

Lecture Notes in Civil Engineering

Erol Tutumluer  
Soheil Nazarian  
Imad Al-Qadi  
Issam I. A. Qamhia *Editors*

# Advances in Transportation Geotechnics IV

Proceedings of the 4th International  
Conference on Transportation  
Geotechnics Volume 3

 Springer

# Lecture Notes in Civil Engineering

Volume 166

## Series Editors

Marco di Prisco, Politecnico di Milano, Milano, Italy

Sheng-Hong Chen, School of Water Resources and Hydropower Engineering,  
Wuhan University, Wuhan, China

Ioannis Vayas, Institute of Steel Structures, National Technical University of  
Athens, Athens, Greece

Sanjay Kumar Shukla, School of Engineering, Edith Cowan University, Joondalup,  
WA, Australia

Anuj Sharma, Iowa State University, Ames, IA, USA

Nagesh Kumar, Department of Civil Engineering, Indian Institute of Science  
Bangalore, Bengaluru, Karnataka, India

Chien Ming Wang, School of Civil Engineering, The University of Queensland,  
Brisbane, QLD, Australia



**Lecture Notes in Civil Engineering (LNCE)** publishes the latest developments in Civil Engineering—quickly, informally and in top quality. Though original research reported in proceedings and post-proceedings represents the core of LNCE, edited volumes of exceptionally high quality and interest may also be considered for publication. Volumes published in LNCE embrace all aspects and subfields of, as well as new challenges in, Civil Engineering. Topics in the series include:

- Construction and Structural Mechanics
- Building Materials
- Concrete, Steel and Timber Structures
- Geotechnical Engineering
- Earthquake Engineering
- Coastal Engineering
- Ocean and Offshore Engineering; Ships and Floating Structures
- Hydraulics, Hydrology and Water Resources Engineering
- Environmental Engineering and Sustainability
- Structural Health and Monitoring
- Surveying and Geographical Information Systems
- Indoor Environments
- Transportation and Traffic
- Risk Analysis
- Safety and Security

To submit a proposal or request further information, please contact the appropriate Springer Editor:

- Pierpaolo Riva at [pierpaolo.riva@springer.com](mailto:pierpaolo.riva@springer.com) (Europe and Americas);
- Swati Meherishi at [swati.meherishi@springer.com](mailto:swati.meherishi@springer.com) (Asia - except China, and Australia, New Zealand);
- Wayne Hu at [wayne.hu@springer.com](mailto:wayne.hu@springer.com) (China).

**All books in the series now indexed by Scopus and EI Compendex database!**

More information about this series at <http://www.springer.com/series/15087>

Erol Tutumluer · Soheil Nazarian · Imad Al-Qadi ·  
Issam I. A. Qamhia  
Editors

# Advances in Transportation Geotechnics IV

Proceedings of the 4th International  
Conference on Transportation Geotechnics  
Volume 3

 Springer

*Editors*

Erol Tutumluer  
Department of Civil and Environmental  
Engineering  
University of Illinois at Urbana-Champaign  
Urbana, IL, USA

Imad Al-Qadi  
Department of Civil and Environmental  
Engineering  
University of Illinois at Urbana-Champaign  
Urbana, IL, USA

Soheil Nazarian  
Department of Civil Engineering  
The University of Texas at El Paso  
El Paso, TX, USA

Issam I. A. Qamhia  
Department of Civil and Environmental  
Engineering  
University of Illinois at Urbana-Champaign  
Urbana, IL, USA

ISSN 2366-2557

ISSN 2366-2565 (electronic)

Lecture Notes in Civil Engineering

ISBN 978-3-030-77237-6

ISBN 978-3-030-77238-3 (eBook)

<https://doi.org/10.1007/978-3-030-77238-3>

© The Editor(s) (if applicable) and The Author(s), under exclusive license to Springer Nature Switzerland AG 2022

This work is subject to copyright. All rights are solely and exclusively licensed by the Publisher, whether the whole or part of the material is concerned, specifically the rights of translation, reprinting, reuse of illustrations, recitation, broadcasting, reproduction on microfilms or in any other physical way, and transmission or information storage and retrieval, electronic adaptation, computer software, or by similar or dissimilar methodology now known or hereafter developed.

The use of general descriptive names, registered names, trademarks, service marks, etc. in this publication does not imply, even in the absence of a specific statement, that such names are exempt from the relevant protective laws and regulations and therefore free for general use.

The publisher, the authors and the editors are safe to assume that the advice and information in this book are believed to be true and accurate at the date of publication. Neither the publisher nor the authors or the editors give a warranty, expressed or implied, with respect to the material contained herein or for any errors or omissions that may have been made. The publisher remains neutral with regard to jurisdictional claims in published maps and institutional affiliations.

This Springer imprint is published by the registered company Springer Nature Switzerland AG  
The registered company address is: Gewerbestrasse 11, 6330 Cham, Switzerland

# Contents

## Tunnels

<b>Investigation on the Dynamic Response of a High-Speed Railway Tunnel Located Beneath an Airport Runway and Uneven Settlement of the Runway</b> .....	3
Feizhi Xiao, Jizhong Yang, and Yao Shan	
<b>Influence of Shield Slurry Property on Filter Cake Quality in Sand Stratum</b> .....	17
Weitao Ye, Longlong Fu, and Shunhua Zhou	
<b>Dynamic Response and Long-Term Settlement of Four Overlapping Tunnels Subject to Train Load</b> .....	33
Xiangliang Zhou, Quanmei Gong, Zhiyao Tian, and Yao Shan	
<b>Dynamic Stability of Soft Soil Between Closely and Obliquely Overlapped Metro Tunnels Subjected to Moving Train Loads</b> .....	49
Hui Li, Quanmei Gong, Honggui Di, Weitao Ye, and Zhi Liu	
<b>Research on Calculating Quantity of Utility Tunnel with Revit Secondary Development</b> .....	63
Qi Zhang, Qian Su, and Yan Yan	
<b>The Influence of Variation in Groundwater Table on Ground Vibrations from Underground Tunnels</b> .....	75
Chao He, Shunhua Zhou, Honggui Di, and Xiaohui Zhang	
<b>Experimental Studies on Three Types of Vibration Isolators for Buildings Near Subways</b> .....	89
Tao Sheng, Xue-cheng Bian, Wei-xing Shi, Jia-zeng Shan, and Gan-bin Liu	
<b>Dynamic Response of Floating Slab Track with Variation on Failure Position of Steel Spring</b> .....	103
Xiaolin Song, Linfeng Xue, Fangzheng Xu, and Jianping Wei	

<b>The Effect of Boundary Permeability on the Dynamic Response of the Layered Saturated Ground Subjected to an Underground Moving Load</b> .....	113
Yijun Li, Anfeng Hu, Kanghe Xie, and Rong-tang Zhang	
<b>The Effect of Excavation Unloading on the Deformation of Existing Underlying Shield Tunnel</b> .....	125
Min-yun Hu, Jing-tian Yang, Li-dong Pan, Kong-shu Peng, and Yu-ke Lu	
<b>Intelligent Construction in Earthworks: Technology and Management</b>	
<b>Field Testing of Automatic Frequency Control for Intelligent Compaction of Embankments</b> .....	143
Carl Wersäll and Andreas Persson	
<b>An Experimental Study on the Estimation of Field Compaction States and Stress-Strain Properties of Unbound Granular Materials from Laboratory Test Results</b> .....	153
Sou Ihara, Kairi Magara, Mitsutaka Okada, Hiroyuki Nagai, Shohei Noda, Yoshiaki Kikuchi, and Fumio Tatsuoka	
<b>A Stress-Dependent Approach for Estimation of Drum-Soil Contact Area</b> .....	167
Aria Fathi, Cesar Tirado, Sergio Rocha, Mehran Mazari, and Soheil Nazarian	
<b>An Earthworks Quality Assurance Methodology Which Avoids Unreliable Correlations</b> .....	179
Burt G. Look	
<b>Intelligent Construction for Infrastructure—The Framework</b> .....	193
George K. Chang, Guanghui Xu, Antonio Gomes Correia, and Soheil Nazarian	
<b>Geo-statistical Evaluation of the Intelligent Compaction Performance in a Reclaimed Base Project</b> .....	205
Maziar Foroutan, Ahmad Ghazanfari, Hamid Ossareh, and Ehsan Ghazanfari	
<b>CCC Systems for Vibratory and Oscillatory Rollers in Theoretical and Experimental Comparison</b> .....	217
Johannes Pistor, Mario Hager, and Dietmar Adam	
<b>Numerical Assessment of Impacts of Vibrating Roller Characteristics on Acceleration Response of Drum Used for Intelligent Compaction</b> .....	231
Zhengheng Xu, Hadi Khabbaz, Behzad Fatahi, Jeffrey Lee, and Sangharsha Bhandari	

**Evaluating the Influence of Soil Plasticity on the Vibratory Roller—Soil Interaction for Intelligent Compaction** ..... 247  
 Sangharsha Bhandari, Behzad Fatahi, Hadi Khabbaz, Jeffrey Lee, Zhengheng Xu, and Jinjiang Zhong

**De-icing Test of the Externally Heated Geothermal Bridge in Texas** ..... 261  
 Omid Habibzadeh-Bigdarvish, Teng Li, Gang Lei, Aritra Banerjee, Xinbao Yu, and Anand J. Puppala

**Climatic Effects on Geomaterial Behavior Related to Mechanics of Unsaturated Transportation Foundations**

**Effect of Relative Density on the Drained Seismic Compression of Unsaturated Backfills** ..... 277  
 Wenyong Rong and John S. McCartney

**Frost Heave Protection of Concrete Pavement Subgrades** ..... 289  
 Chigusa Ueno, Yukihiko Kohata, and Kimo Maruyama

**Effect of Traffic Load on Permeability of Remolded Kaolin** ..... 305  
 Jian Zhou, Linghui Luo, Hao Hu, Jie Xu, and Yicheng Jiang

**Characterization of an Expansive Soil in Southwest Brazilian Amazon—Behavior of an Expansive Subgrade in a Flexible Pavement** ..... 323  
 Victor Hugo Rodrigues Barbosa, Maria Esther Soares Marques, Antônio Carlos Rodrigues Guimarães, and Carmen Dias Castro

**Moisture Influence on the Shakedown Limit of a Tropical Soil** ..... 337  
 Gleyciane Almeida Serra, Antonio Carlos Rodrigues Guimaraes, Maria Esther Soares Marques, Carmen Dias Castro, and Artur Cortes da Rosa

**Long-Term In-Situ Measurement of Soil Suction in Railway Foundation Materials** ..... 349  
 Rick Vandoorne, Petrus Johannes Gräbe, and Gerhard Heymann

**A Tool for Estimating the Water Content of Unsaturated Railway Track Formation Layers** ..... 363  
 Ivan Campos-Guereta, Andrew Dawson, and Nick Thom

**Hydro-Mechanical Behavior of Unsaturated Unbound Pavement Materials Under Repeated and Static Loading** ..... 377  
 Ehsan Yaghoubi, Mahdi M. Disfani, Arul Arulrajah, Jayantha Kodikara, and Asmaa Al-Taie

**Development of a Linear Equilibrium Suction Model Based on TMI and Climatic Regions for Oklahoma** ..... 391  
 Amir Hossein Javid, Hussein Al-Dakheeli, and Rifat Bulut

<b>Use of Steel Slags in Earthworks—Hydraulic Properties of Steel Slags and Granulometrically Modified Steel Slags Under Saturated and Unsaturated Conditions</b> .....	403
Elissavet Barka and Emanuel Birle	
<b>Long-Term Performance of Ballastless High-Speed Railway Track Under the Conditions of Ground Water Level Variations</b> .....	415
Hongming Liu, Xuecheng Bian, Lili Yan, and Yunmin Chen	
<b>Mechanism of Pore Pressure Increase of Saturated Granular Materials Subjected to Repeated Loads</b> .....	423
Chuang Zhao, Xuecheng Bian, Yunmin Chen, and Lili Yan	
<b>Experimental Study on Soil–Water Retention Properties of Compacted Expansive Clay</b> .....	433
Debojit Sarker and Jay X. Wang	
<b>Rainfall-Induced Deformation on Unsaturated Collapsible Soils</b> .....	447
Hamed Moghaddasi, Ashraf Osman, David Toll, and Nasser Khalili	
<b>Experimental Study on the Effect on Stress Release Holes to Decrease Frost Heaves of Fine Particle Fillers in Northern China</b> .....	457
Tianxiao Tang, Yupeng Shen, Xin Liu, and Ruifang Zuo	
<b>Numerical and Experimental Study of the Unsaturated Hydraulic Behavior of a Railroad Track Profile Considering Fouled Ballast Subjected to Tropical Climate Condition</b> .....	467
Guilherme Castro, José Pires, Rosângela Motta, Robson Costa, Edson Moura, Liedi Bernucci, and Luciano Oliveira	
<b>Laboratory Study on Frost Heave of Ballast</b> .....	483
Feng Guo, Yu Qian, Yi Wang, Dimitris C. Rizos, and Yuefeng Shi	
<b>Study of the Influence of Rainwater on the Railway Track</b> .....	493
Luisa Carla de Alencar Menezes, Antonio Carlos Rodrigues Guimarães, and Carmen Dias Castro	
<b>Slope Stability</b>	
<b>Predicting the Stability of Riverbank Slope Reinforced with Columns Under Various River Water Conditions</b> .....	513
Cong Chi Dang, Liet Chi Dang, and Hadi Khabbaz	
<b>Landslide at Govindghat—Investigation and Stabilization Measures</b> .....	525
Ravi Sundaram, Sanjay Gupta, Minimol Korulla, Rudra Budhbhatti, and Pankaj Mourya	

**Earth Pressure, a Load, or a Resistance: Formulation of the ‘What You Design is What You Get’ Model for Stability Design of Propped Cantilever Walls** ..... 541  
C. K. S. Yuen

**Maintenance Planning Framework for Rock Slope Management** ..... 555  
Roman Denysiuk, Joaquim Tinoco, José Matos, Tiago Miranda, and António Gomes Correia

**Geohazard in Consequence of Ignoring Primary Stress State and Failure to Observe the Construction Process of Stabilizing Constructions Designed** ..... 569  
Juraj Ortuta and Viktor Tóth

**Inverse Analysis of a Failed Highway Embankment Slope in North Texas** ..... 583  
Burak Boluk, Sayantan Chakraborty, Anand J. Puppala, and Navid H. Jafari

**Investigating the Effect of Direction of Grass Roots on Shear Strength of Soil and Stability of Embankment Slope** ..... 595  
Jakob Schallberger and Lalita Oka

**Runoff Water Management on Karstic Terrain and Stability of Slopes and Foundations in Northern Spain** ..... 607  
F. Collazos Arias, J. C. Mas Bahillo, D. Castro-Fresno, J. Rodriguez-Hernandez, E. Blanco-Fernandez, L. Castanon-Jano, D. Garcia-Sanchez, and I. Beltran Hernando

**Application of FEA in a Highway Fill Embankment Slope Stability Failure Study** ..... 623  
Jiliang Li and Thiago Leao

**Assessment of Innovative Slope Repair Techniques** ..... 635  
M. G. Winter, I. M. Nettleton, R. Seddon, D. Leal, J. Marsden, and J. Codd

**Challenges Associated with Construction of Highways on Steep Side Slopes Covered with Colluvium from Hunter Expressway Project Australia** ..... 649  
Sudarshan Aryal and Robert Kingsland

**Asset Management**

**Analysis of BIM Implementation on Railway Infrastructures Through an Application to Rail Track Rehabilitation and Inspection** ..... 665  
José Neves, Zita Sampaio, and Manuel Vilela



<b>Targeted Asset Management on Ageing UK Railway Embankments—Wrabness</b> .....	677
Ian Payne, Simon Holt, Isaac Griffiths, and Stuart Fielder	
<b>Integrated Technology Geological Surveys</b> .....	691
Gennadii Boldyrev	
<b>Present Demands on Earth Structures in Transport Engineering in Europe</b> .....	699
Ivan Vaníček, Yvonne Rogbeck, Joost Bredeveld, Daniel Jirásko, and Martin Vaníček	
<b>Multidomain Approach for Track Maintenance and Renewal</b> .....	715
Amine Dhemaied, Gilles Saussine, Aurélie Schwager Guillemenet, Jean Michel Cornet, Quang Anh Ta, and Mathilde Koscielny	
<b>Case Histories</b>	
<b>Assessment of CPT Data on Liquefaction Mitigation with Rammed Aggregate Piers®</b> .....	727
E. Kurt Bal, L. Oner, I. K. Ozaydin, and T. B. Edil	
<b>Observational Method Applied to the Decision Optimizing of Foundation Method in Kujala Interchange on Silty Clay Subsoil</b> .....	739
Monica Susanne Löfman and Leena Korkiala-Tantt	
<b>Design and Performance of Low Capacity Roads on Peat Foundation Soils in Ireland</b> .....	753
Ciaran Reilly and Fintan Buggy	
<b>A Long-Term Record of Water Content and Pore Water Pressure in a Vegetated Clay Highway Cut Slope</b> .....	767
J. A. Smethurst, A. Sellaiya, A. P. Blake, and W. Powrie	
<b>High-Speed Railway Vibrations—An Approach to Tackle Dynamic Instability</b> .....	781
Saeed Hosseinzadeh, Peter Schouten, and Gerhard Schulz	
<b>Field Behavior of GRS Bridge Approach Under Large Subsoil Settlement: A Case Study</b> .....	795
Chunhai Wang and Huabei Liu	
<b>Geotechnical Investigation of Urban Roads with Composite Pavement Structures Using Destructive and Non-destructive Testing</b> .....	807
Maziar Moaveni, Abbas A. Butt, Satish Gundapuneni, Adam D. Groves, and Sean M. Widener	

**Challenges in Developing Sustainable Infrastructure Case History: Boubyan Clay** ..... 819  
 Waleed Abdullah, Fahad AlOqaili, Ananth Ramasamy, Srour AlOtaibi, and Shaikha AlTheyab

**Initiation of 2014 Oso Landslide Using 3D Slope Stability Analyses: Effect of Infiltration** ..... 833  
 Pourya Kargar and Abdolreza Osouli

**Evaluating the Performance Benefits for Low-Volume Roadways Constructed with Geosynthetic Wicking Fabrics: A Case Study in Northern New England** ..... 843  
 Mohamed Elshaer and Christopher Decarlo

**Assessing the Risk of Critical Velocity Effects at Railway Sites Using Site Investigation and Advanced Laboratory Testing** ..... 857  
 A. Duley, B. N. Madhusudhan, L. Le Pen, D. Thompson, and W. Powrie

**Design and Construction of a Very High Embankment Using Geosynthetic Reinforcement** ..... 871  
 Mariya Dayana, Budhmal Jain, Satya Kumar Sunkavalli, and Reginald Subramaniam

**Repeated Load Saturated Soil Behavior Linked to Two Derailment Case Studies** ..... 889  
 Theodore Sussmann

**Deep Foundations**

**Study on Pile-Soil Interaction Mechanism and Failure Modes of CFG Rigid Pile Composite Foundation in the Fluid-Plastic Soft Soil of High-Speed Railway** ..... 907  
 Tai-Feng Li, Jian-Ping Yao, Zhi-Bo Cheng, Qian-Li Zhang, Yin Gao, Jin-Fei Chai, Jing-Yu Liu, and Xin-Gang Zhang

**Analysis and Reconstruction of Rock Joint Surface Based on DCT Algorithm** ..... 923  
 Lianheng Zhao, Dongliang Huang, Shuaihao Zhang, Xiang Wang, Yingbin Zhang, and Shi Zuo

**Numerical Study of the Long-Term Settlement of Screw–Shaft Pile Reinforced Subgrade Under Cyclic Train Load** ..... 935  
 Fu- Hao Li, Xiao-Lei Zhang, and Shi-Jin Feng

**Influence of Pile Side Grouting Reinforcement on the Compressive Load Bearing Capacity of Existing Piles** ..... 947  
 Xinran Li, Quanmei Gong, Yao Shan, and Xiaofan Nie

**Influence of Metro Vehicle Operation on Adjacent High-Speed Railway Bridge Pier** ..... 963  
Guohui Cheng, Yao Shan, and Xiangliang Zhou

**Application Research and Structural Optimization of Vibration Isolation of Row Piles in High-Speed Railway Based on the Concept of Phononic Crystal** ..... 975  
Xiaobin Chen and Hao Tang

**Attenuation Characteristics of Plane Waves by Metabarriers with Negative Parameters** ..... 987  
Jiahua Zhou, Xingbo Pu, and Zhifei Shi

**Shearing Behaviour of Jointed Rocks Under Monotonic and Cyclic Loading with Varying Gouge Materials** ..... 999  
Nirali B. Hasilkar, Lalit S. Thakur, and Nikunj Amin

**Model Research on the Deformation Behavior of Geogrid Supported by Rigid-Flexible Piles Under Cyclic Loading** ..... 1013  
Kaifu Liu, Yonghao Cai, Yi Hu, Dazhi Wu, and Zhenying Zhang

**Resistance Characteristics of Piles Under Distributed Lateral Loading in the Perpendicular Pile Axis Direction** ..... 1023  
Atsushi Mohri, Kazuki Sakimoto, Takamune Yamaguchi, Yoshiaki Kikuchi, Shohei Noda, Shinji Taenaka, Shunsuke Moriyasu, and Shin Oikawa

**Dynamic Behaviors of Piled Embankment Under High-Speed Train Loads** ..... 1041  
Xiang Duan, Ying Wu, Xuecheng Bian, and Jianqun Jiang

**Settlement and Capacity of Piles Under Large Number of Cyclic Loads** ..... 1049  
Renpeng Chen, Chunyin Peng, Jianfu Wang, and Hanlin Wang

# About the Editors

**Erol Tutumluer** is Abel Bliss Professor in the Department of Civil and Environmental Engineering and the Director of International Programs at the University of Illinois at Urbana-Champaign, USA, where he is also the Paul F. Kent Endowed Faculty Scholar. He has research interests and expertise in characterization of pavement and railroad track geomaterials, i.e., subgrade soils and base/ballast unbound aggregate, soil/aggregate stabilization, geosynthetics, applications of artificial intelligence and deep learning techniques to transportation infrastructure, structural health monitoring of transportation facilities using sensors, modeling granular foundation systems using innovative techniques, sustainable use of foundation geomaterials and construction practices for transportation infrastructure, discrete element analysis of ballast, dynamic response measurement and analyses of track systems, and mechanistic analysis and design. Dr. Tutumluer has served as an investigator on over 100 research projects and graduated 21 Ph.D. and 44 MS students, and authored/co-authored over 350 peer reviewed publications from his research projects. Dr. Tutumluer is the current Chair of the ISSMGE Technical Committee 202 on Transportation Geotechnics.

**Soheil Nazarian** is a Professor in the Department of Civil Engineering at the University of Texas at El Paso, USA. He has over 35 years of industry and academic experience in the area of transportation infrastructure, with an emphasis on structures materials, such as that of highways and bridges. His academic experience includes research and teaching positions at the Universities of Texas at Austin and El Paso, as well as the Director at the Center for Transportation Infrastructure Systems at UTEP. He holds a patent for the Moveable Seismic Pavement Analyzer, which is a nondestructive testing device used in evaluation of transportation infrastructure. Prof. Nazarian has been a contributor in over 100 research projects focused on nondestructive materials testing and materials applications, as well as the author of more than 300 industry related articles and publications.

**Imad Al-Qadi** is a Professor in the Department of Civil and Environmental Engineering and the Director of the Advanced Transportation Research and Engineering Laboratory (ATREL), the Illinois Center for Transportation (ICT), and the Smart

Transportation Infrastructure Initiative (STII) at the University of Illinois at Urbana-Champaign, USA. He is also the President of the Transportation Engineering Solutions and Technologies, Inc. Al-Qadi's scholarly record features 700+ authored/co-authored publications, more than 400 of which are fully refereed papers (+280 in periodic journals). His research resulted in the development of new tests, testing specifications, advanced modeling and simulation of pavement loading, pavement layer interface and crack development, and analysis of radar electromagnetic wave interactions with civil engineering materials, roads, and bridges.

**Issam I. A. Qamhia** is a Postdoctoral research associate at the University of Illinois at Urbana-Champaign (UIUC). Dr. Qamhia holds a Ph.D. degree in civil engineering with transportation geotechnics specialization from UIUC, and M.S. and B.S. degrees in civil engineering from the University of Wisconsin Milwaukee and Birzeit University, respectively. He has over nine years of experience in aggregate characterization. His areas of expertise include repeated load testing, morphological shape characterization, tomography scanning, freeze-thaw testing, aggregate packing studies, as well as field characterization of bound and unbound aggregates through nondestructive and accelerated full-scale pavement testing. Dr. Qamhia has authored/co-authored more than 45 peer reviewed publications in prestigious international journals and conferences of repute, and is a frequent reviewer of journals and international conferences.

# Tunnels

# Investigation on the Dynamic Response of a High-Speed Railway Tunnel Located Beneath an Airport Runway and Uneven Settlement of the Runway



Feizhi Xiao, Jizhong Yang, and Yao Shan

**Abstract** The rapid development of the high-speed railways and air transportation networks is leading to an increasing demand of the combination of these two modes of transport. Some modern integrated transport hubs have been operated, and at least 32 airports in China are planning to combine air transportation with high-speed railway transportation. To realize the “seamless transfer” between the airport and the high-speed railway station, some high-speed railways were constructed beneath airport runways. It is necessary to study the dynamic interaction between these two kinds of infrastructures. Based on a project with a high-speed railway tunnel beneath an airport pavement in south China, an aircraft–runway interaction model and a vehicle–tunnel–foundation coupling model are proposed to investigate the dynamic response of the complete system. In this paper, the cumulative plastic deformation of the airport runway caused by the dynamic load of high-speed trains is comprehensively predicated. The influence of the aircraft dynamic load on the deformation of the tunnel and the operation safety of high-speed trains is investigated. The results show that the settlement of airport runway rises to 9.80 mm after ten years of operation of the high-speed railway. The amplitudes of the vertical and horizontal displacement of the tunnel affected by the aircraft dynamic load are 0.192 mm and 0.099 mm, respectively. The rate of wheel load reduction of the high-speed train is not evidently excited by the aircraft dynamic load.

---

F. Xiao (✉) · J. Yang  
China Railway Eryuan Engineering Group Co. Ltd, Chengdu, China  
e-mail: [xiaofz@ey.crec.cn](mailto:xiaofz@ey.crec.cn)

J. Yang  
e-mail: [yangjiz@ey.crec.cn](mailto:yangjiz@ey.crec.cn)

Y. Shan  
Shanghai Key Laboratory of Rail Infrastructure Durability and System Safety, Shanghai, China  
Key Laboratory of Road and Traffic Engineering of the Ministry of Education, Tongji University, Shanghai, China

Y. Shan  
e-mail: [shanyao@tongji.edu.cn](mailto:shanyao@tongji.edu.cn)

**Keywords** High-speed railway tunnel · Aircraft–train interaction · Dynamic response · Operation safety

## 1 Introduction

With the development of China high-speed railway and expansion of urban areas in recent years, the development of comprehensive transport hubs has become an increasing concern in large cities. Comprehensive transport hub integrates multiple modes of transportation, such as railway, aviation and urban transportation. Some high-speed railway tunnels inevitably passed under the existing airports. Both aircrafts and high-speed trains have high requirements for infrastructure deformation. Thus, it is necessary to investigate the construction, and operation requirements are met in the intersection between the airport runway and the high-speed railway.

In recent years, several constructions of tunnels beneath airport runways were carried out. Most of them were highway tunnels and subway tunnels with an operation speed of less than 100 km/h. There is still no precedent of a high-speed railway with a speed of 350 km/h passing under the airport. Previous studies concerning the tunnels constructed beneath the airport mainly concentrated on the following two aspects.

Based on the strict criteria of foundation deformation of the airport, the influence of the tunneling on the deformation of the airport infrastructure has been widely investigated. Gao et al. [1] monitored the variation of the plane curvature of the apron and the differential settlement of the pavement plates by an in-situ test. Xiao and Lai [2] analyzed the airport runway settlement and surrounding soil disturbance caused by shield tunneling. The reasonable buried depth of the shield tunnel was proposed. With the similar methodology, the settlement characteristics of the airport pavement due to the tunnel construction have been investigated [3–5]. Wei [6] utilized a finite element analysis (FEA) model to analyze the effect of train load on the vibration characteristics of the tunnel and of the airport runway. The results indicated that the main stress of the tunnel increased, and the vertical displacement decreased with the increase of buried depth.

Otherwise, some researchers indicated that the impact load of the aircraft played an important role on affecting the service performance of the tunnel structure. Based on a modern integrated transport hub in east China, Zhang et al. [7] analyzed the stress of the tunnel under the aircraft load. Gao et al. [8] used an FEA model to calculate the dynamic response of the tunnel structure under the moving aircraft load. The displacement and tunnel lining stress were employed as criteria.

In view of the above, two main issues were mainly concerned in existing research works: (1) the deformation of the airport pavement due to the tunnel construction and the long-term dynamic train load; (2) the influence of the impact load of the aircraft on the construction safety and service performance of the buried tunnel. However, the operation speed of the rail transit tunnel was limited to 100 km/h in previous cases. To investigate the dynamic interaction between the high-speed railway tunnel (350 km/h) and the airport runway, an aircraft–runway interaction



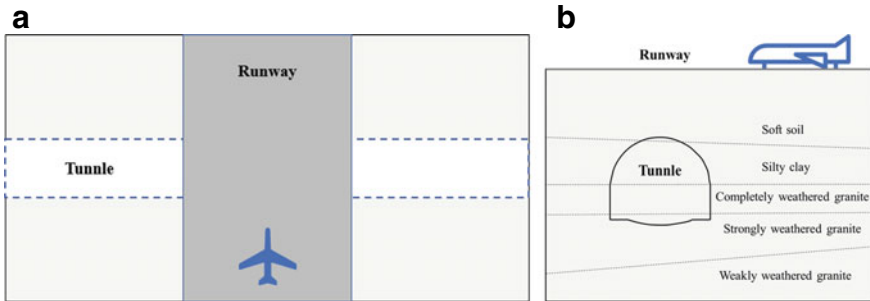
model and a vehicle-tunnel-foundation coupling model are proposed in this paper. The long-term settlement of the runway due to the dynamic train load is predicated as well as the effect of aircraft load on the operation safety of the high-speed train.

## 2 Background

A high-speed railway tunnel is planned to be constructed beneath an airport runway in south China. The railway is a double line passenger dedicated line with a design operation speed of 350 km/h. The tunnel is 15.5 m in width and 12.7 m in height. There is an underground transfer hall in front of the terminal to realize convenient transfer between the railway station and the airport. The layout of these two infrastructures and the distribution of the strata are illustrated in Fig. 1.

The width of the runway is 60 m. The buried depth of the tunnel is 10 m, and the tunnel bottom is located in strongly weathered granite.

This is the first case around the world that the high-speed railway tunnel with an operation speed of 350 km/h constructed beneath the airport runway with shallow buried depth. Compared with the existing underpass cases, the irregularity control in this case is stricter. The train loads in higher frequencies may lead to greater ground settlement and affect the operation safety of the aircraft. Thus, it is necessary to investigate the safety of the intersection. In addition to the two aspects concerned in the existing research works, the stricter criteria of the track irregularity is another significant issue needed to be paid attention to.



**Fig. 1** Layout of runway and tunnel and the distribution of the strata. **a** Sketch of railway and airport. **b** Cross section of high-speed railway tunnel

### 3 Long-Term Settlement of the Runway Due to the Dynamic Train Load

To investigate the influence of the high-speed train load on the deformation of airport runway, a vehicle-tunnel-foundation coupling model is proposed. The high-speed train load is applied to obtain the deviatoric stress in the soil. Combined with the cumulative plastic strain model of the soil, the uneven settlement of the ground is calculated.

#### 3.1 Model

A FEA model of the vehicle-tunnel-foundation system is realized in software MIDAS GTS (refer to Fig. 2). Lv et al. [9] indicated that the length of the model in the horizontal direction should be longer than 8 times the diameter of the tunnel to prevent the wave reflecting. To guarantee the calculation accuracy, the length, the width and the height of the model are chosen as 200 m, 120 m and 52 m, respectively (refer to Fig. 2). According to results in the literature [10], the size of the finite elements should be smaller than the 1/6 of minimum wavelength of the shear wave in different soil strata. Considering the calculation efficiency, the mesh size of soil in the vicinity of the tunnel is chosen as 1.4 m.

The tunnel, soil, airport runway and track slab are simulated by three-dimensional solid elements. The vehicle system is established based on multi-body dynamics. The coupling between the vehicle system and the track is realized by wheel-rail contact forces. The linear elastic model is used for tunnel, airport runway and track slab. The Mohr-Coulomb model is used for soil.

In the dynamic analysis of the model, the reflection of the wave is generated at the boundary of the model, thus affecting the correctness of calculation results. To eliminate the influence of boundary, the three-dimensional viscoelastic artificial boundary around the periphery of the model is utilized to simulate the soil in semi-infinite space. It is realized by adding a parallel spring damping system to the boundary nodes and setting the tangent and normal spring stiffness and damping coefficient. According

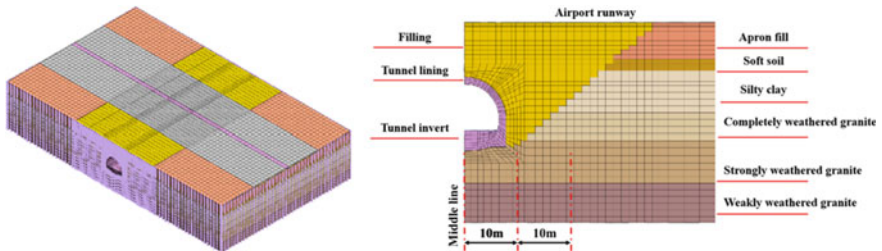


Fig. 2 Vehicle-tunnel-foundation FEA model

to the recommended coefficients [11], the modified coefficients of viscoelastic artificial boundary in tangential and normal directions are chosen as 0.67 and 1.33, respectively.

### 3.2 Analysis of Calculation Results

**Model Parameter.** Parameters of the soil strata and of the slab track (CRTS I double block) are listed in Tables 1 and 2, respectively.

**Wheel/rail force.** CRH380 series electric multiple units (EMUs) are temporarily recommended for the train of this line with a maximum operation speed of 350 km/h. The vehicle model is illustrated in Fig. 3, and the vehicle parameters are shown in Table 3.

The German low interference spectrum of the track irregularity is used as the excitation of the system. The calculated wheel–rail contact force as a function of the time is shown in Fig. 4.

**Results.** To simulate the process of train passing through tunnel, the calculated wheel–rail contact force is applied on the FEA model of runway-soil-tunnel system. The traffic of the high-speed railway line consists of approximately 50 trains per day, including 34 low-speed (80 km/h) trains and 16 high-speed (350 km/h) trains. The deviator stress field of the foundation subjected to the passing trains with different operation speeds is calculated by utilizing the vehicle-tunnel-foundation coupling

**Table 1** Parameters of soil stratification

Classification	Parameter			Thickness (m)
	$E$ (MPa)	$G$ (MPa)	$\mu$	
Runway cement concrete	35,000	15,217.4	0.15	0.4
Cement-stabilized macadam base	400	166.7	0.2	0.38
Apron filling	100	40	0.25	6.8
Filling	120	49.2	0.22	10
Soft soil	30	11.1	0.35	2.14
Silty clay	60	23	0.3	7.9
Completely weathered granite [12]	50	19.2	0.3	5.17
Strongly weathered granite [12]	150	60	0.25	7.04
Weakly weathered granite [12]	400	166.7	0.2	7.4

**Table 2** Parameters of slab track

	Specifications	$E$ (MPa)	$\mu$	Density (kg/m <sup>3</sup> )
Rail	60 kg/m	206,000	0.3	7800
Slab	–	36,500	0.17	2500

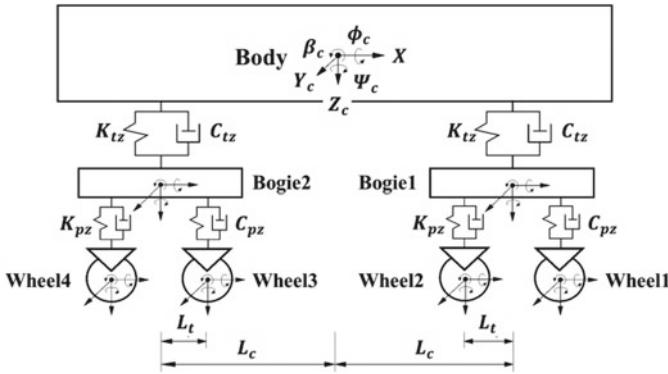
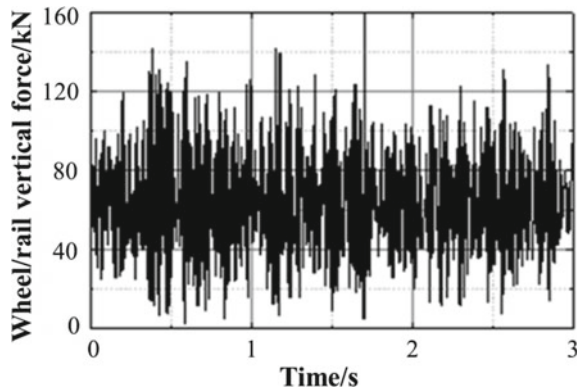


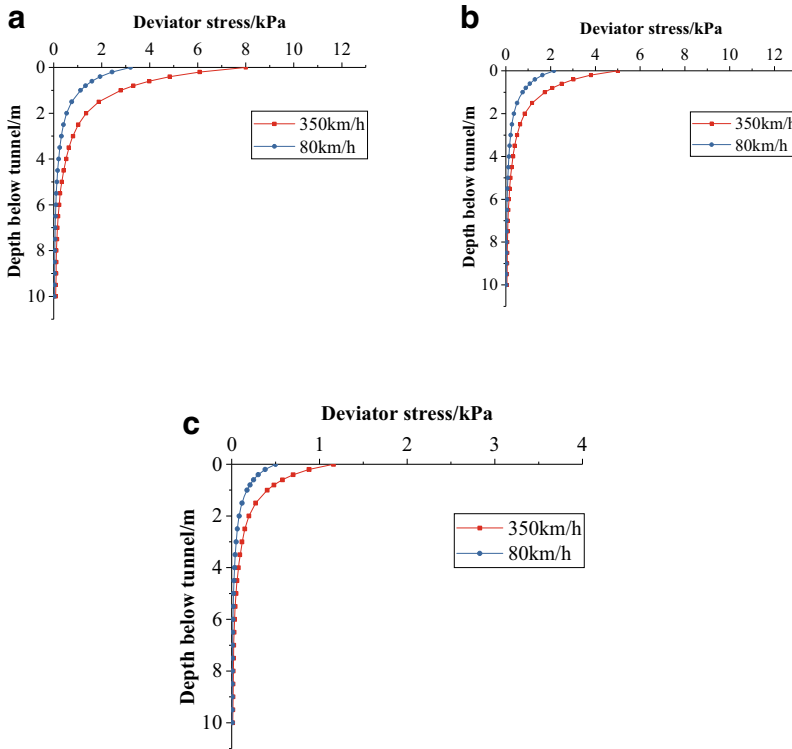
Fig. 3 Vehicle rail coupling model

Table 3 Vehicle parameters

Parameter	Value	Parameter	Value
Mass of the vehicle body	33,766 kg	Stiffness of secondary suspension	2291 kN/m
Mass of the bogie	2400 kg	Damping of primary suspension	196 kN s/m
Mass of the wheelset	1850 kg	Damping of secondary suspension	1174 kN s/m
Pitch inertia of the vehicle body	186700 kg m <sup>2</sup>	Bogie semi-pivot spacing	8.75 m
Pitch inertia of the bogie	1753 kg m <sup>2</sup>	Bogie semi-wheelbase	1.25 m
Stiffness of primary suspension	2352 kN/m		

Fig. 4 Wheel–rail contact force





**Fig. 5** Deviator stress at different position. **a** Deviator stress at the middle line. **b** Deviator stress at 10 m from the middle line. **c** Deviator stress at 20 m from the middle line

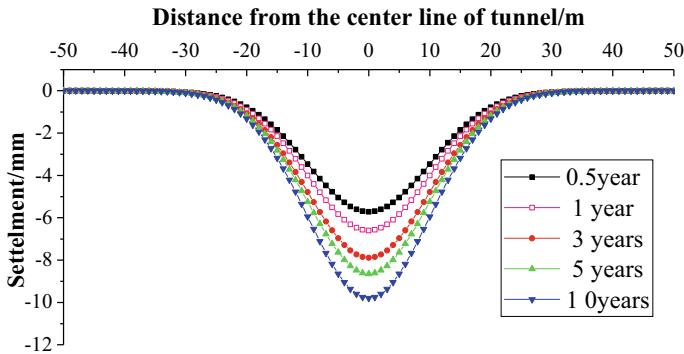
model. The deviator stresses of the soil as functions of the depth beneath the tunnel are shown in Fig. 5. The corresponding position of each figure is shown in Fig. 2.

The deviator stress can be used to calculate soil cumulative plastic strain with regard to a certain number of cyclic train loads. Then, the differential settlement of airport runway can be obtained by integrating soil strain along the depth [13]. The soil cumulative plastic strain model improved by Li and Selig [14] is employed,

$$\varepsilon_p = a \left( \frac{\sigma_d}{\sigma_s} \right)^m N^b, \quad (1)$$

where  $\varepsilon_p$  is the cumulative plastic strain (%);  $a$ ,  $b$  and  $m$  are the parameters for soil type, soil properties and stress state, respectively;  $\sigma_d$  is the deviator stress;  $\sigma_s$  is the soil static strength;  $N$  is the number of repeated load applications. Parameters  $a$ ,  $b$  and  $m$  are chosen based on the laboratory tests [14].

The foundation differential settlements along the runway in cases with different operation periods are shown in Fig. 6. The magnitudes of the differential settlements along the runway with operation periods of 0.5 year, 1 year, 3 years, 5 years and



**Fig. 6** Ground settlement evolution after different operation periods

10 years are 5.71 mm, 6.60 mm, 7.89 mm, 8.65 mm and 9.80 mm, respectively. Both the criterion of the total foundation settlement and the criterion of the differential settlement listed in the “Code for Geotechnical Engineering Design of Airport” are met.

## 4 Influence of Aircraft Load on Service Performance of the Tunnel and the Operation Safety of the High-Speed Trains

The take-off and landing loads of aircraft may cause large deformation and additional stresses of tunnel linings, which directly affect the structure durability and the operation safety of the passing trains, e.g., the rate of wheel load reduction.

### 4.1 Deformation and Stresses of the Tunnel Linings Under Aircraft Loads

Based on the model described in Chap. 3, the impact load of the aircraft is applied to predict the structural deformation. The buried depth of the tunnel is 10 m, and the compactness of the backfill above the tunnel is chosen as 96%. The FEA model is shown in Fig. 7.

Figure 8a shows the lining deformation of the tunnel in the most unfavorable position under the aircraft load. The overall deformation diagram of the tunnel is shown in Fig. 8b. The results reveal that the deformation of the tunnel bottom is relatively small, while the maximum deformation of structure is observed on the tunnel top.

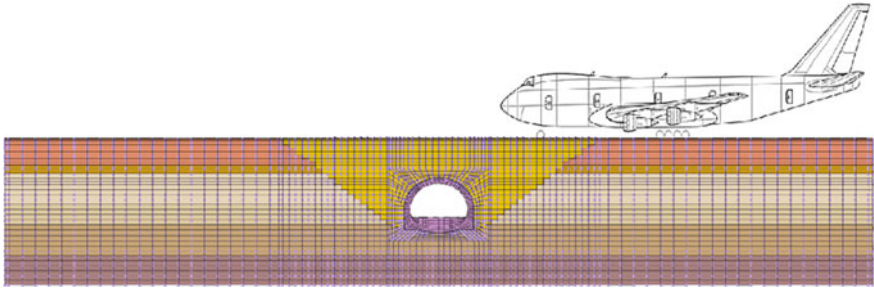


Fig. 7 Tunnel deformation model

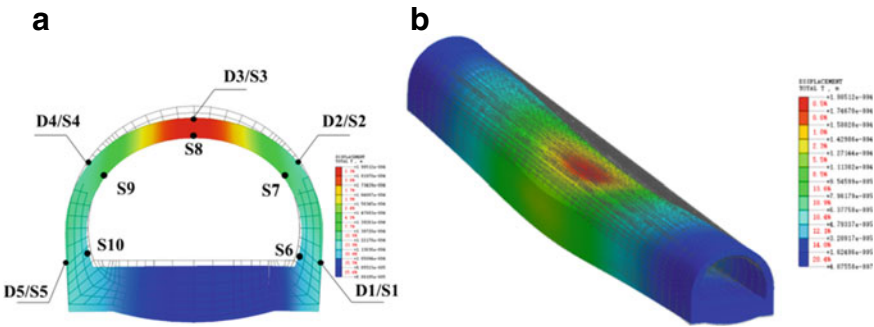


Fig. 8 Deformation of the tunnel. a Deformation in the cross section. b Overall deformation of tunnel

The amplitudes of the deformations and stresses of all measuring points are listed in Tables 4 and 5. The maximum vertical deformation of the tunnel is 0.192 mm, and the maximum horizontal deformation is 0.099 mm. Under the impact load of the aircraft, the deformation of the tunnel structure is very small. The maximum principle

Table 4 Maximum deformation of measuring point

Point	D1	D2	D3	D4	D5
Maximum vertical deformation/mm	0.154	0.156	0.192	0.178	0.179
Maximum horizontal deformation/mm	0.066	0.081	0.076	0.099	0.071

Table 5 Maximum stresses of measuring point

Point	S1	S2	S3	S4	S5	S6	S7	S8	S9	S10
$\sigma_1$ /kPa	39.8	52.9	25.6	45.5	45.4	51.4	44.2	73.9	23.0	79.0
$\sigma_3$ /kPa	-58.4	-46.0	-114.1	-33.7	-95.8	-83.5	-129.0	-41.0	-113.4	-93.8

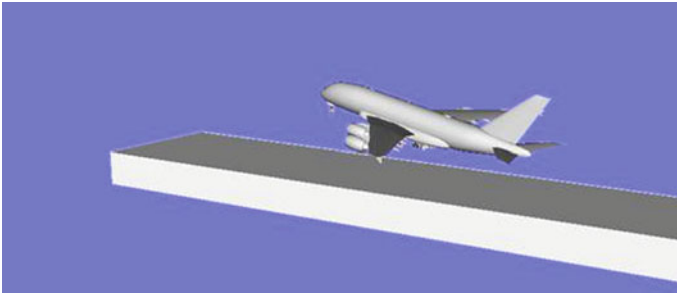
stress ( $\sigma_1$ ) is 79.0 kPa, and the minimum principal stress ( $\sigma_3$ ) is  $-129.0$  kPa. The effect of the aircraft load on the service performance of the tunnel is not obvious.

## 4.2 Dynamic Response of the Track Due to the Aircraft Load

A multi-body dynamic model is employed to investigate the tire–pavement interactions during the aircraft taxiing. The maximum take-off mass of the Boeing 747-400 aircraft is approximately 398 t, and the aircraft taxiing speed is chosen as 260 km/h. The dynamic simulation model of B747-400 is illustrated in Fig. 9.

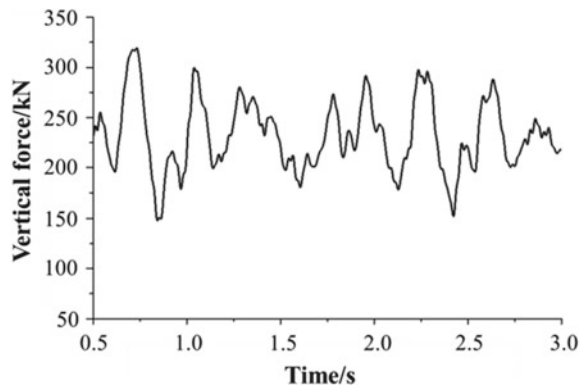
With the excitation of the Class-A highway spectrum, the dynamic tire–pavement contact forces are obtained. The vertical force of a single tire of the main landing gear during the taxiing process before the take-off is shown in Fig. 10:

The impact force of the aircraft directly affects the dynamic irregularity of the high-speed track. The most unfavorable condition was selected to investigate the dynamic response of the track. When the Boeing 747 is passing over the tunnel, the high-speed train is passing through the tunnel with a speed of 350 km/h. The wheel

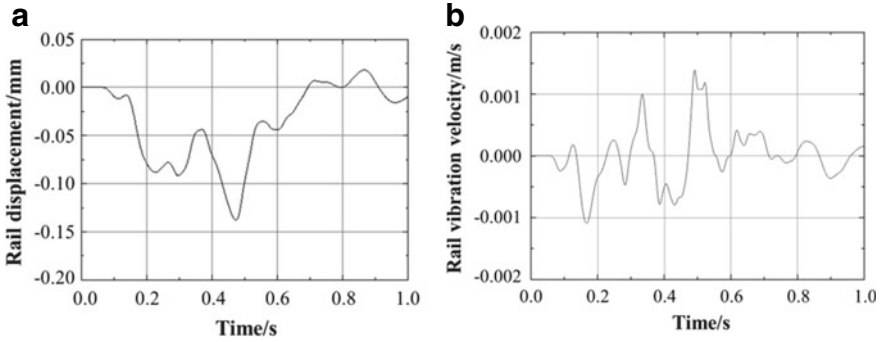


**Fig. 9** Dynamic model of aircraft

**Fig. 10** Vertical force of a single tire







**Fig. 11** Rail vibration displacement and velocity. **a** Rail vibration displacement. **b** Rail vibration velocity

load reduction rate is calculated to evaluate the operation safety of the high-speed train.

Figure 11a shows the rail vertical displacement as a function of the time. When the aircraft is approaching the top of the tunnel, the vertical deflection of the rail is amplified. The maximum value of rail displacement rises to 0.14 mm. The rail deflection decreases when the aircraft leaves the tunnel.

Figure 11b shows the vertical velocity of the rail as a function of the time. The amplitude of the velocity is approximately 0.0013 m/s.

According to the vehicle–track coupling model, the displacement and the velocity of rail are utilized to calculate the wheel–rail contact force. Then, the rate of wheel load reduction  $r$  is obtained by

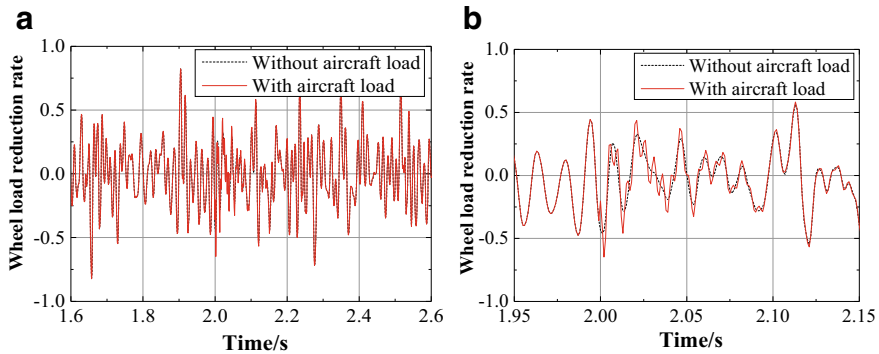
$$r = 1 - \frac{P_d}{P_s}, \quad (2)$$

where  $P_d$  is the dynamic wheel–rail contact;  $P_s$  is the static wheel load.

The time history curve of the wheel load reduction rate during the first vehicle of CRH380 EMUs passes through the tunnel at a speed of 350 km/h is illustrated in Fig. 12. Although the vertical deflection and velocity of the rail are changed when the aircraft passes over the tunnel, the variation of the vertical force is not obvious. Figure 12b shows that the aircraft load has small effect on the wheel load reduction rate. Therefore, the take-off and landing of aircraft have no obvious influence on the operation safety of the high-speed railway.

## 5 Conclusion

In this paper, a series of FEA simulations are carried out to investigate the interactions between a buried high-speed railway tunnel and an airport pavement based



**Fig. 12** Wheel load reduction rate. **a** Full period. **b** Zooming on the results

on an intersection project in south China. The long-term settlement of the runway foundation due to the dynamic train load is predicted as well as the effect of aircraft load on the operation safety of the high-speed train. Three conclusions can be drawn:

1. Under the long-term cyclic loads of the high-speed train, the settlement trough along the runway is generated. Both the criterion of the total foundation settlement and the criterion of the differential settlement listed in the “Code for Geotechnical Engineering Design of Airport” are met after 10 years’ operation of the high-speed railway.
2. Under the long-term aircraft loads, the maximum vertical and horizontal deformations of the tunnel are 0.192 mm and 0.099 mm, respectively. The influence of the aircraft load on the service performance of the tunnel is very small.
3. The impact force of the aircraft on the pavement has limited effect on the deflection and the vertical velocity of the track. The wheel load reduction rate of the high-speed train is stable during the take-off and the landing of aircraft.

## References

1. Gao A, Ma X, Jin H et al (2010) Deformation of airport apron caused by shield tunnel underpassing. *Urban Rapid Rail Transit* 23(1):74–77
2. Xiao M, Lai Y (2011) 3D numerical analysis on subsidence control of shield tunnel excavation under airport runways. *Tunnel Constr* S1:32–37
3. Zhou S, Rong J, Chen L et al (2012) Construction control of large diameter slurry shield undercrossing airport. *Chin J Rock Mech Eng* 31(4)
4. Liu Z (2015) Study on movement of airport runway induced by shallow tunneling under the protection of ultra-long pipe-roofing. Beijing Jiaotong University
5. Jiang X (2017) Discussion on the scheme of intercity railway tunnel passing under airport taxiway. *Railw Stand Des* 1:71–75
6. Wei H (2012) Study on influence of train vibration on tunnel structure and airport runway lying above. Chongqing Jiaotong University

7. Zhang R, Yang Z, Chen Z (2008) Discussion of relative issues on interval tunnel of rail transit crossing airport runway. *Underground Eng Tunnels* 11(3):11–14(18):75
8. Gao F, Fu G, Hu W (2012) Influence of moving aircraft loads on airport tunnel. *J Chongqing Jiaotong Univ (Nat Sci)* 02:50–54
9. Lv A, Jiang B, You C (1999) Research on the meshing range of finite element method for back-analysis of displacement. *Chin Civil Eng J* 32(1):26–30
10. Lai J, Wang K, Qiu J et al (2016) Vibration response characteristics of the cross tunnel structure. *Shock Vibr*
11. Gu Y, Liu J, Du Y et al (2007) 3D consistent viscous-spring artificial boundary and viscous-spring boundary element. *Eng Mech* 24(12):31–37
12. Li R, Wu L (2004) Research on characteristic indexes of weathering intensity of rocks. *Chin J Rock Mechan Eng* 23(22):3830–3830
13. Shan Y, Zhou S, Zhou H et al (2017) Iterative method for predicting uneven settlement caused by high-speed train loads in transition-zone subgrade. *Transp Res Rec* 2607(1):7–14
14. Li D, Selig E (1996) Cumulative plastic deformation for fine-grained subgrade soils. *J Geotechn Eng* 122(12):1006–1013

# Influence of Shield Slurry Property on Filter Cake Quality in Sand Stratum



Weitao Ye, Longlong Fu, and Shunhua Zhou

**Abstract** Slurry preparation and pressure maintenance of slurry balance shield should be carefully treated during tunneling in complex sand stratum. On basis of the slurry shield tunnel project in Fuzhou, slurry pressure was determined by two different theoretical methods. Then, an indoor test was conducted to explore the influence of constituents on slurry property. The influence of slurry properties on filter cake forming process under different slurry pressure was also analyzed through slurry penetration test. The test results indicate that the bentonite and silt soil had dominated influence on relative density, while the bentonite and CMC had dominated influence on viscosity. It is found that the water discharge, which is the index to evaluate the effect of filter cake, decreases firstly and then increases as slurry relative density increases. The water discharge also decreases as slurry viscosity increases. Meanwhile, the influence of viscosity on the water discharge was found less than that of relative density. Finally, a segmented slurry control scheme suitable for sand stratum in Fuzhou was presented.

**Keywords** Slurry shield · Slurry property · Slurry penetration test · Filter cake · Water discharge

## 1 Introduction

Slurry shield is widely used in tunnels beneath rivers or in high permeable strata [1, 2]. When the property of shield slurry is suitable for the strata, a filter cake is formed on the excavation face which is significant to maintain the stability of the face during tunneling. Otherwise, the slurry particles will flow away through the pore which may result in potential instability of the excavation face [3–5]. Therefore, the focal point

---

W. Ye · L. Fu (✉) · S. Zhou

Shanghai Key Laboratory of Rail Infrastructure Durability and System Safety, Shanghai, China  
e-mail: [longlongfu@tongji.edu.cn](mailto:longlongfu@tongji.edu.cn)

Key Laboratory of Road and Traffic Engineering of the Ministry of Education, Tongji University, Shanghai, China

in slurry shield tunneling is to prepare a kind of high-quality slurry to hold effective support pressure on the excavation face.

Currently, the slurry used in slurry shield mostly consists of water and bentonite. Sometimes additives are used in order to enhance the property of the slurry. There are different kinds of additives that include polyanionic cellulose (PAC), carboxymethyl cellulose (CMC), polyacrylamide and other polymers for different functional requirements [6, 7]. Fritz [8] found a combined action of all additives including Caebocel C190, bentonite, sand and vermiculite for the successful construction of Zimmerberg Base Tunnel. Cui [9] found a kind of additive called biodegradable pregelatinized starch (PGS) which is harmless to the environment.

With the above constituents, the key point is to determine the suitable components and corresponding proportion of the slurry. It is an effective way to evaluate the performance of filter cake through water discharge [10–13], pore pressure [14] and the form of filter cake [15, 16] by slurry penetration tests. It is believed that the water discharge decreases with the increase of slurry viscosity and relative density which is the mass of a substance divided by the mass of the same volume of water. Correspondingly, the conversion of pore pressure is more effective. In addition, it is revealed that sand stratum is mainly filled by small bentonite and clay particles, and gravel stratum is filled by cluster of slurry particles. However, the influence of slurry properties on the filter cake quality is so far explored by single factor analysis according to the existing studies.

In this paper, the combined effect of slurry relative density and viscosity is synthetically considered. Meanwhile, the role of slurry relative density and viscosity on the form of filter cake is analyzed after the tests. Then, a segmented slurry control scheme is given and applied in site, which proved that the proposed slurry proportion is suitable to the sand stratum in Fuzhou.

## 2 Engineering Background and Slurry Pressure Setting

### 2.1 Engineering Background

The interval between Jinxiang Station and Xiangban Station is shown in Fig. 1 which is 1580 m long. Slurry shield passes through the medium-coarse sand layer in the section near the station and the silt soil layer under the river which has high

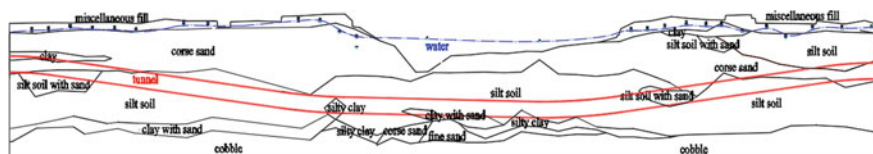


Fig. 1 Strata profile of shield tunneling construction in Fuzhou

requirements for the construction control of the shield and the preparation of the slurry.

## 2.2 Slurry Pressure Setting

Static earth pressure theory and Terzaghi loosening earth pressure theory are used to calculate the earth pressure of the first 600 rings in Jinxiang–Xiangban interval. In the section of deep soil layer, it is useful to calculate earth pressure by Terzaghi loosening earth pressure theory, while static earth pressure theory can be used to calculate earth pressure for thin soil layer across the river.

Horizontal static earth pressure can be calculated by

$$\sigma_v = P_0 + \sum \gamma_i h_i$$

where  $P_0$  is surface load,  $\gamma$  is the unit weight, and  $h$  is the soil depth. Terzaghi loosening earth pressure can be calculated by

$$\sigma_v = \frac{B(\gamma - c/B)}{K \tan \varphi} (1 - e^{-K \tan \varphi \cdot Z/B}) + P_0 e^{-K \tan \varphi \cdot Z/B}$$

where  $K$  is the lateral soil pressure coefficient,  $c$  is the cohesion force of soil,  $\varphi$  is the internal friction angle of soil,  $B$  is the width of Trapdoor, and  $Z$  is depth of tunnel.

Based on the full earth pressure theory, the earth pressure can be calculated according to the stratum parameters of Jinxiang–Xiangban interval in Fuzhou. Considering water pressure and building pressure, the final slurry pressure is shown in Fig. 2.

## 3 Shield Slurry Preparation

### 3.1 Laboratory Test

Laboratory test is designed to explore the influence of different materials and proportion on slurry relative density and viscosity. Shield slurry used in the tests consists of bentonite, silt soil and carboxymethylcellulose which is called CMC for short. The use of silt soil from the tunnel in Fuzhou is for green and economic recycle.

In order to explore slurry properties under different materials and proportion, five groups are designed by controlling variable method which focus on the changes of slurry relative density and viscosity. The results are taken for 1 h and 1 day.

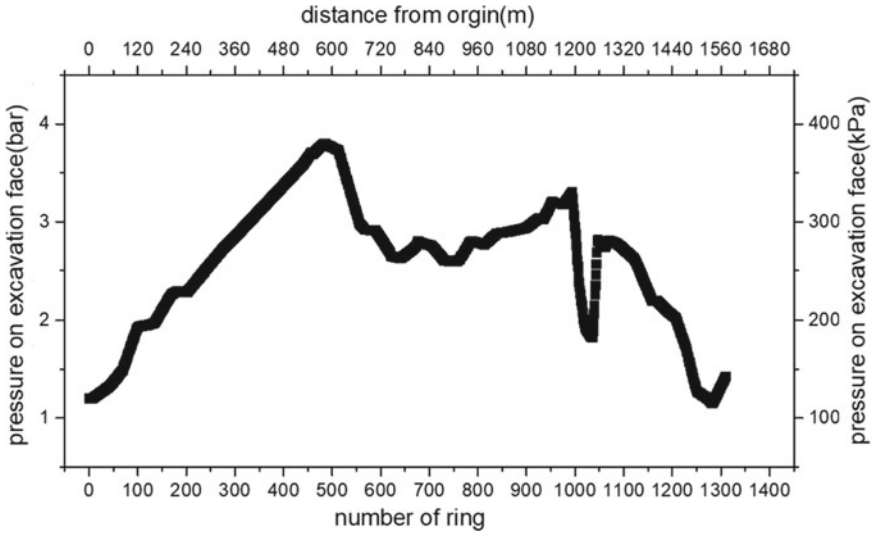


Fig. 2 Slurry pressure of Jinxiang–Xiangban interval

### 3.2 Influence of Materials on Shield Slurry

It is shown in Fig. 3 that slurry relative density increases with the increase of bentonite and silt soil. By tests #1, #2, #4 and #5, the effect of bentonite on slurry relative density is slightly greater than that of silt soil, which is due to the deposition of some coarse particles from silt soil. Meanwhile, slurry standing time has little effect on slurry relative density.

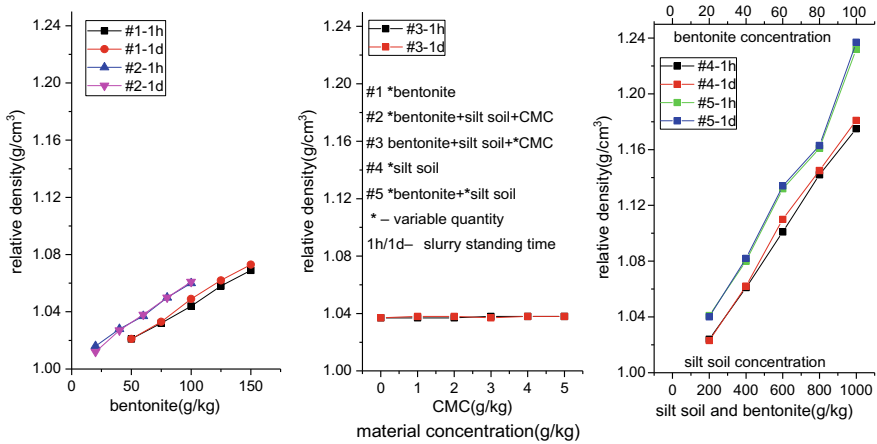


Fig. 3 Slurry relative density under different materials

As shown in Fig. 4, slurry viscosity increases with the increase of bentonite and CMC. It is seen from test#3 that the effect of CMC on slurry viscosity is remarkable. By test#5 and #6, silt soil has little influence on the increase of slurry viscosity. By test#1, test#2 and test#3, CMC and bentonite have synergistic effect on the increase of slurry viscosity. Meanwhile, slurry standing time has great effect on slurry viscosity.

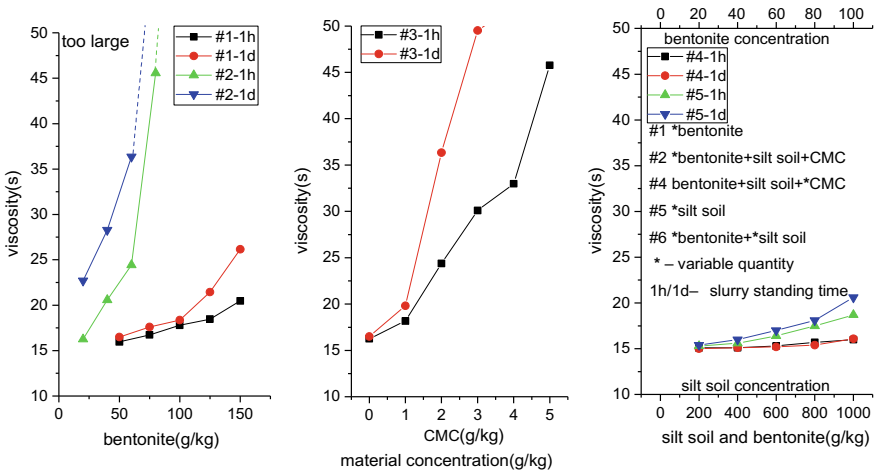
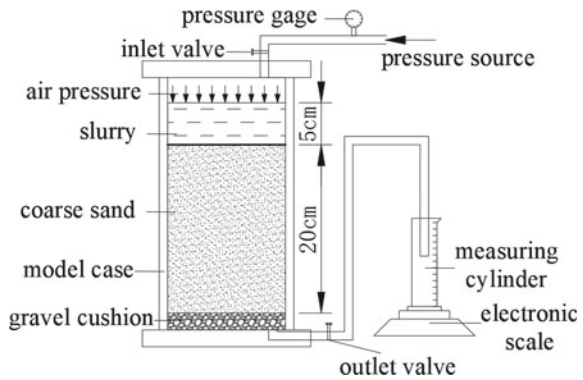


Fig. 4 Slurry viscosity under different materials

Fig. 5 Test apparatus of slurry infiltration





## 4 Slurry Penetration Test Design

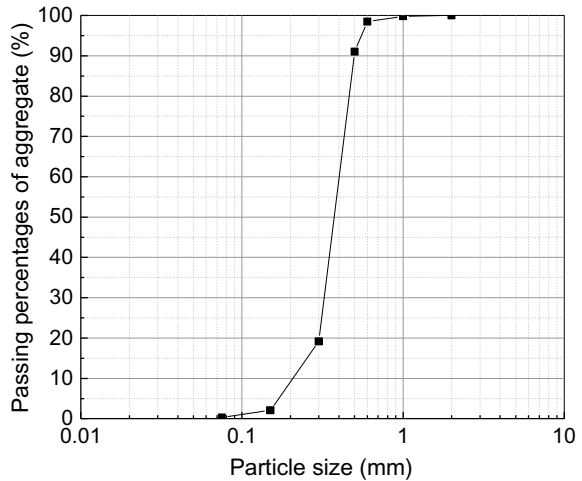
### 4.1 Experimental Apparatus

A self-made device is adopted in slurry penetration tests which is shown in Fig. 5. The main body of the device is an organic glass cylinder whose inner diameter is 14 cm and height is 30 cm. The upper part of the device is an aluminum plate which is connected to the external air compressor by an outlet hole. The bottom of the device is provided with a water outlet hole, and the filtration water is collected by measuring cup in the test and weighted by electronic scale constantly. The materials in the device are divided into three layers from bottom to top which include gravel cushion, coarse sand and slurry.

### 4.2 Experimental Materials

Initial shield slurry is made with water and bentonite. Then, silt soil is added to the slurry to adjust relative density, while CMC is added to the slurry to adjust viscosity. The stratum material is from medium-coarse sand stratum in Fuzhou whose sand grains gradation is shown in Fig. 6.

**Fig. 6** Grading curve of medium-coarse sand



### 4.3 Experimental Procedure

Follows are the methods of the laboratory tests. First, prepare slurry and make it fully hydrated. Second, configure the middle coarse sand in the test. The sand is put into the cylinder by five parts. Third, saturate the middle coarse sand and set still for 12 h. After the completion of saturation, fill the container with the slurry. Forth, apply preset slurry pressure, and each stage lasts 3 min. During the tests, record the filtration water discharge each 10 s.

### 4.4 Experimental Scheme

The effects of slurry pressure, relative density and viscosity are studied by factorial design. There are 16 groups divided by slurry relative density and viscosity which are shown in Table 1. According to the pressure calculated in the second section, the test pressure is divided into four levels from 0.1 to 0.4 MPa. Besides, the relative density deviation is controlled at  $\pm 0.01$ , and the viscosity deviation  $d$  is controlled at  $\pm 1$  s.

**Table 1** Experimental scheme under different experimental factor

Group	Relative density	Viscosity (s)	Bentonite (g)	Silt soil (g)	CMC (g)	Water (g)
1	1.05	18	60	125	0.6	1000
2	1.05	22	60	100	1	1000
3	1.05	26	60	120	2.2	1000
4	1.05	30	60	125	3.2	1000
5	1.12	18	80	550	0.3	1000
6	1.12	22	80	450	0.4	1000
7	1.12	26	80	480	2.6	1000
8	1.12	30	80	460	3	1000
9	1.18	18	80	700	0.1	1000
10	1.18	22	80	850	0.3	1000
11	1.18	26	80	800	0.8	1000
12	1.18	30	80	700	1.3	1000
13	1.25	18	100	1000	0	1000
14	1.25	22	100	1100	0.3	1000
15	1.25	26	100	980	0.8	1000
16	1.25	30	100	1160	1.1	1000

## 5 Results of Laboratory Experiment

### 5.1 Final Water Discharge

The final water discharge of slurry penetration tests is showed in Fig. 7. It is found that the final water discharge is the largest when the slurry relative density is 1.05. When the slurry relative density is 1.12 and 1.18, the results are smaller. But it becomes larger with a slurry relative density that is up to 1.25. It can be concluded that the final water discharge decreased firstly and then increased as slurry relative density increased.

Compared with the results under different viscosity in Fig. 7, when the slurry relative density is 1.05, the final water discharge decreases during the process slurry viscosity increases from 18 to 26 s, but increases when slurry viscosity is 30 s. In other slurry relative density, the final water discharge decreases with the increase of viscosity.

Under the same relative density of shield slurry, the maximum difference of the final water discharge with different slurry viscosity is 3.6 L/m<sup>2</sup> at 0.4 MPa. Under the same viscosity of shield slurry, the maximum difference of the final water discharge with different slurry relative density is 7 L/m<sup>3</sup> at 0.4 MPa, which shows that the influence of slurry viscosity on the results of the tests is less than that of slurry relative density.

It is known that the final water discharge increases with the increase of test pressure from Fig. 7. When the test pressure is larger, the penetrating speed of fine particles in the slurry and the accumulating speed of coarse granules on the surface will be faster.

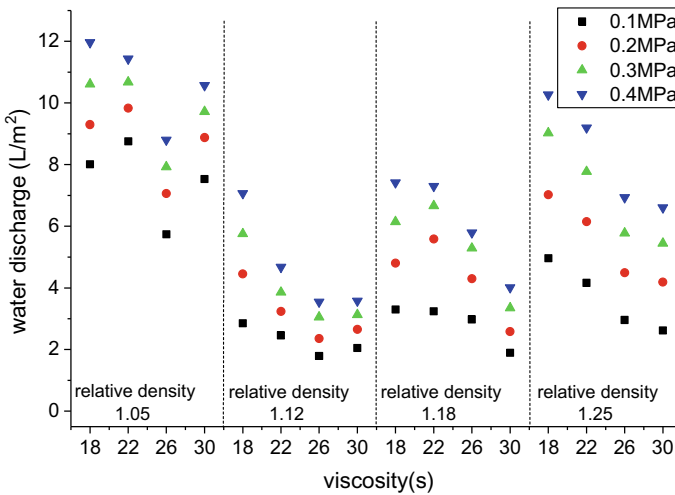


Fig. 7 Final water discharge in the tests

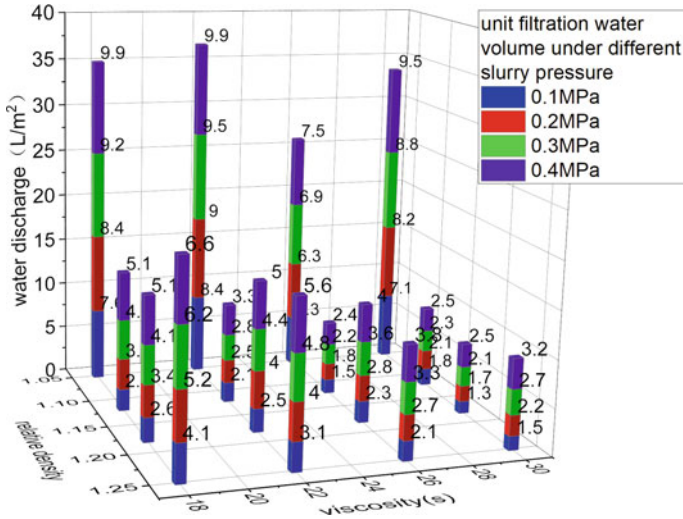


Fig. 8 Water discharge during filter cake forming process

### 5.2 Water Discharge During Filter Cake Forming Process

The final water discharge can be divided into two parts. One is water discharge during filter cake forming process which reflects the form of filter cake and the velocity of its formation. The other is the water discharge per second after filter cake formation which reflects the penetrability of the filter cake.

Figure 8 is the comparison of the water discharge of filter cake forming process under different experimental factors. The water discharge decreases firstly and then increases with the increase of relative density and increases with the increase of viscosity. When the slurry relative density is 1.05, the water discharge is larger, which means the influence of relative density is dominant. When slurry relative density is more than 1.12, relative density and viscosity have the same affection on the test results.

### 5.3 Water Discharge Per Second After Filter Cake Formation

Figure 9 is a comparison map of the water discharge per second after the formation of filter cake. As shown in Fig. 9, the larger the slurry viscosity is, the smaller the water discharge per second is, while the larger the slurry relative density is, the larger the water discharge per second is. Combined with the form of filter cake after the test, it is known that the contents of CMC and bentonite are significant to the permeability of filter cake.

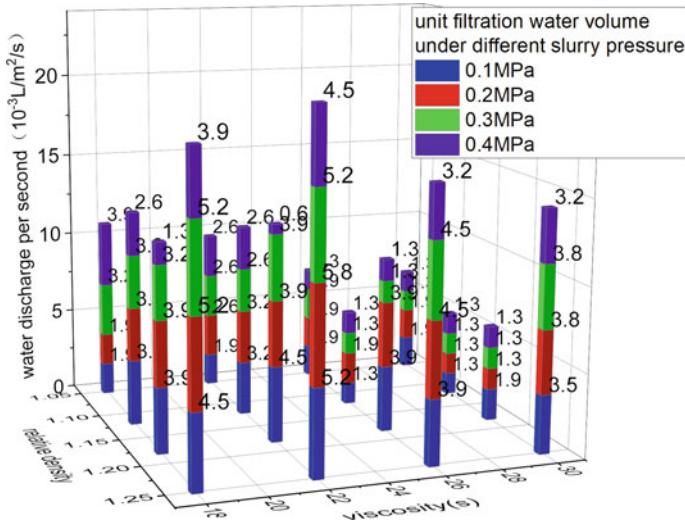


Fig. 9 Water discharge per second after filter cake formation

### 5.4 Filter Cake Formation Time

At present, there are many definitions of filter cake formation time. Wei Daiwei defined the time when pore pressure conversion reaches the maximum as filter cake formation time. Wu Di took the time when pore filling rate is up to 80% as filter cake formation time. In this paper, filter cake formation time is regarded as the time when the water discharge is stable or when the slope of discharge–time curve is less than  $5.1 \times 10^{-3} \text{ L/m}^2/\text{s}$ .

Figure 10 is the comparison of filter cake formation time under different experimental factors. It is found that filter cake formation time decreases with the increase of slurry relative density. The larger slurry relative density is, the more particles in slurry are, so the stratum can be permeated or accumulated faster. Filter cake formation time decreases with the increase of slurry viscosity because the cohesiveness between particles is better when slurry viscosity is larger. Thus, the space network structure can be formed faster in the particles filling process.

### 5.5 The Form of Filter Cake

The form of slurry penetration can be obtained after tests, and the typical form of which under the constant viscosity of 26 s and different relative density are shown in Fig. 11.

Table 2 lists the form of slurry penetration under different slurry relative density. It is known that when slurry relative density is larger, the slurry penetrating distance

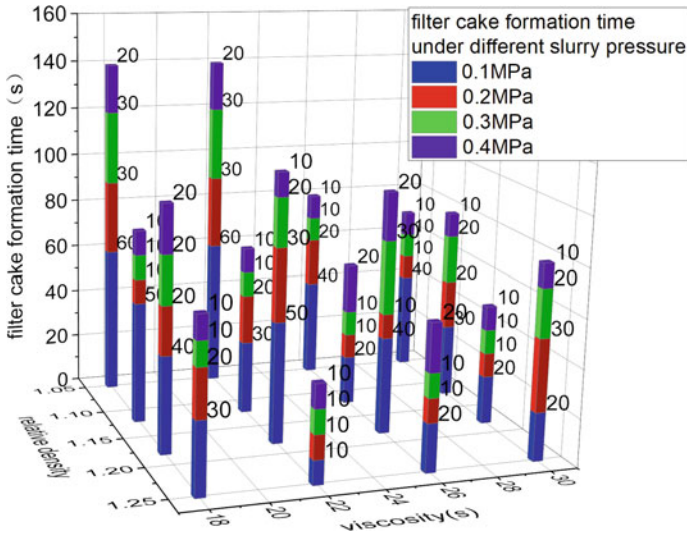


Fig. 10 Filter cake formation time

is shorter, and the filter cake is thicker, which means when slurry relative density increases, the form of filter cake changes from clogging in stratum to filter cake.

## 6 Slurry Control Scheme and Application

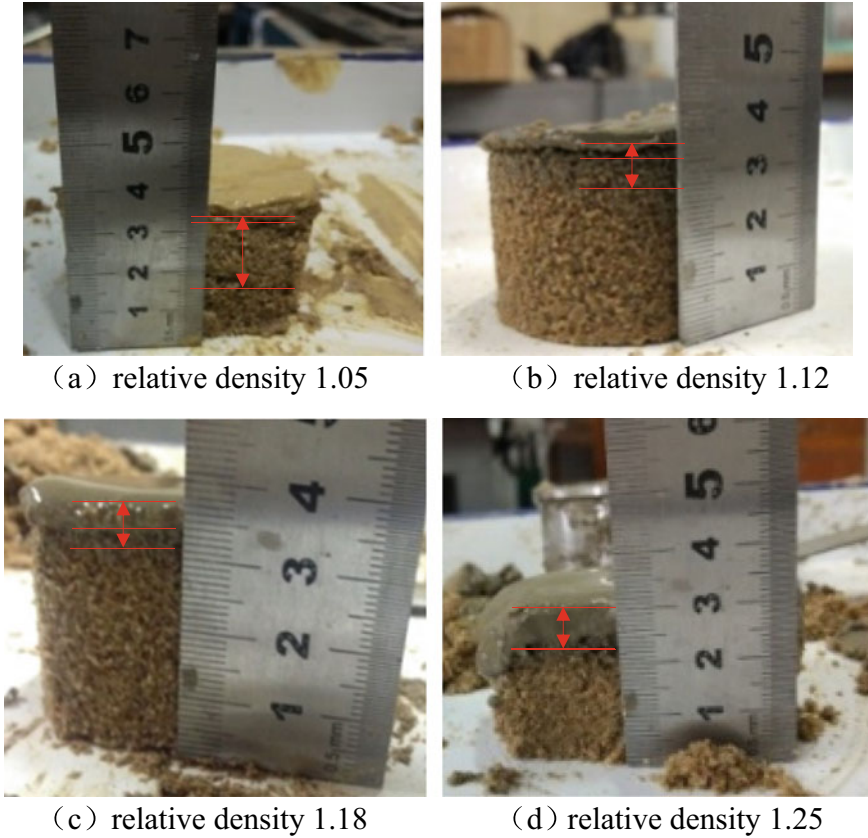
### 6.1 Slurry Control Design

The slurry shield in Fuzhou adopts a cutter head which has six spokes. The time required for two adjacent spokes to reach the same position is filter cake formation time which means filter cake will be destroyed by six times for a circle. Table 3 lists the two failure time intervals of filter cake.

The slurry control plan is given by cutter speed, filter cake formation time and the water discharge of tests, as shown in Table 4. Silt soil layer under the river has a small permeability coefficient. When the slurry pressure is enough, the stability of tunnel face can be controlled, so the properties of the slurry can be reduced properly.

### 6.2 Application in Site

During slurry shield tunneling through the layer under the river in Fuzhou, it is useful to take silt soil from silt ground layer as one of slurry materials. The proportioning



**Fig. 11** Form of slurry penetration under different slurry densities

**Table 2** Form of slurry penetration under different slurry density

Relative density	The form of filter cake	Thickness of filter cake (mm)	Slurry penetrating distance (mm)
1.05	Filter cake and clogging	1	15
1.12	Filter cake and clogging	2	5
1.18	Filter cake and clogging	4	3
1.25	Filter cake	6	0

of slurry is bentonite: silt soil: CMC: water = 80:600:2:1000. The 20th–50th rings in Jinxiang–Xiangban interval are taken as the test section. In this section, slurry relative density is controlled between 1.12 and 1.18, and viscosity is 26–30 s. At the same time, revolution of the shield cutter is controlled at 0.5–1.5 rpm which is shown in Fig. 12. In Fig. 13, it is known that the torque of cutter head is stable, and

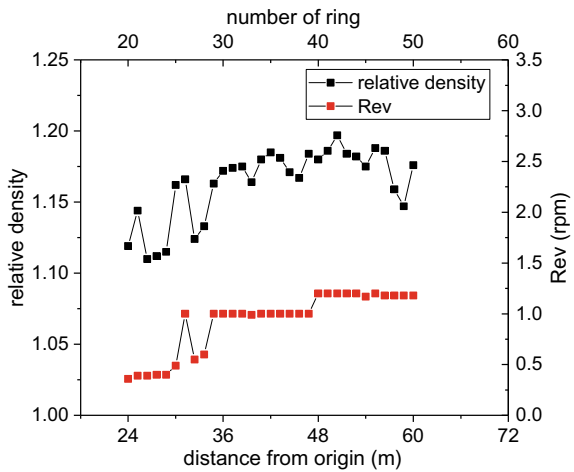
**Table 3** Time interval between two destruction of filter cake

The form shield cutter head	Rotation rate (rpm)	Time of a lap (s)	Two failure time intervals of filter cake (s)
Six spokes distribute 60° uniformly	0.3	200	33.3
	0.5	120	20
	0.8	75	12.5
	1	60	10
	1.5	40	6.7
	2	30	5

**Table 4** Proposed projects of slurry preparation

Stratum	Relative density	Viscosity (s)	Materials
Sand	1.15 ± 0.03	26–30	Bentonite, silt soil and CMC
Silt soil	1.15 ± 0.05	22–30	Bentonite, silt soil and CMC

**Fig. 12** Slurry relative density and revolution of the shield cutter of 20th–50th rings



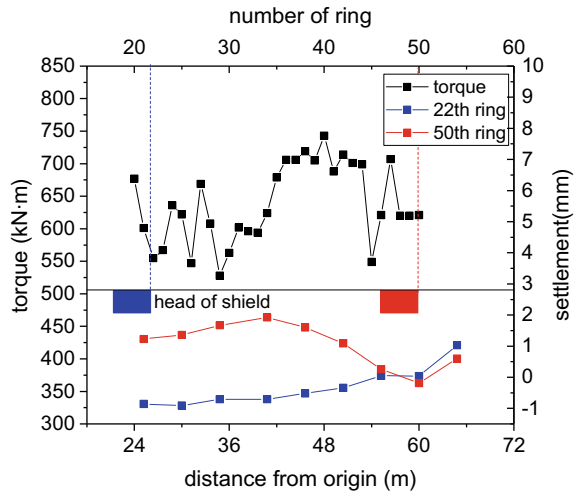
the ground settlement is small which proves the proportioning of slurry from tests result is suitable.

## 7 Conclusions

1. The bentonite and silt soil have dominated influence on the relative density of the slurry, while the bentonite and CMC have dominated influence on viscosity



**Fig. 13** Torque of cutter head and the ground settlement of 20th–50th rings



in slurry preparation. Meanwhile, slurry standing time has great effect on slurry viscosity.

2. The water discharge decreases firstly and then increases with the increase of slurry relative density which however decreases as slurry viscosity increases. Meanwhile, it increases as slurry pressure increases. When the slurry relative density is larger and the slurry viscosity is higher, the formation time of filter cake is shorter and the water discharge is smaller during filter cake forming process.
3. The form of slurry penetration in coarse sand stratum is filter cake and clogging. When slurry relative density is larger, the slurry penetrating distance is shorter and the filter cake is thicker, which means the form of filter cake changes from clogging in stratum to filter cake as slurry relative density increases.
4. On the basis of the results of laboratory tests, the complex strata and the slurry shield machine, a segmented slurry control scheme is presented. The in-situ construction shows that the segmented slurry control scheme performed well.

## References

1. He C, Feng K, Fang Y (2015) Review and prospects on constructing technologies of metro tunnels using shield tunneling method. *J Southwest Jiaotong Univ* 50(1):97–108 (in Chinese)
2. Mengshu W (2014) Tunneling by TBM/shield in China: state-of-art problems and proposals. *Tunnel Constr* 34(3):179–187
3. Henry LB, Filz GM, Davidson RR (1998) Formation and properties of bentonite filter cakes. In: *Proceedings of sessions of ASCE annual convention, Boston*, pp 69–88
4. Anagnostou G, Kovari K (1994) The face stability of slurry shield-driven tunnels. *Tunnell Undergr Space Technol* 9(2):165–174. [https://doi.org/10.1016/0886-7798\(94\)90028-0](https://doi.org/10.1016/0886-7798(94)90028-0)

5. Li Y, Emeriault F, Kastner R et al (2009) Stability analysis of large slurry shield-driven tunnel in soft clay. *Tunnel Undergr Space Technol Incorporating Trenchless Technol Res* 24(4):472–481
6. Fritz P (2007) Additives for slurry shields in highly permeable ground. *Rock Mech Rock Eng* 40(1):81–95
7. Wang Z, Zhang C, Zhang D (2017) Mud preparation and seepage test for slurry shields driving in sandy cobble ground. *J Railw Eng Soc* 34(1):112–117
8. Fritz P, Hermanns SR, Heinz A (2002) Modified bentonite slurry for slurry shields in highly permeable soils. In: 4th international symposium geotechnical aspect of underground construction in soft ground. Toulouse, France
9. Cui W, Liu D, Song H, Pu G (2019) Development and experimental study on environmental slurry for slurry shield tunneling. *Constr Build Mater* 416–423
10. Watanabe T, Yamazaki H (1981) Giant size slurry shield is a success in Tokyo. *Tunn Tunnel* 13(1):13–17
11. Wu D, Zhou S, Wen X (2015) Laboratory test and application of filter cake formation in sand during slurry shield construction. *Chin J Rock Mech Eng (Supp. 2)*:3460–3467
12. Min FL, Zhu W, Han XR (2013) Filter cake formation for slurry shield tunneling in highly permeable sand. *Tunnel Undergr Space Technol* 38:423–430
13. Min FL, Zhu W, Xia S, Wang R, Wei D, Jiang T (2014) Test study on airtight capability of filter cakes for slurry shield and its application in a case. *Adv Mater Sci Eng* 2014:1–8
14. Daiwei W, Wei Z, Fanlu M (2014) Experimental study of forming time of filter cake and conversion rate of slurry pressure in slurry shield in sand stratum. *Rock Soil Mech* 35(2):423–428
15. Cheng L, Jun S, Ping Y et al (2014) Mesoscopic analysis and model test on formation process and state division of slurry membrane. *J Geotechn Eng* 36(3):435–442
16. Ryu YM, Kwon YS, Kim T et al (2019) Slurry clogging criteria for slurry shield tunneling in highly permeable ground. *KSCE J Civ Eng* 23(6):2784–2793

# Dynamic Response and Long-Term Settlement of Four Overlapping Tunnels Subject to Train Load



Xiangliang Zhou, Quanmei Gong, Zhiyao Tian, and Yao Shan

**Abstract** With continued development of urban rail transit networks, the quantity of overlapping metro tunnels is increasing. Long-term service performance of the tunnel structure can be threatened a lot by complicated dynamic response of tunnel–ground system under train load, especially in the overlapping cases. Based on a case of four overlapping tunnels in soft clay region, dynamic response of the tunnel–ground system and long-term settlement of the tunnels are investigated with finite element method (FEM) and empirical method. It is shown that, maximum acceleration and dynamic principal stress of the lining in overlapping zone are 48.2% and 19.8%, respectively, larger than that in non-overlapping zone. The ten-year accumulation settlement of the tunnel in overlapping zone is 173.7% larger than that in non-overlapping zone. Uneven settlement occurs in the overlapping zone, and the radius of curvature of the tunnel (12,461 m) exceeds the requirements of the specification (15,000 m). Grouted reinforcement can control the uneven settlement well. Radius of curvature of the tunnel can be refined to 33,967 m, which meets the requirements of the specification.

**Keywords** Overlapping tunnels · Train load · Dynamic response · Long-term settlement · Grouted reinforcement

---

X. Zhou · Q. Gong · Z. Tian · Y. Shan (✉)  
Shanghai Key Laboratory of Rail Infrastructure Durability and System Safety, Tongji University,  
Shanghai 201804, China  
e-mail: [shanyao@tongji.edu.cn](mailto:shanyao@tongji.edu.cn)

Key Laboratory of Road and Traffic Engineering of the Ministry of Education, Tongji University,  
Shanghai 201804, China

X. Zhou  
e-mail: [1733262@tongji.edu.cn](mailto:1733262@tongji.edu.cn)

Q. Gong  
e-mail: [gongqm@tongji.edu.cn](mailto:gongqm@tongji.edu.cn)

Z. Tian  
e-mail: [tianzy@tongji.edu.cn](mailto:tianzy@tongji.edu.cn)

# 1 Introduction

With urgent demand of traffic accessibility, the scale of urban rail transit networks is constantly expanding. As a result, the quantity of overlapping metro tunnels is increasing. Dynamic response of the structure–foundation system in overlapping cases is much more complicated than that in a single operation tunnel. Complicated dynamic response of the overlapping area may induce significant long-term subsoil deformation, which threatens long-term service performance of the tunnel.

Dynamic response of a single tunnel structure subject to train vibration has been investigated by various methods. Acceleration duration curves of the tunnel lining under train vibration were measured in field tests [1, 2]. Numerical models were also established to analyze the acceleration and dynamic stress on the tunnel lining [3, 4]. Dynamic responses of tunnels in an elastic half space were studied by analytical method [5]. Furthermore, dynamic responses of two parallel tunnels or two overlapping tunnels have also been studied in the literatures [6–8]. The general law shows that dynamic responses of tunnel lining in multi-tunnel situation are larger than that in single tunnel situation.

Long-term settlement of foundation under train load has also been noticed in literatures. The settlement contains two parts [9, 10]: (1) plastic settlement caused by cumulative plastic strain; (2) consolidation settlement caused by dissipation of cumulative pore pressure. There are two types of computational algorithms used to calculate plastic settlement of the foundation subject to dynamic train load: a constitutive model and an empirical model. The constitutive model includes the yield criterion, hardening rules, and flow rules [11, 12]. Numerical analysis was combined with soil constitutive models to calculate the soil plastic deformation of the subgrade caused by train loads. This method has definite physical significance that reflects the deformation mechanism of subgrade soil subject to cyclic train loading. However, it requires many calculations, even with a few cyclic loading applications, and therefore is unrealistic for predicting the long-term uneven settlement of foundation after millions of loading cycles. In engineering, an empirical model can be used more easily than a constitutive model. Considering calculation cost, the realistic and common used algorithm to calculate the above-mentioned two parts settlement is based on empirical models: Step 1, numerical model or analytical model can be used to calculate the dynamic deviator stress of subsoil under once train operation; Step 2, empirical models can be used to describe the relationship of cumulative plastic strain and cumulative pore pressure in soil element with times of the applied repeated load under the certain dynamic deviator stress, which were obtained from laboratory tests [13–16]; step 3, the plastic settlement of subsoil can be calculated by integrating soil strain along the depth, and the consolidation settlement can be calculated by Terzaghi's one-dimensional consolidation theory. Through the above process, long-term settlement of a single tunnel case [16] or two tunnels overlapping case [9] has been predicted. The results show that the settlement in multi-tunnel cases is always greater than that in a single tunnel case.

Most of the aforementioned studies concentrate on a single tunnel case or two tunnels overlapping case. Few studies focused on a four overlapping tunnels case, which is a more common case in practical. In this paper, based on ABAQUS software, a tunnel-foundation FEM model is established to analyze the dynamic response of tunnel lining and the foundation soil in the situation of four overlapping tunnels under train vibration. Long-term settlement of the tunnels in overlapping zone and non-overlapping zone is calculated and analyzed. These findings can provide a reference for maintenance of the service performance of four overlapping tunnels.

## 2 Engineering Background

Nanjing Metro Line 3 has been in operation since 2015. Metro Line 5, designed to cross below Metro Line 3, is expected to be in service in 2022. The lining of Metro Lines 3 and 5 is both 6.2 m in outer diameter and 5.5 m in inner diameter.

The typical profile is presented in Fig. 1. Buried depth of the two tunnels of Metro Line 3 is 9.8 m. The clear distance between the tunnels of Metro Line 3 and 5 is only 1.95 m. The groundwater level is 0.5 m below the ground surface. The typical strata are composed of 2.5 m thick filling, 2 m thick silty clay-A, 12.5 m thick mucky silty clay, 6.5 m thick silty clay-B, and silty clay layer-C to the depth of 50 m. Metro Line 3 is located within the mucky silty clay layer, and Metro Line 5 is mainly located in the mucky silty clay layer silty clay layer-B.

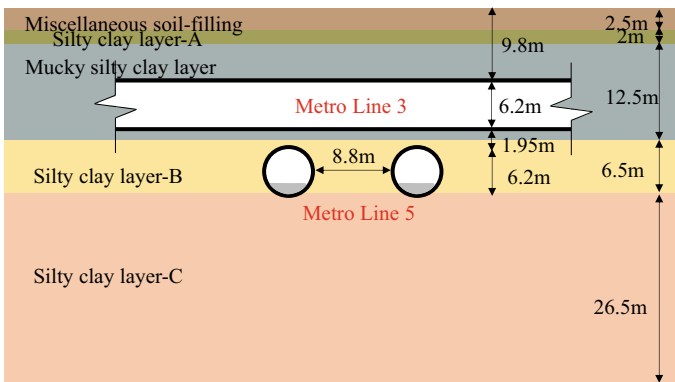


Fig. 1 Typical soil profile at the site

**Table 1** Parameter settings for finite element analysis

Materials	Unit weight $\gamma$ /(kN/m <sup>3</sup> )	Dynamic elastic modulus $E$ /(MPa)	Poisson ratio $\nu$
Miscellaneous soil-filling	19.3	41	0.33
Silty clay layer-A	19.4	69	0.31
Mucky silty clay layer	17.9	31	0.38
Silty clay layer-B	20.1	73	0.32
Silty clay layer-C	20.3	56	0.32
Track bed	25	31,500	0.2
Lining	25	27,600	0.2

### 3 Numerical Calculations

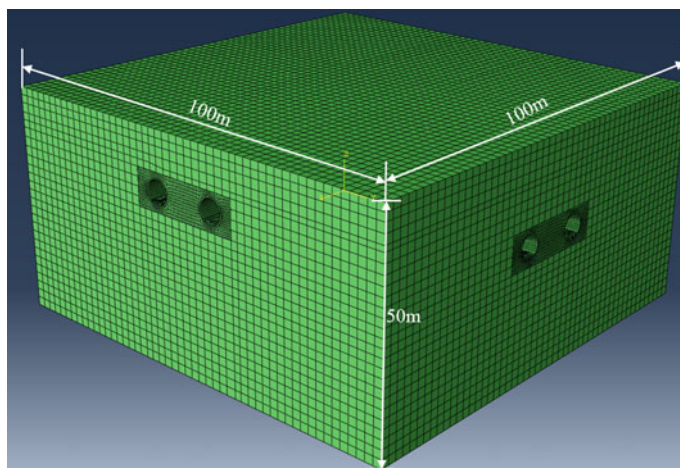
#### 3.1 Description of Calculation Model

Tunnel–ground FEM model was established to compute dynamic response of four overlapping tunnels and subsoil under train load. The experience in the literatures [17–19] shows that an elastic constitutive model is accurate enough to calculate the dynamic deviatoric stress in subsoil under train vibration. Thus, for calculation simplification, the soil and structures are considered to be described with linear–elastic constitutive. The parameters settings are shown in Table 1.

To eliminate boundary effects, horizontal scale of the model is 8–10 times of the tunnel diameter, the size of the finite elements is smaller than the 1/6 times minimum wavelength of soil layers, and a high accuracy calculation results can be reached [20]. The minimum shear wave velocity is 146 m/s (in mucky silty clay). The frequency of shear wave under subway train load is 10 Hz [21, 22]. Therefore, the minimum shear wavelength is 14.6 m. When the size of the finite elements is less than 2.43 m, it can meet the accuracy requirements of dynamic calculation. Thus, the model length is 100 m in horizontal direction; the bottom boundary of the model is 30 m below the ground level, and the upper surface of model is the free face of the ground level. The model mesh is divided into 0.5–2 m regular hexahedral elements. The finite element model is presented in Fig. 2.

#### 3.2 Selection of Measuring Point

Bai and Li [7] studied dynamic responses of two overlapping tunnels case and found that the dynamic amplification effect was most significant when the trains met at the intersection of the tunnels. Moreover, in this case, four trains would reach the longest meeting time at the intersections when the trains met at the intersection. Thus, the case that trains of Metro Line 5 and trains of Metro Line 3 meet at the intersection



**Fig. 2** Finite element model

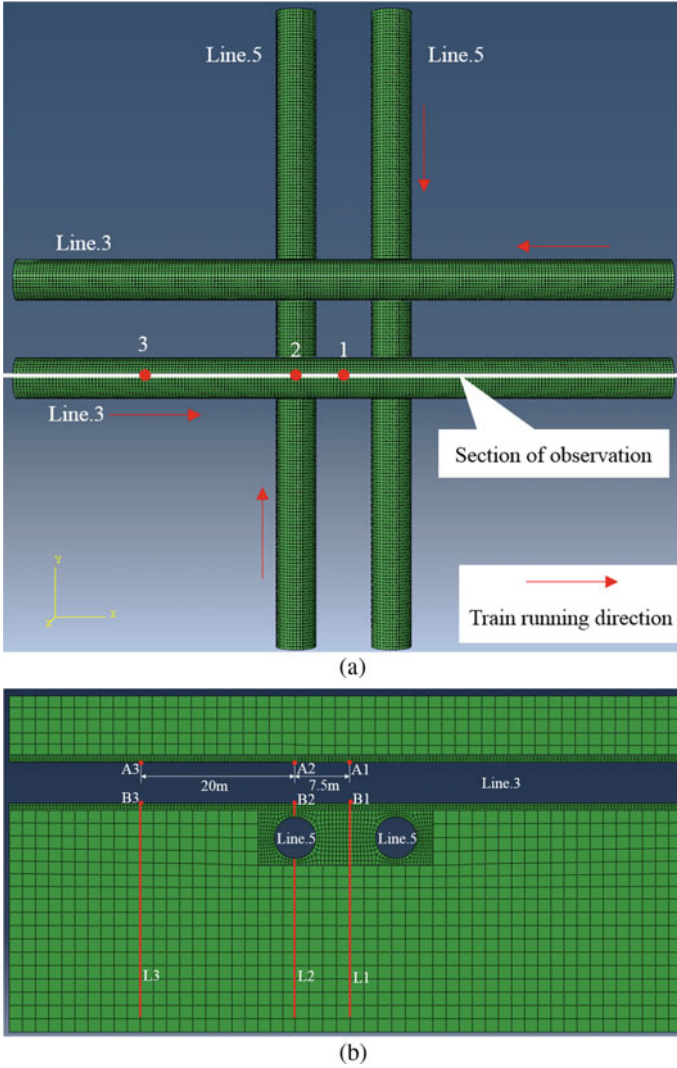
can be considered as the most unfavorable situation, which is the studied case in this paper.

One of the tunnels in Metro Line 3 is chosen for analysis. As is seen in Fig. 3, three vertical sections are chosen for analysis. Section 1 is the center of overlapping zone on Metro Line 3, Sect. 2 is the intersection of Metro Line 3 and 5, and Sect. 3 is thought to be in the non-overlapping zone (the reason will be discussed later). On the tunnel lining, tunnel vault (A) and tunnel invert (B) are chosen for analysis. In subsoil, the soil elements on the red lines  $L1$ ,  $L2$ , and  $L3$  are chosen for analysis.

### 3.3 Load Application

The wheel–rail contact force is transmitted through the fastener to the track bed and then to the tunnel structure. In this paper, the train load is simulated by applying a concentrated force at the corresponding position of the fastener. The fastener force time history curve of a fastener is shown in Fig. 4. The speed of train running is 54 km/h, and phase difference is applied to adjacent fasteners to simulate metro driving.

The fastener force time history curve of a fastener shown in Fig. 4 is obtained from the vehicle–track vertical coupled dynamic model [23] in Fig. 5. Each train carriage consists of a vehicle body, two bogies, and four wheels sets. The vertical and pitch motion of the vehicle body and bogie and the vertical motion of the wheel set are considered. Suspensions are simulated as springs and dampers. The train adopts three same carriages, which can reflect the periodic distribution of the train axle along the bogie and the vehicle body. The parameters of vehicle refer to the type A vehicle of Nanjing Metro. A pair of rails is modeled by using an infinity Euler beam with

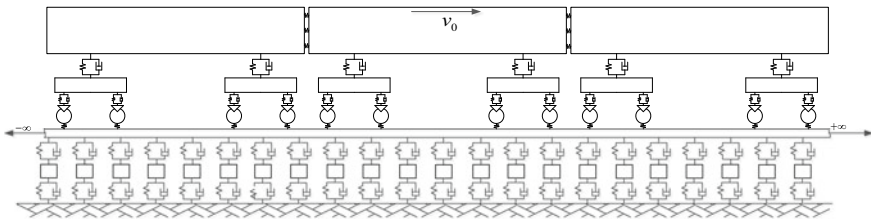
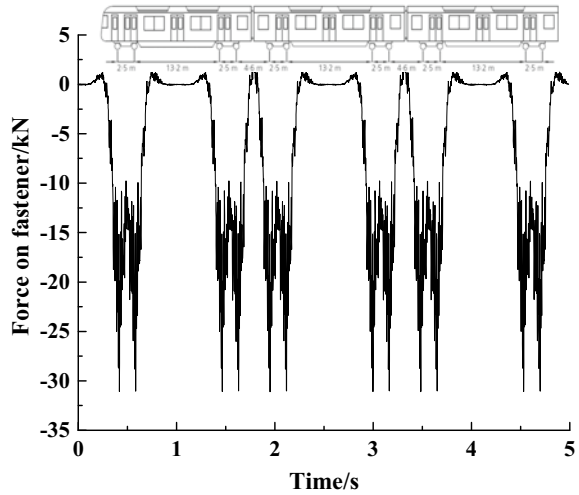


**Fig. 3** Selection of measuring point: **a** plan and **b** profile

discrete supporters. The infrastructure of the rails is treated as a discrete system with supporter units which shall be arranged according to the actual spacing of fasteners. Each support unit of the track consists of two-layer spring-damper system, and the support block is replaced with equivalent discrete mass bodies. Meanwhile, Hertz's theory [24] is applied to calculate the wheel-rail contact force.



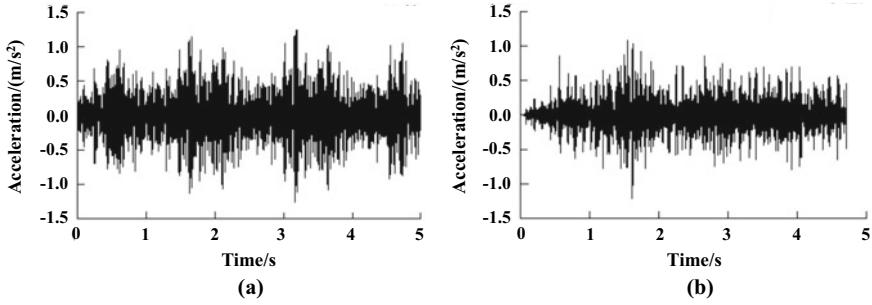
**Fig. 4** Time history curve of fastener force



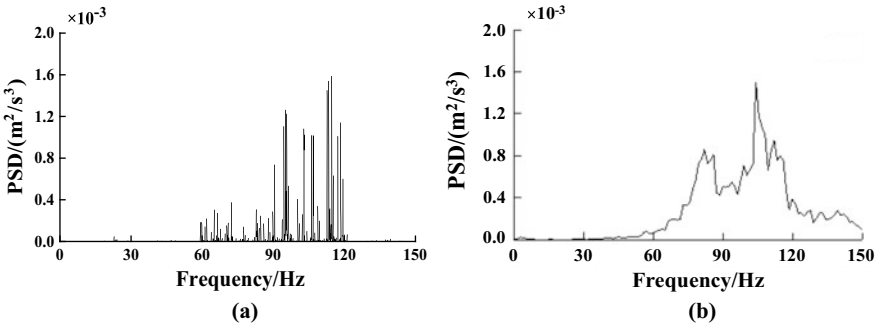
**Fig. 5** Vehicle-track vertical coupled dynamic model

### 3.4 Verification of the Numerical Model

Si [25] measured the vertical acceleration on the track slab in a metro tunnel of which the train type, running speed, and tunnel structure parameters are the same with this study. Considering the case in Si [25] is a two parallel tunnels, the numerical acceleration in the non-overlapping section is chosen to be compared with the measured data in Si [25], the time history curve of vertical acceleration in the center of the track bed is shown in Fig. 6, and the power spectral density (PSD) of vertical acceleration is shown in Fig. 7. As shown in Fig. 6, acceleration amplitude in the center of the track bed in this numerical simulation is  $1.26 \text{ m/s}^2$  that is quite similar with the results in field measurement ( $1.18 \text{ m/s}^2$ ). As shown in Fig. 7, the energy distribution range of the numerical acceleration is basically consistent with that in the field measured acceleration, which is also concentrated in the range of 60–120 Hz. These results indicate the reliability of the numerical models.



**Fig. 6** Time history curve of vertical acceleration in the center of the track bed: **a** numerical and **b** measured



**Fig. 7** Power spectral density of vertical acceleration in the center of the track bed: **a** numerical and **b** measured

### 3.5 Calculation Method for Long-Term Settlement

**Settlement caused by cumulative plastic strain.** The settlement caused by the cumulative plastic strain can be calculated by integrating soil strain along the depth:

$$S_d = \int \varepsilon_h^p dh \quad (1)$$

where  $\varepsilon_h^p$  = cumulative plastic strain;  $h$  = the depth;

The equation for calculating the cumulative plastic strain under repeated loading proposed by Chai and Miura [12] is expressed as follows:

$$\varepsilon^p = a \left( \frac{q_d}{q_f} \right)^m \left( 1 + \frac{q_s}{q_f} \right)^n N^b \quad (2)$$

where  $q_d$  = dynamic deviator stress;  $q_s$  = the initial static deviator;  $q_f$  = the static failure deviator stress;  $a$ ,  $m$ ,  $b$ , and  $n$  are parameters related to the physical and

mechanical properties of subsoil, and  $n = 1.0$  is suggested by Chai;  $N$  = number of repeated load applications, and  $N = 327,300$  times/year.

The dynamic deviator stress  $q_d$  can be calculated as

$$q_d = \sigma_{1d} - \sigma_{3d} = \sqrt{3J_{2d}} \\ = \sqrt{\frac{1}{2} \left[ (\sigma_{xd} - \sigma_{yd})^2 + (\sigma_{yd} - \sigma_{zd})^2 + (\sigma_{zd} - \sigma_{xd})^2 \right] + 3 \left( \tau_{xyd}^2 + \tau_{yzd}^2 + \tau_{zxd}^2 \right)} \quad (3)$$

where  $J_{2d}$  is the second invariant of the dynamic stress deviator. In this paper, soil deviator stress is calculated by tunnel-foundation interaction model.

The initial static deviator  $q_s$  can be calculated as

$$q_s = \sigma_{1s} - \sigma_{3s} = \sqrt{3J_{2s}} \quad (4)$$

where  $J_{2s}$  is the second invariant of the static stress deviator.

The static failure deviator stress  $q_f$  can be calculated as

$$\begin{cases} q_f = 2\tau_f \\ \tau_f = c_{cu} \cdot \frac{\cos \varphi_{cu}}{1 - \sin \varphi_{cu}} + \frac{(1 + K_0)}{2} \sigma_z \cdot \frac{\sin \varphi_{cu}}{1 - \sin \varphi_{cu}} \end{cases} \quad (5)$$

where  $\tau_f$  = undrained shear strength;  $c_{cu}$  = soil cohesion;  $\varphi_{cu}$  = soil internal friction angle;  $K_0$  = soil lateral pressure coefficient, and  $\sigma_z$  = soil gravitational stress.

**Settlement caused by dissipation of cumulative pore pressure.** Cumulative consolidation settlement caused by dissipation of cumulative pore pressure can be calculated by Terzaghi's one-dimensional consolidation theory:

$$S_v = \sum_{i=1}^n m_{vi} h_i u_i \quad (6)$$

where  $m_{vi}$  = the coefficient of volume compressibility of the  $i$ th element;  $h_i$  = the thickness of the  $i$ th element;  $u_i$  = the cumulative pore pressure of the  $i$ th element.

The equation for calculating the cumulative pore pressure under repeated loading proposed by Hyde [13] is expressed as follows:

$$\frac{u}{p_c} = \alpha_2 N^\gamma \quad (7)$$

where  $p_c$  = the initial consolidation pressure;  $\alpha, \gamma$  are parameters related to the physical and mechanical properties of subsoil, can be calculated as

**Table 2** Soil parameters of long-term settlement calculation

Soil layers	Parameters of cumulative plastic strain			Parameters of pore pressure			
	$a$	$m$	$b$	$A$	$B$	$C$	$D$
Miscellaneous soil-filling	1.28	2.51	0.182	0.225	1.316	0.217	-0.018
Silty clay layer-A	1.17	2.58	0.178	0.206	1.203	0.212	-0.017
Mucky silty clay layer	1.31	2.47	0.212	0.204	1.347	0.252	-0.022
Silty clay layer-B	1.15	2.61	0.174	0.202	1.182	0.207	-0.018
Silty clay layer-C	1.19	2.57	0.181	0.2100	1.202	0.216	-0.019

$$\begin{cases} \alpha = A \left( \frac{q_d}{2p_c} \right)^B \\ \gamma = C \left( \frac{q_d}{2p_c} \right)^D \end{cases} \quad (8)$$

The initial consolidation pressure  $p_c$  can be calculated as

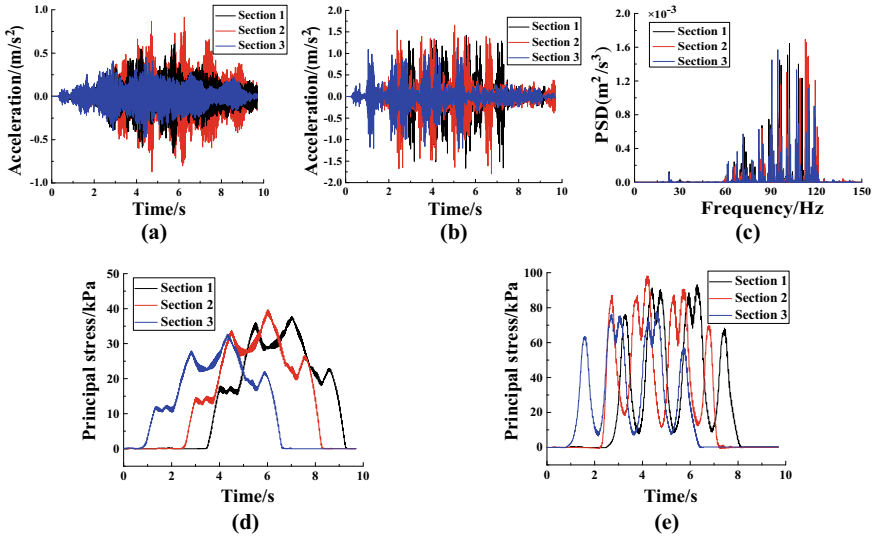
$$p_c = \frac{(1 + 2K_0)}{3} \sigma_z \quad (9)$$

Dynamic triaxial test of Nanjing soft soil was carried out by Luo [26]. In this paper, the experimental results are fitted to determine the relevant soil parameter. As a result, the parameters for long-term settlement calculation are illustrated in Table 2.

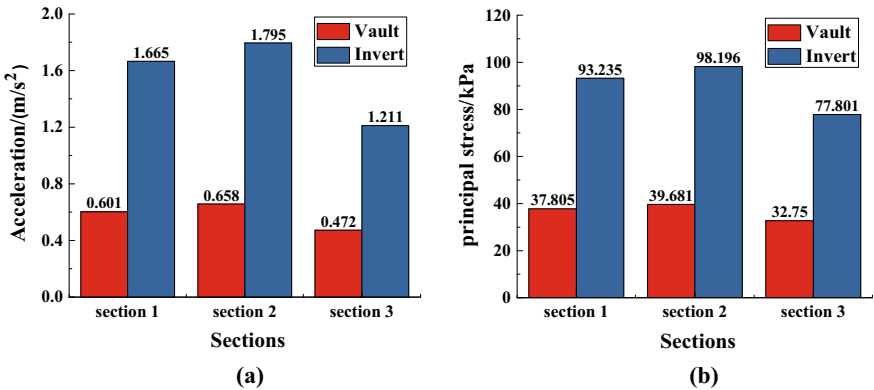
## 4 Computation Result Analysis

### 4.1 Dynamic Response of Overlapping Tunnel

The vertical acceleration and maximum principal stress of tunnel vault and invert in Sects. 1, 2, and 3 are presented in Fig. 8. The amplitudes of acceleration and maximum principal stress on the analysis sections are presented in Fig. 9. The general law can be drawn that (1) amplitudes of acceleration and maximum principal stress on tunnel vault are always smaller than that on tunnel invert; (2) amplitudes of acceleration and maximum principal on the three sections: Sect. 2 > Sect. 1 > Sect. 3; (3) in the low-frequency range (0-50 Hz), there is a peak value of acceleration energy at 23.1 Hz,

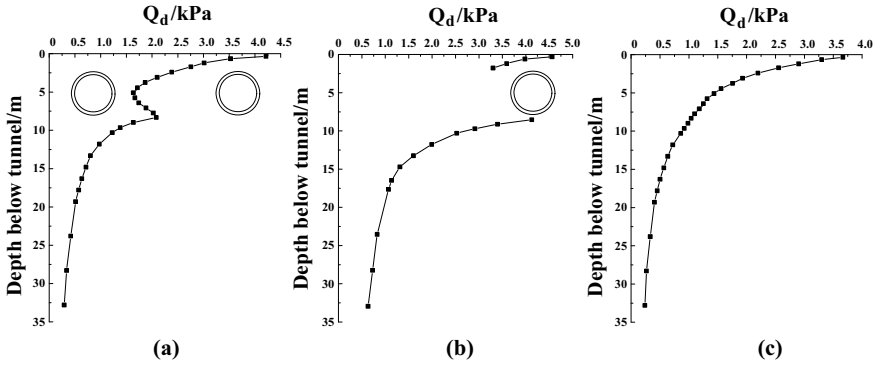


**Fig. 8** Dynamic response of the tunnel: **a** time history curve of vertical acceleration of tunnel vault, **b** time history curve of vertical acceleration of tunnel invert, **c** power spectral density of vertical acceleration of tunnel invert, **d** maximum principal stress of tunnel vault, and **e** maximum principal stress of tunnel invert



**Fig. 9** Amplitude of dynamic response on the analysis sections: **a** vertical acceleration and **b** maximum principal stress

which is excited by the wheel axle passing through adjacent sleepers with an interval of 0.625 m when the train runs at a speed of 54 km/h. In the high-frequency range, the acceleration energy distribution range of the three sections is basically the same, which is mainly concentrated in the range of 60–120 Hz. However, the amplitude of vibration energy in the overlapping area is greater than that in the non-overlapping area.



**Fig. 10** Dynamic deviator stress reduction coefficient with depth: **a** Sect. 1, **b** Sect. 2, and **c** Sect. 3

The results shown that there is an amplification effect of dynamic response in the overlapping area. The acceleration amplitude on Sect. 2 is 48.3% larger than that on Sect. 3, and the maximum principal stress amplitude on Sect. 2 is 19.8% larger than that on Sect. 3. The maximum principal stress is much smaller than the tensile stress of concrete, and long-term settlement of subsoil will be discussed later.

## 4.2 Long-Term Settlement of Overlapping Tunnel

Dynamic deviator stress of subsoil along the depth at Sects. 1, 2, and 3 is presented in Fig. 10. General law of the dynamic deviator stress shows that: Sect. 2 > Sect. 1 > Sect. 3. The dynamic deviator stress of the subsoil just below the tunnel is 3.65 kPa of Sect. 3 and 4.62 kPa of Sect. 2.

At Sect. 1, due to running of Metro Line 5, the dynamic deviator stress decreases with depth till the tunnel spring of Metro Line 5, then increases to the extremum (2.23 kPa) at the tunnel invert of Metro Line 5, and decreases in the subsoil. At Sect. 2, the dynamic deviator stress reduces with depth till the tunnel vault of Metro Line 5—3.25 kPa. The dynamic deviator stress at the tunnel invert (4.18 kPa) is much larger than that at the tunnel vault (3.25 kPa), and then, the stress decreases with depth in the subsoil. As for Sect. 3, the dynamic deviator stress reduces to 50% of its maximum value at the depth of 4 m below the tunnel, 20% at the depth of 11.6 m, which are in agreement with the results in the literature [14], proving the results in this simulation.

Long-term settlement of subsoil is computed using formula (3–11). The development of tunnel settlement (subsoil deformation) with year is presented in Fig. 11. The settlement caused by cumulative plastic strain is larger than the settlement caused by consolidation under excessive pore pressure. The settlement develops sharply in the first year and then develops slowly in the subsequently years. After 10 years' operation, the total settlement of Sects. 1, 2, and 3 is 28.3 mm, 46.2 mm and 16.9 mm,

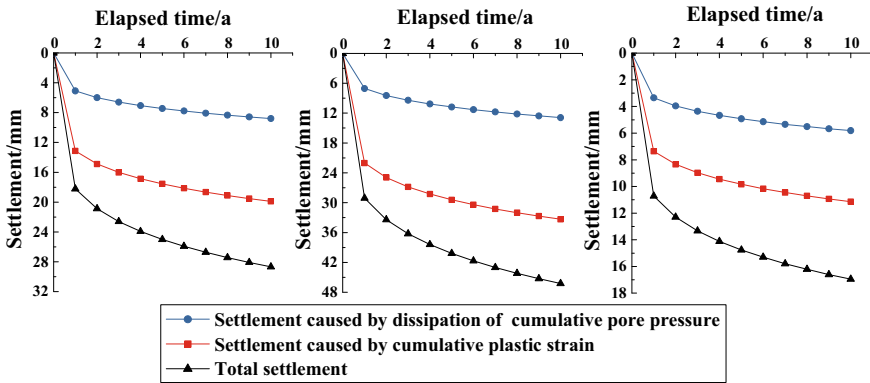
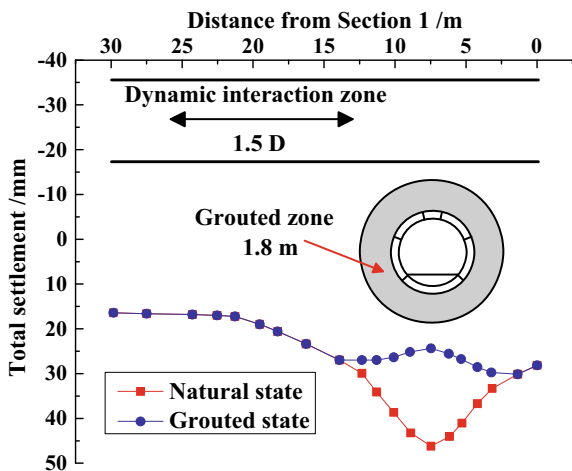


Fig. 11 Development of tunnel long-term settlement with times: a Sect. 1, b Sect. 2, and c Sect. 3

respectively. The ten-year accumulation settlement of the tunnel in overlapping zone (Sects. 2) is 173.7% larger than that in non-overlapping zone (Sects. 3). Finally, a “W”-shaped settlement trough will appear in the overlapping area (Fig. 12 shows a half of the trough). In the tenth year, radius of curvature of the tunnel of Metro Line 3 is 12,461 m, and the relative bending is 1/692 due to the accumulated subsoil deformation, which exceeds the specification requirements of the radius of curvature greater than 15,000 m and the relative bending less than 1/2500 [27]. Thus, measures should be taken to control the significant uneven settlement.

To avoid uneven settlement induced from train vibration, grouted reinforcement is designed to be taken with a zone of 1.8 m outside of the linings Metro Line 5. Settlement of the reinforced case is also computed and compared with the natural state case. Material properties of soil will be improved after grouted reinforcement, and

Fig. 12 Total settlement of tunnel as a function of distance from Sect. 1



the experimental parameters ( $a$ ,  $b$ ,  $m$ ) after soil reinforcement can be referred from literature [28]. As a result, settlement along the tunnels after ten years of grouted state case is shown in Fig. 12, compared with the natural state case. It is shown that uneven settlement can be controlled well with grouted reinforcement, and the maximum settlement of the tunnel is reduced from 46.2 to 26.9 mm after reinforcement. The radius of curvature of the tunnel is refined to 33,967 m, and the relative bending is reduced to 1/2717, which meets the requirements of the specification [28]. In addition, Sect. 3 that is 1.5D (D is the diameter of tunnel) away from the overlapping zone is hardly affected by the dynamic amplification effect from the overlapping zone (as seen in Fig. 12, and settlement is hardly changed in the sections that is 1.5D away). Thus, Sect. 3 is reasonable to be thought as a study point in the non-overlapping zone compared with the overlapping zone.

## 5 Conclusions

Dynamic responses of four overlapping tunnels were analyzed using 3D FEM model, and the long-term settlements of the overlapping tunnels were evaluated. The following conclusions can be drawn.

1. Compared with non-overlapping zone, there is a dynamic amplification effect in the overlapping zone. The acceleration and maximum principal stress value reach the maximum value at the intersection of the tunnels. The amplitudes of acceleration and maximum principal stress of lining in overlapping zone are 48.2% and 19.8% larger than that in non-overlapping zone, respectively.
2. There is an amplification effect of subsoil dynamic deviator stress in overlapping zone. In non-overlapping zone, the dynamic deviator stress decreases to 50% of the maximum value at the depth of 4 m below the tunnel and reduces to 20% at the depth of 11.6 m below the tunnel. In the overlapping area, due to the interaction effect of the lower tunnel, there is an extremum of dynamic deviator stress at the position of lower tunnel invert.
3. The settlement caused by cumulative plastic strain is larger than the settlement caused by consolidation under excessive pore pressure. The settlement develops sharply in the first year and then develops slowly in the subsequent years. The dynamic interaction zone of overlapping tunnel (overlapping zone) is about 1.5D (D is the diameter of tunnel). Due to the difference of dynamic response in overlapping and non-overlapping zone, quite large uneven settlement may occur on the tunnels, which can lead to deterioration of its service performance. The ten-year accumulation settlement of the tunnel in overlapping zone is 173.7% larger than that in non-overlapping zone. The radius of curvature of the tunnel of Metro Line 3 is 12,461 m, and the relative bending is 1/692 due to accumulated settlement, which exceeds the requirements of the specification. Grouted reinforcement can control the uneven settlement well. The maximum settlement of the tunnel is reduced from 46.2 to 26.9 mm by the tenth year, radius of the



tunnel curvature is refined to 33,967 m, and the relative bending is reduced to 1/2717 after reinforcement, which meet the requirements of the specification.

**Acknowledgements** This research was supported by National Natural Science Foundation of China (51708424) and the Fundamental Research Funds for the Central Universities, the People's Republic of China.

## References

1. Degrande G, Schevenels M, Chatterjee P et al (2006) Vibrations due to a test train at variable speeds in a deep bored tunnel embedded in London clay. *J Sound Vib* 293(3–5):626–644
2. Jin Q, Thompson DJ, Lurcock DE et al (2018) A 2.5D finite element and boundary element model for the ground vibration from trains in tunnels and validation using measurement data. *J Sound Vibr* 422:373–389
3. Yuan LQ, Men YM, Liu HJ (2013) The dynamic response simulation analysis of U-shaped metro tunnel. *Appl Mech Mater* 470:857–861
4. Deng FH, Mo HH, Zeng QJ et al (2006) Analysis of the dynamic response of a shield tunnel in soft soil under a metro-train vibrating load. *J China Univ Min Technol* 16(4):509–513
5. Zhou SH, He C, Di HG et al (2017) An efficient method for predicting train-induced vibrations from a tunnel in a poroelastic half-space. *Eng Anal Bound Elem* 85:43–56
6. Lin ZP (2016) Analysis on dynamic response of overlapped tunnel structure under vibration load. *J Railw Sci Eng*
7. Bai B, Li CF (2007) Three-dimensional elastic dynamic response of close crisscross tunnels subjected to subway loading. *Rock Soil Mech* S1:715–718
8. Yuan Z, Boström A, Cai YQ et al (2019) Analytical solution for calculating vibrations from twin circular tunnels. *Soil Dyn Earthq Eng* 117:312–327
9. Gao GY, Li SY, Tu MJ (2015) Analysis of settlement of cross tunnels under cyclic metro loading. *Rock Soil Mech* 36(s1):486–490
10. Cui XZ, Zhang MN, Li SC et al (2015) Effects of embankment height and vehicle loads on traffic-load-induced cumulative settlement of soft clay subsoil. *Arab J Geosci* 8(5):2487–2496
11. Dafalias YF (1986) Bounding surface plasticity (I): mathematical formulation and hypoplasticity. *J Eng Mech* 112(9):966–987
12. Prevost JH (1985) A simple plasticity theory for frictional cohesionless soils. *Int J. Soil Dyn Earthq Eng* 4(1):9–17
13. Li DQ, Selig ET (1996) Cumulative plastic deformation for fine grained subgrade soils. *J Geotech Eng* 122(12):1006–1013
14. Chai JC, Miura N (2002) Traffic-load-induced permanent deformation of road on soft subsoil. *J Geotech Geoenviron Eng* 128(11):907–916
15. Hyde AFL, Ward SJ (1985) A pore pressure and stability model for a silty clay under repeated loading. *Geotechnique* 35(2):113–125
16. Chai JC, Wu HN, Xu YS et al (2014) Evaluation of train-load-induced settlement in metro tunnels. *Proc ICE-Geotech Eng* 167:1–11
17. Dong L (2008) Research on dynamic characteristics of high-speed railway subgrade and deformation properties under cyclic train load. Master dissertation. Beijing Jiaotong University, Beijing, China
18. Wei X, Huang MS (2009) A simple method to predict traffic-load-induced permanent settlement of road on soft subsoil. *Rock Soil Mech* 30(11):3342–3346
19. Wei X, Wang G, Wu ZL (2010) FEM of traffic-load-induced settlement of road on soft clay. *Rock Soil Mech* 31(6):2011–2015

20. Liao ZP (2002) Introduction to wave motion theories in engineering. Science Press, Beijing
21. Yang M (2018) Study on vibration response of shield tunnel-stratum-ground building system due to subway train loads in ground fissure site. Master dissertation. Changan University, Xian, China
22. Yuan LQ (2014) Dynamic response analysis of the soil-metro tunnels interactions in ground fissures area under vibration loads of train. Master dissertation. Changan University, Xian, China
23. Zhai WM (1992) The vertical model of vehicle-track system and its coupling. *Dynamics* 14(3):10–21
24. Timoshenko SP, Goodier JN (1970) Theory of elasticity. McGraw-Hill Book Companies, Inc., pp 520–592
25. Si JB (2018) The train induced dynamic response of the railway embankment and the underpass metro tunnel system. Master dissertation. Tongji University, Shanghai, China
26. Luo JH (2016) Research on the constitutive model and settlement prediction for deep soft soil under metro moving load. PhD dissertation. Southeast University, Nanjing, China
27. Ministry of Housing and Urban Rural Development of the People's Republic of China (2013) CJJ/T 202-2013, Technical code for protection structural of urban rail transit. China Construction Industry Press, Beijing
28. Zhao D (2013) The research of dynamics property and longtime subsidence about corrosion weathered red layer under base of subway tunnel. Central South University, Changsha, China

# Dynamic Stability of Soft Soil Between Closely and Obliquely Overlapped Metro Tunnels Subjected to Moving Train Loads



Hui Li, Quanmei Gong, Honggui Di, Weitao Ye, and Zhi Liu

**Abstract** The problem in dynamic stability of soft soil between closely and obliquely overlapped metro tunnels during operation will aggravate cumulative settlements which affects the safety of metro systems. Based on Shenzhen Metro Line 5 and Line 11 overlapped tunnels, a three-dimensional vehicle-track-tunnel-soil model has been established. Meanwhile, the dynamic shear strain and its transfer characteristics of the soft soil layers between overlapped tunnels under moving train loads has been studied. In longitudinal direction, the most unfavorable position for the soft soil is located in the place where the maximum overlapped degree exists between two tunnels. In transverse direction, the dynamic shear strain in soft soil between tunnels diffuses obliquely at a certain angle from the arch waist of tunnel and gradually decreases with the increase of distance. It also increases nonlinearly with the number of operating lines. Besides, the dynamic stability of soft soil was evaluated by the cyclic threshold shear strain parameters of Vucetic and the value exceeds the linear cyclic threshold shear strain. The plastic deformation of soft soil under moving train loads will accumulate obviously and the dynamic stability problem cannot be ignored. Therefore, high-pressure jet grouting pile is adopted to reinforce the soft soil between two tunnels. And the result shows that the dynamic shear strain of soft soil after reinforcement is much smaller than that before.

---

H. Li · Q. Gong (✉) · H. Di · W. Ye

Shanghai Key Laboratory of Rail Infrastructure Durability and System Safety, Tongji University, Shanghai 201804, China

e-mail: [gongqm@tongji.edu.cn](mailto:gongqm@tongji.edu.cn)

Key Laboratory of Road and Traffic Engineering of the Ministry of Education, Tongji University, Shanghai 201804, China

H. Li

e-mail: [huli1996@tongji.edu.cn](mailto:huli1996@tongji.edu.cn)

H. Di

e-mail: [2012dihonggui@tongji.edu.cn](mailto:2012dihonggui@tongji.edu.cn)

W. Ye

e-mail: [yeweitao@tongji.edu.cn](mailto:yeweitao@tongji.edu.cn)

Z. Liu

Shenzhen Metro Group Co., Ltd, Shenzhen 518173, China

**Keywords** Overlapped metro tunnels · Soft soil · Dynamic stability · Dynamic shear strain · Soil reinforcement

## 1 Introduction

With the rapidly growing population in metropolitan areas, the metro plays an important role in relieving urban traffic pressure and bringing convenience to people's daily life. Meanwhile, the influence of vibration produced by the train operations on surrounding environment cannot be ignored [1]. The long-term cyclic train loads can lead to cumulative settlements in soft soil which affect the safety of metro systems [2, 3]. Besides, these phenomena are more serious in overlapped structures [4]. Gao et al. [5] found the settlement caused by simultaneous operation of two trains is much greater than the sum of single train. Jia et al. [6] pointed out a vibration amplifying area existence within a certain distance in horizontal direction of overlapped tunnels. Besides, Yu et al. [7] concluded the distance between overlapped tunnels has a great effect on ground vibration. Therefore, an investigation on dynamic response of the soft soil induced by underground railways between overlapped tunnels is necessary and desirable.

Numerical modeling approaches are able to consider the nonlinear behaviors of soil, patterns of train load as well as dynamic response of structures. Degrande et al. [8] presented a 3D coupled finite element–boundary element model to simulate the dynamic interaction between tunnel and soil due to the operation of metro trains. By considering segmental joints, Gharehdash and Barzegar [9] used a 3D elastic–plastic finite difference method to study the dynamic response of a tunnel and surrounding soil under vibrations. Yaseri et al. [10] developed a scaled boundary finite-element method to analyze vibrations from underground tunnels. He et al. [11] presented a 3D analytical method from a tunnel embedded in multi-layered half-space to predict ground vibrations. However, the above-mentioned studies mainly focus on single tunnel model.

As a result, most numerical models only consider the dynamic response of single tunnel and surrounding soil, ignoring the influence between tunnels. On the other hand, the existing researches of overlapped tunnels focus more on ground vibration and cumulative settlement, having less attention on dynamic stability of the soil. For soft soil which can be easily affected by cycling vehicle loads, the dynamic stability is even more needed in engineering practice. Therefore, based on Shenzhen Metro Line 5 and Line 11 overlapped tunnels, a 3D vehicle-track-tunnel-soil model has been established in this paper. This model has also been validated by comparison with the measured data of Line 5. Furthermore, the dynamic shear strain and transfer characteristics of the soft soil layers between overlapped tunnels under moving train loads have been studied. The dynamic stability of soft soil was evaluated by the cyclic threshold shear strain parameters [12]. Then a highly efficient method of soil reinforcement was presented.

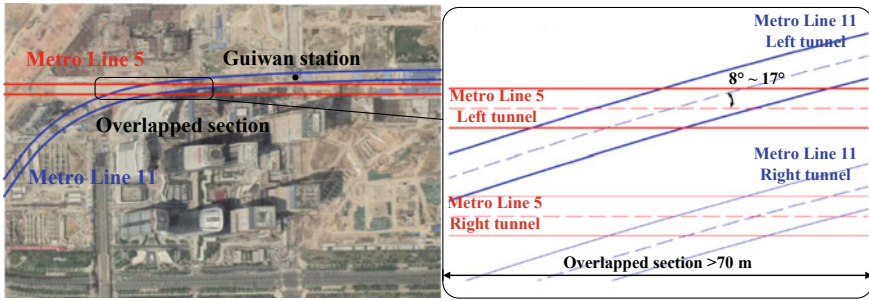


Fig. 1 Schematic diagram of overlapping of Metro Line 5 and Line 11 in Shenzhen, China

## 2 Numerical Method of Dynamic Response Between Overlapped Tunnels

### 2.1 The Closely and Obliquely Metro Tunnels

With the development of rail transit in China’s metropolitan areas, the formation of overlapped metro tunnels is inevitable. Most typically, Shenzhen Metro Line 5 passes over Metro Line 11 tunnels in an oblique angle of  $8^{\circ}$ – $17^{\circ}$ , which can be seen from Fig. 1. These overlapped tunnels with a distance of less than 3 m are over 70 m in length. Besides, the weak intercalations between the tunnels are silt and sandy clay. And the design speed of Line 5 is 80 km/h, as for Line 11 is 120 km/h, which is much faster than the average velocity. Combined with these complex engineering situations, the 3D vehicle-track-tunnel-soil model established in this paper includes two main parts: 3D track-tunnel-soil model and vehicle-track coupled model.

### 2.2 Three-Dimensional Track-Tunnel-Soil Model

Figures 2 and 3 show the transverse section of overlapped metro tunnels under the soil layers together with the finite-element mesh of 3D ABAQUS model close to the actual engineering conditions. The size of the simulated region (140, 225, and 50 m in length in the  $x$ -,  $y$ -, and  $z$ -direction, respectively) is selected through sensitive studies beyond which further extension of lengths has a negligible effect on the half-space response. The 3D track-tunnel-soil model consists of four overlapped tunnels, track beds, and the corresponding soil layers, in which the upper tunnels pass over lower tunnels in an oblique angle of  $8^{\circ}$ – $17^{\circ}$ . In addition, the upper tunnels have an internal radius of 2.7 m and an external radius of 3 m. The lower tunnels have much larger size, with an internal radius of 3 m and an external radius of 3.35 m. The tunnels are also modeled as a whole, without considering the circumferential and longitudinal joints of segments. The depth of the tunnels at their center is taken to be 10 and

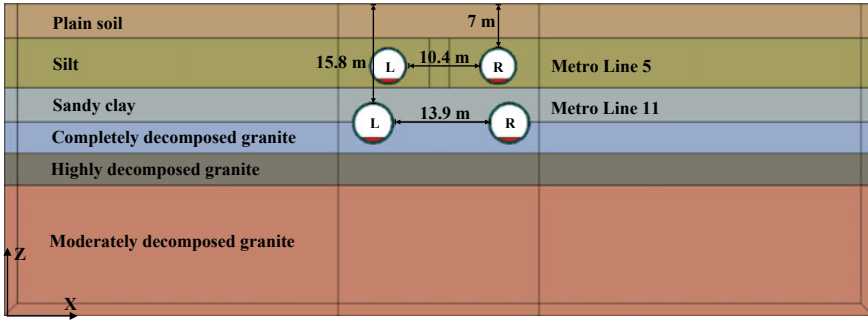


Fig. 2 The transverse section of overlapped metro tunnels together with the soil layers

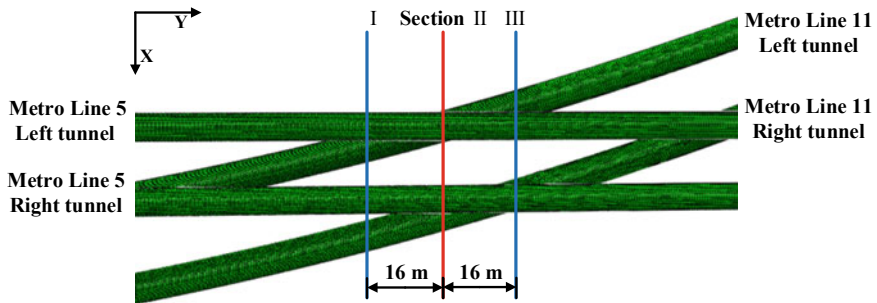


Fig. 3 Section setting of numerical model

19.15 m. The soil is considered to be formed by horizontally layered soil with the material properties listed in Table 1. The material models used in the FE analysis are all linear elastic.

For a dynamic finite element analysis, an artificial boundary is required to define a finite region that can simulate the original unbounded domain well. This model adopts

Table 1 Material properties for the homogeneous model

Material	$h$ (m)	$\rho$ (kg/m <sup>3</sup> )	$E_d$ (MPa)	$\nu_d$
Tunnel	/	2500	34,500	0.20
Track bed	/	2500	30,000	0.20
Plain soil	5.5	1750	27	0.48
Silt	8.0	1560	18	0.48
Sandy clay	5.5	1860	81	0.47
Completely decomposed granite	5.0	1900	117	0.46
Highly decomposed granite	5.0	1950	153	0.45
Moderately decomposed granite	21.0	2550	450	0.45

the 3D infinite element boundary, which can simulate the absorption of reflected and scattering waves on the boundary. Translations in vertical and rotations are restrained at the bottom of model. Meanwhile, translations in transverse direction and rotations are restrained at the vertical faces of model. There are 3 sections set in this model along the y-direction, spaced 16 m apart, to study the influence of overlap degrees on the dynamic shear strain of soft soil, as shown in Fig. 3.

Since the presence of damping and radiation attenuation is caused by the increment of propagation distance, waves will not propagate unlimited in soil layers. The Rayleigh damping coefficients are calculated from the damping ratio of material and the natural frequency of the whole model in order to reflect the dissipation of vibration in soil layers. They can be expressed as:

$$[C] = \alpha[M] + \beta[K] \quad (1)$$

where  $[M]$  is the mass matrix;  $[K]$  is the stiffness matrix;  $\alpha$  and  $\beta$  are the damping coefficients.

If the damping ratio  $\xi_i$  remains unchanged in a certain frequency range  $w_i \sim w_k$ , according to the orthogonal condition of vibration mode, the damping coefficients can be determined:

$$\begin{cases} \alpha = \frac{2w_i w_k}{w_i + w_k} \xi \\ \beta = \frac{2}{w_i + w_k} \xi \end{cases} \quad (2)$$

In order to determine these damping coefficients, two circular frequencies  $w_i$  and  $w_k$  are needed. In this paper, the vibration frequency is relatively high, and the main frequency range from 1 to 150 Hz, which is shown in Table 2.

In this numerical model, most of elements are eight-node linear brick elements, the average element size is approximately 0.3 m in both width and height around the tunnel and gradually increases from the tunnel to the boundaries. The sizes are generated to meet the requirements for simulating highest frequency of loading considered [13].

The train loads are simulated as moving point loads. Considering the phase differences of each point load, the fastener forces calculated from vehicle-track coupled model are applied to the track beds of tunnels. Besides, the left and right trains of Line 5 and 11 are simulated to travel in the opposite directions, and these trains meet at the cross-section which has the maximum overlapped degree of tunnels (Sect. 2).

**Table 2** Rayleigh damping coefficients and circular frequencies for the homogeneous model

$w_i$ (Hz)	$w_k$ (Hz)	$\alpha$	$\beta$
1	150	0.624	0.000105

### 2.3 Vehicle-Track Coupled Model and Cycling Vehicle Load

To simulate the moving train loads mentioned above, the classical vehicle-track vertical coupled dynamic model is adopted to calculate the fastener force caused by the train operations. Considering wheel sets, bogies, and 3 vehicles, the model has 7 rigid-bodies and 10 degrees of freedom which is simulated as a multi-rigid-body system, as shown in Fig. 4. The parameters of vehicle refer to the A-type vehicle in Shenzhen Metro, in order to reflect the periodic law of train operations. All the parts of the vehicle in service neglect their deformation, the operation speed is assumed to be constant as well as the accelerations and decelerations of the vehicle parts are also ignored in this model. And the connections between the parts are replaced with the equivalent spring-damper systems. A pair of rails is modeled by using the infinity Euler beam with discrete supporters. The infrastructure of the rails is treated as a discrete system with sleeper supporter units which shall be arranged according to the actual spacing of fasteners. Each support unit of the track consists of two-layer spring-damper system and the support block is replaced with equivalent discrete mass bodies. Meanwhile, the normal forces between the wheel and rail are calculated by nonlinear spring based on Hertz contact theory. Then, the wheel-rail vertical coupled cross iterative approach is adopted to calculate the fastener force under different

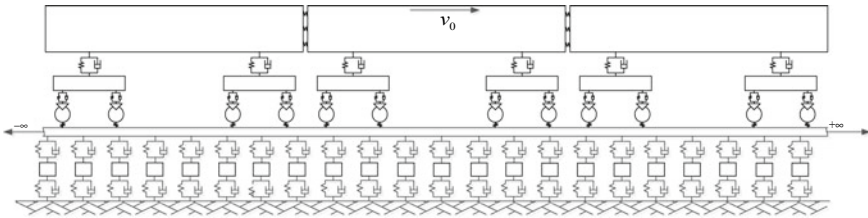


Fig. 4 Schematic diagram of vehicle-track coupled model

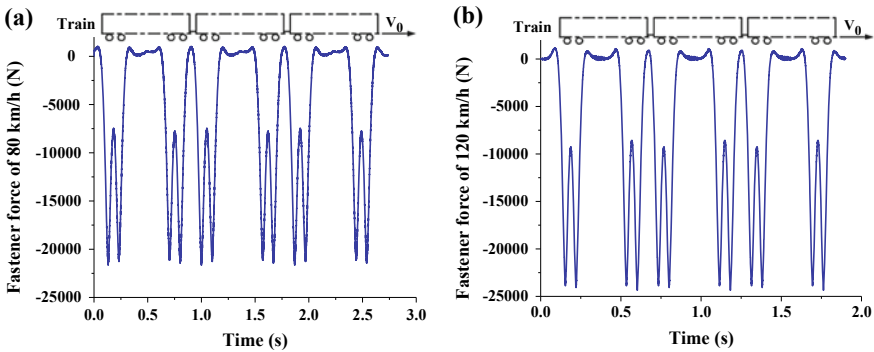
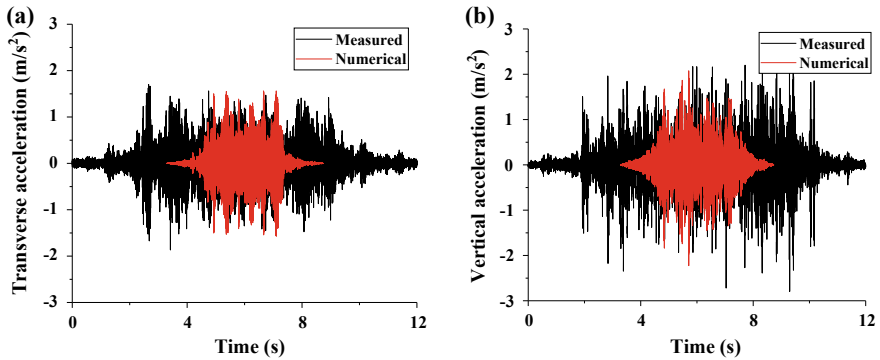


Fig. 5 Time history of fastener force under different speeds a 80 km/h and b 120 km/h





**Fig. 6** Acceleration in the center of the track bed **a** transverse and **b** vertical

running speeds of metro trains. The time history of fastener force is shown in Fig. 5. The negative value indicates the direction of fastener force is vertically downward.

## 2.4 Verification of the Numerical Model

During the case of four-line operation, the vertical and transverse accelerations are obtained from the track bed center in left tunnel of Line 5 (Sect. 2). Meanwhile, the numerical data are compared with the measured data in the same position in Fig. 6.

The train is simulated as 3 vehicles in the numerical model comparing with the 6 vehicles in reality. In Fig. 6, the calculated transverse acceleration amplitude is  $1.5 m/s^2$  and the vertical acceleration amplitude is  $2.0 m/s^2$ . The numerical results closely match the field data which have the same acceleration amplitude and peak separation, indicating the reliability of both numerical models and input parameters.

## 3 Numerical Results and Discussions

### 3.1 Characteristics of Dynamic Shear Strain Distribution

The soft soil between the tunnels of Metro Line 5 and 11 are silt and sandy clay, which can easily result in unrecoverable plastic deformation subjected to long-term train loads. Therefore, using dynamic shear strain to evaluate the dynamic stability of the soft soil. The dynamic shear strain can be divided into longitudinal shear strain along the tunnel ( $\gamma_{xy}$ ), vertical shear strain along the tunnel ( $\gamma_{xz}$ ) and vertical shear strain along the cross-section ( $\gamma_{yz}$ ). Comparing the above dynamic shear strains during the train operation in left tunnel of Line 5, the vertical shear strain along the tunnel ( $\gamma_{xz}$ ) has the maximum value which indicates the dominant position of dynamic stability.

In this paper below, the dynamic shear strain all refers to the vertical shear strain along the tunnel ( $\gamma_{xz}$ ) and its distribution is shown in Fig. 7.

The largest dynamic shear strain of soil is concentrated on the place near the arch waist of tunnel and the boundary between soil layers (less than arch waist). Besides, the dynamic shear strain of left and right sides near the tunnel is opposite in direction and their absolute value is close to each other. Considering dynamic shear strain distribution, the value diffuses obliquely at a certain angle from the arch waist of tunnel and gradually decreases with the increase of distance. Therefore, under the influence of train loads, the dynamic stability of soil near arch waist is the most significant problem, followed by the boundary between soil layers.

In the same condition as above, select the points near the arch waist (which has the maximum dynamic shear strain) in different sections to study the influence of overlap degree on dynamic shear strain of soft soil. The results are shown in Fig. 8.

It can be seen from Fig. 8 that the dynamic shear strain with positive direction in Sect. 2 is 8% higher than other sections; the dynamic shear strain with negative direction in Sect. 2 is 5% higher than others. These prove that the overlap degrees of tunnels have a positive effect on dynamic shear strain of soft soil. More attention should focus on the place which has the maximum overlapped degree between two tunnels.

Fig. 7 Dynamic shear strain distribution of soil around the tunnel

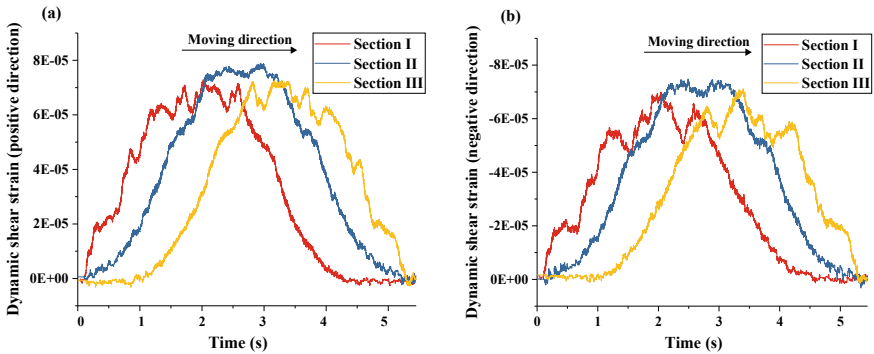
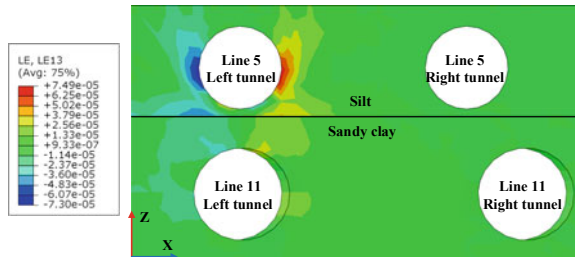
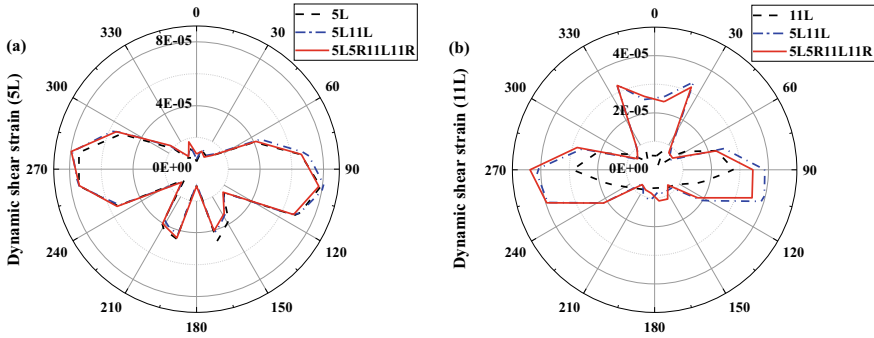


Fig. 8 Time history of dynamic shear strain in different sections a positive direction, b negative direction



**Fig. 9** Dynamic shear strain distribution of soil around the tunnel under different conditions **a** the left tunnel of Line 5, **b** the left tunnel of Line 11

In order to study the influence of multi-line operation on dynamic shear strain, the following conditions are simulated respectively: the single-line operation in the left tunnel of Line 5 (5L), the single-line operation in the left tunnel of Line 11 (11L), the double-line operation in the left tunnels of Line 5 and 11 (5L11L), the four-line operation in both tunnels of Line 5 and 11 (5L5R11L11R). During the case of multi-line operation, all these trains operate simultaneously and meet at the cross-section which has the maximum overlapped degree of tunnels (Sect. 2). In Fig. 9, there is a comparison of maximum dynamic shear strain around the tunnel during different conditions. In this figure, 0° represents the soil near the arch top of tunnel and 180° represents the soil near the arch bottom of tunnel.

For the soil around tunnel of Line 5, the maximum dynamic shear strain during the double-line operation (5L11L) and four-line operation (5L5R11L11R) increases by 5.7 and 6.5% compared with the single-line operation (5L). For Line 11, the maximum dynamic shear strain during the double-line operation (5L11L) and four-line operation (5L5R11L11R) increases by 45.4 and 51.9% compared with the single-line operation (11L). By the available, the dynamic shear strain of soft soil between tunnels increases nonlinearly with the number of operating lines. The dynamic shear strain of soil around the tunnel of Line 11 is much easier affected by multi-line operation than Line 5, which indicates the effect of moving train load in the soft soil transmits more easily from the top down. And the increment of the four-line operation is close to double-line operation, which means the interaction of train operation between the left and right lines is less.

The dynamic shear strain distribution of soil is close to symmetry. In Fig. 9a, the soil around tunnel of Line 5 reaches the maximum value at both sides of the arch waist, the minimum value at the arch top. There is a significant increment at the arch bottom than in other positions. Meanwhile, in Fig. 9b, the soil around tunnel of Line 11 reaches the maximum value at same place of Line 5, but gets the minimum value at the arch bottom which is contrary with Line 5. In particular, there is a significant increment at the arch top of Line 11 which can be easily affected by the operation of Line 5 (upper tunnels). During the case of two-line operation (5L11L) and single-line

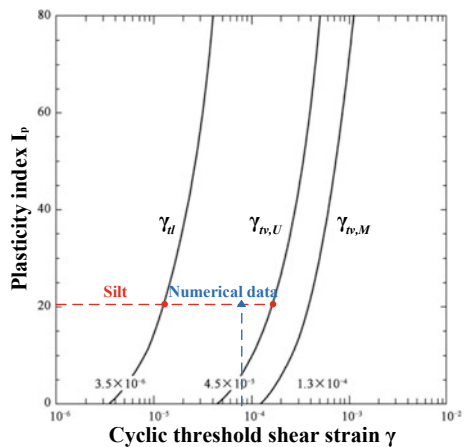
operation (11L), the biggest increment at arch top can be 338.9% which is even larger than the 51.9% increment of arch waist. Above all, the moving train load operated in upper tunnels has more effects on the arch top of lower tunnels.

### 3.2 Cyclic Threshold Shear Strain Parameters and Dynamic Stability Analysis

Dynamic parameters of soil include dynamic strength, dynamic elasticity modulus, and shear modulus, damping ratio as well as dynamic shear strain threshold. The dynamic shear strain is one of the most important factors to control the dynamic response of soft soil subjected to long-term vibration loads. In this paper, using the cyclic strain thresholds [12] that represent the change in cyclic behavior and properties of soil to divide these different cyclic strain regimes. In the above theories, there are two types of cyclic threshold shear strains for different types of soil based on previously published data, the linear cyclic threshold shear strain,  $\gamma_{tl}$ , and the volumetric cyclic threshold shear strain,  $\gamma_{tv}$ , with  $\gamma_{tv} > \gamma_{tl}$ . For cyclic shear strains below  $\gamma_{tl}$ , soil behaves essentially as a linear elastic material. Between  $\gamma_{tv}$  and  $\gamma_{tl}$ , soil behaves markedly nonlinear but remains largely elastic because permanent changes of its microstructure still do not occur or are negligible. Above  $\gamma_{tv}$ , soil becomes increasingly nonlinear and inelastic, with significant permanent microstructural changes taking place under cyclic loads. Because of the discreteness of data, the volumetric cyclic threshold shear strain,  $\gamma_{tv}$  can be divided into the average  $\gamma_{tv,M}$  and the lower limit  $\gamma_{tv,U}$  [14], which shows in Fig. 10.

In the previous study, the maximum dynamic shear strain of soil is located in the silt layer, whose plasticity index  $I_p$  is 20.2. During the case of four-line operation, the maximum dynamic shear strain of silt layer,  $7.973 \times 10^{-5}$ , is even larger than

**Fig. 10** Categorization of cyclic shear strains with respect to response to cyclic loads



the linear cyclic threshold shear strain  $\gamma_{tl}$ ,  $1.3 \times 10^{-5}$ , and close to the lower limit volumetric cyclic threshold shear strain  $\gamma_{tv,U}$ ,  $1.7 \times 10^{-4}$ . These indicate the silt layer will have unrecoverable plastic deformation subjected to long-term train loads which will affect the safety of metro systems. Therefore, the appropriate reinforcement measures should be taken to reinforce the soft soil between the two tunnels.

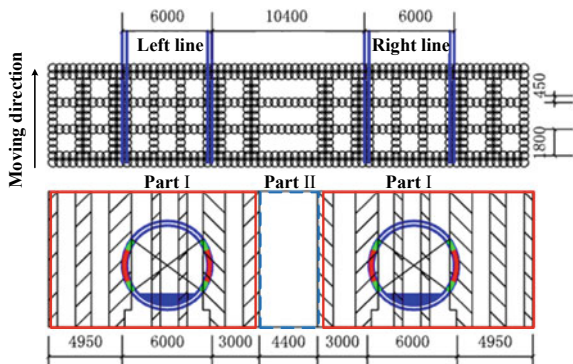
### 3.3 Reinforcement Measures and Effect Evaluation

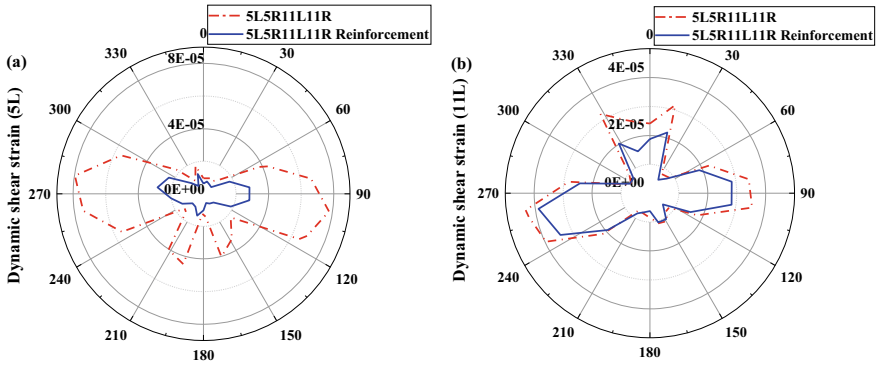
In order to meet the need of dynamic stability of soft soil between closely and obliquely overlapped tunnels during operation,  $\phi$  600 high-pressure jet grouting pile is adopted to reinforce the silt layer where Line 5 is located. The silt layer is reinforced with a length of 225 m longitudinally as well as within 4.95 m outside the tunnels on transverse direction. In vertical, the reinforcement area shall within 2 m around tunnels and keep a reasonable distance from existing tunnels (Line 11), as shown in Fig. 11.

Using composite modulus method to calculate the elastic modulus of reinforcement areas and adjust material parameters of 3D track-tunnel-soil model. In this model, the elastic modulus of area around tunnels (Part I) shall be 126 MPa and the area between two tunnels (Part II) shall be 99 MPa. Figure 12 shows the comparison between dynamic shear strain of silt layer before and after reinforcement during four-line operation.

After reinforcement, the maximum dynamic shear strain of soil around the left tunnel of Metro line 5 decreases from  $7.973 \times 10^{-5}$  to  $2.847 \times 10^{-5}$ , which is 35.7% before reinforcement. At the same time, the value around the left tunnel of Metro line 11 decreases from  $4.377 \times 10^{-5}$  to  $3.887 \times 10^{-5}$ , which is 88.8% before reinforcement. By the available, the reinforcement of the silt layer not only has a good effect on decreasing the dynamic shear strain of soil around the tunnel of Line 5, but also have a certain effect on Line 11. Of course, there are significant decrements at the arch bottom of Line 5 and arch top of Line 11 after reinforcement than other

Fig. 11 Reinforcement of silt layer around the tunnel





**Fig. 12** Comparison of dynamic shear strain of soil around the tunnel before and after reinforcement **a** the left tunnel of Line 5, **b** the left tunnel of Line 11

positions. In conclusion, the reinforcement measure mentioned above has a good guarantee effect on the dynamic stability of soft soil subjected to long-term train loads.

In addition to the above, it should be noted that there are so many important factors that will influence the dynamic stability of soft soil between two tunnels. For instance, changing the cross angle of overlapped tunnels, choosing the effective floating slab track system (FSTS), increasing the distance between tunnels will have a positive effect on the dynamic stability of soft soil. Therefore, further research on the influence of different factors on the dynamic stability of soft soil between overlapped metro tunnels subjected to moving train loads is warranted.

On the other hand, the reported field study of the dynamic response of overlapped metro tunnels during operation is rather limited; therefore, further research on comparisons between simulations and in situ measurement is needed.

## 4 Conclusions

In this paper, a 3D vehicle-track-tunnel-soil model has been established and the model is validated by comparison with the measured data of Line 5. Furthermore, the dynamic shear strain and transfer characteristics of the soft soil layers between overlapped tunnels subjected to moving train loads have been studied. Besides, the dynamic stability of soft soil was evaluated by the cyclic threshold shear strain parameters. The main conclusions in this paper were as followed:

1. In longitudinal direction, the most unfavorable position for soft soil is located in the place where has the maximum overlapped degree between two tunnels.
2. In transverse direction, the dynamic shear strain of soft soil between tunnels diffuses obliquely at a certain angle from the arch waist of tunnel and gradually

- decreases with the increase of distance. There is a dynamic shear strain amplifying area existence within the boundary between soil layers which is less than the arch waist of tunnel.
3. The dynamic shear strain of soft soil between tunnels increases nonlinearly with the number of operating lines. In vertical direction, the effect of moving train load in soft soil transmits more easily from the top down and the moving train load operated in upper tunnels has more effects on the soil near arch top of lower tunnels. The interaction between the left and right lines is less during train operation.
  4. During multi-line operation, the dynamic shear strain of soft soil between tunnels exceeds the linear cyclic threshold shear strain of Vucetic which means the plastic deformation of soft soil will accumulate obviously. Therefore, high-pressure jet grouting pile is adopted to reinforce the soft soil between two tunnels. And the result shows that the dynamic shear strain of soft soil after reinforcement is much smaller than that before.

**Acknowledgements** The authors wish to thank the National Natural Science Foundation of China for their financial support (No. 51978523, No. 51778485).

## References

1. Hussein MFM, Hunt HEM (2007) A numerical model for calculating vibration from a railway tunnel embedded in a full space. *J Sound Vib* 305(3):401–431
2. Gao GY, Chen QS, He JF, Liu F (2012) Investigation of ground vibration due to trains moving on saturated multi-layered ground by 2.5d finite element method. *Soil Dyn Earthq Eng* 40
3. Zhou SH, Di HG, Xiao JH et al (2016) Differential settlement and induced structural damage in a cut-and-cover subway tunnel in a soft deposit. *J Perform Constr Facil* 30(5):04016028
4. Jin XJ, Li S, Li C et al (2017) Environmental vibration responses of close parallel tunnels under train loads. *J Vibr Shock* 36(6):218–222
5. Gao GY, Li SY, Tu MJ et al (2015) Analysis of settlement of cross tunnels under cyclic metro loading. *Rock Soil Mech* 36(1):486–490
6. Jia YX, Liu WN, Sun XJ et al (2009) Vibration effect on surroundings induced by passing trains in spatial overlapping tunnels. *J China Railw Soc* 31(2):104–109
7. Yu YL, Xu HQ, Li ZW et al (2011) Ambient vibration analysis of adjacent parallel multi-tunnels under train loads. *Chin J Geotech Eng* 33(11):1801–1806
8. Degrande G, Clouteau D, Othman R, Arnst M, Chebli H, Klein R et al (2006) A numerical model for ground-borne vibrations from underground railway traffic based on a periodic finite element–boundary element formulation. *J Sound Vib* 293(3–5):645–666
9. Gharehdash S, Barzegar M (2015) Numerical modeling of the dynamic behaviour of tunnel lining in shield tunneling. *KSCE J Civ Eng* 19(6):1626–1636
10. Yaseri A, Bazyar MH, Hataf N (2014) 3d coupled scaled boundary finite-element/finite-element analysis of ground vibrations induced by underground train movement. *Comput Geotech* 60:1–8
11. He C, Zhou S, Di H, Guo P, Xiao J (2018) Analytical method for calculation of ground vibration from a tunnel embedded in a multi-layered half-space. *Comput Geotech* 99:149–164
12. Vucetic, Mladen (1994) Cyclic threshold shear strains in soils. *J Geotech Eng* 120(12):2208–2228

13. Yang YB, Kuo SR, Hung HH (2015) Frequency-independent infinite elements for analysing semi-infinite problems. *Int J Numer Meth Eng* 39(20):3553–3569
14. Hu YF, Li NF (2010) *Theory of ballastless track subgrade for high speed railway*. China Railway Publishing House



# Research on Calculating Quantity of Utility Tunnel with Revit Secondary Development



Qi Zhang, Qian Su, and Yan Yan

**Abstract** A practical cost estimation about the design model of the utility tunnel is essential for the management of the utility tunnel in the design stage. However, the process for quantity calculation based on the design model from the utility tunnel is inefficient because of the inaccurate recognition. Issues in quantity calculation will be resolved with the method related to Revit secondary development (RSD) proposed in the paper. On the basis of Application Programming Interface (API), programming language C#, and programming platform Visual Studio, we established a tight correspondence between the design model of utility tunnel and the external database for quantity calculation. Consequently, results of the quantity calculation based on utility tunnel depended on the clarified model of utility tunnel were available. A case of utility tunnel in the new southern district of Nanjing was studied. It has shown that the results of RSD are better than that of the existing third-party calculation software, in terms of recognition accuracy and data integrity. The results of the study verified the reliability of method proposed in the paper.

**Keywords** Utility tunnel · Quantity calculation · Method · Secondary development · Revit

## 1 Introduction

Ground pipe gallery is the public tunnel that could be able to accommodate multiple municipal pipelines, and it plays a crucial role in relieving traffic congestion [1]. Recently, the speed of ground pipe gallery construction has been accelerated in China, and the total mileage of ground pipe gallery was more than 7800 km by April

---

Q. Zhang · Q. Su (✉) · Y. Yan  
Southwest Jiaotong University, Chengdu 610031, Sichuan, People's Republic of China  
e-mail: [suqian@126.com](mailto:suqian@126.com)

Q. Zhang  
e-mail: [zhangqisuper@126.com](mailto:zhangqisuper@126.com)

Y. Yan  
e-mail: [yanyanyale@foxmail.com](mailto:yanyanyale@foxmail.com)

2018. With the rapid expansion of underground pipe gallery construction, researchers have become to focus on effective cost estimation of it in the design stage [2]. As the basis of cost estimation, the result of quantity calculation not only is significant in the control and determination of cost but also directly affects the quality of cost estimation [3]. In general, there are three standard methods for quantity calculation: manual computation, computer-aided table (e.g., Excel), and graphic calculation [4]. However, various problems (e.g., heavy workload, high repeatability and low efficiency) has been found in manual computation and computer-aided table, making neither of these methods is suitable for quantity calculation [4, 5]. Although quantity could be recognized intelligently from design drawing by graphic calculation, the recognition accuracy is not high enough in the process of drawing identification [6]. Therefore, improvement in the accuracy of quantity calculation has been paid attention to.

Building Information Modelling (BIM) is a model based on 3D technology, and it has the capacity in containing information about a building itself, which makes it feasible to modify and extract relevant information at different stages (e.g., planning, design, and construction) [7]. Besides, the quantity calculation of a building with BIM has been proved [8].

Liu et al. [9] provided the relationship between various information (e.g., quantity) and BIM. Kang et al. [10] researched the quantity calculation with BIM. The result showed that BIM is time-saving and high-precision. Wang et al. [11] accomplished a real-time quantity calculation by developing the construction resource management system of BIM 4D. Deng et al. [12] applied BIM on multiple design schemes of a national road for quantity calculation, and it turned out to be effective. Wei et al. [13] created a calculation method of auxiliary materials required in house construction.

The model of the underground pipe gallery based on BIM was usually completed with Revit. At present, there are two main ways to calculate the quantity of the model: the QTO (Quantity TakeOff) inside Revit and the third-party calculation software [14, 15]. As a third-party method, the quantity of Revit model is calculated by the software with a plug-in inside designed for extracting the data from the Revit. However, it is easy to lead to quantity data leakage because of the process of extracting by plug-in, and it would affect the accuracy of calculation result. Besides, as Chinese character has the feature of multiple meaning, it would be more likely for recognition error during the process of extraction when the item of Revit model needs be recognized with Chinese character for further calculation, which strictly in accordance with the software manual. The QTO of Revit is believed to be more accurate and objective for calculation, but it cannot completely satisfy the Chinese requirement [16]. To ensure the normalization of calculation result, classificatory and denominate information of the model item, which should be in accordance with the Chinese standard specification, is required within the quantity calculation result based on Revit model. However, calculation result of the QTO inside Revit cannot meet the requirement. Besides, attribute information related to quantity of Revit model is likely to be dropped during the process of calculation conducted by the QTO inside BIM. Besides, a survey to employees of construction firms located in southeastern U.S.

[17] indicates the QTO inside Revit cannot provide 100% of data needed to execute the quantity take-off, which reduces the accuracy of calculation results.

This paper proposes the method that is suitable for quantity calculation of underground pipe gallery modeled in Revit. Be basis with secondary development in BIM by using API, C#, and Microsoft Visual Studio, it turns out the quantity calculation result by this method proposed is proved to be accurate, integrated, and applicable. This paper is structured as follows. Section 2 states the methodology applied with secondary development. In Sect. 3, a contrast analysis is performed to demonstrate the applicability of the method proposed with an illustrative case. Section 4 concludes the paper and discusses the perspectives.

## 2 Methodology

### 2.1 Method Design

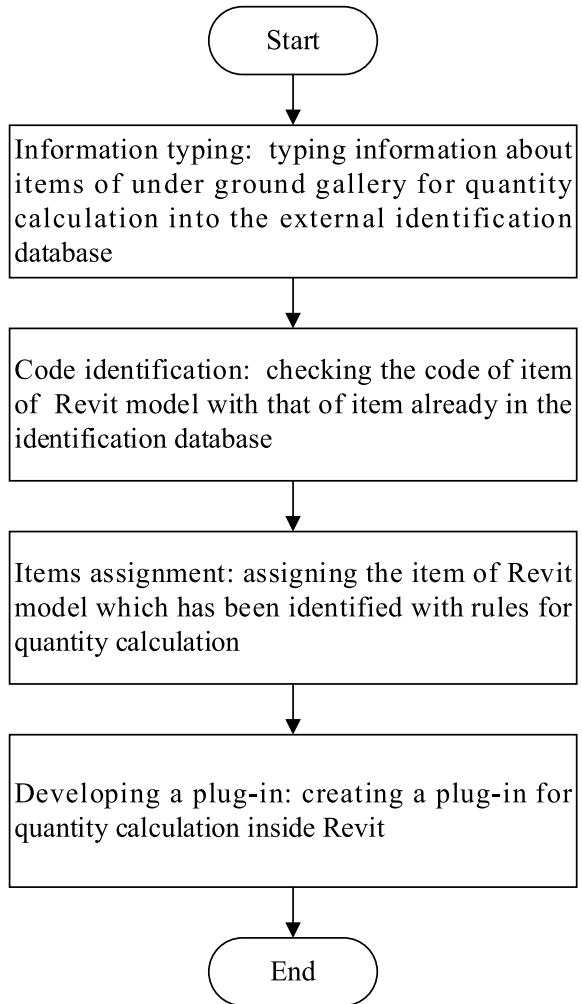
The proposed method consists of four steps. In the first, information about items of the underground gallery for quantity calculation should be imported into the external database, according to relevant national standards (e.g., Specification of Quantity Billing in Construction Projects). Secondly, after the modeling of underground pipe gallery in Revit, the method runs to identify the item of the model with the same component that existed in the database through checking the code of the item, as the more accurate identification of code. Thirdly, the item identified would be assigned with quantity calculation rule which satisfies the Chinese standard. Finally, calculation results could be obtained by employing the proposed method with a Revit plug-in.

Figure 1 shows the method flowchart. The method steps are described in detail in the following paragraphs.

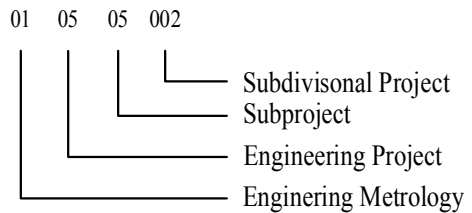
### 2.2 Information Typing

Information about the items of the underground gallery for quantity calculation (e.g., the name, code, and calculation object of the item) should be typed into the identification database. All the information typed should be in accordance with relevant national specifications strictly, especially the code. As the only marking during the identification process, the code (see Fig. 2) is represented by nine Arabic numerals, with requirements of Specification of Quantity Billing in Construction Projects in China and actual design. The first and second digit of code stands for specification in engineering metrology (e.g., house building and decoration engineering), the third and fourth digit of code stands for specification in engineering project (e.g., concrete

**Fig. 1** Flow chart of the proposed method



**Fig. 2** The structure of code



and reinforced concrete engineering), the fifth and sixth digit of code stands for specification in subproject (e.g., cast-in-situ reinforcement concrete plate), and the rest of digits stand for the subdivisional project (e.g., flat-slab).

### 2.3 Code Identification

The process of code identification is shown in Fig. 3. As the unique recognition symbol, each part of code related to the item of the Revit model needs to be checked whether it is matched with that in the identification database. If the code of item could be matched with the code in the identification database, the process of code identification will be done and ready for next steps. Otherwise, if not matched, the result of identification would be marked with 0, and the process of identification would be discontinued.

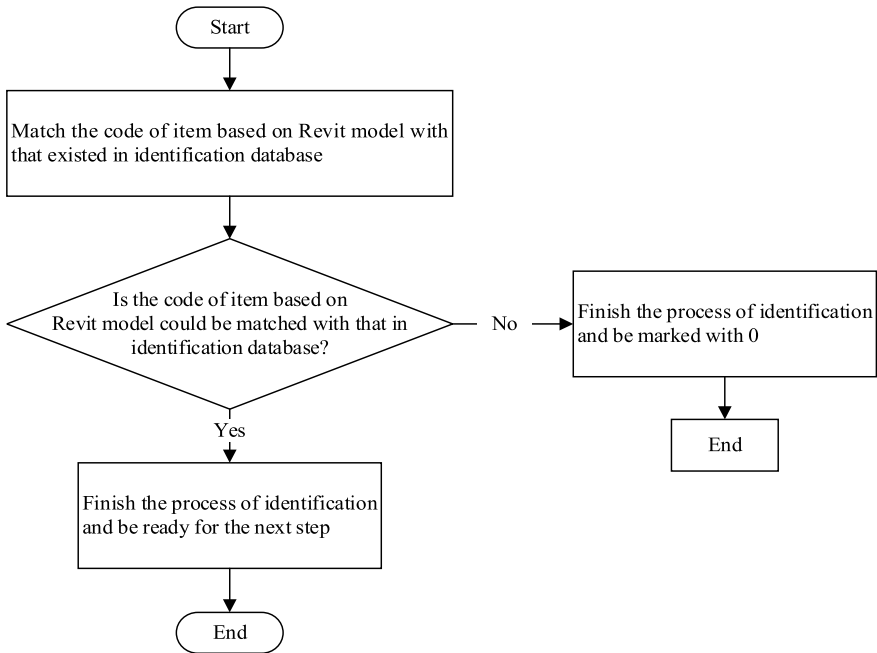


Fig. 3 Flowchart of code identification

## 2.4 Items Assignment

In order to make results of quantity calculation precisely and meet the requirements of Chinese specifications, it is necessary to assign the item of the design model with rules for quantity calculation. The process of assignment is accomplished by procedural programming. The main program is shown below.

```

If(category==record.Category&&family==record.Family&&type==record.Type)
{
  IsDistinguish=1;
  elementData.Number=record.Number;
  elementData.ComputationalStandard=record.QuantityStandardId;
  elementData.ComputationalStandardString=record.QuantityStandardIdString;
  elementData.IsDistinguish=IsDistinguish;
  if(record.QuantityStandardID==Convert.ToInt32(QuantityStandardEnum.None))
  {
    elementData.Quantity=0;
  }
  else if(record.QuantityStandardId==Convert.ToInt32(QuantityStandardEnum.Amount))
  {
    elementData.Quantity=1;
  }
  else if(record.QuantityStandardId==Convert.ToInt32(QuantityStandardEnum.Area))
  {
    elementData.Quantity=Convert.ToDouble(elementData.Area);
  }
  else if(record.QuantityStandardId==Convert.ToInt32(QuantityStandardEnum.Volume))
  {
    elementData.Quantity=Convert.ToDouble(elementData.Volume);
  }
  else if(record.QuantityStandardId==Convert.ToInt32(QuantityStandardEnum.Ton))
  {
    elementData.Quantity=0;
  }
  else if(record.QuantityStandardId==Convert.ToInt32(QuantityStandardEnum.Length))
  {
    elementData.Quantity=Convert.ToDouble(elementData.Length)/100;
  }
}

```

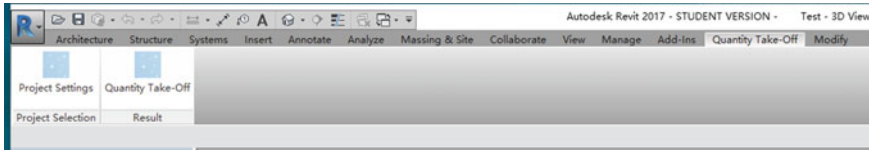


Fig. 4 The plug-in for quantity calculation in Revit

### 2.5 Developing Plug-In

To conduct quantity calculation conveniently in Revit, a plug-in is built. On the basis of Revit API.dll, Revit APIUI.dll and the other interface for Revit, an external command for quantity calculation based on secondary development is implemented with Microsoft Visual Studio [18], and it could be set in the options tab of Revit as a plug-in (see Fig. 4) by loading Add-in Manager and Revit lookup.dll from Software Development Kit (SDK). By clicking the plug-in, the result of quantity calculation based on the design model is available.

## 3 Application Analysis

A case of underground pipe gallery in Nanjing, Jiangsu Province, China is being studied. The chosen case is about a ventilation shaft in the underground pipe gallery whose cross-section dimension is variable because of the available depth of ground surface soil, and under such circumstances, it is necessary to get the accurate quantity calculation result, as the basis for the project cost budget. The section of the ventilation shaft is a double tank. Meanwhile, the net width of the section is  $(3.8 + 2.0)$  m, and the clear height of the section is 3.6 m, with the buried depth is 3 m. The structure of the underground pipe gallery is reinforced concrete. Thereinto, its design working life is 100 years, and seismic fortification intensity is  $7^\circ$ . To visualize the result and improvement of the proposed method, A calculation software commonly employed in China is used to make comparisons. Relevant information in the administrative document of the underground pipe gallery is set as an evaluation criterion for calculation results of different methods. Design model of the ventilation shaft is shown in Fig. 5. Results are listed in Table 1.

As seen in Table 1, calculation results by the proposed method are close to results from the document. However, calculation results of “010504001-Concrete walls-Straight walls-450 mm” and “010504001-Concrete walls-Straight walls-500 mm” calculated by the software are significantly different from the results from the document. Besides, “010504003- Concrete walls-Shear walls-450 mm” and “010504003-Concrete walls-Shear walls-500 mm” are found in calculation results by the software, which does not appear in results of design document and have been highlighted. To explore the reason for calculation bias, detailed calculation results were exported

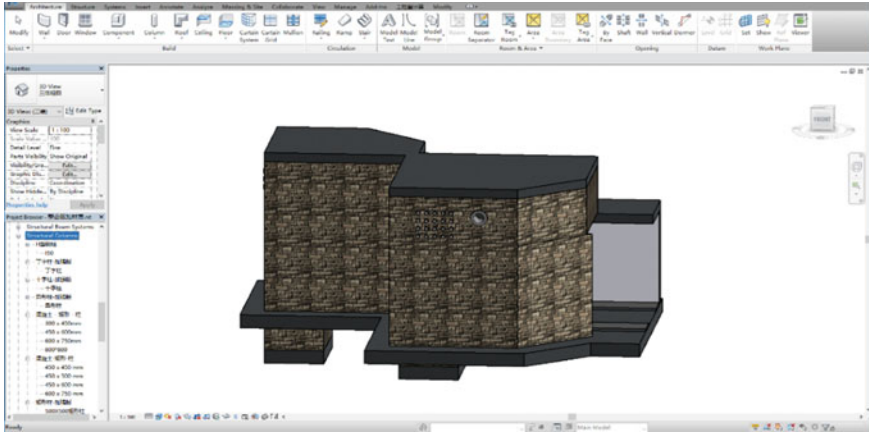


Fig. 5 The design model of ventilation shaft in Revit

Table 1 Quantity calculation results from different methods and design document

Code	Subproject	Name	Type (mm)	Results of the method proposed	Results of calculation software	Results of the document
010504001	Concrete walls	Straight walls	300	12.20 m <sup>3</sup>	12.20 m <sup>3</sup>	12.19 m <sup>3</sup>
			450	100 m <sup>3</sup>	<b>70.46 m<sup>3</sup></b>	101.21 m <sup>3</sup>
			500	5.21 m <sup>3</sup>	<b>3.01 m<sup>3</sup></b>	5.32 m <sup>3</sup>
010505002	P.C. in situ	Flat slab	100	35.63 m <sup>2</sup>	35.68 m <sup>2</sup>	33.87 m <sup>2</sup>
			350	102.12 m <sup>2</sup>	103.12 m <sup>2</sup>	101.82 m <sup>2</sup>
			500	140.85 m <sup>2</sup>	142.61 m <sup>2</sup>	141.26 m <sup>2</sup>
010504003	Concrete walls	Shear walls	450	\	<b>29.54 m<sup>3</sup></b>	\
			500	\	<b>2.20 m<sup>3</sup></b>	\

from calculation software, as also seen in Table 1. From Table 1, it is easy to find out the sum calculation result of “010504001- Concrete walls-Straight walls-450 mm” and “010504003-Concrete walls-Shear walls-450 mm” is 100 m<sup>3</sup>, which is almost equal to the result of “010504001- Concrete walls-Straight walls-450 mm” from design document. Moreover, it is obvious to find out the sum calculation result of “010504001- Concrete walls-Straight walls-500 mm” and “010504003-Concrete walls-Shear walls-500 mm” is 5.21 m<sup>3</sup> at the same time, which is much close to the result of “010504001- Concrete walls-Straight walls-500 mm” from the document. Based on detailed analysis and discussion, a wrong recognition for items of Revit model has been made, which leads to weirdly sorting them during the process for obtaining data by the calculation software, and it would be able to get inaccurate and incomplete calculation results.



**Table 2** Cost estimation results from different methods and design document

Methodology	Cost estimation (CNY)
The method proposed	84.23
Calculation software	68.08
Results of document	84.44

It indicates that some errors existed in the process of importing the data from the Revit model into the calculation software. Meanwhile, the recognition accuracy and ability to ensure data integrity of the method proposed is validated. It can be interpreted that the result calculated by the proposed method is much close to that of the administrative document, which demonstrates its applicability.

To estimate the impact of the method proposed and the calculation software in cost estimation, based on quantity calculation results and the underground pipe gallery construction unit price promulgated by Ministry of Housing and Urban–Rural Development of the People’s Republic of China (MOUHURD), A comparison table of cost estimation is given (see Table 2). As seen in Table 2, there is a slight deviation in cost estimation result between the method proposed and the document (less than 0.2486%), however, the estimation result by the software is greatly different from the result of the document (more than 19.37%). It is clear that the current quantity calculation method (e.g., calculation software) may have a difference on the effectiveness of cost estimation, while the method proposed could provide the basis for accurate cost estimation.

## 4 Conclusion and Perspective

This paper develops the method based on secondary development to get quantity calculation results of underground pipe gallery model in Revit. The method proposed includes four main steps: information typing, code identification, item assignment, and developing a plug-in. Items for quantity calculation, which is in accordance with relevant national specifications, are typed into the external identification database. In the second step, each segment of the code related to the item from the Revit model needs to be checked whether it is matched with that in the external identification database, on the condition that the identification of code is more accurate than that of Chinese character. If the code of item from Revit model could be matched with that in the external identification database, the process of code identification would be done and ready for next steps. In the third step, programming completed in Microsoft Visual Studio would be used to assign with the calculation rule which meets the requirement in China, to make the calculation result more precise. In order to conduct the processes of quantity calculation conveniently, a plug-in based on RevitAPI.dll, RevitAPIUI.dll, Revitlookup.dll, and Add-in manager is established into Revit in the fourth step.

A case is conducted to illustrate the performance of the proposed method by analyzing the difference in results obtained from the method proposed and the calculation software. The method proposed is proved to get improvement in recognition accuracy and data integrity, in comparison to the performance of the calculation software. Furthermore, the applicability of the method proposed is testified.

This study reveals a great potential for applying new approaches of quantity calculation in the design stage of underground pipe gallery. The proposed method could lay the foundation of cost estimation. Then, to verify the effectiveness of the method proposed ulteriorly, more kinds of commercial calculation software (used in or outside China) would be compared with the method proposed in recognition accuracy and data integrity, and improvements on the method proposed would be made depending on the comparative performance. Further, we can develop the method proposed into the cost estimation platform for effective management of cost in the design stage by introducing the price system of cost estimation.

## References

1. Jorge CE, Julian CP (2012) Understanding the major drivers for implementation of municipal sustainable policies in underground space. *Int J Sust Dev World* 19(6):506–514. <https://doi.org/10.1080/13504509.2012.732973>
2. Rifat S (2004) Conceptual cost estimation of building projects with regression analysis and neural networks. *Can J Civ Eng* 31(4):677–683. <https://doi.org/10.1139/104-029>
3. Winston H, Richard DM, Nelson P (2000) On the accuracy of regulatory cost estimates. *J Policy Anal Manage* 19(2):297–322. [https://doi.org/10.1002/\(SICI\)1520-6688\(200021\)19:2<297::AID-PAM7>3.0.CO;2-X](https://doi.org/10.1002/(SICI)1520-6688(200021)19:2<297::AID-PAM7>3.0.CO;2-X)
4. Tuan TA, Park JY (2014) Development of integrated design methodology for various types of product—service systems. *J Comput Des Eng* 1(1):37–47. <https://doi.org/10.7315/JCDE.2014.004>
5. Won J, Lee G, Cho C (2013) No-scheme algorithm for extracting a partial model from an IFC instance model. *J Comput Civ Eng* 27(6):585–592. [https://doi.org/10.1061/\(ASCE\)CP.1943-5487.0000320](https://doi.org/10.1061/(ASCE)CP.1943-5487.0000320)
6. Choi J, Kim H, Kim I (2015) Open BIM-based quantity take-off system for schematic estimation of building frame in early design stage. *J Comput Des Eng* 2(1):16–25. <https://doi.org/10.1016/j.jcde.2014.11.002>
7. Barlish K, Sullivan K (2012) How to measure the benefits of BIM-A case study approach. *Autom Constr* 24:149–159. <https://doi.org/10.1016/j.autcon.2012.02.008>
8. Lee SK, Kim KR, Yu JH (2014) BIM and ontology-based approach for building cost estimation. *Autom Constr* 41:96–105. <https://doi.org/10.1016/j.autcon.2013.10.020>
9. Liu HX, Lu M, Al-Hussein M (2016) Ontology-based semantic approach for construction-oriented quantity take-off from BIM models in the light-frame building industry. *Adv Eng Inf* 30(2), 190–207. <https://doi.org/10.1016/j.aei.2016.03.001>
10. Kang JH, Anderson SD, Clayton MJ (2007) Empirical study on the merit of web-based 4D visualization in collaborative construction planning and scheduling. *J Constr Eng Manag* 133(6):447–461. [https://doi.org/10.1061/\(ASCE\)0733-9364\(2007\)133:6\(447\)](https://doi.org/10.1061/(ASCE)0733-9364(2007)133:6(447))
11. Wang HJ, Zhang JP, Chau KW, Anson M (2004) 4D dynamic management for construction planning and resource utilization. *Autom Constr* 13(5):575–589. <https://doi.org/10.1016/j.autcon.2004.04.003>

12. Deng Y, Cheng JC, Anumba C (2016) Mapping between BIM and 3D GIS in different levels of detail using schema mediation and instance comparison. *Autom Constr* 67:1–21. <https://doi.org/10.1016/j.autcon.2016.03.006>
13. Wei H, Zheng S, Huang R (2017) BIM-based method calculation of auxiliary materials required in housing construction. *Autom Constr* 78:62–82. <https://doi.org/10.1016/j.autcon.2017.01.022>
14. Whang SW, Park SM (2016) Building information modeling (BIM) for project value: quantity take-off if building frame approach. *Int J Appl Eng Res* 11(12):7749–7757. <https://doi.org/10.13140/RG.2.1.4982.9366>
15. Olawumi TO, Chan DW (2019) Building information modeling and project information management framework for construction projects. *J Civ Eng Manag* 25(1):53–75. <https://doi.org/10.3846/jcem.2019.7841>
16. Yang B, Zhang B, Wu J, Wang Z (2019) A BIM-based quantity calculation framework for frame-shear wall structure. *Struct Eng Int* 29(2):282–291. <https://doi.org/10.1080/10168664.2018.1550352>
17. Olsen D, Mark Taylor J (2017) Quantity take-off using building information modeling (BIM), and its limiting factors. *Procedia Eng* 196:1098–1105. <https://doi.org/10.1016/j.proeng.2017.08.067>
18. Richter J (1999) *Programming applications for microsoft windows*, 4th edn. Microsoft Press, Redmond

# The Influence of Variation in Groundwater Table on Ground Vibrations from Underground Tunnels



Chao He, Shunhua Zhou, Honggui Di, and Xiaohui Zhang

**Abstract** This paper investigates the influence of the variation in the groundwater table on ground vibrations from underground tunnels by an analytical model. The saturated porous medium is used to model the soil layer under the groundwater table, and the dry single-phase medium is applied to simulate the soil above the groundwater table. The transfer matrix method and wave transformation are applied to derive the solution for a tunnel in a dry/saturated layered half-space. Ground vibrations from a tunnel in a three-layered half-space are computed by using the proposed model. The numerical results demonstrate that the vibration levels increase as the groundwater table drops. The displacement field is similar to that of a saturated half-space when the groundwater table is above the tunnel, while it is similar to that of a dry single-phase half-space as the groundwater table is under the tunnel.

**Keywords** Train-induced vibration · Underground tunnel · Saturated porous medium · Groundwater table · Transfer matrix method

---

C. He (✉) · S. Zhou · H. Di · X. Zhang  
Shanghai Key Laboratory of Rail Infrastructure Durability and System Safety, Tongji University,  
Shanghai 201804, China  
e-mail: [hec\\_tjtt@tongji.edu.cn](mailto:hec_tjtt@tongji.edu.cn)

Key Laboratory of Road and Traffic Engineering of the Ministry of Education, Tongji University,  
Shanghai 201804, China

S. Zhou  
e-mail: [zhoushh@tongji.edu.cn](mailto:zhoushh@tongji.edu.cn)

H. Di  
e-mail: [dihongguila@126.com](mailto:dihongguila@126.com)

X. Zhang  
e-mail: [988xiaohui@tongji.edu.cn](mailto:988xiaohui@tongji.edu.cn)

## 1 Introduction

Vibrations induced by subway traffic has a significant influence on the environment [1]. The vibrations transmitting to the nearby buildings may cause annoyance to residents and interference with sensitive equipment. Therefore, more and more attention has been paid to predict the train-induced vibrations.

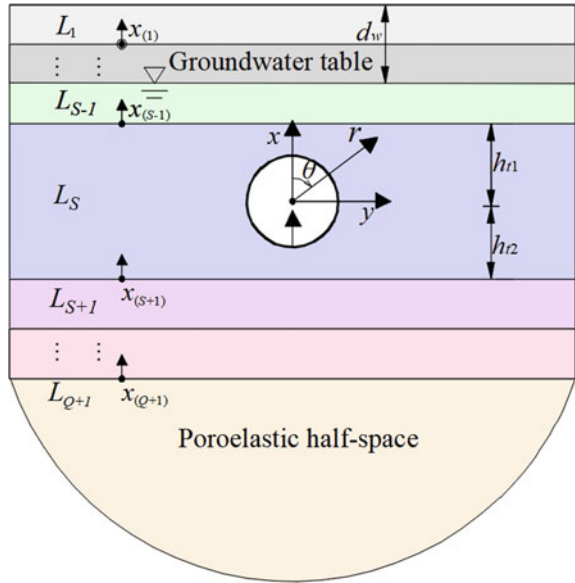
The numerical methods, such as the finite element (FE) model [2–5], finite element–boundary element (FE-BE) model [6–12], finite/infinite element model [13, 14], and finite element finite-perfectly matched layers model [15, 16], have become popular tools to predict the ground vibrations induced by railway traffic. On the other hand, analytical methods with high-computational efficiency were also widely developed to calculate subway-induced vibrations. For example, Forrest and Hunt [17, 18] proposed the pipe-in-pipe (PiP) model to predict ground vibrations from a tunnel in a full-space, which was further improved by many researchers [19–22]. He et al. [23] developed a theoretical model to investigate the effect of the tunnel ring joint on the dynamic responses from underground tunnels. Hussein et al. [24] firstly developed a fictitious force method, which a layered Green’s function was applied to the PiP model to extend it to a layered half-space. However, due to the assumption that the tunnel response is not affected by ground surface and layer interfaces, the accuracy of this model deteriorates when the distance between the tunnel and the ground surface or layer interfaces is less than twice the tunnel diameter. He et al. [25, 26] recently proposed a 3D analytical method to calculate ground vibrations from a single tunnel or twin tunnels in a multi-layered elastic half-space. Since fully couple is considered between the tunnel and surrounding soil in this method, a good accuracy can be obtained even for a close distance between the tunnel and ground surface or layer interfaces. However, those models for the vibration prediction from tunnels in a multi-layered half-space simplified the soil as a single-phase medium. In practice, many subway lines were constructed in the saturated soil, and the groundwater table changes with the seasons.

This paper is aimed to investigate the influence of variation in groundwater table on ground vibrations from underground tunnels. The soil is considered as a dry/saturated multi-layered half-space. A dry single-phase elastic medium is used to simulate the soil above the groundwater table, while the soil under the groundwater table is modeled as a saturated porous medium. The transfer matrix method is applied to deal with wave propagation in the multi-layered medium. The tunnel is considered as a cylindrical shell. The tunnel is coupled with the soil via the boundary conditions at the tunnel-soil interface.

## 2 Formulation

As shown in Fig. 1, the soil involving  $Q$  horizontal layers on the top of a homogeneous half-space is simulated by Biot theory [27, 28]. The groundwater table is located at

**Fig. 1** A circular subway tunnel embedded in a multi-layered half-space with the groundwater table at a depth of  $d_w$



a depth  $d_w$  under the ground surface. For the sake of simplicity, capillary action is not accounted for in this study. Therefore, a dry single-phase elastic medium is applied to model those soil layer, which can be simulated through special parameter setting to eliminate the effect of pore water. The tunnel is embedded in the  $S$ -th layer (source layer). As the geometries and material of the tunnel and soil are assumed to be invariant in the longitudinal direction, the proposed model can be derived in the frequency and wavenumber domains via the following Fourier transforms:

$$\hat{f}(k_z, \omega) = \int_{-\infty}^{+\infty} \int_{-\infty}^{+\infty} f(z, t) e^{i(k_z z + \omega t)} dz dt \tag{1}$$

where  $z$  is the longitudinal coordinate and  $t$  is the time;  $k_z$  denotes the longitudinal wavenumber, and  $\omega$  denotes the angular frequency.

The Biot's theory [27, 28] is used to simulate wave propagation in the saturated porous medium. If the tunnel is not situated at the  $q$ -th layer (i.e.,  $q \neq S$ ), the displacement  $\hat{\mathbf{u}}^{(q)}$ , pore-fluid pressure  $\hat{p}^{(q)}$  and soil stress  $\hat{\boldsymbol{\tau}}^{(q)}$  are obtained through the derivations proposed by Zhou et al. [9], which are written as:

$$\hat{\mathbf{u}}^{(q)} = \frac{1}{2\pi} \int_{-\infty}^{+\infty} \sum_{j=1}^4 \left[ A_{dj}^{(q)} \hat{\phi}_{dj}^{(q)}(x_{(q)}, k_y, k_z, \omega) + A_{uj}^{(q)} \hat{\phi}_{uj}^{(q)}(x_{(q)}, k_y, k_z, \omega) \right] dk_y,$$

$$\begin{aligned}\hat{p}^{(q)} &= \frac{1}{2\pi} \int_{-\infty}^{+\infty} \sum_{j=3}^4 \left[ A_{dj}^{(q)} \hat{\vartheta}_{dj}^{(q)}(x_{(q)}, k_y, k_z, \omega) + A_{uj}^{(q)} \hat{\vartheta}_{uj}^{(q)}(x_{(q)}, k_y, k_z, \omega) \right] dk_y, \\ \hat{\tau}^{(q)} &= \frac{1}{2\pi} \int_{-\infty}^{+\infty} \sum_{j=1}^4 \left[ A_{dj}^{(q)} \hat{\psi}_{dj}^{(q)}(x_{(q)}, k_y, k_z, \omega) + A_{uj}^{(q)} \hat{\psi}_{uj}^{(q)}(x_{(q)}, k_y, k_z, \omega) \right] dk_y\end{aligned}\quad (2)$$

where  $k_y$  denotes the horizontal wavenumber and  $\omega = 2\pi f$  represents the angular frequency.  $\hat{\phi}$ ,  $\hat{\vartheta}$ , and  $\hat{\psi}$  are the wave functions for solid displacements, pore-fluid pressure and stresses, respectively, and  $A_{dj, uj}$  are the corresponding unknown coefficients. The subscripts  $d$  and  $u$  represent that the plane waves are transmitted downward and upward. The expressions of those wave functions are given in Ref. [29].

According to Eq. (2), the variables in at the  $q$ -th layer (i.e.,  $q \neq S$ ) can be re-expressed in the double wavenumber and frequency domains as

$$\begin{aligned}\hat{\hat{\Omega}}^{(q)}(x_{(q)}, k_y, k_z, \omega) &= \left[ \hat{\hat{u}}_x^{(q)} \hat{\hat{u}}_y^{(q)} \hat{\hat{u}}_z^{(q)} \hat{\hat{p}}_{,x}^{(q)} \hat{\hat{\tau}}_{xx}^{(q)} \hat{\hat{\tau}}_{xy}^{(q)} \hat{\hat{\tau}}_{xz}^{(q)} \hat{\hat{p}}^{(q)} \right]^T \\ &= \begin{bmatrix} \mathbf{D}_d^{(q)}(k_y, k_z, \omega) & \mathbf{D}_u^{(q)}(k_y, k_z, \omega) \\ \mathbf{S}_d^{(q)}(k_y, k_z, \omega) & \mathbf{S}_u^{(q)}(k_y, k_z, \omega) \end{bmatrix} \begin{bmatrix} \mathbf{E}_d^{(q)}(x_{(q)}) & \mathbf{0} \\ \mathbf{0} & \mathbf{E}_u^{(q)}(x_{(q)}) \end{bmatrix} \begin{bmatrix} \mathbf{A}_d^{(q)} \\ \mathbf{A}_u^{(q)} \end{bmatrix}\end{aligned}\quad (3)$$

where the coefficient matrixes  $\mathbf{D}_d^{(q)}$ ,  $\mathbf{D}_u^{(q)}$ ,  $\mathbf{S}_d^{(q)}$ ,  $\mathbf{S}_u^{(q)}$ ,  $\mathbf{E}_d^{(q)}$ , and  $\mathbf{E}_u^{(q)}$  are determined by Eq. (2).  $\mathbf{A}_d^{(q)}$  and  $\mathbf{A}_u^{(q)}$  are the  $4 \times 1$  unknown coefficient vectors.

Then, through the transfer matrix method [25], the unknown coefficient vectors  $\mathbf{A}_d^{(S-1)}$ ,  $\mathbf{A}_u^{(S-1)}$  in the  $(S-1)$ -th layer and  $\mathbf{A}_d^{(S+1)}$ ,  $\mathbf{A}_u^{(S+1)}$  in the  $(S+1)$ -th layer are related via:

$$\mathbf{A}_d^{(S-1)} = -(\mathbf{RT}_{d21}^{(1)} - \mathbf{T}_{d11}^{(1)})^{-1}(\mathbf{RT}_{d22}^{(1)} - \mathbf{T}_{d12}^{(1)})\mathbf{A}_u^{(S-1)} = \mathbf{Q}_d\mathbf{A}_u^{(S-1)}\quad (4)$$

$$\mathbf{A}_d^{(S+1)} = -\left[\mathbf{T}_{u21}^{(Q+1)}\right]^{-1}\mathbf{T}_{u22}^{(Q+1)}\mathbf{A}_u^{(S+1)} = \mathbf{Q}_u\mathbf{A}_u^{(S+1)}\quad (5)$$

with

$$\mathbf{R} = -\mathbf{E}_u^{(q)}(h_1)\left[\mathbf{S}_d^{(1)}\right]^{-1}\left[\mathbf{S}_u^{(1)}\right]\mathbf{E}_u^{(q)}(h_1)\quad (6)$$

where the expressions of the transfer matrixes  $\mathbf{T}_{dij}^{(q)}$  and  $\mathbf{T}_{uij}^{(q)}$  ( $i, j = 1, 2$ ) were given by He et al. [25].

The wave field in the source layer  $L_S$  contains the up- and down-going plane waves and the outgoing cylindrical waves. Thus, the variables  $\hat{\hat{\mathbf{u}}}^{(S)}$ ,  $\hat{\hat{P}}^{(S)}$  and  $\hat{\hat{\tau}}^{(S)}$  are expressed in the wavenumber and frequency domains as

$$\begin{aligned}\hat{\mathbf{u}}^{(S)} &= \frac{2}{\pi} \int_0^{+\infty} \sum_{j=1}^4 (A_{dj}^{(S)} \hat{\phi}_{dj}^{(S)} + A_{uj}^{(S)} \hat{\phi}_{uj}^{(S)}) dk_y + \sum_{m=-M}^M \sum_{j=1}^4 A_{mj}^t \hat{\chi}_{mj}(r, \theta, k_z, \omega), \\ \hat{p}^{(S)} &= \frac{2}{\pi} \int_0^{+\infty} \sum_{j=3}^4 \left[ A_{dj}^{(S)} \hat{\vartheta}_{dj}^{(S)} + A_{uj}^{(S)} \hat{\vartheta}_{uj}^{(S)} \right] dk_y + \sum_{m=-M}^M \sum_{j=1}^4 A_{mj}^t \hat{\kappa}_{mj}(r, \theta, k_z, \omega), \quad (7) \\ \hat{\boldsymbol{\tau}}^{(S)} &= \frac{2}{\pi} \int_0^{+\infty} \sum_{j=1}^4 (A_{dj}^{(S)} \hat{\psi}_{dj}^{(S)} + A_{uj}^{(S)} \hat{\psi}_{uj}^{(S)}) dk_y + \sum_{m=-M}^M \sum_{j=1}^4 A_{mj}^t \hat{\eta}_{mj}(r, \theta, k_z, \omega)\end{aligned}$$

where  $\hat{\chi}_{mj}$ ,  $\hat{\kappa}_{mj}$ , and  $\hat{\eta}_{mj}$  represent the outgoing cylindrical wave functions for solid displacements, pore-fluid pressure, and stresses, respectively, with  $A_{mj}^t$  being the corresponding unknown coefficients. The expressions of those wave functions were given in Ref. [29].

To handle the boundary conditions of the interfaces, the cylindrical waves need to be transformed into the corresponding plane waves. This requirement can be solved by the following integral representations of Hankel function of the first kind [30]:

$$H_n^{(1)}(\gamma r) e^{im\theta} = \frac{1}{\pi} \int_{-\infty}^{+\infty} \frac{i^{-m}}{k_x} e^{i(m\beta + k_y y + k_x x)} dk_y, \quad x > 0 \quad (8)$$

$$H_n^{(1)}(\gamma r) e^{im\theta} = \frac{1}{\pi} \int_{-\infty}^{+\infty} \frac{i^m}{k_x} e^{i(-m\beta + k_y y - k_x x)} dk_y, \quad x < 0 \quad (9)$$

in which  $\gamma = \sqrt{k_x^2 + k_y^2}$  is the radial wavenumber.

When  $x^{(S)} > 0$ , substituting Eqs. (8) into (7) gives the variables  $\hat{\tilde{\Omega}}^{(S)}$  of  $L_s$  in the double wavenumber and frequency domains as

$$\hat{\tilde{\Omega}}^{(S)} = \begin{bmatrix} \mathbf{D}_d^{(S)} & \mathbf{D}_u^{(S)} \\ \mathbf{S}_d^{(S)} & \mathbf{S}_u^{(S)} \end{bmatrix} \begin{bmatrix} \mathbf{E}_d^{(S)}(x_{(S)}) & \mathbf{0} \\ \mathbf{0} & \mathbf{E}_u^{(S)}(x_{(S)}) \end{bmatrix} \begin{bmatrix} \mathbf{A}_d^{(S)} \\ \mathbf{A}_u^{(S)} \end{bmatrix} + \begin{bmatrix} \mathbf{D}'_u \mathbf{E}'_u(x_{(S)}) \mathbf{A}^t \\ \mathbf{S}'_u \mathbf{E}'_u(x_{(S)}) \mathbf{A}^t \end{bmatrix} \quad (10)$$

When  $x^{(S)} < 0$ , Substituting Eqs. (9) into (7) gives the variables  $\hat{\tilde{\Omega}}^{(S)}$  of  $L_s$  in the double wavenumber and frequency domains as

$$\hat{\tilde{\Omega}}^{(S)} = \begin{bmatrix} \mathbf{D}_d^{(S)} & \mathbf{D}_u^{(S)} \\ \mathbf{S}_d^{(S)} & \mathbf{S}_u^{(S)} \end{bmatrix} \begin{bmatrix} \mathbf{E}_d^{(S)}(x_{(S)}) & \mathbf{0} \\ \mathbf{0} & \mathbf{E}_u^{(S)}(x_{(S)}) \end{bmatrix} \begin{bmatrix} \mathbf{A}_d^{(S)} \\ \mathbf{A}_u^{(S)} \end{bmatrix} + \begin{bmatrix} \mathbf{D}'_d \mathbf{E}'_d(x_{(S)}) \mathbf{A}^t \\ \mathbf{S}'_d \mathbf{E}'_d(x_{(S)}) \mathbf{A}^t \end{bmatrix} \quad (11)$$

where the components of matrixes  $\mathbf{D}'_u$ ,  $\mathbf{D}'_d$ ,  $\mathbf{S}'_u$ ,  $\mathbf{S}'_d$ ,  $\mathbf{E}'_u(x_{(S)})$ , and  $\mathbf{E}'_d(x_{(S)})$  are given by



$$\begin{cases} D_u^t(j, l + 4m + 4M) = D_u^{(S)}(j, l)T_{umj}/k_{xj}^{(S)} \\ D_d^t(j, l + 4m + 4M) = D_d^{(S)}(j, l)T_{dmj}/k_{xj}^{(S)} \\ S_u^t(j, l + 4m + 4M) = S_u^{(S)}(j, l)T_{umj}/k_{xj}^{(S)} \\ S_d^t(j, l + 4m + 4M) = S_d^{(S)}(j, l)T_{dmj}/k_{xj}^{(S)} \end{cases}, \quad \begin{matrix} j = 1, 2, 3, 4 \\ l = 1, 2, 3, 4 \\ m = -M, \dots, M \end{matrix}$$

$$E_u^t(j + 4m + 4M, l + 4m + 4M) = \begin{cases} e^{ik_{xs}^{(S)}x(s)}, & j = l = 1, 2 \\ e^{ik_{xp1}^{(S)}x(s)}, & j = l = 3 \\ e^{ik_{xp2}^{(S)}x(s)}, & j = l = 4 \\ 0, & j \neq l \end{cases}, \quad [\mathbf{E}_d^t(x(s))] = [\mathbf{E}_u^t(x(s))]^{-1} \quad (12)$$

in which  $k_{xj} = k_{xs}$  for  $j = 1, 2$ ,  $k_{xj} = k_{xp1}$  for  $j = 3$ , and  $k_{xj} = k_{xp2}$  for  $j = 4$ ;  $T_{umj}$  and  $T_{dmj}$  are expressed as

$$T_{umj} = i^{-m} = \begin{cases} e^{im\beta_s} \\ e^{im\beta_{p1}} \\ e^{im\beta_{p2}} \end{cases}, \quad T_{dmj} = i^m = \begin{cases} e^{-im\beta_s} & \beta_s = \arcsin(k_y/k_{rs}), & j = 1, 2 \\ e^{-im\beta_{p1}} & \beta_{p1} = \arcsin(k_y/k_{rp1}), & j = 3 \\ e^{-im\beta_{p2}} & \beta_{p2} = \arcsin(k_y/k_{rp2}), & j = 4 \end{cases} \quad (13)$$

Next, according to the continuity conditions at the upper interface ( $x_{(s)} = h_{t1}$ ) and lower interface ( $x_{(s)} = h_{t2}$ ), the combination of Eqs. (3), (4), (5), (9) and (10) gives the relationship between  $A_{dj}^{(S)}$ ,  $A_{uj}^{(S)}$ , and  $A_{mj}^t$  as

$$A_{dj}^{(S)} = \sum_{m'=-M}^M \sum_{j'=1}^4 L_{jm'j'}^d A_{m'j'}^t, \quad A_{uj}^{(S)} = \sum_{m'=-M}^M \sum_{j'=1}^4 L_{jm'j'}^u A_{m'j'}^t \quad (14)$$

with

$$\begin{aligned} [L_{jm'j'}^d] &= -[\mathbf{K}_{u1}^{-1}\mathbf{K}_{d1} - \mathbf{K}_{u2}^{-1}\mathbf{K}_{d2}]^{-1}[\mathbf{K}_{u1}^{-1}\mathbf{K}_{t1} - \mathbf{K}_{u2}^{-1}\mathbf{K}_{t2}], \\ [L_{jm'j'}^u] &= -[\mathbf{K}_{d1}^{-1}\mathbf{K}_{u1} - \mathbf{K}_{d2}^{-1}\mathbf{K}_{u2}]^{-1}[\mathbf{K}_{d1}^{-1}\mathbf{K}_{t1} - \mathbf{K}_{d2}^{-1}\mathbf{K}_{t2}], \\ \mathbf{K}_{d1} &= [(\mathbf{D}_d^{(S-1)}\mathbf{Q}_d + \mathbf{D}_u^{(S-1)})^{-1}\mathbf{D}_d^{(S)} - (\mathbf{S}_d^{(S-1)}\mathbf{Q}_d + \mathbf{S}_u^{(S-1)})^{-1}\mathbf{S}_d^{(S)}]\mathbf{E}_d^{(S)}(h_{t1}), \\ \mathbf{K}_{u1} &= [(\mathbf{D}_d^{(S-1)}\mathbf{Q}_d + \mathbf{D}_u^{(S-1)})^{-1}\mathbf{D}_u^{(S)} - (\mathbf{S}_d^{(S-1)}\mathbf{Q}_d + \mathbf{S}_u^{(S-1)})^{-1}\mathbf{S}_u^{(S)}]\mathbf{E}_u^{(S)}(h_{t1}), \\ \mathbf{K}_{t1} &= [(\mathbf{D}_d^{(S-1)}\mathbf{Q}_d + \mathbf{D}_u^{(S-1)})^{-1}\mathbf{D}_u^t - (\mathbf{S}_d^{(S-1)}\mathbf{Q}_d + \mathbf{S}_u^{(S-1)})^{-1}\mathbf{S}_u^t]\mathbf{E}_u^t(h_{t1}), \\ \mathbf{K}_{d2} &= [(\mathbf{D}_d^{(S+1)}\mathbf{Q}_u + \mathbf{D}_u^{(S+1)})^{-1}\mathbf{D}_d^{(S)} - (\mathbf{S}_d^{(S+1)}\mathbf{Q}_u + \mathbf{S}_u^{(S+1)})^{-1}\mathbf{S}_d^{(S)}]\mathbf{E}_d^{(S)}(-h_{t2}), \\ \mathbf{K}_{u2} &= [(\mathbf{D}_d^{(S+1)}\mathbf{Q}_u + \mathbf{D}_u^{(S+1)})^{-1}\mathbf{D}_u^{(S)} - (\mathbf{S}_d^{(S+1)}\mathbf{Q}_u + \mathbf{S}_u^{(S+1)})^{-1}\mathbf{S}_u^{(S)}]\mathbf{E}_u^{(S)}(-h_{t2}), \\ \mathbf{K}_{t2} &= [(\mathbf{D}_d^{(S+1)}\mathbf{Q}_u + \mathbf{D}_u^{(S+1)})^{-1}\mathbf{D}_d^t - (\mathbf{S}_d^{(S+1)}\mathbf{Q}_u + \mathbf{S}_u^{(S+1)})^{-1}\mathbf{S}_{de}^t]\mathbf{E}_d^t(-h_{t2}) \end{aligned} \quad (15)$$

Next, the variables in the source layer  $L_s$  also need to be expressed in the cylindrical coordinate system to impose the boundary conditions of cavity surface. The following relationships are introduced to satisfy this requirement [30]:

$$\begin{aligned} e^{i(k_y y - k_x x)} &= \sum_{m=-M}^M i^{-m} e^{im\beta} J_m(\gamma r) e^{im\theta}, \\ e^{i(k_y y + k_x x)} &= \sum_{m=-M}^M i^m e^{-im\beta} J_m(\gamma r) e^{im\theta} \end{aligned} \quad (16)$$

The substitution of Eqs. (14) and (16) into (7), the variables  $\hat{\mathbf{u}}^{(S)}$ ,  $\hat{\mathbf{P}}^{(S)}$ , and  $\hat{\boldsymbol{\tau}}^{(S)}$  are expressed in the cylindrical coordinate system as

$$\begin{aligned} \hat{\mathbf{u}}^{(S)} &= \sum_{m=-M}^M \sum_{j=1}^4 \left[ \frac{1}{2\pi} \int_{-\infty}^{+\infty} \hat{\chi}_{mj}^R \sum_{m'=-M}^M \sum_{j'=1}^4 (T_{umj} L_{jm'j'}^d + T_{dmj} L_{jm'j'}^u) A_{m'j'}^t dk_y + A_{mj}^t \hat{\chi}_{mj} \right], \\ \hat{\mathbf{P}}^{(S)} &= \sum_{m=-M}^M \sum_{j=3}^4 \left[ \frac{1}{2\pi} \int_{-\infty}^{+\infty} \hat{\kappa}_{mj}^R \sum_{m'=-M}^M \sum_{j'=1}^4 (T_{umj} L_{jm'j'}^d + T_{dmj} L_{jm'j'}^u) A_{m'j'}^t dk_y + A_{mj}^t \hat{\kappa}_{mj} \right], \\ \hat{\boldsymbol{\tau}}^{(S)} &= \sum_{m=-M}^M \sum_{j=1}^4 \left[ \frac{1}{2\pi} \int_{-\infty}^{+\infty} \hat{\eta}_{mj}^R \sum_{m'=-M}^M \sum_{j'=1}^4 (T_{umj} L_{jm'j'}^d + T_{dmj} L_{jm'j'}^u) A_{m'j'}^t dk_y + A_{mj}^t \hat{\eta}_{mj} \right] \end{aligned} \quad (17)$$

Next, the solution for the cylindrical shell can be obtained following the derivation of the method proposed by Forrest and Hunt [17] and He et al. [26], which is given by

$$\mathbf{K}_{tm} \left[ -\hat{U}_m, \hat{V}_m, \hat{W}_m \right]^T + \left[ \hat{Q}_{rz m}, -\hat{Q}_{r\theta m}, -\hat{Q}_{rr m} \right]^T = \left[ \hat{F}_{z m}, \hat{F}_{\theta m}, \hat{F}_{r m} \right]^T \quad (18)$$

where the expression of the  $3 \times 3$  coefficient matrix  $\mathbf{K}_{tm}$  was provided by He et al. [26].  $\left[ \hat{F}_{z m}, \hat{F}_{\theta m}, \hat{F}_{r m} \right]^T$  represent the load components applied to the inside surface of shell. For a unit point load with a frequency  $f_0$  and velocity  $v_0$  radially applied to the shell at the tunnel invert, the expression of the load is as follow:

$$\left[ \hat{F}_{z m}, \hat{F}_{\theta m}, \hat{F}_{r m} \right]^T = \left[ 0, 0, \frac{\varepsilon_m (-1)^m}{2\pi a} \delta(w - 2\pi f_0 + k_z v_0) \right]^T \quad (19)$$

Combining Eqs. (17) to (19), the continuity conditions at the tunnel-soil interface give

$$\sum_{j=1}^4 \left[ \frac{2}{\pi} \int_0^{+\infty} \varepsilon_m (\mathbf{K}'_{tm} \hat{\chi}_{mj}^R(r=a) + \hat{\eta}_{mj}^R(r=a)) \sum_{m'=0}^M \sum_{j'=1}^4 (T_{umj} L_{jm'j'}^d + T_{dmj} L_{jm'j'}^u) A_{m'j'}^t dk_y + A_{mj}^t (\mathbf{K}'_{tm} \hat{\chi}_{mj}^R(r=a) + \hat{\eta}_{mj}^R(r=a)) \right] = [0, 0, \frac{\varepsilon_m(-1)^m}{2\pi a} \delta(w - 2\pi f_0 + k_z v_0)]^T \quad (20)$$

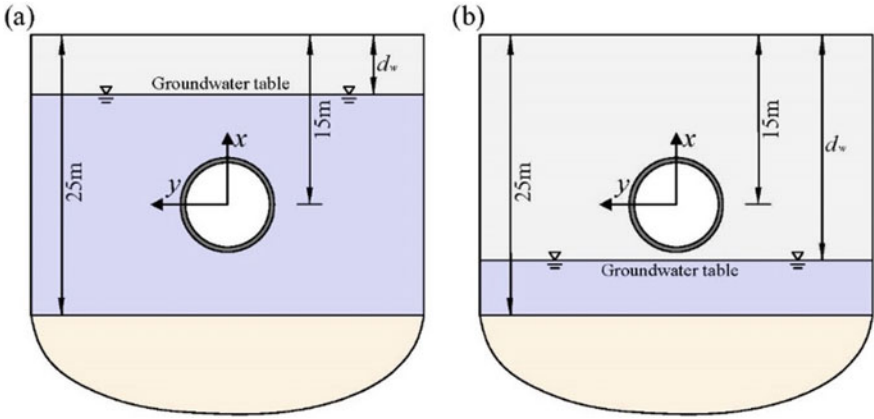
In addition, the tunnel is assumed to be fully impermeable. Therefore, the pore-fluid pressure gradient vanishes at the outside surface of the shell, which yields

$$\sum_{j=3}^4 \left[ \frac{2}{\pi} \int_0^{+\infty} \varepsilon_m \frac{\hat{\kappa}_{mj}^R}{\partial r} \right]_{r=a} \sum_{m'=0}^M \sum_{j'=1}^4 (T_{umj} L_{jm'j'}^d + T_{dmj} L_{jm'j'}^u) A_{m'j'}^t dk_y + A_{mj}^t \frac{\partial \hat{\kappa}_{mj}^R}{\partial r} \Big|_{r=a} = \mathbf{0} \quad (21)$$

The unknown coefficients  $A_{mj}^t$  can be calculated from Eqs. (20) and (21) for each  $m$ . The coefficients  $A_{dj}^{(q)}$  and  $A_{uj}^{(q)}$  can subsequently be determined by the transfer matrix method.

### 3 Numerical Results and Discussion

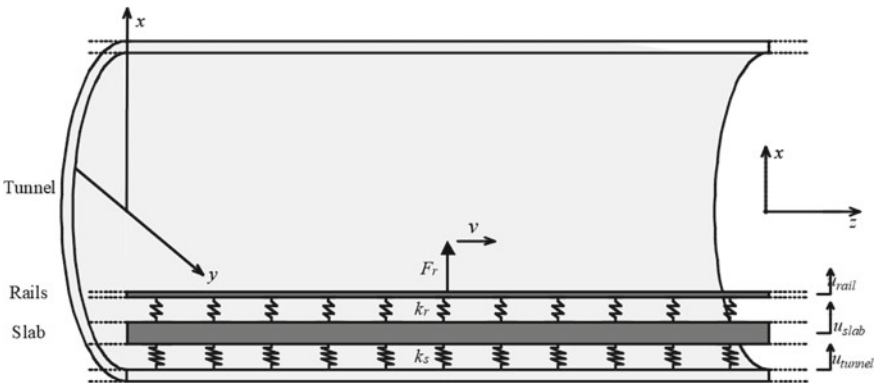
In this section, the impact of the variation in the groundwater table on train-induced vibrations is investigated by a numerical case. A single tunnel in a three-layered half-space is considered, as shown in Fig. 2. The depth of the tunnel center to the ground surface is 15 m, and the total thickness of the first and second layers is fixed at  $h_1 + h_2 = 25$  m. The tunnel that is made of concrete with a Young's modulus  $E_t = 50$  GPa, Poisson's ratio  $\nu_t = 0.3$ , density  $\rho_t = 2500$  kg/m<sup>3</sup>, and material damping ratio  $\beta_t = 0.015$  has a mean radius  $a = 3$  m and thickness  $h = 0.25$  m. Table 1 presents the parameter values used to model the soil layers. The first layer is above the groundwater table, which has the same lamé constant as the second layer, and density  $\rho_b = (1 - \phi)\rho_s = 1089.6$  kg/m<sup>3</sup>. By assigning the parameters  $\rho_f = 0.001$  kg/m<sup>3</sup>,  $\alpha = 0.001$ ,  $M = 1000$  Pa,  $K = 10^5$  m<sup>3</sup>kg<sup>-1</sup> s, the effect of pore water can be ignored [31]. Four values of the depth of the groundwater table are considered, which are  $d_w = 5$  m, 10 m, 20 m, and 25 m. The cases of  $d_w = 5$  m and 10 m indicate that the groundwater table is above the tunnel, as shown in Fig. 2a, while the cases of  $d_w = 20$  m and 25 m represent that the groundwater table is under the tunnel (Fig. 2b).  $d_w = 0$  m that represents a saturated poroelastic layered half-space is considered as a reference case.



**Fig. 2** A single tunnel embedded in a three-layered half-space: **a** under the groundwater table and **b** above the groundwater table

**Table 1** Parameter values defining the properties of the three soil layers

Parameter	First layer	Second layer	Third layer
First lamé constant, $\lambda$ (Pa)	$0.58 \times 10^8$	$0.58 \times 10^8$	$2.33 \times 10^8$
Second lamé constant, $\mu$ (Pa)	$0.25 \times 10^8$	$0.25 \times 10^8$	$1.0 \times 10^8$
Density of bulk material, $\rho_b$ (kg/m <sup>3</sup> )	1089.6	1489.6	1489.6
Material damping ratio, $\beta_s$	0.05	0.05	0.05
Density of pore fluid, $\rho_f$ (kg/m <sup>3</sup> )	0.001	1000	1000
Porosity, $\phi$	0.4	0.4	0.4
First Biot parameter, $a$	0.001	1	1
Second Biot parameter, $M$	1000	$6.13 \times 10^9$	$6.13 \times 10^9$
Tortuosity, $a_\infty$	1	1	1
Hydraulic permeability coefficient, $K$ (m <sup>3</sup> kg <sup>-1</sup> s)	$1.0 \times 10^5$	$1.0 \times 10^{-7}$	$1.0 \times 10^{-7}$



**Fig. 3** Geometry of a double-beam track system in a circular tunnel

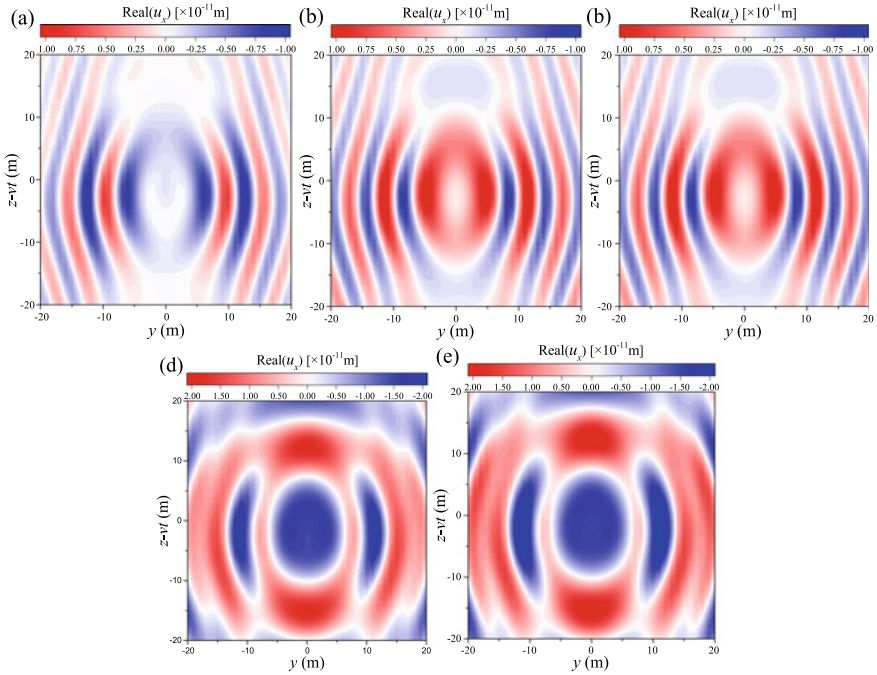
**Table 2** Parameter values defining the properties of the track structures

Parameter	Value
Bending stiffness of two rails, $E_r I_r$	$10 \times 10^6 \text{ Pa}\cdot\text{m}^4$
Loss factor of rails in bending, $\eta_r$	0.03
Mass of two rails per unit length, $m_r$	100 kg/m
Normal stiffness of rail pads, $k_{rp}$	$40 \times 10^6 \text{ N/m}^2$
Loss factor of rail pads, $\eta_{rp}$	0.1
Bending stiffness of slab in the vertical direction, $E_s I_s$	$1430 \times 10^6 \text{ Pa}\cdot\text{m}^4$
Loss factor of slab in bending, $\eta_r$	0.05
Mass of slab per unit length, $m_s$	3500 kg/m

As shown in Fig. 3, track structures are subsequently considered as a double-beam model. The rails and slab are simulated as an Euler–Bernoulli beam with infinite length, respectively, while the rail pad and slab bearings are simplified as spring with continuous supports. The derivations of the fully track model were given by Forrest and Hunt [18]. The parameter values used to simulate the track structures are presented in Table 2.

Figure 4 presents the real part of the vertical displacement ( $\text{Real}(u_x)$ ) on the ground surface induced by a unit harmonic load of 40 Hz moving on the rails at 20 m/s. The displacement fields in Fig. 4a–c show the similar trend, and the same wavelength. It is indicated that when the groundwater table is above the tunnel, the displacement distribution tends to that of the saturated poroelastic layered half-space. However, when the groundwater table drops below the tunnel, as shown in Fig. 4d, e, the displacement fields change, and the wavelength increases. The displacement field in those cases tends to that of a dry single-phase layered half-space.

To quantitatively assess the effect of the variation in the groundwater table on vibrations, the insert gain (IG) that represents the difference of vibration levels between the four cases and the reference case ( $d_w = 0 \text{ m}$ ) is defined as  $\text{IG} = 20\log(|u|/|u'|)$ . Figure 5 shows the vertical displacements and insert gain at three observation points on the ground surface induced by a harmonic load moving at 20 m/s. In the low-frequency region, the variation in the groundwater table has a small influence on the ground vibrations. The vibration levels increase slightly as the groundwater table drops down. However, the effect of the variation in groundwater table on the ground vibrations becomes significant when the frequency increases, inducing IG values up to 20 dB. Due to the existence of the pore water, the compression modulus of the soil increases. Therefore, as the groundwater table drops down, the soil stiffness decreases, resulting in higher vibration levels. However, when the groundwater table is under the tunnel, the further drop in the groundwater table has little effect on the ground vibration levels.

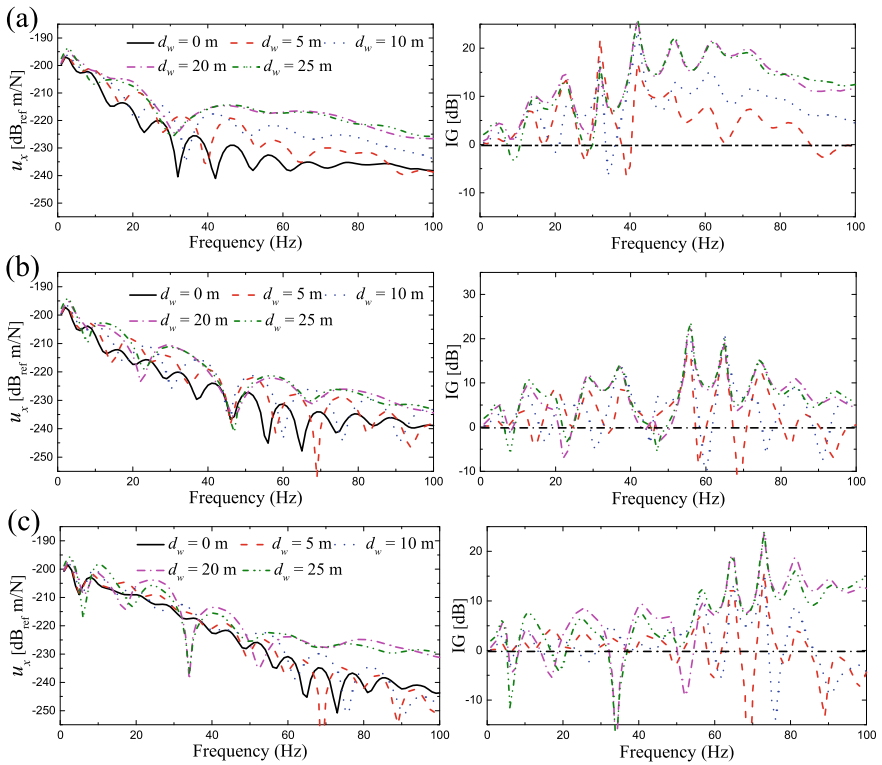


**Fig. 4** Vertical displacement fields on the ground surface in the cases of **a**  $d_w = 0$  m, **b**  $d_w = 5$  m, **c**  $d_w = 10$  m, **d**  $d_w = 20$  m, and **e**  $d_w = 25$  m induced by a unit harmonic load of 40 Hz moving on the rails at 20 m/s

### 4 Conclusions

An analytical model was proposed in this study to investigate the influence of the variation in the groundwater table on the ground vibrations induced by underground railways. The transfer matrix method was applied to deal with wave propagation in the dry/saturated multi-layered half-space. By using the boundary conditions on the tunnel-soil interface, the tunnel was coupled with the multi-layered soil.

The influence of the variation in groundwater table on the ground vibrations was subsequently investigated through a numerical case. The displacement field is similar to that of a saturated layered half-space when the groundwater table is above the tunnel, while it is similar to that of a dry single-phase layered half-space when the groundwater table is below the tunnel. When the groundwater table is above the tunnel, the ground vibration levels increase as the groundwater table drops. When the groundwater table is under the tunnel, the variation in groundwater table has little effect on the ground vibration levels.



**Fig. 5** Vertical displacements and IG at points **a** (15 m, 0 m, 0 m), **b** (15 m, 5 m, 0 m), and **c** (15 m, 10 m, 0 m) on the ground surface for different groundwater table

**Acknowledgements** This project is supported by Projects of International Cooperation and Exchanges NSFC under grant number 51761135109 and the Fundamental Research Funds for the Central Universities.

## References

1. Thompson DJ, Kouroussis G, Ntotsios E (2019) Modelling, simulation and evaluation of ground vibration caused by rail vehicles. *Veh Syst Dyn* 57(7):936–983
2. Yang J, Zhu S, Zhai W, Kouroussis G, Wang Y, Wang KY et al (2019) Prediction and mitigation of train-induced vibrations of large-scale building constructed on subway tunnel. *Sci Total Environ* 668:485–499
3. Kouroussis G, Zhu S, Olivier B, Ainalis D, Zhai W (2019) Urban railway ground vibrations induced by localized defects: using dynamic vibration absorbers as mitigation solution. *J Zhejiang Univ-Sci A* 20(2): 83–97
4. Zhai W, He Z, Song X (2011) Prediction of high-speed train induced ground vibration based on train-track-ground system model. *Earthq Eng Eng Vib* 9:545–554

5. Bian XC, Jin WF, Jiang HG (2012) Ground-borne vibrations due to dynamic loadings from moving trains in subway tunnels. *J Zhejiang Univ-Sci A (Appl Phys Eng)* 13(11):870–876
6. Sheng X, Jones CJC, Thompson DJ (2006) Prediction of ground vibration from trains using the wavenumber finite and boundary element methods. *J Sound Vib* 293(3–5):575–586
7. François S, Schevenels M, Galvín P, Lombaert G, Degrande G (2011) A 2.5D coupled FE-BE methodology for the dynamic interaction between longitudinally invariant structures and a layered halfspace. *Comput Meth Appl Mech Eng* 199:1536–1548
8. He C, Zhou SH, Guo PJ, Di HG, Zhang XH (2018) Modelling of ground vibration from tunnels in a poroelastic half-space using a 2.5-D FE-BE formulation. *Tunn Underg Sp Tech* 82:211–221
9. He C, Zhou SH, Guo P, Di HG, Xiao JH (2018) Dynamic 2.5-D Green's function for a point load or a point fluid source in a layered poroelastic half-space. *Eng Anal Bound Elem* 77:123–137
10. Jin QY, Thompson DJ, Lurcock DEJ, Toward MGR, Ntotsios E (2018) A 2.5D finite element and boundary element model for the ground vibration from trains in tunnels and validation using measurement data. *J Sound Vib* 422:373–389
11. Zhou S, He C, Guo P, Yu F (2019) Dynamic response of a segmented tunnel in saturated soil using a 2.5-D FE-BE methodology. *Soil Dyn Earthq Eng* 120:386–397
12. Chebli H, Othman R, Clouteau D, Arnst M, Degrande G (2008) 3D periodic BE-FE model for various transportation structures interacting with soil. *Comput Geotech* 35:22–32
13. Yang YB, Hung H (2008) Soil vibrations caused by underground moving trains. *J Geotech Geoenviron Eng* 134(11):1633–1644
14. Yan YB, Liang XJ, Huang H, Wu YT (2017) Comparative study of 2D and 2.5D responses of long underground tunnels to moving train loads. *Soil Dyn Earthq Eng* 97:86–100
15. Lopes P, Alves Costa P, Ferraz M, Silva Cardoso A (2014) Numerical modeling of vibrations induced by railway traffic in tunnels: from the source to the nearby buildings. *Soil Dyn Earthq Eng* 61–62:269–285
16. Zhu ZH, Wang LD, Alves Costa P, Bai Y, Yu ZW (2019) An efficient approach for prediction of subway train-induced ground vibrations considering random track unevenness. *J Sound Vib* 455:359–379
17. Forrest JA, Hunt HEM (2006) A three-dimensional tunnel model for calculation of train-induced ground vibration. *J Sound Vib* 294(4–5):678–705
18. Forrest JA, Hunt HEM (2006) Ground vibration generated by trains in underground tunnels. *J Sound Vib* 294(4–5):706–736
19. Hussein MFM, Hunt HEM (2007) A numerical model for calculating vibration from a railway tunnel embedded in a full-space. *J Sound Vib* 305(3):401–431
20. Hussein MFM, Hunt HEM (2009) A numerical model for calculating vibration due to a harmonic moving load on a floating-slab track with discontinuous slabs in an underground railway tunnel. *J Sound Vib* 321(1):363–374
21. Zhou SH, He C, Di HG, Guo PJ, Zhang XH (2017) An efficient method for predicting train-induced vibrations from a tunnel in a poroelastic half-space. *Eng Anal Bound Elem* 85:43–56
22. Jones S, Hunt H (2011) Voids at the tunnel-soil interface for calculation of ground vibration from underground railways. *J Sound Vib* 330(2):245–270
23. He C, Zhou SH, Guo PJ, Di HG, Yang XW (2019) A three-dimensional semi-analytical method for calculating vibrations from a moving load on a periodic jointed tunnel. *Comput Geotech* 114:103150
24. Hussein MFM, François S, Schevenels M, Hunt HEM, Talbot JP, Degrande G (2014) The fictitious force method for efficient calculation of vibration from a tunnel embedded in a multi-layered half-space. *J Sound Vib* 333:6996–7018
25. He C, Zhou SH, Di HG, Guo PJ, Xiao JH (2018) Analytical method for calculation of ground vibration from a tunnel embedded in a multi-layered halfspace. *Comput Geotech* 99:149–164
26. He C, Zhou SH, Guo PJ, Di HG, Xiao JH, Yu F (2019) Theoretical modelling of the dynamic interaction between twin tunnels in a multi-layered half-space. 456:65–85
27. Biot MA (1956) Theory of propagation of elastic waves in a fluid-saturated porous solid, I, low frequency range. *J Acoust Soc Am* 28:168–178



28. Biot MA (1962) Mechanics of deformation and acoustic propagation in porous media. *J Appl Phys* 33:1482–1498
29. Zhou SH, He C, Guo PJ, Di HG, Zhang XH (2020) Modelling of vehicle-track-tunnel-soil system considering the dynamic interaction between twin tunnels in a poroelastic half-space. *Int J Geomech* 20(1):04019144
30. Boström A, Kristensson G, Ström S (1991) Transformation properties of plane, spherical and cylindrical scalar and vector wave functions. In: Varadan VV, Lakhtakia A, Varadan VK (eds) *Field representations and introduction to scattering*. Elsevier, Amsterdam, pp 165–210
31. Lu JF, Jeng DS, Williams SA (2008) 2.5-D dynamic model for a saturated porous medium: Part I. Green's function. *Int J Solids Struct* 45(2):378–391

# Experimental Studies on Three Types of Vibration Isolators for Buildings Near Subways



Tao Sheng, Xue-cheng Bian, Wei-xing Shi, Jia-zeng Shan, and Gan-bin Liu

**Abstract** This paper presents three types of vibration isolators to enhance the comfort for residents inside buildings near subways. Stacked sandbags formed the first type of isolator. An elastic and closed capsule filled with sand and rubber particles is the second type of isolator. The third type of isolator is laminated thick rubber bearing with a sliding bottom. The materials and components of the three isolators are described first. Then, the vertical stiffness values, the damping ratios, and the ultimate bearing capacities of the above isolators are tested in a laboratory, and the suppression effectiveness for subway-induced vertical vibrations are investigated by two full-scale buildings near subway transportation. The results indicated that the bearing capacity of the first isolator is the lowest, but the damping ratio is the highest. For the second isolator, the vertical stiffness and damping ratio can be adjusted by changing the mixture ratio of sand particles, and the bearing capacity is improved significantly. For the third isolator, the damping ratio is the smallest, but the sliding bottom is capable of isolating earthquake ground motions. After installation of the three isolators, the human comfort inside the buildings satisfied the limit values, proving that they are effective as base isolation methods for buildings near subways.

**Keywords** Stacked sandbags · Vertical stiffness · Subways · Field experiment · Base isolation

---

T. Sheng (✉) · G. Liu  
Ningbo University, Ningbo 315211, China  
e-mail: [shengtao@nbu.edu.cn](mailto:shengtao@nbu.edu.cn)

G. Liu  
e-mail: [liuganbin@nbu.edu.cn](mailto:liuganbin@nbu.edu.cn)

X. Bian  
Zhejiang University, Hangzhou 310058, China  
e-mail: [bianxc@zju.edu.cn](mailto:bianxc@zju.edu.cn)

W. Shi · J. Shan  
Tongji University, Shanghai 200092, China  
e-mail: [jzshan@tongji.edu.cn](mailto:jzshan@tongji.edu.cn)

# 1 Introduction

Subway transportation advantages include convenience, punctuality and low pollution, and therefore a large number of subway lines are planned, constructed or are under construction all over the world. Especially in the Asian countries, the construction of subway networks has been a critical investment area since the beginning of this century. However, such transportation networks may have negative influences on human comfort inside buildings near them due to vibrations.

Generally speaking, there are three ways to solve this problem: source reduction methods [1, 2], wave barriers in the ground [3, 4] and passive isolation methods of buildings [5, 6]. Base isolation is one of the passive isolation methods and has been proved to be one of the most effective ways by Cryer [7], Sharif [8], Sheng et al. [9] and many other researchers [10, 11]. But the isolators used for buildings near subway transportation are much more complicated and expensive. Moreover, there are even several defects for the existing isolators. For example, the vertical steel spring isolator [12] struggles to resist corrosion under humid conditions. Besides, the bearing capacity of the steel spring is so small that only appropriate for lightweight buildings. The laminated thick rubber isolator proposed by Sheng et al. [9] and Pan et al. [11] cannot resist large shear deformations under earthquake ground motions. So some more reliable vibration isolators should be deeply developed to meet all the requirements under different engineering conditions.

Matsuoka et al. [13], Nakagawa et al. [14] and Liu et al. [15] discovered that friction forces between soil particles in a soil bag are a benefit to dissipating vibration energy. Inspired by the above research works, this paper presents two new types of geosynthetics isolators to suppress the vertical vibrations of a building near subway transportation. Then, for the buildings near subway transportation and in seismic areas, a new type of isolator is developed from laminated thick rubber isolator to enhance earthquake resistance functions. Furthermore, the mechanical properties and suppression effectiveness of the new isolators are verified by pseudo-static tests and field experiments.

## 2 Designs of the New Isolators

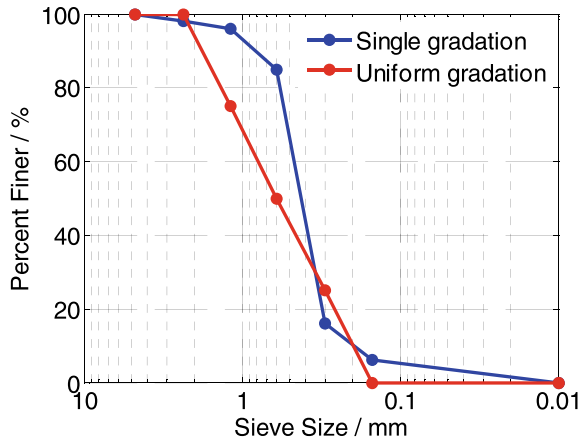
### 2.1 Stacked Sandbags

The sample size of each sandbag in this research is about 35 cm long, 25 cm wide and 8 cm thick. The bags are made of PET continuous filament nonwoven geotextiles, the properties of which are listed in Table 1. For the PET bags, the tensile parameters in the warp direction are the same as those in the weft direction. As a comparison, the properties of the PE bags applied by Liu et al. [15] are also listed in Table 1. As shown in the table, the tensile modulus of the PET bag is only one-tenth of that of the PE bag, so the vertical stiffness of stacked PET sandbags is speculated to be much

**Table 1** The properties of the PET bag and the PE bag [16]

Parameter	PET bag	PE bag
Mass per unit area (g/m <sup>2</sup> )	150	110
Thickness (mm)	1.2	Not listed
Tensile strength (kN/mm)	8	25 (warp); 16.2 (weft)
Tensile modulus (kN/m)	14.2	161 (warp); 138 (weft)
Tensile elongation (%)	50	25

**Fig. 1** Particle size distributions of the filling sand

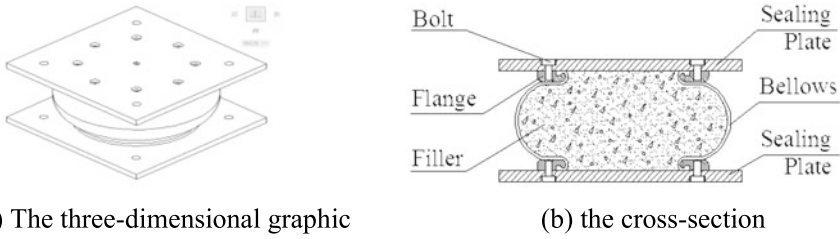


lower than ever before. At the same time, the tensile elongation of the PET bag is two times more than that of the PE bag, so the bearing capacity of PET sandbags may be enough for buildings.

Approximately 25 kg of dried sand particles are filled in each bag, and the bag mouth is sealed by high-strength cotton thread with a manual sewing machine. The sand with single and uniform gradations are filled in the bags to bear the weight of the buildings, respectively. The particle size distributions are shown in Fig. 1.

## 2.2 The Improved Geosynthetics Isolator

The air spring has an enclosed space which is much similar to a sandbag. The capsule of the air spring is composed by structural composite materials, which have excellent performances of durability, toughness and wear resistance [17]. In addition, the tensile strength of the capsule is much higher than that of the PET material, and the elastic modulus is much lower. So, the stacked sandbags are developed to be a new type of vibration isolator in this paper, which is composed by an air spring and filled particle materials. In theory, the bearing capacity of the new isolator will be much larger than that of stacked sandbags, and the vertical stiffness will be much smaller.



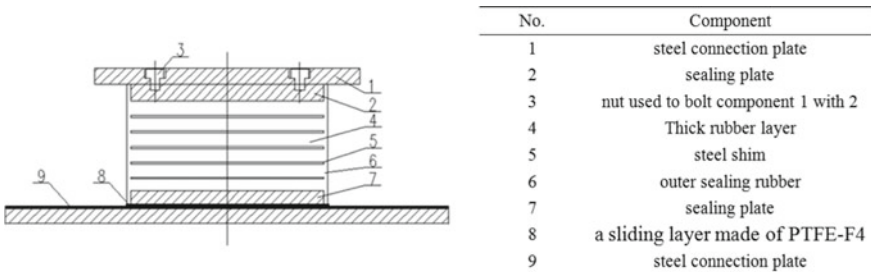
**Fig. 2** The new type of geosynthetics isolator

The three-dimensional graphic and the cross-section of the new isolator are depicted in Fig. 2.

In order to adjust the vertical stiffness and the damping ratio of the isolator, the filled particle materials are composed by sand and rubber particles. In theory, when the proportion of sand particles increases, the damping ratio increases. Similarly, when the proportion of rubber particles increases, the vertical stiffness value decreases.

### 2.3 Laminated Thick Rubber Isolator

The laminated rubber bearing is characterized as high bearing capacity and small horizontal stiffness, so it is widely used for seismic isolation. In theory, the thicker the rubber layer is, the smaller the vertical stiffness of the rubber bearing is. But the thickened rubber layer might reduce the shear deformation capacity of the isolator, so a horizontal sliding layer made of polytetrafluoroethylene (PTFE, F4) plate is designed to ensure the stability and safety of the isolator under earthquake ground motions. The basic configurations and main components of the new isolator are illustrated in Fig. 3.



**Fig. 3** The thick rubber isolator and the main components [18]

**Table 2** Testing cases for the second isolator

Cases		1 (%)	2 (%)	3 (%)	4 (%)	5 (%)
Proportions	Sand	100	75	50	25	0
	Rubber particles	0	25	50	75	100

### 3 Test Programs

#### 3.1 Mechanical Property Tests

The three new isolators were loaded from 0 kN to rupture failure status with a hydraulic universal testing machine to investigate the ultimate bearing capacity, at the speed of 1 kN/s. When the number of layers exceeds seven, the stacked sandbags are unstable. So, the sandbags were stacked from one to seven layers in the following tests. The diameter of the improved geosynthetics isolator is 280 mm, and the diameter of the laminated thick rubber isolator is 240 mm. For the geosynthetics isolator, there are five testing cases which are listed in Table 2.

To investigate the vertical stiffness values and damping ratios, the isolators were cyclically loaded and unloaded four times, similarly to the loading method proposed by Liu et al. [19]. To verify the shear performances, the laminated thick rubber isolator was tested by a horizontal reflexive frame and a hydraulic universal testing machine. The testing photos of the three isolators are shown in Fig. 4.

#### 3.2 Field Experiments

A full-scale one-story masonry building was built near an existing subway trestle in Ningbo, China. Figure 5a shows the front elevation of the masonry building, and Fig. 5b shows the photo of the building. A systematic field experiment was operated in this paper to investigate the suppression effectiveness of the first and the second isolators for vertical vibrations inside the building. The photos of the installed isolators are shown in Fig. 5c, d.

Moreover, a full-scale two-story masonry building was built above an existing subway tunnel in Shanghai, China. Then, a systematic field experiment was operated to investigate the suppression effectiveness of the third isolator for subway-induced tri-axial vibrations. Figure 5e shows the side elevation of the building, and Fig. 5f shows the photo of the building. The position relationship between the two-story building and the subway tunnel is shown in Fig. 5g. The photo of the installed rubber isolator is shown in Fig. 5h.

The dimensions of the one-story building were  $3.0 \times 2.8 \times 2.8$  m, corresponding to length  $\times$  width  $\times$  height. The dimensions of the two-story building were  $4.5 \times 3.0 \times 5.6$  m, corresponding to length  $\times$  width  $\times$  height. A base isolation layer and



(a) Compression test of stacked sandbags.



(b) Compression test of the geo-synthetics isolator.



(c) Compression test of the rubber isolator.



(d) Compression-shear test of the rubber isolator.

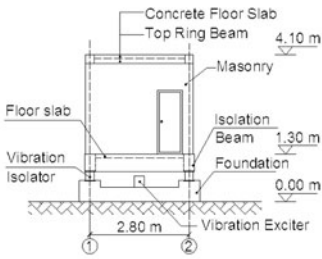
**Fig. 4** Mechanical properties tests of the three isolators

a top ring beam were designed for each of the buildings, both of which were made of reinforced concrete. The thickness of the floor slabs was 100 mm.

## 4 Results and Discussion

### 4.1 Mechanical Properties

The tested force–deformation curves of the different stacked layers and different gradations are illustrated in Fig. 6a. The steep local drops in the force–deformation curves of Fig. 6a are seen as rupture failure statuses. The tested values of vertical stiffness and damping ratio of stacked sandbags are listed in Fig. 6b. The ultimate compressive stress of the sandbag filled with uniform gradation is a little smaller than that filled with single gradation. Therefore, uniform gradation is more suitable for the isolator. When the layer number increases from one to seven, the tensile strain of the outside package increased significantly, and the ultimate bearing capacity becomes lower and lower. The ultimate compressive strength of seven-layered sandbags in



(a) The front elevation of the building.



Full-scale building

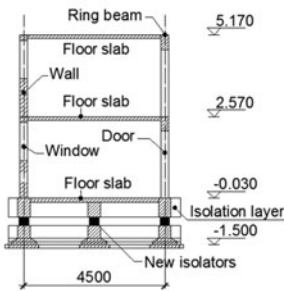
(b) The photo of the building.



(c) The installed stacked sandbags.



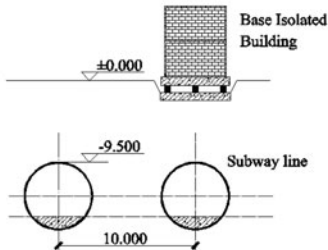
(d) The installed geosynthetic isolator.



(e) The side elevation of the two-story building.



(f) The photo of the two-story building.



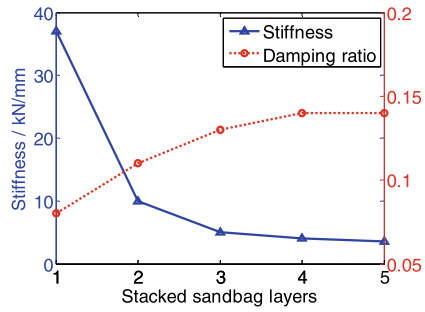
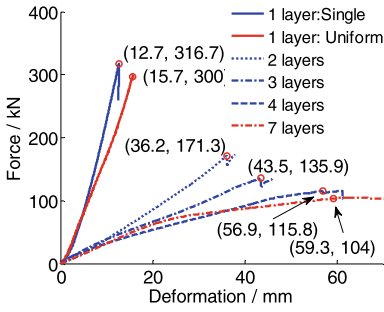
(g) The building and the subway tunnel.



(h) The installed thick rubber isolator.

Fig. 5 The building and the site of the field experiments





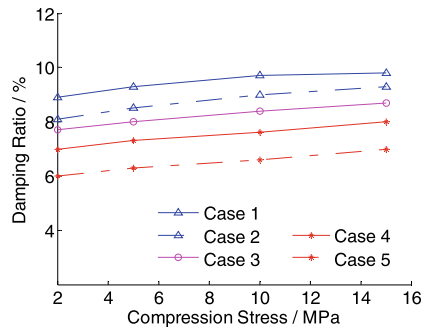
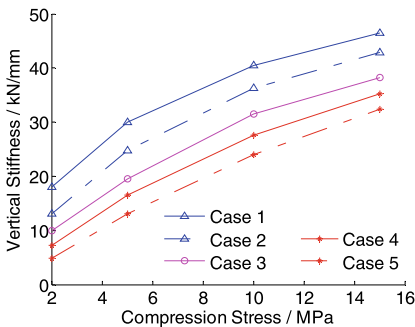
(a) Ultimate bearing capacity. (b) Vertical stiffness and damping ratios.

Fig. 6 Tested results of the stacked sandbags

Fig. 6a is nearly 1.2 MPa which is much larger than that of an ordinary soil foundation. The vertical stiffness of the seven-layered sandbags is as low as 3 kN/mm, and the damping ratio is as high as 15%, which is appropriate for vertical vibration isolation of buildings.

Besides, the strength, the vertical stiffness, and the damping ratio of seven-layered sandbag is almost the same as those of four layered sandbag, proving that the mechanical properties of the isolator becomes stable when the layer number increases from four to seven. Because the height-width ratio of seven-layered stacked sandbags is too large to ensure the stability, the recommended layer of the isolator is four.

The testing vertical stiffness values and damping ratios of the improved geosynthetic isolator are shown in Fig. 7. As the external form of the isolator gradually changes when the compressive stress increases, the vertical stiffness in Fig. 7a increases gradually. The hardening phenomenon of rubber particles under compressive stress also leads to the increasing phenomenon of the vertical stiffness. Furthermore, in Fig. 7a, b, the more the sand particles are included in the isolator, the larger



(a) Vertical stiffness values. (b) Damping ratios.

Fig. 7 Tested results of the geosynthetic isolator

the vertical stiffness and the damping ratio are. This phenomenon proves that the sand particles are benefits to increasing vertical stiffness and dissipating energy. So, changing the mixture ratio of sand particles is an effective way to adjust the vertical stiffness and damping ratio. When only filled with sand particles, the damping ratio is high to 10%, which is similar to a high-damping rubber bearing. In addition, the damping ratios in Fig. 7b are almost the same when the compressive stress increases, proving the damping ratio has no relationship to the compressive stress.

The tested value of ultimate bearing capacity of the geosynthetics isolator is more than 40 MPa, which is much larger than that of stacked sandbags and appropriate for most buildings near subway transportation. However, the testing phenomenon showed that the sand particles were crushed when the compression stress was more than 25 MPa. In this case, the vertical stiffness becomes a stable constant when the compression stress increases. Because the bearing capacity is determined by the capsule, the degradation has no negative influence. The designed compression stress of the isolator is less than 10 MPa, and therefore the degradation could be avoided or delayed.

Figure 8a depicts the vertical force–displacement curves of the thick rubber isolator, and Fig. 8b depicts the horizontal force–displacement curves. In Fig. 8b, a thick rubber isolator with a fixed bottom was also tested to compare with the new type of isolator with a sliding bottom. The pressure in Fig. 8b is 4.5 MPa.

The results in Fig. 8a show that the vertical stiffness of the isolator is nearly a constant value under different pressure loads. The damping ratio calculated from the hysteresis loop is only 2%. In Fig. 8b, the ultimate shear deformation are 100% of  $T_r$  for the isolator with a fixed bottom. The parameter  $T_r$  is the total thickness of rubber layers. As requested by the seismic design code of China [20], the ultimate shear deformation of a laminated rubber isolator should be larger than 55% of  $D$  and 300% of  $T_r$ . The parameter  $D$  is the diameter of the isolator. Obviously the isolator with a fixed bottom does not satisfy the design requirement, because the rubber layers are much thicker than those of a normal rubber isolator. After adding a sliding bottom,

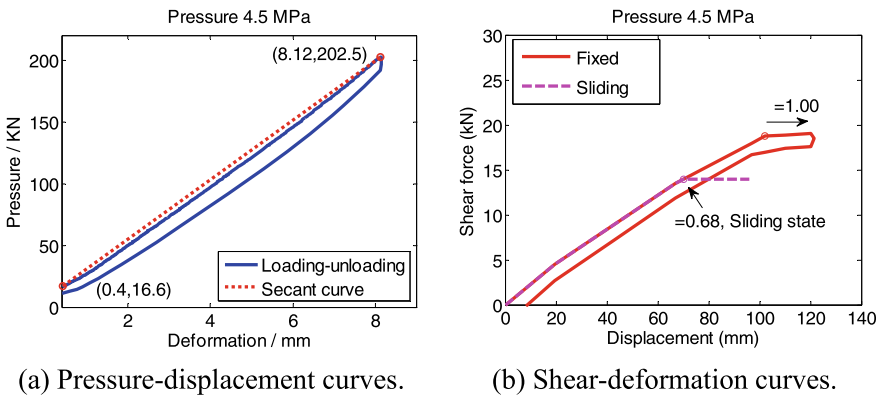


Fig. 8 Tested results of the thick rubber isolator

the isolator starts to slide when the shear deformation reaches 68% of  $T_r$ . So, the sliding layer is effective to protect the isolator and upper structure from instability failure under large shear deformations.

## 4.2 Suppression Effectiveness of the Field Experiments

The natural frequency of the floor slab in the one-story building is identified as 80 Hz by knocking tests. After the installation of stacked sandbags, the isolation frequency in Fig. 5c is identified as 4.5 Hz. After the installation of geosynthetics isolators, the isolation frequency in Fig. 5d is identified as 5.6 Hz. The mix proportion of sand is 25%, and that of rubber particles is 75%. Both of the isolation frequencies are much lower than the natural frequency of the floor slab.

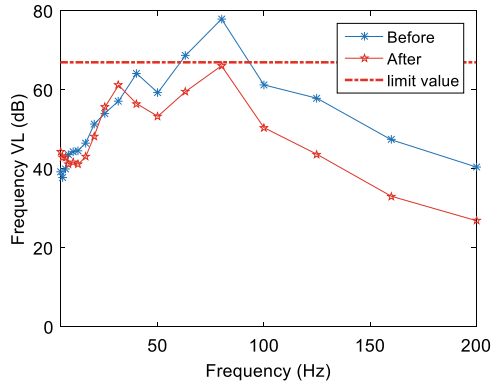
The natural frequency of the floor slab in the two-story building is identified as 60 Hz by knocking tests. After the installation of thick rubber isolators, the isolation frequency in Fig. 5f is identified as 9.4 Hz.

As recommended by the standards of ISO 2631-2 [21], frequency vibration levels (abbreviated as “frequency VLs”) are selected to evaluate the human vibration comfort inside the buildings. For the statistical significance, the frequency VLs are averaged over the measured data corresponding to at least five individual train-passing events. Figure 9 shows the averaged frequency VLs after the installation of different isolators. According to the standard of China, The limit value for human vibration comfort is determined to be 67 dB in this paper.

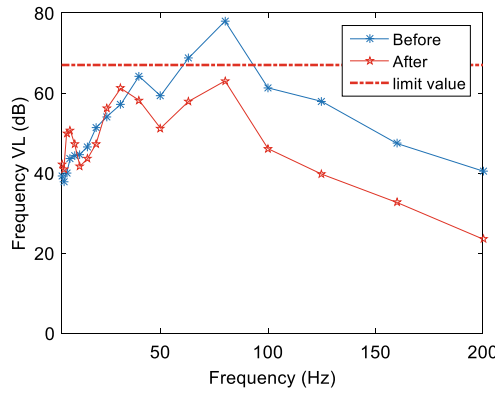
In Fig. 9a, the peak value of frequency VLs decreases by 13 dB after the installation of stacked sandbags. In Fig. 9b, the peak value decreases by 15 dB. In Fig. 9c, the peak value decreases by 26 dB. All of the peak values satisfy the limit value of human comfort. According to the principles of structure dynamics, because the damping ratio of stacked sandbags is the highest, the suppression effectiveness is the lowest. Nevertheless, the characteristic of high damping ratio is a benefit to resisting resonance caused by other low-frequency environmental vibrations.

## 5 Conclusions

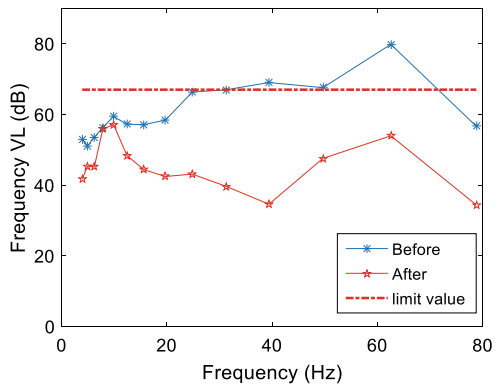
- The ultimate compressive strength of four-layered sandbags is nearly 1.2 MPa which is much higher than that of an ordinary soil foundation. The vertical stiffness of the four-layered sandbags is as low as 3 kN/mm, and the damping ratio is as high as 15%. These characteristics are appropriate for vertical vibration isolation of buildings near subways.
- Changing the mixture ratio of sand particles inside the geosynthetics isolator proved to be an effective way to adjust the vertical stiffness and damping ratio. When only filled with sand particles, the damping ratio is 10%, which is similar



(a) Before and after the installation of stacked sandbags.



(b) Before and after the installation of geosynthetics isolators.



(c) Before and after the installation of rubber isolators.

**Fig. 9** Tested values of frequency vibration levels inside the buildings

to a high-damping rubber bearing. The ultimate bearing capacity is appropriate for most buildings.

- The damping ratio of laminated thick rubber isolators is only 2%. The sliding layer is effective to protect the isolator and upper structure from instability and failure under large shear deformations.
- After the installation of three types of isolators, the peak value of frequency, VLs decreased by 13 dB, 15 dB and 26 dB, respectively. All the peak values satisfied the limit value for human comfort, proving the three isolators are effective for the base isolation of buildings near subway transportation.

**Acknowledgements** Financial support from the Natural Science Foundation of Zhejiang province, China (Grant Nos. LY18E080011), the National Natural Science Foundation of Ningbo, China (Grant Nos. 2019A610402) are gratefully acknowledged.

## References

1. Lombaert G, Degrande G, Vanhauwere B (2006) The control of ground-borne vibrations from railway traffic by means of continuous floating slabs. *J Sound Vib* 297:946–961
2. Sheng T, Zhang SL, Shan JZ, Shi WX (2015) In-situ measurement and analysis of subway-induced environmental vibration and the effectiveness of vibration-source suppression methods. *J Vibr Measure Diagn* 35(2):352–358 (in Chinese)
3. Coulier P, Cuéllar V, Degrande G, Lombaert G (2015) Experimental and numerical evaluation of the effectiveness of a stiff wave barrier in the soil. *Soil Dyn Earthq Eng* 77:238–253
4. Yang Y, Ge P, Li Q, Liang X, Wu Y (2018) 2.5D vibration of railway-side buildings mitigated by open or infilled trenches considering rail irregularity. *Soil Dyn Earthq Eng* 106:204–214
5. Newland DE, Hunt HEM (1991) Isolation of buildings from ground vibration: a review of recent progress. *Mech Eng Sci* 205(1):39–52
6. Cho T (2013) Experimental and numerical analysis of floating floor resonance and its effect on impact sound transmission. *J Sound Vib* 332(25):6552–6561
7. Cryer DP (1994) Modeling of vibration in buildings with application to base isolation. Doctor Engineering Thesis. University of Cambridge, UK
8. Sharif AK (2000) Dynamic performance investigation of base-isolated structures. Doctor Engineering Thesis. Imperial College of Science Technology and Medicine, UK
9. Sheng T, Li YM, Zhang H, Shi WX, Yang Y (2015) Field experiment study of subway nearby building's base isolation by laminated thick rubber isolator. *J Build Struct* 36(2):35–40 (in Chinese)
10. Talbot JP, Hunt HEM (2003) Isolation of buildings from rail-tunnel vibration: a review. *Build Acoust* 10(3):177–192
11. Pan P, Shen S, Shen Z, Gong R (2018) Experimental investigation on the effectiveness of laminated rubber bearings to isolate metro generated vibration. *Measurements* 122:554–562
12. Wagner H (2004) Vibration control systems for trackbeds and buildings using coil steel springs. In: *Proceedings of acoustics*. Gold Coast, Australia, pp 99–104
13. Matsuoka H, Liu SH (2006) A new earth reinforcement method using soilbags. Taylor & Francis/Balkema, Netherlands
14. Nakagawa Y, Chen GL, Tatsui T (2009) Verification of vibration reduction characteristics with soilbag structure. In: *Proceeding of the 4th Asia regional conference on geosynthetics*. Shanghai, China, pp 603–608

15. Liu SH, Gao JJ, Wang YQ (2014) Experimental study on vibration reduction by using soilbags. *Geotext Geomembr* 42(1):52–62
16. Sheng T, Bian XC, Liu GB, Xiao C, Chen Y, Li Y (2020) Experimental study on the sandbag isolator of buildings for subway-induced vertical vibrations and secondary air-borne noise. *Geotext Geomembr* 48(4):504–515
17. Presthus M (2002) Derivation of air spring model parameters for train simulation. Master Thesis. Lulea University of Technology, Sweden
18. Sheng T, Shi WX, Shan JZ, Hong FY, Bian XC, Liu GB, Chen Y (2020) Base isolation of buildings for subway-induced environmental vibration: field experiments and a seismic-analytical prediction model. *Struct Des Tall Spec Build* (on line)
19. Liu JF, Xie HP, Xu J (2008) Experimental study on damping characteristics of rock under cyclic loading. *China J Rock Mech Eng* 27(4):712–717 (in Chinese).
20. Ministry of Construction of China (2010) GB50010-2010: code for seismic design of buildings. China Architecture and Building Press, Beijing
21. ISO2631-2 (2003) Mechanical vibration and shock-evaluation of human exposure to whole-body vibration - Part 2: vibration in buildings (1 Hz to 80 Hz)

# Dynamic Response of Floating Slab Track with Variation on Failure Position of Steel Spring



Xiaolin Song, Linfeng Xue, Fangzheng Xu, and Jianping Wei

**Abstract** The steel spring floating slab track is widely adopted for its remarkable performance on vibration isolation. With the increase of the operation time of floating slab track, the damage or failure of the steel spring is inevitable, which will have a bad effect on the track dynamics and vibration-mitigating effects. The steel spring's forces were calculated by the vertical coupled dynamics model for the metro and the floating slab track. The dynamic response of tunnel and soil subjected to the steel spring's forces was analyzed. The influence of steel spring failure position of floating slab track on the dynamic response of infrastructure was investigated. The results showed that the failure position had a significant effect on the dynamic characteristics. Although the infrastructure displacement varies little with the failure position, the reaction forces of the steel springs and acceleration of the track, the tunnel, and the soil notably increased when the steel spring failed at the end of the track. The tunnel acceleration with one pair of damaged springs at the end of track is 40% greater than that with the same failure springs in the middle of track.

**Keywords** Floating slab track · Steel spring · Dynamic response · Failure position

## 1 Introduction

Floating slab track is widely used in city metro system for its excellent performance in vibration isolation [1]. Steel spring floating slab has lower dominant frequency and longer service life than rubber one and has better vibration-mitigating effects [2]. Steel spring floating slab tracks are getting more popular in the special vibration-sensitive sections and became main technique for reducing track vibration in metro traffic. The correlational research on floating slab track is becoming a topical subject in the domain of urban rail transportation. Much important work on floating slab track has already addressed different aspects. Due to the variation of track structures, vehicle types, operation environments, surrounding infrastructure parameters,

---

X. Song (✉) · L. Xue · F. Xu · J. Wei

State Key Laboratory of Traction Power, Southwest Jiaotong University, Chengdu 610031, China  
e-mail: [xlsong@swjtu.edu.cn](mailto:xlsong@swjtu.edu.cn)

and other factors, a way to fine-tune the floating slab track parameters to mitigate vibration may not be directly applicable to the other systems. A solution may not be applicable to all scenarios for all metro tracks in different locations. Many researchers focused on the parameter optimization and structural design for the floating slab track [3–5]. The comparison of vibration-mitigating effects and dynamic performances has already aroused widespread attention from different perspectives [6–8]. The dynamic characteristics and life analysis of steel spring and other track components are other hot issues. However, with the increase of the operation time of floating slab track, the damage or failure of the supporting component, such as the rail fastener and the steel spring, is inevitable. The failure of steel spring will have a bad influence on the vibration-mitigating effects and dynamic performances of the track [1]. Unfortunately, correspondent studies on the floating slab are very limited [9, 10]. Therefore, it is necessary to investigate the influence of the failure of the steel spring on the dynamic response of floating slab track and the metro infrastructure. In this paper, the influence of the failure position of the steel spring on the vibration characteristics of the floating slab track will be investigated.

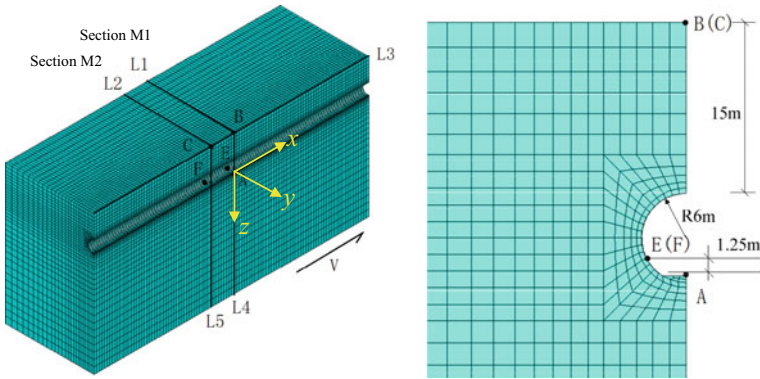
## 2 Numerical Analysis Model and Its Parameters

When a metro train runs along a tunnel, the wheel/rail force will be transferred via the track, the tunnel, and the surrounding infrastructure to the ground. Especially, the floating slab track parameters are related to vehicle types, operation environments, parameters of surrounding soils. In order to investigate the influence of the failure position of steel spring on the dynamic response of the track-tunnel-soil system, the train, the track, the tunnel, and the soil were all involved in the whole system numerical model. The whole model was composed by the train-track coupled sub-model and the 3D finite element (FE) sub-model of the tunnel-soil. The link between the two sub-models is the reaction forces of steel springs, which can be calculated by the train-track coupled model. The loads subjected to the FE model are the reaction forces of steel springs.

As the train-track coupled model and the corresponding parameters were detailed introduced in the literature [1, 11] according to the classical train-track coupled dynamics, the model and its parameters will not be mentioned in this paper.

According to the real parameters of one real metro line, the three-dimensional FE model of the tunnel and surrounding soil was established by the eight-node brick solid element SOLID45, as shown in Fig. 1. The length of the model was 125 m, which was five times of one slab length. The width and the thickness of the model were 80 m and 60 m, respectively. The buried depth, the diameter, and the lining thickness of the tunnel were 15 m, 6 m, and 0.3 m, respectively. The nodes at the bottom boundary are fixed in all directions. Vertical and horizontal constraints were enforced to the cross sections through both ends. The symmetrical boundary condition was subjected to the symmetrical plane (XOZ Plane). To minimize the effect of the boundary condition on the numerical result, the 3D viscoelastic artificial boundary was applied to the FEM





**Fig. 1** Three-dimensional finite element model of tunnel and soil

model. The lining and the foundation base of the tunnel are made of C55 concrete. The surrounding soils of the tunnel were composed of 9 layers of soil, which was homogeneous and isotropic in each layer. The detailed dynamic material parameters referred to literature [1, 12] and will not be listed.

In Fig. 1, five monitoring lines and two monitoring sections were marked on the FE model. Two monitoring sections *M1* and *M2* corresponded to the cross-section through the central and the end of the middle floating slab. Two lateral monitoring lines (Line 1 and Line 2) corresponded to the ground lines through the Section *M1* and *M2*, and the vertical monitoring lines (Line 4 and Line 5) were the intersection of Section *M1* and *M2* with track central section. The longitude Line 3 corresponded to the intersection of the track central section with the ground. Point *E* and Point *F* located in the tunnel wall, 1.25 m above the rail top.

The nodes at the bottom boundary are fixed in every direction. Vertical and horizontal springs were applied at both end sections. In order to avoid the influence of boundary, the non-reflected boundary is used in the three-dimensional finite element model.

### 3 Numerical Calculation and Results Analysis

As the failure position of the steel springs may have a notable influence on the dynamic response of the overall system. With the increase of the damaged steel springs, the combination of the failure position will become very multiple and complicated. In this paper, only one pair of the steel spring damaged in the middle floating slab was investigated. The failure position located in the end, the quarter, and the middle of the slab, which was respectively named Case 1, Case 2, and Case 3. For Case 2 and Case 3, the damaged springs were No. 6 and No. 11, respectively. The diagram of the failure position were shown in Fig. 2. The reaction forces of the

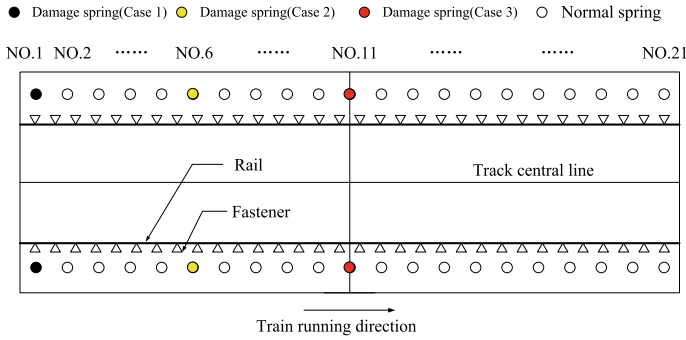


Fig. 2 Diagram of failure position for steel springs

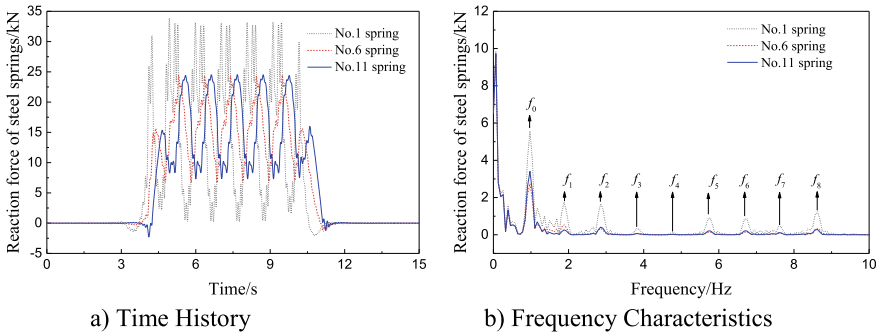


Fig. 3 Reaction force of different steel springs

different steel springs were displayed in Fig. 3, which were the excitation of the FE model.

### 3.1 Effect of Failure Position on Vibration of Track and Tunnel

The rail displacement through section *M1* and *M2* in different cases (different damage position) were shown in Fig. 4, and the peak displacement were shown in Fig. 5.

From Figs. 4 and 5, it could be seen that in Section *M1*, the peak rail displacement varied in a small range, and the displacement in Case 1 was slightly increased than that in other cases. The maximum increment was only 9.58%. However, in section *M2*, the displacement in Case 1 was greater than that in other cases, and the maximum increment reached 23.37%. It also showed that when the springs failed in the end position, the rail displacement was greater than that when the springs failed in the

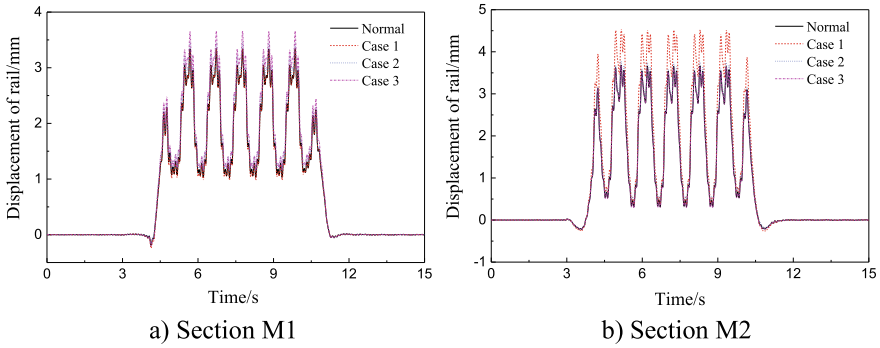


Fig. 4 Rail displacement when steel spring damages in different position

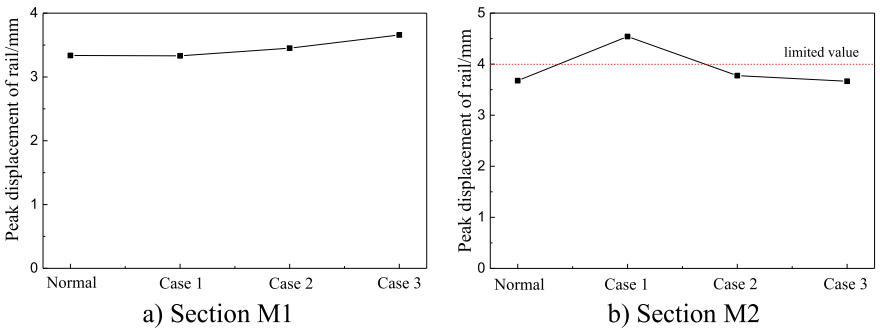


Fig. 5 Rail peak displacement when steel springs damage in different position

middle position. That was to say the springs failed in the end position had a worse effect not only on the rail displacement but also on the influenced range.

Figure 6 illustrated the acceleration of the tunnel wall in different points when springs failed in different positions, and Fig. 7 summarized their peak values in different cases.

Figures 6 and 7 showed that when one pair of steel springs failed in different places, the dominated frequencies of the vibration acceleration of the tunnel wall remained unchanged. It also indicated that when the springs were damaged in the end, the acceleration of the tunnel wall was greater than that when the springs failed in the middle section. The maximum increment of the peak accelerations in Point *E* and Point *F* were 22.02% and 38.15%, respectively. The minimum increase occurred when the middle springs failed. In a word, the steel springs failed in the end had a worse effect on the vibration of the tunnel wall.

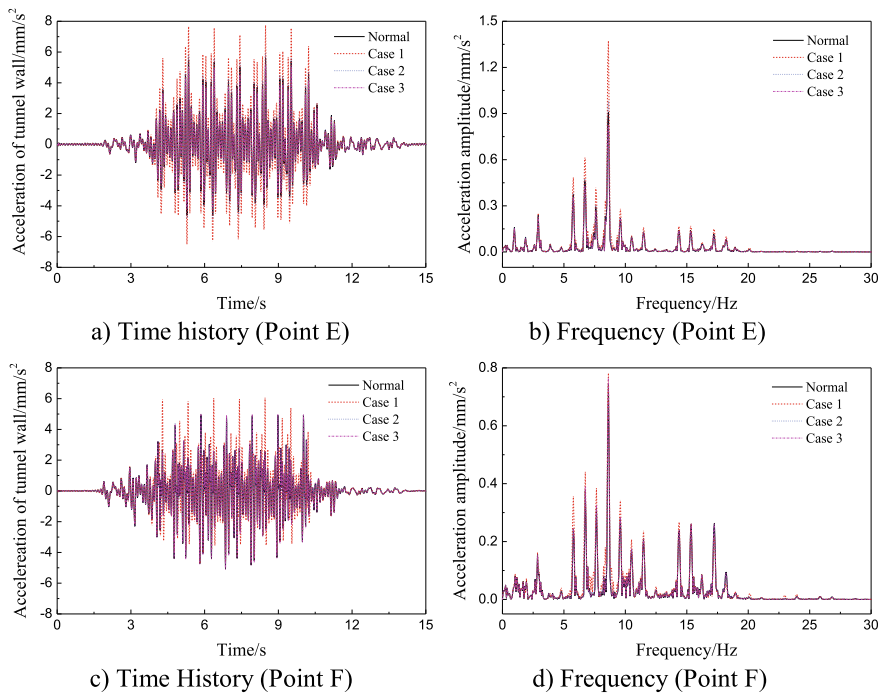


Fig. 6 Acceleration property of tunnel wall when steel springs damage in different positions

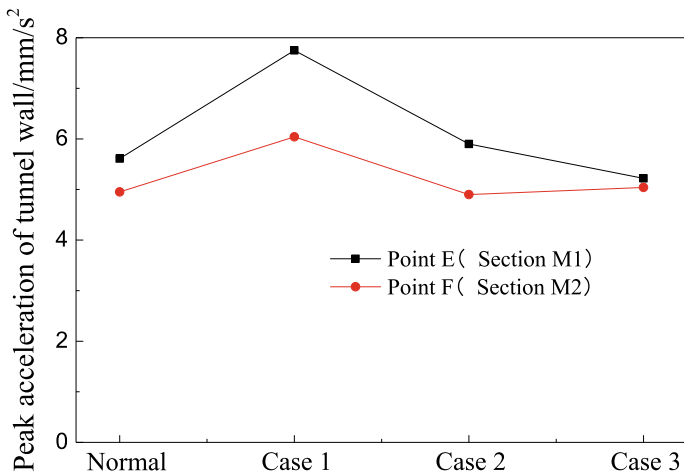


Fig. 7 Peak acceleration of tunnel wall when steel springs damage in different positions

### 3.2 Effect of Failure Position on Vibration and Attenuation of Soil

When the steel springs failed in different position, the lateral distribution of the displacement and the acceleration of the ground was shown in Fig. 8. The longitudinal distribution of the ground acceleration and the displacement along the Line 3 was shown in Fig. 9, while the vertical distribution (along Line 4) of the acceleration and the displacement of the soil was summarized in Fig. 10.

It is indicated from Fig. 8 that no matter where the springs failed, the failure position had little influence on the lateral distribution of the ground displacement, and the displacement variation could be negligible not only along Line 1 but also along Line 2. When the springs failed in the end, the ground acceleration increased remarkably, especially along Line 2. The peak acceleration of Point C increased 50.3% than that with no damage, while it only increased only 9.2% in Point B.

It also showed that in Case 1, when one pair of the springs failed in the end, the ground acceleration increased sharply. The acceleration reached its maximum at the ground 4.165 m away from section M1 along Line 3, and its value increased from 2.02 to 3.1 mm/s<sup>2</sup>. Similar to the lateral distribution of the ground displacement, the

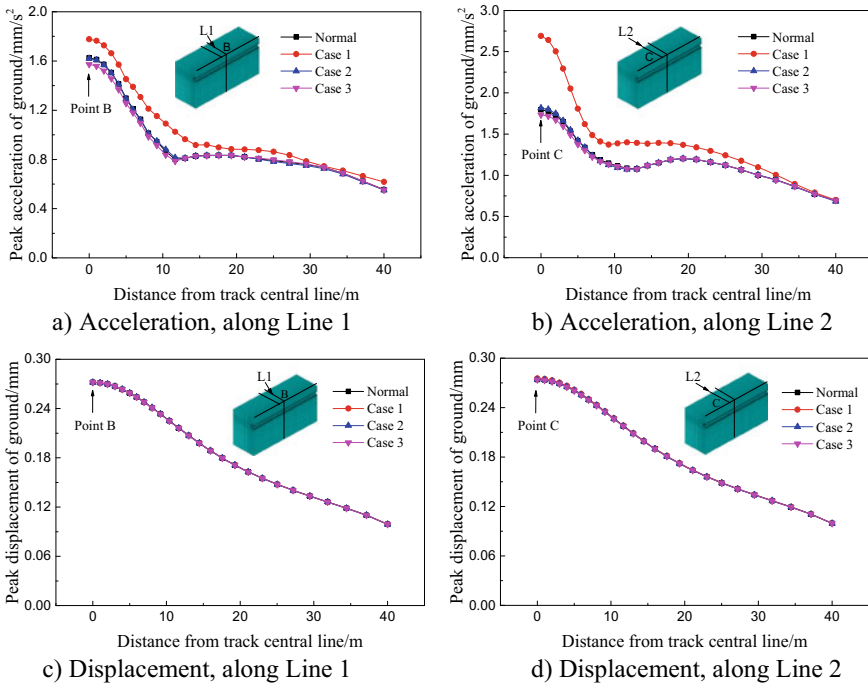


Fig. 8 Lateral distribution of displacement and acceleration of ground

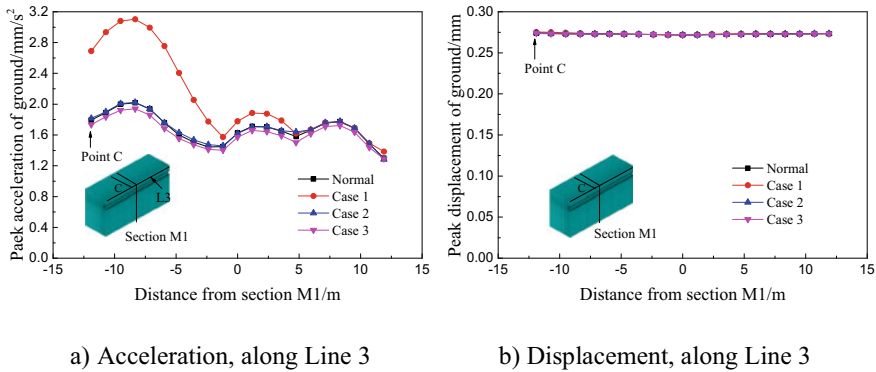


Fig. 9 Longitudinal distribution of displacement and acceleration of ground

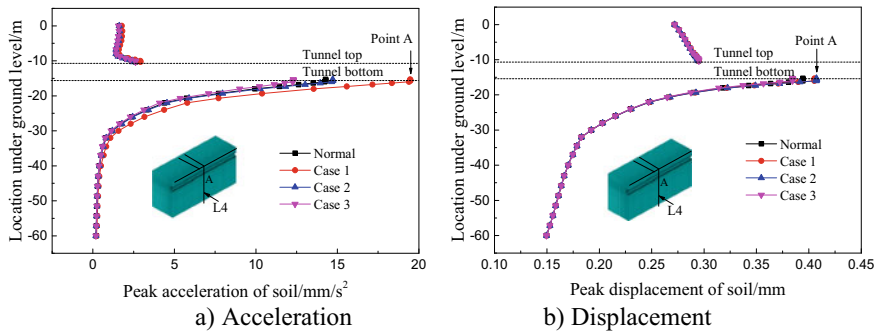


Fig. 10 Vertical distribution of displacement and acceleration of soil

effect of the failure position of the steel springs on the longitudinal distribution could be ignored.

When the springs damaged in the end, the acceleration of the tunnel bottom increased from 14.28 to 19.47 mm/s<sup>2</sup> compared with that with no damaged springs, and the increment achieved to 36.34%. However, the increment was only 13.87 and 3.08% in Case 3 and Case 2. No matter where one pair of the springs damaged or not, the variation of the vertical distribution of the soil displacement could be ignored. The maximum difference is only 5.1%.

### 4 Conclusions

The acceleration of the track, the tunnel wall, and the surrounding soil varied considerably with the damage position of the one pair of the springs. When the springs failed in one end of the floating slab, the acceleration increased remarkably than

that with no damaged springs. The maximum increment of the acceleration respectively reached 23.37% for the rail, 38.15% for the tunnel, and 50.3% for the ground. However, the damaged position had little influence on the displacement of the track, the tunnel, and the soil.

**Acknowledgements** This research was partially supported by the National Natural Science Foundation of China (NSFC) under grant 51735012 and 52078433, the Science and Technology Department of Sichuan Province under grant 2020YFH0007, and the State Key Laboratory of Traction Power of China under grant 2019TPL-T05.

## References

1. Xu F, Song X, Yang J (2019) Influence of steel spring failure of floating slab track on vibration characteristics of infrastructure. *Advances in environmental vibration and transportation geodynamics*, Springer
2. Xia H (2010) *Traffic induced environmental vibrations and controls*. Science Press, Beijing
3. Rajaram S, Nelson J (2019) High-performance floating slab track: design and construction improvements based on lessons learned from prototype slabs. *Transp Res Rec* 2673(1):300–309
4. Wang J, Wu T (2007) On vibration isolation performance of floating slab track. *J Shanhai Jiaotong Univ Chin Edn* 41(6):1021
5. Kouroussis G, Olivier B, Ainalis D, Zhu S, Zhai W (2019) Railway ground vibrations and designing dynamic vibration absorbers for urban rail transit In: *Proceedings of the 26th international congress on sound and vibration*
6. Jiang B, Ma M, Li M, Liu W, Li T (2019) Experimental study of the vibration characteristics of the floating slab track in metro turnout zones. *Proc Instit Mech Eng Part F J Rail Rapid Transit* 233(10):1081–1096
7. Zhu Z, Wang L, Costa P, Bai Y, Yu Z (2019) An efficient approach for prediction of subway train-induced ground vibrations considering random track unevenness. *J Sound Vib* 455:359–379
8. Shi L, Ye X, Zhang P, Guo L (2019) A comparative study on vertical dynamic responses of three types of elevated railway tracks subjected to a moving train. *Mathe Probl Eng*
9. Wei X, Shi W, Jiang J, Zhang J, Ding Z (2019) Effects of steel spring damage on vibration performance of metro train-floating slab track system. *J Vibr Shock* 38(11):228–234
10. Yu G, Shen J, Chen K (2015) Influence of railway-support failure on the dynamic response characteristics of steel spring floating slab track. *Noise Vibr Control* 35:78–81
11. Zhai W (2019) *Vehicle-track coupled dynamics theory and applications*. Springer, Singapore
12. Yin Z (2008) *Research on the buildings vibration and noise caused by subway*. Tongji University, Shanghai

# The Effect of Boundary Permeability on the Dynamic Response of the Layered Saturated Ground Subjected to an Underground Moving Load



Yijun Li, Anfeng Hu, Kanghe Xie, and Rong-tang Zhang

**Abstract** In this paper, the effect of boundary permeability on the dynamic response of a layered poroelastic half-space under moving loads in a tunnel is studied analytically. The tunnel is modeled by an Euler–Bernoulli beam located between two horizontal layers. The Biot’s dynamic equations for the poroelastic soil medium are solved by utilizing the Helmholtz decomposition and Fourier transformation. Combining the boundary conditions and the continuity conditions between each layer, the explicit analytical solutions for the dynamic response of each layer in the transformed domain are obtained by the transmission and reflection matrices (TRM) method. The solutions in time–space domain are expressed in terms of infinite Fourier-type integrals, which are evaluated by an adaptive version of extended integral trapezoidal formula. The validity and accuracy of the proposed methodology and numerical integration scheme are confirmed by comparison with some existing results. Two different boundary permeabilities are considered, and the numerical results show that the influence of the boundary permeability on the dynamic response is related to the permeability of the soil and the moving load speed.

**Keywords** Boundary permeability · Layered poroelastic half-space · Tunnel · Dynamic response

---

Y. Li (✉) · R. Zhang

School of Civil Engineering and Architecture, Wuhan Polytechnic University, Wuhan 430023, China

e-mail: [yijunli@whpu.edu.cn](mailto:yijunli@whpu.edu.cn)

R. Zhang

e-mail: [peterzhang@whpu.edu.cn](mailto:peterzhang@whpu.edu.cn)

A. Hu · K. Xie

Research Center of Coastal and Urban Geotechnical Engineering, Zhejiang University, Hangzhou 310058, China

e-mail: [anfenghu@zju.edu.cn](mailto:anfenghu@zju.edu.cn)

K. Xie

e-mail: [zdkhxie@zju.edu.cn](mailto:zdkhxie@zju.edu.cn)



## 1 Introduction

The environmental effect induced by the underground trains is an issue that needs to be of concern in the whole design and operation stages of the subway. Various models have been established to estimate the vibrations induced by underground moving trains. The simplified 2D beam model with an Euler–Bernoulli beam to simulate the tunnel structure has been proposed to investigate the ground vibration qualitatively [1–3]. The 3D PiP model [4, 5] was established and developed by Forrest and Hunt to calculate the train-induced vibration in a full-space. Lu [6] investigated the dynamic response of a porous full-space with a cylindrical hole subjected to a moving axisymmetric ring load. Yuan [7] provided a benchmark analytical solution for the vibration of a half-space from the tunnel by using the transformation between the cylindrical waves and the plane waves. Many researchers have used the 2.5D BEM and FEM to simulate the generation and propagation of vibrations from underground railways [8–13]. The soil in the above studies is assumed to be a homogeneous medium. Taking into account the layered property of the ground, some layered models have been used to investigate the wave propagation in the layered ground subjected to the trains in the tunnel [14–16]. It is proved that the effect of pore water cannot be ignored in the dynamic analysis [17], and the analytical solutions for the vibration of the layered saturated ground from the underground tunnel are rarely reported.

Therefore, based on Biot’s theory for the saturated poroelastic medium [18, 19], the dynamic response of the multi-layered saturated ground with an embedded Euler beam to simulate the tunnel structure is studied by employing the TRM method [20, 21]. The motion equations of saturated layered are solved using the continuity conditions and the boundary conditions of the coupled system. The results in the time–space domain are calculated using the FFT method.

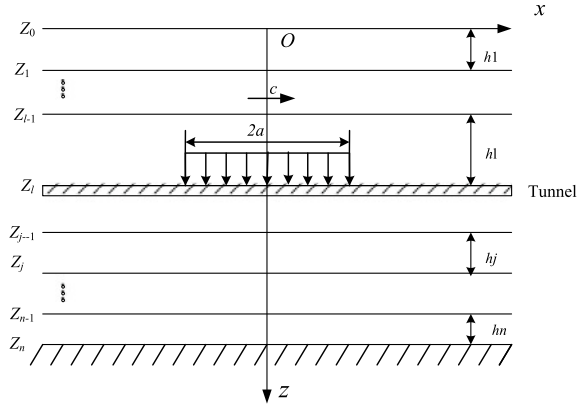
In practical engineering, the ground surface is usually untreated except for the paved or built-on surface. Therefore, two different drainage conditions of the ground surface are considered to investigate the dynamic response of the layered ground, which are the permeable boundary condition corresponding to the natural (untreated) surface and the impermeable boundary condition corresponding to the ground surface with a concrete floor or a bituminous pavement.

## 2 Physic Model and General Solutions

The model of layered saturated ground-beam coupled system is shown in Fig. 1. It is assumed that the deformations are plane strain in the  $x - z$  plane, i.e.,  $\varepsilon_{xy} = \varepsilon_{yy} = \varepsilon_{yz} = 0$ . The constitutive relations for the poroelastic medium can be expressed as [18, 19]:

$$\sigma_{ij} = \lambda \delta_{ij} \theta + \mu (u_{i,j} + u_{j,i}) - \alpha \delta_{ij} p \quad (1)$$

**Fig. 1** Model of layered saturated ground-beam coupled system



$$p = -\alpha M\theta + M\zeta \tag{2}$$

where  $u_i$  and  $w_i$  denote the average solid displacement and the pore fluid displacement relative to the solid matrix in the  $i$ -direction ( $i = x, z$ ), respectively;  $\sigma_{ij}$  is the total stress of the bulk material, and  $p$  is the excess pore fluid pressure (suction is considered negative);  $\theta = u_{i,i}$  is the dilatation of the solid skeleton;  $\zeta = -w_{i,i}$  is the volume of fluid injection into a unit volume of the bulk material;  $\delta_{ij}$  is the Kronecker delta;  $\lambda$  and  $\mu$  are Lamé constants;  $\alpha$  and  $M$  are Biot's parameters accounting for compressibility of the poroelastic medium.

The motion equations for the bulk material and pore fluid can be expressed in terms of the displacements  $u_i$  and  $w_i$  as [18, 19]:

$$\mu u_{i,jj} + (\lambda + \alpha^2 M + \mu)u_{j,ji} + \alpha M w_{j,ji} = \rho \ddot{u}_i + \rho_f \ddot{w}_i \tag{3}$$

$$\alpha M u_{j,ji} + M w_{j,ji} = \rho_f \ddot{u}_i + m \ddot{w}_i + b \dot{w}_i \tag{4}$$

where the dot over a variable denotes the time derivative;  $\rho$  and  $\rho_f$  are mass densities of the bulk material and the pore fluid, respectively;  $\rho = n\rho_f + (1 - n)\rho_s$ ,  $\rho_s$  is the density of the solid skeleton, and  $n$  is the porosity of the porous medium;  $m$  is the density-like parameter that depends on  $\rho_f$  and the geometry of the pores;  $b$  is a parameter accounting for the internal viscous friction due to the relative motion between the solid matrix and the pore fluid. The parameter  $b$  is equal to the ratio between the fluid viscosity and the intrinsic permeability of the medium (i.e.,  $b = \eta/k$ ).

Equations (3) and (4) can be solved by introducing the following Helmholtz decomposition:

$$u_i = \text{grad}\phi_1 + \text{curl}\varphi \tag{5a}$$

$$w_i = \text{grad}\phi_2 + \text{curl}\Phi \quad (5b)$$

By substituting the Eqs. (5) into Eqs. (3) and (4), the general solutions in frequency-wavenumber domain for displacements  $u_i$  and  $w_i$  ( $i = x, z$ ), stresses  $\sigma_{ij}$  ( $i, j = x, z$ ) and pore fluid pressure  $p$  can be obtained by using the Fourier transformation [17]:

The motion equation of the Euler–Bernoulli beam is as follows:

$$\rho_B \frac{\partial^2 W}{\partial t^2} + EI \frac{\partial^4 W}{\partial x^4} = F(t) + a[\sigma_{zz}(x, H - 0, t) - \sigma_{zz}(x, H + 0, t)] \quad (6)$$

where  $W(x, t)$  denotes the vertical displacement of the beam;  $\rho_B$  and  $EI$  are the mass density and bending stiffness of the beam, respectively;  $a$  is a characteristic length associated with the length of the structure in the  $y$ -direction;  $F(t)$  denotes the moving point load;  $\sigma_{zz}(x, H - 0, t)$  and  $\sigma_{zz}(x, H + 0, t)$  denote the vertical stress in the soil beneath and above the tunnel, respectively.

The boundary and continuity conditions corresponding to the coupled system in Fig. 1 can be expressed as:

When  $z = 0$ ,

$$\sigma_{xz}(x, 0) = 0 \quad (7a)$$

$$\sigma_{zz}(x, 0) = 0 \quad (7b)$$

When  $z = z_i$  ( $i = 1, 2, \dots, n - 1$ ),

$$u_x^{(i)}(x, z_i) - u_x^{(i+1)}(x, z_i) = 0 \quad (8a)$$

$$w_z^{(i)}(x, z_i) - w_z^{(i+1)}(x, z_i) = 0 \quad (8b)$$

$$u_z^{(i)}(x, z_i) - u_z^{(i+1)}(x, z_i) = 0 \quad (8c)$$

$$p^{(i)}(x, z_i) - p^{(i+1)}(x, z_i) = 0 \quad (8d)$$

$$\sigma_{xz}^{(i)}(x, z_j) - \sigma_{xz}^{(i+1)}(x, z_j) = 0 \quad (8e)$$

$$\begin{cases} \sigma_{zz}^{(i)}(x, z_i) - \sigma_{zz}^{(i+1)}(x, z_i) = F(t) - \left( \rho_B \frac{\partial^2 W}{\partial t^2} + EI \frac{\partial^4 W}{\partial t^4} \right) \\ u_z^{(i)}(x, z_i) = u_z^{(i+1)}(x, z_i) = W(x, t) \end{cases} \quad (i = l) \quad (8f)$$

$$\sigma_{zz}^{(i)}(x, z_i) - \sigma_{zz}^{(i+1)}(x, z_i) = 0 \quad (i \neq l) \quad (8g)$$

Two different drainage conditions of the free surface are considered. For the drained free surface:

$$p(x, 0) = 0. \quad (9a)$$

For the undrained free surface:

$$w_z(x, 0) = 0 \quad (9b)$$

If the bottom layer (i.e., the  $n + 1$ th layer) is a half-plane, as a result of the radiation and finiteness conditions at infinity, the exponentially increasing terms of the  $n + 1$ th layer will be discarded.

While if the  $n + 1$ th layer is the rigid bedrock, the boundary conditions are:

$$u_x^{(n)}(x, z_n) = 0 \quad (10a)$$

$$u_z^{(n)}(x, z_n) = 0 \quad (10b)$$

$$w_z^{(n)}(x, z_n) = 0$$

### 3 The Development of the TRM Method

The solutions for the dynamic response of the  $j$ th layer can be expressed as follows:

$$\psi^{(j)}(\xi, \omega, z)_{6 \times 1} = \begin{bmatrix} D_d^{(j)}(\xi, \omega) & D_u^{(j)}(\xi, \omega) \\ S_d^{(j)}(\xi, \omega) & S_u^{(j)}(\xi, \omega) \end{bmatrix} \times \begin{bmatrix} W_d^{(j)}(\xi, \omega, z)^T & W_u^{(j)}(\xi, \omega, z)^T \end{bmatrix} \quad (11a)$$

$$\psi^{(j)}(\xi, \omega, z)_{6 \times 1} = \begin{bmatrix} \hat{u}_x^{(j)} & \hat{u}_z^{(j)} & \hat{w}_z^{(j)} & i\hat{\sigma}_{xz}^{(j)} & \hat{\sigma}_{zz}^{(j)} & \hat{p}^{(j)} \end{bmatrix}^T \quad (11b)$$

$$W_d^{(j)}(\xi, \omega, z) = \begin{bmatrix} B^{(j)} e^{-\gamma_1^{(j)}(z-z_{j-1})} & D^{(j)} e^{-\gamma_2^{(j)}(z-z_{j-1})} & F^{(j)} e^{-\gamma_3^{(j)}(z-z_{j-1})} \end{bmatrix}^T \quad (11c)$$

$$W_u^{(j)}(\xi, \omega, z) = \begin{bmatrix} A^{(j)} e^{-\gamma_1^{(j)}(z_j-z)} & C^{(j)} e^{-\gamma_2^{(j)}(z_j-z)} & E^{(j)} e^{-\gamma_3^{(j)}(z_j-z)} \end{bmatrix}^T \quad (11d)$$

where  $W_d^{(j)}(\xi, \omega, z)$  and  $W_u^{(j)}(\xi, \omega, z)$  are termed as down-going and up-going wave vectors, and the matrixes  $D_d^{(j)}(\xi, \omega)$ ,  $D_u^{(j)}(\xi, \omega)$ ,  $S_d^{(j)}(\xi, \omega)$ , and  $S_u^{(j)}(\xi, \omega)$  can be deduced from the expression  $R(z)$  of Eq. (8).

From Eqs. (11c) and (11d), the following equations can be obtained:

$$W_d^{(j)}(\xi, \omega, z_{j-1}) = [B^{(j)}(\xi, \omega) \quad D^{(j)}(\xi, \omega) \quad F^{(j)}(\xi, \omega)]^T \quad (12a)$$

$$W_u^{(j)}(\xi, \omega, z_j) = [A^{(j)}(\xi, \omega) \quad C^{(j)}(\xi, \omega) \quad E^{(j)}(\xi, \omega)]^T \quad (12b)$$

$$W_d^{(j)}(\xi, \omega, z) = E^{(j)}(z - z_{j-1})W_d^{(j)}(\xi, \omega, z_{j-1}) \quad (12c)$$

$$W_u^{(j)}(\xi, \omega, z) = E^{(j)}(z_j - z)W_u^{(j)}(\xi, \omega, z_j) \quad (12d)$$

where

$$E^{(j)}(\hbar) = \begin{bmatrix} e^{-\gamma_1^{(j)}\hbar} & 0 & 0 \\ 0 & e^{-\gamma_2^{(j)}\hbar} & 0 \\ 0 & 0 & e^{-\gamma_3^{(j)}\hbar} \end{bmatrix}$$

The continuity conditions in frequency-wavenumber domain can be expressed as:

$$\psi^{(j)}(\xi, \omega, z_j) = \psi^{j+1}(\xi, \omega, z_j), \quad (j \neq l), \quad (13)$$

According to equations given in Eq. (13), the down-going and up-going wave vectors at the interface  $z = z_j$  can be deduced:

$$\begin{bmatrix} W_d^{(j+1)}(z_j) \\ W_u^{(j)}(z_j) \end{bmatrix} = \begin{bmatrix} T_d^{(j)} & R_u^{(j)} \\ R_d^{(j)} & T_u^{(j)} \end{bmatrix} \begin{bmatrix} W_d^{(j)}(z_j) \\ W_u^{(j+1)}(z_j) \end{bmatrix} \quad (15)$$

where  $\begin{bmatrix} T_d^{(j)} & R_u^{(j)} \\ R_d^{(j)} & T_u^{(j)} \end{bmatrix} = \begin{bmatrix} -D_d^{(j+1)} & D_u^{(j)} \\ -S_d^{(j+1)} & S_u^{(j)} \end{bmatrix}^{-1} \begin{bmatrix} -D_d^{(j)} & D_u^{(j+1)} \\ -S_d^{(j)} & S_u^{(j+1)} \end{bmatrix}$ .

The matrixes  $R_d^{(j)}(\xi, \omega)$  and  $R_u^{(j)}(\xi, \omega)$  in Eq. (15) represent reflection matrixes for the down-going and up-going  $P_1$ ,  $P_2$ ,  $S$  waves incident on the  $j$ th interface, while  $S_d^{(j)}(\xi, \omega)$  and  $S_u^{(j)}(\xi, \omega)$  denote transmission matrixes for the down-going and un-going  $P_1$ ,  $P_2$ ,  $S$  waves incident on the  $j$ th interface.

When the  $n + 1$ th layer is the rigid bedrock, the following relations can be obtained by the boundary conditions at the interface  $z = z_n$ :

$$W_u^{(n)}(z_n) = R_d^{g(n)}W_d^{(n)}(z_n) = R_{de}^{g(n)}W_d^{(n)}(z_{n-1}) \quad (16b)$$

where  $R_d^{g(n)} = -(D_u^{(n)})^{-1}D_d^{(n)}$  and

$$\begin{bmatrix} T_{de}^{g(j)} & R_{ue}^{g(j)} \\ R_{de}^{g(j)} & T_{ue}^{g(j)} \end{bmatrix} = \begin{bmatrix} T_d^{g(j)} & R_u^{g(j)} \\ R_d^{g(j)} & T_u^{g(j)} \end{bmatrix} \begin{bmatrix} E^{(j)}(h_j) & 0 \\ 0 & E^{(j+1)}(h_{j+1}) \end{bmatrix}$$

When  $j = n - 1$ ,

$$\begin{cases} W_d^{(n)}(z_{n-1}) = T_{de}^{g(n-1)} W_d^{(n-1)}(z_{n-2}) \\ W_u^{(n-1)}(z_{n-1}) = R_{de}^{g(n-1)} W_d^{(n-1)}(z_{n-2}) \end{cases} \quad (17b)$$

where

$$\begin{cases} T_{de}^{g(n-1)} = \left( I - R_{ue}^{(n-1)} R_{de}^{g(n)} \right)^{-1} T_{de}^{(n-1)} \\ R_{de}^{g(n-1)} = R_{de}^{(n-1)} + T_{ue}^{(n-1)} R_{de}^{g(n)} T_{de}^{(n-1)} \end{cases}$$

Then, the wave vectors of soil layers below the buried moving load (i.e.,  $l < j < n$ ) can be deduced recursively.

While for the layers above the buried moving load (i.e.,  $0 < j < l$ ), one can get the following equations according to the boundary conditions on the free surface primarily

$$W_d^{(1)}(z_0) = -\left( S_d^{(1)} \right)^{-1} S_u^{(1)} W_u^{(1)}(z_0) = R_{ue}^{g(0)} W_u^{(1)}(z_1) \quad (19b)$$

When  $j = 1$

$$\begin{cases} W_u^{(1)}(z_1) = T_{ue}^{g(1)} W_u^{(2)}(z_2) \\ W_d^{(2)}(z_1) = R_{ue}^{g(1)} W_u^{(2)}(z_2) \end{cases} \quad (20b)$$

where

$$\begin{cases} T_{ue}^{g(1)} = \left( I - R_{de}^{(1)} R_{ue}^{g(0)} \right)^{-1} T_{ue}^{(1)} \\ R_{ue}^{g(1)} = R_{ue}^{(1)} + T_{de}^{(1)} R_{ue}^{g(0)} T_{ue}^{(1)} \end{cases}$$

Then, similarly, the recursion formula of the wave vectors for soil layers above the buried moving load can be deduced.

As a result, the wave vectors of arbitrary layers need to be derived from the up-going wave vector of the  $l$ th layer (i.e.,  $W_u^{(l)}(z_l)$ ) and the down-going wave vector of the  $l + 1$ th layer (i.e.,  $W_d^{(l+1)}(z_l)$ ) recursively.

The wave vectors  $W_u^{(l)}(z_l)$  and  $W_d^{(l+1)}(z_l)$  can be obtained by the continuity conditions given in Eqs. (9c)–(9h):

$$\begin{bmatrix} W_u^{(l)}(z_l) \\ W_d^{(l+1)}(z_l) \end{bmatrix} = \begin{bmatrix} D_d^{(l)} R_{ue}^{g(l-1)} E^{(l)}(h_l) + D_u^l & - (D_u^{(l+1)} R_{de}^{g(l+1)} E^{(l+1)}(h_{l+1}) + D_d^{(l+1)}) \\ S_d^{(l)} R_{ue}^{g(l-1)} E^{(l)}(h_l) + S_u^l & - (S_u^{(l+1)} R_{de}^{g(l+1)} E^{(l+1)}(h_{l+1}) + S_d^{(l+1)}) \end{bmatrix}^{-1} \begin{bmatrix} O \\ Q \end{bmatrix} \quad (22b)$$

where  $Q = \begin{bmatrix} 0 & \widehat{F} & 0 \end{bmatrix}^T$  and  $\widehat{F} = 4\pi f_0 \frac{\sin(\xi a)}{\xi} \delta(\omega + c\xi) \cdot \delta(\cdot \cdot \cdot)$  is the Dirac's delta function.

$O$  is the empty matrix of  $3 \times 1$ , i.e.  $O = [0 \ 0 \ 0]^T$ .

Besides, if the  $n + 1$ th layer is the half-plane, the up-going wave in the  $n + 1$ th layer will vanish. The boundary condition can be expressed:

$$W_u^{(n+1)}(\xi, \omega, z) = 0, \quad z \geq z_n \quad (23a)$$

Then, we can get the following expression

$$R_{de}^{g(n+1)} = 0 \quad (23b)$$

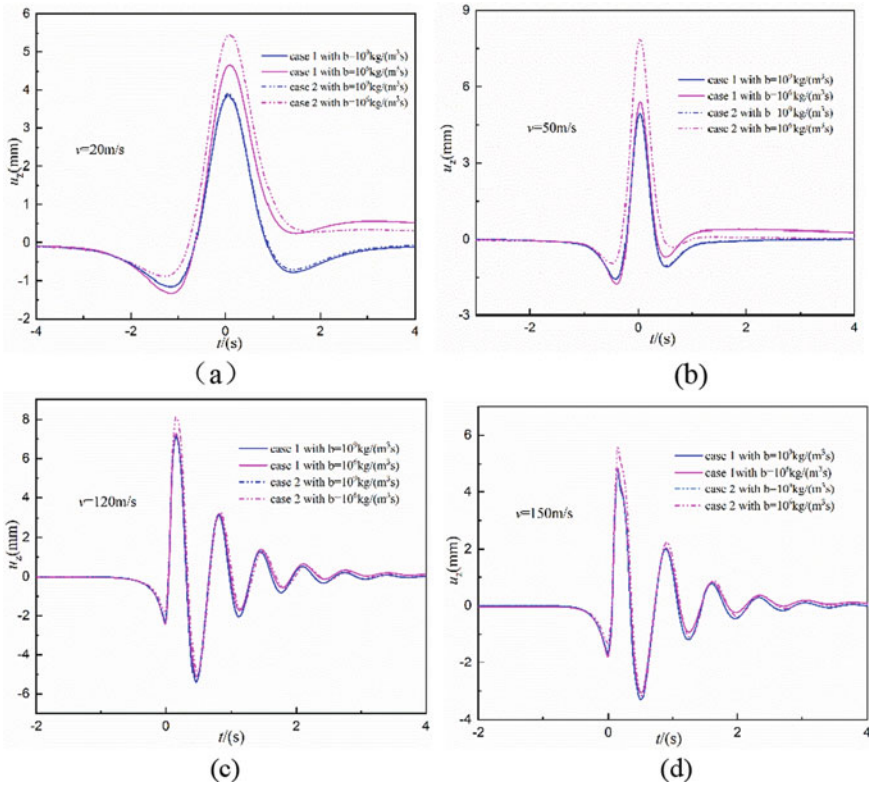
For the undrained poroelastic half-plane, the solution procedure is the same with what adopted above. The difference only exists in the expression  $R(z)$  in Eq. (8): The order of terms  $w_z$  and  $p$  should be made a transposition to present the boundary condition.

Then, the analytical solutions for dynamic response in time–space domain can be obtained by performing the double-inverse Fourier transform to Eq. (11).

## 4 Numerical Results

Two soil cases are considered. Case 1: The boundary condition of the ground surface is assumed to be drained, and the vibration results are depicted with the solid lines; Case 2: The boundary condition of the ground surface is assumed to be undrained, and the vibration results are depicted with the dashed lines. The parameter  $b$  denotes the permeability of the poroelastic soil, and the bigger the value of  $b$ , the lower the permeability of the soil. The results with  $b = 10^9 \text{ kg}/(\text{m}^3\text{s})$  are shown by the blue lines, while the results with  $b = 10^6 \text{ kg}/(\text{m}^3\text{s})$  are shown by the red lines.

The time histories of the surface vertical displacement under moving loads with different velocities are depicted in Fig. 2. It can be observed that the better the soil permeability, the more significant the effect of the boundary drainage condition on the surface vibration. And the influence of the soil permeability on surface vertical



**Fig. 2** Time histories of the surface vertical displacement

displacement is more obvious when the surface of the ground is undrained than that when the surface of the ground is drained.

Besides, by comparing the gaps between the displacement peaks in each graph in Fig. 2, it can also be found that the impact of the boundary permeability on the vertical displacement is also associated with the moving load velocity. Taking  $b = 10^6\text{ kg/(m}^3\text{s)}$  as an example, the impact of the boundary permeability increases with the increase of the load speed when the load speed is lower than the critical speed. When the load speed is faster than the critical speed, the effect of the boundary permeability decreases and the influence of the load speed becomes not obvious with the vibration curves exhibiting oscillations.



## 5 Conclusions

For the saturated poroelastic soil medium, the drainage condition of ground surface is of great significance to the dynamic response of the saturated poroelastic half-space subjected to the underground moving load. And the surface drainage condition associating with the soil permeability affects the vertical displacement of the ground surface, which is more obvious when the moving load speed is lower than the critical velocity.

**Acknowledgements** The work described in this paper is supported in part by the National Science Foundation of China (No. 51978612).

## References

1. Metrikine AV, Vrouwenvelder A (2000) Surface ground vibration due to a moving train in a tunnel: two-dimensional model. *J Sound Vibr* 234(1):43–66
2. Koziol P, Mares C, Esat I (2008) Wavelet approach to vibratory analysis of surface due to a load moving in the layer. *Int J Solids Struct* 45(7–8):2140–2159
3. Yuan ZH, Xu CJ, Cai YQ et al (2015) Dynamic response of a tunnel buried in a saturated poroelastic soil layer to a moving point load. *Soil Dyn Earthq Eng* 77:348–359
4. Forrest JA, Hunt HEM (2006) A three-dimensional tunnel model for calculation of train-induced ground vibration. *J Sound Vib* 294(4–5):678–705
5. Forrest JA, Hunt HEM (2006) Ground vibration generated by trains in underground tunnels. *J Sound Vib* 294(4):706–736
6. Lu JF, Jeng DS (2006) Dynamic response of a circular tunnel embedded in a saturated poroelastic medium due to a moving load. *J Vibr Acoust* 128(6):750–756
7. Yuan ZH, Boström A, Cai YQ (2017) Benchmark solution for vibrations from a moving point source in a tunnel embedded in a half-space. *J Sound Vib* 387:177–193
8. Andersen L, Jones CJC (2006) Coupled boundary and finite element analysis of vibration from railway tunnels—a comparison of two-and three-dimensional models. *J Sound Vib* 293(3–5):611–625
9. Gupta S, Stanus Y, Lombaert G et al (2009) Influence of tunnel and soil parameters on vibrations from underground railways. *J Sound Vib* 327(1–2):70–91
10. Xu QY, Xiao ZC et al (2015) Comparison of 2D and 3D prediction models for environmental vibration induced by underground railway with two types of tracks. *Comput Geotech* 68:169–183
11. Yang YB, Hung HH (2008) Soil vibrations caused by underground moving trains. *J Geotech Geoenviron Eng* 134(11):1633–1644
12. Bian XC, Jin WF, Jiang HG (2012) Ground-borne vibrations due to dynamic loadings from moving trains in subway tunnels. *J Zhejiang Univ Sci A (Appl Phys Eng)* 13(11):870–876
13. He C, Zhou SH, Di HG et al (2018) A 2.5-D coupled FE–BE model for the dynamic interaction between saturated soil and longitudinally invariant structures. *Comput Geotech* 82:211–222
14. Hussein MFM, François S, Schevenels M et al (2014) The fictitious force method for efficient calculation of vibration from a tunnel embedded in a multi-layered half-space. *J Sound Vib* 333(25):6996–7018
15. He C, Zhou SH, Di HG et al (2018) Analytical method for calculation of ground vibration from a tunnel embedded in a multi-layered half-space. *Comput Geotech* 99:149–164

16. Sheng X, Jones CJC, Thompson DJ (2003) Ground vibration generated by a harmonic load moving in a circular tunnel in a layered ground. *J Low Freq Noise Vib Active Control* 22(2):83–96
17. Cai YQ, Sun HL, Xu CJ (2007) Steady state responses of poroelastic half-space soil medium to a moving rectangular load. *Int J Solids Struct* 44(22–23):7183–7196
18. Biot MA (1956) Theory of propagation of elastic waves in a fluid-saturated porous solid. Part I: low-frequency range. *J Acoust Soc Am* 28(2): 168–178
19. Biot MA (1962) Mechanics of deformation and acoustic propagation in porous media. *J Appl Phys* 33(4):1482–1498
20. Debarros FCP, Luco JE (1994) Response of a layered viscoelastic half-space to a moving point load. *Wave Motion* 19(2):189–210
21. Lu JF, Hanyga A (2005) Fundamental solution for a layered porous half space subject to a vertical point force or a point fluid source. *Comput Mech* 35(5):376–391

# The Effect of Excavation Unloading on the Deformation of Existing Underlying Shield Tunnel



Min-yun Hu, Jing-tian Yang, Li-dong Pan, Kong-shu Peng, and Yu-ke Lu

**Abstract** Deformation measurements from 17 real cases of excavation spanning subway tunnels in soft soil were collected for examining the deformation reaction of the tunnels due to the above unloading. The investigation showed that (1) tunnel may be uplifted owing to the above excavation; (2) the deformation of the tunnel section due to above unloading exhibits vertical elongation and horizontal shortening, and the transversal shape of the tunnel changes from approximate circle to vertical ellipse; (3) the main influential factors include the excavation unloading ratio ( $N$ ), the excavation area ( $A$ ), and the excavation shape coefficient ( $\alpha$ ). It indicates that, with the increase of excavation depth and the increase of unloading ratio ( $N$ ) of foundation pit, the rebound of tunnels may increase, and the higher the width of the excavation, the larger the range of vertical uplift that will be induced around the tunnel. For 12 out of the 17 examined cases, the vertical uplift measurements of the tunnels are smaller than the alarmed value of 10 mm, indicating that the maximum displacement of the tunnel can be controlled by purposed engineering measures, such as pre-reinforcement of the soil around the tunnel, installation of the anti-pulling piles around tunnel, and stacking around the bottom of the excavation. 2-D FEM modelling was also carried out to study the effect of excavation characters and the effectiveness of the control procedures. The combination procedure of soil improvement by cement mixing and anti-pulling pile installation is verified to be effective to reduce the adverse impact from above excavation on tunnels.

**Keywords** Pit excavation · Subway tunnel deformation · Real case study · Finite element method analysis · Engineering measure

---

M. Hu (✉) · J. Yang  
Zhejiang University of Technology, Hangzhou, China  
e-mail: [huminyun@zjut.edu.cn](mailto:huminyun@zjut.edu.cn)

L. Pan  
Poly Zhejiang Real Estate Development Co. Ltd., Hangzhou, China

K. Peng  
Huadong Engineering Corporation Limited, Hangzhou, China

Y. Lu  
Zhejiang University of Technology Engineering Design Group Co. Ltd., Hangzhou, China

## 1 Introduction

In recent decades, the underground space exploitation has been accelerated due to the increasing stress of transportation in the urban area in east China. Various underground structures, such as underground fast-ways, subway stations, subway tunnels, municipal pipes, etc., are being laid into limited underground areas and normally within a depth of 30 m, where, in most of the cases, saturated soft soil strata extend through the engineering depth. At the same time, all sorts of excavations, such as foundation pits and underground pedestrian passages, are being constructed in the crowded urban area. Inevitably, there are cases that deep braced excavations are to be/has been constructed over an existing tunnel pipe. For the sake of the safety assessment and protection of the underlying tunnel, attention has been paid to the impact of the excavation on displacement/deformation of the underlying tunnels.

Theoretical and numerical analysis lead to the basic recognition of the impact of an excavation on constructed tunnels. Theoretical analysis on basis of Mindlin's solutions was carried out on Pasternak's elastic foundation model [1] or on Kerr's foundation model [2–4]. The derivations were in terms of the additional stresses in the tunnel structure, the cross-sectional deformation, and the longitudinal deflection of the tunnel pipe. Although theoretical calculations established the framework of the analysis, they were based on ideal ground conditions and for specific working states. Numerical analysis contributed further to the effect of ground improvement on the tunnel displacement and deformation and to tunnel's reflection to the above unloading process [5–15].

Up-to-date researches show that tunnel undergoes uplift displacement when an excavation is constructed overhead, leading to differential longitudinal settlement, which may cause cracks and then leakage and threaten the service of the tunnel. It was realized that the vertical displacement control is the key point for tunnel protection. For the purpose of the vertical displacement control, the character of an excavation, such as the depth, the size, and the construction sequence, should be considered, and the effect of engineering measures, such as ground improvement, should be assessed. However, field observations, which could directly reflect the effect of overhead excavation on tunnels and could assess the effectiveness of engineering measures, are seldom reported.

In this study, field measurements from 17 real cases were summarized to categorize the main factors that have impact on the tunnel's reaction. Furthermore, 2D FEM analysis was carried out to study the influence of the various factors under certain engineering control measures.

## 2 Case Analysis

17 cases [8, 16–28], each with a retained excavation spanning existing shield tunnel(s), were collected for investigation purposes. Most of the tunnels in study

were located in clayey soils. For the protection of the running tunnels, it was requested for the retaining structures' construction that the vertical displacement of the tunnel below the excavation should be strictly controlled. Therefore, engineering measures were taken for each specific case, such as ground improvement around the tunnel, anti-pulling piles installation, and planned sectional digging/block excavation method, as shown in Fig. 1. For the vertical displacement analysis, the effect of the depth, the area, and the shape of excavation were discussed.

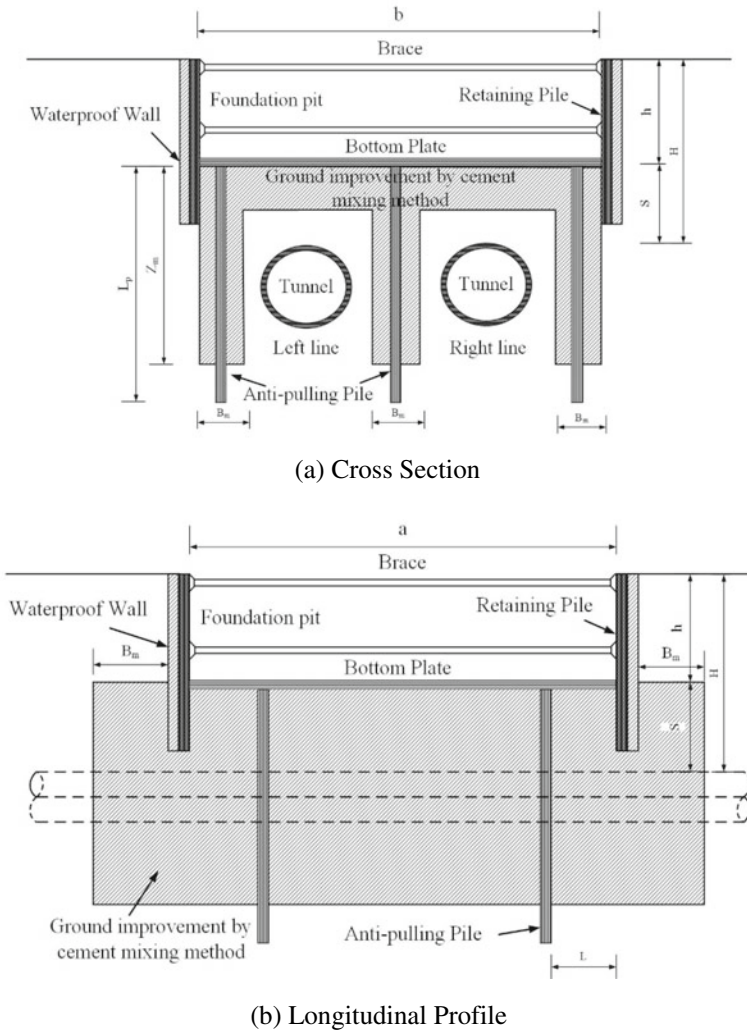
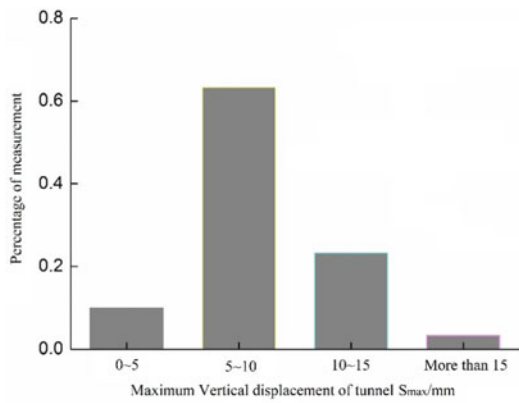


Fig. 1 Schematic illustration of excavation and protected tunnel

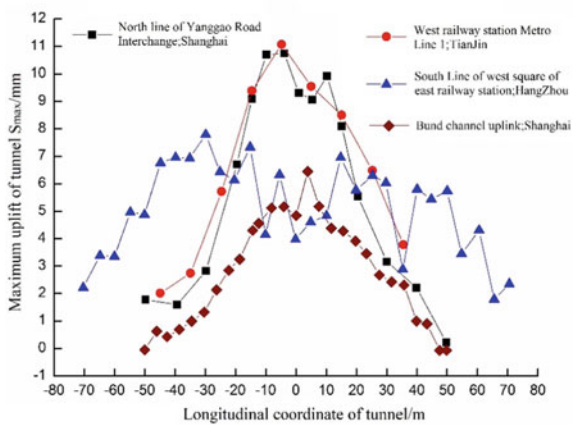
### 2.1 The Vertical Displacement of Tunnels

In term of the design of the retained excavation, other than the strength of the retaining structure and the stability of the excavated soil ground, a key point of consideration is to control the displacement of the underlying existing/running tunnels. Figure 2a gives the statistical outcome of the maximum vertical displacement of the tunnels resulted from the above excavations. It can be seen that most of the maximum heave values are less than 10 mm, which is the upper threshold of the controlling value, validating the effectiveness of the engineering measures. However, in 7 cases, about 41%, the measurements exceed the upper limit. Figure 2b gives the longitudinal heave of 4 tunnels. And it shows that the influence range of the heave extends normally up to 50 m on each side.

**Fig. 2** Uplifting displacement of the underlying tunnels



(a) The maximum heave of tunnels



(b) Heave in the longitudinal direction

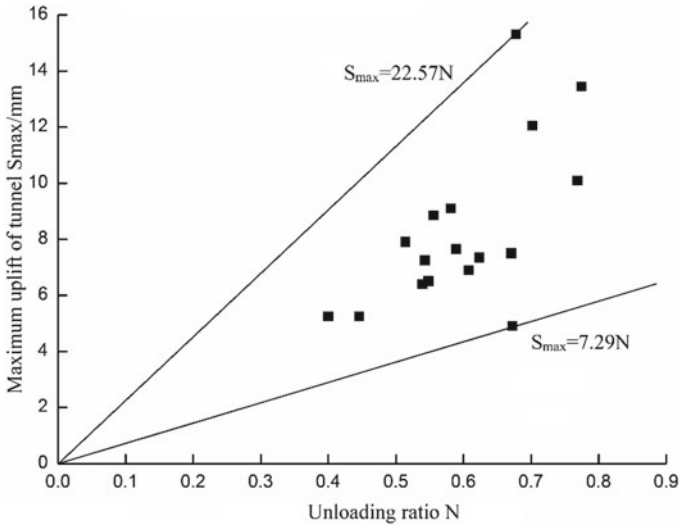


Fig. 3 The relationship of  $s_{max} \sim N$

### 2.2 The Effect of the Depth of Excavation

The depth of excavation indicates the amount of unloading, which leads to the heave of the beneath tunnel. But, the effect of this unloading on the heave of tunnel is also related to the buried depth of the tunnel itself. Unloading Ratio ( $N$ ) was therefore defined [19] as the ratio of the excavation depth  $h$  to the buried depth  $H$  of the tunnel top,  $N = h/H$ .

Figure 3 presents the relation between  $N$  and the maximum heave of the tunnel,  $s_{max}$ , according to the collected data. It can be observed that  $s_{max}$  tends to increase with  $N$  although the data scattered. The increment rate of  $s_{max}$  with  $N$  is between 7.29 and 22.57. The dispersion of the data may due to other factors, such as type of soil, method of excavation, etc.

### 2.3 The Effect of the Size of Excavation

The size of excavation indicates the unloading area. Figure 4 shows the variation of  $s_{max}$  with the excavation area ( $A$ ) above the tunnel. The data scatter in the statistical range of areas, indicating that the heave of the tunnel cannot be simply related to the area of excavation.

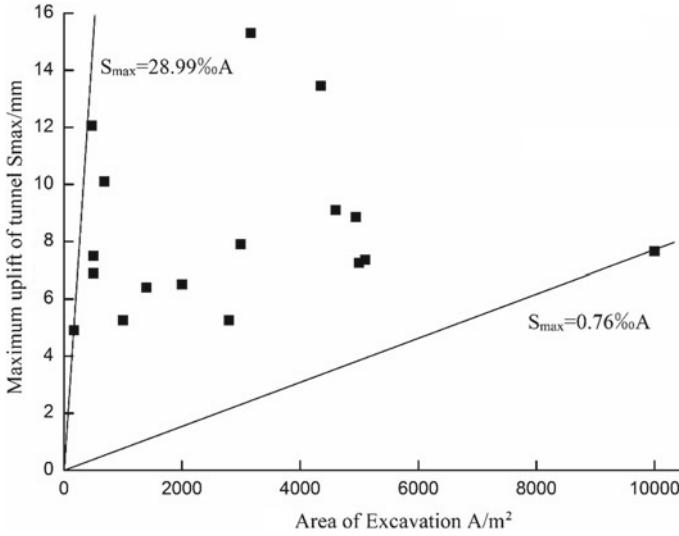


Fig. 4 The relationship of  $s_{max} \sim A$

### 2.4 The Effect of the Shape of Excavation

The shape of excavation can be described by the coefficient of shape ( $\alpha$ ), which is expressed as

$$\alpha = 2\sqrt{ab}/(a + b) \tag{1}$$

where  $a$  and  $b$  are the length and width of the excavation respectively. The length is along the tunnel’s axis, and the width is perpendicular to the axis of tunnel, as shown in Fig. 1. Figure 5 shows the variation of  $s_{max}$  with  $\alpha$ . It indicates that  $s_{max}$  tends to increase with  $\alpha$ . The effect of the width of an excavation on tunnel heave will be further evaluated by FEM simulation in below.

### 2.5 Summary of field observations

In the 17 cases, the maximum uplift vertical displacement of the shield tunnels below the excavated pits was between 4.0 and 15.9 mm. Among them, 12 cases showed smaller displacement than the alarm value of 10 mm, indicating that the maximum heave of the shield tunnel below the foundation pit could be controlled by proper measures. The measured values of the horizontal displacement of the tunnels were small compared to vertical reflections, so, for safety control, the vertical displacement should be assessed properly. The deformation of the tunnel’s cross section due to



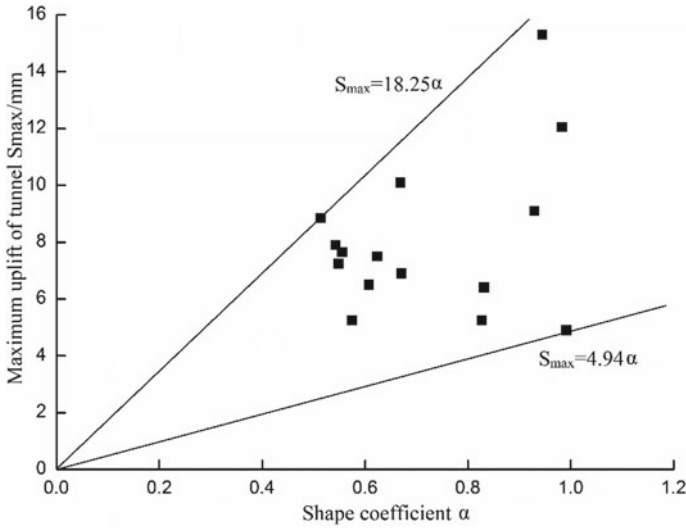


Fig. 5 The relationship of  $s_{max} \sim \alpha$

above excavation exhibited the tendency of vertical elongation and horizontal shortening. The shape of the longitudinal heave of the tunnel is like a Gaussian distribution curve, and the maximum heave of the tunnel mostly occurs below the center of the pit. The influential range of pit excavation was about 2–3 times the width of the pit.

The geometric characteristics of the excavated pit, including excavation depth, excavation unloading ratio  $N$ , excavation area  $A$  and the shape coefficient  $\alpha$ , have direct effect on the displacement/deformation of the tunnel. It also proved that engineering measures, such as soil improvement, installation of anti-pulling piles, and excavation in blocks in strictly limited time, are effective to control the impact of the excavation on the tunnel.

Although the field measurements can help identify the main factors from the excavation on the tunnel’s deformation, specific studies should be carried out to clarify the relationship between the factors and the vertical deformation of tunnel, also the relationship between the controlling methods and the controlled deformation.

### 3 FEM Modelling of Protected Tunnel

In order to further clarify the influence of excavation on the underneath tunnel, 2D FEM simulation analyses were carried out with a protected tunnel model. Two categories of problems were investigated: (i) the effect of the size of the excavation, including the depth and the width; (ii) the effectiveness of protection measures, including the ground improvement plan and the length of the anti-pulling piles. The

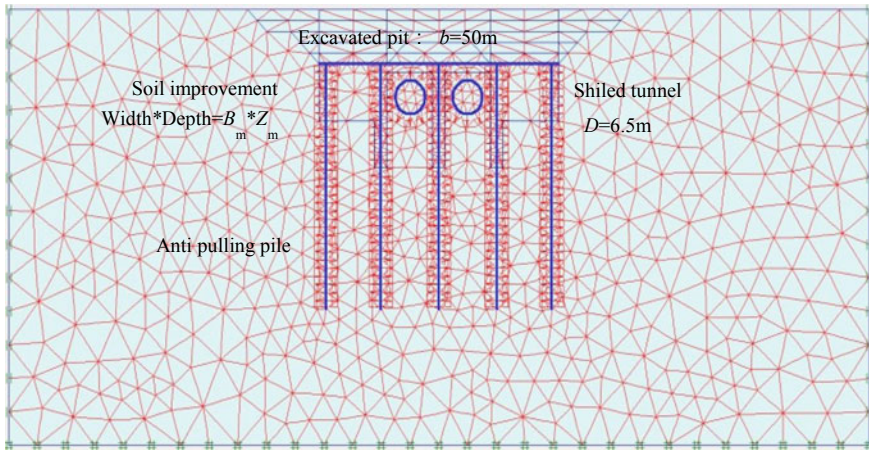


Fig. 6 2D FEM model

anti-pulling piles installation and soil improvement by deep mixing method were finished before the excavation started.

### 3.1 Geometric Model

Figure 6 gives the 2D FEM model (Horizontal  $\times$  Vertical = 180 m  $\times$  80 m) of a pit excavation being constructed over a double-line shield tunnels ( $D = 6.5$  m) where anti-pulling piles and ground improvement were employed on both sides of the tunnels for protection purposes. The modelling program was carried out by PLAXIS 2D code. 15-node triangular isoparametric solid element were used for modelling the soil layers and the improved ground, and ‘plate’ elements were used for concrete members, such as piles and the liner of the tunnels. Goodman elements were set for the contact surface between piles and soil. The boundary conditions were set as horizontal rollers at the bottom and vertical rollers at the sides. There were totally 1730 elements and 15,299 nodes.

### 3.2 Soil Model and the Parameters

In FEM simulation, a homogeneous soil layer was considered and the hardening soil model was adopted to describe the soil’s behavior. When the soil is improved by mixed-in-place method, the parameters should be adjusted. The soil parameters in the modeling analysis were given in Table 1. The behavior of concrete piles, the bottom plate of pit, and liners of tunnel were considered elastic. The reduction of the

**Table 1** Soil's parameters in Hardening Soil model

Soil	$c'$	$\varphi'$	$\psi$	$E_{50}^{\text{ref}}$ (MPa)	$E_{\text{oed}}^{\text{ref}}$ (MPa)	$E_{\text{ur}}^{\text{ref}}$ (MPa)	$\nu_{\text{ur}}$	$p_{\text{ref}}$ (kPa)	$K_0$	$m$	$R_f$
Silty clay	5.5	28	0	20	10	60	0.2	100	0.5	0.5	0.9
Improved soil	170	40	10	120	120	360	0.2	100	0.43	0.5	0.9

**Table 2** Structure parameters in FEM simulation

Member	Modulus of elasticity $E$ ( $10^4$ MPa)	$EA$ (kN/m)	$EI$ (kN m <sup>2</sup> /m)	Poisson's ratio $\mu$
Anti-pulling pile	3.00	$1.2 \times 10^7$	$1.6 \times 10^5$	0.15
Bottom plate	3.00	$2.3 \times 10^7$	$1.1 \times 10^6$	0.2
Tunnel liner	3.45	$1.1 \times 10^7$	$1.1 \times 10^5$	0.15

rigidity of tunnel liners due to the assembling method was taken into account. The elastic parameters for underground structures were shown in Table 2.

## 4 Result and Discussion

### 4.1 The Effect of the Depth of Excavation

When the width of excavation was set to be 50 m and the top of the tunnel was at the depth of 12 m, the depth of excavation was increased from 2 to 10 m to investigate the influence of the unloading ratio  $N$  ( $=0.2-1.0$ ) on the uplift displacement of the tunnel. The result was shown in Fig. 7.

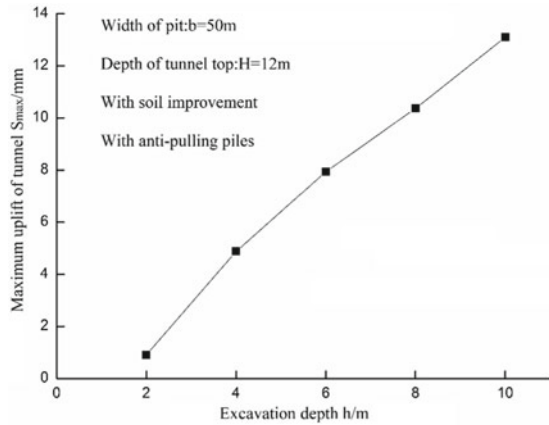
Figure 7a gives the increment of the uplift displacement of tunnel with the excavation depth, and Fig. 7b illustrates this relationship in term of  $s_{\text{max}} \sim N$ . It can be seen that  $s_{\text{max}}$  increased steadily with depth of excavation  $h$ , which is in consistency with observations as shown in Fig. 2, indicating that the unloading process is crucial to the uplift displacement of tunnel.

### 4.2 The Effect of the Width of the Excavation

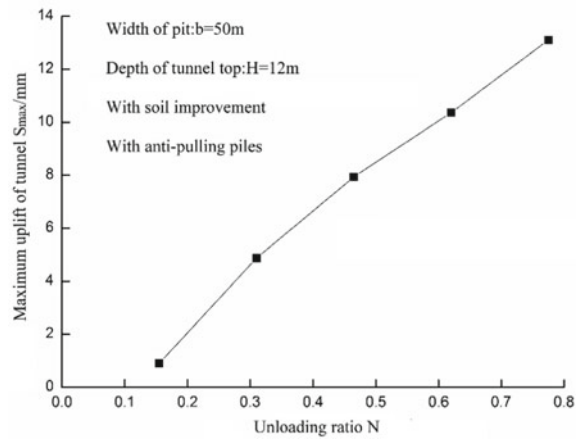
To examine the effect of the width of excavation, the depth of pit was set to be 10 m and the top of the tunnel was at the depth of 12 m. The width varied from 10 m to 180 m (as a large extensive excavation).

Figure 8 shows that the uplift displacement of tunnel increases with the width of excavation. The rate of increment of vertical displacement with width of pit is not a

**Fig. 7** Influence of excavation depth on tunnel’s vertical displacement



(a) The relationship of



(b) The relationship of  $s_{max} \sim N$

constant. After the width of the pit is 60–70 m, about 10 times the tunnel’s diameter, the increment rate of the heave gradually slows down.

### 4.3 The Effect of Ground Improvement

The effectiveness of ground improvement by cement mixing method was evaluated by changing the depth, the width, and the strength of improved soil. In the model, the width of excavation was set to be 50 m, the top of the tunnel was at the depth of 12 m, and the gap between the bottom of pit and the top of tunnel was of  $S = 3, 5,$  and 7 m. Herein, there was no installation of anti-pulling piles.

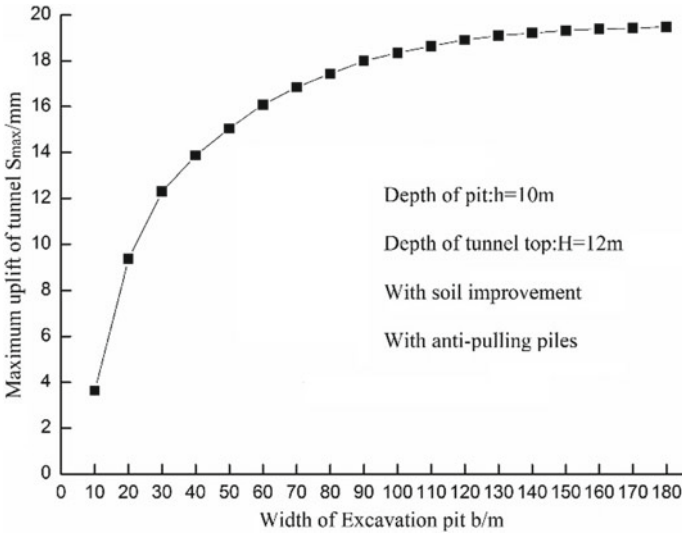


Fig. 8 Influence of excavation width on tunnel's vertical displacement

The depth of the improvement ( $Z_m$ ) changed from 0 to 20 m under the designed bottom of pit. Figure 9 gives the variation of the uplift displacement of the tunnel with the depth of soil improvement. It can be observed that the deeper the soil improvement is, the smaller the uplift movement occurs. When  $Z_m$  is less than 10 m, the uplift movement of the underlying tunnel reduces with the increase of the improved depth,

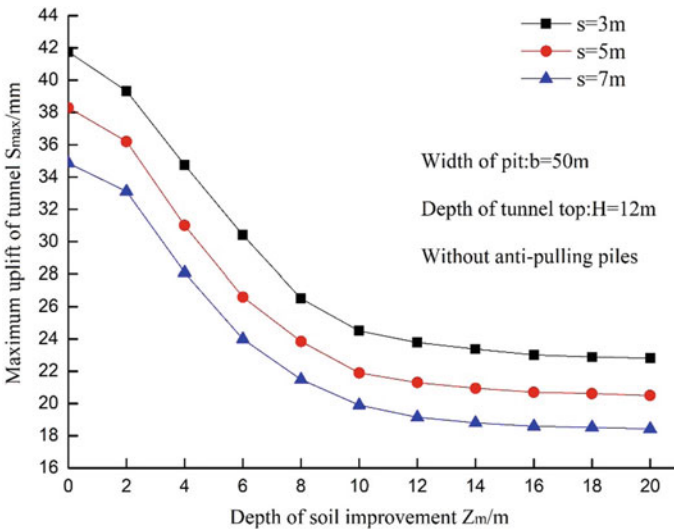


Fig. 9 The relationship of  $s_{max} \sim Z_m$

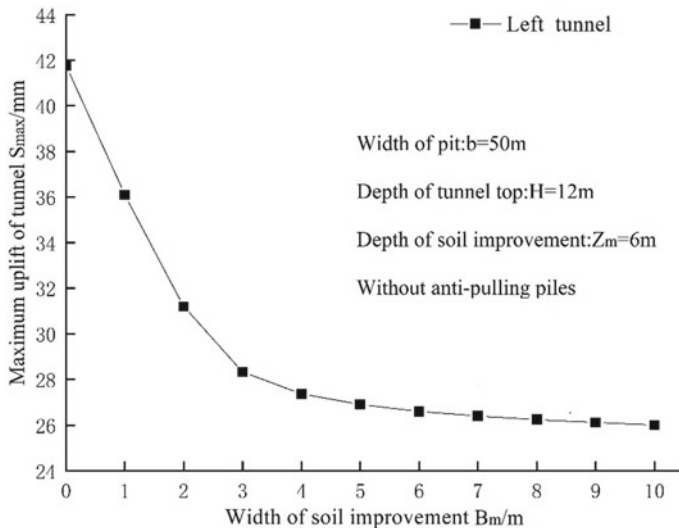


Fig. 10 The relationship of  $s_{max} \sim B$

but, for all three gaps between the bottom of excavation and the top of tunnel, after  $Z_m$  is over 10 m, the reduction of the uplift movement sharply slows down.

In order to investigate the effect of the width of the improved soil ( $B$ ), the depth of the improvement ( $Z_m$ ) was set to be 8 m and the gap between the bottom of pit and the top of tunnel was 3 m. When  $B$  is changed from 0 to 10 m, Fig. 10 shows the variation of the tunnel’s maximum uplift  $s_{max}$ . It can be seen that width of the soil improvement around the tunnel has an obvious impact on tunnel’s displacement reduction, but when the improved width is more than 3 m, which is about half of the tunnel’s diameter, the reduction of tunnel uplift doesn’t change much with width increase.

If cement concentration in the mixed soil is increased, soil’s shear strength and the elastic modulus can be increased. Figure 11 shows the variation of  $s_{max}$  with soil’s elastic modulus increment due to soil cementation. It is observed that the uplift displacement of tunnel decreases with the enhanced soil modulus. In this modelling, to get an elastic modulus of  $E = 400$  MPa is the most effective of all 3 cases, whereas after  $E = 600$  MPa, the increment of  $E$  can not help much in controlling the uplift displacement of tunnel.

#### 4.4 The Effect of the Length of Anti-Pulling Pile

In this modelling, the width of excavation was 50 m, the top of tunnel was at the depth of 12 m and the depth of excavation was 10 m. Soil improvement by cement mixing method was set to 10 m deep under the pit bottom and 3 m wide on each side

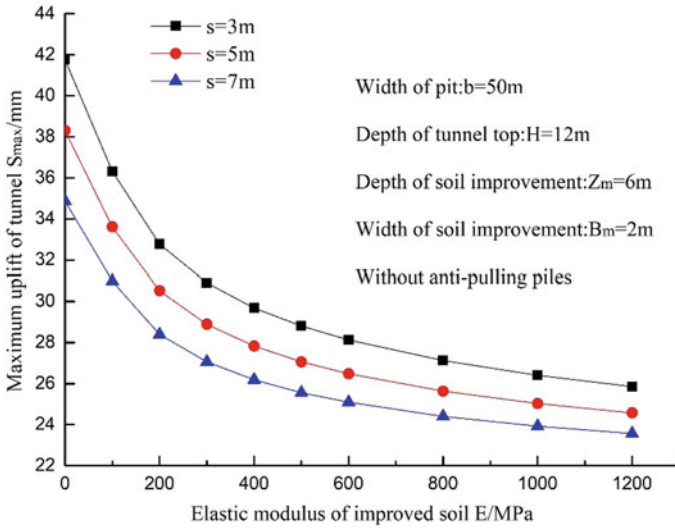


Fig. 11 The relationship of  $s_{max} \sim E$

of the tunnels. The anti-pulling piles were installed on both sides of tunnel with the length of 20 m, 25 m, 30 m, 35 m, and 40 m, respectively.

Figure 12 gives the variation of uplift displacement of tunnel with the length of anti-pulling pile under 3 different distances between the pit bottom and the tunnel

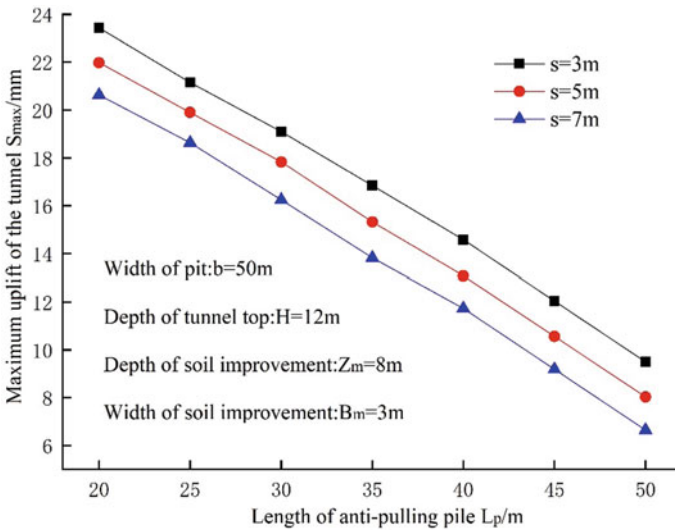


Fig. 12 The relationship of  $s_{max} \sim L_p$

top. It can be seen that the installation of anti-pulling piles can effectively control the vertical displacement of tunnels, and with longer piles, the uplift of the tunnel will be better controlled. It is clear that the combined method with both soil improvement and anti-pulling tunnels can promisingly lead to a satisfactory controlling.

## 5 Conclusions

In this study, deformation measurements from 17 real cases of excavation over-spanning in-use subway tunnels were collected for tunnel reaction analysis in terms of vertical displacement. The measurement shows (1) when excavation was processed to the full depth, the tunnels' displacement could be characterized by uplift movement, while the horizontal displacement of the tunnels was little affected; (2) the deformation of the tunnel cross-section due to over-spanning excavation exhibits *vertical stretch* and *horizontal contraction*, and the shape of the tunnel section tended to be a vertical ellipse; (3) the main influential factors of the excavation are unloading ratio  $N$ , the excavation area  $A$ , and the shape coefficient  $\alpha$ . It indicates that with the increase of excavation depth/unloading ratio  $N$ , the maximum vertical displacement of tunnels tends to increase, and the same trend appears when the width of excavation increases. (4) in 12 out of the 17 cases, the uplift values of tunnels were smaller than the alarm value of 10 mm, indicating the effectiveness of pioneer engineering measures, such as pre-reinforcement of the soil around the tunnel, the installation of anti-pulling piles beside tunnel and stacking at the bottom of the excavation.

2-D FEM modelling was carried out to clarify the effect of excavation characters and the effectiveness of the control procedures. It is shown that, for tunnel protection, the width and, especially, the depth of an overhead excavation should be strictly controlled. The combination procedure of soil improvement by cement mixing and anti-pulling pile installation is verified to be effective. However, both the soil improvement and the anti-pulling piles should be installed in the near field of the tunnels.

**Acknowledgements** This work is funded by the project of National Natural Science Foundation of China (51878616) and by the support from Huadong Engineering Corporation Limited of China.

## References

1. Zhou ZL, Chen SG (2015) Analysis of uplift deflection of subway tunnel due to adjacent pit excavation. *Chin J Geotech Eng* 37(12):2224–2234 (in Chinese)
2. Huang X, Huang HW (2012) Longitudinal deflection of existing shield tunnels due to deep excavation. *Chin J Geotech Eng* 34(7):1241–1249 (in Chinese)
3. Zong X (2016) Study of longitudinal deformation of existing tunnel due to above excavation unloading. *Rock Soil Mech* 37(S 2):571–577 (in Chinese)



4. Jiang Z (2014) Theoretical analysis on deformation of pipeline caused by adjacent foundation pit excavation. *Chin J Undergr Space Eng* 10(2):362–368 (in Chinese)
5. Lo KY, Ramsay JA (1991) The effect of construction on existing subway tunnels—a case study from Toronto. *Tunnels Deep Space* 6(3):287–297
6. Marta D (2001) Tunnel complex unloaded by a deep excavation. *Comput Geotech* 28:469–493
7. Shama JS, Hefny AM (2001) Effect of large excavation on deformation of adjacent MRT tunnels. *Tunn Undergr Space Technol* 16:93–98
8. Hu ZF, Yue ZQ (2003) Design and construction of a deep excavation in soft soils adjacent to the Shanghai Metro tunnels. *Can Geotech J* 40(5):933–948 (in Chinese)
9. Wang WD, Wu JB (2004) Numerical modeling of affection of foundation pit excavation on metro tunnel. *Rock Soil Mech* 25(S11):251–255 (in Chinese)
10. Zhang ZG, Zhang XD (2007) Numerical modeling analysis on deformation effect of metro tunnels due to adjacent excavation of foundation pit. *J Wu Han Univ Technol* 29(11):93–97 (in Chinese)
11. Wang HR (2011) Design and monitoring of the deep excavation in complicated environment. *Chin J Undergr Space Eng* 5:769–976 (in Chinese)
12. Deng X (2013) Numerical analysis of effect of excavation on underlying existing metro tunnel and deformation control. *Rock Soil Mech* 34(5):1459–1468 (in Chinese)
13. Lin H, Chen JY (2015) Numerical analysis on influence of foundation pit excavation on deformation of adjacent existing tunnel. *J Central South Univ (Sci Technol)* 46(11):4240–4247 (in Chinese)
14. Du L, Wang YP (2016) Numerical analysis of influence of pit unloading on underlying metro tunnel. *J Shandong Univ Sci Technol (Nat Sci)* 35(6):62–67 (in Chinese)
15. Wang DJ, Wang WT (2017) Construction influence of pit excavation on underlying subway tunnel. *Chin J Undergr Space Eng* 13 (S1):223–232 (in Chinese)
16. Zhang D (2013) Analysis on behavior of shield-bored metro tunnel caused by construction of large-scale foundation pit located above: case study on foundation pit of west square Hangzhou east railway station. *Tunnel Constr* 33(11):897–902 (in Chinese)
17. Li Y, Chen JY (2011) Numerical analysis of effect of large-scale unloading on underlying shield tunnels. *Chin J Geotech Eng* 35(S2):643–646 (in Chinese)
18. Xiao M (2014) Construction technology of deep foundation excavation in some sunken plaza above metro tunnel. *Constr Technol* 43(17):4–6 (in Chinese)
19. Wei G (2013) Measurement and analysis of impact of foundation pit excavation on below existed shield tunnels. *Rock Soil Mech* 34(5):1421–1428 (in Chinese)
20. Ji MJ (2011) Control of foundation pit construction causing tunnel displacement. *China Municipal Eng* 2:36–39 (in Chinese)
21. Zhou YQ, Yuan JR (2004) Numerical simulation analysis of foundation excavation and environment protection. *Undergr Space* 24(5):719–722 (in Chinese)
22. Huang HW, Huang X (2012) Numerical analysis of the influence of deep excavation on underneath existing road tunnel. *China Civil Eng J* 45(3):182–189 (in Chinese)
23. Li ZG, Liu H (2005) Influence analysis of deep-dip excavation on down tunnel based on the measured displacement. *Chin J Undergr Space Eng* 1(4):620–623 (in Chinese)
24. Chen Y, Zhang DM (2004) Analysis of monitoring data on tunnel heaving due to unloading of foundation pit excavation. *Undergr Space* 24(5):748–751 (in Chinese)
25. Hu RL (2012) Numerical analysis of deformation of operating tunnel caused by deep foundation pit construction. *China Municipal Eng* 2:92–95 (in Chinese)
26. Li JP (2009) Numerical analysis of influence of deep excavation on underlying metro tunnel. *Chin J Undergr Space Eng* 5(S):1345–1349 (in Chinese)
27. Zheng ZP (2010) Protecting design of existing metro tunnel with the up crossing project of north square of West Tianjin railway station. *Chin Overseas Archit* 7:162–163 (in Chinese)
28. Wei G (2005) Measurement and analysis of impact of foundation pit excavation on below existed shield tunnels. *Rock Soil Mech* 34(5):1421–1428 (in Chinese)

# **Intelligent Construction in Earthworks: Technology and Management**

# Field Testing of Automatic Frequency Control for Intelligent Compaction of Embankments



Carl Wersäll  and Andreas Persson

**Abstract** A newly developed intelligent compaction method, automatic frequency control (AFC), has been tested in full-scale field tests. The technique utilizes measurements on the drum to determine the resonant frequency of the dynamic roller-soil system and provides continuous feedback to the roller for automatic adjustment of the frequency. This facilitates compaction at the resonant frequency, even for spatially varying soil properties. Previous tests have been conducted with simplified conditions in indoor full-scale tests and in field tests on low embankments. Those tests showed an increased compaction effect with higher surface stiffness that could likely reduce the number of required passes. This paper describes an additional field test, where a rock-fill embankment has been compacted under realistic conditions. The results confirm that compaction is conducted more efficiently when utilizing AFC, compared to conventional compaction. In addition, AFC increases compaction homogeneity, which provides an embankment less sensitive to rearrangement in the serviceability limit state. Implementing this novel technique can thus reduce costs and environmental impact.

**Keywords** Intelligent compaction · Frequency · Field testing

## 1 Introduction

The current technology for vibratory compaction of embankments was developed during the 1950s, 1960s, and 1970s. In the last 40 years, however, most developments have been in control systems (such as continuous compaction control, CCC), engines, safety, and driver comfort while the fundamental process in which the embankment material is compacted has remained unchanged. Rapid technological development

---

C. Wersäll (✉)

Department of Civil and Architectural Engineering, KTH Royal Institute of Technology, 10044 Stockholm, Sweden  
e-mail: [cwersall@kth.com](mailto:cwersall@kth.com)

A. Persson

Dynapac Compaction Equipment AB, Post Box 504, 37123 Karlskrona, Sweden  
e-mail: [andreas.persson@dynapac.com](mailto:andreas.persson@dynapac.com)

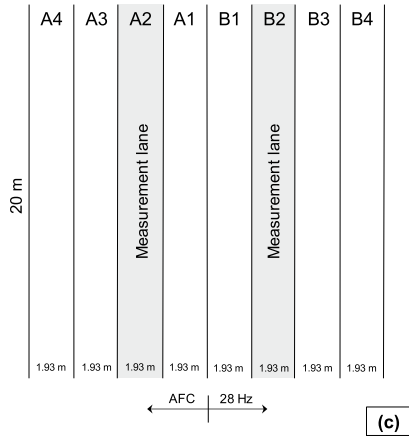
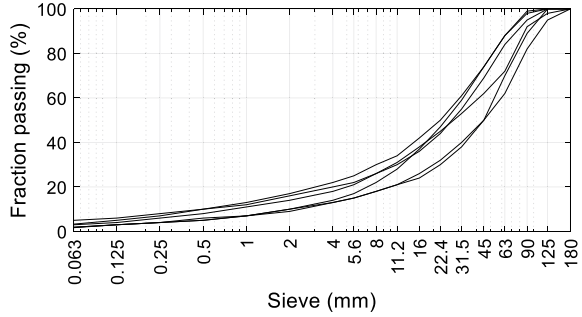
in computers, electronics, artificial intelligence, etc. now provides new possibilities for further development of construction machines, including vibratory rollers. Recent developments include unmanned roller navigation [1] and application of artificial intelligence to roller compaction [2]. Utilizing the current availability of advanced control and feedback systems, a novel intelligent compaction method has been developed that automatically and continuously adjusts the vibration frequency of the drum so that the dynamic roller-soil systems are in a state of resonance. The technique, called automatic frequency control (AFC), is based on findings from small-scale laboratory tests [3, 4] and full-scale indoor tests [5, 6]. These investigations found that resonance is the most effective and energy-efficient frequency in which to operate. Compaction at the resonant frequency has previously been discussed by several authors [7–9]. Automatic frequency adjustment is also available in the Amman Compaction Expert system [10] but does not utilize the full effect of resonance and is combined with adjustment of amplitude.

The first full-scale test with a fully functioning AFC system was conducted in the field on low embankments [11] and found that a higher degree of compaction was obtained while fuel consumption decreased by up to 15%, thus reducing the required operating time and fuel consumption, which implies lower costs and environmental impact. AFC also avoided loosening at the top of the layer, producing a significantly higher surface stiffness. This test had the main limitations that compaction was conducted in a single layer on low embankments and only in single compaction lanes, without compaction of the adjacent material. To study the use of AFC in realistic embankment construction, a subsequent field test was conducted where a 1.5 m high rock-fill embankment was compacted in two layers. In contrary to previous tests, the embankment was compacted over its entire surface to account for realistic conditions. One half of the embankment was compacted using AFC and the other half with a fixed standard frequency. The results from this test are presented in this paper.

## 2 Methods and Materials

The embankment was constructed using crushed rock 0–150 mm according to Swedish regulations for sub-ballast material [12]. Sieve analyses, conducted on samples taken from the embankment, are shown in Fig. 1. At the test site, the subsoil consisted of a compacted stiff gravelly silty till. The embankment was constructed in two layers, where Layer 1 had a compacted thickness of 0.5 m and Layer 2 had a compacted thickness of 1.0 m. Filling was conducted with a bulldozer to avoid separation. Layer 1 was compacted using AFC in 18 passes at high amplitude and 6 passes at low amplitude. For both amplitude settings, no progress in CCC values could be detected at the end of compaction, indicating that maximum compaction had been obtained. The embankment after the end of compaction is shown in Fig. 2a. The roller was a prototype roller based on a Dynapac CA6500D with a static linear load of 65 kN/m that could operate at either a fixed frequency or at a variable frequency

**Fig. 1** Sieve analysis of samples obtained from the embankment



**Fig. 2** Experimental setup; **a** trial embankment; **b** prototype roller; **c** compaction lanes

with AFC, continuously and automatically adjusted to obtain resonance. The fixed frequency was set to 28 Hz and the frequency range for AFC was 17–28 Hz. All passes were conducted at a high amplitude, where the nominal amplitude was 2.1 mm. The roller is shown in Fig. 2b.

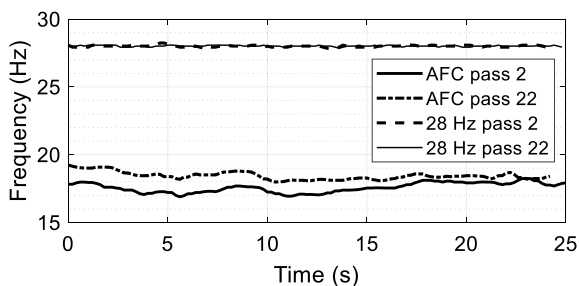
The embankment surface was compacted in 8 lanes with 20 cm overlap. Since the drum width was 2.13 m, each lane had a width of 1.93 m. The total width of the compacted surface was approximately 16 m and each lane was 20 m long. One half of the embankment was compacted by AFC and the other half using the fixed frequency 28 Hz. Figure 2c shows the measurement lanes, where *A* indicate that AFC was enabled and *B* that the frequency was fixed at 28 Hz. First, AFC was enabled and lane A1 was compacted in two passes, followed by two passes on A2, A3, and A4. AFC was then disabled and lanes B1, B2, B3, and B4 were compacted in two passes. This procedure was repeated until all lanes had been compacted in 22 passes. All measurements were conducted on lanes A2 and B2.

Drum acceleration, eccentric position, and roller position (GPS) were logged in all passes on lanes A2 and B2, facilitating analysis of frequency, displacement amplitude, CCC values, and contact force. Vertical deformation within the top 600 mm of the embankment was measured by Epsilon Measuring Units (EMUs). The sensors consist of copper wire, wrapped around circular discs. These coils are placed in vertical alignment in the embankment material at 150–250 mm spacing. When inducing an electric current in one coil, a current can be detected by adjacent coils through electromagnetic induction and this current can be correlated to the distance between the sensors [13]. Through this procedure, the depth-dependent compression that results from compaction can be analyzed. EMUs were placed in two sections below lane A2 and in two sections below lane B2. Each section consisted of four coils, providing three measurement distances. Readings were taken after 0, 2, 4, 8, 12, 16, and 22 passes. Settlement of the embankment surface was measured by leveling in 33 points on lane A2 and 33 points on lane B2 after 0, 2, 4, 8, 12, 16, and 22 passes. In addition, two vertical soil pressure cells were placed at one-meter depth, i.e., in the interface between Layer 1 and Layer 2, to measure the vertical dynamic stress during compaction. One pressure cell was placed below the center of A2 and the other below the center of B2.

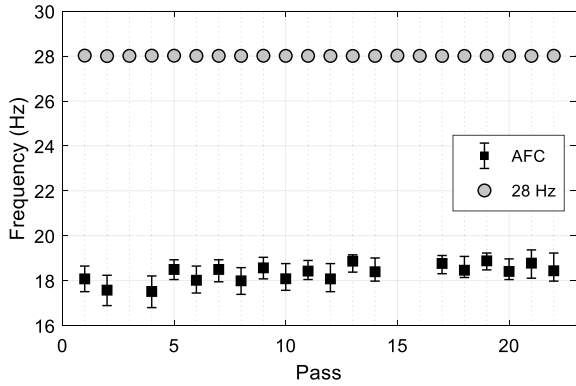
### 3 Results and Discussion

The variation of frequency over pass 2 and pass 22 is shown in Fig. 3. At the fixed frequency, it is constant at the pre-set value of 28 Hz. When AFC is enabled, the frequency is lowered significantly, while continuously varying with soil stiffness. Due to the increased stiffness during the compaction process, the resonant frequency, and thus the compaction frequency, is slightly larger in pass 22 than in pass 2. Figure 4 shows the average frequencies for all passes. Due to equipment malfunction, data was not recorded for AFC in passes 3, 15, and 16. Naturally, the fixed frequency was always constant while AFC implied a varying and slightly increasing frequency. The dynamics of the system, and thus the resonant frequency, somewhat depend on the rotation direction of the eccentric mass in relation to the rotation direction of the

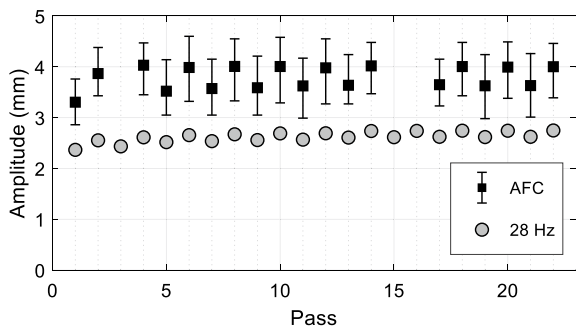
**Fig. 3** Frequency variation over individual passes



**Fig. 4** Average frequencies. The bars indicate maximum and minimum frequencies



**Fig. 5** Average amplitudes. The bars indicate maximum and minimum amplitudes

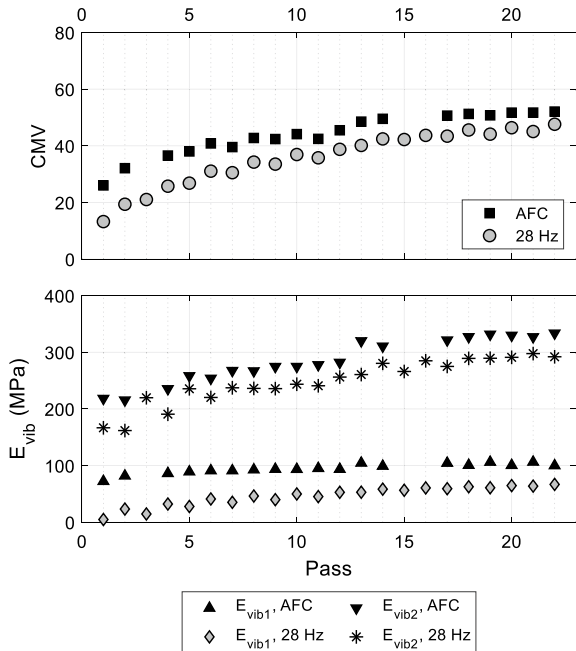


drum. Thus, the excitation frequency during AFC operation depends on whether the roller is moving forward (odd passes) or backward (even passes).

Figure 5 shows the average displacement amplitudes (henceforth denoted *amplitude*). The amplitude depends heavily on frequency and the variation is significantly larger for AFC (the variation of amplitude in individual passes of compaction at 28 Hz is too small to indicate in the figure). However, the amplitude is significantly larger when AFC is enabled, which is consistent with previous studies. Although the centrifugal force is more than twice as high at the fixed frequency (proportional to the square of frequency), the amplitude is larger for AFC due to resonant amplification.

CCC measurement values are shown in Fig. 6. The presented quantities include the Compactometer Value (CMV) and  $E_{vib}$  (here denoted  $E_{vib1}$ ). Also shown is the unloading modulus of  $E_{vib}$  (here denoted  $E_{vib2}$ ), which was developed in the SwePave project [14] and shown to be more related to actual soil stiffness than the other two quantities by Wersäll et al. [15]. The increase of all values is apparent up to approximately 13 passes, after which the increase is more modest, indicating small additional compaction. Although all measurement values are higher for AFC, it does not imply that stiffness is necessarily higher since all CCC quantities are significantly influenced by the vibration frequency, amplitude, and other operational conditions.

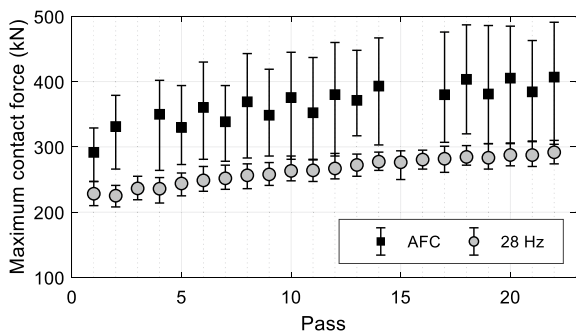
**Fig. 6** Average CMV,  $E_{vib}$  loading ( $E_{vib1}$ ) and  $E_{vib}$  unloading ( $E_{vib2}$ )



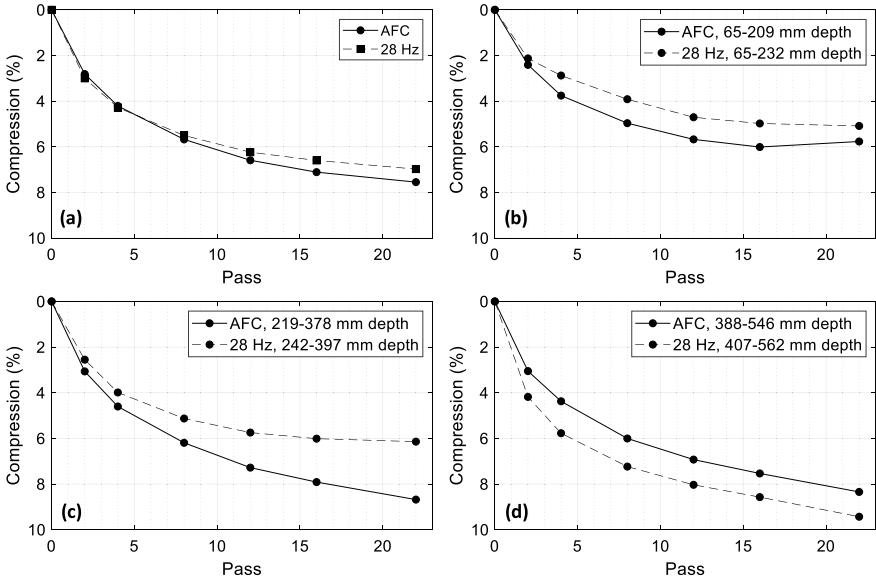
In the calculation procedure for  $E_{vib}$ , using the measured eccentric position and acceleration, the maximum contact force in each cycle can be calculated. Figure 7 presents an average of the maximum contact force for each pass. The bars show the range of values for that pass. Since the force is frequency-dependent, the variation is higher for AFC than for the fixed frequency. It is clear, however, that the contact force is significantly higher at resonance (AFC), despite a lower centrifugal force.

The measurements obtained from the EMUs are displayed in Fig. 8. The results from the two sections in each lane are averaged to obtain a more representative value. Figure 8a shows the total compression of the three measurement distances. The compression is slightly higher for AFC, implying that the compaction is more

**Fig. 7** Average of maximum contact force in each cycle







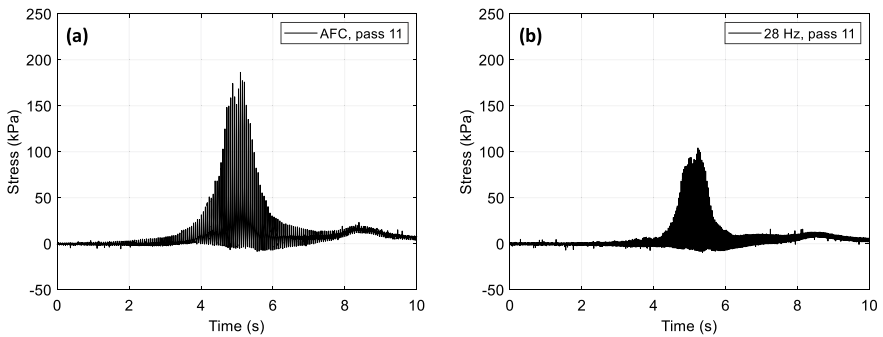
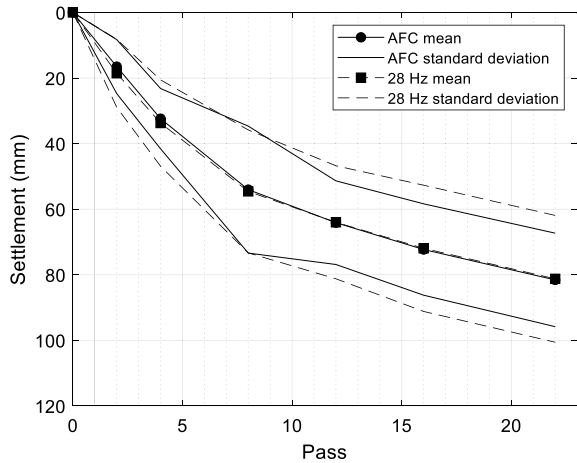
**Fig. 8** Compression measured by EMU sensors; **a** total compression; **b** top layer; **c** middle layer; **d** bottom layer

efficient and produces a more well-compacted layer. The remaining figures show the compression for each measurement distance, where the depth is the average for the two sections. The depths are slightly different due to variations in the actual installed depth. Figures 8b and c, present the upper and middle layers, respectively. In both cases, AFC improves the degree of compaction compared to conventional compaction. In the bottom layer, however, the fixed frequency gives higher compression, as shown in Fig. 8d. An increased stiffness due to enhanced compaction close to the surface has been shown in previous tests [6, 11] and imply that subsequent passes at low amplitude or static passes can be avoided. Since the compression is more similar in the three layers for AFC than for fixed frequency, the compaction profile is more homogenous throughout the layer. This may have a positive effect on the long-term performance of the embankment, as discussed by Wersäll et al. [11]. The results above are in line with previous findings.

The settlements are shown in Fig. 9. Although the compression, measured by EMU coils, was larger for AFC, the average settlements are identical for the two compaction methods. This was observed also in the previous test and the reason could be either larger settlement of the underlying layer (due to a slight increase in depth-effect at a high frequency) or lateral soil displacement. However, the standard deviation is smaller for AFC, indicating that spatial variation is less, suggesting that homogeneity is enhanced also in the lateral direction.

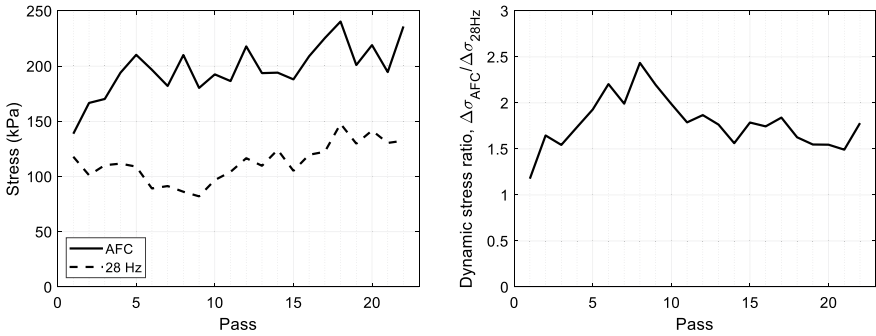
Vertical normal dynamic stress measurements at one-meter depth during pass 11 are shown in Fig. 10. The measured vertical stresses show a similar behavior as

**Fig. 9** Settlement of the embankment surface



**Fig. 10** Vertical stress at one-meter depth during the 11th pass; **a** AFC and **b** 28 Hz

reported by Rinehart and Mooney [16]. The maximum measured stress for each pass is shown in Fig. 11a, illustrating that AFC produces a significantly higher stress, and thus a higher shear strain, within the embankment. The dynamic stress ratio between AFC and fixed frequency,  $\Delta\sigma_{AFC}/\Delta\sigma_{28\text{ Hz}}$ , can be shown as in Fig. 11b. The dynamic stress-induced by compaction using AFC is between 1.2 and 2.4 times the stress-induced at 28 Hz (with a mean value of 1.8), most likely due to resonant amplification of deformations within the embankment. Although this and previous studies have found that compaction is slightly enhanced at greater depths for a high frequency, the measured stress is significantly higher, which may seem counterintuitive. However, considering that the roller speed is constant, a higher frequency produces a larger amount of cycles per unit length which may be the reason for obtaining a better compaction at a lower stress.



**Fig. 11** Vertical dynamic stress at one-meter depth during all passes; **a** maximum stress; **b** ratio of dynamic stress for AFC and 28 Hz

### 4 Conclusions

In order to verify previous field tests, investigating the properties of embankments compacted by the novel technique AFC, a 1.5 m rock-fill embankment was constructed under realistic conditions. The results confirm that the displacement amplitude and the contact force between the drum and the soil are significantly increased and the compression of the compacted layer is higher, although the depth-effect is somewhat decreased. In addition, the vertical dynamic stress at one-meter depth is nearly doubled. The tests also confirm that a higher degree of vertical homogeneity, in regard to compaction, is obtained. Additionally, the results indicate that lateral homogeneity is enhanced. A more homogeneously compacted embankment decreases stiffness and stress gradients, which is beneficial for reducing rearrangement and operational settlements. All of the above is obtained at a lower frequency and with a significant reduction of fuel consumption. The beneficial compaction results and the reduced fuel consumption, in combination with the possible reduction of the number of passes, imply that AFC can produce a better-compact embankment at a lower cost and environmental impact.

**Acknowledgements** This research is funded by the Swedish Transport Administration, the Development Fund of the Swedish Construction Industry, Better Interaction in Geotechnics, Dynapac Compaction Equipment AB and Peab AB.


### References

1. Zhang Q, Liu T, Zhang Z, Huangfu Z, Li Q, An Z (2019) Unmanned rolling compaction system for rockfill materials. *Autom Constr* 100:103–117
2. Imran AS, Barman M, Commuri S, Zaman M, Nazari M (2018) Artificial neural network-based intelligent compaction analyzer for real-time estimation of subgrade quality. *Int J Geomech* 18(6):04018048

3. Wersäll C, Larsson S (2013) Small-scale testing of frequency-dependent compaction of sand using a vertically vibrating plate. *Geotech Test J* 36(3):1–10
4. Wersäll C, Larsson S, Rydén N, Nordfelt I (2015) Frequency variable surface compaction of sand using rotating mass oscillators. *Geotech Test J* 38(2):1–10
5. Wersäll C, Nordfelt I, Larsson S (2017) Soil compaction by vibratory roller with variable frequency. *Géotechnique* 67(3):272–278
6. Wersäll C, Nordfelt I, Larsson S (2018) Resonant roller compaction of gravel in full-scale tests. *Transp Geotech* 14:93–97
7. Anderegg R (2000) ACE Ammann compaction expert—automatic control of the compaction. In: Gomes Correia A, Quibel A (eds) *Compaction of soils and granular materials*, Paris, France. Presses de l'école Nationale des Ponts et des Chaussées, Paris, France, pp 83–89
8. Anderegg R, Kaufmann K (2004) Intelligent compaction with vibratory rollers: feedback control systems in automatic compaction and compaction control. *Transp Res Rec* 1868(1):124–134
9. White DJ, Jaselskis EJ, Schaefer VR, Cackler ET, Drew I, Li L (2004) Field evaluation of compaction monitoring technology: Phase I. Final report, Iowa DOT Project TR-495, Ames, Iowa
10. Anderegg R, Von Felten DA, Kaufmann K (2006) Compaction monitoring using intelligent soil compactors. In: DeGroot DJ, DeJong JT, Frost D, Baise LG (eds) *GeoCongress 2006: Geotechnical engineering in the information technology age*, Georgia, USA. ASCE, Reston, VA, USA, pp 1–6
11. Wersäll C, Nordfelt I, Larsson S (2020) Roller compaction of rock-fill with automatic frequency control. *Proc Inst Civ Eng Geotech Eng* 173(4):339–347
12. Byggtjänst S (2013) AMA Anläggning 13: Allmän material - och arbetsbeskrivning för anläggningsarbeten [General material and work description for civil works] (In Swedish). Svensk Byggtjänst, Västerås, Sweden
13. Janoo V, Irwin L, Knuth K, Dawson A, Eaton R (1999) Use of inductive coils to measure dynamic and permanent pavement strains. In: *Proceedings of the 1st international conference on accelerated pavement testing*, CD-ROM, Reno, NV, USA, pp 18–20
14. Ekdahl U, Bengtsson PE, Ryden N (2004) A new framework for analytical pavement design based on systematic control during construction work. In: *Proceedings of the 14th Nordic Geotechnical Meeting*, pp E55–E80
15. Wersäll C, Åkesson F, Persson A (2019) Dynamic roller characteristics and CCC using automatic frequency control. In: *Proceedings of international intelligent construction technologies group conference 2019*, Beijing, China
16. Rinehart RV, Mooney MA (2009) Measurement of roller compactor induced triaxial soil stresses and strains. *Geotech Test J* 32(4):347–357

# An Experimental Study on the Estimation of Field Compaction States and Stress-Strain Properties of Unbound Granular Materials from Laboratory Test Results



Sou Ihara , Kairi Magara, Mitsutaka Okada, Hiroyuki Nagai,  
Shohei Noda, Yoshiaki Kikuchi, and Fumio Tatsuoka

**Abstract** Field fill materials often contain gravel particles larger than the allowable limit for standard laboratory compaction tests. In such cases, the maximum dry density  $(\rho_d)_{\max}$  of a material containing large gravels is obtained by correcting laboratory test results for specimens without large gravels. Usually, the Walker–Holtz (WH) method is used for this correction, but there are many materials whose gravel ratio ( $P$ ) is 0.3 – 0.4, which is usually considered to be the application limit. Moreover, accurate stress-strain properties under field compaction conditions are necessary for relevant stability analysis of soil structures including embankments. However, with unbound granular materials, it is difficult to obtain undisturbed samples for laboratory tests or to carry out field shear tests. Also, large-scale triaxial compression tests on specimens containing large gravels are difficult to perform in ordinary engineering practices. In this study, a series of laboratory compaction tests were performed changing the maximum particle size ( $D_{\max}$ ), compaction energy level (CEL) and  $P$  to examine the validity of the WH method and a series of drained triaxial compression tests were performed varying the  $D_{\max}$  and the degree of compaction. Based on the test results, a method to modify the WH method is proposed to properly estimate the  $(\rho_d)_{\max}$  value after adding or removing gravel particles when compacted at a certain CEL. Also, a method is proposed to correct the strength for a given gravel ratio to estimate the in-situ strength from the strength obtained from laboratory tests.

**Keywords** Compaction control · The degree of compaction · Gravel content

---

S. Ihara (✉) · K. Magara · M. Okada · S. Noda · Y. Kikuchi · F. Tatsuoka  
Tokyo University of Science, Noda, Chiba 278-8510, Japan

H. Nagai  
Hazama-Ando Corporation, Minato-ku, Tokyo 107-8658, Japan  
e-mail: [nagai.hiroyuki@ad-hzm.co.jp](mailto:nagai.hiroyuki@ad-hzm.co.jp)

## 1 Introduction

In the conventional control of field soil compaction of embankments for roads, railways and residential and industrial areas, etc., the dry density  $\rho_d$  and the water content  $w$  are measured in the field and controlled based on the maximum dry density  $(\rho_d)_{\max}$  and the optimum water content  $w_{\text{opt}}$  obtained by standard laboratory compaction tests performed on representative samples of the field fill material at a specified compaction energy level (CEL) (usually Standard or Modified Proctor,  $1E_c$  or  $4.5E_c$ ). Field fill materials often contain large particles, such as gravels and rock fragments, the size of which exceeds the allowable limit for standard laboratory compaction tests. In this case, it is necessary to estimate the values of  $(\rho_d)_{\max}$  and  $w_{\text{opt}}$  of the field fill material by correcting the values obtained by laboratory compaction tests on samples obtained by removing gravel particles of which the sizes exceed the allowable limit. When the gravel ratio  $P$  (will be described later in Chap. 2) of a given field fill material is lower than 0.3 or 0.4, the Walker–Holtz (WH) method [1, 2] is usually used for this estimate. The WH method assumes that the  $\rho_d$  value of the fine particle portion inside the whole sample after adding large particles is the same as the value of the sample comprising only fine particles compacted at the same CEL. However, it is known that, with an increase in  $P$  of the whole sample, the CEL transmitted to the fine particle portion inside the whole sample decreases, therefore the  $\rho_d$  value of the fine particle portion decreases. Besides, this trend may not be negligible even when  $P$  is lower than 0.3 or 0.4.

In addition, stability analysis of soil structure requires relevant shear strength values of compacted fill material. Because the stability may decrease as a fill material becomes wet or saturated, the strength under wet or saturated conditions is usually used in design. Like the laboratory compaction tests, the shear strength characteristics are often evaluated by performing triaxial compression (TC) tests on samples obtained by removing gravel particles of which the sizes exceed the allowable limit for standard TC tests.

There are studies that approach each problem [3, 4], but there are few researches that studied these two issues related to each other by performing compaction tests and TC tests on the same soil type compacted in the same way. In this research, a set of samples having different maximum particle diameters  $D_{\max}$  were prepared by consecutively removing larger particles from a typical field fill material. A series of laboratory compaction tests were then performed on these samples at  $\text{CEL} = 1E_c$  and  $4.5E_c$  to evaluate the effects of  $P$  on the value of  $(\rho_d)_{\max}$  for various values of  $D_{\max}$  and CEL. Also, a series of laboratory consolidated-drained TC tests were performed on these samples to evaluate the effects of  $P$  on the shear strength characteristics of specimens compacted otherwise under the same conditions.

## 2 Walker–Holtz Method

In the WH method, the dry density  $\rho_d'$  of a sample after adding large gravel particles with the same CEL as a sample before adding gravel particle is obtained by Eq. (1):

$$\rho_d' = \frac{\rho_d \cdot \rho_s}{(1 - P) \cdot \rho_s + P \cdot \rho_d} \tag{1}$$

where  $\rho_d$  is the dry density of the sample before adding gravel particles;  $\rho_s$  is the density of gravel particles; and  $P$  is the mass ratio of the added gravel to the whole sample after adding gravel particles. In this study, it is reasonably assumed that the density of particles other than the gravel particles is the same as  $\rho_s$ . In addition, the  $S_r$  value does not change by adding gravel particles when following Eq. (1). In the WH method,

On the other hand, the dry density  $\rho_d''$  of the portion composed of fine particles not containing large gravel particles inside the whole sample containing large gravel particles compacted at a certain CEL is correctly obtained by Eq. (2):

$$\rho_d'' = \frac{(1 - P) \cdot \rho_d \cdot \rho_s}{\rho_s - P \cdot \rho_d} \tag{2}$$

where  $\rho_d$  is the dry density of the whole sample before removing the gravel particles; and  $P$  is the mass ratio of gravel particles to the whole sample. Note that we need no assumption to derive Eq. (2).

## 3 Soil Samples and Test Methods

The field fill material used to construct a road embankment in Kamaishi City, Iwate Prefecture, Japan (hereafter called Kiten soil) was used in this study. Figure 1 shows

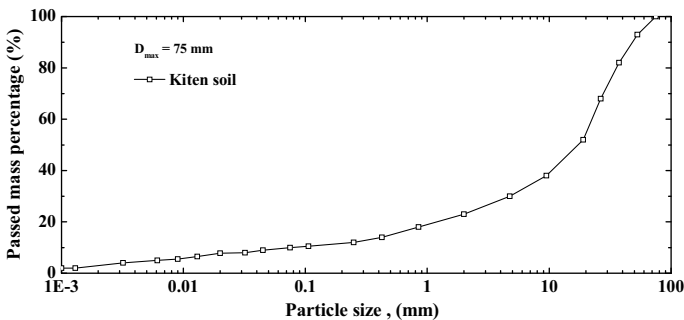


Fig. 1 Grading curves of original material

the grading curve of the field material with  $D_{max} = 75$  mm. A set of samples with  $D_{max} = 53$  mm, 37.5 mm, 19 mm, 9.5 mm 4.75 mm, and 2 mm were produced by consecutively removing larger gravel particles.

The mold having an inner diameter of 15 cm and a volume of 2209 cm<sup>3</sup> was used for laboratory compaction tests on samples with  $D_{max} = 37.5, 19, 4.75,$  and 2 mm. A 2.5 kg rammer was dropped freely from a height of 30 cm, and the number of tamping was 55 for each of in total three layers. The CEL, in this case, is  $1E_c$ , and  $E_c$  is the energy per unit volume and is calculated by Eq. (3).

$$E_c = \frac{W_R \cdot H \cdot N_L \cdot N_B}{V} \tag{3}$$

where  $W_R$  is the weight of the rammer;  $H$  is the drop height of the rammer;  $N_L$  is the number of layers;  $N_B$  is the number of tamping per layer; and  $V$  is the volume of mold.

Furthermore, a 4.5 kg rammer was dropped freely from a height of 45 cm and tamped 55 times for each of in total 5 layers. The CEL in this case is  $4.5E_c$ . A mold having an inner diameter of 30 cm and a volume of 25,000 cm<sup>3</sup> was used for samples with  $D_{max} = 75$  and 53 mm. For  $1E_c$ , a 10 kg rammer was dropped freely from a height of 45 cm. The number of tamping was 104 times for each of in total 3 layers. For  $4.5E_c$ , a 10 kg rammer was dropped freely from a height of 45 cm and the number of tamping was 468 times for each of in total 3 layers. The total mass of a whole compacted sample was measured before and after oven-drying.

A series of drained TC tests were performed on specimens with  $D_{max} = 19, 9.5,$  and 4.75 mm. Table 1 shows the compaction conditions of the specimens having different  $D_{max}$  values.  $[D_c]_{1E_c}$  in the table represents the degree of compaction at  $1E_c$ . The specimens were prepared by compaction in 5 layers in the mold. In order to evaluate effects of  $D_{max}$  on shear strength at the same  $\rho_d$  value, the tests were performed on specimens compacted to  $\rho_d = 1.872$  g/cm<sup>3</sup> and  $S_r = 80\%$  for each  $D_{max}$ . The specimens were 100 mm in diameter and 200 mm in height for  $D_{max} = 19$  mm; and 75 mm in diameter and 150 mm in height for  $D_{max} = 9.5$  mm and 4.75 mm. After saturation, the specimen was consolidated to an effective confining pressure of 50 kPa with a back pressure of 300 kPa, and loaded monotonically at an axial strain rate of 0.01%/min under drained conditions.

**Table 1** TC specimens

$D_{max}$ (mm)	19			9.5			4.75		
$S_r$ (%) when compacted	60	70	80	60	70	80	60	70	80
$[D_c]_{1E_c}$ (%)	95	95	95 96 100	95	95	90 95 100 105	95	95	90 95 100 102



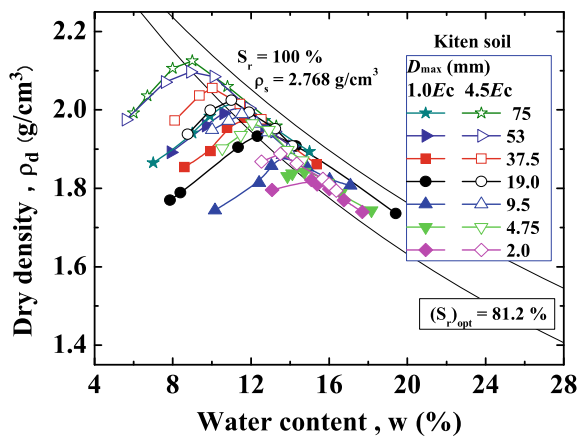
## 4 Results and Discussions (Laboratory Compaction Tests)

### 4.1 Results

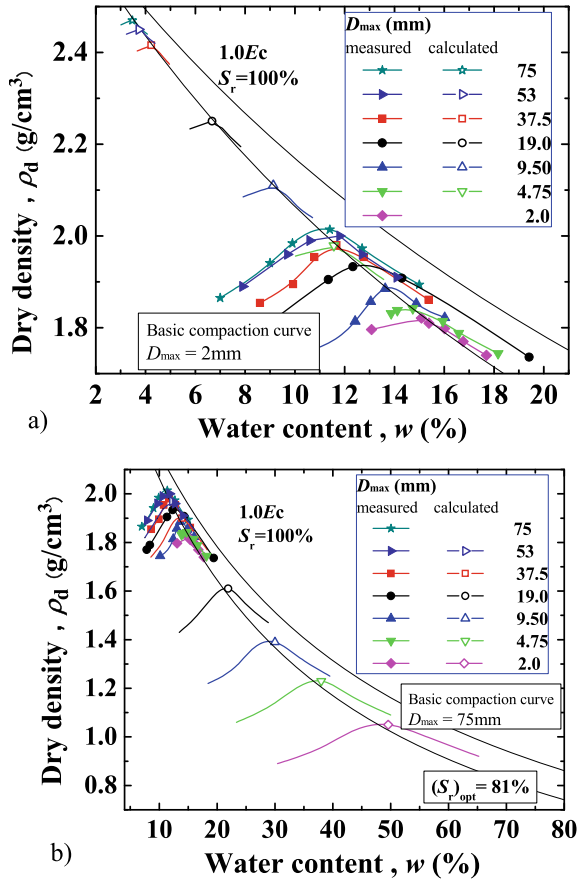
Figure 2 shows the compaction curves for  $1E_c$  and  $4.5E_c$  of the samples having different  $D_{max}$  values. The  $(\rho_d)_{max}$  value increases as the  $D_{max}$  value increases and as CEL increases. In comparison, the  $S_r$  value when  $\rho_d = (\rho_d)_{max}$  along each compaction curve, which is defined as the optimum degree of saturation  $(S_r)_{opt}$  [5], is quite independent of  $D_{max}$  and CEL and has value of 81%.

In Fig. 3a, the curves with data points are the measured compaction curves of the specimens with  $D_{max} = 75, 53, 37.5, 19, 9.5, 4.75,$  and  $2$  mm of Kiten soil compacted at  $1E_c$ . The set of solid curves are the compaction curves of the specimens are those calculated by Eq. (1) when adding particles larger than 2 mm in diameter to the basic specimen with  $D_{max} = 2$  mm. It may be seen that the  $(\rho_d)_{max}$  value for  $1E_c$  is over-estimated by Eq. (1) to a larger extent with an increase in  $D_{max}$  (i.e., with an increase in the mass ratio  $P$  of particles larger than 2 mm to the whole sample containing these added large particles). On the other hand, the compaction curves of the portion of fine particles with  $D_{max} = 53, 37.5, 19, 9.5, 4.75,$  and  $2$  mm inside the basic sample with  $D_{max} = 75$  mm compacted at  $1E_c$  were calculated by Eq. (2). In Fig. 3b, these calculated compaction curves are compared with the measured curves of the specimens comprising fine particles that were compacted at  $1E_c$ . The  $(\rho_d)_{max}$  value calculated by Eq. (2) becomes smaller than the measured one obtained by compaction at  $1E_c$ . This means that the  $(\rho_d)_{max}$  value for  $1E_c$  is under-estimated by Eq. (2) to a larger extent with an increase in  $D_{max}$ .

Fig. 2 Compaction curves for different  $D_{max}$  values



**Fig. 3 a** Compaction curves for  $1E_c$  of the specimens obtained by adding large particles to the basic sample with  $D_{max} = 2$  mm calculated by Eq. (1) and measured curves of these samples compacted at  $1E_c$ ; **b** Compaction curves of the fine particle portion inside the basic specimen with  $D_{max} = 75$  mm compacted at  $1E_c$  calculated by Eq. (2) and measured compaction curves of specimens composed of the same fine particles compacted at  $1E_c$

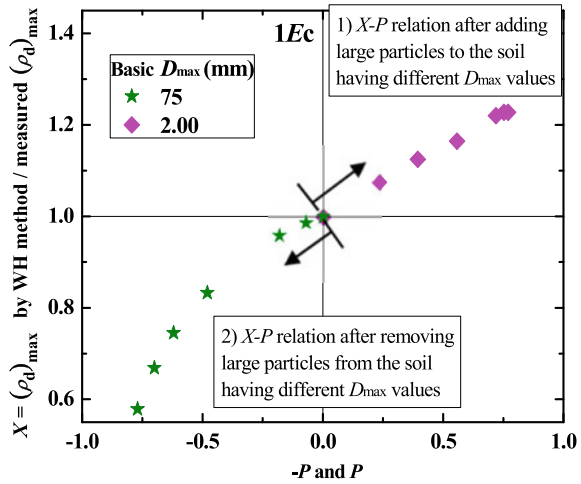


### 4.2 Modification of the WH-Method

It is seen from Fig. 3a that it is necessary to modify Eq. (1) to obtain the correct  $\rho_d$  value of a specimen after adding larger particles that are compacted at a certain CEL from the  $\rho_d$  value of the basic specimen compacted at the same CEL. It is seen from Fig. 3b that it is also necessary to modify Eq. (2) to obtain the correct  $\rho_d$  value of a specimen after removing larger particles that is compacted at a certain CEL from the  $\rho_d$  value of the basic specimen compacted at the same CEL. To unify these trends of behavior in a single framework, the maximum dry density ratio  $X$  was defined as the ratio of the  $(\rho_d)_{max}$  value when compacted at a certain CEL calculated by Eqs. (1) or (2) to the measured  $(\rho_d)_{max}$  value of the same sample compacted at the same CEL.

In the top-right quarter zone of Fig. 4, the  $X$  values of the specimens to which different amounts of gravel particles larger than 2 mm in diameter were added to the basic specimen with  $D_{max} = 2$  mm are plotted against the gravel mass ratio  $P$  of these specimens after adding particles larger than 2 mm. These data were obtained from

**Fig. 4**  $X$ - $P$  relation from data for compaction at  $1E_c$  in Fig. 3a, b



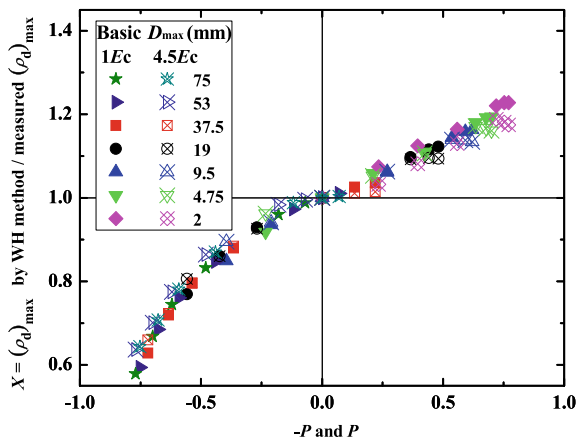
those plotted in Fig. 3a. The  $X$  value increases consistently from 1.0 as  $P$  increases from zero. That is, as  $P$  increases, the  $(\rho_d)_{max}$  value after adding gravel particles when compacted at a certain CEL is over-estimated to a larger extent than if calculated by Eq. (1) based on the  $(\rho_d)_{max}$  value of the basic specimen compacted at the same CEL. Importantly,  $X$  is noticeably higher than 1.0 when  $P = 0.3 - 0.4$ , which is conventionally considered as the upper limit for the application of the WH method.

In the bottom-left quarter zone of Fig. 4, the  $X$  values of the specimens from which different amounts of gravel particles smaller than 75 mm in diameter were removed from the basic specimen with  $D_{max} = 75$  mm are plotted against  $-P$ , where  $P$  is the mass ratio of the gravel particles that were removed from the basic specimen with  $D_{max} = 75$  mm. These plots were obtained from the data presented in Fig. 3b. The  $X$  value decreases consistently from 1.0 as  $P$  increases. That is, as  $P$  increases from zero, the CEL transmitted to the fine particle portion becomes smaller than  $1E_c$ , which was applied to the whole of the basic specimen containing gravel particles. By this mechanism, the calculated dry density becomes smaller than the value obtained by compaction at  $1E_c$ .

Figure 5 shows the  $X$ - $P$  relations obtained for the two different CELs ( $1E_c$  and  $4.5E_c$ ) and different basic  $D_{max}$  values equal to 75, 53, 37.5, 19, 9.5, 4.75 and 2 mm. It may be seen that the  $X$ - $P$  relations for these different CEL and basic  $D_{max}$  values are rather unique. This result is consistent with the results of the previous experimental study [6] showing that the  $X$ - $P$  relation is rather unique regardless of the basic  $D_{max}$  value and CEL, and regardless of the different soil types with similar particle size distributions.

The results shown above indicate that to obtain the correct value of  $(\rho_d)_{max}$  for a given value of CEL after adding large gravel particles, the value obtained by Eq. (1) should be divided by the factor  $X$  obtained from the curve shown in Fig. 5. Similarly, to obtain the correct value of  $(\rho_d)_{max}$  for a given value of CEL after removing large

**Fig. 5**  $X$ - $P$  relation for different basic  $D_{\max}$  values at  $CEL = 1E_c$  and  $4.5E_c$

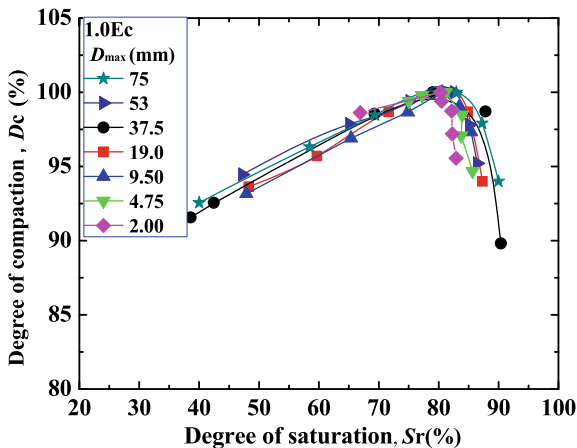


gravel particles, the value obtained by Eq. (2) should be divided by the factor  $X$  obtained from the curve shown in Fig. 5.

### 4.3 Estimation of $\rho_d$ Other than $(\rho_d)_{\max}$

It is often required to estimate a  $\rho_d$  value other than the  $(\rho_d)_{\max}$  value after adding gravel particles to a given sample. In this respect, Fig. 6 shows the  $[D_c]_{1E_c}$ - $S_r$  relation of the samples having different  $D_{\max}$  values obtained from the data presented in Fig. 2. Even if  $D_{\max}$  changes, the optimum degree of saturation  $(S_r)_{\text{opt}}$  does not change noticeably, while the  $[D_c]_{1E_c}$ - $S_r$  relation still remains rather unique. These results are consistent with the findings reported by Tatsuoka [5] that the  $(S_r)_{\text{opt}}$  value

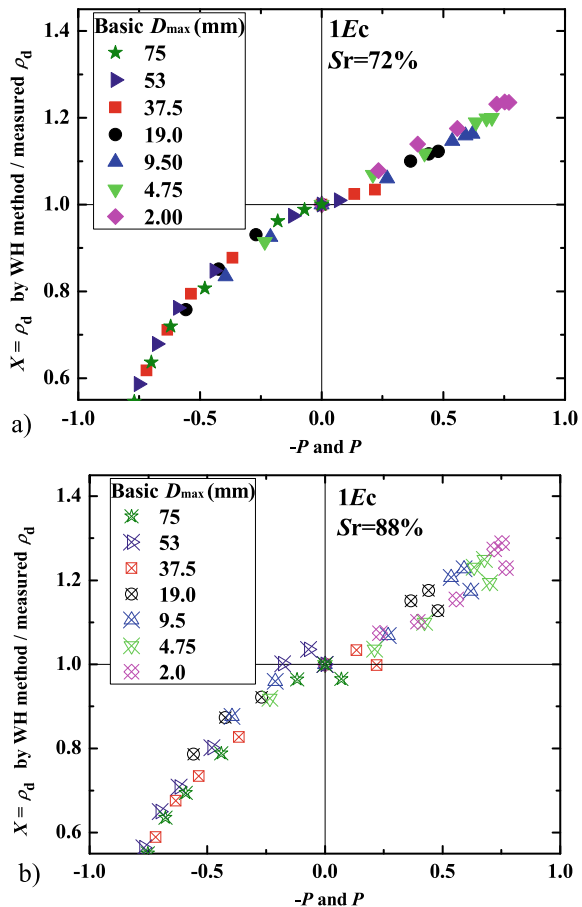
**Fig. 6**  $[D_c]_{1E_c}$ - $S_r$  relation for different  $D_{\max}$



and this relation are rather insensitive to changes in the soil type and CEL. The result presented in Fig. 6 suggests that  $\rho_d$  values after adding gravel particles to, or removing gravel particles from, a given sample are correctly estimated by modifying the values obtained by Eqs. (1) or (2) and applying the same  $X$ - $P$  relation for  $(\rho_d)_{max}$  as presented in Fig. 5.

To confirm this point,  $X$ - $P$  relations other than the one for  $(\rho_d)_{max}$  were examined. To this end,  $X$  was defined as the ratio of the  $\rho_d$  value when compacted at a certain CEL and a certain  $S_r$ . Then the  $X$  values were obtained from the ratio of the  $\rho_d$  value calculated by Eqs. (1) or (2) to the measured value of the same specimen compacted at the same CEL and  $S_r$ . Figure 7a and b show the  $X$ - $P$  relation when compacted to  $S_r = 72\%$  and  $88\%$ . From Fig. 7a for  $S_r = 77\%$ , which is lower than  $(S_r)_{opt} = 81\%$ , the  $X$ - $P$  relation is rather unique and in fact it is nearly the same as the relation shown in Fig. 5. In contrast, in Fig. 7b for  $S_r = 88\%$ , which is higher than  $(S_r)_{opt} = 81\%$ , the relation is not as unique as the one shown in Fig. 5. This trend corresponds

Fig. 7  $X$ - $P$  relation: a  $S_r = 72\%$  and b  $S_r = 88\%$



to the fact that the  $D_c-S_r$  relation scatters in has relatively largely scatter when  $S_r > (S_r)_{opt}$ .

In summary, we can conclude that the  $X-P$  relation for  $(\rho_d)_{max}$  is rather unique even when  $D_{max}$  changes exceeding the maximum allowable particle size for the mold of the laboratory compaction tests. Also, the  $X-P$  relation for  $\rho_d$  other than  $(\rho_d)_{max}$  is nearly the same as that for  $(\rho_d)_{max}$  corresponding to the fact that the  $D_c-S_r$  relation is rather unique regardless of  $D_{max}$ .

The detailed procedure based on the analysis described above to obtain the degree of compaction of the field sample that includes large gravel particles is described below.

#### 4.4 $(\rho_d)_{max}$ of Field Sample Including Large Gravel Particles

The degree of compaction for  $1E_c$  of fill material compacted in the field, hereafter denoted by  $[D_c]_{1E_c,A}$ , is obtained by Eq. (4):

$$[D_c]_{1E_c,A} = (\rho_d)_A / [(\rho_d)_{max,1E_c}]_A \quad (4)$$

where  $(\rho_d)_A$  is the field dry density, and  $[(\rho_d)_{max,1E_c}]_A$  is the  $(\rho_d)_{max}$  of the field fill material compacted at  $1E_c$ . When laboratory compaction tests cannot be performed on a given field fill material due to the inclusion of gravel particles too large in size,  $[(\rho_d)_{max,1E_c}]_A$  is usually estimated by Eq. (1) (i.e., the WH method) from the maximum dry density  $[(\rho_d)_{max,1E_c}]_F$  obtained by laboratory compaction tests at  $1E_c$  on the specimen obtained by removing large gravel particles from the original sample of field fill material. It may be seen from Figs. 4 and 5 that, in the case of adding gravel particles to a given basic material, even when  $P$  is in range of 0.3–0.4,  $X$  is approximately 1.1. This means that the field degree of compaction  $[D_c]_{1E_c,A}$  is under-estimated by a factor of approximately  $1/1.1 \approx 0.9$ . This difference of 10% in  $[D_c]_{1E_c,A}$  is not negligible in usual geotechnical engineering practice. In view of the above, it is proposed that even when  $P$  is lower than 0.3 or 0.4 and always when  $P$  is higher than 0.3 or 0.4, Eq. (1) is replaced by Eq. (5) to obtain a proper value of  $[(\rho_d)_{max,1E_c}]_A$  for use in Eq. (4):

$$[(\rho_d)_{max,1E_c}]_A = \frac{[(\rho_d)_{max,1E_c}]_F \cdot \rho_s}{(1 - P) \cdot \rho_s + P \cdot [(\rho_d)_{max,1E_c}]_F} \cdot \frac{1}{X} \quad (5)$$

In this case, the  $X$  value is obtained by substituting the  $P$  value of a given field fill material into the  $X-P$  relation relevant for the given type of field fill material (such as the one presented in Fig. 5). In this way, it becomes possible to avoid an unreasonable underestimation of the field degree of compaction.

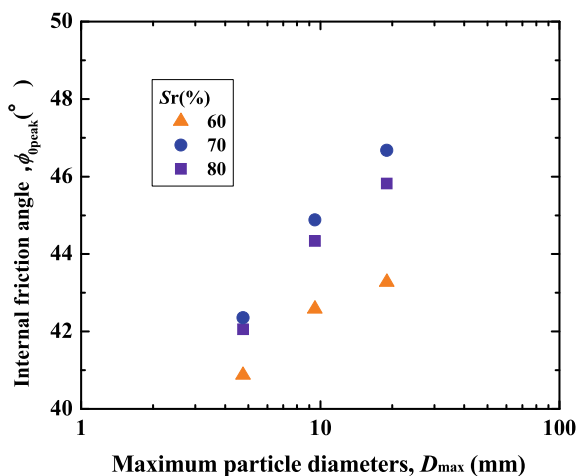
### 5 Results and Discussions (Triaxial Compression Tests)

From the TC test results, the internal friction angles  $\phi_{0peak} = \sin^{-1}\{(\sigma_{1f} - \sigma_{3f})/(\sigma_{1f} + \sigma_{3f})\}$  (for  $c = 0$ ) were obtained, where  $\sigma_{1f}$  and  $\sigma_{3f}$  are the axial and lateral stresses at the peak deviator stress. Figure 8 shows the  $\phi_{0peak}-D_{max}$  relation for  $[D_c]_{1Ec} = 95\%$  for three different  $S_r$  values. Regardless of the value of  $S_r$ , the  $\phi_{0peak}$  value increases as  $D_{max}$  increases. The  $\phi_{0peak}$  value at  $S_r = 70\%$  is slightly higher than that at  $S_r = 80\%$ . However, when compared under the same CEL, the  $[D_c]_{1Ec}$  value at  $S_r = 80\%$  becomes higher than the value at  $S_r = 70\%$  and the  $\phi_{0peak}$  increases correspondingly. As a result, under the same CEL, there is nearly no difference between the  $\phi_{0peak}$  values at  $S_r = 70$  and  $80\%$ . On the other hand, even for the same  $[D_c]_{1Ec}$ , the  $\phi_{0peak}$  at  $S_r = 60\%$  is clearly lower than that of the specimens at  $S_r = 70$  and  $80\%$  and this difference increases as  $D_{max}$  increases. These results support the proposal by Tatsuoka and Correia [7] that the field compaction target is set at  $S_r = (S_r)_{opt}$  to ensure high strength and stiffness after wetting or saturation.

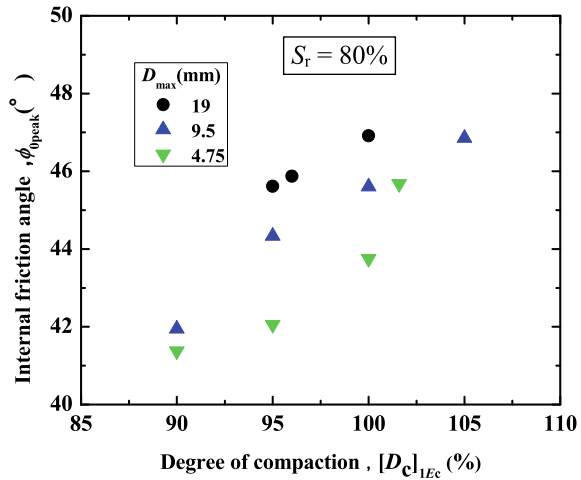
Figure 9 shows the  $\phi_{0peak}-[D_c]_{1Ec}$  relation at  $S_r = 80\%$  for three different  $D_{max}$  values. When compared at the same  $[D_c]_{1Ec}$ , the  $\phi_{0peak}$  value noticeably increases as  $D_{max}$  increases. It is likely that this trend is due to the fact that, as  $D_{max}$  increases, the uniformity coefficient of specimen increases, which results in an increase in  $(\rho_d)_{max}$  therefore an increase in  $\rho_d$  for the same  $[D_c]_{1Ec}$ . On the other hand, Fig. 10 shows the  $\phi_{0peak}-\rho_d$  relation at  $S_r = 80\%$  for the three different  $D_{max}$  values. It may be seen that the  $\phi_{0peak}$  value is determined by  $\rho_d$  regardless of  $D_{max}$ . It seems that this result is due to that the effects of the following factors are cancelled: (1) as  $D_{max}$  increases,  $[D_c]_{1Ec}$  for the same  $\rho_d$  value decreases due to an increase in  $(\rho_d)_{max}$  (Fig. 2); while (2) as  $D_{max}$  increases, the  $\phi_{0peak}$  at the same  $[D_c]_{1Ec}$  increases (Fig. 8).

It is known that, for a wide range of grading characteristics, the  $\phi_{0peak} - \rho_d$  relation is not unique. However, if such a unique  $\phi_{0peak}-\rho_d$  relation as the one shown in

Fig. 8  $\phi_{0peak}-P$  relation for different  $S_r$  ( $[D_c]_{1Ec} = 95\%$ )



**Fig. 9**  $\phi_{0peak}-[D_c]_{IEc}$  relation for different  $D_{max}$



**Fig. 10**  $\phi_{0peak}-\rho_d$  relation for different  $D_{max}$

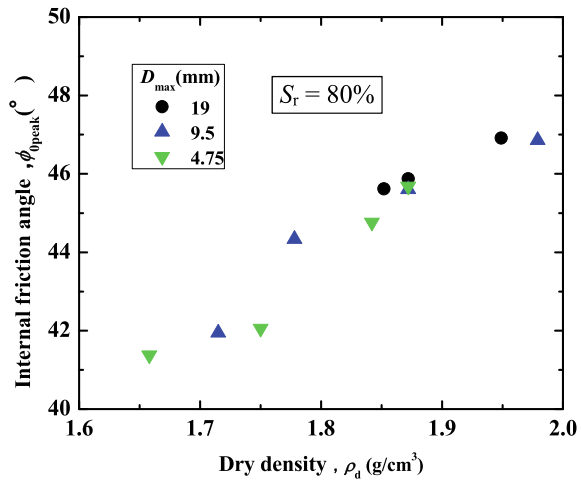


Fig. 9 is confirmed under certain limited conditions, we can determine design strength parameters by referring to such a  $\phi_{0peak}-\rho_d$  relation shown in Fig. 10. Otherwise, it is recommended to determine a design strength parameter by referring to the  $\phi_{0peak}-[D_c]_{IEc}$  relation obtained by TC tests performed on samples after removing large gravel particles with necessary correction for  $D_{max}$ . The results shown in Fig. 9 indicate that it is on the safe side when the effects of  $D_{max}$  are ignored. When the  $[D_c]_{IEc}$  value ensuring a given design strength parameter can be determined following such a procedure as explained above, the target value of  $[D_c]_{IEc}$  in field soil compaction control is determined by referring to this  $[D_c]_{IEc}$  value.



## 6 Conclusions

The following conclusions can be derived from the results of a series of laboratory compaction tests and drained triaxial compression tests on a set of specimens having different maximum particle sizes  $D_{\max}$  obtained by consecutively removing larger particles from a field fill material:

- When assuming that the same CEL as the one applied to the whole sample is transmitted to the portion with fine particle (i.e., the WH assumption), the dry density  $\rho_d$  at a certain  $S_r$  (including  $(\rho_d)_{\max}$  at  $(S_r)_{\text{opt}}$ ) of soil containing large gravel particles compacted at a certain CEL is over-estimated when estimated from the  $\rho_d$  value at the same  $S_r$  of the specimen after removing gravel particles compacted at the same CEL. Similarly, when based on the WH assumption, the  $\rho_d$  value at a certain  $S_r$  of the gravel-removed sample compacted at a certain CEL is under-estimated when estimated from the  $\rho_d$  value at the same  $S_r$  of the specimen containing gravel particles compacted at the same CEL. In both cases, the error is not negligible even when the gravel mass ratio  $P$  is lower than 0.3–0.4.
- In order to appropriately estimate the  $\rho_d$  value at the same CEL of a specimen after adding gravel from the  $\rho_d$  value compacted with a CEL of the specimen before adding gravel particles, it is necessary to modify the conventional equation based on the WH assumption by incorporating a correction factor  $X$  that is a function of the gravel mass ratio  $P$ . This method is applicable over a wide range of  $P$ , from below 0.3 to higher than 0.4.
- The following findings were made from drained TC tests on saturated specimens of gravel-removed samples having different  $D_{\max}$  values:
- When compacted at the same values of  $[D_c]_{1Ec}$  and  $S_r$ , the angle of internal friction  $\phi_{0\text{peak}}$  noticeably increases as  $D_{\max}$  increases. This is due likely to the fact that, as  $D_{\max}$  increases, the uniformity coefficient of the sample increases, which results in an increase in  $(\rho_d)_{\max}$ , thereby an increase in  $\rho_d$  for the same  $[D_c]_{1Ec}$ . This result indicates that it may be on the safe side to estimate the  $\phi_{0\text{peak}}$  value of fill material which includes large gravel particles from the value of gravel-removed specimens for the same  $[D_c]_{1Ec}$ . This effect may be taken into account when necessary.
- As  $S_r$  becomes noticeably lower than the optimum degree of saturation  $(S_r)_{\text{opt}}$ , the  $\phi_{0\text{peak}}$  value for the same CEL becomes lower than the value when  $S_r = (S_r)_{\text{opt}}$ . This fact supports compaction control setting the field compaction target at  $S_r = (S_r)_{\text{opt}}$ .
- With the same  $\rho_d$ , the  $[D_c]_{1Ec}$  value decreases with an increase in  $D_{\max}$ . Due to the combined effects of this factor and factor a) above, when compacted at the same  $\rho_d$  value, the  $\phi_{0\text{peak}}$  value becomes rather independent of  $D_{\max}$ . At least within the test conditions employed in this study, taking advantage of this simple empirical rule, the  $\phi_{0\text{peak}}$  value of gravel-including field fill material can be estimated from the value of gravel-removed sample for the same  $\rho_d$  value.

**Acknowledgements** This research is part of the joint research with Hazama-Ando Corporation. The authors sincerely appreciate their help in performing this study.

## References

1. Walker FC, Holtz WG (1953) Control of embankment material by laboratory testing. *Trans Am Soc Civ Eng* 118(1):1–25
2. Holtz WG, Lowitz (1957) Compaction characteristics of gravelly soils. Bureau of Reclamation, Earth laboratory report, No. EM-509
3. Mitsuo T (2004) Comparison between laboratory and field compaction characteristics on coarse-grained materials. *J Jpn Soc Dam Eng* 14:20–30
4. Uemoto Y, Shibuya S, Yosuke H, Kawai S (2011) Influence of grain size distribution characteristics on compaction and deformation-strength characteristics of gravelly fill material. *Jpn Geotech J* 6(2):181–190
5. Tatsuoka F (2015) Compaction characteristics and physical properties of compacted soil controlled by the degree of saturation, Keynote Lecture, Deformation characteristics of geomaterials, Proceedings of 6th international conference on deformation characteristics of geomaterials, Buenos Aires, pp 40–78
6. Ihara S, Noda S, Kikuchi Y, Tatsuoka F (2019) Experimental evaluation of the effects of gravel particles on the dry density of compacted soil. In: *The 4th international conference on geotechnics for sustainable infrastructure development*, Hanoi
7. Tatsuoka F, Gomes Correia A (2018) Importance of controlling the degree of saturation in soil compaction linked to soil structure design. *Transp Geotech* 17:3–27

# A Stress-Dependent Approach for Estimation of Drum-Soil Contact Area



Aria Fathi , Cesar Tirado , Sergio Rocha , Mehran Mazari ,  
and Soheil Nazarian 

**Abstract** The conventional method of estimating the contact area of compaction rollers is based on simplifying assumptions such as the homogeneous and linear elastic behavior of the underlying compacted geomaterials. This study evaluates a stress-dependent approach for estimating the contact area of roller compaction considering the nonlinear behavior of compacted geomaterials. For this purpose, a finite element model was developed to simulate the roller compaction of unbound materials considering both the nonlinear behavior of geomaterials and the soil-drum interaction by means of using advanced contact algorithms. The contact area of the drum was estimated based on the stress distribution at the soil-drum interface for more representative pavement responses than those obtained from Hertzian models. The contact areas from this approach showed good agreement with those measured in the field.

**Keywords** Contact area · Soil-drum interaction · Compaction roller · Finite element method · Nonlinear behavior · Unbound materials

---

A. Fathi (✉)

GeoDesign Engineering Services, Terracon Consultants Inc., Phoenix, AZ 85282, USA  
e-mail: [aria.fathi@terracon.com](mailto:aria.fathi@terracon.com)

C. Tirado · S. Rocha · S. Nazarian

The University of Texas At El Paso, El Paso, TX 79968, USA  
e-mail: [ctirado@utep.edu](mailto:ctirado@utep.edu)

S. Rocha

e-mail: [srocha@utep.edu](mailto:srocha@utep.edu)

S. Nazarian

e-mail: [nazarian@utep.edu](mailto:nazarian@utep.edu)

M. Mazari

California State University Los Angeles, Los Angeles, CA 90032, USA  
e-mail: [mmazari2@calstatela.edu](mailto:mmazari2@calstatela.edu)

## 1 Introduction

The knowledge of the contact stress distributions and the contact width for a variety of soil types is necessary to accurately predict the stress fields [1, 2]. The contact interaction between a rigid rolling cylinder (drum) and the soil surface depends mostly on the soil type and dynamic behavior of the drum [3, 4]. Such interactions are better explained in terms of the contact width and the stress–strain paths at the contact area. Hertz [5] presented the fundamental contact theory by addressing the contact of two elastic masses with curved surfaces.

The experimental data collected with the instrumented roller compactors reveal complex nonlinear roller vibration behaviors, which include the loss of contact between the drum and the soil, as well as the drum and the frame rocking [6–8].

Different numerical modeling techniques have been used for estimating the response of the roller. Quibel [9] and Kröber [10] predicted the loss of contact (i.e., decoupling of the drum from the soil) using the lumped parameter modeling. Kopf and Erdmann [11] used an iterative process to calculate the drum contact width, as well as stiffness and damping parameters based on a cone–spring–damper model proposed by Kargl [12]. Rinehart et al. [2] studied the stress and strain paths during the vibratory soil compaction on a uniform embankment layer as well as on a two-layer soil system and compared the stress and strain paths to the laboratory resilient modulus results. The authors found that the presence of a thick stiff base layer makes the contact area smaller. Pistol [13] defined continuous compaction control (CCC) as an integrated method to identify soil stiffness. Herrera et al. [14] proposed a data reduction methodology to backcalculate the mechanical properties of compacted soils using CCC data, identifying the potential use of CCC as an in-situ dynamic test for quality control purposes. Musimbi et al. [15] compared the results of an iterative BEM approach with the results of the Hertzian theory application and a field investigation on different types of layered soils to study the drum–soil contact width. They found that the Hertzian theory better predicted the contact width for granular materials as compared to clayey soils due to low elastic modulus of clay.

Asaf et al. [16] used the discrete element method (DEM) to simulate the interaction between a rigid wheel and the soil surface. They concluded that DEM provided reasonable results on contact mechanics as compared to the other theoretical and experimental studies. Buechler et al. [17] employed DEM to study the contact mechanism of a static drum on the soil surface. Their predicted contact widths from the DEM analyses were greater than those predicted by the Hertz theory and were close to the BEM results predicted by Rinehart et al. [2]. Buechler et al. also found that granular soils exhibited greater contact widths as compared to the cohesive soils.

Finite element (FE) models are also versatile tools for obtaining the responses of geomaterials under different rollers. Even though simple two-dimensional (2D) FE modeling approach considers a uniform distribution of responses along the length of the drum, they are rapid to execute [18]. Some FE models include contact models that can better address the stress field and contact width. The execution time can become rather excessive for routine use as the problem is extended to three-dimensional

(3D) with dynamic loading, and as the plastic and nonlinear geomaterial behaviors are included in the model.

Various researchers considered the unbound granular and subgrade materials as linear elastic [18–20], while other have included the Drucker–Prager/cap model. Hügel et al. [21] and Wang et al. [22] further modeled soils using viscoplastic models. More recently, the MEPDG stress-dependent material model has been implemented in several finite element models [23] to simulate the vibratory roller compaction of the soils.

In this paper, a 3D nonlinear FE model [23, 24] simulating the roller proof-mapping of one- and two-layer geosystems upon completion of compaction is used for computing the contact area between the drum and the soil underneath. The FE model used included a contact model to simulate the interaction between the drum and the geosystem. The inclusion of the nonlinear behavior of the geomaterial allows more realistic conditions than the simplifying Hertzian contact theories that consider homogeneous and linear elastic behavior of the surfaces. The following sections explain the components and strategies undertaken in this study.

## 2 Methodology

Since the numerical modeling of soil response due to roller compaction is complex, an FE technique is necessary to evaluate the interaction of the roller with the geosystem. LS-DYNA<sup>®</sup>, which is an explicit and implicit multi-purpose FE program that, was used to address this need. Figure 1 shows a 3D view of the geosystem and the roller. A 3D mesh was assembled to represent a roller imparting energy to the geomaterials

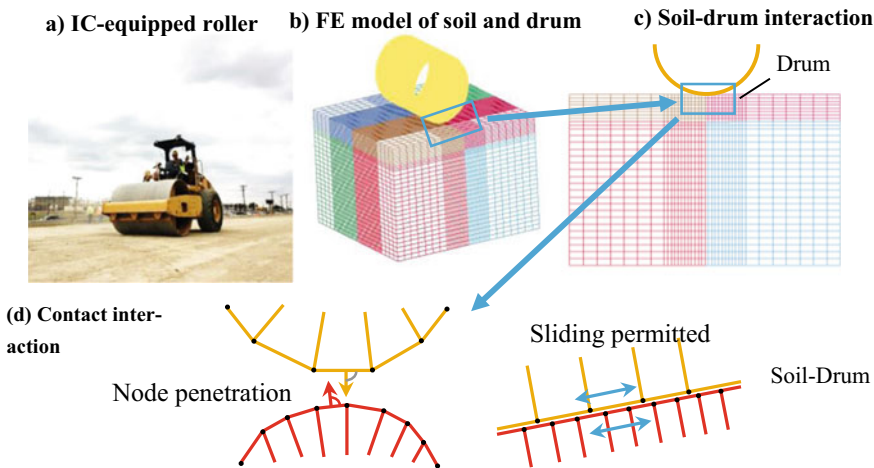


Fig. 1 Schematic representation of drum–soil system [23, 24]

at a given amplitude and vibrating frequency. The drum of the roller compactor was modeled with rigid shell elements with common dimensions of IC rollers, i.e., 2 m wide and 0.75 m in radius. Due to the size of the drum, the geomaterial was modeled as 4 m wide, 4 m long, and 2.5 m deep with non-reflective boundaries. A mesh consisting of about 64,000 brick elements was used to represent the geosystem. Smaller elements with  $50 \times 50 \times 50$  mm dimensions were used underneath the roller up to 0.5 m in depth, 0.6 m longitudinally, and 1.2 m transversally from the center of the roller, after which the elements become larger. To establish better the drum–soil contact, about 75,000 shell elements were used to simulate the drum. The soil–drum system was modeled with different levels of complexity including static and dynamic analyses during stationary and moving conditions. Fathi [24] and Nazarian et al. [25] showed that the numerical responses obtained from FE models with different complexity levels are highly correlated. This study makes use of a nonlinear quasi-static stationary model to evaluate the drum’s contact width.

A material model proposed by Ooi et al. [26] was considered to account for the load-induced nonlinear behaviors of geomaterials. Ooi et al. model is in the form of:

$$M_r = k'_1 P_a \left[ \frac{\theta}{P_a} + 1 \right]^{k'_2} \left[ \frac{\tau_{\text{oct}}}{P_a} + 1 \right]^{k'_3} \quad (1)$$

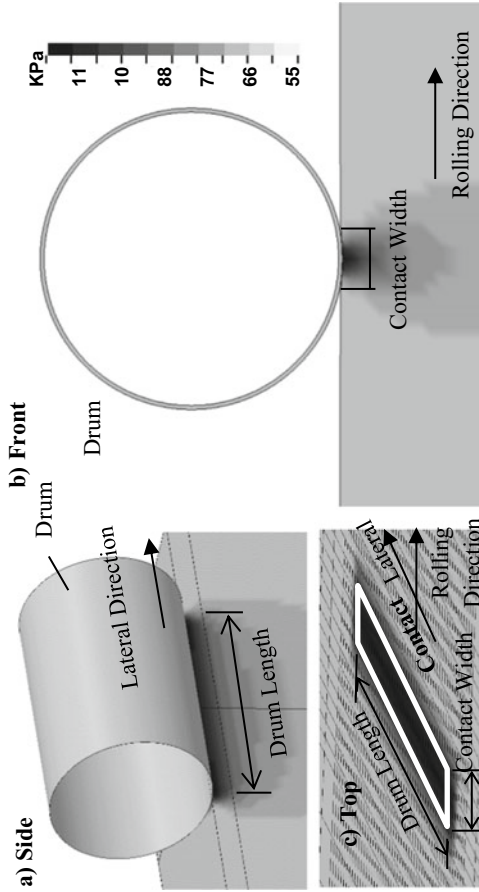
where  $M_r$  is resilient modulus,  $P_a$  is the atmospheric pressure of 100 kPa,  $\theta$  is the bulk stress,  $\tau_{\text{oct}}$  is the octahedral shear stress, and  $k'_1$ ,  $k'_2$ , and  $k'_3$  are the model parameters (determined from fitting the laboratory data to the model).

## 2.1 Contact Width

Figure 2 shows different views of the contact area and the stresses in the geosystem due to drum loading. One of the limitations encountered with the use of the automatic single surface contact model was that the nodes along the drum (master surface) that are in contact with the geosystem (slave surface) are not explicitly defined. For this reason, the contact width of the drum has to be estimated based on the stress distribution at the soil–drum interface. The contact area,  $A_c$ , can be estimated from:

$$A_c = \frac{F_c}{\sigma_{\text{ave}}} \quad (2)$$

where  $F_c$  is contact force, and  $\sigma_{\text{ave}}$  is average vertical stress within the contact area of the drum.



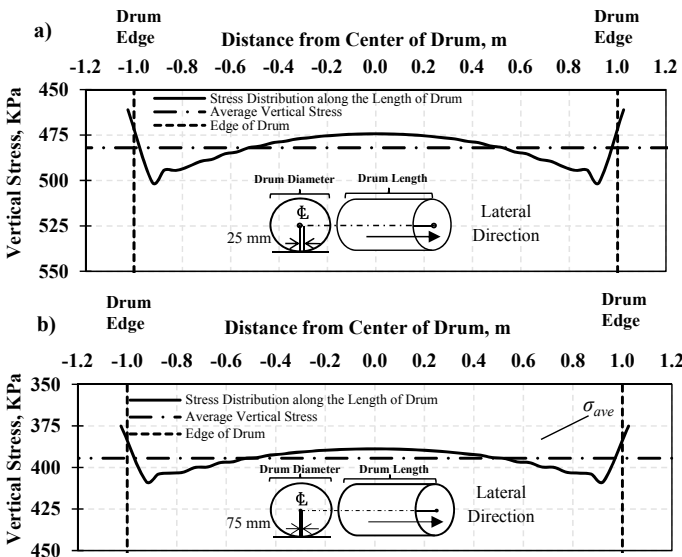
**Fig. 2** Cross-sectional views of pavement and drum for the visualization of contact area at drum-soil contact

### 3 Results and Discussion

The stress distribution along the drum length at two different distances from the centerline of the drum is shown in Fig. 3. The stress increases along the soil surface underneath the drum when closer to the edges of the drum. Likewise, a drop in stress occurs of about 90 kPa from a distance of 25–75 mm from the centerline of the drum cylinder in contact with the soil.

The stress distribution of geomaterial in the rolling direction is shown in Fig. 4. The vertical stress decreases with respect to distance. Even though at 200 mm away from the centerline the stress is close to zero, that distance cannot be defined as the extent of the contact width. A criterion for defining the contact width is necessary, due to the cylindrical curvature of the drum and the size of elements along the pavement surface (50 mm-sided cubic elements). As a simplifying assumption, the contact width is assumed to be constant along the length of the drum. The contact width was set at the distance where the magnitude of the averaged stress is 85% of the peak observed stress. This arbitrary criterion was then compared with field measurements performed at different sites with distinct types of geomaterials.

The contact width under a static drum load was estimated for four different drums shown in Table 1, on top of single- and two-layer geosystems. The drums become larger and heavier in the order listed. A set of 200 cases were simulated per drum, for each group of geosystems, consisting of a single-layer (subgrade only) and two-layer systems with top layer (base) thicknesses of 150 and 300 mm on top of the



**Fig. 3** Stress distribution of surface soil elements along the length of drum at **a** 25 mm away from the center line of drum, **b** 75 mm away from the center line of drum



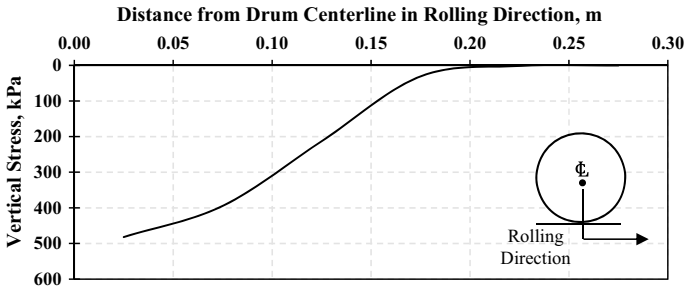


Fig. 4 Stress distribution from drum centerline in rolling direction

Table 1 Rollers selected for assessing contact width

Drum <sup>a</sup>	W (KN)	Centrifugal force (KN)	L (m)	D (m)	No. of cases
I	7.45	15.1	1.00	0.60	600
II	88.55	30.2	1.50	1.10	600
III	88.55	78.3	1.50	1.10	600
IV	58.84	169.0	2.00	1.50	600

<sup>a</sup>W—operating weight + eccentric force, L—length of drum, D—diameter of drum

subgrade and the feasible ranges of nonlinear *k* parameters described in Table 2. The descriptive statistics of the contact width for those drums are summarized in Table 3. The contact width increases as the drum becomes larger.

The contact widths of a Type IV roller drum, described in Table 1, were measured while static at two subgrade sections and four base course materials. The subgrade sites consisted of a sandy subgrade and clayey subgrade sections, while two distinct base layers were laid on top of each subgrade type. The contact width of the drum

Table 2 Feasible range of layer properties [27]

Pavement properties	Range of values
$k'_1$	100–3000
$k'_2$	0–3.0
$k'_3$	–4.0–0

Table 3 Descriptive statistics of contact width for different-sized drums

Drum	Contact width (mm)		
	Mean	Median	Standard deviation
I	143.1	142.8	2.8
II	210.5	208.6	4.5
III	212.4	211.4	5.2
IV	264.0	262.2	6.4

was measured by spray-painting the pavement structure underneath, in front of and behind, and along the length of the drum, as shown in Fig. 5. In addition to the measurement of the contact width, in-situ modulus spot testing with a lightweight deflectometer (LWD) was conducted by the research group. Figure 6 shows the contact width measurements at the six locations.

Table 4 lists the selected FE models with representative resilient moduli similar to LWD field surface moduli, and their respective contact widths. Figure 7 compares

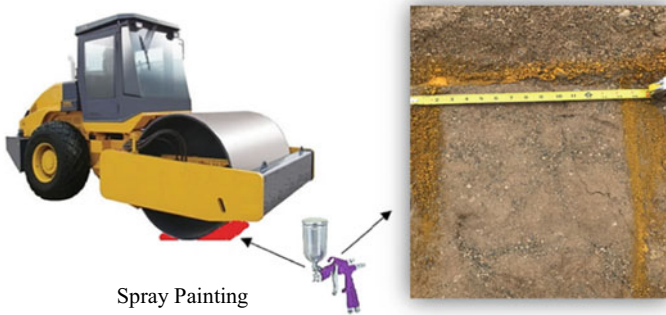


Fig. 5 Schematic view of contact width measurement at field

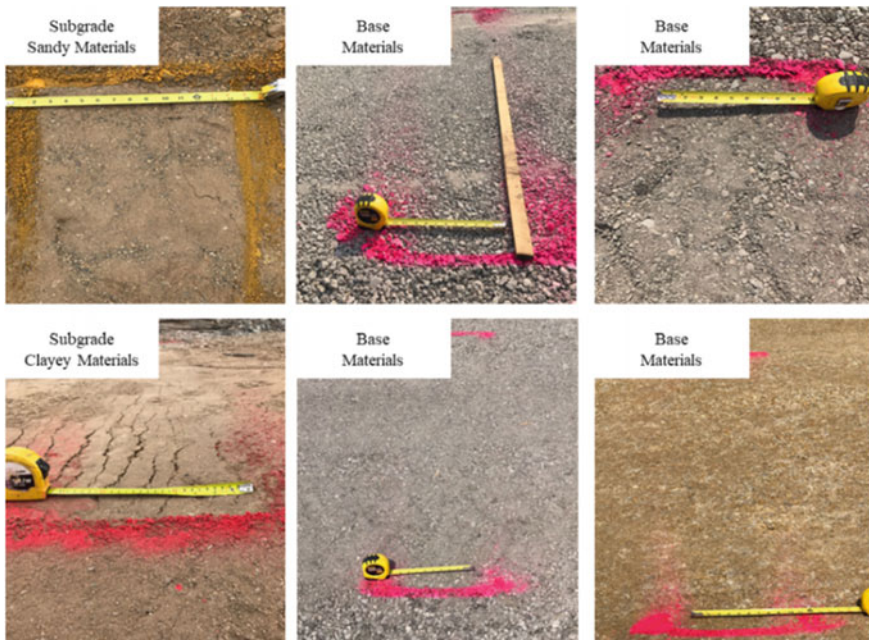
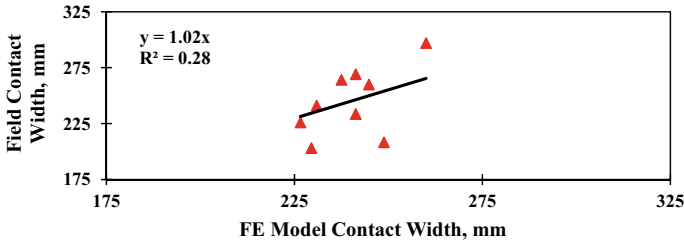


Fig. 6 Measured contact widths at different test sections

**Table 4** Contact width measurements obtained from field sections and similar representative resilient moduli FE models

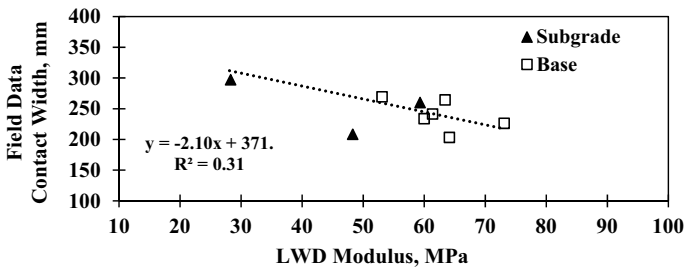
Case	Field measurement		FE analysis	
	LWD modulus, MPa	Contact width, mm	Resilient modulus, MPa	Contact width, mm
Clayey subgrade	59.3	260	59.2	244
Sandy subgrade	48.3	208	48.8	248
Sandy subgrade	28.3	297	34.6	260
Base	64.1	203	62.1	229
Base	53.1	269	53.7	241
Base	63.4	264	63.8	238
Base	61.4	241	61.1	231
Base	59.9	234	59.4	241
Base	73.0	226	73.2	227



**Fig. 7** Comparison of contact width measured from field and FE analysis

the field contact width measurements with the corresponding results obtained from FE analyses. The FE results are in agreement with the measured field contact width.

Figure 8 shows that the measured contact width decreases with an increase in the LWD modulus. In other words, the less stiff the geomaterial is, the wider the contact width will become.



**Fig. 8** Measured field contact width versus LWD modulus for bases and subgrades

## 4 Summary and Conclusions

This study proposed a stress-dependent approach for estimation of the contact area of the compaction rollers considering the nonlinear behavior of the geomaterials. A 3D finite element simulating the proof-mapping process was developed to evaluate the interaction of the roller with the geosystem using an advanced contact model. The stress distribution at the soil–drum interface was used for determining the contact area between the drum and unbound materials. This approach was conducted for different rollers of varying sizes. To validate the stress-dependent approach, different test sites were visited including various types of unbound materials for single-layer (subgrade only) and two-layer (subgrade and base) geosystems.

The contact area was measured by spraying the paint around the drum at static condition at the visited test sites. The comparison between the field measurements and numerical observations revealed a good correlation between the two representing the capability of the developed approach for yielding promising results.

**Acknowledgements** The authors would like to thank the National Cooperative Highway Research Program (NCHRP) for funding this study. The contents of this paper reflect the authors' opinions, not necessarily the policies and findings of NCHRP.

## References

1. Mooney MA, Rinehart RV (2009) In situ soil response to vibratory loading and its relationship to roller-measured soil stiffness. *J Geotech Geoenviron Eng Am Soc Civ Eng* 135(8):1022–1031
2. Rinehart R, Berger J, Mooney M (2009) Comparison of stress states and paths: vibratory roller-measured soil stiffness and resilient modulus testing. *Transp Res Record: J Transp Res Board, Transp Res Board Natl Acad* 2116:8–15
3. Yoo T-S, Selig ET (1979) Dynamics of vibratory-roller compaction. *J Geotech Eng Divis ASCE* 105(10):1211–1231
4. Van Susante PJ, Mooney MA (2008) Capturing nonlinear vibratory roller compactor behavior through lumped parameter modeling. *J Eng Mech* 134(8):684–693
5. Hertz HR (1882) Ueber die Berührung fester elastischer Körper (On the contact between elastic bodies). *J für die reine angewandte Mathematik* 1882(92):156–171
6. Adam D, Kopf F (2004) Operational devices for compaction optimization and quality control (Continuous compaction control & light falling weight device). In: *International Seminar on Geotechnic Pavement and Railway Design and Construction*, Millpress, Rotterdam, The Netherlands, Athens, Greece, pp 97–106
7. Anderegg R, Kaufmann K (2004) Intelligent compaction with vibratory rollers: feedback control systems in automatic compaction and compaction control. *Transp Res Record: J Transp Res Board, Transp Res Board Natl Acad* 1868:124–134
8. Mooney MA, Rinehart RV, van Susante PJ (2006) The influence of heterogeneity on vibratory roller compactor response. In: DeGroot DJ, DeJong JT, Frost D, Baise LG (eds) *GeoCongress 2006: geotechnical engineering in the information technology age*. American Society of Civil Engineers, Atlanta GA, pp 1–6
9. Quibel A (1980) Le comportement vibratoire: Trait d'union entre le choix des paramètres et l'efficacité des rouleaux vibrants (The vibratory behavior: interactions between vibration parameters and the effectiveness of vibratory rollers). In: *Colloque International sur le*

- Compactage (International conference on compaction, Session VII Compaction Equipment), ENPC, LCPC, Paris, pp 671–676
10. Kröber W (1988) Untersuchung der Dynamischen Vorgänge bei der Vibrationsverdichtung von Böden (Analysis of dynamic operation during the vibrational compaction of soil). Technische Universität
  11. Kopf F, Erdmann P (2005) Numerische Untersuchungen der Flächendeckenden Dynamischen Verdichtungskontrolle FDVK (Numerical analysis of continuous compaction control). Österreichische Ingenieur Architekten Zeitschrift (OIAZ) 150(4–5):126–143
  12. Kargl G (1995) Modellversuche zur Ermittlung des Last-Deformationsverhaltens geschichteter Modellböden unter ebenen und zylindrisch gekrümmten Belastungsflächen und vergleichende Computerberechnungen. Technische Universität Wien
  13. Pistor J (2016) Compaction with oscillating rollers (Doctoral thesis). Vienna University of Technology, Vienna. Thurner H, Sandström Å (n.d.) Continuous compaction control, CCC. In: Proceedings of the international conference on compaction, Paris, pp 237–245
  14. Herrera C, Costa PA, Caicedo B (2018) Numerical modelling and inverse analysis of continuous compaction control. *Transp Geotech* 17:165–177
  15. Musimbi OM, Rinehart RV, Mooney MA (2010) Comparison of measured and BEM computed contact area between roller drum and layered soil. In: Fratta DO, Puppala AJ, Muhunthan B (eds) *GeoFlorida 2010: Advances in analysis, modeling & design (GSP 199)*. ASCE, West Palm Beach, FL, pp 2444–2453
  16. Asaf Z, Shmulevich I, Rubinstein D (2006) Predicting soil-rigid wheel performance using distinct element methods. *Trans Am Soc Agric Biol Eng* 49(3):607–616
  17. Buechler SR, Mustoe GGW, Berger JR, Mooney MA (2012) Understanding the soil contact problem for the LWD and static drum roller by using the DEM. *J Eng Mech Am Soc Civ Eng* 138(1):124–132
  18. Mooney MA, Facas NW (2013) Extraction of layer properties from intelligent compaction data. Final Report for NCHRP Highway IDEA Project 145, Transportation Research Board of the National Academies, Washington, DC
  19. Patrick J, Werkmeister S (2010) Compaction of thick granular layers, NZ Transport Agency Research Report No. 411. NZ Transport Agency Research Report 411, New Zealand Transport Agency, Wellington, NZ
  20. Xia K, Pan T (2010) Understanding vibratory asphalt compaction by numerical simulation. *Int J Pavement Res Technol* 4(3):185–194
  21. Hügel HM, Henke S, Kinzler S (2008) High-performance ABAQUS simulations in soil mechanics. In: 2008 ABAQUS users' conference, Newport, RI, pp 1–15
  22. Wang L, Zhang B, Wang D, Yue Z (2007) Fundamental mechanics of asphalt compaction through FEM and DEM modeling. In: Wang L, Masad E (eds) *Analysis of asphalt pavement materials and systems analysis: engineering methods*, GSP 176. American Society of Civil Engineers, Boulder CO, pp 45–63
  23. Carrasco C, Tirado C, Wang H (2014) Numerical simulation of intelligent compaction technology for construction quality control. CAIT-UTC 029 Report, El Paso, TX
  24. Fathi A (2020) Extracting mechanical properties of compacted geomaterials using intelligent compaction technology. Doctoral dissertation, The University of Texas, El Paso
  25. Nazarian S, Fathi A, Tirado C, Kreinovich V, Rocha S, Mazari M (2020) Evaluating mechanical properties of earth material during intelligent compaction. NCHRP Research Report, 933
  26. Ooi PS, Archilla AR, Sandefur KG (2004) Resilient modulus models for compacted cohesive soils. *Transp Res Rec* 1874(1):115–124
  27. Velasquez R, Hoegh K, Yut I, Funk N, Cochran G, Marasteanu M, Khazanovich L (2009) Implementation of the MEPDG for new and rehabilitated pavement structures for design of concrete and asphalt pavements in Minnesota. MnDOT Research Report MN/RC 2009–06. University of Minnesota, Minneapolis, MN

# An Earthworks Quality Assurance Methodology Which Avoids Unreliable Correlations



**Burt G. Look**

**Abstract** In earthworks, testing using density ratio is applied widely in quality control. Density ratio tests take significant time for results to be reported. Yet because of its widespread usage, this now acts as an impediment to the development of alternative methods of testing. Modern geotechnical and pavement designs are based on modulus and strength values. It is, therefore, reasonable to investigate the use of alternative test methods which measures these parameters directly. Several in-situ devices have been available to industry for the past 2 decades and research has shown these have significant benefits. However, studies then try to correlate those measured parameters with the density ratio. Correlating to density is flawed. Given the poor correlations associated with relating density to other measured parameters an alternative approach was developed. This is based on matching probability density functions (PDFs) for quality assurance (QA). This methodology first recognizes density is normally distributed, but other more accurate tests are non-normally distributed. The derived best fit distribution is compared with the normally distributed density measurements. Data using a range of alternative testing equipment was used for this QA method of matching PDFs. The methodology has been successfully used on a major earthworks project in Australia.

**Keywords** Earthworks · Density testing · Probability density functions

## 1 Introduction

In earthworks testing using dry density ratio (DDR) is applied widely in quality control (QC). DDR tests may take significant time for results to be reported. This QC approach is not representative of current Quality Assurance (QA) testing philosophy.

Modern geotechnical and pavement designs are based on modulus and strength values. It is, therefore, reasonable to investigate the feasibility to use alternative test methods for QA purposes, which measure these parameters directly. Several

---

B. G. Look (✉)

FSG—Geotechnics and Foundations, Spring Hill, QLD 4000, Australia

e-mail: [blook@fsg-geotechnics.com.au](mailto:blook@fsg-geotechnics.com.au)

in-situ devices have been available to industry for the past 2 decades and research has shown these have significant benefits. However, studies then try to correlate those measured parameters with the density ratio. Correlating to density is flawed as DDR is not a fundamental parameter. An alternative testing approach is required which encapsulates the QA required but avoids the direct paired correlation approach.

The dry density ratio (DDR) compares the compacted field density with the laboratory maximum dry density (MDD), which can be Standard or Modified compaction. A specified density ratio is really a targeted means to reducing the air voids.

The emphasis on density has led to the belief that it is the key parameter, yet it is an index only, i.e. we assume an increased density ratio (aka relative compaction) means an increased strength or modulus or reduced permeability. Technology has now advanced to measure those parameters directly, yet many road and approving authorities still use density testing as the main quality evaluation parameter because of our longstanding experience. The compaction model has not advanced with the change in both testing and compaction equipment.

Given the poor correlations associated with relating density to other measured parameters an alternative approach was developed based on quality assurance schemes. This is based on matching the probability density functions (PDFs). This methodology first recognizes density measurements are normally distributed, but other more accurate tests are non-normally distributed. The derived best fit distribution is compared with the normally distributed density measurements. Data from several sites using a range of alternative testing equipment, was used to assess this method of matching PDFs. The methodology has been successfully used on a major earthworks project in Australia. The lessons learnt are presented along with the background rationale for progressing such alternative test in earthworks QA.

## 2 Sample Preparation for Testing

Prior to carrying out the laboratory compaction test, the sample should be suitably prepared. Australian Standards AS 1289 1.1 [1] requires that the soil clod size be reduced to pass a 10 mm screen. Blight and Leong [4] shows the effect of clod sizes and sample wetting on the compaction curve. These sample preparation and curing take time prior to the tests. For high plasticity clays, this curing time can be up to 4–7 days, but 1–2 days for low plasticity clays (Table 1).

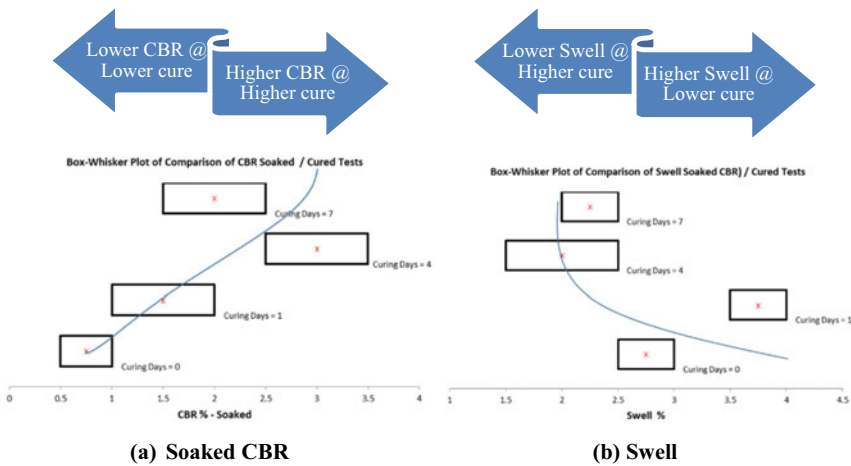
The effect of curing time for soaked CBRs and the corresponding swell values are shown in Fig. 1a, b, respectively. This was a high plasticity clay ( $PI = 47\%$ ) from Bundamba, Queensland. This shows if sample preparation and curing times are not carried out, the test results will be affected. This down time results in project delays and equipment onsite not being fully occupied.

Many contractors often place additional lifts before the test results are known. This has a risk but is based on the assumption that they have done a good job at compaction and the tests are simply validating what they already know.

**Table 1** Minimum curing times based on condition of sample (AS1289 5.1.1, 2017) [2] and (AS1289 6.1.1, 2014) [3]

Plasticity	Within 2% of OMC (h)	Greater than 2% of OMC (h)
Sands and granular materials <sup>a</sup>	2	2
Low (LL < 35%)	24	48
Medium (35% < LL < 50%)	48	96 (4 days)
High (LL > 50%)	96 (4 days)	168 (7 days)

<sup>a</sup>Included crushed rocks and manufactured materials with fines content <12%



**Fig. 1** Soaked CBR—effect of curing time on CBR value (mean, upper and lower quartile)

Density ratio tests are therefore used as a quality control (QC) tool and not in Quality Assurance (QA). QA aims to prevent defects. QC aims to identify and fix defects. Quality Assurance makes sure you are doing the right things, the right way, while Quality Control makes sure the results of what you’ve done are what you expected.

### 3 What Do Engineer Want from Testing

A survey of 54 engineers [6] on ranking what attributes are desirable in a test equipment showed that accuracy is the most preferred attribute of any test. The preference ranking order for the 8 attributes of a test equipment from that survey was.

1. Accuracy



2. Precision
3. Time to conduct test/Ease of use
4. Time to process results/Ease to process and report
5. Amount of data obtained/Capital cost of equipment.

This could be broken down into age and employer. Those with less than 5 years of experience preferred ease of use and ease to process and report. A contractor would have time to conduct and process results highly ranked. This ranking was used to assess various equipment [6].

### ***3.1 Alternative Equipment Used or QA Testing***

Over the past 2 decades, several devices have been developed that provide a more direct measure of the modulus or strength of an in-situ material. However, these various values and units of measurements are not consistent with the historical reliance of density testing results for QC purposes. Using density as a reference test then leads to requests for correlations to the DDR results as if that index was the end product. Yet DDR was meant to be an index only of the likely strength or modulus. To measure strength or modulus and then correlate back to an index test shows how tradition encourages this force fit from a primary to the 2nd order index parameter. A peak strength or modulus is not necessarily coincident with a specific MDD and OMC.

Measured modulus values depend on the material compaction, its quality, and its interaction with deeper underlying layers. Thus, density is just one contributing factor to modulus, and a weak correlation should be expected. The importance of controlling Degree of Saturation (DOS) in soil compaction is discussed in Tatsuoka and Correia [12]. They show a systematic approach to controlling DOS at the end of compaction as the compacted state cannot be estimated only by strength and stiffness.

Poor correlation between modulus and density measurements was reported in Meehan et al. [10] with the effect of moisture content critically important. McLain and Gransberg [9] searched for correlations between potential alternatives to the nuclear density gauge. The tests included Light Falling Weight Deflectometer (LFWD) and Clegg Impact Values (CIV). The results showed that no definite relationship between Nuclear Density Gauge (NDG) and Modulus or CIV results could be found. Mazarai et al. [8] quantify the equipment and operator-related variabilities from a database of stiffness measurements made with four devices on eighteen separate specimens. It was found that most devices are reasonably repeatable and reproducible as long as the moisture content and density are rigidly controlled. This conclusion leads to parallel testing of modulus and density rather than replacement testing.

Nazarian et al. [11] reported on a Modulus-Based Construction Specification for Compaction of Earthwork and Unbound Aggregate. They concluded the adaption of the modulus-based specification needs to be approached in the context of the

levels of uncertainty associated with the current well-established density criteria. It was shown that achieving quality compaction (defined as achieving adequate layer modulus) is only weakly associated with achieving density.

Similar poor correlations will be shown in this paper on many projects over the years. Field result trials were used to benchmark various alternative equipment and compared with traditional density QC measurements. A methodology is presented which avoids the conundrum of accepting a test with a poor paired correlation with density. Without such an alternative methodology, superior tests are unable to supplant the traditional density-based QC approach. Continuous parallel testing is not cost-effective and often creates conflicting data. The nascent technology of Intelligent Compaction (IC) has its own compaction “modulus” which provides a further motivation to have a methodology as an independent test needs to be readily available to check such results.

### 4 Precision and Accuracy of Various Tests

The various test instruments were compared to density for 5 sites with the coefficient of variation (COV) shown in Fig. 2. The COV represents the range of precision, and the density test is the standout leader (COV = 2.0%) as compared to the plate load tests with a COV of 77%. However, precision is the 2nd preference as compared to accuracy. Accuracy was assessed in terms of how well the results compared with each other for similar high, low, and median values for the 5 test sites. The number of matches between tests for the 5 sites were compared as an indicator of accuracy

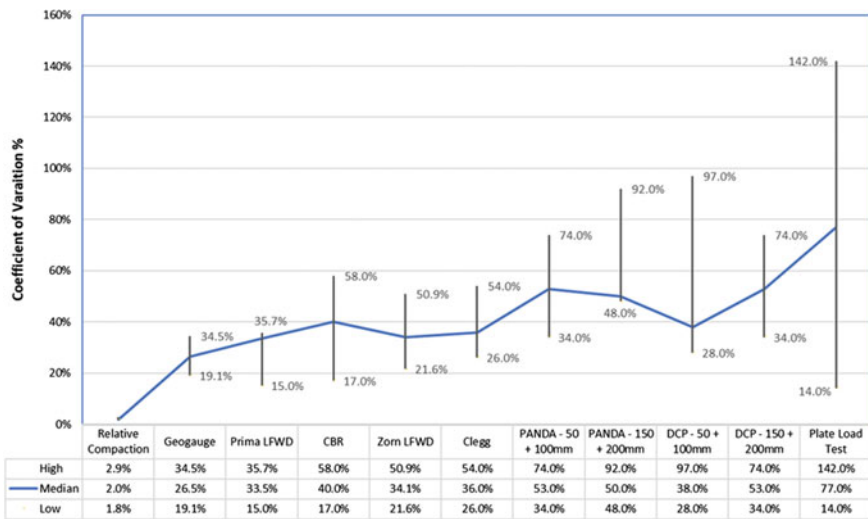


Fig. 2 Variability for equipment tested over 5 sites

**Table 2** Equipment and tests matching to other tests over 5 sites

Tests compared for 5 sites	No. of matches	Rank
Plate load test (PLT)	22	1
PANDA—50/100 mm	19	2
PANDA—150/200 mm and CBR	17	3
LFWD—PRIMA	16	5
Clegg and DCP 150/200 mm	15	6
Dry density ratio	13	8
Geogauge and LFWD—ZORN	11	9
DCP 50/100 mm and moisture ratio	9	11

(Table 2). For depth tests such as the Dynamic Cone Penetrometer (DCP) or PANDA the accuracy and precision would vary if 50/100 mm or 150/200 mm depth test results are used.

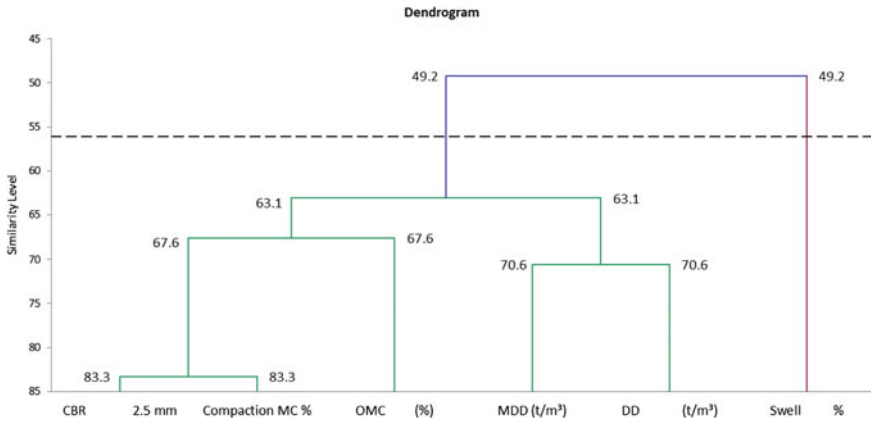
The (incorrect) assumption prior to these trials was that density and PLTs (two “standard” tests) were aligned i.e. a high density would produce a high PLT modulus value and vice versa. The PLT had the highest accuracy with 22 matches with other equipment. Thus, the lowest precision test (PLT) had the highest accuracy. Amount of data was not well ranked as an attribute, but the PLT would provide the most data and the density test provides the least data.

## 5 Dendrograms for Assessing Compaction Relationships

In statistics, hierarchical clustering builds trees (Dendrograms) to represent clustered data. The groups of data are nested and organized as a tree with each group in linking to other successor groups. StatTools (version 7) is an add-in to Microsoft Excel and was used for the cluster analysis. The Cluster Analysis command searches for patterns in a data set in order to classify observations or variables into groups of similar items. The analysis supports a variety of agglomerative hierarchical methods and distance measures. The *clade* is a branch in the tree. Clades that are close to the same height are similar to each other and clades with different heights are dissimilar.

Figure 3 shows the dendrogram for the Cooroy (CH) clay soaked CBR. This clustering provides visual evidence that the CBR is more closely clustered to the compaction moisture and the OMC rather than the density. This could also have been derived numerically as seen in the correlation matrix (Table 3). CBR is most strongly correlated with the compaction moisture content (0.691) and least with the dry density (0.037). CBR is negatively correlated with swell (−0.834). This suggests that CBR for this expansive clay is most correlated to the swell value after soaking for the 4 days.

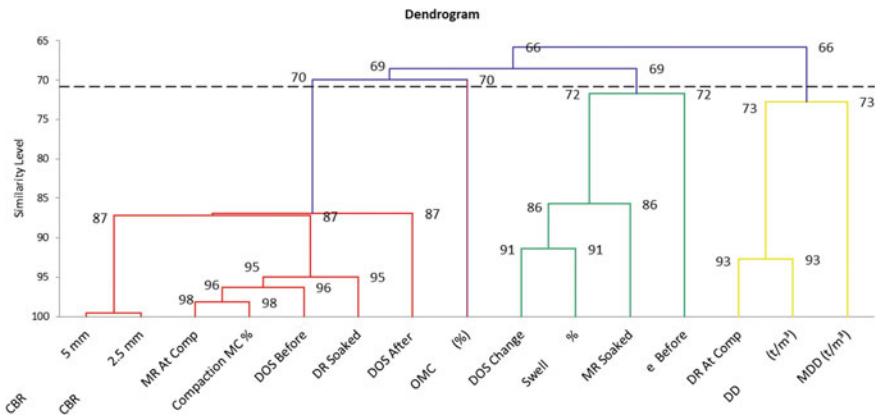
Figure 4 shows the same data dendrogram with the clustering for 15 relationships. The CBR is least related to the DDR at compaction, the dry density, and the MDD.



**Fig. 3** Dendrogram of 6 key measurements in a soaked CBR test

**Table 3** Correlation matrix for 6 No. test outputs

Correlation matrix	Comp. MC %	DD (t/m <sup>3</sup> )	OMC (%)	MDD (t/m <sup>3</sup> )	CBR @ 2.5 mm	Swell %
Comp. MC %	1.000					
DD (t/m <sup>3</sup> )	-0.299	1.000				
OMC (%)	0.229	-0.380	1.000			
MDD (t/m <sup>3</sup> )	-0.043	0.455	-0.343	1.000		
CBR @2.5 mm	0.691	0.037	0.399	0.317	1.000	
Swell %	-0.851	0.059	-0.143	-0.379	-0.834	1.000



**Fig. 4** Dendrogram of 15 parameters in a soaked CBR test

Note that all samples were compacted above 90% MDD, a low Density/CBR relationship does not suggest no or little compaction as that would certainly have an effect on the CBR value. The soaked CBR at 2.5 mm and 5.0 mm are clustered together and the CBR is most strongly related to the Moisture ratio (MR) and moisture content (MC) at compaction, and the compaction the Degree of saturation (DOS) before and after soaking.

Similar dendrogram analysis of in situ tests with compaction parameters show some tests were associated more with the moisture/CBR while other tests are more associated with the DDR. Thus, the non-efficacy of correlating another test result to DDR.

## 6 Density PDF Used to Match Other Test Data

With a “new” equipment and an existing testing system (DDR testing) the first step is to investigate the association between the two sets of data. A poor correlation often results. The density tests are normally distributed, while most of the other tests are not normally distributed. A good correlation also requires both to have the same distribution functions. Look [5] discuss the issues of assuming a normal PDF for tested soil and rock materials. Look [7] show how statistically based compaction quality control requires PDF matching.

Given that paired relationships are unsatisfactory, a different methodology is required if these instruments are to be used for QA tests. A method of matching PDFs is proposed to advance the use of the various instruments. Without such an approach the industry will keep on back checking to the DDR index which provides the poor correlations which then creates suspicion on the use of modern and more accurate test equipment. At the same time, research is consistently showing many of these instruments are superior as QA measurement tools as compared to the density ratio status quo.

The PDFs for the best fit and normal distributions are compared for the DCP in Fig. 5. A normal PDF would be an incorrect assumption and using a DCP with a normality assumption results in a poor QC assessment. The Normal PDF is ranked No. 11 in goodness of fit tests. The paired matching of the DCP and DDR is shown in Fig. 6 with an  $R^2 = 0.06$  for the best-fit trend line. This poor correlation shows an increasing DCP value resulting in a decreasing DDR, when both should be increasing.

The approach of matching PDFs rather than paired correlations is shown in Fig. 7. Using the appropriate PDF, the 5% value of both the DCP and Density ratio are paired. Then a similar pairing for the 10% value, 25% value, median, and so on. Figure 8 shows the data can now be paired with a high correlation. The same data with a paired PDF matching approach now results in a strong correlation.

A similar approach is also shown for LFWD tests paired with DDR results. Figure 9 shows this paired correlation with the “low” LFWD passing values and the “high” failing values when such an approach is adopted. The low  $R^2$  value alone should discount such an approach. But the persistence of site supervisors to insist on

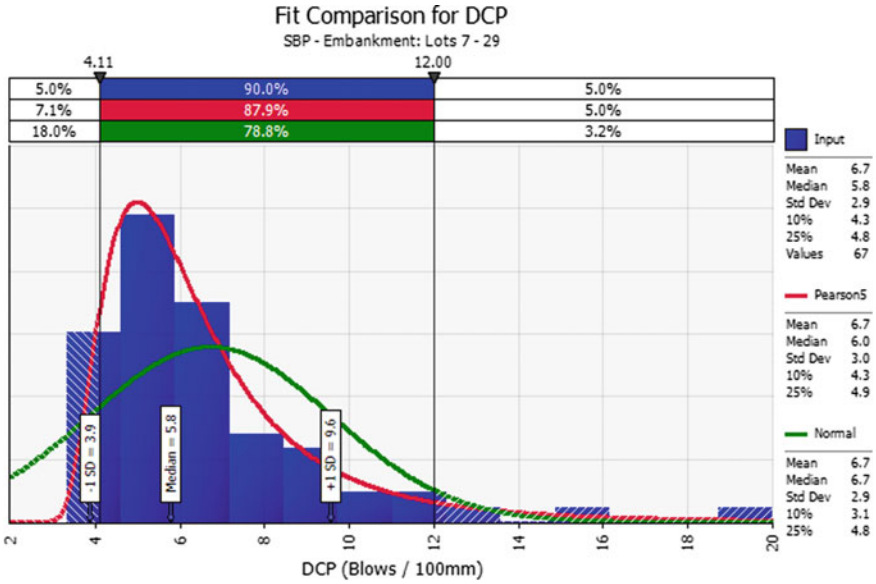


Fig. 5 DCP tests with a non-normal PDF

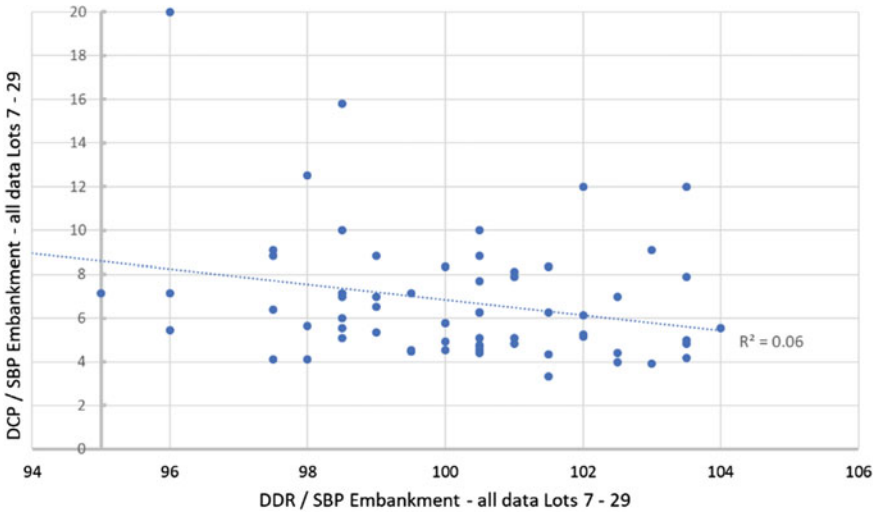


Fig. 6 Paired matching of DDR and DCP with low correlation

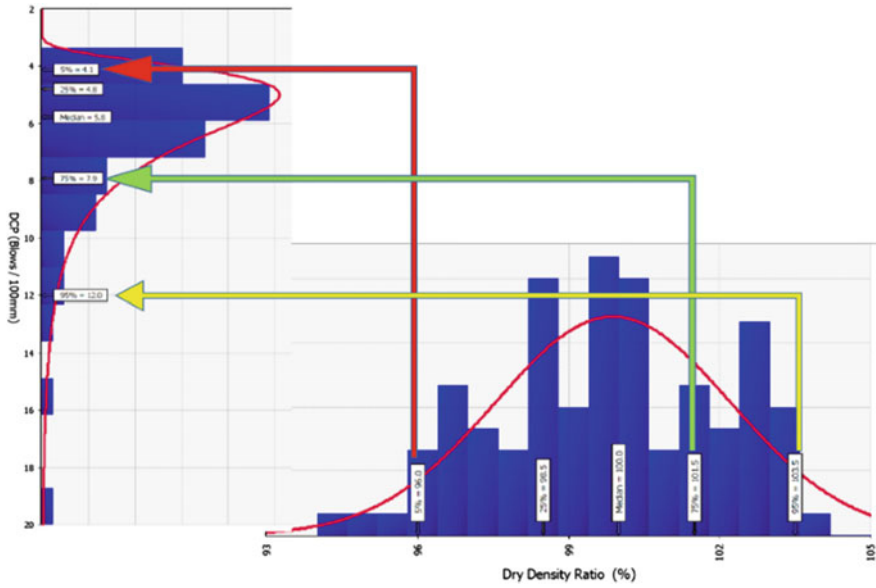


Fig. 7 Matching the dry density ratio and DCP PDFs

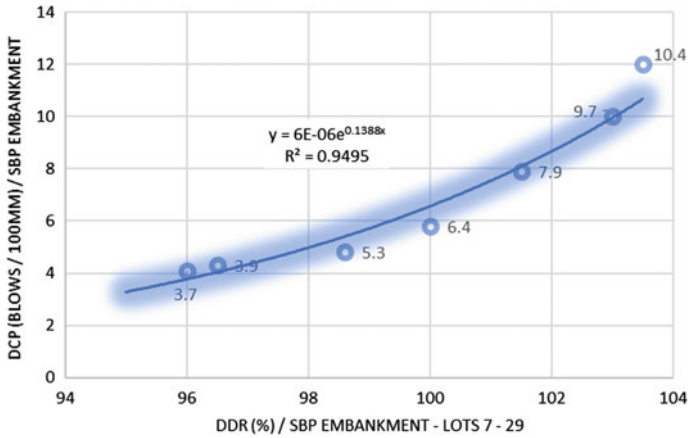


Fig. 8 Matched PDFs for DDR and DCP are correlated

a correlation with the density ratio continues to be the impediment of implementation of superior tests. Modulus values above 100 MPa can “fail” a 100% DDR tests and values below 30 MPa can “pass” a DDR criterion.

Figure 10 shows the LFW tests with the best fit PDF as compared with a normal PDF. The normal PDF was ranked 11 in the goodness of fit test. If a normal PDF was used, the statistical errors become apparent, as large negative values can now occur

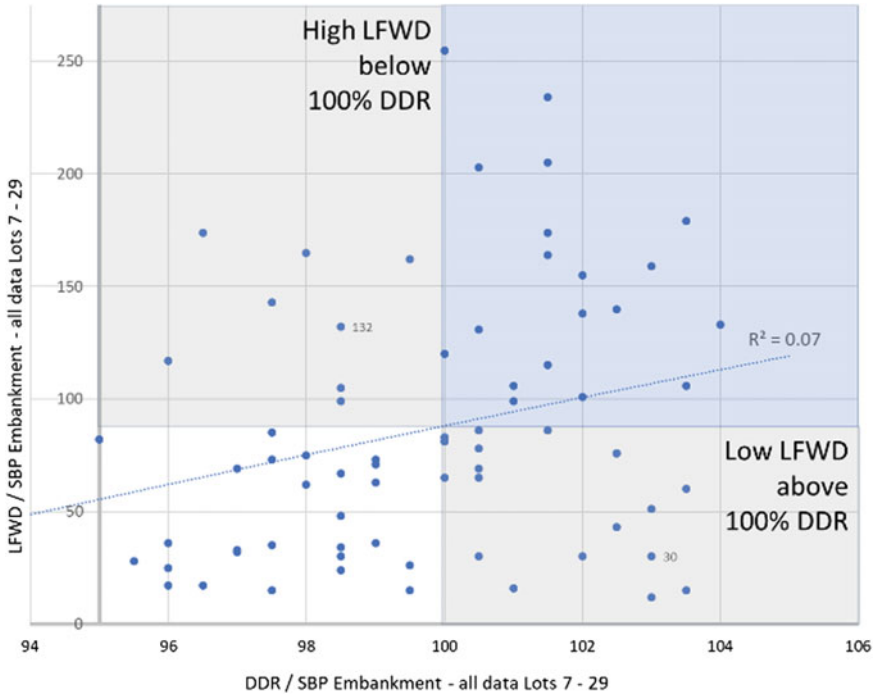


Fig. 9 Paired matching of DDR and LFWD (Prima) tests

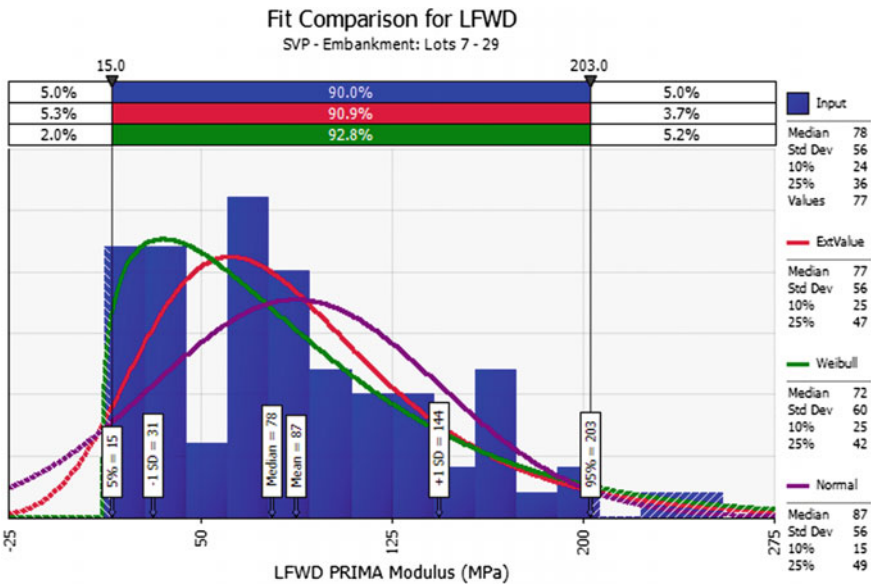


Fig. 10 LFWD (Prima) tests with a non-normal PDF



at the lower 5% tail. A bounded Weibull PDF would provide the best fit PDF in this case.

Using the procedure of matching PDFs for the LFWD, the corresponding QA values are obtained as shown in Fig. 11. The resulting paired fit by this matching PDF method results in an  $R^2 = 0.98$ . This should be compared with Fig. 9 which had a trend line with an  $R^2 = 0.07$ . This is the same data with a transformed analysis.

These results are summarized in Table 4 with both the LFWD and the DCP results. Note that DCP has both a low accuracy and precision as was shown in Table 3 but is shown here not as progressive tool but for those who rely on this commonly used measuring tool. This is a material-specific relationship for this test site as different materials can have different moduli for the same 95% relative compaction [7]. This material was 60% gravel size with 20% of both sand and fines.

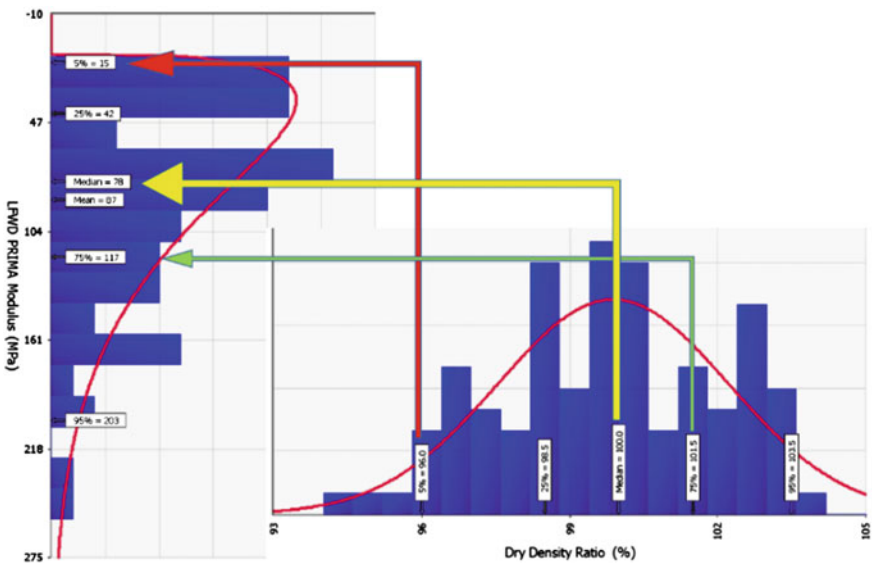


Fig. 11 Matching the dry density ratio and LFWD PDFs

Table 4 In-situ test QA for 2 different tests as obtained by the method of matching PDFs

DDR (%)	LFWD (PRIMA) @ 100 kPa (MPa)	DCP Blows /100 mm
96	15	4
98	30	5
100	60	6
103	160	10
Very high precision	Medium precision	Low precision
Very low accuracy	Medium accuracy	Low–medium accuracy

## 7 Conclusions

Current QC tests rely on density testing. Yet because of its widespread usage and historical success, this now acts as an impediment to the development of alternative methods of testing. The time lag to complete laboratory evaluation of sampled materials, provides a bottle neck during construction. Several in-situ devices have been available to industry for the past 2 decades and have significant benefits. However, with 2 sets of data, most researchers then use a paired correlation and at high densities obtain a low regression coefficient with associated uncertainty. This is due to the low precision of the PLT or LFWD ( $COV > 50\%$ ), while the dry density ratio has a high precision ( $COV < 5\%$ ), but low accuracy. Both the PLT and LFWD have a non-normal PDF as compared to the density tests which have a normal PDF.

A statistical method of matching PDFs was shown to provide a reliable approach, for other testing to be applied for QA assessment without the spurious correlations that would otherwise occur. This would then result in an improved accuracy of testing, faster turnaround of results, and is an easier test, that can cross check the emerging IC technology. However, current lack of standards and lower precision of these tests introduces other considerations in quality assessment. As a priori there is an assumption that a valid relationship exists between any two tests at the same site, on the same material and at a given time of testing. Changes in soil suction and degree of saturation may affect the result if not time coincident.

**Acknowledgements** Dr David Lacey was active in acquiring and analysis of some of the test data presented.

## References

1. Australian Standard (2001) Methods of testing soils for engineering purposes. Method 1.1: sampling and preparation of soils. AS 1289
2. Australian Standard (2017) Methods of testing soils for engineering purposes. Method 5.1.1: determination of the dry density/moisture content relation of a soil using standard compactive effort. AS 1289
3. Australian Standard (2014) Methods of testing soils for engineering purposes. Method 6.1.1: determination of the California bearing ratio of a soil. AS 1289
4. Blight GE, Leong EC (2012) Mechanics of residual soils, 2nd edn. CRC Press
5. Look B (2015) Appropriate distribution functions in determining characteristic values. In: 12th Australia New Zealand conference in geomechanics, Wellington, New Zealand
6. Look B (2018) Compaction QA limitations: benefits of alternative testing methods. In: AGS victoria symposium on geotechnics and transport infrastructure
7. Look B (2020) Overcoming the current density testing impediment to alternative quality testing in earthworks. *Austr Geomech J* 55(1):55–74
8. Mazari M, Garcia G, Garibay G, Abdallah I, Nazarian S (2013) Impact of modulus-based device variability on quality control of compacted geomaterials using measurement system analysis. In: TRB 2013 annual meeting

9. McLain K, Gransberg DD (2016) Contractor-furnished compaction testing: searching for correlations between potential alternatives to the nuclear density gauge in missouri highway projects. *Int J Qual Innov* 3(1)
10. Meehan C, Tehrani F, Vahedifard F (2012) A comparison of density-based and modulus-based in situ test measurements for quality control. *Geotech Testing J* 35(3):387–399
11. Nazarian S, Mazari M, Abdallah I, Puppala I, Mohammad L, Abu-Farsakh M (2014) Modulus-based construction specification for compaction of earthwork and unbound aggregate. Draft final report, National Cooperative Highway Research Program NCHRP Project 10-84, Transportation Research Board
12. Tatsuoka F, Correia A (2018) Importance of controlling the degree of saturation in soil compaction linked to soil structure design. *Transport Geotech* 17:3–23

# Intelligent Construction for Infrastructure—The Framework



George K. Chang , Guanghui Xu, Antonio Gomes Correia,  
and Soheil Nazarian

**Abstract** Due to the impact of modern information technology, the construction of transportation infrastructure has entered the “Intelligent Era.” The conventional construction technology is also undergoing a paradigm shift. In this paper, the term “intelligent construction” is defined, and the status quo of global transportation infrastructure construction with emerging intelligent construction technologies is summarized. The framework of intelligent construction is presented on all aspects of the integration of modern information technology and the conventional highway technologies. The essential elements of intelligent construction include sensing, analysis, decision-making, and execution. Big data, machine learning, and expert system are applied to provide practical technical solutions for intelligent construction. This paper also elaborates on the process of intelligent decision-making and auto-feedback machine controls. Finally, the future development of intelligent construction is laid out. The globally coordinated efforts by the International Society for Intelligent Construction (ISIC) will help the leading development and implementation of intelligent construction into the future.

**Keywords** Intelligent construction · Framework

---

G. K. Chang (✉)

Transtec Group, 6111 Balcones Drive, Austin, TX, USA

e-mail: [GKChang@TheTranstecGroup.com](mailto:GKChang@TheTranstecGroup.com)

G. Xu

Southwest Jiaotong University, Chengdu, Sichuan, China

e-mail: [GHxhome@163.com](mailto:GHxhome@163.com)

A. G. Correia

University of Minho, Guimaraes, Portugal

e-mail: [agc@civil.uminho.pt](mailto:agc@civil.uminho.pt)

S. Nazarian

University of Texas, El Paso, TX, USA

e-mail: [nazarian@utep.edu](mailto:nazarian@utep.edu)

G. K. Chang · G. Xu · A. G. Correia · S. Nazarian

International Society for Intelligent Construction, Okemos, MI 48864, USA

# 1 Definition of Intelligent Construction for Infrastructure

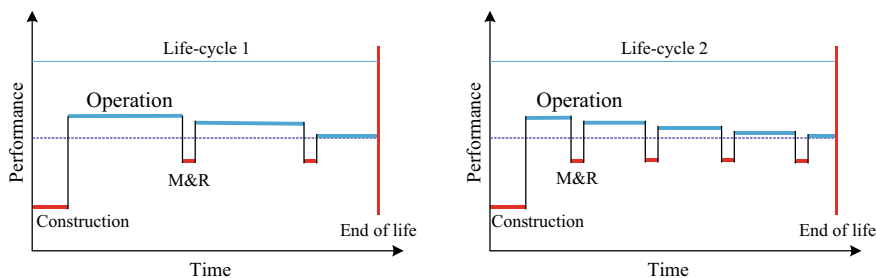
**Definition** The term “intelligent construction for infrastructure” has been referenced by the industry and academics for several years without a clear definition. The following is the definition provided in this paper:

Intelligent construction for infrastructure is a combination of model science and innovative construction technologies. It includes the applications of intelligent perception/sensing, intelligent computing/analysis, intelligent decision-making, and intelligent feedback controls to the life-cycle of infrastructure: from the survey, design, construction, operation, and maintenance/rehabilitation by adapting to changes of environments and minimizing risks.

**Introduction** Conventional infrastructure construction and intelligent technologies used to be in different fields. As the technologies advanced rapidly and reacted to changes in workflows, these two fields are merging into called “intelligent construction.” In modern days, it is common to see advanced technologies being used at construction sites, such as Automated Machine Guidance (AMG), Unmanned aerial vehicles (UAV), etc. Behind the scenes, Building Information Modeling (BIM) is gradually adopted to manage the life-cycle of infrastructure more efficiently. However, the real intelligent construction is beyond automation, but inherently built-in intelligence to “sense, analyze, and assist in decision-making.”

Construction of infrastructure can vary significantly in terms of linear, vertical, sizes, and associated materials and construction machinery and technologies. Regarding the quantity, the construction for roadways is the highest. The construction quality control (QC) for roadways is also relatively more complicated than those for bridges and tunnels. The key issues with roadway construction are dealing with the compaction of earth materials and pavement mixture materials that are affected by the variability of materials types, moisture, and temperatures.

**Life-Cycle and Construction Quality** Modern days management of infrastructure often covers the life-cycle of the asset. Construction quality reflects the needs of subsequent maintenance and rehabilitation (M&R) (Fig. 1). Unfortunately, most construction projects are often of questionable quality due to a low-bid system that is widely used.



**Fig. 1** Comparison of life-cycles of systems with varied construction qualities

**Improve QC with Information Technologies** To improve the construction of infrastructure, one cannot merely rely on conventional construction machinery and technology. One of the critical findings of construction quality studies is that 80% of premature failure of infrastructure is due to workmanship [1]. Therefore, the industry starts to invest in technologies other than conventional methods. One dominating technology that the industry starts to adopt is information technologies. The information technologies start with small computer chips, including chips in circuit boards, then the circuit boards are integrated into construction machinery and management systems (Fig. 2). Such an application allows the conventional methods and machinery with the added capabilities to sense and collect data, analyze data into information, and utilize the information to make better decisions. Application for the quality control for the entire construction process (from material production to final compaction) is gradually adopted by the industry (Fig. 3).

**Characteristics of Intelligent Construction** Intelligent construction can be considered integration of conventional construction methods, machinery with modern information technologies. However, one should remember that automation is not intelligent construction. True intelligent construction shall consist of four crucial elements: perception, analysis, decision-making, and execution (Fig. 4). Perception

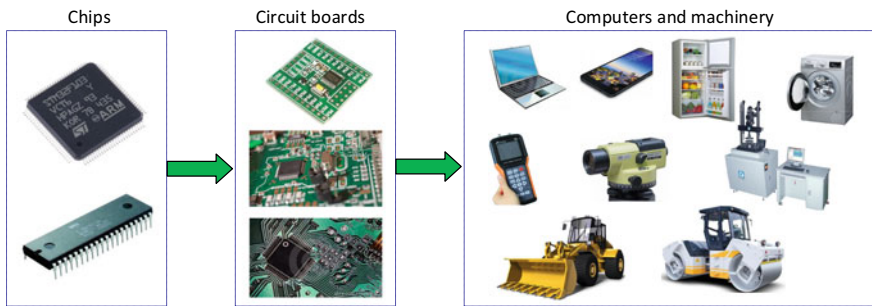


Fig. 2 Information technologies used in computers and construction machinery



Fig. 3 An example of quality control for the entire construction process ( Source Vogele)

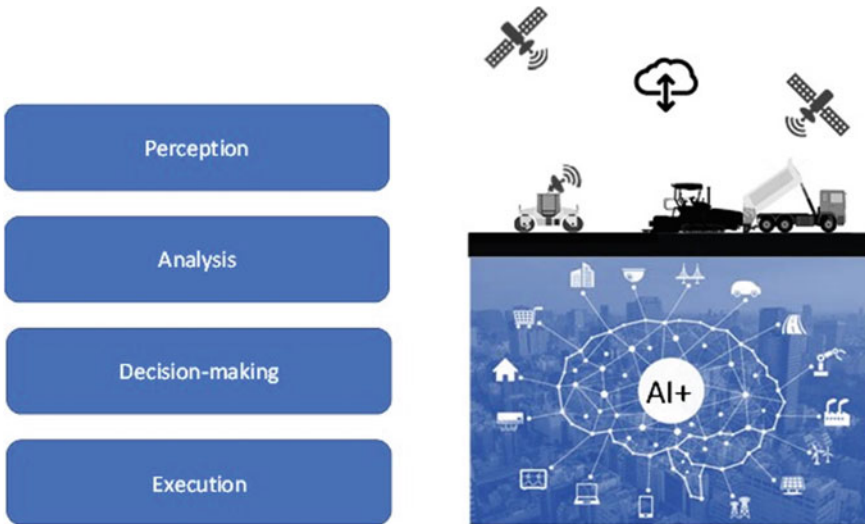


Fig. 4 Fundamental elements of intelligent construction integrated with AI

is not merely to sense and collect data, but to obtain the meaning of the data. Analysis and decision-making would be an inherent intelligent algorithm with aid from a certain level of Artificial Intelligence (AI). Finally, execution would involve a certain level of feedback or auto-feedback systems.

**The Framework of Intelligent Construction** The framework of intelligent construction includes intelligent designs, intelligent construction technologies, and intelligent M&R (Fig. 5).

**Step-By-Step Implementation Starting with Intelligent Compaction (IC)** The implementation of such a framework needs to be in a step-by-step process. Based on the experiences of the authors, the implementation shall start with the intelligent compaction (IC) that has proven and mature track records of implementation since the 1970s. IC is an instrumented roller-based system that can measure one hundred

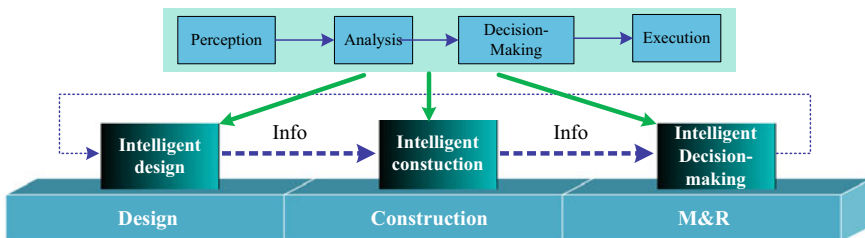


Fig. 5 The framework of intelligent construction

percent coverage of compacted areas. The core of IC is the real-time accelerometer-based measurement system, Intelligent Compaction Measurement Value (ICMV), that can be used to monitor the stiffness of the compacted materials during the compaction process. IC is a proven QC tool and will soon be evolved to be an acceptance tool. Successful implementation of IC would help the implementation of other intelligent construction technologies such as feeding as-built layer modulus data to BIM for pavements [2].

## 2 Construction Managed by Systematic Methods

**The Definition of Systematic Methods** It is imperative to use systematic methods to implement the framework of intelligent construction due to the inherent complexities. There are a variety of systematic methods that utilize mathematical models and computer programs. However, the definition of systematic methods can be generalized as an organic structure of many interacting elements that can be dynamically adapting to changes of conditions and feedbacks from environments to maintain its functions and stability. A system may involve in a wave pattern, as exemplified by the AI system from the 1950s to the current days [3].

**The Fundamental Elements of Systematic Methods** In the systematic methods for roadway construction, the fundamental elements are: designs (including roadway materials and pavement structure), construction (as-built information such as layer moduli measured by intelligent compaction), analysis (stresses and strains of the roadway structure under traffic loadings and environmental effects), condition surveys (including structural and functional testing data), controls (including restriction of overloaded heavy vehicles).

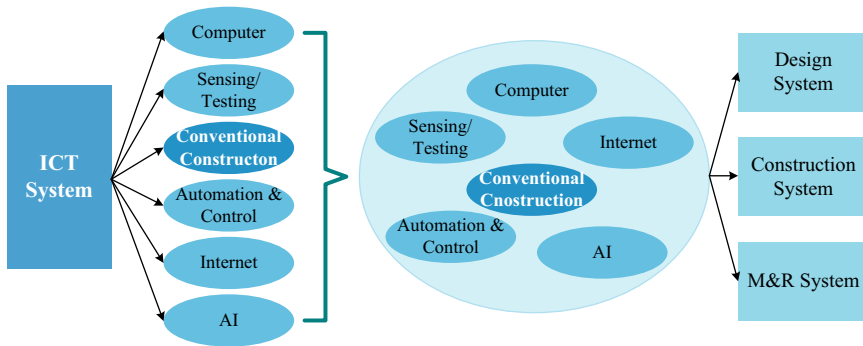
**The Usages of Black Boxes** Any system includes inputs, processes, and outputs. Ideally, a white box or grey box approach can be used if the algorithm of the process is known (e.g., back-calculation of falling-weight deflectometer data to generate pavement layer moduli). When the processes of complex systems are often unknown or too complicated to characterize them into mathematical models, a black box approach needs to be taken with the aid of AI and machine learning.

**The System of Roadway Structures** As an example in roadway construction, the system includes subgrade, subbase, and pavement layers. The inputs to this system are traffic loadings and effects from moisture and temperatures. The outputs of this system are the stresses and strains for each pavement layer.

**The System of Artificial Intelligence** Regarding AI, the core of the system consists of training data, computing algorithms, etc. that will be elaborated on in later sections.

**The System of Intelligent Construction Technologies** The system of intelligent construction technologies consists of many elements such as personnel, technologies,





**Fig. 6** Interaction of many elements within the system of intelligent construction

equipment, materials, information, capital, etc. (Fig. 6). It is an extensive, complex, nonlinear system. The input to this system is the land. The outputs of this system are infrastructure for all modes of transportation mentioned above. The elements are multi-disciplinary, interacting, and assembled into an organic structure or system. As mentioned above, this system consists of three sub-systems: intelligent designs, intelligent construction, and intelligent M&R.

**The Information Technology System for Data Sharing** As the system of intelligent construction grows, the increasing complexity makes it only possibly to be managed by information systems. The core of the system to function is data sharing. However, the fundamental rules of such an information system still need to be followed, including hierarchical structure, horizontal/vertical interaction, compatibility protocols, and an open system.

### 3 Construction Machine Learning

**Computers that Emulate Human Brains** Machine learning is one of the core technologies in intelligent construction. The first generation of such technologies is the expert system. It is followed by an artificial neural network (ANN) and genetic algorithm (GA) to emulate human brains that achieve initial but limited success. Machine learning then leads to another wave of AI revolution in the past few years.

**The Essence of Machine Learning** The essence of Machine Learning is computer code enhanced/involved with training data. There are various training: supervised learning, unsupervised learning, semi-supervised learning, and reinforced learning that lead to various computing methods. The most recent machine learning method, reinforced learning, allows the system model to adjust and adapt based on feedback from the training data.

**Neural Network** As an illustration, the conventional linear regression with the least square technique is a simple method to obtain the rule for the prediction of results based on a set of experimental data. The same set of data can be used to train a three-layer neural network to generate a model, not seen externally, for the prediction of results. The machine learning process involves systems of artificial neurons to react to the excitation from the training data. The reaction that may be nonlinear from each neuron is then weighted and summed. The layers of neurons consist of the input layer, the hidden layer, and the output layer. The input layer handles the inputs and passes them on to corresponding neuron units of the hidden layer without any computation. The hidden layer is the core of the neural network that performs linear (summation of weighted inputs) or nonlinear (excitation functions) computation. The outputs are then transmitted from the hidden layer to the corresponding neuron of the output layer with weights and adjustment. It should be stressed that the weights/adjustments in the input layer and the output layer are different. Therefore, all three layers form a coupled nonlinear system. Once the neural network is established, the next step is to train this system with data to order to decipher the hidden rules that are difficult to model with conventional mathematical methods. During the training, the weighting and adjustment are changed with a variety of techniques, such as the loss function, the steepest-descent method, refreshing the weightings, the slope computation with backpropagation.

**Deep Learning Method** Deep learning employs multiple layers with two to ten hidden layers that use different computation methods than those in a neural network. Deep learning uses pre-processing of data to reduce the burden of computing in a later process. Some methods use the Convolutional Neural Networks (CNN) in one of the hidden layers and the compression (“pooling”) in another hidden layer, also to reduce the computing efforts in later stages. The applied convolutional integration in computing is in discrete form for processing two vectors into the third vector. Such processes include convolutional cores and filtering. However, one should not rule out other emerging methods such as the congregation category and other statistical techniques [3] (Fig. 7).

**Machine Learning and Construction** Though machine learning has been widely used in many industries, it is just started in construction research and development. However, it is anticipated that construction technologies with machine learning will emerge in the industry in the near future. An example of such innovation will include the true intelligent compaction roller that can integrate roller technologies, the highest-level of Intelligent Compaction Measurement Value (ICMV) system, and machine learning (Fig. 8).

## 4 Entering the Big Data Era

**Construction Data and Machine Learning** As described above, machine learning requires a lot of good quality data for training. When applied to construction, it

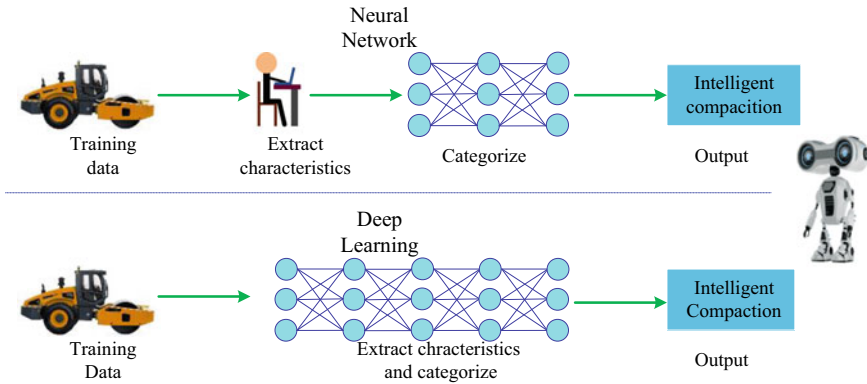


Fig. 7 Comparison between neural network and deep learning for intelligent compaction

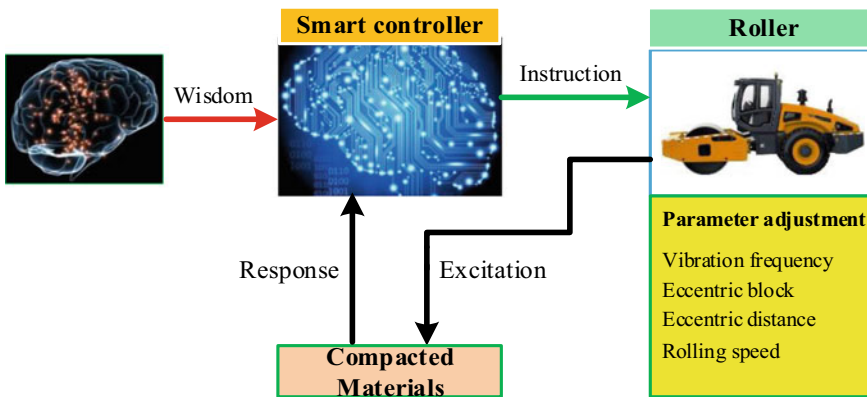
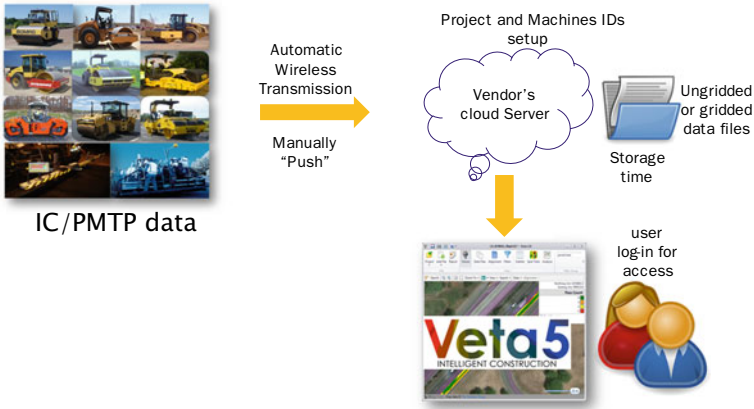


Fig. 8 The true intelligent compaction roller system

cannot be stressed more about the quality construction data (e.g., there was such a compaction industry product that fail due to lack of quality data in training). Raw construction data will need cleaning and mining to extract such quality data.

**Digitization of Construction Data and Information** Modern days intelligent construction often makes use of sensors and telematics to collect and transmit data to the Cloud. The issues for data security, integrity, storage, and ownership are mounting. The construction industry and owns/agencies are at a steep learning curve to handle and resolve those issues.

**Uses of Data** The use of data is quality control (QC) for contractors/industry, quality assurance (QA) for owners/agencies. The line between QC and QA can be murky, which causes issues such as the intelligent compaction (IC) and paver-mounted thermal profile (PMTP) data QA required in the US federal highway (FHWA) requirements for incentives/disincentives of federal-funded construction projects.



**Fig. 9** Intelligent construction data flow from machines to Veta

**Tools for Data Analysis** Software tools for intelligent construction data analysis are crucial for the success of the implementation. An example of such tools is the Veta Intelligent Construction Data Management software that is funded by the US FHWA and transportation pooled fund study, TPF-5(334). The purpose is to create and maintain a standard public-domain software tool that drives the standardization for the intelligent construction industry and simplify/facilitates data management (Fig. 9) [4]. Further information can be found on the Intelligent Construction Clearing House [2].

## 5 Integration of Intelligent Technologies

To implement intelligent construction, the most daunting task is the integration of construction with intelligent technologies. The integration takes a tremendous investment of capital and human resources, training, changes of workflow, institutional changes as well as collaboration among industry partners. Building Information Modeling (BIM) is an appropriate concept for such integration to manage the life cycle of infrastructure assets (Fig. 10). BIM for infrastructure has proven initial success in European countries, China, and some parts of the US.

Data standards such as Industry Foundation Class (IFC) and LandXML are also crucial to make BIM work. Visualization is also an integral part of BIM that serves as a powerful communication tool for all parties. The implementation of BIM is not trivial. A framework for BIM for Pavements (BFP) has been proposed by the authors (Fig. 11). This proposed TPF study is to develop BFP guidelines and public-domain tools to assist departments of transportation (DOTs) for BFP implementation; form partnership between DOTs and industry to advance BFP technologies; and assist

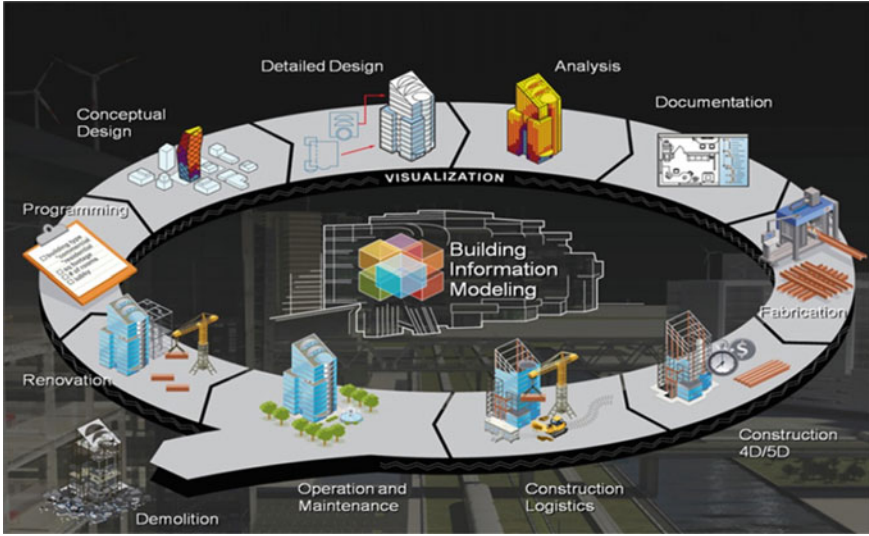


Fig. 10 Illustration for BIM for Infrastructure (Courtesy WisDOT)

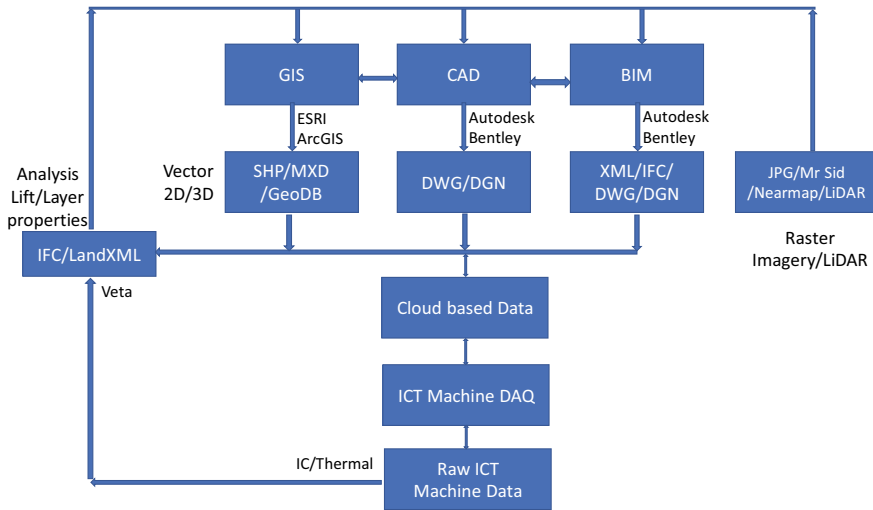


Fig. 11 The proposed framework for BIM for Pavements

DOTs with enhancing financial effectiveness by improving efficiency and cost-saving in pavement design, construction, and maintenance with BFP.

## 6 Future of Intelligent Construction

To facilitate the future development and implementation of intelligent construction, the authors have founded the International Society for Intelligent Construction (ISIC) in 2016 with the vision to create a platform for the globally coordinated efforts to advance and implement intelligent construction technologies worldwide [5]. One of ISIC's primary efforts is to create subcommittees that would lead the future development of prioritized fields for intelligent construction:

**SC1—Perception and Control** All technologies related to data acquisition and controls, including sensing technologies, data collection technologies, e.g., Global Navigation Satellite System (GNSS), Light Detection and Ranging (LiDAR), Unmanned Aerial Systems (UAS), Internet, monitoring technologies (e.g., materials, paving, and intelligent compaction), Automated Machine Control (AMC), Automated Machine Guidance (AMG), and Autonomous Control Machinery (ACM), etc.

**SC2—Data Analysis and Management** All technologies related to data analysis and management, including data science (e.g., Big Data, data communication protocols, and standards), signal analysis, Cloud computing, and digital information platforms, etc.

**SC3—Artificial Intelligence (AI) and Engineering** Application of AI on construction, including intelligent algorithms/computing and methodologies (e.g., engineering expert systems, neural networks, machine learning, etc.)

**SC4—Integration and Innovation** Application with fundamental theories and integrated technologies during design, construction, and rehabilitation/maintenance stages, e.g., stress analysis, augmented reality technologies (BIM, Virtual Reality (VR), Augmented Reality (AR), 3D visualization), the interaction between construction machinery and constructed media, risks forecast/evaluation, management, and decision-making, etc.

**SC5—Green and Safety** Conservation of natural resources, environmentally friendly technologies. Application of automated sensing/safety technologies on construction and operation, and forewarns of all kinds of disasters and recovery, etc.

**SC6—Education and Training** Promotion and popularization of intelligent construction technologies with education and training, including the development of teaching materials, and workshops, etc.

The authors anticipate the above efforts would take intelligent construction to the next levels for technology innovation, education, and implementation in the future.

## References

1. Woolever M (2010) Study on the premature failure of pavement construction projects. Vermont Department of Transportation (VTRAN)
2. Intelligent Construction. Clearing House. [www.IntelligentConstruction.com](http://www.IntelligentConstruction.com). Last accessed 27 Oct 2019
3. Negnevitsky M (2017) Artificial intelligence: a guide to intelligent systems, 3rd edn. Edison-Wesley, UK. ISBN-13: 978-1408225745
4. Veta—Intelligent construction data management software. <https://www.intelligentconstruction.com/veta/>. Last accessed 27 Oct 2019
5. International Society for Intelligent Construction. [www.IS-IC.org](http://www.IS-IC.org). Last accessed 27 Oct 2019

# Geo-statistical Evaluation of the Intelligent Compaction Performance in a Reclaimed Base Project



Maziar Foroutan, Ahmad Ghazanfari, Hamid Ossareh,  
and Ehsan Ghazanfari

**Abstract** One of the main objectives of utilizing intelligent compaction (IC) technology is to increase the uniformity and consistency of compaction operation. In this study, intelligent compaction measurement values (CMVs) in a reclaimed base project in Route 117, Vermont were used to perform a geo-statistical analysis. Semi-variogram models were constructed to investigate the spatial structure and uniformity of compaction during the first and second reclaimed phases. The uniformity of the compaction operation was evaluated using the semivariogram model parameters (range, sill, and nugget). Furthermore, the semivariogram models of in-situ spot measurements were generated to verify the suitability of different types of measurements in capturing the geo-spatial trends in pavement layers. Then, the spatial statistics of each measurement were compared to the univariate statistics. It was found that the data variance might be closely related to each other, but there is no relation between these values and the spatial uniformity of the compacted area. The results indicated that the spatial structures of both compacted layers (i.e., first and second reclaimed layers) were successfully captured through all three types of measurements, where the second reclaimed phase revealed a higher degree of uniformity. In addition, geo-statistical analysis of both reclaimed layers revealed a higher degree of uniformity in dynamic cone penetration index (DCPI) data compared to other compaction measurements. On the other hand, a relatively high degree of inconsistency observed among the CMV measurements. It should be acknowledged that the

---

M. Foroutan (✉) · E. Ghazanfari  
Department of Civil and Environmental Engineering, University of Vermont, 33 Colchester Ave,  
Burlington, VT 05405, USA  
e-mail: [maziar.foroutan@uvm.edu](mailto:maziar.foroutan@uvm.edu)

E. Ghazanfari  
e-mail: [ehsan.ghazanfari@uvm.edu](mailto:ehsan.ghazanfari@uvm.edu)

A. Ghazanfari · H. Ossareh  
Department of Electrical and Biomedical Engineering, University of Vermont, 33 Colchester Ave,  
Burlington, VT 05405, USA  
e-mail: [ahmad.ghazanfari@uvm.edu](mailto:ahmad.ghazanfari@uvm.edu)

H. Ossareh  
e-mail: [hossareh@uvm.edu](mailto:hossareh@uvm.edu)



conclusions of this study are based on data from only one project, specific to the characteristics/conditions of that project.

**Keywords** Intelligent compaction (IC) · Geo-statistical analysis · Uniformity of compaction · Reclaimed base project · In-situ spot measurements

## 1 Introduction

Compaction is one of the most important operations in pavement construction since it has significant impact on pavement service life and costs of maintenance and rehabilitation [1]. Poor compaction of pavement layers can potentially lead to different types of distress such as fatigue cracking, rutting, shoving, and raveling [2]. An important criterion to achieve a desirable compaction quality is the compaction uniformity [2–4]. In addition, the pavement construction codes and analysis tools are mostly designed based on a uniform material [5]. Intelligent compaction (IC) is an innovative technology intended to improve the compaction uniformity and consistency in pavement construction [1, 5]. Using the global positioning system (GPS) and accelerometers, the IC roller can provide real-time compaction measurement values (CMVs) that are tied to the physical space [6]. To get a better insight into the IC roller performance, the uniformity of ICMVs need to be evaluated and compared with in-situ measurements (e.g., nuclear gauge density, dynamic cone penetration, core density). It should be emphasized that CMV is considered as Level 1 intelligent compaction measurement value (ICMV), and therefore, conclusions based on CMV data should be approached with caution.

Univariate statistics are traditionally implemented to evaluate the degree of uniformity during the compaction process [3]. However, these methods are not able to capture and evaluate the geo-spatial structure of the compacted layers [7–9]. Geo-statistical analysis is a statistical tool that can describe the spatial/temporal pattern of the collected data and predict the values at unknown locations based on the spatial/temporal autocorrelation [10]. Identical univariate statistics do not guarantee the same spatial structure; therefore, implementing a geo-statistical analysis is necessary to evaluate uniformity and spatial continuity of the compacted area [3, 11].

Several studies investigated the spatial patterns of IC data and evaluated the uniformity and spatial continuity of different layers upon completion of IC [3, 4, 7, 8, 12, 13]. However, these studies were not conducted on reclaimed base projects, where the material exhibit higher degree of non-homogeneity compared to other types of pavement projects. Given the increase in the number of reclaimed base projects in recent years, the uniformity of IC measurements and in-situ spot measurements need to be investigated and compared in reclaimed base projects.

As such, the main objective of this study is to evaluate the uniformity and spatial continuity of CMVs, nuclear gauge density (NGD), and dynamic cone penetration (DCP) measurements upon completion of the IC compaction process on two different reclaim phases. To this end, the semivariogram models were generated to capture

the geo-spatial structure of the IC data and in-situ spot measurements. Since the spot measurements involve less uncertainty, the uniformity and spatial continuity of the IC measurement were compared to the spot measurements. In addition, the geo-spatial statistics were compared to the univariate statistics in order to verify the ability of the semivariogram models in evaluating the uniformity of the compaction process.

## 2 Background and Methodology

### 2.1 Project Description and In-Situ Measurements

IC technology was implemented in Route 117 Vermont, a reclaimed asphalt pavement (RAP) project. At the initial phase of the project, the existing asphalt layer was milled to remove 4 inches of the distressed pavement. Then, through the first reclaiming phase, the remaining amount of asphalt and a portion of the underlying base were pulverized to the depth of 10 in. Once the first reclaiming phase was completed, the road was graded, shaped, and then compacted by the CS56B Caterpillar IC roller. Then, a 6-inch layer of the emulsion mixed with the reclaimed base material was injected during the second reclaiming phase (i.e., full depth reclamation). Next, the entire road was cut/filled to grade and compact using the IC rollers in order to achieve the desired level of compaction. The in-situ density/moduli measurements were performed through the NGD and DCP tests and coordinates (i.e., Easting and Northing) of each measurement were manually recorded using a GPS rover rod. Figure 1 illustrates the reclaiming process, IC roller operation, and in-situ spot measurements. A geo-statistical analysis was performed on CMV, NGD, and dynamic cone penetration index (DCPI) data to evaluate and compare the spatial variability of these compaction measurements during the first and second reclaimed phases.

### 2.2 Compaction Measurement Values (CMVs)

In this study, the CMVs from the CS56B Caterpillar IC roller were used for data analysis. CMV is a dimensionless compaction quality measurement, which is a function of the roller configuration (e.g., the weight and diameter of roller drum) and roller parameters such as speed, frequency, and amplitude [3, 4]. The dynamic response of IC roller is used to determine CMVs [13], where the CMV can be calculated as below [3, 13]:

$$\text{CMV} = C \times \frac{A_{2\Omega}}{A_{\Omega}} \quad (1)$$



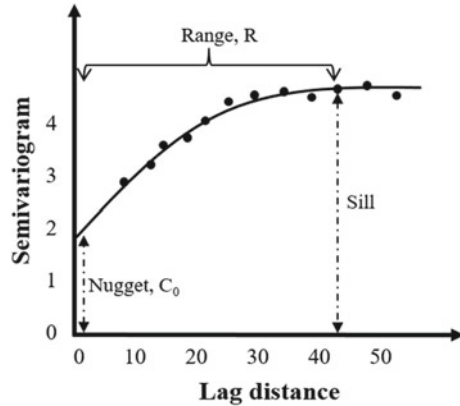
**Fig. 1** Photographs of **a** reclaiming, **b** compacting, **c** NGD, and **d** DCP test

where  $C$  = Constant (300 in the Caterpillar roller),  $A_{\Omega}$  = Acceleration amplitude of the fundamental component of the vibration, and  $A_{2\Omega}$  = Acceleration amplitude of the second harmonic component of the vibration. IC data analysis has shown that  $A_{2\Omega}$  is proportional to the force amplitude ‘ $F$ ’ of the roller blows, and  $A_{\Omega}$  is approximately equivalent to the displacement ‘ $s$ ’ during the blow [14].

### 2.3 Geo-statistical Analysis

Geo-statistical analysis is a statistical tool, which can be used to assess the uniformity and spatial continuity of the compacted area [15]. The geo-spatial autocorrelation between the CMV/NGD/DCPI measurements can be captured using the semivariogram models [3, 4]. In other words, semivariogram is meant to investigate the spatial patterns where the measurements that are closer in space are more correlated than the measurement that are farther apart from each other [3, 4, 7, 14]. The semivariance is defined as one-half of the average squared differences between data values that are separated at a lag distance of  $h$  [15]. Once the semivariance is calculated

**Fig. 2** Schematics of a semivariogram model



for various lag distances, the semivariogram model can be generated by plotting the semivariance values against different lag distances [16, 17]. Figure 2 demonstrates the graphical representation of a semivariogram model. The following expression represents the mathematical formula to determine the estimated semivariance:

$$\gamma(h) = \frac{1}{2N(h)} \sum_{i=1}^{N(h)} [V_{\alpha+h} - V_{\alpha}]^2 \tag{2}$$

where  $N(h)$  the number of data pairs that are separated by lag distance of  $h$  from each other, and  $V_{\alpha}$  and  $V_{\alpha+h}$  are the CMVs/NGD/DCPI measured at location  $\alpha$  and  $\alpha + h$ .

There are different mathematical models, such as power, exponential, Gaussian, and spherical model, that can be used to fit the calculated semivariance values [17]. The mathematical formulations of these models are represented as follows:

$$\text{Power model: } \omega \left[ \frac{h}{a} \right]^2 \tag{3}$$

$$\text{Exponential model: } \omega \left[ 1 - \exp\left(-\frac{3h}{a}\right) \right] \tag{4}$$

$$\text{Gaussian model: } \omega \left[ 1 - \exp\left(-\sqrt{3} \frac{h^2}{a^2}\right) \right] \tag{5}$$

$$\text{Spherical model: } \omega \left[ \frac{3}{2} \left(\frac{h}{a}\right) - \frac{1}{2} \left(-\frac{h^3}{a^3}\right) \right] \tag{6}$$

where  $a$  is the range,  $\omega$  is the sill, and  $h$  is the lag distance. Initially, the semivariogram model can be visually selected based on the binned semivariance. For instance, the

Gaussian model can be fitted when there is an obvious plateau at the beginning of binned data. The exponential model is usually used when the statistical dependence of data gradually decays at a sill value. Then, the least square or the weighted least square methods can be implemented to select the best fitted model. Based on the schematic of the semivariogram model (see Fig. 2), nugget, range, and sill are three main parameters that determine the characteristics of a semivariogram model [15]. Range is defined as the distance that the semivariogram reaches a plateau, while sill can be defined as the plateau that the semivariogram reaches at the range [14]. In other words, range is the maximum distance that the measurements are spatially autocorrelated, and sill corresponds to semivariance at sill. A larger range value is an indication of greater degree of uniformity (less spatial variability) [3, 4, 7]. On the other hand, since the sill value approximately represents the standard deviation of data, lower sill values represent higher levels of uniformity. Furthermore, sampling error and very short scale variability may cause some discontinuity from the origin [3, 4, 7], which is defined as the nugget effect and it is shown as  $C_0$  in the schematic.

In this study, the CMV data were collected during the compaction operation, while NGD and DCPI data were collected upon the completion of the compaction process at first and second reclaim layers. A total of 27 DCP and NG measurements were performed on a 160 ft section of the road during the first reclaim phase, where 15 in-situ measurements were performed on a 90 ft. long portion of the road in the course of second reclaim phase. The location of the data points was recorded using a GPS rover to perform a geo-statistical analysis. A geo-statistical analysis was performed on CMV, NDG, and DCPI data (using Rstudio, academic use version) to evaluate the uniformity and spatial continuity of the compacted area during the first and second reclaim phases.

## 3 Results and Discussion

### 3.1 First Reclaim Phase

The geo-statistical analysis was performed on CMV, NGD, and DCPI data to evaluate the uniformity and spatial continuity of the compacted area during the first reclaim phase. The normal score transformation was performed to ensure the scale of all three datasets are identical. The semivariogram models were generated based on the original and normal score transformed data (see Figs. 3, 4, 5 and 6). The semivariance values resulted from CMV, NGD, and DCPI data were binned using the method of equal number of data points (i.e., 27 data points) in each bin. A comparison between the original semivariogram and semivariogram after normal score transformation revealed that the range values remain unchanged after transformation, while the sill values were close to 1. According to Fig. 3, exponential semivariogram models fitted to the binned semivariance of original and normalized CMV data indicated that the measurements are autocorrelated to the distance of 48 ft. (i.e., range = 48 ft.), where

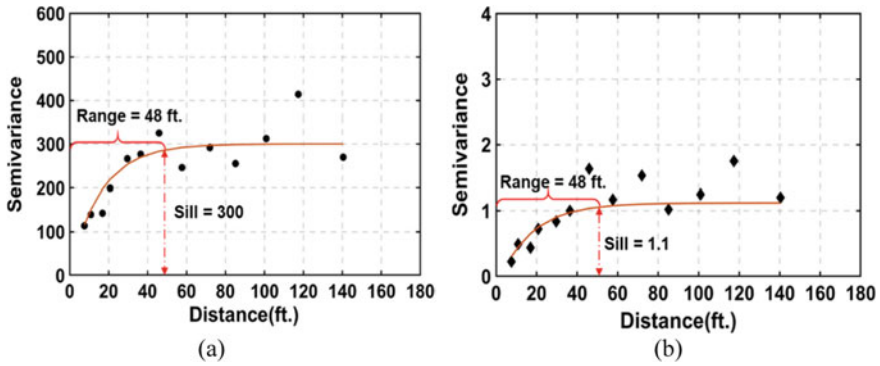


Fig. 3 a Original semivariogram and b normalized semivariogram of CMVs during the first reclaim phase

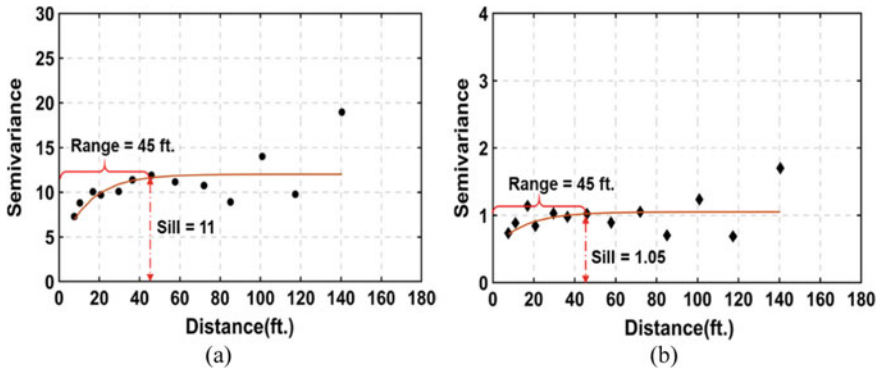


Fig. 4 a Original semivariogram and b normalized semivariogram of NGD during the first reclaim phase

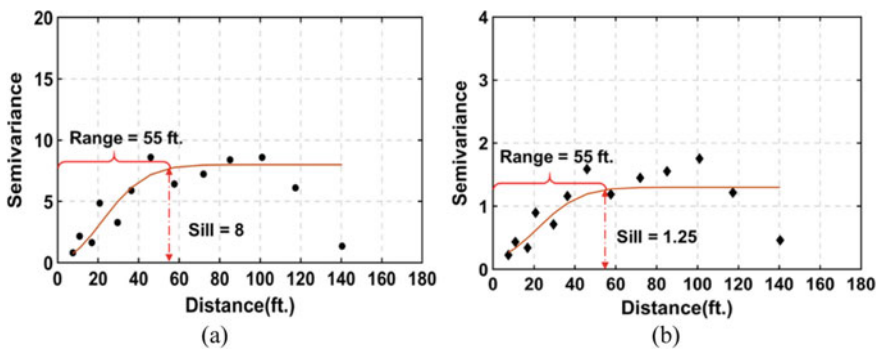
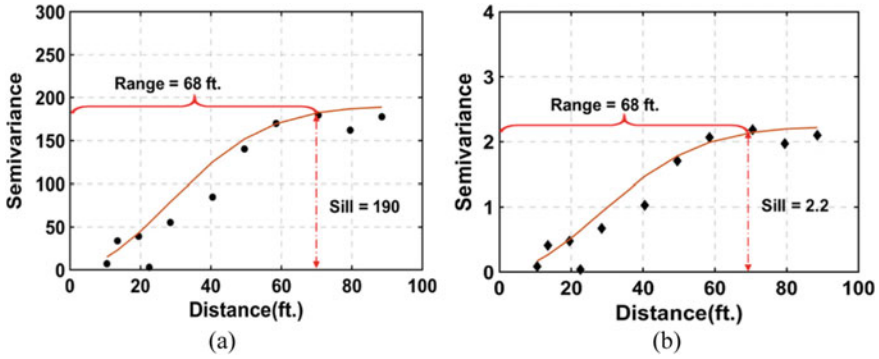


Fig. 5 a Original semivariogram and b normalized semivariogram of DCPI during the first reclaim phase



**Fig. 6** a Original semivariogram and b normalized semivariogram of CMVs during the second reclaim phase

the sill values of the original and normalized semivariogram models were estimated to be 300 and 1.1, respectively. In other words, there would be no statistical dependence between the roller CMVs separated by a distance larger than 48 ft. Furthermore, exponential semivariogram models were fitted to the binned semivariance values resulted from geo-spatial analysis of original and normalized NGD data. As evident from Fig. 4, no spatial autocorrelation exists at lag distances larger than 45 ft., and the corresponding sill values for the original and normalized semivariogram were ~11 and ~1.05, respectively. In this case, the spatial trend of NGD data revealed that there is a potential for this data to get autocorrelated at a larger lag distance since an increasing trend is observed in the model. The Gaussian semivariogram model fitted to DCPI data is illustrated in Fig. 5, where an identical range value of 55 and sill values of 8 and 1.25 were resulted from original and normalized semivariograms, respectively. Table 1 represents the spatial and univariate statistics of different compaction measurements on the first reclaim phase.

**Table 1** Summary of spatial and univariate statistics

Compaction data	Spatial statistics						Univariate statistic	
	Original			Normalized			$\mu$ (Mean)	$\sigma$ (Std. deviation)
	Nugget	Range	Sill	Nugget	Range	Sill		
CMV	5	48	300	0.1	48	1.1	43.8	15.6
NGD	3	45	11	0.5	45	1.05	134.3	3.3
DCP	0	55	8	0.2	55	1.25	6.7	2.2



### 3.2 Second Reclaim Phase

In order to investigate the uniformity and consistency of the compaction operation during the second reclaim phase, a geo-spatial analysis was performed on the original and normal score transformed CMV, NGD, and DCP data collected at this phase (see Figs. 6, 7, and 8). The semivariance values were grouped into the bins with a fixed size of 3 ft. The semivariogram range values were identical before and after transformation, while the sill values were in the range of 1.55–2.7. Figure 6a, b indicate the semivariogram plots of original and normalized CMV data, where Gaussian models are fitted to the semivariance values. As can be seen, no spatial autocorrelation exists after the lag distance of 68 ft, where the corresponding sill values are ~190 and ~2.2 for the original and normalized semivariograms. According to Fig. 7, Gaussian semivariogram models fitted to original and normal score transformed semivariance of

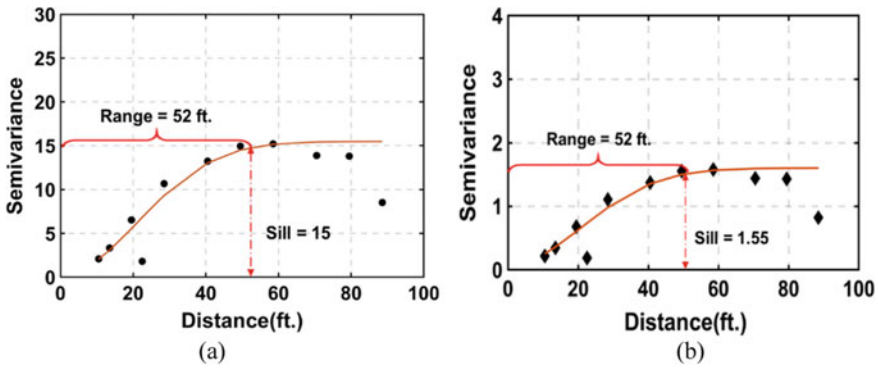


Fig. 7 a Original semivariogram and b normalized semivariogram of NGD during the second reclaim phase

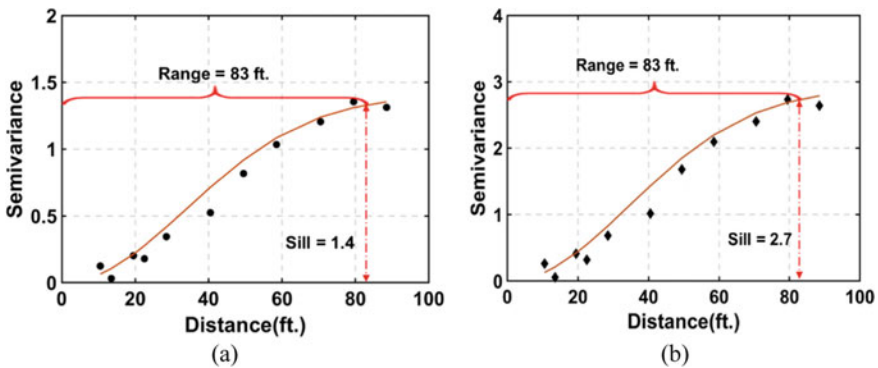


Fig. 8 a Original semivariogram and b normalized semivariogram of DCPI during the second reclaim phase



**Table 2** Summary of spatial and univariate statistics

Compaction data	Spatial statistics						Univariate statistic	
	Original			Normalized			$\mu$ (Mean)	$\sigma$ (Std. deviation)
	Nugget	Range	Sill	Nugget	Range	Sill		
CMV	2	68	190	0.1	68	2.20	43.8	15.6
NGD	0	52	15	0.08	52	1.55	134.3	3.3
DCP	0	83	1.4	0.18	83	2.70	6.7	2.2

NGD measurements are spatially autocorrelated at 52 ft., while the sill values were 1 and 1.55, respectively. In addition, the semivariogram models for DCPIs (Fig. 8) resulted in the highest autocorrelation distance, where the range value was 83 ft., and the sill values for the original and normalized semivariogram models were approximately 1.4 and 2.7, respectively. Table 2 represents the summary of the univariate and spatial statistics of each compaction measurement.

### 3.3 Discussion

Geo-statistical analysis of roller measurements and in-situ measurements (i.e., NGD and DCPI) was performed on the data collected through both reclaim phases. According to the resulting semivariogram models, the spatial trend of the compacted area was captured using all three types of measurements. Although the data collection area in the second reclaim phase was smaller than that of the first reclaim phase, the semivariogram models indicated that the range values resulted from the second reclaim phase data were systematically higher than those from the first reclaim phase. This can be an indication of higher degree of uniformity and spatial continuity of the second reclaim phase. Although it is difficult to interpret the sill values upon data transformation, since this parameter is affected by standard deviation, the original sill values were lower during the second reclaim phase. In addition, a further investigation of the spatial variability of different compaction measurement methods revealed that there was higher degree of uniformity and consistency among the DCPI, which is reflected in relatively higher range value in both reclaim phases. However, it should be noted that the lower sampling rate associated with the spot measurements data might result in missing a range smaller than the sampling rate. Although the range values are significantly higher than sampling intervals, increasing the sampling rate during spot measurements can enhance the reliability of this comparison. The higher level of uniformity and consistency of DCPI data compared to NGD values revealed that DCPI data could be a more reliable option for calibrating the IC roller measurements in this project. This result is consistent with [18] where the regression model constructed using CMVs and DCPI data showed the highest regression value in this project.

The CMV data revealed a high degree of non-uniformity and inconsistency which is reflected in large sill values (sill = 300 and 190) suggested by the semivariogram models. This observed inconsistency among the IC measurements can be attributed to the non-homogeneity of the compacted material or changing the roller parameters (e.g., frequency and amplitude) during the compaction operation [18, 19], as was the case in this study. A similar study in the literature, where the spatial structure of the CMV data on a 130 ft. base layer was investigated, reported a range value of 62.3 ft and a sill value of 947.3 [3]. A comparison between the results presented in [3] and our study suggests that the range value is similar, but there is significant discrepancy in the sill value. This indicates that compared to [3], the level of inconsistency of roller measurements in the current project was less. According to [8], the results of the geo-statistical analysis of the CMV data collected on 800 ft. section of a road base layer resulted in a range value of 13.1 ft. and a sill value of 51.5. The range value reported in [8] is much smaller than those in [3] and the current study. In addition, a comparison between the univariate statistics and spatial statistics revealed that usually the changes in the variance of data proportionally changes the sill parameter of the semivariogram models, but the spatial variability of the measurements cannot be correlated to the univariate statistics. Other studies also have shown that the variance and sill parameter are closely related to each other [3, 4, 8]. It should be noted that the authors are currently collecting and analyzing data from similar IC projects to compare the results and provide comparative analysis.

## 4 Conclusion

Based on the results of this study, the following conclusions can be drawn:

- The spatial structure of the compacted area (during both reclaim phases) was successfully captured through different compaction quality measurement schemes (IC measurements and spot measurements).
- The range values are systematically higher during the second reclaim phase that can be inferred as higher degree of uniformity and continuity.
- The semivariogram models revealed that the DCPI data has the highest range values that can be inferred as a high degree of uniformity thorough the compacted area. It should be considered that this conclusion can be affected by increasing the sampling rate during DCP measurements.
- The standard deviation can be an indication of the degree of non-uniformity and inconsistency of the collected data, but it is not able to explain the differences between the spatial structure of the compacted area.
- The higher degree of inconsistency in IC roller measurements can be attributed to non-homogeneity of the underlain layers and variations in some of the compaction parameters, such as frequency and amplitude during the compaction process.
- It should be acknowledged that these conclusions are based on data from only one project and therefore cannot be generalized for all IC projects.

## References

1. Kamali-Asl A, Ghazanfari E, Dewoolkar MM (2016) Suitability of intelligent compaction for relatively smaller-scale projects in Vermont
2. Adlinge SS, Gupta AK (2013) Pavement deterioration and its causes. *Int J Innov Res Dev* 2(4):437–450
3. Hu W, Shu X, Jia X, Huang B (2018) Geostatistical analysis of intelligent compaction measurements for asphalt pavement compaction. *Autom Constr* 89:162–169
4. Xu Q, Chang GK (2013) Evaluation of intelligent compaction for asphalt materials. *Autom Constr* 30:104–112
5. Xu Q, Chang GK, Gallivan VL, Horan RD (2012) Influences of intelligent compaction uniformity on pavement performances of hot mix asphalt. *Constr Build Mater* 30:746–752
6. Hu W, Shu X, Jia X, Huang B (2017) Recommendations on intelligent compaction parameters for asphalt resurfacing quality evaluation. *J Constr Eng Manag* 143(9):04017065
7. Dondi G, Sangiorgi C, Lantieri C (2013) Applying geostatistics to continuous compaction control of construction and demolition materials for road embankments. *J Geotech Geoenviron Eng* 140(3):06013005
8. White DJ, Thompson MJ, Vennapusa P, Siekmeier J (2008) Implementing intelligent compaction specification on Minnesota TH-64: synopsis of measurement values, data management, and geostatistical analysis. *Transp Res Rec* 2045(1):1–9
9. Hu W, Shu X, Huang B, Woods M (2017) Field investigation of intelligent compaction for hot mix asphalt resurfacing. *Front Struct Civil Eng* 11(1):47–55
10. Kyriakidis P (2016) Geostatistics. In: *International encyclopedia of geography: people, the earth, Environment and technology: people, the earth, environment and technology*, pp 1–13
11. Mazari M, Tirado C, Nazarian S, Aldouri R (2017) Impact of geospatial classification method on interpretation of intelligent compaction data. *Transp Res Rec* 2657(1):37–46
12. Thompson MJ, White DJ (2007) Field calibration and spatial analysis of compaction-monitoring technology measurements. *Transp Res Rec* 2004(1):69–79
13. Mooney MA (2010) Intelligent soil compaction systems, vol. 676. Transportation Research Board
14. Sandström AJ, Pettersson CB (2004) Intelligent systems for QA/QC in soil compaction. In: *Proceedings, 83rd annual transportation research board meeting*, pp 11–14
15. Isaaks EH, Srivastava RM (1989) *An introduction to applied geostatistics*. Oxford University Press, New York
16. Wang J, Lu X, Feng Y, Yang R (2018) Integrating multi-fractal theory and geo-statistics method to characterize the spatial variability of particle size distribution of minesoils. *Geoderma* 317:39–46
17. Vennapusa PK, White DJ, Morris MD (2009) Geostatistical analysis for spatially referenced roller-integrated compaction measurements. *J Geotechn Geoenviron Eng* 136(6):813–822
18. Foroutan M, Bijay KC, Ghazanfari E (2010) Evaluation of correlations between intelligent compaction measurement values and in-situ spot measurements. In: *Geo-congress 2020: geotechnical earthquake engineering and special topics*, American Society of Civil Engineers, Reston, VA, pp 602–611
19. Foroutan M, Ghazanfari E (2019) Implementation of intelligent compaction (IC) for pavement construction in Vermont (Report No. 2020-02). Vermont Agency of Transportation. [https://vtr.ans.vermont.gov/sites/aot/files/documents/VTRC17\\_2\\_FinalReport.pdf](https://vtr.ans.vermont.gov/sites/aot/files/documents/VTRC17_2_FinalReport.pdf)

# CCC Systems for Vibratory and Oscillatory Rollers in Theoretical and Experimental Comparison



Johannes Pistorl , Mario Hager, and Dietmar Adam

**Abstract** Intelligent Compaction (IC) and Continuous Compaction Control (CCC) systems have seen major developments in recent years. The Institute of Geotechnics of TU Wien investigated established CCC systems for vibratory rollers and developed a novel system for work-integrated compaction control with oscillatory rollers. The various CCC systems in the market yield to numerous measurement levels and units with each manufacturer pursuing their own system. This has become a great challenge for contractors and authorities and resulted in a demand for a single measure to be able to combine and compare results from different rollers. The theoretical basis and differences of common CCC systems for vibratory and oscillatory rollers are explained in the paper. Moreover, experimental field tests have been performed with a tandem roller with vibratory and oscillatory excitation. Five different CCC values—CMV, Omega,  $E_{\text{vib}}$ ,  $k_B$  and CCC for oscillatory rollers—were evaluated based on acceleration measurements. The results of the theoretical and experimental investigations are presented and compared to create a better understanding of why results of different CCC systems or rollers cannot simply be converted into each other.

**Keywords** CCC · IC · Intelligent compaction · Roller compaction

## 1 Introduction

Dynamic rollers for near-surface compaction are used for a wide range of engineering structures. The quality of earthwork strongly depends on the state of compaction of

---

J. Pistorl (✉) · M. Hager · D. Adam  
TU Wien, Karlsplatz 13/220-2, 1040 Vienna, Austria  
e-mail: [johannes.pistorl@tuwien.ac.at](mailto:johannes.pistorl@tuwien.ac.at)  
URL: <http://www.igb.tuwien.ac.at>

M. Hager  
e-mail: [mario.hager@tuwien.ac.at](mailto:mario.hager@tuwien.ac.at)

D. Adam  
e-mail: [dietmar.adam@tuwien.ac.at](mailto:dietmar.adam@tuwien.ac.at)

the individual layers. Therefore, both the compaction equipment and the compaction method have to be carefully selected taking into account the material used. The layer thickness must be selected taking into account material properties such as grain size distribution, maximum grain size and degree of non-uniformity, water content and water permeability, roller type and machine parameters.

The concept of vibration excitation for drums was implemented for the first time in 1958 [1] and, together with its further developments such as rollers with directional vibration and feedback-controlled rollers, has become the most common form of excitation for dynamic drums in earthworks. The main advantage of vibratory rollers over static rollers is their significantly higher vertical load due to dynamic excitation, which results in a better compaction depth.

A second type of dynamically excited drums are oscillating drums. The Swedish company Geodynamik AB developed the principle of oscillatory roller compaction at the beginning of the 1980s [2]. The dominant compaction direction of the oscillating rollers (horizontal) results in a lower compaction depth compared to vibratory rollers of the same size and weight. This has to be taken into account on site by reducing the thickness of the filled layers.

Systems for a Continuous Compaction Control (CCC) were developed for both types of excitation. While various systems for vibratory rollers have been used during the last decades, only one CCC system has recently been developed for oscillatory rollers.

## 2 Overview of CCC Systems and Previous Investigations

### 2.1 CCC with Vibratory Rollers

In 1975 the company Geodynamik AB developed a roller-mounted compaction meter in cooperation with Lars Forssblad (of Dynapac) and introduced the compaction meter and the compaction meter value (CMV) in 1978. The CMV is described in more detail below. The new method was presented at the First International Conference on Compaction held in Paris, France, in 1980 [3, 4]. Many of the roller manufacturers, e.g., Caterpillar, Ingersoll Rand, subsequently adopted the Geodynamik CMV-based system.

In the late 1980s, Bomag developed the OMEGA value and the corresponding Terrameter system. The OMEGA value provided a continuous measure of compaction energy and at that time, it served as the only CCC alternative to CMV. In the late 1990s, Bomag then developed the measurement value  $E_{\text{vib}}$ , which provided a measure of dynamic soil modulus (e.g. [5]). Ammann followed suit with the development of the soil stiffness parameter  $k_B$  [6]. These latter  $E_{\text{vib}}$  and  $k_B$  parameters signaled an important evolution towards the measurement of more mechanistic soil properties, e.g. soil stiffness and deformation modulus.

**Compactometer (CMV/RMV)** The Compactometer was the first commercially used system for continuous compaction control with vibratory rollers and is still used by the manufacturers such as Caterpillar, Dynapac, HAMM and Volvo.

The acceleration sensor (named A-Sensor) measures the vertical accelerations on an undamped part (e.g. the bearing) of the vibratory drum. Early research showed that various indices incorporating drum acceleration amplitude and the amplitude of its harmonics (i.e., multiples of the operating frequency) can be correlated to soil compaction and underlying stiffness [4]. From this early research, the compaction meter value (CMV) was proposed [3] and is computed as:

$$CMV = C_1 \frac{A_{2\omega}}{A_\omega} \tag{1}$$

where  $A_\omega$  is the amplitude of vertical drum acceleration at the fundamental (operating) frequency  $\omega$  and  $A_{2\omega}$  is the drum acceleration amplitude of the first harmonic, i.e., twice the eccentric excitation frequency.  $C_1$  is a constant established during site calibration ( $C_1 = 300$  is often used). The ratio of  $A_{2\omega}/A_\omega$  is a measure of nonlinearity.

CMV is determined by performing spectral analysis of the measured vertical drum acceleration over two cycles of vibration. The reported CMV is the average of a number of two-cycle calculations. Geodynamik typically averages the values over 0.5 s; however, this can be modified to meet the manufacturer needs.

A sister parameter called the resonance meter value (RMV) is defined as:

$$RMV = 100 \frac{A_{0.5\omega}}{A_\omega} \tag{2}$$

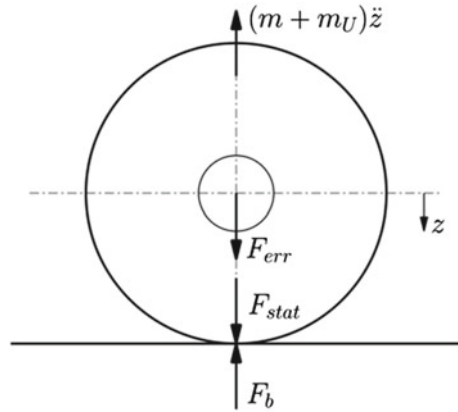
where  $A_{0.5\omega}$  is a subharmonic acceleration amplitude caused by jumping, i.e., the drum skips every other cycle. Therefore, the name of the parameter is misleading since no resonance effects but operation mode “Double-Jump” is causing the subharmonic acceleration amplitude. The RMV is used to indicate whether the roller is double-jump motion.

**Terrameter (OMEGA and  $E_{vib}$ )** The Terrameter system of Bomag also measures the accelerations in the bearing of the drum. The system uses two accelerometers, mounted with an inclination of 45° relative to the horizontal plane and arranged orthogonally to each other.

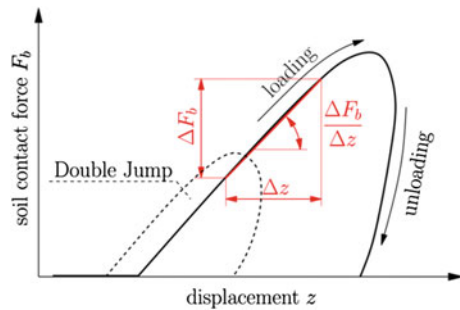
The Terrameter analyses the equilibrium of forces on the drum in vertical direction to calculate the soil contact force  $F_b$  from the vertical drum acceleration  $\ddot{z}$  under consideration of the static force  $F_{stat}$  and the excitation force  $F_{err}$  (see Fig. 1). The vertical displacements  $z$  can be obtained from a two times integration of the acceleration signal. Displacements  $z$  and soil contact force  $F_b$  can be used to plot a force-displacement diagram for each period of excitation (see Fig. 2).

The OMEGA value was the first CCC value of the Terrameter. It is defined as the area under the force-displacement diagram for two consecutive periods of excitation  $T_E$  to minimize the influence of the operation mode Double Jump:

**Fig. 1** Equilibrium of vertical forces for the calculation of  $F_b$



**Fig. 2** Force–displacement diagram of the drum for the calculation of OMEGA and  $E_{vib}$



$$OMEGA = C_3 \oint_{2T_E} F_b z dt \tag{3}$$

Factor  $C_3$  [1/Nm] is a roller-dependent factor to make OMEGA a dimensionless value ranging from 0 and 1000. OMEGA is proportional to the energy transmitted into the soil.

In 1999 Bomag introduced the  $E_{vib}$ , which replaces the OMEGA value and is currently used with the Terrameter system. In contrast to OMEGA the vibration modulus  $E_{vib}$  [MN/m<sup>2</sup>] is not a dimensionless value but a physically interpretable measure, which describes a soil stiffness by analyzing the inclination of the force-displacement curve between two defined points (40% and 90% of the maximum contact force). The  $E_{vib}$  is calculated recursively using a Poisson’s ratio of  $\nu = 0.25$ :

$$\frac{\Delta F_b}{\Delta z} = \frac{E_{vib} 2b_0 \pi}{2(1 - \nu^2)(2.14 + 0.5 \ln C_E)} \tag{4}$$

with

$$C_E = \frac{E_{vib}(2b_0)^3\pi}{16(1 - v^2)(m + m_U + m_R)gr} \tag{5}$$

where  $r$  and  $b_0$  are the radius and the half width of the drum and  $m$ ,  $m_U$  and  $m_R$  denote the mass of the drum, the eccentric mass and the mass of the roller frame respectively. Bomag seems to use adapted versions of these equations in the field.

Moreover, Dynapac uses a modified version of the  $E_{vib}$ , which is determined during the unloading phase of the load-displacement curve and called  $E_{vib 2}$  [7].

**Ammann Compaction Expert ( $k_B$ )** The ACE<sup>®</sup> system (Ammann Compaction Expert) was developed for feedback-controlled rollers by the Ammann Group. It calculates the CCC value  $k_B$  in the time domain based on a force-displacement diagram. The soil stiffness parameter  $k_B$  with the unit MN/m is a physically interpretable parameter, such as the vibration modulus  $E_{vib}$ .

The ACE system uses two different equations for the calculation of  $k_B$  depending on the mode of operation. For continuous contact the  $k_B$  value can be calculated as

$$k_B = \omega^2 \left[ (m + m_U) \frac{(m_U e_U \text{Vario}) \cos \varphi}{A_{(z)}} \right] \tag{6}$$

where  $A_{(z)}$  is the amplitude of the displacement and  $\varphi$  is the angle of phase shift between excitation force and displacement. The dimensionless factor Vario is used for a reduction of the dynamic excitation. In case of a periodic loss of contact,  $k_B$  is calculated using the contact force at the change from loading to unloading phase ( $F_{b(\dot{z}=0)}$ ) and the corresponding amplitude of the drum displacement  $A_{(z)}$ :

$$k_B = \frac{F_{b(\dot{z}=0)} - (m + m_U + m_R)g}{A_{(z)}} \tag{7}$$

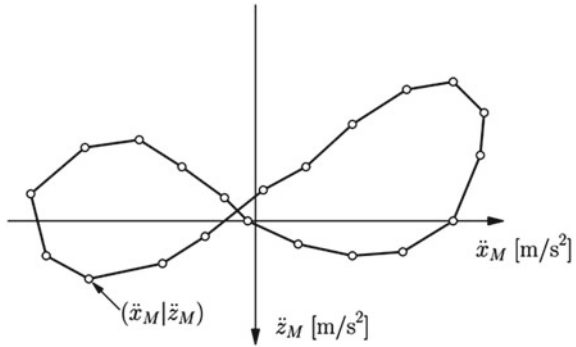
## 2.2 CCC with Oscillatory Rollers

While various CCC systems for vibratory rollers are available only one CCC system for oscillatory rollers has been developed in the past; the Oszillometer of the Swedish company Geodynamik AB.

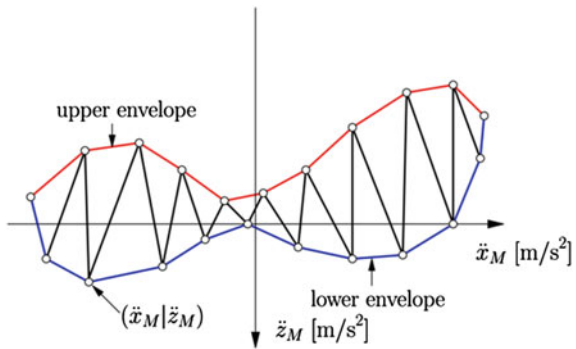
**Novel CCC System for Oscillatory Rollers** A research cooperation of the German roller manufacturer HAMM AG and the TU Wien developed a novel CCC system for oscillatory rollers [8]. The accelerations in horizontal and vertical direction are measured in the bearing of the oscillating drum. The measured accelerations can be plotted in a diagram with horizontal accelerations on the abscissa and vertical accelerations on the ordinate for each period of excitation. This diagram typically shows a



**Fig. 3** Digital acceleration data for one period of excitation sorted and connected in chronological order [9]



**Fig. 4** Digital acceleration data for one period of excitation sorted and connected according to the increasing horizontal acceleration (zig-zag-pattern), and upper and lower envelopes [9]



recumbent eight-shape of accelerations. Experimental and theoretical investigations proved a correlation between the aforementioned shape and the stiffness of the soil.

Each sampling point of the acceleration measurements is defined by a horizontal ( $\ddot{x}_M$ ) and a vertical acceleration ( $\ddot{z}_M$ ) (see Fig. 3). For the calculation of the CCC value, all sampling points are sorted and connected according to the increasing horizontal component, which results in a zig-zag-pattern in the diagram. Furthermore, the upper and lower envelope is calculated by identifying and connecting local maximum and minimum points of the zig-zag-pattern (see Fig. 4). The area of the eight-shape can be assessed by calculating the area between the upper and the lower envelope by trapezoidal integration. The calculated area equals the CCC value for oscillating rollers and adopts the theoretical unit of  $m^2/s^4$ .

### 2.3 Results from Previous Investigations

Adam and Kopf [12] performed numerical studies on CCC values for vibratory rollers. They investigated the influence of the roller’s mode of operation—as a result

of the soil stiffness and the relative drum amplitude—on the CCC values CMV, OMEGA,  $E_{vib}$  and  $k_B$ . Selected results from this study are depicted in Fig. 5.

CMV and OMEGA drop down considerably when passing to “Double-Jump” mode and show a significant dependency on the drum amplitude. OMEGA is closely related to the energy transferred to the ground, which explains the strong link to the drum amplitude.

$E_{vib}$  and  $k_B$  are less influenced by the modes of operation and show a minor dependency on the drum amplitude as expected due to their definition as stiffness values.

Nevertheless, a perfect independency of machine parameters cannot be achieved. Since the level and the course of all CCC values depend on the roller parameters they have to be adjusted and need to be kept constant for the entire measurement procedure.

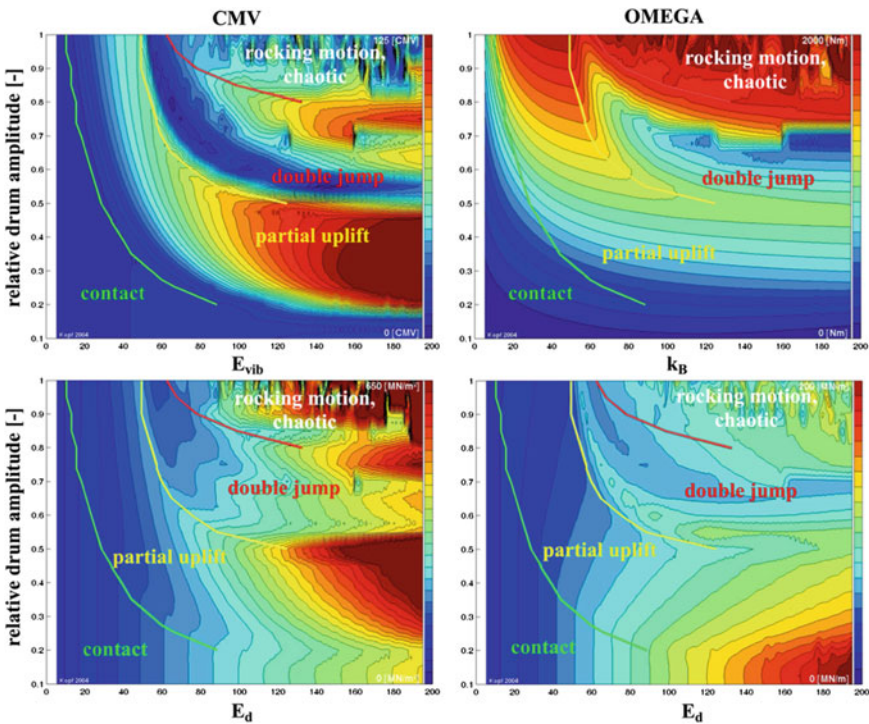


Fig. 5 Influence of modes of operation on CCC values [12]

### 3 Experimental Field Tests on CCC Performance

Large-scale in situ tests were performed in the scope of the aforementioned research project to investigate the performance of various CCC systems based on acceleration measurements obtained from a tandem roller.

#### 3.1 *Compaction Device*

A tandem roller HAMM HD<sup>+</sup> 90 VO [10] was used as compaction device. The roller comprises a total mass of 9830 kg and two drums of roughly 1900 kg vibrating mass each. The typical travel speed during compaction is 4 km/h for this type of roller and was used throughout the majority of the tests. The roller is equipped with a HCQ processing unit – similar to a Compactometer—, which calculates the H<sub>MV</sub> (basically the CMV/RMV) value for vibratory test runs.

Depending on the rotational direction of the eccentric masses the vibratory drum at the front of the roller operates with a vertical amplitude of 0.34 mm or 0.62 mm respectively. For the smaller amplitude, a frequency of 50 Hz was used most of the time while 40 Hz was the standard frequency for vibratory compaction with the large amplitude.

The oscillatory drum is mounted on the rear of the HD<sup>+</sup> 90 VO roller. It uses a tangential amplitude of 1.44 mm and a typical excitation frequency of  $f = 39$  Hz. However, the roller for the experimental field tests was modified to be able to use frequencies from  $f = 20$  Hz up to  $f = 70$  Hz.

#### 3.2 *Test Layout and Measuring Equipment*

A test area was prepared and equipped in a gravel pit near Vienna for the experimental field tests. The test area comprised four parallel test lanes of loose sandy gravel (to be compacted) with a length of 40 m and two layers of 0.4 m and 0.3 m thickness (see Fig. 6). The test field was filled on the highly compacted surface of the gravel pit. The four test lanes were intended for static, oscillatory, vibratory, and combined oscillatory and vibratory compaction. Two ramps at the beginning and at the end of the test lanes served for roller handling, speeding up and down the roller as well as lane changes. A fifth test lane was prepared on the highly compacted ground of the gravel pit.

The test field was equipped with tri-axial accelerometers, a deformation-measuring-device and an earth pressure cell to evaluate the impact of the roller on the soil and the surrounding area. The majority of the results of these measurements is not discussed in this paper, but can be found in literature [8, 9, 11].

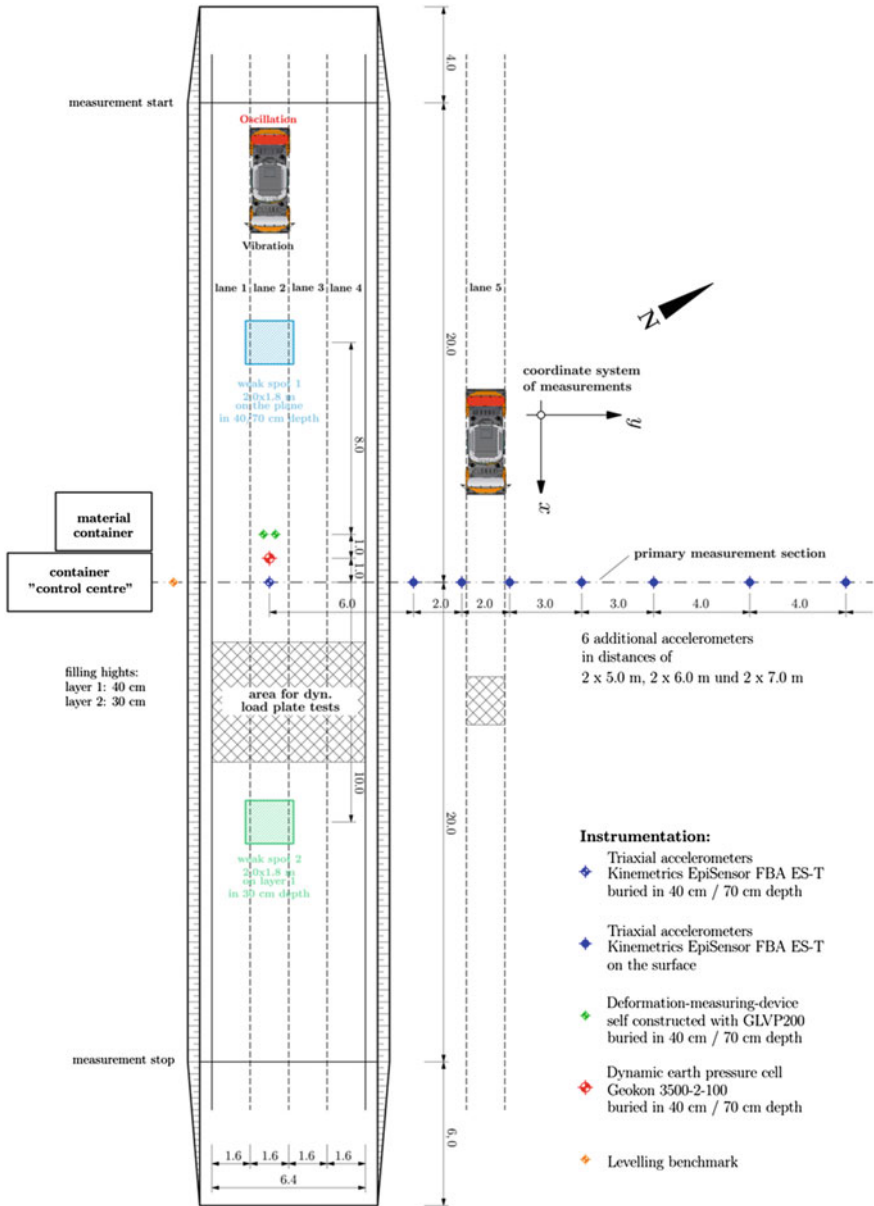


Fig. 6 Test layout of the experimental field tests [8]

Four conventional mattresses were buried under test lane 2 to simulate non-compacted weak spots in the test field and to investigate the influence of these weak spots on CCC values. Two mattresses were placed on the highly compacted ground of the gravel pit before filling the first layer. Weak spot No. 1 was therefore buried in a depth of 0.25 m after filling the first layer and a depth of 0.55 m after filling the second layer. Weak spot No. 2 was prepared by placing two mattresses on top of the first layer after finishing all tests on the first layer. After filling the second layer, weak spot No. 2 was located in a depth of 0.15 m below ground level (see Fig. 6).

The oscillatory drum of the roller was equipped with four accelerometers with a sensitivity of  $\pm 10$  g and the vibratory drum with accelerometers with a sensitivity of  $\pm 30$  g. The accelerometers were mounted on the left- and the right-hand side on the bearing of the drum to measure the accelerations in horizontal and vertical direction on the undamped part. The positive direction of the horizontal accelerations  $\ddot{x}$  was defined in the direction of roller travel; the positive vertical accelerations  $\ddot{z}$  pointed downwards (see Fig. 6). The accelerometer signals and all other measurement data were recorded with a sampling rate of 1000 Hz.

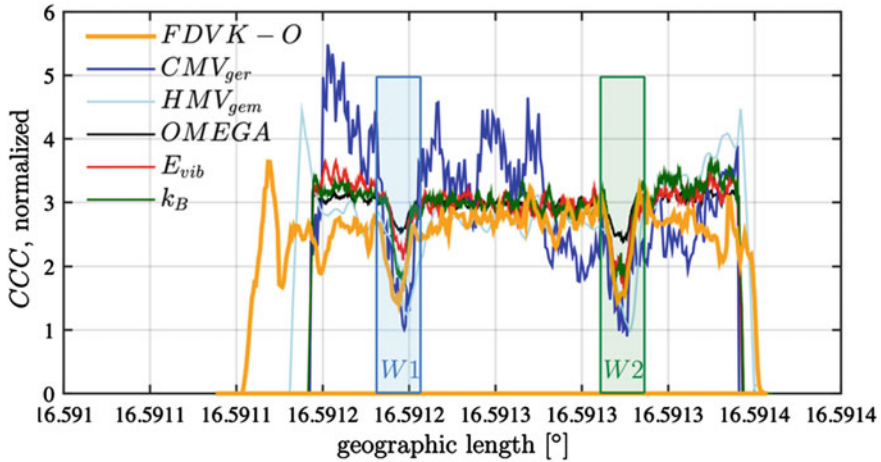
## 4 Results from Experimental Field Tests

In the following, the results of the calculated CCC values for oscillatory rollers are compared to the measured and calculated CCC values for vibratory rollers for selected test runs on layer 2 of lane 2 of the test field. The CCC values for the oscillatory roller and the CCC values for vibratory rollers cannot be calculated on the basis of measurement data of one single test run.

The simultaneous excitation of oscillatory and vibratory drum causes additional accelerations in the bearings of each drum, which interfere with the calculation of CCC values.

Therefore, the excitation has to be limited on one type of excitation for each CCC test run. For the comparison of vibratory and oscillatory CCC values, measurement data of two consecutive test runs on the highly compacted second layer of lane 2 of the test field is used. During these passes, no increase in compaction was to be expected, so that an influence on the CCC values by the changing stiffness ratios between the passes can be largely ruled out.

Figure 7 compares the CCC value for oscillatory rollers with all the CCC values established on the market for vibratory rollers. The oscillatory test run was performed with the standard parameters  $f = 39$  Hz and  $v = 4$  km/h, while all CCC values of the vibratory excitation were determined on the basis of a test run with a small vibration amplitude of 0.34 mm, an operating frequency of  $f = 50$  Hz and a travelling speed of  $v = 4$  km/h. The  $E_{\text{vib}}$  and  $k_{\text{B}}$  values were determined for two excitation periods each, with a mean average smoothing over 30 individual values being used for the representation in Fig. 7. In addition, all CCC curves were divided by their mean value, as otherwise no comparison would be possible due to the different units and measurement levels of the CCC systems.

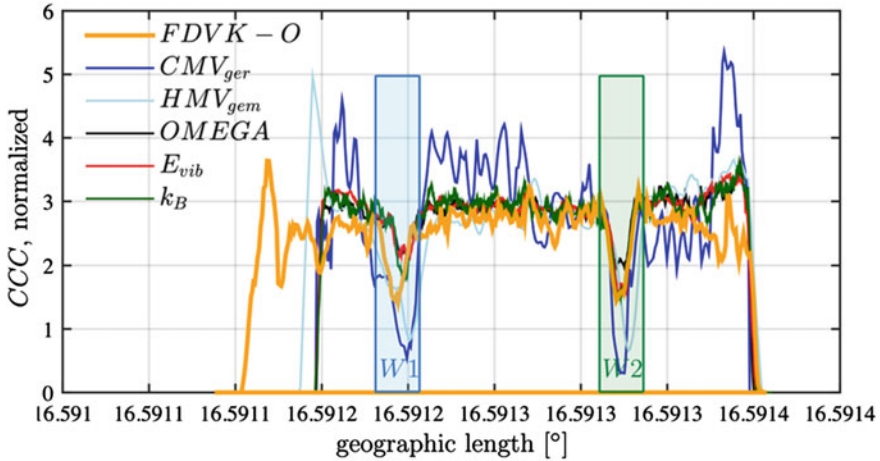


**Fig. 7** Course of popular CCC values for vibratory rollers and a novel CCC value for oscillatory rollers on the compacted layer 2 of the test field. Oscillation:  $f = 39$  Hz,  $v = 4$  km/h. Vibration: small amplitude,  $f = 50$  Hz,  $v = 4$  km/h

The calculated  $CMV_{ger}$  value and the measured  $HMV_{gem}$  value of the pre-installed Compactometer system is based on the same algorithm and clearly shows the influence of the two weak spots, similar to the CCC value for oscillatory rollers (FDVK-O). In particular, the unprocessed  $CMV_{ger}$  value is subject to pronounced scatter in the homogeneous areas of the test field, which reduces its significance. The roller integrated Compactometer obviously smoothes the  $HMV_{gem}$  value, which yields to more “stable” results. The online calculation of  $HMV_{gem}$  is based on a data evaluation in the frequency domain and therefore, performed piecewise which results in a time lag compared to  $CMV_{ger}$ .

The first CCC value of the Terrameter system, the OMEGA value, provides very constant results in the homogeneous areas of the test field, but the two weak spots show a much smaller influence on the size of this value. As already emphasized by Hager in [13], the  $E_{vib}$  value of the Terrameter and the  $k_B$  value of the ACE system is the most advanced CCC values for vibratory rollers and are classified as Level 3 measures in the US FHWA Intelligent Compaction Measurement Value (ICMV) road map document, while  $CMV$  and OMEGA are considered Level 1 and Level 2, respectively.

Figure 8 compares the course of the CCC value for oscillatory rollers of the previously considered test run with the CCC values for vibratory rollers of a test run with a large vibration amplitude of 0.62 mm, an excitation frequency of  $f = 40$  Hz and a travel speed of  $v = 4$  km/h. The statements previously made about the compaction parameters OMEGA,  $E_{vib}$  and  $k_B$  remain valid, even when the large vibration amplitude is used. The CCC values  $CMV_{ger}$  and  $HMV_{gem}$  determined in the frequency domain, on the other hand, show an influence by the increased amplitude of the excitation in the form of pronounced scatter and the underestimation of the



**Fig. 8** Course of popular CCC values for vibratory rollers and a novel CCC value for oscillatory rollers on the compacted layer 2 of the test field. Oscillation:  $f = 39$  Hz,  $v = 4$  km/h. Vibration: large amplitude,  $f = 40$  Hz,  $v = 4$  km/h

stiffness above the weak spots. Due to the large vibration amplitude, the vibratory drum approaches the mode of operation “Double Jump”, to which the frequency-based CCC values react sensitively. This shows a great strength of the CCC value for oscillatory rollers which is, due to its definition, independent of the mode of operation of the oscillatory drum.

However, it should be noted in the comparison that the measuring depths of the CCC system for oscillatory rollers and the CCC systems for vibratory rollers differ significantly. While oscillatory rollers primarily compact the soil by dynamic horizontal forces, the vibratory roller achieves not only a greater depth effect but also a greater measuring depth due to the predominantly vertically directed dynamic excitation.

## 5 Conclusions

The theoretical background of four commonly used CCC values for vibratory rollers (CMV, OMEGA,  $E_{vib}$ , and  $k_B$ ) and a novel CCC value for oscillatory rollers has been explained and results from previous investigations have been reviewed briefly. Experimental field tests have been performed to evaluate the CCC values based on acceleration measurements on a tandem roller with a vibratory and an oscillatory drum. The presented results demonstrate that all investigated CCC values are able to map the stiffness conditions of the soil and to detect weak spots with accuracy.

It has been confirmed that the mode of operation of a vibratory drum has a significant influence on most CCC values for vibratory rollers, especially on CMV and

OMEGA. The differences in the depth effect and the resulting reduced measuring depth have to be considered for CCC with oscillatory rollers. The results from the conducted field tests show that various CCC values cannot simply be converted into each other due to the great differences in the theoretical background (and the resulting Levels of ICMV) of CCC algorithms, even if all CCC values are determined on the basis of acceleration measurements on one and the same roller.

## References

1. Kenze F (2005) *Faszination Straßenbau*. Motorbuch Verlag, Stuttgart
2. Geodynamik AB (1982) *Oscillatory roller*. Stockholm
3. Thurner H, Sandström Å (1980) *Compaction meter on vibrating rollers*. Dynapac Research, Solna
4. Forssblad, L.: *Compaction meter on vibrating rollers for improved compaction control*. In: *Proceedings of international conference on compaction*. Paris, pp 541–546
5. Kröber W et al (2001) *Dynamic soil stiffness as quality criterion for soil compaction*. In: *Geotechnics for roads, rail tracks and earth structures*. Tokyo
6. Anderegg R, Kaufmann K (2004) *Intelligent compaction with vibratory rollers*. In: *Transportation research record 1868*. Transportation Research Board, Washington, DC, pp 124–134
7. Dynapac Compaction Equipment AB (2019) *Instruction manual for vibratory roller CC4000 VI*. Dynapac Compaction Equipment AB, Sweden
8. Pistol J, Adam D (2018) *Fundamentals of roller integrated compaction control for oscillatory rollers and comparison with conventional testing methods*. *Transport Geotech* 17:75–84
9. Pistol J (2016) *Compaction with oscillating rollers*. Doctoral thesis, in German. TU Wien, Vienna
10. Ag HAMM (2015) *Datasheet HD+90 VV/HD+90 VO*. HAMM AG, Germany
11. Pistol J et al (2013) *Ambient vibration of oscillating and vibrating rollers*. In: *Proceedings of the Vienna congress on recent advances in earthquake engineering and structural dynamics 2013 (VEESD 2013)*. Paper 167, Vienna
12. Adam D, Kopf F (2004) *Operational devices for compaction optimization and quality control*. In: *Proceedings of international seminar on geotechnics in pavement and railway design and construction*. Athens, pp 97–106
13. Hager H (2015) *Theoretical and experimental comparison of Continuous Compaction Control (CCC) values*. Master thesis, in German. TU Wien, Vienna



# Numerical Assessment of Impacts of Vibrating Roller Characteristics on Acceleration Response of Drum Used for Intelligent Compaction



Zhengheng Xu , Hadi Khabbaz , Behzad Fatahi , Jeffrey Lee ,  
and Sangharsha Bhandari 

**Abstract** Intelligent compaction (IC) is an emerging technology for efficient and optimized ground compaction. IC combines the roller-integrated measurements with the Global Positioning System (GPS), which performs the real-time quality control and assurance during the compaction work. Indeed, IC technology is proven to be capable of providing a detailed control system for compaction process with real-time feedback and adjustment on full-area of compaction. Although roller manufacturers offer typical recommended settings for rollers in various soils, there are still some areas needing further improvement, particularly on the selection of vibration frequency and amplitude of the roller in soils experiencing significant nonlinearity and plasticity during compaction. In this paper, the interaction between the road subgrade and the vibrating roller is simulated, using the three-dimensional finite element method capturing the dynamic responses of the soil and the roller. The developed numerical model is able to simulate the nonlinear behavior of soil subjected to dynamic loading, particularly variations of soil stiffness and damping with the cyclic shear strain induced by the applied load. In this study, the dynamic load of the roller is explicitly applied to the simulated cylindrical roller drum. Besides, the impact of the frequency and amplitude on the level of subgrade compaction is discussed based on the detailed numerical analysis. The adopted constitutive model allows to assess the progressive settlement of ground subjected to cyclic loading. The results based on the numerical modeling reveal that the roller vibration characteristics can impact the

---

Z. Xu · H. Khabbaz (✉) · B. Fatahi · S. Bhandari  
University of Technology Sydney (UTS), Sydney, NSW 2007, Australia  
e-mail: [Hadi.Khabbaz@uts.edu.au](mailto:Hadi.Khabbaz@uts.edu.au)

Z. Xu  
e-mail: [Zhengheng.Xu-1@student.uts.edu.au](mailto:Zhengheng.Xu-1@student.uts.edu.au)

B. Fatahi  
e-mail: [Behzad.Fatahi@uts.edu.au](mailto:Behzad.Fatahi@uts.edu.au)

S. Bhandari  
e-mail: [Sangharsha.Bhandari@student.uts.edu.au](mailto:Sangharsha.Bhandari@student.uts.edu.au)

J. Lee  
Australian Road Research Board (ARRB), Brisbane, QLD 4006, Australia  
e-mail: [Jeffrey.Lee@arrb.com.au](mailto:Jeffrey.Lee@arrb.com.au)

influence depth as well as the level of soil compaction and its variations with depth. The results of this study can be used as a potential guidance by practicing engineers and construction teams on selecting the best choice of roller vibration frequency and amplitude to achieve high-quality compaction.

**Keywords** Intelligent compaction · Finite element modeling · Vibrating roller compactor · Acceleration response

## 1 Introduction

Continuous compaction control (CCC) is an emerging and appealing technology because it provides continuous assessment of soil stiffness since the technology first began in over 40 years ago. Nowadays, roller-integrated monitoring, in conjunction with the Global Positioning System (GPS) signal incorporated within the CCC vibratory roller, performs the real-time quality control. Moreover, the integration of measurement values with the roller operation allows “intelligent compaction” wherein the roller’s excitation force can be automatically adjusted based on the real-time feedback to achieve the most efficient compaction effort. Intelligent compaction (IC) technology can be utilized to achieve a more endurable performance and a more uniform compaction [1].

Several intelligent compaction measurement values (ICMVs) are used in practice to reflect the compaction quality, such as compaction meter value (CMV), compaction control value (CCV), vibration modulus ( $E_{VIB}$ ) and modulus of subgrade reaction or soil stiffness ( $k_s$ ). The mechanistic measurements derived from IC roller allow practicing engineers and construction teams to evaluate the quality of the compacted ground; hence, a thorough understanding of qualitative control of the soil–drum system is of prime importance. Historically, in the development stage of roller-integrated soil compaction, a dimensionless parameter, CMV, was heuristically measured based on the correlation between the underlying layer stiffness and soil density via harmonic signal [2]. CMV is influenced by the roller operation parameters and the roller dimensions [3–5]. In addition, the CCV of vibratory roller as an extension of CMV, together with recording soil temperature and sub-harmonic content of the drum acceleration, could allow the measurement of the compaction level of the asphalt [1, 6]. More recently, BOMAG has developed a vibratory modulus ( $E_{VIB}$ ) value based on Lundeberg’s theory and one-degree-of-freedom lumped parameter theory [7–10]. Furthermore, a composite nature of soil stiffness ( $k_s$ ) of underlying layers has been interpreted from the drum response and the excitation force, considering a rigid cylinder on the elastic half-space theory [7, 8, 11–13].

Indeed, the soil stiffness is strongly correlated to the loading conditions or strain levels, and there is an increasing emphasis on investigation of soil stiffness in the field based on the roller response [14]. Therefore, the majority of experimental studies

have been conducted to assess the correlation between soil stiffness and roller characteristics, such as the drum frequency and amplitude [11, 13, 14]. However, referring to some recent studies, the interaction between compacted soil and drum reveals a notable nonlinearity [12–15].

The measured soil stiffness reflects on the composite response of layered strata [12] and further analysis would be required to obtain characteristics of each newly compacted layer. The assumption of added masses for the simulation of the soil has been generally adopted in many lumped parameter models; thus, those models are unable to explicitly portray the decoupling behavior of soil–drum system because of overly simplified nature of simulations of inertial and dissipative properties for the soil modeling [13]. Thus, a discretized computational numerical model can be recommended to capture the complex soil–drum interaction behavior, while it can simulate the nonlinear behavior of the soil subjected to cyclic loading.

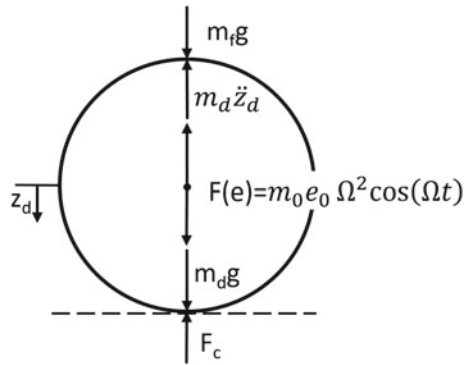
To better understand the response of the soil underneath the roller, developing a representative model to study the sophisticated interaction between the layered soil and the vibratory drum is necessary. Thus, in this study a three-dimensional finite element model is utilized to investigate the dynamic responses of soil–drum system. The key motivation for the paper is to assess the feasibility of the proposed numerical model and reveal the impacts of the roller vibration characteristics on the soil response via the numerical simulation. While many previous studies had investigated the roller response when full compaction state in the soil was reached, in this study the roller response when the soil is being compacted from weak state to stronger state is simulated. Moreover, the cyclic load is explicitly applied on the simulated cylindrical roller drum; and the roller properties are varied in terms of excitation frequency, amplitude and weight to assess the impacts on the level of subgrade compaction. These simulation results can be indicators for practicing engineers and construction teams to select optimized roller parameters and obtain a better understanding of intelligent compaction readings to achieve a high-quality soil compaction. It should be noted that detailed field experiments would help to further assess the suitability of the established numerical model for interpretation of intelligent compaction measurements.

## 2 Development of a Finite Element Model for Simulating Soil–Drum Interaction

### 2.1 Roller Characteristics

In this study, a typical rigid smooth drum was modeled with length and diameter of 2.1 m and 1.5 m, respectively. Referring to Fig. 1, a single drum roller typically adopted for soil compaction, together with a counter-rotating eccentric masses to provide directional eccentric force amplitude ( $F_{ev} = m_0 e_0 \Omega^2$ ). The resultant eccentric mass moment ( $m_0 e_0$ ) was set between 1 and 5 kg m. In addition, the employed

**Fig. 1** A free body diagram of 1-DOF lumped mass model of vibratory roller compactor



**Table 1** Operational parameters of vibratory roller

Parameter	Value	Unit
Length of drum	2.1	m
Diameter of drum	1.5	m
Mass of frame	2534	kg
Mass of drum	4466	kg
Eccentric mass moment inducing vibration	1.0–5.0	kg m
Vibration excitation frequency	25–35	Hz

*Note* Data from Kenneally et al. [13]

excitation frequency ranged from 25 to 35 Hz. Details of the roller properties are summarized in Table 1. The vibratory roller had a total weight of 7000 kg, which was used as the total weight of the simulated drum in this study.

As shown in Fig. 1, a single-degree-of-freedom (SDOF) roller was employed to analyze the intersection between soil and drum, while other parts of the roller including the frame, cabin and back tire were not simulated explicitly. The drum is isolated from the machine frame via low stiffness rubber, and thus, the influence of the frame is rather small, explaining why the frame inertia (i.e.,  $\ddot{z}_f$ ) is commonly neglected [10, 11, 13, 14]. The externally applied load on the soil could lead to the dissipation of excess pore pressures, resulting in a soil consolidation [16]. It should be noted that the magnitude of the vibration force is not equivalent to the effective compaction force [17]. In addition, to acquire the effective compaction force, a more complex soil–drum modeling is required. However, to validate the soil response adopting HS-Small model utilized in this study, the roller behavior was simplified. The drum–soil contact force is determined from simple force equilibrium (Fig. 1, Eq. (1)). The full contact conditions between soil and drum were continuously maintained.

$$F_c = m_0 e_0 \Omega^2 \cos(\Omega t + \varphi) + m_d g + m_f g - m_d \ddot{z}_d - m_f \ddot{z}_f \quad (1)$$

where  $z_d, \dot{z}_d, \ddot{z}_d$  are the displacement, velocity and acceleration of vibratory roller drum, and  $F_c, m_0e_0, \Omega, m_d, m_f$ , are the soil reaction force, the eccentric mass moment, the frequency of operating roller, the mass of the drum, the mass of the frame, respectively;  $\varphi$  is the phase lag between the excitation force ( $m_0e_0\Omega^2 \cos(\Omega t)$ ) and the drum displacement;  $\ddot{z}_f$  is the acceleration of vibratory roller frame, and it was neglected in this study.

## 2.2 Modeling of Soil

The nonlinear elasto-plastic stress–strain relationship is what typically observed in soils subjected to dynamic loading [18]. It is important to employ well-established constitutive models to capture the variations of resilient modulus helping to characterize the nonlinear response of underlying soil under repeated loading [10, 19]. In this study, to precisely capture the soil plasticity and nonlinearity in the cyclic loading, the hardening soil with small-strain stiffness (HS-Small) model developed by Benz [20] was employed. HS-Small model is an extension of the hardening soil model (HS model), extended with the extra elastic overlay model, and is capable of capturing the high stiffness at small strains.

HS-Small model is able to evaluate the stress-dependent stiffness and plasticity-induced soil stiffness degradation [21]. Equation (2) can be used to illustrate the stress dependency of the shear modulus  $G_0$  in the adopted HS-Small model. Additionally, referring to Brinkgreve et al. [22], there are three major parameters that can characterize the behavior of soil simulated using the HS-Small model, including (1) the confining stress-dependent stiffness for primary deviatoric loading ( $E_{50}$ ), (2) the unloading–reloading stiffness from the drained triaxial test ( $E_{ur}$ ) and (3) the tangent stiffness modulus from an oedometer test ( $E_{oed}$ ), as expressed in Eqs. (3)–(5), respectively.

$$G_0 = G_0^{\text{ref}} \left( \frac{c \cos \varphi - \sigma'_3 \sin \varphi}{c \cos \varphi + p^{\text{ref}} \sin \varphi} \right)^m \tag{2}$$

$$E_{50} = E_{50}^{\text{ref}} \left( \frac{c \cos \varphi - \sigma'_3 \sin \varphi}{c \cos \varphi + p^{\text{ref}} \sin \varphi} \right)^m \tag{3}$$

$$E_{ur} = E_{ur}^{\text{ref}} \left( \frac{c \cos \varphi - \sigma'_3 \sin \varphi}{c \cos \varphi + p^{\text{ref}} \sin \varphi} \right)^m \tag{4}$$

$$E_{\text{oed}} = E_{\text{oed}}^{\text{ref}} \left( \frac{c \cos \varphi - \frac{\sigma'_3}{K_0} \sin \varphi}{c \cos \varphi + p^{\text{ref}} \sin \varphi} \right)^m \tag{5}$$

**Table 2** Soil parameters based on hardening soil model with small-strain stiffness

Parameter	Symbol	Value	Unit
Unsaturated unit weight	$\gamma_{\text{unsat}}$	17	kN/m <sup>3</sup>
Saturated unit weight	$\gamma_{\text{sat}}$	20	kN/m <sup>3</sup>
Triaxial compression stiffness	$E_{50}^{\text{ref}}$	50,000	kN/m <sup>2</sup>
Primary oedometer stiffness	$E_{\text{od}}^{\text{ref}}$	50,000	kN/m <sup>2</sup>
Unloading/reloading stiffness	$E_{\text{ur}}^{\text{ref}}$	150,000	kN/m <sup>2</sup>
Rate of stress dependency	$m$	0.5	–
Poisson’s ratio	$\nu_{\text{ur}}$	0.2	–
Cohesion	$c$	0	kN/m <sup>2</sup>
Friction angle	$\Phi$	31	°
Dilatancy angle	$\Psi$	0	°
Shear strain at 0.7 $G_0$	$\gamma_{0.7}$	$1.0 \times 10^{-4}$	–
Small-strain stiffness	$G_0^{\text{ref}}$	$1.2 \times 10^5$	kN/m <sup>2</sup>
Over-consolidation ratio	OCR	1.0	–

Note Data from Brinkgreve et al. [22]

where  $G_0^{\text{ref}}$ ,  $E_{50}^{\text{ref}}$ ,  $E_{\text{ur}}^{\text{ref}}$  and  $E_{\text{od}}^{\text{ref}}$  are the shear modulus, secant, unloading/reloading and tangent stiffness related to the reference pressure  $p^{\text{ref}}$  (a default setting of  $p^{\text{ref}} = 100$  kPa), respectively;  $m$  is the factor defining of the level of stress dependency;  $\sigma'_3$  is the minor principal stress; and  $K_0^{\text{nc}}$  is the stress ratio in primary compression.

The HS-Small constitutive model is able to represent the nonlinear behavior of the natural subsoil in the small- and large-strain ranges. Comparing to the conventional linear elastic and elastic-perfectly plastic Mohr–Coulomb models, the HS-Small model is favorable to simulate the modulus degradation of the soil and damping characteristics with the cyclic shear strain mobilized in the soil [20]. HS-Small model can simultaneously take into account hysteretic soil damping (at small strains) and soil plasticity behavior (at large strains). The function proposed by Hardin and Drnevich [23], utilized to represent the correlation between the cyclic shear strain ( $\gamma_c$ ) and secant shear modulus ( $G_s$ ) in this study, is expressed as below;

$$G_s = \frac{G_0}{1 + \frac{\alpha \gamma_c}{\gamma_{0.7}}} \tag{6}$$

where parameters  $G_0$  and  $\gamma_{0.7}$  represent the small-strain shear stiffness, and the shear strain at which the secant shear modulus ( $G_s$ ) is reduced to 0.7  $G_0$ , respectively. The recommended value for  $\alpha$  (the constant in Eq. (6)), resulting in good agreement with laboratory measurements, is 0.385 [23].

In this study, the properties of sandy soil reported by Brinkgreve et al. [22] were applied, which are summarized in Table 2. Having calculated the model based on the above-mentioned data, the average compressional wave velocity ( $p$ -wave) and the

shear wave velocity (*s*-wave) at  $p = p^{ref} = 100 \text{ kPa}$  were 438.0 m/s and 268.2 m/s, respectively.

### 2.3 Finite Element Model

To characterize the soil–roller interaction, a model consisting of vibratory drum resting on the soil deposit was modeled in three-dimensional (3D) finite element software, PLAXIS 3D (2017). Roller parameters reported in Table 1 were assigned to the drum simulated in this study.

The simulated drum–soil system is portrayed in Fig. 2. The roller was modeled as a rigid body consisting of a 2.1-m-length and 1.5-m-diameter drum. The vibration excitation force ( $F_e = F_{ev} \cos(\Omega t)$ ) induced by an eccentric mass configuration, which rotates around the drum’s longitudinal axis, was applied as a vertically vibrating harmonic load to the roller. It should be noted that due to the counter-rotating eccentric masses, the horizontal forces were canceled out, and therefore they were neglected in this study similar to what was adopted in other studies [12].

A soil deposit was modeled with a width of 10 m, a length of 10 m and a depth of 10 m. It should be noted that the full response depth associated with vibratory roller was estimated to be from 0.6 to 1.0 m [24]. Thus, 10 m was deemed sufficient for modeling purposes. Consideration of interface element has a notable impact on the numerical predictions while soil is interacting with structures [25, 26]. In this

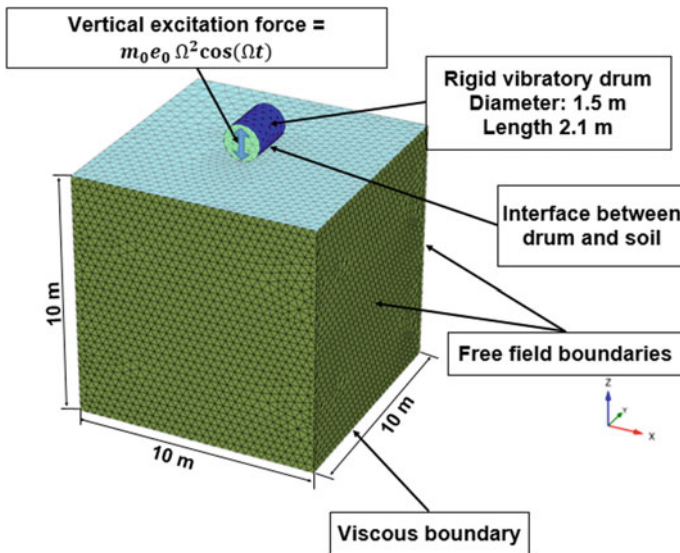


Fig. 2 Adopted three-dimensional numerical model capturing interaction between vibratory roller and the ground

study, to simulate the interaction between soil and drum, the interface elements with the same properties as the surrounding soil were introduced with  $R_{inter} = 1$ , while the zero tension limit was introduced [22]. The free field boundaries coupled with viscous dampers were applied for lateral boundaries to avoid the wave energy rebound into the soil body through applying resistant tractions in the tangential and normal directions [23]; for bottom border, a nonreflecting boundary condition (i.e., viscous boundary) was employed to reduce wave reflection in computational borders as recommended by Herrera et al. [14] and Kenneally et al. [13]. The formulations for the adopted tangential and normal resistant tractions are summarized as follows:

$$t_n = -\rho C_p V_n \tag{7}$$

$$t_s = -\rho C_s V_s \tag{8}$$

where  $V_n$  and  $V_s$  are normal and shear components of the velocity;  $C_p$  and  $C_s$  are  $p$ -wave and  $s$ -wave velocities, respectively. Figure 3 shows the adopted three-dimensional numerical model for the vibratory roller, supported by the sandy soil. There were 186,193 elements in the finite element model. The three-dimensional model was utilized to conduct an implicit nonlinear time integration with a time step of  $2.5 \times 10^{-4}$  s. Indeed, there were three different loading stages adopted in this numerical modeling to assess the soil response to the drum vibration during the compaction process. The first phase was application of gravity loading only; the second stage was dynamic loading phase, where the vibration load was applied on the drum followed by the third stage which was a static condition while roller was removed to establish the permanent deformation of the soil after completion of the soil compaction. The results of the conducted numerical modeling and parametric studies are presented and discussed in the following sections.

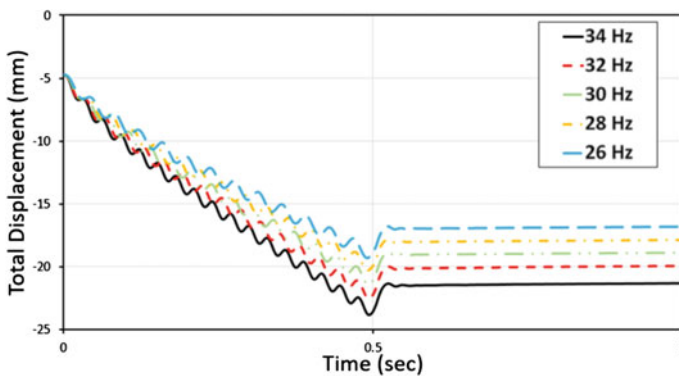


Fig. 3 Settlement (permanent displacement) of soil due to harmonic dynamic loading



### 3 Results and Discussion

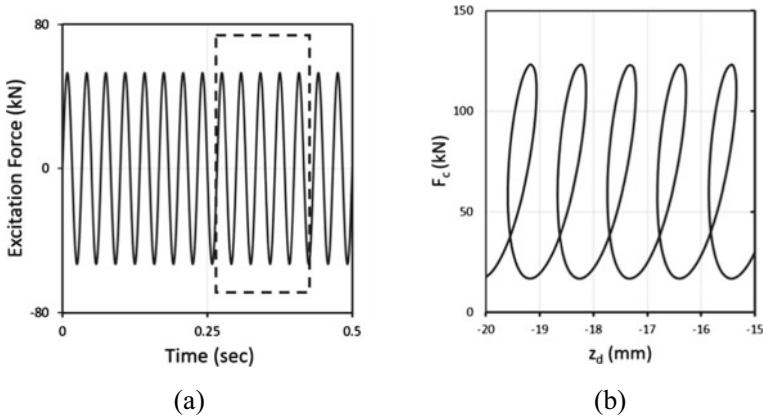
To better investigate the soil response due to vibratory roller behavior, impacts of roller frequency, amplitude and weight of roller were assessed in this study. In the adopted numerical model, the excitation force caused by the rotating eccentric masses was applied to the rigid drum, while different vibration frequencies as well as various eccentric mass moments and different weight of roller  $[(m_d + m_f)g]$  were considered to evaluate the drum response.

#### 3.1 Effects of Vibration Frequency

Vibratory roller frequency as a fundamental parameter in the dynamic system has a crucial impact on the soil compaction process. In order to scrutinize the impact of the vibratory drum, varied frequencies while keeping the eccentric mass moment  $m_0e_0 = 2 \text{ kg m}$  and weight of drum and frame equal to 7000 kg constant were considered. The impact of roller excitation frequency on the soil response was studied by varying frequency from 26 to 34 Hz. It could be noted that the first natural frequency of the soil deposit was estimated to be 110–183 Hz (i.e.,  $V_p/(4H)$ ) corresponding to roller influence depth of 0.6–1.0 m.

Figure 3 presents the time history of soil displacement in conjunction with different vibration frequencies of roller. Referring to this figure, the soil gradually settled due to roller vibration, where  $f = 34 \text{ Hz}$  exhibited the highest degree of soil compaction for the adopted sandy soil. The observations, based on the conducted numerical modeling in this study, exhibit when the vibration frequency is close or equal to the natural frequency of the soil, the vibratory roller can achieve the optimum compaction, and the observed results are consistent with the results reported by other researchers [27–29]. Regarding the operation frequency  $f = 34 \text{ Hz}$ , the initial soil settlement (i.e., 4.8 mm) was observed before vibration just due to the self-weight of the roller. Furthermore, the maximum vertical settlement of the soil in dynamic phase is 23.8 mm and reached residual settlement of 21.5 mm when the roller was removed. It should be noted that as expected the initial soil settlement (i.e., 4.8 mm) was larger than the recoverable soil settlement (i.e., 2.3 mm) since the initial loading stages comprised of both elastic and plastic components, whereas the unloading stage comprised of only elastic component. Figure 3 presents the soil settlement accumulates as a result of plastic deformation during each loading cycle as the dynamic time increased. The irreversible deformation occurred in the soil indicates the gradual compaction of the soil and incremental increases in the yield stress in the soil.

Indeed, the roller vibration frequency closest to the first mode natural frequency of the ground (i.e., roller vibration frequency of 34 Hz) resulted in more ground displacement and soil compaction as expected [30]. Therefore, as the excitation frequency acquired a lower value than the natural frequency of the soil, the accumulated soil settlement was reduced as evident in Fig. 3.



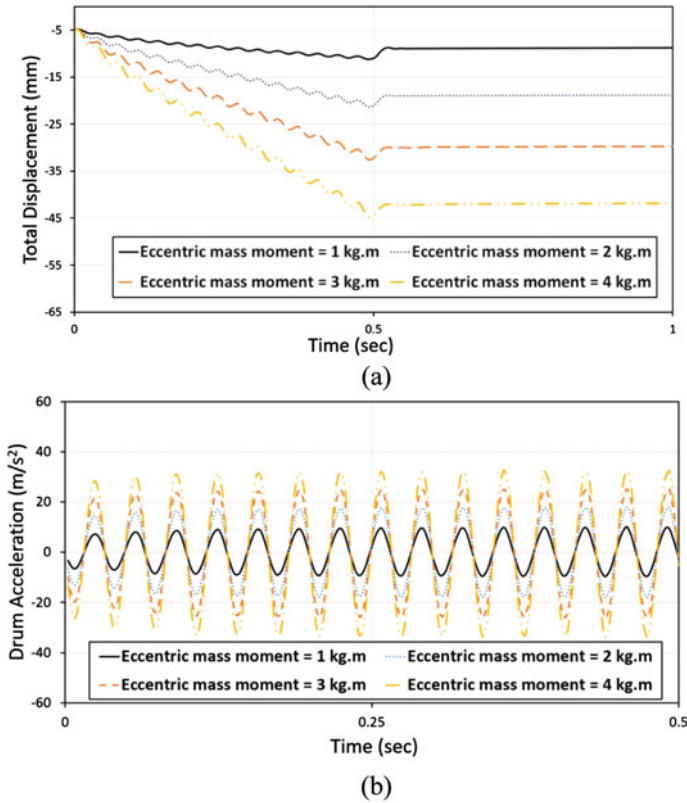
**Fig. 4** **a** A sample of applied excitation force vs time for frequency = 30 Hz and **b** soil reaction force vs soil surface displacement

Figure 4a, b presents the time history of excitation force with a frequency of 30 Hz and the corresponding soil reaction force—cyclic soil-surface displacement relationship. The energy lost in the soil due to soil damping and plastic deformations is evident in Fig. 4b.

### 3.2 Effects of Amplitude

The nominal amplitude of the vibratory drum displacement is directly impacted by the eccentric mass [31]. To consider the impacts of the excitation force amplitude of the roller on the soil and drum interaction and therefore the compaction process, several different magnitudes of eccentric mass moments while keeping the vibration frequency constant equal to  $f = 30$  Hz were adopted in this study. A number of constant eccentric mass moments varying from 1 to 4 kg m were investigated to provide directional eccentric force amplitude. In general, a lower eccentric mass moment is capable of providing smaller excitation force amplitude, and it is usually used for proof rolling and finishing passes to avoid over-compaction; conversely, a higher eccentric mass moment is utilized in the early stage of compaction [13]. Figure 5a illustrates the evolution of the accumulation of soil displacement with time as a function of varying eccentric mass moment. It should be noted that in the range of applied eccentric mass moment, the full contact condition between the soil and drum was continuously maintained.

For a given vibration frequency of  $f = 30$  Hz and soil parameters reported in Table 2, the soil settlement increased with eccentric mass moment with the maximum observed when  $m_0e_0 = 4$  kg m, as shown in Fig. 5a. The results show that an increase in the eccentric mass moment led to an increase in the compacted soil displacement,



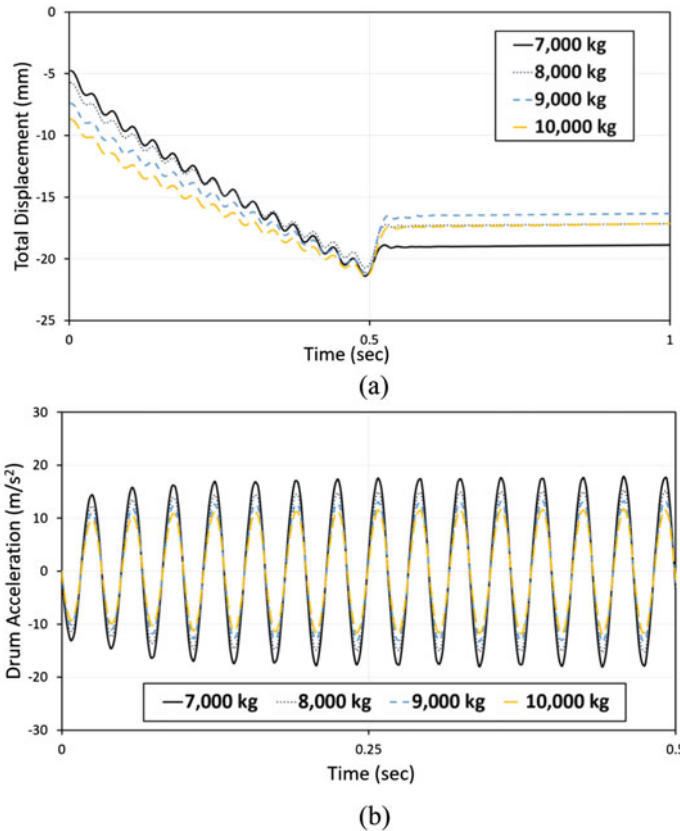
**Fig. 5** a Accumulation of soil displacement versus time in conjunction with different roller masses; and b drum acceleration verse time

which is consistent with the observations reported by other researcher [27]. Additionally, the similar correlation between the acceleration and eccentric mass moment was observed by Pietzsch et al. [31], while the drum acceleration amplitude increased with the drum excitation mass moment. Corresponding to the operating eccentric mass moment  $m_0e_0 = 4 \text{ kg m}$ , the drum showed the maximum acceleration response with time as a result of the highest excitation force. Due to the constant weight of roller, when the excitation force is more (i.e., higher  $m_0e_0$ ), the corresponding acceleration is consequently more. Thus, the drum acceleration increased with eccentric mass moment as observed in Fig. 5b. Obviously, a low eccentric mass moment from vibratory roller results in less accumulation of soil displacement in the soil in comparisons to the high eccentric mass moment. As recommended by Kenneally et al. [13], to avoid the irregular vibration induced by chaotic jump or bifurcation for the very dense soil, the lower eccentric mass should be utilized in finishing passes.

### 3.3 Effects of Roller Weight

The roller mass was altered from 7000 to 10,000 kg in this study for the further assessment while eccentric mass moment  $m_0e_0 = 2 \text{ kg m}$  and frequency of drum equal to 30 Hz were held constant. Figure 6a shows the correlation between drum acceleration response and time for rollers of different weights.

Figure 6a examines the soil settlement with time during compaction. Indeed, the soil settlement gradually increased due to accumulated plastic deformation in the soil. It should be noted that the initial soil settlement corresponding to 7000 kg roller (i.e., 4.8 mm) was less than the corresponding value for 10,000 kg roller which was 8.7 mm, due to the reduced self-weight of the roller. Furthermore, the initial settlement due to self-weight of the roller was larger than the unloading settlement induced by the roller removal, since the initial settlement comprised of both elastic and plastic components as evident in Fig. 6a. The 7000 kg roller showed the highest



**Fig. 6** a Accumulation of soil displacement versus time in conjunction with different roller masses; and b drum acceleration verse time

acceleration response as observed Fig. 6b and resulted in the most compacted state of the soil. It should be noted that the 7000 kg roller exhibited the most compacted state of soil within the range of the studied parameters. The results exhibit that the soil total displacement due to compaction increased with the drum acceleration, which is also in close agreement with the results reported by Cao et al. [32]. While the excitation force is constant, the increased weight of roller resulted in reduced the roller acceleration and therefore vibratory compaction. Obviously, the 7000 kg roller resulted in least initial settlement (see Fig. 6a) due to its lowest self-weight and the largest final settlement (i.e., 19.0 mm) due to the increased vibration acceleration.

## 4 Conclusions

This paper investigated the characteristics of rollers using a three-dimensional finite element simulation to represent the drum–soil interaction while capturing soil hardening with small-strain stiffness variations. The effects of the vibration of frequency and the amplitude as well as the weight of roller on soil compaction process and the roller response were analyzed and discussed via the numerical modeling predictions.

The numerical predictions in this study have indicated that while the vibration frequency was changed between 24 and 34 Hz for a given eccentric mass moment of  $m_0e_0 = 2$  kg m, the optimal compaction was achieved when vibration frequency of 34 Hz was adopted. Indeed, this vibration frequency (i.e., 34 Hz) was the closest to the natural first mode frequency of the effective soil deposit beneath the roller. Furthermore, the initial soil settlement due to self-weight of the roller was larger than the soil expansion after removal of roller since the loading stage comprised of both elastic and plastic components, whereas the unloading stage comprised of only elastic component.

The observations based on the conducted numerical modeling in this study exhibited that for the eccentric mass moment ( $m_0e_0$ ) ranging from 1 to 4 kg m, the maximum contact force was reached when  $m_0e_0 = 4$  kg m, wherein the drum experienced the maximum acceleration with time. Thus, the largest final settlement was observed for  $m_0e_0 = 4$  kg m, and it is not recommended to operate the roller under high eccentric mass moment in the finishing passes to avoid over-compaction. Furthermore, among rollers with different weights considered and for a given eccentric mass moment, the lightest roller experienced the highest acceleration and thus resulted in the largest final settlement due to the highest induced acceleration.

Although the numerical predictions were comparable to the previously published data, further field experiments would help to further assess the suitability of the established numerical model for interpretation of intelligent compaction measurements. The numerical results of this study show that the proposed three-dimensional finite element model adopting nonlinear elastic–plastic soil model capturing soil hardening and damping variations with shear strain can be used to simulate the complex interaction between the soil and the roller drum subjected to roller vibration and can be used to interpret the intelligent compaction results and optimize the process.

Indeed, this study can be used as a potential guidance by practicing engineers and construction professionals on selecting the best choice of roller vibration frequency, eccentric mass moment and weight of roller during intelligent compaction process to achieve high-quality final product.

## References

1. Xu Q, Chang GK, Gallivan VL (2012) Development of a systematic method for intelligent compaction data analysis and management. *Constr Build Mater* 377:470–480
2. Forssblad L (1980) Compaction meter on vibrating rollers for improved compaction control. In: *Proceedings of the international conference on compaction*, vol 2, pp 541–546
3. Thurner H (1980) The compactometer principle: Contribution to the discussion in Session IV. In: *Proceedings of international conference on compaction*, vol 2, Paris
4. Thurner H, Sandström Å (1980) A New device for instant compaction control. In: *Proceedings of international conference on compaction*, vol 2, Paris, pp 611–614
5. Machet JM (1980) Compactor-mounted control devices. In: *Proceedings of international conference on compaction*, vol 2, Paris, pp 577–581
6. Chang G, Xu Q, Rutledge J, Horan B, Michael L, White D, Vennapusa P (2011) Accelerated implementation of intelligent compaction technology for embankment subgrade soils, aggregate base, and asphalt pavement materials
7. Lundberg G (1939) Elastische berührung zweier halbräume. *Forsch Geb Ingenieurwes* 10:201–211
8. Kröber W, Floss R, Wallrath W (2001) Dynamic soil stiffness as quality criterion for soil compaction. In: *Geotechnics for roads, rail tracks and earth structures*, pp 189–199
9. Hertz H (1895) Über die Berührung fester elastischer Körper (On the contact of elastic body). *Gesammelte Werke*, Leipzig
10. Nazarian S, Fathi A, Tirado C, Kreinovich V, Rocha S (2020) Evaluating mechanical properties of earth material during intelligent compaction. Pre-publication draft of NCHRP research report 933. Transportation Research Board, Washington, DC
11. Anderegg R, Kaufmann K (2004) Intelligent compaction with vibratory rollers: feedback control systems in automatic compaction and compaction control. *Transp Res Rec* 1868(1):124–134
12. Van Susante PJ, Mooney MA (2008) Capturing non-linear vibratory roller compactor behavior through lumped parameter modeling. *J Eng Mech* 134(8):684–693
13. Kenneally B, Musimbi OM, Wang J, Mooney MA (2015) Finite element analysis of vibratory roller response on layered soil systems. *Comput Geotech* 67:73–82
14. Herrera C, Costa PA, Caicedo B (2018) Numerical modeling and inverse analysis of continuous compaction control. *Transp Geotech* 17:165–177
15. Mooney MA, Rinehart RV (2009) In situ soil response to vibratory loading and its relationship to roller-measured soil stiffness. *J Geotech Geoenviron Eng* 135(8):1022–1031
16. Ho L, Fatahi B, Khabbaz H (2018) Analytical solution to one-dimensional consolidation in unsaturated soil deposit incorporating time-dependent diurnal temperature variation. *Int J Geomech* 18(5):04018029
17. Torres AN, Arasteh MI (2017) Intelligent compaction measurement values (ICMV)—A road map. US Department of Transportation, Federal Highway Administration, Technical Brief, FHWA-HIF-17-046, Washington, DC
18. Han B, Zdravkovic L, Kontoe S, Taborda DM (2016) Numerical investigation of the response of the Yele rockfill dam during the 2008 Wenchuan earthquake. *Soil Dyn Earthq Eng* 88:124–142
19. Ooi PSK, Archilla AR, Sandefur KG (2004) Resilient modulus models for compactive cohesive soils. *Transp Res Rec: J Transp Res Board* 1874:115–124

20. Benz T (2009) Small-strain stiffness of soils and its numerical consequences. *Bautechnik* 86(SUPP/1):16–27
21. Schanz T, Vermeer PA, Bonnier PG (1999) The hardening soil model: formulation and verification. In: *Beyond 2000 in computational geotechnics*, pp 281–296
22. Brinkgreve R, Kumarswamy S, Swolfs W, Foria F (2017) *Plaxis 2017*. Delft, Netherlands
23. Hardin BO, Drnevich VP (1972) Shear modulus and damping in soils: design equations and curves. *J Geotech Eng* 7(8):667–692
24. Adan D (2007) Roller integrated continuous compaction control (CCC) technical contractual provisions and recommendations. In: *Design and construction of pavements and rail tracks: geotechnical aspects and processed materials*, pp 111–138
25. Fatahi B, Basack S, Ryan P, Zhou WH, Khabbaz H (2014) Performance of laterally loaded piles considering soil and interface parameters. *Geomech Eng* 7(5):495–524
26. Fatahi B, Nguyen QV, Xu RS, Sun WJ (2018) Three-Dimensional response of neighboring buildings sitting on pile foundations to seismic pounding. *Int J Geomech* 18(4):04018007
27. Masad E, Scapas A, Rajagopal KR, Kassem E, Koneru S, Kasbergen C (2016) Finite element modeling of field compaction of hot mix asphalt. Part II: Applications. *Int J Pavement Eng* 7(1):24–38
28. Wersall C, Larsson S (2016) Influence of force ratio and frequency on vibratory surface compaction. In: *Geotechnics for sustainable infrastructure development*, pp 841–846
29. Li S, Hu C (2018) Study on dynamic model of vibratory roller-soil system. In: *IOP conference series: earth and environmental science*, vol 113, p 012187
30. Dieter P, Poppy W (1992) Simulation of soil-compaction with vibratory roller. *J Terra-Mech* 29(6):587–597
31. Pietzsch D, Poppy W (1992) Simulation of soil compaction with vibratory rollers. *J Terramech* 29(6):585–597
32. Cao Y, Liang N, Qin M, Lu Z (2010) Research on the correlation between vibration acceleration of roller and compaction degree of subgrade soil. In: *ICCTP 2010: integrated transportation systems: green, intelligent, reliable*, pp 2974–2982

# Evaluating the Influence of Soil Plasticity on the Vibratory Roller—Soil Interaction for Intelligent Compaction



Sangharsha Bhandari , Behzad Fatahi , Hadi Khabbaz , Jeffrey Lee , Zhengheng Xu , and Jinjiang Zhong 

**Abstract** Use of intelligent compaction (IC) is a growing technique for compaction in the field of construction. It provides an efficient way of evaluating the soil compaction level with a higher degree of certainty than traditional quality control methods. IC involves the interpretation of measured values received through the accelerometer and other sensors attached to the roller. The key objective of this paper is to analyse the dynamic roller–soil interaction via a three-dimensional nonlinear finite element model, capturing soil nonlinear response and damping in both small and large strain ranges as a result of dynamic load applied via the vibratory roller. In particular, the impact of soil plasticity index (PI) on the response of a typical vibratory roller is assessed. Indeed, the soil plasticity impacts stiffness degradation with shear strain influencing the soil stiffness during compaction and the roller response. The numerical predictions exhibit that the soil plasticity can significantly influence the response of the roller and the ground settlement level; hence, practising engineers can consider the soil plasticity index as an influencing factor to interpret the intelligent compaction results and optimize the compaction process.

---

S. Bhandari (✉) · B. Fatahi · H. Khabbaz · Z. Xu  
University of Technology Sydney (UTS), 15 Broadway, Ultimo, NSW 2007, Australia  
e-mail: [Sangharsha.Bhandari@student.uts.edu.au](mailto:Sangharsha.Bhandari@student.uts.edu.au)

B. Fatahi  
e-mail: [Behzad.Fatahi@uts.edu.au](mailto:Behzad.Fatahi@uts.edu.au)

H. Khabbaz  
e-mail: [Hadi.Khabbaz@uts.edu.au](mailto:Hadi.Khabbaz@uts.edu.au)

Z. Xu  
e-mail: [Zhengheng.Xu-1@student.uts.edu.au](mailto:Zhengheng.Xu-1@student.uts.edu.au)

J. Lee  
Australian Road Research Board (ARRB), Brisbane, QLD 4006, Australia  
e-mail: [Jeffrey.Lee@arrb.com.au](mailto:Jeffrey.Lee@arrb.com.au)

J. Zhong  
Logan City Council, Logan Central, QLD 4114, Australia  
e-mail: [JinjiangZhong@logan.qld.gov.au](mailto:JinjiangZhong@logan.qld.gov.au)



**Keywords** Intelligent compaction · Soil plasticity · Vibratory roller · Finite element modelling · Modulus degradation

## 1 Introduction

Compaction by using the vibratory roller is one of the most prevalent methods of ground improvement for many years. This process helps improve the strength of the soil to withstand the structural loads applied on top [1, 2]. Although the dynamic rollers are very efficient for compaction of granular materials, a sufficient number of spot tests are required to verify the quality of compaction attained [3]. To overcome this shortcoming, continuous compaction control (CCC) has evolved and driven research studies in this field. CCC is an integrated technology for the measurement of mechanistic properties of the soil during the process of compaction [3]. Data acquisition systems are attached to the roller to collect operation and performance data continuously during the compaction process [4]. With the development of technology, advanced monitoring system has been developed which provides real-time feedback with the support of built-in global positioning system (GPS), accelerometer, other sensors and display boards by interpreting the signal received by accelerometer and sensors, and the technology has been renamed as intelligent compaction (IC) [3]. In the last four decades, many studies have been performed to transform the response of the roller into a numerical value known as measurement values (MVs). Nowadays, there are several MVs utilized to capture the compaction quality such as compaction control value (CCV), compaction meter value (CMV), soil stiffness ( $k_s$ ), vibration modulus ( $E_{vib}$ ) and the machine drive power (MDP) [3]. During the vibratory compaction process, a dynamic interaction between compaction drum and the soil underneath is present, which can impact the soil settlement. Several factors such as soil stiffness, speed of roller, excitation load, frequency and weight of the roller as well as the dynamic soil–roller interaction have substantial impacts on the roller–soil interaction during the compaction process [1–5].

Roller–soil interaction during compaction is highly dependent on soil properties. Soil properties such as stiffness, cohesion, friction angle and plasticity index can have great impacts on the compaction process, while partially soil characteristics change when subjected to cyclic loading [6]. Plasticity index (PI) is represented as the numerical difference of Atterberg's limits (liquid limit (LL) and plastic limit (PL)) which presents the soil moisture content range, where soil behaves plastically [7]. Vucetic and Dobry suggested that cyclic shear stiffness and damping ratio of fine-grain soils are strongly dependent on the PI [8].

This paper attempts to simulate the complex three-dimensional vibratory compaction process, capturing the interaction between the soil and the roller. The main aim of this paper is to investigate the influence of PI on the roller response during the process of compaction, helping to interpret the roller response during intelligent compaction. The findings of this paper aim to help practising engineers to assess the importance of PI on the vibratory roller response and possibly introducing

PI as one of the indices required to assess the ground stiffness and compaction level during the construction, adopting intelligent compaction technology.

## 2 Three-Dimensional Finite Element Model

In this study, a finite element model using PLAXIS 3D (2018) software was developed to study the vibratory roller–soil interaction. The objective of this modelling was to investigate the response of the soil and roller to the vibratory load for soils with different plasticity indices.

### 2.1 Adopted Soil Model

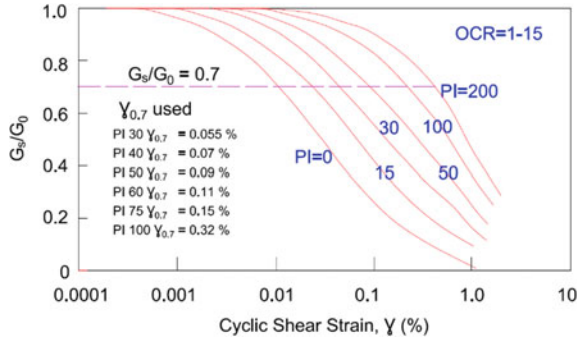
Prediction of the settlement observed in the soil is quite complex due to the presence of both elastic and plastic deformation. Among different available constitutive models, hardening soil (HS) model was developed to allow elastic and plastic deformations of soil to occur concurrently while approaching the Mohr–Coulomb failure envelope [9–11]. Small strain hardening soil (HSS) model is an upgraded version of the HS model, which is capable of capturing the larger stiffness of soils at small strains [11, 12]. HS and HSS models, available in PLAXIS software, use almost the same set of material properties [10–12]. Apart from the hardening model parameters (i.e.  $E_{50}^{\text{ref}}$  = secant stiffness at reference pressure  $P_{\text{ref}}$  (i.e. 100 kPa);  $E_{\text{od}}^{\text{ref}}$  = tangent oedometer stiffness at  $P^{\text{ref}}$ ;  $E_{\text{ur}}^{\text{ref}}$  = loading/unloading stiffness at  $P^{\text{ref}}$ ;  $m$  = power for stress-level dependency of stiffness;  $c$  = cohesion;  $\Phi$  = friction angle;  $\psi$  = dilatancy angle;  $\nu_{\text{ur}}$  = Poisson’s ratio), to represent higher stiffness at small strains, HSS model adopts shear modulus at small strain ( $G_0^{\text{ref}}$ ) and shear strain level at which secant shear modulus is reduced to about 70% of  $G_0^{\text{ref}}$  ( $\Upsilon_{0.7}$ ) [11, 12]. Indeed, soils exhibit the nonlinear stress–strain relationship during cyclic loading, while the degradation of the soil stiffness occurs with shear strain [14]. Referring to Santos and Correia [14],  $\Upsilon_{0.7}$  helps to delineate a distinctive shear modulus decay curve with the use of normalized shear strain ( $\Upsilon^*$ ) given by Eq. (1).

$$\Upsilon^* = \Upsilon / \Upsilon_{0.7} \quad (1)$$

Hardin–Drnevich relationship explains that the stress–strain curve in the small strain range can be expressed by a hyperbolic law which is given by Eq. (2) [12, 13].

$$\frac{G_s}{G_0} = \frac{1}{1 + \frac{\Upsilon}{\Upsilon_r}} \quad (2)$$

**Fig. 1** The relation between  $G_s/G_0$  and  $\Upsilon$  for soils with varying PI (data obtained from Vucetic and Dobry [8])



where  $G_s$  is secant shear modulus and  $G_0$  is initial shear modulus at very small strain (i.e.  $<10^{-6}$ ).  $\Upsilon_r$  is termed as threshold shear strain and expressed as  $\Upsilon_r = \tau_{max}/G_0$ , where  $\tau_{max}$  is failure shear stress. Santos and Correia [14] proposed  $\Upsilon_r = \Upsilon_{0.7}$ , where secant modulus ( $G_s$ ) reduction is assumed to be 70% of the initial value and revised Eq. (2) as Eq. (3) [12–14].

$$\frac{G_s}{G_0} = \frac{1}{1 + a \left| \frac{\Upsilon}{\Upsilon_{0.7}} \right|} \tag{3}$$

where  $a = 0.385$ .

Indeed, the stiffness decay  $G_s/G_0$  due to increasing shear strain very much depends on the soil plasticity index (PI) as laboratory measurements by Vucetic and Dobry [8], shown in Fig. 1, reported. Figure 1 indicates that cyclic stiffness degradation is more significant for the soils with lower PI than higher PI.

In this study, 8-m-deep soil layer was simulated below the roller; top 0.5 m was modelled as a weak cohesive soil, and the rest of deposit below was assumed as old alluvium of stiff nature. Thus, the soil compaction could mainly densify the top layers of the soil. PI of the top layer was varied from 30 to 100, and therefore, the value of  $\Upsilon_{0.7}$  was changed in the numerical model reflecting on the impacts of soil plasticity on the roller’s response and induced soil settlement. Soil properties reported by Möller [15] and Aghayarzadeh et al. [16] were used for this study and are summarized in Table 1.

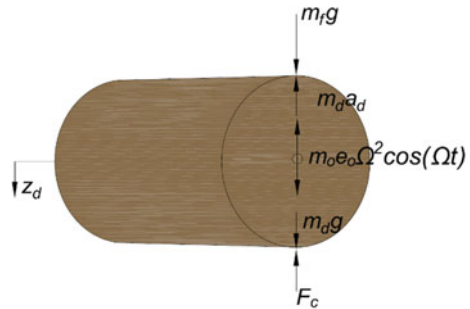
## 2.2 Adopted Roller Characteristics and 3D Model

As shown in Fig. 2, in this study, a rigid cylindrical roller with a length of 2.1 m and diameter of 1.5 m was modelled. The static load was provided by the weight of the roller, which was 6800 kg. The excitation force of roller is generally induced by the eccentric mass ( $m_0$ ) which is placed at the moment arms ( $e_0$ ) inside the roller, and the typical vibration mass moment is 0–5 kg m [9]. In this study,  $m_0e_0 = 1.0$  kg m

**Table 1** Small strain hardening soil properties used in this model

Parameter	Symbol	Topsoil layer [16]	Bottom soil layer [15]	Unit
Density	$\rho$	1800	1900	kg/m <sup>3</sup>
Secant stiffness	$E_{50}^{ref}$	12,000	55,000	kN/m <sup>2</sup>
Tangent stiffness	$E_{oed}^{ref}$	7000	55,000	kN/m <sup>2</sup>
Unloading/reloading stiffness	$E_{ur}^{ref}$	88,000	165,000	kN/m <sup>2</sup>
Power for stress level dependency	$m$	0.9	0.5	–
Poisson’s ratio	$\nu_{ur}$	0.2	0.2	–
Cohesion	$c$	7	6	kN/m <sup>2</sup>
Friction angle	$\Phi$	31	30	
Dilatancy angle	$\Psi$	0	0	
Threshold shear strain	$\gamma_{0.7}$	$5.5 * 10^{-4} - 3.2 * 10^{-3}$	$2.5 * 10^{-2}$	–
Reference shear modulus	$G_0^{ref}$	88,000	225,000	kN/m <sup>2</sup>

**Fig. 2** Vertical forces acting on the dynamic roller

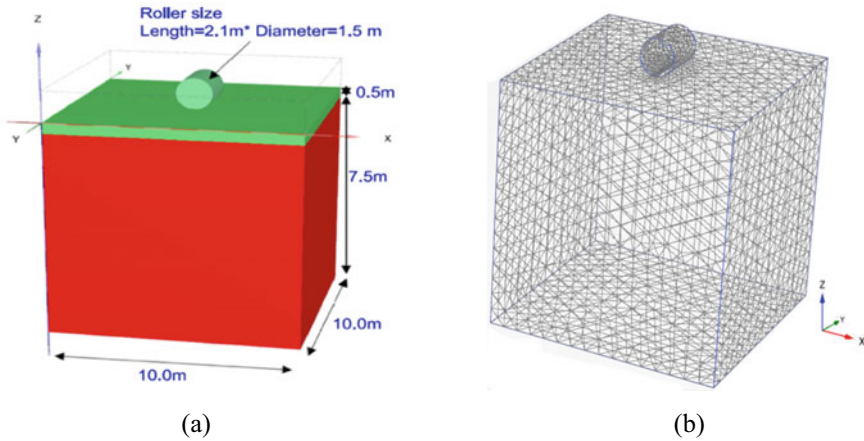


was adopted. Referring to Kenneally et al. [9], the vibration frequency of 30 Hz was adopted in this study, which is a median range for typical rollers. The reaction force from the ground applied to the roller during the vibratory compaction can be written as follows [9].

$$F_c = m_o e_o \Omega^2 \cos(\Omega t) + m_d g + m_f g - m_d a_d \tag{4}$$

where  $F_c$  is the reaction force of the soil;  $m_o e_o$  is the mass moment;  $\Omega = 2\pi f$  (where  $f$  is vibration frequency of the roller);  $m_d$  is the mass of the drum;  $m_f$  is the frame mass, and  $a_d$  is the measured acceleration of the roller during compaction.

The soil beneath the roller undergoes many cycles of loading and unloading during the compaction process. The 3D finite element model was employed to simulate the interaction between soil and drum during the vibratory compaction process. Although the 3D model allows realistic details of the problem to be considered



**Fig. 3** **a** 3D model dimensions adopted to study the roller–soil interaction and **b** finite element mesh adopted in this study

and can provide more accurate and realistic outcomes, the complexity of modelling aspects and computational time increases significantly. In this study, the multilayer soil model was developed as shown in Fig. 3. Length and breadth of the soil block were kept 10 m. It should be noted that the total depth of 8 m for the depth of soil was deemed sufficient considering the roller dimensions reported in Fig. 3. The eccentric loading induced by harmonic excitation force (i.e.  $m_0 e_0 \Omega^2 \cos(\Omega t)$ ) was applied as a dynamic vertical load to the compaction drum with a frequency of 30 Hz. A total of 240,350 elements were used to create the finite element mesh to analyse the model, while the calculation time increment was taken as  $3.3 \times 10^{-4}$  s. It should be noted that it was assumed in this study that the only vertical vibratory force was applied, and for the sake of simplicity, tangential forces due to oscillation compaction were ignored.

The numerical calculations were performed in four phases. In the first phase, the gravity loads were applied to the soil deposit, and equilibrium was established. In the second phase, the self-weight of the roller was applied to investigate the soil settlement due to the static load of the roller. Furthermore, a sinusoidal dynamic load was applied in the third phase to replicate the vibration action. In this phase, the displacement of the roller, acceleration of the roller and settlement of the ground were continuously monitored, which could be used to establish the soil reaction force during the compaction. Finally, in phase four, the roller was removed from the soil surface, and the soil was allowed to reach equilibrium, simulating the post-compaction state of the soil.

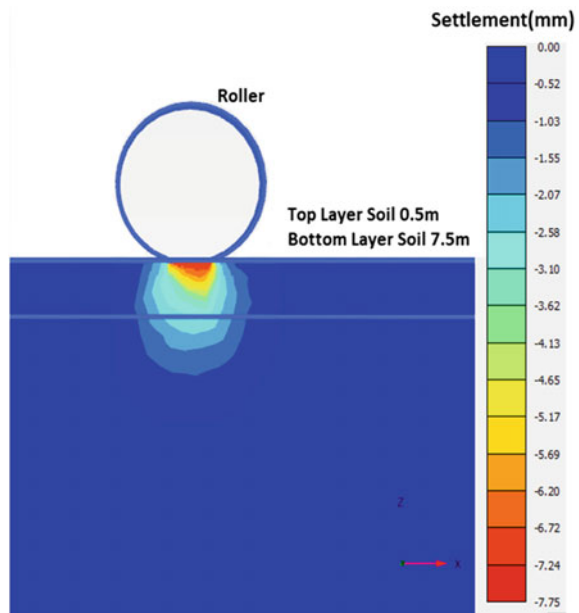
### 3 Results and Discussion

To highlight the importance of soil plasticity on the roller response and roller–soil interaction, a numerical parametric study was conducted by changing the backbone curves as a function of soil plasticity index (PI) as described in Fig. 1. It should be noted that the modelling parameters of the roller, such as weight and dynamic load, were kept constant for all models. Figure 4 shows an example of observed settlement profile of the ground below the middle of the roller after 0.5 s of vibration for the soil with  $PI = 30$ .

Soil properties and particulate parameters impacting the soil stiffness have significant effects on the roller response during the vibratory compaction. Plasticity index (PI) is one of the crucial properties of the soil which can impact the soil stiffness during cyclic loading and needs to be considered when interpreting intelligent compaction data. It should be noted that while the PI of the topsoil layer varied from 30 to 100, all other parameters of the soil model remained the same in this study.

Figure 5 illustrates the time history of soil displacement below the roller for soils of different PI values. Among all the cases, the case with the lowest considered  $PI = 30$  exhibited the most significant soil settlement and densification. The static settlement in the first phase due to the self-weight of the roller was varying from 0.89 to 2.41 mm when soil PI changed from 100 to 30, respectively. Indeed, Fig. 5 shows that the soil with lower values of PI experienced more settlement as a result of roller weight than the cases with higher values of PI. Furthermore, during the application dynamic vibration load of the roller, gradual increment in the settlement was observed

**Fig. 4** Soil settlement observed after the application of a dynamic load of roller for 0.5 s when  $PI = 30$



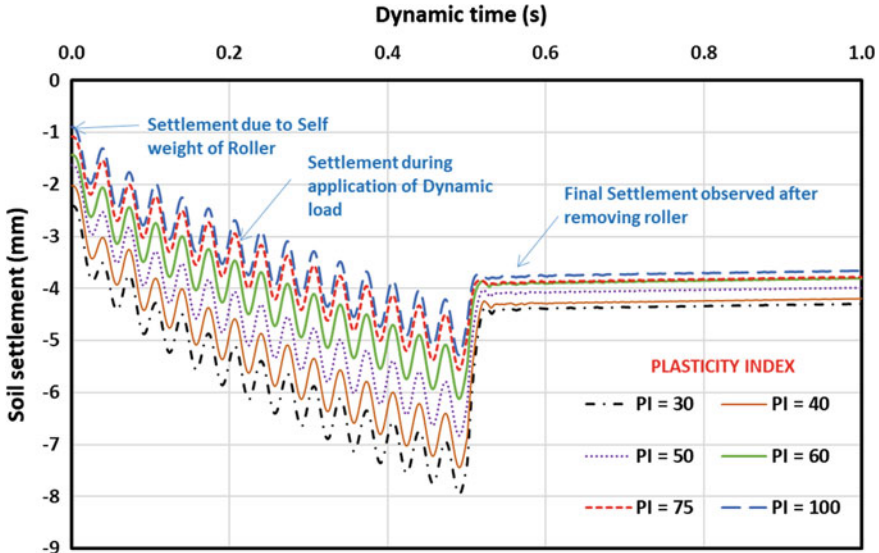


Fig. 5 Settlement observed during different phases of the model

with the local sinusoidal behaviour in response to the sinusoidal vibration load. After the complete cycle of dynamic load for 0.5 s, the total soil settlement (i.e., vertical displacement of the rigid roller) observed before removing the roller was between 4.77 and 7.42 mm corresponding to plasticity indices between 100 and 30, respectively. At the final stage where the roller was removed, soil experienced elastic heave as expected. As shown in Fig. 5, it was observed that there was a gradual decrease in the permanent soil settlement as the PI increased from 30 to 100. Vucetic and Dobry [8] had reported that the soils with higher plasticity indices are generally composed of more fine particles which have comparatively high surface areas and result in a high number of particle contacts which increase the electrical and chemical bonding between the particles and therefore have more capacity to withstand the large shear strains before undergoing permanent deformations. Conversely, in soils with lower PI, the particles start to slide at the adjoining surface at lower strains which results in higher permanent deformations.

The recovered settlement after removing the roller reflects on the elastic properties of the soil, and the permanent settlement was a result of accumulated plastic deformations which also indicates the increased soil compaction/compression level.

Figure 6 illustrates the soil reaction force ( $F_c$ ) during vibratory compaction versus roller displacement for various PI for a given roller vibration frequency (i.e., 30 Hz) and amplitude (i.e.,  $m_0e_0 = 1.0$  kg m). The response revealed an expected soil cyclic damping in addition to the energy loss due to soil plastic-permanent deformations. Figure 7 shows the variations of reaction force ( $F_c$ ) with time which shows that the roller was on continuous contact with the soil during the entire compaction process. For PI = 30, the maximum reaction force observed during the process was



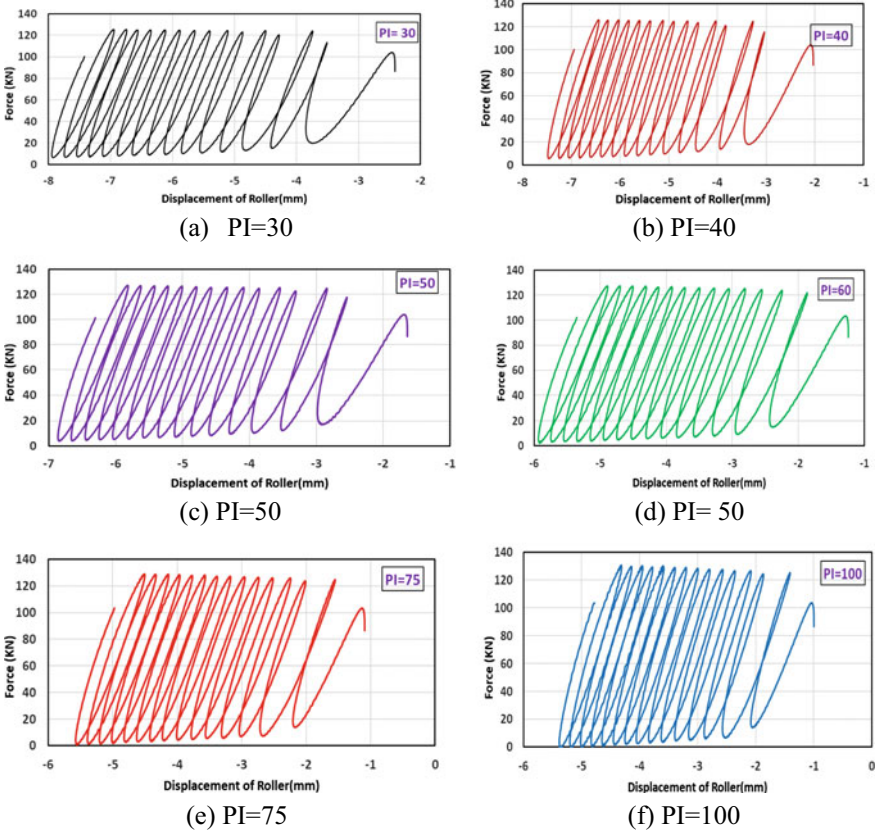


Fig. 6 Soil reaction force with gradual increment in settlement in different cases (PI = 30–100)

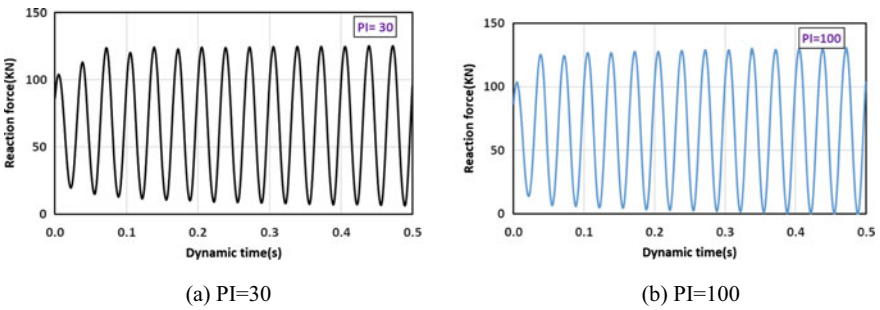
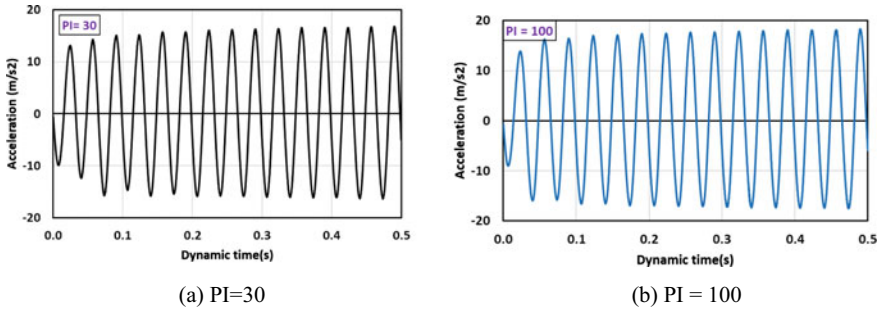


Fig. 7 Reaction force measured with time for two different cases (PI = 30 and PI = 100)





**Fig. 8** Acceleration response of the roller with time for two cases (PI = 30 and PI = 100)

125.48 kN and the minimum value was 6.28 kN. For PI = 100, the maximum reaction force measured was 130.55 kN and the minimum was 0.28 kN. Figure 8 shows the acceleration response of the roller for the given eccentric mass moment of  $m_0e_0 = 1.0 \text{ kg m}$  and  $f = 30 \text{ Hz}$ , which were used to obtain the reaction force of the soil based on Eq. (4).

## 4 Australian Field Experience

In recent years, there are increasing interests in Australia to utilize intelligent compaction technologies to improve the uniformity and quality of road construction. A number of test sites were tested in 2019. For example, Fig. 9 is a fill embankment site consisting of granular fill material (PI < 10%) located in an industrial development site near Yatala QLD. A Dynapac smooth drum roller (model CA4600) equipped with the Trimble CMV technology was used to proof roll a compacted area at the different moisture content (approximately between 8 and 10%). The IC roller operation parameters are:

- Amplitude 1 mm
- Frequency 25 Hz
- Speed 1.6–3.2 kph
- Measurement only made in forward vibration mode.

In comparison, Fig. 10 is a pavement reconstruction project of a Logan City Council road near Eagleby QLD, where a Caterpillar smooth drum roller (model CS64B) was compacting sections of thin granular pavement over high-plasticity clay material (PI > 40%). The soaked CBR value is about 1.5%, and experience shows that the subgrade area will be difficult to compact. The IC roller operation parameters are:

- Amplitude 1 mm
- Frequency 25 Hz



**Fig. 9** Photograph of low-plasticity fill site tested with IC technology



**Fig. 10** Photograph of high-plasticity subgrade site tested with IC technology

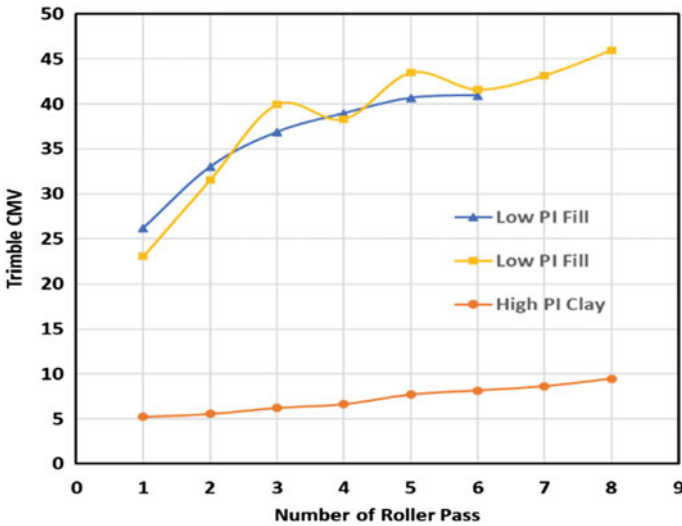


Fig. 11 Comparison of Trimble CMV values on site with different plasticity

- Speed 1.6–4.8 kph
- Measurement only made in forward vibration mode.

Figure 11 shows the compaction curves collected at a different site (measured CMV plotted against a number of roller passes). The yellow line shows the increase in CMV for the granular fill site with moisture content at dry of optimum. Similarly, the blue line corresponds to the same granular fill site but compacted at optimum moisture content. It is noted that there is only a 1% moisture difference between the optimum and dry of optimum case; therefore, it is not unexpected that the compaction curves are very similar. The key point to note is that when the fill was wet of optimum (i.e., moisture content of 10%), the compaction curve plateau was at a CMV of 26.7 after 3 roller passes. No further compaction can be achieved using the current roller compaction setting.

The compaction curve shown in Fig. 11 is the average CMV of the designated compaction zone. For the area compacted at optimum moisture content, it has a standard deviation of 9.1 and COV of 27%. Similarly, for the area compacted dry of optimum, the standard deviation is 12.1 and COV of 36%.

On contrast, the orange line is the compaction curve for the high-plasticity clay site (field moisture content is around 34%). As the CMV is an indication of the stiffness of the underlying material, it makes sense that the wet clay material has a much lower in situ stiffness (i.e., higher deformation measured by the onboard accelerometer) than the granular fill material. It is speculated that if the clay is exposed for a prolonged period (e.g. after a long drought period), the compaction curve for the high plasticity clay material will be different and is expected to have a steeper climb in CMV with increasing roller passes. Furthermore, the rate of increase of the high-PI material is

much lower than the granular fill material. This field observation supports the Plaxis finite element model presented in this paper.

## 5 Conclusions

Three-dimensional finite element simulation was conducted to investigate the impact of soil plasticity index (PI) on the compaction process and roller response. In this study, a layered soil was simulated, where small strain hardening soil (HSS) model was employed to consider variations of soil stiffness with shear strain as well as soil plastic deformations as a result of exceeding the yield stress. The model captured the nonlinear roller–soil interaction for both large and small strain conditions. The interaction between the soil and roller was captured to study the attained settlement and acceleration response of the roller. Impacts of soil plasticity index were captured by altering the backbone curves as a function of PI as recommended by Vucetic and Dobry [8] by adjusting the threshold shear strain  $\gamma_{0.7}$ , which is an input model parameter. Maximum permanent deformation was observed for the soil with the lowest adopted PI (i.e. 30) which was 4.29 mm. Furthermore, while the PI was increased from 30 to 100 and keeping all other parameters constant, a gradual decrease in damping of the roller–soil system was observed. Following a nonlinear trend, 3.66 mm of permanent settlement was observed for the soil with PI = 100. It was evident that total settlement attained due to vibratory compaction was more for the soils with lower PI since they could deform easier at the low-strain loading conditions. On the other hand, higher plasticity soils could absorb more strains internally before undergoing permanent deformations.

The numerical simulations attempted to capture the nature of compaction work on the site in which the soil undergoes both elastic and plastic deformations. This simulation clearly shows that there is a significant impact of soil plasticity in the compaction process. Further, this research will also provide a basis to perform further research in this topic related to intelligent compaction, recommending that soil plasticity index can be considered as a factor in interpreting the results or optimizing the intelligent compaction procedure. Indeed, field study to assess the impacts of soil plasticity index on roller response to validate the findings of this study is highly recommended.

## References

1. Van Susante PJ, Mooney MA (2008) Capturing nonlinear vibratory roller compactor behavior through lumped parameter modeling. *J Eng Mech* 134(8):684–693
2. Sanstrom A, Geodynamik A (1994) Numerical simulation of vibratory roller on cohesion less soil
3. Mooney M, Rinehart RV, Facas NW, Musimbi OM, White DJ, Vennapusa PKR (2010) Intelligent soil compaction systems. NCHRP

4. Meehan CL, Tehrani FS (2011) A comparison of simultaneously recorded machine drive power and compactometer measurements. *Geotech Testing J* 34 (2011)
5. Fatahi B, Van Nguyen Q, Xu R, Sun W (2018) Three-Dimensional response of neighboring buildings sitting on pile foundations to seismic pounding. *Int J Geomech* 18(4):1–25. [https://doi.org/10.1061/\(ASCE\)GM.1943-5622.0001093](https://doi.org/10.1061/(ASCE)GM.1943-5622.0001093)
6. Ho L, Fatahi B (2016) One-Dimensional consolidation analysis of unsaturated soils subjected to time-dependent loading. *Int J Geomech* 16(2):1–19. [https://doi.org/10.1061/\(ASCE\)GM.1943-5622.0000504](https://doi.org/10.1061/(ASCE)GM.1943-5622.0000504)
7. ASTM International (2002) Standard test methods for liquid limit, plastic limit, and plasticity index of soils. In: *Erosion and sediment control technology standards*, pp 80–93
8. Vucetic M, Dobry R (1991) Effect of soil plasticity on cyclic response. *J Geotech Eng* 117(1):89–107
9. Kenneally B, Musimbi OM, Wang J, Mooney MA (2015) Finite element analysis of vibratory roller response on layered soil systems. *Comput Geotech* 67:73–82
10. Surarak C, Likitlersuang S, Wanatowski D, Balasubramaniam A, Oh E, Guan H (2012) Stiffness and strength parameters for hardening soil model of soft and stiff Bangkok clays. *Soils Found* 52(4):682–697
11. Herold A, Von Wolfersdorff P-A (2009) The use of hardening soil model with small-strain stiffness for serviceability limit state analyses of GRE structures. In: *GIGSA GeoAfrica conference*, Cape Town, pp 1–10
12. Brinkgreve R, Kumarswamy S, Swolfs W, Foria F (2017) *Plaxis 2017*. Delft, Netherlands
13. Hardin BO, Drnevich VP (1972) Shear modulus and damping in soils: design equations and curves. In: *Proc ASCE: J Soil Mech Found Div* 98(SM7):667–692
14. Santos J, Correia A (2001) Reference threshold shear strain of soil. Its application to obtain a unique strain-dependent shear modulus curve for soil
15. Möller SC (2006) Tunnel induced settlements and structural forces in linings. *Institute für Geotechnik, Universität Stuttgart, Stuttgart, Germany*, pp 108–125
16. Aghayarzadeh M, Khabbaz H, Fatahi B, Terzaghi S (2020) Interpretation of dynamic pile load testing for open-ended tubular piles using finite-element method. *Int J Geomech* 20(2)

# De-icing Test of the Externally Heated Geothermal Bridge in Texas



Omid Habibzadeh-Bigdarvish , Teng Li , Gang Lei , Aritra Banerjee , Xinbao Yu , and Anand J. Puppala 

**Abstract** In recent years, a geothermal heat pump de-icing system (GHDS) has been introduced as an alternative for conventional snow and ice removal systems (CSRS). Application of the CSRS for bridges highly prone to ice formation is not a satisfactory solution as it has a negative impact on the environment, bridge deck condition, motorist safety, and travel time. Although GHDS has proved to be a sufficient and feasible solution, it is only applicable to new bridges. However, a new method of GHDS has been developed which utilizes an external hydronic pipe attached to the bottom surface of the bridge deck and is applicable even for existing bridges. In this study, the performance of the external hydronic heating system, installed and tested on the full-scale mock-up bridge deck, was investigated in Texas. The system has experienced several cold events and de-icing tests, in which it was successful in maintaining the surface temperature above freezing. However, the results show the system is capable of de-icing the bridge deck and provide an ice-free surface. In order to enhance the de-icing operation, the system requires about 8 h of preheating; however, less time is required during mild events. Furthermore, the system is energy-efficient with a coefficient of performance (COP) of more than 4.

**Keywords** Externally heated bridge deck · Geothermal heat pump system · Bridge deck de-icing · Snow melting · De-icing system · Geothermal energy

---

O. Habibzadeh-Bigdarvish · T. Li · G. Lei · X. Yu (✉)  
Department of Civil Engineering, University of Texas at Arlington, Arlington, TX 76019, USA  
e-mail: [xinbao@uta.edu](mailto:xinbao@uta.edu)

A. Banerjee  
Assistant Professor, Department of Civil and Environmental Engineering, University of Delaware,  
Newark, DE 19716, USA

Formerly Research Scientist, University of Texas at Arlington Research Institute, Fort Worth, TX,  
USA

A. J. Puppala  
A.P. and Florence Wiley Chair Professor, Zachry Department of Civil and Environmental  
Engineering, Texas A&M University, College Station, TX 77843, USA



## 1 Introduction

Approximately, 70% of the US population and transportation network are affected by snowy weather and receive more than 5 in. average snowfall annually [1]. Bridges are the key elements of the transportation network negatively affected by severe winter weather. De-icing the bridge deck surface is critical to ensure the safety and mobility of the motorist. The conventional snow and ice removal system (CSRS) uses the de-icing chemical, such as de-icing salt, which is not only corrosive to the bridges but also provokes environmental issues. It also has proven to be insufficient in minimizing traffic delays and safety issues [2, 3]. However, a new method has been proposed for bridge deck de-icing and snow melting, which can prevent the aforementioned problems.

Geothermal energy is a green and renewable source of energy and a reliable alternative for fossil fuels. The geothermal energy is harvested through the application of ground loop heat exchangers or energy geostructures (e.g., foundations, diaphragm walls, tunnel liners, or anchors) and has been used for different heating and cooling purposes [4–9]. One application of geothermal energy is for snow melting or de-icing the bridge deck. Thus, a geothermal heat pump de-icing system (GHDS) was developed, which utilizes geothermal energy as a reliable and renewable source of energy. In this system, the heat carrier fluid, mostly water-based antifreeze solution, is circulated between the ground loop heat exchanger (GLHE) and hydronic heating loops embedded in the bridge deck. Moreover, the heat pump is employed in the system to help the heat carrier fluid reach the ideal temperature appropriate for melting snow and ice on the surface. Also, the life-cycle cost–benefit analysis (LCCBA) of this system indicated that its application is economically viable for the bridges with a minimum annual daily traffic volume of 7000 vehicles, and benefit to cost ratio (BCR) of 2.6 can be achieved for the 50 years life-cycle and daily traffic volume of 24,000 vehicles [3].

The conventional hydronic heating systems are developed based on the hydronic loops embedded in the bridge deck concrete during the construction of the new bridge and have been studied by different research groups [10–14]. However, as the majority of existing bridges are also in need of de-icing, externally heating hydronic pipes are developed for geothermal heating of the bridge deck. The hydronic loops are attached to the bottom surface of the bridge deck and covered with a sufficient layer of insulation material [15]. In recent years, the Texas Department of Transportation (TxDOT) has investigated the implementation of this system on Texas bridges [16]. However, the main objective of the research was to develop a system that is not only limited to new bridges. Preliminary studies of the externally heated geothermal bridge deck were carried out using a finite element model, and their results showed more heating time in comparison with the internal heating system is required. The proposed system can successfully de-ice the bridge deck in a mild winter weather condition [17]. In another research, the feasibility of this system was tested on a lab-scale bridge deck in the environmental chamber; the system performance was tested on various conditions, including room temperature as low as 40 °F. This study provides detailed

information on system performance as well as the empirical prediction equation to estimate deck temperature at given ambient and supplied heating fluid temperatures [15].

However, it is essential to investigate the feasibility and performance of the externally heated geothermal bridge deck in the actual winter weather conditions. In this study, the process of design and construction of the full-scale mock-up of the externally heated geothermal bridge deck in Texas, USA, is demonstrated, and the results of the system operation during a severe cold event are discussed.

## 2 Design and Construction

### 2.1 Test Site Conditions

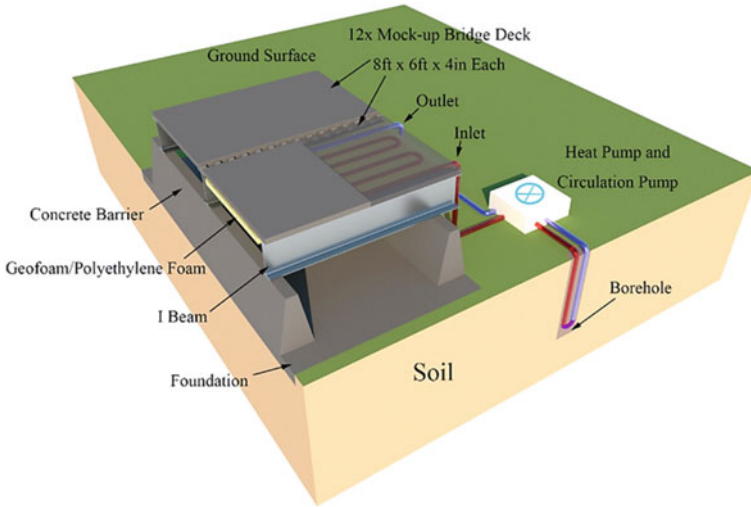
The mock-up of the externally heated bridge deck was constructed in the DFW metroplex in Texas, USA. The test site has a humid subtropical climate characterized by moderate rainfall, mild temperatures, and abundant sunshine [18]. Although the region is familiar with mild winters, several snowstorms in recent years were experienced, such as the snowstorm on March 4–5, 2015, which was the fourth-largest ever recorded in a 24-h period during the month of March in the region. Over a period of two days, 3.5 in. of snowfall was recorded, and the average ambient temperature during snowfall was recorded around 28 °F. Moreover, the subsurface investigation showed the site has relatively uniform soil layers, including sandy clay with alternating sand/gravel seams covering the top 40 ft. which is followed by a limestone layer. The boring logs stop at 60 ft. Based on local knowledge of the region, it is estimated that limestone extends up to a depth, which is of interest to the study. The groundwater table was encountered at 15 ft. below ground surface at the time of drilling. The undisturbed temperature of the soil also was observed to be about 70.5 °F.

### 2.2 Design of the Heated Deck and GLHE

**Bridge deck.** The dimensions of the whole bridge slabs are designed 16 ft. × 36 ft. including 12 standard PCP panels. However, only a section of the bridge with 16 ft. × 24 ft. dimension was assigned for the application of the heating system. The remaining portion was considered as the control section, which would aid in comparing the efficiency of the heating system. Figure 1 shows the 3D model of the whole system.

The mock-up bridge deck consists of three zones: an external heating zone (i.e., hydronic pipes are attached to the bottom surface), an internal heating zone (i.e., hydronic pipes are embedded in the bridge deck concrete), and a control zone. Besides





**Fig. 1** 3D model of the mock-up geothermal bridge design

the external heating system, which is the focus of this project, the internal heating system was also constructed to be tested for comparison purposes. Moreover, the end section of the bridge deck was also considered as a control area with no heating. The hydronic loops at the bridge deck consisted of 0.5 in. internal diameter polyethylene (PEX) pipe with an 8 in. centerline spacing.

**Design heat flux.** Geothermal snow-melting systems were designed to provide sufficient heat flux to the bridge deck surface. The required heat flux at the bridge deck surface is determined as the heat flux maintained at the bridge deck surface in order to prevent snow/ice formation under specified winter weather conditions. Generally, two approaches for the estimation of snow-melting heat fluxes for the mock-up bridge are utilized. The first approach is using the ASHRAE handbook. It provides the design heat flux for different cities in the USA, in which Amarillo is the only city from the state of Texas [19]. It is assumed that the bridge in this study is located in Amarillo, Texas, and from the ASHRAE Handbook the design heat flux corresponding to a snow-free area ratio of 0.5 and 95% reliability is chosen as 108 Btu/hr.ft<sup>2</sup> representing an average case [19]. In another method, Chapman and Katurnich [20] derived a general equation (Eq. 1) for computing steady-state energy balance for required total heat flux ( $q_o$ ) at the upper surface of a snow-melting slab during a snowfall [20]. Based on the equation, there are four environmental factors that determine the heating requirement for snow melting: rate of snowfall, air temperature, relative humidity, and wind velocity.

$$q_o = q_s + q_m + A_r(q_h + q_e) \quad (1)$$

where  $q_o$  is the heat flux required at the snow-melting surface in Btu/hr.ft<sup>2</sup>;  $q_s$  is the sensible heat flux in Btu/hr.ft<sup>2</sup>;  $q_m$  is the latent heat flux in Btu/hr.ft<sup>2</sup>;  $A_r$  is the snow-free area ratio, dimensionless;  $q_h$  is the convective and radioactive heat flux from the snow-free surface in Btu/hr.ft<sup>2</sup>;  $q_e$  is heat flux of evaporation in Btu/hr.ft<sup>2</sup>.

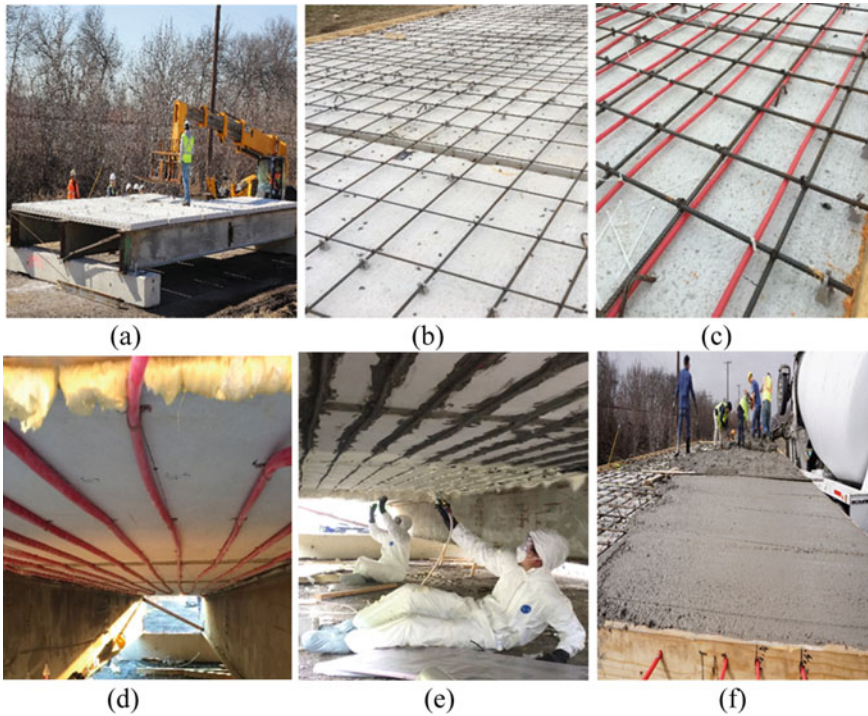
However, the second approach is using Eq. 1 in which the snowstorm at DFW in March 2015 is considered as the scenario representing an extreme case; the total required heat flux for this snowstorm is calculated as 342.8 Btu/hr.ft<sup>2</sup>. Considering the weather history of the region, it is acceptable to select a moderate case for the required heat flux. However, the required heat flux of 108 Btu/hr.ft<sup>2</sup>, corresponding to the average case scenario, is chosen to design the geothermal system upon that. Moreover, the total heating load for the heated area is calculated as 20,736 Btu/hr.

**Ground loop heat exchanger (GLHE).** In this project, GLHEPRO software has been utilized as a strong tool for the calculation of GLHE size [21]. The software is developed based on the g-functions method presented by Eskilson [22]. The design parameters including minimum and maximum entering water temperatures, undisturbed soil temperature, soil and grout thermal conductivity, and diameter of the pipe are important to the proper design of the GLHE. However, considering the total heating load, the weather history of the region and consulting with local contractors, a single borehole of 435 ft. (from ground level) deep and 5.5 in diameter was designed to be sufficient for the system. Moreover, a 3-ton geothermal heat pump, 4 circulation pumps, and an expansion tank are assigned to work in the geothermal system.

### ***2.3 Construction of Mock-up Bridge and De-icing System***

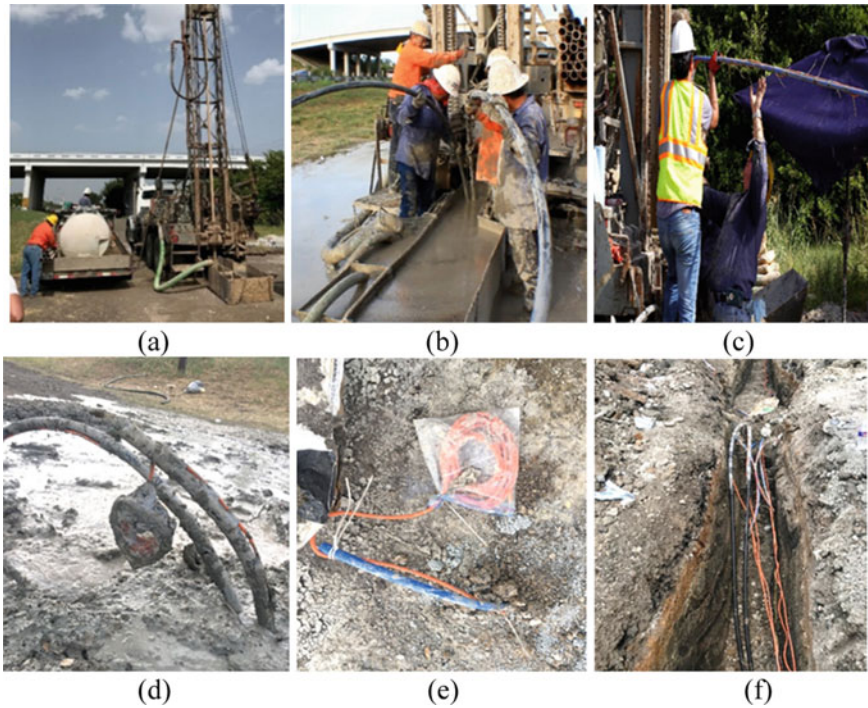
The construction process of the mock-up bridge and the geothermal de-icing system is shown in Fig. 2. The model bridge was constructed during February and March of 2018. Following the bridge deck setup, the hydronic loops on both the internal and external heating zones were installed. The internal heating loops installation followed the conventional method, and they were attached to the rebar and buried by casting concrete on the deck. However, the external heating pipes were first attached to the bottom surface of the externally heated zone using two-hole straps, and then the pipes were covered with cement paste to increase the thermal contact between pipe and concrete. Finally, thermal insulation foam was applied on the whole surface to prevent heat loss in the bottom direction. Moreover, control valves were installed to control the operation mode and the heated section of the bridge deck.

Besides one geothermal borehole, GLHE construction work involves five temperature monitoring boreholes (TMB). TMBs were drilled and equipped with temperature sensors to monitor the temperature field at different distances with respect to the geothermal borehole. In order to connect the GLHE to the control room, a trench with a 5 ft. depth was excavated. 1.25 in. header pipes were connected to the GLHE using socket fusion and sensor cables were laid down on the bottom of the trench and finally backfilled with the excavated soil. Due to the vulnerability of sensor cables,



**Fig. 2** Construction stages of the bridge deck: **a** setting up the PCP panels on the I-beams; **b** tying rebar on the PCP panels; **c** installation of the internal heating pipes; **d** installation of the external heating pipes; **e** external heating pipes covered with cement paste and polyurethane foam on the deck bottom is applied; **f** casting of 4" thick concrete on the deck

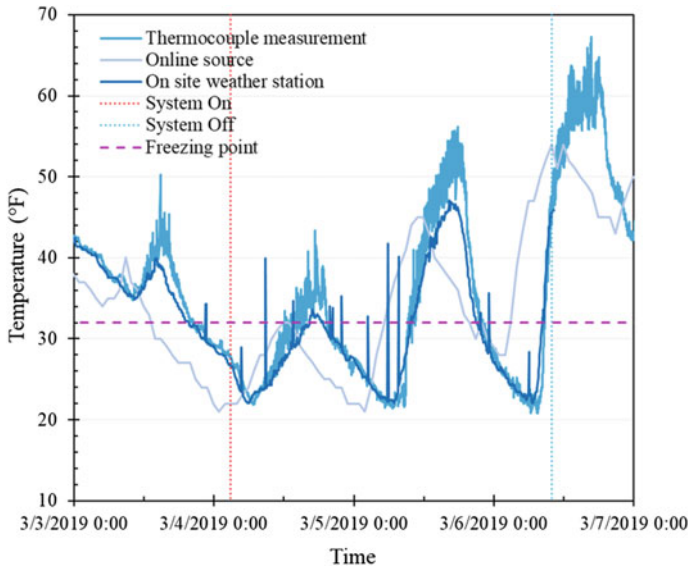
the backfilling operation was performed with extreme caution. Lastly, a control room was built to host the system's main components, including one heat pump, two flow centers, four circulating pumps, and one expansion tank. In fact, in the control room, the pipes of the bridge side were connected to the ground side. In addition, a bypass was designed for the heat pump to operate the system in two modes: full-load operation and bypass operation. In the full-load operation mode, the control valves at the heat pump are closed and the flow goes through the heat pump. In the full-load operation mode, the geothermal heat pump is active, while in bypass mode, the geothermal heat pump is off, and the heat carrier fluid is directly circulating through the bypass. Flow meters are also installed for measuring the flow rate in each side. Finally, after all pipes connections were performed, the system was flushed with 20% propylene glycol solution and tested for any possible leakage (Fig. 3).



**Fig. 3** Construction stages of the GLHE: **a** drilling rig on site; **b** insertion of ground loop; **c** insertion of TMB’s PEX pipe; **d** final stage of geothermal borehole; **e** final stage of temperature monitoring borehole; **f** installation of the pipes and cables in the trench

### 3 System Operation and Performance

The geothermal de-icing system was experimented on in several cold events of the 2018–2019 winter. The goal of all tests was to melt snow/ice on the surface of the bridge deck or maintain the surface temperature above freezing throughout a cold front. As the system was designed to operate in different modes based on the operational condition of the system, the geothermal heat pump was allowed to switch off when the cold front was mild. Moreover, the heated zones, i.e., the internally heated zone and externally heated zone, could be selected for operation using the control valve. However, as the focus of winter tests were on the externally heated zones, most of the tests were operated on this zone by closing the control valve of the internally heated zone. The results associated with the system performance during the coldest event which was experienced by the system are discussed in this study. In this specific event, the system was operated from 3/4/19 2:50 AM through 3/6/19 9:53 AM in full-load mode in the externally heated zone. Moreover, the bridge experienced 7 h of freezing temperatures before the system was turned on the weather conditions were closely monitored and collected from different sources,



**Fig. 4** Ambient temperature measurement from different sources

namely thermocouple measurements on site, weather station data from the site, and online weather data [23]. The monitored weather data during the test is shown in Fig. 4. During the cold front, the de-icing system experienced a total of 36.1 h of freezing temperatures. The average of the freezing ambient temperature was 25.7 °F, and the minimum ambient temperature was recorded as 20.8 °F which was reported as the record low temperature in the past 20 years for March. Moreover, the difference between online source data and on-site measurements is due to a 15-mile distance of the online source station from the test site.

Figure 5 presents the inlet and outlet temperature of the hydronic heating pipes during the test. However, due to large fluctuation of the inlet and outlet temperature and to better illustrate the results, the hourly average of the inlet and outlet temperature are also plotted in the same Fig. 5. The inlet temperature and outlet temperature follow the same trend during the test and show a slight variation due to ambient temperature changes. The monitoring data illustrates that the bridge deck was heated with heating fluid with an average temperature of 108 °F at the inlet; the outlet temperature was recorded as 103 °F as the average temperature, with approximately 5 °F temperature drop.

Figure 6 compares the temperature variation of the heated zone and the non-heated zone, along with ambient temperature data. The temperature data for both the externally heated zone and internally heated zone (not active, therefore, referred to as a non-heated zone) are obtained from the sensor at 1 in below the surface in the center of each zone. However, it should be noticed that the difference between temperature in the heated and non-heated zone before the test began is due to the system operation in the previous test in which the system was operating in bypass mode for the external



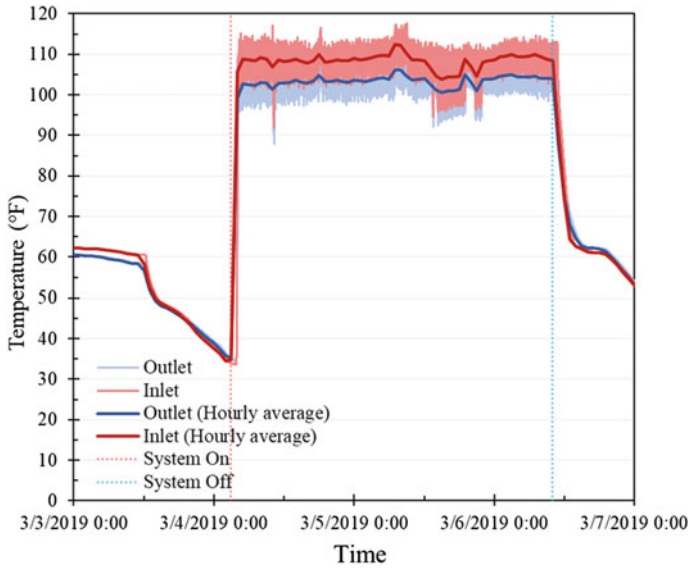


Fig. 5 Inlet and outlet temperature of the bridge deck hydronic pipes

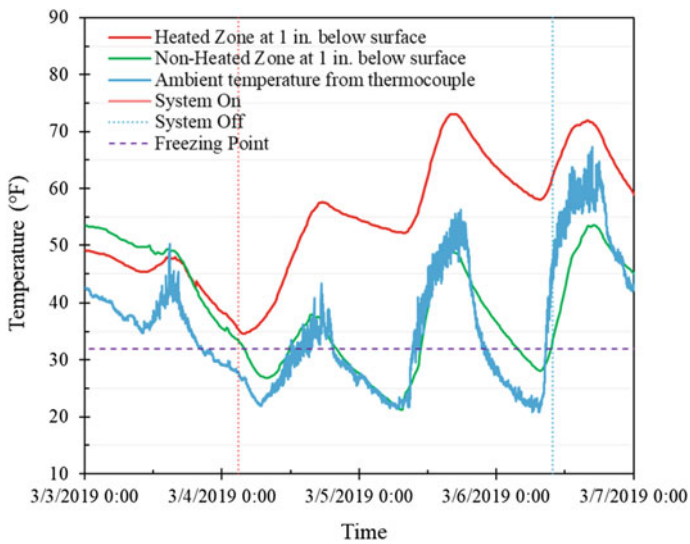


Fig. 6 Heated and non-heated zone temperature variation

and internal heated sections and ended at 3/3/19, 11:17 AM. As mentioned earlier, the bridge experienced 7 h of freezing temperature before the system was switched on for this test. The idling gap of the geothermal system between the previous and this test is about 15.5 h. The heat stored from the previous test gradually dissipated and the bridge was close to being in equilibrium with the ambient temperature before the start of the system. However, after the onset of the geothermal heat pump, the temperature on the heated zone starts to increase and follows a different trend concerning the non-heated zone. The temperature in the non-heated zone still closely matches the ambient temperature, which also indicates the validity of the monitored data. In the end, when the test was over, and the system turned off, the temperature in the heated zone drops and slowly merges to the non-heated zone temperature and both follow the ambient temperature variation. The on-site observation proved the 8 h of idling time was required when the bridge deck of the control zone was in close equilibrium with the ambient temperature. The hours required to rise the bridge deck surface temperature to 32 °F are considered as the time required for preheating. It is worthwhile to mention that the recorded temperatures in Fig. 6 belong to 1 in below the surface, and it has a slightly higher temperature with respect to exact surface temperature on the heated zone. The minimum of 32.5 °F on the heated zone is recorded slightly after the test began in the early morning of 3/4/2019 when the air temperature reached 22 °F. Following about 24 h of operation, the heated surface temperature achieved 52 °F, while air and non-heated surface temperatures are dropped to about 21.5 °F. However, after approximately 48 h of operation, the heated surface temperature is reached 58 °F, while air and the non-heated surface temperature recorded as 21.5 °F and 28 °F, respectively.

Moreover, as no precipitation was forecasted and experienced during the test, the project team decided to make snow on the bridge deck surface using a snowmaking gun about 24 h after system operation. Although the ambient temperature was suitable for making snow, the snowmaking was not successful due to the high humidity greater than 60%. The water drops became ice pellets, and a uniform ice layer was observed in the non-heated zone. In the end, it was observed that the surface of the non-heated zone was fully covered with ice while the heated zone was completely ice-free (Fig. 7).



**Fig. 7** Final stage of the de-icing test, the ice-free surface in the heated zone while the non-heated zone is fully covered with ice

The power consumption of the entire system was monitored to study the geothermal system performance. As the GHDS was tested under the heating mode; therefore, it is appropriate to evaluate the energy efficiency of the system using the coefficient of performance (COP), which is given as:

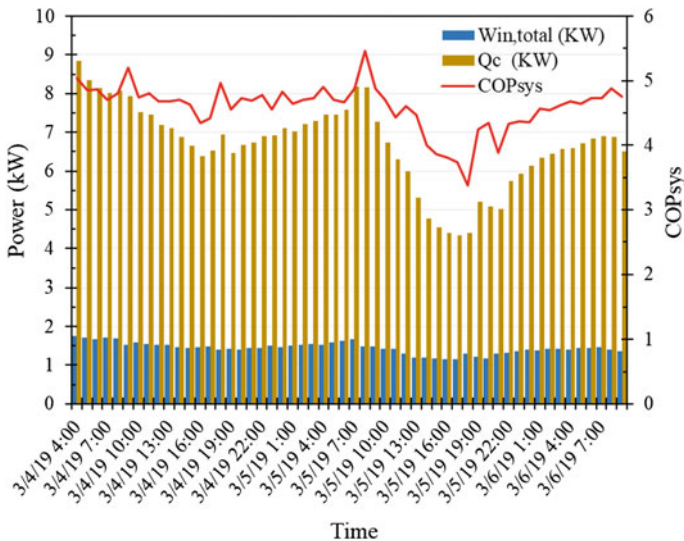
$$COP_{sys} = \frac{\dot{Q}_c}{\dot{W}_{in,total}} \tag{2}$$

$$\dot{Q}_c = \dot{m}C_p(T_{c,o} - T_{c,i}) \tag{3}$$

$$\dot{W}_{in,total} = \dot{W}_{hp} + \dot{W}_p \tag{4}$$

where  $\dot{Q}_c$  and  $\dot{W}_{in,total}$  are the thermal energy output produced by the heat pump and total input power, respectively. The mass flow rate is denoted by  $\dot{m}$ , and  $C_p$ ,  $T_{c,o}$ , and  $T_{c,i}$  are the specific heat of the fluid, outlet, and inlet fluid temperatures of condenser, respectively. Moreover,  $\dot{W}_{hp}$  and  $\dot{W}_p$  represent the electrical power consumed by the heat pump unit and the pumps, respectively.

Figure 8 shows the monitored power consumption of the whole system and compares it with the thermal energy output of the system. During the 54 h of operation, the average system power consumption was 1.4 kW per hour while on average the system delivered about 6.6 kW of energy to the bridge deck per hour. Moreover, the results indicate the average COP of this test was 4.6 which shows the efficient performance of the system.



**Fig. 8** Comparison of the system power consumption, the thermal energy output of the system, and coefficient of performance (COP)



## 4 Conclusion

This research discusses the system performance of the mock-up of the externally heated geothermal bridge deck in a severe cold event during the winter of 2018–2019 in Texas. In this event, the de-icing system experienced a total of 36.1 h of freezing temperatures with the minimum ambient temperature recorded as 20.8 °F. The outcome of the test proves the feasibility of the externally heated hydronic system in maintaining the surface temperature of the heated zone above freezing during the cold front and de-icing test. The geothermal heat pump was operated with an output temperature of 104–112 °F. The results show that the system requires about 8 h of preheating for de-icing the bridge deck, which allows the surface to reach 32 °F. A de-icing test was performed after 24 h of preheating, and no ice formulation was observed on the heated area during the test. Moreover, the system could produce heat energy more than four times the total electricity consumption of the whole system.

**Acknowledgements** The authors appreciate the financial support provided for this study by the Texas Department of Transportation (TxDOT). The help from the research supervisor, Sonya Badgley; James Kuhr; and TxDOT engineers, Richard Williammee and Justin Thomey is also acknowledged. We thank Mark Hurley, Sunil Adhikari, Rahul Yadav, Hiramani Raj Chimauriya, and Samrat Raut for assistance with the construction of the mock-up bridge. Special thanks to the Fort Worth maintenance group and Tom Weatherspoon for the machinery help.

## References

1. FHWA (Federal Highway Administration) (2017) Snow and ice, road weather management program. [http://ops.fhwa.dot.gov/weather/weather\\_events/snow\\_ice.htm](http://ops.fhwa.dot.gov/weather/weather_events/snow_ice.htm)
2. Fischel M (2001) Evaluation of selected deicers based on a review of the literature. The SeaCrest Group. Louisville, CO. Report Number CDOT-DTD
3. Habibzadeh-Bigdarvish O, Yu X, Lei G, Li T, Puppala AJ (2019) Life-cycle cost-benefit analysis of bridge deck de-icing using geothermal heat pump system: a case study of North Texas. *Sustain Cities Soc* 47:101492
4. Brandl H (2006) Energy foundations and other thermo-active ground structures. *Geotechnique* 56(2):81–122
5. Zhang G, Xia C, Sun M, Zou Y, Xiao S (2013) A new model and analytical solution for the heat conduction of tunnel lining ground heat exchangers. *Cold Reg Sci Technol* 88:59–66
6. Nam Y, Chae H-B (2014) Numerical simulation for the optimum design of ground source heat pump system using building foundation as horizontal heat exchanger. *Energy* 73:933–942
7. Mimouni T, Dupray F, Laloui L (2014) Estimating the geothermal potential of heat-exchanger anchors on a cut-and-cover tunnel. *Geothermics* 51:380–387
8. Sterpi D, Angelotti A, Habibzadeh-Bigdarvish O, Jalili D (2018) Assessment of thermal behaviour of thermo-active diaphragm walls based on monitoring data. *J Rock Mech Geotech Eng*
9. Sterpi D, Angelotti A, Habibzadeh Bigdarvish O, Jalili D (2018) Heat transfer process in a thermo-active diaphragm wall from monitoring data and numerical modelling. In: 9th European conference on numerical methods in geotechnical engineering, vol 1, pp 731–736
10. Lund JW (1999) Reconstruction of a pavement geothermal de-icing system. *Geo-Heat Cent*

11. Minsk LD (1999) Heated bridge technology-report on ISTEA Sec. 6005 Program,” United States. Federal Highway Administration
12. Spitler JD, Ramamoorthy M (2000) Bridge deck de-icing using geothermal heat pumps. In: Proceedings of the fourth international heat pumps in cold climates conference, pp 17–18
13. Balbay A, Esen M (2010) Experimental investigation of using ground source heat pump system for snow melting on pavements and bridge decks. *Sci Res Essays* 5(24):3955–3966
14. Ghasemi-Fare O, et al (2015) A feasibility study of bridge deck de-icing using geothermal energy. Mid-Atlantic Universities Transportation Center
15. Yu X, Hurley MT, Li T, Lei G, Pedarla A, Puppala AJ (2019) Experimental feasibility study of a new attached hydronic loop design for geothermal heating of bridge decks. *Appl Therm Eng*, 114507
16. Yu X, Puppala AJ, Zhang N (2017) Use of geothermal energy for deicing approach pavement slabs and bridge decks, Phase I, Texas. Department of Transportation. Research and Technology Implementation Office
17. Li T, Lei G, Yu X, Zhang N, Puppala AJ (2018) Numerical feasibility study of an externally heated geothermal bridge deck. *IFCEE* 2018:758–767
18. Koppen W (1936) *Das geographische system der klimat*, Handb. der klimatologie, p 46
19. American Society of Heating (2015), 2015 ASHRAE handbook: heating, ventilating, and air-conditioning applications, Inch—Pound Edition
20. Chapman WP, Katunich S (1956) Heat requirements of snow melting systems. *ASHAE Trans* 62:359–372
21. Spitler JD (2000) GLHEPRO-a design tool for commercial building ground loop heat exchangers. In: Proceedings of the fourth international heat pumps in cold climates conference
22. Eskilson P (1987) Thermal analysis of heat extraction boreholes
23. Weather history for Arlington, TX, November 2018 to March 2019. Weather Underground, The Weather Company. <https://www.wunderground.com/history>

**Climatic Effects on Geomaterial Behavior  
Related to Mechanics of Unsaturated  
Transportation Foundations**

# Effect of Relative Density on the Drained Seismic Compression of Unsaturated Backfills



Wenyong Rong and John S. McCartney

**Abstract** It is critical to accurately predict the seismic compression of backfill soils supporting bridge decks, pavements, or railways as small backfill settlements may have substantial impacts on the performance of these overlying transportation systems. Although several studies have evaluated the seismic compression of loose unsaturated soils, there has not been significant focus on the seismic compression of denser soils. This study presents the results from series of strain-controlled cyclic simple shear tests performed on unsaturated sand specimens having different initial relative densities and initial matric suctions representative of near-surface backfills. Although the seismic loading process may involve rapid, undrained shearing, the cyclic simple shear tests were performed in drained conditions with a slow shearing rate to isolate the effect of matric suction. The results showed that soils with higher initial suctions (or lower initial degrees of saturation) experienced smaller volumetric strains, but the effect of suction (or degree of saturation) decreases as the relative density increases.

**Keywords** Seismic compression · Unsaturated backfills · Matric suction · Relative density

## 1 Introduction

Seismic compression is defined as the accrual of contractive volumetric strains in soils during earthquake shaking and has been recognized as a major cause of seismically induced damage to civil infrastructure [12], i.e., transportation systems. The state-of-the-practice method used to predict contractive volumetric strains of soils during earthquake involves use of a chart developed by Tokimatsu and Seed [13] correlating

---

W. Rong · J. S. McCartney (✉)  
Department of Structural Engineering, University of California, San Diego, La Jolla, CA  
92093-0085, USA  
e-mail: [mccartney@ucsd.edu](mailto:mccartney@ucsd.edu)

W. Rong  
e-mail: [w1rong@eng.ucsd.edu](mailto:w1rong@eng.ucsd.edu)

volumetric strain with cyclic stress ratio and corrected standard penetration blow count. This chart was developed based solely on results from cyclic simple shear tests on saturated and dry quartz sands from Silver and Seed [11]. However, natural soil layers near the ground surface are often above the water table and may be unsaturated, especially for the compacted backfill soil layers in engineered transportation systems, i.e., roadways, retaining walls and slopes, bridge abutment, etc., which are designed with the intention of remaining in unsaturated conditions by provision of adequate drainage. In earthquake-prone areas, it is of great significance to predict the potential maximum seismically induced settlements of backfills as small settlements may have a significant effect on the normal operation of these transportation systems.

The behavior of unsaturated backfill soils during earthquake shaking is uncertain. At one extreme, liquefaction without volume change is expected in fully saturated soils, while at the other extreme, volumetric contraction is expected in dry soils. Several experimental studies have characterized the seismic compression of unsaturated sand at various relative densities under undrained shearing or without consideration of drainage conditions [3–6, 9, 10, 14, 16]. While some of these studies did not observe a clear trend in the volumetric strain with matric suction (or degree of saturation) for a limited number of cyclic shear strain amplitudes (e.g., [3, 5, 16]), they did not control unsaturated conditions or measure changes in degree of saturation or matric suction during shearing. The lack of a clear trend may also be due to the wet tamping method used to reach different initial suctions, which might result in large uncertainties in soil structures. Although denser soils showed higher resistance to seismic compression at the same unsaturated state [3, 16], the controlling or the dominant factor affecting seismic compression of unsaturated soils has not been discussed. Unno et al. [14] and Kimoto et al. [6] performed undrained and drained cyclic triaxial tests on unsaturated soils with various levels of suction and observed volumetric contraction of dense and loose sands along with the buildup of both the pore water pressure and the pore air pressure. They observed a clear effect of the degree of saturation with liquefaction occurring in some tests on sands at higher degrees of saturation and a clear effect of relative density with denser state resulting in smaller seismic compressions. However, only two initial suctions and relative density values were evaluated, and they did not separate the effects of relative density and degree of saturation on the seismic compression as well. Le and Ghayoomi [8] observed lower seismic compressions for unsaturated specimens with higher suctions in drained cyclic simple shear test. Rong and McCartney [10] performed drained cyclic simple shear tests (constant suction) on unsaturated sands in the funicular regime and the seismic compression was observed to have a log-linear relation with matric suction, but only the relative density of 0.45 was evaluated in these studies and the effect of relative density remains unknown. Therefore, further experimental study on seismic compression of unsaturated specimens with various initial suctions and various relative densities is needed to help understand the governing mechanisms.

To evaluate the effect of relative density on the seismic compression of unsaturated soils, a series of cyclic simple shear tests on unsaturated specimens with four different initial suctions at each of the three relative densities were performed in

this study, representing the general compaction states of near-surface backfills in transportation systems. Although the seismic loading process may involve rapid, undrained shearing, the cyclic simple shear tests were performed in drained conditions with a slow shearing rate to provide a worst-case scenario on the measured seismic compression.

## 2 Effective Stress for Unsaturated Soils

Many mechanical properties of soils, i.e., the shear strength, shear modulus, and damping ratio, are fundamentally influenced by the effective stress. To extend the mechanistic framework established for saturated soils to unsaturated soils, Bishop [2] proposed the following effective stress for unsaturated soils:

$$\sigma' = (\sigma - u_a) + \chi(u_a - u_w) \quad (1)$$

where  $\sigma$  is the total normal stress on a given plane,  $u_a$  is the pore air pressure,  $u_w$  is the pore water pressure, the difference between the total normal stress and the pore air pressure represents the net normal stress, the difference between the pore air pressure and the pore water pressure is the matric suction (also denotes as  $\psi$ ), and  $\chi$  is Bishop's effective stress parameter. Many definitions of the effective stress parameter  $\chi$  have been proposed in the literature, some related to the suction and others related to the degree of saturation. Lu et al. [7] proposed a term called the suction stress  $\sigma^s$  that incorporated all interparticle forces and assumed  $\chi$  is equal to the effective saturation  $S_e$  so that the soil water retention curve (SWRC), which quantifies the relation between suction and the degree of saturation within soils, can be integrated into the definition of effective stress. Specifically, the effective saturation can be related to the suction through the van Genuchten [15] SWRC model, given as follows:

$$S_e = \left\{ \frac{1}{1 + [\alpha_{vg}(u_a - u_w)]^{N_{vg}}} \right\}^{1 - \frac{1}{N_{vg}}} \quad (2)$$

where  $\alpha_{vg}$  and  $N_{vg}$  are the van Genuchten [15] SWRC fitting parameters. The effective stress definition of Lu et al. [7] obtained by combining Eqs. (1) and (2) is given as follows:

$$\sigma' = (\sigma - u_a) + \left[ \frac{u_a - u_w}{\left(1 + [\alpha_{vg}(u_a - u_w)]^{N_{vg}}\right)^{1 - \frac{1}{N_{vg}}}} \right] \quad (3)$$

In this equation, the term in brackets can be referred to as the suction stress  $\sigma^s$ , and the relationship between suction stress and matric suction (or degree of saturation)

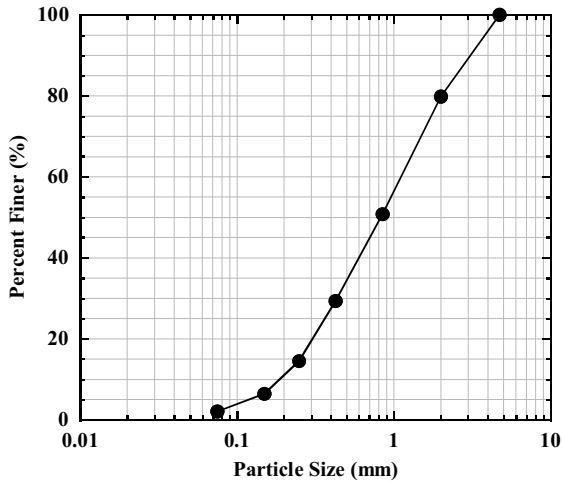
is referred to as the suction stress characteristic curve (SSCC). In this study, Eq. (3) will be used to quantify the effective stress state of unsaturated soils.

### 3 Sand Properties

The sand used in this study is classified as a well-graded sand (SW) according to the Unified Soil Classification System (USCS). The particle size distribution curve of the well-graded sand is shown in Fig. 1. The mean grain size  $D_{50}$  and the effective grain size  $D_{10}$  are 0.8 mm and 0.2 mm, respectively. The sand has a coefficient of uniformity of  $C_u = 6.1$  and a coefficient of curvature of  $C_c = 1.0$ . The specific gravity is 2.61, and the maximum and minimum void ratios are 0.853 and 0.371, respectively (Table 1).

The SWRC of the well-graded sand at different relative densities were measured using a hanging column that can apply higher suction magnitudes to the residual

**Fig. 1** Particle size distribution curve of the well-graded sand



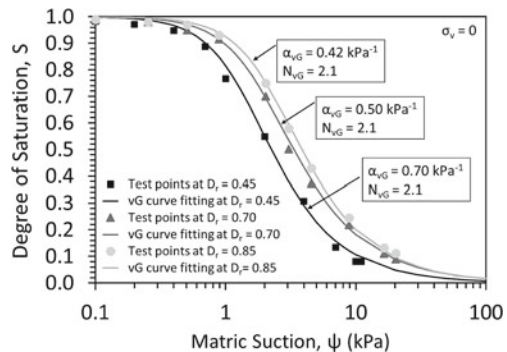
**Table 1** Summary of the basic mechanical of the well-graded sand

Parameter	Value
Specific gravity, $G_s$	2.61
Effective grain size, $D_{10}$ (mm)	0.20
Mean grain size, $D_{50}$ (mm)	0.80
Coefficient of curvature, $C_c$	1.00
Coefficient of uniformity, $C_u$	6.10
Maximum void ratio, $e_{max}$	0.853
Minimum void ratio, $e_{min}$	0.371

saturation of the sand. To determine the SWRC, a pre-determined mass of dry sand was poured at a constant rate from a funnel into a Buchner funnel having a fritted glass disk with an air-entry suction of 50 kPa at the bottom that was filled with de-aired water. It was found that a target density of 0.45 could be reached reliably without tamping, however, to reach higher initial relative densities, i.e.,  $D_r = 0.70$  and 0.85, different tamping efforts were needed. This initially saturated specimen was incrementally desaturated by applying negative water pressures ( $u_w$ ) to the hanging column while leaving the surface of the specimen open to the atmosphere (which means pore air pressure  $u_a = 0$ ). Once the outflow of water from the bottom boundary remained constant over a time between readings of 30 min, the sand specimen was considered to be at hydraulic equilibrium. Test results including the primary drying path for different relative densities are shown in Fig. 2, which also shows the fitted van Genuchten [15] SWRCs. The best-fit SWRC model parameters for the well-graded sand at different relative densities are summarized in Table 2.

The best-fit values of the parameters  $\alpha_{vG}$  and  $N_{vG}$  for the drying path were used to define the SSCCs at different relative densities, which were plotted in terms of both matric suction and degree of saturation as shown in Fig. 3a and b, respectively. As  $N_{vG}$  is slightly larger than 2.0 at all three relative densities, the SSCCs will not increase monotonically with suction [7]. Instead, the SSCCs increase with suction (or decreasing degree of saturation) up to the maximum values at intermediate matric suctions before decreasing back to zero at higher suctions.

**Fig. 2** SWRCs of the well-graded sand at different relative densities



**Table 2** van Genuchten fitting parameters of the sand at different relative densities

Relative density, $D_r$	$\alpha_{vG}$ ( $\text{kPa}^{-1}$ )	$N_{vG}$	Saturated volumetric water content, $\theta_s$	Residual volumetric water content, $\theta_r$
0.45	0.70	2.10	0.39	0
0.70	0.50	2.10	0.33	0
0.85	0.42	2.10	0.31	0



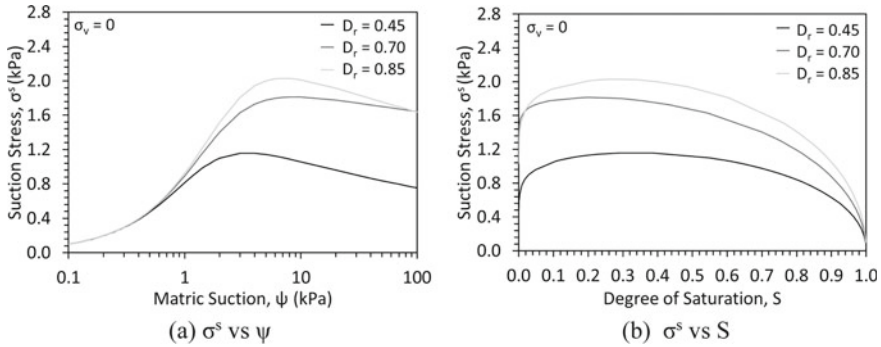


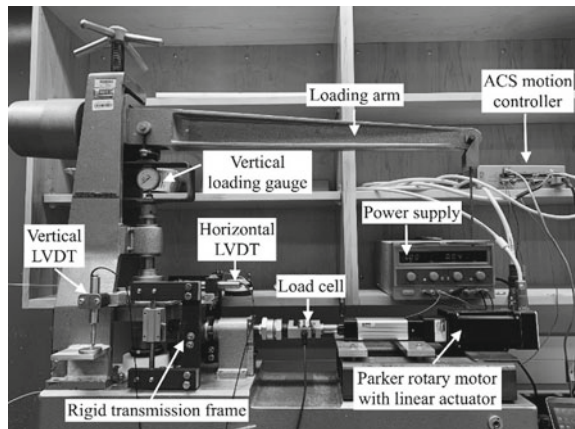
Fig. 3 SSCCs of the well-graded sand at different relative densities **a**  $\sigma^s$  versus  $\psi$ , **b**  $\sigma^s$  versus  $S$

### 4 Simple Shear Device with Suction-Saturation Control

Cyclic simple shear tests allow the principal stress axes to rotate smoothly during cyclic shearing and permit simulation of the stress-strain response of soils in a free-field soil layer due to upward horizontal seismic shear wave propagation, while permitting evaluation of the associated changes in pore water pressure and/or volume change. A monotonic simple shear apparatus manufactured by the Norwegian Geotechnical Institute (NGI) was modified to perform cyclic simple shear tests over a range of shear strain amplitudes and unsaturated conditions (different matric suctions or degrees of saturation) by incorporating a hanging column setup, details of the modification can be found in Rong and McCartney [10]. The overall view of the simple shear apparatus including different components is shown in Fig. 4.

The specimen housing designed to test unsaturated soils in the modified cyclic simple shear device is shown in Fig. 5. The top platen incorporates a coarse porous stone which facilitates air drainage while providing a rough surface to transmit shear

Fig. 4 Cyclic simple shear apparatus for unsaturated soils



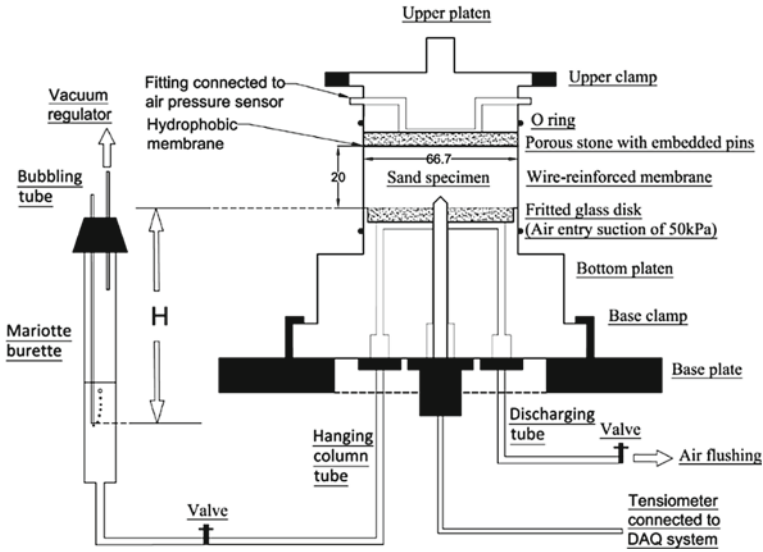


Fig. 5 Schematic view of the specimen housing used in the NGI-type apparatus

stresses to the top of the specimen. The bottom platen incorporates a high air-entry porous disk that transmits water from a hanging column consistent with ASTM D6836, which has a central port to accommodate a tensiometer (model T5 from UMS) to monitor changes in matric suction during cyclic shearing. The cylindrical specimen has a height of 20 mm and a diameter of 66.7 mm, resulting in a height to diameter ratio of  $H/D = 0.3$ , which is less than the maximum value of 0.4 set by ASTM D6528 [1]. The specimen is confined within a wire-reinforced rubber membrane manufactured by Geonor, which minimizes radial deformations of the specimen during preparation, application of vertical stresses, and cyclic shearing but allows vertical and shear deformations.

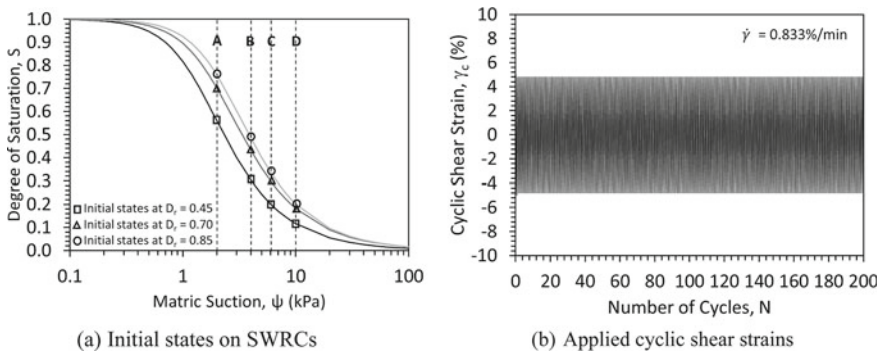
## 5 Preparation of Unsaturated Specimens with Different Relative Densities

The bottom platen of the specimen housing was first fastened on the simple shear device using the T-clamps, and T5 tensiometer was inserted through the porous glass disk and sealed into place. To prepare unsaturated test specimens with different relative densities and different initial suctions, saturated specimens at different relative densities were first prepared, and suction was applied subsequently to reach different initial suctions. Like approaches adopted in measuring the SWRCs, pre-determined mass of dry sand was poured from a funnel into the chamber surrounded by the wire-reinforced rubber membrane that was filled with de-aired water to form the

uniformly distributed saturated specimen. The target relative density of 0.45 could be reached reliably without tamping, but to reach higher relative densities of 0.70 and 0.85, the specimen was carefully compacted with different amount of energy at three layers. Saturated specimens at different relative densities were then desaturated to different target matric suctions using the hanging column. Water outflow was monitored while monitoring the tensiometer reading to confirm the initial unsaturated states. Once the reading of the tensiometer was constant and the water outflow did not change over an interval of 30 min, the unsaturated specimen is assumed to be at hydraulic equilibrium.

## 6 Testing Procedure and Testing Program

Unsaturated specimens with four initial suction values at the three relative densities, marked *A, B, C, D* as shown in Fig. 6a, were evaluated in this study so that effect of relative density on the seismic compression of unsaturated backfills in drained conditions can be analyzed. As the cyclic shearing was performed in drained conditions, the valve on the hanging column burette was kept open and suction was maintained constant while monitoring any outflow of water. Constant shear strain amplitude of 5% was applied with the same number of cycles  $N = 200$  for all tests in this study, which aims to apply sufficiently large values to result in measurable seismic compressions, as shown in Fig. 6b. A shear strain rate of 0.833%/min was chosen to ensure drainage for both the pore water and the pore air based on the matric suction measurement in preliminary testing, which led to a period of 6 min. A vertical stress of 50 kPa was applied to the top of the specimen in all tests, which is representative of a near-surface unsaturated backfill soil layer in transportation systems. Before starting the cyclic shearing test, the actual height of the specimen under the applied vertical stress was measured so that the volumetric strain during cyclic shearing can



**Fig. 6** Initial unsaturated conditions and the applied shear strains in the test, **a** initial states on SWRCs, **b** applied cyclic shear strains

**Table 3** Initial states of the unsaturated specimens

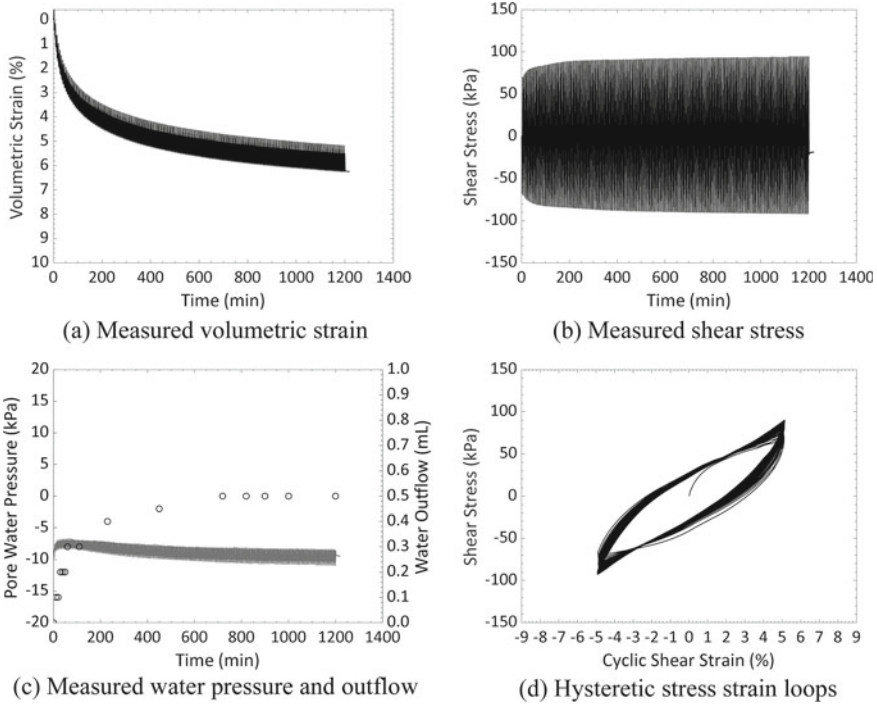
$D_r$	Specimen	$h_0$ (mm)	$\psi_0$ (kPa)	$S_0$	$w_0$	$\theta_{w0}$
0.45	A-45	20.03	2.05	0.55	0.135	0.214
	B-45	19.98	3.98	0.31	0.075	0.119
	C-45	19.85	5.94	0.20	0.050	0.079
	D-45	20.04	10.08	0.12	0.028	0.045
0.70	A-70	20.06	1.98	0.70	0.134	0.233
	B-70	19.85	3.95	0.42	0.081	0.141
	C-70	19.95	6.02	0.28	0.054	0.094
	D-70	19.94	10.10	0.17	0.032	0.055
0.85	A-85	19.89	2.05	0.75	0.129	0.233
	B-85	19.84	3.92	0.49	0.085	0.153
	C-85	19.97	6.02	0.34	0.058	0.104
	D-85	20.02	9.98	0.20	0.035	0.063

be calculated. The initial states of the unsaturated specimens, like the initial specimen height  $h_0$ , initial matrix suction  $\psi_0$ , initial degree of saturation  $S_0$ , initial gravimetric water content  $w_0$ , initial volumetric water content  $\theta_{w0}$ , are presented in Table 3.

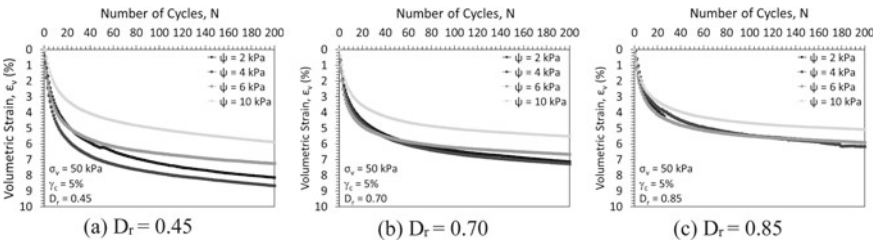
## 7 Experimental Results and Discussion

An example of the time histories of the measured variables in the test are shown in Fig. 7 for the unsaturated specimen having an initial suction of 10 kPa at the relative density of 0.70, during the application of 200 cycles of the shear strain amplitude of 5%. Volumetric contraction was observed, and it was found to gradually increase with number of cycles but with a decreased rate, as shown in Fig. 7a. As volumetric contraction occurs, the shear stress required to maintain the same shear strain amplitude gradually increases with cycles of shearing, as shown in Fig. 7b. Pore water pressure was measured directly with the T5 tensiometer at the bottom of the specimen, as shown in Fig. 7c. It was found to increase a little bit at the beginning of shearing but stabilized to the negative value of the initial suction in the subsequent loading cycles due to dissipation or redistribution of the pore water pressure. Water was observed to outflow primarily in the first 100 cycles (the first 600 min) and became stabilized subsequently, as shown in Fig. 7c as well. The hysteretic stress-strain relationship is shown in Fig. 7d.

Volumetric strains experienced by the unsaturated specimens fluctuated remarkably in each cycle due to the applied large cyclic strains. Evolutions of the medium volumetric strain in each cycle for all the specimens are shown in Fig. 8 for the three relative densities. Matric suction was observed to have a non-negligible effect at lower relative densities, especially for the specimens at  $D_r = 0.45$  as shown in Fig. 8a. The



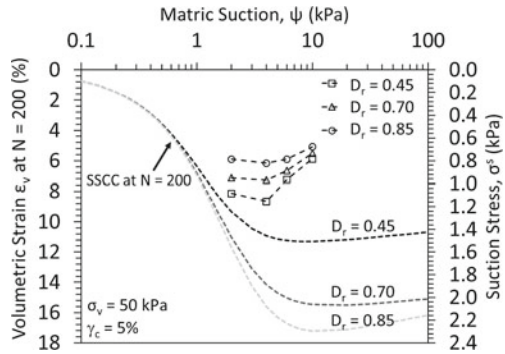
**Fig. 7** Typical time histories measured during cyclic shearing of an unsaturated specimen having an initial suction  $\psi_0 = 10$  kPa at the relative density of 0.70, **a** measured volumetric strain, **b** measured shear stress, **c** measured water pressure and outflow, **d** hysteretic stress-strain loops



**Fig. 8** Evolution of volumetric strains of unsaturated specimens subjected to  $\gamma_c = 5\%$  **a**  $D_r = 0.45$ , **b**  $D_r = 0.70$ , **c**  $D_r = 0.85$

volumetric strains at the end of shearing deviated significantly for different matric suctions with the smallest value of 5.5% at the suction of 10 kPa and the largest value of 8.7% at the suction of 4 kPa. For all the relative densities evaluated in this study, higher suction led to a stiffer response in drained conditions and thus less seismic compression, which agrees well with the findings in Kimoto et al. [6].

**Fig. 9** Synthesized results with the evolutions of SSCCs at different relative densities



Volumetric strains for unsaturated specimens at all relative densities at the end of shearing ( $N = 200$ ) were plotted against matric suction as shown in Fig. 9. It can be seen that higher relative density resulted in smaller volumetric contractions for the same suction level; however, this effect is weakened with increased suctions, especially at the highest suction of 10 kPa. At each relative density, suction plays an important role on the seismic compression with lower volumetric strain observed for specimens with higher suctions. However, the effect of suction can be alleviated or lessened by increasing the relative density. Evolutions of the SSCC can be inferred from the tracked water outflows and the degree of saturation, as shown in Fig. 9 as well. Compared with the initial SSCCs in Fig. 3a, suction stress shifted to the right in the higher suction range at the three relative densities with a remarkable shift at  $D_r = 0.45$  and slighter changes at  $D_r = 0.70$  and  $D_r = 0.85$ , which were primarily due to the different amount of volumetric contractions at each relative density.

## 8 Conclusion

In this study, a series of strain-controlled cyclic simple shear tests were performed on unsaturated sands with four initial suctions at each of the three relative densities in drained conditions, which represented the worst-case scenario for the near-surface compacted unsaturated backfills in transportation systems. Test results indicated that matric suction could lead to stiffer responses of unsaturated specimens in drained conditions, with the smallest volumetric contraction happened at the highest suction value. However, the dependence of the volumetric response on suction can be alleviated or weakened by increasing relative density. In addition, increasing relative density can remarkably decrease the seismic compression at lower suction values, but not an efficient approach for unsaturated soils in the residual saturation with high suctions.

## References

1. ASTM D6528 (2017) Standard test method for consolidated undrained direct simple shear testing of cohesive soils. ASTM International, West Conshohocken, PA
2. Bishop AW (1959) The principle of effective stress. *Teknisk Ukeblad* 106(39):859–863
3. Duku PM, Stewart JP, Whang DH, Yee E (2008) Volumetric strains of clean sands subject to cyclic loads. *J Geotech Geoenv Eng* 134(8):1073–1085
4. Ghayoomi M, McCartney JS, Ko HY (2011) Centrifuge test to assess the seismic compression of partially saturated sand layers. *Geotech Test J* 34(4):321–331
5. Hsu CC, Vucetic M (2004) Volumetric threshold shear strain for cyclic settlement. *J Geotech Geoenv Eng* 130(1):58–70
6. Kimoto S, Oka F, Fukutani J, Yabuki T, Nakashima K (2011) Monotonic and cyclic behavior of unsaturated sandy soil under drained and fully undrained conditions. *Soils Found* 51(4):663–681
7. Lu N, Godt JW, Wu DT (2010) A closed form equation for effective stress in unsaturated soil. *Water Resour Res* 46(5):55–65
8. Le KN, Ghayoomi M (2017) Cyclic direct simple shear test to measure strain-dependent dynamic properties of unsaturated sand. *Geotech Test J* 40(3):381–395
9. Okamura M, Soga Y (2006) Effects of pore fluid compressibility on liquefaction resistance of partially saturated sand. *Soils Found* 46(5):695–700
10. Rong W, McCartney JS (2020) Drained seismic compression of unsaturated sand. *J Geotech Geoenv Eng*. [https://doi.org/10.1061/\(ASCE\)GT.1943-5606.0002251](https://doi.org/10.1061/(ASCE)GT.1943-5606.0002251)
11. Silver ML, Seed HB (1971) Deformation characteristics of sands under cyclic loading. *J Soil Mech Found Divis* 97(8):1081–1098
12. Stewart JP, Bray JD, McMahon DJ, Smith PM, Kropp AL (2001) Seismic performance of hillside fills. *J Geotech Geoenv Eng* 127(11):905–919
13. Tokimatsu K, Seed HB (1987) Evaluation of settlements in sands due to earthquake shaking. *J Geotech Eng* 113(8):861–878
14. Unno T, Kazama M, Uzuoka R, Sento N (2008) Liquefaction of unsaturated sand considering the pore air pressure and volume compressibility of the soil particle skeleton. *Soils Found* 48(1):87–99
15. van Genuchten MT (1980) A closed-form equation for predicting the hydraulic conductivity of unsaturated soils. *Soil Sci Soc Am J* 44(5):892–898
16. Whang DH, Stewart JP, Bray JD (2004) Effect of compaction conditions on the seismic compression of compacted fill soils. *Geotech Test J* 27(4):1–9

# Frost Heave Protection of Concrete Pavement Subgrades



Chigusa Ueno, Yukihiro Kohata, and Kimo Maruyama

**Abstract** The Japanese road authority specifies that, in designing pavement subgrade, non-frost heaving materials shall be used for 70% of the frost penetration depth of the subgrade. However, some concrete pavements in snowy/cold regions have been found to have cracks that are categorized as structural damage caused by frost heaving. To examine the necessity for revising the subgrade design, an onsite survey to clarify the frost damage of concrete pavements and an evaluation of the impact of frost heaving on the lifespan of pavements by using FEM analysis and fatigue calculation were conducted. It was estimated from the onsite survey that the void between the concrete pavement and the subgrade, which was generated by frost heaving, would reduce the lifespan of the concrete pavement. To clarify this point, an FEM model was created to reproduce the frost heaving and an analysis was done using this model. In the analysis using the model that reproduced frost heaving, the tensile bending stress due to wheel loads at the bottom of the concrete slab increased. The pavement life was obtained in a fatigue calculation that incorporated the increase in tensile stress. The result was that a concrete pavement had structural cracks in a short period of a few dozen days after it experienced frost heaving. Based on these findings, we propose that, in designing concrete pavement subgrade in snowy/cold regions, it may be appropriate to use non-frost-heave-susceptible materials for the entire frost penetration depth.

**Keywords** Concrete pavement · Subgrade · Frost heaving

---

C. Ueno (✉) · K. Maruyama  
Civil Engineering Research Institute for Cold Region, Hiragishi 1-3-1-34, Toyohika-ku, Sapporo,  
Hokkaido 062-8602, Japan  
e-mail: [ueno-c22aa@ceri.go.jp](mailto:ueno-c22aa@ceri.go.jp)

K. Maruyama  
e-mail: [k.maruyama@ceri.go.jp](mailto:k.maruyama@ceri.go.jp)

Y. Kohata  
Muroran Institute of Technology, 27-1 Mizumoto-cho, Muroran, Hokkaido 050-8585, Japan  
e-mail: [kohata@mmm.muroran-it.ac.jp](mailto:kohata@mmm.muroran-it.ac.jp)



## 1 Introduction

In recent years, social demand for cost reductions in the development, maintenance, and management of capital assets has been increasing. In road pavement management as well, life cycle costs are required to be minimized by securing high durability for facilities and extending their lifespans. Under such circumstances, concrete pavements have been attracting attention for its higher durability and greater lifespan extension than asphalt pavements. However, in the snowy/cold regions of Japan, concrete pavements have not been used very much because there is a fear of structural damage from frost heaving and a decrease in the bearing capacity of the subgrade during the thawing season.

In this study, we conducted an onsite survey of existing road pavements to clarify the conditions of damage from the frost heaving of concrete pavement slabs (Co slabs). Then, the influence of the space between the Co slab and the base course generated from frost heaving on the life of the concrete pavement was evaluated by FEM analysis and fatigue calculation. The analysis and calculation were found that it is difficult to control damage from frost heaving by using the current design method, in which subgrade re-placement is done for 70% of the theoretical deepest frost penetration and that it is appropriate to construct the subgrade using non-frost heaving materials for the entire frost penetration depth.

## 2 Design Standards as a Measure Against Frost Heaving

The frost heaving countermeasure for road pavements in Japan involves replacing mainly the subgrade materials with non-frost heaving materials. The depth of replacement is specified as “70% of the theoretical deepest frost penetration” [1]. In this study, the appropriateness of the current design standard was investigated.

## 3 Mechanism of Co Slab Damage from Frost Heaving

When frost heaving occurs in the subgrade, it is considered that cracks are generated in the Co slab based on the mechanism as shown in Fig. 1.

The left-hand subfigure as shown in Fig. 1 shows the case in which frost penetrates into the subgrade of frost heave-susceptible materials and water is supplied from the road shoulder. As shown in the left-hand subfigure, an ice lens forms in the subgrade on the side of the shoulder. This ice lens pushes up the Co slab. When this location is repeatedly subjected to wheel loading, longitudinal cracks are generated. This may also cause transverse cracks at times. The right-hand figure in Fig. 1 shows how the transverse cracks are generated in the Co slab. Ice lenses may develop when water freezes at the subgrade locations below the concrete slabs as indicated in Fig. 1.

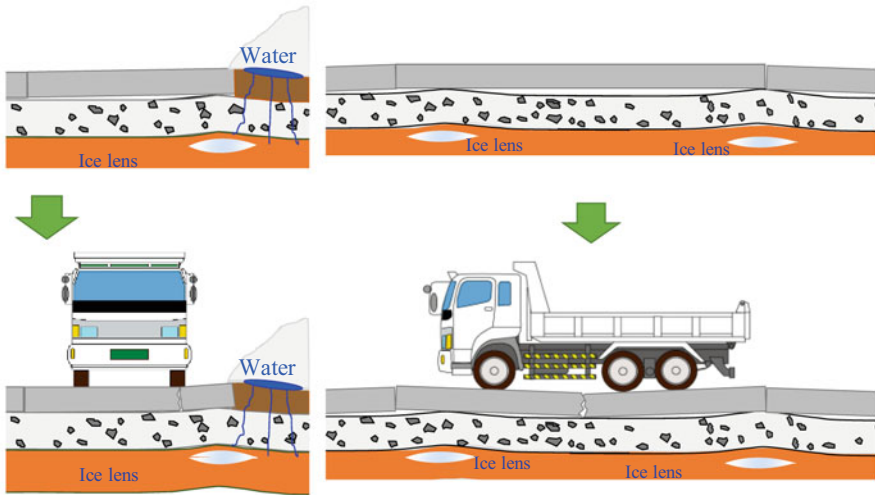


Fig. 1 Mechanism of crack generation from frost heaving

When wheel loads repeatedly stress the slabs directly above subgrade ice lenses, transverse cracks may develop.

#### 4 Fact-Finding Onsite Investigation on Existing Concrete Pavements

We conducted an onsite investigation in a snowy-cold area on concrete pavement constructed using the conventional design method. The locations for this investigation were two road sections (A and B) with concrete pavement. The photograph of the investigation location is shown in Fig. 2. The overview of the investigation sites are

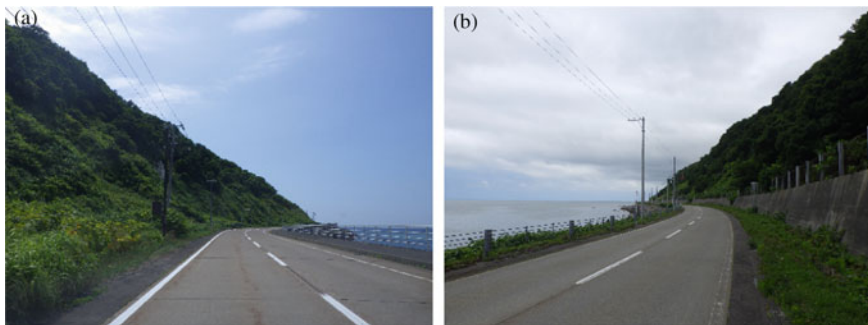


Fig. 2 Locations for this investigation (Left: Location A, Right: Location B)

**Table 1** Overview of the investigation sites

Locations	Years in service (year)	Length (m)	Amount of large vehicle traffic (no. of vehicles /day)	Typical topography	Desirable joint spacing estimated based on traffic amount (m)	Frost heave susceptibility of the subgrade	Drainage characteristics of the subgrade
A	17–28	4886	39	Consecutive embankment immediately along the coastline	7.5	Non-frost heave susceptible	Impermeable layer (Bedrock)
B	27–34	8053	169		8.0	Frost heave susceptible	Permeable layer (Gravelly soil)

**Table 2** Investigated items

Locations	Visual inspection	Survey of frost heave amount	FWD test
Section A	○	–	–
Section B	○	○	○

indicated in Table 1. Sections A and B had very similar topographical characteristics that is mainly consecutive embankment immediately along the coastline.

The three investigated items are shown in Table 2. The investigation for the amount of frost heaving and the FWD survey were done only at Section B, where structural cracks were found in the visual inspection. These will be discussed in the next section.

## 4.1 Investigation Methods

### Visual inspection

Visual inspection for the entire length of the two sections of concrete pavement was done on foot. We counted the number of Co slabs with transverse cracking that penetrated the Co slab and the number of Co slabs with longitudinal cracking that covered at least the half of the entire length of the Co slab as shown in Fig. 3. These types of cracks indicate structural damage to the Co slab.

### Survey on the amount of frost heaving

To clarify the relationship between the cracks found in the visual inspection and frost heaving, we conducted a survey on the amount of frost heaving.



**Fig. 3** Structural damage in the Co slab (Left: transverse cracking, Right: longitudinal cracking)

The targets were the Co slabs with transverse cracking (Fig. 3). The survey ran from December 2016 to March 2019. In the survey, we measured the road surface height before the start of frost heaving in December and defined this height as the reference value. At each location where we had obtained the reference value, we measured the road surface height in late February and early March of the next year, which is considered to be the time of the most severe frost heaving in the surveyed area. The differences between the reference value and the values measured in the frost heave season were recorded as the amount of frost heaving.

### **FWD investigation**

In the FWD investigation, weights are dropped onto the pavement to determine its deflection. The outlines of the investigation are shown in Fig. 4. The  $D_0$  deflection was measured by FWD. The investigation conditions are shown in Table 3.

## **4.2 Investigation Results**

### **Visual inspection**

The pavement structures at the inspected locations and the inspection results are shown in Fig. 5. Both of the inspected sections had a pavement structure that includes low-frost-heave-susceptible materials to 70% of the theoretical deepest frost penetration for 20-year probability. The subgrade material of the Section A was bedrock, which is considered to have low-frost heave susceptibility. In contrast, the subgrade material at Section B was frost heave susceptible.

When the number of cracks and the frequency of cracks were examined, Section B with frost heave-susceptible subgrade material had higher values than Section A. We estimated that, based on the inspection results, cracking relates to the frost heave susceptibility of the subgrade materials.

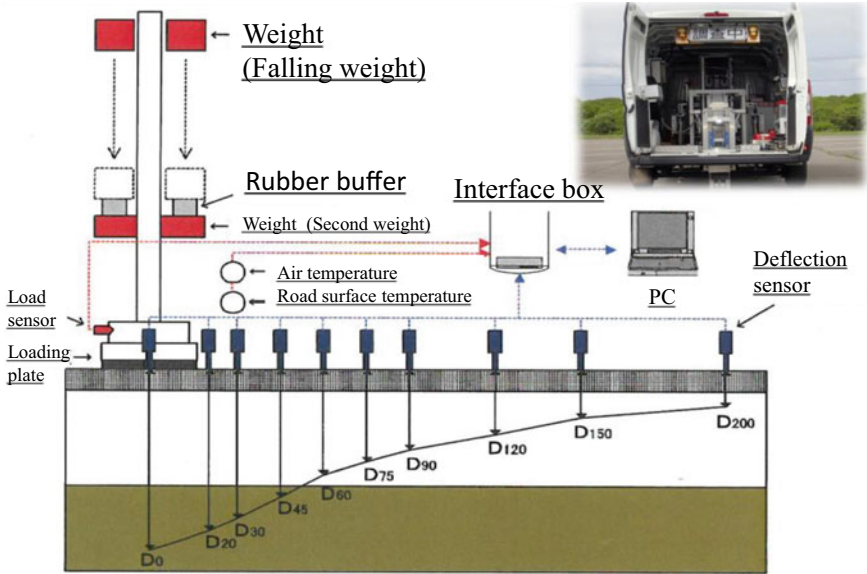


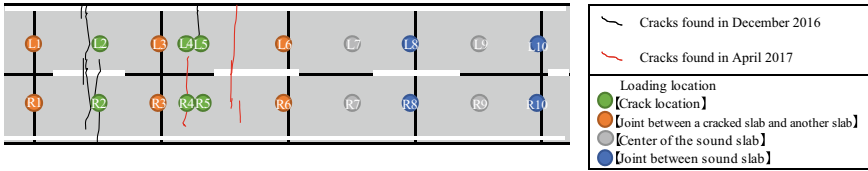
Fig. 4 FWD investigation

Table 3 FWD investigation conditions

Loadings	Number of loadings	Frequency	Road surface temperatures
98 kN	4 times	100 Hz	18.3–20.5 °C

	Section A	Section B
	Concrete pavement slab t=20cm	Concrete pavement slab t=25cm
	Base course (crusher run) t=25cm	Base course (crusher run) t=40cm
	Anti-frost layer (crusher run) t=25cm	Anti-frost layer (crusher run) t=15cm
	Subgrade [Non-frost heave susceptible]	Subgrade [Frost heave susceptibl]
Number of transverse cracks (cases)	0	40
Number of longitudinal cracks (cases)	0	7
Frequency of crack occurrence (cases/km)	0.00	8.63

Fig. 5 Pavement structure and the results of visual survey



**Fig. 6** Locations for the FWD investigation and the cracks on the Co slab

**Table 4** FWD investigation results

No.	L1	L2	L3	L4	L5	L6	L7	L8	L9	L10
$D_0$ (pm)	241	166	268	371	587	288	148	238	174	238
No.	R1	R2	R3	R4	R5	R6	R7	R8	R9	R10
$D_0$ (pm)	265	172	417	402	285	317	155	224	170	270

### Survey on the amount of frost heaving

The greatest frost heaving (13 mm) was observed at Section B.

### FWD investigation

At Section B, where frost heaving was found, we conducted the FWD investigation to clarify the bearing capacity of the pavement body on April 20, 2017. The locations for FWD investigation and the cracks on the Co slab are shown in Fig. 6, and the FWD results are shown in Table 4. The  $D_0$  deflection was great at the locations near the newly found cracks indicated by red lines in Fig. 6, and a marked decrease in the bearing capacity of the pavement body was found in this investigation.

### Discussion on the findings of the onsite investigation

The  $D_0$  deflection of the Co slab measured at the locations with newly found cracks was about twice those at the sound locations, which suggests that voids may have been generated under the pavement slab. As shown in Fig. 1, it can be estimated that the cracks were generated by frost heaving and subsequent fatigue.

The period from the day when the greatest amount of frost heaving was observed to the day when the cracks were found was about 2 months. It was verified that structural damage occurs in a short period from the generation of unevenness in the pavement slab caused by frost heaving. The survey results compelled us to consider the need to review frost heave countermeasures in pavement design.

## 5 FEM Evaluation of the Influence of Frost Heaving

The onsite investigation showed that a possible cause of the early cracking is the voids between the base course and the Co slab generated by frost heaving. To verify the influence of this phenomenon on the Co slab, we conducted FEM analysis.

However, it is difficult to actually measure the void between the base course and the Co slab. Therefore, the asphalt pavement surface, which has the flexibility to follow and reflects the shape of the subgrade, was used to estimate the frost heave shape. And a virtual Co slab was placed on this surface to derive the size of the void between the base course and the Co slab. Then, these voids were reflected in the FEM model.

### 5.1 Creation of a Model for Verification

The shapes and heights of frost heaving were measured in an area of 3.5 m × 10.0 m, which is similar to the size of the Co slab used for the FEM analysis. 10 m joint spacing is the design standard for concrete pavement in Japan. Therefore, we assumed this joint spacing in our model analysis. Elevations of an asphalt pavement slab for the analysis were measured on a 0.5 m mesh in winter. The difference between the measured values and the initial value measured in the fall was determined to be the amount of frost heaving. The contours of the measured values are shown in Fig. 7. The direction of the axis is the same as that of the FEM analysis. From the figure, it is

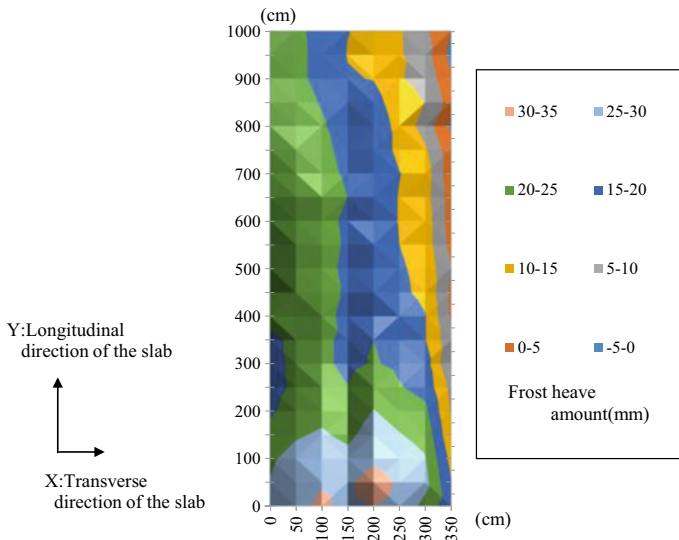


Fig. 7 Contour of unevenness from frost heaving

found that there were uneven amounts of frost heaving that resulted in the pavement surface unevenness.

Using the measurements, we calculated the thickness of each void generated between the bottom surface of the Co slab, which was assumed as a plane surface, and the uneven base course surface and input the values into the FEM model. The greatest thickness of the void between the Co slab and the base course surface was about 19 mm.

A model for this verification (the frost heave model) was created by defining void thickness of less than 5 mm as “the base course is fixed to the Co slab,” that from 5 mm to less than 10 mm as a “5 mm void,” that from 10 mm to less than 15 mm as a “10 mm void,” and that from 15 mm to less than 20 mm as a “15 mm void.”

### 5.2 Analysis Conditions

Pave3D [2] was used for the FEM analysis. The model was 3.5 m in width, 10.0 m in length, and 3.5 m in depth, values that were chosen by assuming a piece of Co slab. The conditions of the ground for the analysis model are shown in Table 5. For the elastic modulus and Poisson’s ratio of the Co slab and the granular material, the representative values shown in the Handbook on Pavement Design [1] were used. The elastic modulus of subgrade with a decreased bearing capacity during the thawing season is obtained by multiplying the lowest limit value of the design CBR of 3 by 10 [1, 3].

The pavement thickness was determined based on the cross-section of the pavement at Section B, which was designed as a 20-year design pavement. For the frost penetration depth, 1000 mm, which is the 20-year-probability greatest frost penetration depth in the surveyed area, was used.

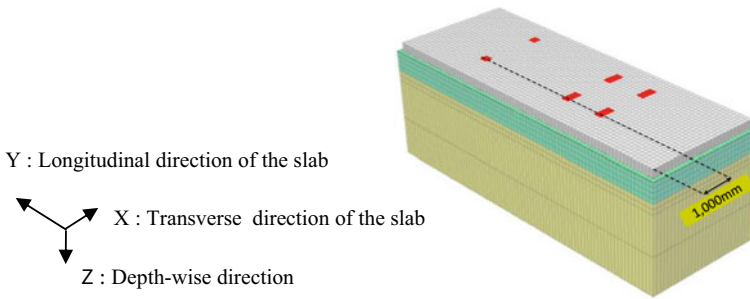
The element division space for the analysis was 125 mm for the X- and Y-axes. The element division space for the Z-axis of the Co slab was 50 mm.

The loading condition was determined by measuring the load imparted by a dump truck with a total weight of 196.2 kN, and the condition obtained in the measurement

**Table 5** Conditions of the ground for the analysis model

	Slab thickness (mm)	Elastic modulus (MPa)	Poisson’s ratio	Density (kg/m <sup>3</sup> )
Concrete pavement slab	250	28,000	0.2	2500
Base course	600	200	0.35	2040
Subgrade	2650	100	0.4	–
Subgrade (when the bearing capacity is reduced)	150	30	0.4	–





**Fig. 8** Loading location

was used [4]. The loading locations are shown as red marks in Fig. 8. In the  $X$ -axis direction, the center of the loading location for the road shoulder side of the front wheel was set at a point 1000 mm from the longitudinal free end. In the  $Y$ -axis direction, the point of greatest tensile stress in the Co slab was determined by repeated calculation. The calculation determined the  $Y$ -axis loading location to be the point where the load of the rear wheel was directly above the void created between the base course surface and the Co slab.

### 5.3 Analysis Details

The analysis was done by using four models. (1) The standard model: This was without any unevenness of the upper surface of the base course. (2) The frost heave model: This was with frost heaving voids between the base course and the Co slab. (3) The low-bearing-capacity model: This was created by considering the decrease in the bearing capacity of the subgrade during the thawing season. The bearing capacity decrease from 100 to 30 MPa in a layer from 850 to 1000 mm in depth of subgrade. (4) The compound model: The FWD test suggested the possibility that voids were generated during the thawing season at the locations where frost heaving had occurred between the Co slab and the base course. The test results also suggested that the subgrade bearing capacity was reduced. In this model, the bearing capacity of the frost heave model was reduced to 30 MPa in the layer from 850 to 1000 mm.

### 5.4 Analysis Results

The values and the locations of generation of the greatest tensile stress for each model are shown in Table 6. The greatest tensile stress for the frost heave model was 1.42 MPa, which is about 6 times the greatest tensile stress (0.23 MPa) of the standard model. The greatest tensile stress of the low-bearing-capacity model was

**Table 6** Analysis results

	Maximum tensile stress (MPa)	Comparison with the standard model	Location of maximum tensile stress generation
(1) Standard model	0.23	–	Lower surface of the slab end
(2) Frost heave model	1.42	6.2 times	Lower surface of the slab end
(3) Bearing capacity decrease model	0.46	2.0 times	Lower surface of the slab end
(4) Compound model	1.60	7.0 times	Lower surface of the slab end

0.46 MPa. The greatest tensile stress of the compound model was 1.60 MPa, which was greater than that of the frost heave model, and about 7 times that of the standard model.

From the above, it was verified that the tensile stress generated in the Co slab increases with the increase in the unevenness of the slab from frost heaving and with the decrease in bearing capacity of the subgrade during the thawing season.

## 6 Evaluation of the Influence of Frost Heaving on the Model by Degree of Fatigue

Using the standard model and the frost heave model explained in the preceding section, we investigated how the void between the Co slab and the base course caused by frost heaving influenced the pavement life. In this evaluation, we evaluated the life of the pavement by using the theoretical design method for the concrete pavement described in the Handbook on Pavement Design and the degree of fatigue.

### 6.1 Creation of a Model for Verification

To reproduce the state of concrete pavement in service in snowy-cold areas, we set the conditions for this evaluation as follows.

For calculating thermal stress, we compared the thermal distribution described in the handbook to the measured values, and we used the thermal distribution described in the part of the book on “locations with small thermal differences,” which resembled the measured value distribution. The measured values were the data for the Co slab near Section B.

The pavement thickness was set as 250 mm, the number of lanes was set as 2, the slab length was set as 10.0 m, the slab width was set as 3.5 m, and the lane width was set as 3.25 m. For the traffic conditions, we used the survey results for another

section whose traffic volume (547 heavy vehicles/day) was close to that for Section B (341 heavy vehicles/day), because surveyed vehicle weight data were unavailable for Section B.

For the standard model, three design periods for determining the degree of fatigue were set: (1) 20 years, which is the standard in Japan, (2) 35 years, which is the design service period for Section B, and (3) the period during which the degree of fatigue exceeds 1.0 (i.e., the time until one transverse crack that has penetrated the slab goes across the entire width of the slab, as shown in Fig. 2).

The calculation conditions for degree of fatigue are shown in Table 7. Particularly, for examining the degree of fatigue, the target location was set as the longitudinal free end of the slab and the target form of crack was set as transverse crack, based on the FEM analysis results.

For bending strength, 5.4 MPa ( $n = 9$ ) was used, which was the average value for the core sampled during the onsite survey from the existing Co slab in Section B.

**Table 7** Calculation conditions for degree of fatigue

<i>Targets for the pavement</i>	
Cracking ratio (performance index value) (cm/m <sup>2</sup> )	10
Reliability (%)	90
<i>Conditions of the pavement slab</i>	
Type of pavement	Ordinary concrete pavement
Bending strength (MPa) *Average value of the sample core from the existing road	5.4
Elastic modulus (MPa)	28,000
Poisson's ratio	0.2
Temperature expansion coefficient (1/°C)	$10 \times 10^{-6}$
Transverse joint spacing (m)	10
Joint	Dowel bar used
<i>Traffic conditions</i>	
Percent heavy vehicles	Suburban area
Number of heavy vehicles that travel when the temperature difference between the upper and lower surfaces of the concrete slab is positive/total traffic volume of heavy vehicles	0.60
Number of heavy vehicles that travel when the temperature difference between the upper and lower surfaces of the concrete slab is negative/total traffic volume of heavy vehicles	0.40
Paved road shoulder of sufficient width	Exists
<i>Paved road shoulder of sufficient width</i>	
Important point	Longitudinal free end
Assumed cracks	Transverse cracks

### 6.2 Calculation of Compound Stress

The calculation method described in the Handbook on Pavement Design has no items that address frost heaving, as shown in Eq. (1); therefore, we attempted to include the influence of frost heaving, as shown in Eq. (2).

$$\sigma_m = \sigma_{ei,j} + \sigma_{tk} \tag{1}$$

$$\sigma_m = \sigma_{ei,j} + \sigma_{tk} + \sigma_{fi,j} \tag{2}$$

where

- $\sigma_m$  compound stress (MPa).
- $\sigma_{ei,j}$  wheel load stress when the wheel load  $P_i$  passes the travel location  $j$  (MPa).
- $\sigma_{tk}$  thermal stress from the temperature difference  $k$  between the upper and lower surfaces of the concrete slab (MPa).
- $\sigma_{fi,j}$  the wheel load stress increase from frost heaving when wheel load  $P_i$  passes the travel location (MPa).
- $\sigma_{fi,j}$  was obtained from the item “the difference in the greatest tensile stress among models under each condition” in the handbook and for the time when the wheel load  $P_i$  passes over the travel location  $j$

**Table 8** Maximum tensile stress

Axel load $P_i$ (kN)	Wheel passes per day	Maximum tensile stress applied to the end of pavement slab (MPa)				Difference in stress (MPa)	
		Standard model		Frost heave model			
		Travel location $j = 105$ cm	Travel location $j = 15$ cm	Travel location $j = 105$ cm	Travel location $j = 15$ cm	Travel location $j = 105$ cm	Travel location $j = 15$ cm
9.8	1229	0.03	0.12	0.25	0.43	0.22	0.31
19.6	252	0.06	0.23	0.42	0.80	0.37	0.57
29.4	274	0.09	0.35	0.60	1.16	0.52	0.82
39.2	49	0.12	0.46	0.78	1.53	0.67	1.07
49.0	23	0.15	0.58	0.97	1.90	0.82	1.32
58.8	10	0.18	0.69	1.14	2.26	0.97	1.57
68.6	2	0.21	0.81	1.32	2.63	1.12	1.82
78.4	2	0.23	0.92	1.50	3.00	1.27	2.07
88.2	0	0.26	1.04	1.69	3.37	1.42	2.33
98.0	0	0.29	1.15	1.87	3.73	1.57	2.58

**Table 9** Results of trial calculation for degree of fatigue

	Design period	Degree of fatigue
		20 years
Standard model	35 years (Equivalent to the service years)	0.74
	48 years	1.01
Frost heave model	18 days	1.06

Table 8 shows the calculated values when the wheel load  $P_i$  acts at the travel location  $j$  of 105 cm and at that of 15 cm from the longitudinal free end as the representative values for the calculated greatest tensile stress, and it shows the difference between the stresses at the two locations. At higher wheel loads and loading locations closer to the longitudinal free end, the difference between the stress for the standard model and that for the frost heave model and the value that is added to the compound stress tend to increase.

### 6.3 Calculation for the Degree of Fatigue

We calculated the degree of fatigue by inputting the conditions set above and the compound stress obtained above into the formula for calculating the degree of fatigue. In obtaining the degree of fatigue, we used the “fatigue curve verified based on the data for concrete pavement in Japan” described in the handbook.

The results of calculation are shown in Table 9. The degree of fatigue exceeds 1.0 in the hatching cell at Table 9. For the standard model, the degree of fatigue did not exceed 1.0 when the service years were set as 35 years, which is the current design service years for Section B, and exceeded 1.0 under the conditions for the service period of 48 years. In the frost heave model, the degree of fatigue exceeded 1.0 after 18 days in service.

From the above results, it was found that there is the possibility of structural damage within a month after frost heaving from freezing that penetrates the subgrade of a Co slab. Even for the Co slab that remains sound without structural damage for more than 20 years under the conditions without frost heaving, structural damage from frost heaving was found to occur early.

### 6.4 Comparison with the Results of the Onsite Survey

It is estimated that the structural damage occurred in Section B, where cracks across the entire width of the Co slab were found in the onsite survey described above, because the tensile stress generated in the Co slab under vehicle travel increased due to the generation of voids between the Co slab and the base course surface and

the decrease in the bearing capacity of the subgrade, as shown in the results of the FEM analysis and the degree of fatigue calculation. In the onsite survey, cracks were found about two months after we found the greatest amount of frost heaving. The calculation of the degree of fatigue by FEM analysis was obtained a result in which cracks similar to these would be generated in a short period of time.

## 7 Conclusion

The main findings in this study are as follows.

- In the concrete pavement slab (Co slab), we found cracks that were likely caused by frost heaving and the decreased bearing capacity of the subgrade at the locations where frost heave-susceptible materials were used for the subgrade within the freeze-penetration depth.
- The analysis results showed that even for a Co slab that would not suffer structural damage until 48 years in service, structural damage occurs in a matter of few days when freezing reaches the subgrade and frost heaving occurs.

From the above, it was clarified that the pavement life decreases at locations where the subgrade materials within the frost penetration depth are frost heave susceptible and when unevenness occurs on the lower surface of the Co slab. In designing subgrades for concrete pavements in snowy/cold areas, we consider it appropriate to use non-frost heaving material for the entire frost penetration depth of the subgrade.

## References

1. Japan Road Association (Public corporation): Handbook on pavement design, p 114 (2006)
2. Japan Cement Association (General incorporated association) Homepage. <http://www.jcassoc.or.jp/tokusetsu/jcapave3d/>. Last accessed 21 Apr 2015
3. Hokkaido Regional Development Bureau: Road Design Guidelines, pp 1–5–3 (2019)
4. Abe R, Tako J (2007) Study on tensile strains of asphalt pavement under dynamic loading. Mon Rep Civ Eng Res Inst Cold Reg 653:12

# Effect of Traffic Load on Permeability of Remolded Kaolin



Jian Zhou, Linghui Luo, Hao Hu, Jie Xu, and Yicheng Jiang

**Abstract** Soil anisotropic strength and strain behavior under principal stress rotation, caused by traffic loading, have been widely studied, while anisotropic permeability is of little concern. Large settlement will be induced by consolidation or secondary consolidation of soft clay, particularly for reclaimed clay. Permeability behavior is thus very important. Since current experimental setups do not take into account the influence of dynamic loading on the permeability of soil, hollow cylinder apparatus (HCA) was modified so that it can be utilized to determine the hydraulic conductivity of clay. HCA is usually used to simulate complex stress paths and to determine anisotropic strength and stiffness of soil under different directions of major principal stress. As no permeation experiment has been conducted by HCA before, firstly this paper proposes the test procedure for measuring the hydraulic conductivity of samples. Then, a series of permeation experiments under different  $K_0$  consolidations were conducted. Horizontal and vertical permeabilities were measured before and after traffic loading. Experimental results show that under  $K_0$  consolidation condition, the anisotropic permeability of remolded kaolin increases with the applied axial stress in spite of the same  $K_0$  value. Hydraulic conductivity decreases in both vertical and horizontal directions after traffic loading. Dynamic load has a greater impact on permeability behavior in its main consolidation direction, which leads to an increase in the anisotropy ratio of permeability. Findings in this paper will help understand the settlement and uneven settlement of embankments in soft ground, where permeability is normally regarded as a constant.

**Keywords** Anisotropy · Permeability · Traffic load · Settlement

---

J. Zhou (✉) · L. Luo · H. Hu · J. Xu · Y. Jiang

Research Center of Coastal and Urban Geotechnical Engineering, Zhejiang University, Hangzhou 310058, China

e-mail: [zjelim@zju.edu.cn](mailto:zjelim@zju.edu.cn)

J. Zhou · H. Hu · J. Xu · Y. Jiang

Engineering Research Center of Urban Underground Development of Zhejiang Province, Hangzhou 310058, China

L. Luo

Shanghai Municipal Engineering Design Institute (Group) Co. Ltd., Shanghai 200082, China

## 1 Introduction

The permeability characteristics of clay play an important role in the field of geotechnical engineering and have been extensively studied [1–5]. However, most research studies have not taken anisotropy and dynamic loading effect into consideration. In fact, there are significant differences between the vertical and horizontal permeabilities; moreover, the micro-study of soil shows that the dynamic loading will reconstruct the micro-structure of soil [2–4], which has great impact on permeability properties.

While the most commonly two types of permeability measuring apparatus are neither not ideal. As for conventional oedometer, there is some unavoidable void space between the specimen and the rigid wall, making some preferential leakage occur along the wall when permeating; therefore, the permeability coefficient measured by oedometer is often larger than actual value [5]. What's more, only one-dimensional consolidation stress can be applied in the oedometer so that it cannot be used to study the influence of complex stress paths and dynamic loadings on soil permeability characteristics. Another common instrument is flexible-wall triaxial permeameter, it can effectively deal with the side-wall leakage and confining pressure control problems, which ensures the accuracy of permeability measuring. However, most triaxial parameters are not equipped with axial strain sensors so it is hard to obtain the change of specimen size during the test processes and neither cannot simulate stress rotation, which means the simulated dynamic load of conventional triaxial cell is different from the actual situation.

Nowadays, dynamic problems are broadly involved in practical engineering and need more attention. Hence, new equipment for better accuracy and complex stress state is more attractive. Part of the experimental results shows the void ratio, and the pore distribution of the soil specimen changed significantly after the traffic loading, which means the permeability coefficient of soil will change a lot, and in addition, permeability behavior has relevance to the settlement and uneven settlement of embankment in soft ground, so the law of permeability variations after dynamic load and the principle behind the law needs to be explored.

Hollow cylindrical apparatus (HCA), with axial strain transducer and pressure control system, usually used to simulate complex stress paths and cyclic rotation of principal stress directions, is available to solve the problems mentioned above. After adding a new base pressure controller and corresponding seepage software in ZJU-HCA system, it can be applied to determine the hydraulic conductivity of clay samples (the modified equipment and test procedures are detailed in the appendix part). The effects of traffic load on permeability and its anisotropy of remolded clay under different  $K_0$  consolidation conditions were experimentally investigated in this paper.



**Table 1** Physical properties of remolded clay

Specific gravity $G_s$	Liquid limit $w_l$ (%)	Plastic limit $w_p$ (%)	Initial void ratio $e_0$	Dry density $\rho_0$ (g/cm <sup>3</sup> )	Water content $w$ (%)
2.68	65.35	40.04	1.56	1.62	56.14

## 2 HCA Testing Procedure

### 2.1 Specimen Preparation

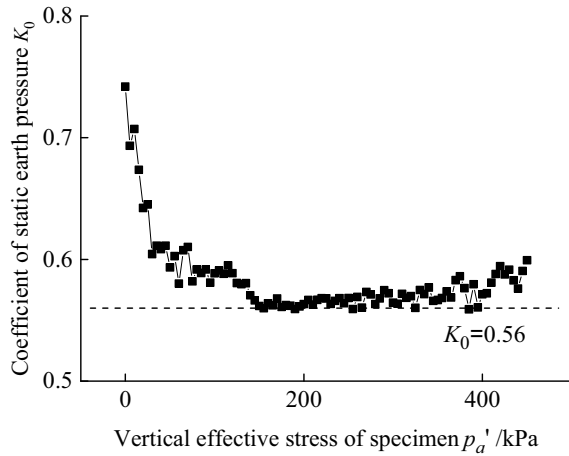
A hollow cylindrical specimen with a geometry of 30 mm × 50 mm × 200 mm (inner radius × outer radius × height) was used in all the tests discussed in this paper. To ensure the homogeneity and comparability of all the specimens, using commercial Malaysia kaolin as the raw material, the required amount of kaolinite was mixed with ultra-pure water to prepare a slurry to ensure the mass ratio of mixed water and soil was 2:1 [6], then poured the slurry into a plexiglass bucket and consolidate it under one-dimensional consolidation stress of around 100 kPa, which achieved by three stages of loading, and each stage endures 24 h. The physical property parameters of the remolded clay after preparation are shown in Table 1, and the parameters in the table are the average values of six group specimens.

### 2.2 Experimental Method

In order to study the influence of traffic load on the permeability of remolded clay under  $K_0$  consolidation condition, a series of permeability experiments were conducted like cutting high-quality (undisturbed) specimens in different directions of the remolded clay prepared and testing them in HCA permeameter to obtain the vertical and horizontal hydraulic conductivities. The horizontal pressure coefficient  $K_0$  of soil is measured by  $K_0$  consolidation module in GDS triaxial test system, which can control back pressure, cell pressure and axial stress at the same time and keep the specimen in  $K_0$  consolidation state without lateral strain. The variational rule of  $K_0$  in the test is shown in Fig. 1, and it can be found that the coefficient  $K_0$  of the remolded kaolin tends to be stable when vertical effective stress is close to 200 kPa; therefore, the ratio of horizontal to vertical effective stress  $K_0$  of the soil can be determined as 0.56.

The purpose of this paper is to investigate the influence of traffic load on the permeability characteristics of soils, so it is necessary to select appropriate dynamic load parameters. Referring to Xiao's laboratory simulation method of subway(metro) traffic load [7, 8], the amplitude of the deviator stress  $(\sigma_z - \sigma_\theta)/2 = 15$  kPa and torsional shear stress  $\tau_{z\theta} = 8$  kPa are selected; furthermore, taking into account the low frequency and large number of cyclic characteristics of traffic load, the frequency

**Fig. 1**  $K_0$  coefficient diagram of remolded kaolin

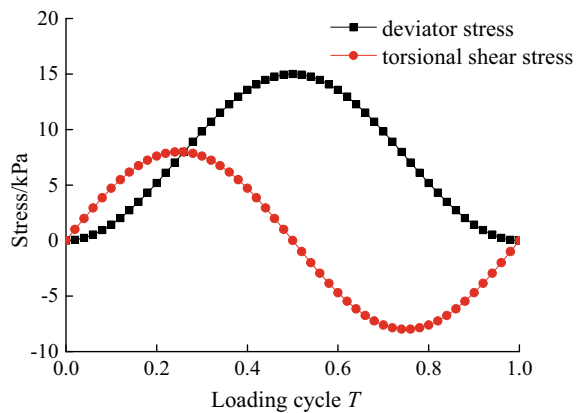


$f = 0.5$  Hz and periods  $N = 10,000$  are also chosen to match the experiment. The theoretical repeated stress on the specimen within one cycle was shown in Fig. 2.

Many of the underground structures are shallow buried; hence, the effective axial stress of  $K_0$  consolidation in all test is not more than 300 kPa. To avoid the influence of the saturation degree of back pressure on the measurement of  $k$ , the back pressure of all test groups is set to 100 kPa. Measuring the hydraulic conductivity of clay by constant head method, the hydraulic gradient is taken as 10 according to flexible-wall permeability test specification [9].

For measuring the permeability anisotropy ratio of clay, the flow direction needs to be defined. Referring to previous research works [2, 6], the direction perpendicular to the sedimentary plane of soil is defined as V-direction and the direction parallel to that is H-direction. The detailed test scheme is shown in Table 2.

**Fig. 2** Time history curve of loading stress



**Table 2** Test scheme

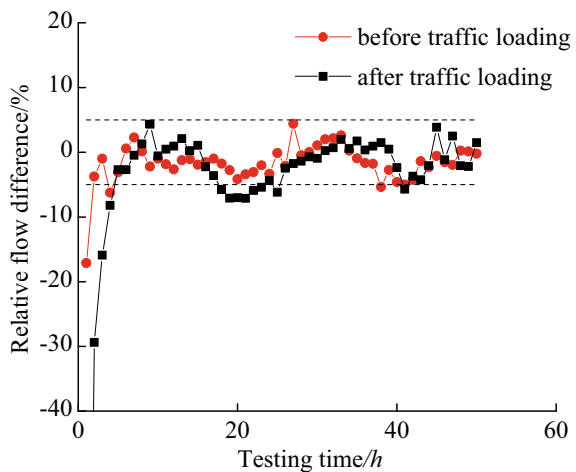
Test number	Effective cell pressure $P_c$ /kPa	Effective axial pressure $P_a$ /kPa
V1	56	100
V2	112	200
V3	168	300
H1	100	56
H2	200	112
H3	300	168

### 3 Experimental Results

#### 3.1 Data Processing Method

As no permeation experiment has been conducted by HCA before, seepage stability standard needs to be developed. ASTM D5084 [9] suggests that the seepage flow can be considered as stable when the ratio of inflow to outflow rate is between 0.75 and 1.25. Chapuis [5] once used rigid-wall oedometer to study the permeability of silt clay and pointed out when both the inflow velocity difference and the outflow velocity difference not exceeding 1% that can be defined as seepage stability stage. When utilizing HCA to determine the hydraulic conductivity of clay, there is still a stable stage to be studied to guarantee the reliability of calculated data. Referring to existing approaches above, this paper takes 3600 s (1 h) as a unit time and calculates the relative flow difference and the permeability coefficient per unit time. Figure 3 shows the relative flow difference curve over time (take V2 as an example). It can be found that the relative flow difference is initially large but gradually stabilizes to a

**Fig. 3** Relative flow difference curve of V2 sample in permeation stage before and after traffic loading



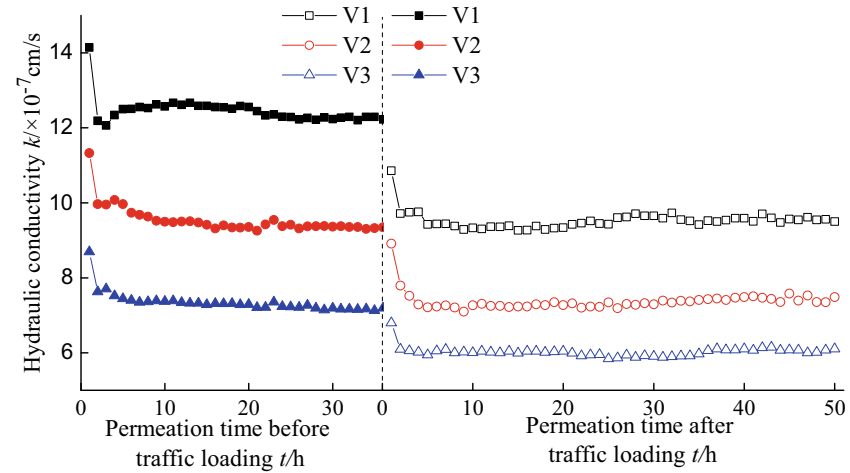
certain extent and the fluctuation after traffic loading is much larger, but the relative flow difference less than  $\pm 5\%$  can still be considered as the stability indicator. Yet the anisotropy ratio of hydraulic conductivity  $r_k$  ( $r_k = k_h/k_v$ ,  $k_h$  and  $k_v$  are the hydraulic conductivity in the horizontal and vertical directions.) is usually less than 1.6, if taking the relative flow difference less than  $\pm 5\%$  as the stability indicator, then the exact anisotropy ratio  $r_k$  cannot be obtained and the stable stage after dynamic loading needs longer time to approach (or sometimes cannot approach).

Consequently, when the difference in average hydraulic conductivity within unit time (1 h) is less than 2% in continuous 24 h before dynamic loading and 5% after, simultaneously the hydraulic conductivity has no obvious increasing or decreasing tendency that can be regarded as the seepage stability criterion. It is reliable to calculate the average  $k$  in this period. The following test data are processed according to the method above.

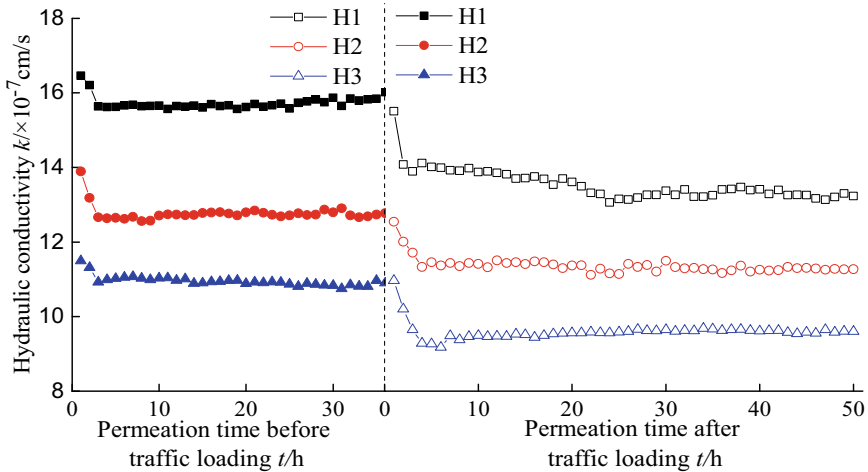
### 3.2 Permeability Results

The curve of vertical and horizontal hydraulic conductivity with time before and after dynamic load of different specimens is given in Fig. 4, and more detailed results can be located in Table 3. Firstly, it can be found that similar to the variation regularity of the relative flow difference, the hydraulic conductivity before and after traffic loading will tend to be stable over time. The calculated  $k$  after different one-dimensional consolidation stress is between  $7.23 \times 10^{-7}$  and  $15.85 \times 10^{-7}$  cm/s. Moreover, the measurements indicate that regardless of the permeation direction, as the clay is compressed one-dimensionally, the hydraulic conductivity of specimen decreases obviously. It also can be observed that in spite of the same  $K_0$  value, both the vertical and horizontal hydraulic conductivities decrease after traffic loading, and the decrease range is 17.01–19.30% in vertical and 11.81–16.34% in horizontal under different consolidation condition, which means traffic loading does reduce the permeability.

Due to the inconsistent effects of dynamic loading on the vertical and horizontal hydraulic conductivity, the permeability anisotropy ratio of remolded kaolin certainly will change after traffic loading. Figure 5 illustrates the variation of anisotropy ratio  $r_k$  versus consolidation stress level, and it can be seen that the  $r_k$  ranges from 1.28 to 1.51 before traffic loading and increases with the increase of consolidation stress. The range is consistent with the experimental results obtained by previous scholars, in a way, that indicates the effectiveness of the HCA permeameter. In addition, it is illustrated that the  $r_k$  of clay increases by 5.96–12.50% after dynamic loading; however, no evidence could be found the increase is corresponding to consolidation stress. The test results show when the effective consolidation stress is 200 kPa,  $r_k$  increased the most at 12.50% after traffic loading.



(a) Vertical



(b) Horizontal

**Fig. 4** Variation of the hydraulic conductivity against the permeation time before and after traffic loading of different samples

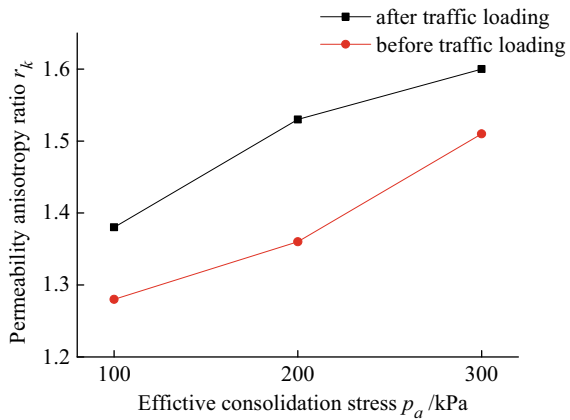
### 4 Discussion

Based on the results above, for the remolded kaolin clay before traffic loading, both the vertical and horizontal hydraulic conductivities decrease as the consolidation stress increases, while the ratio of horizontal to vertical hydraulic conductivity increases monotonically from 1.28 to 1.51 as the effective stress increases from 100 to 300 kPa. For similar material, this compares well with the value ranges from

**Table 3** Comparison of permeability test results of  $K_0$  consolidated specimens before and after dynamic load

Test number	The measured hydraulic conductivity before traffic loading $k_b/ \times 10^{-7}$ (cm/s)	The measured hydraulic conductivity after traffic loading $k_a/ \times 10^{-7}$ (cm/s)	Measured difference value before and after traffic loading/% $(k_a - k_b)/k_b$
V1	12.36	9.58	-18.53
V2	9.37	7.40	-19.30
V3	7.23	6.00	-17.01
H1	15.85	13.26	-16.34
H2	12.79	11.28	-11.81
H3	10.93	9.61	-12.08

**Fig. 5** Relationship between  $P_a$  and  $r_k$



1.0 to 2.0 reported by other researchers [10–12]. It can also be demonstrated that the traffic loading has a great impact on the permeability characteristics of clay, in particular reducing the hydraulic conductivity in different directions and enlarging the anisotropy ratio.

In view of the existing experimental work, the influence of traffic loading on clay permeability can be interpreted from two aspects.

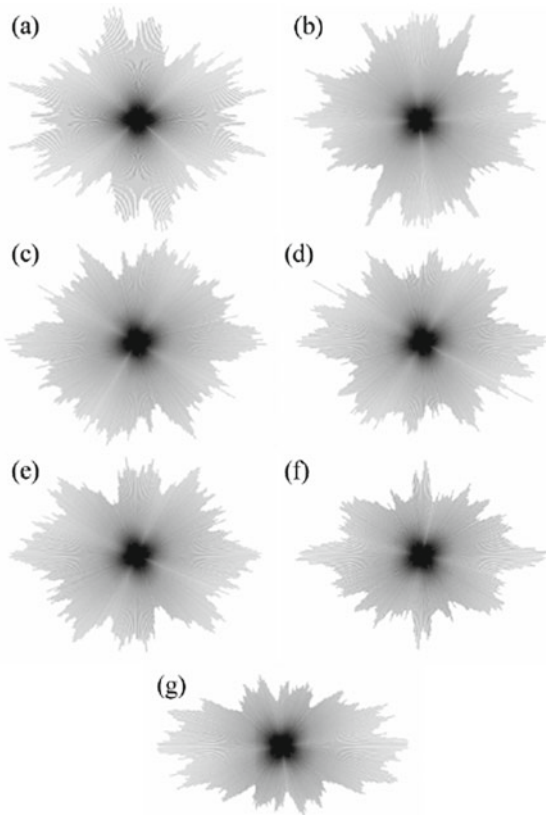
One is that the dynamic loading will cause accumulated strain, which means its void ratio will significantly reduce. In fact, soil permeability is closely related to its void ratio, and almost all the prediction formulas of hydraulic conductivity are bound up with void ratio at present. Generally, the smaller the void ratio is, which equates to the number of pores available for fluid to pass through is reduced, the smaller the hydraulic conductivity is for the same soil. So the dynamic loading makes the  $k$  smaller than it was before.

Another effect is that the dynamic load makes the micro-structure of soil reconstructed. Some micro-structure photographs of clay show that the soil particles have

the trend of directional arrangement under  $K_0$  consolidation condition, and as the stress increases, the arrangement of the pores gradually concentrates to the horizontal direction (as shown in Fig. 6) and finally renders the  $r_k$  value greater than 1. While the original soil structure is ruined by traffic loading and flocculated structure is reconstructed [13], the change of structure causes the variation of permeability characteristics of clay.

Theoretically, the anisotropy ratio  $r_k$  will decrease if only taking the failure of the layered soft clay structure into consolidation; nevertheless, the measured  $r_k$  after traffic loading is larger than it was before (shown in Fig. 5). A possible deduction on account of test results is that the initial smaller vertical hydraulic conductivity is greatly affected by structural change, while the value of horizontal is less affected, which consequently results in the phenomenon that the anisotropy ratio  $r_k$  obtained by HCA permeameter increases after traffic loading. For most of the settlement and uneven settlement prediction methods of embankment in soft ground, where permeability normally regarded as constant, also ignore the influence of traffic loading on soil permeability behavior and usually get inaccurate solution. More micro-experiments need to be performed to study in this project.

**Fig. 6** Rose maps under different pressures [4]



## 5 Conclusions

In this paper, conventional HCA is modified for exploring the effect of traffic load on permeability of remolded kaolin clay. With the establishment of permeation stable criteria for static and dynamic loading, a series of clay permeability test results before and after traffic loading are obtained. The conclusions can be drawn as follows:

1. Under  $K_0$  consolidation condition, the vertical hydraulic conductivity of remolded kaolin decreases from  $12.36 \times 10^{-7}$  to  $7.23 \times 10^{-7}$  cm/s, while the horizontal value decreases from  $15.85 \times 10^{-7}$  to  $10.93 \times 10^{-7}$  cm/s as the effective stress increasing from 100 to 300 kPa. Accumulated strain caused by traffic loading makes further efforts to reduce the void ratio of soil, leading to a smaller  $k$  value after traffic load.
2. The ratio of the horizontal to the vertical hydraulic conductivity increases from 1.28 to 1.51 with the increase of effective consolidation stress, which is consistent with most experimental work for similar materials. However, differing from the changes of hydraulic conductivity, the anisotropy ratio  $r_k$  get larger after traffic loading. The possible reasons for the results are that the traffic loading reconstructs the micro-structure of clay and has a greater impact on the smaller vertical hydraulic conductivity.

**Acknowledgements** This study is supported by the National Key R&D Program of China (2016YFC0800203) and Natural Science Foundation of China (Grant 51338009 and 511784222). Their supports are gratefully acknowledged.

## Appendix

### The Modified HCA

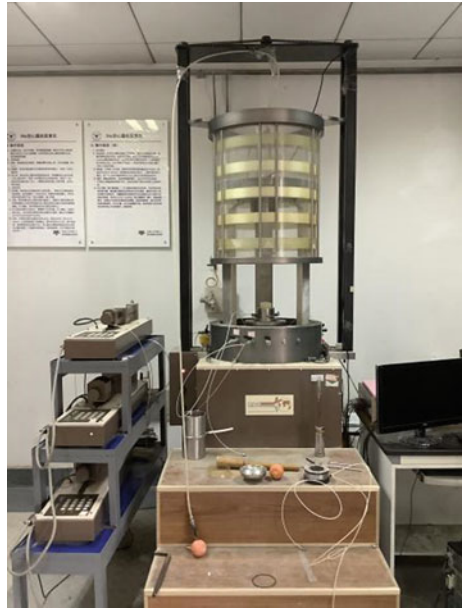
The new permeameter adopted in this paper is composed of additional seepage module software and previous ZJU-HCA system with an added base pressure controller, as shown in Fig. 7. Combined with the additional seepage system, it can be used to measure the hydraulic conductivity of soil under different complex stress paths or dynamic loads. The modified HCA is still mainly composed of hollow cylinder system, pressure controllers, dual-channel control system (DCS) and GDSLAB Software.

In order to realize the seepage function, an additional pressure controller is added, so as to control the back pressure of the top and bottom of the specimen to form a stable hydraulic gradient. The seepage control module is written into the computer control system to collect and read the stress–strain data of the specimen during the seepage process, thus providing a reliable basis for the analysis and calculation of the  $k$  value. The fundamental system of hardware elements of the test instrument is

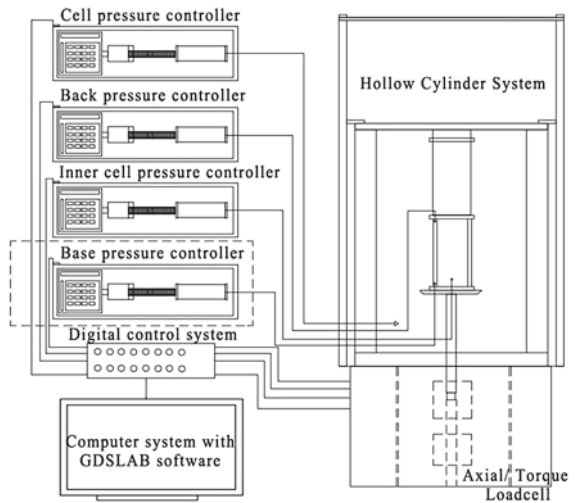


shown in Fig. 8. The base pressure controller in the dashed frame is an additional part of the hardware.

**Fig. 7** Hollow cylindrical apparatus



**Fig. 8** Fundamental system hardware elements



## Specimen Preparation

(1) Preparation of materials and equipment: When conducting remolded soil tests, dry soil and ultra-pure water should be prepared first. To ensure that the specimens are not contaminated by foreign ions, items should be cleaned in ultra-pure water, including high-powered mixers, mixer sticks, graduated beakers, plastic buckets, plexiglass buckets and suitable porous stones. The ultra-pure water used in this paper is from the Municipal Engineering Lab, Zhejiang University. The resistivity of water is between 15.0 and 18.2 M $\Omega$  cm, the electrical conductivity is approximately 0.53  $\mu$ s/cm, and the pH is between 5.60 and 5.80. The kaolin used is the commercial kaolin of Malaysia, and its kaolin mineral content is above 95%.

(2) Preparation of remolded slurry: The remolded slurry is prepared according to the soil–water mass mixing ratio of 2:1. First, take 1000 ml of ultra-pure water from a measuring cylinder and pour it into a plastic bucket. Take 500 g kaolin powder and put aside. Then, place the plastic bucket in a high-power electric mixer (speed: 100–1400 RPM, as shown in Fig. 9), turn on the mixer and mix it at a low speed (about 100 RPM). Slowly pour the measured kaolin powder into the plastic bucket and gradually control the mixer to increase the speed, until all the kaolin powder is poured into the plastic bucket, and the mixer speed increases to 200 RPM, and continue to stir for 5–10 min until the kaolin powder and ultra-pure water are evenly mixed.

(3) Consolidation: Firstly, vaseline was applied to the inside wall of the plexiglass bucket (250 mm diameter  $\times$  600 mm height), and then, slowly pour the remolded slurry into the container along the inner wall and repeat preparation step 2 until a sufficient amount of slurry (about 14–15 times) can meet the requirements of a single group of the test specimen. Let it stand for 24 h to allow the gas inside the remolding slurry to escape to ensure that there are no large pores in the soil specimens after consolidation. After standing, filter paper, porous stone and pressing plate shall be successively added to the surface of the slurry and transferred to the pressure consolidation instrument for loading (as shown in Fig. 10). Load in three stages to 600 kPa (the loading surface diameter is 100 mm, converted to the diameter of 250 mm plexiglass bucket, equivalent to the actual consolidation pressure of 96 kPa), and the loading time of each stage is approximately 48 h until the bottom of the plexiglass bucket with almost no drainage.

(4) Hollow cylindrical specimen preparation: After the remolded slurry is consolidated and the last stage of loading is stable, remove the cover plate screw at the bottom of the bucket and slowly push out the formed kaolin specimen from the other end to ensure the specimen has less disturbance, and the obtained kaolin is as shown in Fig. 11.

Cut formed specimens horizontally or vertically along the main consolidation direction into a solid cylindrical specimen slightly larger than the final hollow cylindrical one (200 mm high  $\times$  100 mm external diameter  $\times$  60 mm internal diameter).

**Fig. 9** High-power mixer and plastic bucket



**Fig. 10** Consolidation system with specimen



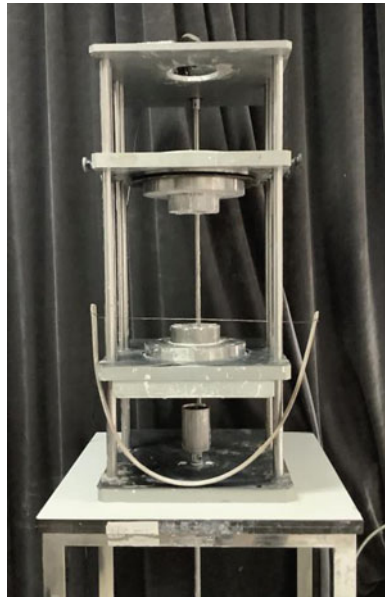
**Fig. 11** Remolded kaolin



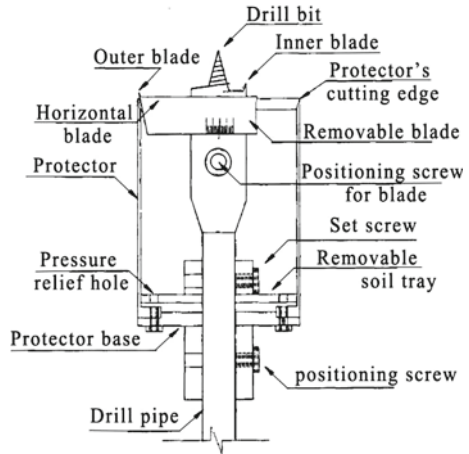
Place the solid cylindrical specimen on the hollow disk of the specimen making table, as shown in Fig. 12. The specimen is then cut from top to bottom using a fret saw attached to the positioning column shown in the figure, start the motor and turn the disk while cutting process. After the specimen's outer wall is formed, remove the fret saw and use a long scraper to repair the specimen's outer wall.

Then wrap the plastic film on the outside of the wall, place a clamping ring on the turntable base, place two pieces of steel protector to close the specimen and tighten it with a stainless steel hoop. The inner wall of the specimen is made by a special inner

**Fig. 12** Specimen making table



**Fig. 13** Special inner cutter



cutter, as shown in Fig. 13. Fix the position of the protecting tube relative to the drill pipe and make the blade slightly exposed along the top of the protect tube. Daub an appropriate amount of vaseline on the outer wall of the protector and each blade of the drill bit, vertically push the drill pipe to make the bit contact with the bottom of the specimen, and then screw the core. The depth of each rotary cut should not be more than 2 cm. Due to the limited depth of the blade, excessive depth of single cut will not improve efficiency but will destroy the soil. After each screw into a certain depth, exit the drill pipe, loosen the positioning screw between the protector and the bit, push the bit up and scoop out the soil inside the protector with a small spoon. After cleaning, reset the bit and tighten the positioning screw, and repeat the coring work until it is finished.

After drilling, remove the steel protector. Use the cap tube to cut the upper and lower ends of the specimen, just like the common triaxial test preparation method, and the final specimens are shown in the Fig. 14.

## Test Procedures

Install the prepared hollow cylinder specimens on the HCA according to the specifications and instructions of the equipment. Then successively carry out the test steps of saturation, consolidation, seepage, reconsolidation, loading and reseepage to measure the hydraulic conductivity of soil before and after cyclic loading.

(1) Saturation: In this paper, all specimens are saturated under 100 kPa back pressure condition, and the effective stress is defined as the actual stress minus the back pressure. Meanwhile, ensure that the soil is not disturbed in the saturation stage. The initial effective cell pressure was set as 5 kPa, and the cell pressure was ensured to increase simultaneously with the back pressure in the saturation stage. Then set back

**Fig. 14** Hollow cylindrical specimen



pressure to increase at a rate of 5 kPa/min until the value of pore pressure coefficient  $B$  measured by the system is larger than 0.98. At this time, it can be considered that the specimen has been saturated (generally takes more than 24 h).

(2) Consolidation: Two consolidation methods are available. One is isotropic consolidation, and the other is  $K_0$  consolidation. When isotropic consolidation is applied, set the axial stress to 0 in HCA advanced loading module, and ensure that all stress components of soil are equal at this time. Then increase the effective cell pressure to the design value at a rate of 5 kPa/min until consolidation is completed. When applying  $K_0$  consolidation to specimen, the axial stress of HCA advanced loading module should be set to increase at a rate of 0.02 kPa /min. Meanwhile, the inner and outer cell pressures should be adjusted according to the actual  $K_0$  coefficient to avoid lateral deformation during the consolidation process. Finally, control the effective axial pressure to reach the design value. The completion marks of the two consolidation modes are back pressure drainage volume less than 100mm<sup>3</sup> per hour.

(3) Seepage: According to the designed hydraulic gradient and the specimen height after consolidation, the pressure difference between the base back pressure and the top back pressure is set to form a stable hydraulic gradient. Since the inner cell pressure controller is not worked by software in this stage, in order to keep the effective cell pressure of soil under stable, the valve connecting the inner and outer cell pressure should be opened. According to the change of soil specimen size in consolidation stage, the equivalent diameter was calculated. The duration of seepage process is generally not less than 36 h.

(4) Reconsolidation: During the seepage process, the size of the top and bottom of the specimen controlled by the controller is different, which results in the uneven

distribution of pore pressure in the longitudinal direction, and the seepage force also causes the uneven deformation of the soil specimen. In order to explore the influence of dynamic load on soil permeability, the influence of uneven pore pressure should be eliminated before the loading process. Therefore, the specimen should be reconsolidated according to the consolidation stress and loading rate designed in test step 2. The completion marks of the reconsolidation stage can also be set as less than  $100\text{mm}^3/\text{h}$  back pressure drainage volume.

(5) Loading: After the completion of reconsolidation, according to the designed dynamic load parameters, cycle number and dynamic shear stress amplitude, the specimen can also be loaded with complex stress path. It should be noted that when exploring the soil permeability characteristics, the specimen should not be damaged during the loading stage, and the size characteristics of the specimen after deformation should still meet the relevant requirements of the seepage process described above.

(6) Reseepage: After the loading process is completed, record the deformation of the specimen and recalculate the equivalent diameter. Correct the specimen size parameters in the software and carry out the seepage test after the loading stage according to the corresponding requirements of test step 3. It should be noted that the time required for this step is generally greater than 48 h to reach the seepage stability stage.

## References

1. Tavenas F, Leblond P, Jean P (1983) The permeability of natural soft clays. Part I: Methods of laboratory. *Can Geotech J* 20(20):629–644
2. Tavenas F, Jean P, Leblond P, Leroueil S (1983) The permeability of natural soft clays. Part II: Permeability characteristics. *Can Geotech J* 20(4):645–660
3. Ding Z, Kong BW, We XJ, Zhang MY, Xu BL, Zhao FJ (2019) Laboratory testing to research the micro-structure and dynamic characteristics of frozen-thawed marine soft soil. *J Marine Sci Eng* 7(85):1–19
4. Zhou J, Deng YL, Cao Y, Yan JJ (2014) Experimental study of microstructure of Hangzhou saturated soft soil during consolidation process. *J Central South Univ (Sci Technol)* 45(6):1998–2005
5. Chapuis RP (2012) Predicting the saturated hydraulic conductivity of soils: a review. *Bull Eng Geol Env* 71(3):401–434
6. Basak P (1972) Soil structure and its effects on hydraulic conductivity. *Soil Sci* 114(6):417–422
7. Xiao JH, Juang CH, Wei K, Xu SQ (2014) Effects of principal stress rotation on the cumulative deformation of normally consolidated soft clay under subway traffic loading. *J Geotech Geoenviron Eng* 140(4):04013046
8. Xiao JH, Hong WY, Wu N (2015) Influence of traffic-loading induced principal stress rotation on the characteristics of soft clay. *Chin J Underground Space Eng* 11(6):1522–1527
9. ASTM D5084–16a (2016) Standard test methods for measurement of hydraulic conductivity of saturated porous materials using a flexible wall permeameter. ASTM International, West Conshohocken
10. Clennell MB, Dewhurst DN, Brown KM, Westbrook GK (1999) Permeability anisotropy of consolidated clays. *Muds Mudstones Phys Fluid Flow Properties* 158(1):79–96

11. Leroueil S, Bouclin G, Tavenas F, Rochelle P (1990) LA.: permeability anisotropy of natural clays as a function of strain. *Can Geotech J* 27(5):568–579
12. Yu LG, Zhou J, Wen XG, Xu J, Luo LH (2019) Factors influencing permeability anisotropy of remolded kaolin. *J Zhejiang Univ (Eng Sci)* 53(2):275–283+372
13. Cao Y, Zhou J, Yan JJ (2014) Study of microstructures of soft clay under dynamic loading considering effect of cyclic stress ratio and frequency. *Rock Soil Mech* 35(3):735–743



# Characterization of an Expansive Soil in Southwest Brazilian Amazon—Behavior of an Expansive Subgrade in a Flexible Pavement



Victor Hugo Rodrigues Barbosa , Maria Esther Soares Marques , Antônio Carlos Rodrigues Guimarães , and Carmen Dias Castro 

**Abstract** The main geotechnical aspects of the southwestern Brazilian Amazon are the absence of rocks to provide gravel for pavements and the widespread occurrence of expansive soils along the natural subgrade, associated with high rainfall indices. Although most of the local soils are rich in 2:1 clay minerals and amorphous material originated from Andes volcanic ashes—which is quite different from other Amazonian soils—geotechnical studies about the behavior of these materials are still very limited. The high volumetric variation of these expansive soils has been causing financial losses and making transportation by land difficult in the region. This paper presents the case study of a pavement built over expansive subgrade in Rio Branco city, state capital of Acre. Disturbed and undisturbed samples were collected in order to evaluate the swelling parameters of the soil. A suction-based model from Texas A&M University was used to predict pavement roughness caused by both expansive soils and traffic. The results showed the high swelling potential of the samples and the importance of developing a methodology for the control of expansive soils when building over these materials at the studied site.

**Keywords** Expansive soils · Amazonia · Flexible pavement

## 1 Introduction

Expansive soils are unsaturated soils that undergo significant volumetric changes when subject to change in suction or water content, commonly associated with seasonal moisture fluctuations. These soils tend to shrink and swell in response to alternate dry and wet conditions, inducing differential movements across lightweight structures such as residential buildings or pavements and causing problems like cracking that is not induced by structural loads.

---

V. H. R. Barbosa (✉) · M. E. S. Marques · A. C. R. Guimarães · C. D. Castro  
Military Institute of Engineering, Rio de Janeiro, Brazil

M. E. S. Marques  
e-mail: [esther@ime.eb.br](mailto:esther@ime.eb.br)

Swelling mechanism of expansive clays is complex and depends on a wide range of variables such as soil characteristics, initial moisture content, climate, vegetation, in situ density, slope of the site and changes brought about by man's action [1]. Nelson and Miller [2] divide these factors into three different groups: the soil characteristics, the environmental factors and stress state.

Considering the mineralogical properties that cause soil volume changes, the clay minerals which are typically associated with expansive soil behavior are smectite or vermiculite [3]. Illites and kaolinites are infrequently expansive but can cause volume changes when particle sizes are less than a few tenths of a micron [2].

Expansive soils are found throughout the world, causing huge financial losses every year. Although the problem is global, in general, regions with more arid climates have more severe expansive soil problems [4]. In Brazil, the problem has been founded in many places, especially in the northeast region [5].

The city of Rio Branco, located at Southwestern Brazilian Amazon has been facing damages associated with expansive soils in its roads and earthworks year by year (Fig. 1). The major concern about local soils is that a significant part is unappropriated for pavement construction due its expansive behavior. Nevertheless, there are few studies focused on understanding the local soils related to pavement construction as well as few design procedures from Brazilian Departments of Transportation. Consequently, suitable project solutions are rarely made.

The objective of this paper is to present results of a typical Acre expansive soil under a geotechnical perspective. It used a simple approach for predicting vertical movements as well as tested a model developed at Texas A&M University to predict pavement roughness caused by both expansive soils and traffic in terms of the serviceability index (SI) and the international roughness index (IRI).



**Fig. 1** Damages to infrastructure due to expansive soils in Rio Branco city

## 2 Background

### 2.1 Literature Review

Unsaturated soil theories have shown significant development over the past four decades. A significant part of these theories was dedicated to study expansive soils, a problematic soil which impacts structures and challenges geotechnical engineers around the world.

Due to the need of supporting lightly loaded structures, it is important to provide tools for practitioners to reliably estimate the volume change behavior of expansive soils in the field [6].

Essentially, when studying a potential heave problem, the engineer must evaluate the stress state profile of the soil and determine suitable physical properties for predicting future behavior [4].

The focus of most prediction methods has been toward estimating the maximum heave potential which occurs when soil attains saturation, usually through linear relationship between void ratio (vertical strain) and net normal stress or soil suction. Likewise, 1-D heaves are the most common analysis methods [6, 7].

Nevertheless, a limitation of these methods is in not providing information of soil movement in the field over time. This led researchers to develop several methods considering the soil suction fluctuation as a function of time within the active zone depth or connecting the soil state variables to volume change movement of the soil. Adem and Vanapalli [6] classify this group in three categories: (1) consolidation theory-based methods that use the matric suction and the net stress as state variables; (2) water content-based methods that use the soil water content as a state variable; and (iii) suction-based methods that use the matric suction as a state variable.

Regarding the classification based on 1-D heave prediction methods, Vanapalli et al. [8] list three categories of techniques or procedures: empirical methods that use soil classification parameters; oedometer test methods that take into account the loading and unloading sequence, surcharge pressure, sample disturbance and apparatus compressibility for reliable determination of the swelling pressure; and soil suction methods where the influence of suction is taken into account through the use of different parameters.

### 2.2 Fredlund (1983) Method

Yoshida and Fredlund [9] proposed a method for predicting 1-D heave in expansive soils involving the use of Eq. (1) and the constant volume swell (CVS) oedometer test.

$$\Delta H = C_s \frac{H_i}{1 + e_0} \log \left\{ \frac{P_f}{P'_s} \right\} \quad (1)$$

where  $H_i$  is thickness of the  $i$ th layer,  $P_f = (\sigma_y \pm \Delta\sigma_y - u_{wf})$  is final stress state,  $P'_s$  is corrected swelling pressure,  $C_S$  is swelling index,  $\sigma_y$  is total overburden pressure,  $\Delta\sigma_y$  is change in total stress,  $u_{wf}$  is final pore-water pressure and  $e_0$  is initial void ratio.

The CVS test involves inundating a sample under load, which is typically 7 kPa. As the sample attempts to swell, the applied load is increased to maintain the sample at a constant volume until there is no further tendency for swelling. This point is referred to as “uncorrected swelling pressure” ( $P_s$ ). The sample is then further loaded and unloaded in the conventional way of a consolidation test.

The CVS test provides two main measurements, namely corrected swelling pressure  $P'_s$  and the swelling index.  $P'_s$  is obtained from an empirical construction proposed by Casagrande which takes into account the effect of sampling disturbance.  $C_S$  is an index parameter which is the slope of the rebound curve determined from the CVS test.

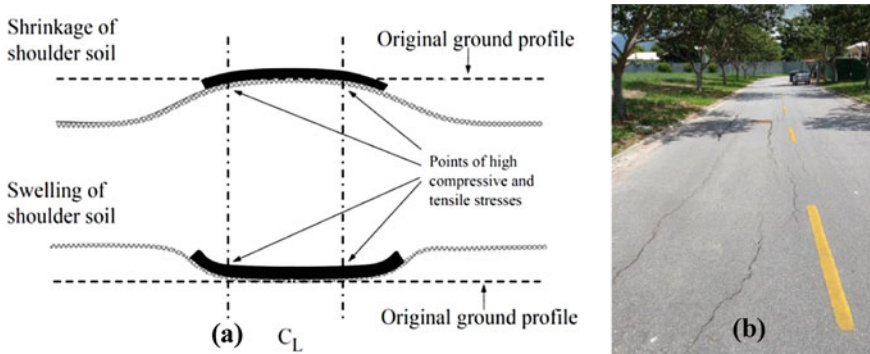
### ***2.3 Design Model to Predict Pavement Roughness on Expansive Soils***

Lytton et al. [10] presented a design program for pavements on expansive soil subgrades, WinPRES, which predict pavement roughness due to both expansive soils and traffic in terms of serviceability index (SI) and international roughness index (IRI) by correlating the roughness analysis to the vertical movement estimated from a vertical movement model.

These models were developed based on finite element studies calibrated to field observation over 15 years of roughness measurements conducted by Texas Transportation Institute (TTI) on Texas pavements.

The designer can specify different levels of reliability and designate several wheel paths for a period desired. Furthermore, it is possible to evaluate the effectiveness of various treatments for reducing roughness caused by expansive clay subgrade including lime or cement stabilized layers, removal and replacement with an inert soil, and vertical and horizontal moisture barrier.

The program considers the properties and effects of local soils, climate and drainage conditions in order to predict the suction that occur in the soil profile due to seasonal variations in moisture, from which vertical shrink–swell movements are estimated. The soil on which the pavement is built is considered at the equilibrium suction. It means that the water responsible for the vertical shrink–swell movement which affects the edge of the pavements comes from the soil and vegetation at the side of the pavement.



**Fig. 2** **a** Conceptual model for generating environmentally induced longitudinal cracks in pavements and **b** example of longitudinal crack occurrence at Rio de Janeiro, Brazil

### 2.4 Mechanisms of Longitudinal Crack Development in Pavements

Zornberg [11] describes the following mechanism that leads to the development of longitudinal cracks (Fig. 2) after long-term observation in Texas Department of Transportation (TxDOT).

## 3 Rio Branco Case Study

### 3.1 General Information

The soils of Rio Branco, a Brazilian city in South America (Fig. 3a), are mainly composed of sedimentary clay with high plasticity and consequently a high expansive potential, which is very common for most part of surrounding region. Despite this, the most part of unsaturated soils presented in the literature still does not include the state of Acre as a region with significant expansive soil deposits in Brazil (Fig. 3b).

According to studies prepared by the Brazilian Company of Mineral Resources (CPRM) at Rio Branco city, mineralogical characterization showed that montmorillonite is the predominant clay mineral in almost all samples analyzed [13]. Similarly, Barbosa [14] found same results studying typical Rio Branco subgrade soils.

An important point about the magnitude of volume change in soils is its high dependency on environmental conditions. Rio Branco has one period of dry and warm climate, between July and August, and other with very wet climate with high rainfall indices, between October and April. According to data from Federal University of Acre, average annual precipitation is 2050 mm. In addition, the region has many freshwater rivers and streams, which are usually seasonally flooded.



Fig. 3 a Location of the study area and b main expansive soil occurrences in Brazil [12]

Some of traditional solutions for pavements built over expansive soils involve the use of gravel both as moisture barriers and as a backfill material after removing some layers of expansive soils. However, as a rule in many cities of Brazilian Amazon, the cost of these materials is very expensive due to the long transport distances from suitable rock deposits. In August 2019, the cost of gravel ( $m^3$ ) at Acre was about 58.0 US dollars per cubic meter, which is 4 times higher than the cost of gravel at Rio de Janeiro, about 14.0 US dollars per cubic meter.

### 3.2 Local Site Investigation

The site studied in this paper is a booming real estate area located at the vicinity of Rio Branco city. Figure 4 shows the typical profile of the flexible pavement studied.

To start with, the occurrence of longitudinal cracks in many asphalt-paved roads after ending of dry season was verified, but still without opening traffic (Fig. 5a). It was also observed at the ground surface of the pavement shoulders the wide spreading of cracking in roughly polygonal patterns (Fig. 5b). The cracks have approximately

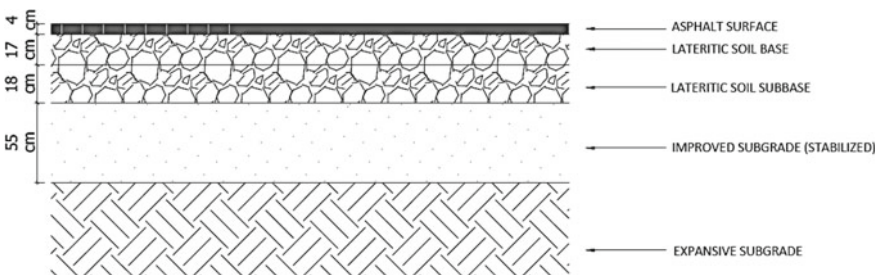


Fig. 4 a Typical pavement section at the studied site





**Fig. 5** **a** Typical longitudinal crack in the site study and **b** occurrence of cracking in roughly polygonal patterns at the studied site

1 in. of width, and excavations have shown that cracks were up to 2 feet deep. It is caused by desiccation that occurs in dry season and is influenced to the presence of root fibers that penetrate the soil profile.

Attempts to evaluate the groundwater level showed that cracking affected the infiltration of moisture insofar as facilitate the infiltration of surface precipitation. In other words, it affects the fluctuation of water in subgrade, with the influence of the mechanism described in 2.4. Plus, it can affect directly the pavement structure if vertical moisture barriers are not used.

### 3.3 Heave Prediction

It is essential in the early identification of expansive soils during the preliminary stages of a project. In order to identify and characterize the expansive soil from subgrade, it used the soil expansivity prediction based on standard classification results, such as grain size analysis and Atterberg limits.

A unidimensional oedometer test was carried out at the Soil Laboratory of Federal University of Acre (UFAC). The test followed the Yoshida and Fredlund [9] procedures, presented in Sect. 2.2. The main objectives were to obtain the corrected swelling pressure,  $P'_s$ , and the swelling index,  $C_s$ .

Since most of heave will occur near ground surface where the biggest difference between the corrected swelling pressure and the total overburden pressure is found, we can assume that heave tends to become zero in a depth where there is no difference between them. The depth where it occurs can be defined as the active depth of swelling, which is predicted by Eq. (2).

$$H = \frac{P'_s}{\rho g} \tag{2}$$

where  $H$  is active depth of swelling,  $\rho$  is total density of the soil (assumed to remain constant with depth) and  $g$  is gravitational acceleration.

The amount of heave is computed considering the stress state changes at the middle of the analyzed layer. The heave in each sublayer is calculated with Eq. 1, and the total heave from the entire expansive soil layer,  $\Delta H$ , is equal to the sum of the heave amounts calculated for each of the subdivided layers (Eq. 3):

$$\Delta H = \sum \Delta h_i \quad (3)$$

### 3.4 Development of Roughness for Case Study

For the flexible pavement in this paper, the design analysis of the studied site was performed using the program WinPRES, with data obtained from borehole logs, laboratory test results, climatic and drainage conditions, dimensions of road, roughness and traffic information.

Thornthwaite moisture index (TMI) was used to characterize the climate in the studied site. According to [15], Rio Branco climate type is B1 (humid), with average TMI value of 30. Falling weight deflectometer modulus of the subgrade soil was 68.95 MPa. The level of reliability for expansive soils was 50% for local roads. The initial serviceability index for flexible pavement was assumed to be 4.2, and the minimum acceptable SI after 10 years is considered at 2.5. All pavement layers were considered as simple inert layer with 1 m of thickness. The slope of the suction versus volumetric water content curve is obtained from the empirical correlation proposed by Lytton et al. [10]. Other parameters used for the case study are presented in Table 1.

## 4 Results and Discussion

### 4.1 Soil Expansivity Classification

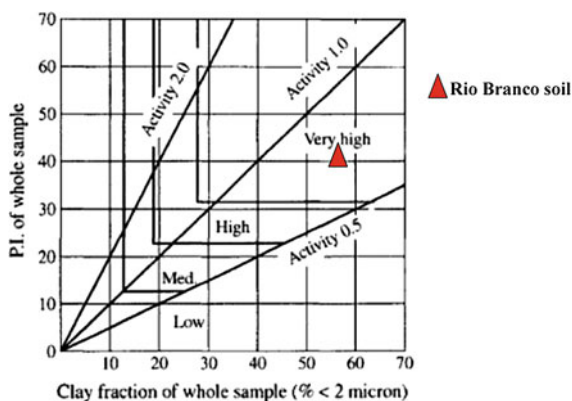
Figure 6 shows the soil expansivity prediction according to Van Der Merwe chart [16]. This classification relates plasticity index and clay fraction, resulting in a very high expansivity for the analyzed soil.



**Table 1** Design parameters for Rio Branco study site

Element data		Design parameters		Study site: Rio Branco local road
<b>LAYER # 1</b>				
Soil type	Inert soil	Number of lanes	1	
Thickness (m)	1.00	Average daily traffic ( $t = 0$ yr)	100	
Liquid limit (%)	50	Average daily traffic ( $t = 10$ yr)	150	
Plasticity index (%)	8	Total $W_{18}$ of outer lane ( $t = 10$ yr)	100,000.0	
Percent passing # 200 (%)	53	Width of pavement (m)	7	
Less than 2 microns (%)	23	Distance from the center of pavement (m)	3.5	
Dry unit weight ( $kN/m^3$ )	18.0	Falling weight deflectometer modulus of subgrade soil ( $kN/m^2$ )	68.95	
<b>LAYER # 2</b>		Structural number (cm)	9.0	
Soil type	Natural soil	Initial serviceability index	4.2	
Thickness (m)	2.00	Initial international roughness index	1.19 m/km	
Liquid limit (%)	69	Reliability	50% for prediction and 80% for design	
Plasticity index (%)	41	Mean Thornthwaite moisture index (TMI)	30	
Percent passing # 200 (%)	100	Depth of root zone (m)	0.5	
Less than 2 microns (%)	56	Depth of vertical barrier (m)	1.5	
Dry unit weight ( $kN/m^3$ )	15.0	Depth of moisture active zone (m)	2.0	

**Fig. 6** Soil expansivity classification based on Van Der Merwe chart



**Table 2** Total heave calculation for Rio Branco study site

Layer no.	Thickness (mm)	Corrected swelling pressure – $P_0 = P'_s$ (kPa)	Initial overburden pressure – $\sigma_v$ (kPa)	<i>Final Stress state</i> – $P_f = \sigma_v \pm \Delta v - u_{wf}$	Heave in each layer – $\Delta h_i$ (mm)
1	200	130.0	22.2	20.0	8.2
2	300	130.0	27.3	25.1	10.9
3	500	130.0	35.3	33.1	15.0
<b>Total heave <math>\Delta H</math>(mm) =</b>					<b>34.2</b>

## 4.2 Oedometer Test Parameters

The results of the constant volume swell (CVS) oedometer test allowed to quantify the initial state of stress along the swelling clay profile. It obtained a corrected swelling pressure ( $P'_s$ ) of 130 kPa and a swelling index ( $C_s$ ) of 0.08. Table 2 presents the calculation of the total heave in the middle of the expansive soil profile (2 m of thickness) assuming change of total stress due to excavation and the placement of fill corresponding to the pavement section shown in Fig. 4.

## 4.3 Roughness Analysis

Figure 7 shows the suction values of the wetting envelope, equilibrium and drying envelope conditions with depth. Suction profile at this location is developed with the equilibrium suction of 209 kPa, which was obtained by correlation equation based on TMI [10]; the limiting surface of 16 kPa for wetting and 3,162 kPa for drying are both estimated by the program using the climate data, the TMI and the drainage condition at the site. Total vertical movements calculated at the edge of the pavement and at the outer wheel path are also shown in Fig. 7.

The loss of serviceability and the increase of international roughness index versus time at a level of reliability of 50 percent are shown in Fig. 8.

## 5 Conclusions

The behavior of the expansive soil subgrade analyzed in Rio Branco based on maximum heave potential for saturated condition indicated a high correlation with the crack pattern on the local pavement, which is suggested by the substantial amount of heave calculated using the constant volume swell oedometer test.

Attempts to associate these cracks with local moisture fluctuations in expansive soils over time led to the use of a model developed at Texas, which is based on

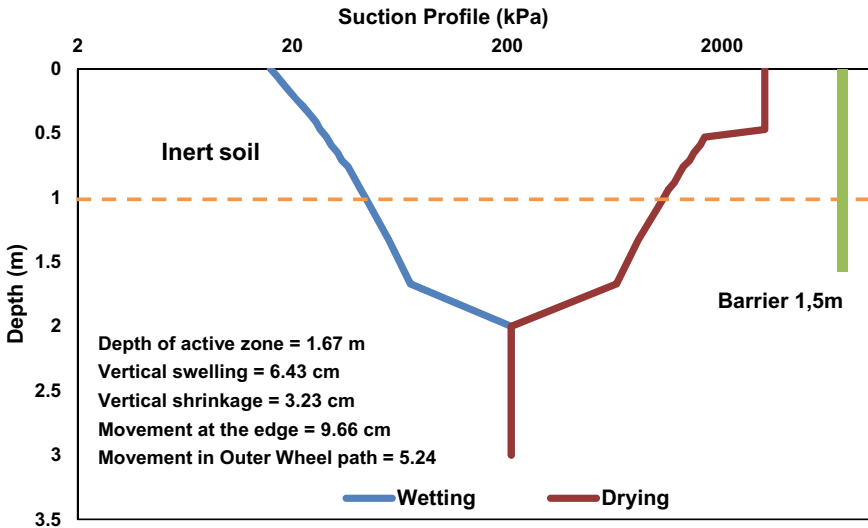


Fig. 7 Suction profile for Rio Branco study site with calculated vertical movement at the edge of pavement and at the outermost wheel path

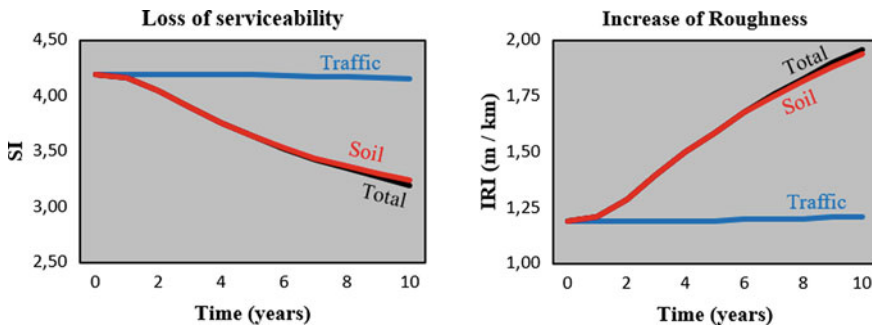


Fig. 8 Serviceability index and international roughness index versus time in the flexible pavement, Rio Branco local road

the roughness analysis. Assuming 2.5 and 2.62 m/km as terminal values for the loss of serviceability (SI) and the increase of international roughness index (IRI), respectively, the results showed that the SI of the pavement system is decreased about 60% after 10 years and IRI is decreased 55% after the same period. Furthermore, both graphs in Fig. 7 highlight the decrease of the pavement was practically due to the environmental and local soil properties, with negligible traffic influence.

In summary, even with more conservative design parameters when considering the low traffic level (structural number = 9.0; vertical moisture barrier = 1.5, inert soil layer of 1.0 m, etc.), this paper showed that the increase of roughness as well as the total movements calculated at the edge of pavement and at the outer wheel

path produced a non-acceptable performance for the pavement system, indicating the need of design alternatives in order to reduce the effects of the expansive subgrade over time.

**Acknowledgements** The authors would like to thank Professor Robert Lytton (University of Texas at Austin), who kindly gave deep recommendations about WinPRES program. The authors would also like to thank all members of Soil Laboratory at Federal University of Acre (UFAC) for their support with several tests on soil samples.






## References

1. Jayatilaka R, Lytton RL (1997) Prediction of Expansive clay roughness in pavements with vertical moisture barriers, vol 7
2. Nelson JD, Miller DJ (1992) Expansive soils—Problems and practice in foundation and pavement engineering. Colorado State University
3. Mitchell JK, Soga K, Wiley J (2005) Fundamentals of soil behavior, 3rd edn.
4. Fredlund DG, Ahmad N, Mermut A (1996) Geotechnical problems associated with swelling clays. In: Vertisols and technologies for their management, vol c, pp 499–524. [https://doi.org/10.1016/S0166-2481\(96\)80016-X](https://doi.org/10.1016/S0166-2481(96)80016-X)
5. Carvalho JC (2015) Solos Não saturados no Contexto Geotécnico. (Unsaturated soils in the geotechnical context). ABMS (in Portuguese)
6. Adem HH, Vanapalli SK (2015) Review of methods for predicting in situ volume change movement of expansive soil over time. *J Rock Mech Geotech Eng* 7(1):73–86. <https://doi.org/10.1016/j.jrmge.2014.11.002>
7. Vanapalli SK, Lu L (2012) A state-of-the art review of 1-D heave prediction methods for expansive soils. *Int J Geotech Eng* 6(1):15–41. <https://doi.org/10.3328/IJGE.2012.06.01.15-41>
8. Vanapalli SK, Lu L, Oh WT (2011) A simple technique for estimating the 1-D heave in expansive soils. In: Unsaturated soils—Proceedings of the 5th international conference on unsaturated soils, vol 2, no May 2016, pp 1201–1207
9. Yoshida RT, Fredlund DG, Hamilton JJ (1983) The prediction of total heave of a slab-on-ground floor on Regina clay. *Can Geotech J* 20(1):69–81. <https://doi.org/10.1139/t83-008>
10. Lytton R, Aubeny C, Bulut R (2004) Design procedure for pavements on expansive soils: vol 1. Re-evaluate current potential vertical rise (PVR) design procedures. Texas Department of Transportation and the U.S. Department of Transportation Federal Highway Administration
11. Zornberg JG, Gupta R (2009) Reinforcement of pavements over expansive clay subgrades. In: Proceedings of the 17th international conference on soil mechanics and geotechnical engineering: the academia and practice of geotechnical engineering, vol 1, pp 765–768
12. Ferreira SRM (2008) Solos colapsáveis e expansivos: uma visão panorâmica no Brasil. In: Machado SL, Carvalho MF (eds) Anais do VI Simpósio Brasileiro de Solos Não Saturados, vol 2. UFBA, Salvador, pp 593–618 (in Portuguese)
13. Oliveira MA (2006) Avaliação Geológico-Geotécnica da cidade de Rio Branco - Acre. (Rio Branco city geological and geological evaluation) (in Portuguese)
14. Barbosa VHR (2017) Estudo de solos do Acre para a produção de agregados calcinados e misturas para Bases em Pavimentação. (Study of soils from Acre in order to produce calcined aggregates and mixtures for base course). Dissertação de Mestrado, Instituto Militar de Engenharia, Rio de Janeiro, RJ, 155 p (in Portuguese)

15. PMACI I (1990) Diagnóstico Geoambiental e Sócio-econômico. Projeto de proteção do Meio Ambiente e das comunidades indígenas. IBGE. Rio de Janeiro (in Portuguese)
16. Van Der Merwe DH (1965) The prediction of heave from the plasticity index and percentage clay fractions of soils. Br J Psychiatry 111(479):1009–1010. <https://doi.org/10.1192/bjp.111.479.1009-a>

# Moisture Influence on the Shakedown Limit of a Tropical Soil



Gleyciane Almeida Serra , Antonio Carlos Rodrigues Guimaraes ,  
Maria Esther Soares Marques , Carmen Dias Castro ,  
and Artur Cortes da Rosa 

**Abstract** This paper presents results from permanent deformation tests carried out on fine tropical soils in order to study the effect of moisture variation. Shakedown limit was defined through repeated load triaxial tests under different stress states for 5000 load cycles. A mathematical model to classify permanent deformation behavior proposed by Werkmeister (Doctoral thesis, Technical University of Dresden [Werkmeister S (2003) Permanent deformation behavior of unbound granular materials in pavement constructions. Doctoral thesis. Technical University of Dresden, 189 pp]) was used to rank the shakedown limit of the materials. In this research, a lateritic clayey soil, according to the classification MCT (Miniature, Compaction, Tropical) from Nogami and Villibor (Brazilian Symposium of Tropical Soils in Engineering, Rio de Janeiro, RJ, pp 30–41, [Nogami JS, Villibor DF (1981) Uma nova classificação de solos para finalidades rodoviárias. In: Brazilian symposium of tropical soils in engineering, Rio de Janeiro, RJ, pp 30–41]), was tested in the optimum content and at the high moisture induced by capillary post-compaction. The resilient behavior was studied to characterize the mechanical behavior of the material. The results of permanent deformation tests showed that fine tropical soils may have a nonsignificant reduction of their shakedown limit, with the increase moisture of 1%. The proposed model showed a good agreement for this tropical soil at an optimum moisture. The understanding of the shakedown phenomenon from tropical soils may help to bridge the gap between the materials accepted by traditional classification and those not accepted, although they present good mechanical resistance.

**Keywords** Shakedown theory · Permanent deformation of soils · Lateric tropical soils

---

G. A. Serra (✉) · A. C. R. Guimaraes · M. E. S. Marques · C. D. Castro · A. C. da Rosa  
Military Institute of Engineering, 80 Praca Tiburcio, Rio de Janeiro, Brazil  
e-mail: [gleyciane.serra@ime.eb.br](mailto:gleyciane.serra@ime.eb.br)

## 1 Introduction

One of the most frequent modes of failure in pavements is rutting. This kind of failure is highly undesirable, since it causes water accumulation in the pavement, reducing the friction between the tire and pavement surface, also, causing saturation of the pavement layers. Pavement structures are designed to dissipate energy from the traffic load in order to maintain stresses and permanent deformation below limits. At the same time, rut development depends on pavement materials under traffic loads and the climatic conditions, thus it is difficult to predict long-term behavior of pavement structure.

Most of the design models are based on the elastic behavior of the pavement. These models consider that just resilient deformation occurs and the failure is attained when stresses are at a critical value. However, pavement collapse is usually caused by the accumulation of small permanent deformations from repeated loads. According to [1], the accumulated permanent deformations promote a gradual deterioration resulting in subsurface slip, rut formation, or surface cracking. Thus, pavement construction must be designed considering also the existence of residual stresses.

After a certain number of load applications, some materials suffer a rearrangement of the particles, leading to plastic deformations called shakedown phenomenon. Several authors reported the occurrence of shakedown at low stress levels [2–5]. It implies that there are some critical stress levels between the elastic and plastic regime that may help to predict the pavements failure.

Shakedown concept has been used to predict the long-term performance of unbound granular materials (UGM) [6–13]. From shakedown studies carried out by University of Nottingham [10], a consistent model was proposed for permanent deformation in UGM. The model defines equations that classify the deformation behavior from the material. When the stresses are within the stable range, called plastic shakedown, the pavement is expected to show good performance. The model does not discuss the influence of moisture content on deformation behavior, and also it may not contemplate other materials, as lateritic tropic soils with high fine content, which tend to be highly susceptible to moisture variation. Although, the model was conceived to analyze UGMs behavior, it would be interesting to use the model to compare permanent deformation of new constituent materials.

Studies of the use of fine tropical soils on low traffic highways road construction were carried out in Brazil [14, 15] in order to reduce costs. The lateritic nature of some tropical soils is the cause of the unique mechanical and hydraulic behavior of these soils. Nevertheless, traditional classifications (SUCS and HRB) are not able to distinguish the nuances of behavior of Brazilian tropical soils. Thus, the MCT (Miniature, Compaction, Tropical) was the methodology proposed by Nogami and Villibor [16] in order to classify these soils.

The studies carried out about permanent deformation in Brazil [17–21] showed a tendency of shakedown occurrence for lateritic soils. Through the analysis of the rate of increase of permanent deformation as a function of the total permanent deformation, it seems that fine lateric soils presented less plastic behavior for lower tensions

than the fine non-lateric soils [20]. Although a pattern was noted, the shakedown limit for tropical soils needs yet to be investigated. There is still field to improve the knowledge about the shakedown phenomenon in Brazilian tropical soils.

For soils, especially in tropical climate regions, the applicability of the permanent deformation attributed to the shakedown concept is an unknown. Since fine soils are more susceptible to moisture than gravel materials, the settlement should be influenced by moisture. Thus, this study seeks to investigate whether there is an influence of post-compaction moisture variation on the shakedown limit through capillary-induced moisture for a typical Brazilian tropical soil.

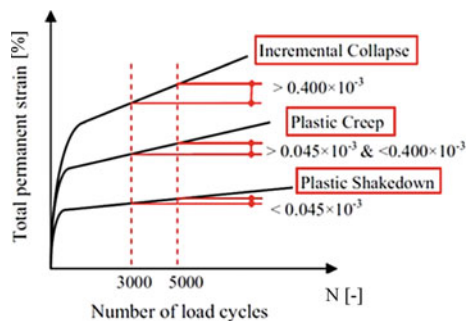
## 2 Shakedown and Permanent Deformation Concepts

Shakedown theory, for design pavement purposes, is related to the accommodation of permanent deformations. Some materials after repeated loading action develop residual stresses that will interact with successive load applications, changing the behavior regime of the material. Such stresses will prevent the layer from exceeding the elastic limit, thus showing only elastic deformations [4].

According to [1], the response of material under repeated loads can be divided in four stages depending on the load level: purely elastic, elastic shakedown, plastic shakedown, and collapse. For paving materials, there is no purely elastic behavior reported in the literature and the elastic shakedown occurs at low stress levels. At this stage, the deformation becomes constant and the structure stable, with an excellent pavement performance. With this basic understanding, it is possible to adopt Melan’s static or Koiter’s kinematic theorems to design pavements [1].

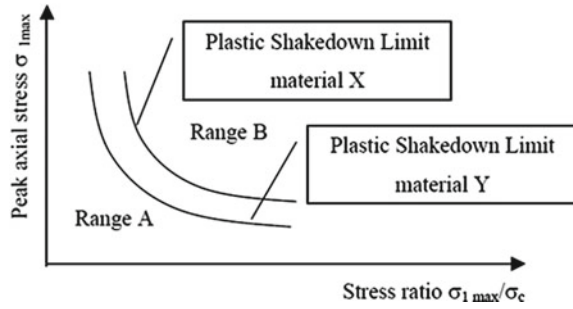
The University of Nottingham developed a consistent study of the behavior of UGM by using the cyclic triaxial test to define the permanent deformation [10]. After observing a pattern in the evolution of deformations in UGM’s, a criterion was set based on the vertical permanent strain accumulated from 3000 to 5000 cycles, in order to classify the permanent deformation behavior in three categories: plastic shakedown, plastic creep, and incremental collapse (Fig. 1).

**Fig. 1** Classification of UGM based on changes in permanent strain [13], as cited in [16]





**Fig. 2** Ranking of materials [10]



The European Committee for Standardization [22] includes a section to rank the materials in shakedown concepts (Fig. 2). It is possible to estimate the shakedown limit to compare and assess the suitability of different materials used in UGMs in pavement constructions. This standard suggests a minimum of three different confining stresses for different stress ratio to find the constants of the equation ( $\alpha$ ,  $\beta$ ) to build plastic shakedown limit, as in Eq. 1.

$$\sigma_{1max} = \alpha \times \left( \frac{\sigma_{1max}}{\sigma_3} \right)^\beta \tag{1}$$

### 3 Material Properties and Testing Procedure

#### 3.1 Material

Soil samples were collected at São Luis, located at the border of Legal Amazon region, and the samples were from a variety of fine lateritic soils in the region, often found at subgrade of highways and depleted land deposits (Fig. 3). This soil was classified as A-4, defined by AASHTO classification method and as ML-CL as per unified soil classification system (USCS). According these classifications, this soil is considered fair to poor performance as subgrade of pavements. In this case, it is recommended to use a subgrade reinforcement to meet the standard. Although, when using MCT classification [16], if the soil is lateritic, it could present a good behavior as subgrade.

A summary of the geotechnical characteristics of the soil is presented in Table 1. The plasticity index is 5%, thus a low plasticity. The sand, silt, and clay content are 64%, 1%, and 35%, respectively. The results of maximum dry density and optimum moisture obtained from the standard Proctor compaction test, at Intermediate energy, were used to prepare the samples of the triaxial tests.



**Fig. 3** Subgrade of a low traffic pavement containing a clayey sand from Sao Luis

**Table 1** Geotechnical characteristics of the soil

Test	Unit	Value
Sand (>0.075 mm)	%	64
Silt (0.005–0.075 mm)	%	1
Clay (<0.005)	%	35
Liquid limit (LL)	%	20
Plasticity limit (PL)	%	15
Specific weight ( $\gamma$ )	$\text{g/cm}^3$	2.61
TRB classification	A-4	–
Unified classification	ML-CL	–
MCT classification	LG' (lateritic clayey)	–
Maximum dry density	$\text{g/cm}^3$	2.04
Optimum moisture	%	10.3

### 3.2 Specimen Preparation

The samples were homogenized at the optimum moisture and to rest under controlled humidity at least 12 h before compaction. Then, the material was compacted in a cylindrical tripart mold with 10 cm radius and 20 cm height in the intermediate Proctor energy (Fig. 4).

In order to analyze the moisture influence, some samples were tested under different conditioning treatments. The moisture content was elevated by capillary over a period of 1 h (30 min on each side of the specimen). After this period, the specimen was again kept during 2 h under controlled humidity. The sample was turned every 30 min in order to homogenize the absorbed water.



**Fig. 4** Specimen in different stages of preparation

### 3.3 Method and Testing Program

Single-stage loading used one specimen for each deviatoric stress. Each specimen was tested for different levels of wheel loads to identify the maximum loads related to shakedown response. The number of 5000 cycles was applied according with the European Standard EN 13287-7:2004 [22].

The European Standard suggests testing at a least at three different confining stresses to rank the material. The confining stresses proposed by the European standard were not enough to this material. It was necessary to run tests with additional confining stresses to reduce the range between the plastic shakedown and plastic creep (Table 2). The test was repeated to the next sample until the material achieved plastic creep. After that, the sample was removed to determine the water content.

**Table 2** Regression coefficients of the models for Sao Luis clayey soil

Stress ratio	Confining stress (kPa)
3	60, 70, 80, 90, 100, 110
4	20, 30, 40, 50, 60, 70
5	20, 30, 40, 50, 60
6	20, 30, 40, 50

## 4 Results and Analyses

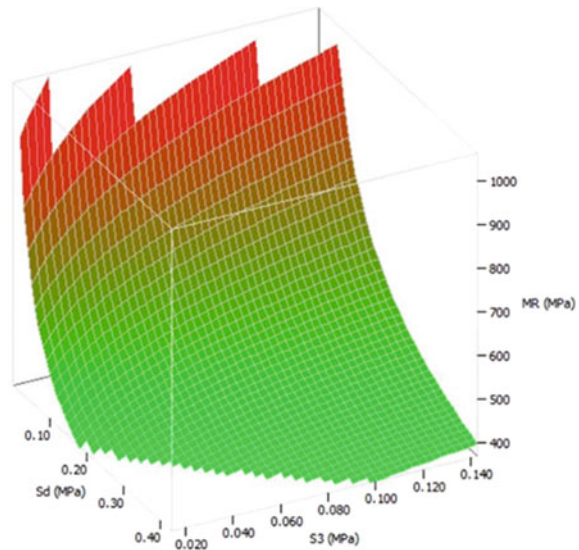
### 4.1 Resilient Behavior

Resilient modulus (RM) is an important propriety for mechanistic approach of pavement design. Thus, the resilient moduli were determined from the triaxial cyclic tests. Three models to predict resilience behavior were analyzed (Table 3). The better fit was the model defined by National Highway Cooperative Research Program (NHCRP) [23]. However, the composite model by Pezo [24], which also shows adequate variability, was adopted to represent the resilient behavior (Fig. 5), since it is the most used model in pavement design in Brazil. The minimum and maximum values predicted by this model were 368 and 1063 MPa, respectively, and the average resilient modulus value resulting from the average of the test values was 639 MPa.

**Table 3** Regression coefficients of the models for Sao Luis clayey soil

Model	References	$k_1$	$k_2$	$k_3$	$R^2$
$M_r = k_1 * \left(\frac{\sigma_d}{P_a}\right)^{k_2}$	[25]	415.62	-0.26	-	0.66
$M_r = k_1 * P_a * \left(\frac{\sigma_3}{P_a}\right)^{k_2} * \left(\frac{\sigma_3}{P_a}\right)^{k_3}$	[24]	415.62	0.21	-0.44	0.84
$M_r = k_1 * P_a * \left(\frac{\sigma_{sum}}{P_a}\right)^{k_2} * \left(\frac{\tau_{oct}}{P_a} + 1\right)^{k_3}$	[23]	117.74	0.35	-0.64	0.92

**Fig. 5** Three-dimensional graph of the composite model of São Luis lateritic clayey soil



**Table 4** Ranges and typical values of MR of materials at the optimum moisture content (NCHRP 1-37A, 2004)

USCS symbol	Descriptions	Resilient modulus (MPa)		Resilient modulus (MPa)
		Low	High	
GW	Gravel or sandy gravel, well graded	272	290	283
GP	Gravel or sandy gravel, poorly graded	245	276	262
GM	Silty gravel or silty sandy gravel	228	290	265
GC	Clayed gravel or clayed sandy gravel	166	259	148
SW	Sand or gravelly sand, well graded	193	259	221
SP	Sand or gravelly sand, poorly graded	266	228	193
SM	Silty sand or silty gravelly sand	193	259	221
SC	Clayed sand or clayed gravelly sand	148	193	166

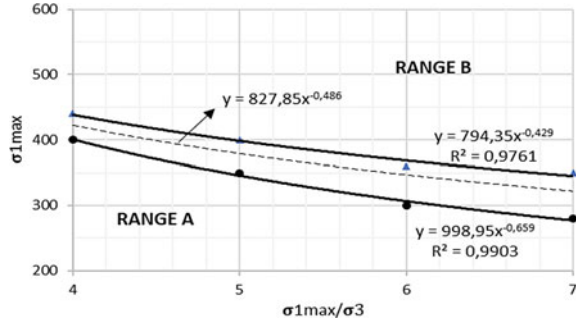
The values of resilient modulus for this material are higher than the average ranges values of RM, suggested by the NCHRP [26], for materials with the same USCS classification (Table 4). This behavior is quite common for lateritic soils, showing the peculiarities of the mechanical behavior of these soils. Discrepancy of values is expected for tropical soils as they are not well represented by traditional classification systems such as USCS.

## 4.2 Shakedown Research

The results of the triaxial tests for the optimum moisture revealed an excellent fit with the standard equation (Eq. 1). Least square regression showed values of 0.98 for upper limit and 0.99 for lower limit (Fig. 6). It was observed that for higher stress ratio, it will be easier for the material to reach range B. Regarding the influence of stresses on vertical deformation, as the confining stress increases, so does the deviation stress necessary to reach the plastic regime, as given in Table 5.

When compared with the results from Werkmeister's studies, the shakedown limit presents higher stress states to change from range A to range B (Fig. 7). There are two aspects that may explain the improvement behavior showed in Fig. 7. The first aspect is chemical origin, which is associated with the wide presence of oxides/hydroxides aluminum and iron in lateritic soils that act as natural cements. Another aspect, by

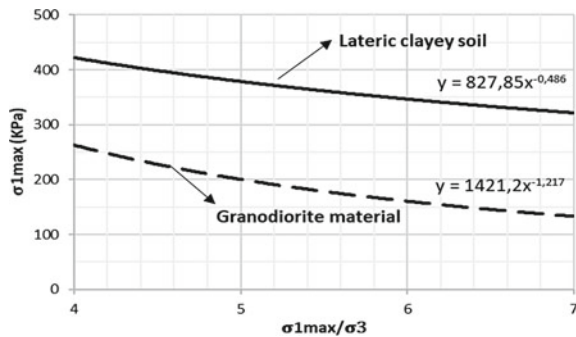
**Fig. 6** Plastic shakedown limit range for Sao Luis lateritic clayey soil



**Table 5** Ranges and typical values of MR of materials at the optimum moisture content (NCHRP 1-37A, 2004)

Ratio stress (kPa)	Deviation stress (kPa)	Confining stress (kPa)	$\varepsilon_{5000} - \varepsilon_{3000} \geq 0.045$	Deformation behavior
3	330	110	0.061	Plastic shakedown
3	300	100	0.04	Plastic limit
4	320	80	0.045	Plastic shakedown
4	280	70	0.033	Plastic limit
5	300	60	0.051	Plastic shakedown
5	250	50	0.028	Plastic limit
6	300	50	0.056	Plastic shakedown
6	240	40	0.027	Plastic limit

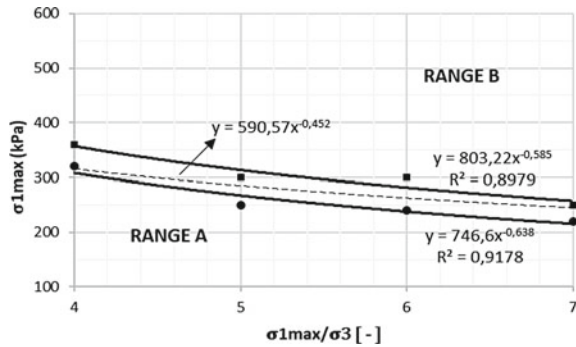
**Fig. 7** Comparison between plastic shakedown limit of Sao Luis lateritic clayey soil and granodiorite from [10]



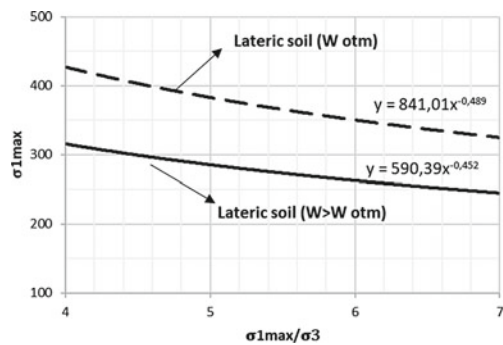
physical origin, is the development of high suction stresses, characteristic of the particle size composition of tropical soils.

The understanding occurred by the effect of moisture from capillarity is important because of possible variations in the groundwater in pavement. In Brazil, there is a high variation of moisture in most of the territory. Some regions are subject to flooding due to high rainfall, such as the legal Amazon. The results from triaxial tests samples, with moisture above the optimum moisture, also showed a good approximation. Figure 8 demonstrated the least square regression values of 0.90 and 0.92 for the range of shakedown limit. Figure 9 shows the shakedown limit results for optimum and water content after conditioning. From a given stress ratio, the moisture variation used (1% above the optimum) did not have significant influence on the shakedown limit. This may be related to the cementation process due to the presence of aluminum hydroxides in the material, which changes the suction stresses. Also, it is observed that as the stress ratio increases, the shakedown limit tends to reduce the materials equal or above the optimum water content.

**Fig. 8** Plastic shakedown limit range for Sao Luis lateritic clayey soil in moisture above the optimum



**Fig. 9** Moisture influence on the plastic shakedown limit for Sao Luis lateritic clayey soil



## 5 Conclusions

A lateritic clayey soil was tested to study the susceptibility to changes in water content. By considering the accumulated permanent deformations between 3000 and 5000 cycles, the present study ranked the material in two different conditions: plastic shakedown and plastic limit. The results obtained at the optimum moisture content were good, and the shakedown limit curve was defined. In addition, the results showed no relevant moisture influence for the samples tested after moisture conditioning. However, the results presented greater dispersion in relation to the equation of European Standard EN 13287-7:2004 for unbound granular materials.

The shakedown concept is well applied to the case of unbound granular material, once after a certain number of loading, these materials tend to get the particles stuck. Even though the same justification for this phenomenon cannot be applied for soil, studies on lateritic soils show an accommodation of permanent deformations similar to the accommodation of UGMs. This peculiarity can be associated with the chemical composition, presence of natural cements, and the high suction stresses, resulting from the granulometric composition of these soils.

## References

1. Collins IF, Boulbibane M (2000) Geomechanical analysis of unbound pavements based on shakedown theory. *J Geotech Geoenviron Eng* 126(1):50–59
2. Sharp RW, Booker JR (1984) Shakedown of pavements under moving surface loads. *J Transp Eng ASCE* 110:1–14
3. Lekarp F, Dawson A (1998) Modelling Permanent deformation behavior of unbound granular materials. *Constr Build Mater Elsevier Science Ltd* 12(1):9–18
4. Sharp RW (1985) Pavement design based on shakedown analyses. In: *Transportation research record 1022*, TRB, National Research Council, Washington, DC, pp 99–107
5. Paute JL, Hornych P, Benaben JP (1996) Repeated load triaxial testing of granular materials in the French Network of Laboratories des Ponts et Chaussées. *Flexible pavements*. In: Correia AG (ed) *Proceedings, European symposium on flexible pavements, Euroflex, 1983*. Rotterdam, pp 53–64
6. Garcia-Rojo R, Herrmann HJ (2005) Shakedown of unbound granular material. In: *Granular matter*, vol. 7. Springer, Berlin, Heidelberg, pp 109–18
7. Nazzal MD, Mohammad LN, Austin A (2011) Evaluation of the shakedown behavior of unbound granular base materials. *Geo-Frontiers 2011*, American Society of Civil Engineers (ASCE), pp 4752–4761
8. Cerni G, Cardone F, Virgili A, Camilli S (2012) Characterisation of permanent deformation behaviour of unbound granular materials under repeated triaxial loading. *J Construct Build Mater Elsevier Sci* 79–87
9. Werkmeister S, Dawson AR, Wellner F (2001) Permanent deformation behavior of granular materials and the shakedown concept. *Transportation Research Record No. 01-0152*, Washington, DC
10. Werkmeister S (2003) Permanent deformation behavior of unbound granular materials in pavement constructions. *Doctoral thesis*. Technical University of Dresden, 189 pp
11. Werkmeister S, Numrich R, Dawson A, Wellner F (2003) Design of granular pavement layers considering climatic conditions. *Transportation Research Board, 82° Annual meeting, 12–16 Jan 2003*, Washington, DC



12. Werkmeister S, Dawson AR, Wellner F (2005) Pavement design for unbound granular materials. *J Transp Eng* ©ASCE/September/October
13. Soliman H, Shalaby A (2015) Permanent deformation behavior of unbound granular base materials with varying moisture and fines content. *Transp Geotech* 4:1–12
14. Nogami JSE, Villibor DF (1995) *Pavimentação de Baixo Custo com Solos Lateríticos*. Editora Villibor, São Paulo, SP
15. Nogami JS, Villibor DF (1991) Use of lateritic fine-grained soils in road pavement base courses. *Geotech Geol Eng* 9(3/4):167–182
16. Nogami JS, Villibor DF (1981) Uma nova classificação de solos para finalidades rodoviárias. In: *Brazilian simposium of tropical soils in engineering*, Rio de Janeiro, RJ, pp 30–41
17. Guimarães ACR (2001) *Estudo de deformação permanente em solos e a teoria do shakedown aplicada a pavimentos flexíveis*. Masters dissertation. COPPE, Federal University of Rio de Janeiro, Rio de Janeiro, RJ
18. Guimarães ACR (2009) *Um método mecanístico-empírico para a previsão da deformação permanente em solos tropicais constituintes de pavimentos*. Doctoral thesis. COPPE, Universidade Federal do Rio de Janeiro, Rio de Janeiro, RJ
19. Delgado BG (2012) *Análise da deformabilidade de um solo tropical do oeste do maranhão como material de sublastro na Estrada de Ferro Carajás*. Masters dissertation. Federal University of Ouro Preto, MG
20. Guimaraes ACR, Motta LMG, Castro CD (2018) Permanent deformation parameters of fine-grained tropical soils. In: *Road materials and pavement design*, pp 1–18
21. Guimaraes ACR, Motta LMG (2008) A study on permanent deformation soils including the shakedown concept. In: *Advances in transportation geotechnics*, pp 149–161
22. European Committee for Standardization (2004) *Unbound and hydraulically bound mixtures—Part 7: cyclic load triaxial test for unbound mixtures*. EN 13286-7
23. National Highway Cooperative Research Program Project 1-28A (2004). *Laboratory determination of resilient modulus for flexible pavement design*. National Cooperative Highway Research Program Research Results Digest No. 285
24. Pezo R (1993) A general method of reporting resilient modulus tests of soils, a pavement engineer's point of view. In: *The 72nd annual meeting of transportation research board*
25. Moosazadeh JM, Witczak W (1981) Prediction of subgrade moduli for soil that exhibits nonlinear behavior. *Transportation Research Record*
26. National Highway Cooperative Research Program Project 1-37A (2004) *Summary of the 2000, 2001, and 2002 AASHTO guide for the design of new and rehabilitated pavement structures*. National Cooperative Highway Research

# Long-Term In-Situ Measurement of Soil Suction in Railway Foundation Materials



Rick Vandoorne , Petrus Johannes Gräbe , and Gerhard Heymann 

**Abstract** Volumetric water content (VWC) and matric suction vary temporally in the foundation layers of pavements and railways due to various influencing environmental factors. The resilient and permanent deformation behaviors of railway foundation materials are strongly linked to the suction within the soil, reinforcing the need for the measurement thereof. This paper reports on the installation of VWC sensors, tensiometers and fixed-matrix soil-water suction sensors in different configurations within the foundation layers of a new 26 tonne/axle railway line near Ermelo in South Africa. Local weather data was recorded using a weather station at the site. The VWC sensors and the fixed-matrix soil-water suction sensors also monitored soil layer temperature. The measurement techniques used are critically compared with regard to their ability to respond to weather events. Practical aspects pertaining to the installation procedures and maintenance required for the different techniques are also reported. It was found that tensiometers require careful consideration to ensure pore-water continuity when installed in the field. Nonetheless, tensiometers were the most reliable and accurate form of measurement in this study. The use of VWC sensors to infer suction in silica flour is a novel idea. However, this method showed limited success in this study. Fixed-matrix soil–water suction sensors provided the best long-term stability and ease of installation. However, the accuracy of these sensors requires further investigation.

**Keywords** Railway foundation · Soil suction · Volumetric water content · Pavement foundation

---

R. Vandoorne (✉) · P. J. Gräbe · G. Heymann  
University of Pretoria, Pretoria, South Africa  
e-mail: [vandoorne.r@gmail.com](mailto:vandoorne.r@gmail.com)

G. Heymann  
e-mail: [gerhard.heyman@up.ac.za](mailto:gerhard.heyman@up.ac.za)

## 1 Introduction

Many road and railway foundations remain in an unsaturated state for the duration of their design life. This may be due to the surfacing layers and/or the drainage systems, which prevent the complete saturation of the founding layers of roads and railways. Despite this, railways are still designed using either completely empirical techniques or mechanistic–empirical techniques based on saturated soil testing and predicted or measured in-situ moisture contents [1].

Unsaturated soil mechanics needs to be considered in order to design and understand the behavior of railway foundations from a fundamental basis. Many of the challenges hindering the adoption of unsaturated soil mechanics in geotechnical design have been addressed [2]. The soil–water retention curve (SWRC) links the soil–water potential (an energy state) to the amount of soil–water present within its pores, which can be expressed either in terms of gravimetric water content  $\omega$ -SWRC, volumetric water content  $\theta$ -SWRC or by the degree of saturation  $S_r$ -SWRC of the soil. Soil–water potential may be divided into osmotic and matric potential, the sum of which is termed total potential. These concepts are well explained by Toll [3] and will not be repeated here to maintain brevity. The absolute value of matric potential is termed matric suction.

The SWRC is vital for the implementation of unsaturated soil mechanics. The SWRC has interrelations with other unsaturated soil property functions such as the suction stress characteristic curve, hydraulic conductivity function and water storage function [4]. These functions dictate the mechanical and hydraulic behavior of unsaturated soil, respectively.

Toll [5] identified that in African countries many low-volume roads constructed from lateritic soils displayed better performance than could be predicted using empirical techniques based on fines content and plasticity. In fact, many of these road materials would be completely rejected based on specifications existing at that time. It was concluded that the fines in these materials allowed higher suctions to develop, which improved mechanical performance of these roads and also decreased their hydraulic conductivity, in turn reducing water ingress and maintaining the developed suctions. The importance of soil suction and fabric has thus been identified.

Figure 1 shows suctions measured on a Kiunyu gravel compacted at different water contents [6]. The lines on the plot show how the suctions changed for three of the samples as they were subjected to wetting and drying after initial compaction. A soil in the field will undergo seasonal drying and wetting cycles after compaction too. From Fig. 1, it can be seen that due to wetting and drying cycles after compaction, a soil at a specific water content may exist at different suctions [5]. This emphasizes the need to measure soil suction rather than water content.

The primary objective of this paper is to summarize the initial findings of a field instrumentation project to remotely measure the real-time temporal variation of matric suction and temperature within the foundation layers of a heavy haul railway line near Ermelo in South Africa. Suction measurement techniques are briefly reviewed in order to select appropriate instrumentation for use in the field. The site

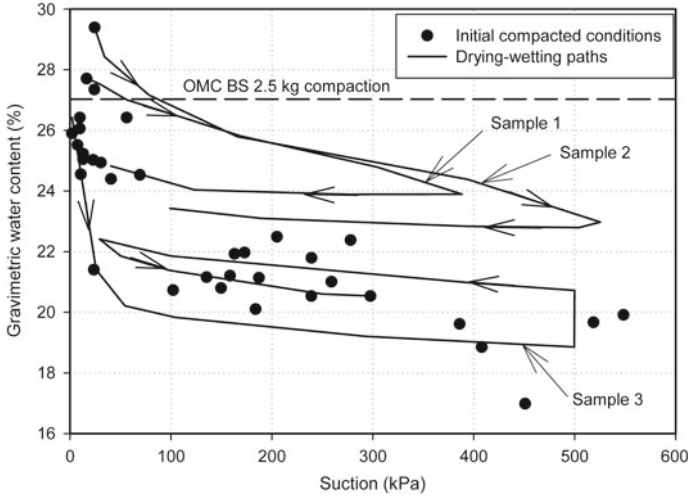


Fig. 1 Suction measurements on Kiunyu gravel (Adapted from Toll [6])

selection and positioning of the sensors are also discussed. The initial data is presented with focus on temporal variations with rainfall events.

## 2 In-Situ Measurement of Soil Suction for Transportation Infrastructure

The measurement of soil suction is vital for the implementation of unsaturated soil mechanics [7]. However, the literature on the in-situ measurement of soil suction within railway foundations is very limited. Furthermore, only some literature is available in this regard pertaining to pavements. This may be due in part to the difficulties associated with the field measurement of soil suction [8].

Suction measurement techniques can be divided into direct and indirect techniques. Direct techniques comprise techniques that directly measure the tensile stress in the soil–water phase. Indirect techniques rely on an intermediate relationship to proceed from a measured parameter to a soil suction value. These techniques are then further subdivided according to whether they measure total or matric suction [9]. A range of typical measurement techniques is summarized in Table 1.

Psychrometers are not ideal for field use as they are highly temperature sensitive; this temperature sensitivity increases as one approaches saturation [8]. This phenomenon is well explained by Kelvin’s law.

The filter paper method is not suited for site use as the filter paper must be physically weighed upon removal from the soil, trying to mitigate any moisture loss which can result in the accumulation of significant errors merely seconds after

**Table 1** Techniques for the measurement of soil suction (Adapted from Masrouri et al. [9])

Sensor	Direct/indirect	Suction component	Suction range (MPa)	Principle
Tensiometer	Direct	Matric	0–1.5	Negative pore-water pressure
Thermal conductivity	Indirect	Matric	0.01–4	Thermal conductivity of porous block
Fixed-matrix porous disk	Indirect	Matric	0.01–100	Water content of porous disk
Filter paper	Indirect	Matric/total	0.1–3	Water content of paper
Psychrometer	Indirect	Total	0.1–100	Relative humidity

removal [10]. Filter papers take more than seven days to equilibrate, which limits the practicality of observing temporal changes.

Thermal conductivity sensors showed some potential for field use according to Van der Raadt et al. [11]; however, their response times were slow and expensive signal conditioning equipment was required. Due to the circuitry of the thermal conductivity sensors, readings of suction can only be taken during site visits [12]. Thermal conductivity sensors also display some hysteresis. Therefore, a sensor installed in an initially wet condition and one installed in an initially dry condition may read different values of suction after equilibration [13]. Difficulties in the utilization of these field measurement techniques meant that seasonal changes in suction were only partially identified by Van der Raadt et al. [11]. If temporal variations of soil suction are to be monitored accurately, alternative measurement techniques have to be explored.

High-capacity tensiometers now regularly measure matric suction up to 1500 kPa [14]. Tensiometers utilize a direct technique for the measurement of matric suction and are, therefore, the instrument with the highest potential accuracy if calibrated and installed correctly. Tensiometers are not subject to the hysteresis associated with many of the indirect measurement techniques. High-capacity tensiometers have been successfully used to measure suction in-situ in a trial embankment near Newcastle, UK [15]. Despite the advantages of tensiometers, these instruments still require regular maintenance and careful consideration during the installation process and may cavitate after prolonged use.

## 2.1 Previous Studies

Van der Raadt et al. [11] used thermal conductivity sensors, thermocouple psychrometers and filter papers to measure soil suction near railway lines in Canada. Culverts

were installed vertically adjacent to the railway at six different locations to a depth of 6 m. Holes were drilled in the sides of the culverts to access the soil at various depths within the profile. The measurements were only taken during site visits as the suction measurement techniques utilized did not lend themselves to remote and continuous logging.

A novel in-situ suction measurement technique was explored by McCartney and Khosravi [16]. They augered a hole in the pavement shoulder and backfilled the hole with silica flour within which they buried volumetric water content (VWC) sensors at different depths. An SWRC for the silica flour was measured in the laboratory. The VWC values were used to back-calculate the suction within the silica flour using the SWRC. Due to thermodynamic considerations, the soil suction in the silica flour is in equilibrium with the soil suction in the pavement layers within which it is located. No other methods were used to compare the novel SWRC back-calculation method against other existing methods [16].

The accuracy of the SWRC back-calculation method is subject to numerous factors warranting further investigation. These factors include:

- Hysteresis of the SWRC of the silica flour
- The accuracy of the VWC determination in the silica flour in the field
- Difference in dry density between the SWRC silica flour and the in-field silica flour
- Potential volume change characteristics of the silica flour.

### **3 Soil Suction Measurement Techniques Utilized**

Three soil suction measurement techniques were utilized in this study. These techniques are summarized in the proceeding sections.

#### ***3.1 Tensiometers***

Low-cost tensiometers have been developed at the University of Pretoria with a material cost of approximately US\$30 each [17]. The tensiometers regularly reach cavitation pressures above 500 kPa. The calibrations done on these tensiometers show a deviation from linearity smaller than 0.1% for the calibration range (0–700 kPa). There is no apparent hysteresis in the sensors, and absolute error is less than 0.5 kPa over the full range. These factors indicate that with good contact between the tensiometers and the soil–water, the sensors will provide accurate readings of the matric suction.

### 3.2 Fixed-Matrix Soil–Water Suction Sensors

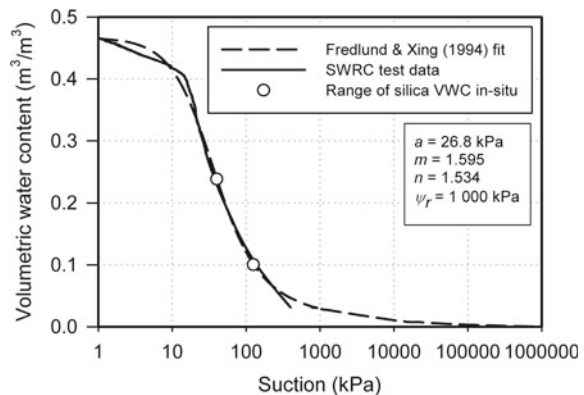
Commercial fixed-matrix soil–water suction sensors are fairly new to the market. The sensors make use of a porous ceramic with a fixed pore size distribution as a dielectric material. The VWC of the porous ceramic is then measured using the capacitance technique [18]. An SWRC for the porous ceramic is determined by the manufacturer and used to relate VWC to suction.

The accuracy of these sensors is still being studied, and some research into this has been conducted by Tripathy et al. [19]. A study on older versions of the sensors by Malazian et al. [20] suggests that there is significant sensor-to-sensor variability, requiring individual calibration of each sensor. Unfortunately, new models of these sensors output a value of suction directly using a pre-programmed calibration curve from the manufacturer. This does not allow for laboratory calibration by the user. The manufacturer of the sensor used in this study gives a rated accuracy of  $\pm$  (10% of the reading + 2 kPa) in the range 9–100 kPa [21]. Ultimately, the accuracy of these sensors still requires more research and information from the manufacturer is limited.

### 3.3 Silica Flour Technique

The silica flour back-calculation technique proposed by McCartney and Khosravi [16] was also used in this study. The silica flour has a modified AASHTO maximum dry density of 1648 kg/m<sup>3</sup> at an optimum gravimetric moisture content of 19.2%. The  $\theta$ -SWRC of the silica flour material used in the study is shown in Fig. 2. The continuous tensiometer technique [22] was used to determine the SWRC of the silica flour at a dry density of 92% modified AASHTO maximum dry density. This value was arbitrarily chosen, and the influence of dry density on the  $\theta$ -SWRC requires further investigation.

**Fig. 2** SWRC of silica flour at 92% modified AASHTO maximum dry density



The Fredlund and Xing [23] equation was used to fit a mathematical relationship to the SWRC data (Fig. 2). The equation fixes the suction at a VWC of 0 m<sup>3</sup>/m<sup>3</sup> to a value of 1,000,000 kPa. There are no suction data for the silica flour beyond 400 kPa, and the SWRC appears to be approaching residual conditions near this point. The fitting parameters are also indicated in Fig. 2.

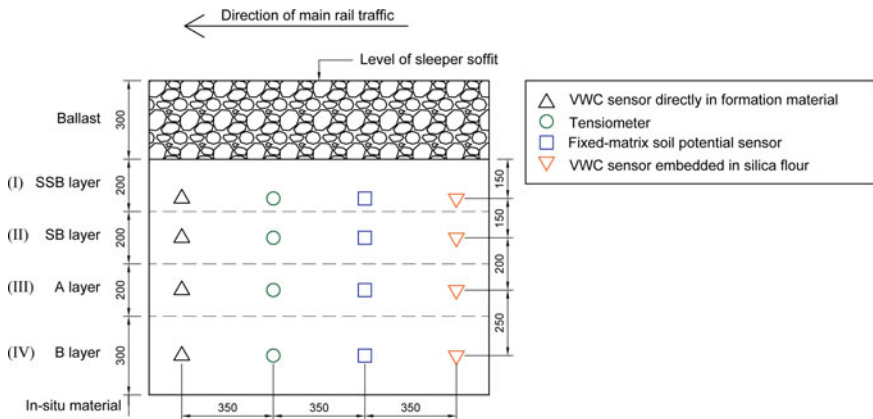
The VWC of the silica flour was measured using soil moisture probes utilizing the capacitance technique. The Topp [24] equation was used to convert the measured dielectric permittivity to VWC. The Topp [24] equation is shown in Eq. (1) where  $\theta_v$  is the VWC (m<sup>3</sup>/m<sup>3</sup>) and  $K_a$  is the dielectric permittivity (dimensionless) measured by the sensor.

$$\theta_v = (-5.3 \times 10^{-2}) + (2.92 \times 10^{-2})K_a - (5.5 \times 10^{-4})K_a^2 + (4.3 \times 10^{-6})K_a^3 \tag{1}$$

The VWC of the silica flour measured in the field to date is bound by the two dots as indicated in Fig. 2. This indicates that the range of suctions in the field falls within the region of the SWRC where reasonable accuracy can be expected based on an analysis of the curve’s slope.

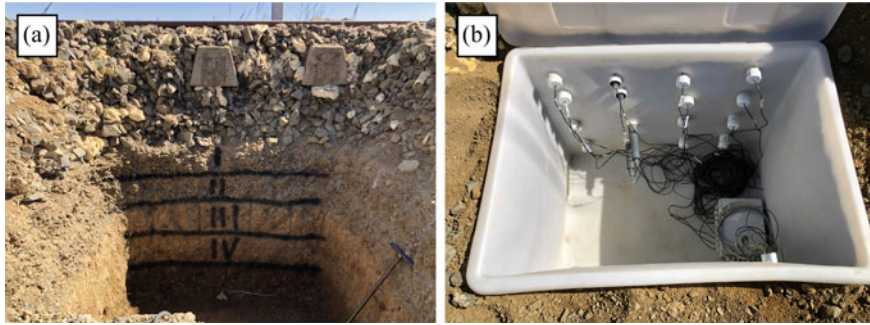
### 4 Site Layout and Sensor Installation

A railway foundation on the Ermelo-Majuba Heavy Haul Coal Line was instrumented on July 26, 2019. The railway line was new and had not been opened to rail traffic yet presenting a good opportunity for the installation. The foundation layers are illustrated in Fig. 3 which also indicates the relative locations of the installed sensors.



**Fig. 3** Longitudinal section indicating the location of the installed sensors within the foundation layers





**Fig. 4** **a** Excavated pit showing the constructed foundation layers. **b** Man hole to facilitate maintenance operations on the sensors if required

The foundation consists of the special subballast (SSB), subballast (SB) and placed fill (A and B) layers. These layers will henceforth be denoted by their abbreviations. The sensors used in this study were buried within every layer of the foundation. No instrumentation was buried in the subgrade beneath the B layer. All layers conform to Transnet Freight Rail's specification for earthworks [25]. Figure 4 shows photographs of the exposed layer works as well as the final installation. A weather station was also installed at the site to record air temperature, relative humidity, solar radiation, wind speed and precipitation.

A pit was excavated adjacent to the railway line as shown in Fig. 4. This pit facilitated access to the foundation layers of the railway structure. Horizontal holes were bored approximately 500 mm beyond the edge of the sleeper toward the center line of the track. PVC tubes were inserted within the bored holes to facilitate sensor maintenance. With the exception of four VWC sensors, each sensor was buried within silica flour material to improve the soil–water interface between the sensor and the railway foundation material. The four VWC sensors that were not buried in the silica flour material allowed direct measurement of the VWC of the foundation layers.

## 5 Results

Preliminary results are presented with a focus on the data for the month of September 2019. The sensors are assumed to have equilibrated during the month of August 2019. Precipitation was recorded for two days in September with 2.0 and 0.5 mm of rainfall occurring on 6 and 23 September, respectively. This period is regarded as a typically dry season at this location.

### 5.1 *Tensiometer and Fixed-Matrix Soil–Water Suction Sensor Results*

The suction data from the tensiometers is shown in Fig. 5. The suction in the SSB layer fluctuated daily with temperature and relative humidity. It is suspected that this tensiometer was not in good contact with the soil–water and requires maintenance and possible reinstallation.

Despite the fluctuations, the tensiometer in the SSB layer still responded to the rainfall events. The tensiometer in the SB layer responded to the 2 mm rainfall event but not the 0.5 mm rainfall event. The suction in the SB layer decreased from 32 to 17 kPa over a 2-week period after the 2 mm rainfall event. The A and B layers showed no response to the rainfall events and maintained a fairly constant suction value of approximately 10 kPa. Therefore, the suction response to rainfall events appears to be inversely related to depth as might be expected. Comparing the magnitude of the suctions in the layers before the first rainfall event, it can be seen that in general the suction appears to decrease with depth into the foundation.

It is insightful to compare the tensiometer suction data with the fixed-matrix soil–water suction sensor data. Daily average suction readings were calculated for the tensiometers and fixed-matrix soil–water suction sensors and are plotted against each other in Fig. 6. The data for the SSB layer has been omitted due to the tensiometer fluctuations. Points plotting on the 45° line would indicate exact correlation between the two sensors for that layer.

The suction data from the sensors in the A and B layers shows better agreement than the SB layer sensors. The A and B layers’ suction data maintains a fairly constant offset of not more than 10 kPa. The data for the SB layer indicates that there is a lag between the response of the fixed-matrix soil–water suction sensor and the tensiometer but that after equilibration a fairly constant offset is also achieved. The fixed-matrix soil–water suction sensors were consistently reading larger suctions than the tensiometers.

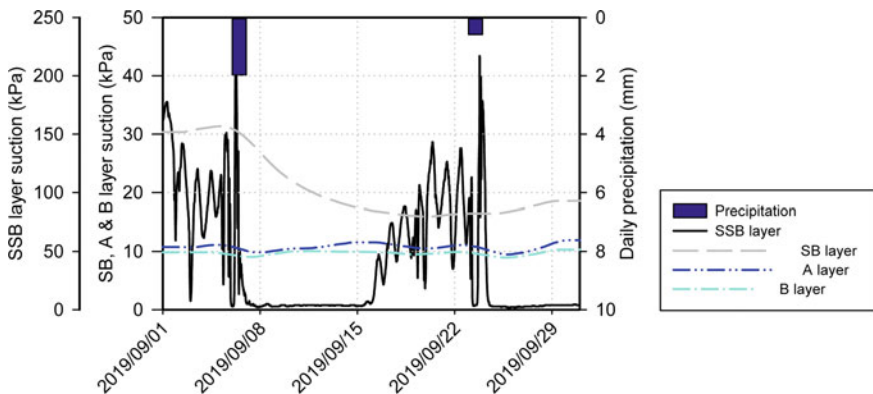
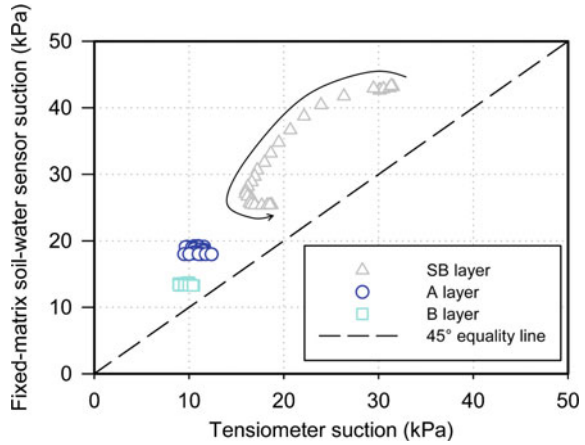


Fig. 5 Temporal variation of suction measured by the tensiometers

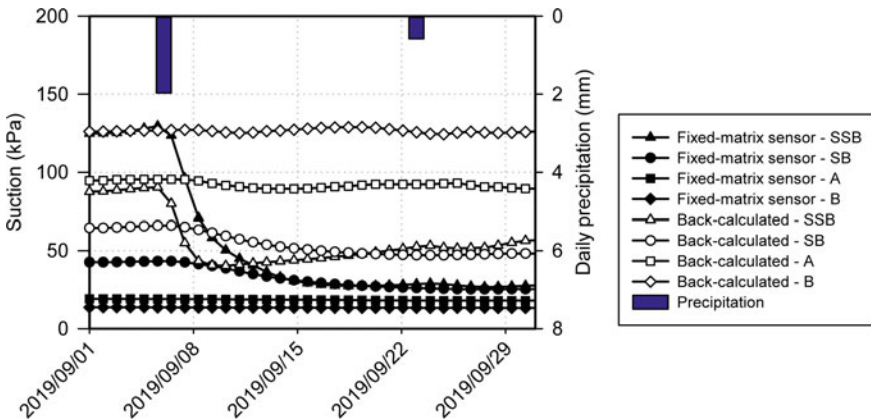
**Fig. 6** A comparison of the suction readings between the tensiometers and the fixed-matrix soil–water suction sensors using daily average suction readings



### 5.2 Back-Calculation of Suction from Silica Flour Volumetric Water Content

The VWC of the silica flour was used to back-calculate the soil suction as described in Sect. 3.3. This data is compared to the data from the fixed-matrix soil–water suction sensors as the techniques are similar in concept. These results are shown in Fig. 7. The black-fill markers indicate data from the fixed-matrix soil–water suction sensors, and the white-fill markers indicate data from the back-calculation procedure. Data from the same layers is plotted using the same symbols.

The SSB and SB layers are the only layers which respond to the rainfall events, similar to what was observed for the tensiometer data. In general, the back-calculated



**Fig. 7** Comparison of the suction readings obtained from the fixed-matrix soil–water suction sensors and the SWRC back-calculation procedure

data does not agree well with the suction data from the fixed-matrix soil–water suction sensors other than displaying similar trends for the SSB and SB layers. The difference in suction values between the two measurement techniques applied for the A and B layers is significant. Differences as large as approximately 100 kPa are evident.

There may be numerous reasons for the significant difference in suction values between the back-calculation procedure and the fixed-matrix soil–water suction sensors. The dry density between the SWRC sample in the laboratory and the silica flour in the field may be significantly different [26]. Furthermore, there may exist air gaps between the tines of the VWC sensor and the silica flour for the A and B layers, causing them to read a relatively low VWC and resulting in the high back-calculated suction values for these layers. Overall, further investigation in the laboratory under controlled conditions is required.

### 5.3 Soil Temperature

Figure 8 shows the temporal variation in soil temperature and air temperature recorded for September 2019. Small daily fluctuations in temperature can be seen for the SSB layer (<1 °C). The other layers appear to show no response to daily air temperature changes.

The air temperature data for the observational period shows minimum and maximum air temperatures of −5 and 31 °C, respectively. Contrastingly, the soil temperature only varied between 13 and 17 °C. This is due to the high thermal mass of the soil. A general increasing trend is observed for both the air and soil temperatures as the seasons shift toward the warmer summer months.

There is a significant response of soil temperature to rainfall events as the cold water infiltrates the surface layer of soil. The air temperature variation was also subdued during this period which may be a contributing factor. However, the soil temperature decreases significantly after both rainfall events which cannot be solely

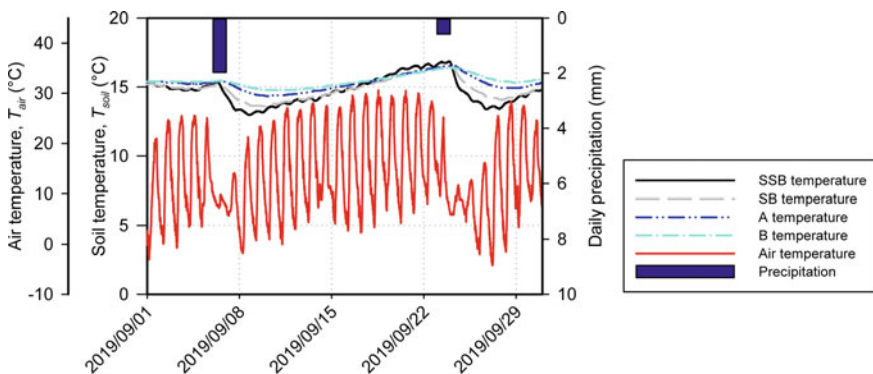


Fig. 8 Temporal variation of soil and air temperatures and the influence of rainfall

due to the subdued air temperature variation. The temperature decrease in the soil is inversely related to depth with the shallowest layer experiencing the largest decrease in temperature after both rainfall events.

## 6 Conclusions

A heavy haul railway foundation on the Ermelo-Majuba Coal Line in South Africa was successfully instrumented with volumetric water content (VWC) sensors, fixed-matrix soil–water suction sensors and tensiometers. A weather station was installed on the site to monitor climatic variables. The data was retrieved remotely and monitored in real time.

Three tensiometers appear to be giving reliable suction data in the subballast (SB) and placed fill (A and B) layers. The tensiometer in the special subballast (SSB) layer requires maintenance to ensure that it is well connected to the soil–water as it is fluctuating abnormally. The fixed-matrix soil–water suction sensors agree with the tensiometer suction data within 10 kPa over the observational period this far. All the suction sensors in the SSB and SB layers showed a suction decrease with an observed 2 mm rainfall event. The magnitude of the suction decrease is inversely related to the depth of the sensor.

Soil temperature appears to decrease significantly in response to rainfall events. The soil temperature in all four of the monitored layers responded to two small rainfall events of 2.0 and 0.5 mm. The magnitude of the response is inversely related to the depth of the layers with the shallowest layers showing the largest change in temperature.

A back-calculation procedure was used to calculate soil suction from the VWC of silica flour in the foundation layers. This procedure showed poor agreement between the tensiometer and fixed-matrix soil–water suction sensor data. Further research is required to identify and measure the influencing factors of this novel method in order to improve its accuracy to an acceptable level.

The field instrumentation described in this paper provides reliable real-time measurement of soil suction, temperature and weather conditions. In the long term, this would make a significant contribution toward the study of climate change and environmental conditions on the behavior of railway foundations and transportation infrastructure in general.

## References

1. Burrow MPN, Bowness D, Ghataora GS (2007) A comparison of railway track foundation design methods. *Proc Inst Mech Eng Part F: J Rail Rapid Transit* 221(1). <https://doi.org/10.1243/09544097JRRT58>

2. Fredlund DG (2006) Unsaturated soil mechanics in engineering practice. *J Geotech Geoenviron Eng* 132(3):286–321. [https://doi.org/10.1061/\(ASCE\)1090-0241\(2006\)132:3\(286\)](https://doi.org/10.1061/(ASCE)1090-0241(2006)132:3(286))
3. Toll DG (2012) The behaviour of unsaturated soil. In BBK, Toll DG, Prasad A (eds) *Handbook of tropical residual soils engineering*, Taylor & Francis Group, London, pp 118–145
4. Lu N, Kaya M, Godt JW (2014) Interrelations among the soil-water retention, hydraulic conductivity, and suction-stress characteristic curves. *J Geotech Geoenviron Eng* 140(5). [https://doi.org/10.1061/\(ASCE\)GT.1943-5606.0001085](https://doi.org/10.1061/(ASCE)GT.1943-5606.0001085)
5. Toll DG (1991) Towards understanding the behaviour of naturally-occurring road construction materials. *Geotech Geol Eng* 9(3–4):197–217. <https://doi.org/10.1007/BF00881741>
6. Toll DG (1988) The behaviour of unsaturated compacted naturally occurring gravel. Ph.D. thesis. University of London
7. Fredlund DG, Rahardjo H (1987) Soil mechanics principles for highway engineering in arid regions. *Transp Res Rec* 1137:1–11
8. Tarantino A, Ridley AM, Toll DG (2008) Field measurement of suction, water content, and water permeability. *Geotech Geol En* 26(6):751–782. <https://doi.org/10.1007/s10706-008-9205-4>
9. Masrouri F, Bicalho KV, Kawai K (2008) Laboratory hydraulic testing in unsaturated soils. *Geotech Geol Eng* 26(6):691–704. [https://doi.org/10.1007/978-1-4020-8819-3\\_7](https://doi.org/10.1007/978-1-4020-8819-3_7)
10. Chandler RJ, Gutierrez CI (1986) The filter-paper method of suction measurement. *Géotechnique* 36(2):265–268. <https://doi.org/10.1680/geot.1986.36.2.265>
11. van der Raadt P, Fredlund DG, Clifton AW, Klassen MJ, Jubien WE (1987) Soil suction measurements at several sites in Western Canada. *Transp Res Rec* 1137:24–35
12. Puppala AJ, Manosuthkij T, Nazarian S, Hoyos LR (2011) Threshold moisture content and matric suction potentials in expansive clays prior to initiation of cracking in pavements. *Can Geotech J* 48(4):519–531. <https://doi.org/10.1139/t10-087>
13. Sattler P, Fredlund DG (1989) Use of thermal conductivity sensors to measure matric suction in the laboratory. *Can Geotech J* 26(3):491–498. <https://doi.org/10.1139/t89-063>
14. Marinho FAM, Take WA, Tarantino A (2008) Measurement of matric suction using tensiometric and axis translation techniques. *Geotech Geol Eng* 26:615–631. <https://doi.org/10.1007/s10706-008-9201-8>
15. Toll DG, Lourenco SDN, Mendes J, Gallipoli D, Evans FD, Augarde CE, Cui YJ, Tang AM, Rojas JC, Pagano L, Mancuso C, Zingariello C, Tarantino A (2011) Soil suction monitoring for landslides and slopes. *Q J Eng GeolHydrogeol* 44(1):23–33. <https://doi.org/10.1144/1470-9236/09-010>
16. McCartney JS, Khosravi A (2013) Field-monitoring system for suction and temperature profiles under pavements. *J Perform Constr Facil* 27(6):818–825. [https://doi.org/10.1061/\(ASCE\)CF.1943-5509.0000362](https://doi.org/10.1061/(ASCE)CF.1943-5509.0000362)
17. Jacobsz SW (2018) Low cost tensiometers for geotechnical applications. In: *Proceedings of the 9th international conference on physical modelling in geotechnics*, London, pp 305–310. <https://doi.org/10.1201/9780429438660-40>
18. Susha Lekshmi SU, Singh DN, Shojaei Baghini M (2014) A critical review of soil moisture measurement. *Measurement* 54:92–105. <https://doi.org/10.1016/j.measurement.2014.04.007>
19. Tripathy S, Al-Khyat S, Cleall PJ, Baille W, Schanz T (2016) Soil suction measurement of unsaturated soils with a sensor using fixed-matrix porous ceramic discs. *Ind Geotech J* 46(3):252–260. <https://doi.org/10.1007/s40098-016-0200-z>
20. Malazian A, Hartsough P, Kamai T, Campbell GS, Cobos DR, Hopmans JW (2011) Evaluation of MPS-1 soil water potential sensor. *J Hydrol* 402(1–2):126–134. <https://doi.org/10.1016/j.jhydrol.2011.03.006>
21. Meter (2017) *Teros 21 users manual*
22. Lourenço SDN, Gallipoli D, Toll DG, Augarde CE, Evans F (2011) A new procedure for the determination of soil-water retention curves by continuous drying using high-suction tensiometers. *Can Geotech J* 48:327–335. <https://doi.org/10.1139/T10-062>
23. Fredlund DG, Xing A (1994) Equations for the soil-water characteristic curve. *Can Geotech J* 31(3):521–532. <https://doi.org/10.1139/t94-061>

24. Topp GC (1980) Electromagnetic determination of soil water content: measurements in coaxial transmission lines. *Water Resour Res* 16(3):574–582. <https://doi.org/10.1029/WR016i003p00574>
25. Transnet (2006) S410: specifications for railway earthworks. Transnet Limited, Pretoria, South Africa
26. Orangi A, Narsilio GA, Wang YH, Ryu D (2019) Experimental investigation of dry density effects on dielectric properties of soil–water mixtures with different specific surface areas. *Acta Geotech*. <https://doi.org/10.1007/s11440-019-00805-x>

# A Tool for Estimating the Water Content of Unsaturated Railway Track Formation Layers



Ivan Campos-Guereta , Andrew Dawson, and Nick Thom 

**Abstract** Water content is one of the causes of railway tracks' poor performance. Implementing its effects into design and management numerical tools is not always straightforward because the relevant descriptive partial differential equations (PDEs) involved are highly nonlinear. The paper describes the creation of a surrogate model to predict water flow in rail-track layers or other multilayered systems, increasing performance of conventional 2D and 3D models so as to enhance their utility and validity for rail-track maintenance management. The model takes advantage of the mainly 1D vertical direction of infiltration through unsaturated layers and the mainly 1D horizontal direction for saturated flow in the lower layers to create an assemblage of one-dimensional domains using a co-simulation technique. Mathematical formulation is included for both of the 1D simulations and for the assemblage. 1D models are verified, and some results of the assembled model are compared with existing experimental results. Available results suggest a suitable predictive model for multilayer flow.

**Keywords** Railways · Drainage · Surrogated model · Co-simulation · Finite element method · Richards' equation · Multilayer flow

## 1 Introduction

While soil water content is highly relevant for the actual response of many public works, its role in the behavior of multilayered railway tracks or road pavements is crucial and has been highlighted by many publications [1–5]. Selig and Waters

---

I. Campos-Guereta (✉) · A. Dawson · N. Thom  
Nottingham Transportation Engineering Centre, Faculty of Engineering, The University of Nottingham, Nottingham NG7 2RD, UK  
e-mail: [ivan.camposguereta@nottingham.ac.uk](mailto:ivan.camposguereta@nottingham.ac.uk); [icamposguereta@gmail.com](mailto:icamposguereta@gmail.com)

A. Dawson  
e-mail: [andrew.nottingham@aol.com](mailto:andrew.nottingham@aol.com)

N. Thom  
e-mail: [nicholas.thom@nottingham.ac.uk](mailto:nicholas.thom@nottingham.ac.uk)



[1] state that one of the main subgrade problems is caused by excessive moisture content and Heyns [2] pointed to ‘poor drainage’ as the major cause of bad track performance. This problem not only affects the subgrade but also the ballast, as one its requirements is to achieve good drainage.

In most rail-track design methodologies and standards, pore pressures are not considered, or they are considered secondarily, the main reason being that its introduction into numerical models usually means passing from relatively simple elastoplastic models to nonlinear models. Many commercial software programs can manage a full hydromechanical coupling analysis, and its application in rail-track design is feasible, but in the operational stage, ‘maintenance management’ and related concepts like ‘Prognostic Health Management’ require predictive approaches under multiple weather conditions and storm events so as to allow the possible outcomes to be predicted. However, each predictive assessment requires a track model that usually has to deal with a huge amount of calculations as conventional water flow simulations in 2D or 3D employ computationally costly techniques to deal with the high nonlinearities introduced (more insights in ‘Prognostic Design’ can be looked up in [6]).

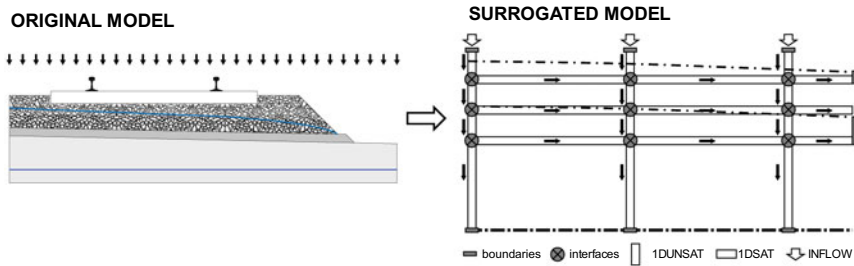
Therefore, the aim of this paper is to describe a tool to perform variably saturated flow simulations to predict the water content of canted multilayered systems (such as in a rail track), trying to increase performance over that of conventional 2D/3D models.

## **2 Simplified Model for Multilayer Variably Saturated Water Flow**

The purpose of the model will be the prediction of water content in a rail-track section but could be extended to the case of a road section, subjected to rain loads. It needs to balance the computational cost and the degree of fidelity with reality. To create such a water content predictive tool, ‘lower-fidelity surrogate models’ are needed, i.e., physically based yet less detailed than usual more accurate simulations, (e.g., 2D or 3D finite element methods (FEM)), herein termed ‘original models’ [7].

A natural way to decrease computational cost is, if possible, to reduce the number of dimensions. For example, many 3D situations can be accurately modeled in 2D, based on symmetry principles.

Many 1D variable saturation models exist for multilayered systems. Often, they include an assessment of infiltration of water from the ground surface into soil but can’t consider the discharge when percolating water reaches a water table between two layers. On the other hand, some 1D models are able to calculate the appearance of water tables and the discharge due to them (e.g., [8, 9]) yet, in most of those models, only steady states are considered. None of them consider infiltration below the water table, dissipation of pore pressures and change in water content in adjacent



**Fig. 1** 1.5DSatUnsat model description. Process of abstraction from ‘original model’ to ‘subrogated model’

soil, nor do they consider layers of higher permeability below more impermeable ones.

The proposed model (herein ‘1.5DSatUnsat’) will perform a co-simulation of assembled 1D simulations, i.e., it combines the characteristics of 1D variably saturated vertical flow simulations (herein ‘1DU<sub>unsat</sub>’ simulations) with 1D saturated horizontal flow simulations (herein ‘1DS<sub>sat</sub>’). The 1DU<sub>unsat</sub> model simulates the infiltration from rain or from upper layers, while the 1DS<sub>sat</sub> model simulates the evolution of water tables for each layer and the horizontal water flow in them. The process of abstraction can be observed in Fig. 1.

This approach assumes that all capillary flow is vertical. By symmetry, this is true for horizontal multilayer systems with an horizontal phreatic line at the bottom, and approximately true for slightly canted layers, but when water table appears symmetry also is maintained from the top of a layer to the water table if the water table is nearly horizontal. Changes of water flow direction (within a vertical plane) will occur with the increase of water table slope, but it will be assumed that this effect has a negligible effect on the inflow to the top of water table. The model also considers that all saturated flow between the top of the water table and the bottom of the layer is effectively horizontal even though the track structure may have slight cants. This has been considered valid by Youngs and Rushton [10] even for pronounced slopes of the water table.

Initial conditions are defined by a phreatic level at the bottom; rain load will be defined at the top of 1DU<sub>unsat</sub> as time-dependent boundary condition; seepage boundary conditions will be defined at the right boundary of 1DS<sub>sat</sub>. The simulation will be done in transient mode and when saturation is reached at the bottom of a layer in one 1DU<sub>unsat</sub> model, 1DS<sub>sat</sub> models activate. Behavior at the 1DU<sub>unsat</sub> and 1DS<sub>sat</sub> contact (interface) will be coupled by some interface equations.

### 3 Water Flow in Variably Saturated Media. Richards' Equation

Water flow in a variably saturated medium is typically modeled applying Richards' equation, which means some assumptions (e.g. not considering water vapor flow). Richards Eq. (1) combine the water-balance equation with Darcy flow.  $\theta$  is the volumetric water content,  $k_w$  is the hydraulic conductivity tensor for a given pressure head,  $h$ ,  $z$  is the vertical coordinate and  $S$  a source/sink term.

$$\frac{\partial \theta}{\partial t} - \nabla \cdot \left( \underline{k}_w \cdot \bar{\nabla}(h + z) \right) - S = 0 \quad (1)$$

Richards' equation can only be solved analytically in very particular cases, and in general, numerical approaches are needed, but this equation is known to be highly nonlinear for several reasons [11–13], and its numerical solution presents lots of challenges that have resulted in many publications dealing with its numerical issues.

Many techniques have been employed to overcome these numerical problems, but many are difficult to implement in 3D or 2D models. Fortunately, some are more easily implemented in 1D, so have been included in the 1.5DSatUnsatsat model.

## 4 Mathematical Model

As no general analytical solution is possible, a numerical approach will be considered. A finite element method (FEM) is suitable because boundary conditions are easy to implement, and because the future implementation of higher-order elements could overcome some of the instabilities that may appear at the interfaces.

### 4.1 1DUnsatsat Simulations

By applying an L2-inner product between the left side of Eq. (1) in its one-dimensional form with a set of test functions,  $v_i$ , integrating by parts to reduce the differentiation order, approximating the dependent variable,  $h$ , and vertical coordinate,  $z$ , as its projection onto a set of basis functions,  $\phi_j$ , and by taking the set of test functions,  $v$ , equal to the set of basis functions,  $\phi$ , the approximation (2) in FEM is obtained, where  $\int_{\Omega_e}$  means integration over the element, index  $n + 1$  refers to the current time step, and index  $k + 1$  to the current iteration, while index  $j$  represents the chosen basis function and its coefficient and index  $i$  represents the chosen test function.

$$\begin{aligned}
 & \sum_i \sum_j \sum_e \int_{\Omega_e} \frac{\theta_j^{k+1,n+1} - \theta_j^n}{\Delta t} \phi_j \phi_i d\Omega_e \dots \\
 & + \sum_i \sum_j \sum_e \int_{\Omega_e} k^{n+1,k+1} \left( h_j^{k+1,n+1} + z_j^{k+1,n+1} \right) \frac{d\phi_j}{dz} \frac{d\phi_i}{dz} d\Omega_e \dots \\
 & - \sum_i \sum_{j \in \Gamma} k^{n+1,k+1} \left( p_j^{k+1,n+1} + z_j^{k+1,n+1} \right) \frac{d\phi_j}{dz} \phi_i \dots \\
 & - \sum_i \sum_j \sum_e \int_{\Omega_e} S_j \phi_j \phi_i d\Omega_e = 0 \tag{2}
 \end{aligned}$$

To numerically solve Eq. (2), linearization techniques have to be applied: the Newton, Picard, modified Picard, Picard/Newton or L-Scheme [12]. Celia, Bouloutas [11] applied the modified Picard method with mass lumping, highlighting the poor mass balance of h-based forms for the Richards’ equation. List and Radu [12] recommended a combined use of the L-Scheme method with the Newton method as a way of increasing convergence, reducing the disadvantages of Newton method (sporadic divergences) and reducing the bad-conditioning of the modified Picard approach. At the moment, 1DUnsat implements only the Picard and Celia-modified Picard methods.

### 4.2 1DSat Simulations

In each of the layers in which a water table can be formed, a 1DSat simulation will be needed. The simulation will be done in that layer but also in the layers above, as the water table can reach more than one layer; nevertheless, results are given for the studied layer. If  $nl$  is the number of layers, then  $nl - 1$  simulations will be needed when the bottom of the 1.5DSatUnsat model is defined by the phreatic level and  $nl$  simulations when the bottom is impermeable.

In this case, Eq. (3) is obtained by applying mass conservation principles combined with Darcy flow over the water table height,  $h$ , and considering the Dupuit–Forchheimer assumption where piezometric head,  $h + z$ , remains constant over the water table height for a given point in the  $x$  coordinate;  $k_{sat}$  is the mean saturated hydraulic conductivity of the layers over the water table height,  $h$ , at point  $x$ ;  $z$  is the vertical coordinate of the bottom of the layer,  $q_v$  is the vertical water inflow along  $x$ ;  $n_{nw}$  is the water capacity above the water table or ‘non-wetted porosity’, which some authors have called specific yield or storage term [8].

$$n_{nw} \cdot \frac{dh}{dt} = \frac{\partial}{\partial x} \left[ k_{sat} \cdot h \cdot \frac{\partial}{\partial x} (h + z) \right] + q_v \tag{3}$$

Following the same methodology as in the previous section, a nonlinear Eq. (4) is obtained. Once again, linearization needs to be performed.

$$\begin{aligned}
 & \sum_i \sum_j \sum_e \int_{\Omega_e} n_{nw} \frac{h_j^{k+1,n+1} - h_j^n}{\Delta t} \phi_j \phi_i d\Omega_e \dots \\
 & + \sum_i \sum_j \sum_e \int_{\Omega_e} k_{sat} (h^{k+1,n+1} + z^{k+1,n+1}) \frac{d\phi_j}{dz} \frac{d\phi_i}{dz} d\Omega_e \dots \\
 & - \sum_i \sum_j \sum_e \int_{\Omega_e} q_{vi} \phi_j \phi_i d\Omega_e \dots \\
 & - \sum_j \sum_{i \in \Gamma} k_{sat} (h^{k+1,n+1} + z^{k+1,n+1}) \frac{d\phi_j}{dz} \phi_i = 0 \tag{4}
 \end{aligned}$$

**Seepage boundary condition** The last term of Eq. (4) represents a column with the inflow-outflow boundary conditions. The model will maintain a symmetry on the left, so in the initial node, imposed water flow will be zero. At the right side a seepage boundary condition needs to be defined. In a two-dimensional analysis, the definition of the seepage boundary does not generally present complications as pressure head will be zero where the water table meets the boundary, but in Eq. (4) at each point  $x$ , piezometric head ( $h + z$ ) has a value meaning that at the boundary pressure head,  $h$ , cannot be zero. Usually and for stationary analysis, this value is defined by imposing a water table height linked in some way to the characteristics of the model. Rushton and Youngs [8] proposed Eq. (5) that relates water table height,  $h_f$ , with the discharge,  $Q_0$ , at the boundary and the permeability,  $k_{sat}$ , by comparison with 2D simulations.

$$h_f = 0.93 \cdot Q_0 / k_{sat} \tag{5}$$

By combining (5) with the value of the outflow given by Darcy equation, the expression proposed by Rushton and Youngs [8] reduces to the imposition of a slope on the water table of 1.075 given by the right side of Eq. (6). Or, more simply, by imposing an outflow at the seepage boundary equal to the left side of Eq. (6) defined by the water table height from the previous iteration.

$$Q_0 = \frac{k_{sat} h_f}{0.93} = -k_{sat} h_f \frac{\partial}{\partial x} (h + z) \Big|_f \Rightarrow \frac{\partial}{\partial x} (h + z) \Big|_f = 1.075 \tag{6}$$

### 4.3 Coupling 1DSat and 1DUnsat into 1.5DSatUnsat

The assembly of the simulation could be done in a monolithic or in a co-simulation approach; in the former case, all constitutive equations are integrated into one system which is solved as a whole, and in the latter each simulation is modeled independently and assembled by passing information between each other at the interfaces [14, 15]. The main advantage of co-simulation is modularity, and parallelization as each simulation is done independently by specifically designed models, but the price is potential instability. Disadvantages of the monolithic approach are its specific development for each problem, and that bigger models need to be run with no subdivisions.

1.5DSatUnsat will perform a co-simulation of 1DSat and 1DUnsat submodels that will be linked at the interfaces where information need to be interchanged, in this particular case by the ‘interface coupling conditions’ given by Eqs. (7), (8), (9) and (10) which are graphically represented in Fig. 2, for the interface (is, iu) which means the interface between the ‘is’ 1DSat (center) and ‘iu’ 1DUnsat simulations (left).

$$\{h_{sat,u(is,iu)}\} = \{h_{sat,s(is,iu)}\} \tag{7}$$

$$\{Q'_{u(is,iu)}\} = \left\{ \frac{dq_h(is,iu)}{dx} \right\} \tag{8}$$

$$\{q'_{u(is,iu)}\} = \{q_{vh(is,iu)}\} \tag{9}$$

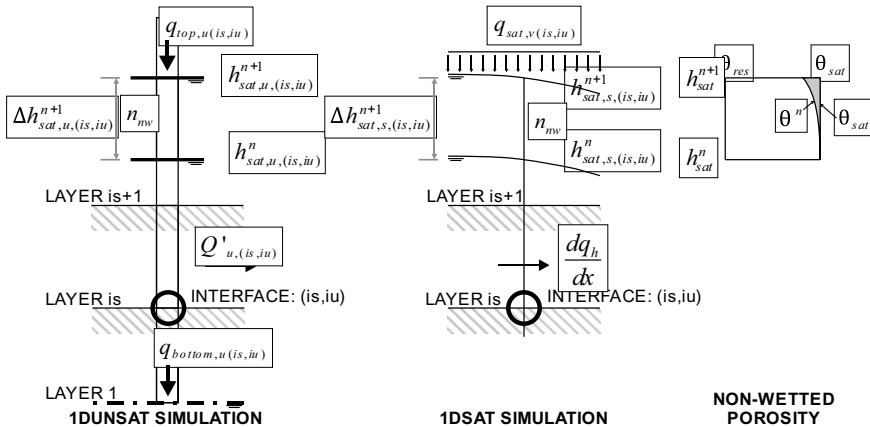


Fig. 2 Coupling variables on the interface (is, iu), between 1DSat, is, and 1DUnsat, iu. On the right is the definition of the ‘non-wetted’ porosity,  $n_{nw}$

$$\left\{ \frac{1}{\Delta h_{\text{sat},u}(is,iu)} \int_{h_{\text{sat},u,n}(is,iu)}^{h_{\text{sat},u,n+1,k}(is,iu)} \theta_{\text{sat}}(h) - \theta(h) \right\} = \{n_{s(is,iu)}\} \quad (10)$$

The water table heights on layer ‘is’,  $h_{\text{sat},u}(is,iu)$  and  $h_{\text{sat},s}(is,iu)$ , have to be the same for both simulations—Eq. (7); the water leaving layer ‘is’,  $Q'_{u(is,iu)}$ , in 1DU<sub>nsat</sub> has to be the same as the variation of the water flow,  $q_{h,(is,iu)}$ , over  $x$  in the 1DSat at the interface ( $is, iu$ )—Eq. (8);  $q_{vh(is,iu)}$  is the inflow over  $x$  in the 1DSat that is calculated from the flow entering and leaving the water table in 1DU<sub>nsat</sub>,  $q'_{u(is,iu)}$ ,—Eq. (9); Eq. (10) shows how the ‘non-wetted porosity’,  $n_{nw}$ , in 1DSat is obtained from 1DU<sub>nsat</sub> as the mean of the non-wetted porosity over the variation of the water table. The shaded area on the right side of Fig. 2 represents the ‘non-wetted voids’ appearing at the water table from one time step to the next.

Different strategies can be considered in how to pass information between the two parts. In Eqs. (7) to (10), information can be passed from left (from 1DU<sub>nsat</sub>) to the right (to the 1DSat) or vice versa, and information can be taken from the previous time step, as in sequential or parallel weak couplings, or in an iterative process from the previous iteration (strong coupling).

The right side of Eq. (8) implies the second derivative of the water table height in the 1DSat simulation, which it is not very accurate if linear elements are considered, so it has been substituted by Eq. (11) by applying the mass balance on the interface as, in a time step ‘ $dt$ ’, the volume entering,  $q_{h,(is,iu)} \cdot dt$ , is equal to the volume in the increase of water table height,  $n_{s(is,iu)} \cdot \Delta h_{\text{sat},s}(is,iu) \cdot dt$ , plus the horizontal water entering minus that leaving  $dx$ ,  $dq_{h,(is,iu)}/dx \cdot dt$ . Hence:

$$\frac{dq_{h,(is,iu)}}{dx} = q_{vh(is,iu)} - n_{nw(is,iu)} \cdot \Delta h_{\text{sat},s}(is,iu) \quad (11)$$

Estimation of the value of  $n_{nw(is,iu)}$  from the left side of Eq. (10) is also numerically difficult and can lead to some errors because of the simplifications to low-order elements. Mass conservation in the 1DU<sub>nsat</sub> simulation in the interface can also be applied, and the increment of water between the water table movement in the time step given by left side of Eq. (12) has to be equal to the water flow entering and leaving the water table given by the right side of Eq. (12).

$$n_{nw(is,iu)} \cdot \Delta h_{\text{sat},u}(is,iu) = q'_{u(is,iu)} - Q'_{u(is,iu)} \quad (12)$$

## 5 Numerical Model Implementation

1DSat and 1DU<sub>nsat</sub> simulations have been implemented in programs Flow1DSat and Flow1DU<sub>nsat</sub> that can be executed independently to the assembled program Flow1.5DSatUns<sub>at</sub>. The algorithms have been coded in Fortran 2003 to make good

use of object-oriented characteristics balanced with functional oriented coding maintaining a good performance. One library includes common classes and functions used by all simulations, 1DSat and 1DUUnsat classes are included in specific libraries that can be used by the isolated Flow1DSat and Flow1DUUnsat programs or by the assembled Flow1.5DSatUnsat, which also has its library.

At this moment, Flow1DSat and Flow1DUUnsat are fully coded and validated with a good match with existing analytical models. In the case of the Flow1.5DSatUnsat model, it shows the expected results for a multilayered system. Some validation has been done against particular cases of the physical two-layered system model performed by Heyns [2], but more validation needs to be done against physical models or against a 2D FEM model.

At the moment of writing this paper, Flow1.5DSatUnsat performs a co-simulation with weak parallel coupling between 1DSat and 1DUUnsat, which means that each of the models is computed by updating information on the interfaces from the previous time step, and those simulations can be done in parallel, after the simulation information is taken for the next time step. Weak coupling means that errors can propagate in time. In this case, 1DSat's main purpose is to define the water table to be for use by 1DUUnsat. Therefore, information from Eq. (7) will be applied from right to left. 1DSat also defines the amount of water,  $Q'_{u(is,iu)}$ , leaving 1DUUnsat that is calculated with Eq. (11). On the other hand, 1DUUnsat's main purpose is to define the inflow into the 1DSat so information from Eq. (9) is applied from left to right.

The value of the non-wetted porosity,  $n_{nw}$ , is calculated after the parallel calculation from (12) taking the 1DUUnsat outflow,  $Q'_{u(is,iu)}$ , which theoretically means that the water tables—Eq. (7)—need to match, whereas the numerical discretization leads to differences. Therefore, a new step is included by forcing the level in 1DUUnsat to match that calculated in 1DSat, and so applying in this way Eq. (7) from right to left so as to obtain new values for  $Q'_{u(is,iu)}$ .

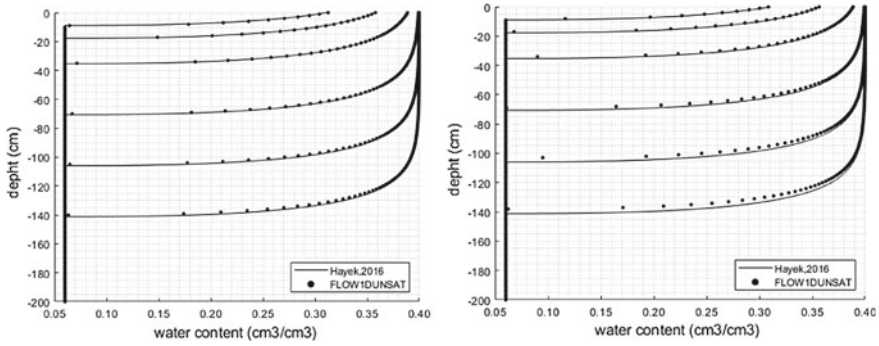
## 5.1 Validation of 1DUUnsat Simulation

The 1DUUnsat simulation has been validated against Hayek's [16] analytical expressions as they are easy to implement, consider the gravity term of the Richards equation and are applied with initially unsaturated materials, which usually means a challenge for numerical models due to the high differences of pore pressures across the saturated/unsaturated boundary.

The Hayek [16] expressions give the water content, saturation or pore pressure evolution over a vertical one-dimensional, initially unsaturated, material which is subjected to a specific time-varying expression of the inflow at the top, but also with the possibility of considering an expression for a Dirichlet condition at the top. The main disadvantage is the need to apply specific power expressions for the water retention curve and for the hydraulic conductivity.

The left side of Fig. 3 shows the result of 1DUUnsat applying the expression for the inflow, and the right side shows the result when the expressions for the pressure





**Fig. 3** Initially dry column 1D water flow with a particular expression of the head at the top boundary (left) or a particular expression of water flow across the top boundary (right). Expressions from Hayek [16]. Water content analytical results by Hayek [16] at 3 h (lowest lines), 6 h, 12 h, 24 h, 36 h and 48 h (uppermost lines) are compared with results from Flow1DUnsat with good match

boundary condition are applied. A total of 200 elements have been selected for the visualization of the results. The main characteristics for the simulation are as follows: an absolute tolerance of  $1 \times 10^{-3}$  mm, use of mass lumping, no relaxation coefficient, use of Picard linearization, a CSR<sup>1</sup> sparse system, with ILUT<sup>2</sup> preconditioning and the FGMRES<sup>3</sup> solver, order 10, for element integration quadrature, dynamic time-stepping with a maximum time step of 0.5 h which is increased by 20% if final iterations are below 5, and decreased by 20% if iterations are above 10 and divided by 3 when above 30. Hydraulic properties are the same as in Hayek [16]. Initial conditions are defined by a phreatic level of  $-5$  m.

## 5.2 Validation of 1DSat Simulation

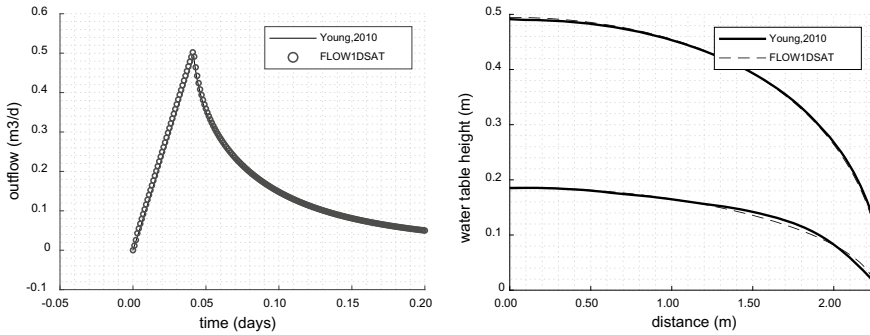
Several 1D models for the flow through one layer exist in the literature, generally based on the Dupuit–Forchheimer approximations. For multilayer systems, only semi-analytical approximations exist [8–10], and most of them apply to stationary régimes.

In Rushton and Youngs [8], a transient numerical model for a 1D one-layered system is included. The model is based on the Dupuit–Forchheimer approximations and seepage boundary conditions varying with time following Eq. 5. In Fig. 4, results from Flow1DSat are compared against Rushton and Youngs [8], in which a one-layer system 2.25 m long is subjected to an inflow of 0.5 m/day during 0.04167 days, with

<sup>1</sup> CSR: Compressed Sparse Row format (sparse matrix storage format).

<sup>2</sup> ILUT: Incomplete Lower Upper factorization (sparse matrix preconditioner).

<sup>3</sup> FGMRES: Flexible Generalized Minimal Residual method (iterative solver).

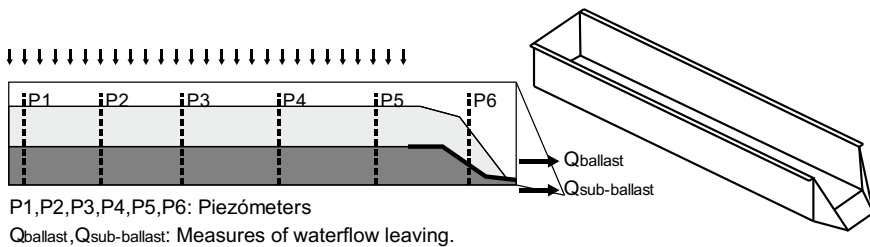


**Fig. 4** One-dimensional one-layer transient analysis by [8] compared to Flow1DSat results. On the left: outflow over time at the seepage boundary. On the right: water tables at the end of recharge (top line) and at 0.2 days

permeability of 4.0 m/s, and a constant non-wetted porosity of  $n_{nw} = 0.04$ . Good matches are apparent.

## 6 Partial Results for 1.5DSatUnsat assembled Model

Heyns [2] performed a series of physical experiments on a flume where a two-layer system of ballast and three different sub-ballast materials with different slopes were subjected to different constant recharges for a limited time before inflow stopped. Saturated permeability for sub-ballast and densities of all materials were obtained, but no unsaturated hydraulic properties were given, and they had to be calibrated to match Heyns [2] results. Flow2DSatUnsat results approximate the experimental ones after calibrating the van Genuchten parameters. But if the Mualem–van Genuchten expressions for water retention curve and permeability are applied to ballast, unrealistic low velocity is obtained, and results get distorted compared to Heyns’ as the saturation front takes time to reach the sub-ballast. To circumvent this problem, a lower ballast layer height is considered (Fig. 5).



**Fig. 5** Flume test filled with sub-ballast and ballast performed by Heyns [2]

**Table 1** Van Genuchten hydraulic parameters for simulation in Fig. 6

Ballast	$\theta_{\text{sat}} = 0.43, \theta_{\text{res}} = 0.045, k_{\text{sat}} = 0.5 \text{ m/s}, \alpha = 200 \text{ m}^{-1}, n = 4.0$
Sub-ballast	$\theta_{\text{sat}} = 0.265, \theta_{\text{res}} = 0.049, k_{\text{sat}} = 5.64 \cdot 10^{-4} \text{ m/s}, \alpha = 3.6 \text{ m}^{-1}, n = 1.56$

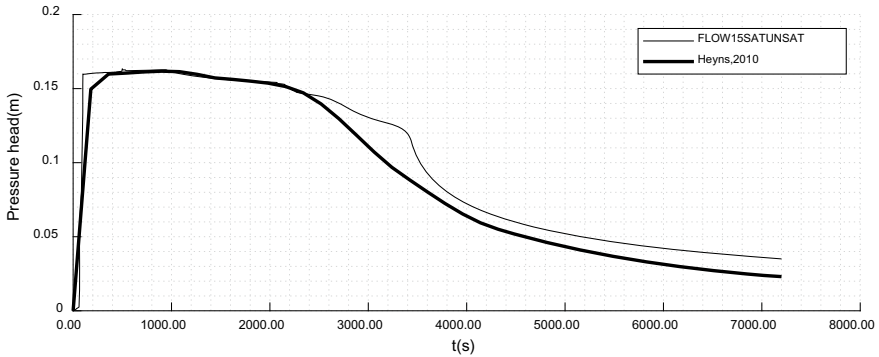
From the experiments performed by Heyns [2], one with enough inflow to involve the two layers has been selected. This was the one with sub-ballast #1, 0% slope, and an inflow of 1.58 m/day (2.60 in/h) over 1.88 m (74in) with a flume length of 2.26 m (89in). The properties of sub-ballast from Heyns [2] are: permeability of 48.76 m/d (80in/h) and dry density of 1.938 t/m<sup>3</sup> with 0% fine content. Van Genuchten hydraulic properties are included in Table 1 and are selected by comparing to typical soils with similar properties included (Table 2). Properties for ballast are taking by extrapolating to a permeability of 0.5 m/s (Fig. 7), while the van Genuchten parameters for sub-ballast are calibrated to the Heyns test to values near to include in Table 2. Water table height is compared with piezometer P3 measures in Fig. 6, with a good match.

The results shown in Fig. 6 have been achieved by ‘weak parallel coupling’ (see above). Strong coupling has been tried but convergence on the interfaces proved difficult because of the differences between the two discretized simulations. Monolithic fully coupled versions were also, but unsuccessfully, tried. Oscillating water flows and non-wetted porosities,  $n_{nw}$ , resulted which might be overcome in future by use of higher-order elements, relaxation techniques or local iterations within each time step.

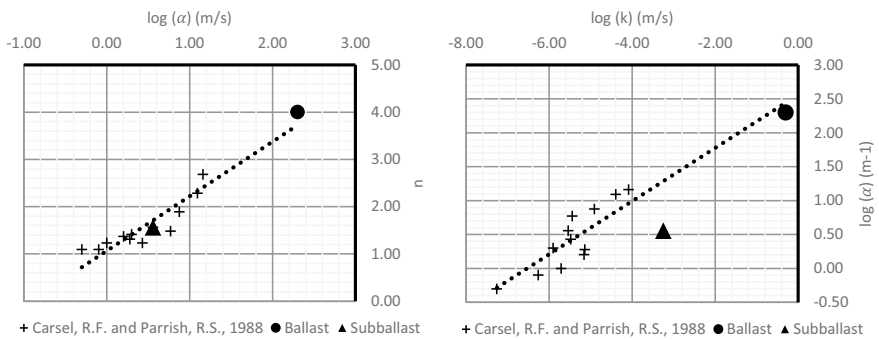
Existing 1D models can predict water table location from rain loads on multilayered systems, but a fixed non-wetted porosity needs to be specified. 1.5DSatUnsat can calculate this varying value even though it changes rapidly with water table rise. Furthermore, 1.5DSatUnsat is able to obtain the values of the dissipation of the pore pressures after rain, not only beneath the water table but also in the unsaturated

**Table 2** Common van Genuchten parameters from Carsel and Parrish [17]

Soil (USDA classification)	$k_{\text{sat}}$ (m/s)	$\alpha$ (m <sup>-1</sup> )	$n$	$\theta_{\text{sat}}$	$\theta_{\text{res}}$
Sand	$8.25 \times 10^{-5}$	14.50	2.68	0.43	0.0450
Loamy sand	$4.05 \times 10^{-5}$	12.40	2.28	0.41	0.0570
sandy loam	$1.23 \times 10^{-5}$	7.50	1.89	0.41	0.0650
Loam	$2.89 \times 10^{-6}$	3.60	1.56	0.43	0.0780
Silt	$6.94 \times 10^{-6}$	1.60	1.37	0.46	0.0340
Silty loam	$1.25 \times 10^{-6}$	2.00	1.41	0.45	0.0670
Sandy clay loam	$3.63 \times 10^{-6}$	5.90	1.48	0.39	0.1000
Clayey loam	$7.22 \times 10^{-6}$	1.90	1.31	0.41	0.0950
Silty clayey loam	$1.94 \times 10^{-6}$	1.00	1.23	0.43	0.0890
Sandy clay loam	$3.33 \times 10^{-6}$	2.70	1.23	0.38	0.1000
Silty clay	$5.50 \times 10^{-8}$	0.50	1.09	0.36	0.0700
Clay	$5.50 \times 10^{-7}$	0.80	1.09	0.38	0.0680



**Fig. 6** Pressure heads at piezometer P3 in a flume with two layers of sub-ballast and ballast from test performed on date 12/8/98 by Heyns [2] (p. 313), compared with results of 1.5DSatUnsat model with hydraulic parameters as in Table 1



**Fig. 7** Values of van Genuchten constants selected for ballast and sub-ballast compared with trends with data included in Table 2

domain, which has great importance in places such as the top of the subgrade or in a fouled ballast.

## 7 Conclusion

A simplified model of the water flow in rail-track layers has been described and is still in development. This model is able to extend the capabilities of current 1D water flow models for multilayered systems by not only predicting the movement of water tables but also the evolution of the water content in the unsaturated domains. This new information has importance in railway management as many problems arise in highly saturated subgrades or with the poor drainage performance of fouled ballast.

The model has a role between that of simplified 1D models and the accuracy of 2D models and could lead the way to faster, yet still reliable, simulations. A fast model with acceptable accuracy to predict water content on rail-track layers could be beneficial in areas such as railway maintenance and infrastructure asset management as a way to assess the risk of failure/distress related to high water content.

## References

1. Selig ET, Waters JM (1994) Track geotechnology and substructure management, Thomas Telford
2. Heyns FJ (2000) Railway track drainage design techniques. University of Massachusetts Amherst
3. Li D, Selig ET (1995) Evaluation of railway subgrade problems, *Transp Res Rec* 1489:17–25
4. Dawson A (2009) Water in road structures: movement, drainage & effects. Springer Science & Business Media
5. Thom N (2008) Principles of pavement engineering. Thomas Telford London
6. Chiachío J et al (2015) Prognostics design for structural health management. In: Emerging design solutions in structural health monitoring systems, IGI Global, pp 234–273
7. Razavi S, Tolson BA, Burn DH (2012) Review of surrogate modeling in water resources. *Water Resour Res* 48(7)
8. Rushton KR, Youngs EG (2010) Drainage of recharge to symmetrically located downstream boundaries with special reference to seepage faces. *J Hydrol* 380(1):94–103
9. Chiachío J et al (2019) A Bayesian assessment of an approximate model for unconfined water flow in sloping layered Porous Media. *Transp Porous Media* 126(1)
10. Youngs EG, Rushton KR (2009) Steady-state ditch-drainage of two-layered soil regions overlying an inverted V-shaped impermeable bed with examples of the drainage of ballast beneath railway tracks. *J Hydrol* 377(3–4):367–376
11. Celia MA, Bouloutas ET, Zarba RL (1990) A general mass-conservative numerical-solution for the unsaturated flow equation. *Water Resour Res* 26(7):1483–1496
12. List F, Radu FA (2016) A study on iterative methods for solving Richards' equation. *Comput Geosci* 20(2):341–353
13. Szymkiewicz A (2004) Modeling of unsaturated water flow in highly heterogeneous soils, in Praca doktorska. Uniwersite Joseph Fourier/Politechnika Gdańska
14. Sicklinger S et al (2014) (2014) Interface Jacobian-based co-simulation. *Int J Numer Methods Eng* 98(6):418–444
15. Vanpachtenbeke M et al (2015) Analysis of coupling strategies for building simulation programs. *Energy Procedia* 78:2554–2559
16. Hayek M (2016) (2016) An exact explicit solution for one-dimensional, transient, nonlinear Richards' equation for modeling infiltration with special hydraulic functions. *J Hydrol* 535:662–670
17. Carsel RF, Parrish RS (1988) Developing joint probability distributions of soil water retention characteristics. *Water Resources Res* 24(5):755–769

# Hydro-Mechanical Behavior of Unsaturated Unbound Pavement Materials Under Repeated and Static Loading



Ehsan Yaghoubi , Mahdi M. Disfani , Arul Arulrajah , Jayantha Kodikara , and Asmaa Al-Taie 

**Abstract** Climatic events such as precipitation result in unbound structural layers of pavements being in a partially saturated condition during their service life. With unsaturated testing being relatively complex and costly, the presence of relatively low matric suction in granular geomaterials, practitioners have been reluctant to explore the utilization of unsaturated geomechanics in the analysis and design of the mechanical behavior of pavement structural layers. In this research, unsaturated mechanical characteristics of three types of recycled geomaterials were firstly investigated using repeated load triaxial testing and the incorporation of their soil–water characteristics in the analysis of their resilient moduli response. This was to demonstrate the importance of understanding the unsaturated mechanical behavior of compacted granular material. Next, a virgin compaction surface (VCS) was developed within a moisture content-based framework to interpret the loading, unloading and wetting-induced volume change of the compacted materials. Outcomes of this research, for the first time, extend the application of the well-established Monash Peradeniya Kodikara (MPK) framework, originally developed for fine cohesive soils, to granular materials. A distinctive attribute of the proposed approach is the relative simplicity in the testing methodology by utilizing the conventional geotechnical testing equipment. The findings of this research can be used for estimation of the settlement of a granular structural layer that is compacted, loaded and then wetted through precipitation or flooding.

**Keywords** Unbound pavement materials · Matric suction · Resilient modulus response · Volumetric behavior · MPK framework

---

E. Yaghoubi (✉) · A. Al-Taie  
Victoria University, Melbourne, VIC 3011, Australia  
e-mail: [ehsan.yaghoubi@vu.edu.au](mailto:ehsan.yaghoubi@vu.edu.au)

M. M. Disfani  
The University of Melbourne, Melbourne, VIC 3010, Australia

A. Arulrajah  
Swinburne University of Technology, Melbourne, VIC 3122, Australia

J. Kodikara  
Monash University, Melbourne, VIC 3168, Australia

# 1 Introduction

Geostructural layers of roads frequently experience a transition between unsaturated and saturated states due to climatic events such as rain and flooding. This causes alteration of the suction stress within the compacted road pavement materials. Despite having influence on the mechanical behavior of granular materials [1], matric suction (hereafter referred to as suction) is of relatively low magnitude in compacted granular soils compared to fine-grained soils, such as clays. Low suction values give rise to two barriers in application of unsaturated geomechanics in the design and analysis of unbound granular pavement layers: (a) potential uncertainties and errors in the measurements of suction and (b) costs and complexities in the laboratory measurement of suction, that is considered unworthy of the effort [2]. In this study, in order to bridge the gap between unsaturated geomechanics research and the current industry practice of using unsaturated geomechanics theories, two steps were taken. In the first step, the importance of the utilization of unsaturated characteristics in the interpretation of the mechanical response of unsaturated granular materials is illustrated. This is shown by comparing the accuracy of three well-known resilient modulus models with and without the incorporation of suction. In the next step, a straightforward moisture content-based approach is proposed and investigated to address the volumetric behavior of unsaturated recycled granular materials.

The proposed scheme of this research was based on an unsaturated testing framework initially developed by Kodikara [3] and has ever since been validated in several research works, such as Islam and Kodikara [4], Abeyrathne et al. [5], Kieu and Mahler [6] and Abeyrathne et al. [7] among others. The abovementioned studies work with fine-grained materials, and hence, a moisture content-based model for granular material is missing. The volumetric behavior of granular materials is known to be of a different nature compared to that of fine-grained soils [8]. This can be due to two factors, being greater internal friction, and lower suction stresses, and hence, the lower sensitivity of volume changes to changes in suction. The current research extends the application of the MPK framework to unbound granular materials. The proposed approach offers two features: (a) It takes the moisture content, as an alternative to suction, to be a state variable, and (b) it utilizes the conventional testing equipment commonly found in geotechnical laboratories. These features are meant to resolve the abovementioned barriers for the incorporation of unsaturated geomechanics in studying the behavior of granular materials. The volume change behavior is a fundamental property of soils and is considered essential for extending the conventional deviatoric, yield and resilient constitutive models into the models that are applicable to unsaturated soils [9].

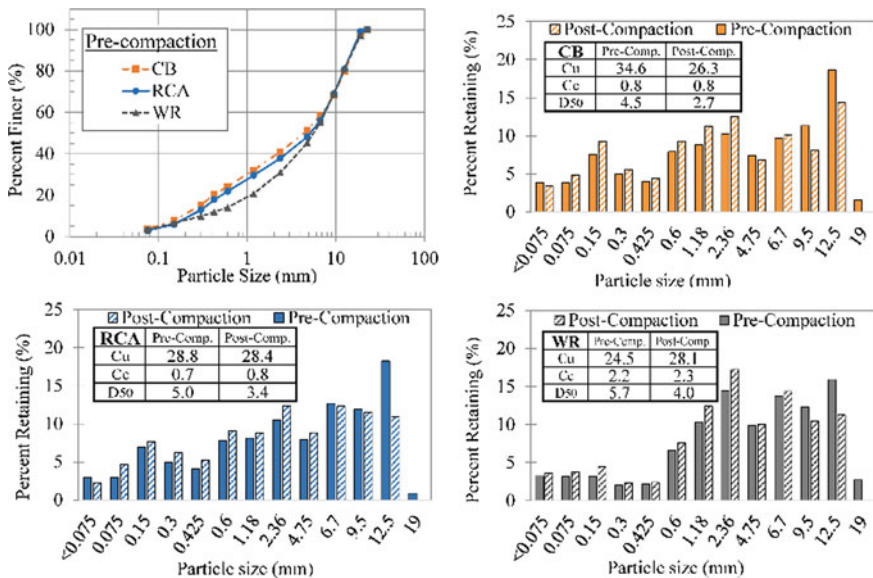
## 2 Materials and Methods

In this research, three types of recycled geomaterials, being crushed brick (CB), recycled concrete aggregates (RCA) and waste excavation rock (WR), were used to encourage sustainability in the design and construction of transportation infrastructures. The physical properties of the materials used in this research, including specific gravity (Gs), optimum moisture content (OMC) and maximum dry density (MDD) following the modified Proctor method, are presented in Table 1. The presented values of California bearing ratio (CBR) indicate the suitability of these materials for pavement base and sub-base applications, according to road authority guidelines, such as AGPT02-17 [10].

In granular materials, aggregate breakage during compaction can result in the alteration of pore size distribution, which affects the unsaturated properties of the compacted materials [11]. Figure 1 demonstrates the particle size distribution of CB, RCA and WR, before and after compaction. Figure 1 also compares the coefficient

**Table 1** Physical and compaction properties of CB, RCA and WR

Material	Gs	OMC (%)	MDD (kg/m <sup>3</sup> )	CBR
CB	2.64	10.8	1990	104–116
RCA	2.69	11.0	1960	141–174
WR	2.82	5.7	2220	118–143



**Fig. 1** Gradation curves, and pre- and post-compaction particle size distribution parameters



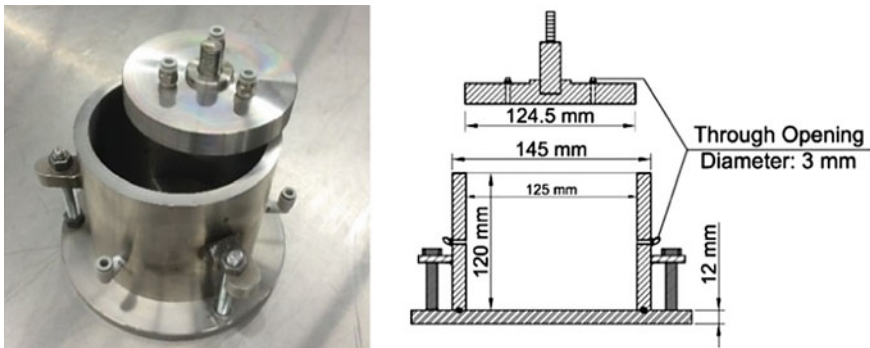
of uniformity ( $C_u$ ), coefficient of curvature ( $C_c$ ) and the mean particle size ( $D_{50}$ ) of the pre- and post-compaction samples. Comparisons between the pre- and post-compaction gradations showed considerable reduction of maximum particle size and  $D_{50}$  which can contribute to the reduction of pore sizes in samples and hence, an increase in suction.

## 2.1 Repeated Load Triaxial Testing

In order to investigate the resilient behavior of the recycled blends, repeated load triaxial (RLT) testing was carried out on the compacted samples following the AASHTO-T307-99 [12] procedure. The testing equipment included a servo-controlled universal testing machine that applied a repeated loading regime of 0.1 s loading period and 0.9 s resting period on samples. The triaxial cell had three openings forming 120-degree angles for mounting three linear variable differential transformers (LVDT) pointing at the mid-height of the specimen. These LVDTs recorded the lateral deformations during the test. Local LVDTs were mounted inside the cell to collect the axial deformation during the test. A split mold with an internal diameter of 100 mm and a height of 200 mm was used for preparing the samples under the modified Proctor compaction energy.

## 2.2 Virgin Compaction Surface Tests

The moisture content-based testing approach of this research sought two aims: (a) development of a virgin compaction surface (VCS) and (b) conducting loading–wetting and loading–unloading–wetting state paths with respect to the VCS. A stainless steel compaction mold (Fig. 2) was designed and manufactured. Three openings



**Fig. 2** Mold developed for the compaction and state path testing

on the wall of the mold and three on the loading plate were machined to allow for the injection of water during the wetting state paths.

For developing the VCS, a series of compaction tests was carried out under a stress range between 100 and 4000 kPa at moisture ratios between 0.1 and the saturation state. Moisture ratio is the product of the moisture content and the specific gravity. Compaction was undertaken by a universal testing machine with the maximum loading capacity of 100 kN in compression, connected to a data logger to collect the stress-deformation data.

The mold presented in Fig. 2 and a universal testing machine were used for undertaking loading, unloading and wetting paths. The loading rate applied on samples drier than OMC was 500 kPa/min. The loading rate for samples wetter than OMC was 50 kPa/min to prevent the entrapment of water. Wetting paths were undertaken by the injection of a pre-determined volume of water into the soil samples through the six openings while the sample was constantly loaded. In each loading, unloading and wetting stages, sufficient time was given to the samples and deformations were observed until the recorded deformation change rate was negligible (no further densification was achieved). More details on sample preparation and the state paths are available in Yaghoubi et al. [13].

### 3 Incorporation of Suction in Resilient Modulus Models

In this section, firstly, the soil water characteristic curves (SWCC) of CB, WR and RCA were estimated. Next, the outcomes of three resilient modulus ( $M_r$ ) prediction models were compared with the RLT test results.

#### 3.1 Soil Water Characteristic Curves

The SWCC of the materials was estimated using two well-established prediction models, namely Aubertin et al. [14] and the Perera et al. [15] models. Input parameters for the models are presented in Table 2. These models were selected as they were suitable for granular materials, and their model input parameters were available for

**Table 2** Input model parameters used for prediction of the SWCC

Parameter	$D_{10}$	$D_{20}$	$D_{30}$	$D_{60}$	$D_{90}$	$P_{200}$	$e$
Used in Aubertin model	•						•
Used in Perera model	•	•	•	•	•	•	•
CB	0.16	0.36	0.72	4.52	14.28	0.041	0.32
RCA	0.20	0.41	0.80	5.56	12.94	0.035	0.37
WR	0.21	0.81	1.50	5.90	12.90	0.036	0.35

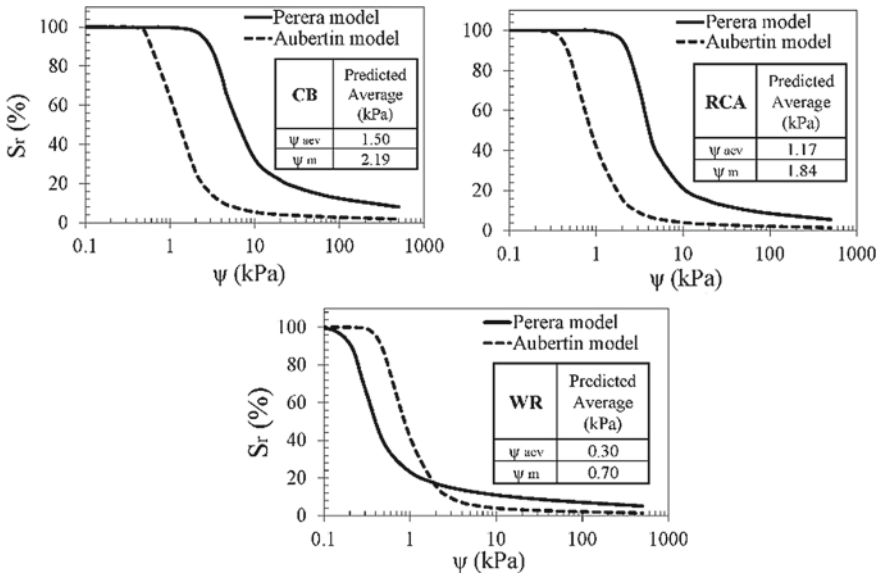


Fig. 3 Estimated SWCC for CB, RCA and WR using Aubertin et al. [14] and Perera et al. [15]

the materials of this research. The post-compaction  $C_u$ , presented in Fig. 1, is also a model input parameter for Aubertin et al. [14]. In Table 2,  $D_i$  refers to the size from which  $i\%$  of the particle are smaller, and  $P_{200}$  refers to the percent passing sieve #200 (0.075 mm) in decimals.

Figure 3 demonstrates the SWCC obtained for CB, RCA and WR using the above-mentioned models, together with the average of air entry value suction,  $\psi_{aev}$ , and the value of suction at the moisture content of the RLT samples,  $\psi_m$ . The moisture content of RLT samples was 95–100% of the OMC values as presented in Table 1. Based on the  $\psi_{aev}$  and  $\psi_m$  values, CB samples showed greater suction compared to RCA and WR samples, possibly due to a greater percentage of fine materials, as well as lower void ratio.

### 3.2 Resilient Modulus Predictions

Deviatoric stress model [16], Eq. 1, modified universal model (aka octahedral model) [12], Eq. 2, and Azam et al. [17] model, Eq. 3, were selected to investigate the incorporation of suction in the resilient models. Among the three models, only the latter takes suction as an input parameter.

$$M_r = p_a \left[ k_1 \left( \frac{\sigma_3}{p_a} \right)^{k_2} \left( \frac{\sigma_d}{p_a} \right)^{k_3} \right] \tag{1}$$

$$M_r = k_1 p_a \left( \frac{\sigma_b}{p_a} \right)^{k_2} \left( \frac{\tau_{oct}}{p_a} + 1 \right)^{k_3} \tag{2}$$

$$M_r = k_0 \left( \frac{\sigma_b}{3 p_a} \right)^{k_1} \left( \frac{\tau_{oct}}{\tau_{ref}} \right)^{k_2} \left( \frac{\psi_m}{p_a} \right)^{k_3} \left[ \left( \frac{RDD(1 - k_4 P - CB/100)}{100} \right) \right]^{k_5} \tag{3}$$

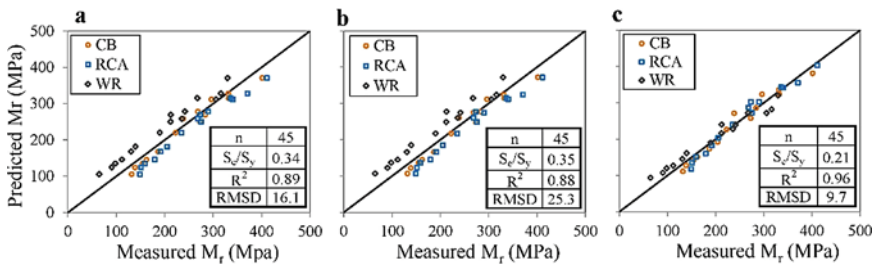
In these equations,  $\sigma_3$ ,  $\sigma_d$  and  $\sigma_b$  are confining, deviator and bulk stresses, respectively,  $p_a$  is atmospheric pressure,  $\tau_{oct}$  is octahedral shear stress,  $\tau_{ref}$  is reference shear stress defined as  $0.471 \times$  maximum shear strength [17],  $k_0$ – $k_5$  are model parameters,  $\psi_m$  is matric suction, and RDD is the relative dry density compared to the highest density of the blends (CB in this research). Equation 3 was originally developed for the mixtures of CB and RCA. For simplifying the model,  $k_4$  is taken as zero to neutralize P-CB (percentage of CB in the blend) and to make the model applicable to all blends.

Table 3 presents the model parameters achieved by regression analysis and fitting the experimentally obtained values of  $M_r$  (45 datasets) to the abovementioned models. These datasets were achieved from 15 sequences of RLT tests on each blend under the range of repeated vertical stresses and static confining stresses recommended in the AASHTO T-307 method. The parameters presented in Table 3 were adopted to predict  $M_r$  values using the models presented in Eqs. 1 to 3.

Figure 4 plots the measured–predicted  $M_r$  values together with three statistical measurements, being standard accuracy ( $S_e/S_y$ ), coefficient of determination ( $R^2$ ) and root mean square deviation (RMSD) for evaluation of the “goodness of fit”. In standard accuracy,  $S_e$  is the standard error of estimate and  $S_y$  is the standard deviation.

**Table 3** Resilient modulus model parameters

Model	$k_0$	$k_1$	$k_2$	$k_3$	$k_4$	$k_5$
Deviatoric stress model	–	2.73	0.382	0.177	–	–
Modified universal model	–	1.237	0.548	0.046	–	–
Simplified Azam et al. model	963.442	0.555	0.005	0.284	0.000	– 3.611



**Fig. 4** Measured versus predicted  $M_r$  using **a** deviatoric stress model [16], **b** modified universal model [12] and **c** simplified Azam et al. [17] model

According to Witczak et al. [18] criteria, when  $R^2 \geq 90$  ( $S_e/S_y \leq 0.35$ ) and  $0.70 \leq R^2 \leq 0.89$  ( $0.36 \leq S_e/S_y \leq 0.55$ ) “Excellent” and “Good” fit are achieved, respectively. Also, lower RMSD indicates a better fit [17]. It is concluded from the goodness-of-fit assessment that utilizing suction, despite being of low magnitude, resulted in a more accurate prediction of the resilient modulus response of the materials. This supports the importance of the application of unsaturated geomechanics theories in the mechanical behavior of unbound granular materials used in pavements.

### 4 Development of a Virgin Compression Surface

The compaction test results extracted from Yaghoobi et al. [13], as per the testing procedure presented in Sect. 2.2, were used to develop the VCS in a space of void ratio,  $e$  (to represent deformation), moisture ratio,  $e_w$  (to represent changes in moisture content) and net stress,  $p$  (to represent loading). The VCSs developed for CB and WR are presented in Fig. 5. This surface is the loosest state of a sample at specific net stress,  $p$ , and moisture state,  $e_w$ . Therefore, once the VCS was developed, it was expected that the independent loading, unloading and wetting state paths can be interpreted within the boundaries of the VCS. The line of optimum (LOO) on the VCS was drawn by connecting the minimum void ratio achieved in each compaction curve (maximum density in static method of compaction). LOO is the boundary between the wet side and the dry side of the VCS. The LOO is important for the determination of the loading rates applied for the samples on the dry and wet side of the VCS.

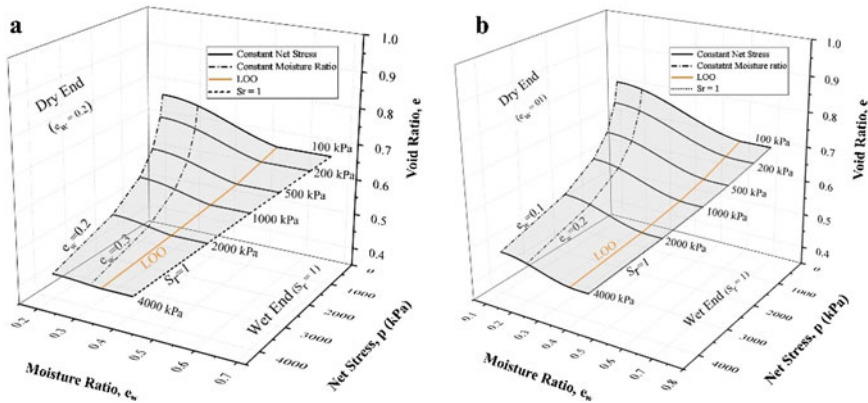


Fig. 5 Virgin compaction surfaces for a CB and b WR

### 5 State Paths with Respect to the VCS

For evaluation of the applicability of the VCS for interpreting the volumetric behavior of the compacted samples, a series of loading–wetting (L-W) state paths and loading–unloading–wetting (L-U-W) state paths were carried out. The net stresses on the paths had a range of between 100 and 4000 kPa. The moisture contents varied between 7.6 and 3.6% for CB and WR, respectively, and the moisture content at saturation.

Figure 6 demonstrates selected L-W state paths starting from a loose state (O) in the  $e - e_w$  and  $e - \log p$  planes. The L-W path simulates a granular layer that has been compacted and undergone the load of a superstructure while being exposed to the precipitation. In both CB (Fig. 6a and b) and WR (Fig. 6c and d), loading paths (O-A and O-A') reached the corresponding stress contours at A and A' (100 and 4000 kPa for CB and 500 and 2000 kPa for WR) verifying that the VCS is capable of predicting the loading paths. However, the wetting paths (A-B and A'-B') only closely followed the VCS under net stresses of 2000 and 4000 kPa.

Figure 7 demonstrates selected L-U-W state paths in the  $e - e_w$  and  $e - \log p$  planes. An example of the L-U-W path could be an embankment fill layer compacted by a roller, unloaded to a stress as low as the effective stress due to the weight of its

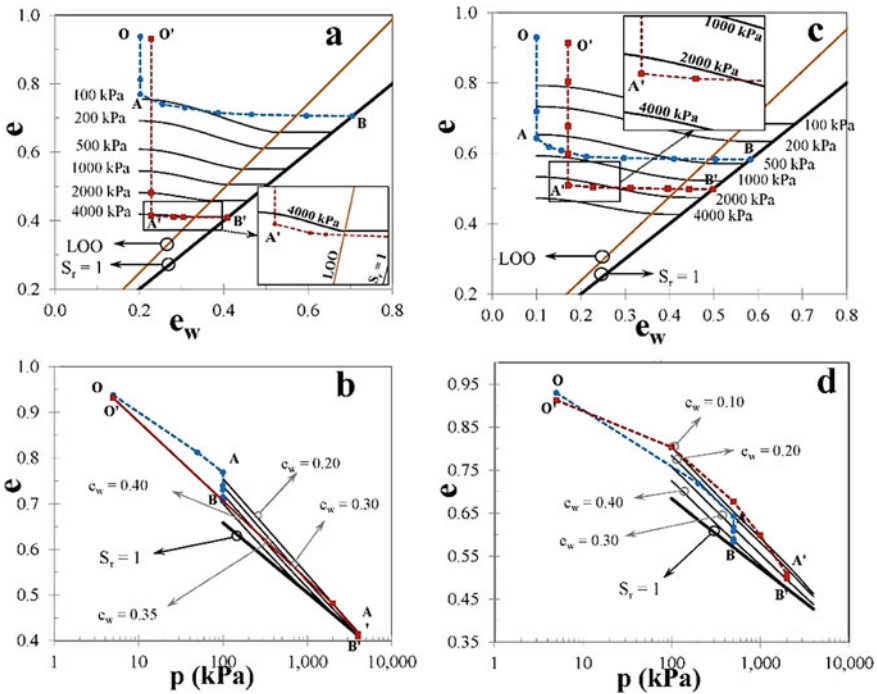
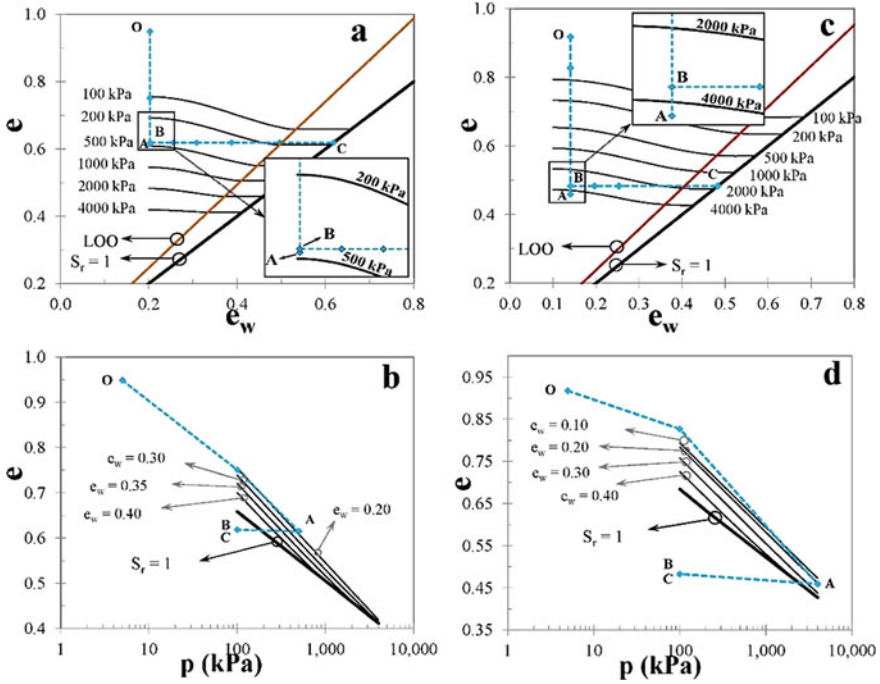


Fig. 6 L-W state paths: a and b for CB in  $e - e_w$  and  $e - \log p$  planes, and c and d for WR in  $e - e_w$  and  $e - \log p$  planes



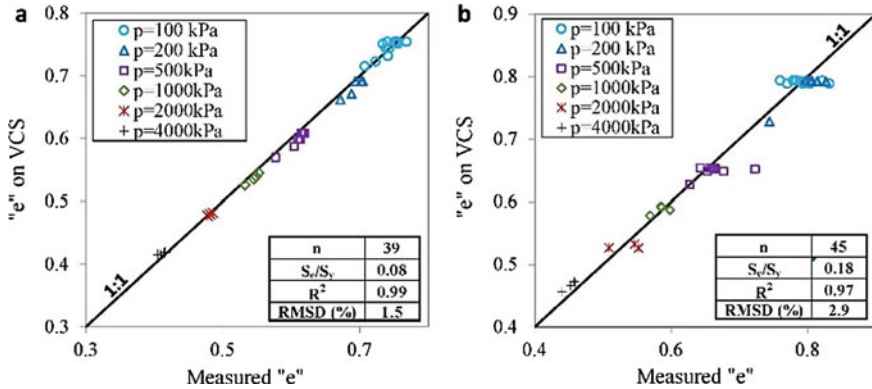
**Fig. 7** L-U-W state paths: **a** and **b** for CB in  $e - e_w$  and  $e - \log p$  planes, and **c** and **d** for WR in  $e - e_w$  and  $e - \log p$  planes

above layers of embankment or pavement, and is finally exposed to a flood event. In Fig. 7a and 7b, a CB sample was loaded to 500 kPa (A), unloaded to 100 kPa (B) and wetted under the net stress of 100 kPa to saturation (C). Figure 7c and 7d illustrate a WR sample loaded to 4000 kPa (A), unloaded to 100 kPa (B) and wetted under the net stress of 100 kPa to saturation (C). Both state paths reached the corresponding stress contour on the VCS at Point A showing that the VCS can predict the loading path. Unloading the samples to 100 kPa, however, did not take the path back to the stress contour of 100 kPa. This matched with the definition of VCS, being the surface developed at the loosest states of a geomaterial at a specific moisture and stress conditions. Therefore, VCS could not predict the unloading path accurately.

The plots presented above and several other L-W and L-U-W state paths showed that the VCS is capable of predicting the loading paths accurately. Figure 8 shows plots of experimentally measured void ratio versus void ratio obtained from VCS for CB and WR. Values of  $S_e/S_y$ ,  $R^2$ , and RMSD presented in Fig. 8 for both VCSs show “excellent” fit between the predicted and measured data following Witczak et al. [18] criteria.

The wetting paths, in contrast, do not follow the surface under net stresses lower than 2000 kPa. Under net stresses greater than 2000 kPa, the wetting path is reasonably close to the VCS; however, the predicted results are not as accurate as of the





**Fig. 8** Measured void ratio versus predicted void ratio for **a** CB samples and **b** WR samples

loading paths. Group of compaction curves of CB and WR shows that the stress of 2000 kPa densifies samples to about 90% of the MDD of modified Proctor compaction. In practical terms, a density of at least 95% of modified proctor MDD is required for the pavement subbase or base compacted layers. For, CB and WR, such densities are achieved under net stresses greater than 2000 kPa, and hence, the VCS provides relatively accurate wetting-induced volume change predictions for practical applications.

For comparison of the wetting-induced deformation in granular and fine materials, volume changes due to wetting paths conducted on kaolin clay from Islam and Kodikara [4] (referred to as source “I” in Table 4) and Pearl clay from Sun et al. [19] (referred to as source “S” in Table 4) were investigated and presented in Table 4.

In Table 4, the changes in the void ratio ( $\Delta e$ ) due to wetting under the constant net stress of  $p$  from the initial degree of saturation ( $(S_r)_{ini}$ ) to a final moisture condition ( $(S_r)_{fin}$ ), being the fully saturated condition, are compared. The LW paths in Sun et al. [19] were presented in  $e-\psi$  (suction) plots. The  $S_r$  values corresponding to initial and final void ratios in each path were obtained using the  $S_r-\psi$  plots (SWCC) presented in their paper. The amount of deformation due to wetting ( $\Delta H$ ) was calculated assuming a geotechnical layer with a thickness of 200 mm. The comparison revealed a significant difference between the deformation of the fine materials and the granular materials used in this research. For instance, wetting a 200-mm layer compacted through and being constantly loaded under the net stress of 4000 kPa from  $S_r = 0.48$  to  $S_r = 1$  resulted in 7.8 mm of deformation in kaolin. In the same amount of change in the degree of saturation, a 200-mm CB layer ended up to a significantly lower deformation of 1.1 mm.

In spite of exhibiting relatively small deformations, in compacted granular pavement materials, volume changes due to wetting can accumulate and result in structural distresses such as rutting. Thus, a prediction model that accurately interprets



**Table 4** Wetting-induced volume changes extracted from the literature versus this research

Source of data	$(S_r)_{ini}$	$(S_r)_{fin}$	$p$ (kPa)	The literature			This research		
				$\Delta e$	$\Delta H$ (mm)	Material	$p$ (kPa)	$\Delta e$	$\Delta H$ (mm)
<i>S</i>	0.55	1.0	98	0.083	7.4	CB	100	0.008	1.0
<i>S</i>	0.56	1.0	196	0.062	5.7	CB	200	0.003	0.4
<i>S</i>	0.63	1.0	392	0.045	4.3	CB	500	0.003	0.4
<i>S</i>	0.67	1.0	588	0.026	2.5	CB			
<i>I</i>	0.263	1.0	100	0.821	54.7	CB	100	0.062	7.0
<i>I</i>	0.364	1.0	1000	0.238	23.2	CB	1000	0.011	1.4
<i>I</i>	0.484	1.0	4000	0.060	7.8	CB	4000	0.008	1.1
<i>S</i>	0.55	1.0	98	0.083	7.4	WR	100	0.002	0.2
<i>S</i>	0.56	1.0	196	0.062	5.7	WR	200	0.002	0.2
<i>S</i>	0.63	1.0	392	0.045	4.3	WR	500	0.001	0.2
<i>S</i>	0.67	1.0	588	0.026	2.5	WR			
<i>I</i>	0.131	1.0	100	0.952	60.8	WR	100	0.079	8.9
<i>I</i>	0.175	1.0	1000	0.310	28.9	WR	1000	0.054	6.9
<i>I</i>	0.233	1.0	4000	0.124	15.6	WR	4000	0.034	4.6

the wetting induced volume changes in unsaturated granular materials can significantly enhance the unbound granular pavement design and analysis. Such a prediction model has recently been developed and presented in Yaghoobi et al. [20] article.

## 6 Conclusions

In this research, two main objectives were sought; firstly, to demonstrate the importance of the application of unsaturated geomechanics in the mechanical behavior of unbound granular materials; secondly, to propose an unsaturated testing approach featured with relative simplicity in order to encourage the engineers to utilize unsaturated geomechanics theories in the design and response analysis of pavement materials. The following outcomes were concluded based on the results of this study:

- Incorporation of suction leads to a more accurate prediction of the resilient modulus for crushed brick, recycled concrete aggregate and waste rock.
- Moisture content-based frameworks are recently being proposed and validated as an alternative to the conventional suction-based schemes for interpretation of the behavior of fine materials. In this research, a virgin compaction surface following the moisture content-based MPK framework was developed and investigated for course-grained geomaterials.

- The virgin compaction surface developed for crushed brick and waste rock showed excellent accuracy in predicting the loading paths. The surface, however, did not show good accuracy in predicting the wetting paths.
- The volume change of compacted fine materials through wetting is significantly greater than that of compacted granular materials. Nevertheless, since the accumulation of small volume changes due to repeated loads of traffic can lead to structural distress in pavements, development of an accurate prediction model is necessary.

An application of the developed virgin compaction surface could be the estimation of the post-compaction dry density (void ratio) of an unbound granular pavement layer at a specific moisture content and compaction effort. Extending the moisture content-based framework to cyclic loading is a future direction for this research.

## References

1. Caicedo B, Coronado O, Fleureau JM, Correia AG (2009) Resilient behaviour of non standard unbound granular materials. *Road Mater Pavement Design* 10(2):287–312
2. Raveendiraraj A (2009) Coupling of mechanical behaviour and water retention behaviour in unsaturated soils: University of Glasgow
3. Kodikara J (2012) New framework for volumetric constitutive behaviour of compacted unsaturated soils. *Can Geotech J* 49(11):1227–1243
4. Islam T, Kodikara J (2015) Interpretation of the loading–wetting behaviour of compacted soils within the “MPK” framework. Part I: Static Compaction 1. *Can Geotech J* 53(5):783–805
5. Abeyrathne A, Kodikara J, Bui H (2016) Prediction of wetting-induced volume change behaviour of compacted unsaturated soils in the context of the MPK framework. In: E3S web of conferences: EDP sciences, pp 17011
6. Kieu M, Mahler A (2018) A study on the relationship between matric suction and the void ratio and moisture content of a compacted unsaturated soil. *Periodica Polytech Civ Eng* 62(3):709–716
7. Abeyrathne A, Sivakumar V, Kodikara J (2019) Isotropic volumetric behaviour of compacted unsaturated soils within (v, vw, p) space. *Can Geotech J* 56(12):1756–1778
8. Macari-Pasqualino EJ, Runesson K, Sture S (1994) Response prediction of granular materials at low effective stresses. *J Geotech Eng* 120(7):1252–1268
9. Sheng D (2011) Review of fundamental principles in modelling unsaturated soil behaviour. *Comput Geotech* 38(6):757–776
10. AGPT02-17 (2017) Guide to pavement technology Part 2: pavement structural design. Sydney, Australia: Austroads Ltd. 283 p
11. Zhang YD, Buscarnera G (2015) Prediction of breakage-induced couplings in unsaturated granular soils. *Geotechnique* 65(2):135–140
12. AASHTO-T307-99 (2007) Standard method of test for determining the resilient modulus of soils and aggregate materials. American Association of State Highway and Transportation Officials, Washington, DC
13. Yaghoubi E, Disfani MM, Arulrajah A, Kodikara J (2019) Development of a void ratio-moisture ratio-net stress framework for the prediction of the volumetric behavior of unsaturated granular materials. *Soils Found* 59(2):443–457
14. Aubertin M, Mbonimpa M, Bussi ere B, Chapuis RP (2003) A model to predict the water retention curve from basic geotechnical properties. *Can Geotech J* 40(6):1104–1122

15. Perera Y, Zapata C, Houston W, Houston S (2005) Prediction of the soil water characteristic curve based on grain-size-distribution and index properties. In: Rathje EM (ed) *Advances in pavement engineering*, vol 130. Geotechnical Special Publication, pp49–60
16. Puppala A, Mohammad L, Allen A (1997) Engineering behavior of lime-treated Louisiana subgrade soil. *Transp Res Record J Transp Res Board* 1546:24–31
17. Azam AM, Cameron DA, Rahman MM (2013) Model for prediction of resilient modulus incorporating matric suction for recycled unbound granular materials. *Can Geotech J* 50(11):1143–1158
18. Witczak M, Kaloush K, Pellinen T, El-Basyouny M, Von Quintus H (2002) NCHRP Report 465: simple performance test for superpave mix design. TRB, National Research Council, Washington, D.C.
19. Da S, Sheng D, Xu Y (2007) Collapse behaviour of unsaturated compacted soil with different initial densities. *Can Geotech J* 44(6):673–686
20. Yaghoubi E, Disfani MM, Arulrajah A, Al-Taie A (2021) A prediction model for the loading-wetting volumetric behavior of unsaturated granular materials. *Soils and Foundations* (in press: <https://doi.org/10.1016/j.sandf.2021.01.012>)

# Development of a Linear Equilibrium Suction Model Based on TMI and Climatic Regions for Oklahoma



Amir Hossein Javid , Hussein Al-Dakheeli , and Rifat Bulut 

**Abstract** There is a need for rational methods to estimate behavior of unsaturated soils for analysis and design of pavement structures. The attributes of a desirable method would comprise low cost, reasonable accuracy and technical soundness. The equilibrium suction has a direct influence on the subgrade resilient modulus and vertical movement due to swelling and shrinking of expansive clays. The current AASHTOWare Pavement ME software package utilizes the enhanced integrated climatic model (EICM) for applying the effects of climate on the pavement materials. The EICM utilizes the depth to groundwater table to compute moisture content and the corresponding suction in the subgrade. However, research studies have revealed that other critical factors also influence the equilibrium suction. In this study, a mechanistic model is presented to predict equilibrium suction considering the effects of the unsaturated soil moisture diffusion coefficient. Based on a statistical analysis, an equilibrium suction prediction model is generated from readily available parameters, i.e., Thornthwaite moisture index (TMI), clay content (%) and relative humidity. The results of this study showed that the regression model provides reasonable prediction accuracy with a small test MSE of 0.03.

**Keywords** Equilibrium suction · Thornthwaite moisture index · Geographic information system · Subgrade soil · Moisture active zone

---

A. H. Javid (✉) · H. Al-Dakheeli · R. Bulut  
School of Civil and Environmental Engineering, Oklahoma State University, Stillwater, OK  
74078, USA  
e-mail: [amir.javid@okstate.edu](mailto:amir.javid@okstate.edu)

H. Al-Dakheeli  
e-mail: [abedalm@ostatemail.okstate.edu](mailto:abedalm@ostatemail.okstate.edu)

R. Bulut  
e-mail: [rifat.bulut@okstate.edu](mailto:rifat.bulut@okstate.edu)

## 1 Introduction

Environmental conditions have a significant effect on the subgrade performance. Of all the environmental factors, moisture has a direct effect on the pavement layer and subgrade property [1–4]. The resilient modulus of the subgrade soil is highly dependent on the degree of saturation and the corresponding matric suction [5–11]. The matric suction in the subgrade soil beneath the pavement reaches an equilibrium condition after a certain period of time after construction [12, 13]. Hence, an accurate estimate of equilibrium suction underneath a pavement structure is necessary to determine the long-term resilient modulus of subgrade soil in response to variations in climatic and surface boundary conditions.

The enhanced integrated climatic model (EICM), which is an integral component of the current AASHTO Pavement ME, plays an important role in defining the short- and long-term pavement materials properties used in the design guide. The EICM involves analysis of water and heat flow through pavement layers in response to climatic, soil and boundary conditions above and below the ground surface in pavement structures. The software uses historical climatic files that have been developed for each state in the USA. These files are in most cases limited in number and region within each state and therefore cannot represent the site-specific climate information. Furthermore, the EICM depends on the groundwater table depth to compute moisture content and the corresponding suction in the subgrade. However, this model would yield inaccurate suction values if the water table data is missing or the water table depth is greater than 7 m [14].

Previous research studies have revealed that other critical factors (e.g., precipitation, field capacity, etc.) also influence the equilibrium suction [15]. These studies have shown a correlation between equilibrium soil suction and Thornthwaite's moisture index (TMI); however, our studies have shown that these suction correlations exhibit large variability. This study is aimed at developing an improved prediction model of equilibrium suction, which would take into account a variety of influence factors. The paper assessed the TMI from the historical climatic data obtained from Oklahoma Mesonet weather stations from 1994 to 2018. Historical climatic data was also employed for classifying climatic regions in Oklahoma using cluster analysis. Thornthwaite moisture index (TMI) contour maps were created using the climatic data and the geographic information system (GIS) platform.

In this study, a mechanistic model is presented to predict equilibrium suction considering the effects of the diffusion coefficient. A regression model was developed to predict equilibrium suction from readily available parameters, i.e., Thornthwaite moisture index (TMI), clay content (%) and relative humidity. The following sections summarize the significant findings of this study.

## 2 Oklahoma Mesonet

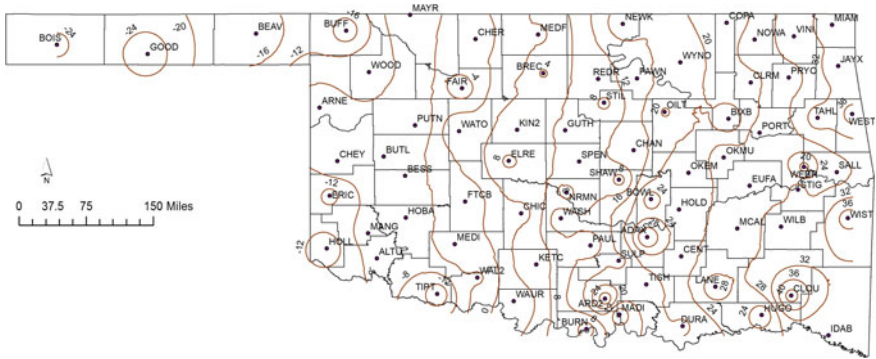
The Oklahoma Mesonet is a network of about 121 automated weather stations that report current weather and soil moisture conditions to a central computer facility every 15 min (Oklahoma Climatological Survey, [climate.ok.gov](http://climate.ok.gov)). There is no other similar network that covers short distances in the collection of climate data in the USA [16]. One of the main objectives in establishing the Mesonet network was to ensure that a station site be as representative of as large an area as possible. Therefore, site locations for Mesonet stations fulfill a number of general requirements for meteorological and environmental purposes. The network was established in the early 1990s jointly by Oklahoma State University and the University of Oklahoma. The Oklahoma Climatological Survey currently oversees Mesonet activities.

A Mesonet station occupies an area of about 100 m<sup>2</sup> and contains a datalogger, solar panel, radio trans-receiver, lightning rod and climate and environmental sensors located on or surrounding a 10 m high tower. The sensors measure more than 20 environmental and soil variables. Climatic variables are measured by a set of instruments located on or near a 10 m tall tower and below ground surface. On and above ground measurements include air temperature measurements at 1.5 m and 9 m above the ground surface, wind speed at 2 m and 10 m, relative humidity at 1.5 m above the ground surface, solar radiation, barometric pressure and rainfall. Soil temperature measurements at 5, 10 and 30 cm below the ground surface under bare and sod soil are recorded. Starting in 1996, a large number of Campbell Scientific 229-L thermal conductivity sensors have been installed at depths of 5, 25 and 60 cm below the ground surface for matric suction measurements. As of September 2019, the Oklahoma Mesonet includes soil moisture sensors at a depth of 5 cm at 121 sites, 25 cm at 101 sites and 60 cm at 76 sites. The soil matric suction measurements are recorded every 30 min, 24 h per day and year-round. A detailed description of the thermal conductivity sensors can be found in [17].

## 3 Thornthwaite Moisture Index (TMI)

The TMI, originally developed by Thornthwaite in 1948, is determined by annual water surplus, water deficiency, and water need. The whole process is computationally intensive and requires soil moisture storage information that may not be readily available in many places. Several other methods were proposed to determine the TMI values in the past decades. Thornthwaite (1948) adopted a relatively simple model for the calculation of the adjusted potential evapotranspiration as compared to some of the sophisticated (yet complex in terms of the parameters involved) models available in the literature. Due to its simplicity, this method has been widely used by many researchers, including [18–27].

Recently, Olaiz et al. [28] performed a comparison study between the four different TMI calculation processes developed from 1948 to 2006 and found out that the model



**Fig. 1** TMI contour map based on Witczak et al. [29] equation

developed by Witczak et al. [29] is comparable to the original TMI calculation process. This study adopted Witczak’s model to calculate the TMI for Oklahoma.

In this study, TMI is calculated for the 77 Mesonet weather stations representing 77 counties in the state for the period of 1994 to 2018. A GIS-based TMI contour map was generated based on the precipitation and monthly average temperature obtained through Mesonet dataset. The ArcGIS software is used to depict the TMI contour map for Oklahoma. Contour maps consist of lines that connect points of equal values of TMI for a certain region. Figure 1 shows the contour map developed using the Witczak et al. [29] method.

The adjusted potential evapotranspiration  $PET_i$  for the month,  $i$ , is calculated using the following equation:

$$PET_i = e_i \left( \frac{D_i N_i}{30} \right) \tag{1}$$

where  $D_i$  is the day length correction factor for the month  $i$  provided by McKeen and Johnson [23];  $N_i$  is the number of days in the month  $i$ ; and  $e_i$  is the unadjusted potential evapotranspiration (cm) for the month  $i$  calculated as

$$e_i = 1.6 \left( \frac{10t_i}{H_y} \right)^a \tag{2}$$

where  $t_i$  is the mean monthly temperature in °C, and  $H_y$  is the annual heat index that is determined by summing the 12 monthly heat index values. The heat index for each month is determined as follows:

$$h_i = (0.2t_i)^{1.514} \tag{3}$$

and  $a$  is a coefficient given by

$$a = 6.75 \times 10^{-7} H_y^3 - 7.71 \times 10^{-5} H_y^2 + 0.017921 H_y + 0.49239 \tag{4}$$

Witczak et al. [29] equation is given as

$$TMI = 75 \left( \frac{P}{PE} - 1 \right) + 10 \tag{5}$$

where  $P$  is the annual precipitation and  $PE$  is the net potential evapotranspiration.

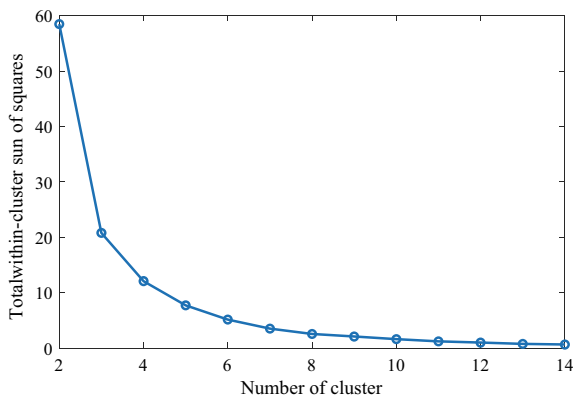
### 4 Oklahoma Climatic Regions

The basic idea of classification is called cluster analysis. Cluster analysis takes a large number of variables and reduces them to a smaller number of groups based on the similarity of the data values within the same group. This study applied  $K$ -means to classify the climatic regions in Oklahoma. The  $K$ -means clustering is a simple and elegant approach for partitioning a dataset into  $K$  distinct, non-overlapping clusters. To perform  $K$ -means clustering, the desired number of clusters  $K$  must be specified; then, the  $K$ -means algorithm will assign each observation to exactly one of the  $K$  clusters [30].

In  $K$ -means analysis, observations are partitioned into  $K$  clusters by minimizing the total within-cluster variation. The within-cluster variation for the  $k$ th cluster is the sum of all of the pairwise squared Euclidean distances between the observations in the  $k$ th cluster, divided by the total number of observations in the  $k$ th cluster. Figure 2 shows the total between cluster total within-cluster ratio variations for different  $k$  clusters.

This study uses the data from 1994 to 2018 for climatic region classification. The number of weather stations within a division is constant. However, the boundaries are still based on the county boundary, since only one weather station is selected

**Fig. 2** Total within-cluster variation for different  $k$  clusters





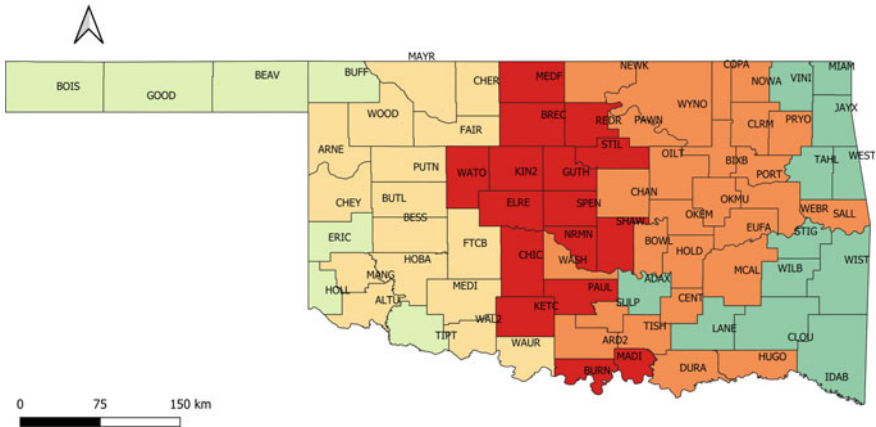


Fig. 3 Five climatic regions in Oklahoma

in each of the 77 counties in Oklahoma. As number of clusters increases, the total within-cluster sum of square becomes smaller. Therefore, this study considered five clusters which reasonably have the total within-cluster sum of square less than 10. Figure 3 shows five climatic regions in Oklahoma.

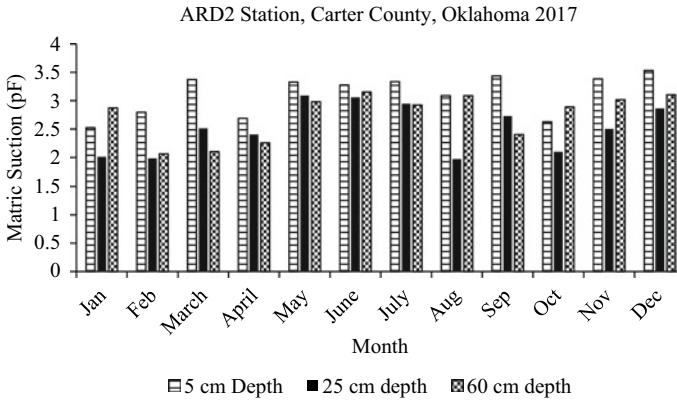
### 5 Matric Suction in Subgrade Soil

The Oklahoma Mesonet weather stations are equipped with CSI 229-L heat dissipation sensors at depths of 5, 25 and 60 cm. The sensors are capable of measuring the matric suctions indirectly through a heat transfer mechanism, which is characterized by measuring the temperature difference. The temperature difference is translated via an empirical calibration equation to estimate the matric potential of the ceramic and soil. The matric potential calibration equation is given by the following equation [16]:

$$MP = -0.717e^{1.788\Delta T_{ref}} \tag{6}$$

where MP is soil matric suction (kPa), and  $\Delta T_{ref}$  is a reference temperature differential (°C).

Equation 1 was used to determine matric suction at various depths for temperature references obtained from Mesonet stations. Figure 4 shows the monthly mean matric suctions for ARD2 station in Love County, Oklahoma, during 2017.



**Fig. 4** Monthly mean matric suction at 5, 25 and 60 cm depths in ARD2 station in Carter county, Oklahoma during 2017

## 6 A Mechanistic Model to Determine Equilibrium Suction

A mechanistic model was developed to determine equilibrium suction by using the diffusion equation proposed by Mitchell [31] and the diffusion coefficient estimate proposed by Javid and Bulut [32]. According to Mitchell, suction change due to the effect of climate, drainage and site cover is a periodic function of time and can be determined by solving the diffusion equation for these boundary conditions. The suction at any depth  $y$  and at time  $t$  can be written as

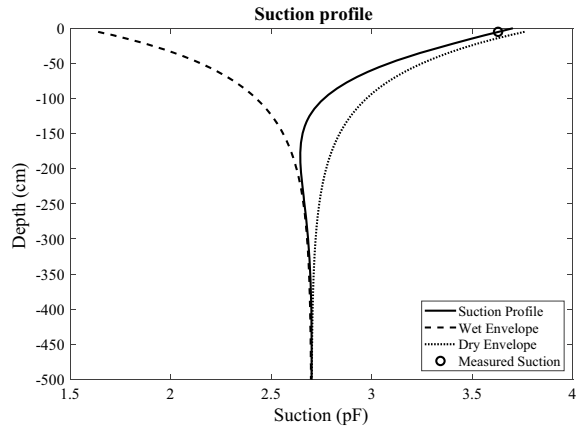
$$u(y, t) = U_e + U_o e^{-\sqrt{\frac{n\pi}{\alpha}} y} \cos\left(2\pi n t - \sqrt{\frac{n\pi}{\alpha}} y\right) \tag{7}$$

where  $U_e$  is the equilibrium suction below the moisture active zone depth [pF (or log kPa)],  $U_o$  is the amplitude of suction variation, and  $n$  is the number of suction cycles per second (1 year = 365 × 24 × 60 × 60 s). The equation is a function of the diffusion coefficient,  $\alpha$ , and as depth increases, the suction decreases exponentially. In other words, the diffusion coefficient controls the rate of moisture content (suction) change.

The diffusion coefficient ( $\alpha$ ) directly controls the depth of the moisture active zone (i.e., the depth of significant seasonal moisture fluctuations) in unsaturated soils [33]. Therefore, it is a major factor that needs to be determined. In this study, the diffusion coefficient is calculated numerically by recursively computing and fitting values from Eq. 7 with respect to measured surface suction obtained from a Mesonet station.

The equilibrium suction at any Mesonet station can be obtained by examining the suction profile. The equilibrium suction for specific sites was determined by recording the suction at a depth of convergence for which an absolute difference between wet and dry envelope became less than 0.1 (pF). The equilibrium suction

**Fig. 5** Matric suction distribution profile for measured suction at 5 cm depth on 07/14/2018 at ARD2 station, Carter county, Oklahoma



for a specific site was determined by recording the suction at a depth of convergence of the suction profiles. Figure 5 illustrates the suction profile at ARD2 station with respect to surface suction measurement at 5 cm on 07/14/2018.

## 7 A Statistical-Based Prediction Model for Equilibrium Suction

A statistical model was also developed to estimate the equilibrium suction in the subgrade soil from climatic parameters and soil properties. The following parameters were considered in the analysis:

- Annual mean relative humidity,
- Annual mean temperature,
- Annual precipitation,
- Annual mean percent sunshine,
- Annual mean wind speed,
- Clay content,
- TMI.

The environmental data was obtained from the Oklahoma Mesonet stations. The clay content was collected using the published results [34]. The equilibrium suction dataset used in the correlations was obtained from the mechanical–empirical model, as stated above. In the correlation process, each dataset was plotted and evaluated for significant trends. For example, the matric suction decreased as annual mean relative humidity increased. The clay content has a direct relation with suction, and as clay content increased, the matric suction increased. The current study revealed that relative humidity (RH), clay content (%) and TMI are statistically significant parameters and have a correlation with the equilibrium suction (pF). In this study,

a generalized linear regression model was fitted to the data. The linear equation obtained through the statistical analysis is shown in the equation below.

$$\begin{aligned} \text{Equilibrium Suction} = & 0.003 \text{ Clay} - 0.066 \text{ RH} - 0.043 \text{ TMI} \\ & + 0.0006 \text{ TMI} \times \text{RH} + 6.98 \end{aligned} \quad (8)$$

The F-test of overall significance provides a formal hypothesis test for the relationship between the suction model and the response variable. The F-test of overall significance was used to determine whether this relationship is statistically significant for the current model. To determine how well a given statistical learning procedure can be expected to perform on independent data, the validation set approach was performed to find the estimate of the test MSE. The validation set was 20% of randomly selected observations from the sample data. The standard MSE obtained through a validation set estimate for the generalized linear model was 0.0312.

## 8 Summary and Conclusions

An improved prediction model, based on mechanistic principles, is presented for predicting equilibrium suction in subgrade soils. The model in this analysis approach can improve prediction of pavement performance by incorporating a more rational estimate of moisture variations beneath the pavement in the subgrade soils. The major contributions of this study are summarized as follows.

- A GSI-based TMI contour map of Oklahoma was developed using the precipitation and temperature data collected from Oklahoma Mesonet.
- A mechanistic–empirical model was developed to determine equilibrium suction based on Mitchell’s steady-state diffusion equation and the diffusion coefficient estimate from measured soil moisture data.
- A general linear model was developed to predict suction from readily available climatic parameters (i.e., relative humidity and TMI) and clay content.
- A GIS-based climatic region map was developed by using the cluster analysis of TMI data. The equilibrium suction values are expected to have similar values within each region.

It must also be noted that the equilibrium suction prediction model is based on Mesonet weather data at specific sites in Oklahoma, subjected to specific weather and drainage conditions. It is expected that alternation in drainage (i.e., ponding) or the soil fabric (i.e., deeper cracks) would result in different predictions. Additional field observations and studies are needed to expand the database to other climates, drainage conditions and soil fabrics.

**Acknowledgements** The authors thank the Oklahoma Department of Transportation (ODOT) and Transportation Consortium of South-Central States (TranSET) for providing funds for this research study.

## References

1. Bulut R, Zaman M, Amer O, Mantri S, Chen L, Tian Y, Taghichian A (2013) Drying Shrinkage Problems In High-Plastic Clay Soils In Oklahoma. (No. OTCREOS11. 1-09-F), Oklahoma Transportation Center
2. Perera YY, Zapata CE, Houston WN, Houston SL (2004) Long-term moisture conditions under highway pavements. In: Geotechnical engineering for transportation projects, pp 1132–1143 (2004)
3. Puppala AJ, Manosuthikij T, Hoyos L, Nazarian S (2009) Moisture and suction in clay subgrades prior to initiation of pavement cracking. (No. 09-1522)
4. Zapata CE, Andrei D, Witczak MW, Houston W (2007) Incorporation of environmental effects in pavement design. *Road Mater Pavement Des* 8(4):667–693
5. Liang RY, Rabab'ah S, Khasawneh M (2008) Predicting moisture-dependent resilient modulus of cohesive soils using soil suction concept. *J Transp Eng* 134(1):34–40 (2008)
6. Oloo S (1998) The application of unsaturated soil mechanics theory to the design of pavements. In: Proceedings of 1st international conference on the bearing capacity of roads and airfields, BCRA'98, vol 3, pp 1419–1428
7. Wolfe W, Butalia T (2004) Continued monitoring of SHRP pavement instrumentation including soil suction and relationship with resilient modulus. (No. FHWA/OH-2004/007)
8. Khoury NN, Zaman MM (2004) Correlation between resilient modulus, moisture variation, and soil suction for subgrade soils. *Transp Res Rec* 1874(1):99–107
9. Gu F, Sahin H, Luo X, Luo R, Lytton RL (2014) Estimation of resilient modulus of unbound aggregates using performance-related base course properties. *J Mater Civ Eng* 27(6):04014188
10. Luo X, Gu F, Zhang Y, Lytton RL, Zollinger D (2017) Mechanistic-empirical models for better consideration of subgrade and unbound layers influence on pavement performance. *Transp Geotech* 13:52–68
11. Zhang J, Peng J, Zheng J, Dai L, Yao Y (2019) Prediction of resilient modulus of compacted cohesive soils in South China. *Int J Geomech* 19(7):04019068
12. Aitchison G (1965) Moisture equilibria and moisture changes in soils beneath covered areas. A symposium in print. Butterworths, Sydney, Australia
13. Basma AA, Al-Suleiman TI (1991) Climatic considerations in new AASHTO flexible pavement design. *J Transp Eng* 117(2):210–223
14. Saha S, Hariharan N, Gu F, Luo X, Little DN, Lytton RL (2019) Development of a mechanistic-empirical model to predict equilibrium suction for subgrade soil. *J Hydrol* 575:221–233
15. Russam K, Coleman JD (1961) The effect of climatic factors on subgrade moisture conditions. *Geotechnique* 11(1):22–28
16. Illston BG, Basara JB, Fiebrich CA, Crawford KC, Hunt E, Fisher DK, Elliott R, Humes K (2008) Mesoscale monitoring of soil moisture across a statewide network. *J Atmos Oceanic Tech* 25(2):167–182
17. Bulut R, Leong EC (2008) Indirect measurement of suction. In *Laboratory and field testing of unsaturated soils*. Springer, Dordrecht, pp 21–32
18. Chan I, Mostyn G (2008) Climate factors for AS2870 for the metropolitan Sydney area. *Aust. Geomech.* 43(1):17–28
19. Fox E (2002) Development of a map of Thornthwaite Moisture Index isopleths for Queensland. *Aust. Geomech. J. News Aust. Geomech. Soc.* 37(3):51
20. Mitchell PW (2012) Footing design for tree effects considering climate change. In: Proceedings 2012 ANZ geomechanics conference, pp 290–295
21. Mitchell PW (2013) Climate change effects on expansive soil movements. In: Proceedings of the 18th ICSMGE, pp 1159–1162
22. Jewell SA, Mitchell PW (2009) The Thornthwaite moisture index and seasonal soil movement in Adelaide. *Aust. Geomech.* 44(1):59
23. McKeen RG, Johnson LD (1990) Climate-controlled soil design parameters for mat foundations. *J Geotech Eng* 116(7):1073–1094

24. Fityus S, Walsh P, Kleeman P (1998) The influence of climate as expressed by the Thornthwaite index on the design depth of moisture change of clay soils in the Hunter Valley. In: Conference on geotechnical engineering and engineering geology in the Hunter Valley. Conference Publications Springwood, Australia, pp 251–265
25. Yue E, Bulut R (2014) Evaluation of climatic factors for the classification of Oklahoma pavement regions. In: Geo-Congress 2014: geo-characterization and modeling for sustainability, pp 4037–4046
26. Li J, Sun X (2015) Evaluation of changes of Thornthwaite Moisture Index in Victoria. *Aust. Geomech. J.* 50(2/3):39–49
27. Karunarithne A, Gad E, Disfani M, Sivanerupan S, Wilson J (2016) Review of calculation procedures of Thornthwaite Moisture Index and its impact on footing design. *Aust. Geomech.* 51(1):85–95
28. Olaiz AH, Singhar SH, Vann JD, Houston SL (2018) Comparison and applications of the Thornthwaite moisture index using GIS. In: PanAm unsaturated soils 2017, pp 280–289
29. Witzczak MW, Zapata CE, Houston WN (2006) Models incorporated into the current enhanced integrated climatic model: NCHRP 9-23 project findings and additional changes after version 0.7. In: Final report, project NCHRP
30. James G, Witten D, Hastie T, Tibshirani R (2017) An introduction to statistical learning. Springer, New York
31. Mitchell PW (1980) The structural analysis of footings on expansive soil. In: Expansive soils, ASCE, pp 438–447
32. Javid AH, Bulut R (2019) Evaluating equilibrium matric suctions under pavement system based on Thornthwaite Moisture Index (TMI). In: Airfield and highway pavements 2019: testing and characterization of pavement materials. American Society of Civil Engineers, Reston, VA, pp 511–521
33. Aubeny C, Lytton R, Tang D (2003) Simplified analysis of unsteady moisture flow through unsaturated soil. *Transp Res Rec* 1821(1):75–82
34. Scott BL, Ochsner TE, Illston BG, Fiebrich CA, Basara JB, Sutherland AJ (2013) New soil property database improves Oklahoma Mesonet soil moisture estimates. *J Atmos Oceanic Tech* 30(11):2585–2595

# Use of Steel Slags in Earthworks—Hydraulic Properties of Steel Slags and Granulometrically Modified Steel Slags Under Saturated and Unsaturated Conditions



Elissavet Barka  and Emanuel Birle

**Abstract** About 6 million tons of steel slag are generated in Germany every year during the production of steel. About 14% of them is landfilled due to some technically or environmentally relevant properties. Nevertheless, increasing costs for the deposition on landfills make their use in earthworks for transportation infrastructure more and more attractive. The utilization of steel slags in earthworks seems to be promising due to their advantageous mechanical properties but requires the protection of soil and groundwater against possible exposure to leached substances. Several construction methods in earthworks are described in a recommendation (M TS E) of the German Road and Transportation Research Association, where soils/materials with environmentally relevant substances can be used with additional capping systems, and without additional liners if they are of low permeability, respectively. Thus, experimental investigations were carried out to study how the permeability of steel slags could be reduced by the addition of clay powders. In order to analyze the seepage flow through earthworks built of such materials, their saturated and unsaturated hydraulic properties have to be determined. These include the coefficient of permeability  $k_f$ , the unsaturated hydraulic conductivity function and the soil–water retention curve, which have been determined carrying out various tests, among others one-dimensional evaporation tests. Based on the experimental results, numerical simulations with the finite element software Seep/W were performed to study the percolation of an embankment section built in a lysimeter. The results showed that the percolation of mixtures of steel slag and clay is low.

**Keywords** Steel slag · Earthworks · Hydraulic properties · Evaporation experiment · Soil water flow · Modeling

---

E. Barka (✉) · E. Birle  
Technical University of Munich, Franz-Langinger-Str. 10, 81245 Munich, Germany  
e-mail: [e.barka@tum.de](mailto:e.barka@tum.de)

E. Birle  
e-mail: [e.birle@tum.de](mailto:e.birle@tum.de)

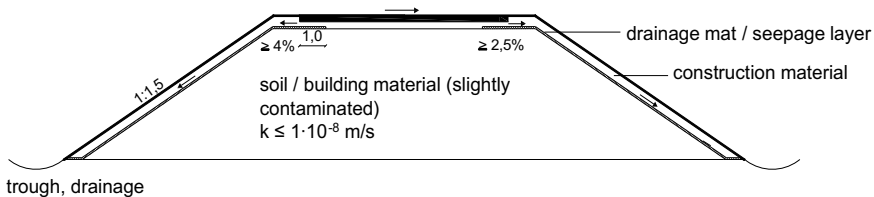
# 1 Introduction

About 6 million tons of steel slag are generated in Germany every year during the conversion of scrap metal or crude iron into steel and processed by crushing and classification into aggregates or building material mixtures, which are mainly used in road and landfill construction [1]. However, currently about 14% of these slags has to be landfilled due to some technically or environmentally relevant properties [1].

A recommendation (M T S E: Merkblatt für technische Sicherungsmaßnahmen im Erdbau, English: recommendations for technical safety measures in earthworks) of the German Road and Transportation Research Association presents several construction methods in earthworks (e.g., for embankments or noise protection barriers) in order to be able to supply mixtures consisting of building materials with environmentally relevant substances for resource-efficient use in earthworks so that their disposal in landfills can be avoided [2, 3]. The aim of the technical safety measures is to minimize the amount of the seepage water through the corresponding building material mixtures. For this purpose, the soils or building materials must be granulometrically modified in such a way that they can be hardly percolated, or they must be protected against seepage by additional capping systems. According to the valid country-specific regulations, it would be possible to use a large amount of the steel slags that are deposited so far as earthwork material in combination with technical safety measures. Accordingly, there is a strong potential to increase the use rate of steel slags and reduce the proportion that currently has to be landfilled. For a use according to the M T S E construction method E (see Fig. 1), the coefficient of water permeability of the steel slags should fulfill the requirement  $k_f \leq 1 \times 10^{-8}$  m/s.

Thus, several steel slags have been investigated both individually, and in varying mixture combinations with clay powders regarding their soil mechanical and hydraulic properties, as well as their leachability. The tests show that steel slags can achieve low permeability and leachability through the addition of fine-grained aggregates so as can also be used without additional capping systems in accordance with the M T S E recommendation [4–8].

Based on the research findings from [9] to achieve low coefficients of water permeability, the fines content of mixed-grained soils should be between 22 and 31 wt%, the content less than 2 mm grain size between 52 and 61 wt% and the content



**Fig. 1** Construction method E according to [3]—embankment made of low permeability soil or building material with environmental relevant substances (variant 2), taken from [3]



less than 0.002 mm grain size between 9 and 12 wt%. Depending on the grain-size distribution curve of the coarse-grained raw materials, it can be necessary to add so-called filling materials to fulfill the requirements on the fines and sand content. For mixing technical reasons, silts and clays of low plasticity (e.g. sandy silts or clays) are chosen for this purpose. In addition to the filler, usually highly swellable bentonites (calcium bentonite, sodium-activated calcium bentonite) are added, as this leads to an additional decrease of effective pore content and water permeability. Depending on the type (soil mechanical and clay mineralogical properties) and the amount of the fine-grained soil to be added it was investigated, which influence four different fine-grained additives have on the compaction and on the hydraulic properties of the mixtures.

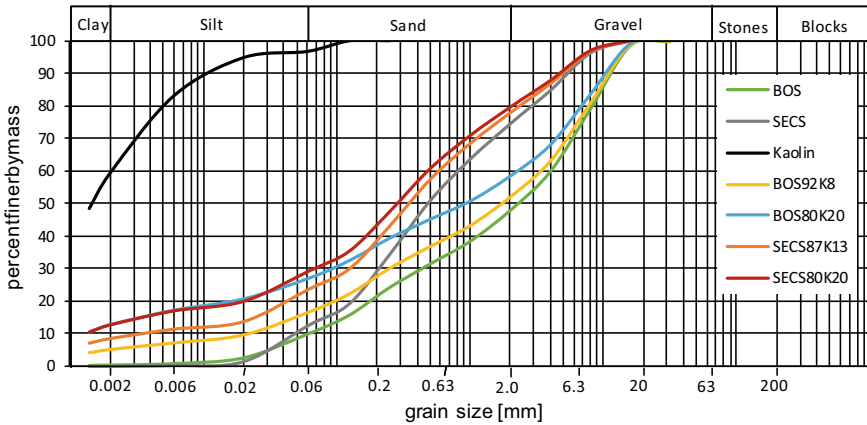
Because earthwork constructions are built above the water table, the investigation of the hydraulic properties under unsaturated conditions seems to be reasonable. The aim of this study was the determination of the hydraulic properties of mixtures consisting of steel slags with clays under saturated and unsaturated conditions, which have been used as input parameters for numerical simulations for the prediction of the water balance of earthwork constructions. The numerical simulations have been performed for an initial saturation at first 40 days applying a defined daily precipitation. After this, a precipitation regime with single precipitations over a period of 47 days was simulated. The precipitation has been determined as a mean value of many weather stations after collection of data of the German Meteorological Service (DWD).

## 2 Materials

Two steel slags in the form of a Linz–Donawitz slag (BOS 0/16 mm) and a secondary metallurgical slag (SECS 0/8 mm) were selected. A kaolin (K) was used as fine-grained additive in accordance to the explanations given in Sect. 1. The grain-size distributions of the basic materials and their mixtures with kaolin are shown in Fig. 2.

The mixing ratios are given in Table 1 as percentage composition of slag and kaolin. The soil mechanical parameters (Proctor density  $\rho_{Pr}$ , optimum water content  $w_{Pr}$  according to DIN 18127 as well as coefficient of water permeability  $k_f$  at the corresponding Proctor optimum according to DIN 18130–1) are also listed in Table 1.

The permeability tests showed that a clay addition of 13–20 wt% resulted in coefficients of water permeability of the granulometrically modified steel slags—compacted with standard Proctor energy—to  $k_f < 1 \times 10^{-8}$  m/s. For several modified steel slags, a further reduction of the permeability to  $k_f < 1 \times 10^{-9}$  m/s could be achieved by an increase of compaction energy (modified Proctor energy). The use of sodium-activated calcium bentonite as an additive, despite its high swelling capacity, did not lead to a significant decrease in the water permeability compared to kaolin or calcium bentonite. This could be attributed to a decrease of the swelling capacity due to the electrolyte concentration of the pore solution of the steel slags. With regard to



**Fig. 2** Grain-size distributions of the investigated basic materials (steel slags) and the mixtures

**Table 1** Soil mechanical properties of the investigated mixtures of steel slags and kaolin

Name	Proctor energy	$\rho_{Pr}$ (g/cm <sup>3</sup> )	$w_{Pr}$ (%)	$k_f$ (m/s)
BOS	Standard	2.25	10.8	$6.7 \times 10^{-7}$
BOS <sub>92</sub> K <sub>8</sub>	Standard	2.30	12.0	$1.9 \times 10^{-8}$
BOS <sub>80</sub> K <sub>20</sub>	Standard	2.14	13.4	$3.7 \times 10^{-9}$
SECS	Standard	2.82	11.1	$2.8 \times 10^{-6}$
SECS <sub>87</sub> K <sub>13</sub>	Modified	2.05	11.4	$2.6 \times 10^{-9}$
SECS <sub>80</sub> K <sub>20</sub>	Modified	1.97	12.6	$1.3 \times 10^{-9}$

environmental and mechanical parameters, the majority of the mixture combinations could be classified as suitable for the M T S E construction methods E [4].

### 3 Unsaturated Hydraulic Properties

#### 3.1 Methods

**Evaporation test.** In the evaporation test, the weight of a soil sample and pressure heads at two height levels are recorded at specified time intervals. The evaluation of the measurements relies on linearization assumptions with respect to time, space and the water content–pressure head relationship according to [10–15]. With this method, a simultaneous determination of the soil water retention curve (SWRC) and the unsaturated hydraulic conductivity is possible. A soil sample is compacted in a Proctor cylinder (height  $H = 12.5$  cm, diameter 15 cm). The compaction plate is removed, and the sample is placed into a water bath in order to become saturated.

After saturation, some water is released by free drainage, which is unavoidable. The sample is placed again on the compaction plate and sealed at the bottom. The upper surface remains open to evaporation. Two tensiometers are installed into the soil column at depths of  $0.25H$  and  $0.75H$  from the surface, respectively [4]. The experimental setup is then placed on a balance, and the evaporation process begins. The experiment is terminated as soon as the upper tensiometer reaches the boiling point of water (100 kPa). The readings of the upper and lower tensiometer are used for the evaluation.

For the determination of the SWRC, the mean volumetric water content  $\theta_i$  for each time step  $t_i$  is derived from the column weight readings taking into account the linearization assumptions. The mean matric suction  $\psi_i$  is also calculated for each time interval as arithmetic mean of the two measured values at the depths of  $0.25H$  and  $0.75H$ .

For the determination of the unsaturated hydraulic conductivity function  $k(\psi)$ , the water flux  $Q$  is calculated from the water volume difference  $\Delta V$  (evaporated soil water for the  $0.5H$ ) per surface area  $A$  and the time interval  $\Delta t = t_i - t_{i-1}$  between two readings. The mean hydraulic gradient  $i_m$  in the time interval is given by Eq. 1, where  $\Delta z$  is the vertical distance of the tensiometers.

$$i_m = \frac{1}{2} \left[ \frac{h_{ti-1,0.25H} - h_{ti-1,0.75H}}{\Delta z} + \frac{h_{ti,0.25H} - h_{ti,0.75H}}{\Delta z} \right] \quad (1)$$

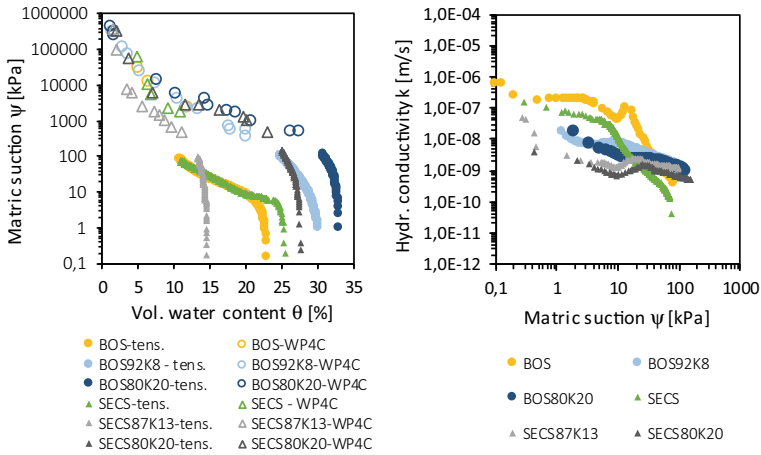
The hydraulic conductivity  $k(\psi)$  is determined using *Darcy–Buckingham law* (Eq. 2).

$$k(\psi) = \frac{\Delta V}{A \Delta t i_m} \quad (2)$$

The hydraulic conductivity is assigned to the mean matric suction  $\psi_m$ , which is calculated as an arithmetic average over the two tensiometers and the considered time interval (Eq. 3).

$$\psi_m = \frac{1}{4} [\psi_{i-1,0.25H} + \psi_{i-1,0.75H} + \psi_{i,0.25H} + \psi_{i,0.75H}] \quad (3)$$

**Chilled-mirror dew point technique.** Measurements of the total suction in the range of approx. 500 kPa to 60 MPa are derived by the chilled-mirror hygrometer WP4C Dewpoint PotentiaMeter supplied by METER Group [16] according to the dew point method [17]. For this purpose, the samples were inserted into the test cells under specified compaction conditions and then saturated. After saturation, the samples were stored closed for at least two weeks for homogenization and afterward exposed to evaporation at the top of the sample step by step. As soon as the desired water content was reached, the samples were sealed and stored for 24 h for homogenization.



**Fig. 3** SWRC derived from the evaporation tests and the WP4C measurements and unsaturated hydraulic conductivity functions of the materials derived from the evaporation tests

### 3.2 Results

The soil water retention curves (drying paths) of the investigated basic materials and the mixtures of them with kaolin compacted at the corresponding Proctor optimum are shown in Fig. 3. The results are derived at lower suctions up to approx. 100 kPa from the evaporation tests and at higher suction ranges from the WP4C device. Figure 3 presents graphically in logarithmic scale the unsaturated hydraulic conductivity functions  $k(\psi)$  for the above-mentioned samples determined from the evaporation tests.

The unsaturated hydraulic conductivity function of the raw steel slags and the mixtures, except from BOS<sub>80</sub>K<sub>20</sub>, shows between approx. 10 and 30 kPa an abrupt change of its development. While the unsaturated hydraulic conductivity should decrease as the suction increases, in those cases a sudden increase occurs for a narrow range of suction. This is probably due to the linearization assumptions regarding the water content and the matric suction over time and space that have been made for the evaluation underestimating these two values with increasing depth and time.

## 4 Numerical Simulations

### 4.1 Calculation Method

The water balance simulations were carried out with the finite element software SEEP/W supplied by GeoSlope International Ltd [18]. For the water transport, the

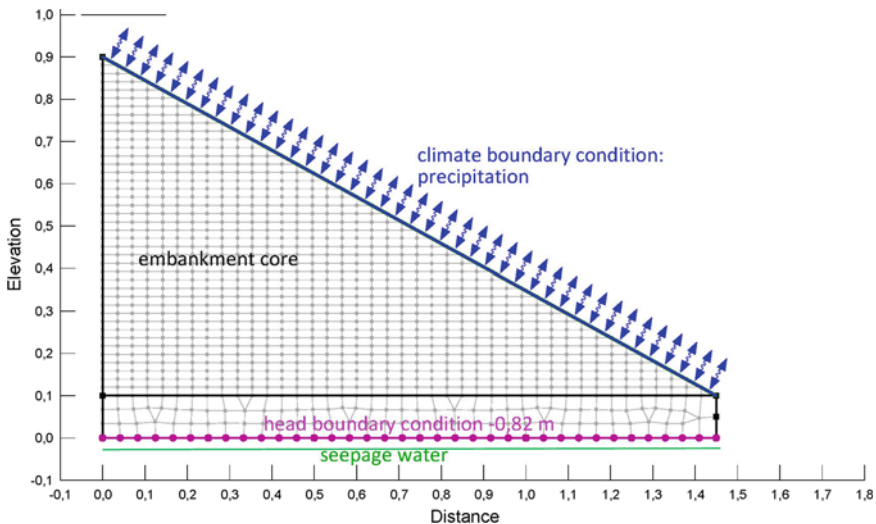
program uses the Richards equation [19]. The water transport in the vapor phase is strongly temperature-dependent, and the equation for the differential heat transfer should also be considered. To solve the equation systems, the relationship between the vapor pressure, the water pressure and the temperature has to be described. This is achieved in SEEP/W via the Kelvin equation modified by [20]. The computations of the evaporation are performed in the program with the relationship of [21] modified by [22].

### 4.2 Modeling

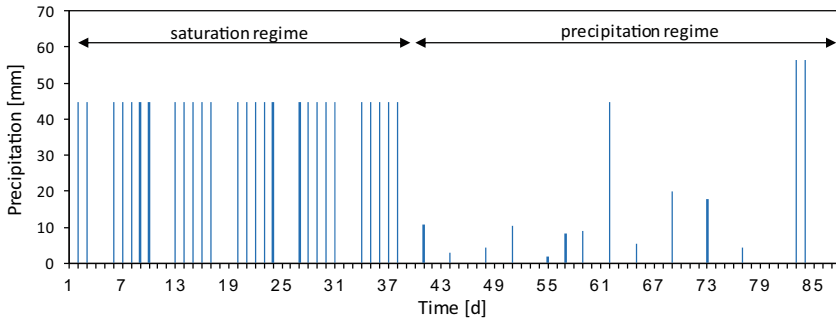
**Model geometry and boundary conditions.** The model geometry represents the actual geometry of the lysimeter that will be used for further experimental investigations of the seepage flow. The lysimeter geometry as well as the boundary conditions and the sections for the seepage water evaluation are shown in Fig. 4.

In the experiments planned, similar to the lysimeter tests done by [23, 24] at the base of the lysimeter, a suction of 8.2 kPa will be applied by suction plates for the collection of the seepage water. To represent the negative pore water pressure of 8.2 kPa applied by the suction plates at the lysimeter base, in the numerical model, a head boundary condition was applied at the bottom of the model. The boundaries at the right and left side are impermeable.

As an initial state of the materials, the initial pore water pressure of the materials was defined according to their initial water content after compaction (using



**Fig. 4** Model geometry of lysimeter with boundary conditions and marked sections of seepage water evaluation



**Fig. 5** Distribution of daily precipitation

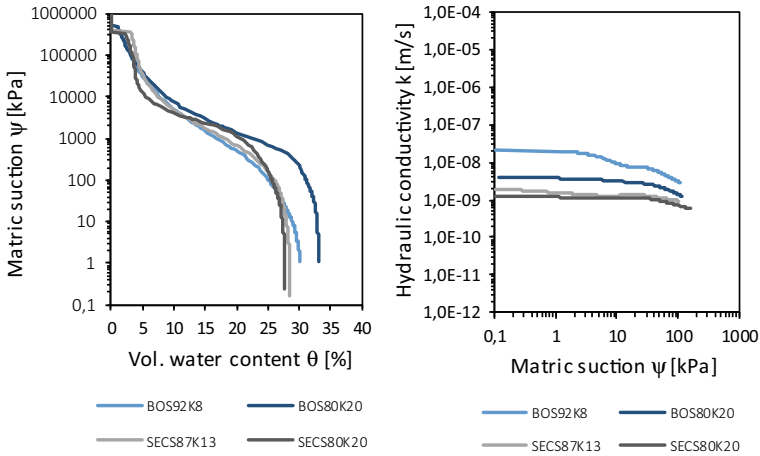
the SWRC). The simulation period was chosen according to the planned lysimeter tests. For an initial saturation at first 40 days, a daily precipitation was defined. After this, a precipitation regime with single precipitations over a period of 47 days was simulated (Fig. 5). The precipitation, which was applied in the simulations, has been determined as a mean value of many weather stations after collection of data of the German Meteorological Service (DWD). The amount of the precipitation has been reduced in some cases up to 40% because of the absence of topsoil in the model, in order to achieve real conditions. Taking into account the amount of precipitation, the rain regime was so chosen that the rainy days meet the 31% of the total period examined.

**Material properties.** The unsaturated hydraulic properties derived from the evaporation tests and the WP4C as mentioned in Sect. 2 have been used as input data for the simulations. By fitting of the data using a trend line, some physically wrong data (e. g. the increase of water permeability with increasing matric suction, which was described in Sect. 2.3) were corrected. Hence, the SWRCs and the unsaturated hydraulic conductivity functions, that have been used in the numerical simulations for the four mixtures, are shown in Fig. 6.

### 4.3 Results and Discussion

The cumulative water balance (precipitation, evaporation, seepage water and surface runoff) of the lysimeters with the four mixtures is illustrated in Fig. 7.

The results of the simulations show that the seepage water for the mixtures BOS<sub>92</sub>K<sub>8</sub> and BOS<sub>80</sub>K<sub>20</sub> is about 5 and 1% with regard to the total precipitation, and the runoff is approx. 93 and 94%, respectively. For the mixtures SECS<sub>87</sub>K<sub>13</sub> and SECS<sub>80</sub>K<sub>20</sub> the seepage water tends to be zero, and the runoff is about 95 and 96% of the total precipitation. This is due to the low coefficients of water permeability and the unsaturated hydraulic conductivities of the two mixtures with SECS and kaolin determined under compaction with modified Proctor energy. With regard to



**Fig. 6** SWRC and unsaturated hydraulic conductivity function of the investigated mixtures used in the simulations

the results of the numerical simulations, the investigated mixtures could be classified as suitable for the M T S E construction method E, since the seepage water determined is negligible.

## 5 Summary and Conclusions

On basis of experimental investigations, it was shown that steel slags can be modified by the addition of fine-grained additives in such a way that they can be used according to the M T S E recommendations without an additional sealing layer (construction method E). The requirement on the coefficient of permeability of  $k_f \leq 1 \times 10^{-8}$  m/s according to M T S E could be met for the steel slags with an addition of 13–20 wt% fine-grained material.

Since earthwork constructions are built above the water table, the investigation of the hydraulic properties under unsaturated conditions is necessary. For this purpose, the unsaturated hydraulic properties of steel slags and mixtures of them with clays have been determined by means of evaporation tests and a chilled-mirror hygrometer. The unsaturated hydraulic conductivity function for most of the investigated materials shows between approx. 10 and 30 kPa an abrupt change of its development. While the unsaturated hydraulic conductivity should decrease as the suction increases, and in those cases, a sudden increase occurs for a narrow range of suction. This is probably due to the linearization assumptions regarding the water content and the matric suction over time and space, which were applied for the evaluation of the evaporation tests.

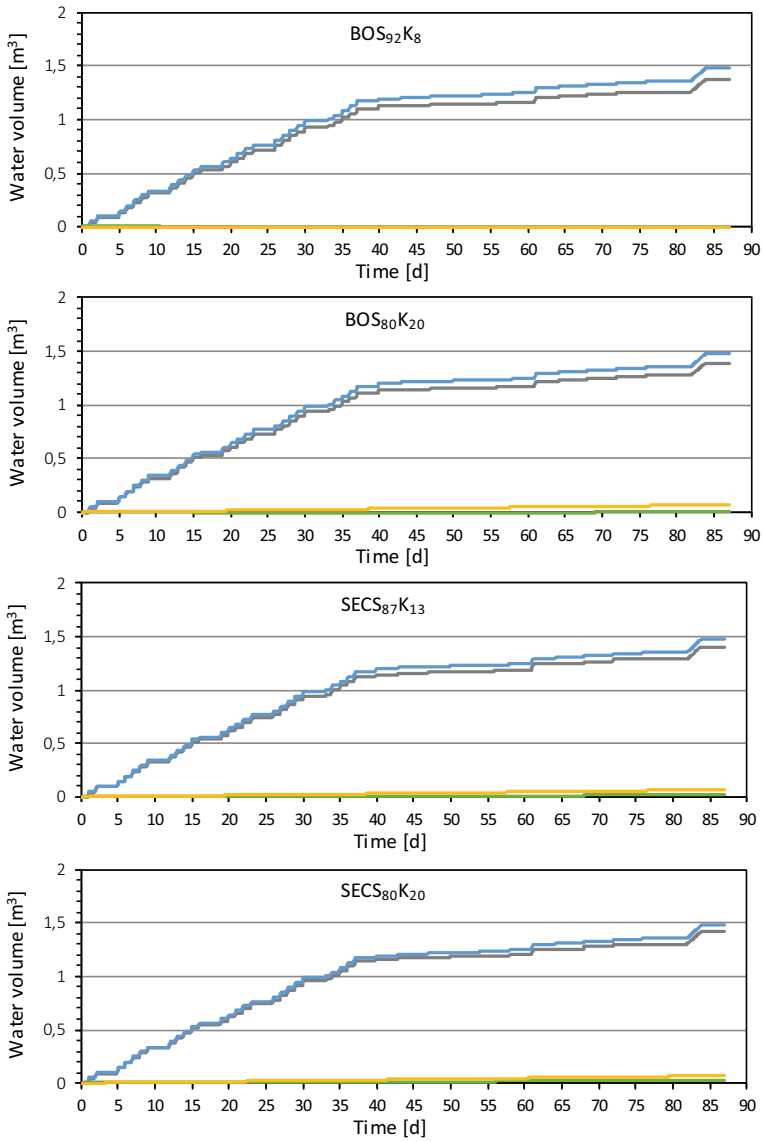


Fig. 7 Water balance of the lysimeters

The determined unsaturated hydraulic characteristics of the mixtures were used as input parameters for numerical simulations for the prediction of the water balance of a lysimeter. In order to avoid unrealistic values and complications at the calculations, the unsaturated hydraulic characteristics have been corrected using a fitting



line. The simulation period covers 40 days of a saturation and 47 days of a precipitation program according to real meteorological data. The results of the numerical simulations show that the seepage water of the investigated materials is about 0–5%. The materials with very low coefficient of water permeability and in further unsaturated hydraulic conductivity tend to have a low leachate under real precipitation conditions. With regard to the saturated and unsaturated hydraulic properties, the investigated mixtures could be classified as suitable for the M T S E construction method E.

**Acknowledgements** Parts of the contribution are based on results obtained within the framework of the IGF projects 18746 N and 20539 N of the research associations VDEh-Gesellschaft zur Förderung der Eisenforschung mbH—VDEh-GmbH. That projects were funded within the framework of the Program for the Promotion of Industrial Community Research (IGF) by the Federal Ministry of Economics and Energy on basis of a resolution of the German Bundestag.

## References

1. Merkel T (2019) Daten zur Erzeugung und Nutzung von Eisenhüttenschlacken 2018. Report Wissenschaftsprojekte des FEhS-Instituts Nr. 26(1):25–26
2. Forschungsgesellschaft für Straßen- und Verkehrswesen (2009) Merkblatt über Bauweisen für Technische Sicherungsmaßnahmen beim Einsatz von Böden und Baustoffen mit umweltrelevanten Inhaltsstoffen im Erdbau-M T S E. Ausgabe 2009
3. Forschungsgesellschaft für Straßen- und Verkehrswesen (2017) Merkblatt über Bauweisen für Technische Sicherungsmaßnahmen beim Einsatz von Böden und Baustoffen mit umweltrelevanten Inhaltsstoffen im Erdbau-M T S E. Ausgabe 2017
4. Bialucha R, Demond D, Birle E, Barka E (2018) Nachhaltige Baustoffverwendung im Erdbau—Einsatz von Eisenhüttenschlacken bei Erdbauwerken mit technischen Sicherungsmaßnahmen. AiF-Forschungsprojekt 18746 N-Abschlussbericht
5. Demond D, Merkel T, Barka E, Birle E (2018) Nachhaltige Verwendung von Stahlwerksschlacken in der M T S E-Bauweise. Report Wissenschaftsprojekte des FEhS-Instituts Nr. 25(1):18–24
6. Barka E, Birle E, Demond D (2019) Geotechnische Untersuchungen an modifizierten Stahlwerksschlacken. Geotechnik 42(4)
7. Barka E, Birle E, Demond D (2019) Use of steel slag in earthworks. In: 10th European slag conference. Thessaloniki, pp 227–237
8. Barka E, Birle E, Demond D (2019) Verwendung von gering durchlässigen Stahlwerksschlacken im Erdbau. In: Fachsektionstage Geotechnik-8. Symposium Umweltgeotechnik, German Geotechnical Society. Würzburg
9. Heyer D, Bienen B, Maurer I (2003) Optimierung der Zusammensetzung gemischtkörniger Abdichtungsmaterialien. BayFORREST-Forschungsvorhaben F157 (Abschlussbericht), Zentrum Geotechnik Technische Universität München
10. Wind GP (1968) Capillary conductivity data estimated by a simple method. In: Proceedings of UNESCO/IASH, symposium water in the unsaturated zone. Wageningen, The Netherlands, pp 181–191
11. Becher H (1971) Ein Verfahren zur Messung der ungesättigten Wasserleitfähigkeit. Aus dem Institut für Bodenkunde der Technischen Universität Hannover, Zeitschrift für Pflanzenernährung und Bodenkunde, Band 128(1)
12. Schindler U (1980) Ein Schnellverfahren zur Messung der Wasserleitfähigkeit im teilgesättigten Boden an Stechzylinderproben. Arch Acker- und Pflanzenbau u Bodenk 24:1–7

13. Peters A, Durner W (2006) Improved estimation of soil water retention characteristics from hydrostatic column experiments. *Water Resour Res* 42:W11401
14. Peters A, Durner W (2008) Simplified evaporation method for determining soil hydraulic properties. *J Hydrol* 356:147–162
15. Peters A, Durner W (2008) A simple model for describing hydraulic conductivity in unsaturated porous media accounting for film and capillary flow. *Water Resour Res* 44:W11417
16. METER Group, Inc (2017) WP4C–Dew point Potential Meter-operator’s manual
17. Lu N, Likos W (2004) *Unsaturated Soil Mechanics*. John Wiley & Sons, INC., Hoboken New Jersey
18. GEO-SLOPE (2012) *Vadose zone modeling with SEEP/W*. Geo-Slope International Ltd., Calgary, Alberta, Canada
19. Richards LA (1931) Capillary conduction of liquids through porous medium. *J Phys* 1:318–333, cited in Fredlund and Rahardjo (1993)
20. Edlefsen NE, Anderson ABC (1943) Thermodynamics of soil moisture. *Hilgardia* 15:31–298, cited in Fredlund und Rahardjo (1993)
21. Wilson GW (1990) Soil evaporative fluxes for geotechnical engineering problems. Dissertation, University of Saskatchewan, Saskatoon, Canada, cited in KRAHN (2004)
22. Penman HL (1956) Estimating evaporation. *Trans Am Geophys Union*, cited in Schöniger and Dietrich (2009)
23. Kellermann-Kinner C, Bürger M, Marks T (2016) Effizienz technischer Sicherungsmaßnahmen im Erdbau–Lysimeteruntersuchungen unter Laborbedingungen. *Berichte der BAST. Bergisch Gladbach*
24. Melsbach M, Birle E (2019) Numerische Modellierung der Lysimeteruntersuchungen der BAST. Final report of R&D 05.0185/2014/CRB. Chair and Testing Institute of Soil Mechanics and Foundation Engineering, Rock Mechanics and Tunneling. Technical University Munich

# Long-Term Performance of Ballastless High-Speed Railway Track Under the Conditions of Ground Water Level Variations



Hongming Liu, Xuecheng Bian, Lili Yan, and Yunmin Chen

**Abstract** High-speed railways will be exposed to high water level caused by extreme water conditions, such as floods and heavy rainfall, which may influence the soil structure of roadbed, leading to excess accumulative deformation under dynamic train loads. The development of uneven deformation of railway track will then exacerbate the wheel–track interaction, which in turn accelerates the degradation of high-speed railway roadbed and jeopardizes the safety of train running. To verify the long-term performance of high-speed railway road under various water level conditions, a full-scale physical model of a ballastless railway and a sequential loading system were developed which can simulate train moving load at speeds up to 360 km/h. Water level in the physical model can be raised and lowered with a water level control system. Train moving loading tests were carried out at three typical water levels: at the subsoil bottom, at the subsoil surface and at the subgrade surface. In each water level condition, three different train velocities: 108, 216 and 360 km/h were simulated for a certain number of cyclic loads. Some results of dynamic pore water pressure are presented in this paper.

**Keywords** Railway settlement · Ground water · Traffic load

## 1 Introduction

Ballastless track bed is now the main form that is used in the newly built high-speed railway lines in China. Compared to traditional ballasted railway track, ballastless railway track (slab track) has higher durability, lower constructing cost and better integrality. However, it is more vulnerable to the deformation of embankment below track slab, which requires more strict construction and maintenance standards. Under

---

H. Liu · X. Bian (✉) · L. Yan · Y. Chen

Department of Civil Engineering, Key Laboratory of Soft Soils and Geoenvironmental Engineering, MOE, Zhejiang University, Hangzhou 310058, China  
e-mail: [bianxc@zju.edu.cn](mailto:bianxc@zju.edu.cn)

H. Liu

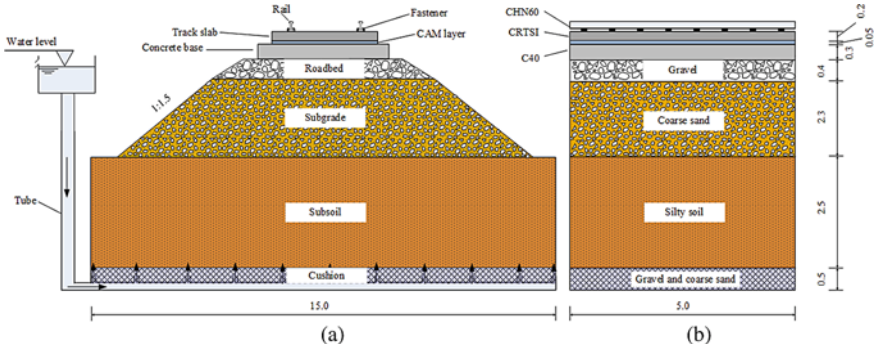
e-mail: [liuhongming@zju.edu.cn](mailto:liuhongming@zju.edu.cn)

extreme weather conditions, such as floods and heavy rainfall, water in the roadbed cannot be drained in a short time, and as a result, decreasing the strength and stiffness of soils in the roadbed and accelerating embankment settlement. Moreover, continuous moving train loads may lead to high excess pore water pressure, causing mud pumping from the joint of track slabs. Consequently, uneven deformation of railway track may develop continuously or even cause cracks in track slab. In China, for example, settlement up to 64.2 cm occurred in the newly built Shi-Tai high-speed railway after several days of heavy rain. Also, in Germany, uneven settlement in Hanover–Berlin high-speed railway line caused the increase of vibration velocity on track slab up to 4 times, making the concrete structure crack [1]. Yang et al. [2] conducted a two-dimensional dynamic finite-element analysis on railway track and pointed out that stress was more likely to approach the failure criterion of soil under higher train speed, increasing the likelihood of failure. Duong et al. [3] conducted a series of physical model tests on a ballast layer overlying a subsoil layer under different conditions, including water content, loading and subsoil dry unit mass, and proposed that the mud pumping was related to the migration of fine particles, and the water content of the subsoil was the most important factor for the migration.

To date, the investigations on the deformation of high-speed railway are mainly in the range of soil unit cell tests, making the complexity of environment condition, soil layers distribution and moving train loads elusive, which cannot gain comprehensive understanding of real deforming patterns of high-speed railway embankment. A full-scale physical model of a ballastless railway was constructed that can simulate train moving load at speed up to 360 km/h in different water level conditions. This paper firstly introduces the full-scale high-speed railway model and then introduces the testing progress. Some results of dynamic pore water pressure are presented in this paper. Testing results of permanent deformation and other related results will be presented in a future publication.

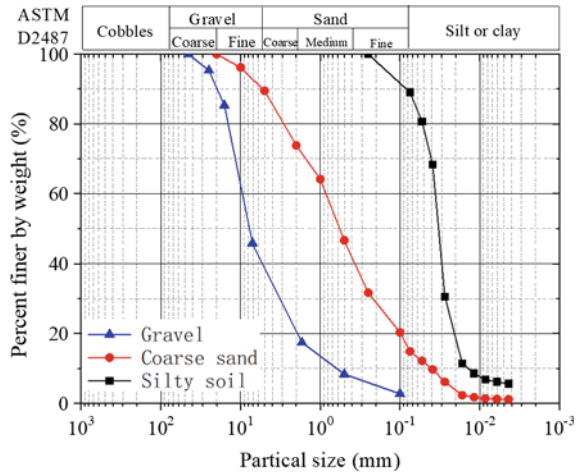
## 2 Full-Scale Model and Testing Progress

In accordance with the Chinese high-speed railway design code, a portion of a full-scale ballastless high-speed railway slab track was built in a steel box with 5 m width, 15 m length and 4 m height. The model consisted of two parts: track structure and embankment. For the track structure, 16 separated CHN60-type rails were fastened on 16 WJ-7-type fasteners, below which is a CRTS I-type track slab with a size of  $4.96 \times 2.4 \times 0.19$  m, a cement asphalt mortar layer and a concrete base with a size of  $5 \times 3 \times 0.3$  m. The embankment is composed of a layer of 0.4-m-thick gravel to support the concrete base, a layer of 2.3-m-thick granular soil as the subgrade and a layer of 2.5-m silty soil as the subsoil. Figure 1 shows the schematic view of this model. And the grain-size distributions of these three geomaterials are plotted in Fig. 2. Table 1 shows the physical parameters of subgrade and subsoil materials. The compaction coefficients and the stiffness parameters measured after compaction of the embankment are listed in Table 2.



**Fig. 1** Overview of physical model of ballastless slab track railway: **a** cross section and **b** vertical section

**Fig. 2** Grading curves of fillings



**Table 1** Physical properties of geomaterials used in the subgrade and the subsoil

Material	Specific gravity	Maximum dry density (g/cm <sup>3</sup> )	Minimum dry density (g/cm <sup>3</sup> )	Liquid limit (%)	Plastic limit (%)	Plastic index
Granular soil	2.66	2.11	1.62	–	–	–
Silty soil	2.67	1.62	–	35	24	11

The loading system was composed of a reaction frame, eight servo-hydraulic actuators and eight spreader beams. Loads were transmitted from the eight actuators through rail segments to the track slab. Simulated train loading was achieved by applying pre-programmed loads obtained from the train-slab track-subgrade coupled

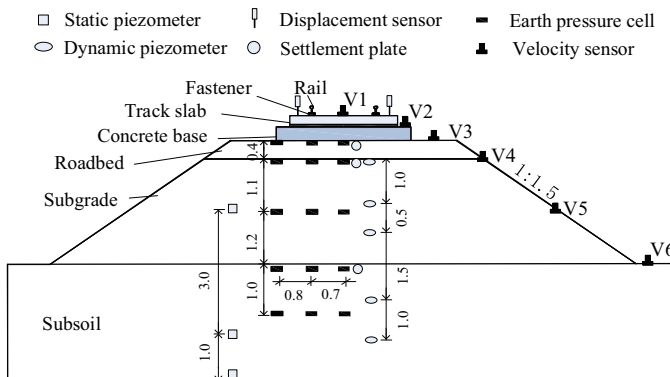
**Table 2** Compaction of the roadbed fillings

Fillings	Compactness quality			
	$k_{30}$ (MPa/m)	$E_{v2}$ (MPa)	$E_{v2}/E_{v1}$	K
Gradation gravel	273–308 ( $\geq 190$ )	269–361 ( $\geq 120$ )	1.78–2.25 ( $\leq 2.3$ )	0.97–0.98 ( $\geq 0.97$ )
Granular soil	362–402 ( $\geq 130$ )	274–301 ( $\geq 80$ )	1.50–1.91 ( $\leq 2.5$ )	0.95–0.97 ( $\geq 0.95$ )

analysis model proposed by Bian et al. [4]. With this loading system, the model can simulate the moving progress with an axle load of 170 kN and the train speed up to 360 km/h, which is comparable to a typical high-speed train running along rails. Figure 3 shows the layout of sensors in cross-sectional vision of model. During the tests, track slab displacement, earth pressure, settlement and pore water pressure in each layer of embankment were measured.

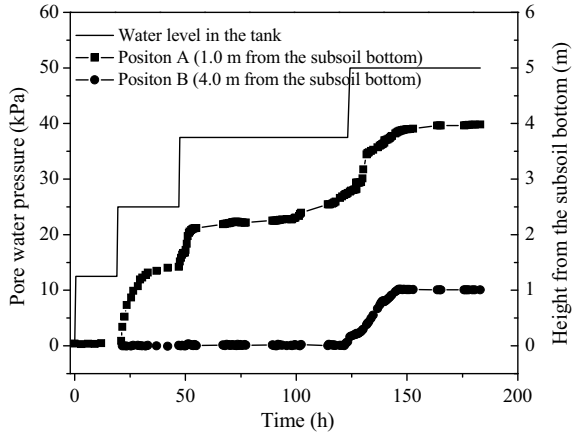
Water level control system consists of a free-lift water tank, main water supply tube and underlaid pipe network with leaking holes. The pipe network is buried in a layer of 20-cm-thick granular and coarse silt to guarantee the homogeneous of water level in the soil. Dynamic pore water pressure sensors buried in subgrade and subsoil can monitor transient and long-term variations of pore water pressure. The result of water level change with water table lifting is shown in Fig. 4.

To explore the long-term deforming patterns of high-speed railway roadbed under different water level conditions, train moving loading tests were conducted on the full-scale railway system with water table at the subsoil bottom, at the subsoil surface and at the subgrade surface, respectively. Table 3 summarized the nine cyclic tests in this study. In each water level condition, three different train velocities were simulated in a certain number of cyclic loads (each cyclic load equals to a train axle passing by) to comprehensively consider the working condition on the field. At the end of



**Fig. 3** Layout of sensors

**Fig. 4** Measured pore water pressure during water level rises



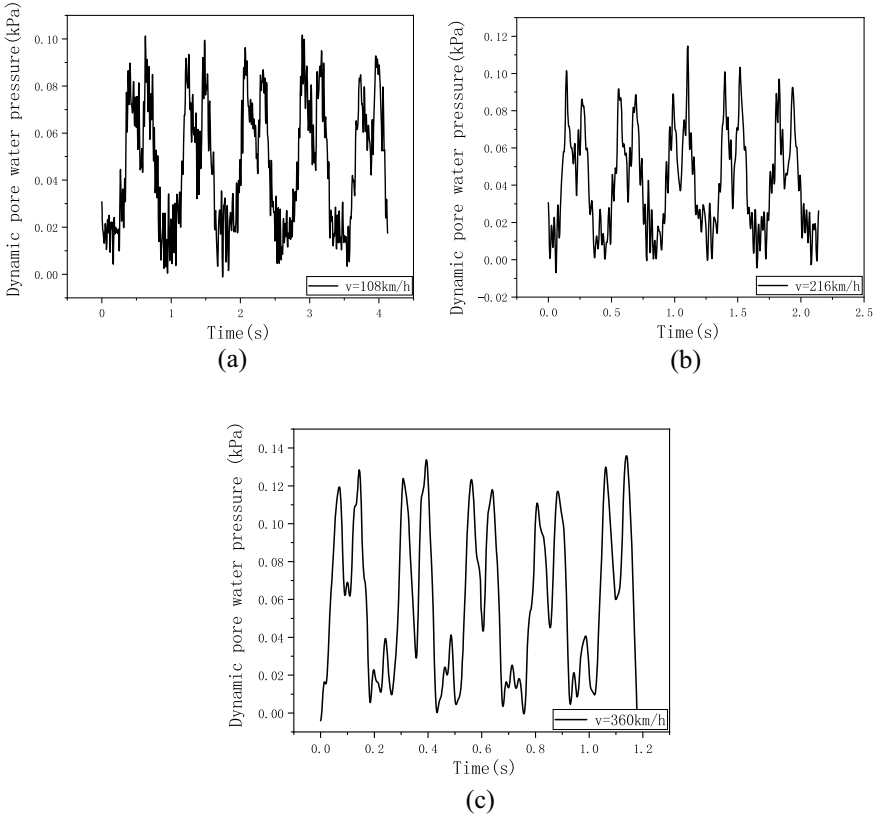
**Table 3** Number of axle load under different conditions

Water table	Number of axle load, <i>N</i>			
	108 km/h	216 km/h	360 km/h	Total
At subsoil bottom	140,000	140,000	140,000	420,000
At subsoil surface	630,000	140,000	867,000	1,637,000
At subgrade surface	780,000	520,000	680,000	1,980,000

each group of tests, train loads were removed for 12 h for the embankment to settle down, after which cyclic loading of a higher train speed was continued.

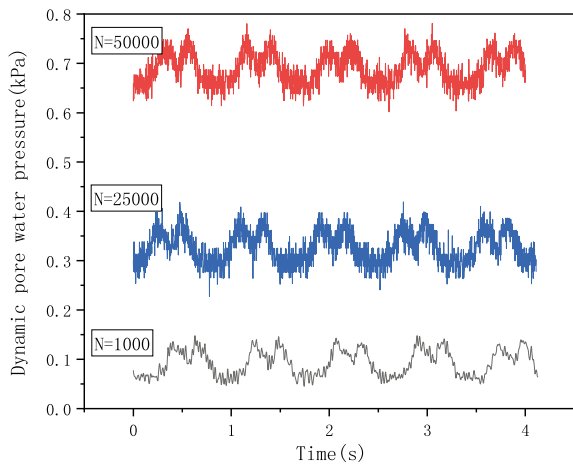
### 3 Testing Results

The development of excess pore water pressure is an important indicator of soil settlement. When water level is at the subsoil surface, the measured dynamic pore water pressure is very small. To study the transient response of dynamic pore water pressure, random five loading cycles of the dynamic pore water pressure (the responding shapes are alike during the whole cyclic loading) measured in subsoil (0.5 m below the subsoil surface) under the condition of water level at the subgrade surface were shown in Fig. 5. The dynamic pore water pressure goes up and down periodically corresponding with train moving loads. The amplitude of dynamic pore water pressure induced by train moving loads is 0.1 kPa at train speed of 108 km/h, which only increases to 0.136 kPa at train speed of 360 km/h. This is attributed to little increase of dynamic soil stress in subsoil with the increase of train speed. Figure 6 shows the dynamic pore water pressure at different no. of train load cycles ( $N = 1000, 25,000, 50,000$ ) at train speed of 108 km/h. There is obvious development



**Fig. 5** Dynamic pore water pressure measured in subsoil at different train speeds: **a** 108 km/h, **b** 216 km/h and **c** 360 km/h

**Fig. 6** Dynamic pore water pressure at different no. of cycle





of residual excess pore water pressure with train loading cycles. And the value of residual excess pore water pressure after 50,000 cycles of train loads is much greater than the amplitude of dynamic pore water pressure. The application of successive loads on the track's superstructure increases the compaction of the underlying soils. In this way, it reduces the void ratio and then pore water pressures increase, even at rest, as shown in Fig. 6. Testing results of permanent deformation and further research will be discussed in a future publication.

## 4 Remarks

Through a full-scale physical model of a ballastless railway, train moving loading tests were conducted with different water levels to explore the long-term performance of ballastless high-speed railway track under the conditions of ground water level variations. Some results of dynamic pore water pressure are presented and discussed. The dynamic pore water pressure goes up and down periodicity corresponding with train moving loads. There is an obvious development of residual excess pore water pressure with train load cycles, which is due to the compaction of the underlying soils due to the application of successive loads on the track's superstructure. Testing results of permanent deformation and further research will be discussed in a future publication.

## References

1. Vogt L, von Wolfersdorff P-A, Rehfeld E (2005) Behaviour of slab track under extreme stress conditions. In: European slab track symposium, Bruxelles
2. Yang LA, Powrie W, Priest JA (2009) Dynamic stress analysis of a ballasted railway track bed during train passage. *J Geotech Geoenviron Eng* 135(5):680–689
3. Duong TV, Cui YJ, Tang AM, Dupla JC, Canou J, Calon N, Robinet A (2014) Investigating the mud pumping and interlayer creation phenomena in railway sub-structure. *Eng Geol* 171:45–58
4. Bian XC, Jiang HG, Chen YM, Jiang JQ, Han J (2016) A full-scale physical model test apparatus for investigating the dynamic performance of the slab track system of a high-speed railway. *Proc Inst Mech Eng Part F J Rail Rapid Transit* 230(2):554–571

# Mechanism of Pore Pressure Increase of Saturated Granular Materials Subjected to Repeated Loads



Chuang Zhao , Xuecheng Bian, Yunmin Chen, and Lili Yan

**Abstract** A series of undrained torsional shear tests were conducted to investigate the variation of excess pore water pressure of saturated sand during undrained cyclic loadings. The test results indicate that there is a threshold of cyclic stress ratio for specimen to reach liquefaction. Above the threshold, the excess pore water pressure gradually increases during undrained cyclic loading and is eventually equal to the initial effective confining stress. The double amplitude of shear strain also increases gradually, showing a weakening development of the shear strength of the specimen. Beneath the threshold, the excess pore water pressure stops increasing eventually regardless of how many cycles are applied. Moreover, the excess pore water pressure rises sharply just after the reverse of the loading direction, which suggests that an evident tendency of negative dilatancy is accordingly induced. The excess pore water pressure cannot always increase with the shear stress, and it decreases when approaching the phase transformation line. Based on introducing a variable that is defined as the increment of the excess pore water pressure during a unit variation of the shear strain, the tendency of volume change of the specimen can be well represented.

**Keywords** Undrained tests · Repeated loading · Saturated sand · Excess pore water pressure · Shear deformation

## 1 Introduction

Pore water pressure gradually increases in practice when the soil materials with high water content are subjected to repeated loadings, such as an earthquake, traffic loadings, and vibrations. Settlements are induced when the generated excess pore water pressure dissipates during and after the seismic events. For example, pore water

---

C. Zhao (✉) · X. Bian · Y. Chen · L. Yan  
Department of Civil Engineering, Zhejiang University, Hangzhou 310058, P. R. China  
e-mail: [zhaochuang@zju.edu.cn](mailto:zhaochuang@zju.edu.cn)

C. Zhao  
Department of Civil Engineering, The University of Tokyo, Tokyo, Japan

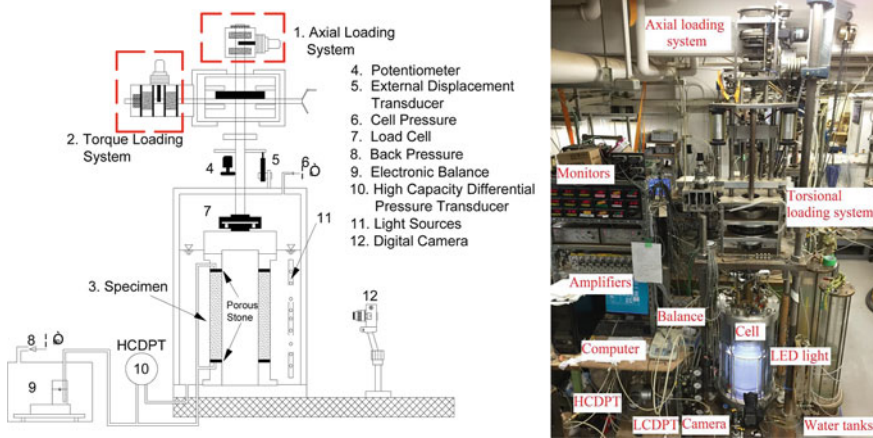
pressure in the ballast or granular soils beneath the concrete board that are of high water content increases gradually under repeated train loads. If the pore pressure rises to a high value compared with the confining stress, the strength of soils would decrease sharply. More seriously, the induced settlement may threaten the safety of passengers and trains when train is running at a quite high speed.

However, most of research mainly focuses on the global increment of pore water pressure with the cycle number during undrained cyclic loadings, little attention has been paid on its substantial mechanism, in particular, the variation of pore water pressure in one cycle. The build-up of pore water pressure in liquefaction tests has been extensively investigated in past decades and is still a representative topic in dynamic soil mechanics [1–3]. Ishibashi et al. proposed a pore pressure prediction model that is seen as one of the most standout models and is mainly used to calculate the residual pore pressure at the end of each cycle [4]. Moreover, an energy-based prediction method is also rapidly developed [5, 6]. In addition, the Biot theory of elastic wave propagation is employed to model the behavior of saturated soils under the repeated loadings [7]. For instance, Bian et al. used the Biot's theory to investigate the generation of pore pressure in a poro-elastic soil under different speeds of train, permeabilities and stiffnesses of soils. However, only numerical and theoretical results were compared without showing the experimental results [8]. In the discrete element method (DEM) simulation, the pore water is usually not reproduced in the model. The calculation of pore water pressure is based on the variation of effective stress acting on the sand particles under the undrained loading condition, which is realized by maintaining a constant volume of the specimen [9]. Even though this consideration has been proved effectively to show the dynamic properties of saturated soils, the pore pressure is only an equivalent substitution, which may not be the case under complicated stress conditions. In short, different methods have different assumptions, which result in various advantages and disadvantages. Therefore, a better understanding of pore water pressure increase during repeated loading contributes to proposing a more realistic and suitable model to further investigate the dynamic behavior of saturated soils.

The aim of this study is to interpret the mechanism of pore water pressure increase of saturated sand during undrained cyclic loadings. Based on a series of typical torsional shear tests, the variation of pore water pressure and the variation tendency of specimen volume are discussed in detail.

## 2 Test Apparatus, Materials, and Procedure

The torsional shear apparatus originally developed at the Institute of Industrial Science (IIS), The University of Tokyo, is schematically shown in Fig. 1, in which the torque and axial force can be monitored using a load cell without coupling effects [10–12]. The axial and shear strains are accordingly measured by an external displacement transducer and a potentiometer, respectively. The volume change of the specimen is measured during consolidation using a digital balance that is placed



**Fig. 1** Schematic diaphragm and photo of the torsional shear apparatus

in a pressure chamber. The initial pore pressure of the specimen can be accordingly adjusted by the back pressure as indicated in Fig. 1. In addition, the effective stress of specimen is measured by a high-capacity differential pressure transducer (HCDPT) with a capacity of approximately 500 kPa.

Silica sand No. 5 ( $G_s = 2.633$ ,  $e_{max} = 1.047$ ,  $e_{min} = 0.688$ ,  $D_{50} = 0.50$ ) was used in this study to prepare the hollow cylindrical specimens with an inner diameter of 120 mm, an outer diameter of 200 mm, and a height of 300 mm using air pluviation method. The specimen was completely saturated using the double vacuuming method to achieve a B value higher than 0.96. Afterward, the specimen was isotropically consolidated at an effective stress of 100 kPa. A prescribed amplitude of shear stress was then applied to the specimen with a vertically prohibited top cap under undrained condition. To directly capture the local deformation of the specimen, a transparent membrane was employed. In addition, a camera was placed in front of the transparent chamber for taking photos during test [11, 12].

### 3 Results and Discussion

#### 3.1 Typical Results

Typical test results on the loose ( $Dr = 32\%$ ), medium dense ( $Dr = 53\%$ ), and dense ( $Dr = 85\%$ ) specimens are shown in Figs. 2, 3, and 4, respectively [11]. The failure line (FL) and phase transformation line (PTL) are also indicated. All the specimens were isotropically consolidated to 100 kPa and sheared at a cyclic stress ratio (CSR) of 0.23. The loose and medium dense specimens reached liquefaction state eventually after being subjected to 1.1 and 4.8 cycles, respectively. However, the dense one did

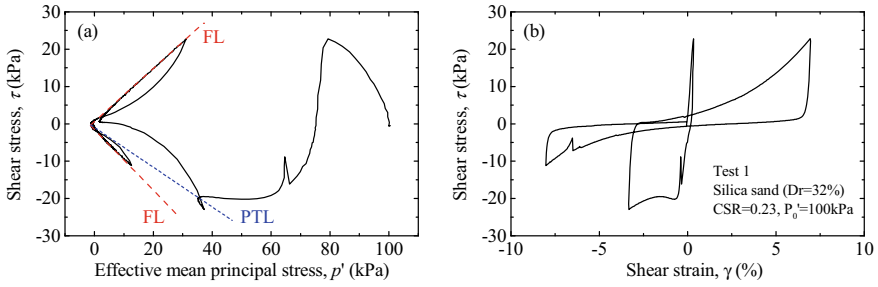


Fig. 2 Typical test results on a loose sand specimen [11]

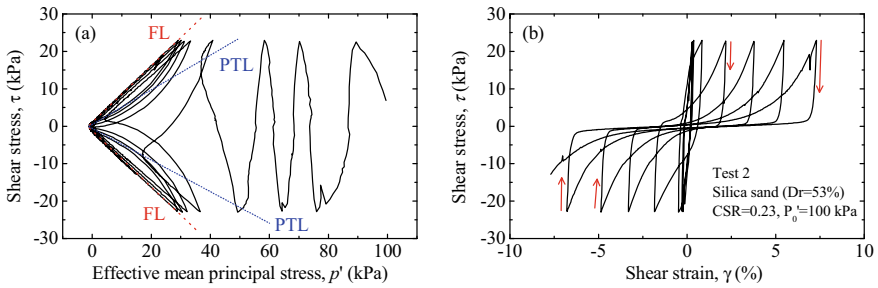


Fig. 3 Typical test results on a medium dense sand specimen [11]

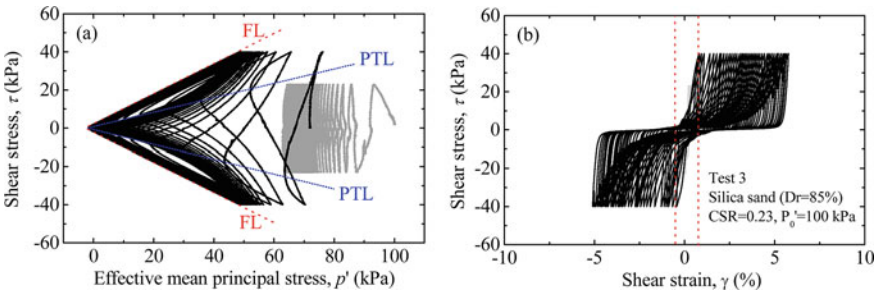


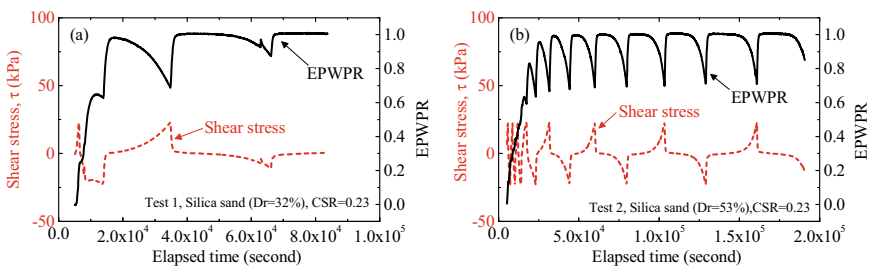
Fig. 4 Typical test results on a dense specimen

not reach liquefaction even 143 cycles had been applied. The test was temporarily terminated and subsequently re-sheared at a CSR of 0.40 and finally reached the liquefaction as shown in Fig. 4. Obviously, the number of cycles for reaching liquefaction increases with the rising relative density of the specimen. During each test, the double amplitude of shear strain increases with the decreasing of effective stress. Moreover, based on the results shown in Fig. 4, there is a threshold of CSR of the dense specimen for reaching liquefaction, under which the specimen cannot be liquefied regardless of how many cycles are applied.

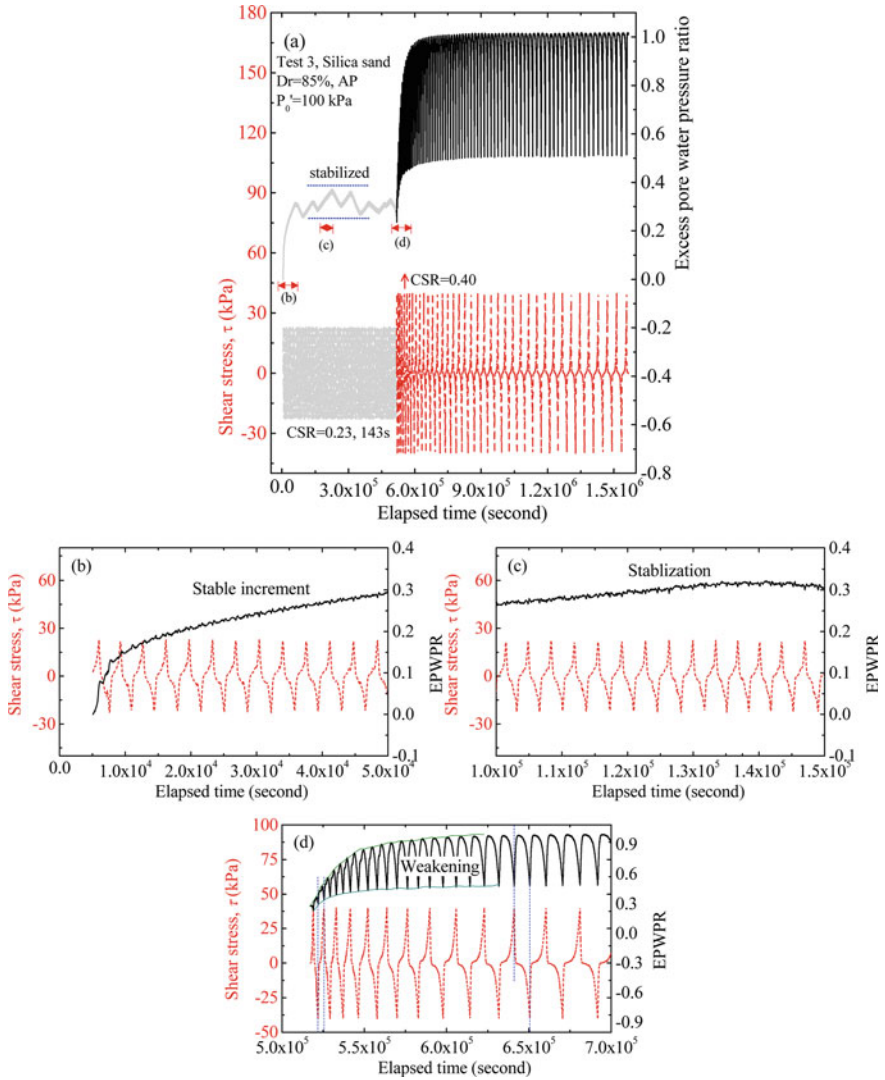
### 3.2 Pore Pressure Increase During Cyclic Loading

Figure 5 shows the time histories of excess pore water pressure ratio (EPWPR) contrasted with those of shear stress. As can be seen in the first several cycles, the excess pore water pressure ratio has a sudden increment when the loading direction is reversed. A decrease of the excess pore water pressure ratio before the reverse of the loading direction is also observed at a higher excess pore water pressure ratio. It indicates that the phase transformation line as shown in Figs. 2, 3, and 4 is accordingly reached. From a mechanical point of view, it is usually assumed that the excess pore water pressure increases because a tendency of negative dilatancy is induced after applying loading. In fact, the specimen was completely saturated and sheared under an undrained condition from a global viewpoint. Therefore, there should be no volume change during the loading. It is still full of difficulty to understand the real behavior of saturated sand in which the pore pressure increases when being applied load.

Similarly, Fig. 6 provides the time histories of excess pore water pressure ratio and shear stress of the dense specimen before and after increasing the CSR from 0.23 to 0.40. Moreover, these time histories curves are divided into three stages as indicated in Fig. 6a. Combined with the results shown in Fig. 4, there is a rapid increase of the excess pore water pressure at the first two cycles after applying the cyclic stress of 23 kPa. Hereafter, the excess pore water pressure ratio shows a stable increment with the cyclic loadings. After more than ten cycles, the excess pore water pressure ratio maintains at approximately 0.3 and has an evident fluctuation in the subsequent 100 cycles from a global point of view. In a detailed illustration as provided in Fig. 6c, the excess pore water pressure ratio is stably kept. After subjected to 143 cycles, the excess pore water pressure and double amplitude of the shear strain are both stably maintained. As discussed earlier, the 23 kPa is lower than the threshold of the shear stress to make the specimen liquefied with finite cycles. Subsequently, the shear stress was increased from 23 to 40 kPa. The excess pore water pressure ratio as shown in Fig. 6a, and Fig. 6d increases gradually. As indicated in Fig. 4a, since the phase transformation line is reached at the first two cycles, the excess pore water pressure increases and decreases periodically with the cyclic loadings. Moreover, the



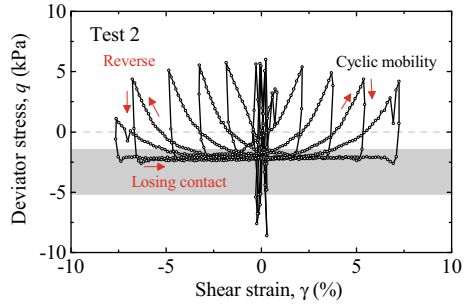
**Fig. 5** Time histories of excess pore water pressure ratio and shear stress of the loose and medium dense specimens



**Fig. 6** Time histories of excess pore water pressure ratio and shear stress of the dense specimen at different stages

amplitude of variation of the excess pore water pressure ratio in each cycle increases at the first several cycles, which indicates a weakening behavior of the specimen. And the amplitude eventually stays at a nearly constant value.

**Fig. 7** Relationship between the deviator stress and shear strain of the medium dense specimen in test 2



### 3.3 Variation Tendency of Specimen Volume

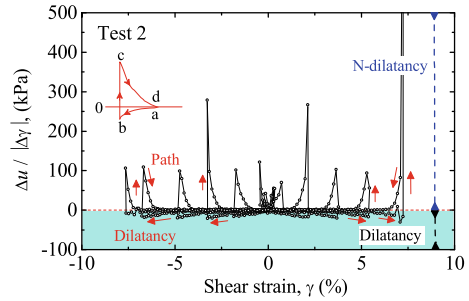
Since the vertical displacement of the specimen was prohibited during the undrained cyclic loadings, some researchers made efforts to use the variation of the deviator stress to represent the tendency of the volume change of the saturated specimen. Figure 7 provides the relationship between the deviator stress and shear strain of the medium dense specimen in test 2. It can be seen that the deviator stress is periodically recovered due to the cyclic mobility. More importantly, the deviator stress decreases to zero rapidly after reversing the loading direction, which is coincident with the variation of excess pore water pressure shown in Fig. 5b. It should be noted that the deviator stress is not zero during the liquefaction. Because the axial force was reset to zero during specimen preparation without considering the weight of the top cap. The weight of the top cap is approximately 2.5 kPa that is nearly equal to the absolute value of the deviator stress during the liquefaction. In addition, the deviator stress increases as the shear stress increases before approaching the peak of the shear stress.

To qualitatively describe the tendency of volume change of the saturated specimen, the increment of excess pore water pressure during an unit variation of the shear strain is defined. It suggests a similar physical meaning as the variation tendency of specimen volume, which results in the variation of the excess pore water pressure. A negative value means that the excess pore water pressure is decreasing as the variation of the shear strain. As shown in Fig. 8, it indicates the dilatancy when the  $\Delta u/|\Delta \gamma|$  is lower than 0. A positive value of  $\Delta u/|\Delta \gamma|$  indicates a trend of the negative dilatancy of the specimen.

It can also be seen in Fig. 8 that there is a slight decrease of the  $\Delta u/|\Delta \gamma|$  in the negative direction (a to b) before approaching the peak of the shear stress, which shows that a dilatancy trend of the specimen is induced. After reversing the loading direction, the dilatancy trend is suddenly changed to the negative dilatancy (b to c). Moreover, the increment of excess pore water pressure just after the reverse, the same as the value of c, is significantly large. However, hereafter, the increment of excess pore water pressure at an unit variation of the shear strain decreases as the shear strain decreases (c to d).



**Fig. 8** Relationship between the  $\Delta u / |\Delta \gamma|_s$  and shear strain of the medium dense specimen in test 2



It is known that membrane penetration is usually induced after applying effective stress to the specimen. However, this membrane penetration gradually disappears due to the increment of the excess pore water pressure under undrained cyclic loadings. The previous space between sand particles that is penetrated by membrane is gradually occupied by the pore water. It can be deduced that pore water migration occurs within the specimen. As announced by the authors, vertical slippage between membrane and specimen is observed both in the triaxial and torsional shear tests during the liquefaction of specimen because the vertical slippage is mainly affected by the resultant force of gravity and buoyancy acting on the sand particles during the liquefaction [11–13]. This is a strong evidence showing that the membrane penetration is completely vanished. From the view of an equilibrant of the global volume of the specimen, the pore water migrates from the inner space of specimen to its outer surface to weaken the membrane penetration. Such migration is certainly induced by a hydraulic gradient within the specimen, where the pore water pressure in the inner space is higher than that in the outer space. Under this circumstance, concurrent with the pore water migration and local pore pressure dissipation, the global pore water pressure within the specimen increases gradually during the undrained cyclic loadings.

From another perspective, the migration of pore water within the specimen is accompanied with the real negative or positive dilatancy of the specimen but from a view of the envelope surface of the specimen. Such kind of consideration will be studied in depth in future.

## 4 Conclusions

The results from a series of undrained cyclic torsional shear tests on saturated sand can be summarized as follows:

- (a) There is a threshold of the cyclic stress ratio for the specimen to reach liquefaction, under which the excess pore water pressure stops increasing eventually and maintains stably in the subsequent cyclic loadings.

- (b) Above the threshold of CSR, the excess pore water pressure increases gradually, which results in an increase in the double amplitude of shear strain. Specimen gradually loses its shear strength and eventually reaches liquefaction.
- (c) The excess pore water pressure does not always increase during the cyclic loading, and it decreases when approaching the phase transformation line because of the tendency of specimen dilatancy.
- (d) After the reverse of loading direction, the excess pore water pressure increases abruptly due to the tendency of negative dilatancy of the specimen. Such tendency of volume change can be well described by the  $\Delta u/|\Delta\gamma|$  during the undrained cyclic shearing.

**Acknowledgements** This work was supported by the National Natural Science Foundation of China (Grant No. 52008369) and the China Postdoctoral Science Foundation (Grant No. 2019M662057). The authors express their highest appreciation to Prof. Junichi Koseki and Mr. Takeshi Sato from the University of Tokyo for their guidance and assistances.

## References

1. Seed HB, Booker JR (1977) Stabilization of potentially liquefiable sand deposits using gravel drains. *J Geotech Eng Div* 103(7):755–768
2. Mitchell RJ, Dubin BI (1986) Pore pressure generation and dissipation in dense sands under cyclic loading. *Can Geotech J* 23(3):393–398
3. Konstadinou M, Georgiannou GN (2014) Prediction of pore water pressure generation leading to liquefaction under torsional cyclic loading. *Soils Found* 54(5):933–1005
4. Ishibashi I, Sherif MA, Tsuchiya C (1977) Pore-pressure rise mechanism and soil liquefaction. *Soils Found* 17(2):17–27
5. Dief HD, Figueroa JL (2007) Liquefaction assessment by the unit energy concept through centrifuge and torsional shear tests. *Can Geotech J* 44(11):1286–1297
6. Jafarian Y, Towhata I, Baziar MH, Noorzad A, Bahmanpour A (2012) Strain energy based evaluation of liquefaction and residual pore water pressure in sands using cyclic torsional shear experiments. *Soil Dynam Earthq Eng* 35:13–28
7. Biot MA (1956) Theory of propagation of elastic waves in a fluid-saturated porous soil. I. Low frequency range. *J Acoust Soc Am* 28(2):168–178
8. Bian XC, Hu J, Thompson D, Powrie W (2019) Pore pressure generation in a poro-elastic soil under moving train loads. *Soil Dynam Earthq Eng* 125:105711
9. Kuhn MR, Renken HE, Mixsell AD, Kramer SL (2014) Investigation of cyclic liquefaction with discrete element simulations. *J Geotech Geoenviron Eng* 140(12):04014075
10. Koseki J, Yoshida T (2005) Sato T (2005) Liquefaction properties of Toyoura sand in cyclic torsional shear tests under low confining stress. *Soils Found* 45(5):103–113
11. Zhao C, Koseki J, Liu W (2020) Local deformation behavior of saturated silica sand during undrained cyclic torsional shear tests using image analysis. *Geotechnique* 70(7):621–629
12. Zhao C, Koseki J (2020) An image-based method for evaluating local deformations of saturated sand in undrained torsional shear tests. *Soils Found* 60(3):608–620
13. Zhao C, Koseki J, Sasaki T (2018) Image based local deformation measurement of saturated sand specimen in undrained cyclic triaxial tests. *Soils Found* 58(6):1313–1325

# Experimental Study on Soil–Water Retention Properties of Compacted Expansive Clay



Debojit Sarker  and Jay X. Wang

**Abstract** The soil–water characteristic curve (SWCC) defines the relationship between water content and matric suction in soil, which contains fundamental information needed for the hydromechanical behavior of expansive soil that generally lies within the unsaturated soil mechanics framework. Moreland clay is highly expansive soil abundant in northern Louisiana, part of Arkansas, and Oklahoma. Unsaturated soil properties for shear strength, permeability, and volume change are needed to identify expansive soil-induced stresses on pavement or railroad track due to seasonal variation of moisture content in the subgrade layers. Determination of the two critical variables obtained from the SWCC, i.e., the air-entry value (AEV) and the residual state suction, is essential for the prediction of unsaturated soil deformations. In this research, an experimental testing program was conducted on the expansive Moreland clay to investigate the soil–water retention properties by adopting the axis translation technique to control suction in the range of 0–1500 kPa. A computer program was developed to fit experimental data, and it was compared with predicted SWCC using empirical relationships. The AEV and the residual state suction, two critical variables, were obtained from the SWCC formulation of Fredlund and Xing equation. Finally, the shrinkage curve was determined to interrelate between elastic deformation and SWCC of Moreland clay.

**Keywords** Soil–water characteristic curve · Expansive soil · Moreland clay · Shrinkage curve

---

D. Sarker (✉) · J. X. Wang  
Programs of Civil Engineering and Construction Engineering Technology, Louisiana Tech University, Ruston, LA 71272, USA  
e-mail: [dsa038@latech.edu](mailto:dsa038@latech.edu)

J. X. Wang  
e-mail: [xwang@latech.edu](mailto:xwang@latech.edu)

## 1 Introduction

The soil–water characteristic curve (SWCC) is described as the relationship between water content (gravimetric or volumetric) or degree of saturation with suction (matric or total) [1]. Among various forms of equations proposed by different researchers [2–7], Leong and Rahardjo [8] pointed out that Fredlund and Xing’s [5] equation was the best fitting. The equation with a correction factor  $C(\Psi)$  is given by the following expression:

$$\theta(\Psi) = C(\Psi) * \frac{\theta_s}{\{\ln[e + (\frac{\Psi}{a})^n]\}^m} = \left[ 1 - \frac{\ln\left(1 + \frac{\Psi}{C_r}\right)}{\ln\left(1 + \frac{10^6}{C_r}\right)} \right] * \frac{\theta_s}{\{\ln[e + (\frac{\Psi}{a})^n]\}^m} \quad (1)$$

where  $a$ ,  $n$ ,  $m$  are the fitting parameters,  $C_r$  is the parameter related to the residual suction, and  $\theta_s$  is the saturated volumetric water content.

Expansive soil experiences a significant volume change due to seasonal variations of moisture content, and it causes pavement and/or building distresses [9–12]. Moreland clay was identified as a highly expansive soil abundant in northern Louisiana, part of Arkansas, and Oklahoma [13, 14]. Identification of the unsaturated soil properties of Moreland clay may lead to the improvement of the design guidelines and specifications for pavement or railroad track on the expansive subgrade soils. The two critical variables obtained from the SWCC, i.e., the air-entry value (AEV) and the residual state suction, are essential for the determination of unsaturated soil properties for shear strength, permeability, and volume change [15–25]. The air-entry value (AEV) is the matric suction where the air begins to enter the most significant pores in the soil, while the residual water content is the water content where a large suction change is required to expel extra water from the soil. Quantification of the relationship between water retention and internal stress state of expansive unsaturated soils is critical, especially at low-to-intermediate saturation, where surface adsorption mechanisms dominate water retention and corresponding stress state [26–28]. The desaturation process, as demonstrated in Fig. 1, takes place over three different stages, i.e., the boundary effect, the transition, and residual stages [1].

As the extension of the research on Moreland clay [13, 14], in this paper, the authors are to disseminate their in-depth research for the engineering properties of the expansive unsaturated soil through compacted specimens. The tests were conducted by employing an oedometer-type pressure plate SWCC device to investigate the water retention capacity of the soil. Similarly, the shrinkage curve was determined to correlate volume changes with soil saturation and desaturation. The goal is to ensure the proper execution of a geotechnical framework involving expansive unsaturated soils during long-term interactions with the environment or during external loading, implying that analyses of water flow and mechanical response are required alongside consideration of the effect of unsaturated conditions on the stress state in the soil.

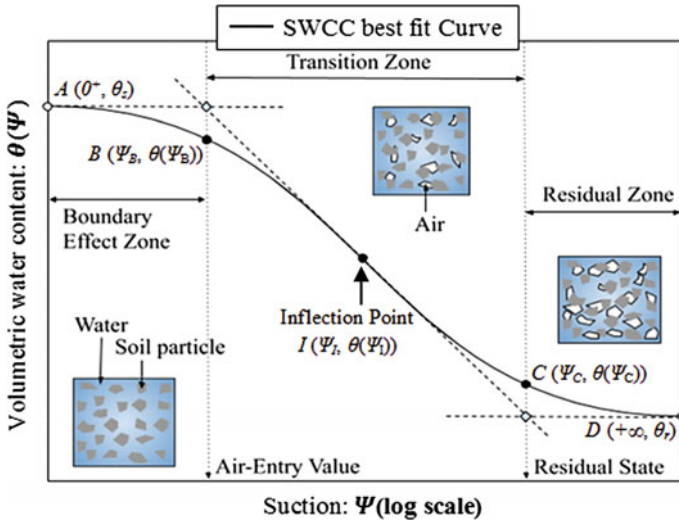


Fig. 1 Different stages of desaturation as defined by the soil–water characteristic curve

## 2 Research Methodology

This study aims to investigate SWCCs and volumetric behavior of compacted expansive Moreland clay. A conventional SWCC best-fit curve is shown in Fig. 1, where  $\Psi_B$  represents the air-entry value, and  $\Psi_C$  is denoted as the residual state suction. Moreland clay was experimentally investigated for its SWCC following ASTM D6836, and it was compared with the empirically predicted SWCC using soil index parameters.

Moreland clay is full of mineral of montmorillonite, abundant mostly in the northern part of Louisiana, part of Arkansas, and Oklahoma [29, 30]. The design of pavement, foundations, and retaining structures sitting in or on Moreland clay requires the ground heave prediction. Tu and Vanapalli [31] showed that heave/shrinkage displacements of expansive unsaturated soils could be predicted from the swelling pressure determined using SWCC as a tool. It is worthwhile to note that the SWCC-based method will result in an accurate heave prediction model compared to full-wetting assumption, which will improve foundation and pavement design over expansive Moreland clay under extreme weather conditions.

### 2.1 A Brief Characterization of the Moreland Clay

The Moreland clay samples were retrieved from the open pit at a church construction site in Bossier City, Louisiana. Disturbed samples were obtained in accordance with the ASTM D1452 standard practice for soil exploration and sampling by auger borings [32]. All the specimens were plastic-wrapped and sealed, and the entire

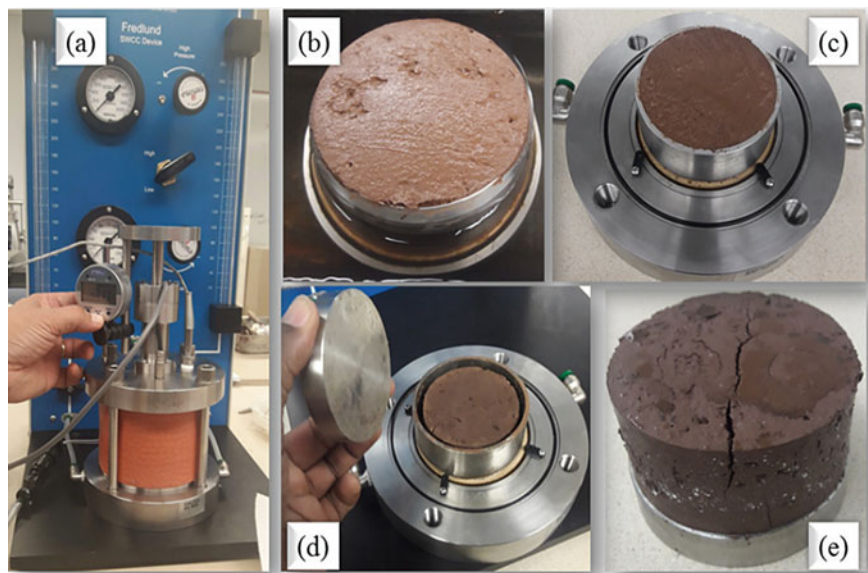
collection was transported and stored in the geotechnical laboratory at the Louisiana Tech University as per the ASTM D4220 standard practice for preserving soil samples [33]. Later, samples were compacted in accordance with the ASTM D1557 standard test methods for laboratory compaction characteristics of soil using the modified effort [34].

The geotechnical index properties were determined according to the ASTM test methods as follows: (i) gravimetric water content by the ASTM D2216 standard test methods for laboratory determination of water (moisture) content of soil and rock by mass [35]; (ii) specific gravity ( $G_s$ ) by the ASTM D854 standard test methods [36]; (iii) liquid limit, plastic limit, and plasticity index by the ASTM D4318 standard test methods [37]; (iv) grain size distribution by the ASTM D6913 standard test methods using the sieve analysis [38]; and (v) soil classification using the unified soil classification system (USCS) by the ASTM D2487 standard practice for classification of soils for engineering purposes [39].

## 2.2 *Experimental Determination of Soil–Water Characteristic Curve*

The SWCC was determined according to the ASTM D6836 standard test methods for determination of the soil–water characteristic curve for desorption using pressure extractor [40] on a 63.5-mm-diameter and 25.4-mm-thick sample obtained from the compacted sample. Predetermined values of matric suction were applied using the SWC-150 Fredlund SWCC device shown in Fig. 2(a), manufactured by GCTS testing systems. Suits et al. [41] provided general recommendations for appropriate use of the equipment and corrections to the SWCC data obtained using the axis translation pressure plate-type devices. The authors concluded that the new oedometer device could be used to obtain an accurate SWCC for a single specimen by applying suction up to 1500 kPa.

According to the ASTM D6836, Method B (pressure chamber with volumetric measurement) was applied for the experimentation. As per Method B, the pore water pressure was maintained at atmospheric pressure, and the pore gas pressure was raised to apply the suction via the axis translation principle. Specimen preparation from a disturbed sample was done by compacting the Moreland clay to the specified water content and density using ASTM D1557. A retaining ring was placed on the surface of the soil after placing the compacted specimen on the bench, and trimming was done until the soil filled in the retaining ring. After that, the gravimetric water content of the specimen was measured using ASTM D2216. As Moreland clay is sufficiently cohesive in nature, the specimen was saturated by inundation in a saturation tray on top of a porous material, as shown in Fig. 2b, and continued for 48 h. As appeared in Fig. 2c, the saturated Moreland clay specimen was placed in contact with a water-saturated porous plate. The application of the matric suction caused water to flow from the specimen until the equilibrium water content corresponding to the applied



**Fig. 2** Experimental setup and sample at different testing stages: **a** the SWC-150 Fredlund SWCC device; **b** a sample kept for saturation; **c** the sample ready for test; **d** the sample after test; **e** the sample taken out of retaining ring

suction was reached. Equilibrium was established by monitoring when water flow came to an end from the specimen.

The water content corresponding suction was determined in two steps. First, the volume of water expelled was measured using a capillary tube. Then, the water content was determined based on the known initial water content of the specimen and the volume of water expelled. After conducting the test, the shrinkage of the Moreland clay specimen can be observed in Fig. 2d. Finally, the specimen was taken out from the retaining ring, as shown in Fig. 2e, and kept in the oven for drying for 24 h.

### 3 Results and Discussion

Table 1 summarizes the geotechnical index properties of the Moreland clay. The saturated water content and the dry unit weight of the compacted sample were found to be 34% and  $1.41 \text{ g/cm}^3$ , respectively. The clay-size fraction (material finer than 0.002 mm) was around 63%. The fine-grained nature of the Moreland clay suggests a high water retention capacity. Overall, the soil was classified as CH (clay with high plasticity) according to the Unified Soil Classification System (USCS).

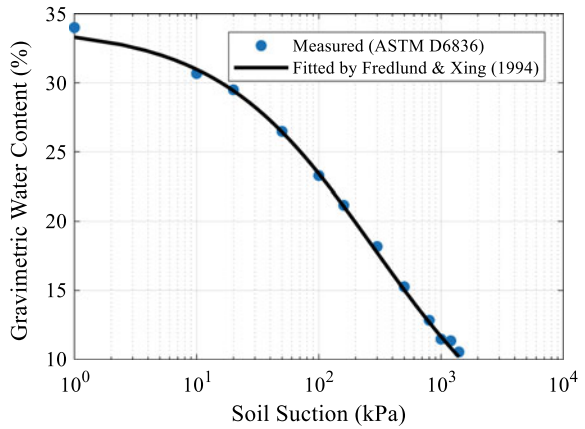
Figure 3 shows SWCC with gravimetric water content, and Fig. 4 presents the SWCC in the form of void ratio. The sample was put in a water tub for 48 h, and the

**Table 1** A summary of the properties of the expansive Moreland clay

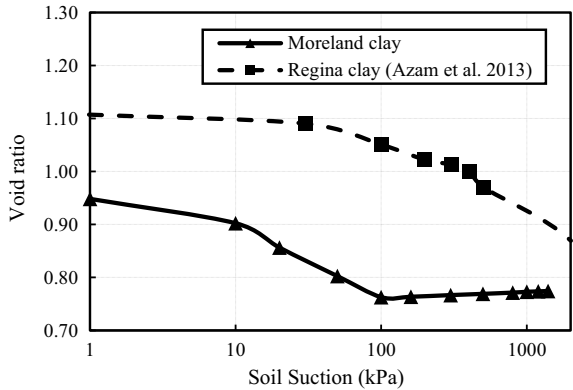
Soil properties	Value	Soil properties	Value
USCS symbol*	CH	Saturated moisture content (%)	34
0.075 mm passing (%)	99	Optimum moisture content (%)	27
0.002 mm passing (%)*	63	Maximum dry density, kN/m <sup>3</sup>	14.52
Specific gravity, $G_s$	2.75	Plastic limit, $PL$ (%)	28
Liquid limit, $LL$ (%)	79	Plasticity index, $I_p$ (%)	51

\*Data from Khan [42]

**Fig. 3** SWCC for desorption with gravimetric water content



**Fig. 4** SWCC for desorption with void ratio



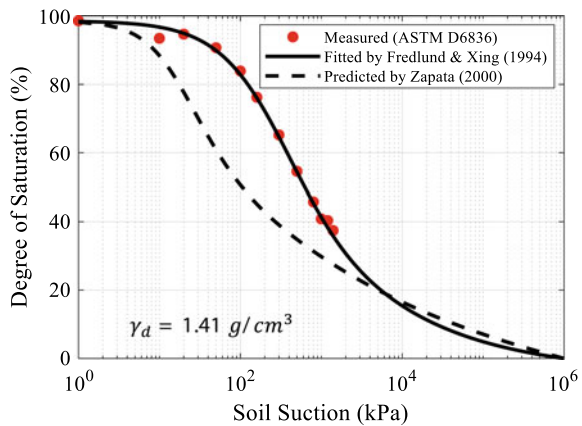


water content was measured at 34% for the compacted sample. A MATLAB-based computer program was developed to fit the measured data using Eq. (1) by a nonlinear least-squares method. The measured gravimetric data fitted well to unimodal distributions with the air-entry value of 50 kPa [47]. Fitting parameters, i.e.,  $a$ ,  $m$ , and  $n$  for the measured SWCC in the form of gravimetric water content, were found to be 169.6, 1.795, and 0.673, respectively. The void ratio was calculated from the dry density at different suctions, and as presented in Fig. 4, the data closely followed unimodal distributions showing an air-entry value of 12 kPa for the compacted sample.

The void ratio vs. suction from the SWCC of Moreland clay was compared with the plot for another expansive soil called Regina clay. Air-entry value from the SWCC in the form of void ratio of Regina clay was found to be 100 kPa for compacted samples [43]. Measured void ratio of Moreland clay exhibited a sharp decrease in void ratio up to the residual condition and became asymptotic to the abscissa after the residual suction and never reached to  $10^6$  kPa on the complete drying stage, which showed a similar pattern as Regina clay for a higher suction range. Figures 3 and 4 clearly show that the more significant part of the shrinkage happens in the full saturation state before the soil starts to desaturate.

Figure 5 presents the SWCC in the form of degree of saturation as a function of soil suction. Similar to Fig. 3, laboratory-measured data depicted a unimodal function with an air-entry value of 50 kPa. Desaturation occurred at an increased rate up to residual suction of 7000 kPa, and the curve finally joined the abscissa at  $10^6$  kPa. The SWCC given in the form of water content versus matric suction is the most precise representation for expansive soils. Fityus and Buzzi [44] postulated that the expansive soil aggregates remain saturated over a more extensive range of suction commonly pervasive in the field. As a result, the gravimetric water content for each suction value catches water drainage through pores and is independent of volume changes because of water adsorption by clay particles. Similarly, the SWCC represented in the form of degree of saturation versus soil suction is the most reasonable for understanding volume decrease in pores because of a suction application. Laboratory-measured data

**Fig. 5** SWCC with the degree of saturation



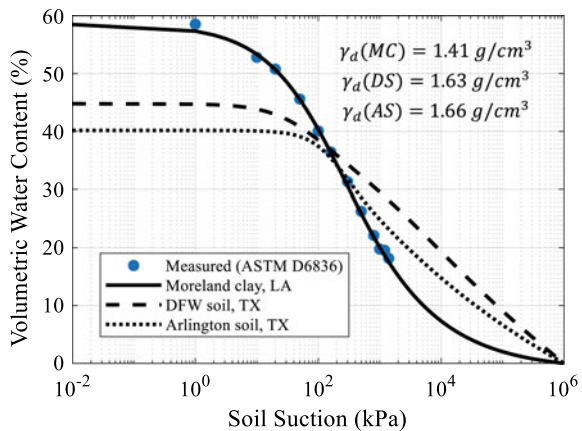
were fitted using Eq. (1) and plotted as “fitted” SWCC in Fig. 5. Fitting parameters, i.e.,  $a$ ,  $m$ , and  $n$  for the measured SWCC in the form of degree of saturation, were found to be 227.1, 1.243, and 1.017, respectively.

SWCC of plastic soils can be predicted using relationships based on the correlations with the commonly obtained soil index parameters such as Atterberg limits and grain size distribution data [45]. Zapata [46] proposed equations to predict the fitting parameters for the Fredlund and Xing [5] equation for plastic soils. The measured SWCC was compared with the predicted SWCC by acquiring the fitting parameters using equations provided by Zapata et al. [47]. Fitting parameters, i.e.,  $a$ ,  $m$ , and  $n$  for the “predicted” SWCC in the form of degree of saturation, was found to be 13.02, 0.54, and 1.56, respectively. There is a significant difference between the measured and predicted SWCC curves of Moreland clay because the family of SWCC curves presented by Zapata [46] for plastic soil was dependent on two parameters only (i.e., percent passing the #200 US standard sieve and Plasticity index).

Figure 6 exhibits the SWCCs of expansive soils at different locations in the form of volumetric water content. Pressure plate test data of expansive soils from two locations in Texas (Dallas-Fort Worth International Airport in Irving, and South Arlington) were obtained from Puppala et al. [48], and suction potentials of these soils were compared with that of Moreland clay. Table 2 summarizes the SWCC fitting parameters of soils from three different locations with 95% confidence interval. The SWCCs of all three expansive soils exhibited similar suction characteristics. The only noticeable difference is that the saturated moisture content (at zero suction) of Moreland clay is much higher than those of the other two soils. This higher value indicates the more ability to hold up water or moisture content, which implies that the Moreland clay undergoes a more considerable swelling when hydrated.

Figure 7 demonstrates the shrinkage behavior for the expansive clay under investigation. Those theoretical lines representing different degrees of saturation were obtained from fundamental phase relationships and using  $G_s = 2.75$ . The initial

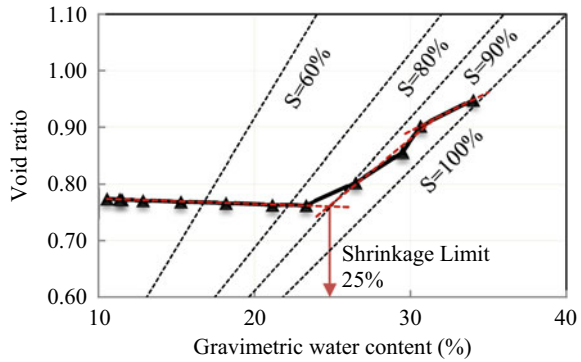
**Fig. 6** SWCCs with volumetric water content



**Table 2** SWCC fitting parameters of soils from different locations

Fitting parameters	Coefficients with 95% confidence bounds		
	Moreland clay	DFW soil	Arlington soil
<i>a</i>	171.2 (42.2, 300.1)	37.36 (26.49, 48.23)	128.1 (111.2, 145)
<i>m</i>	1.802 (1.163, 2.441)	0.2578 (0.1865, 0.3291)	0.312 (0.2565, 0.3676)
<i>n</i>	0.6725 (0.5808, 0.7641)	1.091 (0.7804, 1.402)	1.704 (1.412, 1.996)

**Fig. 7** Shrinkage curve of Moreland clay



unsaturated samples were wetted to achieve the near-saturation conditions and consequently desaturated by applying different suction values. The data depicted in Fig. 7 show an S-shaped shrinkage curve for the compacted sample and the dynamic drying of the investigated expansive soil. The curve is composed of an initial low structural shrinkage pursued by a sharp decrease during normal shrinkage, and after that, by a low decrease during residual shrinkage [49]. Three linear relationships between void ratio and gravimetric water content were obtained from the shrinkage curve of Moreland clay. Equations 2, 3, and 4 represent void ratio as a function of gravimetric water content (*w* in %) at different shrinkage stages, i.e., structural shrinkage ( $e_s$ ), normal shrinkage ( $e_n$ ), and residual shrinkage ( $e_r$ ), respectively. Al-Dakheeli and Bulut [50] reported that the slope of the normal shrinkage curve at equilibrium becomes nearly parallel to the saturation line. The shrinkage curve of Moreland clay depicted similar results. It can be presumed that, during the residual shrinkage, air enters the pores near the shrinkage limit and dismantles the particles that were assembled together because of suction.

$$e_s = 0.0138w + 0.479 \quad \text{for } w \geq 32 \tag{2}$$

$$e_n = 0.0226w + 0.2005 \quad \text{for } 25 \leq w < 32 \tag{3}$$

$$e_r = -0.009w + 0.7838 \quad \text{for } w < 25 \quad (4)$$

Deformation of the expansive subgrade soil is a function of moisture suction in the soil due to climate changes, and it affects the pavement resting on expansive soil. Ikra and Wang [51] simulated the moisture distribution and calculated the heave and shrinkage-induced vertical deformation of the expansive subgrade soils subjected to extreme weather conditions. Khan [42] adopted the distribution of moisture content and the subsequent subgrade deformations across the pavement cross section to analyze the structural behavior of the pavement. Solutions for the pavement structural properties, i.e., shear forces, and bending moments were obtained, and a case study was carried out on the research road farm to market 2 (FM 2) in Texas to validate the results [52–55]. It tends to be noticed that the soil–water retention properties obtained from this research can potentially be used for analyzing distresses on the pavement caused by expansive Moreland clay.

## 4 Conclusion

Knowledge of unsaturated soil properties for shear strength, permeability, and volume change of compacted expansive clays is pivotal for construction because of their relationships to the stability of slopes and bearing capacity of foundations. Laboratory investigation on highly expansive Moreland clay was conducted to determine the unsaturated soil properties following ASTM D6836 using compacted samples. The main conclusions of this research are summarized as follows: The SWCC had the AEV of 50 kPa, the residual suction of 7000 kPa, and the residual volumetric water content of 5%. Moreover, the shrinkage curve of Moreland clay was observed to be S-shaped. It also incorporated a low structural shrinkage followed by a sharp decrease during normal shrinkage, which is nearly parallel to the saturation line, and subsequently by a low decrease during residual shrinkage. The drying gravimetric water content SWCC and the proposed equations for three different shrinkage stages of Moreland clay will allow us to characterize the unsaturated portion of the expansive soil profile similar to that used in saturated soil mechanics. Data from the ongoing characterization of Moreland clay have indicated further that Moreland clay is a highly expansive soil. Prediction of unsaturated soil deformation from soil–water retention properties will encourage geotechnical and pavement engineers to design pavements by considering expansive subgrade soil-induced distresses.

**Acknowledgements** The authors would like to express their gratitude to Mr. Daniel Thompson at Aillet, Fenner, Jolly & McClelland, Mr. Gary Hubbard at Greater Bossier Economic Development Foundation, and Dr. Shams Arafat for their assistance in selecting soil sampling sites and soil sample collection. Some suggestions during weekly discussions from Dr. Ling Cao, a visiting professor from China Three Gorges University, were appreciated.

## References

1. Fredlund DG, Rahardjo H, Fredlund MD (2012) *Unsaturated soil mechanics in engineering practice*, 2nd edn. John Wiley and Sons, Hoboken, NJ
2. Brooks R, Corey T (1964) Hydraulic properties of POROUS MEDIA. *Hydrol Pap Color State Univ* 24:37
3. Mualem Y (1976) A new model for predicting the hydraulic conductivity of unsaturated porous media. *Water Resour Res* 12:513–522. <https://doi.org/10.1029/WR012i003p00513>
4. Van Genuchten MT (1980) A closed-form equation for predicting the hydraulic conductivity of unsaturated soils. *Soil Sci Soc Am J* 44:892–898. <https://doi.org/10.2136/sssaj1980.03615995004400050002x>
5. Fredlund DG, Xing A (1994) Equations for the soil-water characteristic curve. *Can Geotech J* 31:521–532. <https://doi.org/10.1139/t94-061>
6. Kosugi K (1996) Lognormal distribution model for unsaturated soil hydraulic properties. *Water Resour Res* 32:2697–2703. <https://doi.org/10.1029/96WR01776>
7. Seki K (2007) SWRC Fit—a nonlinear fitting program with a water retention curve for soils having unimodal and bimodal pore structure. *Hydrol Earth Syst Sci Discuss* 4:407–437
8. Leong EC, Rahardjo H (1997) Review of soil-water characteristic curve equations. *J Geotech Geoenviron Eng* 123:1106–1117. [https://doi.org/10.1061/\(ASCE\)1090-0241\(1997\)123:12\(1106\)](https://doi.org/10.1061/(ASCE)1090-0241(1997)123:12(1106))
9. Chen FH (2012) *Foundations on expansive soils*. Elsevier
10. Al-Rawas AA, Goosen MFA (2006) *Expansive soils: recent advances in characterization and treatment*, 1st edn. CRC Press
11. Nelson JD, Chao KC, Overton DD, Nelson EJ (2015) *Foundation engineering for expansive soils*. Wiley Online Library
12. Erzincin Y, Erol O (2007) Swell pressure prediction by suction methods. *Eng Geol* 92:133–145. <https://doi.org/10.1016/j.enggeo.2007.04.002>
13. Khan MA, Wang JX, Patterson WB (2017) Swelling–shrinkage properties of expansive Moreland clay. *PanAm Unsaturated Soils 2017*:100. <https://doi.org/10.1061/9780784481707.011>
14. Khan MA, Wang JX, Patterson WB (2019) A study of the swell-shrink behavior of expansive Moreland clay. *Int J Geotech Eng* 13:205–217. <https://doi.org/10.1080/19386362.2017.1351744>
15. Adem HH, Vanapalli SK (2015) Prediction of the modulus of elasticity of compacted unsaturated expansive soils. *Int J Geotech Eng* 9:163–175. <https://doi.org/10.1179/1939787914Y.0000000050>
16. Chiu CF, Yan WM, Yuen K-V (2012) Reliability analysis of soil–water characteristics curve and its application to slope stability analysis. *Eng Geol* 135:83–91. <https://doi.org/10.1016/j.enggeo.2012.03.004>
17. Likos WJ, Song X, Xiao M et al (2019) *Fundamental challenges in unsaturated soil mechanics. Geotechnical fundamentals for addressing new world challenges*. Springer, Berlin, pp 209–236
18. Rao BH, Venkataramana K, Singh DN (2011) Studies on the determination of swelling properties of soils from suction measurements. *Can Geotech J* 48:375–387. <https://doi.org/10.1139/T10-076>
19. Hunt AG (2004) Comparing van genuchten and percolation theoretical formulations of the hydraulic properties of unsaturated media. *Vadose Zo J* 3:1483–1488. <https://doi.org/10.2136/vzj2004.1483>
20. Marinho FAM, Oliveira OM, Adem H, Vanapalli S (2013) Shear strength behavior of compacted unsaturated residual soil. *Int J Geotech Eng* 7:1–9. <https://doi.org/10.1179/1938636212Z.0000000011>
21. Rassam DW, Cook F (2002) Predicting the shear strength envelope of unsaturated soils. *Geotech Test J* 25:215–220. <https://doi.org/10.1520/GTJ11365J>

22. Tahasildar J, Erzlin Y, Rao BH (2018) Development of relationships between swelling and suction properties of expansive soils. *Int J Geotech Eng* 12:53–65. <https://doi.org/10.1080/19386362.2016.1250040>
23. Vanapalli SK, Fredlund DG, Pufahl DE, Clifton AW (1996) Model for the prediction of shear strength with respect to soil suction. *Can Geotech J* 33:379–392. <https://doi.org/10.1139/t96-060>
24. Watabe Y, LeBihan J-P, Leroueil S (2006) Probabilistic modelling of saturated/unsaturated hydraulic conductivity for compacted glacial tills. *Géotechnique* 56:273–284. <https://doi.org/10.1680/geot.2006.56.4.273>
25. Fredlund DG (2018) State of practice for use of the soil-water characteristic curve (SWCC) in geotechnical engineering. *Can Geotech J* 1–11. <https://doi.org/10.1139/cgj-2018-0434>
26. Akin ID, Likos WJ (2020) Suction Stress of clay over a wide range of saturation. *Geotech Geol Eng* 38:283–296. <https://doi.org/10.1007/s10706-019-01016-7>
27. Peron H, Hueckel T, Laloui L, Hu LB (2009) Fundamentals of desiccation cracking of fine-grained soils: experimental characterisation and mechanisms identification. *Can Geotech J* 46:1177–1201. <https://doi.org/10.1139/T09-054>
28. Frydman S, Baker R (2009) Theoretical soil-water characteristic curves based on adsorption, cavitation, and a double porosity model. *Int J Geomech* 9:250–257. [https://doi.org/10.1061/\(ASCE\)1532-3641\(2009\)9:6\(250\)](https://doi.org/10.1061/(ASCE)1532-3641(2009)9:6(250))
29. Khan MA, Wang JX, Sarker D (2018) Stabilization of highly expansive moreland clay using class-C fly ash geopolymer (CFAG). *IFCEE* 2018:505–518. <https://doi.org/10.1061/9780784481592.050>
30. Sarker D, Apu OS, Kumar N, et al (2021) Application of sustainable lignin stabilized expansive soils in highway subgrade. In: *International Foundations Congress & Equipment Expo 2021*. Dallas, TX. <https://doi.org/10.1061/9780784483435.033>
31. Tu H, Vanapalli SK (2016) Prediction of the variation of swelling pressure and one-dimensional heave of expansive soils with respect to suction using the soil-water retention curve as a tool. *Can Geotech J* 53:1213–1234. <https://doi.org/10.1139/cgj-2015-0222>
32. ASTM D1452 (2016) Standard practice for soil exploration and sampling by auger borings. *ASTM Int.* [https://doi.org/10.1520/D1452\\_D1452M-16](https://doi.org/10.1520/D1452_D1452M-16)
33. ASTM D4220 (2014) Standard practices for preserving and transporting soil samples. *ASTM Int.* [https://doi.org/10.1520/D4220\\_D4220M-14](https://doi.org/10.1520/D4220_D4220M-14)
34. ASTM D1557 (2012) Standard test methods for laboratory compaction characteristics of soil using modified effort (56,000 ft-lbf/ft<sup>3</sup> (2,700 kN-m/m<sup>3</sup>)). *ASTM Int.* <https://doi.org/10.1520/D1557-12E01>
35. ASTM D2216 (2019) Standard Test methods for laboratory determination of water (moisture) content of soil and rock by Mass. *ASTM Int.* <https://doi.org/10.1520/D2216-19>
36. ASTM D854 (2014) Standard test methods for specific gravity of soil solids by water pycnometer. *ASTM Int.* <https://doi.org/10.1520/D0854-14>
37. ASTM D4318 (2017) Standard test methods for liquid limit, plastic limit, and plasticity index of soils. *ASTM Int.* <https://doi.org/10.1520/D4318-17E01>
38. ASTM D6913 (2017) Standard test methods for particle-size distribution (gradation) of soils using sieve analysis. *ASTM Int.* [https://doi.org/10.1520/D6913\\_D6913M-17](https://doi.org/10.1520/D6913_D6913M-17)
39. ASTM D2487 (2017) Standard practice for classification of soils for engineering purposes (unified soil classification system). *ASTM Int.* <https://doi.org/10.1520/D2487-17E01>
40. ASTM D6836 (2016) Standard test methods for determination of the soil water characteristic curve for desorption using hanging column, pressure extractor, chilled mirror hygrometer, or centrifuge. *ASTM Int.* <https://doi.org/10.1520/D6836-16>
41. Suits LD, Sheahan TC, Perez-Garcia N et al (2008) An oedometer-type pressure plate SWCC apparatus. *Geotech Test J* 31:100964. <https://doi.org/10.1520/GTJ100964>
42. Khan A (2017) Influence of moisture content distribution in soil on pavement and geothermal energy. PhD Dissertation, Programs of Civil Engineering and Construction Engineering Technology, Louisiana Tech University, Ruston, LA

43. Azam S, Ito M, Chowdhury R (2013) Engineering properties of an expansive soil. In: Proceedings of the 18th international conference on soil mechanics and geotechnical engineering, Paris
44. Fityus S, Buzzi O (2009) The place of expansive clays in the framework of unsaturated soil mechanics. *Appl Clay Sci* 43:150–155. <https://doi.org/10.1016/j.clay.2008.08.005>
45. Ramirez EF (2013) Introducing unsaturated soil mechanics to undergraduate students through the net stress concepts. M.S. Thesis, Arizona State University
46. Zapata CE (1999) uncertainty in soil-water characteristic curve and impacts on unsaturated shear strength predictions. Ph.D. Thesis, Arizona State University, Tempe, AZ
47. Zapata C, Houston WN, Houston S, Walsh KD (2000) Soil-water characteristic curve variability. In: The GeoDenver 2000-unsaturated soils sessions ‘advances in ultrasound geotechnical’. ASCE, pp 84–124. [https://doi.org/10.1061/40510\(287\)](https://doi.org/10.1061/40510(287))
48. Puppala AJ, Punthutaecha K, Vanapalli SK (2006) Soil-water characteristic curves of stabilized expansive soils. *J Geotech Geoenviron Eng* 132:736–751. [https://doi.org/10.1061/\(ASCE\)1090-0241\(2006\)132:6\(736\)](https://doi.org/10.1061/(ASCE)1090-0241(2006)132:6(736))
49. Haines WB (1923) The volume-changes associated with variations of water content in soil. *J Agric Sci* 13:296–310. <https://doi.org/10.1017/S0021859600003580>
50. Al-Dakheeli H, Bulut R (2019) Interrelationship between elastic deformation and soil-water characteristic curve of expansive soils. *J Geotech Geoenviron Eng* 145:04019005. [https://doi.org/10.1061/\(ASCE\)GT.1943-5606.0002020](https://doi.org/10.1061/(ASCE)GT.1943-5606.0002020)
51. Ikra BA, Wang JX (2017) Numerical simulation of moisture fluctuations in unsaturated expansive clay, heave/settlement predictions, and validation with field measurements. In: PanAm unsaturated soils. ASCE, pp 198–208. <https://doi.org/10.1061/9780784481707.021>
52. Khan MA, Wang JW (2017) Application of Euler-Bernoulli beam on winkler foundation for highway pavement on expansive soils. In: Proceedings of PanAm-UNSAT 2017: Second Pan-American Conference on Unsaturated Soils, ASCE. <https://doi.org/10.1061/9780784481691.023>
53. Sarker D, Wang JX, Khan MA (2019) Development of the virtual load method by applying the inverse theory for the analysis of geosynthetic-reinforced pavement on expansive soils. In: Geotechnical special publication. American Society of Civil Engineers, Reston, VA, pp 326–339. <https://doi.org/10.1061/9780784482124.034>
54. Khan MA, Wang JX, Sarker D (2020) development of analytic method for computing expansive soil–induced stresses in highway pavement. *Int J Geomech* 20. [https://doi.org/10.1061/\(ASCE\)GM.1943-5622.0001511](https://doi.org/10.1061/(ASCE)GM.1943-5622.0001511)
55. Wang JX, Sarker D, Ikra B (2018) Development of a mechanistic-based design method for geosynthetic-reinforced pavement on expansive soils and prediction of moisture content fluctuations in subgrades. Southern Plain Transportation Center, Norman, OK



# Rainfall-Induced Deformation on Unsaturated Collapsible Soils



Hamed Moghaddasi, Ashraf Osman, David Toll, and Nasser Khalili

**Abstract** The stability of transportation infrastructure can be affected by seasonal rainfall infiltrated adjacent excavations and natural slopes. The paper investigates the rainfall-induced deformation of an anchored excavation constructed in unsaturated soils. An advanced constitutive model based on the theory of bounding surface plasticity is employed to predict the behaviour of partially saturated soils. The collapse characteristics of unsaturated soils due to wetting are captured in the model by introducing a suction-dependent hardening law. The proposed model has been implemented in a finite difference code with a two-phase flow and deformation formulation. In the numerical algorithms, the validity of the effective stress principle in unsaturated soils is emphasized and the coupling between various phases of porous media has been considered. The problem of an anchored excavation subjected to rainfall is then simulated with the implemented model. The lateral deformation of the supported excavation during the infiltration of water into unsaturated collapsible soils is obtained and compared with the case where the plastic collapse is prevented. Finally, the effect of anchors on minimizing and changing the mode of the deformation is explored.

**Keywords** Rainfall · Unsaturated soils · Constitutive model

## 1 Introduction

The infiltration of rainfall into slopes and excavations poses a serious threat to the safety and stability of infrastructure built on them. Due to the extensive presence of unsaturated soils across the globe, research on rainfall-induced deformation has been an important development in unsaturated soil mechanics. Rainfall seepage can

---

H. Moghaddasi (✉) · A. Osman · D. Toll  
Department of Engineering, Durham University, South Road, Durham DH1 3LE, UK  
e-mail: [hamed.moghaddasi@durham.ac.uk](mailto:hamed.moghaddasi@durham.ac.uk)

N. Khalili  
School of Civil and Environmental Engineering, UNSW Australia, Kensington, NSW 2052, Australia



increase the pore water pressure inside unsaturated soils, leading to a drop in the effective stress thus generating deformation. On the other hand, the infiltration process can substantially alter the hydraulic properties of soils due to the change of the porosity. To explain properly the above hydro-mechanical process, the employment of a coupled flow and deformation model is required [1].

The reduction of the suction during seepage not only creates recoverable deformation via changing the effective stress but also can trigger irreversible wetting-induced collapse. The latter effect of the rainfall cannot be explained successfully by the constitutive models available for saturated soils. With the aid of a coupled multi-phase plasticity model, Cho and Lee [2] investigated the behaviour of a slope subjected to rainfall infiltration. The extended Mohr–Coulomb failure criterion was adopted for the plasticity modelling, and the effect of the change in porosity due to the suction was addressed by a state surface suggested by Lloret and Alonso [3]. This model has been used by Alonso [4] to assess the stability of a slope in overconsolidated clay under rainfall. The mixture theory for multi-phase porous media with an effective stress based plasticity model has been used by Oka et al. [5] to analyse the problem of the seepage through river embankments. Adopting the extended cam-clay model for solid phase, Borja and White [6] conducted a numerical analysis for rainfall-induced deformation of a steep slope and determined the failure mechanism. Recently, Zheng et al. [7] implemented a preliminary unsaturated model (the basic Barcelona model) in a finite difference code. They analysed a steep slope subjected to the rainfall infiltration and predict a wetting-induced plastic deformation.

Most of the fully coupled formulations cited above incorporated preliminary constitutive model for the solid phase and therefore fail to explain comprehensively the collapse behaviour of unsaturated soils. Also, incorporating a constitutive model with independent stress variables will reduce the applicability of the models since a time-consuming process is required for the determination of the model parameters. To overcome these deficiencies, the paper aims at implementing an advanced plasticity model in a coupled hydro-mechanical finite difference code (FLAC). A bounding surface plasticity model is adopted for the constitutive modelling of the solid phase (Khalili et al. [8], Russel and Khalili [9]). The model enjoys the validity of the effective stress principle and includes the hardening effect of suction. The problem of rainfall infiltration into an anchored excavation is then simulated to show the susceptibility of unsaturated soils to wetting collapse.

## **2 Effective Stress Principle, Water Retention and Permeability Model**

From the conceptual viewpoint, the mechanical behaviour of unsaturated soils can be theoretically formulated within the principles explaining the behaviour of multi-phase porous media. For single-phase media, Terzaghi's effective stress law can describe many features of the behaviour of saturated soils. It has been shown that

this theory can be generalized for two-phased porous media as

$$\sigma' = \sigma + \chi p_w \delta + (1 - \chi) p_g \delta = \sigma_{\text{net}} - \chi s \delta \tag{1}$$

where  $\sigma'$  is what we shall call “effective stress”,  $\sigma$  is total stress,  $\delta$  stands for the identity vector,  $\chi$  is the “effective stress” parameter,  $p_w$  and  $p_g$  are wetting (water) and non-wetting (air) pressures,  $s = p_g - p_w$  is the matric suction and  $\sigma_{\text{net}} = \sigma + p_g \delta$  is the net stress. The “effective stress” parameter is a key variable in the above equation. In this study, the wetting degree of saturation,  $S_w$ , has been regarded as the “effective stress” parameter despite the fact that more elaborate relationships, which can better predict the results of experimental data, can be utilized for this parameter (see [10]). The degree of saturation can be expressed in terms the matric suction, which is recognized as the water retention model. Following the work of the van Genuchten [11], the effective degree of saturation can be linked to matric suction as

$$S_{\text{eff}} = \left[ 1 + \left( \frac{S}{p_0} \right)^{1/(1-a)} \right]^{-a} \tag{2}$$

where  $p_0$  and  $a$  are two material parameters, the former has a close link to the suction related to air-entry or air expulsion values and  $S_{\text{eff}}$  is effective degree of saturation defined as  $S_{\text{eff}} = (S_w - S_r^w)/(1 - S_r^w)$ , where  $S_r^w$  is residual wetting fluid saturation. In two-phase porous media, the relative permeability laws for the wetting and non-wetting phases can be correlated to the effective degree of saturation. Aligned with the work of van Genuchten [11], the following expressions hold for the relative permeability models

$$k_r^w = S_{\text{eff}}^b \left[ 1 - \left( 1 - S_{\text{eff}}^{1/a} \right)^a \right]^2 \tag{3}$$

$$k_r^g = (1 - S_{\text{eff}})^c \left[ 1 - S_{\text{eff}}^{1/a} \right]^{2a} \tag{4}$$

where  $a$ ,  $b$  and  $c$  are model parameters and  $k_r^w$  and  $k_r^g$  are relative permeability of the wetting and non-wetting phases, respectively. Having defined the model’s empirical relationships, a theoretical framework based on the principle of the mass and momentum balance can follow to obtain the fluid constitutive laws (see [8]). To obtain a fully coupled flow and deformation model, the employment of the momentum balance equation for the solid phase is also necessary. The constitutive model for the solid phase can finally be obtained by introducing a stress–strain relationship capturing the essential features of the behaviour of unsaturated soil. In this study, an advanced model based on the theory of the bounding surface plasticity is used as the constitutive relationship of the solid phase.

### 3 Bounding Surface Plasticity Model

The bounding surface is the locus of the possible state of stress in the stress space. This surface can be determined from the response of the unsaturated soils in the loosest state. A flexible shape is adopted for the shape of the bounding surface to accommodate versatile behaviour of unsaturated soil

$$F(\bar{p}', \bar{q}, \bar{\theta}, \bar{p}'_c) = \left[ \frac{\bar{q}}{M_{cs}(\bar{\theta}) \cdot \bar{p}'} \right]^N - \frac{\ln(\bar{p}'_c/\bar{p}')}{\ln(R)} = 0 \tag{5}$$

in which  $\bar{p}'_c$  adjusts the size of the bounding surface and  $N$  and  $R$  are material parameters. Further,  $\bar{p}'$ ,  $\bar{q}$ ,  $\bar{\theta}$  stands for the mean “effective stress”, deviatoric stress and lode angle on the bounding surface. It is noted that over-bar indicates parameters given on the bounding surface. It is clear from Eq. (5) that a three-dimensional shape is proposed for the bounding surface. The slope of the critical state line (CSL) has been denoted by  $M_{cs}(\bar{\theta})$  in Eq. (5), which can be expressed in terms of lode angle

$$M_{cs}(\bar{\theta}) = M_{\max} \left[ \frac{2\alpha^4}{1 + \alpha^4 - (1 - \alpha^4) \sin(3\bar{\theta})} \right]^{1/4} \tag{6}$$

where  $\alpha = M_{\max}/M_{\min}$  with  $M_{\max}$  and  $M_{\min}$  are the slope of CSL at triaxial compression and extension. The relationship between  $M_{\max}$  and  $M_{\min}$  is  $M_{\min} = 3M_{\max}/(M_{\max} + 3)$ . The movement of the stress point has been enforced to lie on the loading surface. In this study, an identical shape has been adopted for the loading surface as for the bounding surface assuming that both surfaces are homologous about a centre of homology. The origin of the stress is taken as the centre of homology in this study. Specifying the direction of the plastic strain is another ingredient of the plasticity model involved. Following the work of Russell and Khalili [9], a non-associated plastic potential is selected

$$g(p', q, \theta, p_0) = q + \frac{AM_{cs}(\theta)p'}{A - 1} \left[ \left( \frac{p'}{p_0} \right)^{A-1} - 1 \right] \text{ for } A \neq 1$$

$$g(p', q, \theta, p_0) = q + M_{cs}(\theta)p' \ln \left( \frac{p'}{p_0} \right) \text{ for } A = 1 \tag{7}$$

in which  $A$  is the material parameter and  $p_0$  indicates the size of the plastic potential surface. The last ingredient of the bounding surface plasticity is to identify hardening modules. Following the usual procedure in the theory of the bounding surface plasticity, the hardening module can be decomposed into two terms

$$h = h_b + h_f \quad (8)$$

where  $h_b$  is the hardening modulus on the bounding surface and  $h_f$  is the hardening modulus depending on the distance of the stress point from an conjugate point on the bounding surface. Proposing a hardening modulus as a function of the distance to the bounding surface ensures that smooth elasto-plastic behaviour can be achieved. The following functions can be taken for these moduli (see Khalili et al. [8])

$$h_b = -\frac{\partial F}{\partial \bar{p}'_c} \left( \frac{\partial \bar{p}'_c}{\partial \varepsilon_v^p} + \frac{\partial \bar{p}'_c}{\partial s} \frac{\dot{s}}{\dot{\varepsilon}_v^p} \right) \frac{m_p}{\|\partial F / \partial \bar{\sigma}'\|} \quad (9)$$

$$h_f = \left( \frac{\partial \bar{p}'_c}{\partial \varepsilon_v^p} + \frac{\partial \bar{p}'_c}{\partial s} \frac{\dot{s}}{\dot{\varepsilon}_v^p} \right) \frac{p'}{\bar{p}'_c} \left( \frac{\bar{p}'_c}{p'_c} - 1 \right) k_m (\eta_p - \eta)$$

in which  $\dot{\varepsilon}_v^p$  is the increment for the plastic volumetric strain,  $k_m$  is a material parameter and  $m_p = \frac{\partial g}{\partial p'} / \left\| \frac{\partial g}{\partial \bar{\sigma}'} \right\|$ . Also,  $\eta = q/p$  is the stress ratio,  $\eta_p = (1 - 2(\nu - \nu_{cs}))M_{cs}(\theta)$  is the slope of the peak strength line,  $\nu$  is the specific volume defined as  $\nu = 1 + e$  and  $\nu_{cs}$  is the specific volume at CSL. It is obvious that both volumetric strain and matric suction can generate plastic deformation. This is a unique feature of the model for the simulation of the problems involving the effect of suction change and volumetric deformation. The simultaneous effect of the suction and volumetric strain on the evolution of the size of the bounding surface is predicted by

$$\bar{p}'_c(\varepsilon_v^p, s) = \bar{p}'_{ci} \gamma(s) \exp\left(\frac{\nu_i \Delta \varepsilon_v^p}{\lambda(s) - \kappa}\right) \quad (10)$$

with

$$\gamma(s) = \exp\left(\frac{N(s) - N(s_i)}{(\lambda(s) - k)} - \frac{(\lambda(s) - \lambda(s_i))}{(\lambda(s) - k)} \ln(\bar{p}'_{ci})\right) \quad (11)$$

where  $\nu_i$  and  $\bar{p}'_{ci}$  are the initial specific volume and hardening parameter,  $k$  is the slope of unloading–reloading curve on  $\nu \sim \ln p'$  plane. Also  $N(s)$  and  $\lambda(s)$  are the intercept and slope of limiting isotropic compression line (LICL) on  $\nu \sim \ln p'$  plane at the suction  $s$ ,  $N(s_i)$  and  $\lambda(s_i)$  are corresponding parameters at the initial suction  $s_i$ . LICL can be obtained from the result of the isotropic compression test performed on the loosest soil sample.

### 4 Rainfall-Induced Deformation in an Anchored Excavation

The proposed constitutive model has been implemented in an explicit finite difference code (FLAC) as a user-defined constitutive model. To show the applicability of the model in predicting the response of collapsible soils, the problem of an excavation under rainfall infiltration is simulated. The geometry of the problem is depicted in Fig. 1. The hydraulic properties of the soil are available in Table 1. In this table,  $\mu_w$  and  $\mu_g$  are dynamic viscosity of wetting and non-wetting phases respectively. Also,  $K_w$  and  $K_g$  are bulk modules for wetting and non-wetting phases and  $\kappa_p$  is saturated mobility coefficient defined as the ratio of intrinsic permeability over dynamic viscosity of the water phase. The material properties for the solid skeleton

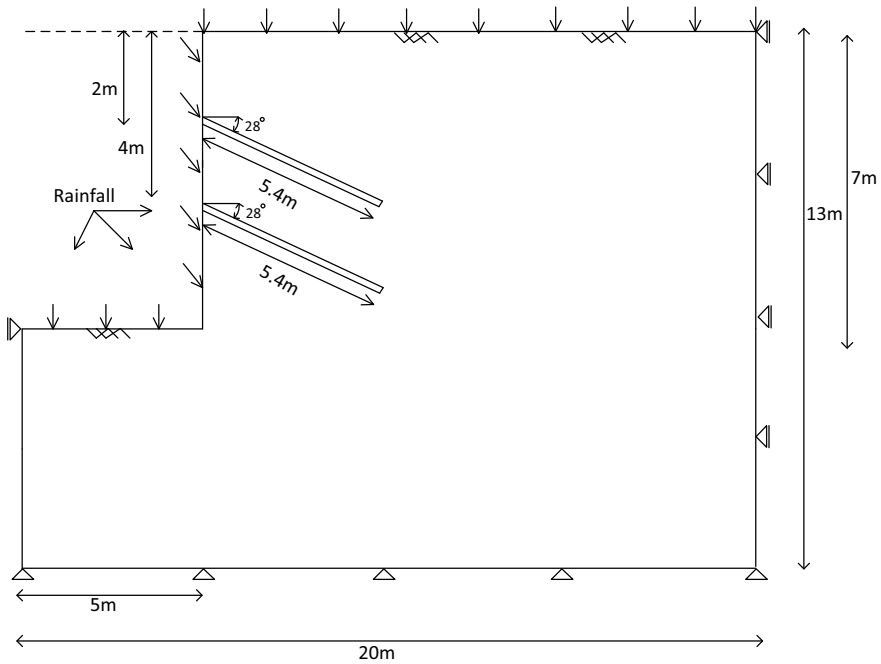


Fig. 1 Sketch of the excavation problem subjected to rainfall

Table 1 Hydraulic properties for soil

$P_0$ (kPa)	$a$	$b$	$c$	$S_{res}$
7	0.58	0.5	0.33	0
$\mu_w/\mu_g$	$K_w$ (MPa)	$K_g$ (Pa)	$\kappa_p$ (m <sup>2</sup> /Pa.s)	
55	2	20	1e - 8	

**Table 2** Mechanical properties of soil

$\kappa$	$\nu$	$M_{cs}$	$N$	$R$	$A$	$k_m$
0.05	0.2	1.1	1.44	2	2	20

**Table 3** Suction-dependent LICL for soil

Suction (kPa)	$s < s_{ae} = 100$	700
$\lambda(s)$	0.2	0.2
$N(s)$	3.112	3.212

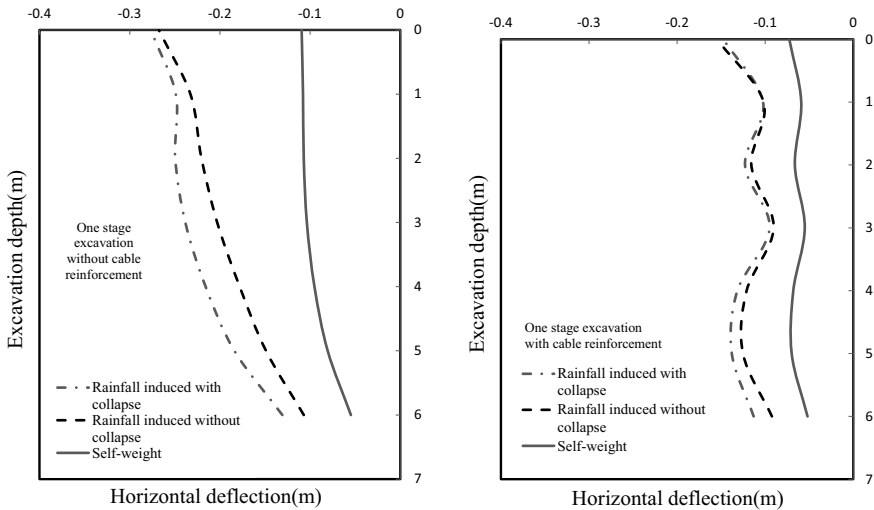
**Table 4** Mechanical properties for anchor

Young’s modulus (GPa)	Yield strength (kN)	Cross section (m <sup>2</sup> )
210	250	5e – 4
Bond stiffness (N/m/m)	Bond strength (N/m)	Spacing (m)
1.5e10	8e5	5

are defined in Tables 2 and 3. In these tables, the elastic parameters of the model (e.g.  $\kappa$  and  $\nu$ ) are determined through calculating the initial tangent stiffness obtained from the stress–strain curve under shearing. The parameters related to the critical state condition ( $M_{cs}$  and  $A$ ) are obtained in the ultimate state of soils achieved in the residual state. The analyses of the behaviour of soils under isotropic loading with various suction indicate the  $\lambda(s)$  and  $N(s)$  from which the model parameters  $R$  have been determined.  $k_m$  is a fitting parameter adjusting the hardening modules during unloading reloading cycles. The parameter  $N$  can also be determined through the shape of bounding surface obtained in the loosest state of saturated soil. Finally, the mechanical properties for anchors are introduced in Table 4.

The unsaturated soil with initial suction of 700 kPa is assumed for the soil behind the wall. The initial specific volume is assigned based on the assumption that the preconsolidation pressure for the whole layer is 1400 kPa. To simulate the effect of rainfall infiltration, zero suction was applied at the ground surface and the inner face of the excavation, which is equivalent to full saturation for the wetting phase. Also a seepage boundary condition was employed at the bottom of excavation to absorb the flow of wetting phase (boundary is impermeable until degree of saturation is 1; afterwards the pore water pressure is set to zero). It is assumed that all of the excavated area was removed in one stage. The suction-dependent LICL was updated during the wetting simulation to reduce the strength of the unsaturated soils, capturing the plastic collapse behaviour.

The horizontal deflection of the excavation was obtained for the case where there was no rainfall on the top surface of the soil (the effect of the self-weight only) and compared to the excavation problem subjected to the rainfall. Also the effect of plastic collapse due to wetting was included in the simulation. This was achieved by



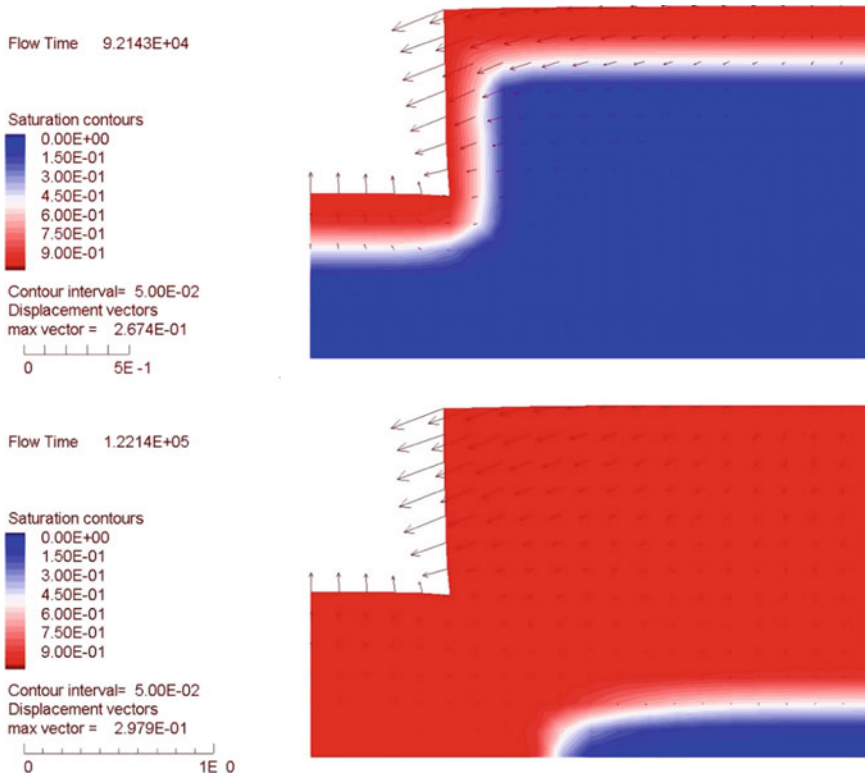
**Fig. 2** Horizontal deflection of an excavation **a** without the instalment of anchors and **b** with instalment of anchors

simulating the excavation problem under single LICL (the strength corresponding to the suction of 700 kPa) and comparing the result with the case of an excavation with suction-dependent LICL. In Fig. 2, the horizontal deflection of the excavation is depicted for the three cases described above. For an unanchored excavation, the increase of the horizontal deflection is predicated upon wetting. If the suction-dependent strength parameters were not involved in the analysis, the model could only predict the excess deflection due to the decrease of the effective stress. However, the full wetting collapse behaviour can be achieved if the variation of the LICL with respect to the matric suction is included.

A similar pattern can be seen for the horizontal deflection of an anchored excavation (see Fig. 2), while different modes of deformation are obtained upon the plastic collapse of the sample. It is also evident that employing anchors can reduce significantly the lateral deflection of the excavation. The change in the degree of saturation during the simulation is depicted in Fig. 3 for the excavation with suction-dependent LICL. It can be seen that there is vertical settlement on the surface of the soil when rainfall penetrates into the soil. Also, large amount of the horizontal deflection occurs if the rainfall infiltrates into the soils.

## 5 Conclusion

The paper studied the deformation of an anchored excavation built on unsaturated soils subjected to rainfall infiltration. Unsaturated soils consist of three phases possessing independent compressibility properties. Relationships for the “effective



**Fig. 3** Change in the degree of saturation and deformation vectors without collapse behaviour **a**  $t = 25$  h (9e4 seconds) and **b**  $t = 34$  h (1.22e5 seconds)

stress” law, degree of saturation and the relative permeability are introduced, which all rely on the variation of suction as a main variable. A non-associated bounding surface plasticity model was developed to predict the behaviour of solid phase. The model offers smooth elasto-plastic behaviour within the bounding surface since a hardening modulus proportional to the distance of the stress point from the image point on the bounding surface is advised. The wetting-induced collapse of unsaturated soils is captured via defining a suction-dependent hardening modulus. A user-defined constitutive model has been written and embedded in an existing finite difference code. With the aid of a coupled flow and deformation model, an anchored excavation under rainfall infiltration is simulated. It has been shown that noticeable lateral deflections can occur if the strength reduction due to the drop of the suction value is permitted in the model. The amount of these deflections can be decreased substantially if a proper set of anchors are installed on the side-wall of the excavation. Finally, the change of degree of saturation during the simulation has been depicted for the whole domain of the problem.



## References

1. Tsaparas I, Rahardjo H, Toll DG, Leong EC (2002) Controlling parameters for rainfall-induced landslides. *Comput Geotech* 29(1):1–27
2. Cho SE, Lee SR (2001) Instability of unsaturated soil slopes due to infiltration. *Comput Geotech* 28(3):185–208
3. Lloret A, Alonso EE, (1980) Consolidation of unsaturated soils including swelling and collapse behaviour. *Géotechnique* 30(4):449–477
4. Alonso EE, Gens A, Delahaye CH (2003) Influence of rainfall on the deformation and stability of a slope in overconsolidated clays: a case study. *Hydrogeol J* 11(1):174–192
5. Oka F, Kimoto S, Takada N, Gotoh H, Higo Y (2010) A seepage-deformation coupled analysis of an unsaturated river embankment using a multiphase elasto-viscoplastic theory. *Soils Found* 50(4):483–494
6. Borja RI, White JA (2010) Continuum deformation and stability analyses of a steep hillside slope under rainfall infiltration. *Acta Geotech* 5(1):1–14
7. Zheng Y, Hatami K, Miller GA (2017) Numerical simulation of wetting-induced settlement of embankments. *J Perform Constructed Facil* 31(3):D4017001
8. Khalili N, Habte MA, Zargarbashi S (2008) A fully coupled flow deformation model for cyclic analysis of unsaturated soils including hydraulic and mechanical hystereses. *Comput Geotech* 35(6):872–889
9. Russell AR, Khalili N (2006) A unified bounding surface plasticity model for unsaturated soils. *Int J Numer Anal Methods Geomech* 30(3):181–212
10. Khalili N, Khabbaz MH (1998) A unique relationship of  $\chi$  for the determination of the shear strength of unsaturated soils. *Geotechnique* 48(5)
11. Van Genuchten MT (1980) A closed-form equation for predicting the hydraulic conductivity of unsaturated soils. *Soil Sci Soc Am J* 44(5):892–898

# Experimental Study on the Effect on Stress Release Holes to Decrease Frost Heaves of Fine Particle Fillers in Northern China



Tianxiao Tang, Yupeng Shen, Xin Liu, and Ruifang Zuo

**Abstract** Seasonal frozen ground is mainly distributed in the north of 30°N, with an area of 5.137 million km<sup>2</sup>, covering approximately 53.5% of the national territory in China. In recent years, with the rapid development of Chinese railway, many lines have been built passing through seasonal frozen areas. At the same time, with the increase of traffic volume, transport capacity would become larger year by year, so the requirements of low frost heave for the subgrades would also be made more stringent. Based on the stress release holes (SRHs), several special experiments are designed and implemented in a one-dimensional freezing condition from a sample's top to bottom, which are targeted to verify the effectiveness and feasibility of SRHs on decreasing frost heaves. Also, a measure to decrease frost heave of subgrade filler in seasonal frozen area is proposed. There are seven laboratory tests carried out in the open system. And the frost heave effect of saturated soil samples within 72 h was explored with a certain HRA set as 4% and SRHs filling materials.

**Keywords** Seasonal frost soil · Stress release holes · Fine particle fillers · Frost heave · Moisture migration

## 1 Introduction

Frozen soil refers to a special soil containing ice with a temperature equal to or below 0 °C [1, 2]. Permafrost, seasonal frozen ground and short-term frozen soil cover about 50% of the global land area, of which seasonal frozen soil covers about

---

T. Tang · Y. Shen (✉) · X. Liu  
School of Civil Engineering, Beijing Jiaotong University, Beijing 100044, P.R. China  
e-mail: [yshen@bjtu.edu.cn](mailto:yshen@bjtu.edu.cn)

Y. Shen  
Beijing Engineering and Technology Research Center of Rail Transit Line Safety and Disaster Prevention, Beijing 100044, P.R. China

R. Zuo  
Road Traffic Design & Research Institute, China Railway Siyuan Survey and Design Group Co., LTD, Wuhan 430063, P.R. China

20% of the land area, and there are about 35% of highway and railway lines through this area. In China, seasonal frozen soil covers approximately 53.5% of the national territory, and there are about 75% of traffic lines operated in seasonal frost area [3, 4]. However, subgrade lesions, such as frost heaves or thaw settlement [5, 6], mud pumping [7, 8] and ballast subsidence [9, 10], are universal during the period of the operation, which would not only affect normal operation of railway lines, but also the traffic safety. There are many effective measures that have been proposed in a targeted manner. Compared with fine particle filler, coarse particle filler can obviously reduce subgrade frost heave [11]. The combined structure of insulation board, asphalt concrete pavement and gravel roadbed has verified the effect in frost heave deformation treatment [12]. In this paper, the effect of SRHs on decreasing frost heave is studied based on the one-dimensional freezing tests, which aim to propose a new idea for treating the frost heaving of the subgrade in the seasonal frost areas.

## 2 Description and Design of Tests

### 2.1 Physical Properties of Soil Samples

The sample soil in this study is taken from the filler of K222 + 800 to K223 + 300 mileage at the Shenmu–Shuozhou heavy-haul railway in Shanxi, China, because the frost heave of this section is more serious as shown in Fig. 1.

The tested soil is a low liquid limit silt, and the soil sample is dark yellow, which is a frost heave-sensitive soil. The particle distribution curve is shown in Fig. 2, and the physical parameters of the silt are shown in Table 1.

**Fig. 1** Damage of frost heave in winter



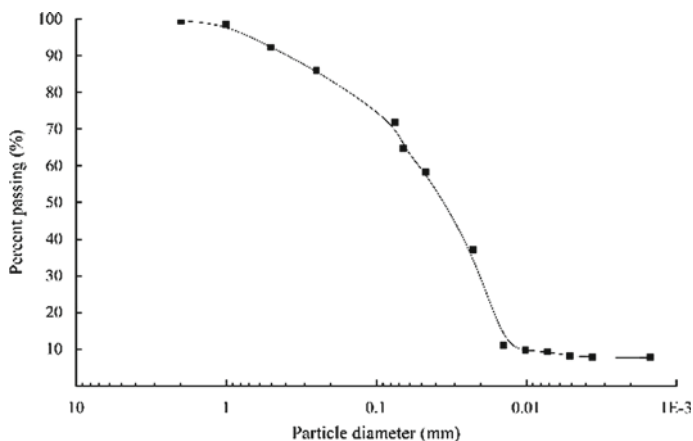


Fig. 2 Accumulative curve of particle size grading of the tested silt

Table 1 Physical parameters of the silt

Soil quality	Soil specific gravity	Liquid limit/%	Plastic limit/%	Plasticity index
Low liquid limit silt	2.745	25.2	17.2	8

## 2.2 Process and Method of Tests

In this paper, the results of 7 laboratory tests are analyzed, and the specific test plan is shown in Table 2. Prepared soil samples are placed in a low-temperature chamber with a constant temperature of 1 °C for 6 h. Then, temperature of the upper top plate (the cold end) is set to - 5 and 1 °C to the lower bottom plate (the warm end), and the water supplement system is turned on at the same time. Tests will last for 72 h. The diameter and height of the soil cylinder are both 150 mm. In the tests, water is supplied by Markov bottle connected with the lower bottom plate (the warm end), and SRHs

Table 2 Experimental conditions of one-dimensional freezing tests

Sample number	Compaction coefficient	Moisture content/%	HRA/%	Filling materials	Freezing time/h
1				/	
2				P1	
3				P2	
4	0.93	20.7	4%	P3	72
5				R1	
6				R2	
7				R3	

**Fig. 3** Soil sample with filling materials



are made through PVC pipe set at the soil sample. Two kinds of materials are selected as the filler of SRHs (Fig. 3), one is a mixture of polystyrene, asphalt and fiber with different proportions (P1, P2 and P3), and the other is a mixture of rubber, asphalt and fiber with different proportions (R1, R2 and R3). The frost heave is measured through the displacement dial indicator set in the upper top plate during the freezing process of the soil sample, and the moisture contents are determined at 10 mm intervals from the warm end as soon as possible after completing the tests.

Note: The hole ratio in area (HRA) is defined as the ratio of the area of the SRH to the sample's area and can be expressed as:

$$\text{HRA} = \left[ \frac{(\pi \cdot r^2)}{(\pi \cdot R^2)} \right] \times 100\% = r^2/R^2 \times 100\% \quad (1)$$

where HRA is the hole ratio in area (%);  $r$  is the radius of SRH (cm); and  $R$  is the radius of soil samples (cm).

The composition and proportioning scheme of the two filling materials are shown in Tables 3 and 4.

**Table 3** First filling material and ratio in quantity

Number	Mass fraction of polystyrene/%	Asphalt/g	Polystyrene/g	Fiber/g
P1	10	200.00	22.78	5.00
P2	15	200.00	36.18	5.00
P3	20	200.00	51.25	5.00

**Table 4** Second filling material and ratio in quantity

Number	Mass fraction of rubber/%	Asphalt/g	Rubber/g	Fiber/g
R1	75	10.00	36.00	2.00
R2	80	10.00	48.00	2.00
R3	85	10.00	68.00	2.00

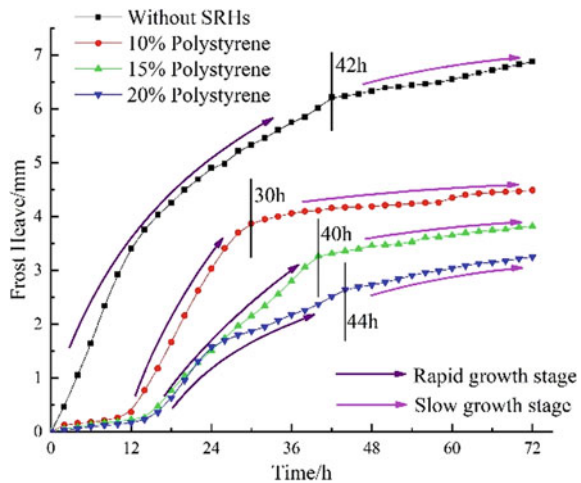
### 3 Analysis of Test Results

#### 3.1 Effect of Filling Materials on Frost Heave

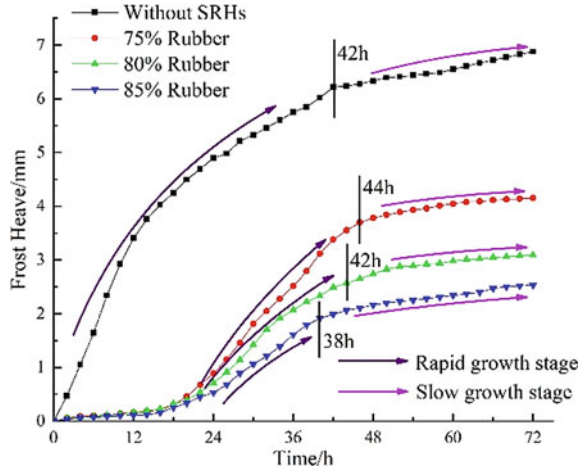
Figures 4 and 5 show the change process of frost heave deformation under different materials filled in the SRHs. According to Figs. 4 and 5, the deformation laws of soil samples are basically the same, and there are obvious phase characteristics during the freezing process which can be described as rapid growth stage and slow growth stage. However, the frost heave of soil samples with SRHs is significantly smaller than that without SRHs, and the development of frost heave also has obvious lag. The frost heave soil samples with SRHs occur with significant increment after 12–16 h.

Compared to frost heaves of the soil sample without SRHs of 6.887 mm after being frozen for 72 h, the soil samples with SRHs have frost heave values of 4.49 mm, 3.82 mm and 3.25 mm under the three conditions of 10% polystyrene, 15% polystyrene and 20% polystyrene, respectively, which are only 0.472–0.653 times that of the sample without SRHs; and the soil samples with SRHs have frost heave values of 4.15 mm, 3.09 mm and 2.53 mm under the three conditions of 75% rubber, 80% rubber and 85% rubber, respectively, which are only 0.368–0.603 times

**Fig. 4** Frost heave of soil samples for SRHs with polystyrene material



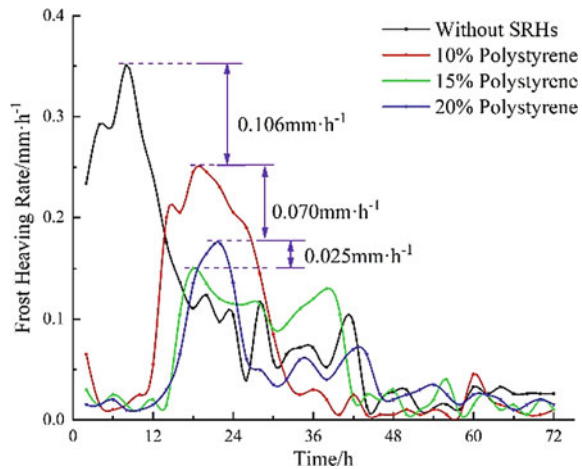
**Fig. 5** Frost heave of soil samples for SRHs with rubber material



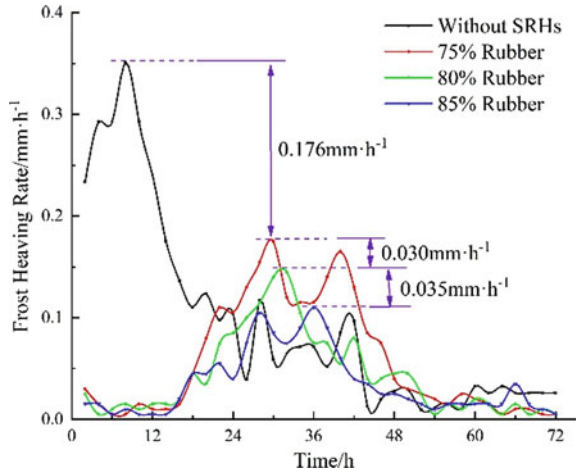
that of the sample without SRHs. The test results show that frost heave can be effectively decreased due to the existence of SRHs, and the effect has a great relationship with the ratio of the filling material in the SRHs, the higher the quality ratio of the skeleton material, the better the effect. Also, the type of the skeleton material has a certain influence on the effect. As can be seen from Figs. 4 and 5, the rubber material is superior to the polystyrene material.

It can be seen from the change of the soil frost heaving rate (Figs. 6 and 7) that the variation of the frost heaving rates of the soil samples with SRHs is smaller than that without SRHs. This is because the soil samples occur with frost heave along the radial direction of SRHs during the freezing process, and then the vertical frost heave would be reduced, so that the frost heaving rates of soil samples with SRHs change smaller.

**Fig. 6** Change of soil frost heaving rates for SRHs with polystyrene material



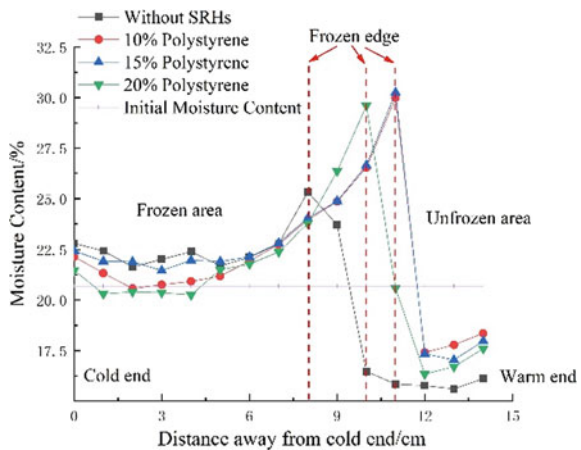
**Fig. 7** Change of soil frost heaving rates for SRHs with rubber material



### 3.2 Effect of Filling Materials on Moisture Migration

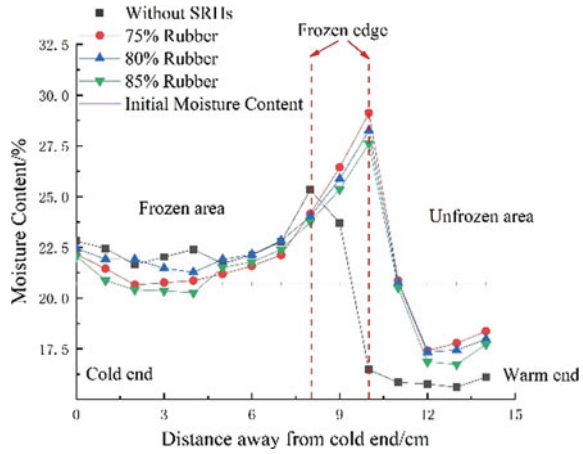
Figures 8 and 9 show the distribution of moisture content after 72 h. The moisture migrates obviously after soil samples frozen, the moisture content of the soil samples in frozen areas is higher than the initial value, and the content in the unfrozen area is lower than the initial content. Meanwhile, the maximum value appears at the frozen edge, and this is because the moisture continuously migrates from the unfrozen area to the frozen edge during the freezing process. Due to the existence of SRHs, the amount of moisture migration at the frozen edge of the soil samples with SRHs was significantly higher than that without SRHs, which indicates that in practical projects, the relationship between the SRHs and the height of the groundwater table should be considered.

**Fig. 8** Moisture content after soil frost heave for SRHs with polystyrene material





**Fig. 9** Moisture content after soil frost heave for SRHs with rubber material



**Table 5** Test results of the soil samples

Sample number	Maximum frost heave/mm	Maximum freezing depth/cm	Maximum frost heaving rate/%
1	6.88	11.86	5.80
2	4.49	13.08	3.43
3	3.82	12.88	2.97
4	3.25	12.72	2.55
5	4.15	12.81	3.24
6	3.09	12.11	2.55
7	2.53	11.93	2.12

## 4 Discussion

Table 5 shows the results of seven laboratory tests. The SRHs and filling materials would deform radially during the freezing process, so that frost heave of soil samples could be decreased effectively. Meanwhile, according to Table 5, rubber has a better effect than polystyrene as a skeleton material on decreasing frost heaves of fine particle fillers.

## 5 Conclusion

In order to study the effect of SRHs on soil frost heave, one-dimensional freezing tests were carried out, and there are three conclusions as follows:

- The frost heave could be decreased with SRHs filled with certain materials, and the effect is significantly obvious. The law of frost heave and moisture migration are basically the same, but moisture migration of soil samples with SRHs is enhanced obviously.
- The filling material in SRHs has a great influence on the frost heave. According to the tests result, rubber is more suitable than polystyrene as a skeleton material due to a better effect on decreasing frost heave.
- In contrast, the moisture migration enhances as a result of SRHs, so that it is recommended that, in practical applications, the size and depth of SRHs should be strictly controlled in consideration of the problem of water intrusion and damage to avoid groundwater intruding into the hole.

**Acknowledgements** This research was financially supported by the National Natural Science Foundation (NSFC) under grants (No. 41772330, No. 41731281 and No. 51578053) and the Scientific Research and Development Program of China Railway (No. P2018G004).

## References

1. Andersland OB, Ladanyi B (1994) An introduction to frozen ground engineering. Chapman and hall, New York
2. Andersland OB, Ladanyi B (2004) Frozen ground engineering. American society of civil engineers, New York
3. Chen XB, Liu JK, Liu HX, Wang YQ (2006) Frost action of soil and foundation engineering. Science Press, Beijing (In Chinese)
4. Xu XZ, Wang JC, Zhang LZ (2005) Frozen soil physics. Science Press, Beijing (In Chinese)
5. Wang TL, Yue ZR, Sun TC et al (2015) Influence of fines content on the anti-frost properties of coarse-grained soil. *Sci Cold Arid Reg* 7(4):407–413
6. Lanis A, Razuvaev D (2017) Systematization of features and requirements for geological survey of railroad subgrades functioning in cold regions. *Sci Cold Arid Reg* 9(3):205–212
7. Tang L, Tian S, Ling XZ et al (2017) Effect of freeze-thaw cycles on the strength of base course materials used under China's high-speed railway line. *J Cold Reg Eng* 31(4):1–12
8. Islam MR, Tarefder RA (2016) Effects of large freeze-thaw cycles on stiffness and tensile strength of asphalt concrete. *J Cold Regions Eng* 30(1):1–8
9. Niu FJ, Li AY, Luo J et al (2017) Soil moisture, ground temperatures, and deformation of a high-speed railway embankment in Northeast China. *Cold Reg Sci Technol* 133:7–14
10. Zhang XY, Zhang MY, Lu JG et al (2017) Effect of hydro-thermal behavior on the frost heave of a saturated silty clay under different applied pressures. *Appl Therm Eng* 117:462–467
11. Hou JF, Zhang RQ, Yu J (2015) Research on frost heaving of subgrade filling in seasonal frozen soil area. *Adv Mater Res* 165:783–787
12. Tai BW, Liu JK, Wang TF et al (2017) Numerical modelling of anti-frost heave measures of high-speed railway subgrade in cold regions. *Cold Reg Sci Technol* 141:28–35

# Numerical and Experimental Study of the Unsaturated Hydraulic Behavior of a Railroad Track Profile Considering Fouled Ballast Subjected to Tropical Climate Condition



Guilherme Castro, José Pires, Rosangela Motta, Robson Costa, Edson Moura, Liedi Bernucci, and Luciano Oliveira

**Abstract** Environmental actions and geotechnical characteristics are vital in the global behavior of railroad track. Climate, can be crucial to railroad geomaterials behavior, especially in tropical regions. In addition, railroad track behavior depends on water content, retention, and suction pressure over time, being dependent on geotechnical characteristics. These aspects directly influence the amount of water available to infiltrate into the soil, which can percolate or be retained, modifying its water content. Thus, unsaturated soil mechanics should be applied to assess climate–track interaction. This paper evaluated the unsaturated hydraulic response of a railroad track profile in Brazil considering fouled ballast under tropical climate conditions through laboratory tests and numerical simulations. Physical–hydraulic tests were performed with railroad track materials. A numerical FEM model was developed to evaluate the infiltration/suction profile and to quantify drainage, considering laboratory results, distinct fouling levels, and seasons. The results reveal that the hydraulic analysis of the track must consider the unsaturated condition of the materials, which will help to understand the ballast fouling influence on track in terms of hydraulic concerns. Significant suction variation was observed in the subballast when fines are strongly present. Thus, the presence of a fouled layer reduces water transfer to the subgrade due to its water barrier effect. Additionally, in the wet season, suction decreased over the fouled ballast in contrast to the one verified in the dry

---

G. Castro (✉) · J. Pires · R. Motta · R. Costa · E. Moura · L. Bernucci  
Polytechnic School University of São Paulo, Prof. Almeida Prado Ave. 83, Butantã, SP, Brazil  
e-mail: [guilhermecastro@usp.br](mailto:guilhermecastro@usp.br)

R. Motta  
e-mail: [rosangela.motta@usp.br](mailto:rosangela.motta@usp.br)

E. Moura  
e-mail: [edmoura@usp.br](mailto:edmoura@usp.br)

L. Bernucci  
e-mail: [liedi@usp.br](mailto:liedi@usp.br)

L. Oliveira  
Vale S.A, Vitória, Brazil  
e-mail: [oliveira.luciano@vale.com](mailto:oliveira.luciano@vale.com)

season. Water balance on the fouled layer surface showed an important amount of runoff, in contrast to the dry period, when a water deficit and high suction values were predominant.

**Keywords** Railroad track · Track drainage · Fouled ballast · Unsaturated soils · Climate action · Water infiltration

## 1 Introduction

Iron ore is the main commodity in the rail freight transport in Brazil, which currently corresponds to 78% (407 million tons) of the total transportation in the country. The amount of iron ore transported increased by 47% (180 million tons) from 2006 to 2018 [1]. Managed by Vale S.A. company, Carajas railroad (892 km long connecting the largest open pit iron ore mine in the world, in Carajas, to Sao Luis Port) is mainly used to transport iron ore in 330 cars per train composition, on average. The closest railroad track from the mine (km 877 + 000) has ballast heavily fouled by iron ore. Costa et al. [2] also identified this condition in another iron ore railroad in Brazil. This problem attracted attention of engineers and researchers considering the failures noticed in sleepers in the fouled ballast layer.

The literature presents studies on the fouled ballast condition [3–7]. However, their authors have analyzed the mechanical response of the fouled ballast in different fouling indexes, not considering climate aspects. Cui [8] says that the presence of fines can considerably affect the hydro-mechanical behavior of the ballast due to its sensitivity to moisture variation. Cui et al. [9] have studied the interlayer formation (ballast with subgrade fines) and the effect of fines, cyclic loads, and the presence of water in it. As the number of fine particles becomes significant with their migration from subgrade to the overlying ballast, they tend to govern ballast pore structure by separating coarse particles between them, thus controlling track drainage and mechanical behavior [6]. Furthermore, it is well-documented that geomaterials used in transportation infrastructure constructions are usually in unsaturated state, being suction a variable to be regarded [8–16]. In other words, even if moisture variation is considered in laboratory analysis of fouled ballast, it may not be representative compared to what happens in the field due to the climate influence. Thus, it is important to firstly identify and to understand the fouled ballast hydraulic behavior and how the latter controls water infiltration and surface runoff (drainage) in the whole track profile.

The negative effect of wet coal fines on the ballast mechanical behavior has already been investigated and showed a great contribution to the loss of shear strength [3, 4]. However, the hydraulic behavior of ballast fouled with iron ore and how it may influence track layers under tropical climate conditions is still unknown. Understanding this may contribute to maintenance procedures as it helps to investigate how this type of fouling material behaves in the track. For all these reasons presented, this paper aims to analyze the hydraulic behavior of a railroad profile considering ballast

fouled with iron ore. The study was based on field inspections, laboratory tests and a SEEP/W finite element software [17] to simulate climate–track interaction with fouled ballast under local tropical climate conditions.

## 2 Ballast Fouling

Ballast fouling is characterized as all fouling material present in the ballast voids. According to Selig and Waters [18], fouling material is characterized by particles smaller than 9.5 mm (sum of the fraction passing the 4.75 mm and 0.075 mm sieves). The same authors stated that sources of fouling usually come from particle breakage (76%) for North American railroads and depend on specific conditions, track environment, and operational conditions. Indraratna et al. [19] attributed fouling as 58% from subballast and subgrade intrusion, 20% from surface infiltration, and 22% from ballast and concrete sleeper abrasion, while Feldman and Nissen [20] reported for heavy haul (HH) track in Australia that fouling is mostly originated from wagon spillage corresponding to around 70–95%. The same has been reported by Pires [21] for HH track in Brazil.

Ballast fouling may cause severe damage to the track such as drainage inhibition, deterioration of the mechanical behavior of the ballast, and loss of stability and track geometry. Therefore, different methods to quantify the level of fouling were proposed, such as Fouling Index (FI), to be a parameter for predicting maintenance cycles [18]. However, these methods quantify only the percentage of the fouling materials by weight (mass), providing a misleading measurement of the actual fouling components due to their different specific gravities (e.g., iron ore and coal). Thus, equations have been developed considering a volumetric approach, such as the Void Contamination Index (VCI) proposed by Tennakoon et al. [22]. VCI refers to the specific gravity, as well as to the dry mass and void ratio of ballast and fouling materials, which makes the evaluation more realistic and sensitive to changes of the fouling material.

Three different zones in terms of load bearing capacity and drainage were identified by Tennakoon et al. [6]: (i) Zone 1 or  $VCI < 25\%$  resulting in inter-particle friction reduction and fines content, which is not enough to avoid ballast “free-drainage”; (ii) Zone 2 or  $25\% < VCI < 50\%$ , showing that strains tend to stabilize and sufficient drainage still occurs; and (iii) Zone 3 or  $VCI > 50\%$  which shows very poor drainage and ballast hydro-mechanical behavior being governed by the fine matrix. Huang et al. [4] also classified fouled ballast in three different phases classified from 1 to 3, being the latter the worst scenario for its water drainage capacity.

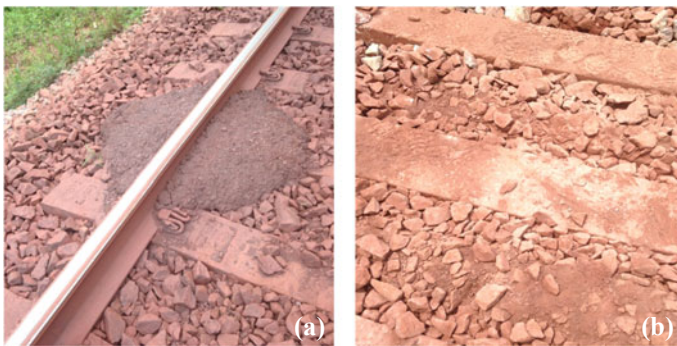
### 3 Experimental Program

#### 3.1 Field Investigation—Site Characteristics

The hydraulic behavior of the fouled ballast under tropical climate influence of a railroad track in Brazil was investigated. The track section is located in Parauapebas, between the Carajas mine and the Sao Luis port and transports iron ore as the main freight. The track profile was composed of 136RE rails, wide-gauge, concrete sleepers, 30 cm of ballast layer, well-graded granular subballast layer over the tropical soil of the region. During the on-site surveys, a high amount of fouled location was detected as given by Fig. 1.

Fouling is known to usually accumulate at the ballast–subballast or ballast–subgrade interface, being also composed of subballast or subgrade fines. However, a high amount of wagon spillage was seen right beside the rails as shown in Fig. 1a. In addition, fines were observed combined with a high amount of water being pumped upward to the top of the sleepers during train passages (Fig. 1b). Considering the possibility of different sources of fouling, both materials were collected and analyzed chemically in laboratory.

Historical climate data from 1981 to 2010 obtained by the National Institute for Meteorology and Statistics (INMET) show that the region is characterized by extreme events. High precipitation rate is observed from January to July (wet season) and a low precipitation rate from August to December (dry season). Net flux (precipitation minus evaporation) shows the highest water surplus from March to April and the lowest water deficit from August to September, when precipitation rate tends to be zero. The average temperature tends to remain between 26 and 29 °C during the year, which is expected in tropical regions. The average rainfall rate reaches around 1500 mm/year (see Fig. 2).



**Fig. 1** **a** Wagon spillage observed beside the rail; **b** fouling material over sleeper surface

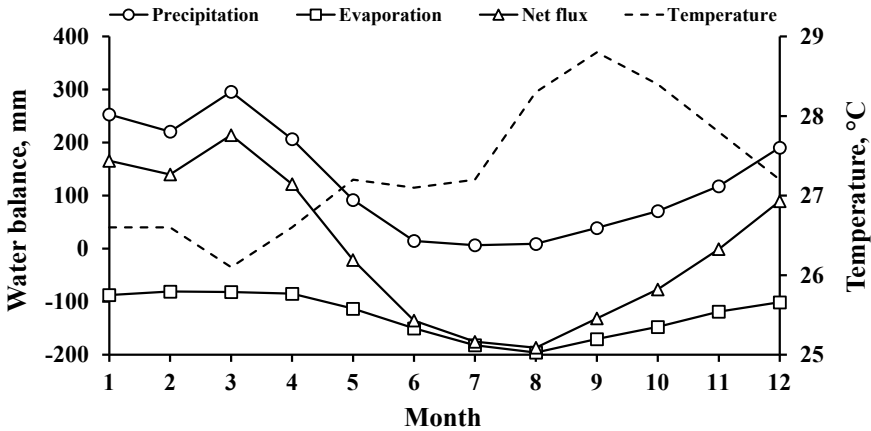


Fig. 2 Historic climate data of the studied region on a monthly basis from 1981 to 2010

### 3.2 Laboratory Tests

Samples of clean ballast, fouled ballast, wagons spillage, mud pumping on top of the sleepers (Top-S), and subballast samples were collected from the track to perform laboratory physical, chemical, and hydraulic characterization. Hydraulic description was determined in laboratory and estimated from physical characteristics and equations from the literature. Figure 3 summarizes the grain size curves of the materials from the track.

Ballast sampling was conducted according to ASTM [23]. Petrographic examination of ballast aggregates was performed according to ASTM [24]. Grain size

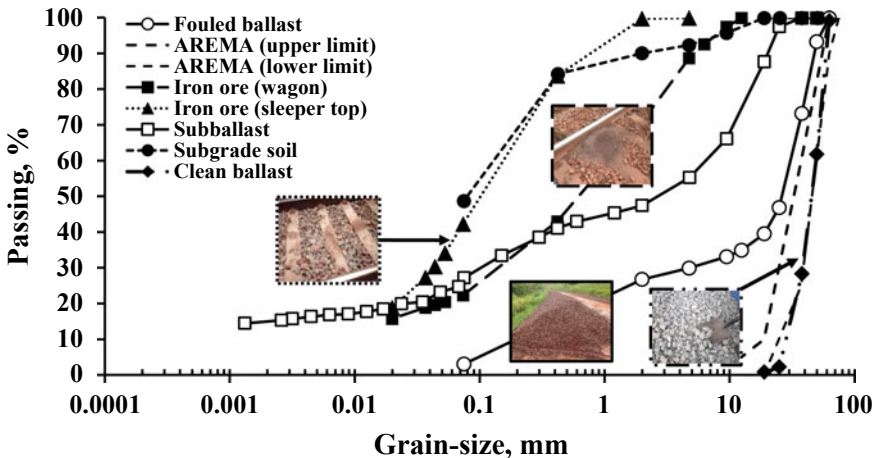


Fig. 3 Grain size distribution of all the materials found in the track

distribution curves of fouled ballast were performed according to ASTM [25]. Grain size curves of fouling materials smaller than 0.075 mm were performed using ASTM [26] standard. Wagon spillage and sleeper top materials grain size curves were also calculated. Subballast grain size analysis was conducted following ASTM [27].

To determine the percentage and composition of the real fouling components, X-ray diffraction (DRX) and chemical analysis were performed. In addition, chemical analysis of iron ore removed from the mine was also performed. The results showed that material coming from wagon spillage was composed of hematite (90%) and goethite (8%) which confirmed the presence of iron ore. Regarding fines material collected on the sleepers, 43%, 36%, and 15% of albite, quartz, and hematite were verified, respectively (see Fig. 4). This proves that such material was also originated not only from iron ore, but also from ballast breakage and attrition since the ballast material presented similar mineralogical origin (quartz, plagioclase, muscovite, and opaque minerals). However, the chemical analysis showed that a high percentage of iron was found only on wagon and mine samples, while material located on the sleepers indicated a predominance of silicon dioxide ( $\text{SiO}_2$ ). Thus, the material on the sleeper top was indicated to be the fouling material which passes mostly a 2.00 mm sieve.

Atterberg limits (e.g liquid limit and plasticity index) of the fouling material and subballast were determined based on ASTM [28]. From liquid limit (LL), plastic limit (PL), and grain size distribution results, USCS and HRB soil classification were carried out for subballast and subgrade characterization according to ASTM [29] and ASTM [30], respectively. An expedite classification applied to tropical soils was also performed with subballast material [31]. Atterberg limits and soil classification results for the materials are shown in Table 1.

DNER-ME [32] or miniature compacted tropical (MCT) test was followed to determine the dry unit weight of fouling material through compaction applying proctor normal compaction energy. MCT methodology requires the use of each material passing a 2.00 mm sieve, compacted in five specimens with 50 mm in height, approximately, into the miniature mold different conditions below and above the

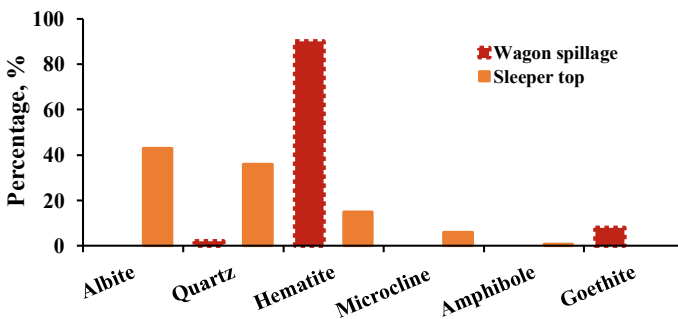


Fig. 4 X-ray diffraction analyses results



**Table 1** Atterberg limits and soil classification of the materials

	LL (%)	PL (%)	USCS	HRD	MCT
Subgrade	28.4	16.9	SC	A-6	–
Subballast	30	17	SC	A-2-6	LA'
Fouling material	15	NP	–	–	–

optimum water content (see Fig. 5). Ballast bulk density and voids were determined according to ASTM [33].

Hydraulic characterization of the subballast soil and fouling material was based on the determination of the saturated hydraulic conductivity ( $K_{SAT}$ ), soil/water retention curves (SWRC), and hydraulic conductivity functions (HCFs). Fouling index and VCI% of the ballast layer were calculated resulting in 33% and 63%, respectively, corresponding to a high fouled ballast condition. Tennakoon et al. [22] state that VCI values higher than 50% are related to a very poor drainage condition because fouling starts governing the hydraulic behavior of the ballast layer. Thus,  $K_{SAT}$  of the fouled ballast was assumed to be fully completed by fines (Phases 2 and 3).

The  $K_{SAT}$  of the subballast soil and fouling material were determined through a variable head permeability test (VHP) which was developed for pavement purposes for determining the saturated hydraulic conductivity of tropical soils [34]. Soil saturation process was conducted through capillarity. Specimens were left in water reservoirs for 7 days. The saturation condition was assumed to be reached after a water column attained a constant value above the soil samples surface. Physical indexes of the saturated specimens were calculated after the VHP test to assure their saturation condition. A weight was placed over the soil samples to prevent expansion and its influence on  $K_{SAT}$  values (see Fig. 5).

Nogami and Villibor [34] studied more than one thousand of different tropical soils in Brazil for MCT classification purposes. The authors were compared both HRB and MCT classification methods asserting that SC (clayey-sand) corresponded to a LA' type (sand or clayey-sand). This type of soil has a  $K_{SAT}$  ranging from  $10^{-4}$  to  $10^{-8}$  cm/s around its optimum moisture content. Lopes [35] also studied a typical LA' soil from the region and determined its  $K_{SAT}$  value and specific gravity ( $G_S$ ) as  $1.22 \times 10^{-6}$  cm/s and  $2.667$  g/cm<sup>3</sup>, respectively. Thus,  $K_{SAT}$  and  $G_S$  values of the subgrade material were assumed to be  $1.2 \times 10^{-6}$  cm/s and  $2.667$  g/cm<sup>3</sup>, respectively. Moulton's [36] equation was used to predict the saturated hydraulic conductivity



**Fig. 5** VHP test for materials passing a 2.00 mm sieve: **a** compaction; **b** saturation; **c** test

of the clean ballast layer, and its minimum value was assumed that obtained in laboratory by Tennakoon et al. [6]. Table 2 summarizes all the physical and hydraulic characteristics of the track materials such as porosity ( $\eta$ ), void index ( $e$ ), maximum dry unit weight ( $\gamma_d$ ), optimum and saturated moisture content ( $w_{OPT}$  and  $w_{SAT}$ ), saturated volumetric water content ( $\theta_{SAT}$ ),  $G_s$ ,  $D_{60}$ ,  $D_{10}$ , and  $K_{SAT}$ .

The stiffening phenomenon of the fouled ballast layer was observed in situ considering the high number of accumulated traffic loads and the difficulty in excavating to collect it. This occurred due to cementation and interlocking of fouling material with ballast particles. Furthermore, fouling material is known to be not compacted in the field but accumulated at the ballast–subballast interface over time. Thus, Menezes [37] and Borges et al. [38] determined the minimum void index of iron ore material (sinter feed) also passing a 2.00 mm sieve in the laboratory resulting in 0.71 and 0.72, respectively. As fouled ballast layer was under the load application point, the compaction of the fouling material (sleeper top) in the laboratory through proctor normal energy resulted in a void index of 0.5. Therefore, this value was assumed to be equivalent to the fouling material compaction condition observed in the field.

### 3.3 Numerical Modeling (SEEP/W)

The geometric characteristics used in the model developed considered a 0.30 m fouled ballast layer placed over a 0.20 m granular subballast and a compacted subgrade, according to those observed in the track site. The water table was assumed to be 10 m based on in situ percussion drilling tests (PDT) results (i.e. deepest water table found). Moreover, we adopted the deepest water table scenario considering that the track site is at a higher elevation, topographically. The track slope was assumed to be 3% according to DNIT [39]. Hydraulic condition variation was investigated at the fouled ballast layer. Point A (see Fig. 6) on the fouled ballast surface was evaluated in terms of drainage and water balance while considering three different fouled conditions (1, 2, and 3). Point B (0.20 m depth) was analyzed in terms of suction variation in the subgrade (see Fig. 6).

To analyze railroad track geomaterials subjected to climate influence, a constitutive relationship known as soil/water retention curve (SWRC) is considered. It should be applied to describe the variation of suction pressure according to moisture content over time. SWRC of all the track materials was determined according to Aubertin et al.'s [40] equation (see Fig. 7a). This equation uses LL,  $D_{60}$  and  $D_{10}$  (diameter passing 60% and 10% of materials), and porosity values (see Eq. 1). The  $D_{10}$  values of subgrade, subballast, and fouling material were also estimated from Aubertin et al. [40], being assumed to be equivalent to typical sandy (0.009 mm) and clayey soils (0.0001 mm), respectively.

$$S_r = \frac{\theta}{\eta} = S_c + S_a^*(1 - S_c); S_c = f(h_{co}; \psi; m); S_a = f(\psi_r, \psi, h_{co}) \quad (1)$$

**Table 2** Hydraulic and physical characteristics of the track materials

Material	$\eta$	$e$	$\gamma_d$ (g/cm <sup>3</sup> )	wOPT (%)	$\gamma_{SAT}$ (g/cm <sup>3</sup> )	$G_s$	w <sub>SAT</sub> (%)	$\theta_{SAT}$ (%)	$D_{60}$ (mm)	$D_{10}$ (mm)	$K_{SAT}$ (m/s)
Subgrade	0.34	0.51	1.768	11.7	2.105	2.667	19.1	33.7	0.12	0.009	1.2E - 08
Subballast	0.20	0.25	2.130	8.4	2.397	2.670	9.5	20.3	7	1E - 04	7.4E - 09
Fouling material	0.27	0.50	2.662	10.2	3.418	3.670	13.6	36.3	0.16	1E - 04	1.2E - 09
Clean ballast	0.43	0.75	1.498	-	2.763	2.621	28.6	42.8	50.0	30	1.2

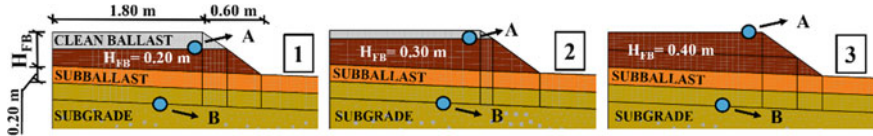


Fig. 6 Model developed: points analyzed and different fouled conditions ( $H_{FB}$ )

where  $S_r$  is the total saturation degree,  $S_a^*$  is the adhesion component,  $\theta$  is the volumetric water content,  $\eta$  is the porosity,  $h_{co}$  is the water capillary height in the soil,  $m$  is the desaturation coefficient,  $\psi$ ,  $\psi_r$  are the instantaneous and residual suction, respectively.

SWCC is directly dependent on the hydraulic conductivity of the porous materials, since the drier the material, the higher the suction and the discontinuity of the water phase on it. This condition hampers water flow decreasing its hydraulic conductivity. Thus, hydraulic conductivity functions (HCFs) were surveyed in the literature to predict the hydraulic conductivity of soils under unsaturated conditions using SWRC data [41]. HCFs of the track materials were calculated through Fredlund et al.’s [41] equation, according to Geo-Slope [17] (see Fig. 7b and Eq. 2).

$$k_w = k_s \frac{\sum_{i=j}^N \frac{\Theta(e^i) - \Theta(\Psi)}{e^i} \Theta'(e^i)}{\sum_{i=1}^N \frac{\Theta(e^i) - \Theta_s}{e^i} \Theta'(e^i)} \tag{2}$$

where  $k_w$  is the conductivity calculated for a specified suction,  $k_s$  is the saturated conductivity,  $\Theta_s$  is the volumetric water content,  $j$  is the least negative pore-water pressure,  $N$  is the maximum negative pore-water pressure,  $\Psi$  is the suction corresponding to the  $j$ th interval,  $i$  is the interval between the range of  $j$  to  $N$ ,  $e$  is the natural number 271,828, and  $\Theta'$  is the first derivative of the Fredlund and Xing [42] equation.

Finally, hourly local climate data were applied to simulate climate–track interaction. The data were provided by the National Institute of Meteorology and Statistics (INMET) such as solar radiation, rainfall, temperature, relative humidity, and wind speed in 2019. Potential and actual evaporation were calculated according to Penman–Wilson’s [17] and Wilson et al.’s [11] equations, respectively, considering that the soil temperature was the same as the air (see Eq. 3). In these analyses, only the wettest and driest months (March–April and August–September) were applied to represent the most extreme seasons (see Fig. 2).

$$q_{AE} = \frac{\Gamma q_n^* + \gamma E_a}{\Gamma + \frac{\gamma}{h_s}}; E_a = [2.625(1 + 0.146u)] p_v^a \left( \frac{1}{h_a} - \frac{1}{h_s} \right) \tag{3}$$

where  $h_a$  is the relative humidity of the air,  $h_s$  is the relative humidity of the soil,  $\Gamma$  is the slope of the saturation vapor pressure verses temperature curve,  $q_n^*$  is the net radiation in terms of water flow,  $\gamma$  is the psychrometric constant = 0.0665 kPa/C,  $u$  is

the wind speed. To compute water flux and runoff on the track surface, the software uses the fluid mass balance equation (see Eq. 4).

$$q_I = q_R + q_P \cos \alpha + q_E \tag{4}$$

where  $q_I$  is the infiltration,  $q_R$  is the runoff,  $q_P$  is the water flux due to rainfall,  $q_E$  is the evaporation, and  $\alpha$  is the slope angle. Considering the possibility of water ponding at any superficial node resulting from the infiltration applied, the pore-water pressure is set to zero and the runoff was calculated through the runoff equation (see Eq. 5).

$$q_R = q_I^{\text{applied}} - q_P \cos \alpha - q_E \tag{5}$$

where  $q_I^{\text{applied}}$  is the water infiltration applied.

## 4 Results and Discussions

A fouled track condition was simulated in a finite element model developed to evaluate the climate–track interaction over two extreme seasons. These seasons were represented by months in the first and the second semester (wet and dry season, respectively). The wettest month (March–April) of 2019 demonstrated that most of the cumulative rainfall turned into runoff as well as high suction values in the fouled layer after rainfall (see Figs. 8 and 9).

It was also observed that only 16% of the total rainfall infiltrated into the fouled ballast corresponding to a very poor track drainage condition. The results confirm the highly fouled condition of the track section with the fouling material reaching the top of the ballast layer as well as accumulation of rainfall water on its almost impervious surface (see Fig. 1).

Furthermore, different levels of fouling were also analyzed considering the variation of the height of the fouled layer or the height of clean ballast at the top (see Fig. 6). Thus, Figure 10 shows a comparison between a 0.20 m and a 0.30 m height fouling layer. From the results, it could be noticed that track drainage capacity increases as fouled ballast height decreases. Thus, water takes more time to be drained from thicker fouled layers, which may contribute to deteriorating superstructure components. However, the barrier formed against water infiltration in the fouled ballast may still improve ballast mechanical behavior, considering that the fouling material cementation (fines from ballast breakage and attrition mixed with iron ore) may increase ballast stiffness and contribute to its hardening, as seen on-site.

Considering the driest month, nothing different was observed from the wettest month, except that it rained only once during the whole season contributing to a high suction fouled ballast condition. This condition turned fouled ballast a very

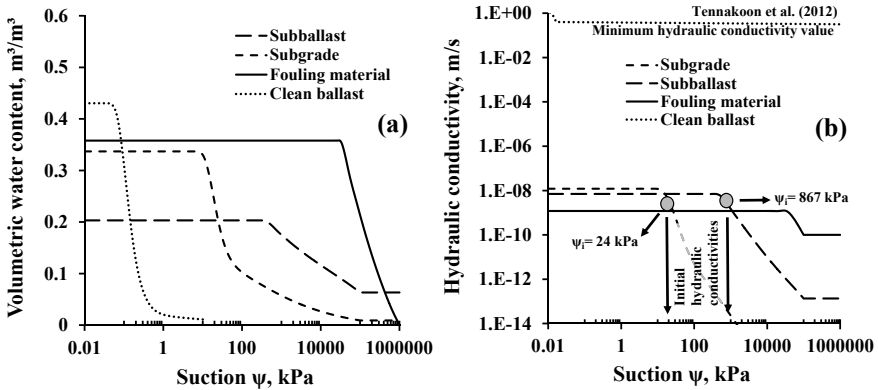


Fig. 7 a SWRCs for the studied materials; b HCFs determined through SWRC data

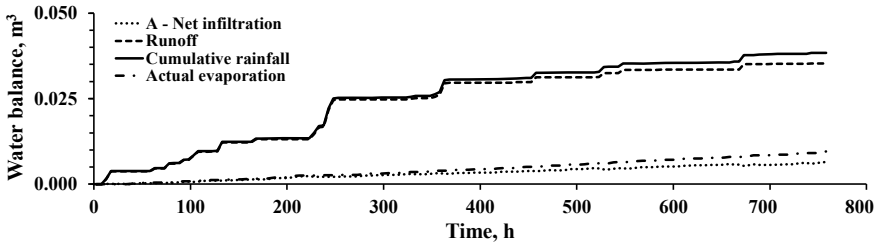


Fig. 8 Water balance at the fouled ballast surface in the wet season

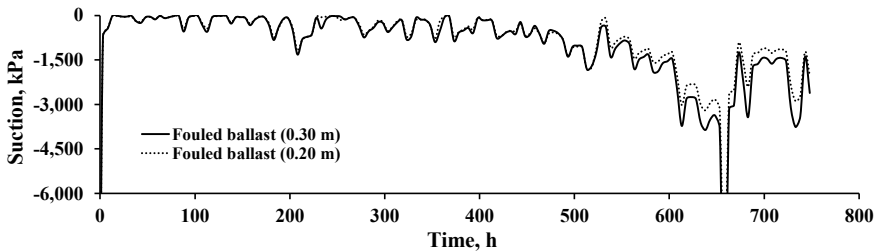


Fig. 9 Water flow at the fouled ballast layer surface (0.20 m depth)

low hydraulic conductivity layer due to its unsaturated condition (see Fig. 6b) and whatever single rainfall event occurs, it will be turned into mostly in runoff and evaporation, as shown in Fig. 11.

After analyzing the subgrade suction variation according to the level of fouling, it could be observed that subgrade suction tends to be unchanged with and without the fouled ballast layer due to a low  $K_{SAT}$  value ( $1.2 \times 10^{-8}$  m/s) (Fig. 12a). However, if subgrade  $K_{SAT}$  increases, such as  $1.2 \times 10^{-6}$  m/s, a slight increase in subgrade

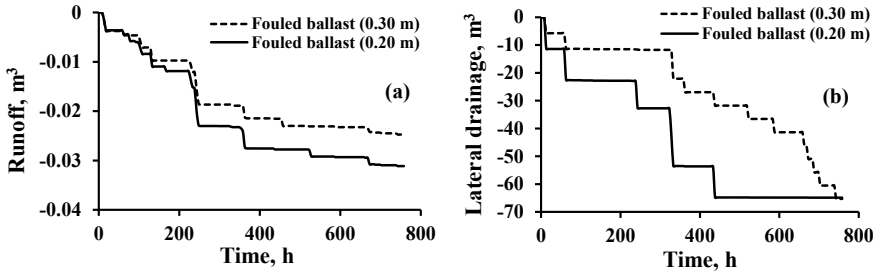


Fig. 10 Drainage capacity of two fouling conditions: 0.20 and 0.30 m height fouling: a runoff; b lateral drainage

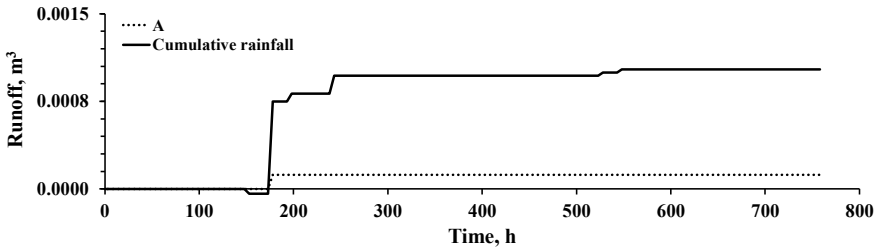


Fig. 11 Runoff at the fouled ballast surface in the dry season

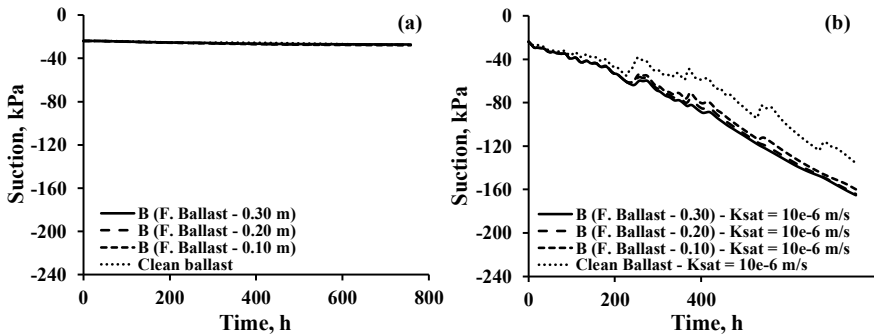


Fig. 12 Subgrade suction variation with time according to different level of ballast fouling: a subgrade  $K_{SAT}$  of  $1.22 \times 10^{-8}$  m/s; b subgrade  $K_{SAT}$  of  $1.22 \times 10^{-6}$  m/s

suction can be noticed with the height of the fouled ballast layer. In addition, this latter case shows that subgrade tends to be more sensitive to climate actions without fouling material in the ballast layer (see Fig. 12b).

It can thus be asserted that 0.20 and 0.30 m of the fouled ballast protected subgrade against moisture content and suction pressure variation, consequently. In other words, subgrade soil tends to be less exposed to climate in a fouled ballast condition with this

type of fouling material, which may work as an alternative material for protecting a relatively low  $K_{SAT}$  subgrade under tropical climate. This may contribute to increase subgrade suction values and to improve subgrade mechanical behavior, consequently. This calls attention to investigate the range of fouling that would concurrently have a beneficial effect for the ballast layer and subgrade soil. It should be highlighted that these results were generated for these railroad environmental and operational conditions.

## 5 Conclusions

This research aimed to better understand the hydraulic behavior of a ballast layer highly fouled with iron ore subjected to tropical climate conditions over the year. Its hydraulic behavior was analyzed through on-site inspections, laboratory tests, and numerical simulations.

- Physical, chemical, and hydraulic analyses were performed to characterize ballast, fouling material, subballast, and subgrade. The results showed that the fouling material is mostly composed of quartz, albite, and hematite indicating not only iron ore but also ballast particle breakage and attrition. Afterward, hydraulic tests showed very low permeability values for the fouling material and high suction values in the fouled ballast layer. This explains the high amount of water accumulated on the fouled ballast surface in the field as well as pumping of fines with water and attrition during trains passages.
- The results from laboratory tests were used to simulate the impact of real climatic conditions on the drainage and hydraulic behavior of a fouled ballast. Hourly climatic data were referred to two extreme weather conditions over 2019, corresponding to March–April (wet season) and August–September (dry season). The results revealed that most water from rainfall events turned into runoff and evaporation, which explains water accumulation in the real track for wet seasons, characterized by a very poor track drainage. Infiltration events were observed to be very low, around 16% of the total rainfall maintaining high suction values in the ballast voids.
- Analyses of different levels of fouling considering fouled layer thickness demonstrated that the lower the fouled layer is, the faster and more efficient the track drainage is. In addition, subgrade suction tends to increase as the amount of fouled ballast increases due to its protection against climate actions. However, the thickness of this type of fouling material that could concurrently contribute to enhancing subgrade and ballast behavior is not known and should be studied. The driest season demonstrated to contribute to an impervious fouled ballast due to its unsaturated condition. To conclude, the prediction and analysis of a railroad track profile under the influence of changes in climate could be well performed by the developed model of this research based on field inspections.



**Acknowledgements** The authors gratefully acknowledge the financial and technical support for this research provided by VALE S.A., the Coordination for the Improvement of Higher Education Personnel (CAPES), and Escola Politécnica—Universidade de São Paulo.

## References

1. ANTT (2019) Evolução do transporte ferroviário de cargas, Superintendência de Infraestrutura e Serviços de Transporte Ferroviário de Cargas, Agência Nacional de Transportes Terrestres, Brasília (In Portuguese)
2. Costa R, Motta R, Bernucci L, Moura E, Alves A, Sgavioli F (2016) Avaliação da contaminação do lastro ferroviário. In: 28<sup>o</sup> Congresso de Pesquisa e Ensino em Transportes, ANPET, Curitiba BRA (In Portuguese)
3. Tutumluer E, Dombrow W, Huang H (2008) Laboratory characterization of coal dust fouled ballast behavior. In: AREMA 2008 annual conference & exposition, Salt Lake City USA
4. Huang H, Tutumluer E, Dombrow W (2009) Laboratory characterization of fouled railroad ballast behavior. *J Transp Res Board* 2117(1):93–101
5. Indraratna B, Tennakoon N, Nimbalkar S, Rujikiatkamjorn C (2013) Behavior of clay-fouled ballast under drained triaxial testing. *Geotechnique* 63(5):410–419
6. Tennakoon N, Indraratna B (2014) Behavior of clay-fouled ballast under cyclic loading. *Geotechnique* 64(6):502–506
7. Indraratna B, Sun Y, Nimbalkar S (2016) Laboratory assessment of the role of the particle size distribution on the deformation and degradation of ballast under cyclic loading. *J Geotech Geoenviron Eng* 142(7):04016016
8. Cui Y (2016) Unsaturated railway track-bed materials. In: Web of conferences E-UNSAT, vol 9, p 01001
9. Cui Y, Duong T, Tang A, Dupla J, Calon N, Robinet A (2013) Investigation of the hydro-mechanical behavior of fouled ballast. *J Zhejiang Univ Sci A (Appl Phys Eng)* 14(4):244–255
10. Fredlund D, Rahardjo H (1993) Soil mechanics for unsaturated soils. Wiley, New Jersey U.S.
11. Wilson G, Fredlund D, Barbour S (1997) The effect of soil suction on evaporative fluxes from soil surfaces. *Can Geotech J* 34(1):145–155
12. Lu N, Likos W (2004) Unsaturated soil mechanics. Wiley, New Jersey U.S.
13. Ferreira T, Teixeira P, Cardoso R (2011) Impact of bituminous subballast on railroad track deformation considering atmospheric actions. *J Geotech Geoenviron Eng* 137(3):288–292
14. Zhang Y, Ishikawa T, Tokoro T, Nichimura T (2014) Influences of degree of saturation and strain rate on strength characteristics of unsaturated granular subbase course material. *Transp Geotech* 1:74–89
15. Hasnain M, McCarter W, Woodward P, Connolly D, Starrs G (2017) Railway subgrade performance during flooding and the post-flooding (recovery) period. *Transp Geotech* 11:57–68
16. Zornberg JG, Azevedo M, Sikkema M, Odgers B (2017) Geosynthetics with enhanced lateral drainage capabilities in roadway systems. *Transp Geotech* 12:85–100
17. Geoslope International (2018) Heat and mass transfer with Geostudio, 2nd edn. GeoStudio. Canada
18. Selig ET, Waters JM (1994) Track geotechnology and substructure management, 1st edn. Thomas Telford Services, London UK
19. Indraratna B, Salim W, Rujikiatkamjorn C (2011) Advanced rail geotechnology—ballasted track. Taylor & Francis Group, London UK
20. Feldman F, Nissen D (2002) Alternative testing method for the measurement of ballast fouling: percentage void contamination. In: Conference on railway engineering RTSA, Wollongong, NSW. Canberra, Australia, pp 101–111

21. Pires J (2015) Integrated maintenance model for heavy haul tracks. Ph.D. Thesis, École Polytechnique Fédérale de Lausanne, Suisse
22. Tennakoon N, Indraratna B, Rujikiatkamjorn C, Nimbalkar S (2012) The role of ballast fouling characteristics on the drainage capacity of rail substructure. *ASTM Geotech Test J* 35(4):1–12
23. ASTM (2011) Reducing samples of aggregate to testing size, *ASTM C 702–11*
24. ASTM (2011) Standard guide for petrographic examination of aggregates for concrete, *ASTM C295/C295M–11*
25. ASTM (2006) Standard test methods for sieve analysis of fine and coarse aggregates, *ASTM C136–06*
26. ASTM (2017). Standard test methods for materials finer than 75- $\mu\text{m}$  (N° 200) sieve in mineral aggregates by washing, *ASTM C117–17*
27. ASTM (2004) Standard test methods for particle-size distribution (gradation) of soils using sieve analysis, *ASTM 6913–04*
28. ASTM (2010) Standard methods for liquid limit, plastic limit, and plasticity index of soils, *ASTM D4318–10*
29. ASTM (2017) Standard practice for classification of soils for engineering purposes (s), *ASTM D2487–11*
30. ASTM (2015) Standard practice for classification of soils and soil-aggregate mixtures for highway construction purposes, *ASTM D3282–15*
31. Nogami J, Villibor D (1981) Um novo sistema de classificação de solos para rodovias. In: *Simpósio Brasileiro de Solos Tropicais em Engenharia, COPPE UFRJ. Rio de Janeiro BRA*, pp 30–41 (in Portuguese)
32. DNER (1994) Solos—Ensaio de compactação em equipamento miniatura, Departamento Nacional de Estradas de Rodagem, *DNER-ME 228/94* (in Portuguese)
33. ASTM.: Standard test method for bulk density (“Unit Weight”) and voids in aggregate, *ASTM C29/C29M* (2017).
34. Nogami J, Villibor D (1995) Pavimentação de baixo custo com solos lateríticos. Escola Politécnica da Universidade de São Paulo, São Paulo BRA (in Portuguese)
35. Lopes L (2017) Análise experimental do comportamento hidráulico e mecânico do pavimento ferroviário. M.Sc thesis. Rio de Janeiro BRA (in Portuguese)
36. Moulton L (1980) Highway subdrainage design Report No. FHWA-TS-80–224. Federal Highway Administration Offices of Research and Development, Washington USA
37. Menezes L (2013) Determinação da curva de retenção de água em solos utilizando bomba de fluxo. M.Sc. thesis. Ouro Preto BRA (in Portuguese)
38. Borges T, Paiva B, Villar L, Gardoni M (2011) Ensaio de laboratório utilizando lisímetro para avaliação do fluxo de água em minério de ferro. In: *7° Simpósio Brasileiro de Solos Não Saturados NSAT. Pirenópolis BRA*. pp 275–282 (in Portuguese)
39. DNIT ISF-211: Railroads—earthwork design procedures, Service Instructions (2015)
40. Aubertin M, Mbonimpa M, Bussiere B, Chapuis RP (2003) A model to predict water retention curve from basic geotechnical properties. *Can Geotech J* 40(6):1104–1122
41. Fredlund DG, Xing A, Huang S (1994) Predicting the permeability function for unsaturated soils using the soil-water characteristic curve. *Can Geotech J* 31(3):521–532
42. Fredlund DG, Xing A (1994) Equations for the soil-water characteristic curve. *Can Geotech J* 31(4):521–532

# Laboratory Study on Frost Heave of Ballast



Feng Guo, Yu Qian, Yi Wang, Dimitris C. Rizos, and Yuefeng Shi

**Abstract** Frost heave is a long-recognized issue contributing to the railway track upheaval in cold regions. Generally, frost heave is believed to happen in the subgrade layer of transportation infrastructure, referred to as the volume expansion of frozen soils, which are susceptible to frost action with the presence of moisture. The aggregate layer, such as highway base course or railroad ballast, is believed not to be prone to the frost heave due to its large void ratio and low capability to hold moisture content. However, recent reports around the world, such as Norway, USA, China, and Japan, etc., indicate the frost heave does happen in the ballast layer even when the moisture content is low. Existing literatures, which often believe track upheaval should not happen on aggregate like ballast, cannot well explain the recently observed phenomenon. In this study, the researchers conduct a series of laboratory experiments aiming to identify the possible reason that cause ballast frost heave in a well-controlled environment. Clean ballast is prepared with different moisture conditions, including half submerged condition and fully submerged condition. The growth of ice and movement of particles are tracked and qualified through image analysis. The findings from this study provide evidence to prove the effect of ice formation on ballast and would help to explain the root cause of ballast frost heave.

---

F. Guo · Y. Qian (✉) · D. C. Rizos

Department of Civil and Environmental Engineering, University of South Carolina, Columbia, SC 29208, USA

e-mail: [yuqian@sc.edu](mailto:yuqian@sc.edu)

F. Guo

e-mail: [fengg@email.sc.edu](mailto:fengg@email.sc.edu)

D. C. Rizos

e-mail: [rizos@cec.sc.edu](mailto:rizos@cec.sc.edu)

Y. Wang

Department of Mechanical Engineering, University of South Carolina, Columbia, SC 29208, USA

e-mail: [yiwang@cec.sc.edu](mailto:yiwang@cec.sc.edu)

Y. Shi

Railway Engineering Research Institute, China Academy of Railway Sciences Co, Ltd, Beijing 100081, China

**Keywords** Ballast · Frost heave · Laboratory experiment · Volume expansion

## 1 Introduction

Frost heave is the process by which the freezing of water-saturated soil causes the deformation and upward thrust of the ground surface [1]. Typically, in the winter, the detrimental effects of frost heave on infrastructure can be upward swelling of the soil, deformation of ground surface, and longitudinal cracks in the center of pavements. The scientific study of frost heave in the soil can be traced back to the 1920s. Taber [2] firstly described the mechanics of frost heave and showed that vertical displacement in soil is due to ice lens segregation, therefore disproving the early hypothesis that frost heave is caused by a simple phase change of pore water to ice phase. Akagawa and Kodama [3] reported frost heave may happen in porous materials such as soil, porous rock, and weathered mortar. Beskow [4] contributed to the early research of frost heave with his conclusion that there is a similarity between unfrozen water content during soil freezing and residual water content encountered during soil drying which encouraged other researchers working on the water transport in frost heave. Bronfenbrener [5] summarized that generally there are three necessary conditions for frost heave to occur: (1) frost susceptible soil, (2) availability of water, and (3) freezing temperatures. Apart from the mentioned research, there is a considerable number of mathematical models have been established to explain the mechanism of frost heave in frost susceptible soils [5–7]. However, frost actions in coarse-grained soils such as ballast and sand are often ignored not only because they have long been recognized as non-frost susceptible, but also because their water content is typically very low, and their location is usually above the groundwater table. Therefore, in the past decades, researchers and engineers from Finland, Sweden, and other cold regions widely used coarse sand and gravel barriers as a separation layer to mitigate and stop frost heave in the roads and railroads [8, 9]. Ironically, recent studies on the railway track in China observed widespread frost heave in railway embankments that occurred in clean ballast where the water content was low. Note the groundwater table was lower than the coarse fill layers, and the frost region within coarse fills did not reach the ballast layer [10]. Besides, Akagawa in Japan found the ballast layer may heave if the moisture condition is favorable since the ballast layer may contain susceptible fines that come from the surrounding environment but not crushed ballast [11]. Unfortunately, the mechanism of frost heave happening in the clean ballast layer remains unclear.

To investigate the ballast frost heave behavior, a series of laboratory experiments in a well-controlled environment were performed. Images were taken for recording and analyzing any changes before and after freezing the ballast layer under different moisture conditions. Results confirmed the frost heave does happen in ballast layer under different moisture levels and needs to be considered for track design and maintenance.

## 2 Laboratory Experiments

### 2.1 Test Materials

Two kinds of materials were used to perform the freeze test in the laboratory, clean ballast, and clean sand. Specifically, the ballast was a granite type 100% crushed aggregate. The grain size distribution of the ballast satisfies the American Railway Engineering and Maintenance-of-Way Association (AREMA) Manual of Engineering (MOE) [12] No. 4 gradation requirements (see Table 1 and Fig. 1). The sands used in this study were engineered materials manufactured by the Unimin Corporation with the uniform grain size distributions, 2 mm for the yellow sand, and 0.5 mm for the purple sand, respectively. All the ballast and sands were washed first and then dried in the oven at 160 °C for 12 h. Materials were stirred during the drying process to ensure they were thoroughly dried. This process ensures all the materials were clean and dry.

### 2.2 Sample Preparation

An acrylic cylinder with of which size is 30.48 cm outside diameter (OD  $\times$  29.85 cm inside diameter (ID)  $\times$  30.48 cm height was used as a container to hold ballast or sand. The Midea WHS-258C1 single door chest freezer with a temperature range between  $-12$  and  $-28$  °C was used to freeze all materials together with the cylinder. For all the tests in this study, the temperature of the freezer was controlled at  $-15$  °C and double checked with another portable thermometer before putting any samples into the freezer and during the specimen freeze period.

Each ballast sample was prepared with 10 kg of clean dry aggregates and compacted slightly to avoid scratches and damaging of the cylinder wall. All the samples were prepared to the void ratio of 0.70, given the specific gravity of the granite was 2.75 g/cm<sup>3</sup>. The level of the top of each sample was checked with the compaction plate. Due to the particulate nature of the aggregate, note the top of each sample would not be smooth.

Each sand sample was prepared with 8 kg of clean dry yellow sands and 1 kg of clean dry purple sand. Yellow sands were poured into the cylinder first as the bottom layer with light compaction and smooth the top first, and then purple sands were poured into cylinder later as the top layer with light compaction and smooth the top. All the samples were prepared to the void ratio of 0.6 for the bottom layer and 0.4 for the top layer, given the specific gravity of the sand was 2.65 g/cm<sup>3</sup>.

After each sample was prepared, the sample image was taken, and the top surface contour of the sample was lightly marked with a pencil on the acrylic surface. Each sample was then carefully placed into the center of the freezer to avoid uneven thermal field. After each specimen was held in the freezer for 24 h, it was gently taken out from the freezer and immediately checked for any volumetric changes. Images of

**Table 1** Ballast gradation in frost heave test

	Percent passing											
	76.2 (mm)	63.5 (mm)	50.8 (mm)	38.1 (mm)	25.4 (mm)	19 (mm)	12.7 (mm)	9.51 (mm)	4.76 (mm)	2.38 (mm)		
No. 4	-	-	100	90-100	20-55	0-15	-	0-5	-	-	-	-
Ballast sample	-	-	100	95	40	8	-	3	-	-	-	-

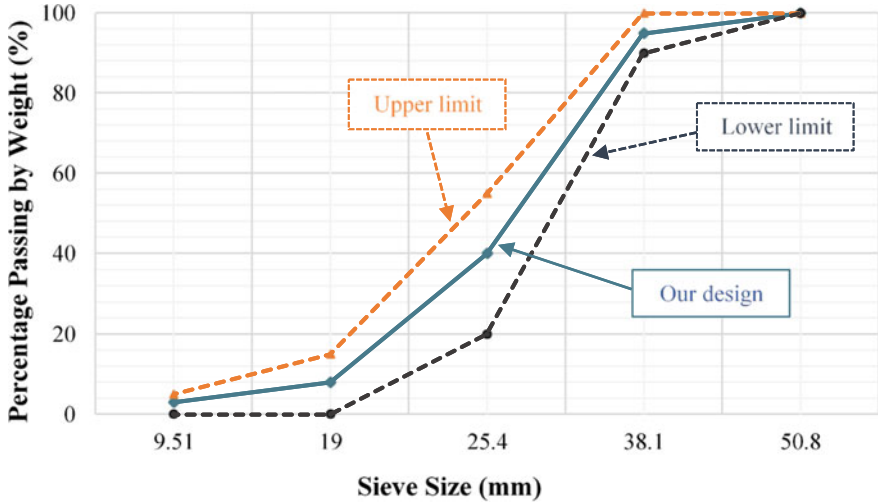


Fig. 1 Ballast gradation in frost heave test



Fig. 2 Steps for laboratory experiment

the samples were taken right after wiping out any surface moisture on the outside of the acrylic wall. Figure 2 shows the detailed test steps.

### 3 Results and Discussion

#### 3.1 Cylinder Freeze Test

To ensure the acrylic cylinder is water-tight and have enough stiffness without any substantial deformation during the freezing stage. A trial test was performed with just water and the cylinder. A total of 3500 ml water was poured into the cylinder which corresponding to 5 cm deep of water in the cylinder. The height and ID of the cylinder were averaged to be 30.5 and 30 cm from four measurements with a caliper before the freezing test.

After 24 h inside of the freezer with a temperature of  $-15\text{ }^{\circ}\text{C}$ , the cylinder was taken out and checked any possible changes in the geometry. The diameter and height

of the acrylic cylinder were averaged as 30.5 and 30 cm with four measurements at the same location before the freezing test. Thus, no major deformation of the cylinder was observed. The water volume was double checked to be 3493 ml after the ice completely melted. The slightly difference was possible due to the handling and residual moisture on the bottom and surface of the acrylic cylinder. It was believed that the test setup was suitable for measuring potential volumetric changes with the results obtained from the control test. The cylinder condition is different from what a ballast layer would experience in the field. However, the purpose of this laboratory test is to investigate if the ice would just grow within the voids between the particles without disturbing the aggregate assembly or the ice would also push the aggregates away from their original positions during the phase changing. During the laboratory test, it was found that the freezing occurred initially on the top surface and then moved downward to the bottom, and this could attribute to the heat isolation effect of the acrylic glass and the wood base of the cylinder.

### **3.2 *Ballast Freeze Test***

Four groups of ballast test were performed with the prepared ballast, water, and the cylinder. For fully submerged tests, a total of 8500 ml water was poured into the cylinder which corresponding to 12 cm deep of water in the cylinder for each specimen. For half submerged tests, a total of 4250 ml water was poured into the cylinder which corresponding to 6 cm deep of water in the cylinder for each specimen. Before freezing, there were four measurements of the height and inner diameter of the cylinder by using a caliper.

It was confirmed that the height and inner diameter of the cylinder were averaged to 30.4 and 30 cm. After 24 h inside of the freezer with a temperature of  $-15^{\circ}\text{C}$ , the cylinder was taken out and checked any possible changes in the geometry. The diameter and height of the acrylic cylinder were averaged as 30.4 and 30 cm with four measurements at the same location after the freezing test. Thus, no major deformation of the cylinder was observed. It was believed that the test setup was suitable for measuring potential volumetric changes with the results obtained from the ballast test.

### **3.3 *Sand Freeze Test***

Four groups of sand test were conducted with dried clean sand, water, and the cylinder under fully submerged condition. For fully submerged tests, a total of 2535 ml water corresponding to 8 cm in bottom layer was poured into cylinder after the bottom layer was prepared and smoothed in each sample. To avoid the disturbance of the top layer, we did not pour water into the top layer. Instead, water was slowly release



from the side wall. Before freezing, there were four measurements of the height and ID of the cylinder by using a caliper.

It was confirmed that the height and ID of the cylinder were averaged to 30.5 cm and 30 cm. After 24 h inside of the freezer with a temperature of  $-15\text{ }^{\circ}\text{C}$ , the cylinder was taken out and checked any possible changes in the geometry. The diameter and height of the acrylic cylinder were averaged as 30.5 cm and 30 cm with four measurements at the same location after the freezing test. Thus, no major deformation of the cylinder was observed. It was believed the test setup was suitable for measuring potential volumetric changes with the results obtained from the sand test.

To prove that these vertical displacements are not purely caused by the water freeze, we performed the comparison test in the control group. In Fig. 3, there is no obvious change or swelling happening indicating the frost heave does occur in the ballast material under half submerged and fully submerged conditions.

Figures 4 and 5 demonstrate the changes for the ballast material with half submerged and fully submerged conditions before and after the freeze. It is clear

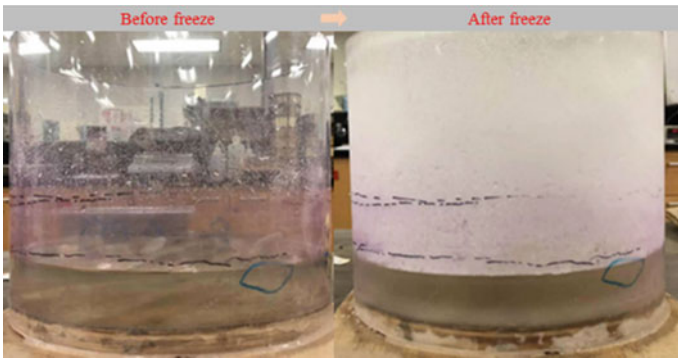


Fig. 3 Cylinder freeze test

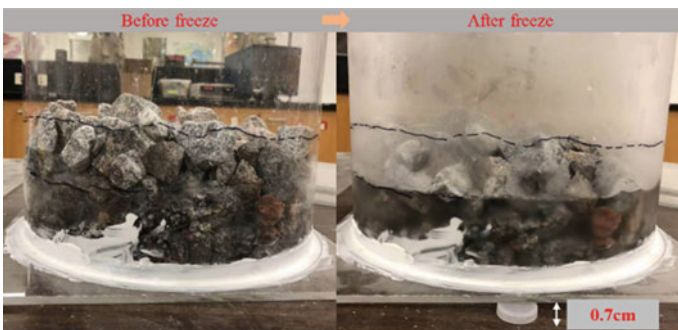


Fig. 4 Ballast freeze test with half submerged condition

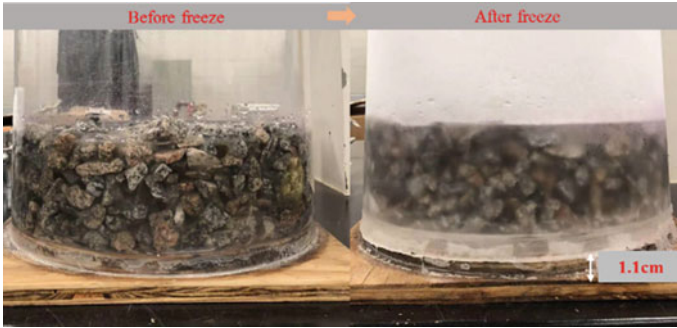


Fig. 5 Ballast freeze test with half submerged condition

to find that after freeze, there are clear swellings toward bottom in both conditions. But the extent of swelling in the half submerged condition is 0.7 cm which not as large as the swelling in fully submerged condition which is 1.1 cm. It should be mentioned that the swelling direction toward bottom indicating the temperature on the bottom is colder than the top. It is reasonable since the refrigerator is at the bottom of the chest freezer.

Figure 6 shows the changes for the sand with fully submerged condition before and after the freeze. It is clear to see that there is obvious separation after freeze with a fully submerged condition. The crack in the yellow sand layer has a width of 0.2 cm and a length of 6 cm. Since sand and ballast are solid particles with less absorption ability, the preconceived opinion that they cannot have frost heave in here is not supported in our case. Under certain moisture conditions, the frost heave does happen in ballast material.

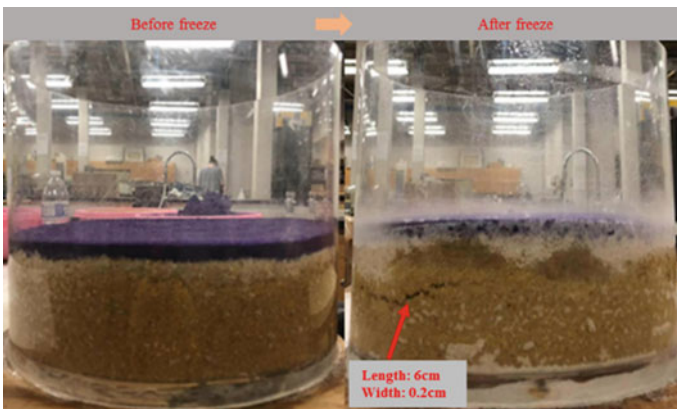


Fig. 6 Sand freeze test

## 4 Conclusion

This study aims to investigate the potential frost heave in clean ballast. Ballast and sand samples with different water levels were prepared and frozen in a controlled laboratory environment. With the limited results obtained from the laboratory, the following conclusions can be drawn:

- Image tracking proves there are vertical displacements on the half merged and fully merged ballast particles.
- Volume expansion of water does not only cause ice to grow into the voids but also pushes particles away
- Sand layer may heave under fully submerged condition
- Ballast layer may heave under certain moisture conditions
- Frost heave may occur on the solid particles that have low moisture absorption capability

**Acknowledgements** This research is partially funded by the new faculty startup fund provided by the College of Engineering and Computer at the University of South Carolina. The opinions expressed in this article are solely those of the authors and do not represent the opinions of the funding agencies.

## References

1. Rempel AW, Wettlaufer JS, Worster MG (2004) Premelting dynamics in a continuum model of frost heave. *J Fluid Mech* 498:227
2. Taber S (1930) The mechanics of frost heaving. *J Geol* 38(4):303–317
3. Akagawa S, Kodama N (2005, January) Frost weathering in rocks and mortar. In *Alaska Rocks 2005*. In: The 40th US symposium on rock mechanics (USRMS). American Rock Mechanics Association
4. Beskow G (1935) Soil freezing and frost heaving with special application to roads and railroads. *Swed Geol Soc Ser C No. 375*, 26th year book No. 3 (translated by J.O. Osterberg, Northwestern Univ., 1947)
5. Bronfenbrener L, Bronfenbrener R (2010) Modeling frost heave in freezing soils. *Cold Reg Sci Technol* 61(1):43–64
6. Fasano A, Primicerio M (1984) Freezing in porous media; a review of mathematical models. *Appl Mathematics Technol* Teubner, pp 288–311
7. Wettlaufer JS (1999) Ice surfaces: macroscopic effects of microscopic structure. *Phil Trans R Soc Lond A* 357:3403–3425
8. Henry KS (1996) Geotextiles to mitigate frost effects in soils: a critical review. *Transp Res Record* 1534(1):5–11
9. Nurmikolu A (2005) Degradation and frost susceptibility of crushed rock aggregates used in structural layers of railway track. Tampere University of Technology

10. Sheng DC, Zhang S, Niu F, Cheng G (2014) A potential new frost heave mechanism in high-speed railway embankments. *Géotechnique* 64(2):144–154
11. Akagawa S, Hori M, Sugawara J (2017) Frost heaving in ballast railway tracks. *Procedia Eng* 189:547–553
12. Arema LMD (2013) American railway engineering and maintenance-of-way association. *Manual for railway engineering*

# Study of the Influence of Rainwater on the Railway Track



Luisa Carla de Alencar Menezes ,  
Antonio Carlos Rodrigues Guimarães , and Carmen Dias Castro 

**Abstract** It is a common practice to use traditional criteria in the selection of materials in railway paving projects as well as the use of optimum moisture in pavement design through the California Bearing Ratio (CBR) method. However, variations in the weather can change the conditions of the infrastructure components over time, especially of the railway tracks since they have no coating and thus are exposed to the elements. These criteria, based only on the mechanical behavior of materials, are not adequate to evaluate the tropical soils and their hydraulic behavior so that soils with good performance can be discarded if more efficient criteria of analysis are not adopted. Therefore, the main objective of this research is to evaluate the variation of humidity over time in the railway platform when subjected to the action of rainwater for five different soil types when used in the sub-ballast layer, from the numerical–experimental analysis, considering as reference case the infrastructure of the Carajás Railway. For this purpose, tests were carried out on the HYPROP and WP4-C equipment in order to obtain the retention and hydraulic conductivity curves of the studied soils. The hydraulic functions in question were performed with the help of the IVFlow program and the input parameters such as section type, precipitation of the region, as well as the van Genuchten hydraulic model as a constitutive model. The results revealed that sample 1 (LS) has the best performance in the presence of water and is suitable for employment in the sub-ballast layer. The other samples presented unsatisfactory results.

**Keywords** Railway track · Moisture · Soil

## 1 Introduction

It is known that in order to achieve a good development in paving projects as well as a consistent mechanistic analysis, one must take into account, among other climatic

---

L. C. de Alencar Menezes (✉) · A. C. R. Guimarães · C. D. Castro  
Military Institute of Engineering, Rio de Janeiro, Brazil

A. C. R. Guimarães  
e-mail: [guimares@ime.eb.br](mailto:guimares@ime.eb.br)

factors, temperature and rainfall. A different rainfall entails a variation of moisture in situ and, therefore, affects the strength and module of the pavement.

The module of the materials is affected by its physical state; therefore, it is influenced by the moisture content of the material. Several studies have shown that moisture changes after compaction promote relevant changes in the module of resilience [1–4].

The study in question has relevant application in the railway sector, considering that the tracks do not have the coating protection, thus becoming more susceptible to the action of precipitation. The effect in the degradation of tracks is observed in situ, but little is known about how the variation of moisture from rainfall occurs. Currently, the railway with higher volume transported is the Carajás Railway (EFC), which is located in a region of high rainfall and high temperatures; that is, the platform is constantly exposed to inclement weather which causes premature wear of the track, once the water accelerates the degradation process of the permanent way.

In regions with tropical climate, for sub-ballast material, lateritic soil is commonly applied. This type of soil is common in these regions; however, the AREMA standard, which guides the design of railway pavements, recommends the use of stone materials as sub-ballast material, according to the characteristics of foreign railways. Thus, one realizes the importance of the study and inclusion of new selection criteria more appropriate to the reality of tropical regions.

Unlike stone materials, the lateritic soil is sensitive to the action of water and its percolation may compromise the railway platform, causing a decrease of the resilient module as well as permanent deformations. In this way, it is consistent that the analysis of the soil water behavior, taking into consideration its permeability, composes the set of criteria for the selection of materials to be used in the rail pavement.

## **2 Theoretical Foundation**

For the theoretical foundation of this study, the following concepts were addressed:

### ***2.1 Railway Infrastructure***

According to [5], the railway can be divided into two basic subsystems: the rolling stock and the permanent way, which encompasses the railway infrastructure and superstructure.

The railway infrastructure, focus of this study, is composed by the railway platform which is composed of leveling, drainage systems, special structures and flyovers and tunnels.

The railway platform is composed of rail, sleeper, equipments for direct fixation of the rails to the sleepers, ballast, sub-ballast and subgrade. These layers, according to

[6], make up the rail pavement. The term “rail pavement” was first used by Professor Jacques de Medina, of COPPE/UFRJ, to distinguish the successive layers that constitute the permanent railway and that work in an integrated way [7]. Its function is to receive the loads from the rail traffic in order to limit the damage to acceptable levels.

## 2.2 Retention Curve

The characteristic curve, retention curve or even suction curve of a soil is described by the suction ratio due to the saturation degree, volumetric moisture content or gravimetric moisture content. The mathematical equation commonly used for retention curves is the equation of [8].

$$\theta = \frac{1}{[1 + (\alpha\psi)^n]^{1-\frac{1}{n}}} \quad (1)$$

The coefficients of this curve relate to different soil properties. Prior knowledge of the retention curve is of fundamental importance for the analysis of the non-saturated soil behavior. Once known the retention curve of a given soil, it is possible to derive the conductivity curve of the material.

## 3 Methodology

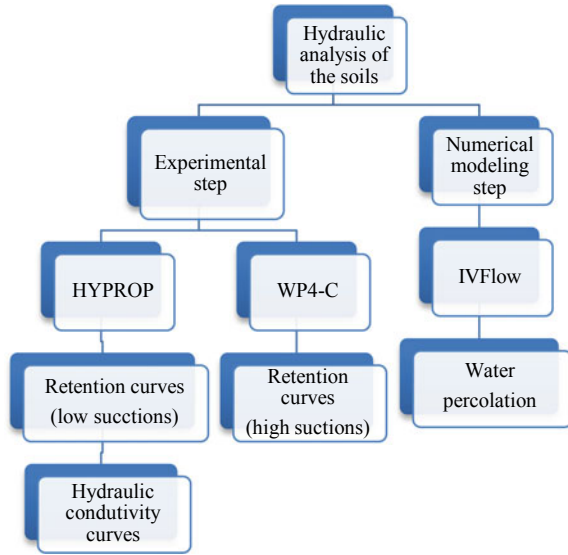
This research is part of an agreement called “Studies for Review of Design Criteria of the Permanent Way,” signed between Military Institute of Engineering (IME) and VALE S.A. in order to evaluate the criteria for selection of materials and assumptions of sizing practiced currently in railway engineering projects. In general, these criteria are based on international studies and, therefore, are not directed to the Brazilian conditions and peculiarities.

For such, 53 samples were collected along EFC in order to perform an analysis concerning its applicability as a layer of rail pavement. According to [8], at the time of collection, one searched for materials that visually would not meet the design criteria, if the traditional methods of selection were considered. However, if more modern methods were used, they could exhibit good behavior.

As a methodology of this study, the following steps were followed: collection of samples, experimental step and numerical modeling as shown in Fig. 1.

Five types of soils and their applicability in the sub-ballast layer of the railway platform from the point of view of the hydraulic behavior of the pavement were studied. However, there will be described in this article the full results for samples 1 and 4, which presented more relevant results.

**Fig. 1** Research flowchart



Sample 1, also known as sample 26, is a thick sandy soil, as visual description at the time of collection, taken at the foot of a slope present at the site of the duplication. The soil was identified by [9] as lateritic sand (LS) according to the MTC classification. In accordance with the creators of this methodology, the soils classified as LS and LS' would be the most recommended to be used in road works and present the following characteristics as shown in Tables 1 and 2.

Applying the criteria laid down by [10], sample 1 would be disapproved once it does not meet the granulometry ranges and value of physical indexes recommended in the standards traditionally adopted. The grain size distribution (%) and the geotechnical characterization of all samples are shown in Tables 3 and 4, respectively.

**Table 1** Granulometric composition of sample 1

Granulometric composition (%)—sample 1 (LA)					
Clay	Silt	Sand			Gravel
		Fine	Medium	Coarse	
9.95	6.75	9.2	57.38	9.75	6.97

**Table 2** Geotechnical characterization of sample 1

Geotechnical characterization—sample 1						
Energy	Compaction			Physical indexes		
	W optimum (%)	MEAS (g/cm <sup>3</sup> )	DR	LL (%)	LP (%)	IP (%)
Intermediate	6	2.07	2.65	17.5	NP	17.5



**Table 3** Grain size distribution of studied samples

	Grain size distribution (%)					
	Clay	Silt	Sand			Gravel
			Fine	Medium	Coarse	
Sample 1	9.95	6.75	9.2	57.38	9.75	6.97
Sample 2	39.2	57.48	3.32	0	0	0
Sample 3	7.43	0.25	83.37	8.9	0.02	0.04
Sample 4	6.69	21.24	70.62	1.45	0	0
Sample 5	22	17	37	21	1	2

**Table 4** Geotechnical characterization of studied samples

	Geotechnical characterization						
	Energy	Compaction			Physical indexes		
		W optimum (%)	MEAS (g/cm <sup>3</sup> )	DR	LL (%)	LP (%)	IP (%)
Sample 1	Intermediate	6	2.07	2.65	17.5	NP	17.5
Sample 2	Intermediate	15.4	1.67	2.71	35.5	0	35.5
Sample 3	Intermediate	6	1.92	2.62	29.4	19.9	9.5
Sample 4	Intermediate	15.4	1.74	2.66	NL	NP	NP
Sample 5	Intermediate	16	1.76	2.64	27	10	17

### 3.1 Experimental Step

Initially, in order to obtain the required parameters for numerical simulation, it was necessary to obtain the characteristic curve and the conductivity curve of the soil of the studied samples. For this, initially, the material available was sieved and the fraction retained on sieve n° 10 (2 mm opening) was discarded, as the equipment HYPROP and WP4-C used for obtaining the hydraulic functions do not allow to work with a higher granulometry material. It was admitted as a basis for such, the claim of [5] that the nature of the fine fraction determines the soil behavior to resilience.

At the Laboratory of Geotechnical in COPPE/UFRJ—Section of Environmental Geotechnics, tests were held for obtaining the retention curve and the conductivity curve of the sample using the HYPROP equipment. The procedure for carrying out the test was conducted as advocated in the device manual.

The HYPROP equipment has its optimal measuring range restricted between the voltage values from 0 to 1000 cm of the water column. However, it was observed the need of obtaining additional points for a better delineation of the retention curve obtained in HYPROP.

With the completion of tests in the WP4-C equipment, it was possible to obtain points from 1000 to 1000,000 cm of the water column, optimal measuring range of

**Table 5** Properties of sample 1

<i>Hydraulic properties</i>	
Hydraulic saturation property (cm/h)	0.0099
Saturation humidity (m <sup>3</sup> /m <sup>3</sup> )	0.2946
Residual humidity (m <sup>3</sup> /m <sup>3</sup> )	0.1817
<i>General information</i>	
Optimal gravimetric moisture (%)	6
Specific dry soil mass (Kg/m <sup>3</sup> )	2070
Water density (kg/m <sup>3</sup> )	1000

the apparatus. The analyses have been carried out at Embrapa Solos—CNPS, located in the city of Rio de Janeiro—RJ.

### 3.2 Numerical Modeling

The second step of the study consisted in numerical modeling with the aid of a software simulation of water infiltration in the railway platform, IVFlow, which uses the finite element method for the solution of Richards equation, that governs the process of transient infiltration of the water in the soil, developed in partnership between the Military Engineering Institute (IME) and VALE S.A.

To build the model were used as parameters of the section values that represent the EFC infrastructure. The conditions for precipitation considered were selected from the program database when selected the study region. The multi-linear option for the hydraulic model was selected, in which the hydraulic functions obtained experimentally fit, as shown in Tables 5, 6, 7, 8, 9, 10, 11 and 12 (Tables 13 and 14).

## 4 Analysis of Results

### 4.1 Retention Curve

The test performed with sample 1 in HYPROP equipment showed its retention curve adjusted in HYPROP-FIT program by the model of Fredlung-Xing bimodal (Fig. 2), option among the five models available that provided better adjustment.

Including the complementary points from the test in WP4-C in the HYPROP-FIT program, a new curve was obtained, which aspect is shown in Fig. 3.

The same procedure was made with sample 5. HYPROP equipment showed its retention curve adjusted in HYPROP-FIT program by the model of Fredlung-Xing unimodal (Fig. 4), option among the five models available that provided better adjustment.

**Table 6** Data of the constitutive multi-linear model of sample 1

Redemption curve		Conductivity curve	
Pressure (cm)	Volumetric moisture (m <sup>3</sup> /m <sup>3</sup> )	Pressure (cm)	Hydraulic conductivity (cm/h)
0.00000	0.2946	0	0.0099
- 2.8184	0.2946	- 29.9916252	0.009995137
- 8.2985	0.2913	- 36.4753947	0.0099328005
- 15.9221	0.2844	- 44.874539	0.006757542
- 21.0378	0.2738	- 57.0164272	0.004263721
- 26.5461	0.2588	- 79.7994687	0.001948896
- 31.7687	0.2447	- 126.765187	0.002040745
- 1000	0.1352	- 245.470892	0.00165878
- 5370.31796	0.0741	- 515.228645	0.000954528
- 12,022.6443	0.0350	- 805.378441	0.002136922

**Table 7** Properties of sample 2

<i>Hydraulic properties</i>	
Hydraulic saturation property (cm/h)	0.0011
Saturation humidity (m <sup>3</sup> /m <sup>3</sup> )	0.4851
Residual humidity (m <sup>3</sup> /m <sup>3</sup> )	0.1822
<i>General information</i>	
Optimal gravimetric moisture (%)	15.4
Specific dry soil mass (Kg/m <sup>3</sup> )	1670
Water density (Kg/m <sup>3</sup> )	1000

**Table 8** Data of the constitutive multi-linear of sample 2

Redemption curve		Conductivity curve	
Pressure (cm)	Volumetric moisture (m <sup>3</sup> /m <sup>3</sup> )	Pressure (cm)	Hydraulic conductivity (cm/h)
0.00000	0.2946	0.0000	0.0011
- 13.2130	0.2946	- 13.2130	0.0060
- 65.3131	0.2913	- 65.3131	0.0025
- 96.8278	0.2844	- 96.8278	0.0015
- 91.6220	0.4746	- 91.6220	0.0010
- 157.7611	0.4695	- 157.7611	0.0010
- 202.3019	0.4641	- 202.3019	0.0012
- 1230.2688	0.4197	- 289.7344	0.0009
- 5370.3180	0.3464	- 427.5629	0.0026
- 14,454.3977	0.18822	- 574.1165	0.0069

**Table 9** Properties of sample 3

<i>Hydraulic properties</i>	
Hydraulic saturation property (cm/h)	0.0013
Saturation humidity (m <sup>3</sup> /m <sup>3</sup> )	0.4907
Residual humidity (m <sup>3</sup> /m <sup>3</sup> )	0.0685
<i>General information</i>	
Optimal gravimetric moisture (%)	6
Specific dry soil mass (Kg/m <sup>3</sup> )	1.92
Water density (Kg/m <sup>3</sup> )	1000

**Table 10** Data of the constitutive multi-linear model of sample 3

Redemption curve		Conductivity curve	
Pressure (cm)	Volumetric moisture (m <sup>3</sup> /m <sup>3</sup> )	Pressure (cm)	Hydraulic conductivity (cm/h)
0.00000	0.4907	0.0000	0.0013
- 4.4157	0.4827	- 2.9923	0.0417
- 41.2098	0.4736	- 4.3752	0.0417
- 95.9401	0.4618	- 4.3551	0.0048
- 171.7908	0.4448	- 45.1856	0.0056
- 262.4219	0.4256	- 138.9953	0.0079
- 395.3666	0.4001	- 231.7395	0.0047
- 19,498.4460	0.2283	- 341.1929	0.0008
- 69,183.0971	0.1576	- 644.1693	0.0002
- 89,125.0938	0.0685	- 264.8500	0.0001

**Table 11** Properties of sample 4

<i>Hydraulic properties</i>	
Hydraulic saturation property (cm/h)	0.0074
Saturation humidity (m <sup>3</sup> /m <sup>3</sup> )	0.3662
Residual humidity (m <sup>3</sup> /m <sup>3</sup> )	0.0621
<i>General information</i>	
Optimal gravimetric moisture (%)	16.5
Specific dry soil mass (kg/m <sup>3</sup> )	1730
Water density (kg/m <sup>3</sup> )	1000

**Table 12** Data of the constitutive multi-linear model of sample 4

Redemption curve		Conductivity curve	
Pressure (cm)	Volumetric moisture (m <sup>3</sup> /m <sup>3</sup> )	Pressure (cm)	Hydraulic conductivity (cm/h)
0.00000	0.3662	0.0000	0.0074
- 5.0119	0.3642	- 5.0119	0.00776
- 1.0917	0.3575	- 11.0917	0.00831
- 25.9418	0.3464	- 41.5911	0.00812
- 49.6592	0.3316	- 63.6796	0.00457
- 67.6083	0.3143	- 71.9449	0.00513
- 76.9130	0.2856	- 89.1251	0.00162
- 2570.3958	0.1190	- 127.9381	0.00048
- 3019.9517	0.1528	- 264.2409	0.00014
- 645.6542	0.0621	- 642.6877	0.00003

**Table 13** Properties of sample 5

<i>Hydraulic properties</i>	
Hydraulic saturation property (cm/h)	0.00417
Saturation humidity (m <sup>3</sup> /m <sup>3</sup> )	0.3849
Residual humidity (m <sup>3</sup> /m <sup>3</sup> )	0.1235
<i>General information</i>	
Optimal gravimetric moisture (%)	16
Specific dry soil mass (kg/m <sup>3</sup> )	1760
Water density (kg/m <sup>3</sup> )	1000

**Table 14** Data of the constitutive multi-linear model of sample 5

Redemption curve		Conductivity curve	
Pressure (cm)	Volumetric moisture (m <sup>3</sup> /m <sup>3</sup> )	Pressure (cm)	Hydraulic conductivity (cm/h)
0.00000	0.3849	0.0000	0.0417
- 5.0119	0.3845	- 2.5293	0.00513
- 1.0917	0.3794	- 2.9648	0.00831
- 25.9418	0.3749	- 4.6666	0.00812
- 49.6592	0.3701	- 8.3946	0.00457
- 67.6083	0.3643	- 18.8365	0.00513
- 76.9130	0.2135	- 34.3558	0.00162
- 2570.3958	0.1764	- 76.3836	0.00048
- 3019.9517	0.236	- 167.8804	0.00014
- 645.6542	0.0621	- 308.3188	0.00003

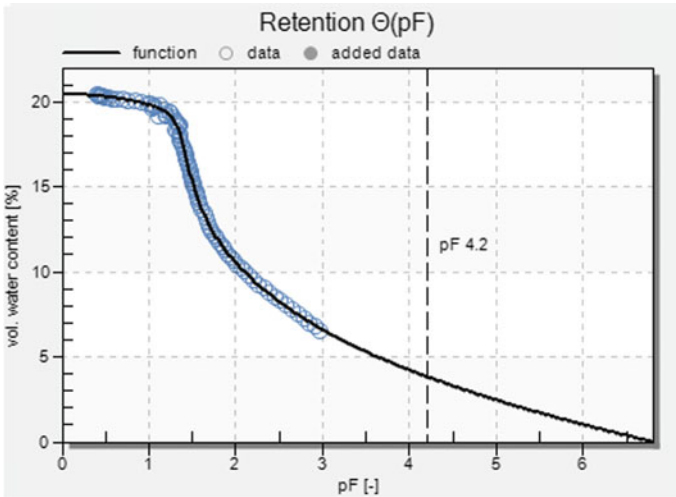


Fig. 2 Sample 1 retention curve obtained in HYPROP

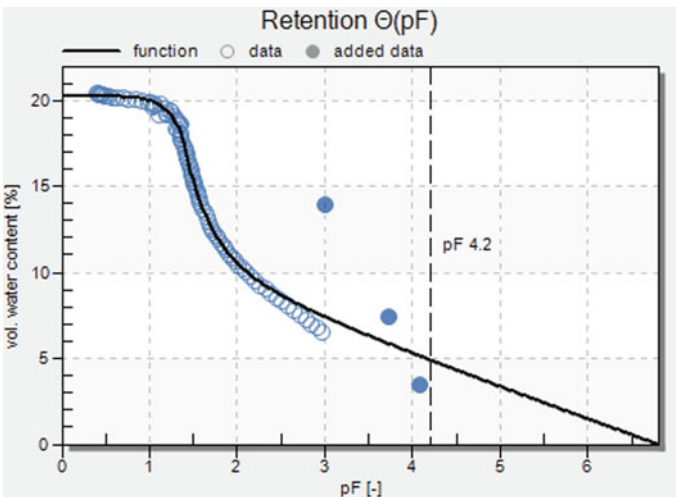


Fig. 3 Sample 1 retention curve obtained in HYPROP 1 and in WP4-C

Including the complementary points from the test in WP4-C in the HYPROP-FIT program, a new curve was obtained, which aspect is shown in Fig. 5.

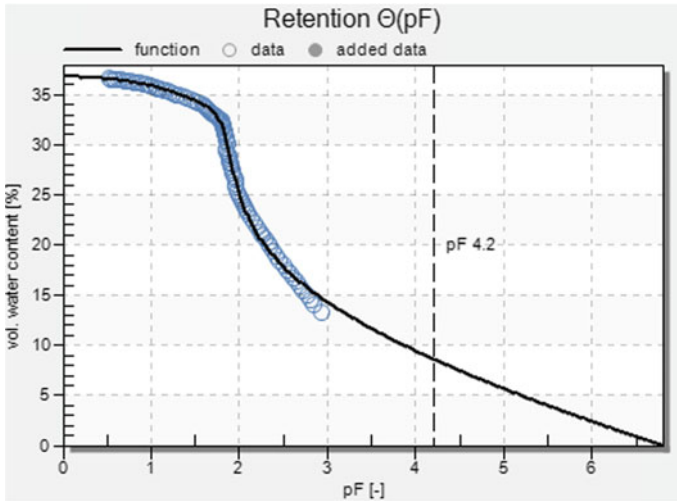


Fig. 4 Sample 4 retention curve obtained in HYPROP

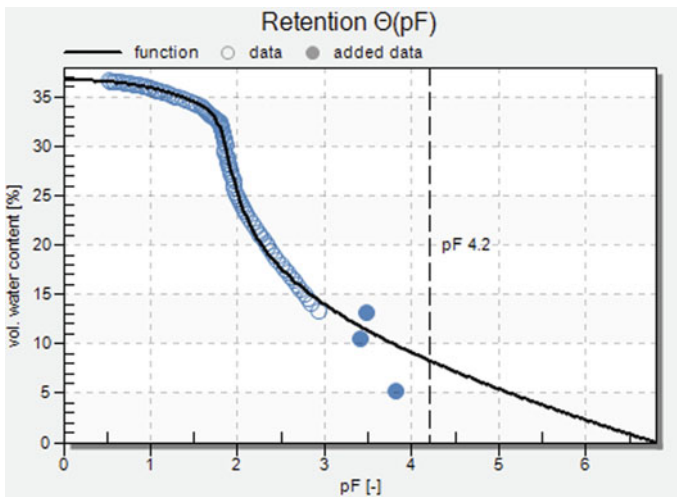


Fig. 5 Sample 4 retention curve obtained in HYPROP 1 and in WP4-C

### 4.2 Simulation

Once having the hydraulic functions of the samples, it was possible to analyze through the IVFlow program their behavior when employed in the sub-ballast layer of the rail pavement subject to the action of rain. The tool provides results through spatial distribution in a given moment (Figs. 6, 7 and 8), temporal graph for a determined point and report summary.

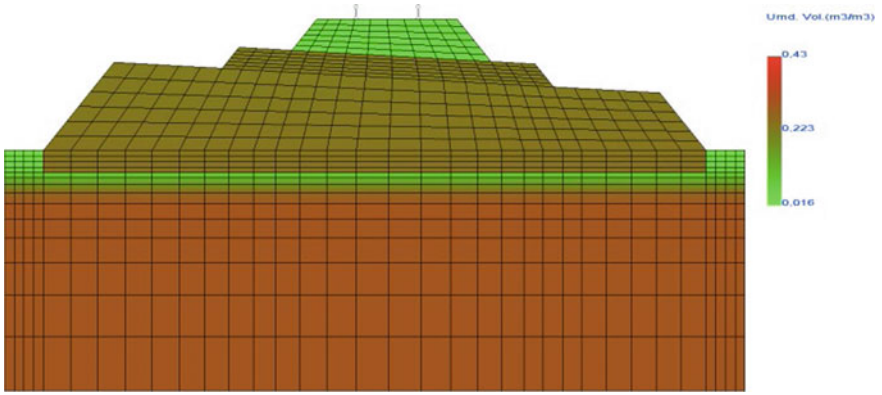


Fig. 6 Volumetric water content at  $t = 0$  (sample 1)

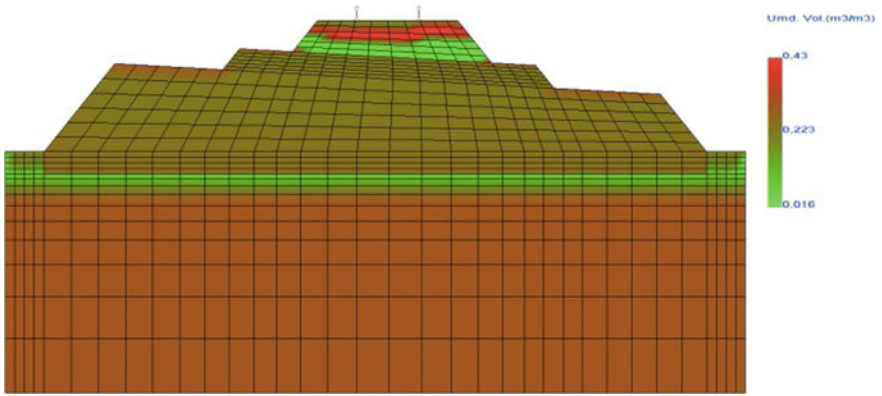


Fig. 7 Volumetric water content at  $t = 10$  min (sample 1)

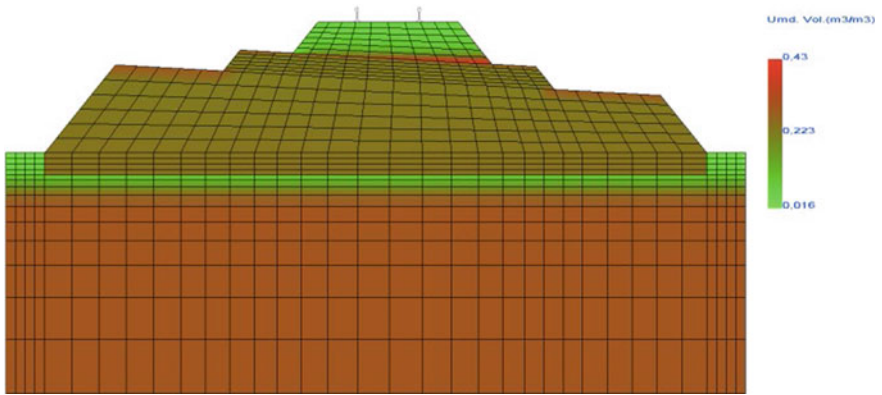


Fig. 8 Volumetric water content at  $t = 3$  h (end of simulation/sample 1)



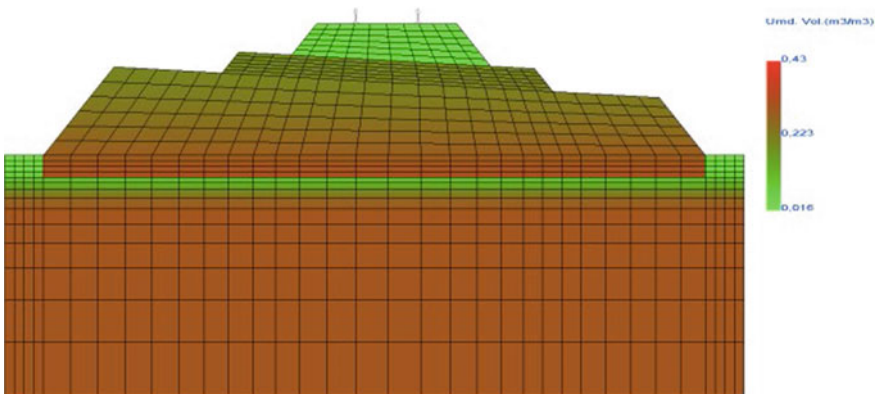
The program generated initially a temporal graph of volumetric water content ( $t = 0$ ). Based on the outputs provided by the program, moisture was detected from the sub-ballast layer that presented a moisture content of  $22.65 \text{ m}^3/\text{m}^3$ , that is, around 3.3% below the saturation moisture and 4.95% above the optimum moisture of the material.

This initial high moisture can be attributed to the infiltration of groundwater by capillary rise, once in the construction of the model it was assigned a water level of 2.6 m and before the precipitation that would be the only possibility of action of the water on the pavement. Realized this situation, the simulations were repeated now assigning a water level of 10 m. However, the layer remained with the same initial moisture content.

Based on the outputs provided by the program, it was detected that the moisture from the sub-ballast layer, when constituted by sample 1, reached a maximum content of 8.2% above the optimum content; that is, the action of rain caused an increase of 3.3% of this content, given that layer already presented a moisture 4.95% above the optimum before the beginning of the simulation. It was also identified that 100% of the layer has suffered a moisture variation greater than 3% in relation to the optimum moisture.

For sample 4 based on the chart, it was possible to verify that before the action of the environment, the sub-ballast layer presented a moisture content that is around 9.6% below the saturation moisture and 4.9% above the optimum moisture of the material. Results for sample 4 through spatial distribution in a given moment are shown in Figs. 9, 10, 11, 12 and 13.

Once the simulation started, subjecting the pavement to the action of the environment for 10 min, the moisture content of the exposed interface increased to 2.4% below saturation, and the other regions did not change their humidity. It was possible to see the advance of the moisture fringe on the railway track (Fig. 10).



**Fig. 9** Volumetric moisture:  $t = 0 \text{ h}$

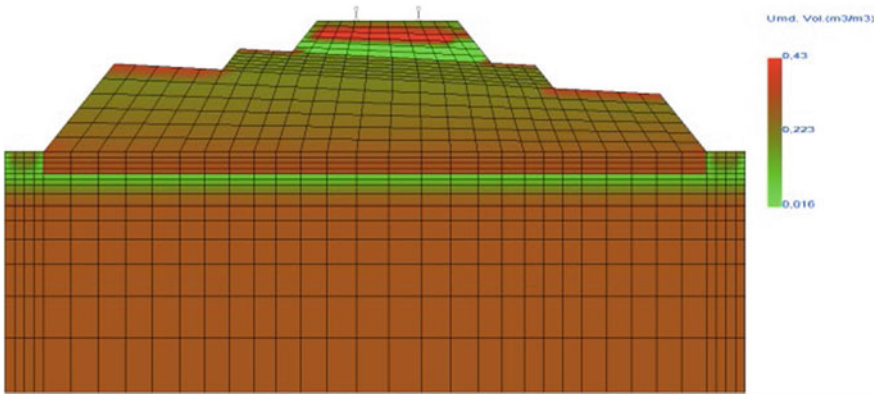


Fig. 10 Volumetric moisture:  $t = 10$  min

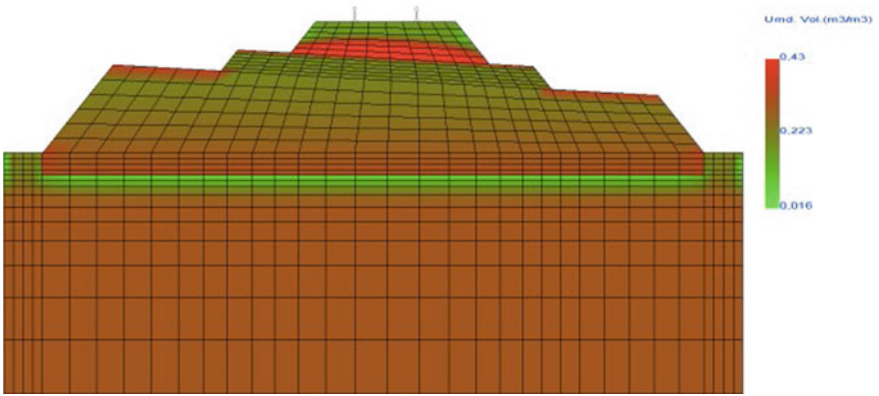


Fig. 11 Volumetric moisture:  $t = 30$  min

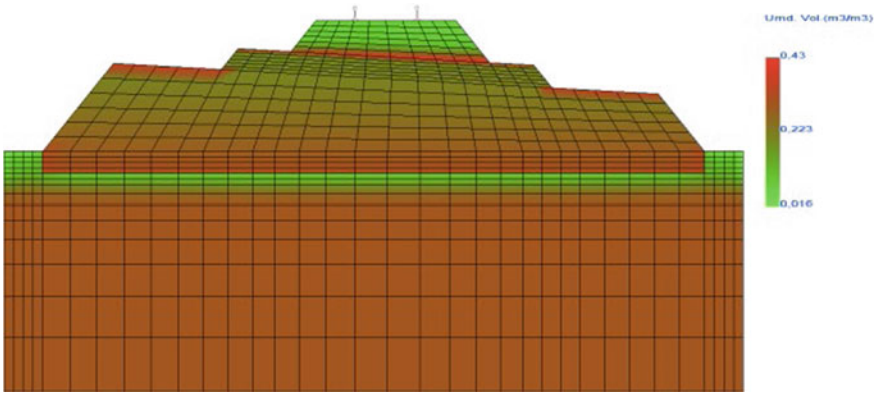
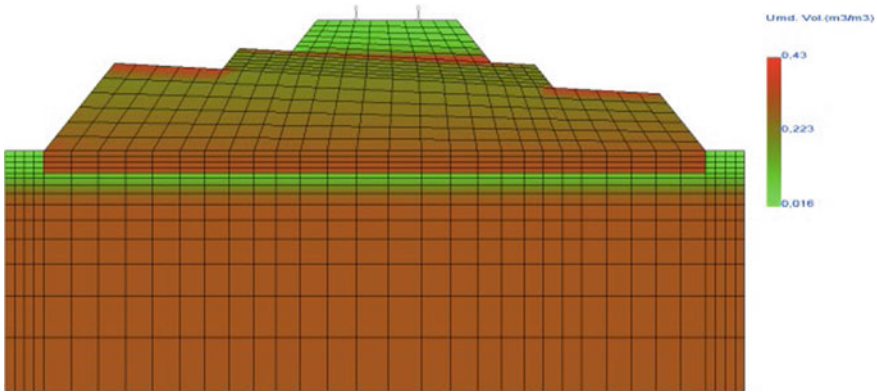


Fig. 12 Volumetric moisture:  $t = 1$  h and 30 min



**Fig. 13** Volumetric moisture:  $t = 3$  h

At 30 min of rain, the moisture at the exposed interface of the sub-ballast and in the border range with the ballast reaches the saturated moisture. The interior of the layer retains its moisture content unchanged (Fig. 11).

Similarly, to the other simulations there was no change in the moisture of the sub-ballast between 30 min and 1 h and 30 min of rain (Fig. 12).

After 3 hours of simulation up to 2.5% reduction in moisture at the top of the layer was observed. The remaining fractions remained at the initial levels.

The IVFlow outputs showed that sample 4 reached a maximum moisture content of 4.65% above the optimum content. Therefore, there was an increase of 9.55% in the moisture content of the sub-ballast that can be attributed to the action of rainwater. The tool also returned that only a fraction of 5.3% of the layer had a moisture variation greater than 1% in relation to the optimum moisture. The output data provided by the program are shown in Table 15.

**Table 15** Output data provided by the program

Sample	Layer	Minimum moisture (m <sup>3</sup> /m <sup>3</sup> )	Maximum moisture (m <sup>3</sup> /m <sup>3</sup> )	Optimum moisture (m <sup>3</sup> /m <sup>3</sup> )
Sample 1 (LA)	Sub-ballast	0.225	0.295	0.124
Sample 2	Sub-ballast	0.469	0.485	0.257
Sample 3	Sub-ballast	0.448	0.491	0.084
Sample 4	Sub-ballast	0.189	0.366	0.285
Sample 5	Sub-ballast	0.346	0.385	0.282

## 5 Conclusion

From the numerical analyses, it was realized that at the beginning of the simulations, before the action of rain, all samples showed moisture above optimum, except sample 4, which preliminarily presented a moisture content of 4.9% below optimum. This behavior can be assigned to the influence exerted by the water level, once in the initial condition the pavement suffers only the action of the groundwater infiltration.

Samples 1 (LS) and 4 (LS') were less susceptible to the water-level influence. The others exhibited initial moistures very close to the saturation content that would lead them to significant changes of resilience module and, therefore, permanent deformations.

Starting from the initial moisture content provided by the program and also using as a criterion the elevation of moisture from the initial conditions, we observed that sample 1 showed better performance, that is, lower elevation of moisture after the action of rain in relation to sample 4. This one had an increase of 9.55%, while the other ranged 3.25% in its content.

Sample 1 also presented low permeability, desirable property to the sub-ballast to behave like a waterproof layer protecting the subbase. Its lateritic character contributes to its applicability due to the formation of rigid blocks, a typical laterite behavior, giving greater capacity to support the pavement. Considering the analysis of hydraulic behavior, we can conclude that the soil of sample 1 is able to compose the rail pavement, even not meeting the traditional criteria practiced nowadays.

## References

1. Selig, ET, Waters, JM (1994) Track geotechnology and substructure management. Thomas Telford Services Ltd., Londres, UK
2. Bernucci LL (1995) Considerações sobre o dimensionamento de pavimentos utilizando solos lateríticos para rodovias de baixo volume de tráfego. Dissertação de Mestrado, Universidade de São Paulo, São Paulo, Brasil
3. Silva BA (2003) Aplicação das metodologias MCT e Resiliente a solos finos do centro-norte do Mato Grosso, Dissertação de Mestrado em Engenharia de Transportes, IME, Rio de Janeiro
4. Takeda MC (2006) Influência da variação da umidade pós compactação no comportamento mecânico de solos de rodovias do interior paulista, Tese de Doutorado em Engenharia Civil, USP, São Carlos
5. Nabais RJS et al (2014) Manual básico de engenharia ferroviária. São Paulo, Brasil: Oficina de Textos
6. Medina J (1997) Mecânica dos Pavimentos. Editora UFRJ, Rio de Janeiro
7. Guimarães ACR, Santana CSA (2014) Relatório—primeira visita técnica à EFC. Projeto IME/Vale: Estudos para Revisão de Critérios de Projeto da Via Permanente. Instituto Militar de Engenharia. Rio de Janeiro
8. Van Genuchten MTH (1980) A closed-form equation for predicting the hydraulic conductivity of unsaturated soils. *Soil Soc Am J* 44:892–898

9. Sousa MAS (2016) Análise geotécnica de solos tropicais de ocorrência ao longo da estrada de ferro Carajás para uso como camadas de pavimento rodoviário, Dissertação de Mestrado, Instituto Militar de Engenharia, Rio de Janeiro, 222 p
10. AREMA—American Railway Engineering Maintenance-of-Way Association (2009) Manual for Railway Engineering. Lanham. Arema, vols I and IV

# **Slope Stability**

# Predicting the Stability of Riverbank Slope Reinforced with Columns Under Various River Water Conditions



Cong Chi Dang, Liet Chi Dang, and Hadi Khabbaz

**Abstract** A numerical analysis on the stability of soil–cement column-reinforced riverbank along a river delta region in Viet Nam is presented in this paper. The numerical analyses based on the limit equilibrium method (LEM) were performed to assess the safety factor of the column-reinforced riverbank system under various river water level (RWL) conditions. Several factors influencing the riverbank slope stability including the position, length, quantity of soil–cement columns, and RWL changes were investigated. The simulated results showed that the riverbank stability is improved with an increase in the column quantity and the column length when subjected to a constant RWL. Moreover, the predicted results by LEM indicated that the column location and the RWL change significantly influence the stability of riverbank with column reinforcement. The column location between the middle and the slope toe had a significant improvement of the riverbank slope stability, where an initial drawdown of RWL resulted in a notable reduction of the riverbank slope safety factor. These factors should be taken into consideration in the design of a riverbank slope, reinforced with columns, under variable RWL. It is worth mentioning that the use of soil–cement column-reinforced riverbank could be a practical and possible engineering countermeasure to prevent a steep riverbank slope under RWL variations from sliding failure.

**Keywords** Riverbank stability · River water level · Soil-cement columns · Slope stabilisation · Numerical modelling · Limit equilibrium method

---

C. C. Dang

Faculty of Civil Engineering, Ho Chi Minh City University of Technology (HCMUT), Ho Chi Minh City, Vietnam

Vietnam National University (VNU-HCM), Ho Chi Minh City, Vietnam

C. C. Dang

e-mail: [1870139@hcmut.edu.vn](mailto:1870139@hcmut.edu.vn)

L. C. Dang (✉) · H. Khabbaz

School of Civil and Environmental Engineering, University of Technology Sydney, Ultimo, NSW 2007, Australia

H. Khabbaz

e-mail: [Hadi.Khabbaz@uts.edu.au](mailto:Hadi.Khabbaz@uts.edu.au)

## 1 Introduction

Soil stability analysis has been a great challenge to geotechnical engineers because the geotechnical structures are complex, involving a complicated soil–structure interaction. Slope failure due to some influential factors consisting of a rapid drawdown of water levels [1, 2], excess soil movement when subjected to larger external loads [3], uncertainty of soil properties [4], threatens human life and their properties. To maintain the slope stability and prevent soil from collapse, practical solutions of geotechnical engineering structures such as retaining walls, piles or columns constructed in slopes are commonly adopted to reduce the probability of the sliding failure to occur.

Numerical methods such as the finite element method (FEM), the finite difference method (FDM) or the distinct element method (DEM) have extensively been adopted and proven as an effectively alternative solution to slope stability analysis [4]. However, the majority of numerical investigations have been conducted and focused on assessment of the natural riverbank slope stability [1, 2, 5] subjected various conditions of water drawdown. They have also taken into consideration the effects of several fundamental influencing parameters such as the bank geometry characteristics, hydrostatic confining pressure, positive and negative pore water pressure vegetation and vertical surcharge load on the slope stability of natural riverbank slopes. Meanwhile, other researchers have paid their primary attention to investigating the stability of slopes stabilised with high strength and stiffness piles based on the numerical method [3, 6–8] and the analytical approach [9, 10]. Nonetheless, investigating the deep cement mixing (DCM), low-strength columns (soil–cement mixture) adopted to increase the stability of riverbank slope have remained very limited although many investigators [11] indicated that DCM columns could be used effectively as retaining walls to support shallow to intermediate excavation depths. Dang et al. [12] investigated the mechanical behaviour of DCM columns foundation [13–22] and stabilised materials with recycled fibre reinforcement [23–31] to be used as fibre reinforced load transfer platform (FRLTP) to support highway embankments built on soft soils, and also confirmed that the application of combined DCM columns and FRLTP improved the embankment deformation and instability. Therefore, it is crucially important to investigate the influence of DCM columns on the stability of riverbank slope. Such investigations could provide a better understanding of the use of DCM columns to reinforce slopes as an alternative and practical engineering solution to the stability improvement of riverbank along rivers when undergoing RWL fluctuations.

In this paper, the effect of DCM column reinforcement on the riverbank stability is examined by numerical analysis using LEM incorporated in SLOPE/W. Several series of numerical parametric studies on the influence of the location, length and numbers of columns on the riverbank stability are performed. The numerical results are presented and analysed to comprehend the riverbank slope stability and the potential failure pattern of column-reinforced riverbank subjected to a constant RWL condition. The key parameters affecting the stability of riverbank slope subjected to different RWL conditions are also examined and discussed in detail. It should be



noted that although, for design methods based on the limit equilibrium method, a safety factor ( $FS = 1$ ) is required to maintain the limit equilibrium state of riverbank slope, a safety factor value greater than one ( $FS > 1$ ) is typically required for the riverbank slope stability during serviceability conditions.

## 2 Description of Case Consideration

The stability analyses based on LEM of a 19 m high and 40 m wide (at crest) riverbank slope reinforced with 1–4 rows of DCM columns are carried out in this study (see Fig. 1). The riverbank is composed of an isotropic and homogeneous silty sand with a cohesion of 10 kPa, a friction angle of  $30^\circ$  and an average unit weight of  $18 \text{ kN/m}^3$ . Another isotropic and homogeneous sand layer with a thickness of 9 m was found below the silty sand. The steady ground-water table is located at a depth of 10 m below the riverbank surface. Details of these soil layers are summarised in Table 1. It should be noted that tangential DCM columns with 1 m diameter ( $D$ ), 9 m length ( $L_c$ ) and a centre-to-centre column spacing ( $s$ ) of 2 m are arranged in a row pattern,

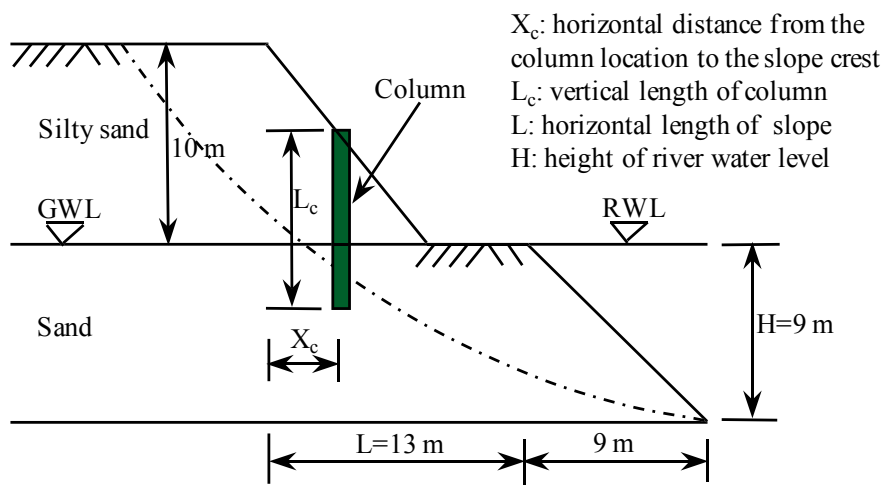


Fig. 1 Typical schematic of a riverbank reinforced with DCM columns

Table 1 Material properties of subgrade soil layers used in this study

Parameters	Silty sand	Sand	DCM columns
Depth (m)	5–15	– 4 to 5	–
$\gamma$ ( $\text{kN/m}^3$ )	18	19	19
$c'$ (kPa)	10	0	75
$\phi'$ ( $^\circ$ )	30	40	42

while horizontal length ( $L = 13$  m) of slope considered is presented in Fig. 1. They are used to improve the riverbank slope stability when river water level varies in a range of  $H = 9\text{--}16.5$  m due to seasonal variations. The DCM columns were assumed to have the unconfined compressive strength ( $q_u$ ) of 1000 kPa; a cohesion value of 75 kPa; and a friction angle of  $42^\circ$  and an average unit weight of  $19$  kN/m<sup>3</sup>, which represents typical DCM column properties used in the examined region [32].

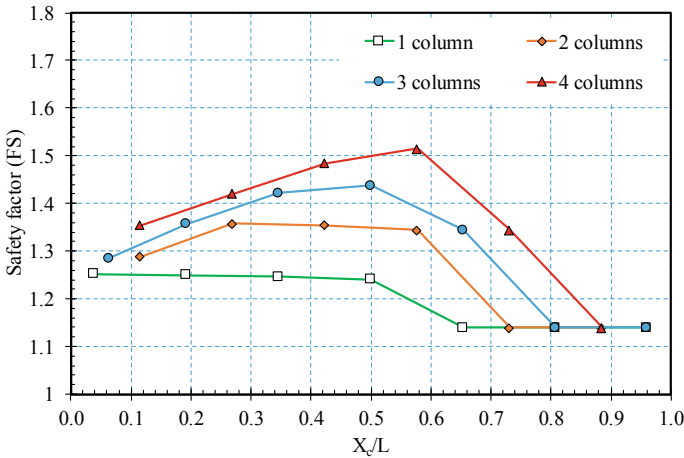
### 3 Numerical Modelling

In this paper, numerical modelling based on LEM of the slope stability of a 19-m-high riverbank reinforced with DCM columns is performed using geotechnical software SLOPE/W. Bishop's method of slices is used to calculate the factor of safety (FS) for the riverbank slope. It is noted that in this numerical simulation, the effect of DCM column quantity on the slope stability of the riverbank is investigated by changing a number of columns ( $n_c$ ) from 1 to 4. Meanwhile, the LEM analyses of the columns reinforced riverbank with various values of column length ranging from  $L_c = 3$  m to  $L_c = 12$  m and the river water level varying in a range of  $H = 9\text{--}16.5$  m due to flooding conditions are performed to examine the influence of the investigated design parameters on the riverbank slope safety of factor. It is also noted that fluctuations of drawdown rate and different vertical surcharge loads may affect the slope stability of the riverbank to some extent [32]. However, they are considered beyond the scope of this LEM analysis and identified as future investigations.

## 4 Results and Discussion

### 4.1 Effect of Column Quantity and Location on the Safety Factor of Riverbank Under a Constant River Water Level

Figure 2 shows the effect of DCM column locations on the safety factor (FS) of the riverbank slope reinforced with columns for different column numbers ( $n_c = 1\text{--}4$ ), river water level ( $H = 9$  m),  $L_c = 9$  m,  $D_c = 1$  m and  $s = 2$  m. As can be seen in this figure, the safety factor generally increased and reached a peak value, followed by a decrease to a certain value when the column location ( $X_c/L$ ) increased in a range between 0 and 1. However, this phenomenon excludes the case of one row of DCM columns reinforced the riverbank slope that presents the FS value remained almost unchanged with an increase in the column location up to  $X_c/L = 0.5$ , followed a reduction of the slope safety factor and then approached a constant value of  $FS = 1.14$ , as shown in Fig. 2. Moreover, it is interesting to note that the DCM columns with  $n_c > 1$  were observed to be more effective for increasing the riverbank slope stability when the column location approached the slope toe (around  $X_c/L = 0.6$ )

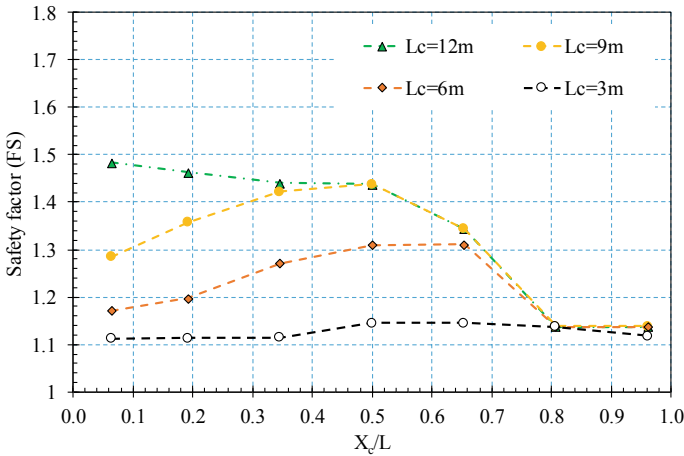


**Fig. 2** Effect of DCM column location and quantity on the safety factor of the riverbank slope stability

considered in this investigation. As Fig. 2 shows, it is also noted that the increase of the riverbank FS with a high rate when the column location ( $X_c/L$ ) increased was predicted for the riverbank reinforced with a greater number of columns ( $n_c > 1$ ). The increase of FS with increasing  $n_c$  could be attributed to a higher shear strength properties of DCM columns used to improve the riverbank slope.

To investigate the effect of both column length and column position on the riverbank slope stability, a series of numerical parametric studies has been conducted. Subsequently, the predicted results are presented in Fig. 3 showing the safety factor of the riverbank slope reinforced with three rows of columns against various column locations for different column lengths ( $L_c = 3 - 12$  m),  $s = 2$  m,  $D_c = 1$  m and  $H = 9$  m. It is observed that the slope safety factor appeared to increase with increasing the column length and the column location ranging from  $X_c/L = 0$  to  $X_c/L = 0.5$ . Except for the case of the slope reinforced with long columns ( $L_c = 12$  m), that shows a slight decrease of FS value against an increase in the column position from the top of the riverbank slope. However, the difference in the increased FS values between the short column and long column-reinforced riverbank slope cases became small and approached the same value when the column location increased further to  $X_c/L = 0.95$ , as plotted in Fig. 3.

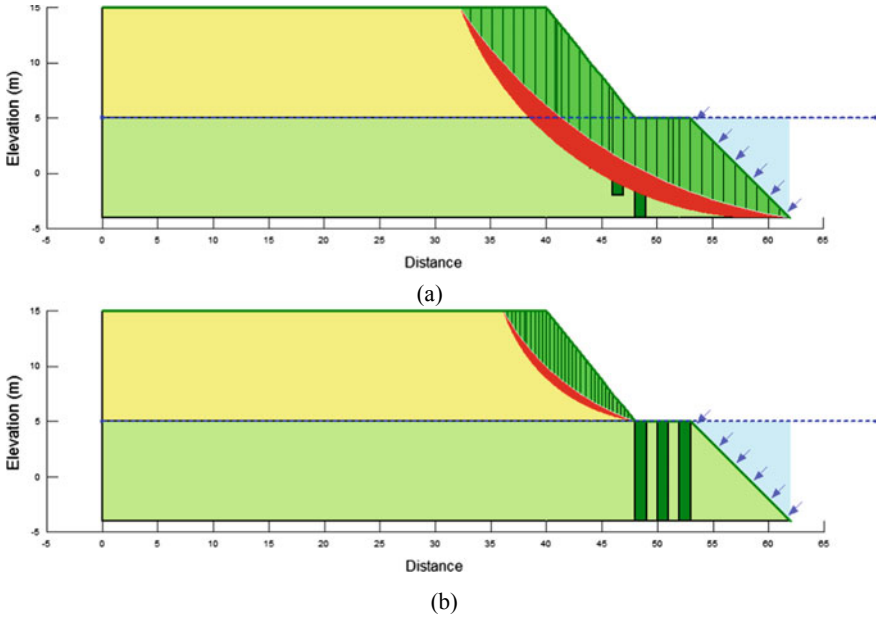
In addition, a special comparison between the two cases of the riverbank slope reinforced with the long column length of  $L_c = 9$  m and  $L_c = 12$  m noted that when the  $X_c/L$  value was small, the slope safety factor was greater for the riverbank with the 12-m-long column reinforcement than that of a 9 m column length. Nevertheless, the safety factor difference between the two cases was smaller as the  $X_c/L$  value increased, and as observed in Fig. 3, it was found to reach approximately the same value for the column location varying between from  $X_c/L = 0.35$  to  $X_c/L = 0.5$ . Although there was a slight reduction of the FS value observed for the riverbank



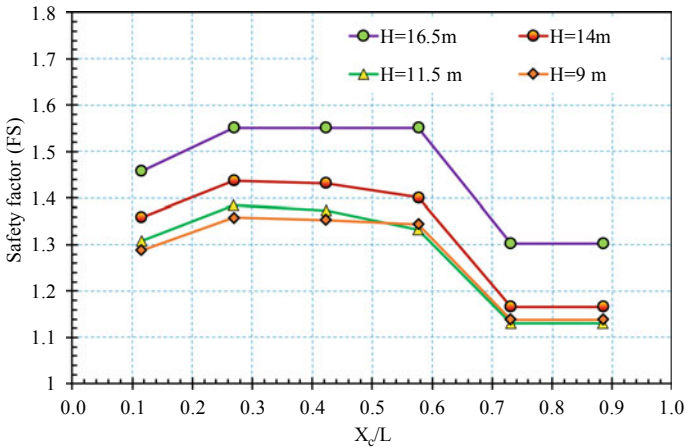
**Fig. 3** Effect of DCM column location with different column lengths on the safety factor of the riverbank slope stability

slope reinforced with the long columns of  $L_c = 12\text{ m}$  when  $X_c/L$  increased to a value of 0.5, about 3% FS reduction was insignificant in view of engineering practice. Therefore, for the riverbank slope reinforced with a long column length of  $L_c = 9 - 12\text{ m}$ , the column length of  $L_c = 9\text{ m}$  and their location in a range of  $X_c/L = 0.35 - 0.5$  could be considered as the optimal length and locations. Meanwhile, as evident in Fig. 3, the optimal column location was predicted to vary in a range of  $X_c/L = 0.5 - 0.65$  for the riverbank slope reinforced with a short column length of  $L_c = 3 - 6\text{ m}$ .

A comparison of failure mechanism of critical slip surfaces of the riverbank reinforced with three columns between different column locations is shown in Fig. 4. As presented in this figure, the critical slip circle of the riverbank reinforced with three columns (Fig. 4a) located at the middle of riverbank slope ( $X_c/L = 0.5$ ) is deeper and passes through both subgrade layers. However, a smaller sliding circle passed through only the upper layer of silty sand is observed for the riverbank reinforced with three columns (Fig. 4b) corresponding to the column location at the extended slope toe ( $X_c/L = 0.8$ ). Referring to Fig. 4b, the column location at the extended slope toe has an insignificant effect on the improved stability of the riverbank slope because the critical slip surface has developed only in the slope of the silty sand layer, which is outside the effective working region by the column improvement. This comparison also indicates the importance of the column location in enhancing the slope safety factor of the riverbank reinforced with soil–cement columns.



**Fig. 4** Comparison of failure mechanism of critical slip surface between riverbank slope reinforced with three rows of DCM columns at various column locations of **a**  $X_c/L = 0.5$  and **b**  $X_c/L = 0.8$



**Fig. 5** Effect of DCM column locations on the safety factor of the riverbank slope stability subjected to different river water levels

## 4.2 Effect of Column Position on the Safety Factor of Riverbank Subjected to Different River Water Levels

Figure 5 displays the safety factor of the riverbank slope reinforced with two rows of tangential DCM columns (2 DCM columns) against various river water levels ( $H = 9 - 16.5$  m) and different column locations ( $X_c/L$ ) with  $L_c = 9$  m,  $s = 2$  m and  $D_c = 1$  m. To study the effect of column position on the safety factor of riverbank subjected to different river water levels (RWL), four different cases of RWL are considered, assuming that ground-water level is equal to RWL in this numerical investigation. It can be seen from Fig. 5 that the safety factor of the reinforced riverbank slope was noticeably depended on the column locations. In addition, as Fig. 5 shows, the slope safety factor was calculated to increase with an increase in the RWL. The calculated results indicate that as can obviously be seen in Fig. 5 for every RWL condition, the highest riverbank slope FS was achieved when the DCM columns were located in a range from the middle to the slope toe (e.g.  $X_c/L = 0.27-0.58$ ). Whereas, the lowest slope FS was predicted when the columns were located in the extended slope toe (e.g.  $X_c/L = 0.73-0.88$ ). These findings demonstrate that the riverbank slope reinforced with 2 DCM columns when subjected to a given RWL condition is susceptible to sliding failure when the columns are located in the extended slope toe. By contrast, when the columns are placed ranging from  $X_c/L = 0.27$  to  $X_c/L = 0.58$ , they are considered as the optimal column locations with respect to a change of RWL from  $H = 9$  m to  $H = 16.5$  m, typical for the examined river delta region.

Moreover, by comparing the two DCM column-reinforced riverbank slope under a low level of river water ( $H = 9$  m) with the same reinforced riverbank subjected to a high RWL of  $H = 16.5$  m, it is found that the critical value of the slope FS in every column location was smaller for the reinforced riverbank slope under a low level of river water. In other words, the low RWL could be more dangerous for causing the slope instability. Thus, it should be taken into account in the design stage of a riverbank slope reinforced with DCM columns in order to ensure the slope stability under the most unstable condition. Meanwhile, as Fig. 5 illustrates, the optimal column location between the middle and the slope toe ( $X_c/L = 0.27 - 0.58$ ) should be considered maximising the column improvement of the slope stability.

## 5 Conclusions

In this study, a practical engineering solution using deep cement mixing (DCM) columns to improving the slope stability of a typical steep riverbank under various river water levels (RWL) in a river delta region has been proposed and investigated applying numerical analysis. The numerical analysis using the limit equilibrium method has been performed to investigate the effect of several design parameters consisting of the column numbers, column length and their location on the slope safety factor and the critical sliding surface of a 19-m-high riverbank slope subjected

to variations of RWL. Based on the numerical results, it is found that DCM columns were remarkably effective in improving the riverbank slope stability. The safety factor of the riverbank slope under a given low RWL increased with increasing the column quantity and the column length as expected. However, when the DCM columns are placed in the optimal locations between the middle and the toe of the slope, a medium column length (corresponding to  $L_c = 9$  m in this investigation) as compared to the longer columns could result in a similar effect on the improved riverbank slope safety factor. The findings also indicate that the column location in the extended slope toe was predicted to have an insignificant impact on increasing the riverbank slope stability and most susceptible to sliding failure irrespective of RWL. Therefore, special attention should be taken when designing the riverbank slope reinforced with columns under an initial drawdown of RWL and when considering the column location in the extended slope toe.

**Acknowledgements** This research is funded by Ho Chi Minh City University of Technology (HCMUT), VNU-HCM, under grant number BK-SDH-2021-1870139. The first author gratefully acknowledges this support.

## References

1. Berilgen MM (2007) Investigation of stability of slopes under drawdown conditions. *Comput Geotech* 34(2):81–91
2. Gao Y, Zhu D, Zhang F, Lei GH, Qin H (2014) Stability analysis of three-dimensional slopes under water drawdown conditions. *Can Geotech J* 51(11):1355–1364
3. Ng CW, Zhang LM, Ho KK (2001) Influence of laterally loaded sleeved piles and pile groups on slope stability. *Can Geotech J* 38(3):553–566
4. Dyson AP, Tolooiyan A (2019) Prediction and classification for finite element slope stability analysis by random field comparison. *Comput Geotech* 109:117–129
5. Duong TT, Komine H, Do MD, Murakami S (2014) Riverbank stability assessment under flooding conditions in the Red River of Hanoi, Vietnam. *Comput Geotech* 61:178–189
6. He Y, Hajarika H, Yasufuku N, Han Z (2015) Evaluating the effect of slope angle on the distribution of the soil–pile pressure acting on stabilizing piles in sandy slopes. *Comput Geotech* 69:153–165
7. Jeong S, Kim B, Won J, Lee J (2003) Uncoupled analysis of stabilizing piles in weathered slopes. *Comput Geotech* 30(8):671–682
8. Lee CY, Hull TS, Poulos HG (1995) Simplified pile-slope stability analysis. *Comput Geotech* 17(1):1–16
9. Ausilio E, Conte E, Dente G (2001) Stability analysis of slopes reinforced with piles. *Comput Geotech* 28(8):591–611
10. Yang M, Deng B (2019) Stability study of slope reinforced with piles under steady unsaturated flow conditions. *Comput Geotech* 109:89–98
11. Waichita S, Jongpradist P, Jamsawang P (2019) Characterization of deep cement mixing wall behavior using wall-to-excavation shape factor. *Tunn Undergr Space Technol* 83:243–253
12. Dang LC, Dang CC, Khabbaz H (2019) Modelling of columns and fibre-reinforced load-transfer platform-supported embankments. *Ground Improvement* 1–19
13. Dang LC, Dang CC, Khabbaz H (2019) Numerical modelling of embankment supported by fibre reinforced load transfer platform and cement mixed columns reinforced soft soil. In: *The*

- XVII European conference on soil mechanics and geotechnical engineering (ECSMGE-2019). ISSMGE, Reykjavik, Iceland
14. Dang LC, Dang CC, Khabbaz H (2018) a parametric study of deep mixing columns and fibre reinforced load transfer platform supported embankments. In: Khabbaz H, Youn H, Bouassida M (eds) *New prospects in geotechnical engineering aspects of civil infrastructures*. Springer, Cham, Switzerland, pp 179–194
  15. Dang LC, Dang CC, Khabbaz H (2018) Numerical analysis on the performance of fibre reinforced load transfer platform and deep mixing columns supported embankments. In: Bouassida M, Meguid MA (eds) *Ground improvement and earth structures*. Springer, Cham, Switzerland, pp 157–169
  16. Dang LC, Dang CC, Khabbaz H (2017) Behaviour of columns and fibre reinforced load transfer platform supported embankments built on soft soil. In: *The 15th international conference of the international association for computer methods and advances in geomechanics*. Wuhan, China
  17. Dang LC, Dang CC, Fatahi B, Khabbaz H (2016) Numerical assessment of fibre inclusion in a load transfer platform for pile-supported embankments over soft soil. In: Chen D, Lee J, Steyn WJ (eds) *Geo-China 2016: material, design, construction, maintenance, and testing of pavement*. ASCE, pp 148–155
  18. Dang LC (2019) *Enhancing the engineering properties of expansive soil using bagasse ash, bagasse fibre and hydrated lime*. University of Technology Sydney, NSW, Australia
  19. Dang CC, Dang LC (2020) Influence of fibre-reinforced load transfer platform supported embankment on floating columns improved soft soils. In: Tutumluer E, Chen X, Xiao Y (eds) *Advances in environmental vibration and transportation geodynamics*. Springer, Singapore, pp 215–227
  20. Dang CC, Dang LC (2020) Evaluation of the at-rest lateral earth pressure coefficient of fibre reinforced load transfer platform and columns supported embankments. In: Ha-Minh C et al (eds) *CIGOS 2019: innovation for sustainable infrastructure, lecture notes in civil engineering*. Singapore, Springer, pp 647–652
  21. Dang CC, Dang LC () Influence of fibre reinforced load transfer platform supported embankment on floating columns improved soft soils. in *The 8<sup>th</sup> International Symposium on Environmental Vibration and Transportation Geodynamics 2018 (ISEV 2018)*. Springer, Changsha, China
  22. Dang C, Dang L, Khabbaz H, Sheng D (2020) Numerical study on deformation characteristics of fibre reinforced load transfer platform and columns supported embankments. *Canadian Geotech J* 58(3):358–50. <https://doi.org/10.1139/cgj-2019-0401>
  23. Dang LC, Fatahi B, Khabbaz H (2016) Behaviour of expansive soils stabilized with hydrated lime and bagasse fibres. *Procedia Eng* 143:658–665. <https://dx.doi.org/10.1016/j.proeng.2016.06.093>
  24. Dang LC, Hasan H, Fatahi B, Jones R, Khabbaz H (2016) Enhancing the engineering properties of expansive soil using bagasse ash and hydrated lime. *Int J GEOMATE* 11(25):2447–2454
  25. Dang LC, Hasan H, Fatahi B, Khabbaz H (2015) Influence of bagasse ash and hydrated lime on strength and mechanical behaviour of stabilised expansive soil. In: *The 68th Canadian geotechnical conference and the 7th Canadian permafrost conference (GEOQuébec 2015)*. Canadian Geotechnical Society, Québec City, Canada
  26. Dang LC, Khabbaz H (2018) Shear strength behaviour of bagasse fibre reinforced expansive soil. In: *International conference on geotechnical and earthquake engineering 2018 (IACGE 2018)*. ASCE, pp 393–402
  27. Dang LC, Khabbaz H (2018) Enhancing the strength characteristics of expansive soil using bagasse fibre. In: Wu W, Yu H-S (eds) *Proceedings of China-Europe conference on geotechnical engineering*, Springer series in geomechanics and geoengineering. Cham, Switzerland, Springer, pp 792–796
  28. Dang LC, Khabbaz H (2018) Assessment of the geotechnical and microstructural characteristics of lime stabilised expansive soil with bagasse ash. In: *The 71st Canadian geotechnical conference and the 13th joint CGS/IAH-CNC groundwater conference (GeoEdmonton 2018)*. Canadian Geotechnical Society, Alberta, Canada



29. Dang LC, Khabbaz H (2019) Experimental investigation on the compaction and compressible properties of expansive soil reinforced with bagasse fibre and lime. In: McCartney JS, Hoyos LR (eds) Recent advancements on expansive soils. Springer, Cham, Switzerland, pp 64–78
30. Dang LC, Khabbaz H, Fatahi B (2017) An experimental study on engineering behaviour of lime and bagasse fibre reinforced expansive soils. In: 19th International conference on soil mechanics and geotechnical engineering (19th ICSMGE). ISSMGE, Seoul, Republic of Korea, pp 2497–2500
31. Dang LC, Khabbaz H, Fatahi B (2017) Evaluation of swelling behaviour and soil water characteristic curve of bagasse fibre and lime stabilised expansive soil. In: Second Pan-American conference on unsaturated soils (PanAm-UNSAT 2017). ASCE, Texas, USA, pp 58–70
32. Dang CC, Dang LC (2020) Numerical investigation on the stability of soil-cement columns reinforced Riverbank. In: Correia AG et al (eds) Information technology in geo-engineering, Springer series in geomechanics and geoen지니어ing. Cham, Switzerland, Springer, pp 879–888

# Landslide at Govindghat—Investigation and Stabilization Measures



Ravi Sundaram, Sanjay Gupta, Minimol Korulla, Rudra Budhbhatti, and Pankaj Mourya

**Abstract** A cloudburst and flash flood in June 2013 in the state of Uttarakhand, India caused landslide at Govindghat located along a major highway. Large boulders in soil matrix were encountered in the area. Water seeping through the open pores between the boulders and erosion of the soil was the major causes of the slope-failure. Erosion of the accumulated debris on the valley side during periods of high discharge in the area also added to the instability. The stabilization measures adopted include a secured drapery of rock anchors and steel mesh on the hill side, nailed gabions at road level, reinforced soil wall to ensure the desired road width, and river-side gabion wall for erosion protection.

**Keywords** Landslide · Cloudburst · Boulder-soil matrix · Seismic refraction tests · Hill-slope stabilization · Erosion protection

## 1 Introduction

A cloudburst in the state of Uttarakhand in northern India triggered several landslides in the fragile Himalayan hill slopes and created havoc in the region. A flash flood in the river Alaknanda flowing in the region further exacerbated the situation. Several buildings and roads in the area were severely damaged / washed away. Of the many

---

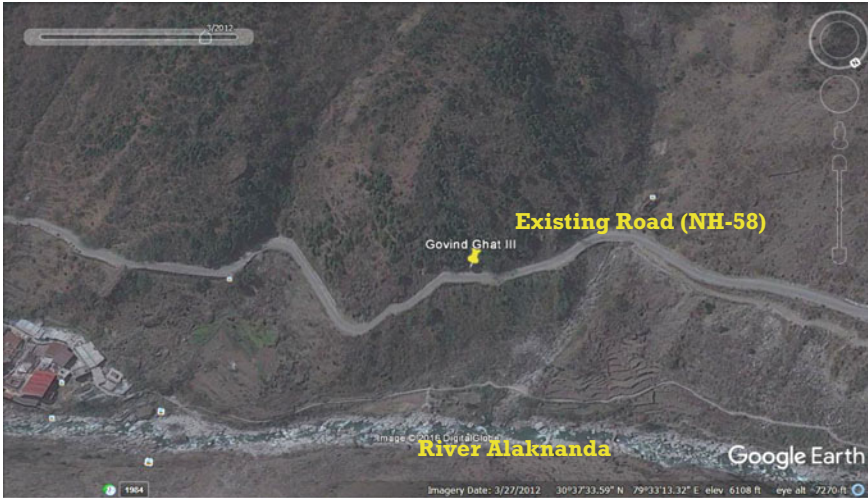
R. Sundaram (✉) · S. Gupta  
CengrsGeotechnica Pvt. Ltd, A-100 Sector 63, Noida, UP, India  
e-mail: [ravi@cengrs.com](mailto:ravi@cengrs.com)

S. Gupta  
e-mail: [sanjay@cengrs.com](mailto:sanjay@cengrs.com)

M. Korulla · R. Budhbhatti  
Maccaferri Environmental Solutions Pvt. Ltd, Gurgaon, Haryana, India  
e-mail: [m.korulla@maccaferri.com](mailto:m.korulla@maccaferri.com)

R. Budhbhatti  
e-mail: [b.rudra@maccaferri.com](mailto:b.rudra@maccaferri.com)

P. Mourya  
Ministry of Road Transport and Highways, Mumbai, India



**Fig. 1** Satellite image—2014 shows no landslide in the area

landslides that blocked traffic along the National Highway 58 as a result of this extreme event, this paper presents the case study of a major landslide at Govindghat. The causes of the slide and the stabilization measures adopted are discussed.

## 2 History and Background of the Slide

Satellite image in 2012 shows no landslide and overall stable conditions along the highway with vegetation on the hill slopes (See Fig. 1). Satellite image of 2014 illustrated in Fig. 2 shows a major landslide along the highway. Since this is the third landslide in the vicinity of Govindghat town, it is identified as Govindghat III.

## 3 Site Conditions

### 3.1 Regional Geology

Geologically, the area belongs to a tectonic fore-deep in the Lesser Himalayas [1]. Govindghat belongs to the Central Crystalline group of rocks and is in the Pandukeshwar formation. The main rock types in this formation include whitish to grey quartzite inter-banded with mylonite-gneiss and garnet-kyanite schist [2]. The quartzites are medium to coarse grained, massive, cross-bedded, and folded. The inter-banded mica-schists are crenulated and contain fibrolite, kyanite, and garnet.



**Fig. 2** Satellite image in 2014 shows major landslide above and below the highway



**Fig. 3** Slopes adjoining the highway at Govindghat with boulder-soil matrix. The photo on the left shows strata above road level, and the one on the right shows the strata below road level

In the landslide area, rocks are not exposed except as a soil-boulder matrix. The boulders are angular and vary in size from less than 0.5 m to 5 m. These boulders are cemented in a sandy matrix. Figure 3 presents photographs of the area.

### 3.2 Stratigraphy

The landslide area at Govindghat III was investigated by two boreholes and one seismic refraction test. Limited boreholes were drilled because of site constraints; however, the borehole data and seismic refraction test were sufficient to clearly assess the stratigraphy.

**Fig. 4** Borehole drilling in progress



Figure 4 illustrates the borehole drilling in progress. Figure 5 presents a photo of the seismic refraction test being done.

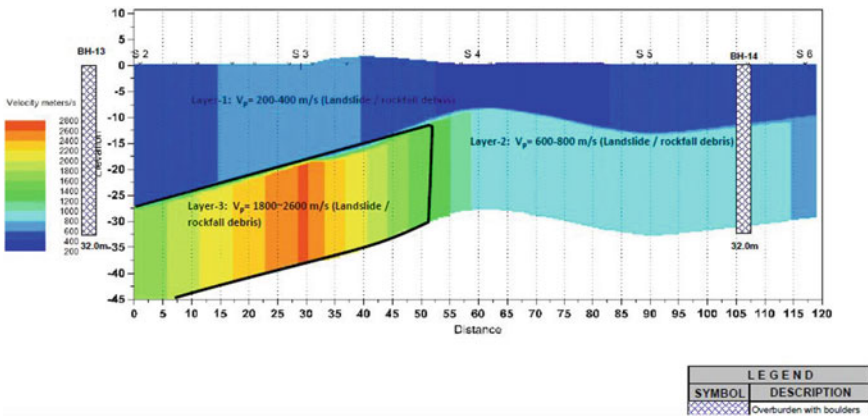
The study indicated the presence of large size boulders and cobbles in a soil matrix to substantial depth, probably extending to the riverbed. Most of it was landslide debris material. The higher recovery and RQD values are due to the large size of the boulders. Figure 6 presents the seismic profile along with the borehole data superimposed on it.

#### **4 Problem Description and Causes of the Slide**

After a detailed study of the slide, the destabilizing forces identified include the following:

- Seepage of water through the open pores through the large boulders on the hill side;
- Erosion of the soil between the boulders-soil matrix during heavy rains, thereby triggering landslide in the foothill below the road; and
- Erosion of the toe on the river side during high discharge of the river.

**Fig. 5** Seismic refraction test in progress



**Fig. 6** Geophysical profile together with borehole data

These are discussed in detail in the sections below [3]. The chainages mentioned are in two parts—the distance in kilometers (whole number) plus additional distance in meters from reference point. For example, Chainage km 499 + 998 means the distance from the reference point is 499.998 km.





**Fig. 7** Stretch with large boulders and open pores. Note the damage to the non-engineered handmade gabion wall

#### ***4.1 Chainage km 499 + 988 to 500 + 030***

In a 42 m stretch between chainage km 499 + 988 to 500 + 030, large boulders ranging in size from 1 to 5 m are seen (See Fig. 7). There is substantial fine material between the large pores that tend to get washed away as rainwater percolates through them. This makes the boulders prone to sliding. Pore-water pressure builds up due to the water percolation which in turn triggers rockfall. The damage to the non-engineered handmade gabion wall at the toe of the slope highlights the problem.

#### ***4.2 Chainage km 500 + 030 to 500 + 138***

In this stretch, the material on the hillslope consists of loose overburden soil and fractured rock (See Fig. 8). The fines get eroded due to seepage during heavy rains and this triggers the landslide. Consequently, the soil debris causes waterlogging of the road as illustrated on Fig. 9.

#### ***4.3 River-Side Erosion***

Erosion of the toe along the Alaknanda River at Govindghat is also one of the causes of landslides in the area. The loose alluvium accumulated on the toe of the river gets eroded, particularly during floods and periods of high discharge during monsoons. This increases the instability, thereby creating conditions favorable for a landslide. The impact of toe erosion is illustrated in Fig. 10.

**Fig. 8** Loose soil with boulders



**Fig. 9** Water and debris accumulated on road



## 5 Stabilization Measures Adopted

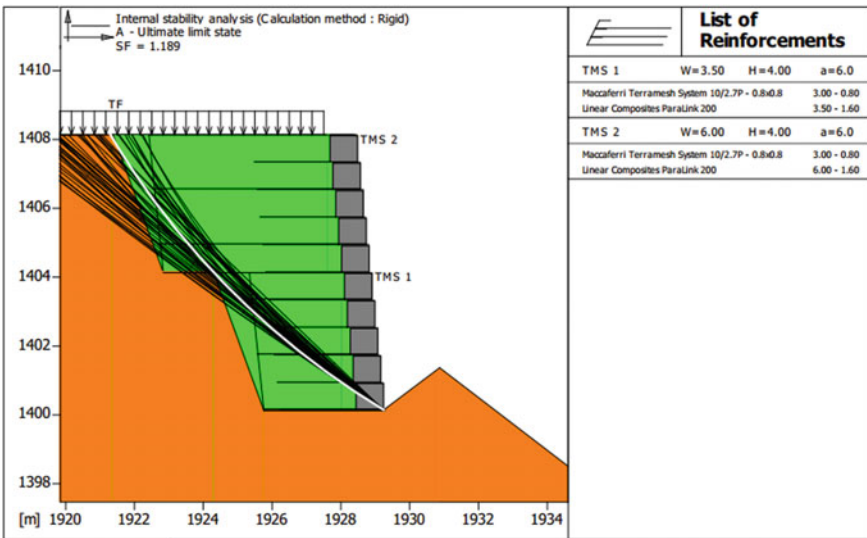
Stabilization measures implemented include the following:

1. For retention of proposed 12-m wide road, reinforced soil wall of 8 m maximum height has been constructed. The wall is designed for the traffic load and very high seismic loads (as per BS 8006 Part-1 [4] and for seismic loading condition, FHWA-NHI-10-024 [5]). The stability analysis was performed using inhouse built software for both static and seismic conditions. This software allows the user to conduct the stability checks using the limit equilibrium method and to do checks of different possible failure mechanism in heterogeneous strata layers with all possible load combinations described in BS 8006 and MoRTH specification [6].





**Fig. 10** Toe erosion on valley side



**Fig. 11** Slope stability analysis of 8 m high reinforced soil wall

Reinforced soil system is advantageous in terms of overall performance, better uniform pressure distribution at the base of the wall, and environmentally friendly [7]. Since the base is flexible, differential settlement can be accommodated.

A typical of software analysis is presented in Fig. 11, and the summary of factor of safety (FoS) is given in Table 1.

**Table 1** Summarized factor of safety for 8 m high reinforced soil wall

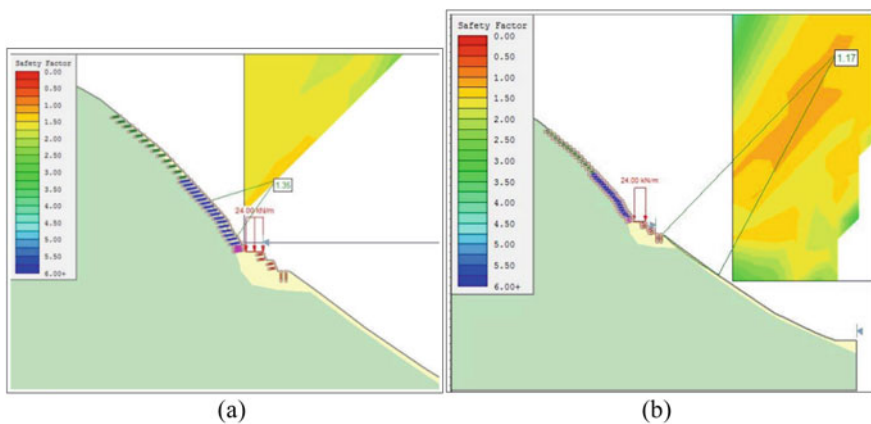
Stability checks	FoS (Static case)		FoS (Seismic case)	
	Required (BS 8006 Part-1)	Actual	Required (FHWA-NHI-00-043)	Actual
Global stability	1	1.377	1	1.197
Sliding	1.3	4.845	1.125	2.242
Bearing capacity	1.35	1.150	1.875	2.598
Overturning	2	8.255	1.5	1.784
Internal stability	1	1.189	1.125	1.272

- For protecting the toe on hill side, nailed gabion wall of 3 m height was provided for entire stretch. By providing nailed gabion, cutting into the hill is reduced as compared to gabion retaining wall, thereby minimizing disturbance to the in-situ strata [8].

Gabions act as a robust fascia for the nails which helps in preventing erosion of the toe and also act as a drainage toe. The nails provide the stabilization effect. The analysis of nailed slope with gabion fascia/drapery system (steel mesh as fascia) and global stability of overall system was carried out using software—‘SLIDE’ of Rocscience Inc., USA. This software evaluates the safety factor or probability of failure of circular or non-circular failure surfaces using vertical slice or non-vertical slice limit equilibrium methods

A typical software analysis output is shown in Fig. 12 and the summary of factor of safety (FoS) is given in Table 2.

- On the hill side, secured drapery consisting of rock anchors with steel mesh was used to secure the large boulders (designed as per Indian Roads Congress



**Fig. 12** Slide analysis results **a** for hill side (static) FoS = 1.35 **b** for valley side (seismic) FoS = 1.17

**Table 2** Summarized factor of safety hill side and valley side slope

Stability checks	FoS (Static case)		FoS (Seismic case)	
	Required (IRC HRB 15)	Actual	Required (IRC HRB 15/IRC 75)	Actual
Hill side	1.3	1.35	1.05	1.06
Valley side	1.3	1.61	1.05	1.17

IRCHRB Special Report 23 [9]) all along the road in the landslide zone. For the design of secured drapery, inhouse built software was used. The analysis for the design of for hill side slope protection and rockfall mitigation was performed using this software, a limit equilibrium approach for the design of secured drapery. A typical output file of the analysis can be seen in Fig. 13. The summary of factor of safety used in the analysis for seismic conditions is given in Table 3. Suitable bioengineering measures are being implemented to enhance the stability of the area.

4. Runoff water was channelized by providing adequate drainage measures including surface run-off deflector and roadside drain which discharges the water collected into a nearby culvert as shown in Fig. 14 (designed as per IRC SP 42 [10]). Figure 15 illustrates the scheme adopted. Rainfall intensity was calculated as per IRC: SP013 and was measured as 14.58 cm/hr. Catchment area delineation was done in Arc-GIS software was used and was calculated as 5.1 hectare. Design discharge from catchment was calculated as per IRC SP 42 and was come out as 1.66 m<sup>3</sup>/sec. Manning's equation was used to calculate allowable discharge for roadside drains and was come out as 2.71m<sup>3</sup>/sec with the factor of safety of 1.63.
5. Protecting the toe exposed to the river, a gabion toe wall has been provided for the whole 150 m stretch along with the gabion mattress as launching apron to protect the exposed toe and reduce erosion as per IRC 89 [11]. The mattress was covered with big boulders (min. 800 mm size). The gabion mattress act as a launching apron, and boulders provided added protection against large boulder impacts to the structure flowing along the river during floods. The protection has been done to 1 m above the high flood level. Figure 16 illustrates the details. The stability analysis of gabion toe wall was performed using inhouse built software. The stability of gabion toe wall, i.e., both internal and external stabilities were checked using limit equilibrium method, and the global stability was checked using theories of Bishop (1955) [12] & Janbu (1956) [13]. External stability of each individual gabion wall against sliding, overturning, and foundation bearing pressures was checked and verified. Internal stability of gabion layers was checked by taking apparent cohesion and apparent angle of internal friction between gabion layers. A typical output of software analysis is presented in Fig. 17, and the summary of factor of safety (FoS) is given in Tables 4 and 5.

The gabions and mattress provided for the project were as per IS 16014 [14].

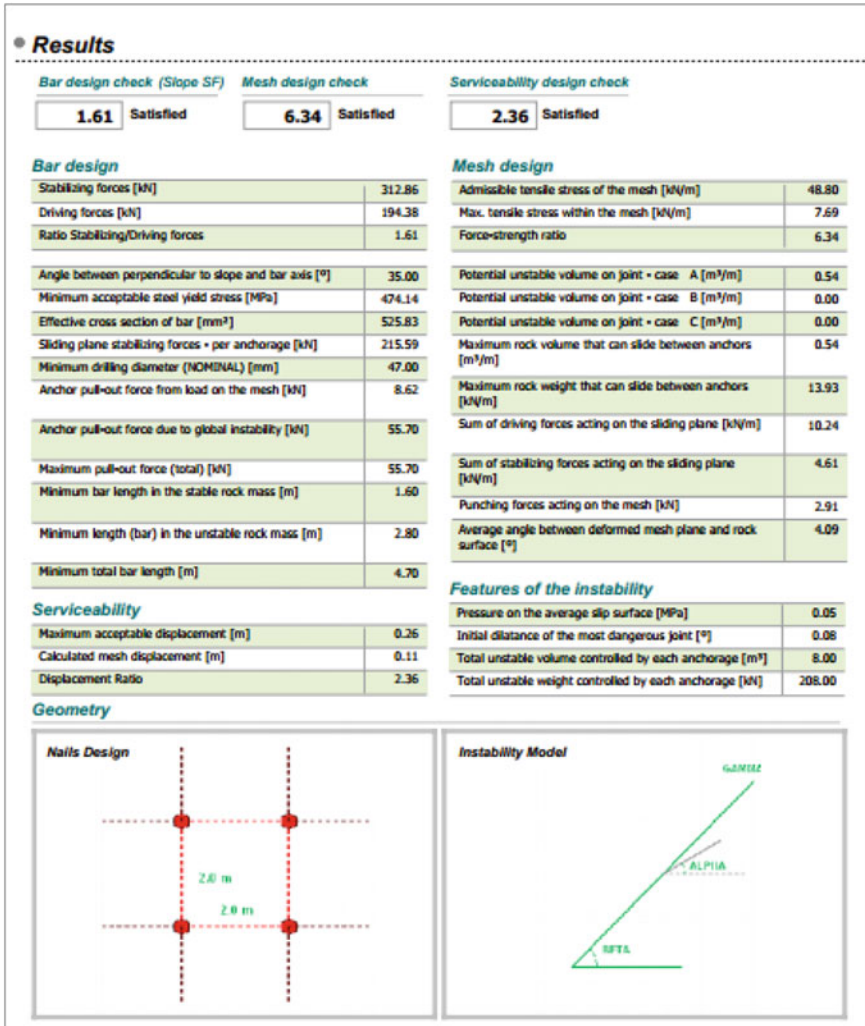


Fig. 13 Analysis of secured drapery system

Table 3 Summarized factor of safety rockfall mitigation (seismic case design)

Stability checks	Required FoS	Actual FoS
Bar design	1	1.61
Mesh design	1	6.43
Serviceability design	1	2.36

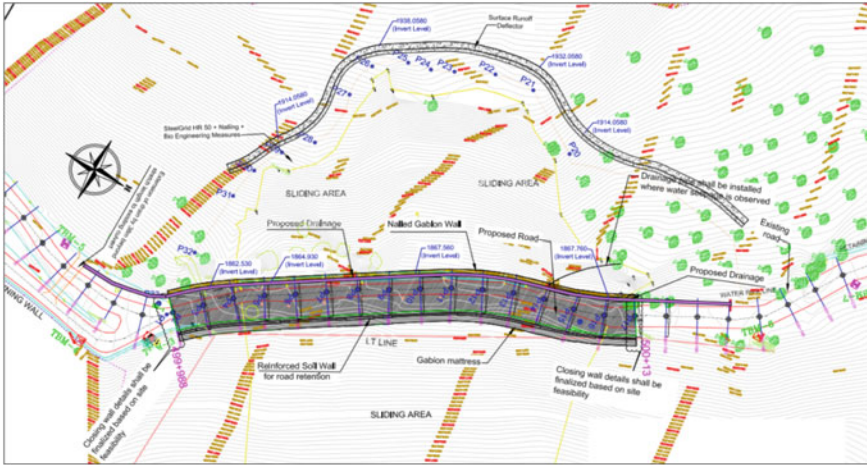


Fig. 14 Drainage plan showing mitigation measures on hill side of the road

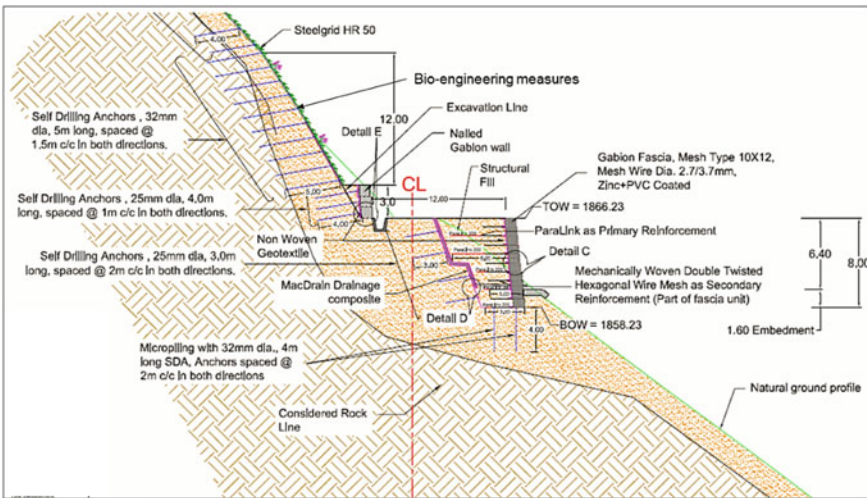
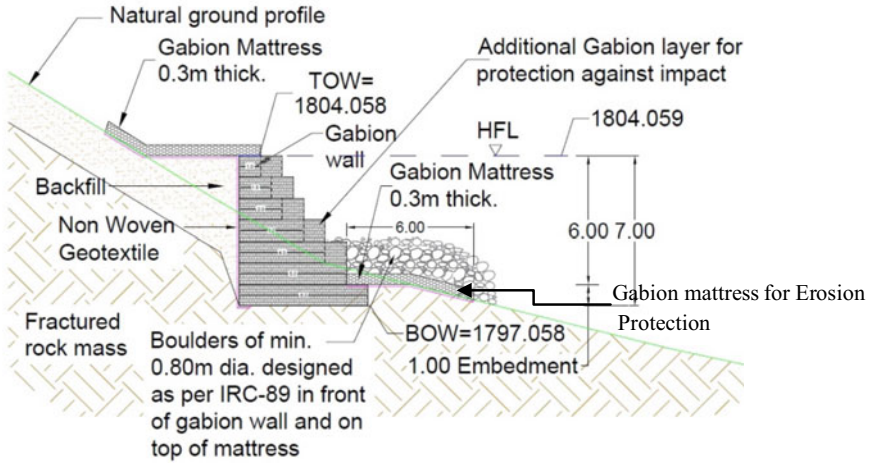


Fig. 15 Reinforced soil wall with secured drapery on hill side and nailed gabions to arrest rockfall (schematic sketch, not to scale)

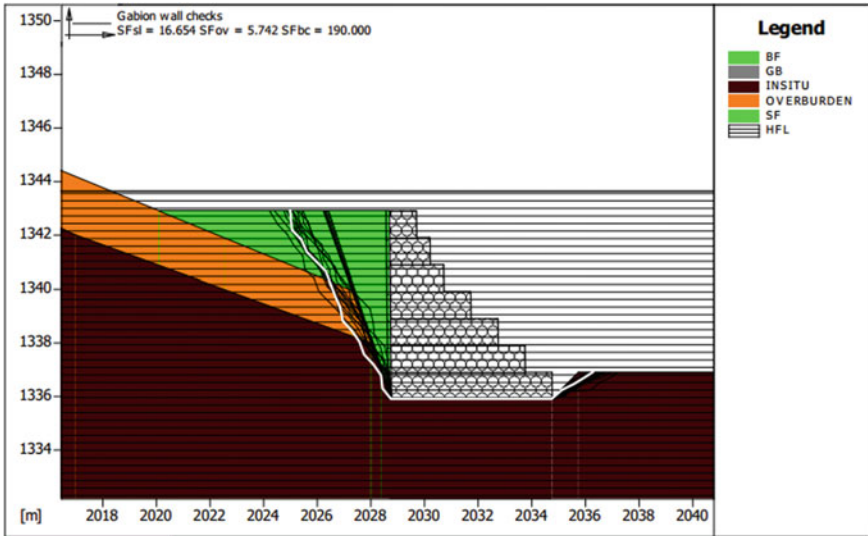
## 6 Present Status

The project is recently completed, and the photographs of the adopted remedial measures at the site are shown in Figs. 19, 20, and 21.





**Fig. 16** River-side Gabion Wall for bank protection (schematic sketch, not to scale) *Note* HFL: High Flood Level (m); TOW: Level of Top of Wall (m); BOW: Level of Bottom of Wall (for 1 m embedment)



**Fig. 17** Slope stability analysis of 7 m high gabion toe wall

**Table 4** Summarized factor of safety for 7 m high gabion toe wall (Static case)

Stability checks	FoS (Static case)		
	Required (IS 14458 Part-2)	FOS for 7 m design height atHFL	FOS for 7 m design height with drawdown
Global stability	1.3	2.177	1.705
Sliding	1.5	16.654	6.585
Bearing capacity	2.5	190	63.750
Overturning	2	5.742	2.159

**Table 5** Summarized factor of safety for 7 m high gabion toe wall (Seismic case)

Stability checks	FoS (Seismic case)	
	Required(FHWA-NHI-00-043)	FOS for 7 m design height at LWL
Global stability	1	1.409
Sliding	1.125	5.765
Bearing capacity	1.875	60
Overturning	2.5	3.845



**Fig. 19** Photograph showing the hill side rehabilitative measures 3-m high nailed gabion wall for toe stabilization and secured drapery system to secure large boulders adopted at site



**Fig. 20** Photograph showing reinforced soil wall constructed at site for road retention



**Fig. 21** Photograph showing the bank protection works adopted at site

## 7 Concluding Remarks

A landslide was triggered on the hill slopes of National Highway 58 at Govindghat in Uttarkhand state, India by a cloudburst and flash flood in June 2013. The geotechnical problems identified were:



- Seepage of water through the open pores through the large boulders on the hill side;
- Erosion of the boulders and soil during heavy rains, thereby triggering landslide in the foothill below the road; and
- Erosion of the toe on the river side during high discharge of the river.

Engineering solutions adopted to stabilize the area include the following:

- Stabilizing the hill slope above road level with a secured drapery of rock anchors and steel mesh;
- Installing 3-m high nailed gabions at road level for toe stabilization;
- Constructing a reinforced soil wall on the valley side (max. 8 m high) to ensure that the desired road width of 12 m is achieved with necessary stability;
- Adequate drainage planning to channelize water into drainage channels for disposal; and
- Protecting the toe erosion on river side with a gabion wall and mattress.

## References

1. Mitigation D, Centre M (2014) Geological investigations in rudraprayag with special reference to mass instability. A DMMC publication, Dehradun, Uttarakhand, India
2. Krishnan MS (1986) Geology of India and Burma. CBS Publishers, New Delhi
3. Korulla M, Budhbhatti R, Meenu PS, Kamal V (2019) Sustainable landslide mitigation measures—demonstration through a live case study in Uttarakhand, frontiers in geotechnical engineering, developments in geotechnical engineering, Chapter-19, Springer Nature Singapore Pte Ltd, pp 395–415
4. BS 8006 Part1, Code of Practice for Strengthened/Reinforced Soils and other Fills (2010)
5. FHWA-NHI-10–024 (2009) Design and construction of mechanically stabilized earth walls and reinforced soil slopes, federal highway administration, Washington, D. C
6. MoRTH, Specifications for road and bridge works, Indian Roads Congress, India
7. Korulla M, Chaurasia S (2018) Sustainable landslide mitigation measures—a case study on Lambagarh, ISGTI Conference, India
8. Korulla M, Mourya PK, Khan S, Kachhal A (2018) Landslide and rockfall mitigation works in Uttarakhand—Case Study, ISGTI Conference, India
9. IRC HRB Special Report 23: Design and construction of rockfall mitigation systems, Indian Roads Congress, India (2014)
10. IRC SP 42, Guidelines for road drainage, Indian roads congress, India (2014)
11. IRC 89, Guidelines for Design and Construction of River Training and Control Works for Road Bridges, Indian Roads Congress, New Delhi (1997)
12. Bishop AW (1955) The use of slip circle in the stability of earth slopes. *Geotechnique* 5:7–17
13. Janbu N, Bjerrum L, Kjaernsli B (1956) Soil mechanics applied to some engineering problems. Norwegian Geotechnical Institute, Oslo, Publ. 16, pp 5–26
14. IS 16014–2012, Mechanically woven, double twisted, hexagonal wire mesh gabions,revet mattresses, rockfall netting (Galvanized Steel Wire or Galvanized Steel Wire with PVC Coating)—Specification

# Earth Pressure, a Load, or a Resistance: Formulation of the ‘What You Design is What You Get’ Model for Stability Design of Propped Cantilever Walls



C. K. S. Yuen

**Abstract** The geotechnical stability design for cantilever retaining walls is often determined by a factor of safety expressed as a ratio between resistance and disturbing load. Many variations of this ratio exist, but most consider the disturbing load extending to the toe level of the wall. Questions are asked: Is the earth pressure a load or a resistance, particularly for the part of wall that penetrates beyond the critical depth at which the wall is at critical rotational equilibrium, and if it is not a load then what is it? The quest to the answers has led the author to formulate the ‘What You Design Is What You Get’, the WYDIWYG model, for stability design of propped cantilever walls. The new design method is shown to be consistent, numerically stable for all soil conditions. The formulation is suitable for Load Resistance Factor Design (LRFD) method, and it allows the Factor of Safety (FoS) to be expressed in terms of the wall critical restoring capacity. For example, the wall designed with a FoS of 2 using this method will have two times the restoring capacity at critical equilibrium, and what you designed is what you get. The calculated FoS can be meaningful and easily comprehensible. The new method could provide a platform for designers to compare between cases and assess adequacy of the level of stability with improved certainty. A worked example is included to demonstrate simplicity of the calculation process.

**Keywords** Embedded cantilever retaining walls · Stability design · Supported excavation

## 1 Introduction

With the advent of urbanization in Sydney, Australia, there is a significant increase in demand in the past decade for supported excavation to accommodate such facilities as car parking and other infrastructure development. Embedded retaining walls are

---

C. K. S. Yuen (✉)  
Transport for New South Wales, South Wales, Australia  
e-mail: [Stanley.Yuen@transport.nsw.gov.au](mailto:Stanley.Yuen@transport.nsw.gov.au)

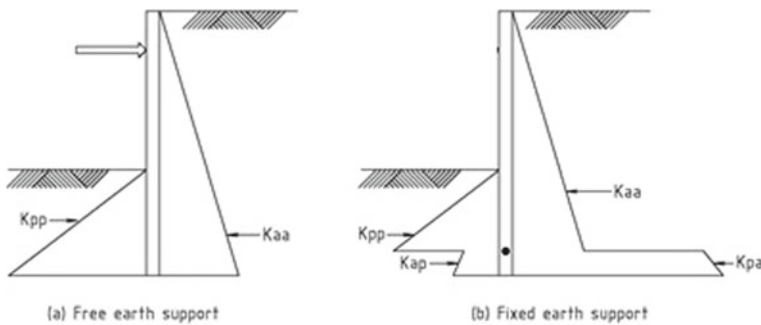
a most popular support type for such excavations. For these walls to be used satisfactorily, they need to be constructed into the ground to mobilize sufficient lateral resistance for stability. In general, these walls are installed to an economical depth for both stability and functional performance which includes strength and deformation design. An optimum balance between these considerations is hence needed. The lateral earth pressure distributions on the wall are fundamental to these designs, but their considerations are quite different between them. For functional performance, the walls are at stable equilibrium, and the pressure distribution due to soil structure interaction is an appropriate choice for realistic estimation of wall performance. There are ample literature discussion on such pressure distributions and on factors affecting them, e.g., Potts and Fourie [5, 6], and readers are referred to them separately. For stability, the pressure distributions need to be idealized at limit states, and this is the focus for discussion in this paper.

Traditionally, the earth pressures on the retained side are regarded as loads and those on the excavation side as resistances. But do they have to be the case for embedded walls, particularly for the part of wall beyond the critical equilibrium depth? The pursuit of answers has led to a different interpretation on the role these pressures play and to a new formulation for determination of a design embedment depth to suit design authority requirements. A worked example is included to demonstrate the straight-forward stability design process.

## 2 Issues with the Current Stability Design

Stability assessment has been a contentious issue for many decades. Earth pressure distribution on the wall is idealized to facilitate calculation of loads for stability design. Most engineers are familiar with the free and fixed earth support models, shown in Fig. 1, for propped and free cantilever walls.

Due to practical difficulty to locate the pivot point in the fixed earth model, free earth support becomes a favorable simpler model to use where the earth pressure on



**Fig. 1** Idealized earth pressure distribution for stability design of propped and free cantilever walls

the retained side is treated as load and that on the excavation side as resistance. The CP2 model [4] is a classic example. Variations of the CP2 model have formed the basis for most common methods such as the British Steel (BS) [2], Strength Factor (SF), and Burland, Potts, and Walsh methods (BP) [3]. Figure 2 shows a schematic distribution of the earth pressures used by these models where the shaded parts are the earth pressure modification represented by the individual model.

Table 1 compares their calculated factor of safety (FoS) for two cases. The first case is for a 5 m deep supported excavation in a uniform soil with an internal friction angle of 35 ° propped at the top of the wall with a toe embedment of 2.28 m. A 10 kPa surcharge is considered at the crest level of the wall, and no groundwater is considered. The second case is similar to the first one with 5 m deep excavation, but in a uniform clay with an undrained cohesion of 40 kPa and a toe embedment of 1.49 m below the excavation level. A minimum fluid pressure of 5 kPa is also considered.

For a problem with the same stability, the results show a surprisingly wide range of calculated FoS values, between 1.26 and 2.66 for the effective case, and between 1.15 and 2.01 for the total stress case. It is not possible to assess the quantum of stability by the sheer calculated values, nor is it possible to compare stability if

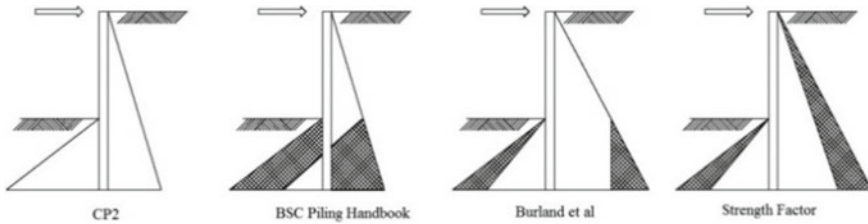


Fig. 2 Schematic pressure distribution used by the common models

Table 1 Comparison of existing design methods

Model	Case 1: Effective stress FoS		Case 2: Total stress FoS	
	Calc <sup>d</sup>	Acceptable	Calc <sup>d</sup>	Acceptable
CP2	1.63	1.5–2.0 <sup>a</sup>	1.36	2.0
BS	2.66	2.0	2.01	2.0
BP	1.72	1.5–2.0 <sup>a</sup>	1.19	2.0
SF <sup>c</sup>	1.26	1.2–1.5 <sup>b</sup>	1.15	1.4–2.0 <sup>b</sup>
WYDIWYG <sup>e</sup>	1.84		1.55	

<sup>a</sup>the acceptable factor varies with strength of the materials and nature of the works

<sup>b</sup>these values vary with design standards

<sup>c</sup>the acceptable factor varies with method of analysis

<sup>d</sup>FoS computed using commercial package WALLAP [7], except the WYDIWYG values

<sup>e</sup>FoS calculated using the proposed method

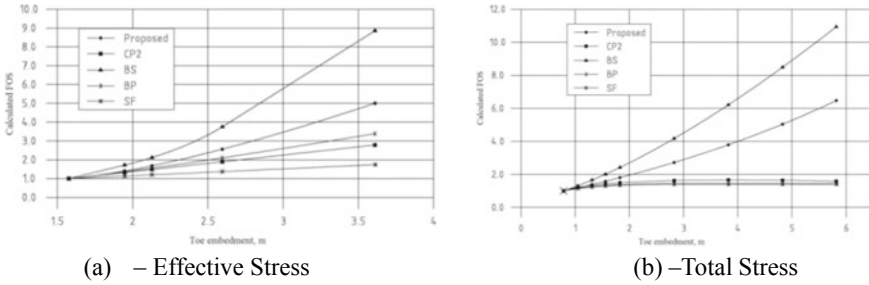


Fig. 3 Sensitivity plots

the designs are using different methods. The FoS of 2.66 by BSC is as stable as 1.26 by SF in the above example. A higher number could convey an impression of a more stable condition and may thus convey a false sense of security when the FoS value is considered alone. On the other hand, a lower value may cause designers to increase wall embedment resulting in excessive conservatism and cost to a design. Neither of this is desirable. Indeed, each of design method is unique and different and is measuring stability using a different scale. Direct comparison between their calculated values for stability hence is not advisable and needs to be treated with caution. The results of the proposed method are also included in the table for comparison purpose.

Sensitivity plots of the above examples are shown in Fig. 3. The calculated FoS to wall embedment responses is consistent with Table 1. All methods are showing positive FoS responses to wall embedment in the effective stress case but not the total stress case, where some methods failed to calculate a realistic value. A problem in the formulation of some methods is obvious.

In Australia, Australian Standard AS 5100 Bridge design [1] is used for most major infrastructures, and for geotechnical design of soil supporting structures all load factors are unity. Stability design of these structures is ensured by multiplying the soil resistance with a geotechnical reduction factor such that the resultant is larger than the disturbance, known as the design action effect. Equation 1 shows this design requirement.

$$\phi_g R_{u,g} \geq E_d \tag{1}$$

where

- $\phi_g$  is the geotechnical reduction factor.
- $R_{u,g}$  is the ultimate geotechnical strength.
- $E_d$  is the design action effect.

This approach is ideally suited to numerical calculation of the functional performance of structures because of the use of unity load factors and the use of characteristic unfactored soil parameters. For geotechnical stability design of cantilever walls, the problem becomes complicated on distinguishing soil loads and resistances

when using the existing models as they are often modified to provide assessment of stability. This renders most of the common methods non-compliant to the standard requirements using the Load Resistance Factor Design (LRFD) approach. Some designers apply geotechnical reduction factors on the passive soil pressure. While this is conforming, the approach is similar to the CP2 method, and it tends to ignore the technical improvements made in the past few decades.

### 3 Earth pressure—A Load or a Resistance

Traditionally, earth pressure is treated either as a load or as a resistance depending on the relative movements between the soil and the structure. If the structure is moving away from the soil, then the active pressure developed is considered as a load, and if it is moving against the soil, then the passive pressure is a resistance. This concept has been used on L-shape retaining walls and other gravity retaining structures. For embedded cantilever walls, the situation is similar but only at the limit equilibrium state.

For acceptable stability, the propped cantilever wall needs to be installed deeper beyond the critical rotational equilibrium depth. Some noticeable changes in the earth pressures could be detected as the wall embedment is increased. Pott and Fourie [5] presented the lateral earth pressure distributions of a 20-m sheet pile wall for a range of excavation depths. The paper considered two at-rest pressure  $k_0$  conditions at 0.5 and 2.0, and their respective pressure distributions are partly reproduced in Fig. 4.

Of interest is the excavation at 13.26 m. Although the example had not calculated the corresponding critical embedment depth for such excavation depth, one could expect it to be shallower than 20 m. The shapes of the pressure distributions on

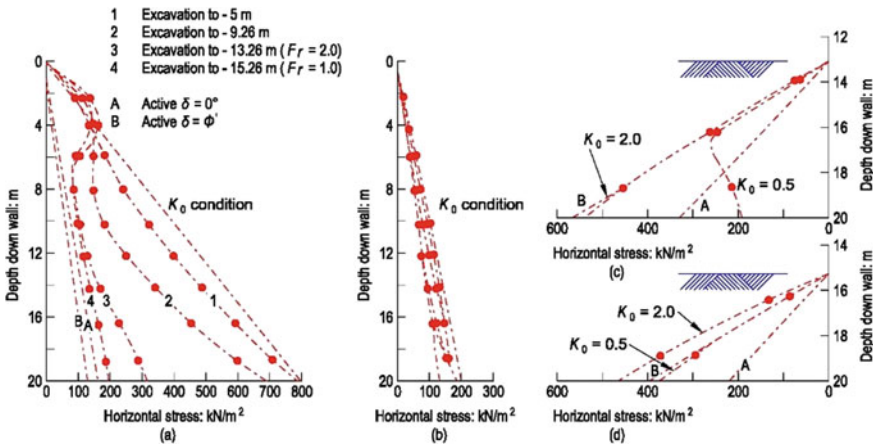


Fig. 4 Lateral earth distributions on the retained side a and b and on the excavation side c & d (After Potts and Fourie [5])

the wall would be similar to that at 15.26 m, line marked 4 in Fig. 4, which was at critical equilibrium for the wall described in the paper with the lateral earth pressures at limiting states on both sides of the wall. For the 13.26 m excavation with the wall toe increased to 20 m, as per line marked 3 in Fig. 4, the wall is stable with a FoS equals to 2. The pressure distribution on the retained side is close to that at critical equilibrium roughly above the critical depth. More significant pressure increases above the active limit occur below such depth. A similar observation could be made on the excavated side except the earth pressure decreases approximately below the critical depth.

It can be ascertained from the observation that the embedment beyond the critical depth brings stability, and there is a corresponding change in earth pressures on the wall, which are no longer at the limiting state. Logic follows that the earth pressure on the retained side of the extra embedment is assisting stability, and it should not be treated as a disturbing load. It serves as a component to provide stability. However, the pressure is acting in the disturbing direction. To mitigate this, one has to also consider the earth pressure on the excavation side. As the passive pressure acts coherently with the active pressure, it is reasonable to consider that the net of these pressures is responsible for the observed stability.

#### 4 The WYDIWYG Method

The above discussion on lateral earth pressure distributions is for a stable propped cantilever wall. For the purpose of evaluating the capacity for stability due to the embedment beyond the critical depth, let us imagine a de-stabilizing process through rotation of the wall. The earth pressure on the retained side, shown line 3 in Fig. 4 above, will gradually move back to the critical line, i.e., line 4; and similar changes could be expected on the excavation side. The wall reaches limiting equilibrium again when the earth pressures are at their respective limits. The maximum reserve for stability thus occurs when limiting earth pressures are developed on the wall.

On the basis of this, the following assumptions could be made for establishment of the WYDIWYG model for stability assessment:

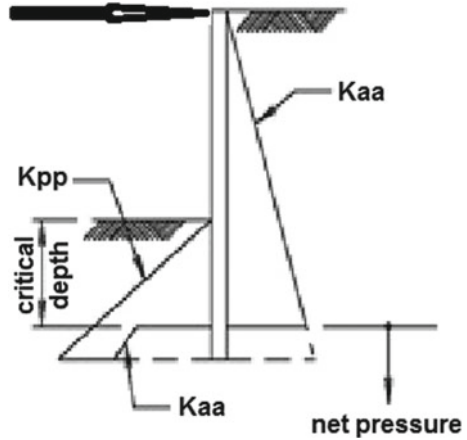
1. The disturbing load on the active side of the wall extends below the excavation level but only to the depth at which the wall is at critical equilibrium
2. The earth pressure on the passive side remains at passive limit above the critical depth
3. The embedded wall beyond the critical depth provides a 'reserve' capacity to stability, and such capacity is derived from the 'net' of the limiting earth pressures from either side of the wall.

The WYDIWYG model is shown in Fig. 5.

where

$K_{aa}$  is the active earth pressure on the retained side of the wall.

**Fig. 5** WYDIWYG model.  
 Note the dotted line represents the portion that is balanced on either side of the wall



$K_{pp}$  is the passive earth pressure on the excavated side.

At the design embedment, the restoring moment capacity is the difference of those from the excavation side and the retained side. Hence, take moment about the support, the reserve moment capacity,  $M_r$ , is:

$$M_r = M_p - M_a \tag{2}$$

where

$M_p$  is the total moment on the excavation side.

$M_a$  is the total moment on the retained side.

Expand Eq. (2) as follows and re-group:

$$\begin{aligned} M_r &= (M_{pcr} + M_{pp}) - (M_{acr} + M_{aa}) \\ &= (M_{pcr} - M_{acr}) + (M_{pp} - M_{aa}) \end{aligned}$$

where

$M_{pcr}$  = the moment above the critical depth on the excavated side.

$M_{pp}$  = the moment below the critical depth on the excavated side.

$M_{acr}$  = the moment above the critical depth on the retained side.

$M_{aa}$  = the moment below the critical depth on the retained side.

At critical depth, the wall is in equilibrium with  $M_{pcr} = M_{acr}$ ; therefore, Eq. (2) may be simplified as follows:

$$M_r = M_{pp} - M_{aa} \tag{3}$$

Using the conventional overturning factor of safety definition,

$$FoS_{\text{overturning}} = M_{\text{restoring}} / M_{\text{disturbing}}$$



Since  $M_{\text{restoring}} = M_{\text{pcr}} + M_r$ , and  $M_{\text{disturbing}} = M_{\text{acr}} = M_{\text{pcr}}$ , the factor of safety can be re-written as:

$$\text{FoS}_{\text{overturning}} = (M_{\text{pcr}} + M_r) / M_{\text{acr}} \quad (4)$$

$$= (M_{\text{pcr}} + M_r) / M_{\text{pcr}}$$

$$= 1 + M_r / M_{\text{pcr}} \quad (5)$$

For a general case in layered materials, it may be shown that

$$\text{FoS}_{\text{overturning}} = 1 + \Sigma M_{\text{ij}} / \Sigma M'_{\text{pcri}} \quad (6)$$

where the summation is of all layers of materials; i layers to the critical depth and j layers to the toe of the wall; the apostrophe indicates the effective moment capacity.

## 5 Discussion and Some Characteristics of the WYDIWYG Method

The proposed method may be regarded as a hybrid between the CP2 and the BSC in that it takes advantage of their simplicity and effectiveness. The new formulation, as shown in Fig. 5, strategically considers the critical equilibrium condition in the upper part of the model. This part is identical to CP2. The portion below the critical depth considers net earth pressures and is similar to BSC.

Most of the models consider a degree of earth pressure modification for enhanced stability assessment. This, however, complicates the determination of loads and resistances in the design calculations, which are needed when using a LRFD approach. The proposed model avoids this by considering only the limit state pressures using a consistent earth pressure theory. The loads and resistances are readily defined. With the existing models, pressure modifications often start from below the excavation level. Using the BSC net pressure model as an example, while this choice provides an assessment on stability, it may be viewed as a premature reduction of disturbing load in the stability calculation. This may explain a consistently high calculated stability value. On the other hand, the active pressures extending to the toe level of the wall on the retained side for the other models would appear to be over-estimating the disturbing loads. This leads to the observed conservatism when using the CP2 method. It may also explain the unreasonable results in the total stress analysis because the increase in resistance is not kept up with the increase in load. In contrast, the new model chooses the critical equilibrium condition as a reference load. The total resistances are made up of the restoring capacity at critical equilibrium and the net pressures from below the critical depth. This effectively allows the

FoS to be expressed as a function of the critical restoring moment, which becomes a convenient quantity to measure stability for a given excavation. By limiting the unreasonable increase of disturbing load, the model avoids the numerical problem in the total stress calculations.

Safety of a design is ensured by adopting a suitable factor required by relevant regulatory authority. In Australia, this factor is represented by the minimum geotechnical reduction factor when designing to AS 5100.3 as per Eq. (1). If the required stability FoS is 2, which is equivalent to a geotechnical reduction factor of 0.5, then using the new approach the design ensures that the wall is stable with a restoring capacity exactly 2 times at its critical equilibrium condition.

Where soil layering occurs the wall embedment can be adjusted by taking into account of the changes in resistance of the soil layers. A stronger foundation material offering a higher lateral resistance would require a shallower embedment and vice versa. The design safety margin is maintained constant, whether it is for total or effective stress analysis. This is again different from some of the existing methods where the margin changes with regard to change of soil conditions. The difference could become more apparent in stratified geological environment with significantly different soil properties.

For the stability calculation to be undertaken effectively, the critical equilibrium depth needs to be determined first. Then using Eq. (4), the required geotechnical reduction is applied to all materials on the excavated side and also to those below the critical depth on the retained side. A similar consideration on groundwater is needed. Equation (6) suggests the reduction factor to be applied on the water components as well. If this is ignored, then the reserve moment capacity could be expected to reduce resulting in a deeper embedment.

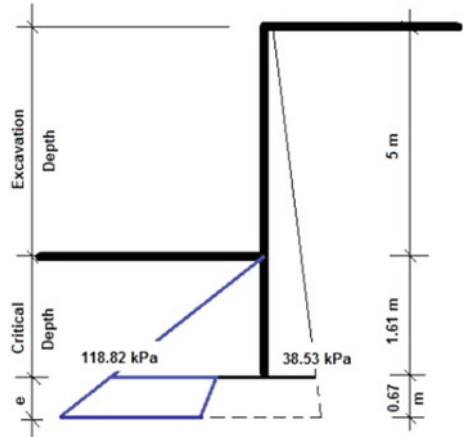
A worked example is given in the next section to demonstrate the calculation process to determine the required wall embedment. The FoS terminology is used in the next section as most engineers are familiar with it, but it may be substituted by the term geotechnical reduction factor as described above if needed.

## 6 A Worked Example

To illustrate application of the WYDIWYG method to embedment design, the effective stress case in Table 1 is used. Instead of calculating the factor of safety (FoS) from a given wall embedment, the target FoS of 1.84 is chosen to suit a given design requirement.

The embedment design using the WYDIWYG method is a two-step process, firstly to calculate the critical wall depth and then determine the critical effective restoring moment. The second step is to proportion the wall embedment to provide the required reserve restoring moment to satisfy the design FoS requirement. The critical wall depth may be calculated by hand for simple problems and for more complex ones involving multiple soil layers and groundwater, it may be worthwhile

**Fig. 6** Earth pressure distribution for effective stress case. *Note* Not to scale, wall shown at critical depth only and prop support not shown



to use appropriately developed calculation programs instead. In the above example, the critical wall depth is calculated by using a commercial software called WALLAP.

The first step in the process is to determine the wall embedment at critical stability, i.e., FoS = 1. The critical embedment depth below the excavation level is calculated to be 1.61 m. The earth pressure distribution is shown in Fig. 6 for ease of reference.

Depth to toe of wall, H, retained side

$$\begin{aligned}
 &= 5 + 1.61 \\
 &= 6.61 \text{ m}
 \end{aligned}$$

The earth pressures at the critical depth are calculated using the following equations:

Earth pressure at critical wall toe, retained side,  $K_{acr}$

$$\begin{aligned}
 &= (\gamma * H + \sigma_s) * k_a \\
 &= (20 * 6.61 + 10) * 0.27 \\
 &= 38.53 \text{ kPa}
 \end{aligned}$$

where

$\gamma$  is the unit weight of soil,  $\text{kN/m}^3$ .

$H$  is the overall length of the wall, m.

$\sigma_s$  is the traffic surcharge, kPa.

$k_a$  is the coefficient of active earth pressure.

Earth pressure at critical wall toe, excavation side,  $K_{pper}$

$$\begin{aligned}
 &= \gamma * h * k_p \\
 &= 20 * 1.61 * 3.69 \\
 &= 118.82 \text{ kPa}
 \end{aligned}$$

where

$h$  is the wall embedment length below the excavation level, m

$k_p$  is the coefficient of passive earth pressure.

The restoring moment capacity at critical equilibrium,  $M_{pcr}$

$$\begin{aligned} &= K_{ppcr}/2 * h * (5 + 2/3 * h) \\ &= 118.82/2 * 1.61 * (5 + 2/3 * 1.61) \\ &= 580.91 \text{ kNm} \end{aligned}$$

The next step is to determine the additional wall embedment to satisfy the required stability. For a given FoS, the required reserve moment capacity can be calculated using Eq. (5):

$$M_r = (\text{FoS}_{\text{overturning}} - 1) * M_{pcr}$$

Since the required FoS is 1.84, the above equation becomes

$$\begin{aligned} M_r &= (1.84 - 1) * 580.91 \\ &= 0.84 * 580.91 \\ &= 487.97 \text{ kNm} \end{aligned}$$

The extra wall embedment is then proportioned to obtain the reserve moment capacity. Take the extra embedment beyond the critical depth to be  $e$ , the earth pressures at the new toe level are expressed as follows:

$$\begin{aligned} K_{aa} &= [20 * (6.61 + e) + 10] * 0.27 \\ &= 38.53 + 5.42e \\ K_{pp} &= 20 * (1.61 + e) * 3.69 \\ &= 118.82 + 73.8e \end{aligned}$$

The reserve moment,  $M_r$ , may be expressed as follows:

$$\begin{aligned} M_r &= (K_{ppcr} - K_{aacr}) * e * (H + e/2) \\ &\quad + [(K_{pp} - K_{aa})/2] * e * (H + 2 * e/3) \\ &= (118.82 - 38.53)e(6.61 + e/2) \\ &\quad + [(73.8e - 5.42e)/2]e(6.61 + 2e/3) \\ &= 22.80e^3 + 266.15e^2 + 530.72e \end{aligned}$$

From above = 487.97 kNm.

Solving the cubic equation,  $e = 0.67 \text{ m}$ , the design wall embedment,  $D$ , is hence

$$\begin{aligned} &= 1.61 + 0.67 \\ &= 2.28 \text{ m} \end{aligned}$$

and the design wall length is  $5 + 2.28 = 7.28$  m.

## 7 Summary and Conclusions

The continued urban development in Sydney triggers increased demand for excavation supports for infrastructure development. Some of the existing stability assessment methods are fraught with problems. The example such as CP2 in Table 1 showed that including all active pressures as loads resulted in under-estimation of the wall stability number, whereas BSC when considering only the net earth pressures could not reliably calculate the stability numbers. BP improved the stability estimates by modifying the loads and resistances. Nonetheless, the approximation commencing from the mud line could not completely overcome the excess load issue, and the problem experienced in the total stress cases remains.

Most of the existing models are not developed to enable conforming designs to LRFD approach, such as that given in Australian Standard AS 5100.3. A review of the existing design methodologies indicates that there are benefits to reformulate the stability model to overcome the issues associated with consistency, reasonableness, and reliability in the stability calculations.

Intuitively increasing wall embedment beyond the critical depth improves stability, and this enables the wall to take on additional load without failure. Clearly, a reserve for stability is created in the process. An examination of the earth pressures on the wall revealed that they no longer exist at limiting states, higher pressure on the retained side, and lower on the excavation side, particularly on the part installed beyond the critical depth. The stability must therefore be derived from the earth pressure changes from the limiting states. It has been argued that the earth pressures over this part of the wall are neither only a load nor only a resistance. The net effect of them is postulated to be responsible for the observed stability and hence should be regarded as a resistance. Calculation of the reserve capacity for stability is made through idealization of the wall with the earth pressures returning to their respective limit state.

Limited sensitivity studies on the proposed method shown in Fig. 3 were undertaken. The results demonstrated that the new formulation calculates consistently throughout the soil strength spectrum. It compares favorably with the existing methods overcoming the long-standing problem in total stress analysis and provides a realistic estimate of the wall stability. Using the critical disturbing load as a new reference datum in stability assessments, the proposed method maintains a constant safety margin for a given design, whether the materials are sand or clay, or layered materials. This is in contrast with the existing methods which tend to vary according to the ground condition due to their formulation.

Accompanying with the new model is a clear distinction of loads and resistance. This makes it suitable for LRFD methods, and conforming design is possible. A worked example has been included to demonstrate the simple design process.

So far the discussion has focused on geotechnical stability only. In order for the wall to sustain this ultimate condition, it needs to withstand the bending moment and shear stresses due to the idealized limiting pressures. For other wall loads and serviceability calculations, design effects from earth pressures due to the conventional soil structure interaction also need to be considered. With the WYDIWYG method, this design process is usually undertaken after the final wall embedment is determined. Or it may be completed simultaneously if the method is codified within a suitable calculation program.

In conclusion a simple, consistent, and reliable way is proposed to calculate the geotechnical stability for propped cantilever walls. The improved assessment for stability design enables designers to better balance between economics of construction and margin of stability in design. The unique way it offers to calculate the geotechnical stability by relating it to a tangible critical equilibrium quantity ensures safety, giving clarity and certainty to design, such that a wall designed with a FoS of 2 will have a restoring capacity exactly two times at its critical equilibrium state. Consistent assessment and meaningful comparison of stability performance may be made.

## 8 Future Work

The use of critical loads for stability calculation in LRFD is not new and has been used satisfactorily in such as L-shape retaining walls. The problem for embedded structures occurs on the role of earth pressures, and the proposed model has provided a different approach to the solution. It is envisaged that this proposed approach could be applicable to some selected geotechnical design areas, notably for stability assessment of laterally loaded geotechnical structures. Going forward, further exploration on plausible application areas will be undertaken. This includes its application on embedded free cantilever retaining walls to demonstrate a simple and effective process, which would otherwise be a challenging mathematical problem when using the conventional fixed earth support model.

**Acknowledgements** The author would like to thank Transport for New South Wales for the permission to publish this paper. Thanks are also due to Mr B Tetleroyd on drafting support. The opinions expressed in this paper are those of the author and do not necessarily represent those of Transport for New South Wales.

## References

1. Australian Standard AS 5100:2017 Bridge design. *Standards Australia*
2. BSC Piling Handbook, 6<sup>th</sup> Edition (1988) *British Steel Corporation*.
3. Burland, J.B., Potts, D.M. & Walsh, N.M (1981) The overall stability of free and propped embedded cantilever retaining walls, *Ground Engineering*, July 1981.
4. Civil Engineering Code of Practice No.2 (1951) Earth Retaining Structures. *Institution of Structural Engineers*.
5. Potts DM, Fourie AB (1984) The behavior of a propped retaining wall: results of a numerical experiment. *Geotechnique* 34(3):383–404
6. Potts DM, Fourie AB (1985) The effect of wall stiffness on the behaviour of a propped retaining wall. *Geotechnique* 35(3):347–352
7. WALLAP, Geotechnical design software – Earth retaining structures by *Geosolve*.

# Maintenance Planning Framework for Rock Slope Management



Roman Denysiuk , Joaquim Tinoco , José Matos , Tiago Miranda ,  
and António Gomes Correia 

**Abstract** This paper presents a computational framework to assist in maintenance planning for geotechnical structures. The most suitable maintenance strategies are determined by optimization regarding the deterioration of structure and the cost of maintenance when satisfying constraints that translate demands for adequate levels of service. Uncertainties are accounted by considering model parameters as random variables. The framework is applied to the case study consisting in optimal maintenance planning for a highway slope belonging to the Portuguese network. The obtained results show the validity and usefulness of this framework. The framework can be also applied to different types of infrastructure assets.

**Keywords** Rock slope management · Maintenance planning · Infrastructure · Optimization

## 1 Introduction

As a developed country, Portugal has nowadays a fairly complete road network, which together with other transportation infrastructures is a fundamental element to ensure all necessary mobility conditions. After several years of investment, the main challenge today is how to guarantee all security and mobility conditions of the road network under increasingly limited budgets. Therefore, there is an urgent need to develop a set of tools able to help decision-makers to take the best decisions with respect to the maintenance strategy to be implemented.

Mathematical modeling, combined with optimization techniques, can be used to devise effective strategies for management of highway assets. Formulating a model, one should make a trade-off between simple and complex models. Simple models omit several details and have the disadvantage of possibly being unrealistic. Complex models include more details and are more realistic, being generally more difficult to

---

R. Denysiuk · J. Tinoco (✉) · J. Matos · T. Miranda · A. G. Correia  
ISISE—Institute for Sustainability and Innovation in Structural Engineering, School of  
Engineering, University of Minho, Guimarães, Portugal  
e-mail: [jtinoco@civil.uminho.pt](mailto:jtinoco@civil.uminho.pt)



solve. Moreover, many real-world problems, including the management of highway assets, require simultaneous consideration of multiple criteria.

Existing asset management systems rely on degradation models to forecast their future states. These models can be either deterministic or probabilistic. A major disadvantage of deterministic models is that they do not consider uncertainties. This can be overcome by using probabilistic models. The most common probabilistic models for modeling deterioration are the Markov chains [1].

The use of forecast models enables to plan maintenance strategies. To assist in this process, optimization of maintenance strategies is performed based on models describing the degradation and effects of maintenance. Early works rely on single-objective optimization [2], where a maintenance strategy minimizing the total cost is sought when considering the degradation as a constraint [3]. With advantages related to the ability of obtaining a set of trade-off solutions efficiently and a posteriori decision making, multi-objective optimization recently has attracted the attention to management of highway assets [4].

Due to the social and economic importance of bridges and pavements, most works focus on these two assets. Concerning the management of slopes, some approaches can be found in the literature that addresses the failure risk assessment and management [5]. These approaches essentially focus on characterizing, in a particular moment, the condition of a given slope or a network of slopes through the quantification of a risk measure related to its probability of failure [6]. For long periods of time, Huisman [7] aimed to determine the relation between time and decay of rock using numerical models. However, such studies do not give indications about the future behavior of slope and the maintenance strategy to follow.

The purpose of the present study is to develop a complete framework for slope management. In the previous work [8] that can be regarded as the first step to the development of this framework, an innovative system named the slope quality index (SQI) was suggested. The SQI system is characterized by its flexibility and is based on the evaluation of different internal and external factors related to the slope quality and stability. By weighting the different factors, a final indicator (the SQI) of the slope stability condition is calculated, which ranges between 1 and 5, corresponding to slopes in very good and very bad condition state, respectively. The system is adopted as the basis for the prediction of the slope degradation over time and is integrated with a methodology for quantifying effects of maintenance actions. This is further extended by combining with multi-objective optimization to address the optimal maintenance planning. The above feature has a particular advantage as it allows obtaining a set of maintenance strategies representing different trade-offs that can be employed for a posteriori decision making. Finally, different approaches to decision making are considered.

## 2 Framework for Maintenance Planning

This section provides details about components of the proposed framework.

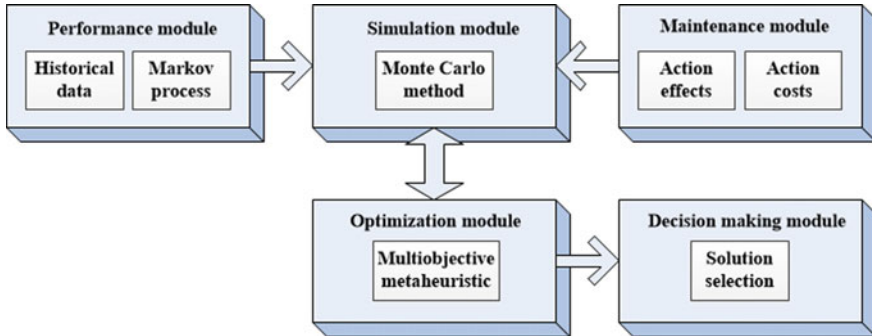


Fig. 1 Flowchart of interactions among modules of the proposed framework

## 2.1 Global Methodology

The structure of the proposed framework is shown in Fig. 1. Although the present study focuses on rock slopes, this framework can be applied to other types of slopes and infrastructure assets. For this, a discrete characterization of the quality index and a quantitative description of maintenance actions must be developed.

The process of planning begins with constructing the degradation model in the performance module. To this end, a Markov chain is used to define a random process based on a historical record of slope inspections. The maintenance module embraces the quantification of effects of maintenance actions and their costs. These are developed on the basis of the expert judgment. The optimization module aims to find the best combination of maintenance actions with respect to the performance and cost. As two clearly conflicting objectives are involved, the problem is naturally posed as a multi-objective optimization problem. This module is linked with the simulation module that accepts a maintenance plan and performs a Monte Carlo simulation to estimate the future degradation (performance) of the given slope. The outcome of the optimization module is a set of Pareto optimal maintenance plans that are fed to the decision-making module. In this module, the decision-maker's preferences are incorporated in order to select the most preferred solution among the available alternatives.

## 2.2 Degradation Model

A continuous-time Markov process is used to model the degradation of slopes. Markov chain is a random process that undergoes transitions from one state to another on a state space. The Markov property states that the next state only depends on current state and not on the sequence of preceding states. The state space of the

Markov process is defined by the values of the slope quality index (SQI) from the set {1, 2, 3, 4, 5} [8]. In the following, the state will refer to the value of SQI.

The transitions between states are defined in the transition matrix:

$$P^{\Delta t} = \begin{bmatrix} p_{11} & p_{12} & p_{13} & p_{14} & p_{15} \\ 0 & p_{22} & p_{23} & p_{24} & p_{25} \\ 0 & 0 & p_{33} & p_{34} & p_{35} \\ 0 & 0 & 0 & p_{44} & p_{45} \\ 0 & 0 & 0 & 0 & p_{55} \end{bmatrix}^{\Delta t} \tag{1}$$

where  $p_{ij}$  is the transition probability between  $i$  and  $j$  from instant  $t$  to  $t + \Delta t$ .

When intervals are not regular, the matrix  $P$  can be computed by solving the Chapman–Kolmogorov equation. This results in the following expression:

$$P = e^{Q\Delta t} \tag{2}$$

where  $P$  is the transition matrix and  $Q$  is the intensity matrix [9].

The intensity matrix,  $Q$ , represents the instantaneous transition probability between the state  $i$  to the state  $j$  ( $j \neq i$ ). It is assumed that, in each time interval, the advance can only occur between adjacent states [9, 10]. Therefore, the elements of  $Q$  are null except for the main diagonal and the diagonal above that, as shown in:

$$Q = \begin{bmatrix} -\theta_1 & \theta_1 & 0 & 0 & 0 \\ 0 & -\theta_2 & \theta_2 & 0 & 0 \\ 0 & 0 & -\theta_3 & \theta_3 & 0 \\ 0 & 0 & 0 & -\theta_4 & \theta_4 \\ 0 & 0 & 0 & 0 & 0 \end{bmatrix} \tag{3}$$

Using the intensity matrix, the transition matrix can be computed for any time interval  $\Delta t$ . By constructing the Markov model, it is meant to estimate the elements of the intensity matrix,  $Q$ .

An initial estimate of  $Q$  can be computed using a historical record of inspections through:

$$\theta_i = \frac{n_{ij}}{\sum \Delta t_i} \tag{4}$$

where  $\theta_i$  represents the transition rate between adjacent states,  $n_{ij}$  is the number of elements that moved from the state  $i$  to  $j$  and  $\sum \Delta t_i$  is the sum of time intervals between observations, whose initial state is  $i$ .

The quality of fit of the initial model is improved by minimizing the following function:

$$\sum_{m=1}^M \sum_{n=1}^N \log(p_{ij}) \quad (5)$$

where  $m$  is the number of transitions observed in element  $k$ ,  $n$  is the number of analyzed elements, and  $p_{ij}$  is the probability of occurrence of observed transition, as predicted by the Markov model.

### 2.3 Maintenance Model

The effects of maintenance actions are modeled based on the experience and data provided by a major Portuguese highway managing company. When a maintenance action is applied, its impact on a slope can be modeled by the following effects: (i) an improvement in the performance at the time of application, (ii) a delay of the degradation process for some period of time, and (iii) a reduction in the degradation rate for a period of time after application. A single maintenance action can produce either one or a combination of the above effects [4, 11].

Maintenance effects are parametrized and modeled as follows. When a maintenance action producing the effect of improvement in the performance is applied, the SQI is updated by reducing its current value by  $\gamma$ . In the case of delaying the deterioration process, the SQI remains constant during a period of  $t_d$ . In the case of reducing the degradation rate, the SQI deteriorates at a rate of  $\delta_r$  during a period of  $t_r$ , which is lower than a normal degradation rate. All these values are determined by experts based on their experience and knowledge. In practice, the effects produced by maintenance actions are not deterministic. They are influenced by uncertainties due to a wide range of factors. Therefore, parameters modeling maintenance effects are defined as random variables. It is assumed that these random variables follow a triangular distribution. The reason behind this choice is that triangular distributions are among easiest ways of introducing randomness. It is characterized by the minimum and maximum values along with a mode (the most probable value).

Depending on the current SQI, the effects produced by the same maintenance action can vary. This issue is addressed by defining different values of the parameters ( $\gamma, t_d, \delta_r, t_r$ ) according to the current SQI value. Thus, considering the values between 1 and 5, at most five different triangular distributions can define each parameter in the maintenance model, with each distribution referring to the current SQI.

### 2.4 Monte Carlo Simulation

As degradation and maintenance models are given by stochastic processes, the future performance of slope is subject to uncertainties. Therefore, a Monte Carlo simulation is used to estimate the future SQI values. The simulation consists in sampling from

probability distributions defined by both models. For a given instance of time, the SQI is characterized by a sample of estimates that represent a probability distribution. The SQI value is estimated by the mean value of that sample.

The transition matrix, whose components represent the transition probabilities between  $i$  and  $j$  from instant  $t$  to  $t + \Delta t$ , is calculated as shown in Eq. (2). Given the SQI value of  $i$  in time  $t$ , the SQI value of  $i'$  in time  $t + \Delta t$  is computed using the probability vector from the  $i$ th row of  $P$ . In particular, the first row is used when  $i = 1$ , the second row is used for  $i = 2$  and so on. A random number  $u \sim U(0, 1)$  is generated and the value of the SQI is determined as:

$$i' = \begin{cases} 1 & \text{if } u < \sum_{j=1}^1 p_{ij} \\ 2 & \text{else if } u < \sum_{j=1}^2 p_{ij} \\ 3 & \text{else if } u < \sum_{j=1}^3 p_{ij} \\ 4 & \text{else if } u < \sum_{j=1}^4 p_{ij} \\ 5 & \text{otherwise} \end{cases} \tag{6}$$

The value of  $i'$  is always greater than or equal to the value of  $i$ . The parameters modeling maintenance action effects are incorporated into the Monte Carlo simulation. In the corresponding year, the values of these parameters are drawn from triangular distributions. If there is an improvement in the SQI, the current value is reduced by  $\gamma$ . In the case of a reduction in the degradation rate, the matrix  $Q$  is multiplied by  $\delta_r$ . A delay in the degradation process is modeled by considering  $P$  as the identity matrix.

### 2.5 Multi-objective Optimization

The problem of optimal maintenance planning for a slope is posed as a multi-objective optimization problem. Formally, it can be defined as:

$$\begin{aligned} \text{minimize : } & f_1 = \max_{1 \leq i \leq t_h} \text{SQI}_i \\ & f_2 = \sum_{j=1}^{t_h} \frac{\text{cost}(\cdot)}{(1+r)^j} \\ \text{subject to : } & \text{SQI}_i \leq 3 \forall i \in \{1, \dots, t_h\} \end{aligned} \tag{7}$$

where  $t_h$  is the time horizon,  $\text{cost}(\cdot)$  is the cost associated with the maintenance action, and  $r$  is the discount rate. The first objective represents the slope performance. The smaller maximum (worst) value of the SQI, the better performance is. The second objective represents the total cost of maintenance activities during the planning horizon. The future costs are discounted to reflect their current values using the concept of the time value of money. Constraints translate requirements for adequate levels of safety and serviceability. At any instance of time, the SQI cannot exceed the value of 3. This is in accordance with quality requirements established by the Portuguese authorities.

For solving the above problem, a multi-objective evolutionary algorithm based on decomposition (MOEA/D) is adopted. MOEA/D decomposes a multi-objective problem into a number of single-objective subproblems using scalarization and optimizes them simultaneously in a single run. For a detailed description of MOEA/D, an interested reader is referred to Li and Zhang [12].

Each population member represents a potential solution to the problem and is encoded as a string of integers. This string corresponds to the plan of maintenance actions to be performed. The string length is equal to the number of years in the time horizon. As an example, consider a string [4 0 2 0 5 0 2 0 1 0]. Each number represents the identification number of maintenance action, whereas the position in the string corresponds to the time of application. Thus, 4 at the first position means that the maintenance action with the identification number of 4 is applied in the first year, 0 at the second position means that no action is applied in the second year and so on.

## 2.6 Decision Making

A solution to multi-objective optimization problem is a product of the search and decision processes. The former refers to generating a set of solutions that are equally important in terms of the Pareto dominance relation. The latter involves selection of a single solution from the obtained set. To enable the distinction between different Pareto non-dominated solutions, an additional preference information must be elicited by the decision-maker.

In the literature, there exist various methods to support decision making in the presence of multiple conflicting criteria. Two different approaches are considered in this study. The first one is adopted from the field of multiple criteria decision making (MCDM). Specifically, compromise programming is used for the solution selection. It is based on the concept that alternatives that are closer to the ideal are preferred to those that are farther away. To be as close as possible to the perceived ideal is a rationale of human choice [13]. The closeness is evaluated by the distance function that using the Chebyshev metric can be defined as:

$$L_\infty(a, w) = \max_{1 \leq i \leq m} w_i \frac{f_i(a) - z_i^*}{z_i^{**} - z_i^*} \quad (8)$$

where  $A$  is a set of non-dominated solutions,  $a$  is a solution from that set,  $w = (w_1, \dots, w_m)$  is a weight vector whose the  $i$ th component represents a relative importance of the  $i$ th objective  $f_i$ ,  $z_i^*$  and  $z_i^{**}$  are the  $i$ th components of the ideal and nadir vectors, respectively. These vectors are composed of the minimum and maximum values of the objectives in  $A$ . The preference information is elicited from the decision-maker in the form of  $w$  that specifies the relative importance of the objectives. Finally, a solution  $a^*$  that meets the best these preferences can be determined as:

$$a^* = \underset{a \in A}{\operatorname{argmin}} L_\infty(a, w) \quad (9)$$

The second approach to decision making addressed in this study is related to the reliability of solutions under effects of uncertainty, which is particularly relevant issue to the problem at hand. As the objective related to the slope performance is derived from the Monte Carlo simulation, repeated evaluations of the same solution produce different results. In the optimization literature, this effect is often referred as to noise. Solutions exhibiting a higher tolerance to noise are preferred in practice. To allow the use of this concept for the solution selection, a proper measure for assessing the solution quality with respect to the noise tolerance and a way to model the decision-maker's preference regarding this criterion must be defined. In what follows, the solution tolerance to noise and robustness are used interchangeably.

The expectation and variance are most commonly used as robustness measures in the field of robust design optimization. Similarly, this study makes use of the variance to determine the tolerance of solution to noise (robustness). For each solution  $a$  from  $A$ , this measure is calculated as:

$$\sigma(a) = \frac{1}{n} \sum_{i=1}^n (x_i - \mu)^2 \quad (10)$$

where  $n$  is the number of evaluations,  $x_i$  is the value of the second objective in the  $i$ th evaluation, and  $\mu$  is the expected value calculated as:

$$\mu = \frac{1}{n} \sum_{i=1}^n x_i \quad (11)$$

A small variance indicates that values of the performance function tend to be close to the mean.

To model the preference information of the decision-maker with respect to robustness, the dispersion parameter  $\varepsilon$  is introduced. This parameter ranges from 0 to 1 and enables the decision-maker to specify the desired degree of robustness for the obtained solutions. Solutions that meet the corresponding requirements form a subset of  $A$  that can be formally defined as:

$$A^\varepsilon = \{a \in A : \bar{\sigma}(a) \leq \varepsilon\} \quad (12)$$

where  $\bar{\sigma}(a)$  is the normalized measure of robustness for the solution  $a$ , which is calculated as:

$$\bar{\sigma}(a) = \frac{\sigma(a) - \sigma^{\min}}{\sigma^{\max} - \sigma^{\min}} \tag{13}$$

where  $\sigma^{\min}$  and  $\sigma^{\max}$  are the minimum and maximum values of  $\sigma$  for solutions in  $A$ , respectively. By specifying the value of the dispersion parameter, the decision-maker filters out solutions that are not robust. For small values of  $\varepsilon$ , the size of  $A^\varepsilon$  is small and contains solutions of high quality. Increasing the value of  $\varepsilon$  embraces a larger set of solutions adding those with lower tolerance to noise. The concept of the dispersion parameter was introduced in Gaspar-Cunha et al. [14], for focusing the search of multi-objective evolutionary algorithms on robust regions of the Pareto front. In that study, the dispersion parameter was used for specifying the preference information a priori (before optimization). This study makes uses of  $\varepsilon$  for a posteriori (after optimization) decision making.

### 3 Case Study

The case study consists in applying the proposed framework to find optimal maintenance strategies for a slope belonging to the Portuguese highway network.

#### 3.1 Experimental Setup

The rock slope under study is located in the west coast of Portugal. It belongs to Beira Litoral and Beira Alta Concession managed by a major Portuguese highway operating company. The current SQI is 2. For planning maintenance strategies, the periods of 10, 20, and 30 years are considered. Table 1 presents the elements of the intensity matrix describing the degradation of the slope. These parameters are computed on the basis of the historical data resulting from visual inspections of all slopes belonging to the highway operator. The intensity matrix has been validated by a goodness-of-fit test as reported in [15]. In accordance with the current practice, the seven maintenance actions have been defined ad their effects quantified on the basis of expert judgment. The description and cost for each of these actions are given in Table 2.

**Table 1** Elements of intensity matrix

$\theta_1$	$\theta_2$	$\theta_3$	$\theta_4$
0.0751	0.0997	0.1480	0.1679



**Table 2** Description and cost of maintenance actions

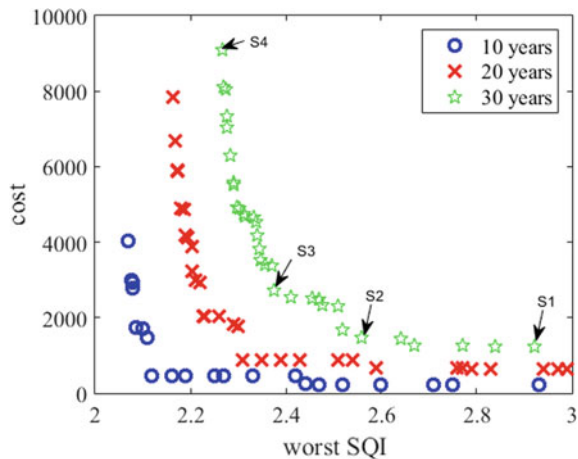
id	Description	Cost (€)
1	Slope bench cleaning	1541.52
2	Deforestation	1073.07
3	Reconstruction of platform ditches	1223.10
4	Reprofiling	1360.8
5	Sealing of cracks with cement grout	1360.8
6	Superficial drainage system cleaning	102.51
7	Banquettes cleaning	1800.00

The optimization is executed with a population size of 100, running for 300 generations. The other parameter settings are as follows. The crossover and mutation probability are 1.0 and  $1/l$ , respectively, where  $l$  is the chromosome length that corresponds to the time horizon. The probability of selecting parents from the neighborhood is 0.8, the neighborhood size is set to 5, and the maximum number of individuals replaced by an offspring is 2. The most suitable configuration of the parameters is determined experimentally. The number of samples used in the Monte Carlo simulation is 100, which corresponds to an adequate trade-off between the accuracy and complexity. The discount rate of 0.01 is used.

### 3.2 Results

For the three time horizons (10, 20, and 30 years), the obtained Pareto optimal solutions are presented in Fig. 2. As expected, there is no single optimal solution but a set of solutions that represent different trade-offs between the performance of

**Fig. 2** Representation of the Pareto optimal maintenance strategies in the objective space

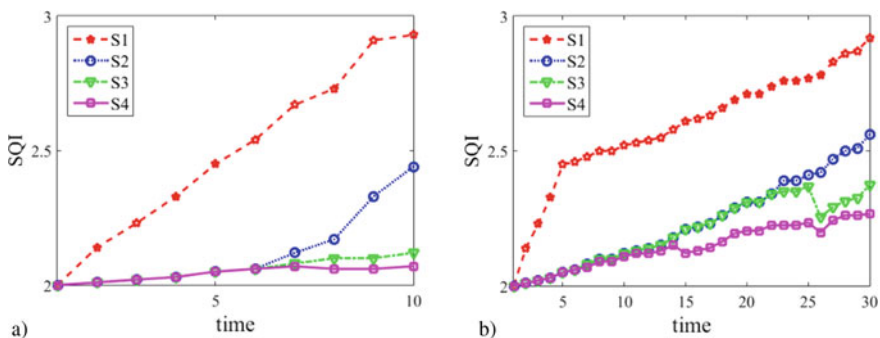


slope and the cost of maintenance. It can be seen that for larger time horizons higher expenses are required for maintenance. For instance, to ensure that the worst quality index of slope is not larger than 2.9, the maintenance costs are €222.2, €645.5, and €1244.2 for 10, 20, and 30 years, respectively.

The obtained Pareto optimal curves in Fig. 2 can be divided into two parts. One part represents scenarios in which the SQI can be improved efficiently. Another part offers solutions with increasingly larger expenses. For instance, consider the solutions obtained for the time horizon of 20 years. It can be seen that the reduction in the SQI from the worst-case scenario to the value approximately equal to 2.3, can be achieved incurring relatively small maintenance costs. However, expenses start growing significantly to accomplish a further improvement in the performance. Also, it can be seen that when the time horizon is increased, the number of solutions that are appealing from practical perspective becomes lower. These results stress the importance of a proper maintenance planning and the need for effective tools to support decision making.

To analyze maintenance strategies lying in different parts of the Pareto fronts, the following four weight vectors are defined:  $w^1 = (0, 1)$ ,  $w^2 = (0.1, 0.9)$ ,  $w^3 = (0.5, 0.5)$  and  $w^4 = (1, 0)$ . These weight vectors reflect different preferences of the decision-maker in accordance with the relative importance attributed to the performance of slope and the cost of maintenance. The vectors  $w^1$  and  $w^4$  correspond to the extreme scenarios when the focus is solely on minimizing the maintenance cost and improving the performance of slope, respectively. Whereas the vectors  $w^2$  and  $w^3$  translate specific trade-offs for these criteria. For the time horizon of 30 years, the compromise solutions corresponding to these weight vectors are highlighted in Fig. 3. For the sake of readability, the compromise solutions for 10 and 20 years are not shown in this figure.

Highway managing companies are often interested in solutions having smaller costs. Considering the time horizon of 10 years, the lowest cost maintenance strategy (solution S1) requires sealing of cracks with cement grout in the end of the considered period, namely in the ninth years. The same maintenance action is suggested being



**Fig. 3** Degradation profiles corresponding to different Pareto optimal maintenance strategies: **a** 10 years; **b** 20 years

applied for several times for the periods of 20 and 30 years. Solution S2 reflects the aspiration in reducing the cost of maintenance with some additional focus on the improvement in the SQI. For 20 and 30 years, the optimal maintenance strategies corresponding to S2 require the same type of maintenance activities increasing the number of interventions by one. For the time horizon of 10 years, solutions S1 and S2 are similar with respect to the type and number of actions though S1 has a lower cost as sealing of cracks with cement grout is delayed in time. This is due to the effect of the concept of the time value of money. Such situation is common in practice. This is because agencies often prefer to delay maintenance activities due to limited budgets. Owing to high maintenance costs, solutions S3 and S4 are unlikely to be interesting from a practical point of view. However, they are important for understanding how the model works.

For the considered compromise solutions, the dynamics of the SQI when implementing the corresponding maintenance strategies are shown in Fig. 3 (time horizon of 10 and 20 years). The plots in this figure clearly show that under suggested maintenance strategies the SQI does not cross the worst allowable value ( $SQI = 3$ ). The worst value of SQI is mostly achieved at the end of the time horizon. This means that a maintenance strategy that is optimal for a certain period of time would not be optimal when the time horizon is increased. These results suggest that the developed framework is able to provide adequate maintenance strategies optimizing the defined criteria and meeting demands for required levels of serviceability.

## 4 Final Observations

As environment becomes increasingly competitive, there is a growing attention to the use of effective tools for decision support. This study suggested a computation framework to assist decision making in maintenance planning for slope. The details of modules composing this framework are presented. The performance module involves building a mathematical model for degradation of slope quality index. This model is based on a time-continuous Markov process derived from a historical record of inspections. It is an important step allowing the prediction of the future performance of slope. The maintenance module comprises models for maintenance effects and costs that are developed on the basis of the expert knowledge. Uncertainties are addressed by modeling parameters as random variables and using a Monte Carlo simulation. Optimization of maintenance strategies is performed from a multi-objective perspective enabling a posteriori decision making.

The application of the proposed framework to maintenance planning for the case study slope demonstrates its validity and usefulness. It was observed that the performance model adequately describes evolution of the slope quality index over time, although a more complete validation with real/historical data is still required, when such information is available. Also, it was confirmed that defining parameters in the maintenance model as variables ranging in some intervals makes the incorporation of expert knowledge easier. This also allows dealing with opinions of several experts

that typically vary. Multi-objective optimization of maintenance strategies appears an effective tool to support decision making. The results are highly dependent on the type of activities and the time of application. When a set of maintenance strategies representing different trade-off is obtained, a careful and more effective planning of resource allocations can be carried out.

**Acknowledgements** This work was supported by FCT—“Fundação para a Ciência e a Tecnologia,” within Institute for Sustainability and Innovation in Structural Engineering (ISISE), project UID/ECI/04029/2013 and through the postdoctoral Grant fellowship with reference SFRH/BPD/94792/2013. This work was also partly financed by Fundo Europeu de Desenvolvimento Regional (FEDER) funds through the Competitiveness Operational Programme—COMPETE and by national funds through FCT within the scope of the project POCI-01-0145-FEDER-007633.

## References

1. Fernando D, Adey B, Walbridge S (2013) A methodology for the prediction of structure level costs based on element condition states. *Struct Infrastruct Eng* 9(3):735–748
2. Miyamoto A et al (2000) Bridge management system and maintenance optimization for existing bridges. *Comput-Aided Civ Infrastruct Eng* 15:45–55
3. Estes AC, Frangopol DM (1999) Repair optimization of highway bridges using system reliability approach. *J Struct Eng* 125(7):766–775
4. Neves LC, Frangopol DM, Cruz PJ (2006) Probabilistic lifetime-oriented multi-objective optimization of bridge maintenance. Single maintenance type. *J Struct Eng* 132(6):991–1005
5. Dai F, Lee C, Yip Ngai Y (2002) Landslide risk assessment and management: an overview. *Eng Geol* 64(1):65–87
6. Uzielli M et al (2008) A conceptual framework for quantitative estimation of physical vulnerability to landslides. *Eng Geol* 102(3):251–256
7. Huisman M (2006) Assessment of rock mass decay in artificial slopes. Ph.D. thesis. Delft University of Technology, Netherlands
8. Pinheiro M et al (2015) A new empirical system for rock slope stability analysis in exploitation stage. *Int J Rock Mech Min Sci* 76:182–191
9. Kalbfleisch J, Lawless J (1985) The analysis of panel data under a Markov assumption. *J Am Stat Assoc* 80(392):863–871
10. Jackson C (2011) Multi-state models for panel data: the msm package for R. *J Stat Softw* 38(3):1–28
11. Denysiuk R et al (2016) A computational framework for infrastructure asset maintenance scheduling. *Struct Eng Int* 26(2):94–102
12. Li H, Zhang Q (2009) Multiobjective optimization problems with complicated Pareto sets, MOEA/D and NSGA-II. *IEEE Trans Evol Comput* 13(2):284–302
13. Zeleny M (1976) The theory of the displaced ideal. In: Zeleny M (ed) *Multiple criteria decision making*. Springer, New York, pp 153–206
14. Gaspar-Cunha A, Ferreira J, Recio G (2014) Evolutionary robustness analysis for multi-objective optimisation: Benchmark problems. *Struct Multidiscip Optim* 49(5):771–793
15. Ferreira C et al (2014) A degradation and maintenance model: application to Portuguese context. In: *Proceedings of bridge maintenance, safety, management and life extension*, pp 483–489

# Geohazard in Consequence of Ignoring Primary Stress State and Failure to Observe the Construction Process of Stabilizing Constructions Designed



Juraj Ortuta and Viktor Tóth

**Abstract** With slope movements man does not encounter every day, but it should be noted that this happens, and it happens more often. These movements are influenced only by two factors, namely nature and humans themselves. Slope deformations are one of the most widespread and to some extent one of the most dangerous country geohazards and represent significant geobarriers to urbanization planning. With gradually expanding populations comes extensive and demanding technical works built in increasingly complex and less favorable geological conditions. In complex geological conditions, it is mainly about understanding the overall geological environment with the development and effectively designing geotechnical structures to ensure long-term stability. The term effective design encompasses a set of geotechnical construction, which complement each other, so that their final effect has the desired influence. In this paper, we have attempted to describe ways of determining global stability, which is directly conditional on the building progress of stabilizing construction. This procedure creates and directs geotechnical engineers. Any change in construction has an impact on the global calculation, which should be adapted and subsequently verified. This calculation also influences new geological and geomechanical conditions that are specified by the construction process. Contractors may skip these essential steps, due to time and cost skips and thus embarks on the risky work, often with fatal consequences.

**Keywords** Geohazard · Slope stability · Primary stress

## 1 Introduction

The mechanism of slope movements is defined as natural procession of general development and the course of slope mass movement. It is also conditioned by

---

J. Ortuta · V. Tóth (✉)

Amberg Engineering Slovakia, S.R.O, Somolického 1/B 811 06, Slovak republic, Slovakia

e-mail: [vtoth@amberg.sk](mailto:vtoth@amberg.sk)

J. Ortuta

e-mail: [jortuta@amberg.sk](mailto:jortuta@amberg.sk)

the geological—tectonic structure of a slope, by slope site topography as well as by operating natural and human activity factors. On the basis of the specific deformation and kinetic mutual coupling of separate parts of a moving mass in entire zone of a slope movement, this integrating mechanism determines that in a given space and time there develops and proceeds a characteristic type of downward slope movements and also a resulting type of slope failure, always with minimal energy consumption. The mass movement mechanism and the type of slope movement, as well as its velocity, can however change in space and time.

## **2 Sliding**

The most widespread slope movement is sliding. It is distinguished by the gravitational movement of soil or rock mass in solid (hard) to plastic state (from very stiff to soft consistence) on a slope without loss of contact with the bed ground.

Analysis of slide movement in respect to kinetics is based on Newton's law of motion, valid for the acceleration of solid bodies in the gravity field. With respect to the variable geometry of landslide, their surficial topography and their sliding surfaces, is possible to solve the kinetics of slide movement just in simple cases or in particular parts with clearly defined sliding mass path.

## **3 Landslides and Line Construction**

Slope deformations generally have a negative impact on planned construction. The greatest interest is mainly focused on landslides threatening the new family houses. It being remembered that many times the owners, who decided to build on the slope without the help of a geologist or geotechnical engineer, can often experience this situation. Linear structures, however, represent a strategic building that has a very wide use for the population and the state.

The complicated geological structure complex in the interaction with the construction of highways and the related occurrence of slope deformations is the biggest problem of most states in the world.

Although the maps of slope stability, in which the landslides and other slope deformations are registered, is being developed. During construction it, the responsible geotechnical engineer often encounter unexpected complications.

Project planning counts on what has been documented in the past, and therefore, are realized remedial arrangement which resulting from a previous survey. As already mentioned, there are cases when the combination of adverse natural conditions and anthropogenic intervention of construction into the natural environment activate slope deformations. One of the most frequent building interventions in the rock environment during construction is the undercut. Nothing unusual, but from

stability view-point, it is very dangerous. Although the stability ratios are calculated, due to the construction of supporting walls, the slope deformations are often unpredictable and thus annoying and mainly over-charge the actual construction.

## **4 Stability Assessment of Slope Deformations in Highway Corridor**

As an example, paper describes the construction of a highway in complicated geological conditions, where the alternation of solid and plastic layers occurs. This alternation results in several shear areas at different depths.

The most significant exogenous geodynamic phenomenon for near the highway included landslide, which is a response to the geological and tectonic structure of the area and its hydrogeological conditions. Slope deformations, that are in multiple locations combined with a movement of rubble's layers, cover the bulk of the area slopes engaged motorway route (or a range). We decided to focus on the first section of the highway, which almost represents one potential landing gear that directly threatens the adjacent railway station and, therefore, the direct northern rail link connecting the Czech Republic, Poland and Slovakia. This section is divided into several homogeneous units.

### **4.1 Section 1**

The route undergoes extensive stabilized slope deformation at the final development stage. First 120 m is applied to potential landslides a frontal planar slip surface in a depth of 7.0 to 8.0 m.

### **4.2 Section 2**

The section of the highway is situated in the accumulation of potential frontal landslide. The rock environment disturbed by sloping movements reaches a depth of 2.1 m–3.0 m. The depth of the sliding body according to the piezometric borehole is 5.0 m.

### **4.3 Section 3**

This section includes a large sliding area with two staged, stepped slides of 250–300 m in length, interconnected by two smaller flat landslides. The surface layer is damaged to a depth of 4–5 m by a potential landslide, where a basic shear surface is assumed to be 9.5–10.5 m deep.

### **4.4 Section 4**

Here is the highway route situated in a compound stabilized slope deformation. The construction sites are situated in the frontal landslide with a thickness deluvial landslide at 7–8 m. The central part of the territory is violated planar and current stabilized landslides, and the upper part of the slope deformations are broken by rubbles. The depth of the shear area is 7.0 m below the terrain.

### **4.5 Section 5**

This is a section where the rock environment is damaged by stabilized frontal landslide with a depth of shear area of 2.1 m–4.1 m.

Already on the basis of this sectional division and a short description of deformations, it is obviously what challenging geological environment. In general, we encounter several, mutually interconnected shear surfaces, either at the basal level (deeper shear areas) or the level of deluvial rubbles movement (shallow shear surfaces).

## **5 Design of Geotechnical Construction for Landslides Stabilization**

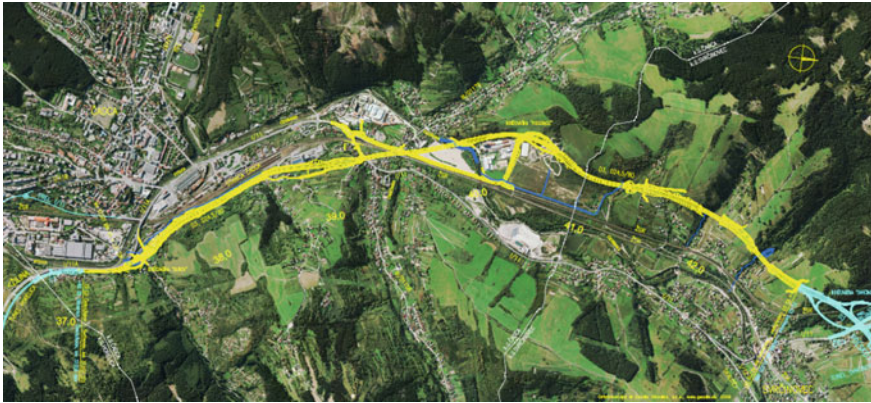
On the whole, the above described part of the newly built highway has been divided into six homogeneous units, and on the basis of geological survey was proposed set of geotechnical constructions, whose task is to stabilize the slope deformations. Figure 1 shows one of these variants.

Given that the problem is not only shear surface but a number of independent ones, it was necessary to choose the most advantageous construction process that would already have its own built steps created a motion-preventing construction unit.

Calculation of stability ration took place on two levels.

Calculation of the global stability of the section, account of the construction process and each step has been assessed separately, to avoid accidental triggering of





**Fig. 1** Plan of the highway D3—section length 6.3 km

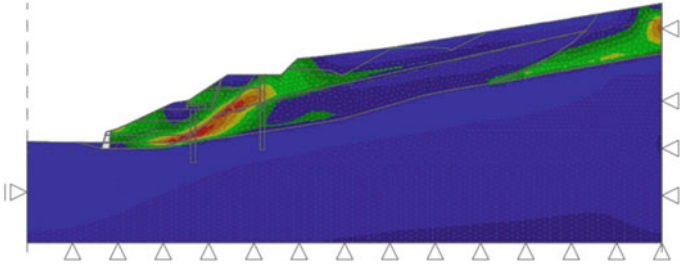
slope movement. If the step results in a decrease of stability to the previous step, and this step is reviewed and selected other process so as to still ensure the continuity of the construction (Figs. 2, 3, 4 and 5):

Calculation of internal stability of individual structures to determine internal forces and subsequent dimensional evaluation (Figs. 6 and 7):

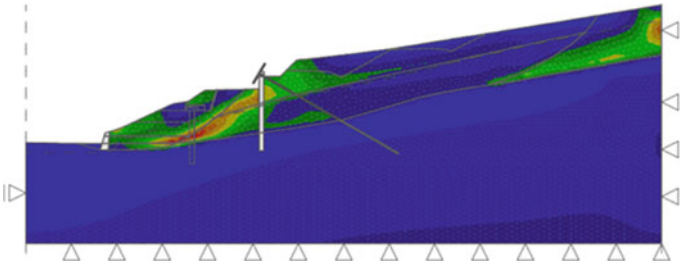
Many times, there is a requirement for control of project documentation sometime, directly from the contractor, supported global stability assessment for individual objects of the construction system. However, this requirement is often based on a misconception that the system can be divided into parts and they carry a proportion of the total degree of global stability.



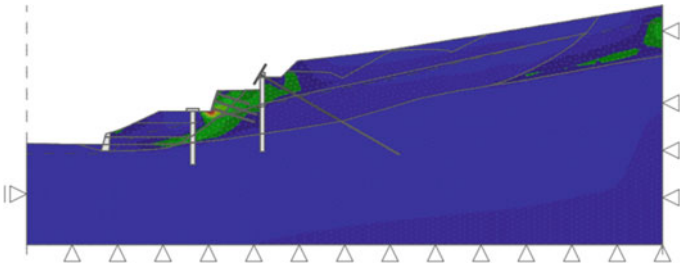
**Fig. 2** Schematic cross section—highway width 24.5 m



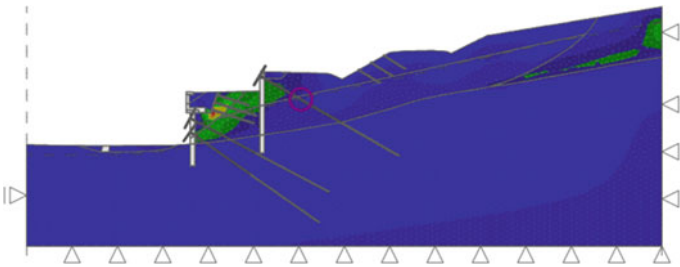
**Fig. 3** Shape of the shear surfaces for the first construction step (phase 0 represents the initial stress state)



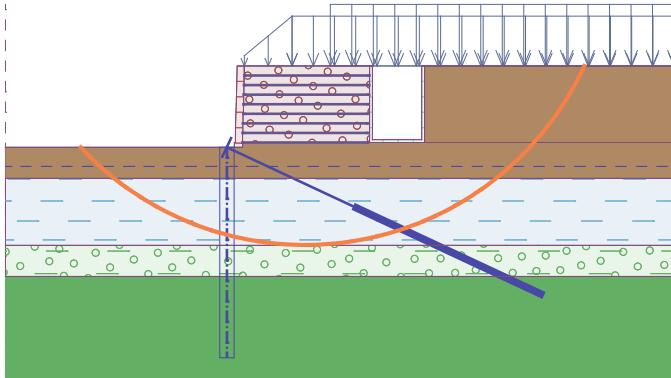
**Fig. 4** Redistribution of the shear displacements after completion of the first object, which now allowed the start of landslide release



**Fig. 5** Construction of another pilot wall, the task of which will be primarily to secure the left-hand highway



**Fig. 6** Final stability system of highway



**Fig. 7** Example of determining global stability for part of a construction with a reinforced structure

## 6 Construction Process and Global Stability

The main task of the geotechnical engineer is to propose a set of measures that will, by their nature, prevent landslides. A set of constructions means that individual parts fulfill their partial role until they build up the next part (gravitational walls, piles, MSE wall) and jointly take over the stability role as a whole.

The individual steps of geotechnical construction must be assumed and, on the basis of the primary stress state in the mass, it must be ensured so as to avoid landslides.

Each step must be supported by stability recalculation and only on the basis of it can be chosen the next procedure or take an auxiliary measure.

In such a construction process, geotechnical engineer works with time as a variable. This procedure must be followed by the contractor and cannot be diverted from it because even the minimum change may mean collapse.

Geotechnical engineer is in constant contact with the geologist who is present on the site. Each change from the assumption is immediately analyzed and inserted into the design model to verify the calculations. In case of non-compliance, they are immediately proposed measures. This does not mean an unnecessary increase in the cost of the work and the time of construction is not extended.

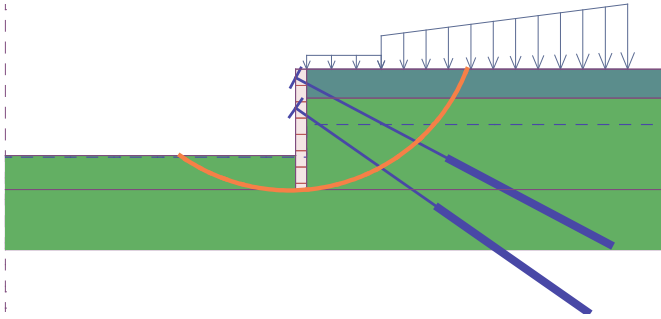
Other examples are the sum of the most common geohazards of the contractor in violation of geotechnics and ignoring nature.

Ignoring the construction process (Figs. 8, 9, and 10):

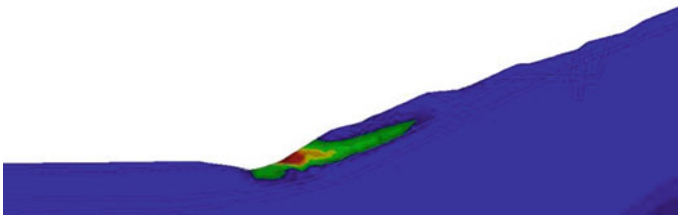
Ignoring the construction time (Figs. 12 and 13).

Geotechnical engineer prescribed not only the construction process but also the time steps that need to be accomplished. This had to be completed within the day so as not to damage the structure.

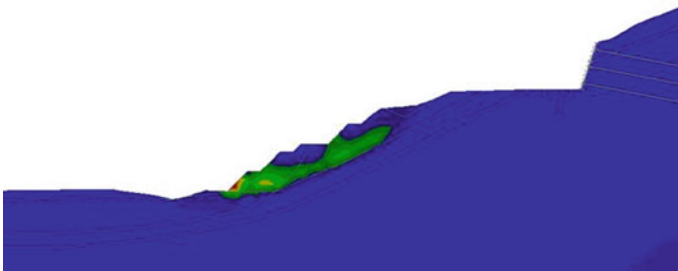
Nailed slope had to be secured by concrete in a day to prevent degradation of the soil and the change in mechanical properties (Fig. 14).



**Fig. 8** Another part of the same object and determination of global stability for piles and anchors



**Fig. 9** Primary stress state with identified landslide



**Fig. 10** Primary stress state with identified landslide

## 7 Risk Analysis and Likelihood of Occurrence an Undesirable Event

In geotechnical engineering, it is necessary to assume that a fault on the part of the contractor will occur during the design itself. It is in this area of construction that the manufacturer's mistakes are of a great nature and have dangerous consequences for the proposed work. It is necessary to count on them during the design, and thus to prevent, respectively, at least reduce the negative impact of improper work. This analysis will increase the safety of the building and increase the safety of workers.



**Fig. 11** Slope adjustment without free cut



**Fig. 12** Slope adjustment without free cut



**Fig. 13** More than a week open unsecured excavation and one-day rain





**Fig. 14** Crack zone

As mentioned above, frequent errors in the process of design geotechnical structures are neglect, respectively, simplifying undesirable effects on the building structure. But, if we are aware of these risks, it is possible to analyze them and under consideration the likelihood of an undesirable occurrence with regard to other aspects of the design under consideration.

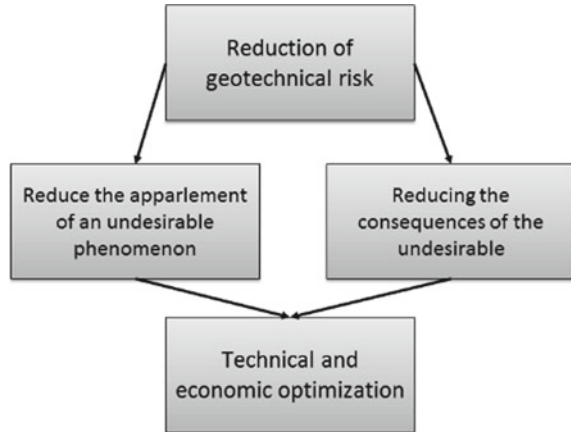
Generally, the risk can be understood as a probability of occurrence of an undesirable and unintended event and a negative consequence of this event. So, if we talk about risk, we are talking about the probability that a threat may occur. The risk is accompanied by uncertainty. It is the event with which the risk is associated may or may not occur. On the other hand, it is a loss, which is the result of unexpected consequences.

The first stage in risk analysis is their identification, a savoir identification of risk, and the identification of the risks that may affect the building structure. Creating a list of potential risks is based on the fact that everything can occur during the static calculation solution and what events it does. At present, there are many techniques and methods for identifying risks (Fig. 15).

The next step is the risk analysis itself. It serves to sort the risks according to their impact on project goals. Quantitative risk analysis serves to determine the likelihood of risks and to link these risks to the objectives of the project. Various risk analysis methods can also be used for building and designing building structures. However, the mathematical method, the method of scenario analysis and the method of using experience are the most optimal.

The main advantage of the matrix method is the ability to capture a great deal of interrelationships between the rock environment and the building structure. The scenario analysis method has the ability to use simulation patterns of construction behavior. In practice, it is being used less and less. The method of exploiting experience is in turn based on similarities with other similar constructions, which have been proposed under similar geological conditions. However, as geological conditions are predominantly different in each building, this method of analysis is rarely applicable.

**Fig. 15** Reduction of geotechnical risk



## 8 Lessons for Contractors

### 8.1 Application of the Observation Method

Natural or artificial environment from natural materials can never be considered as homogeneous, eventhough we are thinking in static assessment. Its real characteristics and the type of behavior of building structures in the rock environment cannot be reliably determined at the stage of preparing the project documentation. And it cannot do even the finest computational procedures.

The use of the observation method during construction will allow the quality of construction projects to be improved. To a certain extent, take into account the behavior of each part of the construction in specific cases. Indeed, the behavior of the construction structure after completion as a whole is decisive. It is therefore necessary to pay increased attention to the monitoring proposal. However, in order to be able to proceed with the design of the observation method during construction, it is necessary to accept a certain acceptable risk during the design.

### 8.2 Procedure of Construction

Another important part of static assessments is, of course, the stage of construction—the construction process, which in most cases is determined by the contractor himself. In this section, all stages of earthworks and building construction should be modeled as they will be carried out on site.

The problem is whether or not to consider this part of the assessment or to simplify it in the calculation model. At that time, complications also occur in simpler constructions, when this fact is neglected most often. It is not a complete rarity when the

proposed abutment walls in the landslide area are also modeled in the 15 stages, only to ensure stability at each stage of construction.

### 8.3 *Geotechnics is no Science*

Geotechnics is no science. This argument we often encounter in practice is very erroneous. Geotechnical constructions account for about 5–10% of all costs on the financial side of the construction site. For civil engineering, it is 30%, and for water constructions, the share of geotechnics is up to 50% of the total cost of the construction work. The largest share of these buildings is of course underground, where the share of geotechnics represents up to 95% of all costs. Based on these statistics, it is clear that the impact of geotechnics is significant for all types of construction and cannot be neglected under normal conditions.

## 9 Conclusion

Slope movements are events man does not encounter every day, but it should be noted that this happens, and it happens more often. These movements are influenced only by two factors, namely nature and humans themselves.

In complex geological conditions, it is mainly about understanding the overall geological environment with the development and effective design of geotechnical structures designed to ensure long-term stability. The term effective design is meant a set of geotechnical construction, which complement each other, so that their final effect has the desired influence. Therefore, the calculation is conditional on precisely the construction process and the time dependency. This is the primary input that geotechnical engineers should identify at the beginning of the design work. This procedure is unalterable and all other work has to come from it. Based on this, it is then possible to simply involve individual suppliers in the building process and effectively manage the overall process.

## References


1. Boehm BW (1991) Software risk management: principles and practices, USA IEEE 0–8186–3342–5/93
2. Frankovská J, Durmeková T (2011) Specific features of weak rock laboratory testing. In 15th European conference on soil mechanics and geotechnical engineering: Proceedings. Geotechnics of hard soils—weak rocks. Athens, Amsterdam : IOS Press, 2011. ISBN 978–1–60750–800–7, pp 337–342
3. Frankovská J, Kopecký M, Turček P (2014) The correlation of surface area with hydraulic conductivity of fine-grained soils. In SGEM 2014. GeoConference on science and technologies



- in geology, exploration and mining: conference proceedings. Sofia : STEF 92 Technology, ISSN 1314–2704. ISBN 978–619–7105–08–7, pp 893–900
4. Frankovská J, Kopecký M, Panuška J, Chalmovský J (2015) Numerical modelling of slope instability. In *Procedia earth and planetary science: world multidisciplinary earth sciences symposium, WMESS 2015*. Praha, ČR, 7. - 11. 9. 2015. 15:309–314
  5. Zhussupbekov A, Frankovská J, Stacho J, Al-Mhaidib AI, Doubrovsky M, Uranhayev, N, Yerzhanov S, Morev I (2015) Geotechnical and construction considerations of pile foundations in problematical soils. In *Japanese geotechnical society special publication [elektronický zdroj]*. 2(79), online, s. 2704–2709. ISSN 2188–8027

# Inverse Analysis of a Failed Highway Embankment Slope in North Texas



Burak Boluk , Sayantan Chakraborty , Anand J. Puppala ,  
and Navid H. Jafari 

**Abstract** Expansive clayey soils undergo significant volumetric changes, and desiccation cracks develop due to wetting and drying cycles. The presence of desiccation cracks changes the soil's hydro-mechanical properties and allows rapid infiltration of rainwater to the underlying deeper layers. The abrupt increase in moisture content and swelling reduces the soil's peak strength to fully softened strength. Consequently, these slopes experience shallow failures that are approximately parallel to the slope surface. The purpose of this study is to assess the impact of weathering cycles by studying the failed highway embankment slope located in Denison, Texas. The experimental laboratory studies, including direct shear test, fully softened strength test, soil water characteristic curve, and soil hydraulic conductivity tests, were conducted on samples that were collected from scarp of the failed slope. A comprehensive inverse analysis was conducted using a finite element method-based software package. The analyzed results suggest that the surficial slope failure was attributed to (i) the formation of desiccation cracks, (ii) increase in soil permeability, (iii) reduction in shear strength, and (iv) the formation of the perched water table in the weathered surficial soil during intense rainfall events.

**Keywords** Fully softened strength · Wetting and drying cycles · Slope stability · Shallow slope failure

---

B. Boluk (✉)

University of Texas At Arlington, Arlington, TX 76019, USA

e-mail: [burak.boluk@mavs.uta.edu](mailto:burak.boluk@mavs.uta.edu)

S. Chakraborty

Birla Institute of Technology and Science Pilani, Pilani, Rajasthan 333031, India

e-mail: [sayantan.chakraborty@pilani.bits-pilani.ac.in](mailto:sayantan.chakraborty@pilani.bits-pilani.ac.in)

A. J. Puppala

Texas A&M University, College Station, TX 77843, USA

e-mail: [anandp@tamu.edu](mailto:anandp@tamu.edu)

N. H. Jafari

Louisiana State University, Baton Rouge, LA 70803, USA

e-mail: [njafari@lsu.edu](mailto:njafari@lsu.edu)

## 1 Introduction and Background

Expansive clayey soils are commonly present in many arid and semi-arid areas of the USA, and several highway embankment slopes are built with highly expansive clays [1, 2]. These highway embankments are in marginal condition since seasonal weathering activities, particularly wetting–drying cycles, have detrimental effects on hydro-mechanical properties of clayey soils [3–6]. Expansive clayey soils experience a significant amount of swelling due to exposure of moisture at near-surface layers from rainfall [7]. Whereas, in the drought season, the same soil tends to shrink, and its volume decreases significantly [8]. At times, extended weathering activity results in several shallow highway embankment slope failures, which constrain mobility services and require high maintenance and expensive rehabilitation measures [9].

The recurring weathering cycles result in surficial desiccation cracks in clayey soil, and these cracks directly influence the soil hydraulic properties [10]. Benson [11] concluded that the permeability value of clayey soil liners might increase around 1000 times after the first three wetting and drying cycles due to the high shrinkage potential. Similarly, Daniel [12] pointed out that the hydraulic conductivity value of clay liner in the field generally increases one to four orders in magnitude after construction. Boynton and Daniel [4] studied the effect of confining stress on the permeability of the clayey soil after the development of desiccation cracks and reported that the permeability value increases significantly up to 30 kPa (627 psf) of confining stress, which can be present at shallow depths.

Wetting and drying cycles result in irreversible changes and damage soil integrity. As a result of irreversible volumetric changes, desiccation crack patterns promote rapid moisture intrusion in the near-surface layers of embankments. Since the moisture content of the clayey soil increases easily, the cracked clayey soil swells, and soil shear strength reduces from peak to fully softened strength (FSS). FSS is defined as the peak strength of normally consolidated clay [13]. By conducting back analyses on failed embankment slopes, Skempton [14] concluded that the development of fissures in clayey soil reduces the peak shear strength to FSS. Kayyal and Wright [(3)] found a similarity between the shear strength of newly compacted clayey soil exposed to wetting and drying cycles and the peak strength of normally consolidated clayey soils. The initial factor of safety (FOS) of the critical slip surface calculations, using peak shear strength of the clayey soil, is generally above one. However, over time, shallow slope failures of 1.2 to 2.4 m (4 to 8 ft) depth occur due to softening behavior [15–17].

The primary purpose of this study is to investigate the probable reason(s) behind the failure of a highway embankment slope located in Denison, Texas, by conducting comprehensive inverse analyses. The peak shear strength parameters of the embankment soil were determined using direct shear (DS) tests and were used to assess the stability of the slope after construction. Whereas FSS parameters were estimated using the Bromhead torsional ring shear (TRS) equipment to study the stability of the embankment slope after exposure to extensive wetting and drying weathering cycles. Soil water characteristic curve (SWCC) was determined in the laboratory,

and the unsaturated hydraulic conductivity of clayey soil was predicted by using van Genuchten's SWCC function [18]. The changes in shear strength parameters and unsaturated hydraulic conductivity properties estimated from laboratory tests were used to perform an inverse climate-coupled slope stability analysis using the commercially available SEEP/W and Slope/W software packages.

## 2 Site Details

The failed embankment slope is located along U.S 75 Frontage Road in Denison, Texas. Before the failure, the slope was having a height of 11.58 m (38 ft) with 3H:1 V slope ratio. While the exact slope failure date is not known, the Texas Department of Transportation (TxDOT) engineers noticed that the slope started to experience several desiccation cracks from 2014, and no major failure was observed until December 2015. However, the road is closed since 2016 as the cracks caused several surficial slope failures and also damaged the pavement structure. In 2018, the length of failure affected zone was 18.3 m (60 ft), and one lane of the road experienced major damage. However, in 2019, due to the effect of continuous weathering cycles, the length of failure affected zone increased to 134.7 m (442 ft), and both lanes of the road were affected by the slope failure (Fig. 1). The soil samples for laboratory testing were collected from the failure scarp after discarding approximately 30 cm (1 foot) of topsoil to avoid the presence of vegetation, fertilizers, and aggregate material from the failed pavement structure. The collected soil samples were stored in sealed buckets



**Fig. 1** Condition of slope in June 2019

and transferred to the laboratory to determine the hydro-mechanical properties of the soil. The details of the experimental program are elucidated in the next section.

### 3 Experimental Studies

#### 3.1 Soil Characterization Tests

Soil characterization tests were conducted as per ASTM and TxDOT standard procedures to determine the basic soil properties. Wet sieve analyses and hydrometer tests were conducted on samples to determine the soil grain size distribution following the ASTM D 422–63 procedure. Plastic and liquid limits were measured in accordance with ASTM D4318. Standard proctor compaction tests were conducted as per ASTM D698-12. One-dimensional (1D) free swell tests and 1D linear shrinkage tests were conducted in accordance with ASTM D 4546–14 and Tex-107-E, respectively.

#### 3.2 Soil Shear Strength Tests

Soil strength parameters are important to understand the reason for slope failure. Newly compacted clayey soil generally imparts enough shear strength, resulting in high FOS of the critical slip surface. However, in the long term, a significant number of wetting and drying cycles detrimentally impacts the clayey soils' hydro-mechanical properties, ultimately reducing the FOS of the critical slip surface to unity. In this study, several inverse analyses were performed using the soil strength parameters, which were obtained from DS and TRS tests.

**Direct Shear Tests.** The shear strength parameters obtained from the DS test represent the initial soil strength before exposure to wetting and drying cycles. DS tests were conducted as per ASTM D3080 using the DS testing equipment shown in Fig. 2a. Cylindrical specimens of 63.5 mm (2.5 in) in diameter and 25.4 mm (1 in) thickness were prepared at the optimum moisture content (OMC) of 19.5% and maximum dry density (MDD) of 16.8 kN/m<sup>3</sup> (107 pcf) as per standard proctor compaction test results (Fig. 2b). The DS test specimens were sheared at normal stresses of 50, 100, and 150 kPa (1044, 2089, and 3133 psf). A slow shearing rate of  $4.4 \times 10^{-3}$  mm/min ( $1.73 \times 10^{-4}$  in/min) was used to simulate a drained condition by allowing sufficient time to dissipate the excess pore water pressure that might have developed during the shearing.

**Torsional Ring Shear Tests.** TRS tests were conducted to estimate the shear strength parameters of a specimen that was exposed to a significant number of wet-dry cycles (FSS parameters). Tests were conducted using the modified Bromhead TRS device as per ASTM D7608-10 (Fig. 3a). The dry soil was mixed with water to attain a moisture content equal to 1.5 times of liquid limit (LL) of soil. The soil slurry

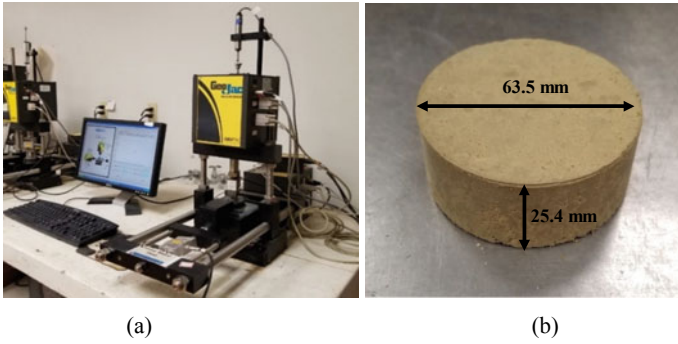


Fig. 2 a DS test apparatus and b DS test specimen

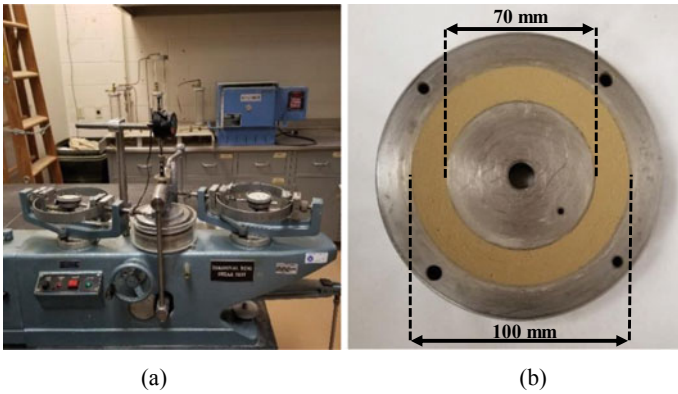


Fig. 3 a Modified Bromhead ring shear test apparatus and b annular ring shear mold

was placed in an annular ring shear mold that has an inside diameter of 70 mm (2.75 in) and an outside diameter of 100 mm (4 in) (Fig. 3b). TRS tests were conducted at the same normal stress levels that were used for the DS test with the shearing rate of 0.018 mm/min ( $7.1 \times 10^{-4}$  in/min).

### 3.3 Unsaturated Soil Properties

Highway embankments are generally present in unsaturated conditions. During rainfall events, the soil suction level and development of pore water pressure are controlled by the unsaturated hydraulic conductivity parameters of the soil. Therefore, the hydraulic properties of the unsaturated soil are important parameters that are required for performing a rainfall-induced slope stability analysis.

SWCC provides information on the variation of volumetric water content at different suction levels. As the unsaturated soil permeability is a function of the degree of saturation, the unsaturated permeability can be indirectly estimated using the SWCC. In the literature, numerous empirical models are defined to estimate the unsaturated permeability of soil [19]. These models generally require saturated permeability value and SWCC best-fitting curve parameters. Therefore, the saturated permeability value of soil was determined using the modified triaxial device, and its details are provided in Bhaskar et al. [20]. The drying path of SWCC was determined using Tempe cell for suction values of 0 to 500 kPa (0 to 10.44 ksf), and dew point potentiometer for suction values ranging from 500 to 120,000 kPa (10.44 to 2,506 ksf). The determined SWCC was fitted using the van Genuchten [18] function to identify the best-fitting parameters.

## 4 Numerical Model Studies

In this study, the impact of weathering cycles on the stability of highway slope was studied using SEEP/W and Slope/W software. Transient seepage analyses were conducted by using SEEP/W software to determine the changes in the pore water pressures during rainfall events. The obtained pore water pressure distributions were transferred to SLOPE/W to determine the FOS of the critical slip surface of the embankment slope.

Several inverse analyses were conducted to identify the cause of slope failure. The numerical analysis model was built according to the geometric configurations provided by TxDOT (Fig. 4). As the slope failure was measured at 2.1 m (7 ft) depth from the slope surface, the analysis was performed by dividing the numerical model into two layers, surface layer, and deep layer. The surface layer was defined as a 2.1 m (7 ft) thick surficial layer, where the soil experienced degradation in hydro-mechanical properties due to weathering cycles. The deep layer starts beneath the

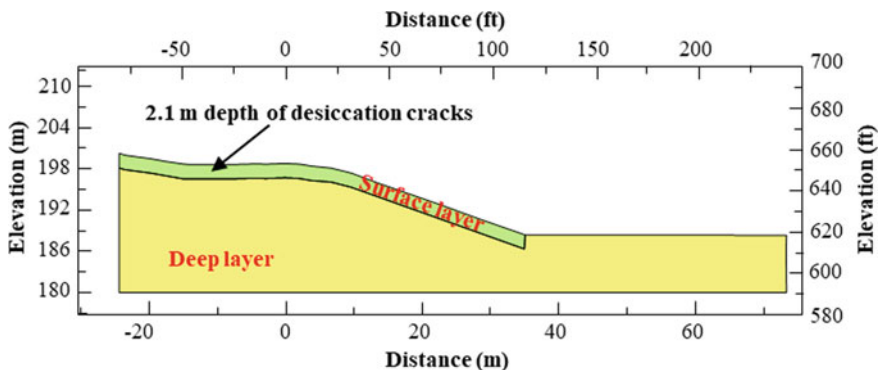


Fig. 4 Numerical analysis model of the slope



surface layer and represents the soil layers that were not affected by wetting and drying cycles.

The slope stability was investigated for two different scenarios: (1) Case 1, portrays the initial condition in which there are no desiccation cracks, and (2) Case 2 shows long-term conditions in which there are desiccation cracks in the surface layer due to weathering cycles. Case 1 analysis was conducted after assigning soil peak shear strength and newly compacted condition of soil hydraulic conductivity value into all the regions of the slope model. Case 2 analysis was conducted using the degraded hydro-mechanical properties in the surface layer. The soil strength was decreased to FSS parameters, and permeability value was increased by 10,000 times, to simulate the presence of desiccation cracks, in accordance with existing literature [12].

In rainfall-induced slope stability analyses, the initial suction level of the slope controls the unsaturated soil properties. During preliminary site investigations, no water table was observed until a depth of 15.7 m (51.5 ft) (up to an elevation of 179.9 m) from the ground surface. Therefore, analyses were conducted assigning the water table at an elevation of 179.9 m. The numerical analyses were conducted by limiting the maximum suction level at 50 kPa (1044 psf) to prevent overestimation of suction-induced soil shear strength [21]. The effect of an increase in the soil shear strength with respect to soil matric suction was incorporated in the analysis using the internal friction angle due to soil matric suction ( $\phi^b$  angle). The  $\phi^b$  value was assumed to be  $15^\circ$  based on the soil air entry value, in accordance with existing literature [22]. After defining the probable entry and exit points of trial slip surfaces, the stability analyses were performed using the Morgenstern-Price method.

Since the exact failure date was not known, rainfall-induced analyses were conducted using rainfall frequency estimates provided by National Oceanic and Atmospheric Administration (NOAA) [23]. The stability of slope was evaluated for two different rainfall durations, a short-duration rainfall of 1 day and a long-duration rainfall of 10 days. As the hourly rainfall variation data is not available, a total amount of 15.77 cm (6.21 in) rainfall was continuously applied to slope model in 1 day with a constant rainfall intensity of  $1.83 \times 10^{-4}$  cm/sec ( $7.19 \times 10^{-5}$  in/sec), to simulate a short-duration rainfall event. For the long-duration rainfall, a total amount of 25.65 cm (10.10 in) rainfall was applied in ten days with a constant rainfall intensity of  $4.43 \times 10^{-5}$  cm/sec ( $1.17 \times 10^{-5}$  in/sec).

## 5 Results and Discussions

### 5.1 Soil Characterization Test Results

The basic soil characterization test results are tabulated in Table 1. Based on the grain size distribution and LL and PI, the soil is classified as a high plasticity clay (CH) using the USCS classification chart. The soil exhibited a high value of 1D



**Table 1** Summary of soil characterization test results

Property	
Clay fraction, CF (%)	55
Liquid limit, LL (%)	58
Plastic limit, PL (%)	37
Plasticity index, PI (%)	21
USCS classification	CH
Optimum moisture content, OMC (%)	19.5
Maximum dry unit weight at optimum moisture content (kN/m <sup>3</sup> /pcf)	16.8 /107
1D free swell strain (%)	7.2
1D linear shrinkage strain (%)	17.7

swelling and shrinkage strains of 7.2% and 17.7%, respectively. The severe swelling and shrinkage strain results are consistent with a high PI value of 21% and a clay fraction (CF) of 55%. The basic characterization test results indicate that the soil is susceptible to degradation in hydro-mechanical properties when exposed to wetting and drying cycles.

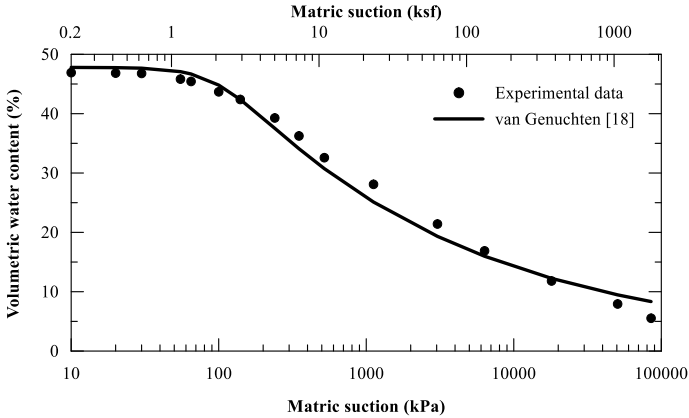
### Soil Shear Strength Test Results.

The soil strength test results showed that the soil specimens experienced a decrease in effective cohesion value from 13.2 kPa (276 psf) to 1.28 kPa (26.8 psf) due to softening behavior. The soil friction angle remained practically the same, with a minor decrease from 23.7° to 23.4°. The soil strength test results are consistent with those observed by previous researchers [24]. These results are supporting evidence that indicates the chances of slope stability issues when exposed to wetting and drying cycles. The drastic reduction in soil cohesion values causes a decrease in shear strength of the surficial soil layers. Therefore, in the long term, the soil shear strength is only contributed by the soil friction angle.

## 5.2 Unsaturated Soil Test Results

The experimental result of the drying path of SWCC is shown in Fig. 5. The experimental data points were fitted with van Genuchten [18] function and the best fitting parameters are presented in Table 2.

The SWCC results indicate that the soil has an  $\alpha$  value of 0.01 kPa<sup>-1</sup>, which can be attributed to the high CF of soil. Soil saturated permeability test showed that soil has a low value of hydraulic conductivity of  $2.68 \times 10^{-10}$  m/s ( $8.8 \times 10^{-10}$  ft/s). This low permeability value also can be attributed to the high fines content of the soil, which fills the voids and results in a low hydraulic conductivity value.



**Fig. 5** Drying path of SWCC of soil

**Table 2** SWCC model parameters

van Genuchten [18] best fitting parameters		
$\alpha$ (kPa <sup>-1</sup> )	$n$	$m$
0.01	2.89	0.095

### 5.3 Numerical Analyses Results

Rainfall-induced slope stability analyses were conducted to illustrate the impacts of weathering cycles on the stability of the embankment slope. Table 3 shows the calculated FOS of the critical slip surface of the embankment slope.

In the newly compacted condition, Case 1, there was no significant amount of moisture intrusion for all the rainfall events. Figure 6 shows the pore water pressure in the middle of the slope between elevations of 195.4 m to 191 m (641 ft to 626 ft) after 15.77 cm (6.21 in) of rainfall in 1 day.

The moisture fluctuation was obtained only within a depth of 3.6 m (11.8 ft) below the surface of the slope (between elevations of 195.4 to 191.8 m). The critical slip surface of the slope had sufficient FOS (minimum 2.84) for all the rainfall amounts. The high FOS value can be attributed to the sufficient post-construction shear strength of the soil, coupled with a low permeability value that prevented rapid moisture intrusion into the deeper layers. Consequently, the presence of a considerable amount

**Table 3** Calculated FOS of the critical slip surface

Total rainfall		
Case #	15.77 cm (6.21 inches)	25.65 cm (10.10 inches)
Case 1	2.84	2.84
Case 2	1.86	0.86

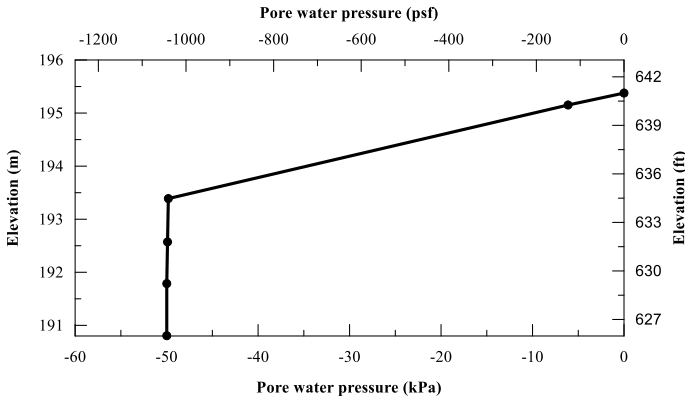


Fig. 6 Pore water pressure diagram for Case 1 after 15.77 cm (6.21 in) rainfall

of negative pore water pressure (soil matric suction) contributed towards the stability of the slope.

In the long term, Case 2, after a total of 25.65 cm (10.10 in) rainfall in 10 days, FOS of the critical slip surface showed a drastic decrease to 0.86. The presence of desiccation cracks in the surficial layer allowed rapid moisture infiltration into the slope, resulting in the accumulation of rainfall water in the surficial layer due to the presence of an underlying layer with low permeability value of  $2.68 \times 10^{-10}$  m/s ( $8.8 \times 10^{-10}$  ft/s). A perched water table was observed to develop in the surficial layer within a depth of 2.4 m (7.9 ft) from the surface (Fig. 7). This development of positive pore water pressure decreased the soil’s effective strength, and slope experienced shallow failure.

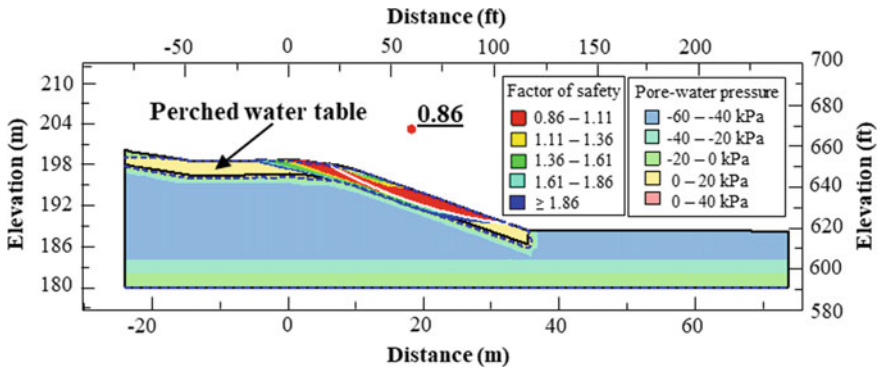


Fig. 7 Calculated FOS of the critical slip surface after 25.65 cm rainfall for Case 2

## 6 Summary and Conclusions

This study focused on investigating the reason behind the failure of a highway embankment slope located in Denison, Texas. Extensive laboratory tests were conducted on the soil collected from the failed embankment site. Rainfall-induced slope stability analyses were performed for different rainfall events, and its effect on the stability of the slope was studied. The analyzed result suggests that the shallow slope failure was attributed to the following reasons.

- Soil samples experienced high swelling and shrinkage strains of 7.2% and 17.7%, respectively. These high amounts of volumetric changes indicate the susceptibility of soil to wetting and drying cycles. Due to the exposure to weathering cycles, the surficial embankment soil lost its integrity and experienced desiccation cracking.
- The development of desiccation cracks in the surficial layer caused the abrupt moisture intrusion into the embankment slope during rainfall events.
- After experiencing wetting and drying cycles, the effective cohesion value of the soil showed a significant decrease from 13.2 kPa (276 psf) to 1.28 kPa (26.8 psf) while the friction angle showed a minor decrease from 23.7° to 23.4°. The reduction in cohesive force resulted in a decrease in the shear strength of the surficial soil layer and was detrimental to the stability of the slope.
- The degraded hydro-mechanical soil properties in the surficial layer, along with the development of positive pore water pressure during an intense rainfall event, led to a significant decrease in effective soil strength and probably resulted in the failure of the slope.

## References

1. Puppala AJ, Manosuthikij T, Chittoori BCS (2013) Swell and shrinkage characterizations of unsaturated expansive clays from Texas. *Eng Geol* 164:187–194
2. Das JT, Banerjee A, Puppala AJ, Chakraborty S (2019) Sustainability and resilience in pavement infrastructure: a unified assessment framework. *Environ Geotech* 1–13. <https://doi.org/10.1680/jenge.19.00035>
3. Kayyal MK, Wright SG (1991) Investigation of long-term strength properties of Paris and Beaumont Clays in Earth Embankments. Final report, No. FHWA/TX-92+ 1195–2F
4. Boynton SS, Daniel DE (1985) Hydraulic conductivity tests on compacted clay. *J Geotech Eng* 111(4):465–478. [https://doi.org/10.1061/\(ASCE\)0733-9410\(1985\)111:4\(465\)](https://doi.org/10.1061/(ASCE)0733-9410(1985)111:4(465))
5. Jafari N, Puppala A, Chakraborty S, Boluk B (2019) Integrated full-scale physical experiments and numerical modeling of the performance and rehabilitation of highway embankments. Final report, No. 18GTLSU06
6. Bhaskar P, Boluk B, Mosadegh L, Banerjee A, Puppala AJ (2020) Effect of fines on hysteretic hydraulic conductivity of unsaturated soil. In *Geo-Congress 2020: geo-systems, sustainability, geoenvironmental engineering, and unsaturated soil mechanics*. Reston, VA, American Society of Civil Engineers, pp 330–339. <https://doi.org/10.1061/9780784482827.037>
7. Chakraborty S, Nair S (2018) Impact of different hydrated cementitious phases on moisture-induced damage in lime-stabilised subgrade soils. *Road Mater Pavement Des* 19(6):1389–1405. <https://doi.org/10.1080/14680629.2017.1314222>

8. Wang M, Kong L, Zhao C, Zang M (2012) Dynamic characteristics of lime-treated expansive soil under cyclic loading. *J Rock Mech Geotech Eng* 4(4):352–359. <https://doi.org/10.3724/SP.J.1235.2012.00352>
9. George AM, Chakraborty S, Das JT, Pedarla A, Puppala AJ (2018) Understanding shallow slope failures on expansive soil embankments in north Texas Using unsaturated soil property framework. *PanAm Unsaturated Soils* 2017:206–216. <https://doi.org/10.1061/9780784481691.021>
10. Chertkov VY (2000) Using surface crack spacing to predict crack network geometry in swelling soils. *Soil Sci Soc Am J* 64(6):1918–1921. <https://doi.org/10.2136/sssaj2000.6461918x>
11. Albrecht BA, Benson CH (2001) Effect of desiccation on compacted natural clays. *J Geotech Geoenviron Eng* 127(1):67–75. [https://doi.org/10.1061/\(ASCE\)1090-0241\(2001\)127:1\(67\)](https://doi.org/10.1061/(ASCE)1090-0241(2001)127:1(67))
12. Daniel DE (1984) Predicting hydraulic conductivity of clay liners. *J Geotech Eng* 110(2):285–300. [https://doi.org/10.1061/\(ASCE\)0733-9410\(1984\)110:2\(285\)](https://doi.org/10.1061/(ASCE)0733-9410(1984)110:2(285))
13. Skempton AW (1970) First-time slides in overconsolidated clays. *Geotechnique* 20(3):320–324
14. Skempton AW (1984) Slope stability of cuttings in brown London clay. *Selected Papers on Soil Mechanics*. Thomas Telford Publishing, pp 241–250
15. Gamez JA, Stark TD (2014) Fully softened shear strength at low stresses for levee and embankment design. *J Geotech Geoenviron Eng* 140(9):06014010. [https://doi.org/10.1061/\(ASCE\)GT.1943-5606.0001151](https://doi.org/10.1061/(ASCE)GT.1943-5606.0001151)
16. Fleming RL, Sills GL, Steward ES (1992) Lime stabilization of levee slopes. In *Proceedings second interagency symposium on stabilization of soils and other materials*, metairie, LA
17. Jafari NH, Puppala A, Boluk B, Cadigan JA, Chakraborty S, Bheemasetti T, Pleasant JE (2019) Predicting the performance of highway embankment slopes. *MATEC Web Conf* 271:02007. <https://doi.org/10.1051/mateconf/201927102007>
18. van Genuchten MT (1980) A closed-form equation for predicting the hydraulic conductivity of unsaturated soils I. *Soil Sci Soc Am J* 44(5):892. <https://doi.org/10.2136/sssaj1980.03615995004400050002x>
19. Mualem Y (1976) A new model for predicting the hydraulic conductivity of unsaturated porous media. *Water Resour Res* 12(3):513–522. <https://doi.org/10.1029/WR012i003p00513>
20. Bhaskar P, Boluk B, Banerjee A, Shafikhani A, Puppala A (2019) Effect of lime stabilization on the unsaturated hydraulic conductivity of clayey soil in Texas. In *Geo-Congress 2019: geotechnical materials, modeling, and testing*, Reston, VA, American Society of Civil Engineers, pp 773–783. <https://doi.org/10.1061/9780784482124.078>
21. Lee LM, Gofar N, Rahardjo H (2009) A simple model for preliminary evaluation of rainfall-induced slope instability. *Eng Geol* 108(3–4):272–285. <https://doi.org/10.1016/j.enggeo.2009.06.011>
22. Zhang F, Fredlund DG (2015) Examination of the estimation of relative permeability for unsaturated soils. *Can Geotech J* 52(12):2077–2087. <https://doi.org/10.1139/cgj-2015-0043>
23. Perica S, Pavlovic S, Laurent MS, Trypaluk C, Unruh D, Martin D, Wilhite O (2018) NOAA Atlas 14: precipitation frequency atlas of the United States 11 (2). Maryland
24. Skempton AW (1970) First-time slides in over-consolidated clays. *Géotechnique* 20(3):320–324. <https://doi.org/10.1680/geot.1970.20.3.320>

# Investigating the Effect of Direction of Grass Roots on Shear Strength of Soil and Stability of Embankment Slope



Jakob Schallberger and Lalita Oka 

**Abstract** The use of grass to protect the slopes from erosion of road embankments is a common practice. However, quantifying the changes in shear strength of such bio-structured (with grass roots) soil is a complex procedure. One of the important factors affecting the shearing resistance of such soils is the direction of grass roots with respect to the slope angle. An experimental investigation was taken up to quantify the changes in shear strength of soil due to the direction of grass roots. Direct shear tests were conducted on field samples from a slope with grass roots and compared with remolded samples without roots. The field samples were obtained by pushing the samplers in a sloping ground in vertical, horizontal, and in 45 ° inclination. Direct shear tests were conducted on these samples by keeping the direction of the roots in perpendicular, parallel, and inclined to the failure plane during the direct shear test. Thirty-five samples were tested with in-situ moisture content, and fifteen samples were tested in saturated conditions. For the samples tested with in-situ moisture conditions, the test results indicate that the soil with the vertical and inclined root direction experienced a similar overall increase in cohesion and a near negligible change in friction angle. However, the samples with roots parallel to the failure plane experienced the least increase in cohesion in comparison with the other two root directions. A similar trend was observed for the samples tested in saturated conditions. Additionally, slope stability analysis was performed using software SLIDE (version 7) to determine the effects of the root direction on the factor of safety.

**Keywords** Slope stability · Grass roots · Shear strength

## 1 Introduction and Background

Maintaining the stability of embankments is one of the important concerns of all road transportation and infrastructure development projects. Road embankments

---

J. Schallberger · L. Oka (✉)  
California State University, 2320 E San Ramon Ave, Fresno, CA 93740, USA  
e-mail: [loka@csufresno.edu](mailto:loka@csufresno.edu)

and retaining walls are typically constructed using granular soils to avoid excessive buildup of pore pressure. However, these soils lack cohesive properties and are susceptible to slope failure. Improving the shear strength of such cohesionless soils is, therefore, a big challenge. While geotextiles are widely used to protect and strengthen the slopes, they are sometimes cost-prohibitive and require regular maintenance. These considerations are especially important for roads located in remote regions. Using plant roots or grass roots to stabilize the slopes is one of the cost-effective solutions. However, predicting the response of such root-reinforced soils is challenging, mostly due to the unknown soil behavioral model. Multiple studies in the past have reported that root-reinforced sandy soils have higher shear strength in comparison with sands without roots (Cazzuffi et al. [1], Comino, and Druetta [2], Eab et al. [3], Fan and Su [4]). Several factors, e.g., root diameter, root tensile strength, and planting density, were found to affect the shear strength of root-reinforced soils (Loades et al. [5]). Effect of Vetiver grass roots on shear strength parameters have been extensively studied by many researchers (e.g., Eab et al. [3], Xu et al. [6], Hamidifar et al. [7]). These researchers have shown a clear evidence of improvement in shear strength and thus improved sliding resistance capacity. While most of these studies were conducted using direct shear tests, it has a major disadvantage of forcing the sample to shear in a horizontal direction. Thus, the direction of the roots with respect to the shearing plane can affect the results. Unfortunately, the problem is further compounded since the existing standardized testing procedure for the direct shear test, ASTM-D-3080 [8], does not include information on the testing procedure for root-reinforced soils. Therefore, this investigation was prompted by the need for more research on the effect of root direction on the shear strength of root-reinforced soils. The soil specimens were obtained from a grass root-reinforced slope by pushing samplers in three directions (vertical, horizontal, and inclined to the slope) to capture the effect of root direction, and direct shear tests were conducted in the laboratory. This paper describes the sampling method and results from the tests. A sample slope stability analysis using software SLIDE (version-7) is also presented.

Use of root-reinforced soil to improve slope stability has been in practice since the thirteenth century (Cazzuffi et al. [1]), but the geotechnical testing of such soils was introduced by the researchers Endo and Tsuruta [9], and Wu et al. [10] in the late twentieth century. Wu et al. [10] and Waldron and Dakessian [11] were among the early researchers to propose the use of Mohr–Coulomb model to estimate the shear strength of root-reinforced soil, and it is still in practice. Recently, some studies (e.g., Cazzuffi et al. [12]) have focused on evaluating the effect of grass species, and soil types and some (e.g., Ji et al. [13], Zhou et al. [14]) have investigated the effects of large root system such as tree roots on the shear strength of the soil.

While there are instances of using triaxial test to measure the shear strength of root-reinforced soils (Zhang et al. [15], Mazzuoli et al. [16]), most studies reported in the literature are based on direct shear tests. This is mainly because of ease in sample preparation; and no difference was found in the end results with remolded specimens (Castellanos and Brandon [17]). However, one of the important drawbacks of the direct shear test is that it forces the failure plane to be horizontal. Although Fitz et al. [18] have documented the role of the direction of failure plane on slope

stability, it is rarely considered in the testing of sands since it is very difficult to obtain undisturbed samples in the sand. Hence, there is evidence in the literature that the direction of roots could play an important role in determining the shear strength of root-reinforced soils, and it will ultimately influence slope stability analyses for the road embankments. A study was therefore undertaken to investigate the effect of root orientation on shear strength of sandy soil and the factor of safety estimation for a slope.

## 2 Testing Program

### 2.1 Field Sampling

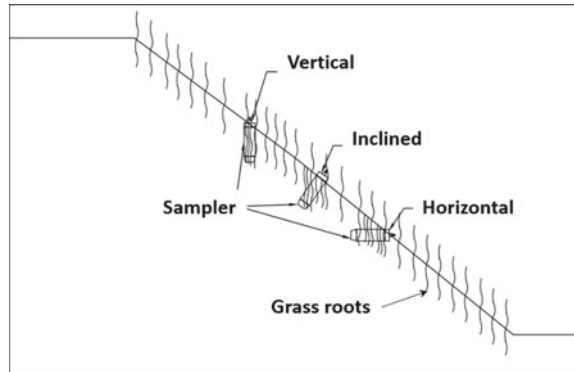
The sampling site was located between the Laton and Riverdale towns in the Fresno County of Central California. Figure 1 shows the details of field measurements and sample collection. The slope profile was determined by staking along the length of slope and measuring the elevations with the help of Zipline Pro-2000 high precision altimeter. A split sampler drive tube consisting of two 6-inch-long samplers was pushed in the sloping ground (covered with grass) with the help of slide hammer. After retrieving the samplers, both ends were covered with plastic caps to retain the moisture content. Additionally, one borehole was drilled to a depth of 35 ft. below the top of the basin for soil profile to be used in the numerical model.



**Fig. 1** Site location and details of field sampling: **a** grass root-reinforced slope, **b** slope length measurement, **c** altimeter, **d** sampling split mold



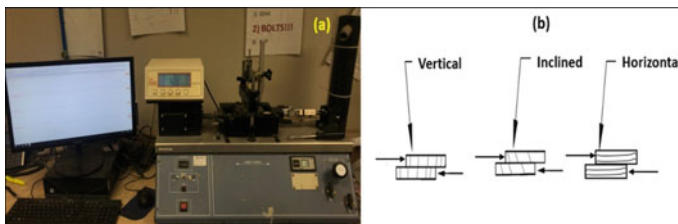
**Fig. 2** Schematic representation of orientation of grass roots during sampling



To overcome the difficulty due to forced horizontal plane during the direct shear test, the soil samples from a natural root-reinforced slope were collected in three directions (vertical, horizontal, and inclined). Figure 2 shows a schematic representation of the orientation of grass roots during sampling. A total of sixty samples were collected from ten locations along the slope consisting of two samples in each direction.

## 2.2 Laboratory Testing

The field samples consisting of root-reinforced soil were brought back to the laboratory. The laboratory testing consisted of measuring unit weight (ASTM-D-7263 [19]), moisture content (ASTM-D-2216 [20]), particle size distribution (ASTM-D-6913 [21]), organic content determination (ASTM-D-2974 [22]), and direct shear tests (ASTM-D-3080 [8]) to measure the shear strength parameters ( $c'$  and  $\phi'$ ). The diameter of each sample was 2.42 inches. A minimum of three direct shear tests with the normal stress increments of 1 ksf, 2 ksf, and 3 ksf were conducted on each directional sample from each sampling location. The rate of shearing was 0.03 inch/min. Figure 3 shows the direct shear test setup and the direction of shearing



**Fig. 3** Direct shear tests: **a** test setup, **b** orientation of grass roots

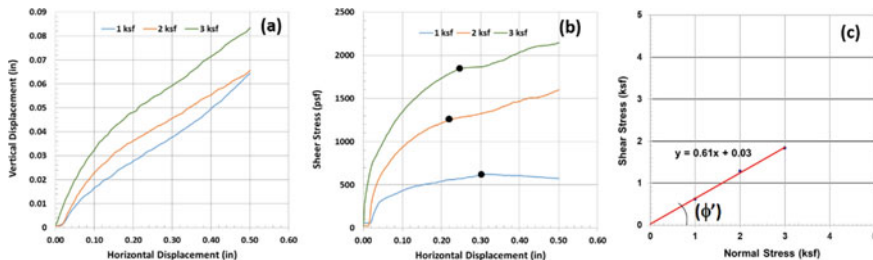
plane with respect to root orientation. A total of 35 samples were tested under in-situ moisture condition, and 25 samples were tested under the saturated condition to capture the effect of saturation on shear strength parameters. Direct shear tests were also conducted on remolded samples without roots with in-situ moisture content and under the saturated condition for comparison.

### 3 Results and Discussions

Table 1 shows the average index properties of the soil, including organic content, which is the ratio of the weight of roots to the weight of soil solids. It is important to note that all the soil samples revealed that the field slope consisted of sandy soil with USCS classification being SP-SM (poorly graded sand with silt). As mentioned earlier, each set of the direct shear test consisted of fixed normal stress increments (1 ksf, 2 ksf and 3 ksf). Figure 4 shows the typical direct shear test data for one set of samples. The combination of peak shear stress ( $\tau_{max}$ ) and corresponding normal

**Table 1** Index properties of the soil

Soil properties	Orientation of roots		
	Vertical	Horizontal	Inclined
Dry unit weight (lb/ft <sup>3</sup> )	99	97.7	99.5
Organic content (%)	0.8	0.7	0.7
Fines content (%)	13.3	11.4	10.9
Plasticity of fines	Non-plastic	Non-plastic	Non-plastic
Soil classification (As per USCS)	SP-SM	SP-SM	SP-SM



**Fig. 4** Typical direct shear test result: **a** vertical displacement versus horizontal displacement, **b** shear stress versus horizontal displacement, **c** mohr–Coulomb failure envelope

stress ( $\sigma$ ) was then selected to develop Mohr–Coulomb failure envelope. The angle of internal friction ( $\phi'$ ) and cohesion ( $c'$ ) was thus estimated for each set of samples.

Figure 5 shows the comparison between the displacement response of the soils with and without grass roots. Inclusion of roots was found to show increased horizontal displacement than soils without roots. Thus, roots were found to make the soil more ductile and thus improved resistance for cracking which typically is a sign of brittleness. Similar behavior is noted by multiples studies (e.g., Comino and Druetta [23]) in the past.

Figure 6 shows the comparison of displacement based on root direction for a typical specimen. It was observed that soils with inclined root orientation experienced more horizontal displacement (ductility) in comparison with horizontal and vertical root orientations. This clearly shows that direction of root influences the deformations that the soil might undergo.

Figure 7 shows shear strength parameters based on the inclusion of grass roots as well as the saturation condition of the test specimens. Figure 7a, c shows that

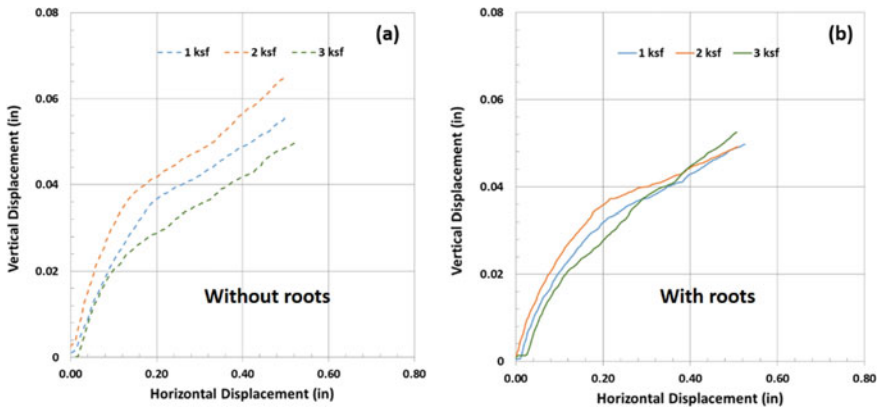


Fig. 5 Comparison of displacements during direct shear tests: **a** for soils without roots, and **b** for soils with roots

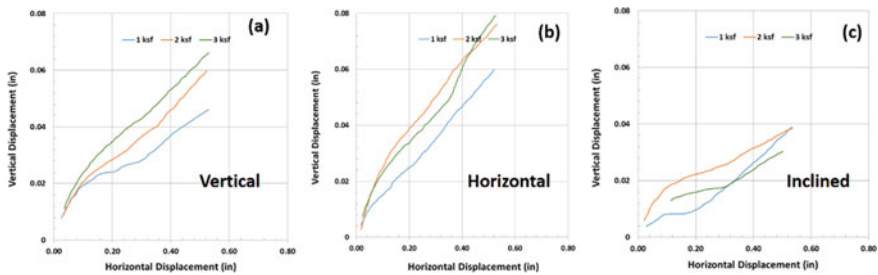
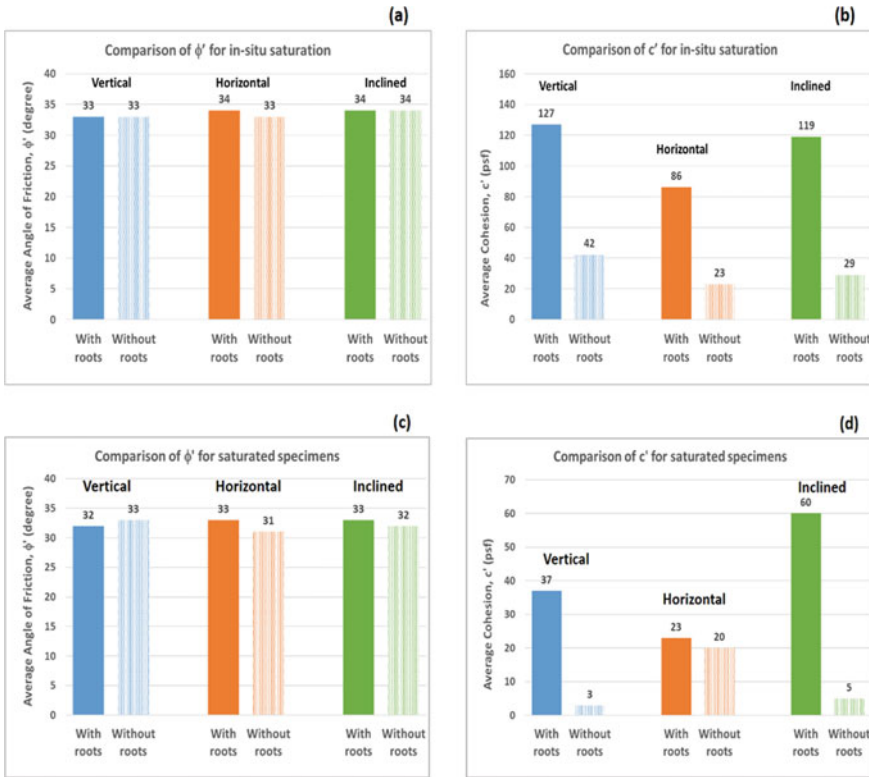


Fig. 6 Comparison of displacements during direct shear tests based on root orientation: **a** for soil with vertical root orientation, **b** for soil with horizontal root orientation, and **c** for soil with inclined root orientation



**Fig. 7** Comparison of shear strength parameters: **a**  $\phi'$  at in-situ saturation, **b**  $c'$  at in-situ saturation, **c**  $\phi'$  at 100% saturation, **d**  $c'$  at 100% saturation

angle of friction ( $\phi'$ ) generally remained unaffected irrespective of changes in root direction or saturation condition, while Fig. 7b and d shows that soils with roots generally experienced increased cohesion in comparison with soil without roots. These findings are similar to the previous studies by Mickovski and Beek [24], and Xu et al. [6]. Additionally, as per Fig. 7b, when tested with in-situ moisture content (partially saturated), soil containing vertical root reinforcement developed the maximum cohesion (127 psf) while soil containing horizontal roots developed the least cohesion (86 psf). On the other hand, Fig. 7d shows that when tested under fully saturated condition, the soil with inclined roots developed the highest (86 psf) cohesion while soil with horizontal roots experienced the least cohesion (23 psf). Figure 7b and d also indicates that cohesion decreased with an increase in saturation. This phenomenon can be attributed to the addition of suction due to the presence of roots. Interestingly, the unsaturated soil specimens with inclined root orientation experienced the highest (310%) increase in cohesion in comparison with unsaturated soils without roots. For the fully saturated samples, the soil specimens with vertical root mobilized the highest (1133%) increase in cohesion in comparison with saturated

soils without roots. Figure 7b and d also indicates that although the specimens with roots in the horizontal direction (parallel to the direction of the shearing plane) did experience an increase in cohesion, their percent increase was least when tested under fully saturated condition. Changes in cohesion are summarized in Table 2.

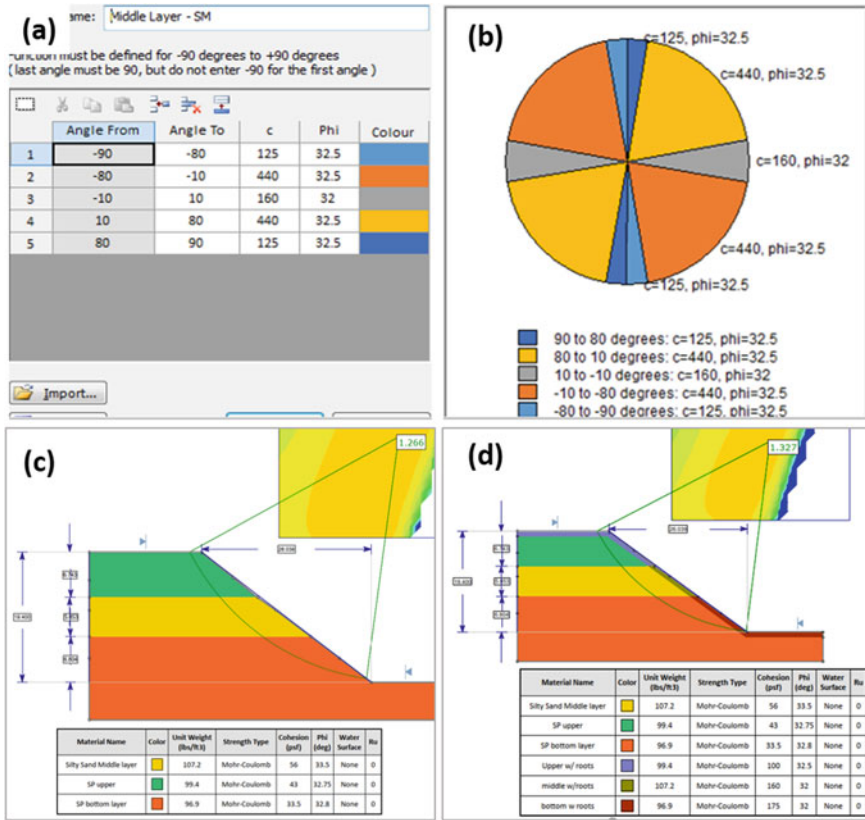
The findings of this study can be effectively applied in slope stability analysis in engineering practice, which consists of determining the factor of safety using the limit equilibrium method. In the case of finite slopes such as road embankments, the factor of safety estimate is based on moment equilibrium of sliding slices or wedges of soil under the slope. Thus, the factor of safety is given by the equation:

$$F_s = \frac{\sum M_R}{\sum M_D} = \frac{\sum c'l_a + \tan \phi' N'}{\sum W \sin \alpha} \quad (1)$$

where  $M_R$  is the resisting moment and  $M_D$  is the driving moment.  $c'$  and  $\phi'$  are the cohesion and angle of internal friction of the soil,  $l_a$  is the length of arc, ( $N' = W \cos \alpha$ ) and ( $W \sin \alpha$ ) are the normal and tangential components of the weight of the sliding wedge of soil, and  $\alpha$  is the radial angle. The critical factor of safety is typically determined iteratively by considering slip surfaces passing through sloping ground. These iterations can easily be performed using any commercially available software. Figure 8 shows computation of the factor of safety using the software, SLIDE (version 7) for slope without grass roots and with grass roots in the vertical direction. The slope profile was constructed using soil properties from this study. The strength parameters of the soil were modeled in the software using the anisotropic function. This function allows the user to input strength parameters depending on how the failure plane passes through the soil with grass roots. The failure plane represents the shear plane in laboratory testing. Therefore, the vertical, horizontal, and inclined directions were all considered in the model for determining factor of safety. Figure 8a and b displays the anisotropic function input parameters. Horizontal, inclined, and vertical sample strength parameters were input from  $0^\circ$  to  $10^\circ$ ,  $10^\circ$  to  $80^\circ$ , and  $80^\circ$  to  $90^\circ$ , respectively. These values are mirrored in the circle for any other failure plane beyond  $0^\circ$  to  $90^\circ$ . Figure 8c and d shows the estimation of factor of safety for slopes with and without grass roots, respectively. Based on the field observations, the roots were assumed to be present only in the top one-foot thick layer. It is, however, entirely possible to have deeper roots depending on species of grass. In this example, the critical factor of safety for slope without grass roots was found to be 1.266, while the critical factor of safety for the slope with grass roots in the vertical direction was found to be 1.327, which is approximately 5% higher than the slope without grass roots. A similar increase in the factor of safety was previously reported by Eab et al. [3], Lin et al. [25], and Liu et al. [26]. Although the numerical model predicted a modest increase in factor of safety, the purpose of this example was to show that numerical tools can easily be applied to predict the behavior of slope with grass roots. By tactically arranging the root reinforcement, practicing geotechnical engineers can easily quantify the differences and recommend slope protection measures.

**Table 2** Summary of changes in cohesion due to root inclusion

	Vertical root orientation			Horizontal root orientation			Inclined root orientation		
	$c'$ With root (psf)	$c'$ Without roots (psf)	Change in $c'$ (%)	$c'$ With root (psf)	$c'$ Without roots (psf)	Change in $c'$ (%)	$c'$ With root (psf)	$c'$ Without roots (psf)	Change in $c'$ (%)
Unsaturated	127	42	202	86	23	274	119	29	310
Saturated	37	3	1133	23	20	15	60	5	1100



**Fig. 8** Slope stability analysis using Slide (version 7): **a** entering anisotropic function, **b** assigning values of anisotropic shear strength parameters, **c** estimating factor of safety for slope without grass roots, and **d** estimating factor of safety for slope with grassroots in the vertical direction

### 4 Conclusions

- An experimental study was undertaken to investigate the effect of root orientation on the shear strength parameters of soil.
- Field samples were collected with vertical, horizontal, and inclined root orientation, which enabled direct shear tests to be performed by keeping root orientation perpendicular, parallel, and inclined to the shearing plane, respectively.
- While root orientation did not affect the angle of internal friction ( $\phi'$ ) of the soils, the development of cohesion ( $c'$ ) was considerably affected by root orientation. The samples with the root orientation perpendicular to the shearing plane were found to mobilize the highest cohesion while root orientation parallel to the shearing plane mobilized the least amount of cohesion.
- Soils with inclined root orientation showed more ductility in comparison with soils consisting of vertical and horizontal root orientations.

- A numerical model incorporating improved soil properties for the surface layer predicted a modest (5%) increase in factor of safety for the vertically root-reinforced slope in comparison with a slope without root reinforcement.

**Acknowledgements** The authors would like to thank BSK Associates, Fresno for their generous support especially with field sampling and laboratory testing. Additionally, the authors would like to thank Mr. Degol Messfin for providing help in conducting laboratory tests. The authors are also thankful to the reviewers for their constructive comments that helped improve the paper.

## References

1. Cazzuffi D, Cardile G, Giofrè D (2014) Geosynthetic engineering and vegetation growth in soil reinforcement applications. *Transp Infrastruct Geotechnol* 1:262–300
2. Comino E, Druetta A (2010) The effect of poaceae roots on the shear strength of soils in the Italian alpine environment. *Soil Tillage Res* 106:194–201
3. Eab KH, Likitlersuang S, Takahashi A (2015) Laboratory and modelling investigation of root-reinforced system for slope stabilisation. *Soils Found* 55:1270–1281
4. Fan C-C, Su C-F (2008) Role of roots in the shear strength of root-reinforced soils with high moisture content. *Ecol Eng* 33:157–166
5. Loades K, Bengough A, Bransby M, Hallett P (2010) Planting density influence on fibrous root reinforcement of soils. *Ecol Eng* 36:276–284
6. Xu L, Gao C, Yan D (2018) Interaction between vetiver grass roots and completely decomposed volcanic tuff under rainfall infiltration conditions. *Geofluids*
7. Hamidifar H, Keshavarzi A, Truong P (2018) Enhancement of river bank shear strength parameters using vetiver grass root system. *Arab J Geosci* 11:611
8. ASTM-D-3080–11 (2011) Standard Test Method for Direct Shear Test of Soils Under Consolidated Drained Conditions, in, ASTM International, PA, pp 1–9
9. Endo T, Tsuruta T (1969) The effect of the tree's roots on the shear strength of soil, Annual Report, 1968, Hokkaido Branch, For. Exp. Stn., Sapporo, Japan, pp 167–182
10. Wu TH, McKinnell WP III, Swanston DN (1979) Strength of tree roots and landslides on Prince of Wales Island Alaska. *Canadian Geotech J* 16:19–33
11. Waldron L, Dakessian S (1981) Soil reinforcement by roots: calculation of increased soil shear resistance from root properties. *Soil Sci* 132:427–435
12. Cazzuffi D, Corneo A, Crippa E (2006) Slope Stabilisation by perennial “gramineae” in Southern Italy: plant growth and temporal performance. *Geotech Geol Eng* 24:429–447
13. Ji J, Kokutse N, Genet M, Fourcaud T, Zhang Z (2012) Effect of spatial variation of tree root characteristics on slope stability. A case study on Black Locust (*Robinia pseudoacacia*) and *Arborvitae* (*Platycladus orientalis*) stands on the Loess Plateau, China, *Catena*, 92:139–154
14. Zhou Y, Watts D, Cheng X, Li Y, Luo H, Xiu Q (1997) The traction effect of lateral roots of *Pinus yunnanensis* on soil reinforcement: a direct in situ test. *Plant Soil* 190:77–86
15. Zhang C-B, Chen L-H, Liu Y-P, Ji X-D, Liu X-P (2010) Triaxial compression test of soil–root composites to evaluate influence of roots on soil shear strength. *Ecol Eng* 36:19–26
16. Mazzuoli M, Bovolenta R, Berardi R (2016) Experimental investigation on the mechanical contribution of roots to the shear strength of a sandy soil. *Procedia Engineering* 158:45–50
17. Castellanos B, Brandon T (2013) A comparison between the shear strength measured with direct shear and triaxial devices on undisturbed and remolded soils. In: *Proceedings of the 18th international conference on soil mechanics and geotechnical engineering, Paris*, pp 317–320
18. Fitz GM, Brandon TL, Duncan JM (1992) Back analysis of olmsted landslide using anisotropic strengths, transportation research record



19. ASTM-D-7263–18 (2018) Standard test methods for laboratory determination of density (Unit Weight) of soil specimens, in, ASTM International, PA
20. ASTM-D-2216–19 (2018) Standard test methods for laboratory determination of water (moisture) content determination of soil and rock by mass, in, ASTM international, PA
21. ASTM-D-6913–14 (2014) Standard test methods for particle-size distribution (gradation) of soils using sieve analysis, in, ASTM International, PA
22. ASTM-D-2974–14 (2014) Standard test methods for moisture, ash, and organic matter of peat and other organic soils, in, ASTM international, PA
23. Comino E, Druetta A (2009) In situ shear tests of soil samples with grass roots in Alpine environment. *Am J Environ Sci* 5:475
24. Mickovski S, Van Beek L (2009) Root morphology and effects on soil reinforcement and slope stability of young vetiver (*Vetiveria zizanioides*) plants grown in semi-arid climate. *Plant Soil* 324:43–56
25. Lin D-G, Huang B-S, Lin S-H (2010) 3-D numerical investigations into the shear strength of the soil–root system of Makino bamboo and its effect on slope stability. *Ecol Eng* 36:992–1006
26. Liu HW, Feng S, Ng CWW (2016) Analytical analysis of hydraulic effect of vegetation on shallow slope stability with different root architectures. *Comput Geotech* 80:115–120

# Runoff Water Management on Karstic Terrain and Stability of Slopes and Foundations in Northern Spain



F. Collazos Arias , J. C. Mas Bahillo, D. Castro-Fresno ,  
J. Rodriguez-Hernandez , E. Blanco-Fernandez , L. Castanon-Jano ,  
D. Garcia-Sanchez , and I. Beltran Hernando

**Abstract** This communication analyzes the latest experiences in slope and foundation drainage and runoff water management to improve resilience in roadway infrastructures. The actions resulted from temporary rain and adverse weather conditions during the months of January and February 2012 and 2013, which caused singular damage to several road slopes in Northern Spain. The objective of the repair was to restore road safety and road stability. Regarding runoff water, heavy rains cause loose and scattered stone movements along the slopes of the La Hermida Gorge and in the limestone rocky massifs that make up the Gorge. There are also many karst caves exiting that load their levels to the fullest and produce impressive waterfalls on the road. The energy of these waterfalls was dissipated, and the water curtain was channeled into the Deva River through an innovative solution. With regard to the drainage of slopes and foundations, the action carried out on the slope of the A-8 motorway includes its stabilization by biological engineering. All the actions presented in this article have proven to be valid throughout the last year of road operation. Furthermore, the monitoring system used in full-scale tests for dynamic barriers according to ETAG-27 is reliable to better understand the force transmission mechanism and also for future design purposes.

**Keywords** Slope · Heavy rain · Stability · Drainage · Foundation · Resilience

---

F. Collazos Arias (✉) · J. C. Mas Bahillo · D. Castro-Fresno · J. Rodriguez-Hernandez ·  
E. Blanco-Fernandez · L. Castanon-Jano  
Department of Transport, Projects and Processes, University of Cantabria, Santander, Spain

D. Garcia-Sanchez · I. Beltran Hernando  
TECNALIA Parque Científico Y Tecnológico de Bizkaia C\Geldo, Edif. 700, 48160 Derio, Spain

# 1 Approach to the Problem

The effect of the storms of February 2012 and 2013 resulted in numerous complications in the environment and on the road that runs through Cantabria and which resulted in three major problems [1]:

1. Disruption of traffic by flooding of the elevation, both by water (Fig. 1) and by materials of the road (Fig. 2).
2. Problems of stability of slopes [2], both in clearings and embankments, which resulted in invasion of part or all of the road by materials and cracking of the roadway, with partial (or total) falls of several meters (Fig. 3).
3. Seat and overturning of walls, with problems, usually sliding at its base (excessive thrust) or the mass of land on which they rested or increased compressibility of the wetting foundation [3].



**Fig. 1** Situation of PK 158,140 MI produced by heavy rains on rocky slope (upstream) without acting



**Fig. 2** Situation in the N-621 produced after intense rains with stone falling

**Fig. 3** Cracking of the roadway with descent of 100 cm in the A-8, Liendo



The problem to be solved Type 1, of management of runoff water, is that of the currents of water that appear after a heavy downpour or in the event of avalanche or thaw fall on the road in the form of a waterfall from the escarpments that border the road, which stop or at least hinder the circulation of the vehicles (Fig. 1). A multitude of karst caves exists, which when episodes as the ones described above take place are filled with water to the maximum and produce impressive waterfalls on the national road. In addition to the waterfalls stones are continuously falling: On average, 50 stones are counted in a day in the stretch of the Gorge (Fig. 2). A count carried out in 2009 in PK 171 + 800 gave as a result 58 incidences of falling stones with a total of 212 stones throughout the year, which compared to the year 2014, gave a result of 21 incidents for the same reason after the performance and with a count of 56 stones (from 3 to 5 cm to 30 cm–30 cm). It should be borne in mind that the purpose of the action in such PK was to channel that waterfall so as not to hinder the traffic due to waterfalls of water. This has reduced the fall of stones (average size of 10 × 8 cm) by 74%.

Regarding the Type 2 problem, there was a large slide of the right road (Fig. 3), in this case embankment of the highway A-8 in PK 167, in Liendo, on February 8, 2013, with strong horizontal and vertical displacement of the right lane, of the order of 30 and 100 cm, respectively. This led to cut traffic in the roadway and to the urgent set up of metal lanes in the central reservation to prevent the slippage from affecting the opposite lane, which is along where the two traffic directions circulated.

Another Type 2 problem occurred in Reinosa on February 5 and 6, 2012, with rainfalls of 134 and 65 mm, respectively, and which caused the rapid melting of snow fallen the previous week in the Campoo Valley, leading to flooding in the area and abnormal river flooding. In Cañeda, the flooding of the Besaya River, which crosses the town, took place; at the height of PK 141.1 of the N-611, the river had

**Fig. 4** Initial situation in Cañeda, road N-611, p.k. 141.1



been previously piped under the road embankment, and probably, by the collapse of a metal tube, the tube was blocked and subsequently broke down at the event with the consequent risk to the road stability (Fig. 4).

Type 3 problems occurred elsewhere such as in the A-67 road, PK 150 + 600 near the village of Pujayo. In this case, there was a head slide on the green wall of 17 m high and 70° slope, which supports the highway in the access to the viaduct of Pujayo. A “spoon” surface slip occurred at an approximate length of 15 m and a height of about 6 m. In other areas of the green wall, the beginning of a rollover/breakage process of the top step of the wall was also observed.

## 2 Climate Conditions

From a regional point of view, the climate of the area is Atlantic, temperate humid, and is conditioned largely by markedly abrupt orography and by the relative proximity to the sea, which exerts a damp ending effect. It is worth noting the abundance of wet-type weather situations, which originate in the Atlantic and northern storms.

In particular, the area of the Gorge of the Hermida has unique physiographic characteristics: The area further north suffers huge influence from Atlantic conditions, while in the south, there are Mediterranean conditions.

### 2.1 Precipitation

For the climate study, the latest precipitation data collected from the Piñeres meteorological observatory, dependent on the State Bureau of Meteorology (AEMET), has been taken into account. They recorded 424 mm of precipitation in February



### **3 Geological and Hydrological Conditions**

#### **3.1 Geology**

The Paleozoic lands (P) are located at the western end of Cantabria, constituting the eastern boundary of the large Paleozoic sedimentary basin of the astur-leonesa area. The oldest outcrops that appear, in the coastal area, are represented by the Ordovician quartzites (Ria de Tina Mayor, surroundings of Pechón and Pesúes). On these materials', large masses of massive limestone during the Carboniferous, mountain limestone, were deposited, protagonists of the relief of the domain of Picos de Europa, whose most prominent features derive from this geological nature. Massive coal age limestones, which show high resistance to erosion, preserve the general morphology of blocks displaced by alpine tectonics. The slopes of the main valleys, whose slopes reach 2000 m, show steep slopes, resulting in a morphology of very steep and deep canyons (location of the study area of the waterfalls). Meanwhile, the relief of the higher areas is dominated by glacial forms (circuses, ridges, "jous"/sinkholes, etc.) and karst forms (naked dolinas and limestone pavement fields), developing a complex underground water drainage system. South of this area, the Liébana area consists of a series of slates, greywackes, sandstones, and sometimes conglomerates, which extend through the valleys [6].

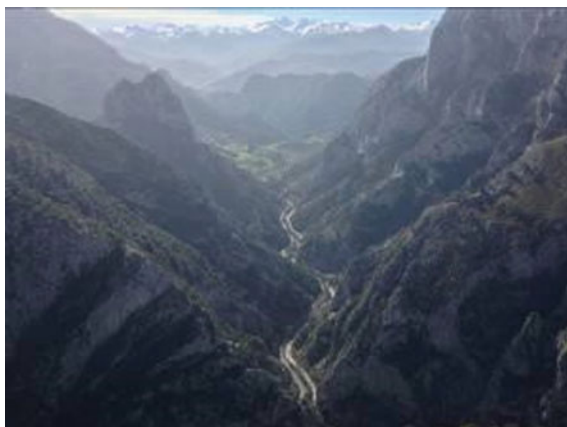
#### **3.2 Hydrology and Hydrogeology**

As for surface hydrology, the slope of the Deva riverbed is considerable, so they dominate rapids and fast boards with total average resources of 1008hm<sup>3</sup>/year and with an average annual-specific contribution of 843 mm. From a hydrogeological point of view, the territory is nestled in the hydrogeological units 01.17 Picos de Europa-Panes and 01.13 Cabuérniga [4].

#### **3.3 Geomorphology**

From a geomorphological point of view, the Gorge of La Hermida is defined as a flowkarstic gorge, combination of river or flow-torrential incision processes, karstification, and gravitational processes associated with high slopes. It is a natural space characterized by a high geodiversity, with points of 1500 m of elevation, which allows the existence of a wide range of processes and forms of relief, inherited from some of the climates of the past and from others active today. It is a natural space characterized by a high geodiversity, where its 20 km of longitudinal development and its more than 1500 m of elevation in some points allow the existence of a wide range of processes and relief forms.



**Fig. 6** Hermida gorge

The current road layout, perfectly integrated into the landscape of the Gorge and located at its bottom, runs through the most recent part of the Gorge, that is to say, the most active and dynamic (Fig. 6).

### ***3.4 Geotechnical***

The limestone formations of the Hermida Gorge corridor are grouped together and have a very similar geotechnical behavior. Massive calcareous formations (mountain limestone formation, laminated black micritiques and Picos de Europa limestones, white and gray micritique masses) would be considered according to Hoek–Brown as a group of good or very good geotechnical characteristics in the condition BLOCKY to MASSIVE, healthy rock matrix with good interconnection between the rock mass, consisting of cubic blocks formed by three families of angular discontinuities [3]. The conditions of the joints are favorable, with hard and clean edges, where the water circulates.

## **4 Solutions Adopted for the Management of Runoff Water in Karstics Areas (the Problem to Be Solved Type 1)**

The energy of these cascades has been dissipated by placing sequences of metal modules based on profiles or rods placed on the ground, dynamic screens complemented by metal mesh and chain screens. The water curtain is channeled to the Deva River by placing a reduced opening metal net. Sometimes, the rocky slope is very close to the road, so runoff water falls directly onto the road, watering it with little chance of drainage, even opening it transiently after a heavy downpour (Fig. 7).



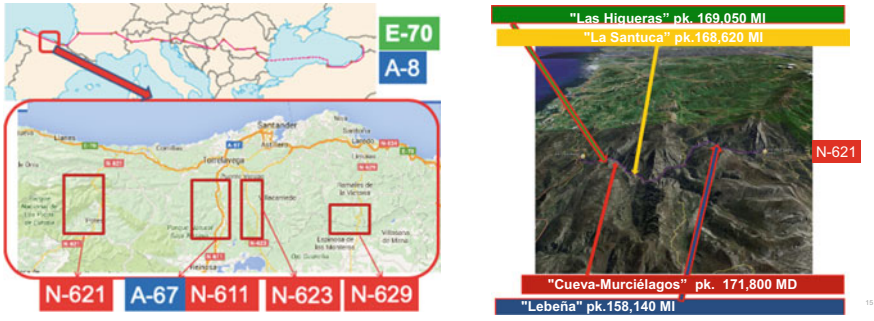


Fig. 7 Map showing the location

The actions carried out within the National Highway N-621 (Fig. 8) is the water-energy absorption of waterfalls based on dynamic screens and screens of chains complemented with metal mesh, arranged according to orography in sequence for the adaptation of the energy.

The water curtain is channeled to the River Deva by placing a dense metal net and performing ditches and sewers crossing under the road.

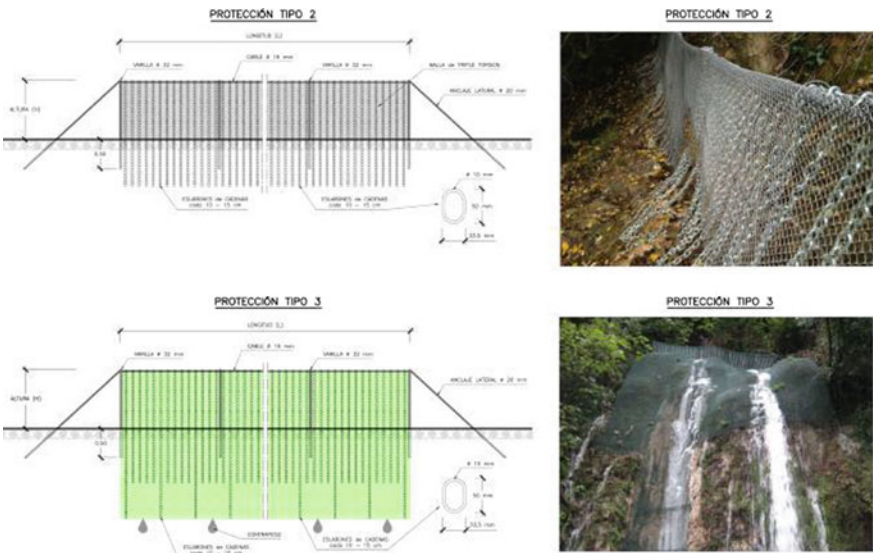


Fig. 8 Type 2 (M2) and Type 3 (M3) protection modules with photography on the right



**Fig. 9** Situation of PK 158,140 MI produced by heavy rains and situation of PK 158,140 MI with the finished stonework (national roadside)

#### ***4.1 PK 158 + 140 MI Cascading Energy of Absorption “Lebeña”***

It is associated with a rocky ballast that descends to the edge of the road, with a variable height between 50 and 75 m and 170. The speed and energy of the water force sprouting from two karst cavities and channeled to the Deva River have been decreased, through five consecutive levels, 1 of M2 and 4 of M1-2. The receiving bowl has been improved by rock bite, and a masonry wall has been executed, with putlog holes being performed and mimetized with the natural environment, which allows for the integration of landscape (Fig. 9).

#### ***4.2 PK 169 + 050 MI Energy Absorption at “Las Higueras” Waterfall***

The speed and energy of the water force that descends from four channels that converge in two and are channeled to the Deva River have been decreased. All this by arrangement of the different modules are shown in Fig. 10.

#### ***4.3 PK 171 + 800 MD Energy Absorption at “Murcielagos” Waterfall***

The speed and energy of the water force that descends from two torrents and channeled to the Deva River have been decreased by: 26. 00 m<sup>2</sup> of dynamic screen (Module No. 1) and 185. 74 m<sup>2</sup> of string screen (Module No. 2) (Fig. 11).



Fig. 10 Situation of the PK 169,050 MI produced by rains. Protection channels 2, 3 y 4

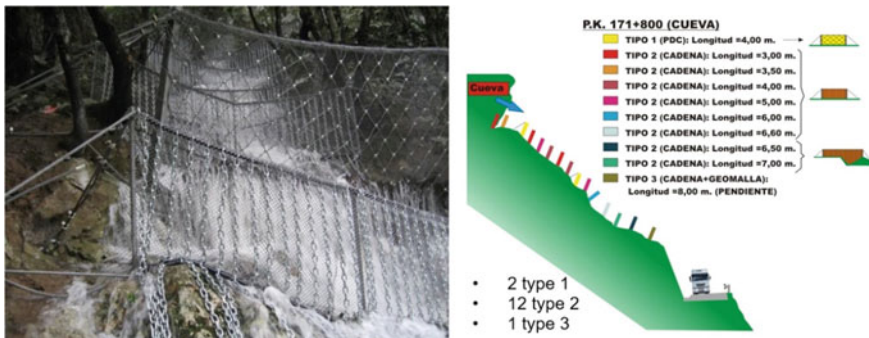


Fig. 11 Operation of modules no. 2 in lower slope in the face of rain events

## 5 Biological Engineering Solutions in A-8 Highway (the Problem to Be Solved Type 2 and 3)

The action carried out on the slope includes its stabilization by means of a measure of biological engineering, consisting in the incorporation of a gravity wall formed by a cell structure of eucalyptus wood logs, with living stakes and container plants, with the aim that the future development of the plant replaces the trunk structure. The structure has been reinforced with a foot of slab. The performance has been completed with the execution of a coronation ditch with its corresponding descent.

With regard to other solutions that were carried out, we could cite the following:

- Mortar piles 60 cm in diameter net. Triangles equilateral mesh of 2,40 m side, in the center 80 m and mesh of equilateral triangles of 2. 70 m side, in the 20 m sides to the sinking area. With a total 248 pilots between 20 and 26 m deep. Preparation of accesses, execution of drain 4 m deep filled with draining material, construction of concrete-coated ditch. Execution of Californian drains and rail stake and topographic control. The movements recorded in the period leading up

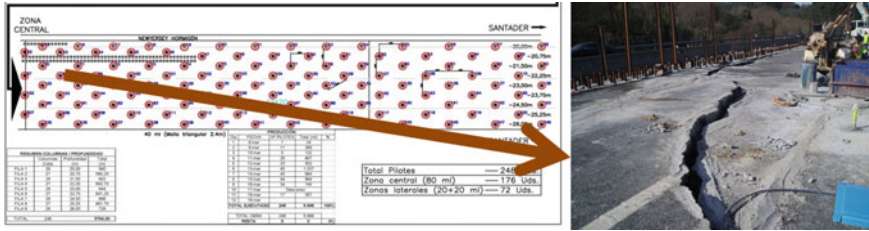


Fig. 12 Embankment stabilization A-8 (E-70)

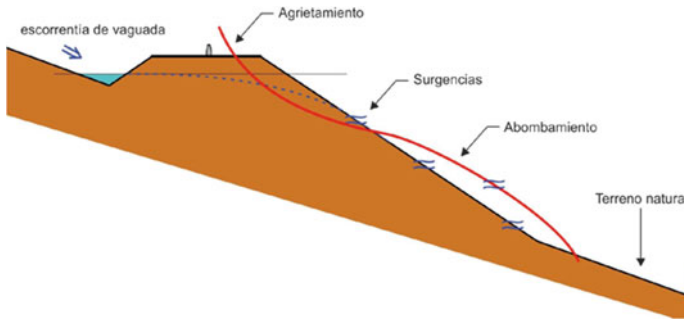


Fig. 13 Embankment stabilization A-8 (E-70). before

to the start of the repair works are elevated, greater than 20 cm at some points. During repair work, up to a maximum of 3–4 cm. After completion of the repair work, the movements on both the carriageway as in the slope practically have disappeared (Figs. 12, 13, and 14).

Walls, rockfill bases and rocky slopes skin, rail staking. Replacement of ARMCO (Fig. 15) tubes with prefabricated three-articulated concrete structure.

## 6 Full-Scale Tests on Dynamic Barriers

### 6.1 Background

Dynamic barriers are flexible metal structures specifically designed to stop detached rocks from slopes, to prevent them from reaching critical infrastructures or even dwellings. They have been a major measure to mitigate rock falls damages in northern Spain and in Cantabria in particular, especially in La Hermida Gorge.

GITECO (Construction Technology Research Group of the University of Cantabria) has collaborated for the last 20 years in different research projects with the company Malla Talud Cantabria in the field of landslides and rockfall protection

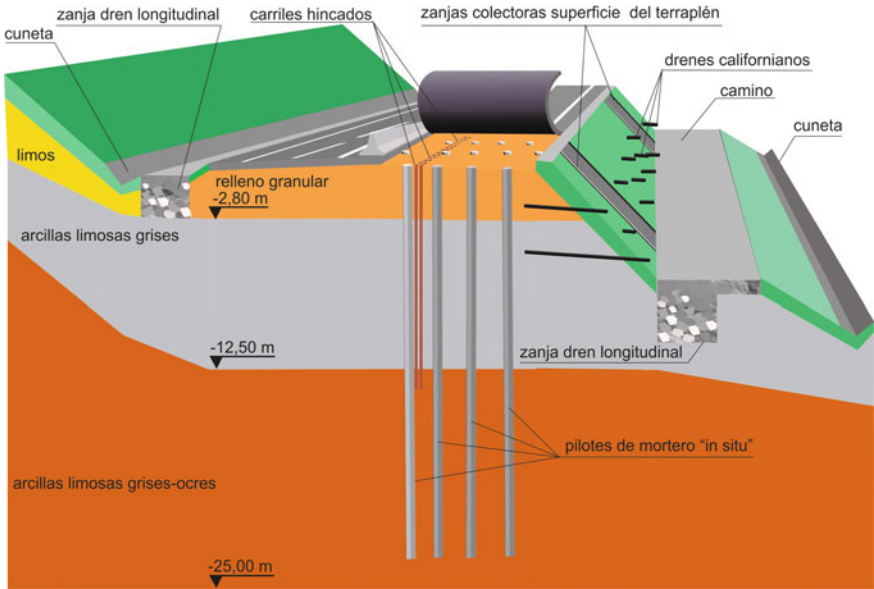


Fig. 14 Embankment stabilization A-8 (E-70). after

Fig. 15 Replacement of ARMCO tubes with prefabricated



systems. One of the main achievements has been to carry out a field test on dynamic barriers following ETAG 27 on two products: IBT-150 and IBT-500. Forces in cables, stresses in foundations, displacements in membrane, and energy dissipaters deformation have been measured through load cells, strain gages and high-speed video cameras, among others.



## 6.2 Test Description

Field tests were carried out on IBT-150 and IBT-500 in 2010 and 2015, respectively, following ETAG-27. The test consists on applying a vertical impact over a dynamic barrier installed in a horizontal position. The dynamic barrier consists of three function modules of 10 m length by 3 m width. The projectile used is a concrete block with standard dimensions that is released with a crane at a certain height producing an impact of a certain potential energy. IBT-150 and IBT-500 are commercial dynamic barriers that have a nominal energy of 150 kJ and 500 kJ, respectively. The test procedure, according to ETAG 27, consists of applying three consecutive impacts on a dynamic barrier, the first two correspond to the service energy level (SEL) while the last one corresponds to the maximum energy level ( $MEL = 3SEL$ ). The nominal energy of each commercial product corresponds to the MEL energy obtained from a full-scale test. The weight and drop height of each block can be defined by a test developer as long as it reaches the desired MEL/SEL level taking into account that a minimum speed of 25 m/s at the moment of impact is always required. If the dynamic barrier can bear the MEL impact, even if certain components might have broken, the test is considered valid.

In the IBT-150 full-scale test, maximum vertical displacement of middle panel was recorded through a high-speed camera. Also, the forces at the central functional module were monitored using two load cells (N1, N2) for 8 mm diameter cables. In addition, four reinforcement cables (N3, N4, N5, N6) and upstream cables (N7, N8, N9, N10) were monitored using load cells for 16 mm diameter cables. Furthermore, specific load cells were fabricated and attached in the GEWI bar, between the rock and the posts, in order to measure the stresses in the foundations as ETAG-27 indicates.

For the particular case of the IBT-500, certain changes were made in the instrumentation with respect to IBT-150 in order to improve data recorded. Foundations were monitored in this case, directly attaching strain gages in the GEWI bars close to the wall (N15, N16). Four load cells for 8 mm diameter cables were placed in the central functional module (N1, N2, N3, N4), eight load cells for reinforcement cables of 22 mm diameter were added (N5, N6, N7, N8, N9, N10, N11, N12), and two more load cells for 16 mm diameter in upstream cables (N13, N14) were set up (Fig. 16).

## 6.3 Test Performance

Both tests were valid since the dynamic barriers stopped the MEL impact; furthermore, both barriers did not present significant damages.

Load cells in sensors worked pretty well detecting the evolution of tensile forces in cables along each impact for around 0.2 s. In the particular case of IBT-150, the specific load cells placed in the GEWI bars did not work as expected due to an inadequate force transmission between the bar and the load cell. In both tests,

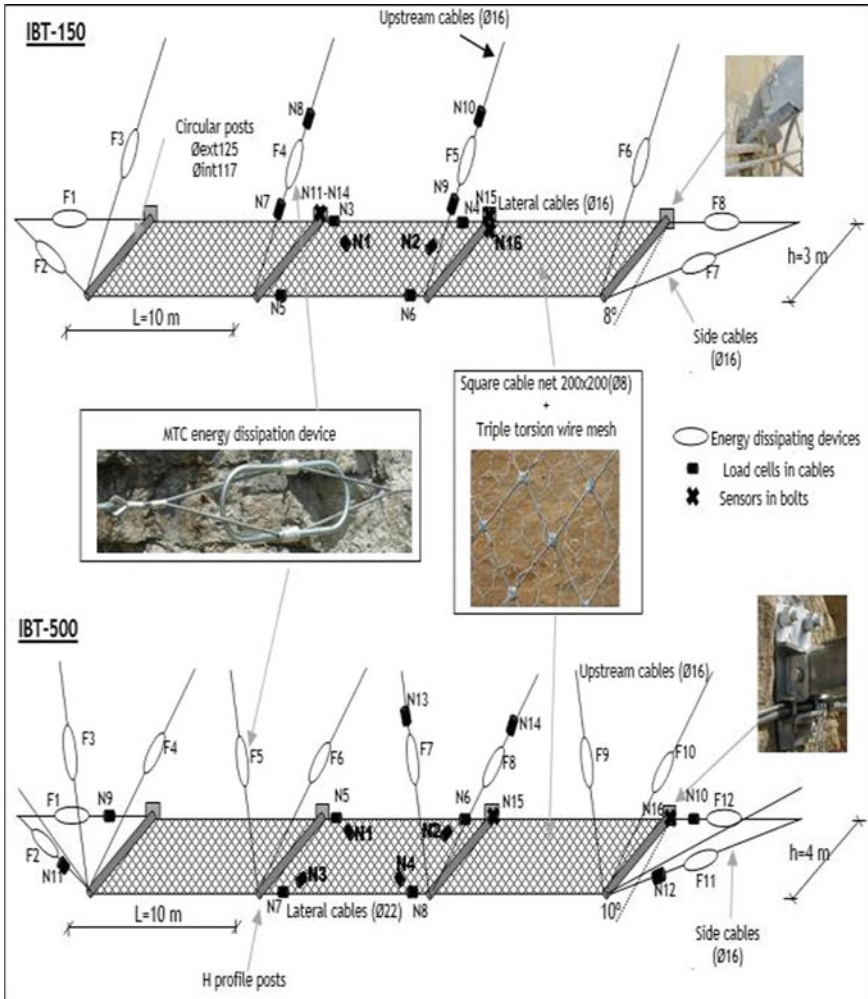


Fig. 16 IBT-150 and IBT-500 full-scale test

reinforcement cables were the components that recorded higher forces and not the cables in the membrane itself. Also, it is considered that the best location to place the load cells in the reinforcement cables is close to the lateral anchors (N9, N10, N11, N12). This is due because of two reasons: They generally record more force than the ones located at the central functional module, and also because it is easier to place them because there are not sewing cables that connect the membrane with them.

Measuring the forces in the foundations, as ETAG-27 establishes, is considered the most difficult task because the types of foundations vary a lot from one model to other for different manufacturers. In this case, the bolts themselves were considered

**Table 1** Characteristics of the SEL and MEL test of both barriers

Barrier type	mSEL (kg)	Vimp (m/s)	ESEL (kJ)	mMEL (kg)	EMEL (kJ)	Vimp (m/s)
IBT-150	148.0	25.27	47.25	504.0	165.0	25.59
IBT-500	460.5	26.94	167.15	1429.5	518.9	26.94

as foundations which are used to join the posts to the ground. Measuring forces in a bolt is not either an easy issue; however, it has been considered that the best method is to stick straightforward strain gages into the GEWI bar.

Although ETAG-27 does not state any specific acceptance criteria for the forces, and stresses recorded with the sensors, they are quite useful for design purposes, especially when a new and larger dynamic barrier is intended to be developed. Data recorded can be used to understand better which are the mechanisms of force transmission among components, also to determine which are the components that bear the higher forces, and finally, to calibrate numerical models [7] for future design purposes (Table 1).

## 7 Conclusions

The weather events that occurred after the interventions were installed are comparable in magnitude and frequency to those that occurred before the interventions were put in place are more extraordinary yet. For example, the amount of precipitation collected last November must be qualified as extraordinary; specifically, in the station of Tresviso, the 648 mm (254.0 mm normal) constitutes the maximum value registered since the series began in 1980. The time passed after the execution of the exposed solutions (1–2 years) has shown that they work efficiently, and it is important to highlight the good results obtained with the use of chain curtains in the Hermida Gorge, which substantially improves road safety under rainy weather conditions (comparing Fig. 1 and Fig. 17); also, it is worth mentioning the stability achieved with the use of the cell structure of eucalyptus trunks on the A-8, which prevents slide accidents during winter.

Full-scale test according to ETAG-27 with the type of sensors used by University of Cantabria has shown to be a good monitoring system to determine maximum tensile forces on different cables, stresses on foundations, and maximum elongations.



**Fig. 17** Situation of PK 158,140 MI produced by heavy rains on rocky slope (upstream) performed the performance



## References

1. Collazos F (2015) Gestión del agua de escorrentía en terrenos kársticos y estabilidad de taludes y cimientos en el norte de España. Actas finales. Presentación oral. XXVth World Road Congress. Seoul (South Korea)
2. Road Congress. PIARC- Seoul (South Korea)
3. Hoek E, Brown K (2002) "Rock slope engineering" I.N.M. London
4. Odón Hernández Holgado (2013) Agencia Estatal de Meteorología. Una aproximación a la nivología en Picos de Europa, pp 34–38
5. Gobierno de Cantabria (2010) Decreto 57/2010, de 16 de septiembre, por el que se aprueba el Plan Especial de Protección Civil de la Comunidad Autónoma de Cantabria ante el Riesgo de Inundaciones, INUNCANT. Santander
6. Mapa Geológico 1:50.000, hoja nº 56 (Carreña- Cabrales), editado por el Instituto Geominero de España (MAGNA)
7. Castanon-Jano L, Blanco-Fernandez E, Castro-Fresno D, Ferreño D (2018) Use of explicit FEM models for the structural and parametrical analysis of rockfall protection barriers. Eng Struct 166:212–222

# Application of FEA in a Highway Fill Embankment Slope Stability Failure Study



Jiliang Li and Thiago Leao

**Abstract** This paper presents the study of a slope stability failure due to a roadway widening using an FEA program. It consists of a case study of static load induced liquefaction in a simple roadway widening project constructed in the north eastern part of Ohio in 2008. The widening required an embankment fill, which moved nearly 4 feet vertically and 1 foot laterally after days of installation. The main objective of the work is to compare different approaches dealing with this static liquefaction situation; in this case, limit equilibrium method (LEM) and finite element analysis (FEA) method are being studied. The use of two approaches is important to show how the results can be compared and to determine the reliability of the factor of safety (FS). The mechanism that caused the rotational slope failure was the liquefaction of sand layers beneath the road embankment. The study explains how this loose sand layer could be simulated with the use of FEA which provides an advanced tool to perform a more complete and accurate analysis. The study concluded that each method has its advantages and limitations; however with the use of FEA, it was possible to build a more realistic model since advanced material model and properties could be defined which are more adequate for such cases as liquefaction in sands.

**Keywords** Slope stability · Static liquefaction · Critical state soil mechanics · FEM

## 1 Introduction

Liquefaction of soils has been a topic of extensive studies over the past decades. Casagrande [1] was one of the pioneers in this research topic, followed by other authors such as Castro [2]. The most common situation able to trigger this phenomenon occurs due to dynamic loads caused by seismic motion. However, static loads also can lead to the loss of shear strength when some such conditions are met. This study presents one of these cases in which an apparently simple structure had some issues due to soil liquefaction, a condition not initially understood or predicted.

---

J. Li (✉) · T. Leao

Department of Mechanical and Civil Engineering, Purdue University Northwest, Hammond, IN, USA

e-mail: [Li1919@Purdue.Edu](mailto:Li1919@Purdue.Edu)

The case presented in this study was described by Weber and Bredikhin [3] and consists of a simple roadway widening constructed in northern Summit County, Ohio, in 2008. It was necessary to construct an embankment with dimensions of 25-foot wide and 15-foot high because of the widening of the road. The issues started after the conclusion of the fill placement activities, with some shear cracks indicating some movement. After the construction of highway fill embankment and a rainstorm in October 2008, this fill movement reached 4 feet vertically and 1 foot laterally; therefore, it would be necessary to understand the failure before continuing the stabilization work.

Some field exploration and soil laboratory tests were performed to determine the cause of the failure. Firstly, the settlement was analyzed and estimated, and it was concluded that this could not be the cause of the failure. The testing results revealed a hydrostatically charged sand layer confined between two clay layers beneath the embankment. The sand at this location could be assumed to be in undrained condition, since the clay layers enclose the flux of pore water to be drained after the external load was applied. These conditions could lead to static liquefaction of the sand layer, a fact that explains the large movement of the fill.

The original study [3] considered limit equilibrium method (LEM) to calculate the factor of safety of the slope and concluded that in fact it was instable. The same study concluded that if the pore water pressure could drain from the sand layer, the static liquefaction would not occur; therefore, the installation of wick drains was adopted to solve the problem. Even being a more simplified approach, the static liquefaction could be demonstrated in this model.

Another approach which could be applied in this situation would be the use of constitutive models to represent the sand layer in this situation. In this case, the consideration of the additional parameters and the undrained condition could show the complete loss of shear strength in the sand. Figure 1 presents a simplified diagram of the analysis procedures generally used in geotechnical engineering. The overview of some of the most commonly used constitutive models is presented by Lade [4]. These models need to be used with finite element and/or finite difference calculations of soil structures problems under axisymmetric, plane strain, and/or general three-dimensional conditions.

Finite element method (FEM) provides a useful tool to apply constitutive models for soil materials and achieve a more realistic approach. FEM has found increasing use in geotechnical engineering practice over the past 50 years. It was first used to solve problems of heat flow and water flow in soils and later was applied to determination of stresses and deformations in excavated slopes and embankments. More recently, it has been used to evaluate the factor of safety defined in the same way as that used in limit equilibrium method.

Griffiths and Lane [5] identify the following as being advantages of the finite element analysis over conventional limit equilibrium analysis:

1. It is not necessary to divide the domain into vertical slices.
2. Since there are no slices, no assumptions are required for side forces between slices.

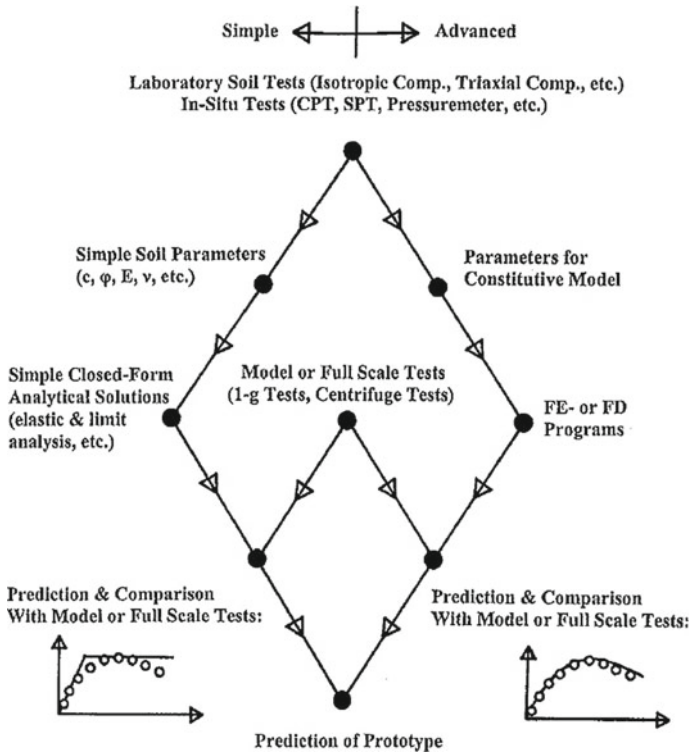


Fig. 1 Simple and advanced procedures for predicting behavior of prototype structures [4]

3. The FEM determines the locations of failure zones by calculation of stresses, without the search for a critical slip surface that is required in limit equilibrium analyses.

## 2 Literature Review

### 2.1 Static Liquefaction

Static liquefaction occurs when the total stress remains constant and the pore pressure increases such that the normal effective stress becomes zero, or when the pore pressure remains constant and the total stress decreases such that the normal effective stress becomes zero [6].

Several works have demonstrated the behavior of loose sands under monotonic loading. These experimental studies consist of analyzing drained and undrained triaxial compression tests and comparing with results from constitutive models. Castro [2] simulated banding sand under undrained condition until the complete

loss of strength. Yamamuro and Lade [7] tested Ottawa sand and observed complete static liquefaction at low confining pressures. Buscanera and Whittle [8] applied an effective stress soil model, MIT-S1 at Toyoura sand to examine the influence of the initial state on the potential for undrained instability. The behavior is approximately the same in all studies and occurs only for loose sand samples.

While shearing in triaxial test, sands show a hardening behavior depending on being in loose, medium, or dense state which results in different volumetric behaviors upon shearing. Loose sand undergoes compaction and medium dense and dense sand will show an initial compaction followed by dilation and increase in volume. In undrained triaxial test, due to the generation of excess pore water pressure, (very) loose sands tend to undergo static liquefaction. Dense sand on the other hand can endure high levels of shear stress partly due to the generation of negative excess pore water pressure.

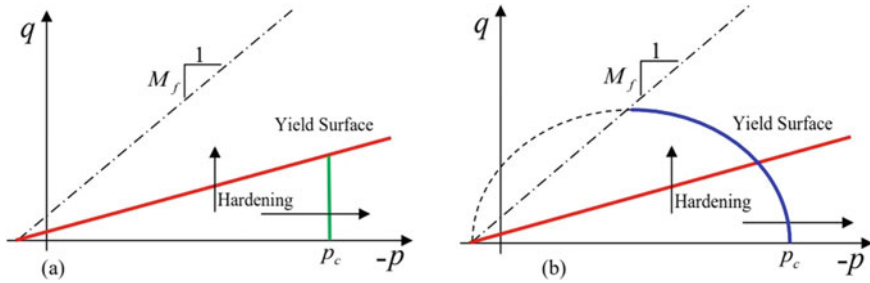
## 2.2 *Constitutive Models*

Some authors have developed constitutive models to represent sand behavior under both drained and undrained monotonic loadings. The first theory that captured the dilation of soils was what became known as critical-state soil mechanics (CSSM), popularized by Schofield and Wroth [9] with the Cam clay idealized theoretical model of soil. Critical-state soil mechanics is basically an effective stress framework describing soil mechanical response.

Other models derived from Cam clay were developed by Roscoe et al. [10] and Burland [11]. However, these models were inadequate to represent sand because of their inability to dilate and yield in a manner approximating real sand behavior. This inability to dilate realistically arises from the assumption that all yield surfaces intersect the critical state.

More recent models based on CSSM were created with more parameters to overcome some limitations of the classical methods. One of these models is the NorSand model. This model was proposed by Jefferies M.G. in 1993 [6]. The main difference between NorSand and Cam clay model is that NorSand assumes a yield surface and stress-dilation relationship known from Cam clay but disassociated hardening from CSL which gives the model capability to reproduce real sand behavior.

The softening–hardening model presented in RS<sup>2</sup> finite element program simulates the plastic deformation in soils that start from the early stages of loading utilizing a hardening law after yielding. The model can utilize up to three yield surfaces that includes deviatoric (shear), volumetric (cap), and tension cut off. This model in its simplest form has one additional model parameter than that of the elasto-perfect plastic model. Figure 2 shows the yield surfaces of the softening–hardening model.



**Fig. 2** Yield surfaces of the softening–hardening model; **a** Deviatoric yield surface (red) and the vertical cap (green); **b** deviatoric yield surface (red) and elliptical cap (blue) [12]

### 3 Methodology

#### 3.1 Software

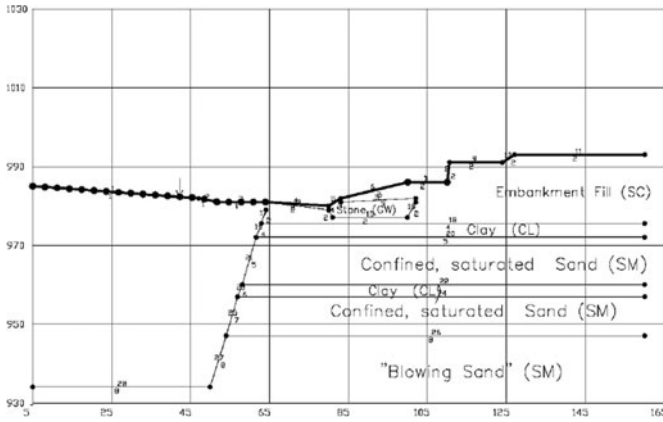
The finite element analysis software adopted in this study is Rocscience—RS<sup>2</sup> version 9 which has incorporated the NorSand advanced constitutive model to simulate static liquefaction [16]

#### 3.2 Models

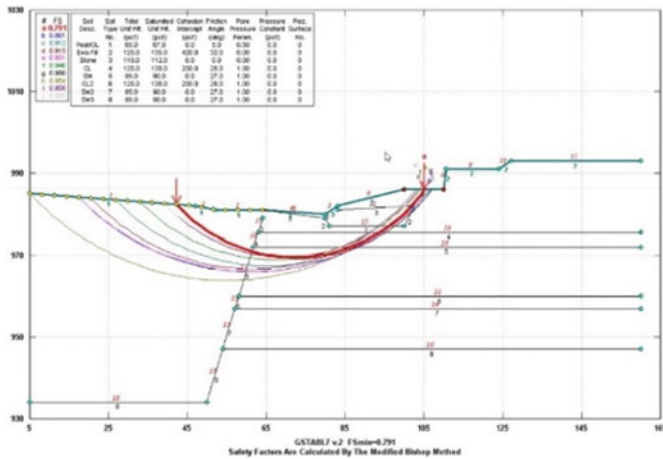
The model considered in [3, 14] used limit equilibrium method with method of slices and Modified Bishop method for the typical section (Fig. 3a–c). The sand layer in undrained condition immediately after a rainstorm in October 2008 was represented by a consideration of pore pressure ratio of 1 as reported in [3, 14].

For the study presented here, two models were created in finite element program RS<sup>2</sup> to simulate the embankment by using a FEM program. The first model represents the entire typical section as shown in Fig. 4. The slope model has been discretized using 2000 six-noded triangular elements. Mohr–Coulomb was initially considered for all materials. Shear strength reduction (SSR) technique was used to calculate the factor of safety. The SSR area considered followed approximately the critical slip surface from deterministic analysis.

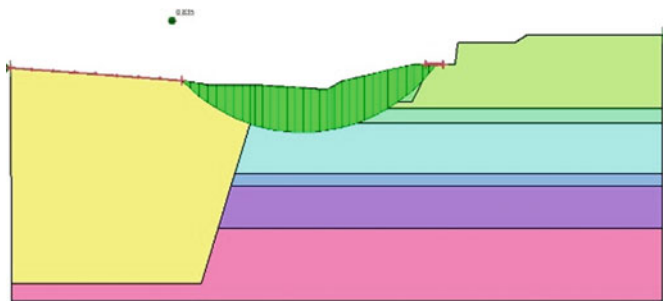
The second model consists of only the sand layer being represented (Fig. 5). The softening/hardening model was considered in this case. In this simulation, the increase in deviatoric strain due to embankment construction is considered to check if the change in deviatoric stresses could indicate static liquefaction properly. In undrained condition, it is assumed that no pore water is able to escape, so no volume change can occur since water is incompressible. Vertical displacement was incremented in a constant rate, and horizontal displacement is also incremented to maintain constant volume.



(a)

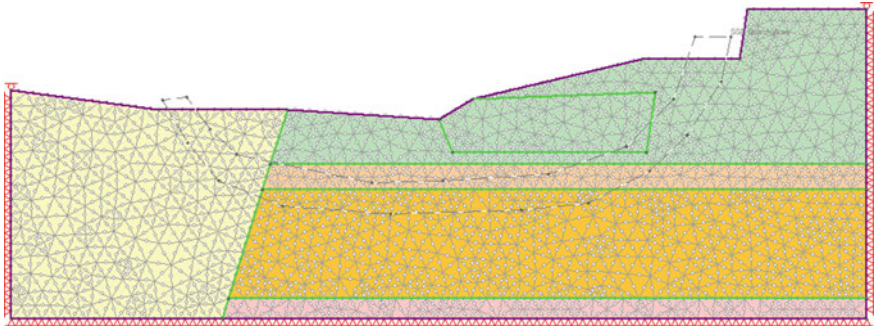


(b)



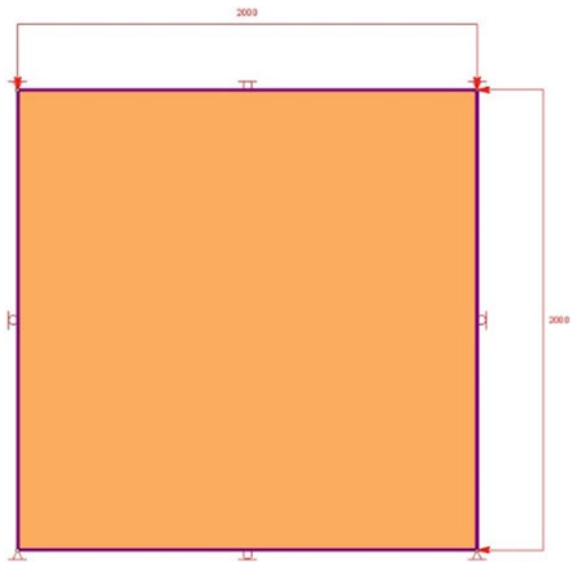
(c)

**Fig. 3** LEM for typical section [3, 14]. **a** Highway fill embankment cross-section materials [3]. **b** Highway fill embankment cross-section slip line search [3]. **c** Slope stability analysis (During failure) [14]



**Fig. 4** Model 1—FEM for typical section

**Fig. 5** Model 2—FEM for sand layer—Undrained condition



**Table 1** Materials properties for Model 1

Layer	$\gamma$ (pcf)	c (psf)	$\phi$ (°)	$\psi$ (°)	E (psf)	$\nu$
Peat/OL	65	0	5	0	105,000	0.35
Embankment Fill	125	420	32	10	440,000	0.30
Clay	125	230	28	5	210,000	0.30
Saturated sand	131	0	27	5	440,000	0.30



**Table 2** Material properties for sand Model 2

Material	Failure friction angle (°)	Zero dilation angle (°)	c (psf)	Hardening parameter
Sand	27	0	0	0.075

### 3.3 Material Properties

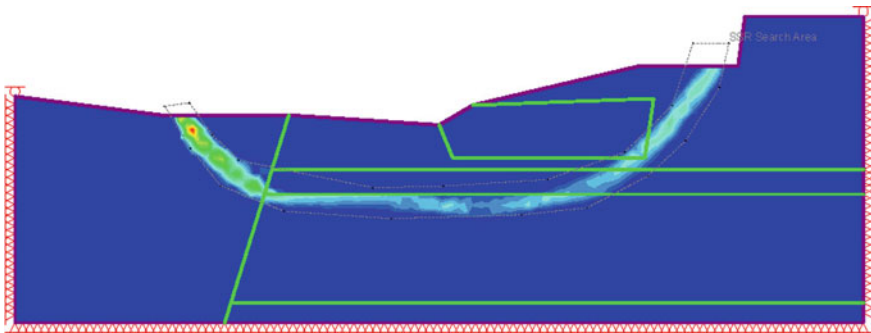
The material properties considered for both models are presented in Tables 1 and 2 based on the synthesis of data from reference [3, 14]. For the first method, the soil is treated as an elastic-perfectly plastic (elastoplastic) material adhering to Mohr–Coulomb failure criteria. Only six soil parameters are required for conducting the analysis:

- $c$  = cohesion
- $\phi$  = friction angle
- $\gamma$  = unit weight
- $\psi$  = dilation angle
- $E$  = Young's modulus
- $\nu$  = Poisson's ratio

## 4 Results and Discussion

In this section, the results of all simulations are presented. Results from RS<sup>2</sup> are compared to the limit equilibrium analysis results.

When the typical section was considered entirely in RS<sup>2</sup> (Model 1), it was not possible to verify the effect of static liquefaction in the model with Mohr–Coulomb model. Even though it was possible to see a region of larger shear stresses in the sand layer (Fig. 6), the critical SSR value was 5.8, much different from the value of 0.79 presented in [3].

**Fig. 6** Shear strains—Model 1

For the second model considered, the results for the sand layer by assuming NorSand model are presented in Figs. 7, 8 and 9. The charts represent the data from each of the 50 iterations considered in the finite element analysis [6]. In the first chart (Fig. 7), it is possible to see that when the deviatoric stress increases, there is a reduction in the effective mean stress, but after the deviatoric stress reaches a peak point, it starts to decrease until 0 psf, showing a complete loss of strength. Figure 8 shows the increase of excess pore water pressure during the increase of soil strain.

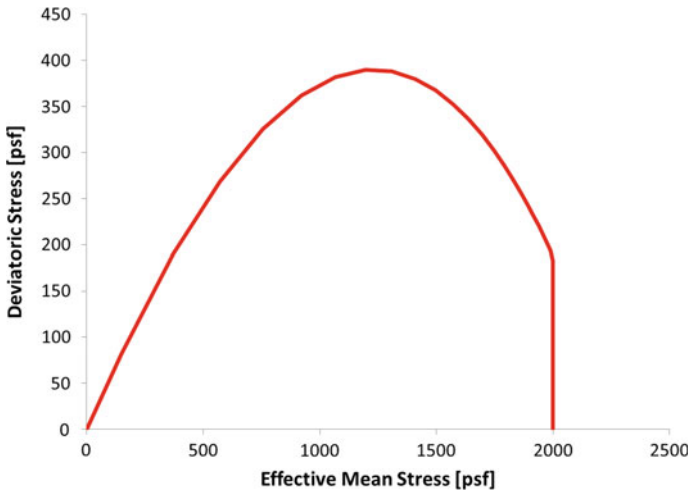


Fig. 7 Plot of deviatoric stress versus effective mean stress

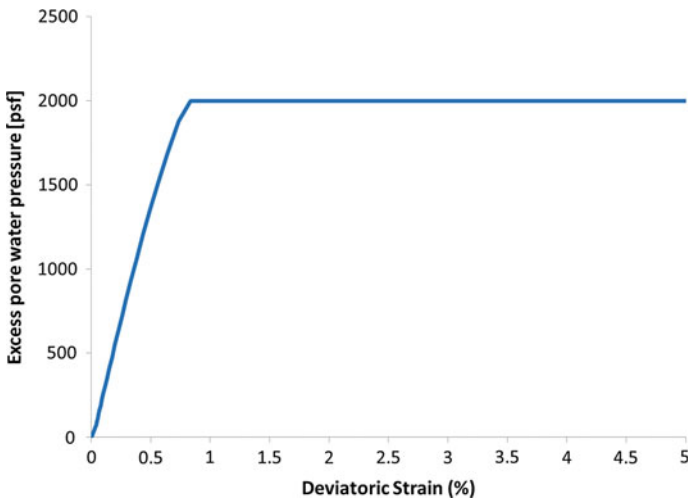
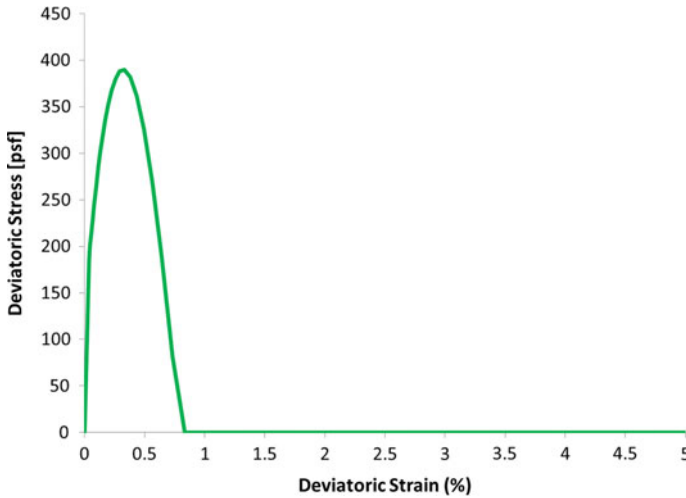


Fig. 8 Plot of excess pore water pressure versus deviatoric strain



**Fig. 9** Plot of deviatoric stress versus deviatoric strain

Because of the undrained condition, total stress remains constant and the normal effective stress becomes zero. The strains at peak deviatoric stress and complete loss strength can be obtained as shown in Fig. 9.

## 5 Concluding Remarks

This paper presented a static liquefaction case study of a highway fill embankment failure resulted from the liquefaction of the loose sand layer. It was demonstrated the importance of the constitutive model considered in the analysis, which should represent some specific characteristics of sands. The use of FEM allowed the representation of static liquefaction when the sand layer was simulated with the softening–hardening material model. In this model, only the sand layer was considered, and a constant deformation was applied in the material representing the increase of vertical stresses due to the embankment construction. The typical section considering Mohr–Coulomb and SSR area could not predict the instability of the slope, since the model could not represent the sand behavior properly. The newly added NorSand constitutive model reported in Rocscience (2019) as verified by its NorSand capability in Rocscience RS2 program [16] could be adopted to model the static liquefaction.

## References

1. Casagrande A (1975) "Liquefaction and cyclic deformation of sands, a critical review". Proc. 5th Pan-American Conf. on Soil Mech. and Found. Engng, Buenos Aires
2. Castro G (1969) "Liquefaction of sand". Harvard soil mechanics series, No. 81. Pierce Hall, Cambridge, Massachusetts
3. Weber MW, Bredikhin AJ (2010) "Static load induced liquefaction, steels corners road embankment failure". International conferences on recent advances in geotechnical earthquake engineering and soil dynamics. <http://scholarsmine.mst.edu/cgi/viewcontent.cgi?article=2830&context=icrageesd>
4. Lade PV (2005) "Overview of constitutive models for soils." Calibration of constitutive models. [https://doi.org/10.1061/40786\(165\)1](https://doi.org/10.1061/40786(165)1)
5. Griffiths DV, Lane PA (1999) Slope stability analysis by finite elements. *Geotechnique* 49(3):387–403
6. Jefferies MG, Been K (2016) "Soil liquefaction. A critical state approach". Taylor & Francis, London and New York. <https://www.crcpress.com/Soil-Liquefaction-A-Critical-State-Approach-Second-Edition/Jefferies-Been/p/book/9781482213683>
7. Yamamuro JA, Lade PV (1997) Static liquefaction of very loose sands. *Can Geotech J* 34(6):905–917. <https://doi.org/10.1139/t97-057>
8. Buscarnera G, Whittle AJ (2013) Model prediction of static liquefaction: influence of the initial state on potential instabilities. *J Geotech Geoenviron Eng* 139(3):420–432
9. Schofield A, Wroth P (1968) *Critical state soil mechanics*, vol 310. McGraw-Hill, London
10. Roscoe KH, Schofield AN, Thurairajah A (1963) Yielding of clays in states wetter than critical. *Geotechnique* 13(3):211–240. <https://doi.org/10.1680/geot.1963.13.3.211>
11. Burland JB (1965) "Some aspects of the mechanical behaviour of partly saturated soils." Moisture equilibria and moisture changes in soils beneath covered areas, pp 270–278.
12. Azami AR, Yacoub T, Curran J (2015) "A practical constitutive model for sands." <https://www.rocsience.com/documents/pdfs/rocnews/fall2015/Azami-Yacoub-Curran.pdf>
13. Been K, Jefferies G (1985) A state parameter for sands. *Geotechnique* 35(2):99–112
14. Li J, Leao TF (2018) Application of nor sand constitutive model in a highway fill embankment slope stability failure study. *Civ Eng J* 4(10):2252–2263
15. Rocscience, RS2 Manual, Toronto, Canada (2015)
16. Rocscience (2019) *NorSand in RS2: An Advanced Constitutive Material Model* <https://www.rocsience.com/about/news-events/norsand-in-rs2-an-advanced-constitutive-material-model>, last accessed March 11/2021

# Assessment of Innovative Slope Repair Techniques



M. G. Winter , I. M. Nettleton, R. Seddon, D. Leal, J. Marsden, and J. Codd

**Abstract** This paper summarises work to evaluate the effectiveness of innovative geotechnical repair techniques for Highways England's slopes. The techniques assessed were live willow poles, fibre reinforced soil (FRS) and electrokinetic geosynthetics (EKG) used in place of conventional approaches in order to reduce the overall impact of various challenges including environmental constraints (habitat and visual), access and utility constraints, and the need to reduce the scale and/or cost of traffic management and traffic delays. Trials of these techniques have been undertaken over the last 20 years or so, but monitoring was generally limited to just a few years post-construction; longer-term evaluation has not generally been undertaken. This paper presents a summary of the assessment of the effectiveness of live willow poles, FRS and EKG as aids to increased stability. The success, or otherwise, of the techniques led directly to recommendations for future use ranging from the development of design guidance and specification information for willow poles, guidance on the execution of further trials of EKG, to the cessation of use of FRS. The results of a life cycle assessment (LCA) are reported, and more generic lessons learnt from the trials and the practical application reported were used to produce guidance for future trials of innovative geotechnical repair techniques.

**Keywords** Slopes · Remediation · Shallow

---

M. G. Winter (✉)

Formerly TRL Limited now Winter Associates, Kirknewton EH27 8AF, United Kingdom  
e-mail: [mwinter@winterassociates.co.uk](mailto:mwinter@winterassociates.co.uk)

I. M. Nettleton

Coffey Geotechnics, Manchester M22 5PR, United Kingdom

R. Seddon

Formerly Coffey Geotechnics now Jacobs, Manchester M15 4GU, United Kingdom

D. Leal

Formerly TRL Limited now Atkins, Aldershot GU11 1PZ, United Kingdom

J. Marsden

Formerly Highways England, Guildford GU1 4LZ, United Kingdom

J. Codd

Highways England, Guildford GU1 4LZ, United Kingdom

## 1 Introduction

Work to assess the effectiveness of innovative geotechnical repair techniques for slopes was commissioned by Highways England. The techniques assessed were the planting of live willow poles, fibre reinforced soil (FRS) and electrokinetic geosynthetics (EKG). These techniques were used in place of conventional approaches in order to reduce the overall impact of various challenges including environmental constraints (habitat and visual), access and utility constraints, and the need to reduce the scale and/or cost of traffic management and traffic delays.

Trials of these techniques have been undertaken over the last 20 years or so, but monitoring was generally limited to just a few years post-construction. Longer-term evaluation had not generally been undertaken with the maximum duration of monitoring generally being around two to three years for formal research trials but often much less for other trials and practical applications. Available information from trials and practical applications undertaken on the English strategic road network (SRN) of the techniques was evaluated, and detailed site inspections and assessments were undertaken as part of this work.

This paper summarises the assessment of the efficacy of the three techniques including the recommendations for future use, summarises a comparative life cycle assessment (LCA) and gives information on the recommendations made with respect to future trials of innovative geotechnical slope repair techniques.

## 2 Willow Poles

The use of vegetation as an aid to slope stability has been widely written about, and the associated benefits are often described as follows [1]:

- Root reinforcement as the root structure develops, which will enhance the initial reinforcement provided by the willow poles.
- Canopy interception of rainfall and subsequent evaporation.
- Increased root water uptake of the water that does infiltrate into the soil and subsequent transpiration via the leaf cover.

Willow poles will, in addition to these benefits, provide immediate reinforcement to the slope as the poles act as either mini-piles or as short soil nails depending on the configuration of the design.

The available information from a series of trials of the planting of live willow poles was considered for sites at the A10 Hoddesdon, M1 J12 Toddington, A5 Milton Keynes and M23 Gatwick. The information from the trials was supplemented by site visits during February 2017, March 2017 and August 2018. At this time, the trial at the M1 had been removed as part of the works to reconfigure Junction 12 at Toddington, and the M23 trial was about to be removed because of works at that

site. The results of the work to determine the efficacy of the use of willow poles to stabilise shallow slope failures are presented in greater detail elsewhere [2].

The trial applications of live willow poles were primarily focused on the environmental benefits of their use to prevent shallow slope failure, but the aesthetic and ecological consequences were also considered.

The trials were informed by a precursor experiment at the A429 Iwade Bypass. The Iwade experiment yielded disappointing results in terms of the survivability of the willow poles and changes to the installation process were made for the trials. The primary lesson learned from the Iwade experiment was that driving the willow poles led to a low survival rate and subsequent trials installed the poles into pre-drilled holes, which were then backfilled. However, it should be noted that poles are usually tamped into the intact ground at the base of the hole in order to aid the process of backfilling, tamping of the backfill and sealing of the top of the annulus at the top of the hole, which gives a much higher survival rate [2, 3].

The monitoring undertaken at the A10, M1, A5 and M23 sites was extensive including meteorological data (sunshine, temperature, precipitation), condition rating and height measurement of the trees, tensiometer (suction) data, standpipe piezometer data, neutron probe data, and mini-rhizotron data to record root development. Invasive root investigations by exhuming the poles were also undertaken to establish root growth and to assess mycorrhizal status and to make direct measurements of moisture content [3]. The suction data was graphic, clearly showing the seasonal trends as well as the effects of plant development in successive growing seasons and, generally, the difference between the planted areas and the control areas without willow poles. The groundwater data, in contrast, showed clear variations only in the seasonal data.

From the monitoring results and subsequent site observations, it was clear that although monitoring was undertaken only in the relatively short-term, the planting of live willow poles has been beneficial in terms of promoting the type of changes and behaviours in the soil that would be expected and that would be beneficial from the point of view of reducing instability.

In addition to the trial sites, a practical application of willow poles, planted around 15 years after the trials, to stabilise a slope was examined at the M6 South of J40 (Fig. 1). At this site, inclinometer readings were taken before, during and after the willow poles were installed. Progressive downslope movements of up to around 50 mm were evident during a period of around 570 days before and during construction. In the 540 days post-construction, these movements largely stopped and/or were reversed (Fig. 2).

Collectively, the trial sites and the practical application used four different species of willow poles (*Salix alba*, *Salix dasyclados*, *Salix spaethii*, *Salix viminalis*) and were located in areas from the south-east of England to the north-west of England, thus encompassing a wide range of climatic conditions.

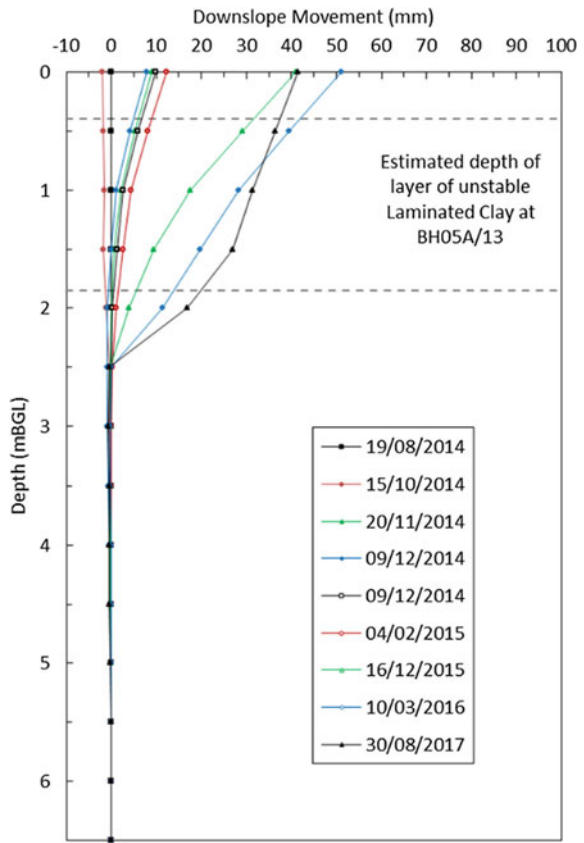
Specific challenges related to the future use of willow poles include:

- The selection of appropriate willow species including in the light of climate change and in consultation with statutory bodies and appropriate professionals.



**Fig. 1** General view of the M6 south of J40 from the B5320 overbridge looking south-east: Left, March 2017 (installation was between November 2105 and February 2016); Right, August 2018 showing growth [2]

**Fig. 2** Downslope movement measured using an inclinometer at BH05A/13 at the M6 South of J40 site showing movement with depth at different times [2]. (BGL—below ground level.)





- Construction issues related to the installation of the poles and the fitment of appropriate tree guards.
- Design and construction costs.
- The types of monitoring that have proven to be useful.
- Maintenance issues, particularly the need to ensure that the willows are appropriately coppiced, and that competing vegetation is eradicated during the period of establishment.
- Future uses for willow pole coppicing products, and
- The need for a long-term end-of-life strategy for willows to allow for, for example, succession planting.

These challenges are fully addressed in design, specification, construction and maintenance guidance for live willow poles installations in which the challenges identified above are fully addressed [2] as updated, expanded and formalised from the original trial work [3]. This covers the principles of design, site survey, sourcing of live willow poles, site preparation, installation of live willow poles, protection of installed poles and maintenance requirements, with an appendix indicating an approach to detailed design.

### 3 Electrokinetic Geosynthetics

The use of EKG treatment typically comprises an active treatment phase, when the EKG installation is electrically powered, and a passive phase when the power is switched off.

EKG treatment provides four primary contributions to enhance slope stability:

- Electroosmotic active dewatering, leading to a reduction in water content, pore water pressures, consolidation and an increase in shear strength.
- Physiochemical changes in the soil, such as cementation, precipitation, ion exchange and flocculation, which can lead to increases in shear strength and stiffness, and a reduction in plasticity.
- Temporary active EKG drainage and permanent passive drainage provided by the EKG cathodes.
- Soil nail reinforcement provided by the EKG anodes with an enhanced soil/nail bond.

The design of the EKG treatment has been undertaken by Electrokinetic Limited and is based on laboratory testing which is specifically targeted at the EKG technique. The installation comprises an array of anodes and cathodes (Figs. 3 and 4). The technique is considered to improve the stability of slopes by a number of processes, the contribution of which can be summarised as follows:

- Reduction of pore water pressures by electroosmotic dewatering.
- Reduction in water content due to electroosmotic consolidation.



**Fig. 3** P45 Slope climbing drill rig installing electrodes: A419 Rat Trap, 2014 [4]



**Fig. 4** Cathode at A21 stocks green. Water flowing from cathode (passive flow) [5]

- Increase in shear strength.
- Soil/grout Interface shear resistance/adhesion increase around the anode electrode soil nail.

Three of the four EKG trials (A21 Stocks Green, M5 Junction 7 and A419 Rat Trap) were undertaken as practical remedial works for known relatively shallow (1 m to 2 m deep) earthwork embankment instability issues. The fourth EKG trial (A56 Woodcliffe) was undertaken to demonstrate, on a small scale, the effectiveness of EKG primarily for active dewatering of fine-grained soils, but also ground improvement. The available information was supplemented by site visits during February 2017, March 2017 and August 2018. The results of the work to determine the efficacy of the use of EKG to stabilise slope failures are presented in greater detail elsewhere [5].

Based on the available information and the inspections undertaken by the authors for this project, the A21 and M5 trials appear to have been successful in stabilising the shallow landslides whilst reducing disruption to the network and damage to ecologically sensitive sites. However, the ground improvements by EKG treatment cannot be rigorously assessed due to limitations in the extent and duration of post-EKG treatment ground characterisation, groundwater monitoring and movement monitoring. The results of the A419 Rat Trap are of uncertain value as the interpretation of the existence of a shallow slide seems to be questionable. However, the trial provides additional information on the installation and operation of the EKG system.

The A56 trial provides a high-quality data set to demonstrate the effectiveness of the active dewatering of a deep (6–12 m) landslide using the EKG technique. However, the detailed rigorous assessment was compromised by the limitations in the extent and duration of post-EKG treatment ground characterisation, groundwater monitoring and movement monitoring. The EKG active dewatering effect on groundwater levels was significant and appears effective in fine-grained soils. This technique has the potential to be a valuable means of groundwater removal and control in fine-grained soils with high water tables, a situation which is often problematic for permanent works, and particularly for the temporary works required to install permanent works.

Specific challenges related to the EKG trials include:

- That there is currently only one supplier of the EKG system possibly complicating procurement.
- The need for more robust and effective system components and monitoring systems (electrical and water discharge).
- The need for early assessment of likely current draw coupled with discrete EKG panels with monitored and controlled current supply.
- The need for post-trial ground investigation, in situ testing, laboratory testing and monitoring to determine effectiveness and the longevity, and thus the design life, of the EKG processes.
- These challenges are addressed in preliminary guidance for trials of EKG slope stabilisation [5]. This covers site selection, site characterisation and monitoring and design.

## 4 Fibre Reinforced Soil

The addition of discrete fibres to improve the physical properties of soil is relatively common practice in countries such as the USA. The use of FRS has been reported to have benefits over other more commonly used slope repair techniques. It allows the reuse of site-won material through the addition of a relatively small proportion of the fibres. The polypropylene fibres are ostensibly inert and therefore are potentially less hazardous than other soil improvement techniques that use lime or cement.

The available information on the use of FRS was considered for sites at the A1(M) Junction 1, M20 Smeeth (Fig. 5) and A27 Polegate (Fig. 6). The reported information from the trials was supplemented by site visits during February and March of 2017. The results of the work to determine the efficacy of the use of FRS to stabilise shallow slope failures are presented in greater detail elsewhere [6].

The trial applications of FRS were primarily focused on their use to prevent shallow slope failures and desiccation cracking. However, it became apparent during the construction works that the addition of fibres to ground softened by rainfall and plant movements allowed work to continue on site when it would otherwise have stopped.

Difficulties in accurately determining the improvement to the geotechnical properties of the soils at the trial sites were reported at both the design and construction stage. At design stage, a 25% increase in the effective angle of shearing resistance was generally adopted. However, post-construction testing at the A1(M) site and slope instability at A27 Polegate suggest that the increase in angle of friction was less.



**Fig. 5** Fibres present at ground surface and to a lesser degree in the exposed made ground [6]



**Fig. 6** A27 Polegate/bay tree lane FRS trial; note arcuate back scar indicating slope failure [6]

It was considered that the three trials did not demonstrate the effectiveness of the FRS as a long-term slope repair technique. Specific difficulties were experienced with mixing the fibres into the soil so as to achieve an effective random distribution leading to ‘clumps’ of fibres being located at the soil surface several years after construction (Fig. 5). This difficulty of mix control is also likely to have contributed to the post-construction failure illustrated in Fig. 6; this is located in an area of supposed FRS but only a very limited fibre presence was found during the authors’ investigations. There were also considerable concerns around the environmental issues surrounding the introducing of plastic fibre into large soil masses including general issues on plastics in the environment and more specific issues regarding the end-of-life waste regulation status and treatment of the FRS mass.

In order to progress further with FRS trials, the following aspects would need significant further consideration:

- In situ sampling and laboratory testing techniques need to be further developed to better determine the effect the addition of fibres has on the geotechnical properties.
- Further research is needed into effective methods of sampling FRS for post-construction validation testing.
- Construction needs to be controlled to prevent FRS being placed too wet of optimum.
- FRS needs to be encapsulated to prevent erosion and fibres migrating into drainage and water courses.
- Further consideration needs to be given to the long-term sustainability and reuse of FRS.

The above would require further research prior to the implementation of any future trials. Given these issues plus the potential environmental challenges associated with reuse, it is considered that FRS technology and knowledge are not sufficiently developed for it to be adopted as a long-term slope repair technique.

Notwithstanding this, the trials demonstrated the potential for FRS to be used to improve the trafficability of soils. Further research was recommended to assess the use of FRS, created with sustainable and biodegradable natural fibres, for temporary ground improvement and the construction of temporary roads and tracks. It was particularly noted that such studies would need to address the key issue of the relationship between the design life of the works and the time taken for biodegradation of the fibres.

## **5 Life Cycle Assessment (LCA)**

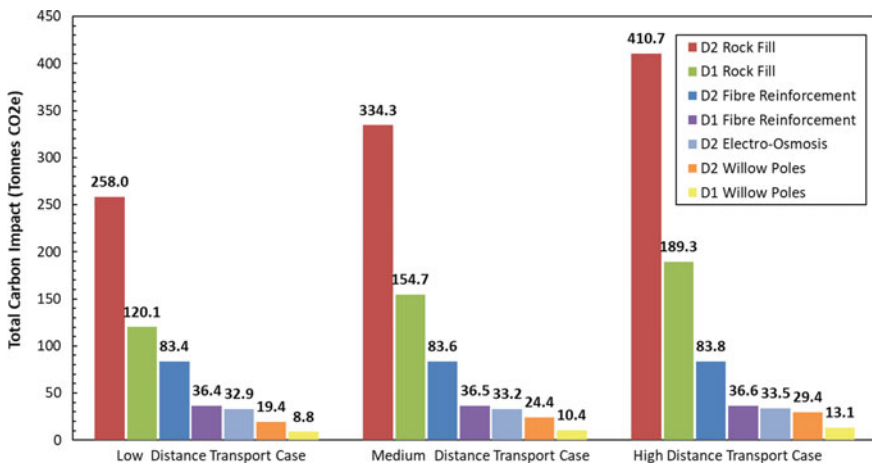
A cradle-to-site comparative LCA was undertaken to assess the environmental impact of the three techniques compared to a dig and replace rock fill control. In general, two failure depths were analysed, 1 m and 2.5 m, although the shallower depth was



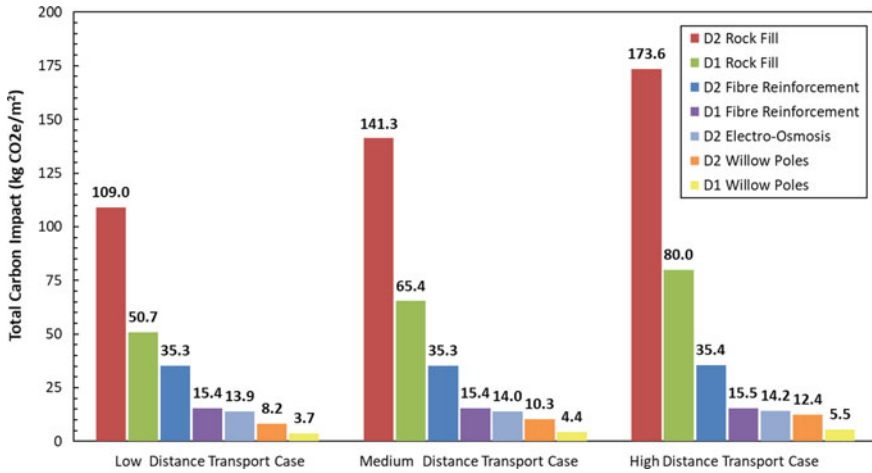
considered uneconomic for EKG, and this was omitted from the analysis. Results were presented for both total carbon (CO<sub>2</sub> equivalent) emissions (Fig. 7) and by area of slope repaired (Fig. 8), allowing alternative means of comparison.

It was found that at both failure depths and for all transport cases, the technique with the greatest environmental impact was the rock fill replacement, which is the conventional technique used as a control. At 1.0 m and 2.5 m failure depth, this technique resulted in 51–80kgCO<sub>2</sub>e/m<sup>2</sup> and 109–174kgCO<sub>2</sub>e/m<sup>2</sup> of failed slope, respectively. The use of willow poles had the lowest impact, resulting in 4–8kgCO<sub>2</sub>e/m<sup>2</sup> for the shallow and deep failure depths, respectively. For the 2.5 m failure depth, EKG was the second-best performing technique, with an average impact of 14kgCO<sub>2</sub>e/m<sup>2</sup>. The FRS technique had an impact ranging between 16–35kgCO<sub>2</sub>e/m<sup>2</sup>. Relative to the granular rock fill replacement, the impact of the willow pole technique was about 7–8%, EKG is 8–13%, and the impact from the FRS technique ranged from 19–32% of the control [7, 8].

For techniques requiring large quantities of materials and movements of these materials across substantial distances (such as the rock fill replacement control and willow pole planting), it was found that transportation accounts for more than 50% of the total impact. The environmental performance of the willow poles and EKG indicates significant environmental benefits and savings when compared to the rock fill replacement. The FRS technique also shows considerable carbon savings compared to rock fill, albeit that there are other issues with its use as highlighted in Sect. 4.



**Fig. 7** Total impact comparison between transport cases and technique [8]. Low, medium and high transport distances were 37 km, 52 km and 77 km, respectively



**Fig. 8** Areal impact comparison between transport cases and techniques [8]. Low, medium and high transport distances were 37 km, 52 km and 77 km, respectively

## 6 Future Trials

This project presented a primary opportunity to evaluate not only the efficacy of the three techniques used for slope repair but also the trials processes itself [9].

Guidance for future trial of innovative techniques covering key issues included:

1. Site selection including the slope morphology, ground conditions, defect type and failure mechanisms are well matched to the technique being evaluated; that accessibility of the site is such as to allow maintenance of the trial; and that network risks and environmental constraints have been fully evaluated.
2. Interaction with other works, in particular, to ensure that other routine site construction and maintenance operations do not undermine the value of the trial site.
3. Location recording and access, to ensure that the trial area can be accessed and that the records of the trial are stored accessibly; to this end, changes were made to the Highways England Geotechnical Data Management System [10] to facilitate more effective access to trial data and information.
4. Verification and monitoring of the trial are planned to ensure that the approach is appropriate to the site, that the technique and that the monitoring period is planned to be of adequate duration, and that those clear success criteria are set in advance.

## 7 Conclusions and Summary

It is concluded that the planting of live willow poles can be a successful approach to improve the stability of shallow slope failures. The evidence suggests that this stability can, with proper maintenance, be applicable in the long term at sites to which a sixty-year design life is applicable. This has been progressed, and design guidance and specification information has been developed as described.

Other opportunities for innovative applications within the field include the option to use willow poles planted at an angle to the vertical such that they act as soil nails and the use of other vegetative species whether to supply poles or to stabilise the surface of slopes subject to erosion. However, it should be noted that other species are not likely to confer the immediate reinforcement benefit afforded by willow poles unless they too can be configured as poles.

The lack of adequate post-EKG trial ground investigation, testing and monitoring prevent any clear assessment of the contribution of the various elements of EKG slope stabilisation to be made. A lack of longer-term monitoring and verification also currently hinders the adoption of the EKG treatment. It was concluded that further EKG trials, building on the lessons learnt, should be undertaken and documented to enable the technique to be taken into more regular use.

Lessons learned from the EKG trials and practical application will need to be incorporated into design guidance and specification in due course, building on the tentative guidance on design and specification for trials developed as part of this work.

It was also noted that the EKG technique has the potential to be a valuable means of groundwater removal and control in fine-grained soils with high water tables, a situation which is often problematic for permanent works, and particularly for the temporary works required to install permanent works.

FRS proved less successful, and the recommendations are for an effective cessation of its use in both trials and applications until such time as the issues surrounding testing, mixing, placement and end-of life/reuse can be fully addressed. Notwithstanding this, it was noted that the use of biodegradable reinforcement for temporary works showed some promise. Such a technique is essentially the fascine technique used to reinforce soft ground since at least Roman times [11], but plastics are now widely enough distributed that they may act as an anthropogenic marker horizon in the future geological record.

The use of innovative techniques such as the planting of willow poles and EKG clearly has the potential to reduce the environmental impact of slope stability measures and the impact on the travelling public. The relatively limited amounts of materials and equipment that are required on site can mean that access to the site can be made off-network, reducing the exposure of road workers, limiting the need for traffic management and thus limiting delays to the travelling public. The results of the LCA also suggest very strongly that carbon emissions are greatly reduced.

Recommendations are also made with a view to improve the value that is rendered from future trials.



## References

1. Winter MG, Corby A (2012) A83 rest and be thankful: ecological and related landslide mitigation options. Published Project Report PPR 636. Transport Research Laboratory, Wokingham
2. Winter MG, Seddon R, Nettleton IM (2018) Innovative geotechnical repair techniques: effectiveness of willow poles. Published Project Report PPR 874. TRL, Wokingham
3. Steele DP, MacNeil DJ, Barker D, McMahon W (2004) The use of live willow poles for stabilising highway slopes. TRL Report TRL619. TRL, Wokingham
4. Anon.: Road Management Services. A419 Rat Trap. Geotechnical Feedback Report. HAGDMS Report No. 28565. Electrokinetic Limited, Newcastle Upon Tyne (2015). (Unpublished.)
5. Nettleton IM, Seddon R, Winter MG (2018) Innovative geotechnical repair techniques: effectiveness of electrokinetic geosynthetics. Published Project Report PPR 890. TRL, Wokingham
6. Seddon R, Winter MG, Nettleton IM (2018) Innovative geotechnical repair techniques: effectiveness of fibre reinforced soil. Published Project Report PPR 873. TRL, Wokingham
7. Leal D, Winter MG, Seddon R, Nettleton IM (2018) Innovative geotechnical repair techniques: comparative life cycle assessment. Published Project Report PPR 889. TRL, Wokingham
8. Leal D, Winter MG, Seddon R, Nettleton IM (2020) A comparative life cycle assessment of innovative highway slope repair techniques. *Transp Geotech* 22:1–8
9. Winter MG, Nettleton IM, Seddon R (2018) Innovative geotechnical repair techniques: recommendations and guidance for management of future Highways England trials with innovative techniques. Published Project Report PPR 891. TRL, Wokingham
10. Power CM, Patterson DA, Rudrum DM, Wright DJ (2012) Geotechnical asset management for the UK Highways Agency. *Eng Geol Spec Publ* 26:33–39
11. Winter MG, Watts GRA, Johnson PE (2006) Tyre bales in Construction. Published Project Report PPR080. Transport Research Laboratory, Wokingham

# Challenges Associated with Construction of Highways on Steep Side Slopes Covered with Colluvium from Hunter Expressway Project Australia



Sudarshan Aryal and Robert Kingsland

**Abstract** A section of the recently completed Hunter Expressway in the Hunter Valley, Australia, traverses steep side sloping topography covered by colluvium overlying weathered coal measures rocks. The rock mass contained seams of very low-strength and highly moisture-sensitive tuffaceous claystone interbedded in sandstone, siltstone and coal. The blocky and transmissive sandstone beds overlay the weaker, aquiclude siltstones and claystones creating a geological terrain vulnerable to rockfalls, surficial colluvium instability and deeper translational failures on the slope next to the alignment. The design of the motorway vertical alignment required a 10 m high reinforced soil wall (RSW) to retain the fill on the downslope side. Foundation works for the RSW were an early construction activity in the area. The construction of the RSW involved a large foundation excavation into the colluvial capped slope which had the potential to destabilize global stability of a marginally stable slope whilst boulder fall hazards presented both a construction and operational risk to be managed. Therefore, the construction of the RSW foundation was assessed as a high-risk activity. The team had to deal with challenges of additional hazards associated with inclement weather during excavation of the foundation. This paper discusses how the risks and challenges were successfully managed during construction through a broad range of mitigation measures including implementation of a responsive design development strategy, stakeholder engagement, on-site close geotechnical engineering oversight and staging of works which led to good design outcomes and allowed the works to be completed without any occurrence of slope instability or safety incident.

**Keywords** Slope · Instability · Australia · Tuffaceous · Claystone

---

S. Aryal (✉)

Mott MacDonald Australia Pty Ltd, L10 383 Kent Street, Sydney 2000, Australia  
e-mail: [sudar.aryal@mottmac.com](mailto:sudar.aryal@mottmac.com)

R. Kingsland

WSP Australia Pty Ltd, L27 680 George St, Sydney 2000, Australia

## 1 Introduction

This paper presents a case history of successfully managing risks of slope instability during construction of a 10 m high reinforced soil wall (RSW) on a steep sloping ground (the site) as part of Hunter Expressway Motorway Project, in the Hunter Valley, Australia. This retaining wall, identified as RW17 in the project documentation, was required to support the carriageway from the downhill side on the existing hillside slope. Foundation excavation for the reinforced block of RW17 involved up to 16 m of excavation of the sloping ground across the carriageway. The excavation undermined stability of the upslope section including temporary earthworks for access tracks, catch drains and part of the existing hillside next to the opposite side of carriageway. Signs of instability were observed at several locations including tension cracks on compacted earthworks, concrete lining for catch drains and in colluvium close to the toe of the existing slope at the edge of carriageway. Groundwater seepage from uphill was visible in the excavation. These observations triggered several actions: immediate review of the construction methodology considering the potential slope failures, review of the retaining wall design, risk mitigation measures to address landslide risks, further geotechnical investigations to more accurately characterize the ground conditions and consideration of potential impacts to the construction program and budget.

This paper describes the project, the original retaining wall design concept, the construction phase mapping and investigations to characterize the ground, the retaining wall design revision and the assessment of slope risk and mitigation measures adopted to address the risk. The final outcomes demonstrate the power of the observational approach.

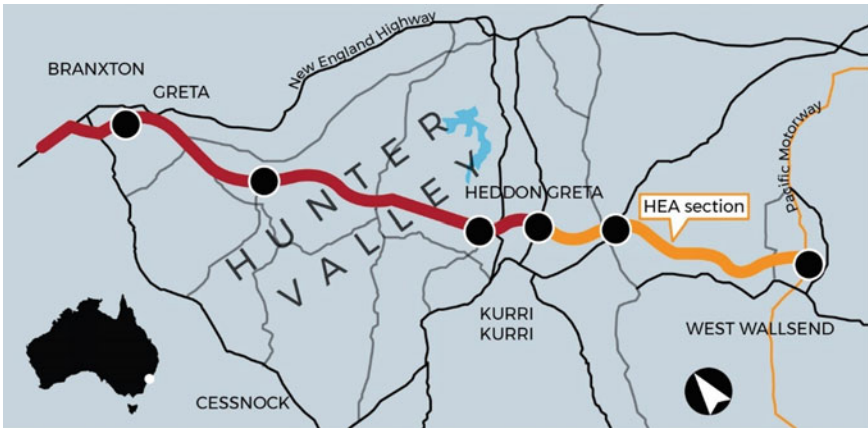
## 2 The Project

### 2.1 Project Description

The \$1.7b (AUD) Hunter Expressway is located 140 km north of Sydney and involved construction of a new 40 km long, four-lane divided carriageway motorway link between the M1 Pacific Motorway near Seahampton, west of Newcastle and the New England Highway, west of Branxton.

At the time, the Hunter Expressway was one of the largest and most complex projects undertaken in New South Wales, presenting environmental, geographical, Aboriginal and European heritage, technical and time frame challenges.

Delivery was established under two contracts: Hunter Expressway Alliance (HEA) for the eastern 13 km and Hunter Expressway Design and Construct (HED&C) contract for the western 27 km section (Fig. 1).



**Fig. 1** Hunter Expressway Project Location with Alliance section shown in orange

The eastern section of the expressway includes the rugged Sugarloaf Range area underlain by old coal mine workings at depths of up to 120 m. Construction commenced in late 2010, and the Expressway was opened to traffic in March 2014.

The Expressway provides a new east–west connection between Newcastle and the Upper Hunter and has reduced travel times, relieved congestion and provided for future traffic growth.

## 2.2 Geological Conditions

The alignment at the site trends along a westerly facing slope of the Sugarloaf Ranges which is underlain by the sediments belonging to the upper part of the Newcastle Coal Measures (NCM). The upper part of the NCM sequence comprises a relatively thick unit of coarse-grained sandstone interbedded with beds of conglomerate, tuffaceous and carbonaceous sedimentary rocks with lenses of coal. The tuffaceous sedimentary rocks comprise tuffaceous sandstone, tuffaceous siltstone and tuffaceous claystone. The tuffaceous claystones are low-strength rocks that are particularly susceptible to weathering and are highly reactive [1].

Structurally, these rocks are cut by a dominant high-angled joint set trending north-north-east to east to north–east with a subordinate joint set trending to the west. Associated with the dominant joint set are some low to moderately angled joints, usually clay lined. The formation also forms prominent escarpments alongside deep valleys which have exploited prominent tectonic joint sets. Valley cutting and associated horizontal stress relief of these thicker rigid sandstone units have resulted in irregular interbed fractures. Colluvial debris of variable thickness masks the frontal slope of these escarpments. The Sugarloaf Ranges are underlain by former

underground coal mine workings predominantly in the Borehole Seam which was mined in various collieries during the early 1900s at typical depths of 70–100 m [2].

### 3 Design Development Phase

#### 3.1 Site-Specific Details

The portion of the Expressway presented in this paper (the “site”) is defined in project nomenclature as Fill 9, Cut 9 and retaining wall RW17. The site traverses a south facing hillside slope in an east–west orientation. The Fill 9 triangular profile embankment is approximately 260 m long with a maximum RW17 height of 11 m at the edge of westbound (WB) carriageway. The edge of the eastbound (EB) carriageway intersects the lower slopes of a thickly vegetated steep ( $28^\circ$  to horizontal) hillside slope. Within the footprint of the carriageway, the ground slopes ease to  $14^\circ$  to horizontal. An aerial view of the site area together with a cross-sectional view from the east looking towards west is captured in Fig. 2.



Fig. 2 Aerial view of site (a) and side view looking west (b)

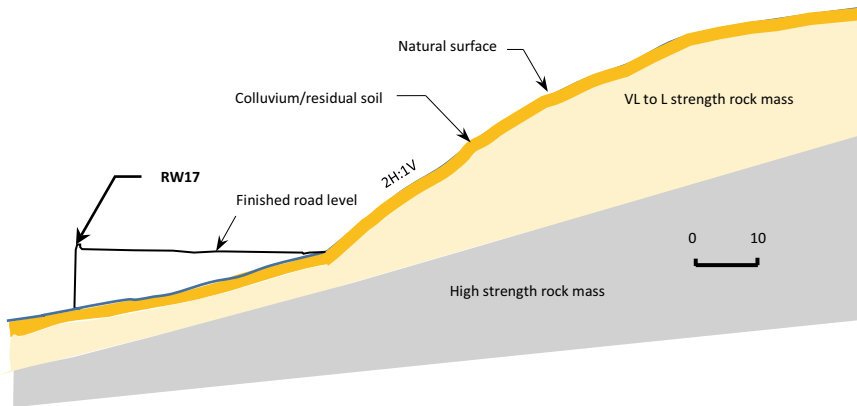


Fig. 3 Simplified geotechnical model for design (design phase)

### 3.2 Geotechnical Basis for Design

**Geotechnical Data.** The detailed design for Fill 9 and RW17 was developed from a geological model inferred from 4 boreholes and 6 test pits. No boreholes were available at the location of RW17 due to ecological and access constraints.

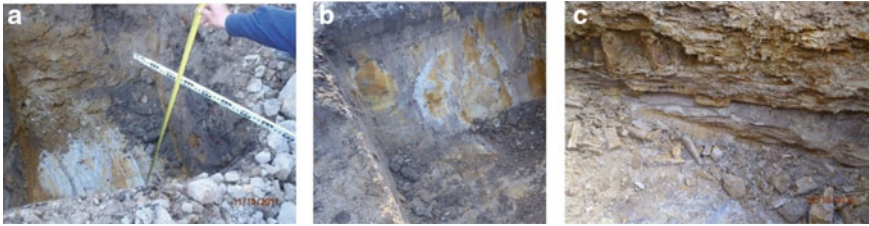
A site geotechnical walkover was carried out; however, the densely forested slope conditions prior to construction clearing, reduced visibility of geological features. From the available data, a simplified geotechnical model was postulated as shown in Fig. 3. This consisted of a thin colluvial layer over fractured sandstone, mostly with low and very low rock substance strength.

**Design.** Foundation design for Fill 9 included stripping of topsoil and vegetation, removal and replacement of unsuitable material and terracing the sloping foundation. Retaining wall RW17 was designed to be founded on weathered sandstone after stripping of the overlying colluvial layer.

## 4 Construction Phase

### 4.1 Construction Works for RW17

**Planning for Foundation Excavation.** Foundation works for RW17 were one of the first construction activities at the site. These included boxing out of the sloping surface to provide a stepped level foundation for the reinforced soil wall (RSW) block up to 11 m wide plus a specified parameter backfill zone extending a further  $H/2$  (i.e. up to 5 m) behind the block forming a temporary excavated face up to 4 m high below the Fill 9 embankment. This substantial excavation into the steep cross-slope would present a significant risk to undermining the existing slope.



**Fig. 4** RSW foundation test pits exposing **a** tuffaceous claystone (light grey-brown on photo); **b** colluvial materials; and **c** fractured sandstone bedrock

**Excavation Works.** Construction access tracks and temporary catch drains were first constructed within the upslope side of the carriageway to allow for excavation works to commence at the site of RW17 on the downslope side.

Six probing test pits were excavated below the stripped surface at different chainages along the wall footing to expose the foundation level to confirm design assumptions. The test pits revealed variable subsurface profiles exposing weak tuffaceous claystones, carbonaceous bands and colluvium below the designated foundation level (Fig. 4). This identified a potential for a translation failure if the weak layers were continuous that warranted further investigation.

As the excavation progressed into the existing slope, it became more apparent that the tuffaceous/carbonaceous bands along with colluvial gullies extended under the expressway foundation.

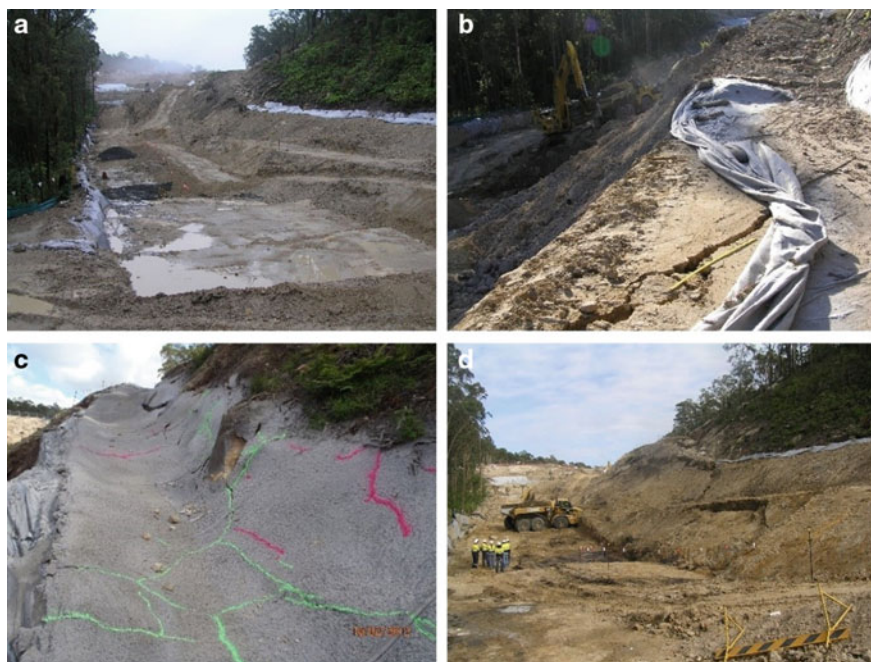
As interim measures, excavations were secured by providing batters suitable for temporary stability, excavated materials were stockpiled in temporary berms around the excavation, and a concrete-lined catch drain was installed at the toe of the existing slope above the site to collect surface runoff (Fig. 5).

**Inclement Weather.** During the foundation excavation, episodes of sustained rain occurred in the area impacting the temporary earthworks. Tension cracks developed upslope of the excavation indicating ground movement, seepages were observed on the fill slopes and additional cracks formed on the concrete-lined drain (Fig. 5); a section of which eventually failed and dislodged down the slope.

**Action Plan.** Following the evidence of instability, an emergency task force team was set up, and an action plan was developed. All construction works ceased and personnel and equipment were moved out of the area which was then cordoned off. Urgent repair works necessary to make the area safe and secure were then completed which included reinstatement of the damaged drain, ripping and recompaction of the cracked berms, a network of temporary subsoil drains installed, reshaping and sealing off the earthworks structures.

**Subsoil Drains.** Seepages occurred in several locations through temporary berms, colluvium and carbonaceous bands in the bedrock. Under the supervision of the on-site geotechnical engineer, subsoil drains targeting major seepage areas were installed by progressively trenching and backfilling in short sections (10 m typically) as one operation. Drains comprised a 300 mm wide trench typically 1–2 m deep with a





**Fig. 5** Impact of rain on work-in-progress earthworks: **a** view following a rain episode, **b** tension crack on temporary berm upslope from RSW foundation excavation area, **c** cracking observed on concrete lining of catch drain along the toe of existing hill slope and **d** view of a slip on temporary berm batter

100 mm slotted PVC pipe with gravel surround, wrapped in geotextile. The network subsoil drains were funnelled to a triple pipe subsurface trunk drainage which was extended under the foundation of RSW to daylight on the slope downstream of RSW, sized to accommodate the large seepage flows.

No further cracking or widening of existing cracking was observed following installation of the drainage.

**Potential Global Slope Instability.** Along with deployment of the repair works directed at stabilizing the area to make it safe for recommencing the works, a “bigger-picture” issue of global stability during construction and in the long term was also a focus of the task force.

The presence of tuffaceous claystone layers beneath the sloping ground under the RW17 wall raised concerns about the potential global instability of the RSW. Tuffaceous claystones are associated with many slope instability issues in the Hunter Region due to their persistence and very low shear strength.

It was also postulated that these bands may underlie the hillslope above the EB carriageway, which would pose a significant risk to global instability for the entire Fill 9 site, not just RW17. This triggered a direction by the project senior management for a comprehensive risk assessment of the current design, construction methodology



and the long-term stability of this expressway section and its potential impact on the in-service expressway.

## 4.2 Risk Assessment

Several risk workshops involving relevant stakeholders including senior construction and design staff and the client representatives were held. Key actions resulting from this process included:

- Thorough review of the stability of the entire site as well as design review of each of Fill 9, RW17 and the existing slope above separately
- Further geotechnical investigation and testing including, detailed geological mapping of the slope, boreholes, test pits and shear strength tests on claystone seam samples [3, 4]
- Boosting of full-time geotechnical advisory staff availability for inspection/mapping, assessment and advice during foundation earthworks and temporary structures
- Work safety measures with restricted access to the site, full-time spotters for further earthworks construction, daily pre-start risk assessment for all workers in the area
- Daily review of construction program to ensure a safe construction environment.

## 4.3 Review of Stability of RW17

**Further Geotechnical Investigations.** In addition to existing boreholes in the vicinity of RSW location, four more boreholes were completed along the RSW footprint to collect subsurface geotechnical data from deeper levels under the RSW foundation for stability review (Fig. 6).

**Findings.** Interpretation of geotechnical data indicated non-homogeneity vertically and laterally with areas of colluvium overlying weathered sandstone interlayered with coal and tuffaceous claystones (Fig. 7). The findings confirmed that the actual foundation conditions were different to what was assumed (i.e. homogeneous bands of weathered sandstone under thin colluvium) for detailed design. These investigation outcomes triggered a revision of the geological model and redesign of the RSW foundation incorporating slope stabilizing piles to satisfy long-term stability. The design of stabilizing piles for RW17 is discussed in more detail in [4].

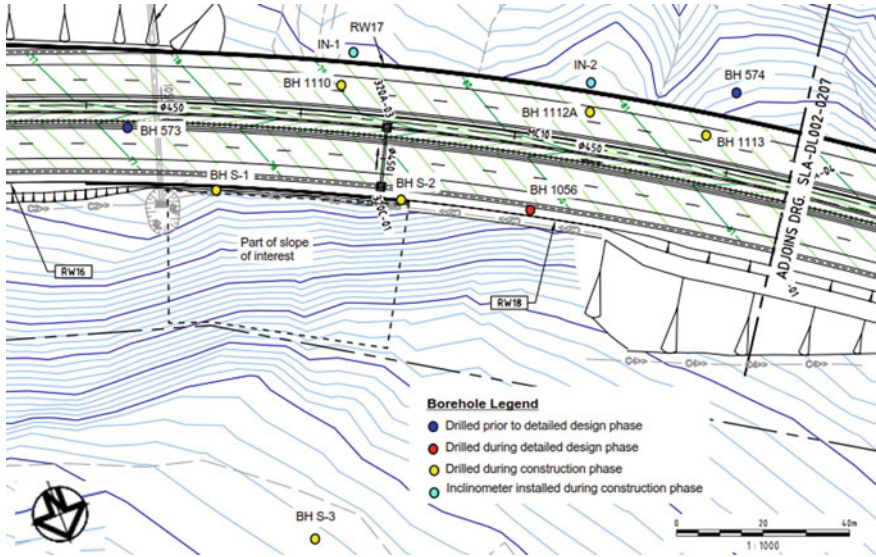


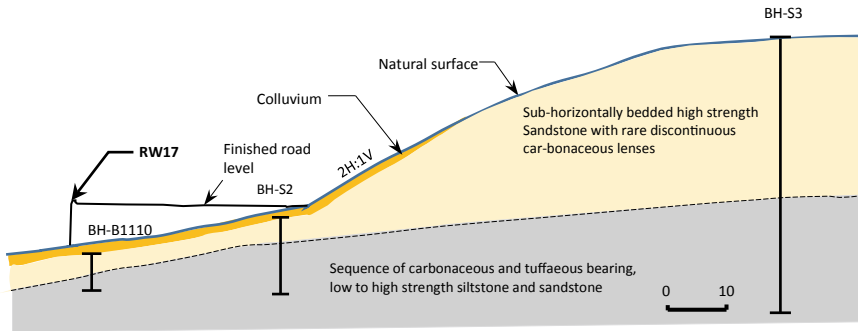
Fig. 6 Borehole locations



Fig. 7 RSW foundation exposing different materials: in situ rock and compacted colluvium

#### 4.4 Fill 9 and Natural Slope Above

Stability of Fill 9 and the natural slope above the project was assessed for two possible scenarios: deep-seated translational failure and slope failure associated with colluvium.



**Fig. 8** Revised geotechnical model (construction phase)

**Investigations for the Presence of Deep Seated Weak Planes.** The gap in subsurface information between the existing boreholes in the vicinity of the EB carriageway was investigated with two boreholes, positioned at the edge of EB carriageway and one borehole drilled from the crest of the hillslope some 70 m north from the alignment. The boreholes targeted the deep subsurface profile details to investigate the risk of global translational failures on weak layers (tuffaceous?) within high strength sandstones.

A review of geological conditions based on more complete data set available indicated that there was a very low risk of global instability as the slope was formed with high and very high strength sandstones and siltstones with no weak layers to a depth of 31 m (around the foundation level of Fill 9). A horizontally bedded sequence incorporating tuffaceous and carbonaceous layers underlies this sandstone unit (Fig. 8).

**Investigation of Colluvium.** Detailed geotechnical mapping and four test pits were completed to assess the nature and distribution of the colluvial cover on the natural slope above the expressway.

The results indicated that the colluvium mostly comprised sandstone boulders, sand and loamy soil, thicker in the lower part of the slope close to the expressway level with occasional unstable boulders resting on fractured in situ sandstone rock mass further up the slope. The fill/colluvium layer thickness in the lower part was variable ranging from about 2 to 5 m overlying a similar bedrock sequence as encountered in the deep borehole. This variability suggested presence of localized narrow infill gullies. The majority of this material would be removed as part of the foundation preparation for Fill 9 and RW17, and therefore, would have no impact on the stability of the road formation.

Despite this favourable outcome, boulder falls remained as a hazard which could impact serviceability of the expressway in the operation phase.

### 4.5 Boulder Fall Risk Mitigation

**Slope Risk Rating.** Slope risk rating, as per RMS slope risk analysis ver. 4 [5], a project requirement for all slopes, was carried out for the existing natural slope. The results showed that there was an unacceptably high risk to road users for boulder fall hazards.

**Risk Mitigation Measures.** The following mitigation options were workshopped with representatives of design, construction and the client:

- Option 1—Remove colluvium (eliminate boulder fall hazard)
- Option 2—Barrier structure (pile wall, precast L-shaped wall, rock fence, etc.) at the toe of the slope (manage risk)
- Option 3—Combination of boulder removal and barrier structure (manage hazard and risk)
- Option 4—Provision of a fall zone (minimize consequence).

The adopted design solution comprised a combination of selected boulder removal with a fall zone and low concrete barrier at the toe. Rockfall analysis was used to assess the required width of the fall zone (Fig. 9).

**Implementation of Design.** Large boulders (estimated 1 tonne or more) with potential for dislodgement and rolling were identified and removed. The fall zone and concrete barrier provided mitigation for remnant boulder falls (Fig. 10).

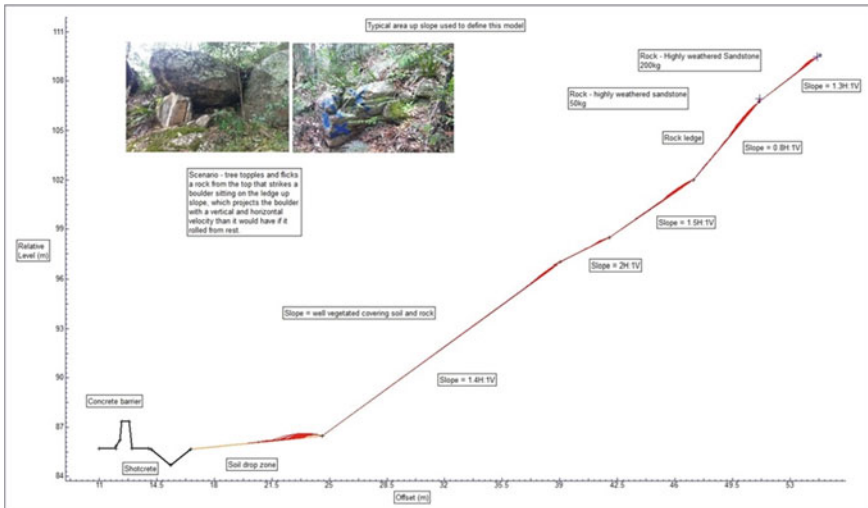


Fig. 9 Output of boulder fall analysis



**Fig. 10** View at constructed solution

## 5 Instrumentation and Monitoring During Construction

Instrumentation and monitoring of the Fill 9/RW17 area comprised daily visual monitoring by geotechnical staff during construction works and slope movement monitoring using two inclinometers installed within 2 m in front of the RSW face. The maximum displacement recorded by the inclinometers several months following completion of the RSW block to full height was 5 mm, well within the predicted value of 20 mm [4].

## 6 Conclusion

A coordinated approach from all relevant stakeholders in dealing with complex situations with a common spirit to deliver the project successfully drove the actions to find an optimal solution. Availability of geotechnical staff on site full time proved to be crucial in making informed risk-based engineering decisions which took into account work safety during construction, quality and standard of the works to project completion and the client's perspective of the whole-of-life costs in the operation and maintenance phase.

Efforts during construction on targeted geotechnical investigations specific to the geotechnical issues unearthed as construction progressed provided a great benefit to the project success as more site and issue-specific data became available enabling adjustment to design to suit the exposed subsurface geotechnical conditions.

**Acknowledgements** The authors wish to acknowledge the support of WSP Australia and Mott MacDonald in the preparation of this paper along with the NSW Roads and Maritime Authority for approval to publish.

## References

1. Aryal S, Kingsland R, Rees P, Russell G, Stahlhut O, Wheatley, D (2013) Hunter Expressway, Australia: dealing with poor ground and subsidence. In: Proceedings of the Institution of Civil Engineers, Civil Engineering special issue 166. ICE Publishing, London, Issue CE5, pp 22–27
2. Kingsland R, Mills K, Stahlhut O, Huang Y (2012) Mine subsidence treatment and validation strategies on Minmi to Buchanan section of the Hunter Expressway. In: Proceedings of the 11th Australia–New Zealand Conference on Geomechanics—Ground Engineering in a Changing World, 15–18 July 2012, Crown Conference Centre, Melbourne, Australia
3. Och D, Kingsland R, Aryal S, Zhang H, Russell G (2014) Case studies of post investigation geological assessments. In: Lollino G et al. (eds) Engineering geology for society and territory, vol 6, pp 387–391
4. Zhang H, Yau S, Kingsland R, Och D (2013) Design of slope stabilizing piles for reinforced soil walls on Hunter Expressway. In: Proceedings of Australian Geomechanics Society Sydney Chapter Symposium, November 2013, pp 115–124
5. Roads and Maritime Services (2014) Guide to slope risk analysis, Version 4. <https://www.rms.nsw.gov.au/business-industry/partners-suppliers/disciplines/geotechnology.html>

# **Asset Management**

# Analysis of BIM Implementation on Railway Infrastructures Through an Application to Rail Track Rehabilitation and Inspection



José Neves , Zita Sampaio , and Manuel Vilela

**Abstract** Having the aim of promoting the application of BIM—Building Information Modeling—in the railway sector, this paper’s main objective is to analyze the BIM implementation in the particular case of rail track rehabilitation and inspection. BIM enables the computational development of projects during their lifecycle including all the phases. Three-dimensional (3D) modeling using Civil 3D® software was applied to the rehabilitation of a rail track in service. The following tasks were carried out: (1) the modeling of the geometry of the railway infrastructure; and (2) the capacity analysis to extract diverse information from the model, in particular the geometric parameters of the rail track: gauge and transversal leveling. Revit® software was also used to model the project. Families were created relating to the sleepers and fastenings and to the rails. Other rail track components, such as the ballast, sub-ballast, geosynthetics, and foundation, were generated as slab layers in the infrastructure component. In order to create a four-dimensional (4D) model that includes the time factor, Navisworks® software was used. The 4D model allows for simulation of the rehabilitation sequence of the rail track, including the application of geotextile and geogrid under the ballast layer. It was concluded that the use of the 3D model can present limitations to the implementation of the BIM methodology, particularly with respect to interoperability in the transference of models between softwares. Regarding the inspection and maintenance of the rail track, some limitations were observed in the storage and processing of relevant information.

**Keywords** BIM · Railway infrastructures · Rail track rehabilitation

---

J. Neves (✉) · Z. Sampaio  
CERIS, IST, Universidade de Lisboa, Avenida Rovisco Pais, 1049-001 Lisboa, Portugal  
e-mail: [jose.manuel.neves@tecnico.ulisboa.pt](mailto:jose.manuel.neves@tecnico.ulisboa.pt)

M. Vilela  
IST, Universidade de Lisboa, Avenida Rovisco Pais, 1049-001 Lisboa, Portugal



## 1 Introduction

Generally speaking, the architecture, engineering, and construction (AEC) industry is increasingly implementing the Building Information Modeling (BIM) methodology in the context of Industry 4.0. BIM is a concept supported in advanced computational technologies and allows for the development of collaborative projects along the various phases of a structure's life cycle: i.e., planning, design, construction, maintenance, management, and demolition [1, 2]. However, BIM is less frequently applied in the segment of transportation infrastructures (roads, railway, airfields, tunnels, bridges, and ports). Given the increasing interest, more research and practice are needed on BIM implementation in the sector of transportation infrastructures [3, 4].

The integration of BIM in railway projects, as in other transport infrastructures, brings important advantages and benefits, namely: greater efficiency in terms of construction and maintenance management; operation management; cost control; sharing of information; and activity coordination [5–10].

Various computational tools currently being applied to transportation infrastructures can be used in a perspective of BIM implementation. Infracore<sup>®</sup> is often used to support the spatial analysis of the infrastructure and has an efficient degree of interoperability with Revit<sup>®</sup> and Civil 3D<sup>®</sup> [11]). Civil 3D<sup>®</sup> emerged in the 1980s, but it is a software that was not developed from a BIM methodology perspective. It is oriented to create, manage, visualize and analyze data related to general civil engineering projects. It has only recently developed interoperability capacities, allowing for the implementation of BIM methodology [12]. In the case of transportation infrastructures, the most common software programs are Revit<sup>®</sup> and Navisworks<sup>®</sup> from Autodesk<sup>®</sup>. They are well-known BIM-based tools and are regarded as the most comprehensive programs for civil engineering applications [3].

With a view to promoting and developing BIM implementation in railway sector, this study has defined its main objective to analyze the implementation of BIM methodology in the particular case of rail track rehabilitation and inspection. The paper presents: (1) three-dimensional modeling (3D) of the geometry of railway infrastructure, including the application of geosynthetics in the stabilization of the ballast layer; (2) the four-dimensional modeling (4D) related to the construction activity planning; and (3) the capacity analysis to extract diverse information from the model, in particular the geometric parameters of the rail track, which are of use for the quality monitoring: Track gauge and transversal leveling.

## 2 Methodology

**General framework.** Figure 1 presents an overview of the proposed methodology to implement BIM in the context of existing transport infrastructure rehabilitation.

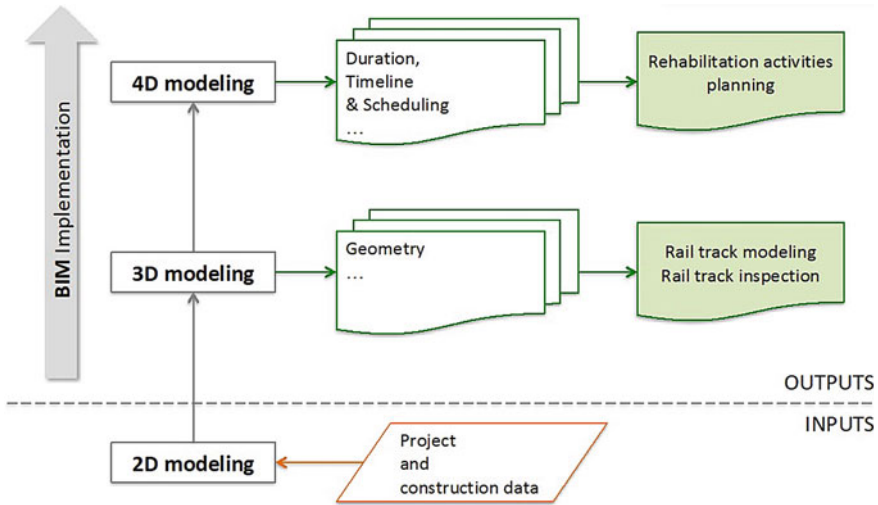


Fig. 1 Schematic illustration of the methodology

Indeed, the rehabilitation action presents an opportunity to initiate the implementation of BIM in this sector. Accordingly, based on all project and construction data available, mostly interpreted from the technical drawings (2D) used as inputs, the process can be developed towards the definition of several activities supported in the model. The research seeks to demonstrate the implementation of 3D and 4D levels of information using BIM software. However, this general methodology can be also implemented up to 5D (costs), 6D (sustainability) and 7D (maintenance) levels [8].

**3D Modeling.** 3D modeling, the most commonly known characteristic of BIM, enables participants to not only see the infrastructure in 3D before earthworks, but also to automatically update said views throughout the infrastructure life cycle, from initial conception to final demolition. 3D modeling also allows the participants to manage their multidisciplinary collaboration more effectively in modeling and analyzing complex spatial and large constructions, as is the case of transportation infrastructures. This BIM dimension is also important for reducing rework. In this paper, 3D modeling was performed using Civil 3D® and Revit® software. For the geolocation and ground modeling, Infracore® software was used. The main outputs of 3D modeling are a more efficient definition and representation of railway geometry and components.

**4D Modeling.** By introducing the time element, a 4D model was created and used to represent the construction site planning and related activities. This fourth dimension of BIM enables the participants to extract the information in each construction phase and to visualize the progress of the construction activity. 4D modeling can provide enhanced control over conflict detection and over the complexity of changes that frequently occur during the construction work. At this level, construction activities and team organization can benefit in terms of planning and scheduling

optimization. The main outputs of 4D modeling are the definition over time of the rehabilitation phases, production flow, and the activities planning and scheduling.

### 3 Case Study

An important renewal of the main railway network is currently being carried out in Portugal by the national railway agency [13]. The case study presented herein is for a section of an important double-track railway line, with a total length of 35 km and characterized by mixed and heavy traffic (passengers and cargo). UIC 60 rails, VAX LU41 NG bi-block concrete sleepers, and the corresponding fastenings were the main components of the track structure. The track gauge was the Iberian type: 1668 mm. This railway line is classified as D4 (22.5 ton/axle; 8 ton/m), according to UIC 700-O. Mainly due to stabilization and drainage problems, this railway section was rehabilitated in 2016 as follows: the complete renovation of the rail track through replacement of rails, sleepers, and fastenings; the placement of a new ballast layer with a thickness of 25 cm; the renovation of the drainage system; the update of the electrification system.

Figure 2 shows the existing fouled ballasted rail track. The passage of traffic over time and a deficient sub-drainage system resulted in the modification and contamination of the ballast aggregates. The infiltration of materials from the subgrade and the surface led to large amounts of smaller particles and the presence of clayed soil. This modification of the ballast layer has negatively affected, over time, the general quality of the rail track, requiring more continuous and expensive maintenance action.

Due to the restrictions that come with a railway in service, the rehabilitation of the ballasted rail track was carried out during the night period (from 5:00 am to 7:00 am). In addition to the laying of a new rail track, the rehabilitation has mainly consisted of



Fig. 2 Cross-section of the ballasted rail track [14]

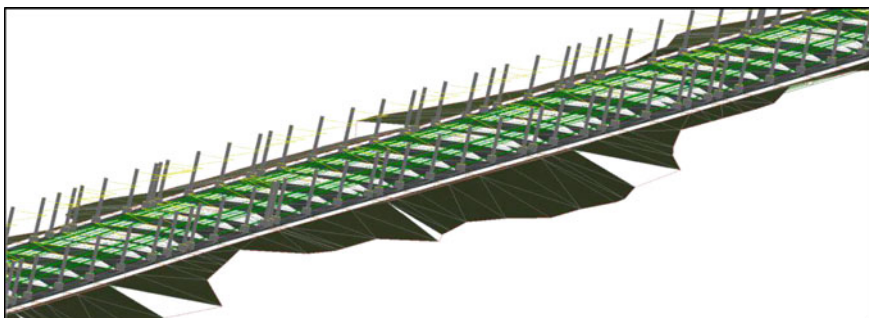


**Fig. 3** Application of geotextile and geogrid [14]

the application of non-woven geotextile and triaxial geogrid after the general removal of the contaminated ballast layer. The geotextile has the functions of separation and filtration with regard to the subgrade soil. The geogrid serves to stabilize the lateral movements of the ballast particles (lateral restraint). A track-mounted undercutting machine rolled out both the geotextile and the geogrid and finally the new ballast layer of 25 cm thickness was placed on top (Fig. 3).

Based on the project and construction data, available on printed versions and digital files of drawings, a straight alignment with a length of 1787 m was selected to be modeled in Civil 3D®. The 3D model includes the subgrade, sub-ballast, and ballast layers; rails, sleepers, and fastenings; sub-drainage components (lateral piles); and catenary system (vertical poles and cantilever).

The geolocation and ground modeling of the construction site was performed through the application of Infracore® software and was then transferred to Civil 3D®. Vertical and horizontal alignments of the railway line were established and, finally, the cross-section was designed. Figure 4 shows the perspective view of a generic part of the 3D model created for the case study. This model was then used for BIM implementation through 3D and 4D modeling using Revit® and Navisworks® software programs, respectively. Based on the 3D model, it was possible to analyze the possibility of extracting information from the model, in particular the geometric parameters of the rail track: gauge and transversal leveling. The 4D model describes



**Fig. 4** The 3D model of the railway generated using Civil 3D® [15]

the sequence of the rail track rehabilitation, including the application of geotextile and geogrid. This BIM model allows for planning the rehabilitation techniques (Fig. 1).

## 4 Results and Discussion

### 4.1 Rail Track Modeling

An attempt was made to export the model created in Civil 3D® to Revit® software. However, due to interoperability difficulties between the two software programs, a new 3D model was developed in Revit®. Based on BIM library, families of parametric objects related to the railway components were created: rails, concrete sleepers, fastenings; rail track substructure (sub-ballast and ballast layers, geosynthetics, and subgrade); and sub-drainage system (two identical pipes placed in a lateral position).

Generally speaking, the various layers of track substructure were modeled as slab elements (subgrade, sub-ballast, ballast, and geosynthetics layers). The corresponding properties of BIM parametric objects were layer thickness and material type: sand in the subgrade and gravel in the ballast/sub-ballast layers. In the case of the geotextile and geogrid, the procedure was similar: The horizontal dimensions were  $25.6 \times 12.0 \times 0.45 \text{ m}^3$  and the thickness was 5.4 mm (assumed value) (Fig. 5). A new material, polypropylene, was created with specific thermal and mechanical properties. Supplementary descriptive and product information on the class, manufacturer, and model was provided (Fig. 6).

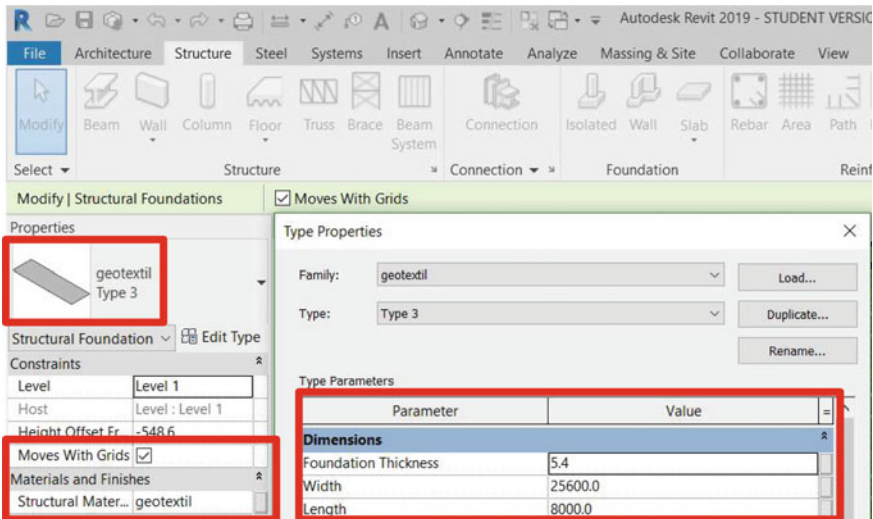


Fig. 5 Geotextile and geogrid modeled in Revit® [15]

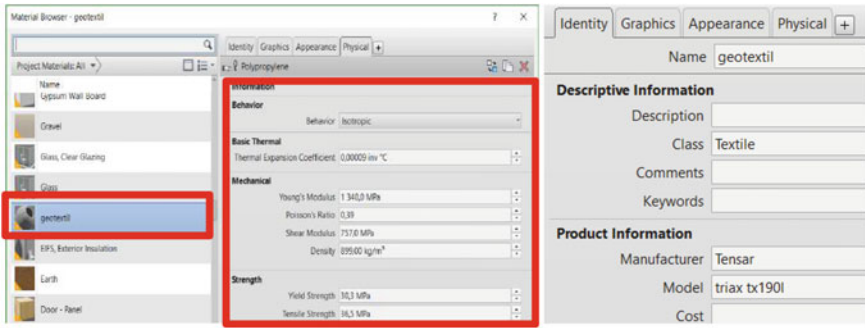


Fig. 6 Association of geotextile and geogrid properties in Revit® [15]

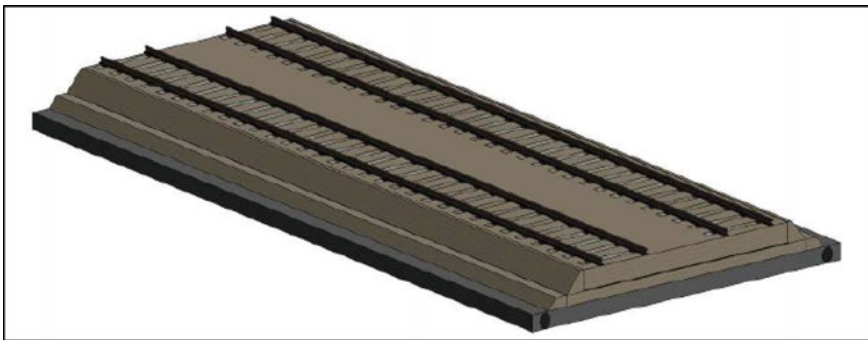


Fig. 7 Final 3D model of the rail track generated using Revit® [15]

Figure 7 represents a perspective of the global 3D model created in Revit® including rail track structure components and lateral drainage pipes.

#### 4.2 Rehabilitation Activities Planning

The 4D model was developed in Navisworks® by associating the time parameter to the construction steps, thus allowing for the rail track rehabilitation planning and scheduling. The 3D model developed in Revit® was successfully exported. To simulate the rehabilitation process, seven activities were defined: (1) existing rail track; (2) replacement of rails, sleepers and fastenings; (3) existing substructure; (4) removal of ballast; (5) application of the geotextile and the geogrid; (6) ballast tamping; and (7) final rail track tamping. The existing rail track and substructure were not real activities but they were included in order to achieve a more realistic simulation of the rehabilitation. The sets (groups of elements) were created through selection



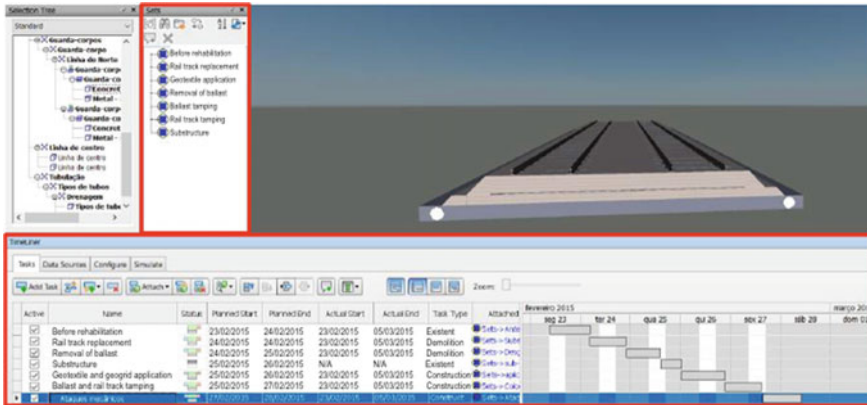


Fig. 8 Sets menu and Gantt chart [15]

of the geometric components of the 3D model associated to each construction phase (Fig. 8).

Subsequently, the duration of each activity was added in accordance with the information obtained from the real work development. Figure 8 illustrates the Gantt chart established directly in Navisworks® for a rail track segment. The Gantt chart was also modified, so that the different construction phases could be visualized.

### 4.3 Rail Track Inspection

Throughout the life cycle of a rail infrastructure, rail track monitoring is an important activity, with a view to ensuring safe conditions for the rail traffic. Regular inspections are aimed at identifying and controlling structural degradations and the overall conditions of the rail track components. According to standard EN 13848-1 [16], the main parameters to consider in the track geometry are the track gauge, leveling, alignment, and twist.

Through the model developed in Civil 3D® it was possible to consider only the track gauge and the transversal leveling. The track gauge is the minimum measured distance between the heads of the rails. Transversal leveling is the difference between the rail surface and a horizontal reference plan.

However, the functionality of these geometric parameters is very simplified and significant improvements should be carried out in the future in a perspective of regular rail track monitoring based on BIM methodology. Most railway agencies and companies have their own quality monitoring systems. It would be desirable to promote the implementation of these management systems from a BIM methodology perspective.

## 5 Conclusions and Recommendations

The paper describes the application of BIM methodology to a case study consisting of the rehabilitation of an existing railway infrastructure with a total length of 35 km. Due to stabilization and drainage problems, the rail track had to be rehabilitated: Replacement of rails, sleepers, fastenings; the placement of a new ballast layer; the renovation of the drainage system; the update of the electrification system. A segment measuring 1787 m was selected to be studied using the BIM methodology.

The implementation of BIM consisted of three steps: (1) development of the 3D model of the railway infrastructure using Civil 3D<sup>®</sup> software and Infracore<sup>®</sup> (ground modeling); (2) 3D modeling of the rail track in the Revit<sup>®</sup> software; and (3) 4D modeling in Navisworks<sup>®</sup> software in order to plan and schedule the construction process of the rail track rehabilitation. Finally, the possibility of extracting information from the 3D model on the rail track geometry in the context of the inspection activity was studied.

The main conclusions of the research relate to the generation of the 3D and 4D models, the analysis of the interoperability capacity between BIM software programs, and the possibility to use BIM methodology in the rehabilitation and inspection of rail tracks:

- The Civil 3D<sup>®</sup> and Revit<sup>®</sup> tools proved to be suitable for the 3D modeling, including all the rail track components (substructure and superstructure), drainage elements (pipes), and electrification system (catenary);
- Using the Navisworks<sup>®</sup> tool, a 4D model was established. Seven sets were created to illustrate the different construction phases, including the application of geotextile and geogrid;
- The interoperability between software packages was analyzed. The integration of the 3D model from Civil 3D<sup>®</sup> into Revit<sup>®</sup> was unsuccessful as most of the elements were not recognized. Interoperability between Revit<sup>®</sup> and Navisworks<sup>®</sup> was possible and facilitated the process of creating the 4D modeling, as they are both from Autodesk<sup>®</sup>;
- Regarding the inspection of the rail track, there were still many limitations regarding the storage and manipulation of this type of information using Civil 3D<sup>®</sup>. But Revit<sup>®</sup> was unable for this purpose.

Some recommendations arise from the implementation of BIM to the case study. Regarding the Revit<sup>®</sup> software, we would recommend more advances in the development of specific families of objects of transport infrastructures. The modeling process would thus be completer and more realistic. A further recommendation has to do with the integration of BIM methodology in the track monitoring systems, including all the usual geometric parameters. It is desirable that further consideration will be given to the possibility of having a proper track inspection system, so that the maintenance planning, coupled with quality control inspection tests, can be more integrated and completer.



Finally, it is expected that in the near future the reported problems of interoperability between BIM software programs will be solved, given the current and foreseeable evolution of digital systems, in line with the technical advances.

**Acknowledgements** The authors would like to thank the Portuguese Railway Infrastructure Agency (“Infraestruturas de Portugal, SA”), for the permission to use and disseminate the project information related to the case study described in the paper, and CERIS (Civil Engineering Research and Innovation for Sustainability).

## References

1. Brewer G, Gajendran T, Goff R (2012) Building Information Modelling (BIM): an introduction and international perspectives. Report. Centre for Interdisciplinary Built Environment Research, School of Architecture and Built Environment, The University of Newcastle. <https://doi.org/10.13140/RG.2.2.13634.58565>
2. Bryde D, Broquetas M, Volm JM (2013) The project benefits of Building Information Modelling (BIM). *Int J Project Manage* 31:971–980. <https://doi.org/10.1016/j.ijproman.2012.12.001>
3. Bradley A, Li H, Lark R, Dunn S (2016) BIM for infrastructure: an overall review and constructor perspective. *Autom Constr* 71:139–152. <https://doi.org/10.1016/j.autcon.2016.08.019>
4. Costin A, Adibfar A, Hu H, Chen SS (2018) Building Information Modeling (BIM) for transportation infrastructure—literature review, applications, challenges, and recommendations. *Autom Constr* 94:257–281. <https://doi.org/10.1016/j.autcon.2018.07.001>
5. Bensalah M, Elouadi A, Mharzi H (2018) Integrating BIM in railway projects: review & perspectives for Morocco & Mena. *Int J Recent Sci Res* 9:23398–23403. <https://doi.org/10.24327/ijrsr.2018.0901.1460>
6. Bensalah M, Elouadi A, Mharzi H (2018) BIM integration to railway—literature & experiences critical review. In: 11th International Colloquium of Logistics and Supply Chain Management LOGISTIQUEA 2018, Morocco, vol 11
7. Bensalah M, Elouadi A, Mharzi H (2017) Optimization of cost of a tram through the integration of BIM: a theoretical analysis. *Int J Mech Prod Eng* 5:138–142
8. Eastman C, Liston K, Sacks R, BIM handbook. Paul Teicholz Rafael Sacks. 2007029306
9. Chong HY, Lopez R, Wang J, Wang X, Zhao Z (2016) Comparative analysis on the adoption and use of BIM in road infrastructure projects. *J Constr Eng Manag* 32(6):1–13. [https://doi.org/10.1061/\(ASCE\)ME.1943-5479.0000460](https://doi.org/10.1061/(ASCE)ME.1943-5479.0000460)
10. AEC Magazine: Autodesk 2017 updates. <https://www.aecmag.com/59-features/1122-autodesk-2017-updates>. Last accessed 14 Mar 2018
11. Kurwi S, Demian P, Hassan TM, Integrating BIM and GIS in railway projects: a critical review. Association of Researchers in Construction Management (ARCOM). <https://dspace.lboro.ac.uk/2134/26491>. Last accessed 15 Nov 2019
12. André A, Ribeiro L (2018) Aplicação de metodologia BIM no âmbito de projetos de regularização fluvial. Os casos de Díli e de Pante Macassar em Timor-Leste. In: 2nd Portuguese BIM Conference, Portugal, pp 221–230 (in Portuguese)
13. Neves J, Lima H, Rodrigues F (2016) The use of geosynthetics in the construction and rehabilitation of transportation infrastructures in Portugal. In: Workshop 1, Geosynthetics in Transportation Geotechnics, 3rd International Conference on Transportation Geotechnics, Portugal. ISBN: 978-972-8692-98-8. <https://doi.org/10.5281/zenodo.61306>
14. Queirós B (2017) Application of geogrids in rail renovation works—case study. In: Proceedings of the 1st Seminar on Transportation Geotechnics, Portugal. ISBN: 978-989-20-8046-8. <https://doi.org/10.24849/spg.cpgt.2017.01>

15. Vilela M (2018) BIM Implementation to transport infrastructure. Master's Thesis, Instituto Superior Técnico, University of Lisbon, Portugal (in Portuguese)
16. EN 13848-1:2003+A1:2008 (2008) Railway applications Track—track geometry quality. Part 1: characterization of track geometry. European Committee for Standardization

# Targeted Asset Management on Ageing UK Railway Embankments—Wrabness



Ian Payne, Simon Holt, Isaac Griffiths, and Stuart Fielder

**Abstract** To prioritise and optimise mitigation with sustainable and value engineered solutions, a targeted asset management (TAM) regime has been established. The early stages have been successfully implemented at an embankment site at Wrabness in Essex which has experienced long-term instability issues. The site is located on sidelong ground leading to the Stour estuary with evidence of natural mass movement and drainage issues. Temporary mitigation, including local toe weighting and drainage improvements, has helped to control slope movements. Detailed geomorphological mapping, interrogation of ground investigation data, slope instrumentation data, and review of track monitoring data have allowed development of good ground models and understanding of geotechnical issues. Early ecology surveys, upfront preliminary designs and site risk zonation have enabled network rail to plan budgets and decide on the works in each five yearly funding cycle.

**Keywords** Asset management · Slopes—stabilisation · Earthworks · Geotechnical engineering · Railway tracks

## 1 Introduction

The Wrabness site is centred on national grid co-ordinates TM 19,091 31,556 and comprises a 900 m long embankment approximately 5 km west of Harwich in Essex, as shown in Fig. 1. The railway is electrified with 25 kV (AC) overhead equipment and has a line speed of 60mph. Originally opened in 1854, and doubled in 1882, the line connects the port of Harwich carrying both passenger and freight traffic.

The site is adjacent to a site of special scientific interest (SSSI) and ecology surveys have been critical in the programme to ensuring protected species such as dormice are not impacted by proposed engineering works.

---

I. Payne  
Network Rail, London, United Kingdom

S. Holt (✉) · I. Griffiths · S. Fielder  
Atkins Limited, Croydon, United Kingdom  
e-mail: [simon.holt@atkinsglobal.com](mailto:simon.holt@atkinsglobal.com)



**Fig. 1** Site location plans

The embankment is constructed on sidelong ground using uncompacted end-tipped locally derived fill, common practice in Victorian age earthwork construction prior to full understanding of geotechnical engineering. Embankment slopes are up to 8 m high on the north side, with very steep upper slope angles and thick ash and ballast layers near the crest.

The site has a long history of instability and resultant issues including track dips, leaning infrastructure and periodic implementation of temporary speed restrictions (TSRs) for the safety of the public.

Network rail (NR) asset management teams have a difficult balance trying to spread their budget and prioritise risk to best ensure public safety. To aid this, consulting engineers, such as Atkins, characterise such sites in detail to ensure optimised and focused mitigation. Targeted asset management (TAM) has been developed to facilitate getting the balance correct and will be demonstrated at Wrabness. Phased site investigation, previous engineering intervention, potential future works and controlling residual risks will also be discussed, drawing upon lessons learnt from the site in the region.

The paper builds on the initial work presented on this site for the 2017 UK Railway Engineering Conference in Edinburgh [1].

## 2 Site Characterisation

### 2.1 *Geomorphological Survey*

A detailed geomorphological survey was undertaken at the site, with key slope features and defects mapped, as shown in Fig. 2. Numerous indicators of stability issues were noted including toe bulges, lobes, historic intervention, track defects and leaning and uprooted trees (Fig. 3). Groundwater issues were evident along the south side where saturated soils were noted along the embankment toe.

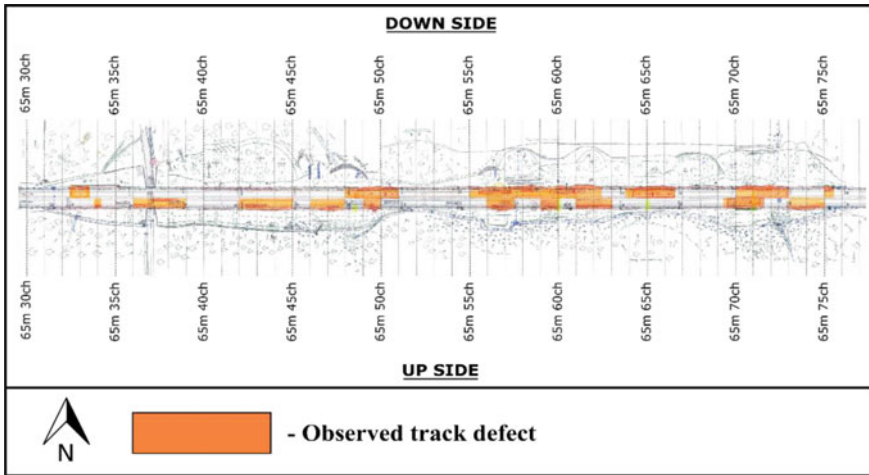


Fig. 2 Detailed geomorphological mapping undertaken winter 2018/19

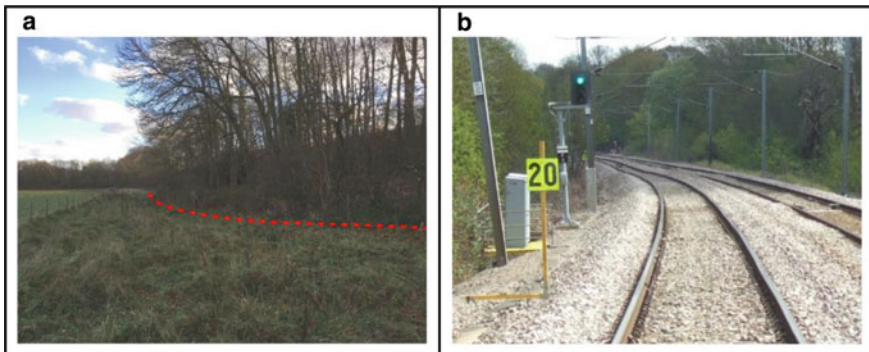


Fig. 3 a—Lower slope lobe feature in eastern part of site, north side. b—Looking East: track dips, thick ballast shoulder, TSR and leaning gantry on the north side slope (left of photo)

## 2.2 LiDAR

NR have biannual LiDAR surveys flown across network and there is ongoing research on how best to use this data to aid asset management. LiDAR imagery of the site (Fig. 4) was used in conjunction with the geomorphological survey to aid interpretation.

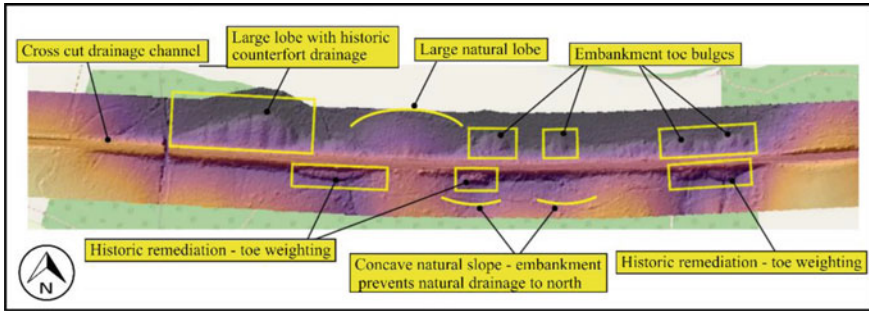


Fig. 4 High resolution LiDAR image of the site

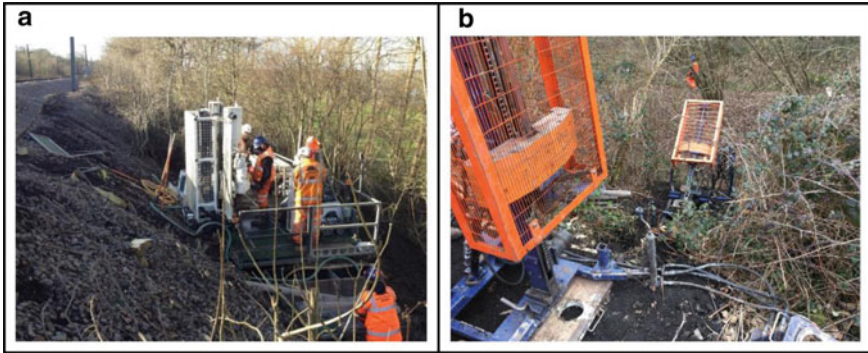
### 2.3 *Trackside Issues*

Track stability issues have been a long-term problem at the site, with reports of instability dating back to the 1960s. More recently, continuous track defects have been recorded at discrete locations along the embankment, with occasional TSRs being required, as shown in Fig. 3. Track maintenance works, including tamping and hand packing of the track in combination with ballast drops, have enabled line speeds to be restored; however, ongoing movements have caused alignment issues to continue and re-occur in the same areas repeatedly.

Typical defects exhibited at the site include track dips and twists, cess level drops, troughing collapse, ballast thickening, depleted ballast shoulders, exposed sleeper ends, leaning trackside structures, spalling of material down slope faces and surface subsidence. Key areas noted by visual assessment are highlighted in Figs. 2 and 5 shows one of the worse affected areas.



Fig. 5 a—Thick ballast shoulder spilling downslope and leaning OLE mast (looking west). b—Drop in cess level with associated ballast thickening and adjacent track dip (looking east)



**Fig. 6** **a**—P60 slope climbing rig set up on steep north side slope (Geotechnics Ltd). **b**—Lightweight limited access modular rig (LLAMR) set up on south side slope (Topdrill Ltd)

## 2.4 Track Monitoring

NR periodically monitor track condition through train mounted equipment undertaking geometry measurements and ground penetrating radar (GPR) to infer trackbed condition, and the results of which are presented in the Linear Asset Decision Support (LADS) tool. LADS data and maintenance records have been used at the site to identify where defects and regular maintenance events occur. Typically, the LADS data at the site shows poor line and level condition on both lines throughout, with numerous maintenance interventions.

## 3 Ground Model

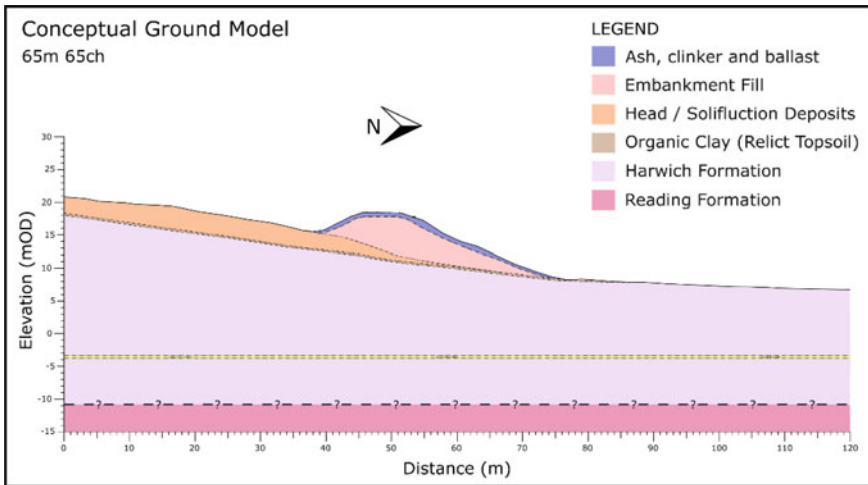
### 3.1 Ground Investigation

Several phases of ground investigation (GI) have been undertaken at the site including installation of inclinometers and piezometers. GI work has required specialist slope access rigs (Fig. 6) and careful health, safety and environmental considerations.

### 3.2 Ground Conditions

Ground models have been developed to allow design and optimisation of mitigation solutions (Fig. 7) and derived from a combination of GI, geomorphological, LiDAR and topographical survey information.





**Fig. 7** Ground model at 65 m 65ch; section line shown in Fig. 8

Embankment fill is heterogenous, with varying amounts of cohesive and granular material, an indicator of both the long-term instability issues and the nature of original end-tipped uncompacted construction [2, 3]. Typically, embankment fill was found to contain a greater proportion of cohesive material in the eastern half of the site and dominantly granular fill in the western half. Cohesive fill is likely to be reworked Thames Group deposits, whilst granular material represents reworked Kesgrave Catchment Subgroup deposits, excavated in nearby cuttings during construction.

Throughout the site, the embankment is topped with a layer of ash and clinker, varying in thickness from less than 0.5 m to over 3.5 m. This layer is likely to represent historic repairs to embankment crest failures and is as a result thicker where movement indicators are observed, or where the upper slope is particularly steep on the north side.

An organic clay layer was encountered in numerous exploratory holes across, with a maximum thickness of 2.7 m. Typically, this organic layer was found to directly underlie the embankment fill or, where present, the naturally reworked head/solifluction deposits. This is thought to represent relic topsoil from before construction of the embankment and/or historic mass movement in the form solifluction mudslides. Head comprising low strength sandy gravelly clays were encountered beneath embankment fill in many exploratory holes and were generally consistent with naturally reworked Harwich Formation. Typically, the deposits were encountered in areas where the embankment sits on the toe of the natural slope as shown in Fig. 7.

Solid geology at the site comprises over 20 m of the Harwich Formation (Thames Group), under which deposits of the Lambeth Group are encountered.



### 3.3 Slope Monitoring

Slope monitoring has been installed at Wrabness through several different phases of GI works and Fig. 8 shows a summary of the key inclinometer and piezometer position within the eastern part of the site.

Historically, the area of the site with the most serious track issues and signs of instability has been the section as shown in Fig. 7. Due to the severity of this area, an automated inclinometer system was installed at the location, along with a surface camera for ‘real-time’ photographs, aiding remote assessment by the asset management team. These inclinometers (BHIN06 and BHIN07) indicate movement at a depth of 5–6 m below ground level, suggesting a deep-seated failure mechanism. Despite the generally progressive increase in recorded displacement, the data indicates a clear seasonal variation, increasing at the start of the winter period, before reaching a maximum at the end of spring or start of summer, and then reducing before the cycle repeats (Fig. 9a).

The inclinometers across the rest of the site generally suggest a gradual downslope movement of embankment fill, occurring primarily at the crest of the north side embankment. This displacement typically occurs in approximately the top 5 m and increases towards ground surface. A maximum displacement of 82 mm was recorded in BH10 (Fig. 9b) occurring since monitoring commenced in March 2016. Similar downslope movement was recorded in BH04 (48 mm). It should be noted that displacements occurring in the top 1 m may be partially attributed to poorly compacted backfill of the inspection pits following inclinometer installation.

Assessment of ground water trends is ongoing including establishing potential links with the seasonal slope movements and drivers of pore water pressure fluctuations [4].

BHIN01 recorded a maximum downslope displacement of 38 mm; however, unlike other locations, the displacement observed in this inclinometer did not increase towards ground surface. Moreover, it appears to approximately correspond to the

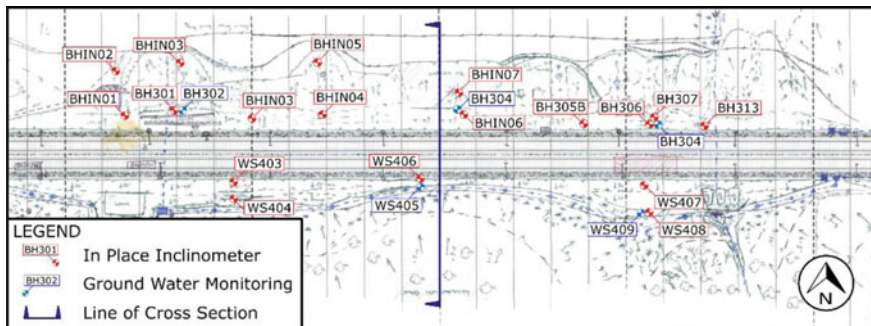
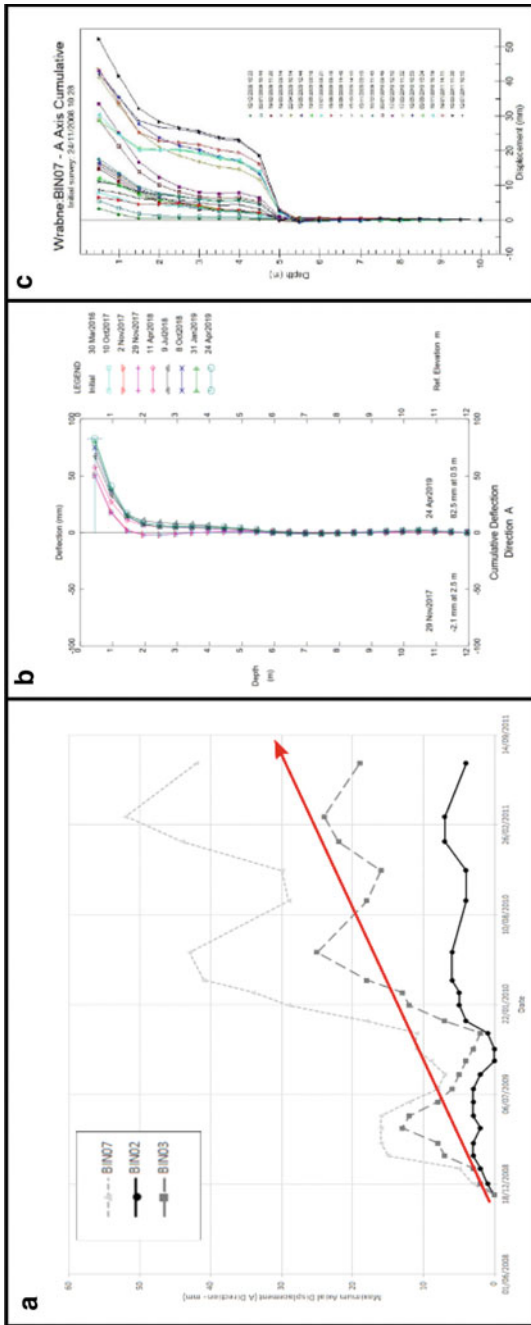


Fig. 8 Location plan of key monitoring location for the eastern end of the Wrabness site



**Fig. 9** a—2008–2011 midslope and toe movement showing overall progressive deterioration and seasonal fluctuation. b—BH10 inclinometer data showing shallow movement in the upper 2 m of the slope. c—BH08 inclinometer data showing deep-seated movement at approx. 5mbgl

depth at which embankment fill transitions from granular to cohesive material, suggesting movement of the granular layer over the cohesive layer.

Displacement in BH301 (20 mm) and BH313 (30 mm) corresponds to the transition between embankment fill and natural ground, at approximately 5.4mBGL and 6.2mBGL, respectively, suggesting downslope movement over natural ground. Clearly, there is movement across the whole site that corresponds to the variability of the ground conditions encountered.

Whilst monitoring has been focused to the north side over the last 10 years, in early 2019, inclinometers and groundwater monitoring points were installed at key locations on the south side to further understand the failure mechanisms. Data is currently limited although there is evidence of movement below areas of track defects as shown in Fig. 2. Whilst the slope is relatively shallow on the south side, movements here highlight the importance of interpreting both sides of the railway to ascertain the global picture, not just focusing on one side in isolation.

## 4 Targeted Asset Management (TAM)

It is recognised that due to the large scale of many of the Earthworks Renewal projects and constrained remedial works budgets, large-scale heavy engineering solutions across entire sites are not feasible. This was recognised during CP5 and Payne et al. [5] report the successful risk management approach at Ashdon Way, eliminating widespread sheet piled walls and prolonging the life of the asset with targeted local cess retention and soil nailing. The process has since been further refined and to prevent further deterioration of earthwork assets and to maintain the operational safety of the railway, the TAM risk management approach is being utilised to identify the scope of remedial works at key sites within the Anglia Earthworks CP6 workbank. The TAM process was set out by Payne et al. [6] and targets stabilisation at the highest risk sections of the earthworks to minimise operational disruption and is undertaken in four stages as outlined below:

- TAM Stage 1 (Option Selection and Outline Design)
- TAM Stage 2 (Costing)
- TAM Stage 3 (Detailed Design)
- TAM Stage 4 (Post-Construction).

Constant collaboration between client, contractor and designer is imperative to ensure the success of the TAM process and ensure that the final design solution manages the instability issues at the site, whilst remaining sustainable. TAM Stage 1 focuses on data collection and considers the current condition of the whole asset. The asset is divided into zones based on information collected and each zone is assigned a risk rating (see Fig. 10) of high, medium or low based on its condition. Outline design and optioneering is then undertaken for high and medium risk zones, allowing the contractor to provide cost estimates for remediation in TAM Stage 2 before NR commit to the works. Following agreement of scope and cost with the

Definition of TAM Risk Category	
Risk Category	Definition
<b>High (H)</b>	Known evidence of regular high priority track issues and or above average slope movements with visual signs of instability with high potential to cause public disruption and a threat to the safe operation of the railway.
<b>Medium (M)</b>	Potential to cause continued track issues and affect maintenance regime. Slope movements are considered at or below average and steady. No imminent signs of failure from visual observations. Continue to monitor and have a future works strategy plan in place should it enter HIGH risk.
<b>Low (L)</b>	Minor track and maintenance issues with no cause for concern, below average slope movements (where data) and no visual indicators of failure.

**Fig. 10** Definitions of TAM risk category

client, detailed design of the works is completed in TAM Stage 3. Finally, TAM Stage 4 is implemented post-construction and involves the continued monitoring and asset management to ensure any risks from unremediated areas are managed.

#### **4.1 TAM Stage 1**

TAM Stage 1 aims to identify the underlying geotechnical issues which are causing instability in the asset and have potential to affect the operational safety of the railway. These issues are recorded in the form of a technical risk register which has three main failure categories:

1. Track and maintenance issues
2. Ground conditions and slope movement monitoring
3. Visual movement indicators.

These categories are subdivided into several subcategories, such as service impacts, slope defects, drainage defects, with a risk rating applied to each as defined in Fig. 10 (full details of these subcategories are recorded in Payne et al. (2019)). Design optioneering is then undertaken for the high and medium risk zones to feed into TAM Stage 2 costing.

Wrabness has been subjected to the TAM Stage 1 process following the detailed site mapping and GI interpretation described earlier. The site was assessed in accordance with the TAM criteria and the output of the TAM risk mapping can be seen in Fig. 11.

Whilst both sides of the embankment were subject to zonation, greater attention is given here to the north side given the higher slope, more regular defects; slope movement data for the south side is still being built up. Zones 8 and 10 were identified as being the highest risk areas driven by the major track and slope defect observations together with the higher recorded inclinometer slope movements.

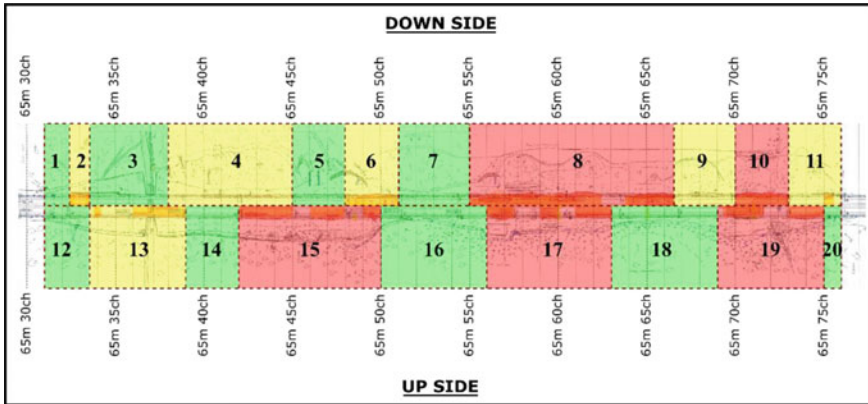


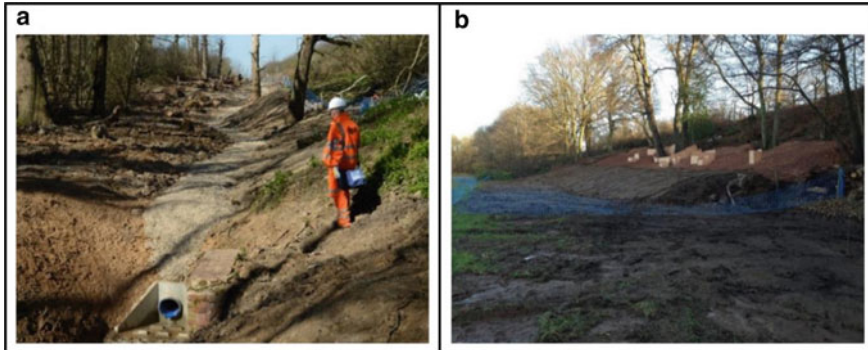
Fig. 11 Wrabness TAM risk zonation map (see Fig. 10 for risk definition)

The TAM zoning process has allowed intervention at the site to be targeted at the highest risk areas to reduce the overall cost of remediation at the site whilst ensuring good management of the asset.

## 5 Intervention

Historical evidence of engineering intervention was reported by Payne et al. [1] including records from a 1966 walkover survey showing counterfort drainage, lump slag and rubble berms as possible toe weighting on the north side and numerous observations of instability, including old major landslips and blocked drainage, on the south side. There are localised engineering works including a 2001 sheet piled wall with gabion wall immediately downslope (possibly to create a working platform) over a 50 m length with Zone 8 on the north side and a toe berm in Zone 17 on the south side. However, there are still signs of problems at track level above both fixes and movement downslope of the sheet piled wall indicating not all the stability mechanisms have been addressed by the historical reactive interventions.

In late 2014, extensive drainage improvement works were undertaken on the south side which included an impermeable toe cut-off drain (Fig. 12) ‘catching’ run-off from the adjacent woodland and reinstating 2 culverts to provide an effective passage below the embankment. The work was undertaken by Volker Fitzpatrick and required extensive ecology surveys with associated controls and close collaboration with the RSPB, winning an Environmental Green Apple Gold Award for outstanding environmental protection. Whilst it is difficult to measure the improvement of the asset as a result of the drainage works, there has certainly been less critical slope movements in the last 4–5 years and as has been proven at many similar sites, intervention must start with addressing the drainage. One means of assessing the improvement was noted during the geomorphological survey in the area beyond



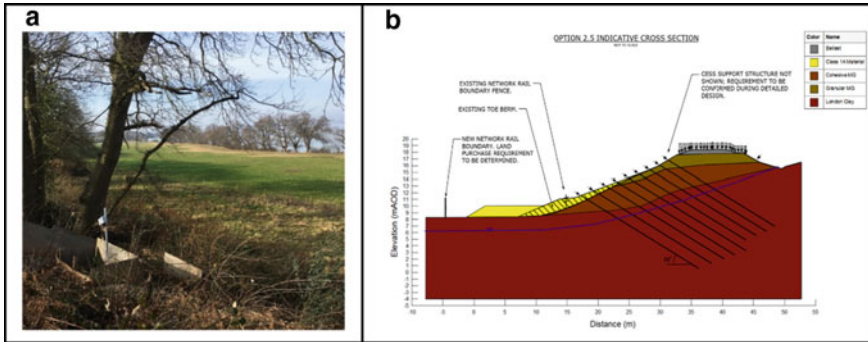
**Fig. 12** **a**—South side cut-off toe drainage installed in early 2015. **b**—Completed Temporary Toe Berm on the north side at 65 m 65ch

limit of the 2014–2015 drainage works. Within Zone 15 a culvert was blocked on both sides of the embankment and the catchment of water from the embankment toe falling from the west and east, plus the woodland run-off from the south, has resulted in very boggy ground at the embankment toe. This coincides with notable issues on the embankment slopes on both sides and higher maintenance on track.

Further, GI was carried out in early 2016 and given access was required from the toe, and the NR minor works team took the opportunity to construct a temporary toe berm around the previously recorded highest and deep-seated movements at 65 m 65ch on the north side (Fig. 12b). As this was a reactive emergency mitigation measure, a short term design betterment approach was adopted given the intention was for a longer-term stabilisation in accordance with design standards (Eurocode 7).

During CP5, it was recognised that fully fixing sites like Wrabness with 120 year design life solutions would be unsustainable and unrealistic. The NR asset management team have to very carefully ensure budgets are spread correctly across the whole region. Whilst Wrabness was subject to drainage refurbishment and a temporary toe berm, other sites were experiencing higher movements and required longer-term mitigation. One such site was Ashdon Way which was close to Basildon station in Essex and on a very busy London commuter line. Payne et al. [1] describe the use of automated inclinometers allowing high active slope movements to be controlled during construction and post-construction arrest of slope movements was evident validating the design. Further, inclinometers were installed in lower risk areas for observational monitoring and a Future Works Strategy Plan (part of TAM Stage 3) was developed to advise NR of the monitoring strategy, trigger levels and outline emergency works options should they be required.

The higher risk TAM zones identified at Wrabness (north side) as shown in Fig. 11 have been subject to TAM Stage 1 optioneering. Given additional land purchase at the toe by NR in 2016 as shown by the new fence line as shown in Fig. 13, design solutions needed to make best use of this space. Preliminary design options were appraised and costed in TAM Stage 2. The unsustainable nature of importing vast volumes of fill for



**Fig. 13 a**—Additional land purchase shown by the new fence line to allow future permanent works/access. **b**—Preliminary TAM Stage 1 Output Engineered Solution of soil nails and cess retention with some additional toe weighting

a full shallow slope regrade and expense of a sheet piled wall meant that soil nailing with cess retention was likely to be the preferred option moving forward, especially given the success on arresting slope movements on other cohesive embankments in the region. A preliminary design option is shown in Fig. 13a that also includes toe weighting with imported granular fill which could be used as a working platform which may also incorporate drainage.

## 6 Conclusions

The Wrabness site provides a good case study of how targeted asset management (TAM) can optimise how Network Rail deal with ageing UK railway earthworks. The railway has been built on a natural landslide and the topography has resulted in an over-steep higher north slope which has suffered both shallow, deep and cyclic ground movements over many years. Groundwater plays a vital part and providing new relief pathways from near surface run-off has slowed slope movements; however, infiltration into an upper ashy embankment with clay core will continue to increase pore pressures and cause instability.

The case study provides a typical example of embankment problems in the region and demonstrates the importance of establishing an accurate ground model linking surface observations, track and maintenance data, and historical information. Good reliable monitoring is essential, whilst more expensive remote monitoring provides accurate trends, greater control and reduces safety risks of attending site. It is important for the designer to target the correct areas and compare movement trends over time and to other sites. Lessons can also be learned from intervention across the region and it is critical to work as a collaborative team to fully understand the balance between risk, mitigation and cost.



There have been many historic interventions and the railway line has been subject to a long history of maintenance which continues to the present day. The patchwork of treatments has kept the line operational, although it has been subject to restrictions following some higher slope movements. Further, detailed design is required, but the early TAM stages have shown that a feasible option can be determined and priced before NR commit to the final works, aiding their budget planning and assessment of further mitigation requirements. Wrabness represents less than 0.1% of the total Earthwork mileage in Anglia, yet initial remediation costings for the high risk zones on the north side were approaching 10% of the total CP6 budget. Resultantly further TAM refinement may be required with continued observational monitoring, which has been successful in controlling risks at other sites in the region.

## References

1. Payne I, Holt S, Griffiths I (2017) Wrabness railway embankment—managing slope instability through phased investigation, monitoring and planned intervention. In: *Railway engineering*, Edinburgh
2. Skempton AW (1996) Embankments and cuttings on early railways. *Construct History* 11:33–49
3. Nowak P, Gilbert P (2015) *Earthworks: a guide*, 2nd edn. Publishing, Thomas Telford Limited, Institution of Civil Engineers
4. Briggs KS, Smethurst JA, Powrie W, O'Brien AS (2013) Wet winter pore pressures in railway embankments. *Proc Inst Civ Eng* 166(5):451–465
5. Payne I, Holt H, Griffiths I (2018) Railway embankment stabilisation: economical asset management. *Proc Inst Civ Eng—Geotech Eng* 171(4):332–344
6. Payne I, Savill F, Holt S, Griffiths I, Fielder S (2019) Targeted asset management approach to mitigating railway earthwork instability—chitts hill embankment, colchester Essex. *Permanent Way Inst: J* 137(4):26–37



# Integrated Technology Geological Surveys



Gennadii Boldyrev

**Abstract** The paper presents the results of the development of integrated technology engineering and geological surveys and design foundations. It is shown that the currently existing information systems for data transmission and processing, information measuring systems allow not only to manage the process of testing soils and process test data, but also to simultaneously perform calculations of the deformation and strength of the foundation. Modern methods of field research of soils, such as static, dynamic and boring sounding, allow to obtain continuous information about the physical and mechanical properties of soils in depth and rather cheaply with an increase in the number of test sites within the studied survey area. The recording of sensing parameters data can be performed at any depth interval. Using known or local correlation equations and sounding data, soil depth characteristics are found. Further, the calculated values of the characteristics of the soils are determined, and then, the deformations and strengths are calculated directly in the field conditions during the soil sounding process. The proposed complex technology combines engineering and geological surveys and the design of building foundations into a single production process. The result is a reduction of the survey time due to the application of soil sounding methods with automated control of the test process and interpretation of test data. In this case, the results of engineering and geological research provide not only information about the properties of soils, but also an assessment of their influence on the behavior of the designed building or structure.

**Keywords** In-situ soil test · Foundation design · Information systems

## 1 Introduction

Currently, foundations of buildings and structures are designed using analytical and numerical solutions. Analytical solutions are given in the corresponding sets of rules (SR) [1]. They are simple, easily programmable, require determination of the

---

G. Boldyrev (✉)

Penza State University of Architecture and Construction, Penza 440026, Russia

e-mail: [g-boldyrev@geotek.ru](mailto:g-boldyrev@geotek.ru)

minimum number of soil characteristics. And many years of practice of their application testifies to the reliability of these solutions. Numerical methods of foundation calculations are much more complicated. In most cases, it is necessary to determine more characteristics/parameters of soil models during engineering-geological and geotechnical investigations. And very often their validity is to be checked using analytical solutions. Due the fact that it is still obligatory to comply with the requirements of the SR, in the development of integrated technology, we propose to use the appropriate analytical solutions for calculating the foundations on deformations and bearing capacity given in the SR. The structure of the proposed technology allows to apply numerical methods of solutions implemented in various programs such as PLAXIS, and FLAC. However, it is not yet clear how to determine all the parameters of soil models directly in the field.

## 2 Soil Testing Methods

Most of the required physical and mechanical characteristics of soils for designing buildings and structures can be determined both in laboratory and in-situ conditions. More attractive is the determination of physical and mechanical characteristics of soils in in-situ conditions, for example using static (CPT, CPTU, SCPTU) and dynamic (SPT, DCPT) penetration tests, Russian screw test (RST), boring sounding (RDT), vane shear test (VS), etc. The first two methods are known and widely used in practice of engineering and geological investigations [2]. Boring sounding is little known and is still rarely used in domestic practice in determining mechanical characteristics of soils and fragmentating the soil thickness into separate layers, despite its shown efficiency [3, 4].

Boring sounding method allows to carry out investigations of soil properties of practically all types similar sandy, clay, gravelly rock, and frozen soils. In this method, the well boring is performed by a screw with a boring tool, the type of which depends on the type of soil. Due to fact that the auger almost without force moving into the ground, it allows to use conventional drilling rig. These machines are widely used in carrying out engineering-geological and geotechnical investigations without their modernization. It will be shown later that combining the static penetration and boring sounding method allows a significant increase in the number of measured parameters, which is useful in constructing correlation dependencies.

## 3 Soil Testing Technology by Means of Boring Sounding

In our opinion, a more promising method of in-situ studies of soil properties is the method of boring sounding method. First, this method is applicable, in contrast to the method of static penetration, not only in clay and sandy soils, but also in gravelly, rocky, and frozen soils. Second, the method allows to determine the modulus of soil

deformation and force resistance to shear without using correlation dependencies. At the same time, other soil characteristics can be found using correlation dependencies, as in the case of static and dynamic penetration.

Boring sounding method involves testing of dispersed and frozen soils by means of measuring a number of parameters during well drilling with a solid or hollow auger, which are given in Table 1.

The device of boring sounding is measuring system including sensors, amplifiers of signals, and analog-to-digital converter which are structurally located in the steel cylinder having standard shafts in end faces [3]. One part of which is connected to the rotator shaft and the other to the shank of the boring column. The device for boring parameters measurement contains “bidirectional action” force sensor for measurement of compression and tension forces, sensor for torque measurement, sensor for rotation speed measurement and inclination. Penetration depth measurement of a boring column and a line speed is carried out by a potentiometer range finder. Range finder indications are transferred by means of interface RS 485 and registered in a computer database.

Sensors of force, moment, slope angle, and rotational speed are connected to ATsP boards powered by a built-in accumulator. ATsP boards are connected to the wireless RS-485/ZigBee modem by RS-485 interface. The modem antenna is brought to an upper part of the device. There is a modem for wireless ZigBee communication from the managing computer. It is connected by means of USB port. For data exchange between ATsP and computer boards, ModBus RTU recording is used. The block which is electronic and transforming with RS-485 interface for the range finder which is located on a mast of the boring device is connected to a computer. The

**Table 1** Parameters measured

The measured parameter	Dimension	Range	Measurement accuracy, % of a range
<i>Disperse not frozen soils</i>			
Torque	kNm	0–0.5	1.0
Feed force/thrust force	kN	0–50	1.0
Hoisting force/weight of a boring column with soil on flanges	kN	0–50	1.0
Rotational speed	RPM	0–300	1.0
Depth	m	30	0.5
Vertical deviation	degree	0–10	0.5
Pore pressure	MPa	0–2	0.5
<i>Additionally, for frozen soils</i>			
Soil resistivity under boring tool	MPa	1–80	1.0
Temperature soil and heating of the soil	°C	– 20- + 110	± 0.1
Heating power	W	0–100	1.0

process of registration and visualization of boring parameters is carried out by ASIS program.

The boring measurement apparatus operates as follows. The upper part of the device is connected to boring machine rotator, and the lower part of the device is connected to a boring column. Range finder is fixed on mast, and its cable is fixed on rotator housing. By means of a button on the upper part of the device, the power supply is switched on and signals from sensors (forces, torque, rotation, movement, inclination) begin to enter the computer in digital form by wireless communication.

Then, boring master activates the rotator and the well drilling process begins. Torque and axial load from boring machine are simultaneously transmitted to the upper part of the device. The torque is measured by a torque sensor, and an axial force is measured by a bidirectional force sensor. At the same time, only torque ( $M$ ) is transmitted to the moment sensor, and only the axial force ( $N$ ) is transmitted to the force sensor. The rotation speed of the device is measured by the rotation speed sensor located in the electronics unit. The movement of the boring column is measured by a laser or potentiometric range finder. The slope of the boring column is measured by an inclination sensor located in the electronics unit. The same sensor can be used for monitoring the angle of inclination of the boring mast. Torque and axial force from the lower shank of the device are transmitted to the boring column sounding the ground.

The described boring sounding device is located in the upper part of the screw column above the soil surface. Therefore, the measured boring parameters are influenced by screw column bending, friction forces between the surface of the screw flange and the soil, friction forces between the moving soil and the well walls, and also other factors. However, these disadvantages can be avoided if the boring sounding device is placed in the first link of the hollow screw string by penetrating an extensible static penetration cone into the structure.

## 4 Interpretation of Measurement Data

Interpretation of the boring sounding involves determination of the following parameters.

*Mechanical power* at rotational motion at the current depth of penetration (kJ/s):

$$A = M \cdot 2\pi\omega \quad (1)$$

where  $M$ —present torque (Nm);  $\omega$ —rotation speed of the boring tool ( $s^{-1}$ ). This parameter characterizes the work spent in a unit of time when boring the well.

*Specific energy*. In 1965, R. Til [5] suggested to use the parameter called specific energy for well-boring process control. The specific energy is the work value necessary for boring a volume of soil:

$$E = Q/A + M \cdot \omega/A \cdot v \quad (2)$$

where  $Q$ —axial force (kN);  $A$ —transverse section of the well ( $m^2$ );  $M$ —torque, (kNm);  $\omega$ —rotation speed (rad/s);  $v$ —speed of boring tool progress (m/s).

Specific energy index is used for optimization of penetration speed into soil of a boring tool at penetration of deep vertical, inclined, and horizontal wells. Penetration speed depends on several factors: axial load, rotation speed, downhole pressure gradient, boring fluid pressure, soil strength, etc. However, in the field of geotechnical surveys, the specific energy indicator is practically not used, despite the fact that well boring is also carried out, but only of lower depth.

For the first time, the parameter of mechanical power in rotational motion was applied in PNIIS (Russia) in 1989 in order soil type identification with different strength. Later, possibility of using this method was shown not only for the soil stratigraphy, but also for the determination of deformation modulus.

In the latter case, the tests are carried out at a given depth by pressing the drill string from hollow augers into the ground with a preliminary measurement of its weight and the weight of the soil on the flanges of the auger. The loading is carried out in steps to a predetermined stabilization of deformations with the measurement of axial load and displacement of the column.

In the case of using a drilling bit in the form of the vane, the undrained strength is determined from the expression:

$$M = \pi c_u \left( \frac{d^2 h}{2} + \beta \frac{d^3}{4} \right) \tag{3}$$

where  $M$ —maximum torque (kHm);  $d$ —vane diameter (m);  $h$ —vane height (m);  $c_u$ —undrained strength (кПа);  $\beta$ —coefficient depending on the distribution of mobilized soil resistance:  $\beta = \frac{2}{3}$  with a uniform distribution of pressure equal to  $c_u$  on the surface of the vane;  $\beta = \frac{1}{2}$  with increasing pressure on the surface of the vane according to the linear law from 0 to  $c_u$  и  $\beta = \frac{3}{5}$  with increasing pressure on the surface of the vane in a parabola from 0 to  $c_u$ .

The shear modulus is found from the expression:

$$G = \frac{HM}{\pi R^4 \varphi} \tag{4}$$

where  $M$ —current measured moment (kHm);  $\varphi$ —vane rotation angle (rad.),  $R$ —radius(m);  $H$ —vane height (m). Since the angle of rotation of the vane and therefore the shear deformations are measured during the test, this allows one to determine both the initial shear modulus and its degradation with increasing shear deformation. The friction forces on the side surface of the vane during its vertical immersion in the soil are found from the expression:

$$f_s = \frac{N}{A_s} \tag{5}$$

where  $N$ —axial load;  $A_s$  —the area of the side surface of the vane. The shear resistance of the soil is found from the expression:

$$\tau = \frac{M}{B} \tag{6}$$

where  $B$ —vane constant ( $\text{cm}^3$ ), taken according to vane type.

### 5 Implementation of the Proposed Technology

The solution to this problem is performed using the ASIS information-measuring system, the composition of which is shown in Fig. 1.

Currently, ASIS information-computing system is a set of measuring instruments (instruments and devices) and a set of control and computing programs for measuring the parameters of sensing and interpreting in-situ data and laboratory tests of soils (Fig. 1). ASIS information-computing system receives signals in digital form from sensors of penetration devices (CPT, CPTU, SCPTU, SPT, DCPT, RDT, VS, etc.), converts them to physical values (see Table 1), performs basic interpretation from the point of view of soil behavior, determines various physical and mechanical characteristics of soils, and calculates deformation of bases of buildings and structures in accordance with the requirements of the SR during the whole process of penetration devices into soil. The linear penetration speed, rotational speed, input force, and other force parameters are monitored and controlled by means of feedback to the drilling rig of the loading mechanism by the ASIS program.

As it was noted earlier, the estimated values of soil characteristics are based on the corresponding correlation equations. Correlation equations, in Geotek Field program, are based on the works of domestic and foreign investigations. Note that correlation equations are presented only as a guide to geotechnical use and must be carefully analyzed and adjusted for local soil varieties. The values of the obtained soil characteristics are estimated and should be clarified by carrying out the corresponding

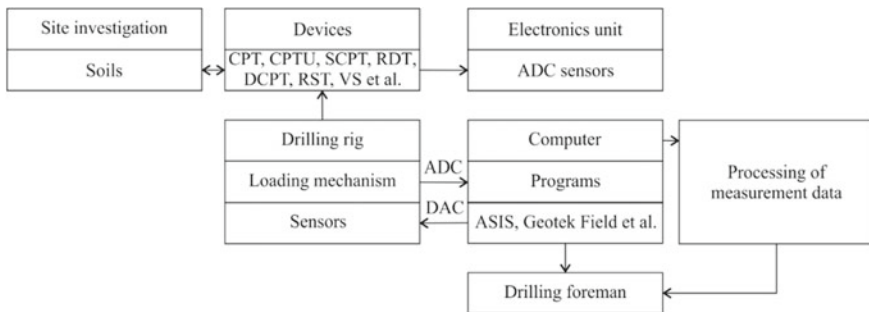


Fig. 1 Structural diagram of ASIS information-computing system

laboratory tests of the soils. At the same time, Geotek Field has a module “Statistics,” which is used to build local correlation equations according to laboratory and field soil tests. Now Geotek Field program includes several modules of calculation of the bases: settlement and tilt of the foundation; base stiffness coefficient; bearing capacity of foundation bases with use of analytical solutions [6–8].

## 6 Conclusion

The proposed complex technology combines engineering-geological and geotechnical investigations and design of structures bases into a single production process. The result is the reduction in investigation time due to the use of soil penetration methods with automated control of the testing process and interpretation of measurement data. At the same time, the result of engineering-geological and geotechnical investigations is not only information on soil properties, but also assessment of their impact on the behavior of the designed building or structure.

## References

1. EN 1997–1 (1977) Eurocode 7. Geotechnical Design. Part 1: General rules
2. Mayne PW, Coop MR, Springman S, Huang AB, Zornberg J (2009) State-of-the-art paper (SOA-1): geomaterial behavior and testing. In: Proceedings 17th international conference soil mechanics and geotechnical engineering, Millpress/IOS Press, Rotterdam, vol 4, pp. 2777–2872
3. Boldyrev G, Novichkov G (2016) The boring sounding of alluvial soils. In: Proceedings of 13th baltic sea geotechnical conference, pp 97–99
4. Boldyrev G, Novichkov G (2016) Evaluation of tip resistance to auger drilling. International conference on geotechnical and geophysical site characterization, 4–8 September, Australia
5. Teale R (1965) The concept of specific energy in rock drilling. *Int J Rock Mech Min Sci Geomech Abstracts* 2:57–73
6. Barvashov VA, Boldyrev GG, Utkin MM (2016) Calculation of settlement and tilt structures taking into account uncertainty of soil bases properties. *Geotechnics* 1:12–29 (in [Russian])
7. Barvachov VA, Boldyrev GG (2017) Sensitivity of structures and geological data. COMPDYN 2017. 6th ECCOMAS thematic conference on computational methods in structural dynamics and earthquake engineering. Papadrakakis M, Fragiadakis M (eds) Rhodes Island, Greece
8. Boldyrev GG, Barvashov VA, Sheynin VI, Kashirsky VI, Idrisob IKH, Diveev AA (2019) Information systems in geotechnical engineering—3D geotechnics. *Geotechnics* XI(2):6–27 (in [Russian])

# Present Demands on Earth Structures in Transport Engineering in Europe



Ivan Vaníček , Yvonne Rogbeck, Joost Bredeveld, Daniel Jirásko , and Martin Vaníček 

**Abstract** One of the major challenges for modern society is to continue providing sustainable, affordable, and available transportation networks for people and goods. The challenge is twofold: (1) new structures should be built in a more resilient and a more durable and affordable manner, and (2) existing structures need to be maintained, retrofitted, or reset for a new purpose. Over recent times, different visions for improving transport engineering in these areas have been defined in Europe. Like many transport and geotechnical engineering platforms, European Large Geotechnical Engineering Platform (ELGIP) declares the readiness of the field of geotechnical engineering to contribute to the realization of these visions. The focus is on both engineering approaches and those which are helping to add a new dimension to Earth Structures in transport engineering—sustainability, availability, and affordability. This paper describes some opportunities that are currently on offer in this field. In Europe, the engineering approach is recorded in EC 7—Eurocode 7 in which the principle of limit state design was accepted, and the geotechnical categories classification is used. The second generation of EC 7 is now undergoing the final phase of preparation. The question on how to consider sustainability in Earth Structures in Transport Engineering is covered by describing geotechnical solutions for reducing energy and resource consumption. Moreover, proactive measures to guarantee transport infrastructure availability and affordability under extreme circumstances (e.g., natural and man-made hazards) are discerned. In conclusion, this paper explains why geotechnical engineering should devote appropriate attention to the use of the

---

I. Vaníček · D. Jirásko (✉)

Czech Technical University in Prague, Thákurova 7, 166 29 Prague 6, Czech Republic  
e-mail: [daniel.jirasko@fsv.cvut.cz](mailto:daniel.jirasko@fsv.cvut.cz)

I. Vaníček

e-mail: [ivan.vanicek@cvut.cz](mailto:ivan.vanicek@cvut.cz)

Y. Rogbeck

Swedish Geotechnical Institute, Statens geotekniska institute, 581 93 Linköping, Sweden

J. Bredeveld

Deltares, P.O. Box 177, 2600 MH Delft, Netherlands

M. Vaníček

Geosyntetika Ltd., Nikoly Tesly 3, 160 00 Prague 6, Czech Republic



building information model (BIM) for Earth Structures in Transport Infrastructure generally.

**Keywords** ELGIP · Transport infrastructure · Earth structures · Sustainability · Availability · Affordability · BIM

## 1 Introduction

Over the most recent period, different visions for transport engineering have been defined in Europe. Politicians and investors (owners) of transport infrastructures should enable engineers to fulfill these visions. Therefore, many transportation and geotechnical engineering platforms are declaring their preparedness to contribute to the realization of these visions. ELGIP—the European Large Geotechnical Engineering Platform have prepared many supporting materials in this direction. Its focus is on both engineering approaches and other approaches which are helping to add a new dimension to Earth Structures in Transport Engineering—in terms of sustainability, availability, and affordability.

The engineering approach is now specified in Europe by Eurocode (EC) 7 Geotechnical Design where the principle of limit state design was accepted. In this paper, some possibilities in this direction will be described with respect to the second generation of EC 7 which is now in a final phase of preparation. The main focus is on risk identification and subsequent risk reduction for basic phases of geotechnical structure design and execution, as in the ground model, the geotechnical design model, the calculation model, and in structure construction (execution) with proposed quality control.

But the earth structures should not only be safe and economically efficient, but also environmentally friendly. Possibilities in this direction are now at the center of interest, as indeed is reducing energy and resource consumption as instanced for example with land and natural aggregates. For an area sensitive (or prone) to natural hazards such as landslides, flood, and rock falls, there is a tendency to increase structure robustness, to guarantee structure operation even on a limited scale and, at the same time, to limit costs for structure maintenance during life time expectancy.

The building information model (BIM) can be a very useful tool to guarantee mutual bonding of the above-mentioned aspects. In this way, it helps to stress the significance of geotechnical engineering, as well as a good cooperative relationship among the individual partners right from the start.

The presented paper will briefly describe the possibilities which geotechnical engineering is now offering and will utilize new achievements in this branch. However, only in some selected cases will a closer specificity be addressed.

## 2 ELGIP Activities

ELGIP was founded in 2002. Now ELGIP is a group of 14 European research organizations, leaders in geotechnical engineering, with the main aim being to promote internationally the profession, its networking, and its societal relevance. A working group on transport infra has over the last 5 years prepared different workshops, as on “Geotechnical risk management for transport infrastructure,” published a vision document “Reduction of geotechnical uncertainties for infrastructure” and also distributed a position paper “The need for improved knowledge and understanding of ground properties in transport infrastructure.” The organizer of the 4th ICTG 2021, after the meeting of the WG of ELGIP and TC 202 of ISSMGE supported not only the idea of closer cooperation, but also publication of the activities of the ELGIP WG at this conference.

Let us start with the main aims summarized in the position paper focused on policy makers, transport engineers, risk managers, geoscientists, and engineers, and their need to collaborate at early stages when planning, building, and maintaining transport infrastructure. Especially, cooperation in the early stages is extremely important as it is a chance to include in the design new ideas giving to the transport infrastructures (TI) such new dimensions as:

- Sustainable TI by using innovative solutions;
- Available TI by guaranteeing secure and resilient solutions;
- Affordable TI by cost optimization.

For example, innovative solutions by slope reinforcement can safeguard land, as well as demands on ground investigation, which is also important in the case of TI widening as additional land buying is a very sensitive problem. Application of large volume waste can limit the demands on natural aggregates, and the volume of embankments can be higher than the volume of cuts. In the final analysis, the position paper argues that planners and policy makers need to put money and efforts where it makes a difference—improved knowledge and understanding of ground properties.

## 3 Safe and Economically Efficient Earth Structures of Transport Engineering

According to [1], the European Commission agreed to sponsor the development of a set of European codes of practice for building structures and in this way to encourage free exchange between member countries going back as far as 1976. Eurocode 7 Geotechnical design was prepared in the 1980s under the umbrella of ISSMGE, but from the 1990s, the work on all Eurocodes was transferred to the European Committee for Standardization (CEN), namely that of Technical Committee 250—CEN/TC250. A subcommittee (SC 7) is responsible for Eurocode 7 (EC 7), of which a final draft was prepared in 2004. After positive voting by national standards bodies

the European standard EN 1997-1, Eurocode 7: Geotechnical Design, Part 1: General rules are valid in most European countries. A similar status was obtained for EN 1997-2. Eurocode 7: Geotechnical Design Part 2: Ground investigation and testing, which came two years later. After another 5 years, the review of existing codes started, and a second generation of the ECs is now prepared and being discussed before final voting. Geotechnical engineering will be more visible as the basic code EC 0 will have a title: Basis of structural and geotechnical design. With respect to EC 7, it will have three parts.

### ***3.1 EC 7—1 Geotechnical Design Part 1: General Rules***

Generally, the design principle assumes limit states with the application of partial factors of safety and distinguishing ULS—ultimate limit state and SLS—serviceability limit states. The second generation of EC 7 utilizes either the “resistance factor approach”—RFA or the “material factor approach”—MFA. In the first case, ultimate limit states involving failure of the ground should be verified using the partial factor for ground resistance and increased factor on effects of actions; while in the second case, ultimate limit states involving failure of the ground should be verified using partial factors for material properties and actions. EC 7 is recommending these partial factors. The National Standards implementing the Eurocodes will comprise the full text of the Eurocodes followed by a National Annex (NA). A NA can only contain information on those parameters, known as nationally determined parameters, which are left open in the Eurocodes for national choice. For SLS, the recommended partial factor is equal to one.

Subsequently, for each geotechnical design situation, it shall be verified that no relevant limit state is exceeded and shall provide a level of reliability no less than that required by EC 7. However, the complexity of each geotechnical design should be determined along with the associated risk, or with an impact (consequence) of failure. Three geotechnical categories are used for any distinction in this direction.

The geotechnical categories classification influences each step of the geotechnical structure design and execution. For example, with simple structures with low risk, the design can use geotechnical parameters which are collected as the result of the experience of our predecessors and are presented in different tabular form based on soil (rock) classification. On the other hand, the structures connected with very high risk deserve the collection of undisturbed samples on which geotechnical parameters are subsequently determined. The number of such samples from each lithological layer (geotechnical unit) should be sufficient for statistical evaluation. In both cases, the designer should select the characteristic (representative) values for geotechnical parameters as a cautious estimate of the value affecting the occurrence of the limit state. Therefore, the GC classification right from the beginning is very desirable. One of the possibilities for such classification is an overview of uncertainties linked with basic steps of the geotechnical structure design and performance as in:

- Ground model—containing geological model + results of lab and field tests;
- Geotechnical design model—where for each lithological layer (geotechnical unit) or discontinuity there is selected a characteristic (representative) value, subsequently used in the next phase namely in the calculation model;
- Calculation model which includes analytical or numerical calculation models;
- Geotechnical construction—sensitivity of geo-technology to the input data.

When checking limit states of a geotechnical structure (during the phase of the calculation model) with the help of the partial factor method, the inequality given below (Eq. 1) shall be verified:

$$E_d \leq R_d \quad (1)$$

where

$E_d$  is the design value of the effect of actions;

$R_d$  is the design value of the corresponding resistance.

### **3.2 EC 7—2 Geotechnical Design, Part 2: Ground Investigation**

EN 1997-2 provides rules for specifying the ground investigation (GI) used to gather information needed for the design and verification of geotechnical structures. The relationship between the GC and demands on sampling was already mentioned. Generally, it is valid that in the phase of ground investigation planning, the relationship between the proposed structure and methods of the ground investigation as well as required geotechnical information should be considered. Therefore, more attention is devoted to the demands of ground investigation for individual geotechnical structures than on own tests, either lab or field. The usefulness of different phases of ground investigation are described in more detail, such as desk study and site inspection, preliminary GI, GI for design, construction, and control and monitoring investigations. This latter one is able to evaluate the differences in the results during this last phase against the results obtained during the phase of the design GI. In the case of large differences, the geotechnical structure should be re-modelled for new information. The range of investigation points should guarantee that all ground volume which will be affected by geotechnical structure will have been investigated. As TIs are generally 2D structures, the verification between individual investigation points in longitudinal direction can be controlled by indirect methods, namely by geophysical ones. Therefore, our attention is focused on quicker and cheaper possibilities with a high predicative value in order to decrease uncertainties connected with the ground model. It is valid not only for ground (subsoil), but also for borrow pit. Attention is also devoted to ground mechanical response to dynamic loads and to parameters for seismic loading. The result of the ground investigation is summarized

in the ground investigation report (GIR), which shall be part of the geotechnical design report (GDR).

### **3.3 *EC 7-3 Geotechnical Design, Part 3: Geotechnical Structures***

The proposal for EC 7-3 includes the following geotechnical structures: Slopes (embankments and cuts), spread foundations, piles, retaining structures, anchors, reinforced (soil) earth structures, and ground improvement. The last two were not specified in the first version and deserve a few additional notes. Still not all geotechnical structures are mentioned there, typically the most difficult structures such as tunnels or high earth and rock-fill dams. General rules are valid for them but should normally include alternative provisions and rules to those in EC 7. For example, in the case of tunnels, a special expert group was established by means of the Joint Research Center (JRC) administered by the European Commission and sponsored by CEN.

With respect to ground improvement, different techniques are classified into:

- Diffused ground improvement as, e.g., different compaction or consolidation methods, different methods of mixing and grouting, or
- Discrete ground improvement as, e.g., different vertical columns as stone, geosynthetic encased columns or jet grouting, vibrated concrete columns.

The distinction between the two basic improvement techniques has a strong impact on characteristic parameters selection. For diffused improvement, the properties of new material should be tested; while for discrete improvement in most cases, the characteristic parameters are determined for basic ground as well for discrete elements.

Ground improvement techniques are studied very intensively as they can help to reduce an expulsion of less appropriate ground from the construction process. Clayey soils with higher moisture content than optimum are a typical example, where stabilization with lime is a preferred way of ground improvement. A different amount of quick lime can lead firstly to a workability improvement (roughly up to 2%), while higher content up to 6% can lead to a strengthening improvement. New characteristic values of geotechnical parameters are selected from the tests performed on stabilized clay at least 28 days after soil stabilization. However, this process is problematic for soils containing sulfates, or where sulfates arise through oxidation of “sulfides,” as in this case, the final result is sensitive to swelling due to creation of mineral ettringite.

From the viewpoint of TIs, the chapter on reinforced ground deals with fill reinforcement (mostly with geosynthetics), slope cuts reinforcement by soil nailing or, respectively, with basal reinforcement. A recommendation is given for the long-term design strength of geosynthetics reinforcement based on ultimate short-term strength. For verification of ULS by analytical methods of slices, the distribution of tensile

forces in a reinforcing element is recommended with a maximum (long-term design force) at a point where the reinforcing element is cutting a potential slip surface.

## 4 The Sustainability Principle

It is now about 30 years since the concept of sustainable development was accepted at the highest level during the International conference “Environmental Summit” in Rio de Janeiro. Over time, this concept was gradually developed in various areas of human activity, including geotechnical engineering, e.g. [2–4] Very briefly stated, the principle is to propose geotechnical structures which are not only safe and economically competitive, but also much friendlier to the environment. However, this concept was accepted by politicians only at the highest level, while here it is a specialist duty to say how we are prepared to fulfill this concept. Usually in the field of TI, the focus is on saving land, natural aggregates, and energy (or here at least setting on lower CO<sub>2</sub> footprint). This can be achieved with implementation of new advances in geotechnical engineering, developing from the fact that this branch always had a very close working contact with the environment. In order to reach this new goal, full acceptance should be declared from all sides of the construction process (investors—owners, ground investigators, designers, contractors) involving them from the very earliest steps. Nevertheless, there are many different questions on how to include any savings into the total (or at least the bidding) price of the project. For example, the price of land should be included as is at the phase of design or that which can be expected during half of the structure life time expectancy. How do we express the benefit when the large volume waste can be used for the TI construction instead of depositing it at different landfills? How can we evaluate the lower CO<sub>2</sub> footprint? Therefore, this means that the technical solution to these problems, which will be presented below giving the simplest examples, should be accompanied by answers to these kinds of above-mentioned questions.

### 4.1 Savings on Land

Annual consumption of land for different activities in Europe is alarming. Many countries declared an effort to significantly safeguard land, in the first instance denoted as greenfield. The transportation network is one of the greatest land consumers. Merely to reduce land consumption or divert it on to less valuable land such as, e.g., brownfields, TI gives roughly two basic possibilities:

- During TI planning to situate it on less valuable land (brownfields) or to find such a traffic route that will need lower embankments and shallower cuts;
- To propose steeper slopes with the help of new techniques, as is, e.g., soil reinforcement.

As steeper slopes enable a saving on not only land, but also natural aggregates and energy they should be preferred, even when this solution may require better protection of slopes against surface erosion.

As buying up of land is always a very difficult task, steeper slope reinforcement (by geosynthetics for fill and soil nailing for cuts) can be a very attractive solution for any proposed existing TI widening, especially if the geomorphology allows it.

## 4.2 *Savings on Natural Aggregates*

TI uses huge amount of natural aggregates, therefore any basic effort is connected with higher utilization of different materials denoted as waste, especially where these are produced in large volume, as in:

- Construction and demolition waste—e.g., bricks, concrete, ceramics;
- Excavated soil during construction activities in cities—e.g., metro, underground garages;
- Mining waste—different waste rocks, debris;
- Industrial waste—e.g., flying ash from electric power stations, slag from metallurgy, waste (tailings) from concentrator factories.

The application of the above-mentioned large volume waste can decrease the need of their deposition on different landfills, so they can change the general principle about balance of the volume of ground excavated in cuts with volume needed for fill. However, the decision in which phase of the revaluation chain the particular residue can be used, depends on:

- Structural stability—sensitivity to structural collapse or sensitivity to swelling;
- Qualification of a leachate character and subsequent contaminant transport modeling—to prove that there is a practically negligible potential risk of environmental contamination.

Recent and current experience shows that there is a high potential for the application of large volume waste. Even a very high mining spoil heap composed from clayey clods deposited by free fall can be used for TI—[5]. There is similar validity for embankment where flying ash was deposited together with classical soil in sandwich arrangement [6]. Only one example of small volume waste can be mentioned. Small pieces of waste glass which are not appropriate for recycling in a glass factory can be transformed to foam glass. Grains of foam glass about the size of sand and gravel have a very low density of about 150–70 kg/m<sup>3</sup>. When used as bridge abutment backfill, such material can reduce fill settlement, also earth pressure and in addition, it has very good insulation and drainage properties.

### 4.3 Savings on Energy

As consumption of energy used for transportation is huge, about 30–40% of all spend energy, there is now a natural trend to reduce it. In the field of transportation geotechnics, there are different possibilities. Instead of the already mentioned (lower demands on excavation and transport), they can be divided into:

- Renewable energy harvesting;
- Savings via application of new geo-technologies;
- Savings via application of geotechnical structures with lower demands on energy or with a lower CO<sub>2</sub> footprint.

ELGIP common European research project COST called GABI was focused on thermo-active structures—energy piles, diaphragm walls, and tunnel lining. Pipes installed in these structures can, with the help of reversible heat pumps, extract heat from surrounding ground in wintertime and deposit there heat in summertime. In transport engineering, this system is applied for tunnels, foundations of bridge piers as well as for bridge abutment. Harvested energy can be used for the transport infrastructure surface, in order to limit extremely low and extremely high temperature there. Toward a similar purpose of utilization, the energy can be harvested also from a low depth. Earth areal heat exchanger can be placed on the contact of the embankment with the ground. Numerical models of heat transfer are exploited to define the total amount of energy which can be extracted for specific ground conditions.

Soil compaction is a basic technology for embankment construction. Selection of the optimal type of compaction technique, as well as thickness of the compacted layer and frequency and amplitude for vibratory technique is the first possibility to limit energy consumption during this process. A significant step forward was achieved with rollers denoted as with continuous compaction control (CCC) or as intelligent compaction. Last year, a special symposium was dedicated to the 40 years anniversary of this technology [7]. Besides the main output—to be informed directly about the compaction result—this technology can decrease energy demands via optimization of roller passes and via savings on classical control in a lab. Other possibilities are tested for rollers with non-standard shape of drum or with non-circular compacting masses.

In building engineering, the term “smart buildings” is now very fashionable, where the term “smart” is mostly connected with structures which need less energy with a lower CO<sub>2</sub> footprint. Politicians have declared the intention to stop or limit atmospheric concentration of CO<sub>2</sub>, and therefore, geotechnical engineers should also try to follow in this direction. For example in [8], there is already approval that classical concrete retaining wall needs more energy with a higher CO<sub>2</sub> footprint than a retaining wall from made from reinforced soil. However, to be able to declare more examples, we need to be more familiar with this energy as a CO<sub>2</sub> calculation, as up to now, it is out with our field of competence.



## 5 The Availability and Affordability Principles

Demands on the mobility of both people and goods have been increasing steadily over time, and safe access to certain places at certain times is expected to be guaranteed not only under usual conditions, but also under circumstances resulting from natural or man-made hazards including accidents.

Three proactive measures mentioned in this chapter include a better forecasting of unusual and emergency events, increasing structural resistance and finally, emergency action planning.

### 5.1 *Resilience of Infrastructure in the Context of Climate Change*

At present, it is obvious that average temperatures have been increasing and registered in most European countries over at least the last 50 years. Therefore from the viewpoint of available and affordable infrastructures, it is important both to adapt the existing infrastructure to any climate change and to consider climate change when designing new constructions. The effects of climate change on the subsurface and on the infrastructure will vary between different countries in Europe; but in all countries, it is important to take this matter into account. Extreme events seem to become yet more extreme and more frequent. Increased and more intense precipitation, sea level rise, increased water flow, storm surge, more surface water, increased periods of freezing and thawing (zero crossings), and more drought in summer can be included among the climate change effects.

Extreme weather may have a significant impact on any infrastructure. Sea level rise and water-related effects may lead to flooding and erosion that also might influence the bearing capacity and the stability of slopes and embankments. The probability of natural hazards like landslides and rock fall will also increase. More thawing and snow melt can increase water content in base or sub base layers in road embankments followed by cracking and degradation of pavements. Heat waves and droughts may induce shrinkage of the soil leading to differential settlements.

Adaptation of existing infrastructure should be undertaken to reduce future damage. The measures can be different depending on the problems. Uncertainty in climate predictions must be considered, and different climate scenarios should be used for assessing the resilience of existing infrastructure. Planned infrastructure should be more robust and designed to be more resilient to changes in conditions. Hazard mapping, risk analysis, and risk management should be performed to help in considering the climate change effect on any infrastructure. Monitoring could be used on existing infrastructure as an early warning system. It is also important to develop the methods available for decision makers.

Many research projects have been studying the different phenomena and the effect they have on infrastructures as in [9] and [10]. There are also a many ongoing research

projects in Europe with the purpose of getting a deeper understanding of the effect of climate change and to find solutions for existing infrastructure and design methods for new infrastructure. One such example is the European project INTACT which deals with the impact of extreme weather on critical infrastructure.

As the expected temperature increase has the highest impact on floods, landslides or rock falls, the interaction of these events with TI is now at the very center of our interest.

## 5.2 Landslides

According to [11], landslides create roughly 17% of all negative impacts caused by natural hazards. As a result, an ELGIP workshop arranged in Paris 2019 was also devoted to this problem. The problem of slope instability is especially sensitive for areas prone to landslides, as is also these areas—with respect to their range—that should be used for TI. Typical problems are connected with:

- Landslides in quick clays;
- Landslides along a contact of quaternary layer with elder fine sediments, as, e.g., claystone;
- Landslides with over-consolidated fissured clays or weak rocks.

The first case is typical only for a limited number of countries and is the subject of interest on International Workshops on Landslides in Sensitive Clays (IWLSC), the last one arranged in Trondheim 2017. Two other cases are more general. An increase of the ground water table in the quaternary layer can decrease slope stability to reach a limit state of instability and can be a reason for shallow planar landslides, [12]. If during such a situation, man-made impacts are also realized, as in cuttings in the lower part of the slope or deposition in the upper part of the slope, the slope instability is more realistic [13, 14] describes large landslides affecting the highway A7 in Granada with a mobilized volume greater than 1.5 million cubic meters. Dolomitic karstified and fractured marbles are overlaying phyllites which are in their upper part highly weathered. Cuts for motorway in phyllites that initiated horizontal deformation with progressive slip development passing through this material for which a residual angle of friction  $13^\circ$  was measured with a ring shear apparatus. In the upper part, the slip surface went through cracks in the marble. Remediation measures were proposed, combining such different possibilities as pore water pressure reduction (by vertical drains), excavation of material in the upper part, and finally, the construction of a retaining wall from diaphragm panels in the lower part.

### 5.3 Floods

Nearly one third of all natural hazard damage is attributed to floods. One of the problems relates to the higher utilization of flood prone areas. Given expected climatic changes, an increase in attention is fully justified. Among the main problems, now investigated are:

- Foundation of bridges;
- TI such as road and railways embankment in direct contact with floods;
- Flood protection measures such as dikes, small dams the surface of which is used for TI.

During floods access to bridges is usually limited or indeed the bridge is closed. Reopening after a flood, wave decrease is associated with a structure check, when attention is not only focused on the upper structure, but preferably also on pier foundation. The higher level and speed of flowing water causes scouring of ground along bridge pier which can lead to failure. Therefore, the depth of scouring for an expected maximum water level has to be calculated and compared to the foundation depth. As the foundation depth is usually low for historical bridges, in that case, the problem is extremely sensitive. Charles bridge in Prague, founded in the fourteenth century, is one such example. Reference [15] described the interaction of bridges with floods for the Po River in Italy.

For direct contact of embankments of TI with floods, two basic examples have a different approach. When the TI embankment is close to, and parallel with, water course surface erosion of slopes, then it creates a very sensitive place. As these most sensitive places can be detected in advance, the protection measures should be realized as soon as possible. When the TI is intersecting the water course, there is a potential problem with culvert blocking. The water level is going up, and seepage through the embankment can start. Practical examples show that partly saturated less permeable material is most dangerous, as enclosed air bubbles can cause upheaval and slope instability [16].

The last case of interaction is typical for dikes and small dams the surface of which is used for TI. The character of any failure tends to be caused by internal or surface erosion. For historical small dams, the sensitive place with respect to the internal erosion is along the old bottom outlet, often a wooden one. The connection with surrounding ground is often affected by the vibration of heavy trucks. Surface erosion is playing a most important role when the crest is overflowing. Asphalt pavement can significantly increase resistance against surface erosion. Similarly, some protection measures on the downstream slope are recommended, e.g., geosynthetics mattresses.

A last note is devoted to the potential flooding of a metro system as occurred in Prague during heavy floods in 2002.

## 5.4 Rock Falls

Due to heavy traffic increases as well as the expected climatic changes, the problem of interaction of TI with rock falls has been getting greater priority in recent times. Protection measures applied on the slope are developed as well as protection barriers at the slope toe. Numerical modeling of individual rock block falls can help to design these barriers for expected impact force. However, the same care is devoted to emergency action planning. In the case of direct access to the individual blocks which can fall down, the installed sensors control their movements and when crossing limits defined in advance, the control point is alarmed or the TI closed [17]. When there is no such access, the slope is observed geodetically or by geophysical methods with respect to observed points or blocks movement. Reference [18] describes the utilization of ground-based radar interferometry for such purposes.

## 6 The BIM Model

For BIM—the building information model there exist different definitions. One of them describes BIM as an information database which can encompass all data starting from the design, through the construction phase, the management facility, on to maintenance and right up to the demolition of structures. A 3D digital model of structure is the basis of the BIM model, enriched by other information such as time, financial expenses, structure management, etc.—by which we can refer further to 4D, 5D, and then generally concerning nD models.

The implementation of the BIM model is a little bit slower for civil engineering structures than for building engineering; but in some countries, this model should be used for significant structures financed from the governmental budget. For the Czech Republic, the starting year is 2022.

Geotechnical engineering is playing an irreplaceable role in the whole process as all structures are founded on ground, and the interaction of an upper structure with ground is secured by foundation structures. Also earth structures as well as underground structures are in interaction with ground, and therefore, partial models entrusted to geotechnical engineers will be covered by models similar to those mentioned in EC 7—the ground model, the geotechnical design model, the calculation model, and finally, a model of the fully realized geotechnical structure placed into the last ground model.

The exploration of such a model will have different levels:

- Information such that the range of the ground investigation corresponds to the demands of structure design;
- Information on whether the structure was constructed in accordance with the previous demands;
- Information about an individual element of the structure—e.g., for each day, the range of compacted layers can be controlled together with results of compaction

control, preferably if continuous compaction control (CCC) was used and having also GPS, and this, together with information from which borrow pit the soil for this layer, was excavated and what properties it had;

- Information for future purposes should a designed geotechnical structure have some problems (e.g., during any interaction with natural hazards or man-made accidents) or in the case where a new proposed structure would be in interaction with an existing one.

The BIM model creates a new level for civil engineering, and our specialist branch can play a very important role here. Therefore, we have to pay close attention to this new approach from the start or as early as possible.

## 7 Conclusion

This paper shows that, according to ELGIP (the European Large Geotechnical Engineering Platform), geotechnical engineering offers many opportunities for contributing to the realization of visions on new and existing transport infrastructure. These opportunities occur in both engineering approaches (EC 7) and approaches which are helping to add new dimension to Earth Structures in Transport Engineering—sustainability, availability, and affordability. In conclusion, to seize all the opportunities (including those described in this paper), geotechnical engineering should devote proper attention to the use of BIM for Earth Structures in Transport Infrastructures.

## References

1. Frank R, Bauduin C, Driscoll P, Kavvas M, Ovesen KN, Orr T, Schuppener B (2011) Designer's guide to Eurocode 7: Geotechnical Design, EC 7-1 General rules. London, Thomas Telford, first ed. 2007
2. O'Riordan N (2012) Sustainable and resilient ground engineering. In: Keynote Lecture, 11th Australia-New Zealand conference on geomechanics, Melbourne, Australia
3. Vaníček I, Vaníček M (2013) Modern Earth structures of transport engineering. *Procedia Eng* 57:77–82. [online] Available from <https://doi.org/10.1016/j.proeng.2013.04.012>
4. Correia AG, Winter MG, Puppala AJ (2016) A review of sustainable approaches in transport infrastructure geotechnics. *Transportation Geotechnics* 7:21–28
5. Dykast I, Pegrimek R, Pichler E, Řehoř M, Havlíček M, Vaníček I (2003) Ervěnice corridor—130 m height spoil heap from clayey material—with transport infrastructure on its surface. In: *Proceedings 13th EC SMGE, Prague, CGtS, vol 4, pp 57–76*
6. Vaníček M (2006) Risk assessment for the case of waste utilization for embankment construction. In: Logar J, Gaberc A, and Majes B (eds) *Proceedings XIII. Danube European conference on geotechnical engineering. Ljubljana, Slovenian Geotechnical Society, vol 2, pp 799–806*
7. Brandl H, Kopf F, Adam D (2005) Continuous compaction control (CCC) with differently excited dynamic rollers. *Bundesministerium für Verkehr, Innovation und Technologie, Straßenforschung Heft 553, Wien, p 150*

8. Heerten G, Völlmert L, Herold A, Thomson DJ, Alcazar G (2013) Modern geotechnical construction methods for important infrastructure buildings. In: Delage P, Desrues J, Frank R, Puech A, Schlosser F (eds) Challenges and innovation in geotechnics. Proceedings 18th ICSMGE, Paris, vol 4, pp 3211–3214
9. Rogbeck Y, Lofroth H, Rydell B, Andersson-Skold Y (2013) Tools for natural management in a changing climate. In: Delage P, Desrues J, Frank R, Puech A, Schlosser F (eds) Challenges and innovation in geotechnics. Proceedings 18th IC SMGE, Paris, 2013, vol 4
10. Lacasse S (2013) Protecting society from landslides—the role of the geotechnical engineer. 8th Terzaghi Oration. In: Proceedings 18th IC SMGE, Paris, vol 1
11. Kalsnes B, Nadim F, Lacasse S (2010) Managing Geological Risk. In: Proc. 11th IAEG Congress, Auckland, New Zealand, pp 111–126
12. Vaníček I, Jirásko D (2019) Interaction of transport infrastructure with landslides. Example for D8. ELGIP Workshop, Paris
13. Katzenbach R (2019) How to analyse and how to avoid landslides. ELGIP Workshop, Paris
14. De la Oliva JLG (2019) Ground investigation and stabilization design for a large landslide in A7 highway, Granada. ELGIP WORKSHOP, Paris, Spain
15. Malerba PG (2011) Inspection and maintenance of old bridges. In: Vaníček I (eds). Sustainable Construction. CTU Press, Prague
16. Vaníček I, Jirásko D, Vaníček M (2020) Modern Earth Structures for Transport Engineering. Engineering and Sustainability Aspects, CRC Press. <https://doi.org/10.1201/9780429263668>
17. Jirásko D, Vaníček I (2017) Practical example of the infrastructure protection against rock fall In: Building up efficient and sustainable transport infrastructure 2017 (BESTInfra2017). IOP Publishing Ltd., Bristol. IOP Conference Series: Materials Science and Engineering, vol 236. ISSN 1757-8981
18. Barla G, Antolini F, Barla M, Mensi E, Piovano G (2019) Ground-Based Radar Interferometry for the monitoring of a deep-seated landslide, Aosta Valley, NW Italian Alps. ELGIP Workshop, Paris

# Multidomain Approach for Track Maintenance and Renewal



Amine Dhemaied , Gilles Saussine, Aurélie Schwager Guillemenet, Jean Michel Cornet, Quang Anh Ta, and Mathilde Koscielny

**Abstract** The French rail network comprises more than 30 thousand kilometers of lines with over 15,000 trains running each day. Most of the lines are more than 100 years old. As a result, the rail network is aging due to natural wear and tear of the materials and environmental conditions despite regular maintenance. Various and non-necessary optimized maintenance practices, either extended or localized, to improve the condition of the railway lines are carried out every day. Besides, accurate knowledge of the substructure condition is necessary to assess the quality of the track line. In order to (a) improve the network performance, (b) increase the traffic on this network, (c) maintain a high level of safety, and (d) improve the comfort and accessibility of infrastructures, the French railway company SNCF planned to use a holistic assessment approach for the rehabilitation and modernization of hundreds of kilometers of rail lines. The results obtained in the studies showed that it is possible to carry out an optimal classification of railway sections which require a structural reinforcement of the platform, propose drainage rehabilitation, or complementary investigations for better decision making. The crossing engineering domain described here has included procedures for assessing the optimum engineering solutions to acceptable long-term performances for railway line. This multidomain approach gives an adapted rehabilitation technique.

**Keywords** Railway · Maintenance · Georadar · Drainage · Hydrogeology

## 1 Introduction

Many French railway lines have been in operation for more than 100 years. Their rehabilitation or adaptation to modern trains or increase of speed requires a detailed characterization of their geotechnical characteristics in order to propose relevant maintenance operations. Accurate knowledge of the substructure condition is important in effectively assessing the potential for service interruptions and the need for

---

A. Dhemaied (✉) · G. Saussine · A. S. Guillemenet · J. M. Cornet · Q. A. Ta · M. Koscielny  
SNCF Réseau, 93574 La Plaine Saint-Denis Cedex, France  
e-mail: [amine.dhemaied@reseau.sncf.fr](mailto:amine.dhemaied@reseau.sncf.fr)

slow orders. An important part of a railroad's track maintenance budget is allocated to correct rough track that is caused by movements in the substructure under repeated train loading. The substructure performance is significantly affected by moisture accumulation thickness of the roadbed layers and water accumulation. This multidomain analysis focuses on an analysis of maintenance operation, layers geotechnical characterization, an evaluation of the drainage system capability, and a survey of hydrogeology condition. The results obtained in the studies showed that it is possible to carry out an optimal classification of railway sections which require a structural reinforcement of the platform, propose drainage rehabilitation or complementary investigations for better decision making. The crossing engineering domain described here has included procedures for assessing the optimum engineering solutions to acceptable long-term performances for railway line. This multidomain approach gives an adapted rehabilitation technique.

## 2 A Holistic Assessment Approach: Background Information

Since 1800s, the predominate design of French railway track structures is the ballasted trackbed. This "classical structure," which does not comprise any sub-ballast or shape layer. It consists of a ballast layer which has been deposited on various supporting soil improvement devices or directly on the ground. This has resulted in the development, under the ballast, of a "plugged" ballast layer, followed by a so-called "intermediate layer" horizon, which is usually stable and compacted by the successive passages of trains. This layer consists of an in situ ballast mixture by interpolation of the ballast in the ground in place (Fig. 1).

The SNCF track inspection program is carried out on a weekly or monthly basis by specific monitoring trains. The collected data are transformed to indicators which enable managers to plan maintenance or renewal actions. These indicators coupled with geotechnical investigations highlight the appearance of defects which may originate from disorders related to components of the track and/or variation in the structures of the railway platform, nature of the subsoil or poor drainage. Besides, for

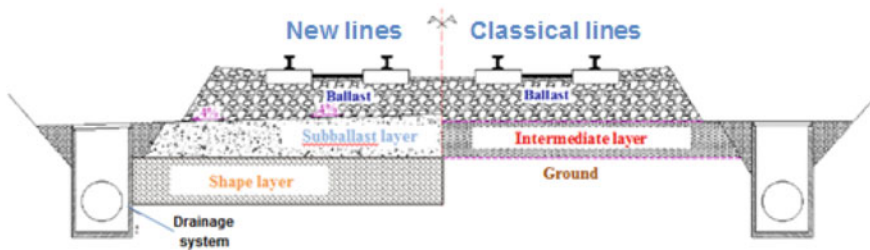


Fig. 1 Comparison between new and classical lines structures ( Source before adaptation: [1])



many old lines (in terms of age and / or last date of regeneration work), restoration of the track geometry requires a complete regeneration of the line.

The identification of railways line portions presenting geotechnical issues (sub-ballast layers and hydraulic disorders) require selecting and collecting appropriate data for better analysis in order to define relevant and optimized works solutions. Therefore, we propose a method to estimate the sections which are predisposed to rapid degradation according to the following characteristics:

- History of maintenance: the number and nature of maintenance operations are an indicator of the degree of degradation and enable to prioritize areas to regenerate,
- Geotechnical investigations: the thickness, nature, and mechanical characterization of under ballast layers are key parameters to determine if geotechnical works are needed,
- Drainage capability and site configuration: the knowledge of the hydric state of the structures enables to determine whether the hydraulic system works correctly or not, and then makes it possible to anticipate the need for hydraulic works and to grant regeneration works sustainability. Railway environment and configuration of the earthwork,
- Hydrogeological context: the hydrogeological risk combined with the configuration of the earthwork is good indicators of possible water-related disorders that impact the platform

### 3 Methodology

As mentioned previously, the input data that are considered are related to the maintenance, the geotechnical properties, the drainage, and the hydrogeological context [2].

#### 3.1 Maintenance

Measurement of track geometry quality is the most used automated condition assessment technique in railway maintenance. Most problems with the track (at least the ones concerning the ballast and substructure) will be visible as track geometry irregularities, but the root cause of the problem is not detected via the track geometry measurements. In these cases taking into account, maintenance parameters are a part of a decision-making approach which allows confirm the root cause of poor track behavior [3]. We propose in our approach to focus on the longitudinal level (NL for “Niveau Longitudinal”) variations.

The main parameters are the four last values of longitudinal level and the cumulative tamping operation over the last 10 years. The analysis consists in identifying the NL evolution which represents the degradation rate of railway track and comparing the maintenance effort to the average for corresponding UIC group.

We also focus on the cumulative number of mechanized and manual maintenance. The analysis' results can help to evaluate the impact of maintenance on the curative work capability to ensure a stable maintenance effort. The clean ballast thickness (BS) is also considered. The parameters combination enables to identify railway track portion weaknesses.

### 3.2 Geotechnical Properties

The maintenance effort is strongly influenced by the properties of the track layers. From the experience and innovative tool, we have the opportunities to conduct geotechnical surveys based on combined use of Georadar technique (Fig. 2), Panda<sup>®</sup> dynamic penetration tests and Geoendoscopy ([2, 4, 5]) (Fig. 3). 2D Georadar evaluations, we obtain a simple representation of the longitudinal section. For the Panda<sup>®</sup> test, in addition to calibrate the Georadar data, we get local information about geotechnical properties of the different layers of the railway platform.

We propose to evaluate the following parameters:

- Mechanical quality of the sub-ballast layers which is evaluate as a mean value of the cone penetration test (when the information is available),
- Thickness of the sub-ballast layers,
- Mechanical quality of the supporting ground in order respect the SNCF Railway classification (when the information is available),
- Moisture level evaluated by the Georadar or/and Geoendoscopy test ([4, 6–8]): the presence of water in the different layers degrades the soils mechanical properties so it is essential to evaluate the saturation level.



**Fig. 2** Georadar vehicle (Source: Ground Control Geophysik & Consulting GmbH), PANDA<sup>®</sup> equipment (Source: Sol Solution's PANDA<sup>®</sup> slides and [6]) and Geoendoscopy

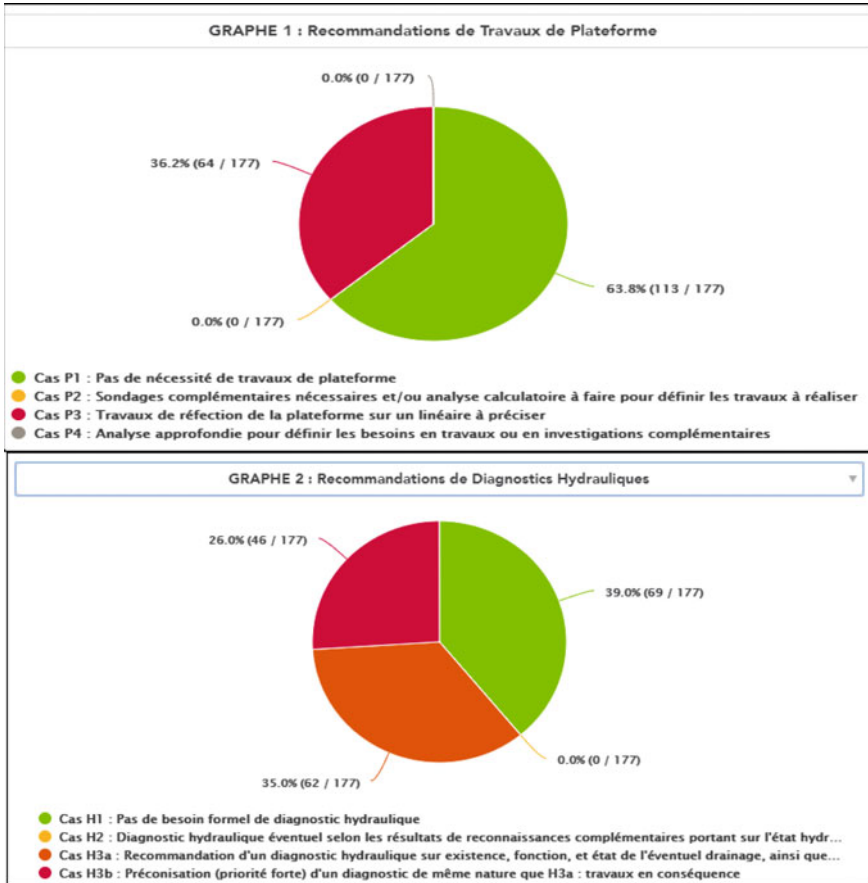


Fig. 3 Pie charts representation with on the top, the platform works recommendations and on the bottom, the hydraulic diagnosis recommendations over the Buchy—Motteville line. The definition of the different “The platform works recommendations” and “Hydraulic diagnostics” cases is detailed in paragraph 4 above. (Source: SNCF Réseau)

### 3.3 Evaluation of Drainage Capability

The purpose of this analysis is to identify areas with hydraulic hazards with respect to drainage. The identification of vulnerable areas can help to identify the root problem in order to ensure sustainability of the railway track. A second objective is to optimize maintenance and/or renewal work to maintain a healthy line.

The main disorders affecting the track’s stability are generally due to poor quality of drainage which plays an important role on the mechanical properties of substructure layers [9]. Under the effect of repeated stress of train circulations and increase in railway load and traffic, trapped waters create progressive and irreversible softening of platforms particularly in sensitive soils (clay, marl, etc.). They contribute rapidly to

reduction of lift which is recognized by the alteration of track geometry appearance of muddy areas. Moreover, the geometry of the track can be affected indirectly by alteration and aging of earth structures.

A diagnosis concerning the hydraulic aspect will make it possible to identify the zones with high criticality in order to study them more finely. The parameters chosen for this analysis are as follows:

- Environment of the line (urban, agricultural, forestry) plays an important role on water circulation and consequently on stability of the railway infrastructure,
- Previous water-related disorders are indicative of a risk. This type of disorder and its repetition (within a close perimeter) can give information about a reason related to water. The number of disorders that will be taken into account in this analysis.
- Classification of earth structures according to internal SNCF references, namely sensitive works (OTS) for water-related hazards, special works classified as water-related hazards (OTP), and current structures (OTC),
- Configuration of earthwork and more specifically if it is cutting or rock trenches, grazing embankments or simple embankments,
- Drainage and drainage devices with regard to the following criteria:
  - Information on the presence or absence of a water drainage system,
  - Hydraulic and mechanical condition, whether good or bad,
  - Drainage functionality: the drainage of the seating structures must be ensured, and there must be no blocking of the flows (no sealed cords, for example). For that purpose, the drainage timing was considered; the top of the drainage must be located lower than the bottom of the intermediate layer and the presence of rising mud traces.

### ***3.4 Hydrogeological Analysis***

The object of this diagnosis is to identify the zones presenting a hydrogeological risk with respect to the rail network (slope, platform, and track) and the configuration of the earthwork.

Hydrogeological risk is a hazard that is related to groundwater. Flows of water and aquifers circulate through enclosures that are of different natures (limestone, marl, sandstone ...). A geological approach is therefore needed to determine whether or not there may be a potential groundwater presence.

The potential presence of an underground water table can lead to indirect or direct disturbances at the level of the platform and track. Phenomena such as muddy ascent, slope slide, and groundwater level variability may result in tracking and/or drainage disorders and flooding of the platform [3]. Two criteria were used to identify potential risk areas:

- Potential presence of aquifer close to the surface of the TN base on the classification of BRGM,
- Configuration of the earthwork according to the three categories: embankment, grading embankment, and excavation.

This hydrogeological diagnosis includes certain limitations such as the data precision, the lack of information on the height of the cuttings, and since most of the parameters are not punctual, evaluation was made for the most critical zone of the 200-m section.

## 4 Results and Case Study

The proposed approach gives a practical framework for engineers according to the SNCF technical references by considering four domains: maintenance, railway geotechnics, hydraulic, and hydrogeology. The evaluation was made for 200-m portions. The combination of the domains allows defining directly civil engineering works and gives practical information for railway track managers.

The expert system, which represents all the combination for decision making, helps to define eight cases:

- Renewal works
  - Case P1: No need of civil engineering work,
  - Case P2: No information,
  - Case P3: Civil engineering is needed on a length that remains to be defined
  - Case P4: Advanced analysis to define the civil engineering works required or the supplementary geotechnical investigations
- Hydraulic diagnoses
  - Case H1: No need of hydraulic diagnosis,
  - Case H2: No information,
  - Case H3a: Recommendation of a hydraulic diagnosis based on the presence, function, and possible drainage state as well as a link with possible former disorders,
  - Case H3b: Recommendation of an hydraulic diagnosis like H3a with a high priority (existence of a disorder related to water and/or a high hydrogeological risk)

Also, this approach was tested on a few projects where works have been initiated urgently: it helped to adapt or modify works methodologies and finally led to better-progressed projects. The next step of this work is the evolution from a system based on expert analysis to the use of neural network techniques based on expert knowledge

and database from numerous diagnoses. Some tests have been done and show some very encouraging results.

### **Case Study: Buchy—Motteville**

In the context of the the Buchy—Motteville line modernization, a diagnosis has been carried out. This modernization is aimed at maintaining a dense traffic over a 30-year period, a 100 km/h speed, and a traffic increase with two dozen trains instead of 10 currently.

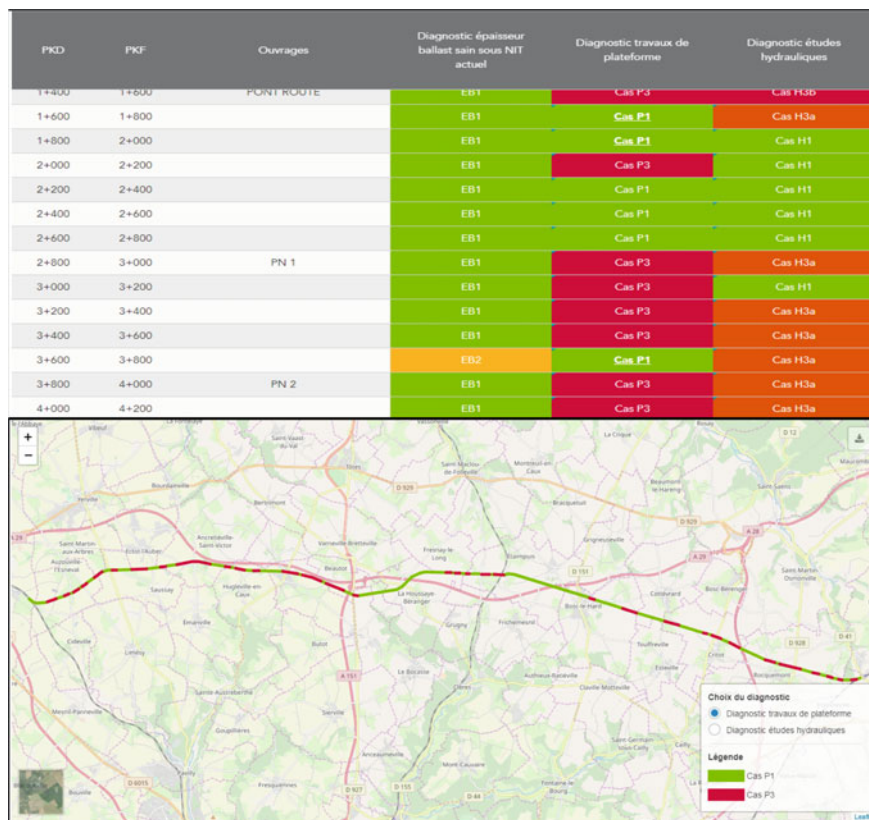
The pie charts below (Fig. 3) represent the line shares that are in good condition or requiring supplementary investigations or engineering works. For example, 36% of the line need platform renewal works, while 64% do not. Moreover concerning the hydraulic state, 51% of the line needs a diagnosis and 39% do not. Other results indicate that 99% of the line presents a compliant clean ballast layer thickness. Beside, 71% of the line needs to be inspected regarding the platform lateral water flow.

The figure above on the top (Fig. 4) shows the results of the analysis of each 200 m section of a railway line: either recommendation for further investigations to be requested and/or geotechnical work to be done and/or hydraulic diagnosis to be performed. Figure 4, on the bottom, summarizes the results as a cartographic representation.

## **5 Conclusions**

Currently, the railway line regeneration program is based on the service life of the track components (rail, sleeper, ballast). The proposed multidomain analysis gives an operational guideline for track renewal or rehabilitation which classifies every portion of railway track by the importance of civil engineering works needed. Thereby, the developed approach aims to provide a system vision for a better definition of the regeneration and maintenance policy. It has been implemented in a web application (DIAG'PLAT) to enable a better integration and capitalization of the data. A national training program has been set up to help the engineers to use this new analysis tool. Several regeneration projects have been improved using this new approach. A machine learning process will be integrated to estimate the network state without conducting geotechnical investigations but by using only maintenance and environmental parameters information.

The approach described in this work is under implementation for management of the regeneration program of the French Railway Network. The authors believe that this holistic assessment approach can be improved and deployed in other railway networks.



**Fig. 4** On the top, an overview of the DIAG’PLAT application interface and on the bottom, the results cartographic representation of the Buchy—Motteville line. The columns of the table correspond, respectively, to: start kilometer point, end kilometer point, the structures, the result of the ballast thickness diagnosis, the result of the platform diagnosis and the result of the hydraulic diagnosis. (Source: SNCF Réseau)

## References

1. Cui YJ, Lamas-Lopez F, Trinh VN, Calon N, Costa D’Aguiar S, Dupla JC, Tang AM, Canou J, Robinet A (2014) Investigation of interlayer soil behaviour by field monitoring. *Transp Geotech* 1(3):91–105
2. Saussine G, Dhemaied A, Amblard J, Cornet JM, Koscielny M, Guillemenet A (2017) A multidomain assessment procedure and rehabilitation criteria of old railway line. In: SNCF Réseau, for the 14th international conference & exhibition of railway engineering 2017, Edinburgh, June 2017
3. Selig E, Waters J (1994) *Track geotechnology and substructure management*, T. Telford, ISBN 9780727720139, LCCN lc95115005.
4. Gourvès R, Barjot R (1995) The Panda ultralight dynamic penetrometer. In: *Proceeding of ECSMF*. Copenhagen, Denmark, pp 83–88
5. Rhayma N, Bressolette P, Breul P, Frogli M, Saussine G (2011) A probabilistic approach for estimating the behavior of railway tracks. *Eng Struct* 33:2120–2133

6. Benz MA (2009) Mesures dynamiques lors du battage du pénétromètre Panda, Ph.D. thesis, Université Blaise Pascal
7. N.P. 94-105 (2000) Contrôle de la qualité du compactage: Méthode au pénétromètre dynamique à énergie variable - Principe et méthode étalonnage du pénétromètre - Exploitation des résultats – Interprétation. Technical report, AFNOR
8. Chaigneau L (2001) Caractérisation des sols de surface à l'aide d'un pénétromètre, Ph.D. thesis, Université Blaise Pascal, Clermont—Ferrand
9. Duong TV, Tang AM, Cui YJ, Trinh VN, Calon N, Dupla JC, Canou J, Robinet A (2013) Effects of fines and water contents on the mechanical behavior of interlayer soil in ancient railway substructure. *Soils Found* 53:868–878



# Case Histories

# Assessment of CPT Data on Liquefaction Mitigation with Rammed Aggregate Piers<sup>®</sup>



E. Kurt Bal , L. Oner , I. K. Ozaydin , and T. B. Edil 

**Abstract** This paper presents the results of pre- and post-improvement cone penetration test (CPT) results executed at the site where Rammed Aggregate Pier<sup>®</sup> elements were used for the liquefaction mitigation. The effectiveness of these elements is attributed to the lateral pre-stressing that occurs in the matrix soil during construction and to the high strength and stiffness of the piers. The improvements provided by Rammed Aggregate Pier<sup>®</sup> elements mitigate liquefaction potential include (i) soil densification (ii) transferring a major portion of the seismically induced shear stresses from the soil to columns (iii) increasing the horizontal stress of the surrounding soil (iv) dissipation of excess pore water pressure. In the case history presented in this paper, the soil profile consisted of a thick hydraulic fill layer (characterized by silty, clayey sand) overlying sea bottom sediments of soft to medium stiff silty clay (CL) and medium stiff silty clay with sand (SM) down to almost 40 m depth which are underlain by a stiff to very stiff silty clay layer. Installation of 50 cm diameter Rammed Aggregate Pier<sup>®</sup> elements which are constructed by Impact<sup>®</sup> System construction procedures (bottom-feed dry displacement method) is aimed to mitigate liquefaction risk in the hydraulic fill layer and to limit settlements, by forming an improved soil crust of desired thickness at the surface. Rammed Aggregate Piers of 16 m length were installed in square and triangular patterns with 1.5 m and 1.7 m on-center spacing, respectively. CPT testing was performed before and after the installation of the piers. The results show that the additional densification and improvement in non-cohesive soils due to vibration and ramming during the pier construction has increased the safety factor against liquefaction by 2.5–3.0 times.

---

E. Kurt Bal · L. Oner (✉)  
Sentez Insaat, Istanbul, Turkey  
e-mail: [loner@sentezinsaat.com.tr](mailto:loner@sentezinsaat.com.tr)

E. Kurt Bal  
e-mail: [ekurt@sentezinsaat.com.tr](mailto:ekurt@sentezinsaat.com.tr)

I. K. Ozaydin  
Yildiz Technical University, Istanbul, Turkey

T. B. Edil  
University of Wisconsin-Madison, Madison, WI, USA  
e-mail: [tbedil@wisc.edu](mailto:tbedil@wisc.edu)

**Keywords** Impact<sup>®</sup> System · Rammed aggregate pier<sup>®</sup> · Liquefaction mitigation · Cone penetration test (CPT)

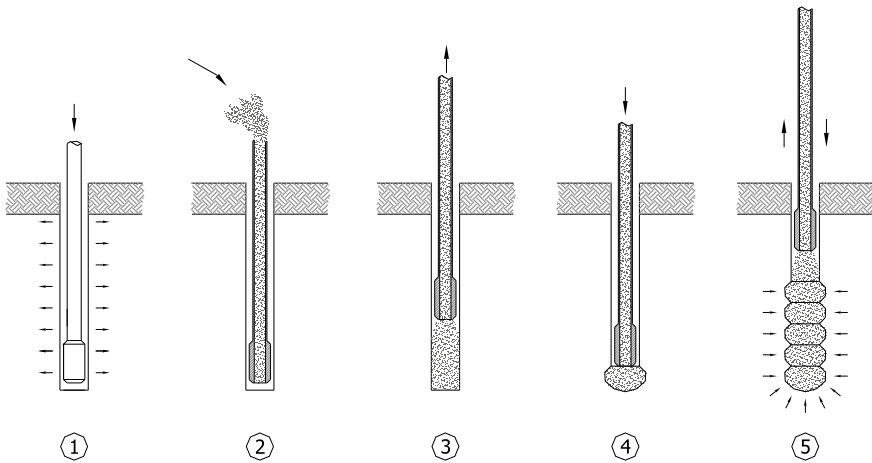
## 1 Introduction

Liquefaction induced differential and total settlements, lateral spreading in saturated sand, or non-plastic silty deposits occur due to earthquake loading. For this reason, soil deposits need to be improved by means of various methods to control earthquake-induced displacements in civil engineering projects. The choice of the appropriate ground improvement technique depends on soil and structure type, project time, and cost. In recent years, Rammed Aggregate Pier<sup>®</sup> elements are frequently preferred to provide cost-effective solution and easy installation for settlement, low bearing capacity, liquefaction, and soil stability problems instead of other traditional soil improvement techniques, such as deep foundations, preloading, and over excavation and replacement. The matrix soil is improved by a closed ended mandrel penetrating into the soil and aggregate material compacted with mechanical energy during Rammed Aggregate Pier<sup>®</sup> installation. It was indicated that construction of new pier at the center of a group of piers is more difficult than construction of new pier at the outside of a group of piers because of lateral stresses and densification of soil mass during Impact<sup>®</sup> System [1]. In this study, the liquefaction potential of the hydraulic fill layer reclaimed by dredging sea bottom sediments was evaluated by using post-improvement cone penetration (CPT) test results executed at the site improved with Rammed Aggregate Pier<sup>®</sup> elements. Within the scope of this paper, after a literature summary related to Impact<sup>®</sup> System, a representative soil profile and the pre- and post-improvement CPT test results will be presented.

### 1.1 Construction of Rammed Aggregate Piers<sup>®</sup>

In the field, Rammed Aggregate Pier<sup>®</sup> elements are installed using Impact<sup>®</sup> System (soil displacement method) construction procedures: (1) a closed ended mandrel with a diameter of 36 cm is pushed into the design depth using hydraulically applied static force assisted with vertical dynamic energy, (2) the mandrel and hopper are filled with aggregate, (3) the ramming action is applied with 100 cm up/67 cm down compaction efforts, during which vertical energy is also introduced resulting in a 50-cm column (Fig. 1).

The significant increase in lateral stress combined with the high density of the stone created by the installation process provides the unique strength and stiffness of the Impact<sup>®</sup> System. In this method, it is provided to increase in lateral stress due to displacement of soil by mechanical vertical ramming actions and to create 50-cm diameter, high stiffness Rammed Aggregate Piers<sup>®</sup> elements. In this project, pier stiffness was measured as between 53 and 240 MN/m<sup>3</sup> by using modulus load test



**Fig. 1** Construction procedure of Impact<sup>®</sup> System (Sentez Insaat, 2005)

results performed consistent with ASTM D-1143 standard [2]. Figure 2 shows the photos of Rammed Aggregate Pier<sup>®</sup> installation taken from the site.

## 1.2 Summary of Literature

Wissmann et al. [3] presented a trial test program funded to evaluate the efficiency of various cost-effective ground improvement methods at Christchurch, New Zealand affected by 2010–2011 Canterbury Earthquake Sequences. The program objective was to investigate the technical viability of using ground improvement to reduce liquefaction vulnerability for the rebuilt or repaired houses. For this purpose, different ground improvement methods were used at three sites in Christchurch in areas severely affected by liquefaction. Rammed Aggregate Pier<sup>®</sup> was one of the ground improvement methods used in this trial program. The testing phase comprised pre- and post-improvement cone penetration testing (CPT) and cross-hole shear wave velocity (VS) testing, vibroseis T-Rex testing, and blast-induced liquefaction testing. Nine test areas were constructed at three sites in Christchurch. The piers were spaced 1.5–3.0-m on-center in a triangular pattern and installed to depths of 4 m in soil profiles that graded sequentially from sandy silt and silty sand to clean sand with depth. CPT results show that pier installations consistently increased CPT tip resistance,  $q_c$  in soil layers with  $I_c < 1.8$  (i.e., lower fines content, FC), whereas a minimal improvement in  $q_c$  occurred in soil layers with  $I_c > 1.8$ . The authors indicate that the observation is consistent with those widely reported in the literature for other soil densification methods. The cyclic resistance ratio (CRR) values for various column spacing using the Boulanger and Idriss [4] liquefaction triggering methodology indicate that for the silty soil layers ( $I_c > 1.8$ ), there is a negligible increase in  $q_c$  and,



Fig. 2 Rammed aggregate pier® installation

hence, CRR. Conversely, measured  $q_c$  and hence computed CRR values increase significantly for soil layers where the  $I_c < 1.8$ . As a conclusion, the Rammed Aggregate Piers® consistently reduce liquefaction susceptibility in both clean sand and silty soils through a combination of soil densification and composite ground shear stiffening.

In the scope of a master thesis at Iowa State University by Zeng [5], pre- and post-installation CPTs were evaluated on the case study data from 16 sites where displacement and replacement aggregate piers were installed. These aggregate piers with a diameter of 50–76 cm were installed in an area replacement ratio,  $A_r$ , ranging from 3.5 to 20% and in the lengths of 2–12 m at the clean sand and clayey layers. The effective improvement data and non-effective improvement data are shown in Robertson’s classification chart (1986) by Zeng (Fig. 3).

The results from this study indicate that the soil is significantly improved for FC of less than 20%, and that soil improvement will reduce when the FC is greater than 20%. However, in sandy soil with less than 20% FC, it is reported that it is difficult to estimate the degree of improvement. In some of the cases in this project where the FC was less than 20%, the CPT results indicate the tip resistance in a very loose sandy layer does not increase as much as in a denser layer. That indicates that the initial relative density somewhat affects the degree of improvement.

Safner et al. [1] presented in situ testing data collected before, immediately after and 1 month after installation of displacement Rammed Aggregate Piers in New Madrid, Missouri. The soil profile consisted of a stiff sandy silt layer (2-m thick), a clean sand layer (1-m thick), a silty sand layer (3-m thick), and another clean sand

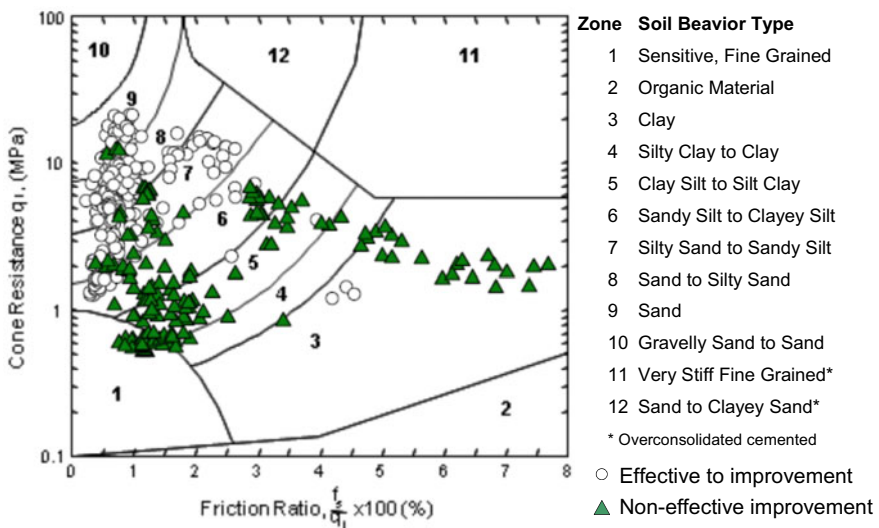


Fig. 3 Effective improvement data and non-effective improvement data shown in Robertson’s classification chart by Zeng [5]

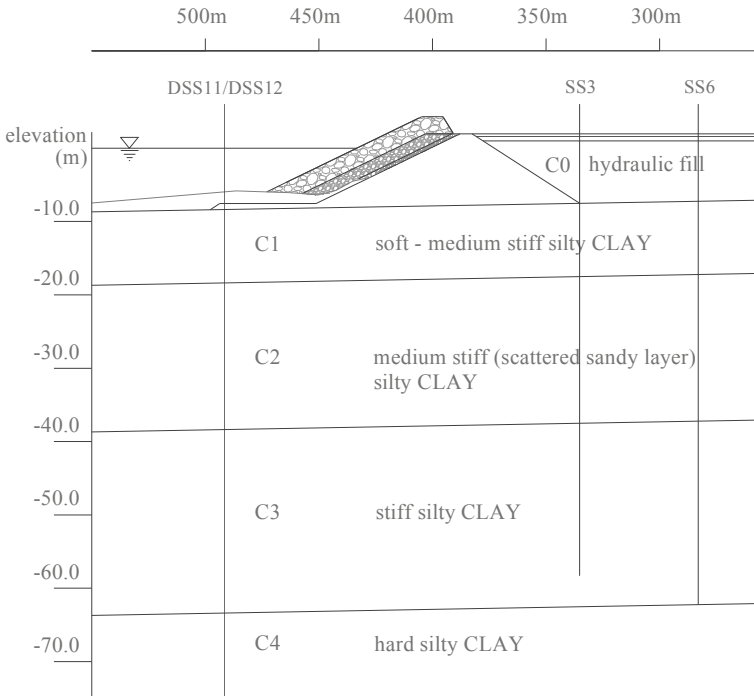
layer (6-m thick). The piers were installed in a triangular pattern with 3-m center-to-center spacing and extended to a depth of 12 m. Cone penetration test results showed a time-dependent strength gain following the disturbance of the loose clean sand layer, increasing roughly 33% in the month after pier installation. Tip resistance values remained generally consistent with 1-day testing in the shallow layers, as well as below pier installation.

Rudolph et al. [6] examined the effect of Rammed Aggregate Pier<sup>®</sup> elements on liquefaction improvement by CPT tests before and after installation at a site which is approximately 2.9–27.4 km from San Andreas, San Gregorio, and Hayward faults. The piers were installed to a depth of 8.5 m below the ground surface and with a square pattern of 1.2-m on center under spread footings and 2.1-m on center for slab support after the execution of the pre-installation CPTs at the site consisting of loose to medium dense silty sand layer scattered by medium stiff to stiff clay, sandy silt layer overlying dense to very dense sandy layer. Post-installation CPTs were executed approximately 4 weeks and 10 weeks after pier installation in order to better account for time-dependence of ground improvement. Liquefaction hazard was assessed by the pre- and post-CPT results using the liquefaction potential index (LPI), as defined by Iwasaki et al. [7]. Within the spread footing area where a closer Rammed Aggregate Pier<sup>®</sup> spacing was used, the reduction in LPI from pre-installation CPT versus post-installation CPT shows a reduction from very high risk (LPI of approximately 17.8) to low risk (LPI of approximately 3.2). Within the slab on-grade area where a wider pier spacing was used, the reduction in LPI from the pre-installation CPT versus post-installation CPT shows a reduction from very high risk (LPI of approximately 17.8) to high risk (LPI of approximately 9.6). Time-dependence of CPT penetration resistance indicates the potential for further liquefaction risk reduction with time.

## 2 Site Investigation and Improvement with Rammed Aggregate Piers<sup>®</sup>

The project site is within a private harbor located at southern shores of Marmara Sea in the city of Bursa, Turkey. The soil profile comprises alluvial deposits consisting of soft to stiff silty clay layers with sandy inclusions. In the western side of the harbor area, a 180 m × 350 m land was reclaimed by hydraulic filling using material dredged from the sea bottom. Based on the findings of the soil exploration borings drilled at the investigation area, soil profile is determined to be as shown in Fig. 4.

The liquefaction triggering potential of silty, clayey, and sandy hydraulic fill layers with varying fines content (12–90%) was identified under a seismic scenario of maximum acceleration  $a_{\max} = 0.4$  g and magnitude  $M_w = 7.5$  by using the approaches proposed by Seed and Idriss [8] and Youd and Idriss [9]. A surcharge load of 60 kPa was envisaged due to container storage. The almost unavoidable settlement problems expected could be somewhat tolerated under container storage,



**Fig. 4** Representative soil profile

as long as the differential settlements are kept within limits not to hinder the operations. But the risk of large lateral soil movements and risk of soil strength and rigidity loss during a strong earthquake could not be tolerated. Especially the hydraulic fill layer (C0) and the underlying soft clay layer (C1) shown in Fig. 4 are expected to possess high level of risks. In order to increase the resistance against liquefaction and strength/rigidity losses during a strong earthquake, to decrease problems which might arise as a result of excessive surface settlements, and to limit the lateral soil movements, it was decided to implement soil improvement down to a depth of 16 m. The main goal of in situ soil improvement to be implemented was chosen to be formation of a homogeneous crust of improved soil properties. The elimination of settlements is considered to be a task not easily (or economically) achievable and found to be not necessary for the proposed use of this land. The detrimental effects of soil liquefaction and differential settlements to be reflected on the ground surface and lateral soil movements are expected to be minimized if a 16 m thick crust on top of the soil profile is generated.



### 3 Evaluation of CPT Data

CPT tests were carried out pre- and post-installation of Rammed Aggregate Piers® in two areas where 1.5-m square and 1.7-m triangular pattern were applied to determine the additional improvement expected to occur at the soil matrix due to vibration and impact applied during installations. Post-installation CPT tests were executed at the center of the column group closest to the pre-installation CPT tests (Fig. 5).

Figure 6 shows plots of all of the pre- and post-improvement CPT tip resistance vs depth for square and triangular groups performed in Zone-1 and Zone-2. In Zone-1 where square and triangular piers were installed in silty- clayey- sandy hydraulic fill with fines content FC of about 6% down to 10 m depth, the tip resistance increased approximately 1.5–2.0 times from 6–8 to 11–13 MPa. In Zone-2 where fines content is in the order of 15%, at square pattern test area the tip resistance increased from 2.2 to 5.8 MPa values, whereas there was no significant and systematic change in penetration resistances in triangular pattern test area.

An overall evaluation of the results point out an increase in CPT cone resistance in silty sand deposits of the hydraulic fill layer after the installation of Rammed Aggregate Piers®, consistent with the expectations and data reported in the literature.

According to Robertson and Wride [10] method of estimating cyclic resistance ratio (CRR) for liquefaction from CPT cone tip resistance, for soils with fines content <15%, or pre- improvement CRR values of 0.10–0.20 are increased to 0.30–0.60 after the installation of piers, reflecting 2–4 times improvement in CRR which corresponds to 2.5–3 times increase in factor of safety against liquefaction.

The variation of tip resistance increase ( $\Delta q_c$ ) with the soil type index ( $I_c$ ) is shown in Fig. 7. The soil behavior types encountered at the site soil profile ranged from 2 (organic soils-clay) to 6 (clean sand to silty sand) based on CPT soil behavior type

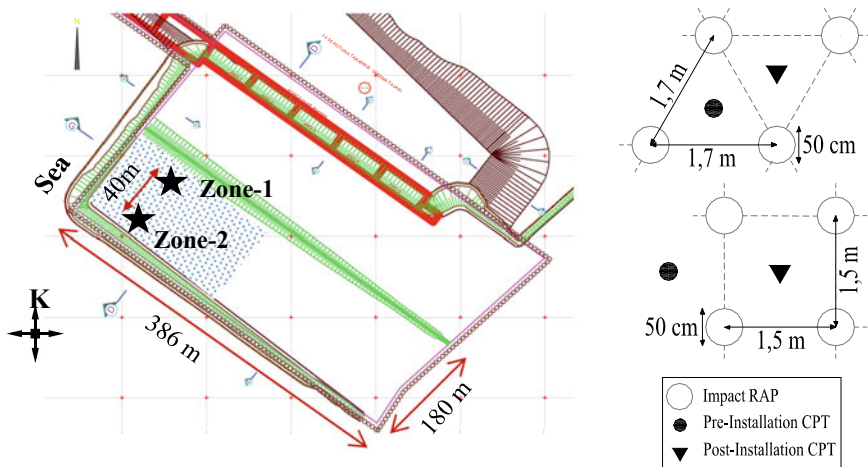
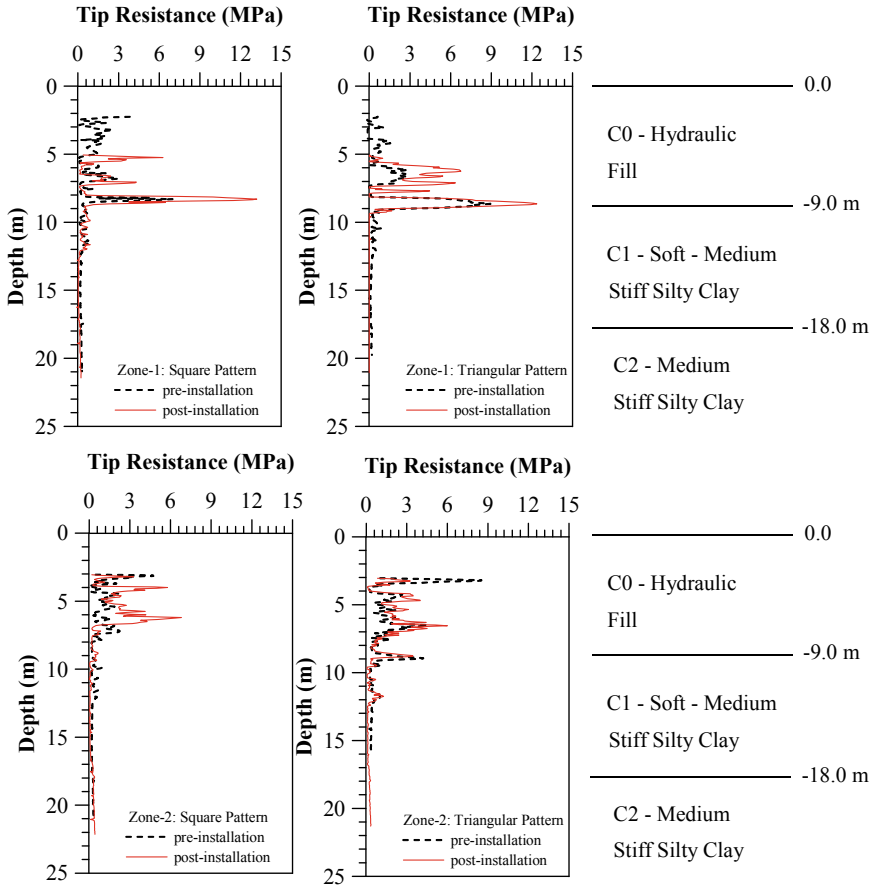


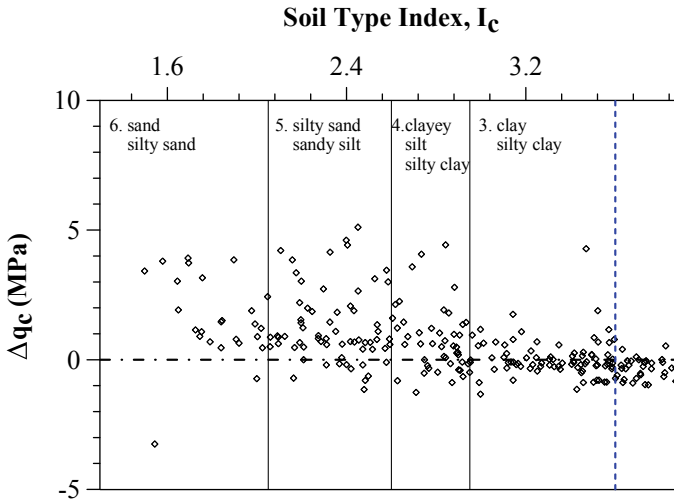
Fig. 5 In situ test layout



**Fig. 6** CPT tip resistance vs depth responses in square and triangular test areas for Zone-1 and Zone-2

chart [11]. The amount of increasing tip resistance ( $\Delta q_c$ ) tended to decrease as the soil behavior type index increased indicating that the level of improvement is more pronounced in sand and silty sand-sandy silt soils, whereas not much noticeable in clayey soils. An additional improvement in sandy soil matrix is achieved due to the vibration and impact effects during the installation of piers.

Furthermore, the presence of rigid columns in a soil deposit is expected to resist a significant portion of the shear stresses arising from earthquake waves leading to a decrease in level of shear stresses in the surrounding soil. The level of mitigation in liquefaction risk due to this effect is closely related to site soil conditions [12].



**Fig. 7** Variation of increase in cone tip resistance ( $\Delta q_c$ ) with soil type index ( $I_c$ )

## 4 Conclusions

In this paper, a case history of recorded increase in CPT cone resistance values at a site where Rammed Aggregate Pier<sup>®</sup> elements were used for soil improvement against liquefaction. The soil conditions at the site comprised of a hydraulic fill of dredged sea bottom sediments consisting of silty clayey sand layers overlying thick soft silty clay layer with sandy seams, grading to stiff-very stiff consistency with depth.

Soil improvement was needed to mitigate liquefaction-related risks as well as limiting total and differential settlements. The effect of 16-m long piers chosen for soil improvement against liquefaction was investigated with the aid of pre- and post-improvement CPT tests. An increase in CPT cone resistance values was recorded in silty sand deposits of the hydraulic fill layer after the installation of piers, consistent with the expectations and results reported in the literature. For soils with fines content <15%, pre-improvement cyclic resistance ratio values of 0.10–0.20 are increased to 0.30–0.60 after the installation of piers, corresponding to 2.5–3 times increase in factor of safety against liquefaction. However, for soils with fines content >15%, there was little or no improvement.

The increase in cone tip resistance increase is observed to be related to soil type index ( $I_c$ ) reflecting the improvement achieved in sandy soil matrix due to the vibration and impact effects during the installation of piers.

It is concluded that soil improvement with Rammed Aggregate Pier<sup>®</sup> elements can be effective in mitigation of soil liquefaction-related risks, as well as limiting the amount of total and differential settlements for soils with low fines content.

## References

1. Safner DA, Zheng J, Green RA, Hryciw R, Wissmann KJ (2017) Rammed aggregate pier installation effect on soil properties. In: ICE Proceedings
2. ASTM D1143–81: Standard test methods for deep foundations under static axial compressive load. ASTM International, West Conshohocken, PA (Reapproved 1994).
3. Wissmann KJ, Ballegooy S, Metcalfe BC, Dismuke JN, Anderson CK (2015) Rammed aggregate pier ground improvement as a liquefaction mitigation method in sandy and silty soils. In: 6th International conference on earthquake geotechnical engineering, 1–4 Nov 2015, Christchurch, New Zealand
4. Boulanger RW, Idriss IM (2014) CPT and SPT based liquefaction triggering procedures. Report No. UCD/CGM-14/01, Center for Geotechnical Modeling, Department of Civil and Environmental Engineering, University of California, Davis, CA
5. Zeng W (2010) Assessment of matrix soil improvement using displacement aggregate piers. Master of Science, Iowa State University, Ames, Iowa
6. Rudolph RW, Serna B, Farrell T (2011) Mitigation of liquefaction potential using rammed aggregate piers. *Geo-Frontiers*, ASCE
7. Iwasaki T, Tokida K, Tatsuoka F, Watanabe S, Yasuda S, Sato H (1982) Microzonation for soil liquefaction potential using simplified methods. In: Proceedings of 2nd international conference on microzonation, Seattle
8. Seed HB, Idriss IM (1971) Simplified procedure for evaluating soil liquefaction potential. *J Soil Mech Found Div*
9. Youd TL, Idriss IM (2001) Liquefaction resistance of soils summary report from 1996 NCEER and 1998 NCEER/NSF workshops on Evaluation of Liquefaction Resistance of Soil. *J Geotech Geoenviron Eng*
10. Robertson PK, Wride CE (1998) Evaluating cyclic liquefaction potential using the cone penetration test. *Can Geotech J*
11. Robertson PK, Cabal KL (2014) Guide to cone penetration testing for geotechnical engineering, 6th edn. Gregg Drilling & Testing Inc., California
12. Green RA, Olgun CG, Wissmann KJ Shear stress redistribution as a mechanism to mitigate the risk of liquefaction. In: Geotechnical earthquake engineering and soil dynamics IV, ASCE (2008)

# Observational Method Applied to the Decision Optimizing of Foundation Method in Kujala Interchange on Silty Clay Subsoil



Monica Susanne Löfman and Leena Korkiala-Tanttu

**Abstract** Observational method is a powerful approach to dealing with uncertainty in subsoil conditions. In the presented case study, Kujala Interchange, constructing test embankments and applying the observational method enabled to replace many initially planned pile slab foundations with ground-supported road embankments. The residual settlements of these embankments were controlled by means of preloading accompanied with monitoring. This paper demonstrates how a decision tree analysis can be employed to assess the feasibility of constructing the test embankments. The prior probability of acceptable settlements of the ground-supported embankments is estimated for a typical soil profile in Kujala area via Monte Carlo simulation. This prior probability is then updated via monitoring results and Bayes' theorem. Lastly, the expected costs of each design alternative are derived based on their respective probabilities and the actual cost savings acquired at Kujala Interchange. The results of the decision tree analysis confirm that constructing the test embankments and minimizing the pile foundations were the optimal decision in this case study. In sum, this paper shows how the observational method can be employed to reduce the expected costs and environmental impact of foundation design characterized by significant uncertainty in subsoil conditions. However, it is concluded that besides monetary costs, one should also include non-monetary consequences such as carbon dioxide emissions.

**Keywords** Observational method · Decision tree · Road embankment · Bayesian updating

## 1 Introduction

Geotechnical engineers have developed many strategies to deal with uncertainty. According to Christian [1], they include (1) ignoring it, (2) being conservative, (3) using the observational method, and (4) quantifying uncertainty. The second

---

M. S. Löfman (✉) · L. Korkiala-Tanttu  
Department of Civil Engineering, Aalto University, Rakentajanaukio 4, 02150 Espoo, Finland  
e-mail: [monica.lofman@aalto.fi](mailto:monica.lofman@aalto.fi)

approach, conservatism, has been widely used with satisfactory results, but it may result in non-economical design solutions in challenging site conditions. Hence, in projects with higher level of uncertainty and greater difficulties to predict the geotechnical behavior, the observational method (OM) might be more suitable [2, 3]. This recommendation to consider OM is also given by the Eurocode 7 for geotechnical design [4].

In Kujala Interchange, which is a part of Highway 12 in Finland, the considerable uncertainty in the geotechnical properties of the silty clay subsoil conditions led the designers to apply observational method. The uncertainty in subsoil properties was partly caused by the high sensitivity of silty layers, which led to sample disturbance. As a result, field vane and oedometer tests were deemed unreliable. Thus, the epistemic uncertainty in both stability and settlement predictions was lowered by monitoring of two 4–5.5 m high test embankments. Besides the test embankments, settlement monitoring was performed in other road sections in the interchange area also during the construction process. As a result, most of the initially planned pile slab foundations could be replaced by ground-supported road embankments; the residual settlements were decreased by applying preloading. In addition, lightweight fills made of recycled foamed glass were used in transition zones. This optimization of foundation method led to construction cost savings of six million euros (6 M€) compared to the initial road plan estimate; compared to the initial plan, the amount of pile slabs was reduced to one third, and the amount of lightweight fills became 1.5 times larger.

This paper utilizes a decision tree analysis to quantify the expected costs of different foundation method alternatives in the case of Kujala Interchange (conservative design versus optimized design, i.e., minimized pile foundations). In addition, this paper demonstrates how one can rationally evaluate whether it is an optimal decision to apply observational method (to construct the test embankments) or not. In sum, this case study shows how the observational method together with decision tree analysis can be employed to reduce both monetary costs and environmental impact of design cases with low-quality site investigations.

## 2 Project Description

Kujala Interchange area forms the Eastern border of Part 1B in Highway 12, Southern Ring Road of Lahti. Part 1B was assessed to be technically the most challenging part of the project. Hence, the selected procurement model was an alliance, which is considered to be suitable model for executing a complex project with considerable risks [5]. VALTARI alliance is formed by the owner parties (Finnish Transport Infrastructure Agency, City of Lahti and Municipality of Hollola) and the service providers Skanska Infra Oy and Pöyry Finland Oy. The geotechnical design of Kujala Interchange was provided by Pöyry Finland Oy, and Skanska Infra Oy was the constructor.

The allowable settlements in Kujala Interchange during service time were defined by the Finnish Transport Infrastructure Agency. The maximum total settlement for road embankments was either 300 mm (class V1) or 400 mm (class V2) during 50 years of operation. The maximum change in longitudinal grade (slope) was set to 0.6 percentage points (p.p) in 50 years and 0.8 p.p./50 years for classes V1 and V2, respectively. In transition zones, no more than half of this maximum change in grade is allowed. Due to this limit, the maximum total settlement was set to 50 mm/50 years at the transitions to the piled structures.

The subsoil in Kujala area consists of 10–25 m of clay and silt. Between the fine-grained soil and bedrock, there is a few meters thick layer of glacial till. The groundwater depth is at 0.3–2 m. The thickness of top clay layer (dry crust) is 2–4 m. The water content of clay and silt layers is 30–90%, and the liquid limit is approximately equal or slightly greater than the water content. The clay fraction is 30–70%. The undrained shear strength is in the scale of 20–50 kN/m<sup>2</sup> in clay and silt layers and up to 200 kN/m<sup>2</sup> in the dry crust layer. The sensitivity is mostly in the scale of 10, but in some silt-rich layers, the sensitivity is up to 60. The overconsolidation ratio (OCR) is mostly in the scale of 1.5–2 but higher (OCR = 4–6) in the dry crust layer.

Two instrumented 4–5.5 m high test embankments were constructed in order to increase the reliability of settlement predictions. These embankments will remain as a part of final interchange ramp structures. The monitoring data was collected for six months before starting the construction at the area; settlements, horizontal displacements (via inclinometers), and pore pressure measurements were recorded every 2–4 h. The data collection was continued for almost 1.5 years. Besides monitoring, an extensive ground investigation program was planned with special focus on ensuring the best possible quality. The settlement predictions were then calibrated using the newly collected data, and it turned out that the subsoil conditions were more favorable than what the preliminary ground investigation implied. Consequently, these test embankments and other monitoring in the area (i.e., observational method) allowed for minimizing the pile foundations in Kujala Interchange.

### 3 Observational Method

The principles of *observational method* were first defined by Peck [6], based on a methodology applied by Terzaghi. Peck [6] states that the observational method can enable considerable savings in time or money or provide the needed assurance for the safety (reliability) of the design. Terzaghi, who applied this method successfully, called it the ‘learn-as-you-go’ method [6]. Christian [1] summarizes the basis of the observational method as follows: ‘It involves (1) considering possible modes of unsatisfactory performance or other undesirable developments; (2) developing plans for dealing with each such development; (3) making field measurements during construction and operation to establish whether the developments are occurring; and (4) reacting to the observed behavior by changing the design or construction process.’

According to Peck [6], observational method is often used to provide affirmation that enough time has elapsed for a certain desirable outcome. In the case of preloading, the desirable outcome would be that enough settlements occur during the available consolidation time in order to minimize the settlements that would occur during the operation time. Peck [6] continues that the observational method can only be used if the engineer can alter the design during construction. Consequently, the specifics of the contract between the owner and the constructor may pose limitations to the usage of observational method. The strength in alliance model, which was the model applied in Kujala Interchange, is that the communication between the constructor, designer, and owner parties is proficient, and optimizing the design solutions is encouraged for by means of bonus and sanctions scheme. The service-providing parties can earn bonuses via working toward solutions that are in accordance with the agreed key objectives [5].

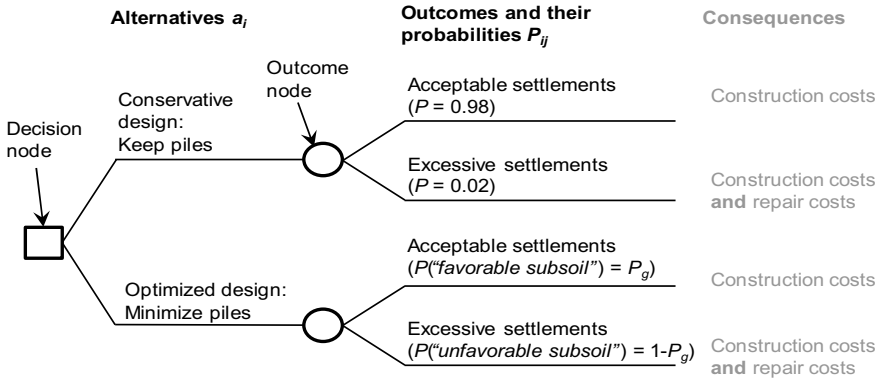
Peck [6] also notes that in some cases the probability of most unfavorable conditions is so high that the usage of observational method is simply not economical. In other words, if the expected probability of needing contingency actions is too high with respect to their cost, the observational method does not provide more favorable option than the conventional design [7]. That is, the engineer should have a prior position that the actual conditions are more favorable (or the same) as predicted before the observations. In the case of Kujala area, the prior position based on engineering judgment was that the geotechnical properties of the silty clay subsoil should be more favorable than what was indicated by the preliminary ground investigations. Moreover, the uncertainty in OCR forced the engineers to consider the most unfavorable conditions (subsoil in OCR = 1 state mostly). As noted by Terzaghi [6], this conservatism-based approach to deal with high uncertainty can be uneconomical.

Observational method has not been widely used in Finland; the usage has been increasing in the field of rock engineering, but in foundation engineering, the systematic use has been more scarce. In his master thesis research, Bäcklund [8] interviewed industry representatives during years 2012–2013 and concluded that the main reason for the rare applications of observational method has been that the geotechnical designers do not fully understand its principles or possible benefits. Nevertheless, the observational method has been successfully applied in other Nordic countries (e.g., [2]). In order to study which is more effective, the observational method or conventional design, one can apply decision optimizing methods such as decision tree analysis [7].

## 4 Decision Tree Analysis

A *decision tree* is an organized graph that presents the information available for the decision making [9]. It is formed by two basic components: alternatives and outcomes [10]. Different events arise from the outcome nodes (chance nodes), and one can assess the probability of these outcomes. Figure 1 presents a basic decision tree for





**Fig. 1** Basic decision tree for the serviceability limit state design of a road foundation (modified after Gilbert et al. [10])

two alternative designs ( $a_i$ ) for Kujala Interchange with their possible outcomes, consequences, and their respective probabilities ( $P_{ij}$ ).

The probability of excessive settlements in the case of conservative design (‘keep the piles’) is usually low; it is here assumed that there is  $P = 0.02$  probability in the case of a design consisting mostly of end-bearing piles supported by the bedrock. On contrary, the probability of excessive settlements in the case of ground-supported embankments is usually much greater. In this study, ‘minimize piles’ (Fig. 1) refers to an optimized design in which pile slab foundations are replaced with ground-supported road embankments at all sections in which it is feasible given the design criteria and the available knowledge on the subsoil conditions. This optimized design will require more site investigations and monitoring compared to over-designing (i.e., ‘keep the piles’).

When the consequences can be defined as monetary costs or value, a common procedure is to adopt the decision criterion known as *maximum expected monetary gain* [11, 12]. In other words, the optimized decision is the design alternative with the smallest expected monetary cost (or the greatest value). This *expected monetary cost* of the  $i$ th design alternative  $E(a_i)$  is derived by weighting the total cost of each outcome ( $C_{ij}$ ) by its probability  $P_{ij}$  [11]:

$$E(a_i) = \sum_j P_{ij} C_{ij} \tag{1}$$

Besides monetary costs, one can also include other consequences such as environmental impact or human health risks. A common procedure is to then combine all the attributes to a single monetary value, or, alternatively, to a utility value [10].

In the simple case presented in Fig. 1, the expected monetary costs of the optimized design alternative for Kujala Interchange are

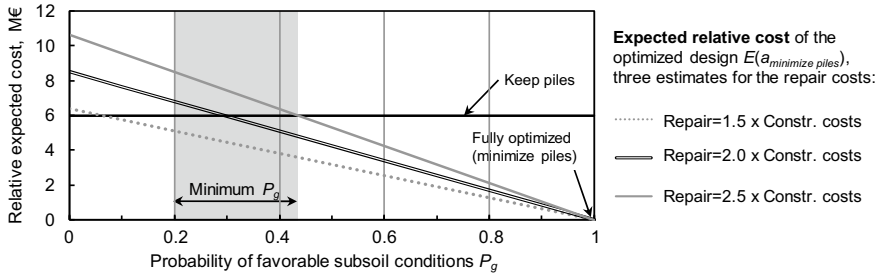


Fig. 2 Expected relative costs for the alternative designs (keep piles versus minimized piles)

$$E(a_{\text{minimize piles}}) = C_{\text{constr.}} P_g + (C_{\text{constr.}} + C_{\text{repair}})(1 - P_g) \tag{2}$$

$$\rightarrow E(a_{\text{minimize piles}}) = (C_{\text{constr.}} + C_{\text{repair}}) - C_{\text{repair}} P_g \tag{3}$$

where  $C_{\text{constr}}$  is the cost of construction,  $C_{\text{repair}}$  is the cost of repair and other costs created by excessive settlements,  $P_g$  is the probability of acceptable settlements, and  $(1 - P_g)$  is the probability of excessive settlements. Probability  $g$  is later referred to as the ‘probability of favorable subsoil conditions’. Figure 2 presents the expected relative cost of the two alternatives (optimized design and ‘keep the piles’ alternative).

In Kujala Interchange area, the expected cost of keeping the piles does not depend on the probability of favorable subsoil conditions  $P_g$ , because the end-bearing piles are supported by the bedrock. On the other hand, the expected cost of fully optimized design (minimizing the piles) decreases linearly as the probability of favorable subsoil conditions  $P_g$  increases. At  $P_g = 1$ , the relative cost of optimized design is zero, whereas the expected cost of keeping the piles is 6 M€ greater. This difference (6 M€) corresponds to the actual cost savings acquired in Kujala Interchange by replacing two thirds of the initially planned pilings with ground-supported embankments).

At  $P_g = 0$ , the intercept of expected cost for optimized design ( $E(a_{\text{minimize piles}})$ ) is defined by the assumed costs of construction and repair ( $C_{\text{constr}} + C_{\text{repair}}$ ). At these low values of  $g$ , the risk of both excessive settlements and stability issues is so large that the conservative design (‘keep the piles’) is usually preferred. Hence, the lowest value for  $C_{\text{repair}}$  should be in the scale of 1.5 times the construction costs (dotted line in Fig. 2); at low values of  $P_g$ , the expected cost of ‘keep piles’ is then lower and thus optimal. However, the authors estimate that the actual monetary repair cost of excessive settlements would be lower; thus, it is assumed that  $C_{\text{repair}}$  here includes other consequences also, such as contingency actions required by low stability, environmental impact, and repair works’ consequences to road users.

Given the assumed relative costs of excessive settlements, minimizing the piles becomes more optimal when  $P_g$  is larger than 0.2–0.4. In the following sections, the site-specific probability of favorable subsoil conditions ( $P_g$ ) for Kujala area is assessed.

## 5 Decision Optimizing for Kujala Interchange

### 5.1 Prior Probability of Favorable Subsoil Conditions

In order to study the feasibility of constructing the test embankments, the probability of acceptable settlements (that is, the probability of favorable subsoil conditions  $P_g$ ) must be high enough. In order to assess this probability, the prior distribution of residual settlement was estimated for a typical soil profile in Kujala.

The preliminary ground investigations in Kujala area revealed that the subsoil is mostly silty clay with a few layers with higher clay content. Taken into account the ground elevation (+80 m above sea level) and geographic location, one can estimate that the subsoil may represent somewhat overconsolidated Baltic Ice Lake sediment. For this sediment type, prior distributions of geotechnical properties are available in the literature. Alternatively, one could utilize a probability of favorable subsoil conditions based on local expertise or other prior knowledge such as established correlations between water content and compressibility index, for example.

In this study, prior distributions for compressibility properties given by Löfman and Korkiala-Tanttu [13] were mostly utilized. The prior distribution for OCR was modified after Gardemeister [14]. Regarding the coefficient of creep (coefficient of secondary compression  $C_{\alpha\varepsilon}$ ), no prior distribution for Baltic Ice Lake sediments was available; hence, a general prior distribution for clay soils given by Löfman [15] was used. The probability distribution of residual settlement in Kujala area was estimated via Monte Carlo simulation (30,000 simulations) in @RISK software [16]. The input parameters for random variables are presented in Table 1.

**Table 1** Input parameters for the random variables used in Monte Carlo simulation

Input†	Unit	Distribution type	Min	Mode/mean	Max	Standard deviation	COV (%)
OCR	–	Truncated lognormal	1.00	1.20/1.80	6.00	0.869	48.2
$C_c$	–	Lognormal	0.00	0.200*/0.586*	$+\infty$	0.6003*	102
$C_s$	–	Lognormal	0.00	0.044*/0.077*	$+\infty$	0.0523*	67.9
$\gamma$	kN/m <sup>3</sup>	Truncated normal	11.0	17.7/17.7	25.0	1.119	6.32
$C_{\alpha\varepsilon}$	%	Triangle	0.00	1.30/1.71	3.82	0.793	46.4
GW	m	Triangle	0.50	1.00/1.17	2.00	0.312	26.7
H	m	Triangle	3.50	4.50/4.50	5.50	0.408	9.07
$\gamma_{\text{fill}}$	kN/m <sup>3</sup>	Normal	$-\infty$	20.0/20.0	$+\infty$	1.000	1.00

†OCR = overconsolidation ratio;  $C_c$  = compression index;  $C_s$  = swelling index;  $\gamma$  = unit weight of soil;  $C_{\alpha\varepsilon}$  = coefficient of secondary compression; GW = depth of groundwater level; H = height of the embankment;  $\gamma_{\text{fill}}$  = unit weight of fill material (crushed rock)

\*Arithmetic statistic

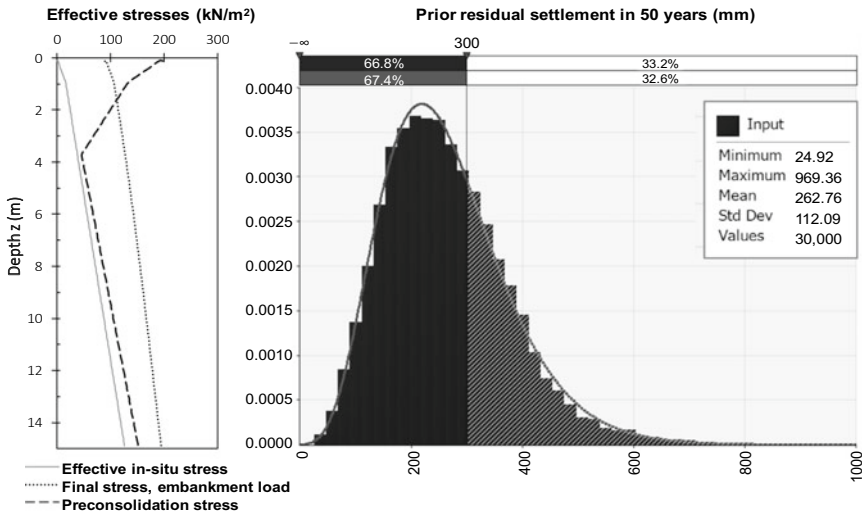


Fig. 3 Mode values of effective stresses (left) and the prior residual settlement (right)

The residual settlement was calculated for a typical soil profile in Kujala area: a 15 m deep clay-silt basin. The OCR in dry crust is usually 5–7 times greater than in deeper soil layers [14], and this was taken into account by applying a decreasing preconsolidation pressure with  $\alpha'_p = 200 \text{ kN/m}^2$  at the ground surface and minimum around depth of 4 m. The maximum value of  $\alpha'_p$  was chosen to be in the same scale as the value determined from two good/fair quality oedometer tests (at 5 m and 10 m) performed in the preliminary ground investigation program. The mode values of  $\alpha'_p$ , effective in-situ stress, and embankment load are presented in Fig. 3 (left).

The negative correlation between unit weight and compression indexes was taken into account by means of a copula function. The initial void ratio of soil was calculated using the compression index, based on a regression analysis performed for the Baltic Ice Lake sediment data analyzed by Löfman and Korkiala-Tanttu [13]. The compressibility of the dry crust was calculated by assuming that the modulus is 50 times the preconsolidation pressure (an empirical relation used in Swedish practice, e.g., [17]).

Figure 3 (right) presents the histogram of residual settlement in millimeters. It was assumed that this residual settlement accumulating during road service time of 50 years is a sum of 20% of the primary consolidation settlement and 50% of the estimated creep. In other words, it is assumed that 80% of primary consolidation occurs already during the construction/preloading stage. Regarding the creep, only 50% of the estimated creep settlement is included in the residual settlement for two reasons: Firstly, the prior distribution used for coefficient of creep included many soft clays and organic clays which are more prone to creep than silty clays (dominant in Kujala area) which are characterized by lower  $C_c$  and lower water content [17, 18]. Secondly, the applied surcharge preloading decreases the creep effects (e.g., [18]).

Figure 3 shows that the probability of settlements smaller than 300 mm is  $P_g = 0.67$ . However, due to the limitations for differential settlements, a 300 mm limit cannot be applied to the whole area. Hence, it is assumed, that on average the prior probability of acceptable settlements is only  $P_g = 0.25$  (which corresponds to a probability of residual settlements being less than  $\approx 180$  mm).

## 5.2 Probability of Favorable Subsoil Given the Observations

Since the prior probability of favorable subsoil conditions is only  $P_g = 0.25$ , one could consider the feasibility of acquiring more information about the actual subsoil conditions via monitoring of test embankments. In general, the additional cost of acquiring more information (e.g., via observational method) may be justified if it eliminates a considerable part of the uncertainty [11].

The reliability of field observations of a test embankment depends on their quality and the measurement period. On the other hand, the time required for a reliable total settlement prediction depends on consolidation properties of the compressing subsoil (drainage paths and permeability). Länsivaara [19] observed (based on 11 clayey soil sites in Finland) that measurement period of one year usually leads to a very reliable settlement prediction, whilst six months periods led to a ‘quite good’ prediction at many sites. If one applies the verbal descriptions of uncertainty collected by Baecher and Christian [12], ‘quite likely’ and ‘very likely, very probably’ correspond to probabilities  $P = 0.80$  and  $P = 0.90$ , respectively.

In Kujala test embankments, the time reserved for settlement observations prior design update was 6 months; however, the observations were continued during construction also, in total over 16 months. In addition, the rate of consolidation (rate of excess pore pressure dissipation) was observed via piezometers. Combined with the settlement monitoring, the observations provide a rather reliable result. Hence, one can estimate that the probability of reliable settlement prediction (given the monitoring measurements) is at least 0.80 and up to 0.90.

The prior probability of favorable subsoil conditions ( $P(G) = P_g$ ), given the monitoring observations that also indicate favorable subsoil conditions ( $A$ ), can be updated with Bayes’ theorem. The updated, posterior probability is defined with

$$P(G|A) = \frac{P(G) * P(A|G)}{P(G) * P(A|G) + P(\bar{G}) * P(A|\bar{G})} \quad (4)$$

The definitions of these probabilities are given in Table 2. Scenario 1 represents an optimistic estimate of the reliability of monitoring-based settlement prediction, whereas Scenario 2 assumes that the probability of inaccurate or false interpretation is greater. For example, the primary consolidation might continue longer than what the measurements indicate, or, the creep might be more significant than what initially estimated.

**Table 2** Likelihoods used to update the probability of favorable subsoil conditions

Outcome of monitoring observations	$G$ : Actual subsoil conditions: favorable (prior = $P_g = 0.25$ )		$\bar{G}$ : Actual subsoil conditions: unfavorable (prior = $1 - P_g = 0.75$ )	
	Scenario 1	Scenario 2	Scenario 1	Scenario 2
<b>A: Observations indicate favorable subsoil</b>	$P_1(A   G) = \mathbf{0.90}$	$P_2(A   G) = \mathbf{0.80}$	$P_1(A   \bar{G}) = \mathbf{0.30}$	$P_2(A   \bar{G}) = \mathbf{0.50}$
$\bar{A}$ : Observations indicate unfavorable subsoil	$P_1(\bar{A}   G) = 0.10$	$P_2(\bar{A}   G) = 0.20$	$P_1(\bar{A}   \bar{G}) = 0.70$	$P_2(\bar{A}   \bar{G}) = 0.50$

As there are two test embankments with somewhat different subsoil profiles, one can update the prior probability two times (two sets of independent measurement data). In the second update, the prior probability  $P(G) = P_g$  in Eq. 4 is replaced by previously updated posterior probability  $P(G | A)$ . After the second update, the posterior probability of favorable subsoil (given monitoring results that indicate favorable conditions) is thus 0.75 in Scenario 1 and 0.46 in Scenario 2.

A similar updating process could also be performed to the case of monitoring results indicating unfavorable subsoil conditions (measured settlements are large, and excess pore pressure dissipated slowly). This outcome would decrease the probability of favorable subsoil conditions even more ( $P_g < 0.25$ ). Hence, one can assume that if the monitoring indicates excessive settlements, the optimal decision by default is to keep the piles.

### 5.3 Optimal Design According to the Decision Tree Analysis

The final decision tree with the expected relative monetary costs is presented in Fig. 4. For all the alternative designs, the assumed repair costs ( $C_{\text{repair}}$ ) were two times the construction cost of the fully optimized design (minimize the piles). The assumed cost of test embankments was 0.25 M€; in Kujala Interchange, the actual cost of the test embankments was in the scale 0.20–0.25 M€. The lowest expected relative cost (corresponding to the optimal design alternative) is marked with bold font.

If no test embankments are built, the optimal decision is to keep the piles (if the probability of favorable subsoil conditions is only  $P_g = 0.25$ ). On the other hand, if the prior probability of favorable subsoil condition is updated using the monitoring, the expected cost of minimizing piles is only  $E(a_{\text{minimize piles}} | A) = 2.5\text{--}5.1$  M€ (lower than expected cost of keeping the piles, 6.4 M€). The lower expected cost corresponds to the highest assumed reliability of monitoring-based settlement prediction (Scenario 1, Table 2).

However, one potential outcome is that the monitoring results will indicate unfavorable subsoil conditions, which would lead to selecting ‘keep piles’ and thus losing the investments put into observational methods. The expected relative cost of test

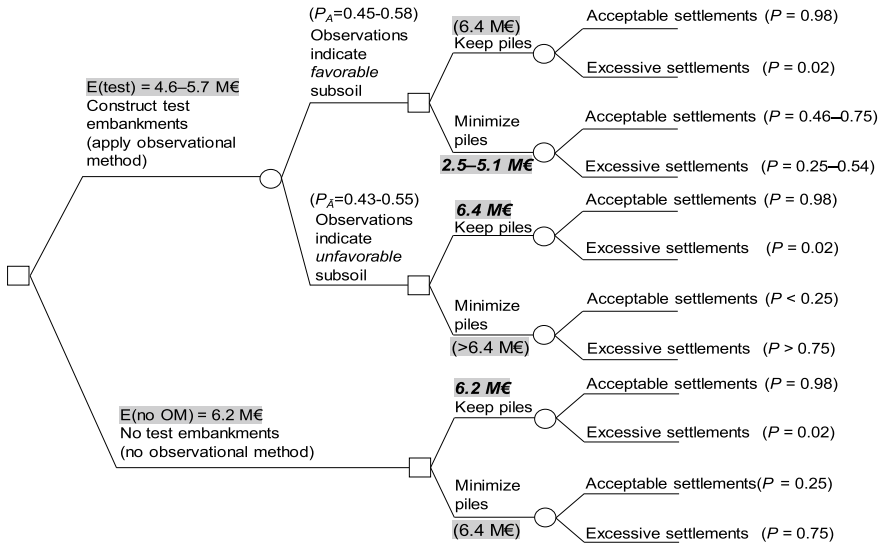


Fig. 4 Decision tree for applying the observational method with expected relative costs

embankments and OM,  $E(\text{test})$ , can be calculated by considering the most optimal alternatives in both monitoring outcomes with [11]:

$$E(\text{test}) = P_A * E(a_{\text{minimize piles}}) + P_{\bar{A}} * E(a_{\text{keep piles}}) \tag{5}$$

where  $P_{\bar{A}}$  is the probability of monitoring results indicating unfavorable subsoil conditions given the prior probability of  $P_g = 0.25$  ( $P_{\bar{A}} = 0.55$  and  $P_{\bar{A}} = 0.43$  in Scenarios 1 and 2, respectively), and  $P_A$  is the probability of monitoring indicating favorable subsoil conditions ( $P_A = 0.45$  and  $P_A = 0.58$  in Scenarios 1 and 2). It was assumed that the probability of observations indicating unfavorable subsoil equals the complement of ‘favorable’ observations (Table 2). It should be noted that because the prior probability of favorable subsoil conditions is only 0.25, larger ‘false positive’ probability is actually beneficial from the perspective of ground-supported embankments.

Expected cost of constructing test embankments and applying observational method  $E(\text{test})$  is thus 4.6 M€ and 5.7 M€ for Scenario 1 and Scenario 2, respectively. This expected relative cost is less than the optimal decision in the alternative of no test embankments (keep piles, 6.2 M€). Thus, the decision to construct the test embankments is supported by the decision tree analysis.

## 6 Discussion

Figure 4 shows that the probability of excessive settlements for the ‘minimize piles’ design with observational method is quite large ( $P = 0.25 - 0.54$ ). Hence, it should be noted that the optimal decision might be the conservative design instead, if the decision maker preferred risk minimization decision criteria instead of maximum expected monetary gain. All in all, the ‘gray area’ in which minimizing piles becomes more optimal than the conservative design (keeping the piles) is the most challenging from the perspective of decision making. In this gray area, including other consequences besides the construction and repair work costs would support the robustness of decision optimizing. For instance, environmental impact such as greenhouse gas emissions should be included in the consequences also. In Kujala Interchange, the minimization of reinforced concrete piled slab foundations lowered the estimated carbon dioxide equivalent ( $\text{CO}_2\text{eq}$ ) by approximately 7000–14,000 tonnes. This minimization of piles caused an increase in the amount of lightweight fills, but the equivalent  $\text{CO}_2\text{eq}$  increase for the fill material used (recycled foamed glass) is only approximately 500 tonnes. Hence, it is clear that the overall climate change impact was reduced via the foundation method optimization.

## 7 Conclusions

This paper demonstrated how a decision tree analysis can be used to study the feasibility of applying the observational method in the foundation type optimization. In Kujala Interchange, the decision to construct the test embankments was supported by the decision tree analysis, even though the estimated prior probability of favorable subsoil conditions was only  $P_g = 0.25$ . However, the most optimal decision can be quite sensitive to the assumed consequences of the unsatisfactory performance of the foundation.

By using real cost savings acquired in the Kujala Interchange case study, it was shown how the observational method can be employed to reduce the expected costs and environmental impact of foundation design. In particular, the observational method can be very effective in projects which are characterized by significant uncertainty in subsoil conditions.

**Acknowledgements** This research was funded by the Finnish Transport Infrastructure Agency. Pöyry Finland Oy provided the monitoring data and estimates for the test embankment costs and the acquired cost savings.



## References

1. Christian JT (2004) Geotechnical engineering reliability: how well do we know what we are doing? *J Geotech Geoenviron Eng* 130:985–1003
2. Prästings A, Müller R, Larsson S (2014) The observational method applied to a high embankment founded on sulphide clay. *Eng Geol* 181:112–123
3. Patel D, Nicholson D, Huybrechts N, Maertens J (2007) The observational method in geotechnics. In: *Proceedings of the 14th European conference on soil mechanics and geotechnical engineering*. Millpress, Rotterdam, pp 371–380
4. CEN: EN 1997-1:2004 (2004) Eurocode 7: geotechnical design. Part 1: general rules. European Committee for standardization, Brussels
5. Finnish Transport Infrastructure Agency (2018) Trunk Road Vt 12, Southern Ring Road of Lahti, Project Part 1B: Project plan for the development phase and Value for Money report 29 May 2018
6. Peck RB (1969) Advantages and limitations of the observational method in applied soil mechanics. *Geotechnique* 19:171–187
7. Spross J, Johansson F (2017) When is the observational method in geotechnical engineering favourable? *Struct Saf* 66:17–26
8. Bäcklund J (2013) Geotekninen monitorointi Suomessa [Geotechnical monitoring in Finland], Master Thesis, Aalto University, Espoo
9. Raiffa H (1968) *Decision analysis: introductory lectures on choices under uncertainty*. Longman Higher Education Division
10. Gilbert RB, Najjar SS, Choi Y-J, Gambino SJ (2008) Practical application of reliability-based design in decision-making. In: Phoon K-K (ed) *Reliability-based design in geotechnical engineering. Computations and applications*. Taylor & Francis, pp 192–223
11. Ang AH-S, Tang WH (1984) *Decision analysis*. In: *Probability concepts in engineering planning and design*. Volume II: decision, risk and reliability. Wiley, pp 5–111
12. Baecher GB, Christian JT (2003) *Reliability and statistics in geotechnical engineering*. Wiley
13. Löfman MS, Korkiala-Tanttu LK (2019) Variability and typical value distributions of compressibility properties of fine-grained sediments in Finland. In: *Proceedings of the seventh international symposium on geotechnical safety and risk* (in press)
14. Gardemeister R (1975) *On engineering-geological properties of fine-grained sediments in Finland*. Technical Research Centre of Finland, Helsinki
15. Löfman MS (2016) *Estimation of the reliability of Perniö Clay parameters and correlations between clay properties*. Master Thesis, Aalto University, Espoo
16. Palisade Corporation (2016) @RISK user's guide. risk analysis and simulation add-In for Microsoft® Excel. Version 7. July, 2016
17. Larsson R (1986) *Consolidation of soft soils*. Swedish Geotechnical Institute, Linköping
18. Mesri G, Ajlouni MA, Feng TW, Lo DOK (2001): *Surcharging of soft ground to reduce secondary settlement*. In: Kwong AKL (ed) *Soft soil engineering*. Taylor & Francis, London
19. Länsivaara TT (2001) *Painuman ennustaminen painumahavaintojen perusteella* [Settlement predictions based on observational approach]. Finnish National Road Administration, Helsinki

# Design and Performance of Low Capacity Roads on Peat Foundation Soils in Ireland



Ciaran Reilly  and Fintan Buggy 

**Abstract** Peat soils exhibit very high organic and moisture contents with corresponding very high compressibility and creep characteristics and very low strength. These poor engineering properties make peat soils particularly unsuitable as a foundation material for road pavements with attendant high risks of instability during both initial construction and in service with unpredictable and often excessive long-term deformations. Almost 20% of Ireland is peatland and roads have been historically constructed directly on peat, albeit with mixed results and often high, long-term maintenance costs. Ground improvement by means of excavation and replacement of peat is frequently adopted and more recently piled embankments are increasingly used in areas of deep peat deposits in Ireland for major roads. However, these mitigation measures can have high construction costs and attendant risks as well as large resultant waste volumes and environmental sustainability impacts. The paper briefly reviews the historical approaches to road construction in peat soils both in Ireland and internationally. Analytical methods to assess flexible pavement foundation stability and deformation under static embankment and dynamic traffic loading are reviewed. A number of case histories of low capacity (less than 2000 AADT) road foundation design and performance on Irish peat soils are described. The benefits of surcharge upon the creep performance of peats are discussed and back calculated, and field performance data from one site is presented. Some conclusions are drawn as to the potential for increased application of geosynthetic base reinforcement and ground improvement approaches in peat soils which are less commonly adopted at present in Ireland.

**Keywords** Mechanistic—empirical design · Sustainability · Geosynthetic reinforcement · Peat · Case histories

---

C. Reilly (✉)  
Ciaran Reilly & Associates, Maynooth, Ireland  
e-mail: [ciaran@ciaranreilly.ie](mailto:ciaran@ciaranreilly.ie)

F. Buggy  
Roughan & O'Donovan, Dublin, Ireland  
e-mail: [fintan.buggy@rod.ie](mailto:fintan.buggy@rod.ie)

## 1 Introduction

Excavation and replacement of peat deposits are the standard earthworks construction technique applied to shallow peat and organic soils on major roads projects in Ireland. This improvement technique is generally robust in terms of long term performance of the road foundations and reasonably economic for modest depths of soft ground, provided that sources of imported replacement fill and areas for deposition of waste peat materials are close to or contiguous with the area of soft ground. Costs, environmental impacts and risks associated with the technique increase as the volume and depth of peat increases (especially above 4 m) and as import fill sources and disposal sites extend further away from the project. The large resultant waste and import volumes have significant environmental sustainability impacts. More recently, piled embankments are increasingly used in areas of deep peat deposits in Ireland for major roads. However, this mitigation measure can have high-construction costs and attendant construction safety risks due to operating heavy piling plant and construction traffic on temporary work platforms.

Osorio et al. [1] provide a useful overview of the historical development and current performance of rampart roads in Ireland's peatlands discussing several road improvement methods to sustain increased traffic volumes and improve performance including temporary surcharge to induce pre-consolidation, vertical drains, lightweight fills and geosynthetic reinforcement within pavement overlays.

The application of surcharge to improve the strength, compressibility and long-term creep characteristics of peat soils is well-documented for both Irish conditions as well as in many other countries where such soils are prevalent (i.e., Canada, USA, Scandinavia, UK, Japan). Hanrahan [2] reports its use in Ireland as early as 1951 and it was extensively applied to the R401 between Edenderry and Rathangan in County Offaly over peat with 7.6 m mean depth in the mid 1950s. Other more recent applications in Ireland include the N6 Athlone Bypass constructed using surcharge over peat layers up to 2 m thick and sections of the Galway Outer Ring Road.

Internationally, Munro [3] reports several case histories of the application of surcharge in Scotland, Finland and Norway, mostly to low volume roads, but including a national trunk road in Scotland. Carlsten [4] cites two case histories of major roads in Sweden being constructed directly over peat 2–3 m and 4–6 m thick, respectively, using surcharge preloading. In Hokkaido, Japan, Hayashi and Nishimoto [5] describe its application to an expressway underlain by 5 m thickness of peat and organic clay.

Pre-consolidation of peat by artificial means can be achieved in many ways as follows:

1. If the peat surface is sufficiently excavated before construction of a new road or during the reconstruction of an existing road, and then its new vertical stress is now lower than it was prior to excavation and the soil is slightly over consolidated. Examples of this approach for new construction are rare in Ireland, but at least one railway between Athenry and Tuam in County Galway was historically

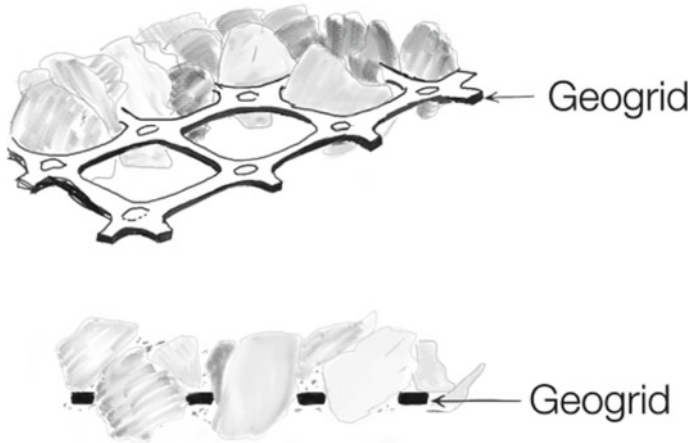
- constructed by this method in the 1860s. The technique was recommended for existing bog roads by Hanrahan [6];
2. If an existing road embankment's fill materials are replaced by light weight fill, then a pre-consolidation effect also results which also provides long-term maintenance benefits for the reconstructed road pavement [1, 7, 8];
  3. If the road embankment is temporarily over loaded by a surcharge fill during construction and the temporary fill is maintained at its full height relative to the final road pavement level and for long enough to permit full consolidation drainage to occur. Normally, this takes place within 2 months as reported by O'Loughlin [9], but the duration varies with degree of over consolidation or surcharge height desired plus peat thickness, permeability and drainage boundary conditions;
  4. If a vacuum pressure is artificially applied to the surface of the peat, this has the same effect as applying a vertical load due to dead weight of surcharge fill. This technique is experimental at present, but has been the subject of a research trial by the NRA and Trinity College Dublin and is reported by Osorio et al. [10].

In Sweden a rule of thumb is to provide at least 25% overstress to the embankment by temporary surcharge (ignoring the effect of buoyancy as fill becomes submerged below a water table). Studies by Yu and Frizzi [11] in Florida suggest that an overstress of at least 50% may be required to produce the most efficient reduction in long term creep.

Difficulties can be experienced when trying to construct embankment and temporary surcharge fills directly above very soft peat soils due to risks of slope instability or local bearing capacity failure of construction plant. To mitigate for this risk the use of geosynthetic reinforcement is common. Typically, a non-woven geotextile separator and a geogrid are placed on the peat surface before any fill is placed or plant operates on it. The separator geotextile prevents the peat pumping or migrating into the fill reducing its strength, while preventing the fill being "lost" into the soft peat. The geogrid acts to laterally confine and reinforce the fill layer, preventing overall or localized failure and reducing deformation. It is usual to place the geosynthetics directly on the peat surface to take benefit from the reinforcing effect of any vegetation growing on the peat and the additional strength offered by any hardened "crust" which may be present.

Such geosynthetic applications may be designed using proprietary methods developed by manufacturers or using methods available in the literature, such as the Giroud-Han method [12, 13]. The majority of these methods take account of the confinement and lateral restraint offered to the imported granular fill by the geosynthetics, as illustrated in Fig. 1, rather than the "tensioned membrane" effect, as deformations required to mobilize the "tensioned membrane" effect are larger than those typically tolerated for roadways.

Geosynthetics can also improve the local or differential settlement performance of pavements on a peat foundation when incorporated into the pavement foundation (typically at the interface between capping and sub base) or in the pavement structural layers. Davitt [14] cites this latter technique as useful in extending the life



**Fig. 1** Interlocking of granular fill particles with geogrid ribs

of overlays on surface dressed macadam bog roads in Ireland and the technique is further reviewed by Keller [15]. Design methods for geosynthetics in these situations have been developed, for example those proposed by Korulla et al. [16], however examples of their application to roads on peat in Ireland are not known to the authors.

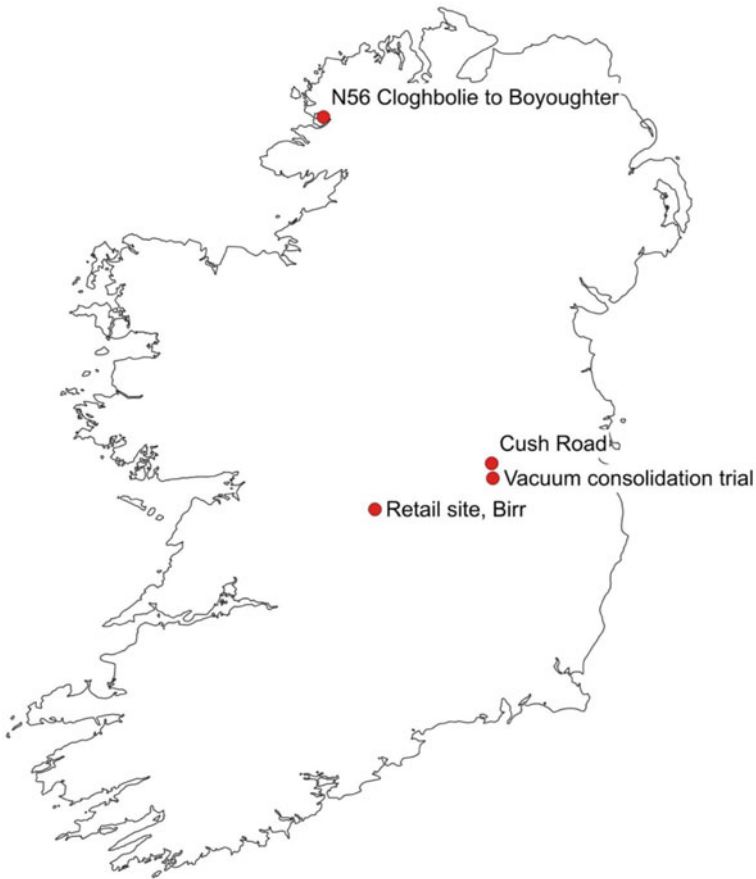
## 2 Summary of Case Histories

Three case histories are discussed in this paper, ranging from the review of a historic failure to a modern-day application of geosynthetics to construct economical temporary roads over drained peat. The locations of the case histories presented, along with the location of the vacuum consolidation trial discussed in Sect. 1, are shown in Fig. 2.

### 2.1 *Cush Road (L1001), Edenderry, County Offaly to Rathangan, County Kildare*

Hanrahan [2, 6–8] reports on novel works carried out to stabilize a section of the Cush Road (L1001) in County Offaly which had deformed to the point of failure at three locations after resurfacing works carried out between August 1953 and March 1954. The project offered a unique opportunity to document the behavior of the road over peat bog over the following 26 years.

The original road was an unpaved gravel road constructed over an average peat depth of 7.6 m. The road was surfaced with tarmacadam in 1936 and, due to increases



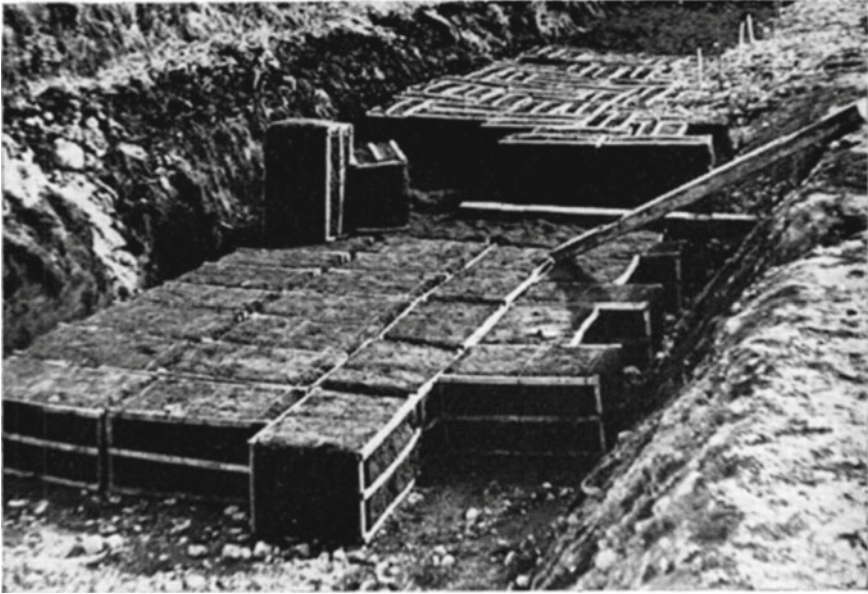
**Fig. 2** Locations of case history sites

in traffic loads, began to disintegrate such that significant repairs were required in 1952. At this time, the average thickness of road construction was 300 mm. Works proposed included:

1. Widening the road from 4.3 to 6.4 m by placing strips of gravel 450-mm thick either side of the existing road construction,
2. Scarify the existing road surface, and
3. Strengthen the road by adding an extra 450 mm of gravel over the full width.

It was thought that the additional settlement generated by an additional surcharge of 450 mm of gravel would be within tolerable limits and could be dealt with by local regrading, with the modest additional surcharge fill load leading to consolidation and hence strengthening of the underlying peat.

Works were completed by March 1954. It was quickly apparent that excessive depths of gravel were added to the road in several places, leading to serious



**Fig. 3** Bales of dried peat used to rebuilt road (Hanrahan, 1964)

adverse effects including settlement, heave and lateral spread. Over three sections with lengths of 60, 55 and 45 m, regrading was insufficient to prevent excessive deformation, and therefore, Hanrahan designed a scheme whereby benefit was taken of preconsolidation effects to reduce the stress on the peat subgrade. This involved removing part of the additional gravel fill and replacing it with light-weight bales of compressed horticultural peat. The compressed peat was then resurfaced with 450 mm of gravel. An example of the placement of these compressed peat bales is shown in Fig. 3.

Remedial measures were completed in November 1954 and the opportunity arose to monitor the road levels. The results of monitoring over the initial 8 years are presented in [7] and reproduced in Fig. 4 where the road levels in 1962 can be compared to an original road level as constructed in 1954. At this time, the road surface over the peat bales was observed to be in good condition and in better condition than elsewhere. Ten trial pits were excavated at this time to determine the make-up of the road and to investigate the condition of the peat bales. It was found that the baled peat had increased in moisture content from 37.5% as it left the factory to 473% after being submerged for 8 years. The bulk density of the peat bales increased from 1.7 to 7.5 kN/m<sup>3</sup> during the intervening 8 years. Typical values for natural peat moisture content of 1150% and undrained strength from field vane shear testing of 6 kN/m<sup>2</sup> were reported. A further set of road levels was taken in March 1980 and settlement against log time is plotted in Fig. 5, where the end of original construction in circa March 1954 = 100 days; observed settlements in July 1962 = 3500 days; and observed settlements in March 1980 = 9500 days. The proportion of overstress

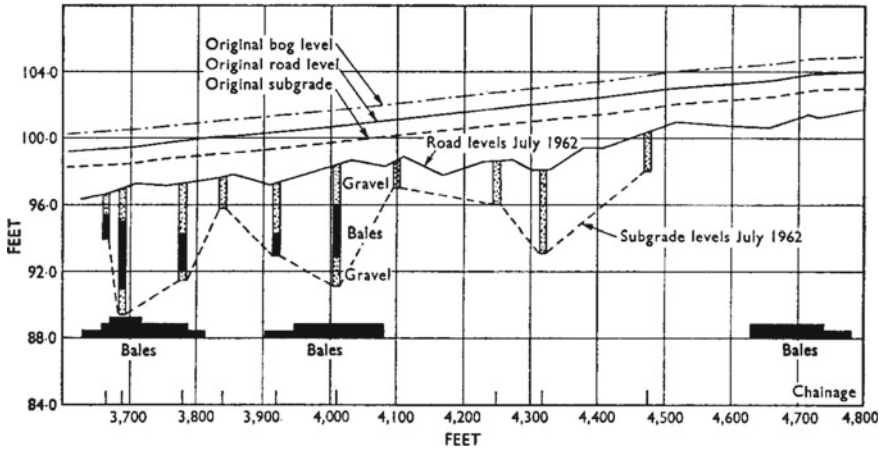


Fig. 4 Road levels and locations of peat bales and trial pits, July 1962 [7]

achieved by the replacement of gravel using lightweight baled peat (i.e., the reduction in vertical effective stress from its prior maximum value to its post-construction long-term value) varied from 65 to 200%. The long-term creep rates  $C_{ae}$ , defined as strain per log cycle of time, were back calculated using the recorded settlement and peat thickness given in the reference publications plus time from the period 1954 to 1980 (26 years) shown in Fig. 5 as follows:

1. Locations 7, 8 and 10 outside of baled peat lightweight fill replacement  $C_{ae} = 0.025-0.06$ ; and
2. Locations 2, 3, 5 and 6 improved by baled peat lightweight fill replacement  $C'_{ae} = 0.006-0.017$ .

Taking an average back calculated field value for normally consolidated, unimproved peat of  $C_{ae} = 0.042$  suggests that back calculated creep improvement ratios ( $C'_{ae}/C_{ae}$ ) for surcharged peat varied from 0.4 to 0.14 and reduced with increasing proportion of overstress as reported by Yu and Frizzi [11]. However, the creep improvement ratios for peat are notably much higher than those reported by Ladd [17] for soft mineral soils.



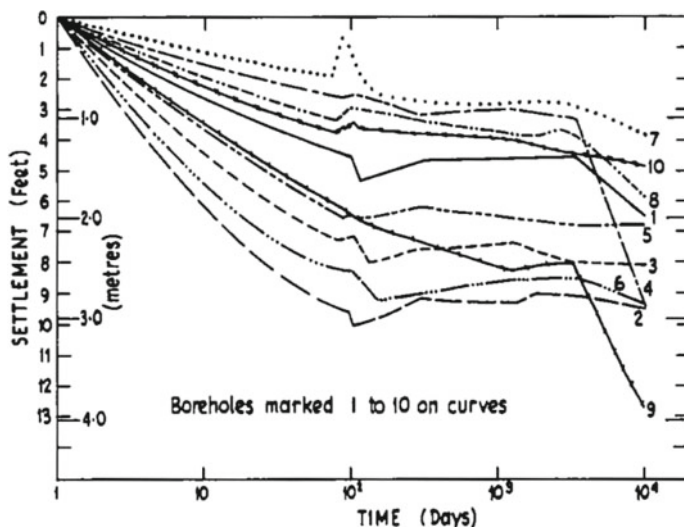


Fig. 5 Observed settlements (Locations 1, 2, 3, 5 and 6 at peat bales), March 1980 [8]

## 2.2 N56 Cloghbolie to Boyoughter, County Donegal

The N56 Cloghbolie to Boyoughter Road involved improvements to 3.5 km of a lightly trafficked (approximately 2000 vehicles/day AADT), 7 m paved width, Type 3 National Secondary Route in County Donegal, in north-west Ireland. Approximately 1.2 km length was located in a deep bog area where the new alignment was around 3 m below the existing road levels. The route was investigated by a range of intrusive and geophysical methods including trial pits, dynamic probing with window sampling, boreholes, 2D resistivity profiling and ground penetrating radar. The peat depth varied considerably from 1 m to in excess of 5 m and a typical interpreted section is shown in Fig. 6. Natural moisture contents generally ranged from 300 to 1200% with a mean of 865%, while organic contents varied from 22 to 80% (mean = 51%) and bulk density of  $11.8 \text{ kN/m}^3$ . Peat was typically underlain by sands and weathered granite bedrock which acted as a basal drainage boundary. A mean field undrained shear strength of approximately  $15 \text{ kN/m}^2$  is estimated from correlation to moisture content [18].

A temporary road diversion was constructed in summer 2012 on a floating 2.5 m wide cycleway using a shuttle service with traffic light control during the excavation of the existing road and its peat foundation and subsequent reconstruction. A typical cross section of the floating cycleway construction is shown in Fig. 7 and consisted of a geotextile separator placed directly on the vegetated peat surface; Tensar TX160 triaxial geogrid; 400-mm thickness of crushed stone capping; 100 mm of C1. 804 subbase; and 40 mm of C1 912 asphalt concrete surface course. Figures 8 and 9 show the cycleway during construction, and Fig. 10 shows the cycleway during temporary

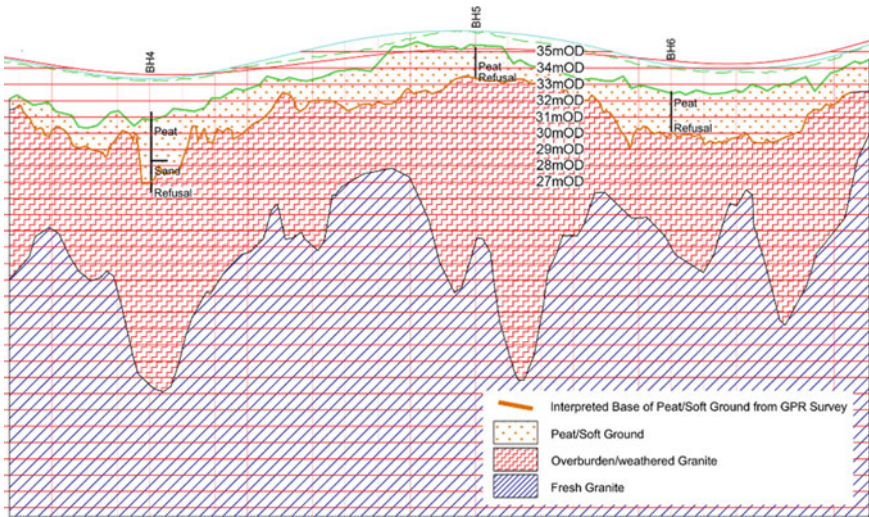


Fig. 6 N56 typical interpreted geologic section from geophysics surveys

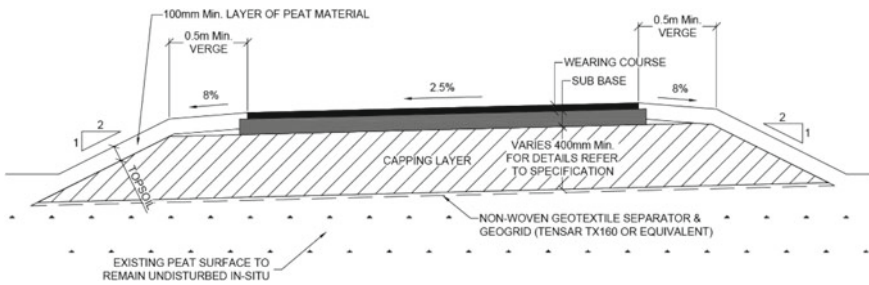


Fig. 7 N56 floating cycleway typical section

service as a diversionary route. The temporary floating road performed well under traffic over a 10 weeks period without evidence of any distress or rutting.

### 2.3 Temporary Access Road at Retail Development, Birr, County Offaly

As part of the upgrade of a retail site (a Lidl supermarket) in Birr, County Offaly, temporary access was required over peat soil for construction plant including tipper trucks, excavators and a piling rig. The road was constructed alongside an existing retail building, which was supported on driven precast concrete piles. A view of the road under construction is shown in Fig. 11.



**Fig. 8** N56 floating cycleway during construction

Two phases of ground investigation were carried out at the site, involving cable percussive boreholes, dynamic probing and trial pits. The first phase of investigation, carried out in 2001 and using the “heavy” dynamic probe apparatus (utilizing a 50 kg weight dropped through 500 mm), showed that the probe fell under its own weight to a depth of between 4.9 and 7.6 m below ground level along the line of the proposed road, meeting dense granular deposits (likely of fluvio-glacial origin) at depths of between 7.2 and 7.8 m below ground level. Natural moisture content of the peat at the site ranged from 285 to 684% with a mean of 500%. This is lower than typical for natural Irish peat and is likely due to local drainage of the peat layer due to other infrastructure works in the vicinity.

Further trial pits and field vane testing carried out between 2016 and 2018 found peat to a depth of 1.0 m to greater than 2.7 m below ground level, overlying soft gray alluvial silts and clay. The peat was described as “dark brown plastic pseudo-fibrous peat with heavily decayed branches and plant material”.

Undrained shear strengths measured at a depth of 1.0 m below ground level in the peat ranged from 35 to 50 kPa, while undrained shear strengths measured in the



**Fig. 9** N56 floating cycleway during construction



**Fig. 10** N56 floating cycleway during use as a temporary diversion route

underlying soft alluvial clay and silt ranged from 12 to 14 kPa. No natural moisture content measurements were made of the peat underlying the proposed road in 2016 or 2018, however by reference to the correlations presented by Carlsten [18], it is expected that the natural moisture content remained at approximately 500%. Ground water was encountered at typically 1.5 m below ground level.

The road required was 4 m wide and approximately 65 m long. The access road was designed using the Giroud-Han method to support an axle load of 80 kN with 5000 axle loadings over the construction period. A rut depth of 50 mm was selected as tolerable. The road was constructed in summer 2018 and removed once construction was complete. The road consisted of a geotextile separator placed directly on the vegetated peat surface; Thrace TG4040S biaxial geogrid; and 450 mm of crushed





**Fig. 11** Temporary access road at retail development site, Birr, County Offaly

stone capping. The access road performed very well over the construction period of approximately 8 weeks, with rutting less than 40 mm observed in service.

### 3 Conclusions

The construction of roads over deep peat deposits remains challenging and comes with relatively high levels of risk. The three case histories presented show a range of measures taken to deal with the challenges of constructing roads across peat in Ireland. The use of lightweight fill (bales of compressed horticultural peat) has been found to be an effective improvement technique to control creep settlements and was demonstrated over a long time frame of 26 years. Currently, temporary fill surcharge and geosynthetics are most commonly deployed to control the overall stability, long-term settlements and local deformations of the road surface. A number of other techniques are reviewed, however for reasons of practicality, familiarity, economy and risk minimization, these are the techniques most often adopted for construction of roads over peat in Ireland.

**Acknowledgements** The authors would like to acknowledge Transport Infrastructure Ireland and Donegal County Council for their kind permission to publish the N56 Cloghbolie case history data and Thrace Synthetic for permission to publish case history data relating to the retail development site in County Offaly. The views expressed in this paper are the sole views of the authors and do not represent the views of the organizations named above, Ciaran Reilly & Associates or Roughan & O'Donovan.

## References

1. Osorio JP, Farrell ER, O'Kelly BC, Casey T (2008) Rampart roads in the peat lands of Ireland: Genesis, development and current performance. *Adv Transp Geotech*, pp 227–233
2. Hanrahan ET (1976) Bog roads. *Inst Civ Eng Irel* 29(10):3–5
3. Munro R (2004) Dealing with bearing capacity problems on low volume roads constructed on peat: The Highland Council
4. Carlsten P (1988) The use of preloading when building roads on peat. *Baltic geotechnical conference*, pp 135–142
5. Hayashi H, Nishimoto S (2008) FE analysis of the long term settlement and maintenance of a road on peaty ground. In: *Advances in transportation geotechnics*. CRC Press, pp 383–388
6. Hanrahan ET (1953) The mechanical properties of peat with special reference to road construction. *Trans Inst Civ Eng Irel* 78:179–215
7. Hanrahan ET (1964) A road failure on peat. *Géotechnique* 14(3):185–202
8. Hanrahan ET, Rogers MG (1981) Road on peat: observations and design. *Am Soc Civ Eng, J Geotech Eng Div* 107(10):1403–1415
9. O'Loughlin CD (2007) Simple and sophisticated methods for predicting settlement of embankments constructed on peat. In: *Proceedings SGE—2007, soft ground engineering conference*, Athlone, Ireland, February 2007. ISBN 1-898-012-83-0, pp Paper 1.4
10. Osorio S, Farrell ER, O'Kelly BC (2010) Peat improvement under vacuum preloading: a novel approach for bog roads in Ireland. *Cork, BCRI Symposium UCC 2010*, pp 255–262
11. Yu KP, Frizzi RP (1994) Preloading organic soils to limit future settlements. Vertical and horizontal deformation of foundations and embankments, ASCE, pp 476–489
12. Giroud JP, Han J (2004a) Design method for geogrid-reinforced unpaved roads. I: development of design method. *J Geotech Geoenviron Eng* 130(8):775–786
13. Giroud JP, Han J (2004b) Design method for geogrid-reinforced unpaved roads. II. Calibration and applications. *J Geotech Geoenviron Eng* 130(8) pp 787–797
14. Davitt S, Lynch J, Mullaney D, Wall W (2000) Guidelines on the rehabilitation of roads over peat. Department of Environment and Local Government, Dublin
15. Keller GR (2016) Application of geosynthetics on low-volume roads. *Transp Geotech* 8:119–131
16. Korulla M, Gharpure A, Rimoldi P (2015) Design of geogrids for road base stabilization. *Indian Geotech J* 45:458–471
17. Ladd CC (1971) Settlement analyses of cohesive soils. Research Report R71-2, Department of Civil Engineering, M.I.T., Cambridge, Massachusetts
18. Carlsten P (2000) Geotechnical properties of some Swedish peats. In: *NGM—2000, Nordic geotechnical meeting*, Helsinki, pp 51–60

# A Long-Term Record of Water Content and Pore Water Pressure in a Vegetated Clay Highway Cut Slope



J. A. Smethurst, A. Sellaiya, A. P. Blake, and W. Powrie

**Abstract** The major highway network in the UK was developed from the 1960s, and the earthworks are generally well engineered. However, as many of the earthworks get older, slope failures are becoming more common, with some posing a threat to the safety of transport operations. Field measurements of soil water content and pore water pressure changes within the surface zone of a highway cut slope in London Clay at Newbury, Berkshire, UK, have been carried out continuously since 2003. This paper describes and gives examples of the long-term field measurements from the site at Newbury and details a number of significant findings from the observations from the site. The paper explains how these have been used to calibrate appropriate models of seasonal cycles of pore water pressure and slope deterioration.

**Keywords** Slope stability · Pore water pressure · Vegetation

## 1 Introduction

Transport infrastructure is often significantly affected by slope failures. Failures in embankments have the potential to undermine roads and railways, while slips in cuttings may cause material to obstruct transport routes, posing risks to drivers and possible derailment of trains.

---

J. A. Smethurst (✉) · A. Sellaiya · A. P. Blake · W. Powrie  
University of Southampton, Southampton, UK  
e-mail: [jas@soton.ac.uk](mailto:jas@soton.ac.uk)

A. Sellaiya  
e-mail: [a.sellaiya@soton.ac.uk](mailto:a.sellaiya@soton.ac.uk)

A. P. Blake  
e-mail: [a.p.blake@soton.ac.uk](mailto:a.p.blake@soton.ac.uk)

W. Powrie  
e-mail: [wp@soton.ac.uk](mailto:wp@soton.ac.uk)

A. Sellaiya  
Tony Gee and Partners, Esher, UK

Much of the rail network in the UK was constructed over 150 years ago, and the earth structures were not built to modern standards. As these structures age, failures have become more common and can pose a threat to the safety of transport operations. Deep-seated failures have been reported in the clay slopes of both railway and highway cuttings and embankments [1, 2]. In the wet winters of 2012/13 and 2013/14 in the UK, around 250 failures occurred in railway earthworks, causing six train derailments [3]. A significant number of more recent highway earthworks built using modern construction techniques also have shown signs of less severe, shallower failures [4].

Climate conditions directly influence the behaviour and failure of slopes. In temperate European climates, the season of peak water demand by vegetation (summer) is out of phase with the season of greatest rainfall (winter) causing seasonal fluctuations in soil water content and pore water pressures within earthworks [5]. Rapid infiltration of rainfall into clay slopes during wet winters leads to high pore water pressures and is generally the cause of slope failures [1]. Pore water suctions generated by vegetation will have a beneficial effect on slope stability only if they are carried through into winter and early spring. In the UK, the pore water suctions generated by light shrub and/or grass cover are rarely sustained through the winter period, although larger vegetation cover can maintain suctions beneficial to stability [6–8].

When stiff overconsolidated clays such as the London Clay are sheared, they will initially reach a peak strength; with further shear deformation, this drops towards a lower residual strength. This strain-softening leaves slopes vulnerable to progressive failure, with a shear band steadily developing from the toe of the slope where the soil initially reaches the post-peak strength. There is clear evidence from both centrifuge model tests and numerical analyses of clay slopes that cyclic stresses representative of those induced by seasonal climate and vegetation can cause strain-softening to occur [9–12]. Over a period of several tens of years, these cycles of pore pressure and effective stress can result in progressive failure.

Knowledge of the effects of climate and vegetation on pore water pressures is important for the validation of numerical models of slope stability that attempt to consider the complex interactions between climate, vegetation and the ground. Such models are essential if the cyclic changes in effective stress that leads potentially to progressive failure, and the influence of climate change on long-term slope stability is to be understood [7].

This paper describes the results of a field study carried out to quantify the hydrological environment and pore water pressures in a cut slope in London Clay. Data were collected over 17 complete winter/summer cycles, including two wet winters (2002/03 and 2013/14) and some exceptionally dry summers (2003, 2018, 2019). This has enabled a thorough understanding of the physical behaviours that occur in response to seasonal variations in weather and lead to a range of observed soil water contents and pore water pressures/suctions, in a clay slope that is representative of significant lengths of the UK highway network. The paper also describes how the field observations have been used to calibrate numerical models of slope deterioration and failure.



## 2 Newbury Monitoring Site

The field study was carried out on a London Clay cutting slope on the A34 Newbury bypass in southern England (Fig. 1). The slope is east facing, 8 m high and 28 m long (Fig. 2), and was constructed in 1997. The London Clay at the site is about 20 m thick, highly weathered to a depth of about 2.5 m below original ground level and underlain by Lambeth Group deposits and the Upper Chalk. After the cutting was excavated, up to about 0.4 m of topsoil was placed over the cut London Clay surface to facilitate the vegetation growth on the slope. A gravel fin drain approximately 600 mm deep, 4 m from the toe of the slope, was installed to drain the road sub-base. The fin drain connects at intervals into a sealed carrier drain that outfalls to the south of the cutting and to which the road gullies are also connected. A cross section through the slope is shown in Fig. 3.

The current groundwater regime in the slope is effectively hydrostatic below the groundwater level. This indicates that within the near-surface zone being monitored, any negative excess pore pressures induced by unloading as a result of excavating the cutting have substantially dissipated.

When the instrumented slope was established in 2002, the vegetation cover was grass and herbs with some small (less than 1 m high) trees and shrubs. The grass was periodically mowed to aid establishment of the planted trees and shrubs. This ceased in late 2002, after which the trees and shrubs in the instrumented section were maintained to a height of less than 1.5 m by heavy pruning. After the first 6 years of monitoring, the vegetation was allowed to grow larger, and the slope now has a thick vegetation cover of shrubs and trees up to 4–5 m in height.

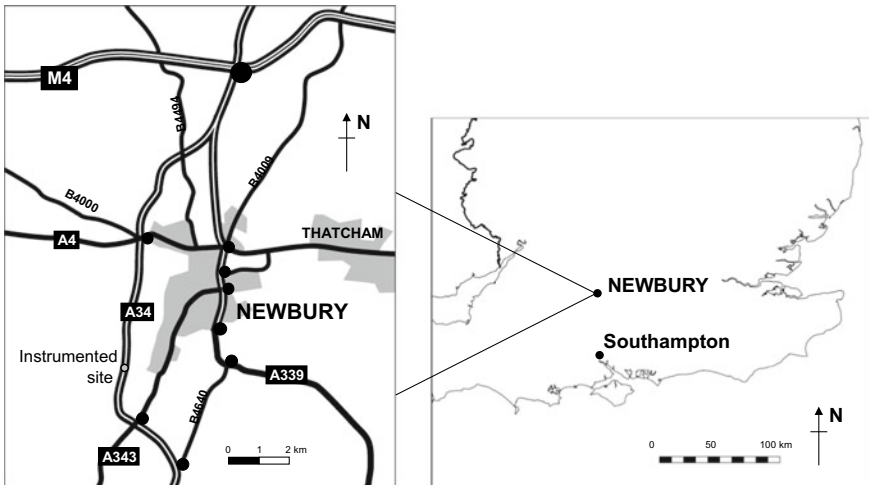
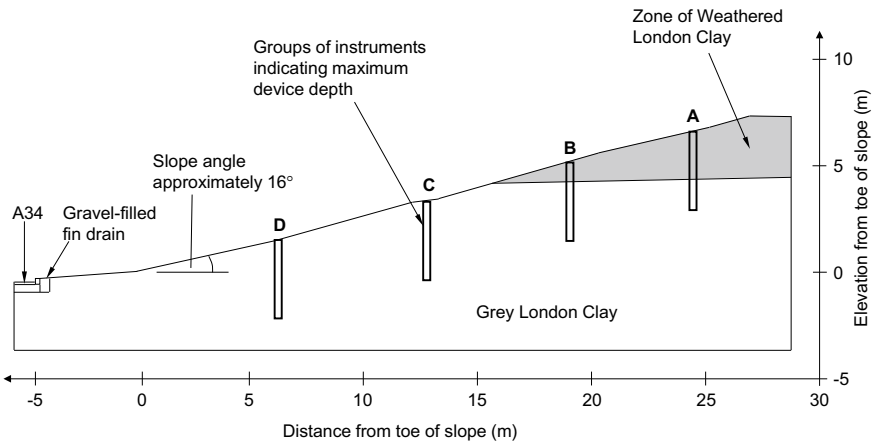


Fig. 1 Newbury site location (redrawn from Ref. [7])



**Fig. 2** Instrumented site at Newbury, looking upslope from close to the toe of the cutting. Picture was taken in April 2015. The slope is now more heavily vegetated than shown here



**Fig. 3** Cross section through the site showing the slope geometry and instrument group locations (redrawn from Ref. [7])

**Table 1** Permeability, unit weight and plasticity index of grey and weathered London Clay at the Newbury site

Property	Grey London Clay		Weathered London Clay	
	Range	Average	Range	Average
Saturated permeability, from double ring and Guelph permeameter tests: m/s	$1.0 \times 10^{-11}$ to $7.3 \times 10^{-6}$	$1.1 \times 10^{-6}$	–	–
Saturated permeability, from borehole bail out tests: m/s	$2.3 \times 10^{-9}$ to $4.4 \times 10^{-9}$	$3.7 \times 10^{-9}$	$3.6 \times 10^{-8}$ to $5.0 \times 10^{-8}$	$4.3 \times 10^{-8}$
Dry unit weight, $\gamma_d$ : kN/m <sup>3</sup>	13.2–15.2	14.6	13.2–16.2	16.0
Plasticity index, $I_D$ : %	32.5–36.4	34.8	31.7	31.7

The London Clay at the site is predominantly a stiff grey clay but contains several bands of silty clay up to 50 mm thick and bands of large clay stones. The weathered London Clay close to the top of the cutting is spatially very variable, changing from a stiff orange-brown clay to a clayey silt over small distances and depths, similar to the description given by Perry et al. [13]. The permeability, unit weight and plasticity index of the London Clay at the site are summarised in Table 1. The dry unit weight was measured from undisturbed block samples obtained from 0.5 m depth for both the weathered and unweathered clays.

The permeability of the clay was measured in the laboratory in a triaxial apparatus using small specimens trimmed from samples collected using 50 mm diameter thin-walled sample tubes. Bulk permeability was measured in the field using borehole bailout tests at 2–3 m below ground level, the double ring infiltrometer and Guelph permeameter close to the surface. The field measurements of permeability followed the ASTM standard [14]; more details of the measurements at the site are given in Refs. [15] and [16]. The variation of permeability with depth is several orders of magnitude, with values of between  $7 \times 10^{-6}$  and  $1 \times 10^{-10}$  m/s close to the ground surface (in the top 0.6 m of the soil profile) and an average value of  $4 \times 10^{-9}$  m/s from the borehole bail out tests. The generally larger and much greater variation in measured permeability close to the slope surface is caused by summer desiccation cracking, and greater soil structure given by roots, animals and decayed organic matter.

### 3 Instrumentation

The site was extensively instrumented to monitor the soil water content, pore water pressure, soil temperature, the free water surface, rainfall, runoff and climatic data required to estimate evapotranspiration.

Arrays of time domain reflectometry (TDR) probes for measuring soil water content, flushable vibrating wire piezometers, water-filled tensiometers and equiten-siometers were installed in four groups spaced 6 m apart down the slope (Fig. 3). The instrumentation included a range of devices (such as Delta-T TDR ThetaProbes for measuring water content) that are more commonly used in agricultural and crop studies for measurements in the plant rooting zone. There was also a desire to measure soil water content due to the difficulties in measuring the large pore water suctions that can develop in clay soils subjected to direct drying by vegetation [5]. The study at Newbury was one of the first geotechnical studies to employ some of these types of instrumentation.

The sensors were installed at depths between 0.3 and 3.5 m, at intervals of 0.3 or 0.5 m. Smethurst et al. [5, 7] provide more detail on the sensor types and the depths at which each type was installed. A climate station was placed on the slope to record air temperature, humidity, wind speed and solar radiation. These parameters were used to estimate potential evapotranspiration using the Penman–Monteith method [17].

Surface runoff together with interflow (i.e. flow of water through the topsoil) was measured using an interceptor drain cut across the face of the slope. The interceptor drain was 6 m long and 35 cm deep, dug through the topsoil into the top of the undisturbed London Clay. A slotted drainpipe with gravel packing channelled water into a tipping bucket flow gauge is capable of measuring up to 15 l/min. The runoff and interflow were measured to enable the full water balance (rainfall, evapotranspiration, soil water storage and runoff) to be understood.

All of the above sensors were connected to a Campbell Scientific data logger with a GSM modem connection, powered by a 12 V car battery recharged by a 10 W solar panel. The data were logged at 10 min intervals and recorded as hourly averages, commencing in late 2002.

Aluminium access tubes for a neutron probe were installed to enable point measurements of water content adjacent to the logger sensors. In 2016, in place inclinometers were also installed to measure seasonal lateral movements within the slope.

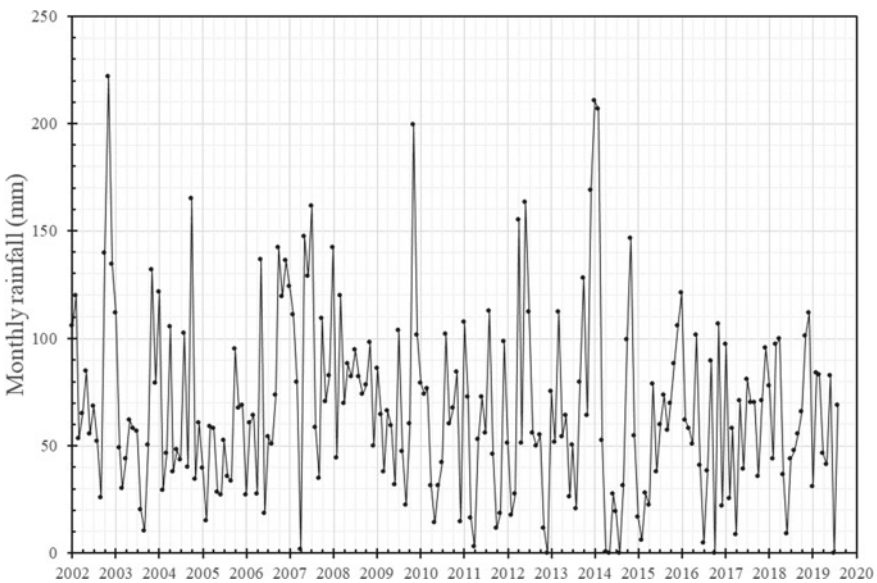
### 4 Monitoring Results

The Newbury site has been monitored over a period of 17 years, starting in late 2002 and continuing to present. The long-term annual rainfall at Newbury is 875 mm, with slightly wetter months in autumn and early winter (having a typical monthly

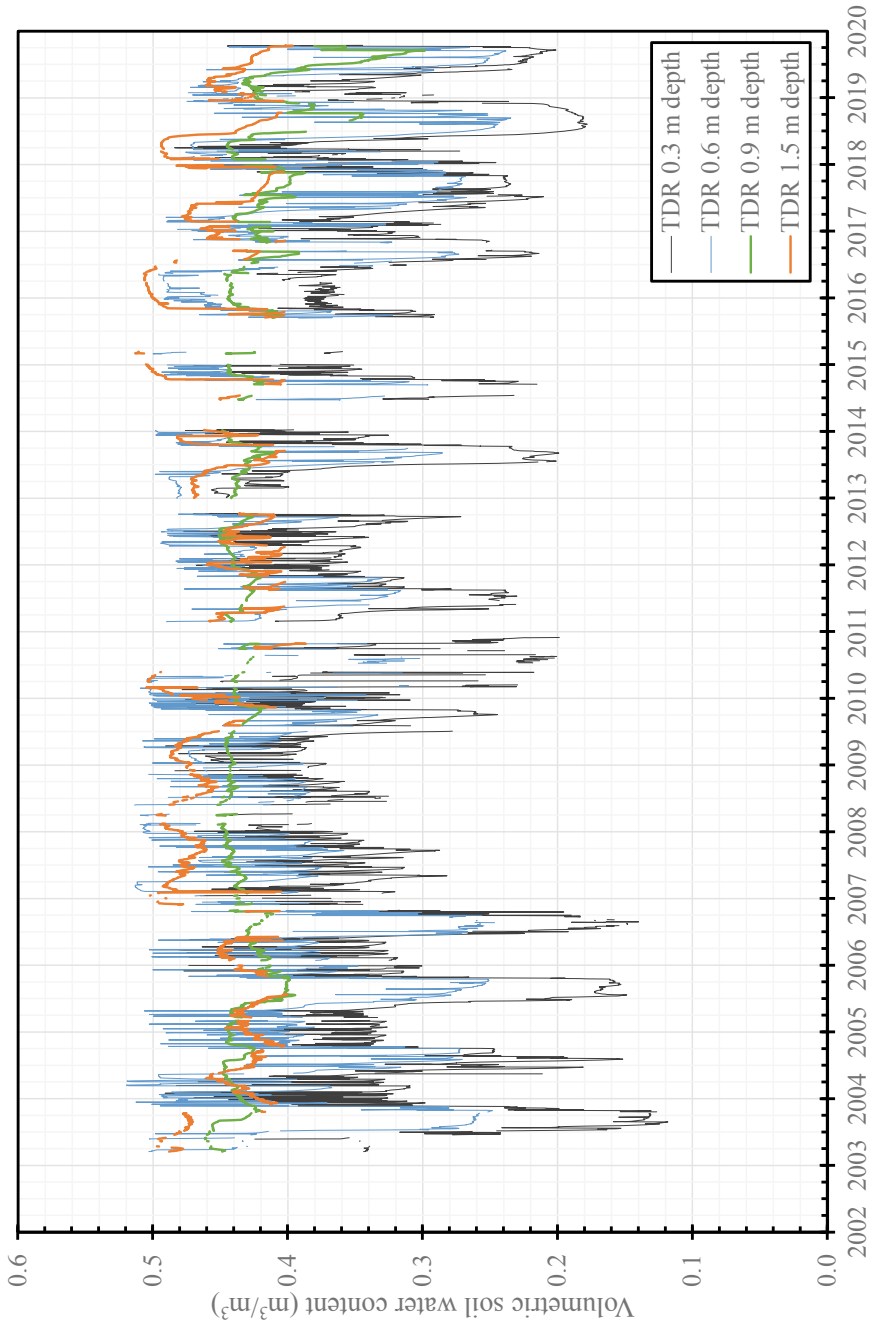
average of 95 mm) and drier months in late spring and summer (with typical monthly averages of 60 mm). Figures 4, 5 and 6 give some examples of the data recorded over the full duration of monitoring: Fig. 4 shows the rainfall, and Figs. 5 and 6 show the soil water content and measured pore water pressures for the instrument group A at the top of the slope. A clear seasonal pattern can be seen in the data, with substantial drying occurring at shallow depths caused by plant evapotranspiration exceeding rainfall in the summer months and rewetting of the soil again in late autumn and winter when evapotranspiration reduces (Fig. 5). The depth of drying is dictated by the typical maximum plant root depth of about 0.8 to 1.0 m. There are some summers, such as 2007 and 2008, that were very wet, during which the reduction in soil water content was only small.

Figure 6 shows that the same seasonality is apparent in pore water pressures. Pore pressures return to fairly high values in many winters, giving a distribution that is close to hydrostatic from about 0.5 m below ground surface level. The plot also shows a gentle but steady reduction in average pore water pressure over the monitoring period. This is caused by the change in vegetation cover as the slope has gone from being mainly grass covered to now being covered with a dense growth of shrubs and small trees. The immature trees can root to slightly greater depths and are likely to transpire more water, and this appears to have caused a small and gradual reduction in the pore water pressures in the slope, most notable by slightly lower values in winter.

Smethurst et al. [7] consider the first 6 years (2003–2008) of water content and pore water pressure observations in detail and in the context of a longer 40-year



**Fig. 4** Monthly rainfall totals measured at Newbury site for period 2003–2019



**Fig. 5** Soil water content measured using TDR ThetaProbes at group A (close to the top of the slope) for period 2003–2019

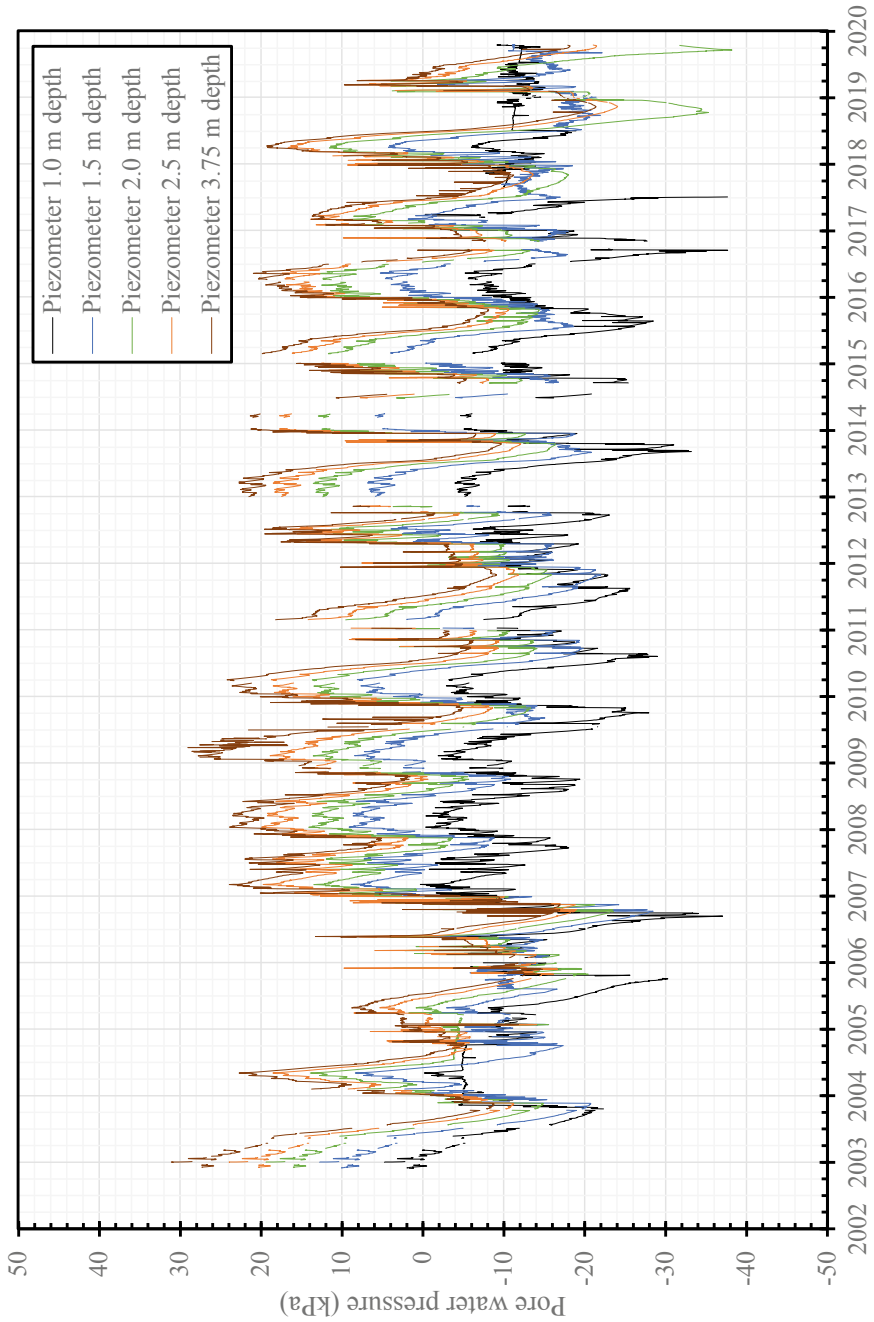


Fig. 6 Pore water pressures measured at instrument group A for period 2003–2019



rainfall dataset. The paper considers data from a wider range of the instrumentation than shown here, to make a series of observations, as follows:

- The grass and small shrub cover on the slope are capable of rooting to about 0.8 m in the clay, and the major summer soil drying occurs over this depth. Large pore water suctions ( $>200$  kPa) are generated in the root zone, but modest suctions also extend deeper, up to about 3.5 m depth in a drier summer. Most winters see close to hydrostatic conditions, particularly in the lower part of the slope.
- The seasonal behaviour seen is closely linked to the observed climate. The actual evapotranspiration (determined from a simple water balance model) remains very similar from year-to-year, but rainfall varies considerably. If the summer (June to August) rainfall exceeds 250 mm, very little soil drying occurs. A water balance model can be used very effectively to link observed weather, water content and suctions in the rooting zone.
- The permeability of the near-surface rooting zone is large during the summer due to desiccation cracking, as evidenced by the occurrence of very little runoff during high-intensity rainfall events and the rapid rewetting of the soil profile in late autumn and early winter. However, the clay does swell in autumn and winter, closing cracks and reducing the near-surface permeability [15].
- Pore water pressure/suction observations coupled with a 40-year rainfall dataset make it possible to characterise approximate return periods for pore water pressures/suctions associated particularly with extremely dry and wet events.

## 5 Use of Monitoring Results to Validate Numerical Models

The Newbury monitoring dataset has been used by four different studies, both to validate partly saturated finite element/difference models investigating soil hydraulic processes and parameter selection (Heppell et al. [18] and Karim et al. [19]) and validate partly saturated coupled mechanical models that are able to simulate cyclic strain-softening driven progressive failure in slopes (Rouainia et al. [11] and Postill et al. [12]). All of the models are driven by climate (daily rainfall and evapotranspiration) applied to the upper slope surface boundary, which drives annual cyclic changes in water content and pore water pressure/suction in the model. All four studies have modelled the Newbury slope, using the field observations to help to calibrate the vegetation evapotranspiration, saturated/unsaturated permeability and water retention relationships required to correctly replicate the measured changes in soil water content and pore water pressure. Some of these relationships can be uncertain; c.f. the wide range of measured saturated permeabilities given in Table 1. The most recent study (Postill et al. [12]) has used the full 17 years of monitoring data presented in this paper to validate simulation results, showing that the model is able to replicate the field measured behaviour, particularly of soil water content and pore water pressure, to both short and prolonged wet and dry periods. The models able to replicate strain-softening and progressive failure show that after many applied



cycles of seasonal pore water pressure, the slope suffers ultimate shallow failure, due to progressive loss of strength [11, 12].

The Newbury dataset is currently being used as part of a UK project called ACHILLES ([www.achilles-grant.org.uk](http://www.achilles-grant.org.uk)), which is carrying out field monitoring, laboratory experiments and numerical modelling to understand deterioration and failure processes in clay earthworks under the influence of weather and a changing climate. The ACHILLES project is led by the University of Newcastle and includes a number of other UK universities and institutions, including the University of Southampton. Field monitoring data are being used both to develop conceptual models and to validate numerical models that seek to understand weather-driven deterioration and ultimate failure in clay slopes; an initial output from this work is the simulation of the Newbury site presented by Postill et al. [12]. The climate-driven models being developed are essential to understand the effects that climate change will have on the rate of deterioration of the slopes (this is demonstrated by Rouainia et al. [11]). The models will also be used to look at potential mitigation and remediation strategies. A planned output of the project will be a set of deterioration curves, showing how the factor of safety of an earthwork against ultimate failure declines with time; an example of such a set of deterioration curves is given by Glendinning et al. [20].

As part of the ACHILLES project, it is planned to make the full 17-year record of processed Newbury site monitoring data, of which sections are shown in this paper, publicly available for others to use in validation of similar models.

## 6 Conclusions

The long-term monitoring of the Newbury highway slope has allowed several important observations of the effect of weather and vegetation on the soil water content and pore water pressures/suctions in a cutting typical of those in overconsolidated clays in the midlands and south of England. The site is unusual in having a long and near-continuous record of observations now spanning 17 years duration. Long-duration observations of this type are likely to be essential in understanding how weather, vegetation and climate (including climate change) influence the long-term deterioration on performance of clay earthwork assets. The well-cited dataset has already provided a means to validate important models that are able to replicate the effect of weather and vegetation on certain modes of cyclic deterioration and failure in infrastructure earthworks, and this work is continuing via the ACHILLES project.

The site will continue to be monitored for the foreseeable future. Whilst initially maintained, the vegetation at the site is now being allowed to develop into a dense thicket of large shrubs and immature trees, so that the effect of the changing vegetation on pore water pressures/suctions can be observed.

**Acknowledgements** The instrumentation and monitoring of the Newbury site have been funded by the UK Engineering and Physical Sciences Research Council grant numbers GR/R72341/01,

EP/F63482/1, EP/K027050/1 and EP/R034575/1. The support of Highways England in both setting up and the continued monitoring and maintenance of the Newbury site is also gratefully acknowledged.

## References

1. Briggs KM, Loveridge FA, Glendinning S (2017) Failures in transport infrastructure embankments. *Eng Geol* 219:107–117. <https://doi.org/10.1016/j.enggeo.2016.07.016>
2. Hughes D, Sivakumar V, Glynn D, Clarke G (2007) A case study: delayed failure of a deep cutting in lodgement till. *Proc Inst Civil Eng—Geotech Eng* 160(4):193–202
3. Department for Transport (2014) Transport resilience review: a review of the resilience of the transport network to extreme weather events. Her Majesty's Stationary Office, London
4. Perry J (1989) A survey of slope condition on motorway earthworks in England and Wales. Research report 199. Transport and Road Research Laboratory
5. Smethurst JA, Clarke D, Powrie W (2006) Seasonal changes in pore water pressure in a grass covered cut slope in London clay. *Géotechnique* 56(8):523–537. <https://doi.org/10.1680/geot.2006.56.8.523>
6. Anderson MG, Kneale PE (1980) Pore water pressure changes in a road embankment. *J Inst Highw Eng* 25:11–17
7. Smethurst JA, Clarke D, Powrie W (2012) Factors controlling the seasonal variation in soil water content and pore water pressures within a lightly vegetated clay slope. *Géotechnique* 62(5):429–446. <https://doi.org/10.1680/geot.10.p.097>
8. Smethurst JA, Briggs KM, Powrie W, Ridley A, Butcher DJE (2015) Mechanical and hydrological impacts of tree removal on a clay fill railway embankment. *Géotechnique* 65(11):869–882. <https://doi.org/10.1680/jgeot.14.P010>
9. Nayambayo V, Potts D, Addenbrooke T (2004) The influence of permeability on the stability of embankments experiencing seasonal cyclic pore water pressure changes. In: *Advances in geotechnical engineering: proceedings of the Skempton conference, vol 2*. Imperial College, London, pp 898–910 (2004)
10. Take WA, Bolton MD (2011) Seasonal ratcheting and softening in clay slopes leading to first-time failure. *Géotechnique* 61(9):757–769
11. Rouainia M, Helm PR, Davies O, Glendinning S (2020) Deterioration of an infrastructure cutting subjected to climate change. *Acta Geotechnica* 15: 2997–3016. <https://doi.org/10.1007/s11440-020-00965-1>
12. Postill H, Helm PR, Dixon N, Glendinning S, Smethurst JA, Briggs KM, El-Hamalawi A, Rouainia M (2021) Numerical modelling of the long-term deterioration of a cut slope in high plasticity clay. *Eng Geol* 280:105912. <https://doi.org/10.1016/j.enggeo.2020.105912>
13. Perry J, Field M, Davidson W, Thompson D (2000) The benefits from geotechnics in construction of the A34 Newbury Bypass. *Proc ICE—Geotech Eng* 143:83–92
14. ASTM: Standard method D 5126-90—Standard Guide for Comparison of Field Methods for Determining Hydraulic Conductivity in the Vadose Zone. 1998. Annual Book of ASTM Standards. Section 4: Construction, Vol. 04.08 Soil and Rock (I): D 420–D 5779. American Society for Testing and Materials, West Conshohocken, PA, 1055–1064 (2001)
15. Dixon N, Crosby CJ, Stirling R, Hughes PN, Smethurst J, Briggs K, Hughes D, Gunn D, Hobbs P, Loveridge F, Glendinning S, Dijkstra T, Hudson AP (2019) In situ measurements of near-surface hydraulic conductivity in engineered clay slopes. *Q J Eng GeolHydrogeol* 52(1):123–135. <https://doi.org/10.1144/qjagh2017-059>
16. Sellaiya A (2019) Cyclic seasonal effects on infrastructure earthworks. Ph.D. Thesis, University of Southampton

17. Allen RK, Smith M, Perrier A, Pereira LS (1994) An update for the calculation of reference evapotranspiration. *ICID Bull* 43(2):35–92
18. Heppell J, Payvandi S, Zygalkis KC, Smethurst JA, Fliege J, Roose T (2014) Validation of a spatial-temporal soil water movement and plant water uptake model. *Géotechnique* 64(7):526–539. <https://doi.org/10.1680/geot.13.P.142>
19. Karim MR, Hughes D, Kelly R, Lynch K (2019) A rational approach for modelling the meteorologically induced pore water pressure in infrastructure slopes. *Eur J Environ Civ Eng*. Published online ahead of print. <https://doi.org/10.1080/19648189.2018.1506824>
20. Glendinning S, Helm PR, Rouainia M, Stirling RA, Asquith JD, Hughes PN, Toll DG, Clarke D, Hudson A, Powrie W, Smethurst JA, Woodman N, Hughes D, Harley R, Karim R, Dixon N, Crosby C, Dijkstra T, Postill H, Chambers J, Dashwood B, Gunn D, Uhlemann S, Briggs K, Muddle D, Loveridge F (2018) Infrastructure slopes: sustainable management and resilience assessment: iSMART. Final Report. <https://doi.org/10.1680/geot.13.P.142>. <https://eprint.ncl.ac.uk/254433>

# High-Speed Railway Vibrations—An Approach to Tackle Dynamic Instability



Saeed Hosseinzadeh, Peter Schouten, and Gerhard Schulz

**Abstract** The experience with the first generation of high-speed railway lines (HSR) has shown that the cyclic-dynamic impact should be considered in order to limit maintenance efforts, disturbance of operations and increase passenger comfort. Due to the country-specific conditions, different methodologies and requirements are applied by different railway authorities. Serviceability and stability requirements need to include the cyclic-dynamic impact. If the operational train speed exceeds the surface Rayleigh wave velocity in soil, deformations will be amplified, which may cause damages to railway tracks or set a demand for extensive maintenance influencing operation of a line. Therefore, it should be ensured that embankment and subsoil conditions meet the required capacity; and that maximum operation speed could be achieved without damages or limitations. It is commonly accepted that the Rayleigh wave velocity associated with generated vibration is identified as being the criterion to be achieved to mitigate the risk of amplifications of ground movements and deterioration of the track system. This is currently considered the state-of-the-art approach by most railway authorities. However, from existing projects in different countries, it seems that the ultimate criterion is dynamic displacements which should be considered along with Rayleigh wave velocity in order to limit maintenance efforts and to increase passenger comfort. This paper aims to discuss the criteria required for a proper design of HSR including a methodology, with showcasing examples of projects both in Germany and the Netherlands.

**Keywords** Railway vibrations · Cyclic-dynamic impact · High-speed rail

---

S. Hosseinzadeh (✉) · P. Schouten · G. Schulz  
Arcadis, 6814 DV Arnhem, The Netherlands  
e-mail: [saeed.hosseinzadeh@arcadis.com](mailto:saeed.hosseinzadeh@arcadis.com)

P. Schouten  
e-mail: [peter.schouten@arcadis.com](mailto:peter.schouten@arcadis.com)

G. Schulz  
e-mail: [gerhard.schulz@arcadis.com](mailto:gerhard.schulz@arcadis.com)

## 1 Introduction

Understanding of railway-induced vibration phenomenon has been of interest to geotechnical and railway engineering practitioners since 1970s [1]. Predicting railway-induced ground-borne vibrations is an inherently complex task involving numerous uncertainties, especially when performing such analysis over kilometres of railway track. Ground-borne vibrations are generated primarily due to the rail–wheel interaction which may also result in ground-borne noise in the buildings located in close proximity to the railway tracks [2] (theoretical background of ground-borne vibration and noise is provided in [3]). In general, one can distinguish two different categories related to vibrations generated by passing trains: firstly, the effect of vibration on the surrounding environment in which both the source of vibration and receiver (e.g., a building) are considered in the study (e.g., [4]), and secondly, the impact of train-induced vibrations on the track itself (theoretical background is contained in [5–8]). The latter is the focus of this paper.

Cyclic-dynamic impact is nowadays considered a priority when designing a new high-speed rail (HSR) or dealing with an increase in train speed or train frequency/track capacity, especially with tracks on earth structures. Railway traffic, especially a HSR, consists of cyclic-dynamic loads, which are transferred from the superstructure to the substructure and the underground. Cyclic-dynamic impact through every load cycle brings about both elastic and plastic deformations [9]. These deformations should meet the requirements regarding serviceability and stability. If the operational train speed exceeds the surface Rayleigh wave velocity in soil, critical train speed phenomenon would occur. This will amplify the deformations and cause damage to railway tracks, set a demand for additional maintenance influencing operation or even lead to the need to reduce the operation speed.

The governing factors for vibration response can be distinguished in two separate categories. These comprise first quasi-static excitation or moving load (e.g., axle load) by which the vibration response close to the track is governed, and second, dynamic excitation by which the vibration response at further distances is governed. An example of the latter is rail unevenness [10].

Dynamic stability of a railway line due to railway-induced vibrations is dependent upon several factors. These include, but are not limited to, ground conditions and soil parameters as studied, for instance, in [11–13], types, configuration and properties of the trains (although, less influential compared to soil parameters as, for instance, indicated in [14, 15]), speed of the trains, weight of trains (i.e., axle loads, e.g., [16]), type and number of the tracks (e.g., ballasted or ballast-less tracks), condition of the tracks (e.g., railway roughness) as, for instance, studied in [17], condition of the wheels or wheel singularities, e.g., out-of-roundness (e.g., [18]), presence of any structures in the vicinity of the track, for example, railway level crossing, turnout, etc., as well as their local defects (e.g., [19]).

Many studies including field tests (e.g., [9]), measurements under operation (e.g., [20, 21]), theoretical analyses (e.g., [22, 23]) as well as numerical modelling (e.g., FEM [24], BEM [25] and a combination of FEM–BEM [26]) have been conducted by

researchers in the past few decades for better understanding of the railway-induced vibrations. In [27], detailed and simplified ways of assessing railway critical speed are provided. At the beginning of the studies in the 1990s and early 2000s, field tests were developed [20]. Due to the availability of higher capacity computers and software development, numerical modelling has become more common since the last 10 years. The computer models are calibrated by the field tests and measurements during operation.

This paper aims to discuss the criteria required for a proper design of a HSR including a methodology, with showcasing examples of international projects.

## **2 Cyclic-Dynamic Impact Assessment**

In each project, the cyclic-dynamic impact assessment is evaluated, where one should first process the data for existing situation with respect to track configuration, ground conditions as well as available measurement data. In parallel, the types of trains, train configurations as well as number of trains for future situations (compared to those of existing situation/in case of speed and/or capacity increase of a track) are important and should also be collected. Afterwards, analytical/theoretical models and/or numerical models are employed in order to determine Rayleigh wave velocity as well as dynamic displacements along the project location. It is notable, however, that the first and foremost way of acquiring an insight into surface wave velocity is direct measurement, even though, it is not always possible in projects to do so, especially in the case of new lines. As such, the indirect approaches are applied through the use of theoretical and numerical models so as to determine Rayleigh wave velocity and dynamic displacements.

### ***2.1 Track Configuration***

Before commencing the cyclic-dynamic impact assessment, one should compile the relevant data with respect to both train configurations as well as superstructure layout. This implies that the type of embankment (e.g., ballasted track or slab track or concrete slab beneath ballast bed), sleeper and rail, train axle loads and speed and geometry, etc., should be clearly identified.

### ***2.2 Soil Parameters***

The relevant soil conditions and parameters including dynamic soil properties need to be known. For this purpose, archival research is carried out in the first place. For instance, in the Netherlands, the national database DINOloket [28] can be used to

retrieve site investigation data conducted in the project area. Additional CPTs/SPTs and boreholes along and within the location of a track are to be carried out to acquire an insight into the soil conditions and damping characteristics of the ground. In parallel, geohydrological characteristics including monitoring of groundwater table should also be collected.

The field and laboratory tests conducted for the project location need to consider the low strain levels with respect to the dynamic shear parameters depending on the respective stress level. For this purpose, soil-dynamic laboratory tests like resonant column tests are suitable. In the field, down-hole tests in boreholes, Seismic Cone Penetration Tests (S-CPTs) in combination with geophysical surface methods (e.g., seismic refraction tomography) are applied.

### ***2.3 Measurements***

The in situ vibration measurements are to be performed along the alignment of the railway track both in the case of an existing line that is upgraded for higher speeds and a new railway line. This helps practitioners determine the ground-borne vibration levels as well as damping characteristics of the underground along railway track. For this purpose, a number of measurements along the railway track are carried out. The number of profiles to be taken depends mainly on the variation in geotechnical conditions, but may also be affected by the vertical alignment of the track. After having collected all the measurement data, a filtering process is performed in which the types of trains are determined in order to provide the input data for a vibration prediction model. The model is used for predicting maximum vibration speed and dynamic displacements by railway traffic.

### ***2.4 Data Analysis and Compilation***

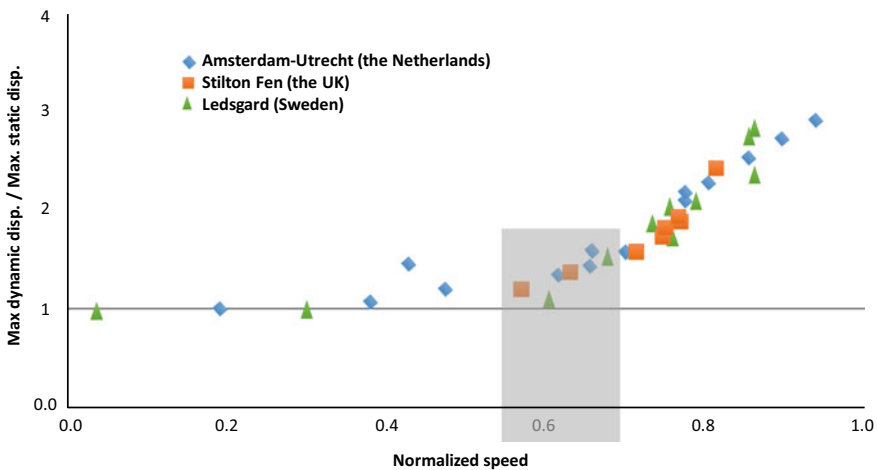
The above-mentioned compiled data should be analysed and used as an input for the model for assessing railway-induced vibration aspects. Once the initial processing is complete, the model will be built up for predicting vibration at different time and locations. In some projects, numerical modelling is used in the first place to predict vibration levels; whereas, it can also be used as a verification tool for the results of analytical models. Measurements are also used to validate the results of numerical modelling.

### 2.5 Design Procedure

It is commonly accepted that the Rayleigh wave velocity associated with generated vibration is identified as being the criterion to be achieved to mitigate the risk of amplifications of ground movements and deterioration of the track system. As shown in Fig. 1, large dynamic amplification in the response of a railway track occurs if the resonance conditions of the system are reached. Resonance appears when the train speed is equal to the phase velocity of the excited waves. From field measurements in the Netherlands, Sweden and the UK (Fig. 1), it can be seen that the closer the train speed is to the Rayleigh wave velocity, the higher the amplification will be. Therefore, the train speed should be limited to around 0.6–0.7 times the Rayleigh wave velocity, which corresponds to a safety factor of around 1.7–1.4. This is called “critical train speed”.

Due to different country-specific approaches and conditions, the Railway Authorities in different countries apply different methodologies. For instance, the German Railways require the evidence of dynamic stability for projects where slab (non-ballasted) track is applied and for projects with ballasted track and a design speed over 200 km/h. The evidence of dynamic stability includes not only the safety margin from the resonance case but also the limitation of dynamic displacements (Fig. 3). The design procedure recommended by German guidelines [30] is shown in Fig. 2.

As shown in Fig. 2, dynamic soil parameters are determined through site investigation on the project site. Determination of train types also includes the configuration of the trains as well as their speeds. In principal, the superstructure, substructure and subsoil can be completely modelled through 3D analyses. However, such modelling is very time consuming, and hence, to simplify the calculations, two different models



**Fig. 1** Normalized train speed versus amplification of displacements (extract and adapted from [29]). Normalized speed is defined as the ratio of train velocity to Rayleigh wave velocity



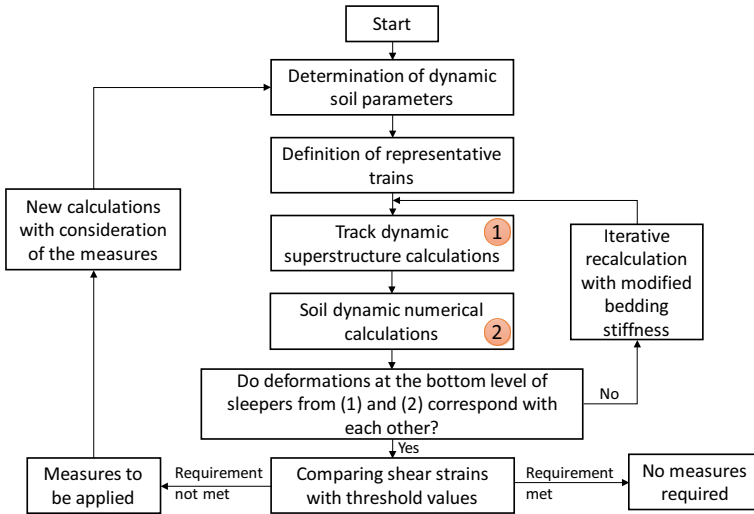


Fig. 2 Design procedure recommended by German guidelines [30]

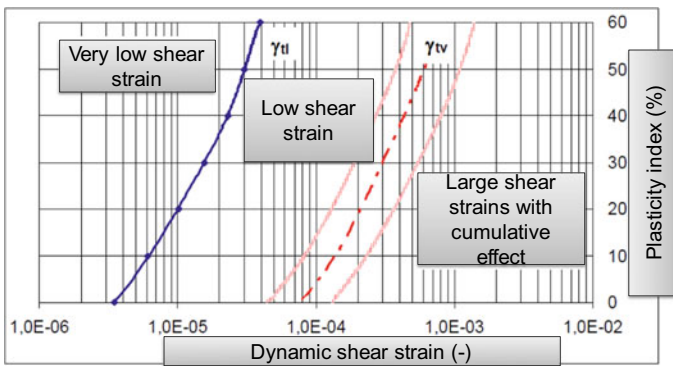


Fig. 3 Threshold values for dynamic displacements based on German guidelines [30]

are recommended. First, track dynamic calculations related to the assumed stiffness of the superstructure including rail and sleeper. Second, numerical calculations related to soil dynamics are carried out with the aid of numerical modelling (e.g., FEM). In case the resulting deformations from calculations related to track dynamics at the bottom of sleepers correspond to those of soil dynamics (iterative process), the generated shear strains will be compared with the allowable shear strain values shown in Fig. 3. The allowable shear strains are below the threshold values displayed on the left-hand side areas separated by a red-dashed line in Fig. 3. In case the calculated shear strains are below the threshold values, dynamic stability is achieved. In

the case of exceeding the allowable values, progressive plastic deformations would occur where abatement measures will be required.

In the Netherlands, a similar approach is applied in which dynamic displacements are assessed through a more detailed analysis in case the train speed exceeds the critical train speed. The following are the key points of design procedure in Dutch practice according to OVS [31]:

- Defining shear wave velocity/Rayleigh wave velocity. In the Netherlands, direct measurements are firstly recommended where the surface wave velocity is directly determined. Since this is not always a feasible option, different methods are used to determine the shear wave velocity from seismic CPTs as follows:
  - Method A: considering the lowest shear wave velocity of the soil profile (up to 10 m depth, although, soft layers with low shear wave velocity mostly appear in top soil layers).
  - Method B: calculation of the shear wave velocity at the surface based on soil profile and soil characteristics.
  - Method C: considering the average shear wave velocity of the top 5–10 m of the soil profile. This method is not included in the standard but is applied as a modification of Method A.
- Performing seismic CPTs and determining dynamic shear modulus from which shear wave velocity profile could be created when a direct measurement is not possible. The experience has proven that these seismic CPTs should be performed at the track location, as conditions next to the track may be different.
- Comparison between the desired operational train speed and critical train speed.
- Defining dynamic stiffness of all layers and perform numerical analysis so as to give an insight into dynamic displacements (in case the critical train speed is exceeded).
- Numerical calculations and defining the dynamic displacements generated through a vertical profile of the ground. In the case of exceeding 2.5 mm of dynamic displacements according to OVS [31], an abatement measure should be considered.

### 3 Case Studies

In this section, some of the projects in which Arcadis has been involved are presented and discussed. Although the names of the projects are not mentioned in view of confidentiality, nevertheless, the project descriptions including ground conditions are provided. The examples selected are from The Netherlands and Germany.

In the Netherlands, the underground conditions are mainly sand layers with different compactness and soft (organic) clay and peat layers. The groundwater table is mainly high (close to the surface). The area is mostly flat, and therefore, railway tracks are at grade or on low embankments. The railway network is very dense, and

the train intensity is high. Also because of frequent stops, the passenger trains run with less than 140 km/h to maximum 200 km/h; whereas, in Germany, the topography and geology are variable. The alignment of high-speed railway tracks requires a frequent transition from tunnels to viaducts to earth structures. The railway tracks are located at grade on earth structures, on embankments (up to 10–20 m high) and in cuts. The operation speed of the high-speed trains is 250–300 km/h. Most of the high-speed lines are also used by freight trains.

### 3.1 Case Study 1 in the Netherlands

In this project, the superstructure of an existing track had to be renovated without substantial earthwork, such that the railway track system could accommodate an increase in the operational train speed from 90 up to 130 km/h (36.1 m/s).

The ground condition at the location of project consists mostly of sandy layers ranging from loosely packed to medium and more densely packed sands. At some locations of the project, a very thin layer of loam to silty sandy clay is locally encountered. The depth profile identified by a seismic CPT is shown in Table 1. In this project, Method A was applied to derive the shear wave velocity.

This indicates that the first 1.0 m below the ground surface does not fully (but almost) meet the requirement concerning the design train speed of 130 km/h (36.1 m/s). However, it is plausible that the ground conditions meet the requirement with respect to the critical train speed as the seismic CPT was carried out in the vicinity of the track location and not in the track. Due to train passages, the upper metre of the sand layer beneath the existing railway track has been compacted. Based on other CPTs performed on the embankment, the fulfilment of the criteria could be proven.

**Table 1** Depth profile used in assessing case study 1

Depth below ground surface (m)	Shear wave velocity (m/s)	Dynamic shear modulus (MPa)	Rayleigh wave velocity (m/s)	Critical train speed (m/s)	Desired operational train speed (m/s)	Critical train speed versus operational speed (-)
1.0	66	7.9	59.4	35.6	36.1	Not OK
2.0	108	20.1	97.2	58.3	36.1	OK
3.0	148	41.6	133.2	79.9	36.1	OK
4.0	145	39.2	130.5	78.3	36.1	OK
5.0	164	51.4	147.6	88.6	36.1	OK
6.0	165	49.7	146.7	88.0	36.1	OK
6.5	215	84.4	193.5	116.1	36.1	OK

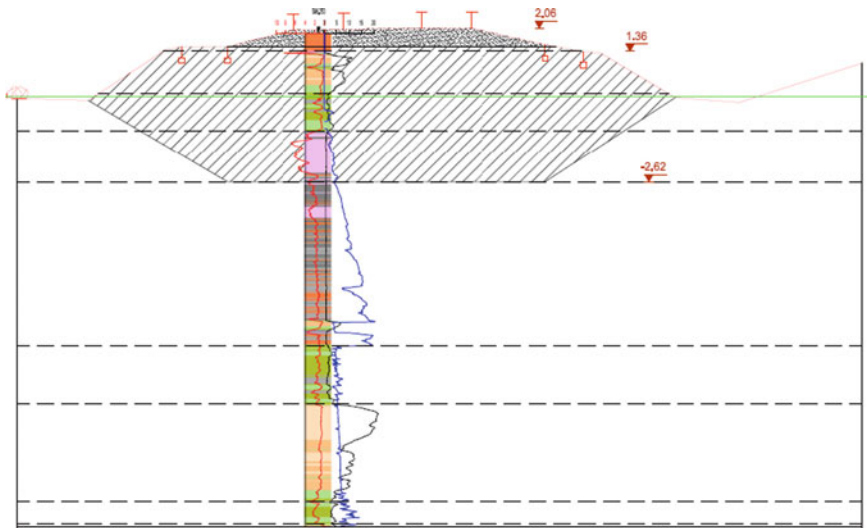
### 3.2 Case Study 2 in the Netherlands

In this project, cyclic-dynamic impact along with stability of an existing line was to be checked for an envisaged increase of train speeds and in the case of not meeting requirements set by standards, abatement measures were to be proposed. The two most critical sections along the railway track of this project are shown below (Table 2). In this section, Method C was applied to derive the characteristic shear wave velocity.

Ground conditions at these locations include mostly loose to medium sand layers with an intermediate peat layer. At these locations, the required operational speed is 140 km/h (equivalent to 38.9 m/s). Therewith this is higher than the critical train speed. Different abatement measures were suggested to be applied in order to fulfil the requirements of dynamic stability. One of them was ground improvement of the

**Table 2** Two most critical sections—used in assessing case study 2

Section	Shear wave velocity (m/s) of the top 5 m of ground stratum	Rayleigh wave velocity (m/s)	Critical train speed (m/s)	Required operational speed (km/h)	Required operational speed (m/s)	Design speed versus operational speed (–)
1	72	64.8	38.9	140	38.9	Not OK
2	61	54.9	32.9	140	38.9	Not OK



**Fig. 4** Ground improvement as an abatement measure

surface track (subgrade) and possibly the underground (Fig. 4). This includes nearly 4 m of ground improvement over a length of approximately 1.5 km.

Further measurements will be applied in this case in order to optimize the abatement measures. More applicable abatement measures to fulfil the requirements of cyclic-dynamic stability are provided in [32] and also mentioned in other case study.

### 3.3 Case Study 3 in Germany

In Germany, intensive studies about cyclic-dynamic impact of railways began in the 1990s, which were also triggered by the decision of Deutsche Bahn to apply slab (non-ballasted) track for the new HSR. The focus of Deutsche Bahn has been to reduce maintenance efforts. Due to the limited knowledge and experience in the 1990s about the cyclic-dynamic impact of railways, Arcadis developed an in situ testing device [9, 20] (see Fig. 5) This testing device can simulate the cyclic-dynamic impact of railways realistically in 1:1 scale in situ, as the comparison of test results and measurements under operation in Fig. 5 shows.

Based on these researches and studies, a methodology has been developed (see above) and published in [30]. This approach is basically a combination of dynamic calculation of the superstructure and numerical soil-dynamic calculation. Dynamic stability is achieved, when the calculated shear strains are below the threshold value (Fig. 3). Figure 6 shows an example related to the results of numerical analysis based on the methodology described in [30]. The method has been validated based on long-term measurements (10 years) along tracks [21]. For cases where shear strain criteria

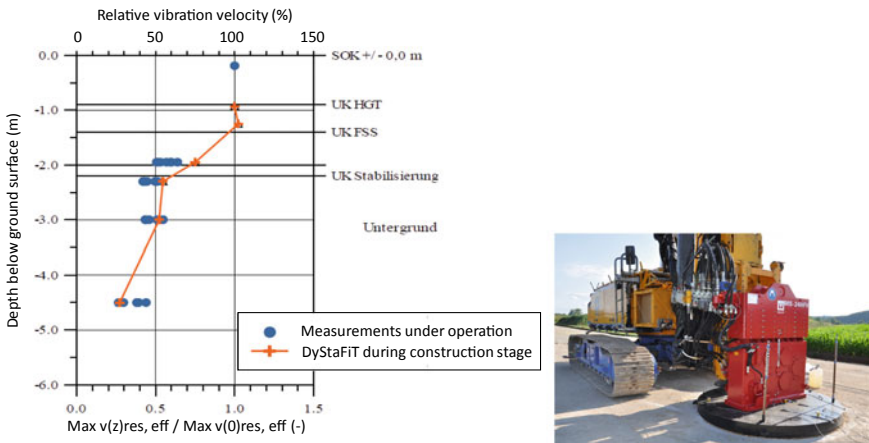


Fig. 5 Left, comparison of test results with the testing device DyStaFiT and measurements under operation [20]; right, the testing device DyStaFiT [20]

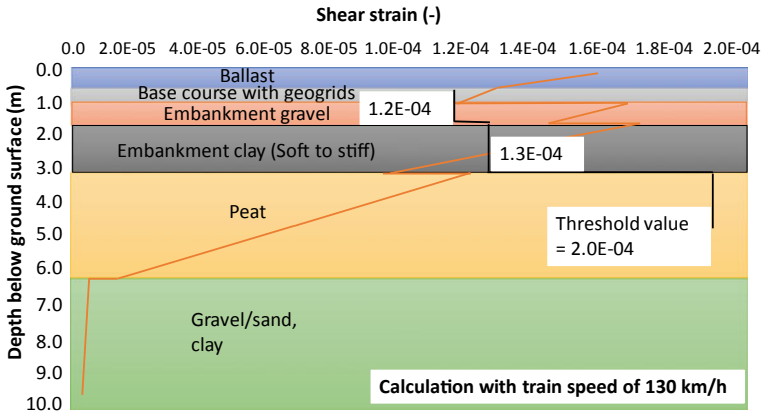


Fig. 6 Numerical analysis results of shear strains and comparison with thresholds [21]

are met, there is a limited maintenance. This method allows for an economical design with reduced maintenance by considering train-track-ground conditions realistically.

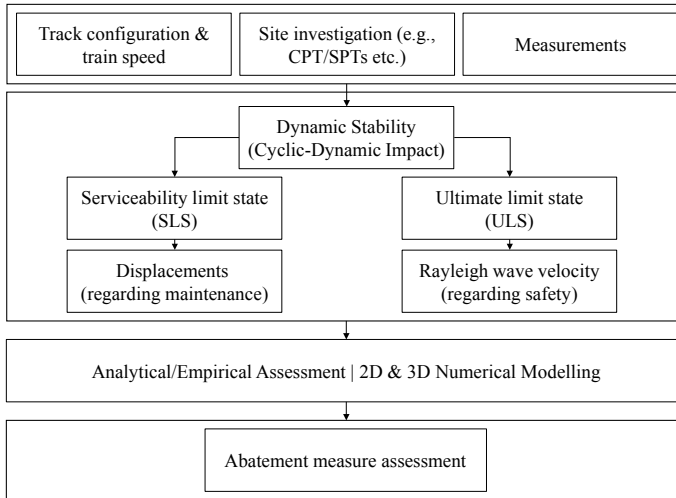
In case the requirements are not met, one can think of different solutions including, but not limited to, abatement measures at the location of vibration source (e.g., the use of slab track instead of conventional ballasted track in order to reduce the cyclic-dynamic impact) and the use of stone columns or dynamic compaction.

### 4 Final Remarks

The following flowchart (see Fig. 7) is a methodology which can be adopted for international projects. In fact, for commencing with a dynamic stability project, one should study three aspects first: These include track configuration, site investigations and measurements. Regardless of the geographical locations and national directives, one can consider two requirements simultaneously (i.e., dynamic displacements as well as Rayleigh wave velocity).

In the Netherlands, first Rayleigh wave velocity is assessed with the use of in situ testing (either through direct measurements of the waves or performing seismic CPTs) in order to determine the shear wave velocity. Afterwards, the critical railway velocity is assumed as 90% of the shear wave velocity (i.e., Rayleigh wave velocity) and a factor of safety for stability of the railway track is applied which is 1.67 (critical railway velocity divided by 0.6).

In this paper, the methodologies used in both the Netherlands and Germany were discussed. For instance, in the Netherlands the number of railway lines with design speeds higher than 200 km/h is limited compared to those in Germany. This explains the more detailed regulations and demands for analysis in Germany when designing a high-speed line with speed higher than 200 km/h. Moreover, different case studies



**Fig. 7** Methodology applied for assessment of cyclic-dynamic impact

with respect to the cyclic-dynamic assessment were shown and two different criteria, namely Rayleigh wave velocity and dynamic displacements were considered. It is commonly accepted that the Rayleigh wave velocity associated with generated vibrations is identified as being the criterion to be achieved to mitigate the risk of amplifications of ground movements and deterioration of the track system. This is currently considered the state-of-the-art approach by most railway authorities. However, in order to further increase safety and passenger comfort and reduce maintenance efforts, dynamic displacements should also be used as the second criterion so as to assess cyclic-dynamic impact.

## References

1. Dawn TM, Stanworth CG (1979) Ground vibrations from passing trains. *J sound Vib* 66(3):355–362
2. Connolly DP, Marecki GP, Kouroussis G, Thalassinakis I, Woodward PK (2016) The growth of railway ground vibration problems—a review. *Sci Total Environ* 568:1276–1282
3. Thompson D (2008) Railway noise and vibration. Mechanisms, modelling and means of control. Elsevier Ltd., Oxford
4. Ma M, Liu W, Qian C, Deng G, Li Y (2016) Study of the train-induced vibration impact on a historic Bell Tower above two spatially overlapping metro lines. *Soil Dyn and Earthq Eng* 81:58–74
5. Krylov VV (1995) Generation of ground vibrations by superfast trains. *Appl Acoust* 44(2):149–164
6. Krylov VV (2017) Focusing of ground vibrations generated by high-speed trains travelling at trans-Rayleigh speeds. *Soil Dyn and Earthq Eng* 100:389–395
7. Madhus C, Kaynia AM (2000) High-speed railway lines on soft ground: dynamic behaviour at critical train speed. *J Sound Vib* 231(3):689–701

8. Mezher SB, Connolly DP, Woodward PK, Laghrouche O, Pombo J, Costa PA (2016) Railway critical velocity—analytical prediction and analysis. *Transp Geotech* 6:84–96. <https://doi.org/10.1016/j.trgeo.2015.09.002>
9. Neidhart T, Schulz G (2011) Dynamic stability of railway tracks—DyStaFiT, an innovation in testing. In: *Proceedings from Georail*, pp 335–346
10. Connolly DP, Costa PA, Kouroussis G, Galvin P, Woodward PK, Laghrouche O (2015) Large scale international testing of railway ground vibrations across Europe. *Soil Dyn and Earthq Eng* 71:1–12
11. Kouroussis G, Conti C, Verlinden O (2013) Investigating the influence of soil properties on railway traffic vibration using a numerical model. *Veh Syst Dyn* 51:421–442
12. Gupta S, Stanus Y, Lombaert G, Degrande G (2009) Influence of tunnel and soil parameters on vibrations from underground railways. *J Sound Vib* 327:70–91
13. Auersch L (2008) The influence of the soil on track dynamics and ground-borne vibration. In: *Proceedings noise and vibration mitigation for rail transportation systems*, Springer, Berlin, Heidelberg, pp 122–128
14. Colaço A, Costa PA, Connolly DP (2016) The influence of train properties on railway ground vibrations. *Struct Infrastruct Eng* 12:517–534
15. Kouroussis G, Connolly DP, Verlinden O (2014) Railway-induced ground vibrations—a review of vehicle effects. *Int J Rail Transp* 2:69–110
16. Lombaert G, Degrande G (2009) Ground-borne vibration due to static and dynamic axle loads of intercity and high-speed trains. *J Sound Vib* 319:1036–1066
17. Hung HH, Chen GH, Yang YB (2013) Effect of railway roughness on soil vibrations due to moving trains by 2.5 D finite/infinite element approach. *Eng Struct.* (57):254–266
18. Kouroussis G, Connolly DP, Alexandrou G, Vogiatzis K (2015) Railway ground vibrations induced by wheel and rail singular defects. *Veh Syst Dyn* 53:1500–1519
19. Kouroussis G, Mouzakis HP, Vogiatzis KE (2017) Structural impact response for assessing railway vibration induced on buildings. *Mech Ind* (18):803
20. Neidhart T, Fischer R, Hotz C, Johmann S (2002) Optimization of the substructure of slab track—verifications under operation by measurements (In German). *Vortrag auf der Erd-und Grundbautagung im Rahmen der INNOTRANS*
21. Wegener D, Fischer R (2016) Dynamic stability of railway tracks on soft soils. *El-Sonderheft Geotechnik*.
22. Krylov V, Ferguson C (1994) Calculation of low-frequency ground vibrations from railway trains. *Appl Acoust* 42:199–213
23. Sheng X, Jones CJC, Thompson DJ (2003) A comparison of a theoretical model for quasi-statically and dynamically induced environmental vibration from trains with measurements. *J Sound Vib* 267:621–635
24. Connolly D, Giannopoulos A, Forde MC (2013) Numerical modelling of ground borne vibrations from high speed rail lines on embankments. *Soil Dyn and Earthq Eng* 46:13–19
25. Galvín P, Romero A, Domínguez J (2010) Fully three-dimensional analysis of high-speed train-track-soil-structure dynamic interaction. *J Sound Vib* 329:5147–5163
26. Yang YB, Hung HH, Chang DW (2003) Train-induced wave propagation in layered soils using finite/infinite element simulation. *Soil Dyn Earthq Eng* 23:263–278
27. Costa PA, Colaço A, Calçada R, Cardoso AS (2015) Critical speed of railway tracks. Detailed and simplified approaches. *Transp Geotech* (2):30–46
28. DINO Homepage, <https://www.dinoloket.nl>. Last accessed 2019/10/23.
29. Madshus C, Lacasse S, Kaynia A, Hårvik L (2004) Geodynamic challenges in high speed railway projects. In: *Geotechnical engineering for transportation projects*, pp 192–215
30. DB Netz AG (2018) *Ballasted railway tracks on soft soils—analysis of dynamic stability—computational method*, 3rd edn (in German).
31. ProRail (2016): *Instruction for design (OVS) for pavement and geotechnics*. OVS00056-7.1 (04) (in Dutch)
32. Schulz G (2011) Advanced geotechnical solutions for modern high speed railway lines. In: *Proceedings from Georail*, pp 143–153



# Field Behavior of GRS Bridge Approach Under Large Subsoil Settlement: A Case Study



Chunhai Wang  and Huabei Liu 

**Abstract** Geosynthetic reinforced soil (GRS) structures with excellent engineering performance are extensively utilized throughout the world in embankment engineering. GRS structures are commonly not utilized for applications where large settlements are anticipated. In this study, a GRS bridge approach reinforced with uniaxial geogrid and backfilled with graded crushed stones was instrumented during and post-construction for almost one year. Owing to the high construction height and the compressibility of the foundation soil, the GRS bridge approach has settled more than 0.3 m and continues to settle. That unexpected settlement induced a series of complicated response mechanisms related to the behavior of the reinforcement and vertical earth pressure at the base of the wall. Overall, even for such large settlements, the GRS bridge approach still performed adequately.

**Keywords** GRS bridge approach · Field instrumentation · Settlement · Working behavior

## 1 Introduction

For remediating the differential settlement between bridge and embankment, the GRS structure is extensively employed as the transitional structure [1–5], with the advantages of low engineering cost, easy implementation, fast construction, and environment-friendliness. To better understand the engineering behavior of the transitional structure, full-scale tests with field instrumentation and numerical analyses were conducted [6–11].

In this study, an 8 m high GRS bridge approach had a settlement that exceeded 0.3 m during and post-construction. It was instrumented for measuring settlement, reinforcement strain, vertical earth pressure, and monitored for almost one year. The objective is to reveal the mechanisms that took place during the deformation behavior of that transitional structure.

---

C. Wang · H. Liu (✉)

School of Civil Engineering and Mechanics, Huazhong University of Science and Technology, Wuhan, China

e-mail: [hbliu@hust.edu.cn](mailto:hbliu@hust.edu.cn)

## 2 Field Overview

The GRS bridge approach was a part of one urban expressway embankment, which was constructed beside the Yangtze River in one city in the center of China. For the purpose of adapting non-uniform settlement and also saving engineering cost, the GRS wall structure with vertical facing was designed to some embankment sections. Between the bridge and embankment, the GRS bridge approach was designed with a quite height of 8 m. Figure 1 shows the overview of the GRS bridge approach during the service period.

The GRS wall consisted of cement-soil mixing pile, base cushion reinforced with triaxial geogrid, strip foundation, pre-casted concrete block facing, uniaxial geogrid, drainage layer, backfill soil, and then pavement structure. Before the construction of the GRS wall, the ground was reinforced by cement-soil bidirectional deep mixing pile to satisfy different sections with different strength standards. A 0.5 m thickness lime-treated soil reinforced with triaxial polypropylene geogrid was assigned under the strip foundation. The foundation adopted a C25 strip concrete foundation. The concrete block facing with the dimensions of 400 mm × 305 mm × 150 mm (length × width × height) connected to adjacent layers blocks and uniaxial geogrid by two nylon anchor rods. The mechanical properties of uniaxial geogrid made of high-density polyethylene (HDPE), provided by the manufacturer according to

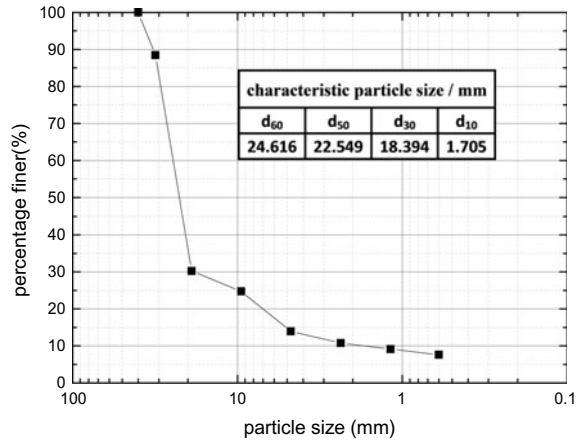


**Fig. 1** Overview of the GRS bridge approach during the service period

**Table 1** Properties of uniaxial geogrid provided by the manufacturer

Parameters	Value
Ultimate tensile strength (kN/m)	70.0
Tensile strength at 5% strain (kN/m)	31.0
Maximum allowable strength after 120 years (kN/m)	25.6

**Fig. 2** Size distribution of the backfill graded crushed stones



ASTM standards, are shown in Table 1. Behind the block facing, a 0.3 m thickness crushed stones were set for drainage and filtration. Considering the drainage and safety requirement, graded crushed stones were used as backfill soil within the bridge approach range. Figure 2 shows a representative size distribution of the backfill graded crushed stones.

The backfill soil of the GRS bridge approach is graded crushed stones with weight of 17.35 kN/m<sup>3</sup>. By simple shear test, the friction angle is  $\varphi = 41^\circ$ , and the cohesion is  $c = 31$  kPa. And the reference stiffness modulus at 50% strength is  $E_{50}^{ref} = 9847.9$  kPa with the corresponding reference confining pressure  $p^{ref} = 100$  kPa.

The GRS bridge approach is a complex GRS structure as shown in Fig. 3, in which the GRS wall was combined with the bridge pier. The reinforcements came from both parallel and perpendicular to the road direction as shown in Figs. 3 and 4. The corner adjacent reinforcement layers were separated by backfill graded crushed stones for avoiding reinforcement overlap during construction. The bridge approach reinforced zone filled with graded crushed stones is 8 m in the height, 8 m in the width, and approximately 34 m in the length.

According to the engineering geologic investigation report, the base condition is quite complex as shown in Fig. 3 and Table 2. The cement-soil bidirectional deep mixing pile was implemented to improve the strength of the weak subsoil layers to not lower than 200 kPa. The base condition as shown in Fig. 3 was complex even after the ground treatment the weak substratum layer still existed.

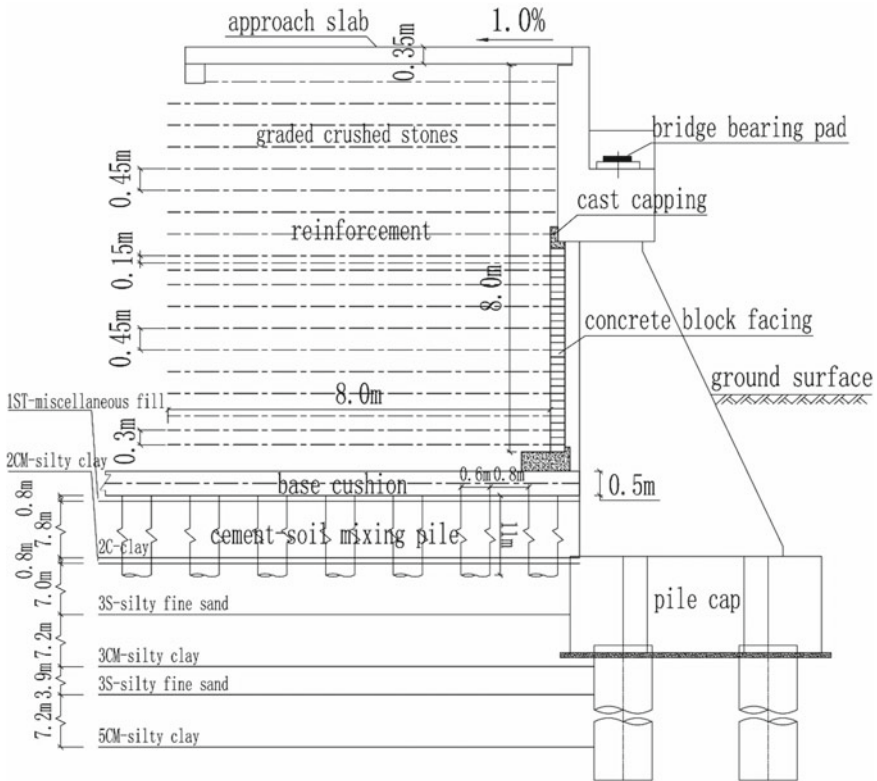


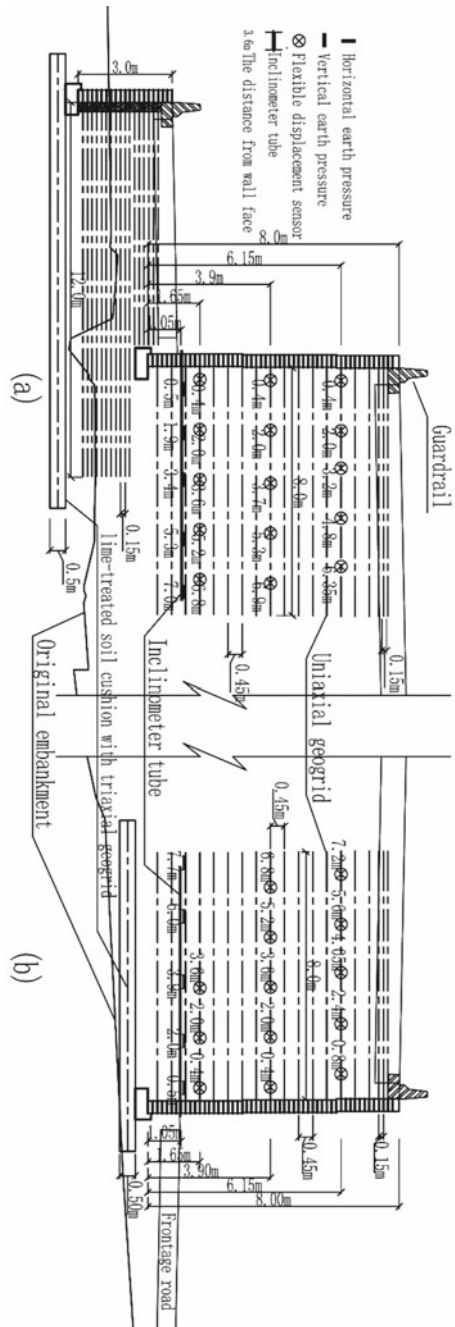
Fig. 3 Illustration of cross-section parallel to the road direction of the GRS bridge approach

### 3 Instrumentation

The instrumented cross-sections were both sides of the GRS bridge approach as shown in Fig. 4. For the convenience of description, the left side of the GRS bridge approach from the embankment to bridge direction was arranged as the Section-A (Fig. 4a). And the other side was arranged as the Section-B (Fig. 4b). The upper tiered wall of Section-A and Section-B was symmetrical, filled with graded crushed stones, combined with pavement structure to 8 m high, and reinforced with the reinforcement length of 8 m, the vertical spacing of 0.45 m.

The monitoring of both sections included vertical earth pressure at the base of the wall, reinforcement strains for three layers by flexible displacement sensor, and settlement along the reinforced zone from the base of the wall by inclinometer tube (Fig. 4). The vibrating-wire earth pressure cell with capacity of 300 kPa and accuracy of 1 kPa was adopted; the flexible displacement sensor based on inductance frequency modulation design has the capacity of 20 mm and the accuracy of 0.01 mm; settlement measurement consists of two parts, one from relative settlement of inclinometer tube

**Fig. 4** Illustration of instrumented cross-sections: **a** Section-A and **b** Section-B



**Table 2** Properties of base by engineering geologic investigation report

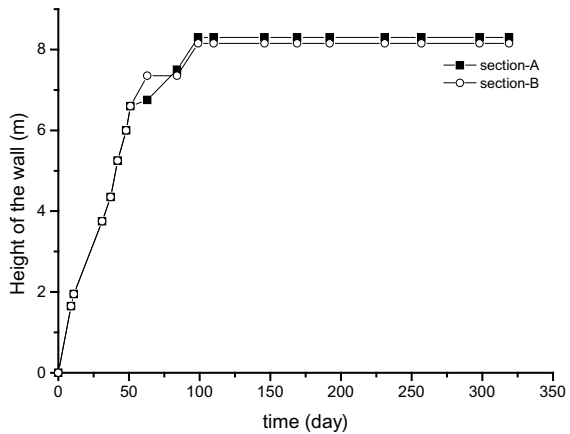
Soil layer no	Soil	Physical properties				Mechanical properties		
		Moisture content	Dry density	Soil particles	Coeff. of permeability	Modulus of compressibility	Consolidated undrained direct shear tests	
		$\omega$	$\rho_d$	$G_s$	K	$E_{s,1-2}$	$c$	$\phi$
		%	t/m <sup>3</sup>	—	m/d	MPa	kPa	°
2C	clay	35.03	1.42	2.73	0.00432	4.43	28.31	15.10
2CM	silty clay	32.91	1.41	2.71	0.00147	4.55	27.11	16.53
3S	silty fine sand	19.90	1.58	2.68	0.86400	13.7	15.00	27.50
3CM	silty clay	33.03	1.41	2.71	0.00432	3.86	21.35	16.74
5CM	silty clay	34.92	1.37	2.70	0.00432	3.44	20.70	17.00

and another from absolute settlement of inclinometer tube porthole compared with reference point by total station. The accuracy is 0.01 mm for the inclinometer and 2 + 2 ppm for the total station.

The construction progress was very fast, the main portion finished by almost two months as shown in Fig. 5. The settlement of both sections during construction was unexpectedly large, which increased a few layers of the block facing compared with the original design, two for Section-A and one for Section-B.

Single drum vibratory roller was used for central backfill compaction, which implemented a static linear load for 51.6 kN/m and centrifugal force for 374/290 kN (high/low amplitude). Within 1 m range from the facing, the backfill was compacted

**Fig. 5** Illustration of construction progress



by operated plate compactor with centrifugal force 15 kN. Each 0.45 m layer was divided into two layers for compaction while construction.

### 4 Analysis of Test Results

Different sensors with different installation positions would have dispersive records. For the convenience of explanation, unified recording time was adopted from the beginning of construction.

#### 4.1 Settlement

In this study, the settlements almost stabilized after 320 days as shown in Fig. 6. With that large settlement appearance, the contractor decided to grout the gap below the approach slab from road surface approximately in day 180.

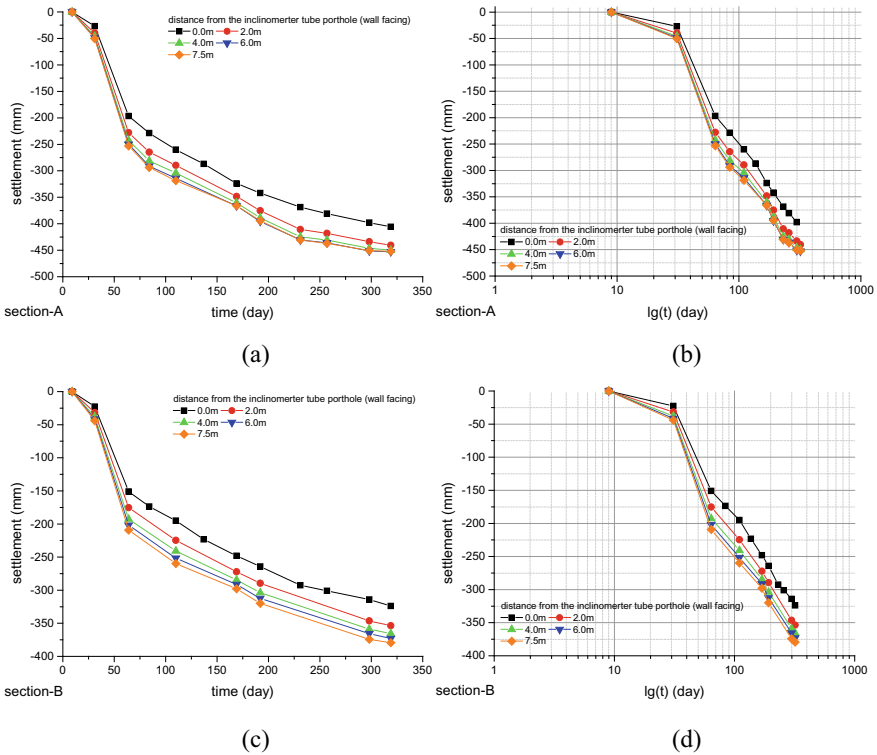


Fig. 6 Settlements of both sections: a, b for Section-A and c, d for Section-B

The settlement of inclinometer tube porthole was approximate  $-196/-151$  mm (Section-A/Section-B) during the main portion of the wall complete in day 60. Meanwhile, the differential settlement appeared between the facing and inside of the wall. Contributed by the strip foundation, the settlement gradually increased with the distance from the wall facing. Affected by the lack of lime-treated cushion and the compressibility of the lower-tiered wall, the settlement of inclinometer tube porthole for Section-A was  $-81$  mm larger than Section-B in day 320.

That large settlement came from three parts. The first one was the complex base situation with high compressibility. According to the engineering geologic investigation report, only silty fine sand layer 3S had a relatively high stiffness. Ground treatment only improved the strength but not enough for stiffness compared with the thickness of weak substratum layers. There was a possibility that the base of embankment could be Yangtze River downstream alluvial soil due to the river change in hundreds of years. The second one was the fast construction speed with a high overlay load. The GRS bridge approach was particularly high with 8 m and upload in a short period of 60 days. The third one was the unreasonable construction process. The construction of the GRS bridge approach began in the late stages of the whole embankment engineering. Because of the mistake of construction arrangement, the ballast preloading technique was adapted for the whole road except for the GRS bridge approach reinforced range. There was no effective measure to reduce the post-settlement for such a sensitive structure.

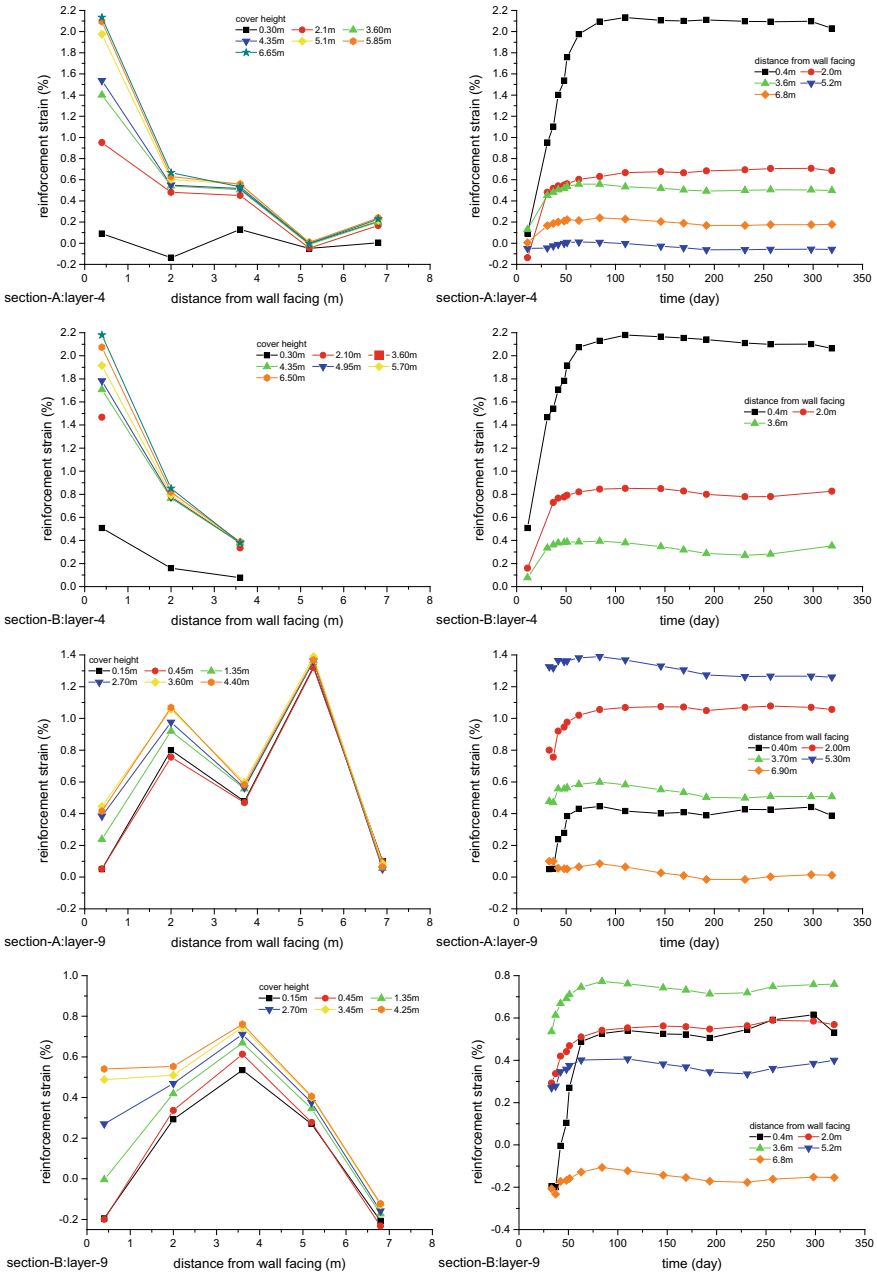
## 4.2 Reinforcement Deformation

The instrumented reinforcement layers and corresponding height were layer-4, layer-9, layer-14 and 1.65 m, 3.90 m, 6.15 m, respectively. The reinforcement deformations were measured by the inductive flexible displacement sensor, which satisfied deformation compatibility with the average tensile deformation between adjacent transverse ribs [12–14].

Figure 7 shows the reinforcement strains during and post-construction. The reinforcement strains were relatively stable after construction completion. The strains of the reinforcement were mainly induced by both construction and settlement. The construction induced reinforcement strains came from both above stone gravity loading and compaction. That compaction induced strains reduced gradually after engineering complete until the contractor grouted from the road surface in day 180. After that, the strains got a little bigger, especially for the higher layer-14.

With the increase of the construction height, the non-uniform settlement between facing and inside of the wall magnified the reinforcement strains close to the wall facing as shown in Fig. 7a. By the result in certain backfill-arching, the distribution of stain along the reinforcement was not uniform.





**Fig. 7** Reinforcement strains of both sections: **a** strains distribution during construction **b** strains during and post-construction

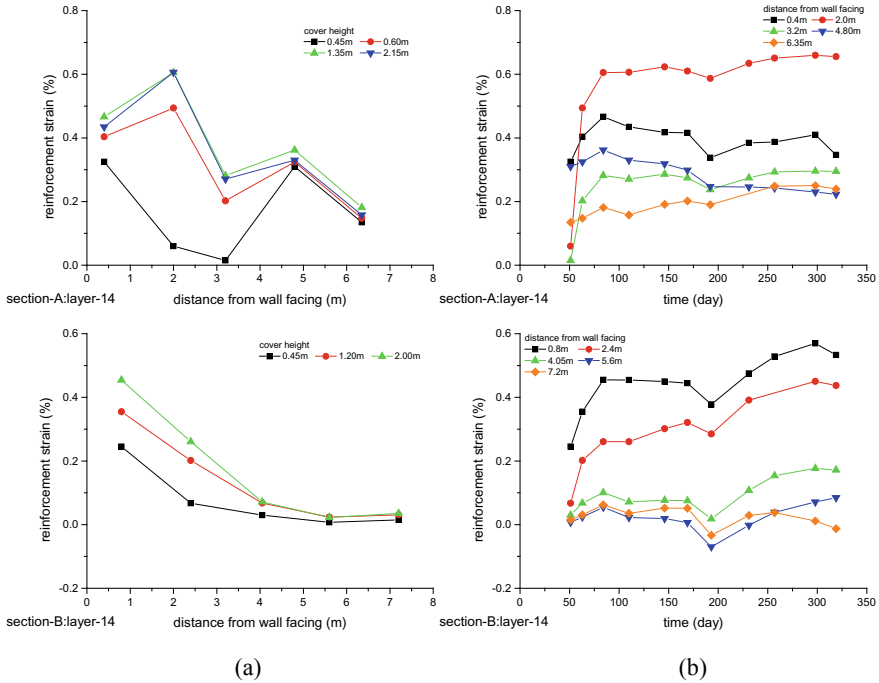


Fig. 7 (continued)

### 4.3 Vertical Earth Pressure at the Base

Unfortunately, four vertical earth pressure sensors of Section-A at the base lost their function, which decreased immediately to almost zero after the compaction of the upper layer probably due to machine damage.

Although the reinforcement could assist the vertical earth pressure evenly distributed, the large settlement caused some unusual mechanics response as shown in Fig. 8. The large settlement, increasing gradually with the distance from the wall facing, inducing the reinforcement zone of the wall deflected backward. However, the vertical earth pressure was not increased with the distance as expected, probably due to the softness of the subsoil. The vertical earth pressure close to the facing was larger than inside one from Section-B. The non-uniform settlement might lead slightly unload at the base rear of the reinforcement zone. And certain backfill-arching improved the pressure in 6 m.

Figure 8b, d shows the vertical earth pressure evolution with days. The expressway started service on day 277, and the traffic load was assumed with 10 kPa. The vertical earth pressure at the base of the wall gradually raised with construction progress, after that was a decline with the compaction effect disappear and a little improvement after the road started service. Compared with the estimated load, the measured results showed good consistency.

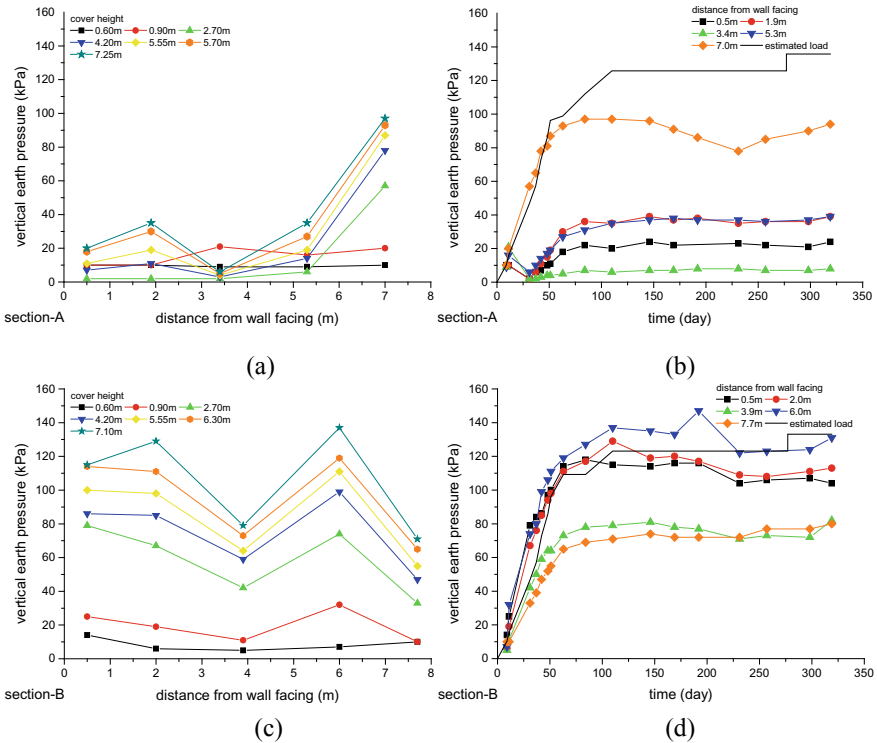


Fig. 8 Vertical earth pressure of both sections: a, b for Section-A and c, d for Section-B

### 5 Conclusion

A GRS bridge approach backfill with graded crushed stones and reinforced with uniaxial geogrid was instrumented and monitored for almost one year. The settlement, reinforcement strains, and vertical earth pressure were measured during and post-construction. The measured responses were analyzed, and the behavior mechanism related to each aspect was discussed. From this case study, the following conclusions were obtained:

1. The high compressibility of the subsoil and unreasonable construction process led to the large settlement of the GRS bridge approach.
2. Reinforcement strain was generated mainly by gravity loading and compaction, after that the strain remains relatively stable. Moreover, the increased strain of reinforcement by large settlements was only close to the wall facing range in this study.
3. The large settlement decreased the vertical earth pressure at the base beneath the wall.

4. Under a large settlement of over 0.3 m, the GRS bridge approach still performed satisfactorily.

## References

1. Wahls HE (1990) Design and construction of bridge approaches. Transportation Research Board
2. White D, Sritharan S, Suleiman M, Mekawy M, Chetlur S (2005) Identification of the best practices for design, construction, and repair of bridge approaches. Department of Transportation, Iowa
3. Berg RR, Christopher BR, Samtani NC (2009) Design of mechanically stabilized earth walls and reinforced soil slopes. No. FHWA-NHI-10-024 Vol I and NHI-10-025 Vol II. Federal Highway Administration, Washington, DC
4. Adams M, Nicks J, Stabile T, Wu J, Schlatter W, Hartmann J (2012) Geosynthetic reinforced soil integrated bridge system, interim implementation guide. Federal Highway Administration
5. Tatsuoka F, Tateyama M, Koseki J, Yonezawa T (2014) Geosynthetic-reinforced soil structures for railways in Japan. *Transp Infrastruct Geotechnol* 1(1):3–53
6. Abu-Hejleh N, Wang T, Zornberg JG (2000) Performance of geosynthetic-reinforced walls supporting bridge and approaching roadway structures. *Advances in transportation and geoenvironmental systems using geosynthetics*, pp 218–243
7. Adams MT, Schlatter W, Stabile T (2007) Geosynthetic reinforced soil integrated abutments at the Bowman Road Bridge in Defiance County, Ohio. *Geosynthetics in Reinforcement and Hydraulic Applications*, pp 1–10.
8. Kost AD, Filz GM, Cousins T, Brown MC (2014) Full-scale investigation of differential settlements beneath a geosynthetic-reinforced soil bridge abutment. *Transp Res Rec* 2462(1):28–36
9. Zheng Y, Fox PJ (2016) Numerical investigation of geosynthetic-reinforced soil bridge abutments under static loading. *J Geotech Geoenviron Eng* 142(5):04016004
10. Nicks JE, Esmaili D, Adams MT (2016) Deformations of geosynthetic reinforced soil under bridge service loads. *Geotext Geomembr* 44(4):641–653
11. Saghebfar M, Abu-Farsakh M, Ardah A, Chen Q, Fernandez BA (2017) Performance monitoring of geosynthetic reinforced soil integrated bridge system (GRS-IBS) in Louisiana. *Geotext Geomembr* 45(2):34–47
12. Yang G, Zhang B, Lv P, Zhou Q (2009) Behaviour of geogrid reinforced soil retaining wall with concrete-rigid facing. *Geotext Geomembr* 27(5):350–356
13. Yang G, Liu H, Lv P, Zhang B (2012) Geogrid-reinforced lime-treated cohesive soil retaining wall: case study and implications. *Geotext Geomembr* 35:112–118
14. Yang GQ, Liu H, Zhou YT, Xiong BL (2014) Post-construction performance of a two-tiered geogrid reinforced soil wall backfilled with soil-rock mixture. *Geotext Geomembr* 42(2):91–97

# Geotechnical Investigation of Urban Roads with Composite Pavement Structures Using Destructive and Non-destructive Testing



Maziar Moaveni, Abbas A. Butt, Satish Gundapuneni, Adam D. Groves, and Sean M. Widener

**Abstract** Effective assessment of bearing capacity of the existing pavement structure as well as proper characterization of materials used in the construction of pavement layers provides critical inputs for rehabilitation design of urban roads. This study presents the findings from a comprehensive pavement geotechnical investigation that was performed on approximately 2300 ft of composite pavement (AC on top of PCC) located on Curtis road in Savoy, Illinois. Non-destructive testing program included falling weight deflectometer (FWD) as well as ground penetrating radar (GPR) at both center and transverse joint locations. Additionally, destructive testing program including pavement borings, pavement coring at crack locations, deep and shallow soil borings, dynamic cone penetration (DCP) testing on aggregate base, and subgrade as well as soil sampling and laboratory testing was performed. GPR scans obtained at three different antenna's frequencies including 2 GHz, 900 MHz, and 400 MHz were analyzed and calibrated by pavement cores to generate pavement layer thickness profiles. Statistical analysis methods were used to identify trends and develop correlations between the laboratory and field test results. This includes finding linkage between the pavement thicknesses obtained through coring and what was estimated using GPR. The findings from this study showed that strength, bonding status, and thickness variability of pavement layers as well as groundwater table and in-situ moisture condition of the subgrade soil significantly affect the surface pavement deflections.

**Keywords** Composite pavements · Falling weight deflectometer · Ground penetrating radar · Geotechnical investigations · Urban roads · Pavement rehabilitation design

---

M. Moaveni (✉)

Savannah State University, Savannah, GA 31404, USA

e-mail: [moavenim@savannahstate.edu](mailto:moavenim@savannahstate.edu)

A. A. Butt

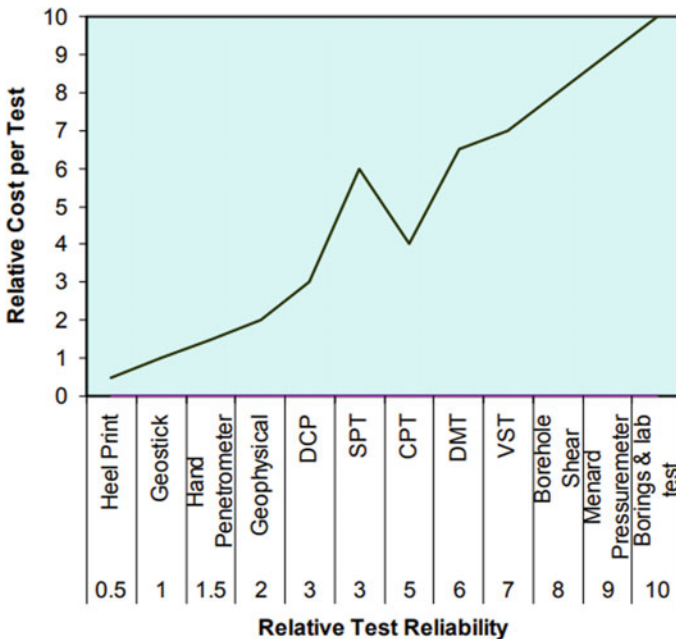
Engineering and Research International, Inc., Savoy, IL 61874, USA

S. Gundapuneni · A. D. Groves · S. M. Widener

Clark Dietz, Inc., Champaign, IL 61820, USA

# 1 Introduction

A comprehensive geotechnical investigation is an initial and mandatory stage that needs to be performed as part of road widening and highway pavement rehabilitation projects. Although original design documents and as-built construction records might be available for the existing pavement structure, the material properties used for the initial design might not remain the same over service life of the project. This can be due to contamination from subgrade soils fines, freezing and thawing cycles as well as degradation of geo-materials caused by repeated traffic loading and environmental conditions. According to the reference manual 05-037 [1] published by National Highway Institute (NHI) related to geotechnical aspects of pavements, an idealized subsurface exploration program for a highway project should include remote sensing to survey the area, geophysical testing, resistivity study, penetrometer testing as well as soil borings, sampling and laboratory testing. This idealized program provides a clear understanding of the existing condition of the road structure. Nevertheless, the cost associated with such a detailed testing program needs to be justified and modified depending on the size of the project and available resources. Figure 1 shows a comparison between different subsurface exploration techniques considering the cost and reliability of each method.



**Fig. 1** Different subsurface exploration alternatives with associated cost and reliability levels [2]. DCP—Dynamic cone penetration, SPT—standard penetration test, CPT—cone penetration test, DMT—flat dilatometer test, VST—vane shear test

The adverse impact of geotechnical problems can increase the construction costs, delay the project schedules, and finally reduce the service life of the pavement. These issues have been very well documented in the literature. Neupane [3] conducted a survey with participation of 53 engineers from state Department of Transportations (DOTs) and 43 engineers from design consultant firms in order to investigate the geotechnical related issues on pavement projects' performance. He found that lack of properly identifying boring locations as well as misclassifying subgrade soils was two major factors with negative impacts on cost and schedule of the highway rehabilitation projects. Chapter 4 of the geotechnical manual published by Illinois Department of Transportation [4] outlines the subsurface explorations and field-testing procedures for highway construction projects. The manual emphasizes that insufficient, poorly planned, and/or poorly executed subsurface explorations could result in unanticipated discovery of weak, wet, or frost susceptible soils; or erroneous predictions of soil behavior during construction that may lead to expensive delays and redesigns.

This paper provides the findings from geotechnical investigations performed on the existing pavement and within the right of way of the proposed lane widenings for the Curtis road project from Prospect Avenue to Route 45 in Savoy, Illinois. The project section was approximately 2300 ft long. The project included lane widening and resurfacing of the existing pavement. This study also provides the recommendations related to strength variability of existing pavement structure including the quality of load transfer efficiency of existing Portland cement concrete (PCC) joints. Moreover, the pavement rehabilitation as well as soil improvement alternatives is discussed in this paper.

## 2 Project Development and Background Data Collection

A review of the available information for the project started in March 2019. Based on the proposed drawings provided, the portion of Curtis road included in this project was marked from Sta. 138 + 46.91 (Centerline of Prospect Avenue) to Sta. 161 + 26.11 (Centerline of Route 45). The elevation and alignment data for the existing pavement and the proposed pavement widening locations were also provided. United States Department of Agriculture (USDA) Soil Survey of Champaign County as well as Geographic Information System (GIS) data obtained from the Champaign County GIS Consortium was reviewed. The soil survey data was overlaid with the existing road at the project location. According to Fig. 2, the proposed alignment of Curtis road traverses mostly Drummer silty clay (152A) with Flanagan silt loam (154A). The soils on the project are common for major land resource area (MLRA) 108 (Illinois and Iowa Deep Loess and Drift) with the poorly drained Drummer series in the flat (0–2% slope) bottom areas and somewhat poorly drained Flanagan series on the flanks of sloping areas (0–2% slope) at the top of slopes. The soils have formed in loess and till deposits of the Wisconsin Glaciations, specifically in the Champaign Moraine.

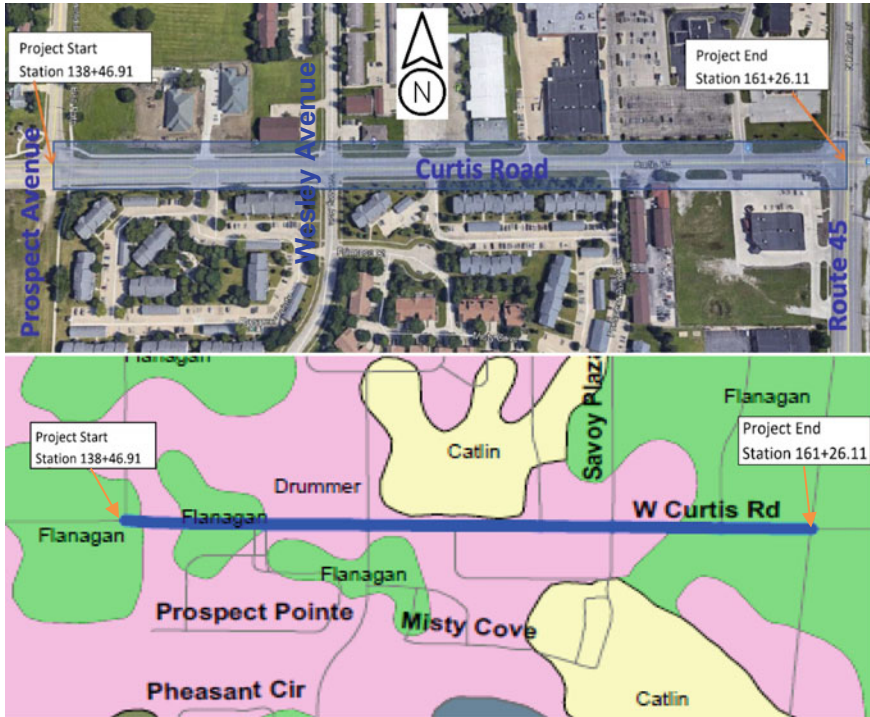


Fig. 2 Curtis road project boundaries and governing soil types based on USDA Champaign County soil survey report

### 2.1 Existing and Proposed Typical Pavement Cross Sections

The existing pavement on Curtis road between Prospect Avenue and Route 45 is asphalt concrete (AC) over PCC except a few locations. The pavement coring showed that existing pavement at sections with AC over PCC had an average AC thickness of 5 in. over an average PCC thickness of 7.8 in. The existing pavement at the few locations with only AC had an average AC thickness of 10.1 in. A layer of crushed stone aggregate and sand was found under the pavement at several locations.

The proposed pavement on Curtis road from the intersection of Wesley Avenue to the intersection of Route 45 was still at the design stage during this study. Nevertheless, for the purpose of this study, it was assumed that the proposed pavement on Curtis road will be 8 in. of PCC over 4 in. of aggregate base course material. It was also assumed that the elevation of the proposed lane widening on Curtis road between Wesley Avenue and Route 45 will match the elevation of the existing pavement surface.



### **3 Field and Laboratory Testing Programs**

#### ***3.1 Non-destructive Deflection Testing (NDT)***

The objective of an NDT program is to measure the pavement's structural response to heavy dynamic loads, similar in magnitude and duration to those produced by moving truck wheel loads. The collected deflection data may be used to determine the pavement layer material properties and foundation support and to group or divide a pavement into uniform sections that exhibit similar responses under a given load. This can aid the designer, so that significantly different pavement sections are not overlooked with random coring. The equipment used for the deflection testing in this study was a trailer mounted KUAB falling weight deflectometer (FWD). The FWD exerts an impulse loading force to the pavement and measures the resulting surface deflections. Nine deflection transducers were used with one transducer placed at the center of the loading plate and the others spaced radially at spacings of -12, 0, 12, 18, 24, 36, 48, 60, and 72 in. from the center of the load plate along a straight line. The resultant set of readings form the deflection basin. The negative 12 in. transducer was used for PCC joint load transfer analysis. The existing pavement was five lanes from Prospect Avenue to Wesley Avenue and three lanes from Wesley Avenue to Route 45. Note that lane numbers were assigned in increasing order from south to north. The FWD testing was conducted at loading levels ranging from 6000 to 12,000 lbs. and at two locations in each lane: (1) at center of lane to represent the slab center locations and (2) in right wheel path at transverse crack locations to represent the transverse joint location in the underneath PCC pavement. The air temperature and surface temperature of the AC layer were also recorded using air transducer and infrared temperature sensor of the FWD, respectively.

#### ***3.2 Ground Penetrating Radar (GPR) Testing***

Ground penetrating radar (GPR) has many uses including determination of pavement layer thicknesses, base and subbase evaluations, geological investigations, bridge deck inspections, and geo-textile performance testing. The GPR equipment used for this study was GSSI's RoadScan™ system with the SIR-30 data acquisition system, a 2.0 GHz air-coupled antenna, 900 and 400 MHz ground-coupled antennas. A GPS unit was used to obtain the spatial coordinates of the points along the pavement section being tested. This system provides an effective tool for quickly collecting the pavement surface thickness data while traveling at posted speed limits. The GPR system can collect data at intervals as small as 1 inch. Therefore, continuous pavement surface thickness profiles can be developed without causing any damage to the pavement structure, which would not be possible with conventional pavement coring. The GPR testing was also performed at two locations including center of the lane and right wheel path. Note that the GPR and FWD testing were performed

simultaneously by integrating the distance measuring instrument (DMI) of the FWD trailer with the GPR data acquisition system. This arrangement will allow real-time analysis of the pavement layer thicknesses in conjunction with the maximum deflection data collected at deflection transducer located at the center of the load plate.

### ***3.3 Soil and Pavement Borings, Sampling, and Testing***

Soil investigation is necessary to determine the suitability of in-place soils as embankment and pavement subgrade. Soil properties determined from laboratory testing provide important inputs for the pavement design. Depths of existing AC and/or PCC pavement layers, depth of soil layers, in-place moisture contents, organic contents, Atterberg limits, particle size distributions, soil classifications, and subgrade supporting rating following Illinois DOT subgrade stability procedure [5] were among the items that were investigated in this project. A total of 19 pavement boreholes were drilled with a 6 inch diameter core rig, and 14 soil borings were augured at various locations from Prospect Avenue to Route 45 to get the representative soil samples from each lane in both east bound (EB) and west bound (WB) directions. An additional ten pavement cores were drilled at the crack locations to determine the condition of the existing structural layers of AC and PCC to examine the crack patterns and the depths of crack propagation with respect to top and bottom surfaces within each layer. Both pavement borehole and core stations/lane number as well as pavement materials and associated thickness for each layer are summarized in Fig. 3. No soil samples were collected at the ten core hole locations. Dynamic cone penetrometer (DCP) testing was also performed at the top of the aggregate and/or soil layer (after removing the pavement core when applicable). The borings were then further advanced manually through the soil layers to a minimum depth of 72 in. whenever possible. Soil samples and pavement core were collected at each borehole location and transported to the laboratory for further analysis. Water table measurements were taken at 5 min and 24 hrs after completion of the sampling at all borehole locations.

## **4 Results and Discussions**

The maximum deflection (D0) obtained from NDT is a good indicator of the overall roadway condition. D0 is a function of foundation support, upper pavement layer thicknesses, strength, and applied loads. In general, for any given thickness, higher D0 values indicate a weaker pavement, and variability of the pavement structure can be observed by viewing the longitudinal profile of the maximum deflections along the length of a roadway. The D0 data measured at a target load of 9000 lbs. were normalized to a standard load of 9000 lbs. considering the pavement temperature

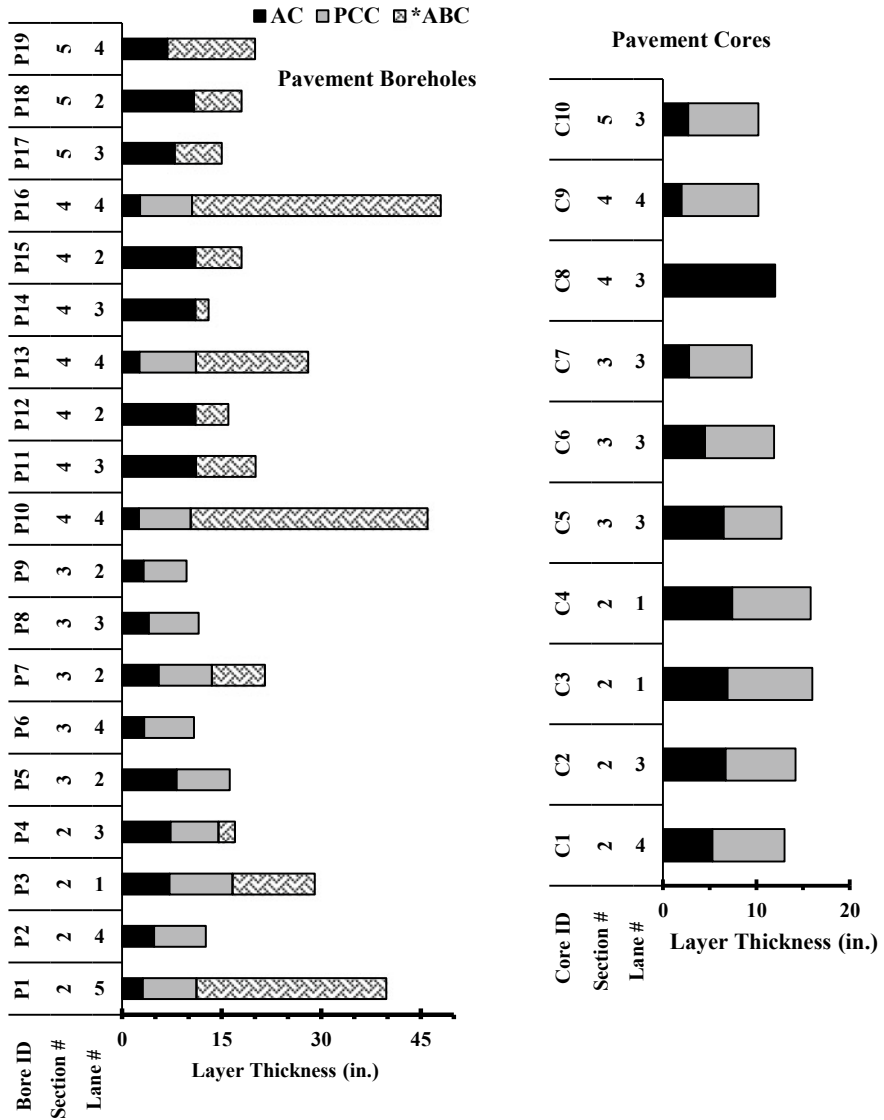


Fig. 3 Pavement borehole and core stations/lane numbers, pavement materials, and thickness for each layer

following Asphalt Institute (MS-17) correction procedure [6]. Both the approach and leave slab deflections could be recorded as part of FWD testing. Thus, percentage of load transfer efficiency of PCC joints as the ratio of approach to leave slab deflection multiplied by 100 [7] was computed. Figure 4 summarizes deflection testing results.

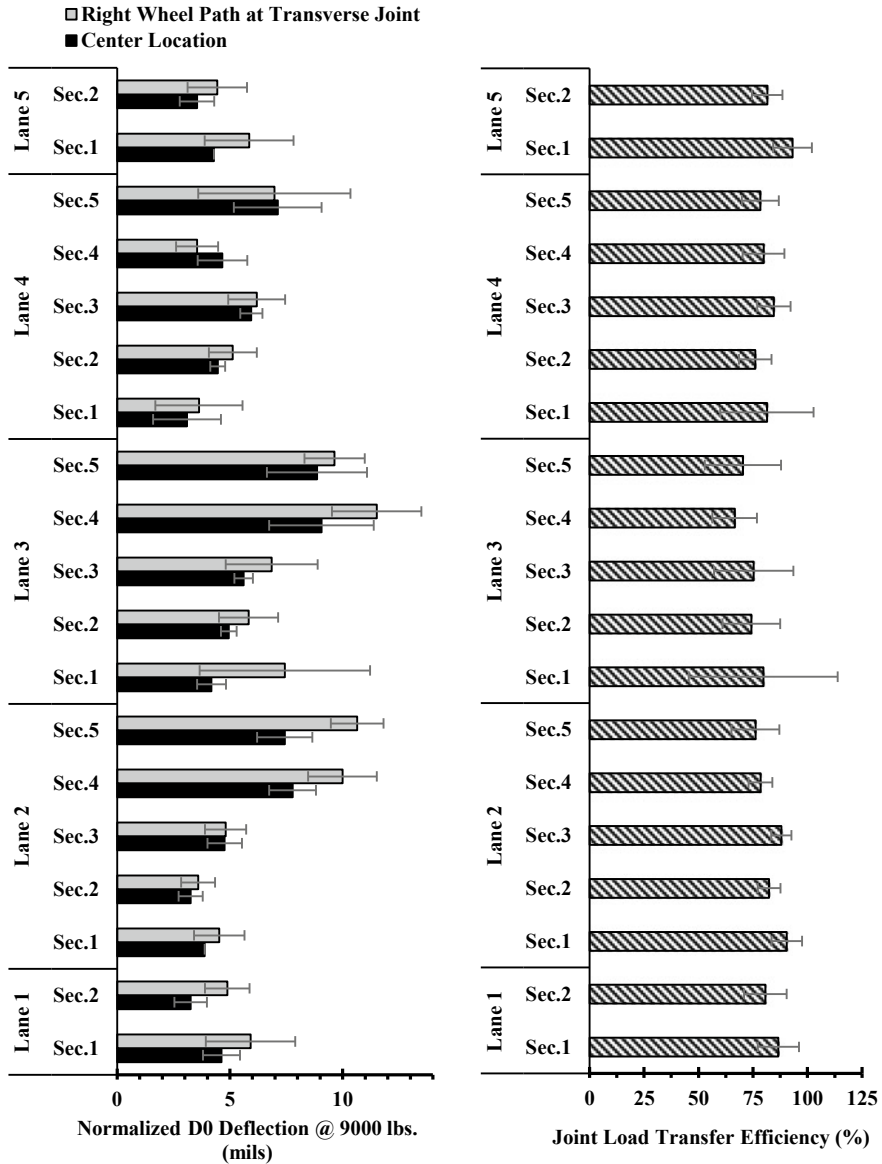


Fig. 4 Normalized D0 deflections and load transfer efficiencies with corresponding standard deviations at different lanes and uniform sections

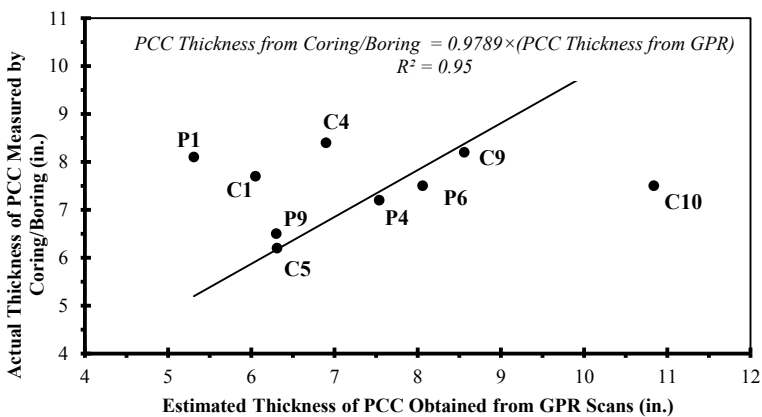
**Table 1** Uniform section numbers and corresponding stations

Station	Uniform section number				
	1	2	3	4	5
Start station	138 + 46	139 + 81	146 + 47	151 + 00	158 + 22
End station	139 + 81	146 + 47	151 + 00	158 + 22	161 + 26

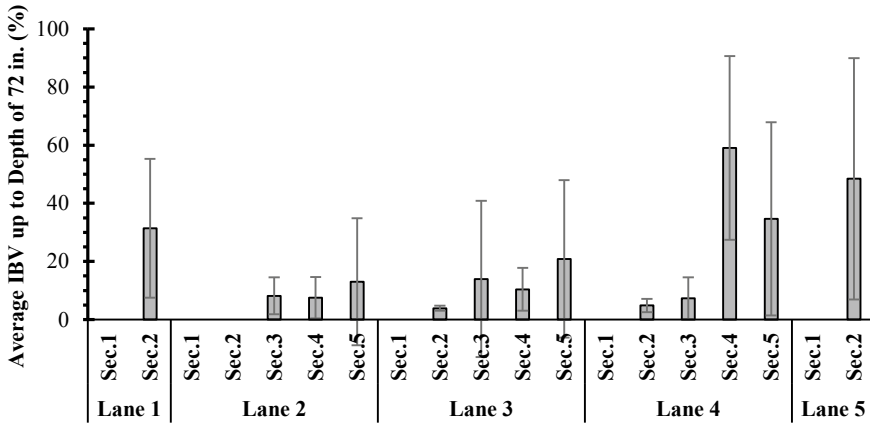
Considering normalized D0 deflection at 9000 lbs. at center and right wheel path transverse joint locations for different lanes, the project length was divided into five uniform pavement sections.

The start and end station numbers for each uniform pavement section is included in Table 1. These boundaries were later used to provide different rehabilitation alternatives for each section. The normalized D0 profile and pavement layer thicknesses obtained from coring (see Fig. 3), showed that from Wesley Avenue to Route 45, pavement structure along lane 4 has relatively lower strength variability as compared to center turning lane (lane 3) and lane 2. Additionally, the deflection values as well as their variabilities recorded for pavement structure of all 5 lanes from Prospect Avenue to Wesley Avenue were found to be lower than the deflection values and variabilities associated with lanes 2, 3, and 4 from Wesley Avenue to Route 45.

GPR data obtained from three different antennas were processed using RADAN® GSSI's software to determine the existing pavement layer thickness. A two-layer analysis approach was used to estimate the depth to the bottom of PCC layer. The estimated thickness of PCC layer obtained from GPR analysis and measured from pavement coring/boring is presented in Fig. 5. This figure shows that a good correlation exists between these two methods for measuring the PCC thickness. Note that low level of accuracy in estimating the PCC layer thickness by GPR was observed for core C10 located in Section 5. After inspecting the surface of the pavement,



**Fig. 5** Estimated thickness of PCC layer obtained from GPR analysis and measured from pavement coring/boring



**Fig. 6** Average Illinois bearing values (IBV) up to the depth of 72 in. at different lanes and uniform sections

a considerable amount of structural distresses was found in Section 5. Pavement surface distress allows greater amount of moisture penetration into the pavement which could interfere with GPR signal.

Immediate bearing values (IBV) [5] were obtained by performing DCP tests on the aggregate base and subgrade soil at the location of 19 pavement borings. Illinois DOT has adopted the term IBV in lieu of the California bearing ratio (CBR), to differentiate it from the soaked CBR used for pavement design. The average IBV results up to the depth of 72 in. are presented in Fig. 6. In general, DCP testing results indicate that the soils provide a relatively low bearing value.

Soil samples collected from 19 pavement borings as well as well as fourteen soil borings were visually classified. In total, six main soil groups and three organic soil groups were identified. A representative soil samples from each group was selected, and several laboratory tests were performed. According to Table 2, most of the soils were classified as silty clay with A-6 and A-7-6 AASHTO designation which confirms the poor bearing capacity of the soil. Organic content test was also performed on the three organic soil groups.

The results presented in Table 3 indicate 4.3–7.3% of organic content was found in the soil samples. The subgrade support ratings (SSR) [5] of five soil samples tested in the laboratory varied from poor to granular. It was recommended that a “Poor” SSR be used for this project. The compressive strength test was also performed on the concrete samples cored from the pavement at P3, P4, P6, P8, and P9 locations.

The results showed compressive strength of the PCC ranging from 7150 to 9300 psi with mostly shear failure. These were acceptable values since the typical PCC 28-days compressive strength is around 5000 psi. Note that it was not possible to perform compressive strength on all the cored samples due to broken cores and/or rebar in the cores.

**Table 2** Laboratory soil test results on six main soil groups

Soil group no.	2B	4	7	8	9	10
Section no.	5	3	4	4	3	5
Sample depth (in.)	7–19	36–44	38–50	28–40	21.5–33.5	30–42
AASHTO classification (group index)	A-1-a (0)	A-7-6 (0)	A-6 (0)	A-6 (1)	A-6 (5)	A-2-4 (0)
ASTM classification	SM	CH	CL	CL	CL	SC
IDOT classification	Sand	Silty clay	Silty clay loam	Loam	Loam	Sandy loam
IDOT subgrade support rating	Granular	Fair	Poor	Poor	Poor	Granular/poor
% Sand	84.9	16.2	10.1	39.6	46.4	70.0
% Silt	11.0	50.7	65.0	42.7	37.1	14.2
% Clay	4.1	33.1	24.9	17.7	16.5	15.8
Liquid limit	NP <sup>a</sup>	50	38	26	39	NP
Plastic limit	NP	21	22	15	20	NP
plasticity index	NP	29	16	11	19	NP

<sup>a</sup>NP—Non-plastic

**Table 3** Organic content test results for organic soil groups (AASHTO T267)

Soil group no.	3	5	6
Section no.	2	4	4
Depth (in.)	17–32	24–36	12–24
Organic content (%)	7.3	4.3	6.6

## 5 Conclusions and Recommendations

A combination of different destructive and non-destructive tests was performed on approximately 2300 ft of composite pavement located in Curtis road in Savoy, Illinois. Based on the findings from this study, milling and overlay with localized patching and joint repairs was recommended for existing pavement in lanes 1 through 5 at Sections 1, 2, and 3. Additionally, full pavement reconstruction was suggested for lane 2 and lane 3 in Section 4 as well as lanes 2 through 4 at Section 5. High deflection values in these lanes and sections were used as the main criteria to identify the proper rehabilitation alternatives. Note that only milling and overlay with localized patching and joint repairs was recommended for lane 4 in Section 4. DCP field testing at boring locations as well as laboratory tests performed on soil samples indicated that

subgrade bearing capacity is at poor condition. Where lane widening or full pavement reconstruction is required, it was decided that subgrade improvement should be performed. This could be achieved by treating top 12 in. of subgrade with lime after removing and replacing organic soil layers in Sections 2 and 4 with suitable material within the top 24 in. of subgrade. Based on IDOT recommendations, 4 in. of aggregate base material should also be placed under 8 in. of PCC pavement. The findings from this study showed that the combination of destructive and non-destructive testing can be effectively used to characterize the composite pavement structure. This includes the successful performance of GPR in estimating the thickness of PCC pavement.

**Acknowledgements** The authors of this paper would like to thank Mr. Timothy Worstell, Mr. Joshua Black, and Mr. Ivan Catron for conducting the field and laboratory tests. The contents of this paper reflect the views of the authors who are responsible for the facts and the accuracy of the data presented. This paper does not constitute a standard, specification, or regulation.

## References

1. Christopher RB, Schwartz C, Boudreau R (2006) Geotechnical aspects of pavements, National Highway Institute Report 05-037, Federal Highway Administration, Washington, DC
2. Handy RL (1980) Realism in site exploration: past, present, future, and then some—all inclusive. In: Proceedings of symposium on site exploration in soft ground using in-situ techniques, Report FHWA-TS-80-202, Federal highway Administration, Washington DC
3. Neupane KP (2016) Causes and impacts of geotechnical problems on bridge and road construction projects. Master Thesis, University of Nevada at Las Vegas
4. Geotechnical Manual (2015) Division of highways. Bureau of Materials and Physical Research, Illinois Department of Transportation (IDOT), Springfield, Illinois
5. Subgrade Stability Manual (2005) Division of highways. Bureau of Bridges and Structures, Illinois Department of Transportation (IDOT), Springfield, Illinois
6. Asphalt Overlays for Highway and Street Rehabilitation (2001). Manual Series 17, 3rd edn, Asphalt Institute
7. AASHTO (1993) Guide for design of pavement structures. American Association of State Highway and Transportation Officials (AASHTO), Washington DC



# Challenges in Developing Sustainable Infrastructure Case History: Boubyan Clay



Waleed Abdullah, Fahad AlOqaili, Ananth Ramasamy, Srour AlOtaibi, and Shaikha AlTheyab

**Abstract** Boubyan Island, which is the largest island within the geographic boundaries of the State of Kuwait, is characterized with its challenging ground conditions. Results of the extensive geotechnical investigation program indicated that the soil profile in the island is comprised of thick, soft, silty clay layer, with thickness ranging between 19 and 26 m, underlain by a dense to very dense fine sand layer. The silty clay layer is characterized as very soft to soft, calcareous, low to intermediate plastic, light brown to brown clay with cone resistance value less than 1 MPa, which is locally referred as “Boubyan Clay.” Due to the existence of the thick, soft Boubyan Clay deposits in the island, ground improvement works in the form of surcharging with prefabricated vertical drains was adopted for limiting settlement of the road embankments after formation and for enhancing stability of the embankments. This paper describes in detail the challenges that Boubyan Clay imposes in developing sustainable infrastructures and in particular the analysis of the embankment slope stability under temporary and permanent load conditions using Morgenstern and Price method of slices by adapting the numerical modeling program of SLOPE/W. Analysis indicated that embankments were stable under temporary as well as permanent loading conditions. Results also proved that margin of safety in the drained long-term loading condition is much larger than those under the undrained loading conditions.

**Keywords** Boubyan clay · Ground improvement · Slope stability

---

W. Abdullah · S. AlTheyab  
Civil Engineering Department, Kuwait University, P. O. Box 5969, 13060 Safat, Kuwait, Kuwait  
e-mail: [waleed.abdullah@ku.edu.kw](mailto:waleed.abdullah@ku.edu.kw)

F. AlOqaili (✉)  
Kuwait International Airport New Passenger Terminal Project, Ministry of Public Works, Kuwait, Kuwait

A. Ramasamy · S. AlOtaibi  
Ministry of Public Works, Kuwait, Kuwait

# 1 Introduction

The State of Kuwait lies on the northeastern part of the Arabian Peninsula. It has a surface area of about 17,818 km<sup>2</sup> and is bounded on the north and west by Iraq, on the west and south by Saudi Arabia, and on the east by the Arabian Gulf (Persian Gulf). Halwagy and Halwagy [5] the State of Kuwait includes ten offshore unpopulated islands: Failaka, Boubyan, Warba, Mischan, Um Al-Nemmel, Auhha, Kubbar, Qaruh and Um Al-Maradim. Figure 1 shows the map of the State of Kuwait and the islands.



Fig. 1 State of Kuwait map

Boubyan Island is the largest island within the geographic boundaries of Kuwait that is located in the northwestern corner of the Arabian Gulf with an area of about 863 km<sup>2</sup>. It is about 40 km long with a width that varies between 25 and 35 km. The soil profile in Boubyan Island is different than soil across the State of Kuwait as it is mainly soft, thick clay, locally known as Boubyan Clay, as opposed to the calcareous silty, sand that covers the rest of the country. The development of the infrastructure of the island is linked to constructing a new container seaport terminal that lies on the eastern shore of the island. Figure 2 shows the master plan of Boubyan Island and the location of the seaport on the eastern shore. The port requires major development around the island as it requires the construction of a dual 3-lane carriageway highway and a parallel twin line railway. The lengths of the highway and the railway are approximately 35 km linking the seaport from the eastern shore of the island to Kuwait from the west through a bridge. Due to the existence of the thick, soft Boubyan Clay deposits in the island, ground improvement works in the form of surcharging with prefabricated vertical drains were adopted. Prefabricated vertical drains were used to limit settlement of the road embankments after formation and for enhancing stability of the embankments' slope during the different stages of construction.

The first part of the paper discusses the geotechnical characteristics of Boubyan Clay and challenges it imposes in developing sustainable infrastructures, while the second part presents the analysis of the embankment slope stability under temporary and permanent load conditions using Morgenstern and Price method of slices by adapting the numerical modeling program of SLOPE/W.

## 2 Challenges Imposed by Boubyan Clay in Development of Sustainable Infrastructures

El-Nahas et al. [3] reported that the clay deposits in Boubyan Island consist of structured marine clay that forms part of the Euphrates Delta Formation. Abdullah et al. [1] reported that the island is located where the Euphrates/Tigris River systems enter the Arabian Gulf, and that the large river systems act as both erosive and depositional environments depending on historical climatic and sea-level changes. Rapid climatic changes following the end of the last ice age (approximately 10,000 years ago) resulted in the production of considerable sediment that has been deposited at the mouth of these river systems, forming a large delta, part of which is now Boubyan Island [1].

Search for the literature on the engineering properties of Boubyan Clay was limited to include only Bao et al. [2], El-Nahas et al. [3] and Abdullah et al. [1]. With no prior local experience and data on Boubyan Clay deposits, investigation programs which included mostly field tests and correlation with limited laboratory tests were carried out for the specific purpose of development of the infrastructure projects in the island.



Fig. 2 Master plan of Boubyan Island

The Geotechnical Assessment Report [8] presented results of the extensive geotechnical investigation program that was carried out along the proposed highway and railway sections. The Geotechnical Assessment Report indicated that the soil profile within Boubyan Island can be characterized with two main layers as follows: The upper major deposit of the island (M1) which is a thick layer of very soft to soft silty clay extending down to depths between 19 and 26 m with an average thick of about 20 m and is characterized as very soft to soft, calcareous, low to intermediate plastic, light brown to brown clay with cone resistance value less than 1 MPa. This silty clay layer is locally referred to as “Boubyan Clay.” Underlying this layer exists a dense to very dense fine sand layer (A3). The land surface of Boubyan Island is generally flat with ground surface varying from +2.1 to 3.4 m KLD. Water table was found around 0.5 m depth from ground surface. Table 1 lists a summary of engineering properties of both M1 and A3 layers. Figure 3 shows the geological profile along east–west highway/railway section of the island.

In Table 1,  $w$  is the mean moisture content,  $G_s$  is the mean specific gravity,  $\gamma$  is the mean bulk unit weight,  $C_a$  is the mean calcium content,  $C_u$  is the undrained cohesion,  $C'$  is the drained cohesion,  $\phi'$  is the drained friction angle,  $C_c$  is the compression index,  $C_r$  is the swelling index,  $C_\alpha$  is the secondary coefficient of consolidation,  $e_0$  is the initial void ratio,  $C_v$  is the vertical coefficient of consolidation, and  $C_h$  is the horizontal coefficient of consolidation, which was taken as 1.5 times  $C_v$ .

The existence of thick, highly compressible soft Boubyan Clay layer, unit M1, and due to its low undrained shear strength created challenges for the construction of the infrastructures included in the master plan, and therefore, ground improvement works were necessary for creating sustainable development in the island with the objectives to minimize the post-construction primary and secondary consolidation settlement to meet the specified design requirements.

Preloading with vertical drains, vacuum dewatering, stone columns and in situ deep mixing are commonly performed in cohesive soils [6]. Therefore, surcharge with prefabricated vertical drain (PVD) was chosen as the ideal ground improvement method for the Boubyan Clay soil along both the 35 km highway and railway and part of the port area to accelerate the consolidation of the soft clay soil by allowing water to dissipate radically to the nearest PVD as well as vertically to the sand filter layer.

Abdullah et al. [1] described the challenges faced in the design, and execution of the preloading/PVD ground improvement project applied to the thick Boubyan Clay was the variations in the horizontal and vertical coefficients of consolidation ( $C_h$  and  $C_v$ , respectively) that were measured in the laboratory, and therefore, preliminary analysis predicted that the time to reach 90% consolidation may vary from three months to one year causing a construction problem. To validate these predictions and given the lack of prior local experience in soft clay in general and scarcity of data on Boubyan Clay deposits in specific, a full-scale pilot project that included an instrumented section under a surcharge load with PVDs was carried out.

Figure 4 shows detailed section of preloading profile with PVD adopted for the road/rail embankment.



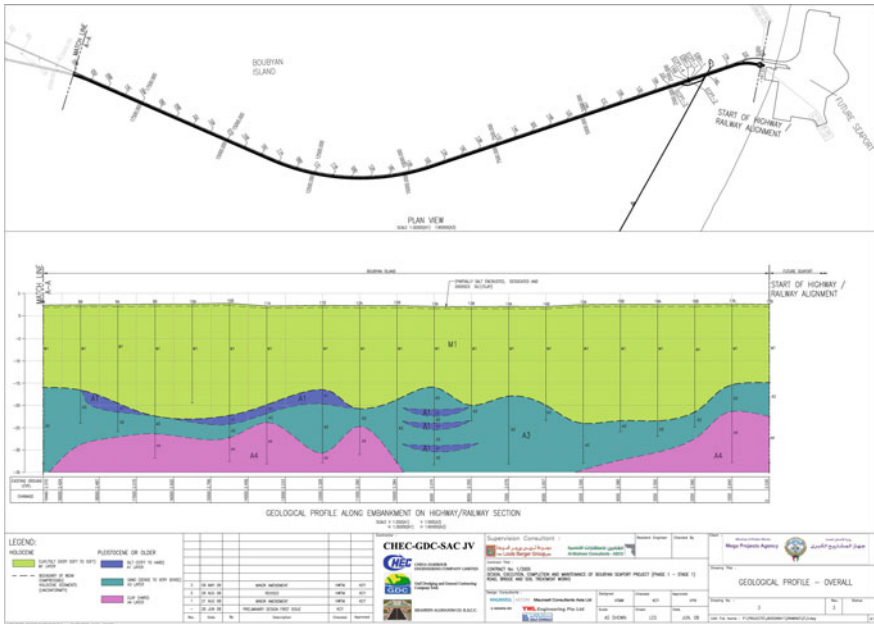


Fig. 3 Geological profile along east-west axis of the island [8]

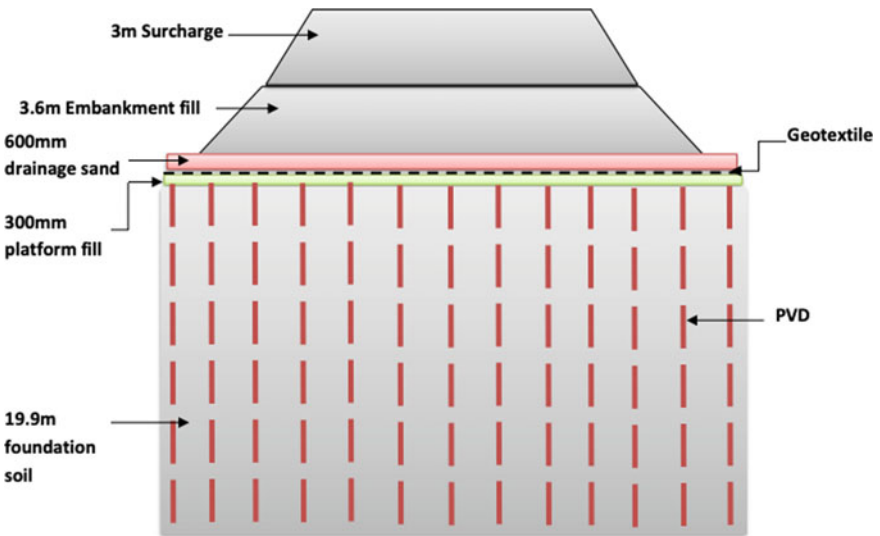


Fig. 4 Elevation cross section of the loading profile



**Table 2** Model geometries used in the stability analysis

Model	Soft clay thickness (m)	Embankment height (m)	Surcharge height (m)
A	26	4.8	3
B	24	4.8	3
C	21	4.8	3
D	19	4.8	3

### 3 Embankment Slope Stability

Road embankments in Boubyan Island are to be constructed over deposits of very soft to soft clay and silt. Preliminary assessment of the stability analysis indicated that a 4.8 m high embankment with side slope of 1V:6H with a maximum of 3 m high of surcharge preloading should be stable with factor of safety greater than the required value of 1.2 for temporary condition and 1.5 for permanent condition by stage construction. Under temporary conditions, a construction traffic loading of 10 kPa has been assumed during construction stage. For the permanent condition, traffic load of 20 kPa has been assumed over the traffic lanes.

Depending on the depth of the soft sediment, four models were created for slope stability analysis, namely A, B, C and D. The four models were proposed to cover all ranges of depth of the clay layer which is between 19 and 26 m. Details of the model geometries are listed in Table 2.

### 4 Method of Analysis

The Morgenstern and Price method of slices was used for embankment overall stability analysis with the aid of the numerical program of SLOPE/W, which considers both force and moment equilibrium for the individual slices.

Slope/W software has many inputs that facilitate the management of data, including forces details on each slide, list of variables amongst other aspects that ensure the correct determination of the stability of the slope [4]. As such, slope stability problems are normally approached with respect to soil strength, geometry, loading imposed, pore water pressure, as well as soil structure interaction [4].

In this project, the analysis involved the use of Morgenstern and Price limit equilibrium technique to determine the minimum/critical factor of safety of slopes provided which had two or more layers. The properties that were important for the analysis included slip surfaces in the slope as well as the Piezometric line. The Piezometric line defines the pore water pressure throughout the domain. The soil above the slip surface in this case was divided into 20 slices for all the stages.

The following stages of construction were proposed and analyzed as follows:

- Stage 1: Construction of embankment height with temporary load



Involved the construction of 4.8 m of embankment with additional 10 kPa for temporary traffic load. The initial normally consolidated undrained shear strength envelope of the soft clay was applicable.

- Stage 2: Construction of surcharge with temporary load  
The soft clay is then subjected to consolidation during post-Stage 1 for a period to 90% primary consolidation. Additional 20 kPa for permanent traffic load was applied on the overconsolidated soft clay. The overconsolidated undrained shear strength was applicable.
- Stage 3: Construction of surcharge with temporary load  
After the soft clay has gone through consolidation during Stage 2 for a period to 90% primary consolidation, further loading of 3 m of surcharge with additional 10 kPa for temporary traffic load was applied on the overconsolidated soft clay. The overconsolidated undrained shear strength was applicable.
- Stage 4: Post-construction of surcharge with permanent load  
After the soft clay has gone through consolidation during post-Stage 3 for a period to 90% primary consolidation, the surcharge load was removed to original embankment level, and permanent load of 20 kPa was applied. The permanent load was applied slowly indicating that the overconsolidated drained shear strength was applicable.

The selected design parameters for the soft sediment and the fill materials are given as shown in Table 3. Due to lack of previous data on the undrained shear strength of the Boubyan Clay and difficulties in obtaining undisturbed samples, normally consolidated and overconsolidate undrained cohesions listed in Table 3 were correlated from cone penetration tests, which were done before the surcharge loading, as shown in Eq. 1 [7]

$$C_u = 0.22 \sigma'_o \tag{1}$$

where  $C_u$  is undrained shear strength, and  $\sigma'_o$  is effective overburden pressure.

**Table 3** Design parameters

Soil layer	Classification	Bulk unit weight $kN/m^3$	N/C undrained cohesion $C_u$ $kN/m^2$	N/C drained cohesion	N/C drained friction $\Phi'$ degree	O/C undrained cohesion $C_u$ $kN/m^2$	O/C drained cohesion	O/C drained friction $\Phi'$ degree
Fill	SW	18	–	0	32	–	0	32
Soft clay	CL	18.1	15:0–10 m 20:10–15 m 27:15–20 m 36:20–26 m	0	30	20.3:0–5 m 26.8:5–10 m 36:10–15 m 40.5:15–20 m 48.3:20–26 m	0	30
Sand	SM	20.3	–	0	36	–	0	36

## 5 Results and Discussion

The summary of the slope stability analysis from Slope W is listed in Table 4 with comparison of design minimum requirement.

- Stage 1 Involved the construction of 4.8 m of embankment with additional 10 kPa for temporary traffic load. The minimum factor of safety obtained from the analysis was 1.215 for all models, which showed that the slope had just about the exact level of factor of safety required (1.2).
- Stage 2 With a permanent traffic load of 20 kPa that was applied on the 4.78 m high embankment soil where the underlying soft clay has been overconsolidated during post-Stage 1. The minimum factor of safety calculated ranged between 1.538 and 1.575. The minimum slope stability for this case was expected not to fall below 1.5. As such, the calculations indicated that the slope was safe.
- Stage 3 Included the additional loading of 3 m of surcharge with 10 kPa for temporary traffic load, the minimum factor of safety calculated between 1.204 and 1.206. This soil layer was expected to have a minimum not below 1.2. The additional temporal load from traffic could be supported without any risks at the factor of safety.
- Stage 4 For the long-term drained slope analysis of the embankment and 20 kPa traffic loading, the critical factor of safety calculate was 3.136 for all the models. Design requirement of minimum factor of safety was 1.5. In this case, the stability of the underlying soil layers was satisfied.

Figures 5, 6, 7 and 8 show the failure surface and minimum factor of safety calculated for Model A for the four stages.

Analysis of the factor of safeties measured for the four stages indicates that the margin of safety in the drained Stage 4, which is under drained loading, is much larger than those in the first three stages (1,2,3), which are under the undrained loading conditions. Therefore, long-term stability of the embankment is satisfied.

**Table 4** Factors of safety calculated by Slope/W

Model	Stage 1	Stage 2	Stage 3	Stage 4
A	1.215/1.2	1.564/1.5	1.204/1.2	3.136/1.5
B	1.215/1.2	1.564/1.5	1.204/1.2	3.316/1.5
C	1.215/1.2	1.538/1.5	1.206/1.2	3.316/1.5
D	1.215/1.2	1.575/1.5	1.206/1.2	3.136/1.5

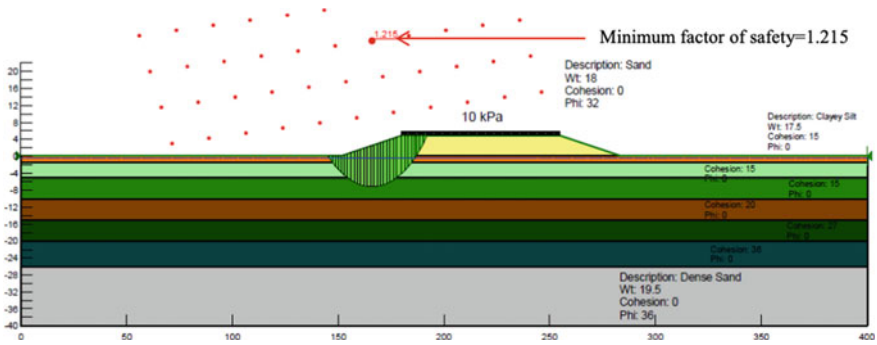


Fig. 5 Failure surface and minimum factor of safety calculated for Stage 1 of Model A

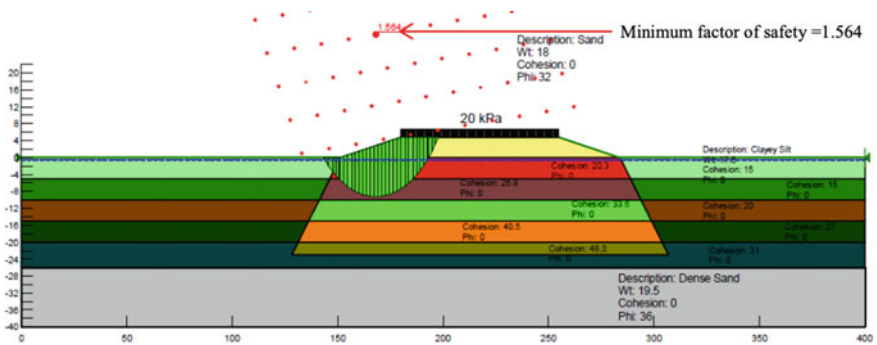


Fig. 6 Failure surface and minimum factor of safety calculated for Stage 2 for Model A

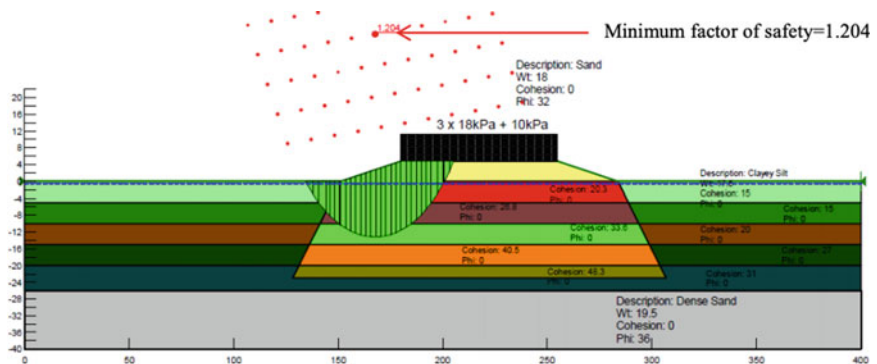
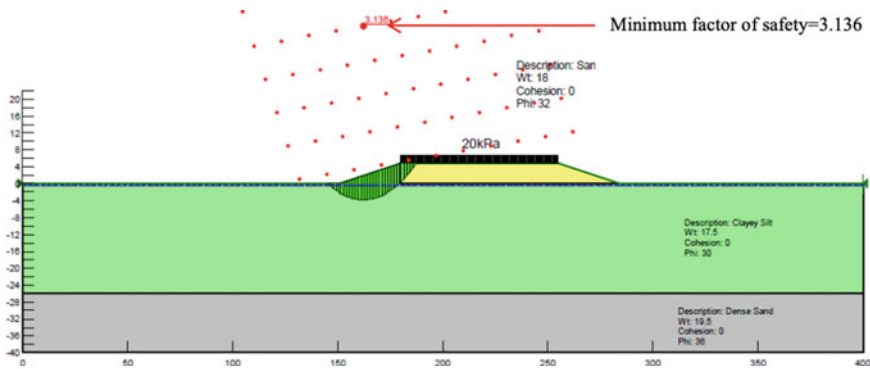


Fig. 7 Failure surface and minimum factor of safety calculated for Stage 3 for Model A



**Fig. 8** Failure surface and minimum factor of safety calculated for Stage 4 for Model A

## 6 Conclusions

This paper presented a background on the Boubyan Clay deposit that cover the whole surface area, approximately 863 km<sup>2</sup>, of Boubyan Island and to depths between 19 and 26 m. The existence of this soft clay presented challenges that faced the development of the mega infrastructures works included in the master plan for Boubyan Island. Challenges included high consolidation settlements and low bearing capacity of the Boubyan Clay that required ground improvement works. Surcharge with prefabricated vertical drain (PVD) was chosen as the ground improvement method for the Boubyan Clay soil along both the 35 km highway and railway and part of the port area.

Further challenges were presented due the lack of available data on the Boubyan Clay and lack of prior local experience to predict the long-term consolidation settlements associated with these mega projects; therefore, to validate these predictions, a full-scale pilot project that included an instrumented section under a surcharge load with PVDs was carried out.

Slope stability analysis of a 4.8 m high embankment with side slope of 1V:6H with a maximum of 3 m high of surcharge under temporary and permanent load conditions was performed using Morgenstern and Price method of slices by adapting the numerical modeling program of SLOPE/W. Analysis indicated that embankments were stable under temporary as well permanent loading conditions. However, margin of safety in the drained long-term loading condition is much larger than those under the undrained loading conditions.

**Acknowledgements** The work presented in this paper would not have been possible without the cooperation and support of the Mega Projects Sector (MPS), Ministry of Public Works (MPW), Kuwait. The authors appreciate the assistance of the MPS Directors and Engineers.

## References

1. Abdullah W, Ramasamy A, Talaat A, AlOtaibi S (2019) Verification of the preloading design of soft clay with prefabricated vertical drains by full-scale field instrumentation and numerical modelling. *Int J Geotech Eng* 13(1):92–101
2. Bao S-f, Huang J-h (2013) Engineering properties of soils on Boubyan Island in Kuwait. *Adv Mater Res* 815:273–278
3. El-Nahas A, Chitambira B, White J, Brew D (2014) Geotechnical characteristics of shallow soil formations at Boubyan Island, Kuwait. In: *Proceedings, 3rd International Symposium on Cone Penetration Testing*, Las Vegas, Nevada, USA
4. GEO-SLOPE International Ltd. (2012) *Stability modeling with SLOPE/W*. Eng Methodol. November 2012 Edition
5. Halwagy R, Halwagy M (1974) Ecological studies on the desert of Kuwait I. The physical environment. *J Univ Kuwait* 1:75–86
6. Hirkane SP, Gore NG, Salunke PJ (2014) Ground improvement techniques. *Int J Inventive Eng Sci* 2(2):11–13
7. Terzaghi K, Peck RB, Mesri G (1996) *Soil mechanics in engineering practice*, 3rd edn. Wiley
8. Ministry of Public Works (MPW) (2009a). *Geotechnical Assessment Report of Boubyan Island Seaport Project (Phase1-Stage1)*. Revision D

# Initiation of 2014 Oso Landslide Using 3D Slope Stability Analyses: Effect of Infiltration



Pourya Kargar and Abdolreza Osouli

**Abstract** March 2014 Oso landslide, which demolished Steelhead Haven Community near Oso, Washington, is the deadliest in US history. Several factors have been suggested for the initiation of this landslide by various researchers including, the heavy rainfall before the landslide, timber harvesting on the upper plateau, river erosion at the slope toe, groundwater rise due to rainfall infiltration, and irregular 3D topography of the slope. This study utilizes 3D limit equilibrium and 3D finite element seepage analyses to investigate the effect of rainfall infiltration in the 7.5 acres timber harvest area at the top of the slope as well as potential changes of groundwater elevation on the initiation of 2014 Oso landslide. To achieve these objectives, the infiltration rate was varied in the harvested area to investigate its effect on the first phase initiation. Also, two potential groundwater levels were examined to assess the sensitivity of the first phase slide mass to changes in groundwater conditions. The 3D factor of safety for the critical slip surfaces was obtained for the two groundwater levels using two conventional limit equilibrium methods. The safety factor for the critical slip surface is slightly different for the first and second groundwater levels. The difference is such small that it can be concluded that a reasonable rise in groundwater level would not have been the triggering factor for the 2014 Oso landslide. The impacts of other potential factors such as shear strength reductions of upper layers due to the rainfall infiltration, timber harvesting, and/or 3D slope geometry effects appear to have been more influential in the initiation of the landslide.

**Keywords** Oso landslide · 3D slope stability analysis · Rainfall infiltration · 3D seepage analysis · Shear strength

---

P. Kargar  
Southern Illinois University, Carbondale, IL, USA  
e-mail: [pkargar@siue.edu](mailto:pkargar@siue.edu)

A. Osouli (✉)  
Southern Illinois University, Edwardsville, IL, USA  
e-mail: [aosouli@siue.edu](mailto:aosouli@siue.edu)

## 1 Introduction

After the occurrence of devastating Oso 2014 landslide with numerous casualties, several researchers contemplated on the cause. Failure mechanism and the initiation of the landslide are two of the main aspects that were analyzed by various studies. The complex topography of the slope and sequence of progressive failures resulted in different interpretations. Keaton et al. [1] using the data collected by a team reconnaissance in the landslide area present some suggestions for the landslide failure and initiation mechanisms. They introduced the Oso 2014 landslide as a two-phase landslide with a deep-seated failure surface which was initiated due to the remobilization of the previous landslides' debris on the slope. However, remobilization of a large volume of ground layers as suggested by them does not follow the observations of other studies, e.g., Stark et al. [2], who also suggests the upper part of the slope as the initiation zone of the landslide. Iverson et al. [3] using their numerical modeling software package (D-Claw) investigated the mobility of the 2014 Oso landslide. They concluded that the disaster of Oso 2014 landslide was due to the high mobility (speed and travel distance) of the landslide debris avalanche flow and ruled out the relevancy of the size of the failure. They speculate that the landslide is triggered at an elevation below the ancient landslide bench in the middle of the slope. However, this speculation is not consistent with their proposed "high mobility of the landslide debris avalanche flow" and other observed facts in the field. Tart [4] utilized the aerial photos captured from the landslide area and presumed that the western part of the ancient landslide bench had been the initiation zone of the landslide. The theory is in contrast with the observations and findings by Stark et al. [2] which introduced the eastern part of the ancient landslide bench as the initiation zone of the landslide. Stark et al. [2], based on their findings from the field observations and 2D limit equilibrium analyses, proposed a two-phase failure mechanism for the landslide. They identified the eastern part of the ancient landslide bench, which had the smallest width, as the initiation location of the landslide. Yerro et al. [5] performed an investigation on the runout of the Oso 2014 landslide using the material point method (MPM). They described this landslide by two primary stages and suggested that the initiation stage had been the mobilization of the soil materials in the middle of the slope.

As can be inferred from above, despite some differences, the majority of the previous studies on Oso 2014 landslide accept a two-phase mechanism for the failure of the slope. However, there is no consensus on the initiation location of the landslide. In addition, all the conducted studies have neglected the complex 3D topography of the landslide area. The factor which seems to have played a significant role in the initiation of the landslide, due to the presence of the ancient landslide bench.

This study aims at revealing the roles of the 3D effect and impact of the timber harvested area at the north side of the bench in the initiation of Oso 2014 landslide. For this purpose, the complex topography of the affected area was considered in a 3D setting. A combination of limit equilibrium (LE) and finite element (FE) methods were utilized to assess the effect of excessive rainfall infiltration due to the elimination

of vegetation on the stability of the landslide slope. Also, employing 3D LE analyses, the role of groundwater table elevation in the landslide initiation was investigated.

## 2 Rainfall Infiltration—Effect of Harvested Area

According to Cao et al. [6] and Henn et al. [7], there has been an extremely wet period of 403 mm rainfall in 21 days preceding the landslide event. They claim that this rate of precipitation makes this period the wettest in the recorded history of the region. Also, the aerial photos of the landslide region show the presence of a timber harvested area (about 7.5 acres) on the eastern corner of the upper plateau (see Fig. 1). The conducted procedure for evaluating the effect of the heavy rainfall period in conjunction with the presence of the harvested area is delineated in the following.

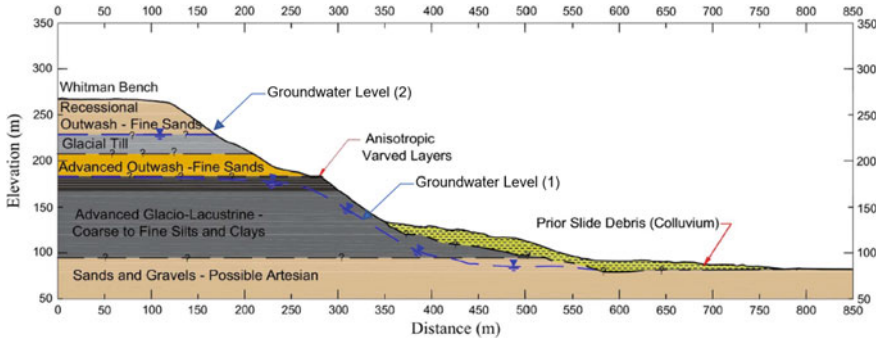
### 2.1 Infiltration Modeling

To model the rainfall infiltration effect on the initiation of the landslide, RS3 software package [8], provided by Rocscience, is deployed. RS3 is a 3D software package able to perform deformation and stress analyses via FE numerical method. The complex topography of the landslide slope and the neighboring area is incorporated into the modeling using the data extracted from LiDAR photography of pre-landslide



**Fig. 1** Timber harvested area on the eastern corner of the 2014 Oso landslide's upper plateau (Image by Gordon Farquharson, University of Washington)





**Fig. 2** 2014 Oso landslide cross section and two potential groundwater levels by Stark et al. [2] inferred from inverse stability analyses and field observations

conditions. Also, the geotechnical profile of the slope, including the thickness of soil layers and the corresponding hydraulic parameters, is implemented using the investigations performed by Stark et al. [2]. Figure 2 illustrates the geotechnical profile of the landslide slope that is considered in the analyses. A horizontal layering was assumed for the geotechnical profile of the area, as a result of the observations made by Stark et al. [2] from the near-vertical landslide head scarp.

Due to the lack of groundwater monitoring prior to the landslide, two potential groundwater levels are assumed by Stark et al. [2], shown by Fig. 2. The study of rainfall infiltration should be addressed by performing transient seepage analysis which requires specification of volumetric water content function for each of the ground materials. This function can be either calculated using laboratory tests or estimated by closed-form solutions and predictive methods. Herein, the volumetric water content function of soil layers was estimated using the van Genuchten method [9] as a closed-form solution. Van Genuchten model parameters were selected based on the type of the materials according to the Vogel et al. [10] study. Table 1 summarizes the hydromechanical parameters used in the present study for modeling the rainfall infiltration including hydraulic saturated conductivity ( $K_{sat}$ ), coefficient of volume compressibility ( $M_v$ ), saturated water content ( $W_{sat}$ ), and residual water content ( $W_{res}$ ).

**Table 1** Materials’ hydraulic parameters for rainfall infiltration analysis

Material type	$K$ (m/day)	$M_v$ (1/kPa)	$\omega_{sat}$	$\omega_{res}$
Recessional outwash	7.200	0.0001	0.43	0.045
Glacial till	0.005	0.0010	0.38	0.070
Advanced outwash	3.500	0.0002	0.43	0.057
Advanced varved glaciolacustrine (low plasticity)	0.315	0.0002	0.39	0.100
Advanced glaciolacustrine (high plasticity)	0.005	0.0002	0.36	0.070
Sands and gravels	7.200	0.0001	0.43	0.045

Regarding the vegetation type in the area along with the hydraulic conductivity of the surficial ground layer, an average infiltration rate equal to 0.6 cm/day was assumed based on the rate of precipitation within the 21 days prior to the landslide. Also, to assess the impact of the timber harvested area, a variety of average infiltration rates from 0.6 to 8 cm/day was allocated to the surface of the harvested area. For modeling the steady-state condition prior to the heavy rainfall, the groundwater table with the lower elevation, shown in Fig. 2, was introduced to the seepage analysis model. The lower groundwater level was selected due to its greater compatibility with the slope’s topography. Then, by running the analysis for 21 days, net pore water pressure was calculated from the combination of the groundwater table and extracted rainfall infiltration from the model. These net pore water pressures were used to assess the effect of rainfall infiltration on the stability of the slope using 3D LE slope stability analyses.

### 2.2 Slope Stability Analyses for Rainfall Infiltration

The effect of rainfall infiltration in conjunction with the presence of harvested area on the stability of Oso landslide slope is captured through 3D LE slope stability analyses. Slide3 software package [11] as a 3D modeling and analysis tool is utilized for this purpose. Table 2 shows shear strength parameters and density of the soil layers depicted in Fig. 2, reported by Stark et al. [2]. The net pore water pressure grids, which are computed by RS3 seepage analyses for different infiltration rates, are introduced to Slide3 slope stability models.

The 3D critical slip surfaces were determined by particle swarm optimization (PSO) method [12] along with the observations of Stark et al. [2] from the landslide’s site. Contrary to many other existing methods, the sliding direction is not pre-defined

**Table 2** Material properties for the slope of 2014 Oso landslide [2]

Material type	Unit weight (kN/m <sup>3</sup> )	Peak friction angle (°)	Range of friction angle (°) <sup>a</sup>
Recessional outwash	20	28	–
Glacial till	20	35	–
Advanced outwash	19	30	–
Advanced varved glaciolacustrine (low plasticity)	20	–	25–34
Advanced glaciolacustrine (high plasticity)	20	–	21–35
Sands and gravels	19	35	–

<sup>a</sup>For the fully softened stress-dependent envelope from torsional ring shear tests

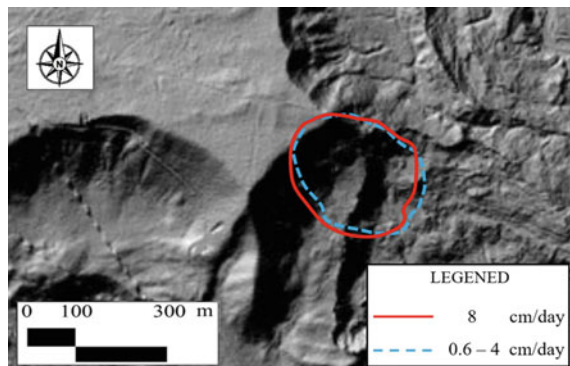
in Slide3, an advantage that eliminates potential bias around the critical slip surface selection.

Spencer slope stability method was employed for safety factor calculations of the slip surfaces affected by rainfall infiltration. This slope stability method satisfies all the moment and force equilibrium equations and is recommended for non-circular slip surfaces [13]. The “ellipsoidal” shape was assumed for the geometry of slip surfaces with respect to the anisotropic nature of the soil layers observed in this landslide.

### 2.3 Results of Rainfall Infiltration Effect Modeling

As a result of the 3D slope stability methodology described above, the critical slip surfaces were obtained corresponding to each of the rainfall infiltration rates on the harvested area. It was observed that increasing the rate of rainfall infiltration leads to a decreasing trend for the safety factor of the critical slip surface located on the eastern part of the ancient landslide bench. Figure 3 depicts the position of the computed slip surfaces regarding the rate of infiltration. As can be seen, the shape of the critical slip surface remains constant by increasing the amount of infiltration rate from 0.6 to 4 cm/day. However, increasing this rate from 4 to 8 cm/day slightly affects the geometry of the critical slip surface. The main finding of this figure is the location of the initial slide of the 2014 Oso landslide. In all of the cases, the eastern part of the ancient landslide bench in which the width is the narrowest is the initiation zone of the landslide. In fact, the variation of rainfall infiltration does not affect the initiation location of the landslide. The computed safety factors for each of these scenarios are reported in Table 3. It shows that the safety factor of the critical slip surface is not considerably varying by increasing infiltration rate from 0.6 to 4 cm/day, but a drastic reduction in safety factor from 1.08 to 1.00 can be expected when the infiltration rate changes from 4 to 8 cm/day.

**Fig. 3** Critical slip surface position of 2014 Oso landslide initial slide for different rainfall infiltration rates in the harvested area on 2013 LiDAR image of the area



**Table 3** Computed safety factor for different rainfall infiltration rates in the harvested area

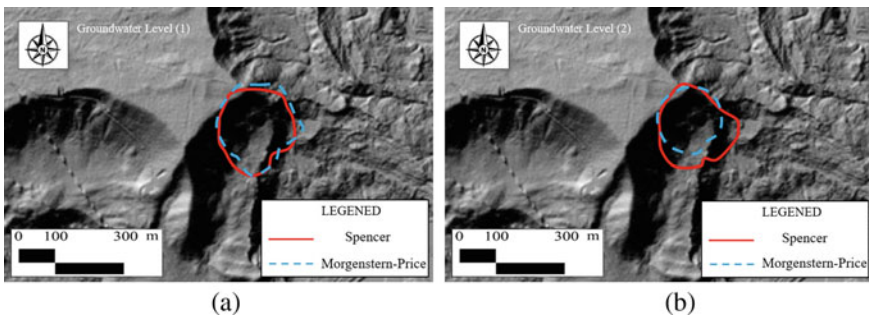
Case number	Infiltration rate (cm/day)	Stability analysis method	Safety factor
1	0.6	Spencer	1.08
2	2.0	Spencer	1.07
3	4.0	Spencer	1.07
4	8.0	Spencer	1.00

### 3 Groundwater Level Effect

To examine the impact of groundwater level on the initiation phase of the 2014 Oso landslide, two different levels for the existing groundwater were considered (see Fig. 2). LE slope stability analyses were performed for each of these two groundwater levels using the Slide3 software package. Accordingly, the PSO method was utilized for searching the critical slip surfaces in 3D conditions. Safety factor of critical slip surfaces was computed by Spencer and Morgenstern–Price methods. All the assumptions for the groundwater level effect study regarding the pre-landslide topography, stratigraphy, geotechnical properties, and slip surface shape followed the assumptions in the analyses conducted for the rainfall infiltration investigation. Figure 4 illustrates the plan view of the computed critical slip surfaces for groundwater levels of (1) and (2) on the LiDAR image of the landslide area with respect to the method of analysis.

This figure implies that the location of the initiation phase of the landslide does not depend on the level of groundwater prior to the landslide. In fact, all the computed critical slip surfaces using different slope stability analysis methods for the two groundwater level cases are formed around the eastern portion of the ancient landslide bench. Table 4 summarizes the safety factor calculated for each of the critical slip surfaces according to the level of groundwater and the method of analysis.

According to the results, elevating the groundwater table from level (1) to level (2), shown by Fig. 2, has led to a 2% decrease in the average safety factor of the



**Fig. 4** Critical slip surface position of 2014 Oso landslide initial slide for different analysis method: **a** groundwater level (1), **b** groundwater level (2)

**Table 4** Computed safety factor for different groundwater levels and analysis methods

Case number	Groundwater level	Stability analysis method	Safety factor
1	(1)	Spencer	1.08
2	(1)	Morgenstern–Price	1.10
3	(2)	Spencer	1.07
4	(2)	Morgenstern–Price	1.07

critical slip surfaces (i.e., from 1.09 to 1.07). Thus, given the assumed geotechnical and topographical characteristics for the slope, groundwater elevation change has had a minor impact on the stability of the landslide slope which implies that the initiation of the 2014 Oso landslide cannot be directly originated from a rise in the groundwater table.

## 4 Conclusion

In this study, the effects of water infiltration, due to a heavy rainfall period prior to the landslide, complex 3D geometry, and change in groundwater level on the initiation of Oso 2014 landslide, were investigated. In addition, the presence of a timber harvested area on the upper plateau of the landslide slope was taken into consideration. For these purposes, a combination of 3D FE seepage analyses and 3D LE slope stability analyses were performed. It was shown that an average infiltration rate of 8 cm/day in the harvested area could have adversely affected the stability of the slope by decreasing its safety factor from about 1.08 to one. In addition, the difference in calculated safety factors of critical slip surfaces for the two assumed groundwater levels was very small. Therefore, it can be inferred that the initiation of 2014 Oso landslide could not have been originated from such assumed change in groundwater elevation. The impacts of other triggering factors such as rainfall infiltration and the consequent shear strength loss of upper layers, timber harvesting, and/or 3D slope geometry effects might have been more influential in the initiation of the landslide.

**Acknowledgements** The authors would like to thank RocScience Inc for providing the RS3 and SLIDE3 software packages to perform study and their technical support.

## References

1. Keaton JR, Keaton JR, Wartman J, Anderson S, Benoît J, de La Chapelle J, Gilbert R, Montgomery DR (2014) The 22 March 2014 Oso Landslide, Snohomish County, Washington. Geotechnical Extreme Event Reconnaissance Association Report GEER-036

2. Stark TD, Baghdady A, Hungr O, Aaron J (2017) Case study: Oso landslide on 22 March 2014—material properties and failure mechanism. *J Geotech Geo-environ Eng* 143(5). [https://doi.org/10.1061/\(ASCE\)GT.1943-5606.0001615](https://doi.org/10.1061/(ASCE)GT.1943-5606.0001615)
3. Iverson RM, George DL, Allstadt K, Reid ME, Collins BD, Vallance JW, Schilling SP, Godt JW, Cannon CM, Magirl CS, Baum RL, Coe JA, Schulz WH, Bower JB (2015) Landslide mobility and hazards: implications of the 2014 Oso disaster. *Earth Planetary Sci Lett* 412(1):197–208
4. Tart RG (2016) Why the Oso landslide caused so much death and destruction. In: *Proceedings of 2016 geotechnical and structural engineering congress*, ASCE, Reston, VA, pp 1545–1554
5. Yerro A, Soga K, Bray J (2017) Runout evaluation of the Oso landslide with the material point method. In: *JTC1 Workshop on Advances in Landslide Understanding*, Barcelona, Spain
6. Cao Q, Henn B, Lettenmaier DP (2014) Analysis of local precipitation accumulation return periods preceding the 2014 Oso mudslide. Department of Civil and Environmental Engineering, University of Washington, Seattle
7. Henn B, Qian C, Lettenmaier D, Magirl C, Mass C, Bower JB, Laurent M, Mao Y, Perica S (2015) Hydroclimatic conditions preceding the March 2014 Oso landslide”. *J Hydrometeorol* 16(3):1243–1249
8. RocScience, RS3, RocScience Inc., Toronto, Canada (2019)
9. van Genuchten MTh (1980) A closed form equation for predicting the hydraulic conductivity of unsaturated soils. *Soil Sci Soc Am J* 44:892–898
10. Vogel T, van Genuchten MT, Cislérova M (2001) Effect of the shape of the soil hydraulic functions near saturation on variably saturated flow predictions. *Adv Water Resour* 24:133–144
11. RocScience, SLIDE3, RocScience Inc., Toronto, Canada (2019)
12. Hajihassani M, Armaghani DJ, Kalatehjari R (2018) Applications of particle swarm optimization in geotechnical engineering: a comprehensive review. *Geotech Geol Eng* 36:705–722
13. Spencer E (1967) A method of analysis of the stability of embankments assuming parallel inter-slice forces. *Geotechnique* 17(1):11–26

# Evaluating the Performance Benefits for Low-Volume Roadways Constructed with Geosynthetic Wicking Fabrics: A Case Study in Northern New England



Mohamed Elshaer and Christopher Decarlo

**Abstract** One of the most challenging issues transportation managers face is maintaining the condition of low-volume roadways during and immediately following wet weather events, such as heavy rainfall and the spring time thaw period. Specifically, high moisture contents in the road base and subgrade weakens the overall structure, causing excessive rutting and structural damage, leading to costly repairs, load restrictions, and/or closures. The main objective of this study is to evaluate the impact on structural performance of low-volume roadways constructed with geosynthetic wicking fabrics, which are designed to act as both a drain to move water out of the pavement structure as well as a moisture barrier to prevent a capillary rise in the unbound layers of the roadway. A low-volume roadway in Northern New England was constructed where a Mirafi® H2Ri wicking fabric was installed in the subgrade layer of the pavement. The pavement section was instrumented with moisture and temperature sensors at different depths to monitor the effect the fabric had on the moisture content of the subgrade. The data, collected and monitored over a period of one year, was then used to predict the stiffness of subgrade layer. The layered elastic analysis was used to predict the rutting performance of the pavement section. These performance predictions were then compared to the previously unmodified section with no fabric installed. Ultimately, the results showed significant improvements in the rutting resistance of the pavement structure with the fabric compared to the unmodified section, particularly during the spring time thaw period due to the improved drainage capability the fabric provides. The findings from this study suggest that geosynthetic wicking fabrics offer significant advantages when installing in roadways to prevent damage during the spring time thaw period in cold regions and could be a useful tool for transportation managers with low-volume roadway networks as well as adapted in pavement design practice.

**Keywords** Low-volume roadway · Unsurfaced roadway · Wicking fabric · Spring time thaw · Structural performance

---

M. Elshaer (✉) · C. Decarlo

Cold Regions Research and Engineering Laboratory (CRREL), US Army Engineer Research and Development Center (ERDC), US Army Corps of Engineers, Hanover, NH 03755, USA  
e-mail: [mohamed.h.elshaer@erdc.dren.mil](mailto:mohamed.h.elshaer@erdc.dren.mil)

## 1 Introduction

A common challenging issue that transportation managers face in cold regions is maintaining the condition of roadways during and immediately following the time of extreme wet weather. For example, extreme changes in moisture content within a pavement structure during the spring thaw period, elevated groundwater table levels, or periods of heavy rainfall, can result in reduced structural performance of the road [1, 2]. In extreme cases, these problems can require measures such as load restrictions or even temporary road closure to be taken to prevent distress formation and excessive damage to the pavement structure. Therefore, solutions are needed to protect pavements experiencing frequent periods of high moisture levels and other environmental issues.

Different approaches can be implemented to maintain the roadway strength during challenging environmental conditions (e.g., spring thaw period) such as (1) load restrictions; (2) replace frost susceptible soils with unsusceptible soils; (3) place a coarse-grained soil as a capillary barrier above the groundwater table; and (4) provide new and innovative materials to protect the unbound layers from excessive moisture content. Most of these methods are expensive and labor-intensive and have not been able to consistently prevent spring load restriction or closure of the road [3]. Consequently, many agencies and researchers started to investigate a different type of material such as geotextile as an alternative solution to mitigate freeze–thaw weakening and excess moisture issues.

One of these new, promising methods is constructing pavements with geosynthetic wicking fabrics. Wicking fabrics are geosynthetics with asymmetric properties. In the longitudinal direction (parallel to the road), the fibers are closed. In the transverse direction, however, the fibers are perforated and hollow to allow the capillary movement of moisture through the fabric. When placed in a pavement structure, the fabric acts in two main ways. First, it allows water migrating down from the surface to drain away to the sides of the roadway where it will not affect the pavement structure. Second, the fabric acts as a moisture barrier to water below, preventing capillary rise from moving moisture from groundwater into the upper layers of the pavements. Combining both of these effects prevent excess buildup of moisture in the pavement, making the structure much more resilient during times of wet weather and the spring thaw time through its improved drainage capacity. The use of wicking fabrics in pavements has been demonstrated with success in a number of sites in the USA.

Perhaps the most profound example of wicking fabric success is that reported by Zhang and Presler [4] where wicking fabrics were installed to prevent frost boils/soft spots in the Dalton highway Beaver Slides area in Alaska, just south of the Arctic Circle. The issue with this road was the shallow groundwater flows each spring downslope and into road embankment causing frost boils and consequently road damage and accidents on the road. The performance of wicking fabric was monitored under different climatic conditions such as rainfall events, freezing,



and thawing processes. The first 2 years of monitoring indicated good overall performance, and remarkable road surface difference was observed between the test section and sections with and without wicking fabric. The authors reported that H2Ri wicking fabric successfully eliminated frost heave and thaw weakening in the first 3.5 ft below the road surface and the soil never reached full saturation. Interestingly, soils below the wicking fabric layer indicated high moisture content and frost heave movement at times, but this had no effect on the performance of the road. The authors concluded that H2Ri wicking fabric is an excellent material for transporting water from the road structure and improving pavement performance.

In this study, an instrumented test section with a H2Ri wicking fabric was constructed in Hartland, Vermont. The site chosen for the section, located at a dam facility managed by the US Army Corps of Engineers, is a gravel surfaced low-volume access road primarily used to transport vehicles and equipment down to the dam facilities. The roadway is located in a shallow cut forming a small valley that the road passes through. The general climate of the site is a typical New England wet-freeze climate where below freezing temperatures are present from late November through early April. The primary reason this site was chosen for the installation and monitoring of the wicking fabric was due to the challenges with using this roadway during the spring thaw period. Typically, the structural integrity of the road was compromised to the point where a single vehicle pass would cause excessive rutting on the surface of the roadway. Because of this, it was decided that this roadway would serve as an ideal test section to investigate the effects of adding wicking fabric to the subsurface layers of the pavement.

This paper presents a method to quantify the structural performance gained from placing the wicking fabric on unsurfaced pavements. The resilient modulus of the unsaturated soil layer was determined based on the measured moisture content. The layered elastic approach was used to predict the vertical compressive strains at the top of subgrade layer and is translated to pavement damage using the transfer function to evaluate the impact of wicking fabric application on the overall pavement performance. A case study is presented to demonstrate the application of the method. The proposed study will give an insight into the performance of unsurfaced low-volume roads due to the wicking fabric application.

## **2 Methodology**

### ***2.1 Site Description***

The construction of the test section was conducted in September of 2017. To start, a total section length of 120 ft. was marked off for the fabric installation. Over the length of this section, the existing roadway was excavated down to a depth of 1 ft. The existing roadway was composed of a thin, 1 in. gravel layer above-compacted

natural subgrade. During the excavation, both layers were kept separate and sampled for further laboratory characterization as described in the following section.

After the excavation, the first array of four Campbell CS650 moisture/temperature sensors was installed in dug pits at a depth of 1.5 ft, slightly higher than the groundwater table. Each sensor was placed approximately every 30 ft. throughout the test section. Next, the wicking fabric was installed upon the excavated roadway.

One point worth noting is that in this study, the wicking fabric was not installed in a conventional manner. The typical installation for the wicking fabrics is for the fabrics to be rolled out parallel to the roadway, so that the moisture-wicking direction is transverse to the travel direction. The intention of this is to drain excess moisture into drainage ditches along the road. Construction of the test section in this manner was not feasible as the existing roadway did not have adequate drainage structures as it was constructed in a narrow cut. To address this, the fabrics were installed in a manner that wicks moisture parallel to the roadway surface by cutting the fabrics into 12 ft. long sheets and rotating them 90° upon installation. These fabric sections were then installed in layers (similar to how shingles are installed) to continuously wick the moisture down the roadway, taking advantage of the natural slope the roadway is built upon. Upon reaching the end of the test section, adequate drainage structures were available as the narrow cuts end here. At this point, the fabric was installed in a conventional manner so move excess moisture to the sides of the roadway into the existing drains. This modified installation and conventional installation can be seen in Fig. 1.

Upon finishing the fabric installation, a 6 in. layer of subgrade was placed back onto the roadway surface and compacted to previous density levels. The second array of Campbell CS650 moisture/temperature sensors were installed in this prepared surface. Lastly, the final 6 in. of subgrade and 1 in. gravel layer was placed back onto the roadway surface and compacted to finish the test section.

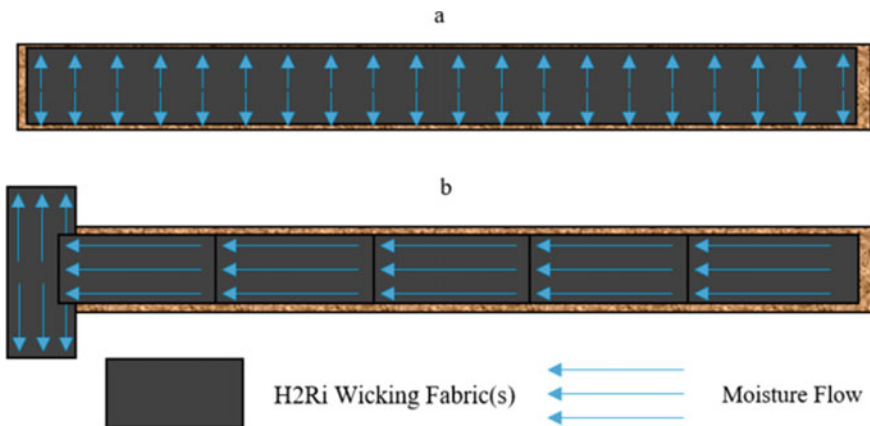


Fig. 1 Conventional wicking fabric installation (a), compared to installation used in this study (b)

## 2.2 Material Characterization

Particle size analysis and Atterberg limits tests were conducted on the subgrade soil samples collected from the field during the construction. Figure 2 shows the particle size distribution curve of the presented soil. Based on these results, the soil was classified as a A-1-b according to AASHTO classification system. In addition, a Proctor test was conducted to determine the optimum moisture content ( $W_{opt}$ ) and maximum dry density of the soil. Also, the in-situ density of soil was determined by the drive-cylinder method. Table 1 shows the physical properties of the presented subgrade soil.

The soil-water characteristic curve (SWCC) proposed by [5] available in the enhanced integrated climate model (EICM) was used to predict the degree of saturation from soil suction. SWCC is essential to determine the potential benefits of the wicking fabric [5]. For effective drainage of the wicking fabric, the suction in the fabric has to be greater than the suction in the soil. Connor et al. (2016) found that if the suction of the soil exceeds 200 kPa, the air can enter and block the microchannels in the wicking fabric, causing the wicking fabric to stop working as a drainage material for soils under unsaturated conditions [6]. Thus, SWCC curve was generated to determine the effectiveness of wicking fabric in draining the water. The matric suction is zero for saturated soils, while a hydrostatic capillary suction was calculated based on the depth to the water table approach [7]. Figure 3 exhibits the predicted SWCC for the presented soil layer plotted as the relationship between the degree of saturation ( $S_r$ ) and matric suction ( $u_a - u_w$ ) using the Fredlund and Xing and Perera's correlation models. As can be seen in the figure, the air entry value for this soil is 0.70 kPa. That means the soil displays unsaturated conditions rather than full saturation condition if the matric suction is beyond 0.70 kPa. As expected, the degree of

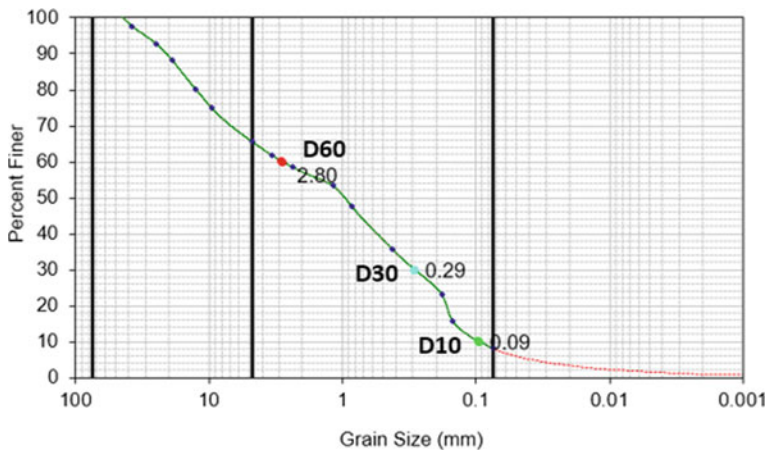


Fig. 2 Particle size distribution curve of the site soil

**Table 1** Physical properties of site soil

Soil type	P#200	D60 (mm)	PI	% of gravel	% of sand	% of fines	$W_{opt}$ %	In-situ dry density (kg/m <sup>3</sup> )	Gs	Max laboratory dry density (kg/m <sup>3</sup> )	porosity
A-1-b	8	2.80	NP	34.4	57.5	8.1	8.5	1876	2.65	1995	0.32

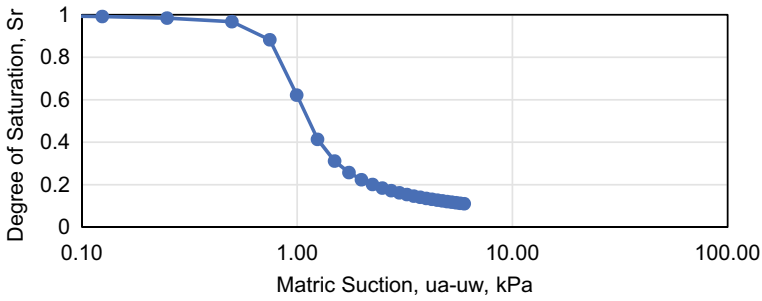


Fig. 3 Predicted SWCC for the presented soil

saturation decreases as the matric suction increases. Based on Conner et al. findings, the wicking fabric has no issue of draining the water for the presented soil.

To determine the structural performance of the roadway constructed with wicking fabric, the resilient modulus of subgrade soil at different moisture conditions must be determined. A forensic investigation was conducted to measure the in-situ resilient modulus of the unsurfaced pavement layers. The dynamic cone penetrometer (DCP) test was conducted in the field on the gravel and soil layers to provide a measure of in-situ resistance to penetration. The in-situ resilient modulus of pavement layers was indirectly calculated based on the DCP measurements as presented in Eq. 1. Then, this calculated resilient modulus was adjusted at different degrees of saturation using the Witczak model in EICM [7] as presented in Eq. 2 given the optimum moisture content and the corresponding degree of saturation.

$$M_{r\text{opt}} = 2555 \left[ \frac{292}{\text{DCP}^{1.12}} \right]^{0.64} \tag{1}$$

$$\log \frac{M_r}{M_{r\text{opt}}} = a + \frac{b - a}{1 + \exp\left[\ln \frac{-b}{a} + k_m (S - S_{\text{opt}})\right]} \tag{2}$$

where  $M_{r\text{opt}}$  the resilient modulus at a reference condition (psi), DCP is in mm/blow  $M_r/M_{r\text{opt}}$  is the resilient modulus ratio;  $M_r$  the resilient modulus at any degree of saturation;  $a$  the minimum of  $\log M_r/M_{r\text{opt}}$ ;  $b$  the maximum of  $\log M_r/M_{r\text{opt}}$ ;  $k_m$  the regression parameter; and  $S - S_{\text{opt}}$  the variation in degree of saturation expressed in decimals. Using the available data from the literature and assuming a maximum modulus ratio of 2.5 for fine-grained materials and 2 for coarse-grained materials, the values of  $a$ ,  $b$ , and  $k_m$  for coarse-grained are  $-0.3123$ ,  $0.3$ , and  $6.8157$ , respectively [7].

### 2.3 Linear Elastic Analysis Method

Layer elastic analysis using KENLAYER software was performed using the adjusted resilient modulus from the measured moisture content over time to calculate the vertical stress and strain on the subgrade layer. Layer elastic analysis was performed for two scenarios (i.e., before and after installing H2Ri wicking fabric) to determine the impact of wicking fabric on the pavement response. The difference between the two scenarios is treating the subgrade layer in terms of the depth and moisture conditions as shown in Fig. 4. For instance, the road was modeled before the wicking fabric installation as one fully saturated gravel layer and one fully saturated subgrade layer on top of the bedrock layer. This was done because prior to the installation, the roadway section was inundated; fully saturated (water observed on top of the surface) from the spring thaw until re-freeze in December.

On the other hand, after wicking fabric placement, the subgrade layer was divided into two sublayers from the top of the subgrade to the bedrock based on the TDR location depths (i.e., TDRs fell in the middle of sublayers) as separation by wicking fabric layer [8]. As mentioned, two TDR sensors were installed at each station of the road at depths 6 and 18 in. Thus, two sublayers (12 in. each) were modeled in the layer elastic analysis using the computed resilient modulus from Eq. 3. The resilient modulus of the surface gravel layer was indirectly calculated from the DCP measurements (DPI of 6 mm/blow) as shown in Fig. 4. In this study, the resilient modulus of the fully saturated materials was not measured before wicking fabric placement due to the fact that the site was inundated. Thus, the resilient modulus at full saturation conditions (before wicking fabric placement) were considered to be half the optimum moisture content value according to MEPDG [9]. The depth to the bedrock was shallow (measured to be 25 in. from the surface) and the modulus assumed to be 250,000 psi based on the Cornell typical values.

To investigate the effects on structural performance, two-vehicle loads were chosen. First, a standard 18 kip highway axle load was chosen as an extreme case with high loads and tire pressures, while a more representative load for unsurfaced

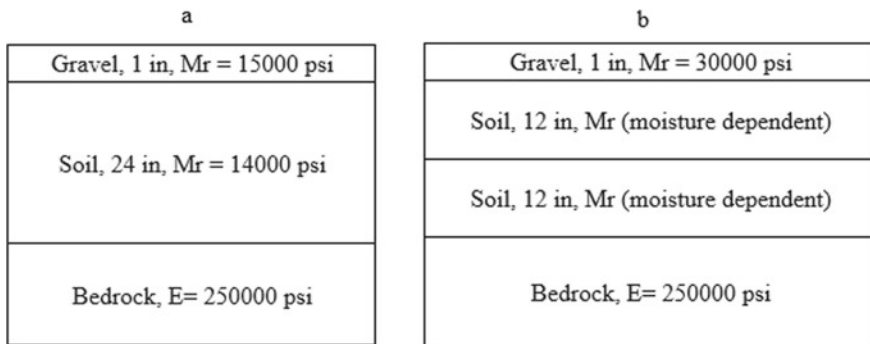


Fig. 4 Pavement cross section **a** before wicking fabric, **b** after wicking fabric

roadways was represented by the heavy expanded mobility tactical truck (HEMTT) which has lower loads and tire pressures. Specifically, a tire load of 9000 lb (40 kN) and 120 psi (0.827 MPa) tire pressure were used for standard highway axle, while a load of 7760 lb (35 kN) and 55 psi (0.379 MPa) were used for HEMTT. Trucks were modeled in the KENLAYER software, and the maximum vertical strains on the subgrade surface under each loading were used for rutting analysis. The vertical strains were used to calculate the number of equivalent single axle loads (ESAL) to rutting failure using this transfer function [10]:

$$\epsilon_z = 0.0058 \times N^{-0.171} \tag{3}$$

where:  $\epsilon_z$  = vertical compressive strain over subgrade;  $N$  = number of standard axle load repartitions leasng to failure (ESAL).

### 3 Results and Discussions

#### 3.1 Analysis of Measured Temperature and Moisture Content Data

Figure 5a, b shows the measured moisture content and temperature above and below the fabric over the course of a year for the two stations in the test section, one being

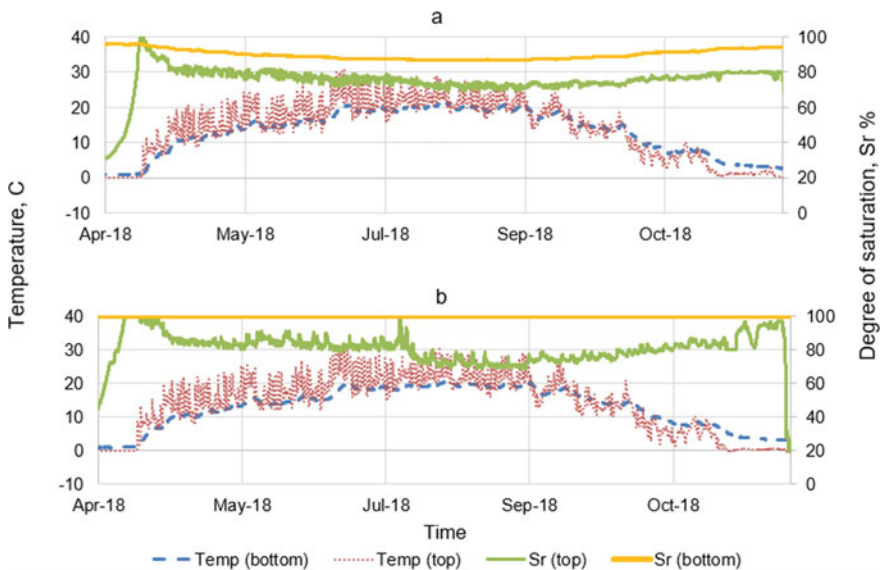


Fig. 5 Monitored temperature and degree of saturation at the a middle station b last station

in the middle and one at the end of the section. The reason these two locations are shown is that the middle point is representative of the majority of the fabric section, whereas the last point is different due to the unconventional construction as described previously.

Looking at the temperature readings for both locations, it is apparent that the temperature of the soil beneath the fabric did not freeze during the course of the year, which is surprising considering typical frost depths for this area are far deeper than 1.5 ft. where the sensors were installed. A likely explanation for this observation is that the road was not subject to winter plowing, and roads with snow cover (serving as an insulating layer) do not undergo significant freezing. This applies to any condition; a late snowfall year or a minimal snow depth. Another explanation could be because of the high groundwater table, which was found to be about 1.75 ft. from the surface during construction, and the natural slope of the roadway preventing the water from freezing.

Looking at the moisture readings in the middle of the section, Fig. 5a. shows that the wicking fabric reduced the degree of saturation of the soil down to 72% above the fabric and 90% below the fabric during the summer months compared to the 100% saturation of the unmodified roadway. In addition, it can be seen during the spring thaw period that the fabric rapidly drained moisture from the top soil layers where the degree of saturation was lowered by 25% in about one week, whereas minimal reduction in saturation was seen in the bottom layer, likely due to the elevated groundwater table. These results suggest that the wicking fabric is draining water from both above and below the fabric throughout the year, where the effect above the fabric is more pronounced.

On the other hand, Fig. 5b. shows different trends with regards to the moisture levels at the point at the end of the section. It should be noted that this point is located both at bottom of the slope the roadway is on and where the last fabric (which all of the other fabrics were draining toward) as placed. In this case, the fabric reduced the saturation levels above the fabric to 86% during the spring and 68% during the summer. Similar to the previous point, there was a sharp decline in the saturation of about 20% during the spring thaw period due to the effects of the fabric. Interestingly, there was no observed effect on the soil beneath the fabric. In this case, it appears that the fabric is only working to drain water from the soil above, perhaps because the fabric is being “overloaded” with water at the bottom of the slope, preventing it from having its intended effect.

Considering the results presented at these two points, it is apparent that the fabric had a significant impact on reducing the moisture content in the soil layers above it, where reductions in saturation were as high as 32% (i.e., the subgrade saturation reached to the optimum moisture content level). On the other hand, both points showed differing results for the soil beneath the fabric where the middle point (which was representative for the majority of the section) reduced the saturation while the point at the bottom of the section saw no change. As mentioned, this is potentially due to the continuous drainage of the moisture to this location in addition to the high groundwater table, thus overloading the fabrics drainage capacity at this location (i.e., the end of the test section).



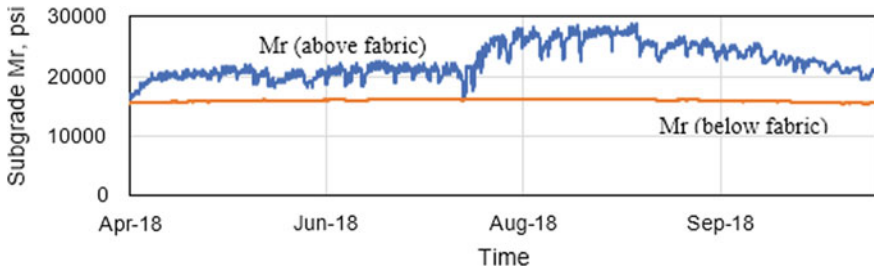


Fig. 6 Resilient modulus of two subgrade sublayers for the last station of the road

### 3.2 Resilient Modulus Prediction

The comparison between the resilient modulus at fully saturated condition (bottom layer) and different unsaturated moisture conditions (top layer) for the last station (i.e., drainage station) on the road over a year is shown in Fig. 6. As can be seen in the figure, there is a 25–45% increase in the subgrade resilient modulus due to a reduction in the moisture content on the upper subgrade layer. This indicates that fabric indirectly improved the stiffness of the subgrade layer.

### 3.3 Pavement Rutting Analysis

Table 2 shows the rutting life predictions of two different vehicle loads (standard 18 kip highway axle and HEMTT) for both the unmodified roadway and the fabric-enhanced roadway at various times of the year, which represent a variety of moisture states in the subgrade. For the purposes of this paper, the rutting performance is quantified in ESALs required for failure. Looking at the results, it can be seen that the presence of the fabric has a significant positive effect on rutting life where a 66.50 times increase of the ESAL for single axle single tire and 79.24 times increase for HEMTT truck type are observed during the summer. The improvement in performance during the other two seasons ranges from 52.50 to 69.51 times depending on the timeframe and load level. The results of the unmodified section agree with the

Table 2 Number of ESALs leading to rutting failure under different truck types

	18 Kip highway-ESAL to failure			HEMTT-ESAL to failure		
	Unmodified	Wicking fabric	Times increase	Unmodified	Wicking fabric	Times increase
Spring	2	105	52.50	263	17,323	65.87
Summer	2	133	66.50	263	20,840	79.24
Fall	2	113	56.50	263	18,280	69.51

site observations before wicking fabric placement where a single vehicle pass would cause excessive rutting on the surface of the roadway. The findings show that the standard single axle single tire is the critical truck type for rutting performance in the unsurfaced pavement structure under saturated conditions. The results indicate that the wicking fabric significantly improved the rutting performance of this unsurfaced roadway regardless of the load type.

It is worth noting that this analysis was conducted in a worst-case scenario where the unmodified roadway was fully saturated. As mentioned previously, this is based on observations from before the fabric was installed. Note that the estimated ESALs after wicking fabric installation were based on the MNDOT empirical transfer function, which could be different in reality. Thus, field validation of the estimated ESALs is still needed to better quantify the rutting life expectancy.

## 4 Summary and Conclusions

Unsurfaced pavements are vulnerable to moisture damage due to the large fluctuations of the moisture content in the subgrade soil which can negatively impact the performance of pavements by influencing the stiffness of the subgrade layer. Wicking fabric application is one of the new innovative methods used to reduce the moisture in the subgrade soil. A method to investigate the impact of wicking fabric on the rutting performance of the road was described in this paper and was demonstrated using a case study in Hartland, Vermont. The monitored moisture contents were used to predict the unsaturated resilient modulus of the subgrade over a year. Matric suction of the soil was predicted from the hydrostatic pressure distribution to evaluate the capability of the wicking fiber to drain the water. The layered elastic approach was conducted using the resilient modulus of the subgrade to determine the impact on the pavement performance after the fabric was installed. The results indicated that the wicking fabric had successfully eliminated the excessive moisture on the site. The conclusions that can be drawn based on the observations from the case study are as follows:

- (1) The monitoring data showed that the moisture contents of the subgrade layer were decreasing after the fabric was installed and did not exceed the full saturation condition for the layer below the fabric at all the road stations except the last station. In addition, a significant reduction in the saturation of the layer above the fabric was observed (i.e., the subgrade saturation reached the optimum moisture content level and up to 10% above the optimum moisture content). This indicates that the wicking fabric had a greater permeability and succeeded to eliminate the negative impact of the thaw weakening issue on the pavements.
- (2) A significant increase in the stiffness of the subgrade was encountered after the fabric was installed (25–45% increase in the subgrade resilient modulus) due to the reduction in the moisture contents.

- (3) A significant increase in the number of load repetitions to rutting failures was observed regardless of the truck type after the fabric was installed.

The use of this study will give an insight into the performance of low-volume pavements after the wicking fabric is installed and can be adapted to reduce the load restriction on the road during spring thaw time or wet areas. Future work will investigate the long-term performance of the wicking fabric and its impact on pavement performance.

## References

1. Zhang Z, Wu Z, Martinez M, Gaspard K (2008) Pavement structures damage caused by Hurricane Katrina flooding. *J Geotech Geoenviron Eng* 134(5):633–643
2. Elshaer M, Ghayoomi M, Daniel JS (2019) Impact of subsurface water on structural performance of inundated flexible pavements. *Int J Pavement Eng* 20(8):947–957
3. Holtz RD, Kovacs WD (1981) *An introduction to geotechnical engineering*. Prentice Hall, Englewood Cliffs, NJ
4. Zhang X, Presler W (2012) Use of H2Ri wicking fabric to prevent frost boils in the Dalton Highway Beaver Slide area, Alaska (No. INE/AUTC 12.23)
5. Fredlund DG, Xing A (1994) Equations for the soil-water characteristic curve. *Can Geotech J* 31(4):521–532
6. Connor B, Zhang X (2016) *Laboratory Performance of Wicking Fabric H2Ri in Silty Gravel, Sand and Organic Silt* (No. 4000130). Alaska University Transportation Center
7. NCHRP (2004) *Laboratory determination of resilient modulus for flexible pavement design*. In: National Cooperative Highway Research Program Research Results Digest, No. 285. Washington, DC: Transportation Research Board, National Research Council
8. Elshaer M, Ghayoomi M, Daniel JS (2018) Methodology to evaluate performance of pavement structure using soil moisture profile. *Road Mater Pavement Des* 19(4):952–971
9. *Mechanistic-Empirical Pavement Design Guide (2008) Interim Edition: A Manual of Practice*. AASHTO, Washington, DC
10. Gupta A, Kumar P, Rastogi R (2015) Mechanistic–empirical approach for design of low volume pavements. *Int J Pavement Eng* 16(9):797–808

# Assessing the Risk of Critical Velocity Effects at Railway Sites Using Site Investigation and Advanced Laboratory Testing



A. Duley , B. N. Madhusudhan , L. Le Pen , D. Thompson ,  
and W. Powrie 

**Abstract** As train speeds increase on existing rail networks, and new high-speed routes are constructed, the likelihood of a line experiencing the large track displacements commonly termed critical velocity effects increases. The phenomenon occurs as the train speed approaches the speed of surface (Rayleigh) waves in the underlying ground. At a certain proportion of this speed the track deflections begin to increase above those for static loading, slowly at first and then more rapidly, reaching a maximum at a “critical” velocity. Larger trackbed deflections may cause increased rates of track deterioration, maintenance needs and in the worst cases risks to safety. Therefore, it is important to be able to predict which sites are susceptible to critical velocity effects and to determine threshold speeds below which they are not influential. Where these thresholds are exceeded mitigation measures can be considered. Reliable prediction of critical velocity effects using numerical modelling and other analytical tools require selection of a representative ground model and parameters. This paper describes a programme of site measurements, sampling and advanced laboratory testing to create a ground model for a site on the UK railway network known to experience critical velocity effects.

**Keywords** Critical velocity · Resonant column · Organic silt · Rayleigh wave · Railway · Railroad · High speed trains · Bender element · Ground model

---

A. Duley (✉)  
Jacobs UK Ltd., Aperture @ Pynes Hill Court, Exeter, UK  
e-mail: [alice.duley@jacobs.com](mailto:alice.duley@jacobs.com)

B. N. Madhusudhan · L. Le Pen · W. Powrie  
Infrastructure Research Group, University of Southampton, Boldrewood Innovation Campus,  
Southampton SO16 7QF, Hampshire, UK

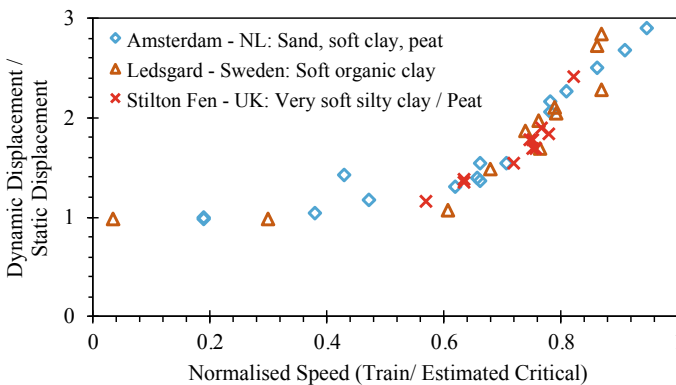
D. Thompson  
Institute of Sound and Vibration, University of Southampton, Highfield Campus, Southampton  
SO17 1BJ, Hampshire, UK

## 1 Introduction

In many countries, there is pressure to increase train speeds on existing rail networks, as well as for higher speed new routes. As train speeds are increased, tracks that have previously performed acceptably may start to deteriorate and in extreme cases experience large movements during the passage of an individual train, as a result of what are commonly termed critical velocity effects. The phenomenon occurs when the train speed approaches the speed of surface (Rayleigh) waves in the underlying ground—defining the critical velocity of a site. These effects are also of potential concern for new high-speed lines where straighter routes may cross areas of soft ground, which have traditionally been avoided owing to their inherently low wave speeds. It is important to be able to predict where critical velocity effects may occur, and where necessary take steps to mitigate them. For economic reasons, it is equally important to avoid such mitigation where it is not necessary.

Critical velocity effects have been observed in many countries. The most well-documented and highly cited occurrence is that at Ledsgård in Sweden, where soft organic clays caused the onset of critical velocity effects at approximately 150 km/h. Track displacements of up to 15 mm were recorded at a train speed of 200 km/h [1]. A strong trend is found across multiple sites when track displacements are normalised relative to low speed (quasi-static) values, and train speeds relative to the estimated site critical velocity (Fig. 1). For reasons of safety and the avoidance of excessive maintenance, it is often recommended that line speeds be limited to a factor of the site critical velocity ( $X_{VC}$ ). Values of 0.6–0.7 are commonly suggested, as this is the normalised speed at which displacement magnitudes begin to significantly increase [2–4].

There is still some uncertainty over the suitable value of  $X_{VC}$ . Some locations run well at higher factors; for example, in Ireland, trains run satisfactorily at critical velocity factors  $X_{VC}$  greater than 0.7 [5]. Whilst the appropriate value for  $X_{VC}$  may be debated, and factors such as the absolute magnitude of displacements must also



**Fig. 1** Normalised displacement-speed curve for a range of critical velocity sites, after [3]

be considered, estimation of the actual critical velocity at a site is important. For example, for  $X_{VC} = 0.6$ , under- or over-estimating the critical velocity by 15% would result in a range of speed limits equivalent to applying  $X_{VC} = 0.5$  or 0.7. This paper summarises, with reference to a case study, a process to produce a ground model from which the critical velocity may be estimated. There are very few other published case study sites available which offer ground properties and measurements of critical velocity effects in action.

### ***1.1 Causes and Modelling of Critical Velocity Effects***

The shear wave velocity of a soil, being related to the Rayleigh wave velocity, is a useful indicator of the likelihood of critical velocity effects. Softer, less dense ground is most likely to be susceptible both because displacements per unit load are greater and the Rayleigh wave speed (and hence the train critical velocity) is lower. Models of railway vibration are often based on the assumption that the ground can be modelled as a layered-elastic half space, with each soil layer behaving in a linear elastic isotropic manner. However, beyond a threshold strain, the shear modulus of a soil degrades with increasing strain, resulting in non-linearity. Damping is also non-linear once the linear strain threshold has been exceeded.

Strains during train passage at Ledsgård were high enough to take the soils beyond any limit of linearity. Maximum cyclic strains at the site were reported as 1% in the embankment and 0.8% in the underlying natural organic clay. The secant shear modulus reduced to 10–50% of the small strain value, whilst the damping ratio increased by 20–100% [1]. Inclusion of these degraded state parameters in an analytical model has a significant impact on the calculated ground displacements and critical velocity at a site, and a model based on non-degraded parameters underestimates track displacements, e.g. [1, 6–8].

Critical velocity effects have been analysed using models of varying degrees of complexity, ranging from linear-elastic 2D, e.g. [9], through 2.5D and 3D equivalent-linear models, e.g. [6, 10], to 3D models with a fully non-linear soil response, e.g. [7, 8]. Whether the aim is to more effectively identify potential problem areas or to produce a full non-linear displacement response estimate, results are only as accurate as the ground model adopted. Soil layering, density, shear modulus and variation in damping with strain are essential for an effective model. Critical velocity effects are most likely on soft soils, for which there is a relative paucity of published shear modulus degradation data.

## **2 Assessing Ground Quality**

Typically, the ground up to a depth of 15–20 m below track level may be excited by train passage. However, owing to the elliptical nature of the ground movement

associated with Rayleigh waves and the attenuation of energy in the upper ground layers, the overall critical velocity is influenced more by the layers of ground closest to the track than those at the full depth of excitation. The stiffness properties of the track itself also play a part.

Ground wave speeds can be directly measured by in-situ and laboratory testing, and inferred via empirical and other correlations with related parameters. The Rayleigh wave speed in a soil is usually approximately 90–95% of the shear wave speed [11]. In-situ testing techniques include MASW (Multi-channel Analysis of Surface Waves), SCPT (Seismic Cone Penetration Test) and other seismic-impulse based techniques. Laboratory techniques include resonant column (RC), bender element (BE) and triaxial tests, all of which require undisturbed samples to be retrieved from the site of interest. Other key modelling parameters such as ground layering, densities and damping can be obtained through a combination of in-situ and laboratory methods.

Laboratory testing is necessary to measure the non-linear relationship between shear wave speed/damping and strain. The degradation of the shear modulus with strain can be measured in triaxial and resonant column tests. Only the resonant column apparatus is able to measure also the strain dependency of soil damping.

The resonant column apparatus has a torsional drivehead to which a cylindrical sample is attached. The base of the sample is fixed. The drivehead is rotated clockwise and anticlockwise through small angles at a range of frequencies, with the response of an accelerometer on the drivehead monitored. The frequency at which the greatest response is measured is the resonant frequency of the specimen. From this, the shear wave speed can be calculated. Damping is measured by monitoring the accelerometer after the sample has been excited at its resonant frequency and then cut off to vibrate freely. Bender elements are very small piezo-electric transducers, which operate as a pair at either end of a sample. A voltage is applied to one end to excite a wave and the arrival time at the other end is recorded, from which the shear wave speed is calculated (Fig. 2).

### 3 Case Study Site

#### 3.1 Background

Following an increase in line speed from 160 to 200 km/h, a site on the UK classic network was found to experience large track displacements along a run of sleepers. To quantify the increased track deflection, site measurements of sleeper velocity during train passage were carried out using geophones. Geophone data from a sequence of sleepers showed that the track was deflecting in excess of 6 mm (Fig. 3). This is large compared with the typically <2 mm movement on well performing routes. It may result in increased rates of track deterioration, which local track maintenance records confirm. Historical geotechnical investigations showed the site to be underlain by a

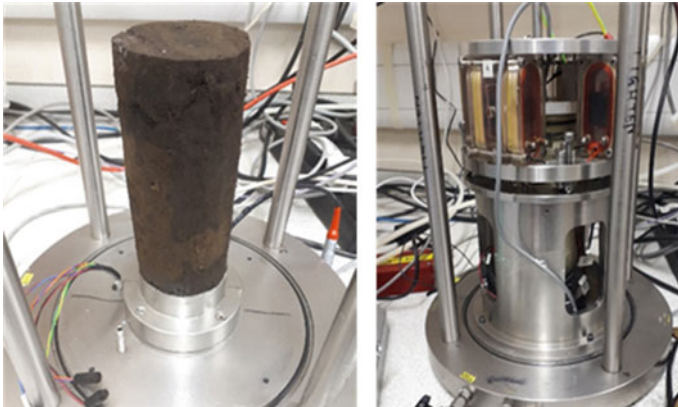


Fig. 2 RC example sample, and RC equipment before pressure cell put in position

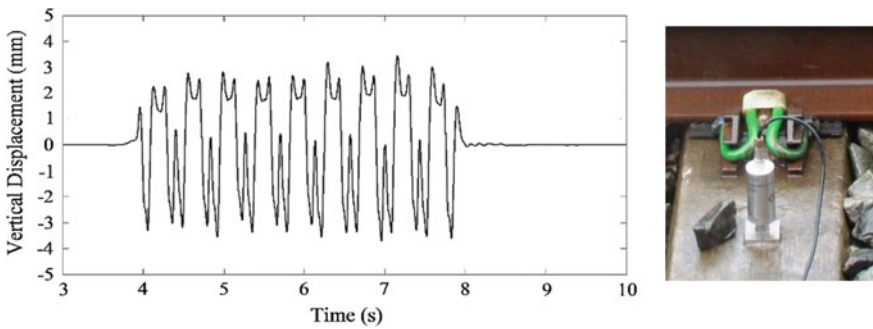


Fig. 3 Typical geophone trace showing track displacement and geophone fitted on sleeper. Note that the 'zero' point for the geophone does not represent the 'zero' point for the track [12]

layer of soft organic material, sitting over layers of stiffer sands and gravel. The soft layer varies between 2 and 4 m in thickness and is present along a 50 m length of track. The site sits within a slight basin and cutting, with several streams and brooks in the area. These factors explain why the site has a high water table.

### 3.2 *In-Situ Ground Investigation*

During a night-time possession of the line, a tracked windowless sampling rig was used to drill two boreholes directly through the centre line of the track. The bores were positioned within sleeper bays at chainages targeting the maximum thickness of the soft layer shown on the historical geotechnical investigation (GHS1), and slightly beyond the previously indicated extent (GHS2). Each bore penetrated 6 m





**Fig. 4** Typical organic silt samples

below sleeper level (BSL), with samples below the trial pit retained inside the casings in 1 m lengths and the bores logged at 1 m intervals. Super heavy dynamic probes (SHDPs) were carried out at both locations from the base of the bore to 10 m BSL.

Sample tubes were transported to the laboratory for full logging and index testing. 15 whole samples suitable for advanced laboratory testing, of at least 150 mm in length, were successfully retrieved from the bores. Of key interest in the results is a layer of soft to very soft organic silt, which extends beneath the ballast to approximately 3–4 m BSL. Soils of this nature tend to have a low shear wave velocity. Examples of the silt materials are shown in Fig. 4. The two bores are summarised in Fig. 5. The ballast layer is thicker than typical (up to 0.9 m)—a possible indication of increased ballast maintenance activity at the site. Below the soft silt are layers of clay, sand and gravel, which are unlikely to be the cause of the critical velocity effects.

### Index Testing

Figure 6 shows the variation in density with depth, based on 50 mm dia. density ring tests completed in the laboratory. There is some variation in density between the two boreholes, with GHS1 consistently denser. Determination of density from density rings is subject to some error in very variable soils such as these. Nonetheless, a large variation with depth was found. The densities in GHS2 were especially low, with values generally between 1100 and 1400 kgm<sup>-3</sup> for the first 3.5 m below ground level. A typical clay soil might be expected to have a density of approximately 2000 kgm<sup>-3</sup>, almost twice the lowest value measured in GHS2. Low density soils tend to have low stiffness, hence likely to be the cause of critical velocity problems at the site.

The variation in moisture content with depth is also shown in Fig. 6. As with density, a significant difference is apparent between the boreholes. The denser GHS1 has generally far lower moisture contents than GHS2, and the values are also more consistent. Greater variability is found for GHS2, with unusually high moisture content being an indicator of the organic material in the soil.

Other index testing was also completed on selected samples. Atterberg tests showed the organic sandy silts to be non-plastic, whilst the firm sandy clay has low plasticity. Ignition tests were carried out on 8 organic silt samples to measure total and volatile solids, resulting in 6 high-organic and 2 medium-organic ratings.

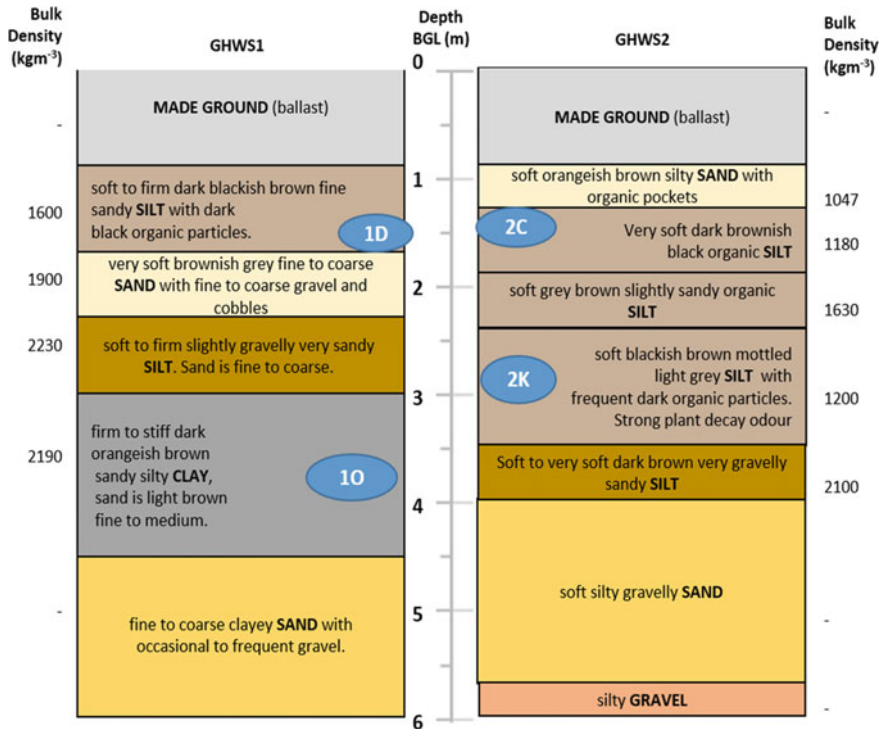


Fig. 5 Borehole summary with selected sample locations

**Super Heavy Dynamic Probe (SHDP) Results**

The SHDP results gave good indications of layer density boundaries, which correlate well to borehole results. Consistent with the density evaluation for the top 6 m of ground in the borehole logs (Fig. 6a), the SHDP results indicate that the ground below this depth is stiffer at borehole GHS1. The average blowcount was approximately 60% greater for GHS1 at depths >7.5 m bSL than for GHS2. At the maximum penetration depth of 10 m bSL the two SHDP blowcounts show a degree of convergence.

Derivation of further parameters from the SHDP relies on converting the blowcounts to SPT equivalents and applying empirical correlations. Common correlations for relative density for non-cohesive materials were applied [13, 14] as the ground is believed to consist of sands and gravels. GHS1 equates to medium-dense and dense material, whilst GHS2 is loose to 7 m bSL, underlain by medium-dense material.

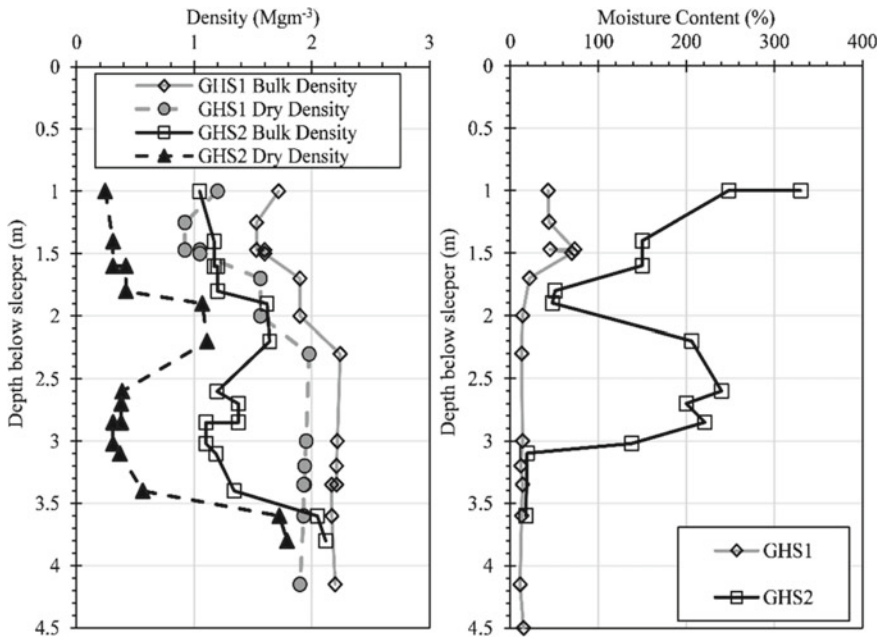


Fig. 6 Density and moisture content variation with depth, both site bores

## 4 Laboratory Testing

### 4.1 Resonant Column and Bender Elements

#### Test Procedure

A standard resonant column apparatus was adapted following the improvement methods of [15] and [16], (Fig. 2). The end caps were modified to contain vertical bender elements, which provide fast, non-destructive direct measurements of shear and compressional wave speeds at very small strains. As the soft soils tested were likely to have resonant frequencies below those typically measured in the RC, calibration focused on the low stiffness/frequency range using brass, nylon and aluminium calibration bars.

Four site samples were selected to represent the most geotechnically interesting materials, and carefully trimmed from the sampling diameter of 100 mm down to the resonant column specimen size of 70 mm. The material type and location of each sample are shown in Fig. 5. Several testing pressures were calculated for each, based on the depth of sample retrieval, the range of likely water tables and possible future surcharges. The test process for each sample was as follows: (1) saturation; (2) consolidation to the lowest test pressure; (3) bender element measurements; (4) resonant frequency measurements at increasing strains, ensuring strains remained recoverable; (5) repeat bender element and very small strain resonant column measurements

to ensure no permanent deformation occurred; (6) steps 2–6 repeated for remaining test pressures.

**Results: Shear Modulus and Shear Wave Speed**

Non-destructive torsional tests were successfully completed on the four soft organic silt samples, at a range of test pressures and strains. The very soft samples necessitated repositioning of the resonant column drivehead during testing due to the large amount of consolidation. Bender element measurements were also successfully taken. The resonant column measured shear moduli, normalised by the small strain shear modulus  $G_0$ , show varying rates of degradation with strain (Fig. 7). The stiffest sample (GH1O- clay) shows greater rates of degradation, and at lower strains than the silt samples. For example, averaged across the testing pressures, at distortional strain levels of 0.01% the shear moduli of the samples showed reductions to GH2K—98%, GH2C—93%, GH1D—87%, GH1O—77%.

Very low shear moduli (and therefore shear wavespeeds) were measured for all the organic silt samples, with  $G_0 > 10$  MPa for most pressures (Fig. 8). The silt samples also showed a very low rate of strength gain with pressure increase in comparison with the clay. The low rate of increase in modulus with pressure of the soft organic silt samples means that soils normally considered to be at a sufficient depth to have a reasonable shear modulus may have a very low value. Threshold strain limits, where the shear modulus begins to degrade, vary by sample and by pressure, but are higher for the organic silts than the clay, consistent with the impact of organic content reported by [17]. Excellent agreement was also found between bender element and resonant column measurements of shear modulus / shear wave speed (Fig. 8). The softest samples have shear wave speeds as low as 70 m/s (250 km/h). In comparison, modern high-speed railways are often designed for 400 km/h running. Poisson’s ratio was derived from the bender element compressional and shear wave measurements.

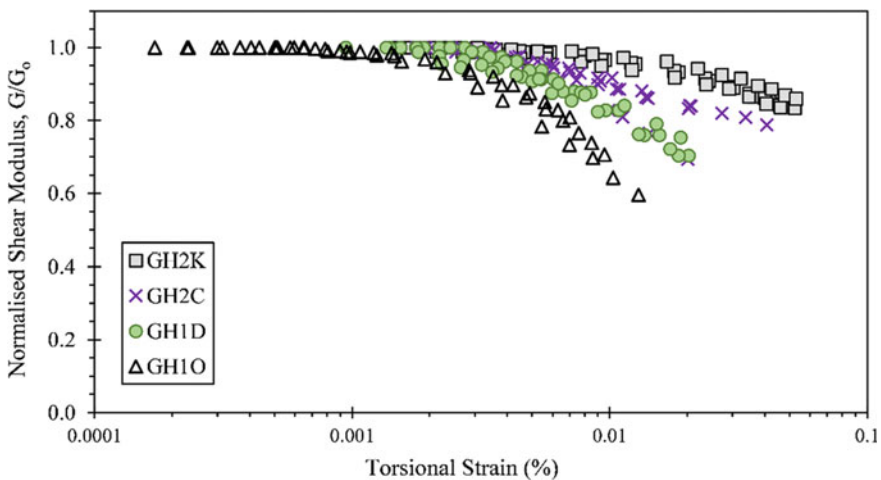


Fig. 7 Normalised resonant column shear modulus degradation with strain for all samples

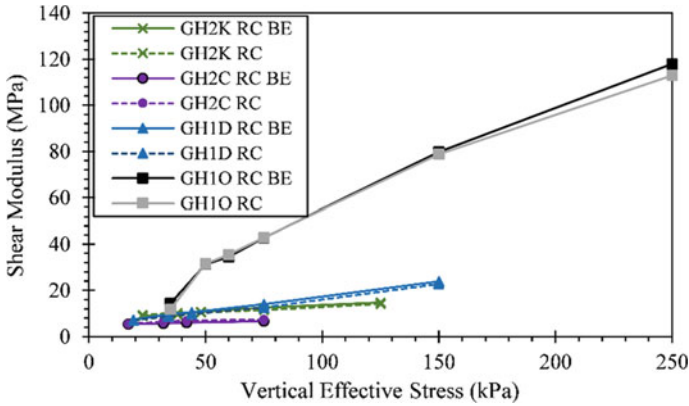


Fig. 8 Small strain shear modulus variation with pressure, resonant column and bender element

**Results: Damping**

The increase in damping ratio with strain was also measured for all samples. Damping is higher for the clay and sandy silt samples than for the soft/very soft organic silts. No significant variation in damping with the applied test pressures was found. The measured values sit within expected ranges for typical clay and organic soil types. A typical result is presented in Fig. 9 for GH2C, a very soft high-organic silt.

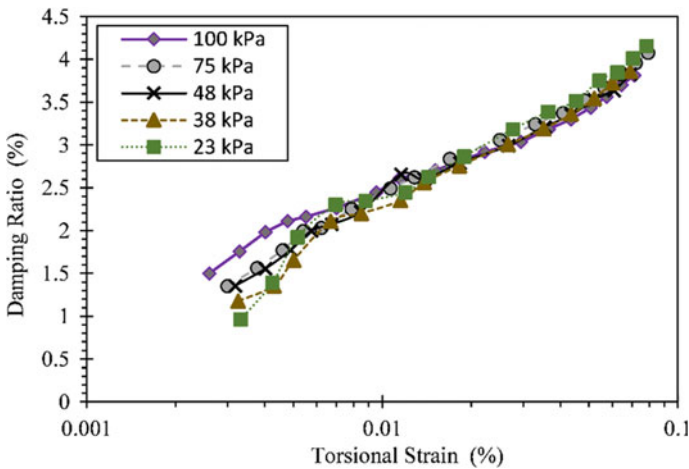


Fig. 9 Example damping variation with strain in resonant column tests: sample GH2K

**Table 1** Site ground model: small strain parameters

Material	Thickness (m)	Bulk density ( $\text{kgm}^{-3}$ )	Shear modulus $G_0$ (MPa)	Shear wave speed $V_s$ ( $\text{ms}^{-1}$ )	Small strain damping ratio (%)	Poisson's ratio
BALLAST type	0.7	1600	57	189	2.0	0.3
Very soft to soft highly organic SILT	2.5	1200	6.8	75	2.1	0.482
Firm sandy silty CLAY	0.7	2100	20	97	3.7	0.497
Clayey SAND and GRAVEL	To depth	2000	52	161	3.0	0.45

## 5 Integration of Laboratory and In-Situ Parameters

To build a ground model, it is necessary to consider data obtained from all sources. The first restriction is that most models include only horizontal layering. For this reason, an average thickness for the important soft silt layer must be selected, which is believed to be a basin of varying thickness with a maximum of 4 m. A value of 2.5 m was chosen, with the thickness and material type of the layers above and below the silt selected from a combination of the historical site boreholes, the new site boreholes and the SHDP. The site is believed to be saturated below the ballast. The final ground model and small strain parameters are presented in Table 1. Accurate modelling will require degraded values of soil parameters to be considered.

Properties were assigned to each material based on laboratory tests on relevant samples. Results for laboratory tests were also compared with other published results for similar soil types where possible, to give added confidence. Typical published values were selected for materials where no laboratory testing took place.

## 6 Conclusion and Recommendations

An extensive site investigation was carried out, including the drilling of new boreholes and the completion of dynamic probe tests. After full index testing of 20 m of borehole samples, a large data set of soil stratigraphy, density and other general index measurements has been produced. Testing of samples in advanced laboratory equipment has been completed, providing data for stiffness and damping variation with strain from the resonant column, with confirmatory shear modulus testing completed with bender elements. The highly organic silt is a material for which little data are published, and so provide a useful dataset for future work. In combination with pre-existing seismic measurements and track displacement measurements, this data

provides all the information required for the use of this site as a new critical velocity case study [18].

Recommendations for assessing ground models for critical velocity sites are as follows:

- In-situ seismic testing is less useful on sites where the underlying ground layers are uneven and the position of the railway is such that suitable test locations are unavailable or inaccessible. Sole reliance on such tests is not recommended, as soils at soft sites may have unusually low densities which are unlikely to be assumed in the seismic dispersion curve analysis.
- Super heavy dynamic probe test data are useful in building an expanded picture of the site stratigraphy rather than relying on boreholes alone, at lower expense and with reduced invasiveness.
- The addition of bender elements to a resonant column test is a very effective method for providing confirmatory measurement of shear wave speed/shear modulus for minimal additional cost and time.
- The resonant column is the only method capable of providing both shear modulus and damping degradation measurements relatively quickly and easily—both key modelling parameters.
- If it is thought that a site may suffer critical velocity effects and advanced laboratory testing is not possible, it is essential to carefully consider the ground material before selecting typical shear moduli and strain degradation/damping variation rates. Organic content and/or the presence of soft materials such as silts will greatly affect the selected values.

**Acknowledgements** The work described in this paper was funded by the UK Engineering and Physical Sciences Research Council (EPSRC) and HS2 Ltd. as part of the Track Systems for High Speed Railways: Getting It Right project (EP/K03765X). The site access was also facilitated by Network Rail and AECOM who assisted with historical records and the site investigation.

## References

1. Madshus C, Kaynia AM (2000) High-speed railway lines on soft ground: dynamic behaviour at critical train speed. *J Sound Vib* 231(3):689–701
2. Hunt GA (1994) Analysis of requirements for railway construction on soft ground. Technical Report LR TM 031. British Rail Research, London, UK
3. Woldringh R, New B (1999) Embankment design for high speed trains on soft soils. In: Twelfth European conference on soil mechanics and geotechnical engineering, 'geotechnical engineering for transport infrastructure'. Balkema, Amsterdam.
4. Powrie W, Yang LA, Clayton CRI (2007) Stress changes in the ground below ballasted railway track during train passage. *J. Rail and Rapid Transit* 221(2):247–261
5. Brough M, Sharpe P, Hoffman A (2013) Investigation, design and remediation of critical velocity sites—a desk study. In: *Railway engineering 2013—12th international conference & exhibition*. London

6. Alves Costa P, Calçada R, Silva Cardoso A, Bodare A (2010) Influence of soil non-linearity on the dynamic response of high-speed railway tracks. *Soil Dyn Earthq Eng* 30(4):221–235
7. Shih JY, Thompson DJ, Zervos A (2017) The influence of soil nonlinear properties on the track/ground vibration induced by trains running on soft ground. *Transp Geotech* 11:1–16
8. Woodward PK, Laghrouche O, Mezher SB, Connolly DP (2015) Application of coupled train-track modelling of critical speeds for high-speed trains using three-dimensional non-linear finite elements. *Int J Railway Technol* 4(3):1–35
9. Connolly DP, Kouroussis G, Giannopoulos A, Verlinden O, Woodward PK, Forde MC (2014) Assessment of railway vibrations using an efficient scoping model. *Soil Dyn Earthq Eng* 58:37–47
10. Sheng X, Jones CJC, Thompson DJ (2003) A comparison of a theoretical model for quasi-statically and dynamically induced environmental vibration from trains with measurements. *J Sound Vib* 267(3):621–635
11. Richart FE (1962) Foundation vibrations. *Trans ASCE* 127(1):863–898
12. Duley A, Le Pen L, Thompson DJ, Powrie W, Watson GVR, Musgrave P, Cornish A (2015) Critical train speeds and associated track movements: a case study. In: *Proceedings of the XVI ECSMGE geotechnical engineering for infrastructure and development*, ICE Publishing, Edinburgh, UK, pp 253–258
13. Terzaghi K, Peck RB (1948) *Soil mechanics in engineering practice*. Wiley, Hoboken
14. USACE (1994) *Engineering manual EM 110-2-2504*
15. Priest JA (2004) *The effects of methane gas hydrate on the dynamic properties of a sand*. Ph.D. Thesis. University of Southampton.
16. Clayton CRI, Priest JA, Bui M, Zervos A, Kim SG (2007) The Stokoe resonant column apparatus: effects of stiffness, mass and specimen fixity. *Geotechnique* 59(5):429–437
17. Kallioglou P, Koninis G, Tika T, Pitilakis K (2008) ‘Shear Modulus and Damping Ratio of Organic Soils’, *Geotechnical and Geological Engineering*
18. Duley A (2018) *Soil parameters for modelling critical velocity effects of railways*. EngD Thesis, University of Southampton



# Design and Construction of a Very High Embankment Using Geosynthetic Reinforcement



Mariya Dayana, Budhmal Jain, Satya Kumar Sunkavalli,  
and Reginald Subramaniam

**Abstract** Kannur International Airport Ltd. (KIAL) is a new Greenfield airport project with airside development on an undulating terrain with an average height of 90 m above mean sea level (MSL) and a maximum height of 142 m. To accommodate the desired Runway length and runway end safety area (RESA) at both the ends along the proposed alignment, it resulted in 45.5 million cubic meters in cutting and filling. The insufficient availability of land for the construction of free slope embankment at RESA 07 end resulted in the design and construction of reinforced soil slope (RSS) system with a maximum slope of 65°. An embankment fill of average 70 m height with steep slopes located in high rainfall area is a unique feature of this project. The fill was reinforced with high-strength uniaxial geogrids laid perpendicular to the slope. Weld mesh wrapped with coir mat acted as fascia units to protect it against surface failure. Considering high rainfall received on this table top airport site, extensive drainage system was designed for the high embankment fill. Gabion wall up to 9 m height were also designed and constructed along the boundary to accommodate the toe of the RSS fill beside the jeepable track at the base level. The design of RSS fill was done using ReSSA software and verified in PLAXIS 2D modeling. The site won excavated laterite soil was used as the fill material for the construction. Extensive field and laboratory tests were conducted during the construction of RSS system for quality assurance.

**Keywords** Airport · Embankment · Gabion · High-strength uniaxial geogrid · KIAL · Laterite soil · PLAXIS

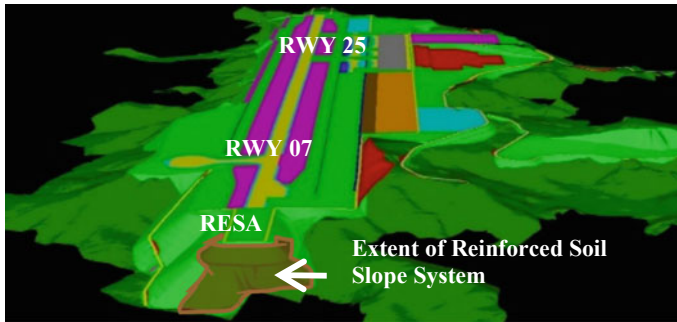
---

M. Dayana (✉) · B. Jain · S. K. Sunkavalli  
L&T Construction, Transportation Infrastructure IC, Mumbai, India  
e-mail: [mariyadayanapj@Intecc.com](mailto:mariyadayanapj@Intecc.com)

B. Jain  
e-mail: [bjain@Intecc.com](mailto:bjain@Intecc.com)

S. K. Sunkavalli  
e-mail: [satyakumar@Intecc.com](mailto:satyakumar@Intecc.com)

R. Subramaniam  
Maccaferri Environmental Solutions Pvt. Ltd, Gurgaon, India  
e-mail: [s.reginald@maccaferri.com](mailto:s.reginald@maccaferri.com)



**Fig. 1** Layout model of KIAL with RSS marking

## 1 Introduction

The Kannur International Airport is a new greenfield airport, recently constructed and commissioned in Kerala, a south-western coastal state of India. The airport has been developed with a single Runway of length 3050 m and a parallel taxiway to aerodrome reference code 4E specifications [1]. The general surface profile in the project area is undulating with an average height of 90 m above MSL and a maximum height of 142 m. Being a table top aerodrome, the runway was provided with the overturn of 60 m and runway end safety area of 240 m on either ends which resulted in a total strip development of 3650 m. Only 3000 m approximately of land along the runway length was at a general elevation of the development platform of 100 m [2]. The rest, toward the runway ends, was at a general elevation of 20–60 m. This resulted in massive earth fill, stability of which was to be ensured. This was further aggravated by the non-feasibility of land acquisition at RESA 07 side to provide a stable earth fill slope (1 V:2H), which therefore became a necessity to provide earth retention system. Various retention schemes and combinations were explored to accommodate such a high embankment with the available land premises. All the proposed schemes were rigorously evaluated against the stability criteria and feasibility of construction. This paper represents a case study detailing the design and construction of a very high embankment using geosynthetics for the provision of runway length and RESA area as shown in Figs. 1 and 2. The aerial view of RSS system during construction is shown in Fig. 3.

## 2 Earth Retention Systems

The major earth retention schemes proposed include: Reinforced cement concrete (RCC) walls, Gabion wall and geogrid reinforced soil systems. In RCC walls and Gabion Walls, a multi-tier approach was evaluated which each tier height worked out to be 10 m. However, the very heavy structural design and material requirements ruled



Fig. 2. 3D model view of RSS system

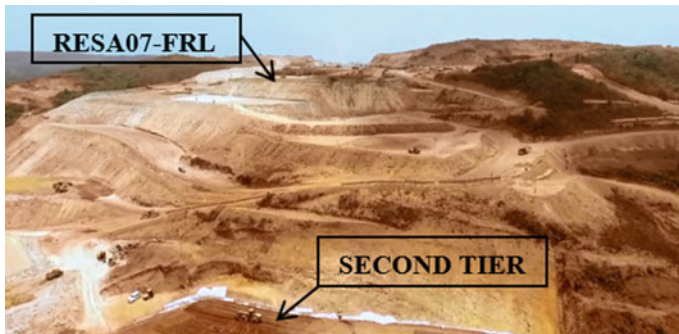


Fig. 3 Aerial view of construction site

out this option as RCC wall and the gabion wall scheme was ruled out due to failure in global stability analysis even though the individual tier stability was satisfied. Finally, the option of employing a geogrid reinforced soil slope system was considered [3]. Various combinations of RSS system were designed and evaluated which includes: Designing the entire system as a single slope, encroachment of airport operational perimeter (AOP) road within the system resulting in the discontinuity of the single slope thereby designing the system with a combination of slopes checking against its stability.

### 3 Geotechnical Investigation

#### 3.1 General

Kannur is characterized with diversified surface terrain and distinctive geomorphic processes. Laterite soil pre-dominates the district of Kannur covering around 62.7%

**Table 1** Foundation parameters

Description	Units	Top layer-soil	Middle layer-weathered rock	Bottom layer-hard rock
Bulk unit weight	kN/m <sup>3</sup>	18	25	25
Cohesion	kPa	15	200	800
Angle of internal friction	Degrees	30	35	35

of the total area [4]. The lateritic soil has excellent strength properties in dry conditions, while the same soil exhibits very low strengths during the wet conditions. All laboratory strength tests are performed in wet condition after a minimum soaking period of 6 h in order to simulate the worst possible conditions during monsoon rains.

### 3.2 Foundation Strata

Engineering properties of the foundation strata were studied by conducting geotechnical investigation at 12 locations in the RSS system area. Boreholes of 150-mm diameter were drilled using hydraulic rotary rig. Standard penetration test (SPT) was conducted in the boreholes at regular intervals of 1.5 m or every change of strata and disturbed and undisturbed samples were collected at various depths for further testing in laboratory. Borehole termination was mainly governed by the presence of hard rock. Boring up to a depth of 5 m was continued in the hard rock strata to confirm its occurrence. Rock core samples were subjected to unconfined compressive strength (UCS) test. Triaxial consolidated undrained test was performed on undisturbed soil samples to determine the shear strength parameters. Ground water level (GWL) in each borehole was determined after 24 h of completion of boring.

Based on laboratory test results, three different foundation strata were observed below the proposed embankment fill as mentioned in Table 1. Rocky strata was met at an average depth of 15 m from ground level. RocLab software [5] output for rock mass strength based on generalized Hoek Brown failure criteria was used for the determination of 'c' and 'phi' property of rock [6]. The water table depth was met 10 m below ground level. As the water table level can go high during monsoon, water table at 2 m depth below toe of RSS system was considered for the slope stability analysis.

### 3.3 Reinforced Soil and Backfill Soil

The engineering properties of the reinforced fill play a key role in the design of RSS system. Based on the design, about 1.2 million cubic meter of reinforced fill was

**Table 2** Design properties of fill soil

Description	Units	Reinforced soil	Backfill soil
Bulk unit weight, $\gamma$	kN/m <sup>3</sup>	18	19
Cohesion, $C$	kPa	10	15
Angle of internal friction, $\Phi$	Degrees	30	25

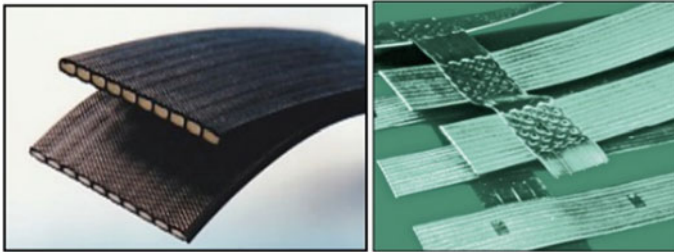
essential. As the project location is situated on an undulating terrain, like embankment fill, huge amount of cutting works were also involved in the construction. So, the idea was to borrow the fill material from the cut locations based on its suitability. Laboratory tests including grain size analysis, Atterberg limit, MDD and direct shear test was conducted on soil samples from cut location and design parameters for reinforced and back fill soil were finalized as shown in Table 2.

## 4 Design of RSS System

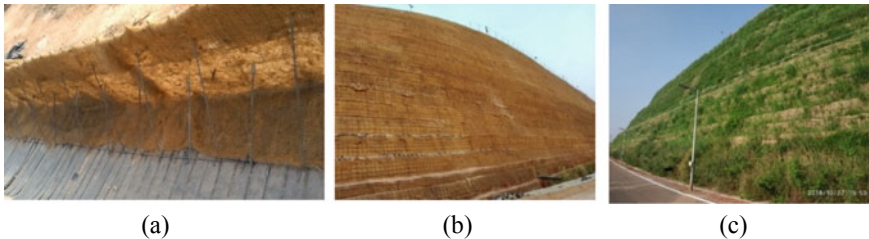
The design of an economic and stable reinforced soil slope system for such a height with curves and bends along with the accommodation of gradually climbing up AOP road at mid height and perimeter Jeep track at the base level was challenging to the designers. To address these challenges a total number of 10 cross sections with varying slope geometry were selected to be designed. Project timeline of 32 months with 8 months of monsoon included demanded for a design to make the construction feasible in 24 months. This was achieved by maintaining the vertical geogrid spacing at 800 mm.

### 4.1 Geogrid Reinforcement

The RSS system was designed for a life of 25 years as per the airport capacity enhancement plan. For this huge fill with the geogrid vertical spacing of 800 mm, use of high-strength uniaxial geogrid became mandatory. Therefore, high-tenacity polyester yarn tendons encased in a polyethylene sheath coated geogrid with ultimate tensile strength of 1200 kN/m was selected as the primary reinforcement (Fig. 4). Geogrids with ultimate tensile strength down to 50 kN/m were also incorporated in the design where suitable so as to economize the design. The long-term design strength of the geogrids was derived considering reduction factors for creep of 1.39, installation damage factor varying between 1.02 and 1.1 based on individual geogrid strength grade, durability factor of 1.12, and an additional ramification factor of 1.1.



**Fig. 4** Primary Reinforcement



**Fig. 5** Facia system: **a** coir mat wrapped weld mesh; **b** elevation view of facia system; **c** Vetiver grass growth

## 4.2 Facia System

65° angled 'L' shaped welded mesh units (8-mm diameter and mesh size-150 mm × 150 mm) were used to maintain slope angle varying from 33° to 65°. Welded mesh unit was wrapped with coir mat to facilitate the growth of vegetation. Vetiver grass was planted throughout the system (Fig. 5). The horizontal and inclined faces of the welded mesh unit were braced by 8-mm diameter hooked steel bars to maintain the geometrical shape and stability of the face during the compaction of the soil. For slope angle steeper than 45°, primary reinforcement at that level was wrapped around the weld mesh units to act as the facing system along with the placement of coir mat. While for slope's gentler than 45°, secondary reinforcement (1 m width) in the form of biaxial geogrid of 20 kN/m tensile capacity was installed between the primary geogrid layers. For slopes gentler than 33°, coir mat was laid on the surface and vegetation growth was facilitated.

## 4.3 Surface and Subsurface Drainage System

The airport project is located in a heavy rainfall area with annual rainfall of 3300 mm. It becomes mandatory to design and provide a detailed surface and subsurface

drainage system to prevent any infiltration of water in to the RSS system. Therefore, drainage in the form of berm drains and chute drains was provided to clear of the surface running water from the RSS system and subsurface drainage system provided on top and back of the RSS system to arrest the infiltrated water from reaching reinforced fill.

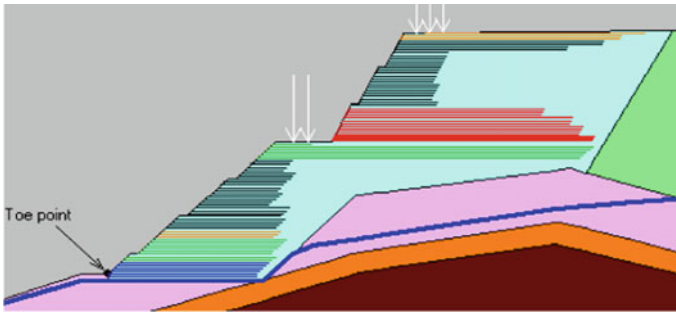
At the rear end of the reinforced fill, chimney drain in the form of 600-mm thick aggregate media sandwiched between non-woven geotextile layers were adopted to prevent the infiltration of water from backfill to the reinforced fill. Aggregates of size between 13.2 and 40 mm were used. An aggregate mount and HDPE pipe network were provided at the bottom of the chimney drain to collect seepage water and carry it outside the RSS fill. The pipe network consisted of geotextile wrapped 315-mm diameter half perforated HDPE longitudinal pipe and 160-mm diameter non-perforated HDPE transverse pipes. At the bottom level of chimney drain, longitudinal pipe run along the perimeter to collect the percolated water through the geotextile wrapped perforations. Transverse pipes were connected at right angles to the longitudinal pipe to drain out the collected water out of the system. Both longitudinal and transverse pipes were installed with adequate gradients to enable the free flow of water that is being collected. Since the reinforced fill coverage area of top tier and bottom tier was diverse, two independent chimney drain systems were provided for both the sections.

Although the top surface of the RESA is sloped as per the specified gradients, considering the high rainfall intensity at the project site, a subsurface drainage system was designed for the complete extent of reinforced soil zone. The arrangement consists of 200 mm thick aggregate layer sandwiched between geotextile layers laid down with a gradient of  $-1\%$  longitudinally towards the rear end and  $-2\%$  transversely from center line of RESA. The system is underlined by an impermeable 1-mm thick geomembrane sheet.

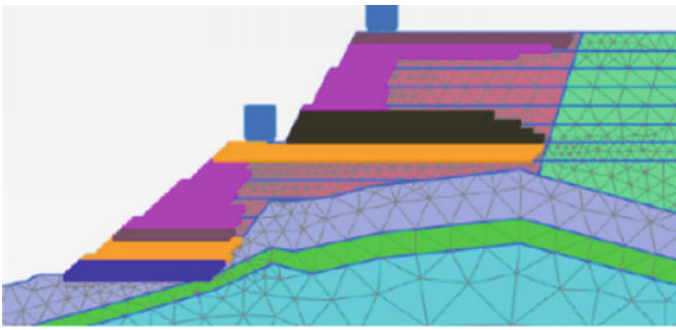
## 5 Design Methodology

The RSS system was designed as per FHWA-NHI-10-025 guidelines [7]. The analysis and design were carried out using ReSSA software and was verified in Plaxis-2D finite element analysis program (Figs. 6 and 7). The seismic analysis was carried out using the pseudo-static approach with improved seismic coefficient and importance factor. Minimum factor of safety for slope stability analysis at the end of construction was considered as 1.3 for static condition and greater than 1.0 for seismic condition. The summary of the design sections is given in Table 3.

ReSSA software is based on the limit equilibrium method. The slope stability analysis was performed for circular slip surface by Bishop's method and for direct sliding along geogrid reinforcement layers by Spencer's method. Rotational and transitional stability analysis were performed and least factor of safety were obtained. The global minimum was obtained by performing the analysis with different bounds for the entry and exit points of the slip circles.



**Fig. 6** ReSSA software model



**Fig. 7** Plaxis software model

Finite element analysis program was carried out under plain strain model using Plaxis-2D AE Version (Plaxis 2013). Mohr–Coulomb model has been considered for soil with 15 node element and linear elastic model have been considered for both soft as well as hard rock strata. Geogrid is defined as an elasto-plastic material. The foundation soil strata layers are modeled and assigned as initial phase. After that the reinforced soil system is slowly built up in number of phases as per the height of the structure. A live load of 24 kPa was considered over the airport operational road at finished level of RESA and on airport operational perimeter Road for 7-m width and air plane loading of 267 kPa was considered for a width of 3.54 m acting at 44.77 m from the edge of embankment. The project falls under Zone III as per Indian Standard Code IS: 1893 [8]. The actual seismic factors as per IIT Kanpur—GSDMA [9] are considered for design which is enhanced beyond IS: 1893. A horizontal seismic coefficient of 0.096 was considered for seismic case. The vertical seismic acceleration coefficient is taken as 0 as most of the damage occurs due to horizontal acceleration.

When the geometry model was complete, the finite element mesh was generated. PLAXIS 2D allows for a fully automatic mesh generation procedure, in which the



**Table 3** Design cross sections of RSS system

Design section	Bottom slope			Top slope			Stretch		
	Total height (m)	Slope angle (Deg)	Height (m)	Remarks	Slope angle (Deg)	Height (m)	Remarks	From	To
447	66.42	27	38.85	FS	43	28.25	RS	440	447
450	69.82	32	40.95	PRS	56	29.23	RS	447	450
452	73.04	38	43.62	RS	62	26.60	RS	450	452
453	71.18	42	41.56	RS	64	29.71	RS	452	453
470	67.38	45	37.41	RS	65	30.00	RS	453	480
480	69.05	36	39.08	RS	65	30.00	RS	480	490
490	70.50	30	40.53	PRS	65	29.97	RS	490	500
535	75.41	29	45.55	FS	65	29.89	RS	500	540
540	84.81	29	55.96	FS	53	29.25	RS	540	542
542	86.78	27	58.76	FS	44	28.53	RS	542	550

Note FS—free slope, RS—reinforced slope, PRS—partially reinforced slope

geometry is divided into element of the basic element type and compatible structural element, if applicable. The generation process is based on a robust triangulation principle that searches for optimized triangle. In addition to, the mesh generation itself a transformation of input data (properties, boundary condition, material sets, etc.) from the geometry model (point, line and clusters) to the finite element mesh (element, nodes and stress points) is made.

The finite element analysis was carried out to calculate the stress and deformations starting from initial phase up to the last layer of soil. In the initial phase, in situ soil is in  $K_0$  condition. After completion of deformation analysis in each phase, C—Phi reduction analysis is carried out to check the stability of the RSS structure in the safety analysis phases. The seismic analysis carried out using the pseudo-static approach.

The contribution of Gabion wall constructed to accommodate Jeep track was not considered in the design since the wall was non-uniform and discontinuous. Where the slope angle is more than  $45^\circ$ , wrap around fascia was considered in the design analysis. Maximum length of 82 m was designed at critical section at AOP road level which acted as basal reinforcement for top 30 m high-steep reinforced slope. The factor of safety values obtained at all sections are found to be adequate ( $FS \geq 1.3$  for static case and  $FS \geq 1$  for seismic case).

## 6 Construction Methodology

### 6.1 Ground Preparation

Initially, full formation width at ground level plus additional extra width as required was cleared, excavated and leveled to the designed foundation level. The existing ground (sloped) surface was excavated to the extent required to accommodate the primary reinforcement. The soil from all areas of cutting was stripped to a suitable depth not less than 150 mm to ensure removal of majority of root matter. This stripped of material (vegetative soil) was then stored as stockpiles for later use in fascia where vegetation is recommended as part of slope erosion protection. Whenever the fill is to be deposited against the face of natural slope or sloping earthworks face, such faces were benched before placing the subsequent fill to ensure adequate bond with the fresh embankment to be added.

The leveled surface was scarified, mixed with water and then compacted by rolling so as to achieve a minimum dry density of 98% MDD for a thickness of 150 mm. If the founding stratum was observed with loose pockets, it was then removed and replaced with suitable backfill material in layers not greater than 200 mm in thickness and compacted to minimum 98% MDD.

## 6.2 Gabion Construction

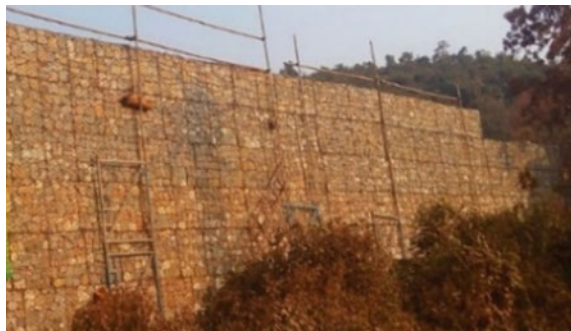
Toe gabion wall was constructed with a batter of  $6^\circ$  to the vertical by slanting the foundation level consequently. Gabions were delivered in bundles with the tie wire. Each gabion panels were straightened on a leveled ground to form a rectangular shape gabion box with the help of wooden mallet and batter/flank. All the gabions placed were connected to each other by lacing. MS pipe/frame formworks were provided at the gabion facia to keep bulges within the specified tolerances, while filling.

Filling was done manually to minimize voids to achieve maximum density as shown in Fig. 8. Stones used for gabion filling were placed in lifts of 300 mm. Stones with flat face were placed at the exposed faces to enhance the appearance and reduce the risk of construction induced damage (Fig. 9). Small-sized stones were provided only at the center of box. Internal cross-ties were provided using lacing wire after every 300 mm of fill connecting the front and back faces. The diaphragm position and overall dimensions of the gabion were checked constantly during the process. Gabion in the upper layer was connected to the top of lower layer along the front and back edges of contact using the same lacing connection. Back face of the gabion



Fig. 8 Gabion filling

Fig. 9 Elevation view of gabion wall



was wrapped with a non-woven geotextile extending 250 mm into the backfill at top and bottom in the form of C-shape wrapping. This prevents backfill being washed into stone voids in the event of rainfall and to drain-off excess water from backfill.

### 6.3 Reinforced Fill and Backfill Construction

Once foundation bed is prepared, weld mesh units were placed in position at slope face and fixed to ground using 8 mm U-pin. It was then wrapped with coir mat, extending 300 mm in to the backfill at bottom and top which is laid over-hung at the face. Diagonal hook bars were fixed to each unit. On reaching next level of mesh unit, the overhung portion of coir mat is wrapped around and fixed using U-pins/ wooden pegs.

The reinforced fill and backfill soil were spread in layers by mechanical means, finished by a motor grader and compacted using 10 T vibratory roller (Fig. 10). The reinforced soil was carefully placed and compacted in area behind the slope face extending up to the end of design reinforcement length. It was compacted in layers of 200 and 300 mm combinations, while backfill soil was compacted in layers of 300 mm thickness. Each layer of reinforced soil fill was compacted to 98% of MDD and backfill soil to 95% of MDD. The compaction was done with the help of self-propelled single drum vibratory roller of 10 ton capacity.



**Fig. 10** Construction activities: **a** dumping; **b** dozing; **c** grading; **d** compaction



**Fig. 11** Geogrid activities: **a** Unrolling of geogrid; **b** stretching and fixing of geogrid

On attaining geogrid level, layout of geogrids was marked on the prepared bed using total station and required grade of geogrid rolls were laid flat by unrolling and placed in continuous longitudinal strips from slope face (Fig. 11). It was then cut from the roll, tightened manually and pinned using 8 mm U-pin at regular interval of 2 m into the soil to ensure no slackness or undulation. Installation of geogrid was followed by placement of vegetative soil of 300 mm width at the slope face except for the gabion fascia location. Vegetative layer was compacted using plate compactor of 1 ton capacity. After every 0.8 m construction height, weld mesh units were placed and the construction activity repeats. Regions where slope angle is steeper than 45° to horizontal, primary geogrid were wrapped around weld mesh units. Wraparound length acts as a secondary reinforcement. After leaving sufficient length for wrapping, remaining installation of geogrid and related works are same as explained earlier.

The curvilinear alignment of the RSS system created non-uniform convex and concave faces for different tiers. Convex face creates gap between the adjacent reinforced zone. Therefore, additional geogrids of same grade to the adjacent section were used to cover the gaps as shown in Fig. 12. The geogrids were laid with a vertical



**Fig. 12** Geogrid arrangement at: **a** convex face; **b** concave face



**Fig. 13** Aerial view of chimney drain alignment in 5th tier

stagger of 200 mm so as to avoid physical contact between geogrids provided at sections adjoining the concave faces.

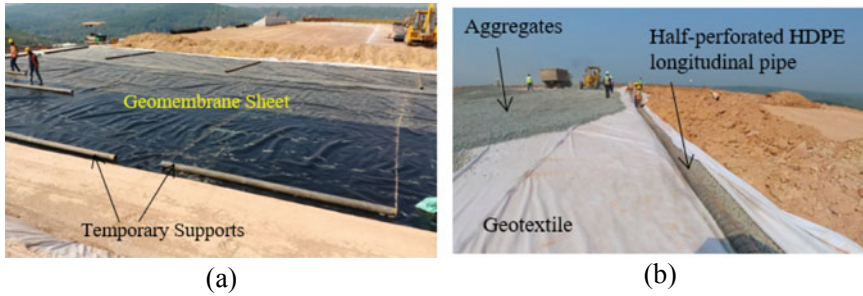
#### **6.4 Chimney Drain**

At rear end of the structural fill, a filter bay or chimney drain of 600 mm width is provided. The filter bay was filled simultaneously as the structural fill was placed and compacted layer by layer. At the interface of soil and filter media, non-woven geotextile was installed as a continuous roll extending upward along the fill height. Adjacent rolls were stitched together at an overlap of 100 mm. Chimney drain was constructed along the cut portion of the natural slope as it formed the rear end of reinforced fill up to third tier and thereafter, it rested on the side slope of backfill. The aerial view of chimney drain alignment in 5th tier is shown in Fig. 13.

315-mm diameter half perforated HDPE pipes were installed at the bottom of chimney drain with perforations facing upward. The perforated pipe was wrapped with geotextile throughout its length with an overlap of 50 mm stitched manually. The pipe was laid with a slope of 2–3% across the system for easy flow of water. Transverse HDPE pipes of specified diameters were connected to the perforated pipe using T-joints by welding. Transverse pipes were laid perpendicular to the chimney drain with a slope of –2% toward fascia. The ends of longitudinal pipe were closed using end caps.

#### **6.5 Subsurface Drainage System**

A systematic approach was followed in the construction of subsurface drainage system at the top. Initially, an impermeable geomembrane sheet was laid horizontally at the bottom most level of the subsurface drainage system as shown in Fig. 14a. The adjacent geomembrane sheets were joined by hot wedge welding with an overlap of



**Fig. 14** Subsurface drainage system

100 mm. The sheet was laid from the facia edge to the chimney drain end protecting the complete extend of reinforced zone. A similar arrangement was also provided below AOP road platform.

As drainage layer was designed with 1% longitudinal and 2% transverse slope, the bed was also prepared with same gradient. Rigorous level checking was done at close intervals to maintain the slope, with trenches made along the transverse direction from the centerline and also at the edges. Bed preparation was followed by the installation of bottom geotextile sheet, filter media and top geotextile sheet forming 200 mm thick filter media (Fig. 14b). Later, geotextile wrapped half perforated 315-mm diameter HDPE pipes were installed in trenches running along the edges of subsurface drainage system with perforations facing upward to collect water.

## 6.6 Quality Assurance and Quality Control

QA and QC performed during construction mainly applies to onsite field testing and associated laboratory tests. For reinforced fill, the maximum size of soil particle permitted was 100 mm and for backfill 2/3rd of compacted bed thickness. Each layer of reinforced fill was compacted to 98% MDD. The compaction was done with the help of 6–8 passes of self-propelled single drum vibratory roller of 10 ton capacity. While compaction within 1 m from the slope face was carried out using vibratory plate compactor having 1 ton capacity. Compacted density of the bed was checked using nuclear density gage testing machine. Subsequent layers were placed only after the bed has been tested and checked. If the moisture content of dumped soil is in excess of OMC, it is spread and left exposed to atmosphere to dry out, while if it is found to be deficient, then soil spread on ground is moisturized by sprinkling water.

All types of geosynthetics are supplied with test certificates indicating its properties. Geogrids were always examined for any kind of physical damage during installation and if found, it goes to scrap. Geogrids were laid straight and tight, perpendicular to the slope face. The alignment of geogrids was marked using total station, which in





**Fig. 15** RSS system: **a** Elevation view; **b** top view

turn checks the geometry of the system. No equipment's or machinery was allowed to pass directly on the geogrids.

Geomembrane sheets were joined by hot wedge welding. Peel test and shear test were carried out to ensure the quality of weld. Minimum value of 350 N/25 mm shear strength and 263 N/25 mm peel strength were obtained and marked satisfied. Also, 'break in the sheet not in the weld' was observed during the test. Air Pressure test was conducted to ensure quality of joint against leakage. The results indicated no drop in pressure more than 4 psi for 2 min and dropped immediately when the end away from pressure gage was opened, thus satisfying the requirement. The aerial view of RSS system after completion is shown in Fig. 15.

## 7 Conclusion

Design and construction of 70-m high reinforced soil slope system with very high-steep slopes along with curves and bends in a high rainfall area at Kannur International Airport was challenging for the contractor, Larsen & Toubro Ltd. Following are the conclusions made:

- The main choice of reinforced soil slope system over the traditional mass retaining structures is found in the flexibility, environmental friendliness and cost effectiveness of the RSS system. Furthermore, it was found faster in terms of construction schedule compared to the traditional methods.
- Choice of welded mesh facia system for slope protection was found to be adequate because of its handling and fabrication easiness at site. However, it is suggested to use this system for the entire reinforced slope region for a faster rate of construction.
- The robustness of the design and construction was proven when the system was exposed to extreme rainfall in two consecutive years. This was engineered in an innovative way fulfilling the requirements of stability and economy.



## References

1. ICAO-Annex 14, Volume I, Aerodrome Design and Operations, Eight Edition, July 2018.
2. Sunkavalli SK, Jain B, Tipnis M (2019) Case study-A state of the art, reinforced soil slope system for runway end safety area at Kannur International Airport, India. International Airfield and Highway Pavement conference. ASCE, Chicago, Illinois, pp 394–406
3. Gharpure AD, Kumar S.: Composite soil reinforcement system for retention of very high and steep fills—a case study. In: 5th European geosynthetic congress. Valencia 2012, vol 5, pp 346–352. ResearchGate (2012)
4. Prasad TK (2018) Landscape of Kannur: a geomorphological appraisal. Impact: IJRHAL 6(7):355–370
5. Rocscience (2007) RocLab. 1.031 edn. Rocscience Inc., Toronto
6. Bakkhtiyari E, Almasi A, Cheshomi A, Jafar H (2017) Determination of shear strength parameters of rock mass using back analysis methods and comparison of results with empirical methods. EJERS 2(11)
7. FHWA-NHI-10-025 (2009) Design and construction of mechanically stabilized earth walls and reinforced soil slopes—volume II, Federal Highway Administration, U.S. Department of Transportation, Washington, DC
8. IS 1893 Part 1 (2002) Criteria for Earthquake resistant design of structures. Bureau of Indian Standards, New Delhi
9. IITK-GSDMA (2007), Guidelines for seismic design of Earth Dams and Embankments. Indian Institute of Technology, Kanpur, India.

# Repeated Load Saturated Soil Behavior Linked to Two Derailment Case Studies



Theodore Sussmann

**Abstract** According to Hay (Railroad engineering, Wiley, New York, 1982), the support of railway track is a critical requirement to achieve the potential of railway track to serve as one of the most cost-effective types of infrastructure in terms of long-term maintenance cost. Uniform resilient support provided to the track structure (rails and ties) is needed to maintain stresses in the track structure that result from the applied train loading within an acceptable range. Excessive track deflection due to poor track support contributes excessive stress to track components. The shallower the support deterioration, the more severe the effect on the track structure and the deeper the support deterioration the more difficult it can be to locate and repair. Saturated-undrained soil conditions would not be expected to compromise track support in railway track built using commonly specified materials. However, changes in track drainage patterns and contamination of open-graded aggregate ballast has been known to result in roadbed saturation and associated softening that is listed in the FRA Railway Accident/Incident Reporting System as derailment cause code T001 Roadbed Settled/Soft. The technical cause of deterioration is often a moisture content increase associated reduction in strength. Repeated load behavior of saturated undrained soils is known to cause specific types of problematic failures that might be mitigated with operational limitations or maintenance. The potential for saturated-undrained repeated load soil failure modes in track can only be assessed if situations susceptible to these conditions can be identified. In this paper, the classic conditions related to these soil failures are discussed as a basis for review of two case studies illustrating the field conditions associated with two distinct failure scenarios.

**Keywords** Case study · Derailment · Pore water pressure · Cyclic mobility

---

T. Sussmann (✉)

U.S. DOT/Volpe Center, Cambridge, MA, USA

e-mail: [Ted.Sussmann@dot.gov](mailto:Ted.Sussmann@dot.gov)

University of Hartford, Hartford, CT 06117, USA

## 1 Introduction

Emerging railway operational scenarios aim to increase the cost-effectiveness of railway transport. Schedule reliability is a central requirement of any robust operational scenario aimed to improve cost-effectiveness [1]. Reliable rail track infrastructure is a critical element of track safety and schedule reliability. The goal of the track design, inspection, and maintenance process is to ensure safety and develop maintenance plans that address safety concerns and ensure track reliability. Each decision made during each phase of the life of track contributes to the reliability of the infrastructure. During track design, the trade-offs between a more robust design and initial cost are quantified and evaluated [2, 3]. Once constructed, the inspection phase is intended to identify safety defects and locations of early rail support failure for correction. As the condition of the track degrades over time, maintenance changes from an abnormal operation to correct a construction error or location that varied from design parameters early in the track life to a routine occurrence as the track deteriorates under traffic, time, and environmental conditions. At this latter stage in the track life, maintenance and inspection efforts target safety risks that sometimes include potential track support failure risks. Efforts to identify the root cause of track deterioration are continually pursued [4] by the industry in an effort to ensure that any repairs improve track structure performance in order to minimize future maintenance outages and limit the risks associated with track degradation. This paper will focus on saturated and undrained soil response under repeated load to identify field conditions potentially susceptible to these types of behavior. The nature of the failure and rate of deterioration is discussed to help link field conditions to the known failure conditions. Two derailments will be considered and linked to these specific track support related geotechnical conditions.

## 2 Railroad Case Studies

When assessing the potential influence of railway track substructure to develop saturated and undrained conditions that could affect roadbed stability, it is important to consider the depth of the layer and local drainage conditions. The risk posed by deeper layers susceptible to poor performance when saturated and undrained can often be minimized with good drainage. However, internal track drainage can become blocked as the ballast gradation becomes more fouled later in the ballast life. Under these conditions, the subballast and even the ballast layer itself might be subject to instability. When assessing the potential for saturated ballast instability it is important to consider:

1. the level of ballast disturbing maintenance or amount of traffic that has passed the site to assess whether the ballast is loose or dense,
2. ballast gradation and degree of ballast fouling,
3. the availability of water in the amounts needed to result in saturation, and

4. the likelihood of saturated and undrained conditions to exist.

Because the industry does an excellent job in identifying problem areas and diagnosing these problems for repair, relatively few examples exist that approach the conditions that would meet the requirements of saturated and undrained failure conditions. One failure attributed to saturated and undrained conditions occurred under test in Pueblo, CO [5] where a thick 15 in. (0.38 m) subballast layer was installed that was well-graded with a high percentage of fine sand size particles and smaller that blocked drainage. The track was subject to excessively heavy rains under traffic and the track settled and deformed excessively. Lacking other explanations, this case is perhaps the first observation of a saturated undrained failure condition in track. Two possible revenue service cases have been identified that appear to exhibit the distinct field conditions conducive to saturated undrained failure. These two cases will be discussed in appropriate detail to link the possible field conditions to the mechanics of saturated and undrained failure under repeated loading.

### 2.1 Cox Landing, West Virginia, 1998

A 1998 derailment in West Virginia was investigated by the National Transportation Safety Board that determined that “the probable cause of this derailment was an unstable roadbed that resulted from inadequate or ineffective measures...to permanently correct known drainage problems in the area” [6]. The site was a hillside adjacent to the Ohio River as shown in Fig. 1.

The NTSB report provides a somewhat more detailed discussion of the importance of drainage:

Although different types of roadbed soil will react differently to an excessive amount of water, complete water saturation will generally destabilize a roadbed. To avoid such saturation, the track system, including ballast and subballast, must be able to guide both rain and drainage water away from the track structure. The track ballast allows water to drain through it, while the subballast should be impermeable, guiding water away from the subgrade... [6].

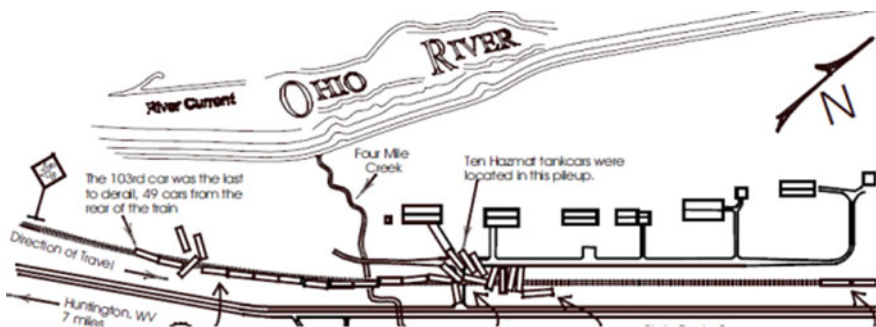


Fig. 1 Derailment site schematic in West Virginia [7]

While some might debate the claimed role of the subballast, the importance of drainage to the track structure is clearly stated and not debatable.

In this derailment, a very high level of maintenance was required to maintain track geometry within FRA track safety limits. A significant amount of track surfacing and alignment maintenance occurred including about twice-monthly repairs during the fall before the derailment [6]. This trend appeared to reestablish itself in the spring although at perhaps a less frequent interval. The track inspector is quoted as stating “the track just goes down” [6], which is interpreted to mean that once surfaced the track could not support the load from passing traffic without track geometry surface degradation indicating significant settlement in the area.

Meteorological reports [6] indicate a noteworthy amount of precipitation. The area had received 6.89 in. (0.175 m) of rain during June, which on average receives 3.51 in. (0.089 m) during the month of June. Even more important is the noted fact that a significant portion, 4.77 in. (0.121 m), of this rainfall occurred in the 11 days preceding the derailment. This fact seems to indicate that a very wet period with no significant dry periods preceded the derailment.

Drainage of the track in the area of the derailment was poor as noted by a local resident quoted in the NTSB report [6] as stating that the drainage ditch between the state highway and the track held standing water “all the time”. The derailment site is on a slope with the Ohio River at the bottom, some residences between the river and the tracks, and a state highway adjacent to and slightly above the tracks (Fig. 1). At the time of the derailment, no cross drains or other outlet for precipitation and runoff from the adjacent land and highway existed [6].

Analysis of the conditions at the site at the time of the derailment identified the major safety issue as “inadequate roadbed drainage and resulting roadbed instability” [6]. This conclusion combined with the track inspectors statements that highlight track settlement concerns clearly indicate the type of instability observed at the site aligns well with the expectations from the types of failures that can occur in saturated and undrained soils. However, a review will be conducted of the evidence that exists to help characterize the required four conditions necessary for saturated, undrained conditions of (1) ballast physical state (dense or loose), (2) gradation or ballast fouling, (3) source of water adequate to cause saturation, and (4) field conditions that approach undrained.

The repeated maintenance of track geometry occurred quite often at this site. Track surfacing for profile and alignment loosens the ballast, which takes significant energy to compact. Under optimum conditions, traffic might re-compact the ballast in a few days to a couple weeks depending on traffic density. However, the track inspector’s statement about the instability of track profile is a clue that compaction was not optimum, and the ballast was quite possibly in a loose state for extended periods.

The drainage conditions appear a bit more obvious since the heavy rain concentrated just prior to the derailment coupled with inadequate drainage highlighted by standing water both point to saturation of the roadbed. While poor drainage might not always indicate undrained conditions, it appears that the standing water and reduced

hydraulic conductivity of the ballast due to fouling indicate conditions approaching undrained.

Under the conditions of loose saturated ballast under repeated load in a saturated and undrained condition, the ballast could have been subject to liquefaction, which is a failure mode of loose, saturated, and undrained soils that will be discussed in the next section on track mechanics. The track inspector's comment about track settlement perhaps indicates some ballast re-compaction under load following maintenance, which would fit with the expectations for loose soils that tend to compact and densify under load. However, the difficulty in compacting fouled, saturated ballast likely indicates that at some point, the tendency toward volume reduction under repeated loading will be offset by the energy required to compact the ballast and void ratio/density will not change appreciably. At that point, continued loading could increase the pore water pressure resulting in the potential for liquefaction. The increase in pore water pressure would also reduce the resistance of the roadbed to applied static loads due to the reduction in the effective stress, which would further exacerbate the ballast deformation.

In this derailment, it appears that a case could be made that the mechanics of the roadbed instability might be attributed to loose, saturated, and undrained fouled ballast. Under these conditions, the ballast might not easily re-compact. The increased pore water pressure that might have developed under train loading would be expected to act as a pressure between particles that will have a tendency to push the particles apart and reduce contact stress between particles. The effect of this behavior is that this pressure reduces interparticle friction, which can destabilize the structure of the roadbed.

## **2.2 *Bronx, New York 2013***

A July 18, 2013 derailment in the Bronx, New York was investigated by the National Transportation Safety Board [8] which determined “that the probable cause of the accident was excessive track gage due to a combination of fouled ballast, deteriorated concrete ties, and profile deviations resulting from...” deferred maintenance. The derailment site is directly adjacent to a tributary to the Hudson River (Fig. 2). The right-of-way in this area consists of two tracks along the river. The land adjacent to the tracks includes a football field and baseball diamond in a low-lying area roughly one to two feet higher in elevation than the tracks. To each side of the sports fields are slopes up to residential areas.

The location is a typical drainage problem area with a significant runoff from the higher, developed residential areas to the low-lying ballfields. Groundwater from the ballfields appears very likely to flow to the river under the tracks. With the tracks roughly 0.3–0.6 m (1–2 ft) above high water level, depending on tides, and between 5 and 7 m (15 and 20 ft) away from the water's edge, roadbed drainage is critical. Clean ballast is necessary in track sections in this close proximity to water sources to promote water flow through the ballast and away from the track structure. The NTSB



**Fig. 2** Track conditions at the point of derailment [8]

report [8] notes that track conditions included fouled ballast and signs of pumping, abrasion of the tie bottom due to track movement under load, and track structure deterioration including rail seat abrasion (between the tie and rail) and signs of rail fastening deterioration including insulators out of position. These conditions point to an advanced stage of track deterioration since rail seat and tie bottom abrasion take time and traffic to develop.

The NTSB accident investigation [8] does not mention the presence or effect of moisture making this not seem like a case of saturated, undrained soil failure. However, a review of local news sources shows the early summer of 2013 to be a particularly significant time for precipitation including extreme flooding of the Mohawk River (largest Hudson River tributary) in June 2013 (Fig. 3). Significant precipitation events just preceding the derailment include:

1. During the 2 months between May 8 and July 8, 2013, New York City received 19.55 in. of rain, which is double the average [9]
2. 6.44 in. of rain on June 7–8, 2013 in New York City [7]. The rain event occurred over 33 sustained hours and was the second biggest June rainstorm in New York City history [9]
3. June 13 flash flooding in Schoharie County New York, just south of the Mohawk River [10]
4. June 28 flooding in Herkimer and Montgomery counties in New York, along the Mohawk River in western New York State [10].

These rainfall events prompted New York Attorney General Eric Schneiderman to have a report published titled “Current and Future Trends in Extreme Rainfall Across New York State” [7]. This report highlights a series of significant rainfall events that affected New York State with the photo of the Mohawk Valley flooding





**Fig. 3** Mohawk River valley flooding [7]

in 2013 on the cover (Fig. 3). The flow of these floodwaters from the Mohawk River to the Hudson River and south toward the derailment zone would occur over a period of time that includes the timeline for the derailment.

The impact of these precipitation events on the level of the Hudson River is obvious in the variations of river level data from the United States Geological Survey (USGS) gaging station at Piermont, NY (15 km (10 mi) north of the derailment toward the Mohawk River) from June 1 to July 18, 2013 (Fig. 4) [11]. The red line in the figure is termed the Mean Higher High Water level, which is “determined by averaging the highest of the 2 high tides that occur each day over a 19-year tidal” period [11]. Review of the data clearly indicates that this 19 year high water level was exceeded routinely for more than a month prior to the derailment including the day just preceding the derailment. These observations were corroborated with a review of Google Earth satellite imagery for the derailment site, where the increase in river level was confirmed. Google Earth imagery for the site shows the water encroaching from a distance of 10 m (32 ft) from the tracks and about 0.6 m (2 ft) below track elevation in 2010 to within 5 m (15 ft) of the tracks and about 0.3 m (1 ft) below track elevation in May 2013.

Based on this analysis, the likelihood is high that water was present in the track structure in sufficient quantity to establish saturation. This could occur without surface indications other than the mud pumping locations noted in [8] that were noted to be fouled with:

1. intrusion of soil [8],
2. deteriorated concrete noted by the gray color of the fouling material in the photos [8], and
3. the near universal presence of ballast breakdown particles in fouled ballast.



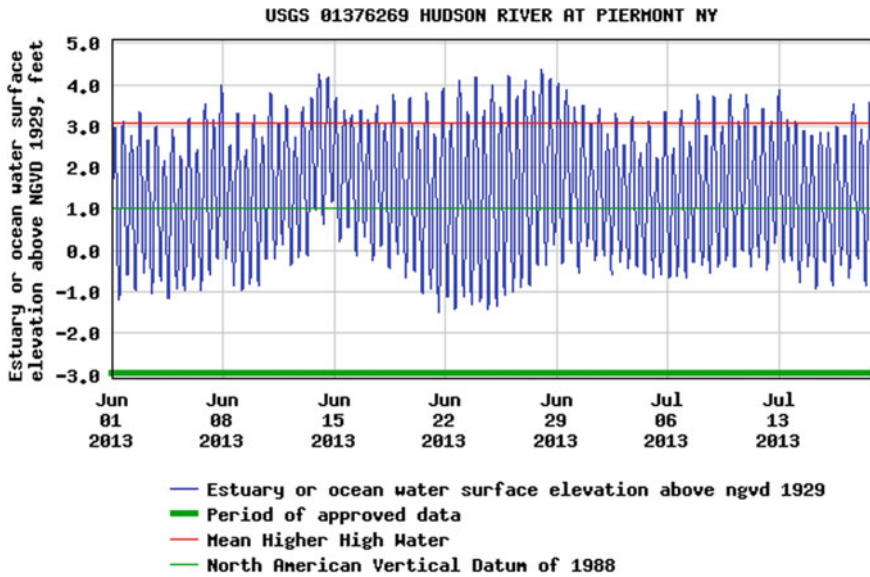


Fig. 4 Hudson River level at Piermont, NY [11]

Under these conditions, it is clear that ballast drainage could have been impeded and the conditions may have been sufficient for undrained behavior.

In this derailment, it appears that a reasonable case could be made that the mechanics of the roadbed instability might be attributed to dense, saturated, and undrained fouled ballast. Ballast is assumed dense at the onset of the failure due to high-traffic volume and stable track geometry that did not require ballast loosening track surfacing maintenance noted in the review of records in the NTSB report [8]. This may indicate that the deformation was rapid meaning that the ballast deformed under relatively few wheel loadings and a short time period, which would fit with the conditions for a saturated and undrained failure from an initially dense condition. Of course, once deformation occurs, the ballast would exist in a looser state from that point forward.

Under the expected initially dense conditions, the ballast would be dilative meaning that the particles are densely packed and unable to pass or override each other under train loading. Due to the high stresses from train loading and the interference from adjacent particles, it is possible that this could result in particle breakage and an associated reduction in volume. The volume reduction would lead to a pore water pressure increase and associated reduction in minor principal effective stress. If this were the conditions in track, then the type of saturated and undrained failure would be termed cyclic mobility.

Under the cyclic mobility failure scenario, the increased pore water pressure acts as a destabilizing pressure between particles that will have a tendency to separate particles. In the dense ballast packing, the high-interparticle forces might not be

reduced adequately to allow particle movement. In this case, the pore water pressure could be relieved at the track surface and manifested as mud boils or mud-pumping and spraying, which appears to be evident from photos of the site [8]. As this failure progresses, the volume reduction and increased pore water pressure will both act to reduce the confinement of the ballast until the particles rearrange to a looser density/higher void ratio leading to increased plastic deformation, settlement, and ultimately track geometry deviations and dynamic loading.

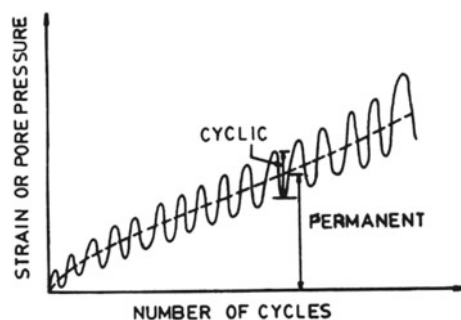
### 3 Relating Track Mechanics to Field Conditions

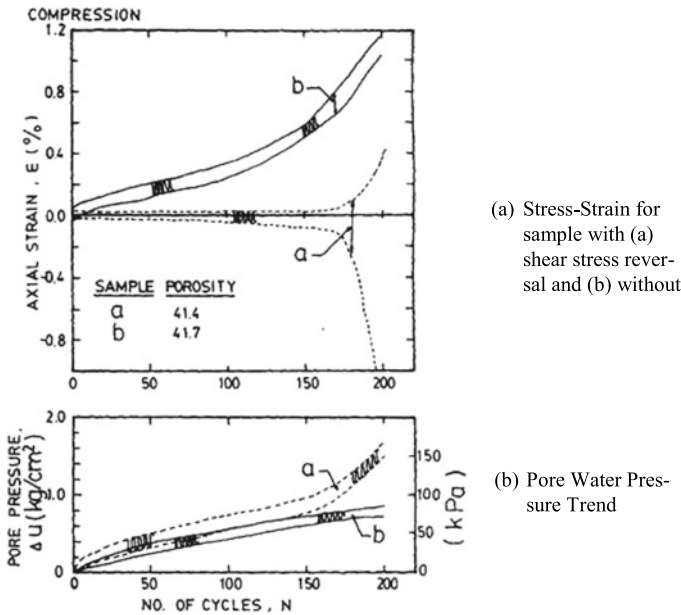
In this section, the mechanics of railway track behavior focusing on substructure considerations are discussed. The discussion is focused on describing each consideration to the extent necessary to make the connections to the field conditions related to each derailment, which will be described in a subsequent section. These descriptions are basic introductions and references are included for the reader interested in a more complete and definitive description.

#### 3.1 Stress State Considerations

The stress state of the soil under load is critical to the understanding of the failure mechanisms. In this paper, saturated undrained repeated load soil behavior is discussed as it relates to two case studies. In repeated load soil behavior of saturated undrained samples, shear stress reversal is of particular concern since it is one of the conditions necessary for rapid increase in pore water pressure noted in lab testing [2, 3, 12]. Figure 5 highlights the differences between cyclic and permanent strain whereby increasing permanent strain or pore pressure is the most significant failure mechanism under repeated load. In samples subject to shear stress reversal the cyclic permanent strain can dominate the behavior at or near failure as shown in Fig. 6.

**Fig. 5** Cyclic and permanent strain under repeat load triaxial testing [12]





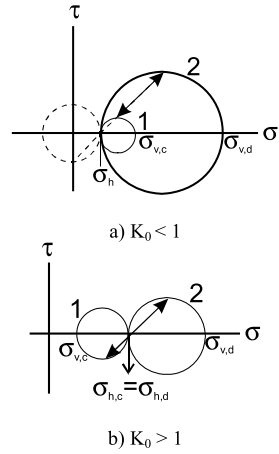
**Fig. 6** Deformation and pore water pressure trends associated with samples tested with and without shear stress reversal [12]

In Fig. 6, sample ‘b’ is similar to the trend presented in Fig. 5, because it was not subject to shear stress reversal. Sample ‘a’ in Fig. 6 is a sample subject to shear stress reversal that undergoes excessive strain during individual load cycles. The increase in cyclic strain is associated with an increase in pore water pressure [12].

Mohr’s Circle is one of the fundamental analytical tools for understanding issues related to state of stress. In addition to concerns related to exceedance of strength limits, the state of stress is important for highlighting problematic conditions such as the potential for development of shear stress reversal. Figure 7a presents the typical Mohr’s Circle for  $K_0$  less than 1. In this case, the unloaded case considering the static self-weight of the track is represented by circle 1 and the stress state with the applied wheel load in addition to the track self-weight is represented by circle 2 (Fig. 7). The change from 1 to 2, does not involve shear stress reversal as the shear stress remains positive along the path noted 1–2 in the figure.

In granular, uniform coarse-graded aggregate ballast used to support track, high  $K_0$  conditions develop under repeated loading [3] from passing wheels applying incremental stress pulses that often compact and interlock particles. Figure 7b presents the state of stress associated with a  $K_0$  condition greater than 1 with the vertical stress less than the horizontal stress in circle 1. From this condition, the applied wheel load is added resulting in circle 2. Under this condition, the added incremental stress due to the wheel load is relatively large and exceeds the deviatoric stress. The minor principle stress is the vertical stress which receives the predominant dynamic loading,

**Fig. 7** Mohr circles for repeated loading



while the major principle stress (horizontal) remains approximately constant creating circle 2 (Fig. 7b). Under these conditions, the shear stress will change from negative to positive along the noted path.

The dashed circle in Fig. 7a shows the state of stress that could develop with a sufficiently large deviator stress to apply a horizontal stress exceeding the vertical stress, possibly induced by large lateral loads induced by passing traffic. In this case, shear stress reversal could also occur.

It is important to understand both the incremental and static loading when analyzing the stress state since the static stresses might exceed the applied train loading depending on the depth of the point in the track being analyzed.

### 3.2 Physical State Considerations

The physical state of geomaterials describes the density and moisture content, among other characteristics-like plasticity. Since most track materials above the subgrade are non-plastic, the physical state parameters discussed in this paper will relate mainly to density as described by the unit weight or void ratio and moisture content. The state diagram describes conditions of saturated, undrained, dynamic soil failure linked to the physical state of the material as measured by either density or void ratio. A dense material (low void ratio and high density) can be expected to behave and fail in a different manner from a loose material (high void ratio or low density) and these differences are described by different regions in the state diagram in Fig. 8 [13].

Figure 8 presents a classic state diagram depicting the steady state line that separates the dense material to the bottom left and the loose materials to the upper right. Materials starting in either region (loose or dense) may change state under loading whereby loose materials will compact under load and dense materials may loosen (dilate). The void ratio and minor principal stress would be expected to shift under

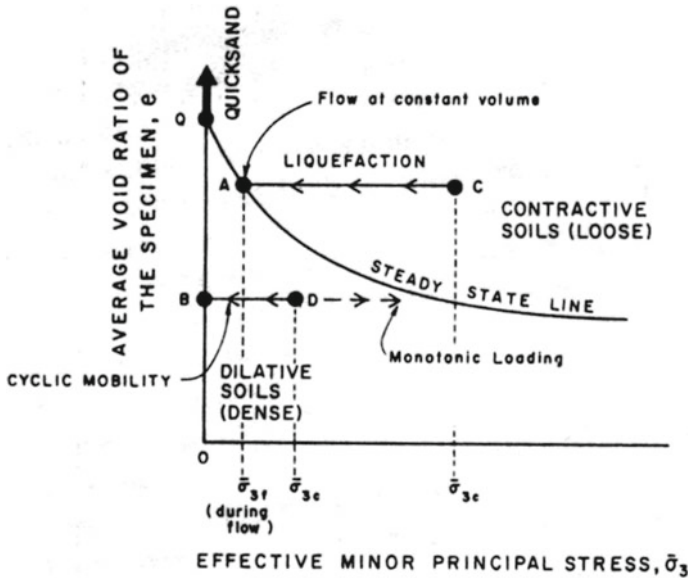


Fig. 8 Classic state diagram [13]

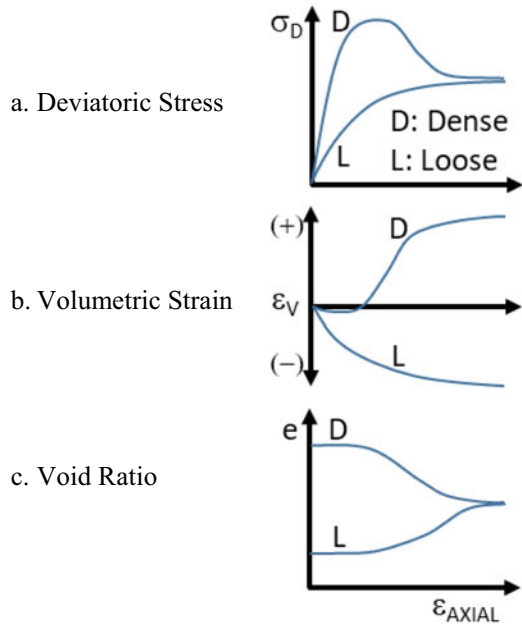
load with a tendency for changes toward the steady state line. However, soils do not tend to readily cross the steady state line and rather often tend to progress toward and along the steady state line under further loading [3].

### 3.3 Stress Strain Response

The stress–strain behavior of soil depends heavily upon the state of stress and physical state of the soil. Figure 9 depicts the stress–strain response under monotonic loading to failure. In Fig. 9a, the deviatoric stress increases more rapidly in dense materials resulting in a higher Young’s Modulus than soil in an initially loose state. In addition, the peak in the deviatoric stress–strain curve for dense soil is a characteristic shared with the lateral resistance of well-compacted (consolidated) track. It is noted that when a soil is tested starting either initially loose or dense, the deviatoric stress at large axial strain approaches a common value in both cases.

In Fig. 5b, the volumetric strain for initially loose soil reduces nearly exponentially with strain. For initially dense soils, some initial reduction in volumetric strain may occur as particles rearrange, but this particle rearrangement ultimately results in a positive volumetric strain (volume increase). This is termed dilation and is characterized by particle-to-particle interference as load is applied whereby the initial dense packing of particles must loosen to allow particles to move past one another. If the particles cannot pass to accommodate the required strain to support the applied

**Fig. 9** Typical stress–strain response of soil after [14]



load at this density, then particle breakage is likely to occur. The increase in volume for dense soil and reduction in volume for loose soil is the mechanism by which the phenomena in Fig. 5c develops whereby the initial loose or dense void ratio changes during testing approaching a common void ratio at large axial strain.

#### 4 Linking Mechanisms to Failures

The repeated load behavior of soil can be somewhat different from the behavior described for a single quasi-static load applied to failure shown (Fig. 9). The relatively common failure mode of earthquake-induced liquefaction occurs in loose sand subjected to earthquake shaking or vibration and other types of dynamic loading, which generates increased pore pressure, resulting in reduced effective confining pressure and ultimately flow along the steady state line (Fig. 8). Although some cases of loose sand might be found in transportation structures such as pavement or track, the occurrence can be limited with good construction practices. Maintenance prior to the Cox Landing, WV site would have loosened the ballast and created conditions susceptible to this type of failure. While, Cox Landing was associated with a deeper seated instability, the presence of poor drainage and possibility for high-pore water pressure to develop under traffic is likely to have contributed to the failure in one of three ways:

1. aggravating existing conditions at the site by contributing additional water under pressure to the deeper failure,
2. resulted in poor load distribution once an upper layer liquefied that accelerated the failure by concentrating additional load deeper in the track structure, and/or
3. destabilization of the roadbed that triggered the derailment.

Under repeated load, soil samples regardless of initial density have a tendency to reduce in volume during testing. As each load pulse is applied, a small amount of rearrangement or breakage occurs that contributes to the volume reduction, although dense soils have less tendency for volume reduction.

Failure modes that may occur in dense soils are below and to the left of the steady state line in Fig. 8 and are described as failure under monotonic loading and cyclic mobility in the figure. Monotonic loading refers to quasi-static load increase that will cause an increase in the minor principle stress of a dense, dilative soil resulting in negative pore water pressure development and a net increase in effective minor principal stress. On the other hand, cyclic mobility refers to the reduction in confining stress under repeated load as previously discussed. The tendency for volume reduction under repeated loading would result in positive pore water pressure that could reduce the effective minor principal stress.

Railway ballast is placed in track loose and then compacted under traffic or under a dynamic track stabilizer. When clean and well-drained, the ballast can compact without the complications offered by the state diagram. In these cases, the clean ballast will densify under traffic. However, the addition of fouling material and moisture will influence the behavior and compaction of ballast.

When ballast deteriorates under traffic, the ballast is expected to be dense, as it has compacted under traffic. When saturated, this tendency toward volume reduction and compaction can be impacted. Traffic loading is quite rapid with repeated load applications in the tens of Hz and associated significant vibrations up to 50 Hz or more. Compounding the problem, railway track has a relatively long drainage path. The shortest drainage path length would be the outer track where water would need to drain the track width plus the shoulder, which is about 2.4–3 m (8–10 ft). Center tracks can be double this drainage length or more. Resistance to flow or ponding at various points have been noted by many authors [2, 3] indicating that saturated conditions likely exist in ballasted railway track, at least temporarily [3]. Under these conditions, wet fouled ballast subject to loading from passing traffic would most likely be subject to the path represented by cyclic mobility (Fig. 8) as the tendency for volume reduction due to ballast breakage at high-interparticle contact stress leads to increased pore water pressure and decreased minor effective principal stress. This appears to have been possible during the derailment in The Bronx where dense compact and fouled ballast combined with significant rainfall and a location adjacent to water and in the path of a significant drainage feature of the nearby area. High-pore water pressure in the ballast appears to be evident as spraying and pumping conditions were noted in the accident investigation [8].

Track maintenance to address track geometry irregularities results in an increase in void ratio (decrease in density). This loosening of ballast usually results in the

ballast being subject to traffic at a reduced speed to reestablish ballast compaction and lateral track resistance to avoid track buckling risks associated with continuous welded rail (CWR) [15]. As the traffic compacts the loose ballast, the void ratio will decrease and pore water pressure could increase if the ballast is saturated. In this case, ballast that might start at point C would move down and to the left toward the steady state line. However, until the ballast is drained or dried, reestablishing ballast compaction to a dense position below the steady state line is problematic, as the saturated ballast will tend to spread or otherwise deform and move along the steady state line. Another option would be for the ballast to densify (decrease void ratio) under constant confining stress resulting in a movement vertically downward in Fig. 4. Under these conditions, the ballast may compact and increase density (reduce void ratio), but the ballast will not tend to cross the steady state line and instead will propagate either to the right (increase confining stress) or the left (decrease in confining stress). Either process is problematic since the loose ballast could reasonably be expected to deform and not provide a solid foundation for track until drained or dried.

## 5 Summary

The ballast is a critical element in the structure of the track providing the support to the tie needed for track to achieve the stability required to ensure safety at a reliability level that supports the cost-effectiveness of the industry. Ballast fouling is a result of deterioration under traffic and external contamination that can change the well-drained, uniformly graded ballast aggregate to a saturated layer of well-graded aggregate subject to excessive deformation. The mechanisms by which this deformation accumulates have been the subject of speculation and often attributed to moisture related strength reduction.

In this paper, two case studies of derailments were presented where conditions approaching the saturated undrained conditions necessary for rapid deterioration of soil under repeated load may have been present. These cases were presented for two reasons: First to promote more advanced discussion and recognition of the complex failure modes that can exist in track and second to identify conditions that might be avoided through targeted risk reduction. For instance, one potential improvement could be ensuring maintenance of fouled ballast occurs during dry periods when possible and recognizing the potential limitations of surfacing and re-compacting wet fouled ballast when maintenance is required in wet periods. Another possible outcome could be that train operations are limited in particularly wet, saturated, or near flood stage conditions. Limiting operations to empty trains or slowing operations appropriately are both possibilities. However, significant data are required to help inform analyses that could support or refute these possibilities since pore water pressure in track has not been measured on any routine basis previously.

Ongoing research by the Federal Railroad Administration is pursuing development of wireless technology to support the basic measurement of pore water pressure



in track. Additional work is planned to demonstrate links between saturated undrained soil behavior and track performance. In the future, lab testing is planned to provide measurements that support improved understanding of the particular conditions of track and ballast failure with the goal of highlighting specific risks and mitigation measures. This effort is geared toward ensuring that ballasted railroad track continues to fulfill its historic role as a highly safe and cost-effective form of infrastructure.

## References

1. Hay WW (1982) *Railroad Engineering*. Second Edition. Wiley, New York, NY
2. Li D, Hyslip JP, Sussmann TR, Chrismer SM (2015) *Railway geotechnics*. CRC, Boca Raton, FL
3. Selig ET, Waters JM (1994) *Track geotechnology and substructure management*. Thomas Telford, London
4. Sussmann TR, Thompson HB (2017) Track structure design for maintenance and rehabilitation with automated track inspection data track. In: *Proceeding of the International heavy haul association meeting*. Cape Town, South Africa, September 2017
5. Read D, Li D (1995) Subballast considerations for heavy axle load track. In: *Technology digest 95-028*. Association of American Railroads, Washington, DC
6. National Transportation Safety Board (1999) *Railroad accident report NTSB/RAR-99/01*. NTSB, Washington, DC
7. New York State Attorney General (2014) Current and future trends in extreme rainfall across New York State. [https://ag.ny.gov/pdfs/Extreme\\_Precipitation\\_Report%209%202%2014.pdf](https://ag.ny.gov/pdfs/Extreme_Precipitation_Report%209%202%2014.pdf). Accessed 10 Apr 2020
8. National Transportation Safety Board (2014) *Railroad Accident Brief NTSB/RAB-14/11*. NTSB, Washington, DC
9. Frydlewicz R (2013) New York City weather archive. <https://thestarryeye.typepad.com/weather/2013/01/new-york-weather-recap-for-2013.html>. Accessed 10 Apr 2020
10. National Weather Service (2017) *Major Floods*, U.S. NWS, Albany, NY. <https://www.weather.gov/aly/MajorFloods>. Accessed 10 Apr 2020
11. National Weather Information Service (2020) Hudson River at Piermont, NY. In: *United States Geologic Survey, NWIS*. [https://waterdata.usgs.gov/nwis/uv/?site\\_no=01376269](https://waterdata.usgs.gov/nwis/uv/?site_no=01376269). Accessed 10 Apr 2020
12. Selig ET, Chang CS (1981) Soil failure modes in undrained cyclic loading. *J Geotech Eng Div 107(GT5):539–551*
13. Castro G, Poulos SJ (1977) Factors affecting liquefaction and cyclic mobility. *J Geotech Eng Div 103(GT6):501–516*
14. Holtz RD, Kovacs WD (1981) *An introduction to geotechnical engineering*. Prentice Hall, Englewood Cliffs, NJ
15. Kish A, Samavedam G, Al-Nazer L (2013) Track buckling prevention: theory, safety concepts, and applications. In: *Federal Railroad Administration, Report Number DOT/FRA/ORD-13/16 (2013)*.

# **Deep Foundations**

# Study on Pile-Soil Interaction Mechanism and Failure Modes of CFG Rigid Pile Composite Foundation in the Fluid-Plastic Soft Soil of High-Speed Railway



Tai-Feng Li, Jian-Ping Yao, Zhi-Bo Cheng, Qian-Li Zhang, Yin Gao, Jin-Fei Chai, Jing-Yu Liu, and Xin-Gang Zhang

**Abstract** In order to solve existing engineering problems, such as variable and dynamic slope stability issues of railway embankments, limited soil bearing capacity, and post-construction settlement of foundations in fluid-plastic soft soil, etc., the Cement-Fly Ash-Gravel (CFG) rigid pile composite foundation has been used as the main foundation design method. However, due to the lower shear strength and the thixotropy of fluid-plastic soft soil, and the lack of research on pile-soil interaction mechanisms especially for the pile-soil modulus ratio, these will influence the effectiveness of CFG rigid pile foundation design. Therefore, it is crucial and essential to study the anti-shear contribution and the failure mode of CFG rigid piles in the foundation treatment of fluid-plastic soft soil. This paper starts with the finite element analysis of the structural mechanism of single rigid piles in the fluid-plastic soft soil under different working conditions. The results show that the stiffness of the pile body itself, the pile-soil modulus ratio, the shear strength of soil, and the angle between pile and the sliding arc tangent of soil are the main influencing factors of the apparent shear strength (defined as the maximum anti-shear force the pile can provide). Furthermore, with an increase of the angle between the pile and the shear plane, the failure modes of piles will gradually transition from the tensile bending failure to compression bending failure. When the pile-soil modulus ratio is greater than 4000:2, the CFG pile and other rigid piles are not suitable for fluid-plastic soft soil foundation. Considering both safety and economy factors, drainage consolidation treatment should be used to improve the shear strength of fluid-plastic soft soil foundation, then follow with the CFG rigid pile composite foundation treatment. Based on research achievements and some investigations from new-built railway

---

T.-F. Li (✉) · J.-P. Yao · Q.-L. Zhang · J.-F. Chai · J.-Y. Liu · X.-G. Zhang  
Railway Engineering Research Institute, China Academy of Railway Sciences Corporation Limited, Beijing 100081, China

Z.-B. Cheng  
Institute of Computing Technologies, China Academy of Railway Science Corporation Limited, Beijing 100081, China

Y. Gao  
Transportation Technology Center, Inc., Pueblo, CO 81001, USA

construction projects, these combined treatment methods can significantly improve the effectiveness of foundation treatment and increase the slope stability of railway embankments.

**Keywords** High-speed railway · Slope stability · Foundation treatment · Fluid-plastic soft soil · Pile-soil interaction · Pile-soil modulus ratio · Apparent shear strength

## 1 Background

For the high-speed railway foundation treatment in the fluid-plastic soft soil region of China, rigid piles such as Cement-Fly Ash-Gravel (CFG) piles, pipe piles, and reinforced concrete pouring piles are widely to be used to solve the problem of insufficient foundation bearing capacity [1, 2] and post-construction settlement. However, in the actual engineering project, there are still a series of engineering problems such as failure of foundation treatment, overall slippage of the subgrade during filling process, and instability and sinking of the railway subgrade in the short term after railway operating [3]. This is mainly due to the lack of understanding of the extremely low shear strength and high thixotropic engineering properties of the fluid-plastic soft soil, and the unclear understanding of the interaction mechanism between pile and soil with large differences in pile-soil modulus [4]. Also, the research on the shear contribution and failure mode of CFG piles in the fluid-plastic soft soil foundation is not deep enough. The traditional limit equilibrium method is still used in the embankment stability analysis, which overestimates the stability of the embankment [5]. This can cause the improper selection of foundation treatment methods in practical engineering.

In order to solve the engineering problems in the treatment of fluid-plastic soft soil foundation, this paper uses a finite element analysis method to numerically analyze the working mechanism of single pile in different conditions in fluid-plastic soft soil. The main research of this paper will focus on the different pile-soil modulus ratios, the different angles between piles and sliding arc tangent, the shear behavior of piles under different shear strength of soil, the failure mode, and the interaction mechanism between piles and soils. The shear contribution of single pile has been defined as the apparent shear strength in this paper. Furthermore, this paper will also explore the relationship between the apparent shear strength and the pile stiffness, the difference of pile-soil modulus, the shear strength of soil, to analysis and find out the possible failure mode of the pile.

## 2 Using FEA Model to Simulate Direct Shear Test

This section will use FEA model to simulate the direct shear test of soil. The main soil sample parameters are shown in Table 1.

In order to calculate the interaction between fluid-plastic soft soil and CFG pile, four types of soil samples were selected in this paper. The first three soil samples (A–C) are typical fluid-plastic soft soil, the parameters are obtained from the in-door tests. The fourth soil sample (D) has been set as an ideal clay, with improved cohesion force and the internal friction angles, compared with the former soil samples. The difference between the clay and the fluid-plastic soft soil in the interaction between pile and soil will be further discussed in this paper, and the soil sample B has been set as the original sample for the comparison analysis.

### 2.1 Calculation Parameters of Direct Shear Test

Table 2 shows the calculation parameters required for the numerical simulation of the direct shear test, as well as the theoretical values of the shear strength, shear force, and the applied force of the shear soil. It is generally believed that the maximum shear force that a shearing soil can provide should theoretically be equal to the applied force it receives.

For the known soil strength parameters and vertical stress, the shear strength of the soil in the failure state can be obtained by Coulomb’s law. Since the shear force is equal to the applied force, after considering the corresponding area, the average applied force of the soil on the acting surface can be obtained.

**Table 1** Parameter of four soil samples in the simulated direct shear test

Soil type	Elastic modulus (MPa)	Cohesion (kPa)	Internal friction angle (°)	Pile-soil modulus ratio
A	8.4	9.4	5.9	4000:2
B	4.0	5.0	5.0	4000:1
C	12.0	14.6	11.2	4000:3
D	20.0	25.0	10.0	4000:5

**Table 2** Parameter of soil sample B in the simulated direct shear test

Vertical stress (kPa)	Cohesion (kPa)	Internal friction angle (°)	Pile-soil modulus ratio	Shear force (N)	Shear strength (MPa)	Applied force (Mpa)
100	5.0	5.0	4000:1	52.51	0.014	0.085
200	5.0	5.0	4000:1	85.92	0.023	0.139
300	5.0	5.0	4000:1	119.34	0.031	0.193

### 2.2 Calculation Method of the Direct Shear Test

The main purpose of this direct shear test simulation calculation is to verify whether the shear strength inside the soil is equal to the external applied force received by the known soil parameters (Mohr–Coulomb model).

In order to get the soil shear stress results, a cubic shear soil sample has been optimized from the original cylinder sample in this FEA model. The soil size was adjusted with the consideration of the true direct shear test model. The direct shear model is mainly composed of four parts: upper shear box, lower shear box, upper shear box cover, and shear soil.

The length, width, and height of the both upper and lower shear box are  $84 \times 84 \times 20$  mm, respectively. In order to minimized the influence to the calculation results, the shear box was set as a rigid body. The dimension of the shear soil is  $61.8 \times 61.8 \times 20$  mm, which can be embedded into the middle grooves of the shear boxes.

A uniform vertical stress of 100–300 kPa is applied to the upper surface of the soil, and the shear displacement is set to 7 mm to ensure that the soil reaches complete shear failure and shear. The shear time duration is set as 420 s, the shear displacement per minute is 1 mm. The theoretical shear strength of the soil under different vertical pressures can be obtained from the relationship between the known shear strength and the vertical pressure.

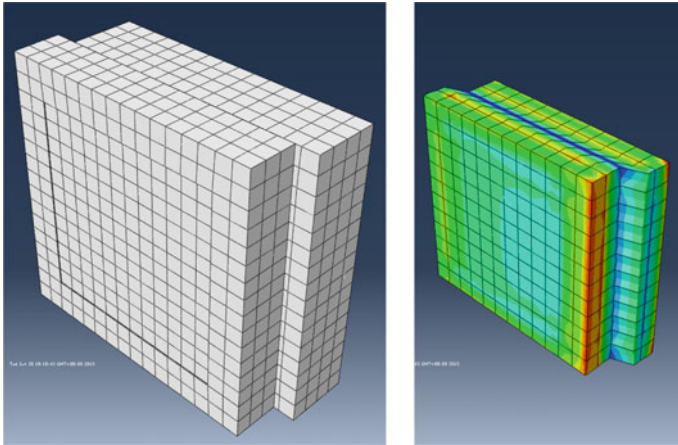
### 2.3 Calculation Results of the Direct Shear Test

The maximum shear displacement has been set as 7 mm in the FEA model, in order to make all soil samples close to or achieve complete shear failure. In the actual direct shear test, it is generally considered that the shear displacement of the soil (non-fluid plastic soft soil) reaches 4–5 mm, and the soil can be considered to have complete shear failure.

This paper will mainly focus on the studies of pile-soil interaction between fluid-plastic soft soil and CFG pile. Therefore, when the vertical stress is small, the soil cannot completely reach the shear failure, as in Case 1 in Table 3 (vertical stress 100 kPa). When the vertical stress is large enough, both Case 2 and Case 3 achieve

**Table 3** Comparison of both numerical and theoretical solution of direct shear simulation

Vertical stress (kPa)	Theoretical shear force (N)	Theoretical shear strength (MPa)	Applied stress (MPa)	Modified shear strength (MPa)	Modified applied stress (MPa)	Modified shear force (N)	Modified applied force (N)
100	52.51	0.014	0.085	0.015	0.089	58.180	55.288
200	85.92	0.023	0.139	0.023	0.141	87.058	86.906
300	119.34	0.031	0.193	0.031	0.192	118.528	118.523



**Fig. 1** The deformation form of shear box and soil after shearing

full shear failure, which is also consistent with the classical Coulomb's law for the shear strength expression of cohesive soil.

However, this equation does not fully consider the case of soil plastic strain. Therefore, it is necessary to correct the simulated shear strength and the simulated applied force stress from the FEA model. After considering a series of factors such as shear time and reverse friction, the modified results are basically consistent with the theoretical results (Table 3), which also proves the accuracy and reliability of FEA model.

Figure 1 shows the deformation shape of the shear box and the sheared soil after shearing. The shear box has been set horizontally, with the applied load vertically. The visual direction of Fig. 1 has been modified to show more detail in a single view.

It can be seen that the FEA model is very similar to the actual direct shear test, and the shear strength of the soil is mainly distributed on the shear plane, which can prove the reliability and accuracy of FEA model.

### **3 Study on Mechanism of Pile-Soil Interaction in Fluid-Plastic Soft Soil Composite Foundation**

#### ***3.1 Numerical Calculation of Interaction Between Single Pile and Soil***

This section will consider the interaction of single pile and soil, which totally includes 52 working conditions, in order to find the pile-soil interaction (four soil types) under different pile body and the sliding arc tangent angle.

Different from the direct shear test, this section will consider the pile-soil interaction between the fluid-plastic soft soil and the CFG pile, so a cylindrical CFG pile model will be inserted into the original shear soil in the FEA model [6].

The diameter of the pile model is 3 mm, with the length as 20 mm, which can be inserted vertically at the middle of the shear soil. The included angles were set between  $-30^\circ$  and  $+30^\circ$ . Four different pile-soil modulus ratios are set from 4000:1 to 4000:5 (shown in Table 4).

### 3.1.1 Calculation Parameters of Pile-Soil Interaction

In order to specifically explain the interaction between single pile and soil, this section will take the working condition 2A as an example to explain the calculation process and calculation results of the single pile-soil interaction. The strength parameters of each soil sample are shown in Table 5:

### 3.1.2 Definition of the ‘Apparent Shear Strength’

From the macroscopic analysis, the stress of soil and pile is considered separately. The resistance provided by pile can be thought as the anti-sliding force provided by the foundation minus the resistance provided by soil. This resistance provided by pile is defined as apparent shear strength. Therefore, the apparent shear strength of the pile in the simulated shear test is numerically equal to the difference between the applied force and the shear force of the soil around the pile.

There is a direct relationship between the apparent shear strength and the pile stiffness, the difference of pile-soil modulus, the shear strength of soil and the included angle between the pile and the sliding arc tangent.

### 3.1.3 Calculation Results of Pile-Soil Interaction.

It can be seen from Table 6 that the simulation results are highly consistent with the actual situation. The shear strength of soil mass is all 0.02 MPa, so it can be calculated that the shear force provided by soil mass in the shear plane is 75.23 N.

Since the CFG pile has a higher ‘shear strength’ than the original soil mass, the applied force stress is slightly improved from the original 0.12–0.13 Mpa, and the total applied force of the soil is 81.96 N. After considering the horizontal cross-sectional area of the pile ( $7.07 \text{ mm}^2$ ) the apparent shear strength of the pile can be calculated as 0.95 Mpa.



**Table 4** Totally 52 working conditions of single pile soil interaction

Soil type	Modulus ratio	The included angle between pile and sliding arc tangent, $\alpha(^{\circ})$												
		30	25	20	15	10	5	0	-5	-10	-15	-20	-25	-30
B	4000:1	27B	23B	19B	15B	11B	7B	<b>3B</b>	31B	35B	39B	43B	47B	51B
A	4000:2	26A	22A	18A	14A	10A	6A	<b>2A</b>	30A	34A	38A	42A	46A	50A
C	4000:3	28C	24C	20C	16C	12C	8C	<b>4C</b>	32C	36C	40C	44C	48C	52C
D	4000:5	29D	25D	21D	17D	13D	9D	<b>5D</b>	33D	37D	41D	45D	49D	53D

**Table 5** Calculation parameters of pile-soil interaction

Working condition (No.)	Pile-soil modulus ratio	Elastic modulus (MPa)	C (kPa)	$\Phi$ (°)	Shear force (N)	Shear strength (MPa)	Applied stress (MPa)
2A	4000:2	8.4	9.4	5.9	75.37	0.020	0.122
3B	4000:1	4.0	5.0	5.0	52.51	0.014	0.085
4C	4000:3	12.0	14.6	11.2	131.38	0.034	0.213
5D	4000:5	20.0	25.0	10.0	162.82	0.430	0.263

**Table 6** Calculation results of apparent shear strength under working condition 2A

Results	Shear strength (Mpa)	Applied stress (Mpa)	Shear force (N)	Applied force (N)	Apparent shear strength (Mpa)
Simulation	0.02	0.13	75.23	81.96	0.95
Realistic	0.02	0.12	—	—	—

### 3.2 Working Mechanism of Single Pile Under Different Pile-Soil Modulus

The difference of pile-soil modulus has a great influence on the shearing effect of pile in soil. The working mechanism of pile body under different pile-soil modulus ratio will be analyzed in this section. The main soil parameters are shown in Table 5.

#### 3.2.1 Failure Modes of Piles Under Different Pile-Soil Modulus

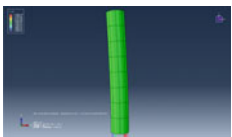
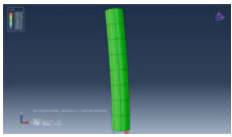

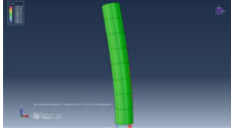
It can be seen from Table 7 that with the decrease of the pile-soil modulus ratio, the failure modes of the pile are as follows: the bending failure, the bending failure with tensile-bending failure, and the tensile-bending failure.

This is because as the strength of the soil increases, the apparent shear strength of the pile increases, and it can bear a larger applied force, which is completely consistent with the theory of pile-soil interaction.

#### 3.2.2 Apparent Shear Strength of Piles Under Different Pile-Soil Modulus

It can be seen from Table 8 and Fig. 2, as the strength of the soil increases in sequence, the apparent shear strength of the pile increases nonlinearly. When the pile-soil modulus is relatively large, the external applied force cannot be transmitted to the pile body completely effectively. Therefore, the apparent shear strength that the pile can provide is limited, such as the working condition 3B in the Table 8, the apparent shear strength of the pile is only 0.667 MPa.

**Table 7** Failure modes of piles under different pile-soil modulus

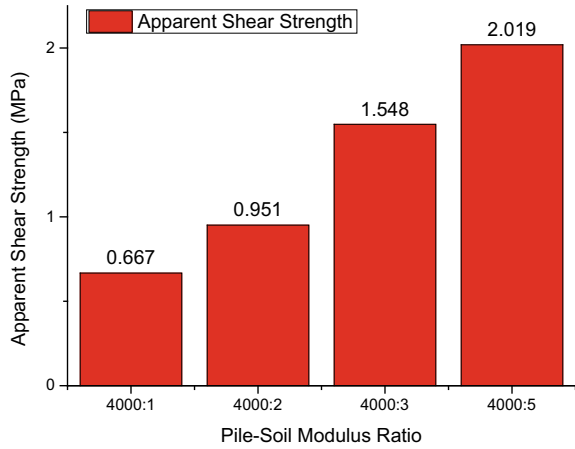
Pile-soil modulus ratio	Working condition	Failure mode	Vertical stress of pile body
4000:1	3B	Bending failure	
4000:2	2A	Bending failure to tensile-bending failure	
4000:3	4C	Tensile-bending failure	
4000:5	5D	Tensile-bending failure	

**Table 8** 'Apparent shear strength' of pile body

Pile-Soil modulus ratio	Working condition	Shear strength (MPa)	Applied stress (MPa)	Shear force (N)	Applied force (N)	Apparent shear strength (MPa)
4000:1	3B	0.014	0.09	52.41	57.13	0.67
4000:2	2A	0.020	0.13	75.23	81.96	0.95
4000:3	4C	0.034	0.23	131.14	142.08	1.55
4000:5	5D	0.043	0.29	162.52	176.79	2.02

In order to improve the stability of the foundation, it is necessary to treat the fluid-plastic soft soil to increase its strength [7], so as to more effectively conduct the external applied force to the CFG pile, hence, the pile can contribute a higher apparent shear strength.

**Fig. 2** Relationship curve between apparent shear strength and pile-soil modulus ratio



### 3.3 Working Mechanism of Single Pile Under Different Included Angle Between Pile and Sliding Arc Tangent

In this section, the working mechanism of the single pile is analyzed when the pile and the sliding arc tangent are at different included angles.

Different included angles reflect the different location of pile body under the subgrade. As the included angle between the pile body and the shear plane increases, the failure mode of the pile body gradually changes from the tensile-bending failure, the bending failure to the compressive-bending failure, and the compression failure.

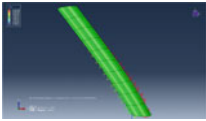
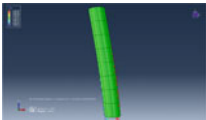
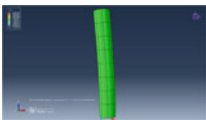
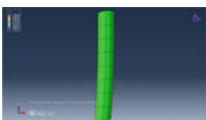
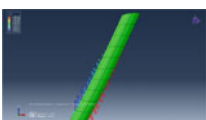
Soil sample A was selected as the soil sample for calculation. The soil strength parameters remained unchanged and only the included angle between the pile and the shear plane was changed from  $-30^\circ$  to  $+30^\circ$ . Every  $5^\circ$  change is one level, for a total of 13 working conditions.

#### 3.3.1 Failure Mode of Pile Under Different Included Angle Between Pile and Sliding Arc Tangent

Table 9 shows the different failure modes of the piles under different included angle between the pile body and the shear plane. It can be seen from the Table 9, with the included angle increases gradually, the failure modes of the piles have undergone tensile-bending failure, bending failure, and compressive-bending failure respectively.

When the included angle between the pile and shear plane is negative, it means that the pile has axial tension, and the failure mode is tensile failure). Working condition 2A shows the failure mode of the pile when the included angle is zero. There is no obvious axial tension and compression inside the pile, and the failure mode of the pile is only general bending failure. When the included angle between the pile and

**Table 9** Failure modes of piles under different included angle of pile and sliding arc tangent

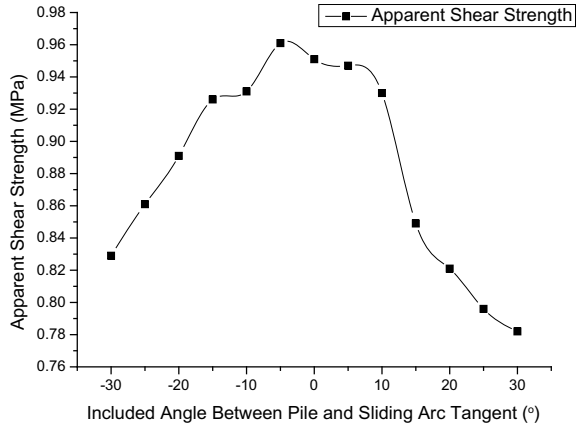
Included angle (°)	Working condition	Failure mode	Vertical stress of pile body
-30	50A	Tensile-bending failure	
-5	30A	Tensile-bending failure	
0	2A	Bending failure	
+5	6A	Compressive-bending failure	
+30	26A	Compressive-bending failure	

shear plane is positive, it indicates that the pile has axial pressure, and the failure mode is bending failure.

### 3.3.2 ‘Apparent Shear Strength’ of Pile Under Different Included Angle

Figure 3 shows the relationship between the apparent shear strength of the pile and the angle of the sliding arc tangent. When the pile body is close to vertical (zero included angle), its apparent shear strength reaches the maximum. When the pile body inclination is positive or negative, the apparent shear strength will decrease correspondingly, and the positive and negative inclination angles are basically symmetrically distributed. When the pile is at the same absolute inclination, the tensile failure can provide more apparent shear strength than the compression failure [8].

**Fig. 3** Relationship between ‘apparent shear strength’ of pile and included angle between pile and sliding arc tangent



**Table 10** Extended parameter of soil sample B in FEA model

Soil type	Elastic modulus	Cohesion	Internal friction angle	Pile-soil modulus ratio
	MPa	kPa	°	
B-1	4	5	5	4000:1
B-2	8	10	5	4000:2
B-3	12	15	5	4000:3
B-4	16	20	5	4000:4
B-5	20	25	5	4000:5

### 3.4 Interaction Mechanism Between Pile and Soil Under Different Soil Strength

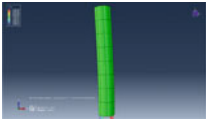




In order to further study the influence of soil strength on pile-soil interaction, this section makes some corresponding adjustments to the original soil sample B.

Table 10 shows the type of soil sample used in the FEA model. The elastic modulus  $E$  and the cohesion force of the soil sample B2–B5 are 2–5 times higher than the original soil sample B1, respectively, the internal friction angle  $\varphi$  remains unchanged.

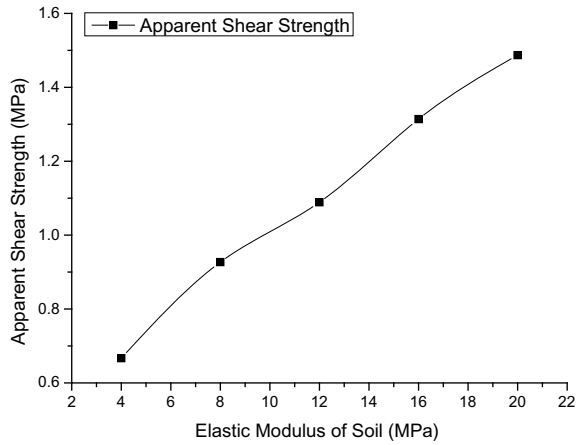
#### 3.4.1 Failure Modes of Piles Under Different Soil Strength

Table 11 shows the failure mode of the pile under different soil strengths. With the increased of soil strength, the failure mode of the pile gradually transitions from bending failure to tensile-bending failure, the increase amplitude is not too obvious. It can be seen from Fig. 4 that as the strength of the soil increases, the apparent shear strength of the pile increases substantially linearly.

**Table 11** Failure modes of piles under different soil strength

Pile-soil modulus ratio	Soil type	Failure mode	Vertical stress of pile body
4000:1	B-1	Bending failure	
4000:2	B-2	Bending failure	
4000:3	B-3	Bending failure	
4000:4	B-4	Bending failure to tensile-bending failure	
4000:5	B-5	Tensile-bending failure	

**Fig. 4** Relationship between soil strength and 'apparent shear strength'



### 3.4.2 Adaptability of Piles Under Different Soil Strength

As the strength of the soil increases, the apparent shear strength of the pile is significantly improved. It should be specially noticed that there is a nonlinear relationship between the increase of the apparent shear strength and the increase of the soil strength. When the elastic modulus of the soil is increased from 4 to 8 Mpa, the cohesion force is increased from 5 to 10 kPa, and the apparent shear strength of the pile is increased by nearly 40%, which is the maximum efficiency.

In the follow-up situation, although the apparent shear strength of the pile has also been improved to a certain extent. However, in an actual engineering project, it is necessary to adopt a stronger ground treatment method, which is less economical.

Therefore, it can be considered that when the pile-soil modulus ratio is greater than 4000:2, the fluid-plastic soft soil foundation is not suitable for rigid pile treatment such as CFG [9]. When the pile-soil modulus ratio is equal to 4000:2, it is the best interaction between pile and soil. At this time, the most effective apparent shear strength can be provided at the most economical cost.

When the soil strength is too low, and the pile-soil modulus is relatively large, the CFG pile cannot provide sufficient apparent shear strength, which will seriously affect the stability of the foundation. Therefore, the reinforcement of the pile-side soil is particularly important.

However, considering the factors of optimal economy and maximum efficiency, the reinforcement of the pile-side soil is not as large as possible. When the pile-soil modulus ratio is less than 4000:2, the foundation treatment has limited increase in the apparent shear strength of the pile, the construction cost is uneconomical, which is not recommended.

## 4 Conclusion

In this paper, the FEA model is used to numerically analyze the mechanism of a single pile under different working conditions in the fluid-plastic soft soil. The shear behavior, failure mode, and interaction mechanism of piles and soils under different conditions of pile-soil modulus ratio, pile and sliding arc tangent included angle, and shear strength of soil is studied.

1. This paper puts forward the concept of apparent shear strength of piles. The use of apparent shear strength in the calculation of subgrade stability can more accurately reflect the shearing effect of piles in the foundation. The traditional method of stability checking, simply using the shear strength of the pile will overestimate the stability of the subgrade.
2. The theoretical value of the apparent shear strength of the pile under different working conditions of pile-soil modulus ratios and included angles of the pile and shear plane is calculated in this paper, which provides a theoretical basis for the calculation of fluid-plastic soft soil subgrade stability. As the pile-soil



modulus ratio decrease, with the strength of the soil increases, the failure modes of the piles are gradually transformed from the bending failure to the tensile-bending failure. This is due to the increase of the apparent shear strength followed with the increase of the soil strength.

3. The angle between the pile and the tangent of the shear plane reflects the position characteristics of different piles under the subgrade. As the included angle increases gradually, the failure mode of the pile gradually changes from the tensile-bending failure and the bending failure to the compressive-bending failure and compression failure.
4. With the increase of soil strength, the failure mode of the pile gradually changes from bending failure to tensile-bending failure, but the increase amplitude is not too obvious. When the pile-soil modulus ratio is greater than 4000:2, the fluid-plastic soft soil foundation is not suitable for rigid pile treatment.

**Acknowledgements** This work was funded by the National Natural Science Foundation of China (Grant U1834206, 41731288) and the Foundation of China Academy of Railway Sciences Co., Ltd. (Grant 2020YJ048).

## References

1. Zhou J, Ye YS, Cai DG (2007) Analysis of calculation method for foreign geosynthetic reinforced pile supported embankments. *China Railw Sci* 28(2):1–6
2. Terashi M (2003) The state of practice in deep mixing methods. *Grouting Ground Treatment* 25–49
3. Kitazume M, Maruyama K (2005) Collapse failure of group column type deep mixing improved ground under embankment. In: *Proceedings of international conference on deep mixing best practice and recent advances*, pp 245–254
4. Gong XN (1999) Development of composite foundation and its application to high rise building. *China Civ Eng J* 32(6):3–10
5. Kitazume M, Kenji M (2007) Internal stability of group column type deep mixing improved ground under embankment loading. *Soils Found* 47(3):437–455
6. Han J, Huang J, Porbaha A (2005) 2D Numerical modeling of a constructed geosynthetic-reinforced embankment over deep mixed columns. In: *Contemporary issues in foundation engineering*, pp 1–11
7. Navin MP, Filz GM (2006) Numerical stability analyses of embankments supported on deep mixed columns. In: *Ground modification and seismic mitigation*, pp 1–8
8. Wu CQ, Xiao DP (2007) Stability analysis of embankment on composite subgrade. *Rock Soil Mech* 28(S1):905–908
9. Dong L, Ye YS, Cai DG et al (2006) Contrast test on soft ground improvement of high-speed rails. *Rock Soil Mech* 27(10):1856–1860

# Analysis and Reconstruction of Rock Joint Surface Based on DCT Algorithm



Lianheng Zhao , Dongliang Huang , Shuaihao Zhang, Xiang Wang, Yingbin Zhang, and Shi Zuo

**Abstract** Research on the mesoscopic geometrical characteristics of joint surfaces has been a topic of considerable interest. Based on discrete cosine transform theory, this paper presents a novel morphology characterization and reconstruction method to quantitatively analyze the 3D geometrical characteristics of rock joints. The joint surfaces are segmented and transformed into standard grid data sets, which are termed, the discrete time-domain signals. Based on discrete cosine transform algorithm, it is possible to convert discrete time-domain signals into a discrete spectrum. Then, the normalized amplitudes of the spectrum are defined as descriptors, which are found to be applicable to characterize and reconstruct the joint surface. Further, the proposed method is used to analyze 205 measured 3D joint samples, and is validated by comparing the surface of the real rock joint with that of reconstructed surface. The research provides an insight into the rapid random reconstruction of joint surfaces, which is beneficial for field identification of discontinuities and providing virtual test samples for numerical modeling.

**Keywords** Discrete cosine transform (DCT) · Rock joint · Morphology · Reconstruction

---

L. Zhao · D. Huang · S. Zhang · X. Wang (✉) · S. Zuo  
School of Civil Engineering, Central South University, Changsha 410075, Hunan, China  
e-mail: [wang.xiang@csu.edu.cn](mailto:wang.xiang@csu.edu.cn)

L. Zhao  
Key Laboratory of Heavy-Haul Railway Engineering Structure, Ministry of Education, Central South University, Changsha 410075, Hunan, China

Y. Zhang  
Key Laboratory of Transportation Tunnel Engineering, Ministry of Education, Southwest Jiaotong University, Chengdu 610031, Sichuan, China

Department of Geotechnical Engineering, School of Civil Engineering, Southwest Jiaotong University, Chengdu 610031, Sichuan, China

## 1 Introduction

Morphological characteristics are important in the study of shear strength of rock joint surfaces. Scholars have carried out series of research studies using shear testing as the basic criterion. Barton et al. [1, 2], based on the back-calculation results of many shear tests used to extract the profiles of joint surfaces proposed the classic Barton-Bandis failure criterion for rock mass and its embedded joint roughness coefficient, *JRC*. Later, Tse and Cruden [3], Yu and Vayssade et al. [4, 5] proposed statistical indices to estimate the *JRC* value: the root mean square ( $Z_2$ ) and structure function ( $SF$ ).

In recent years, numerical simulation has become an effective means to study the shear characteristics of rock joint surfaces. With the development of 3D scanning and printing technology, it is possible to obtain high-precision 3D models of joint surfaces, which brings a wealth of samples for numerical simulations [6] and indoor shear test [7–10]. There are also some studies on the quantitative reconstruction of joint surfaces. Besides 3D scanning, scholars reconstruct the virtual joint surfaces based on specific parameters and study their influence on shear performance of rock mass. In this respect, models are mainly reconstructed based on the dentate line stretching method [11] and the random number generation method [12]. However, the reconstructed joint surfaces are quite different from the 3D scanning results. Zhao et al. [13] carried out the related research based on discrete Fourier morphological analysis method and achieved good results, but limited to 2D joint profiles. The study of 3D joint surface reconstruction methods requires new theories.

This paper proposes a novel method for spectral analysis and reconstruction of joint surfaces. First, the joint surfaces in the field are collected using photogrammetry technology. The standard data sets of joint surfaces and the corresponding database are obtained. Then, samples are decomposed into spectrums using discrete cosine transform (DCT) algorithm and the distribution characteristics of each component are statistically analyzed. The fitting model for the spectrum is proposed and the undetermined coefficients are solved based on the database. Finally, based on piecewise spectral control, a novel method for joint surface reconstruction is proposed using the inverse discrete cosine transform (IDCT) algorithm.

## 2 Photogrammetry-Based Acquisition and Pre-processing of 3D Joint Surface

The acquisition of the joint surface can be done using a camera and a calibration board (Fig. 1a). In practice, the calibration board is placed on the joint surface to calibrate camera parameters and also to create a local Cartesian coordinate system. Then, the camera is moved according to the array scanning frame (Fig. 1b) to ensure the degree of overlap (greater than 60%, see Fig. 1c) in adjacent images [14, 15], and the image sequence is collected directly opposite the joint surface. Then, the image sequence

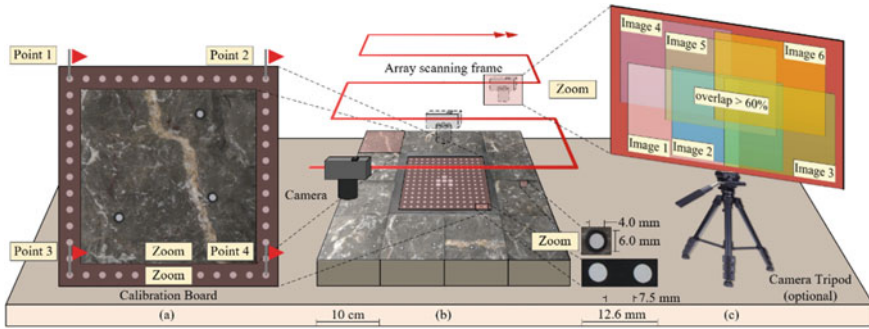


Fig. 1 Array scanning frame for rock joint

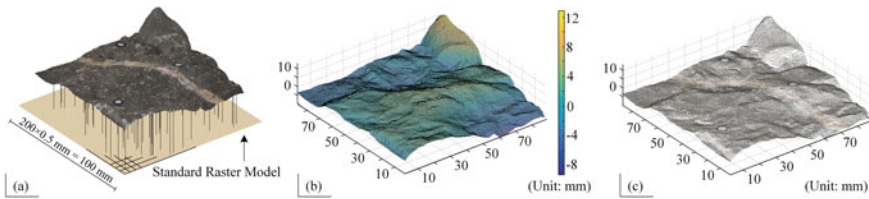


Fig. 2 Workflow of point cloud pre-processing

solving work is completed on the computer to obtain the sparse point cloud. After that, the dense point cloud can be reconstructed. Using the aforementioned procedure, the image resolution becomes 0.05 mm and accuracy also become at least 0.1 mm [16], which makes it suitable for the acquisition of rock joint. Further, the dense point cloud is segmented to form a segmentation point cloud with a projection size of 100 × 100 mm and a number of point clouds of 200,000–300,000. After removing the noise [17], the point cloud can be resampled into a standard raster dataset by the nearest-neighbor interpolation [10], with a sampling interval of 0.5 mm (Fig. 2). A total of 205 samples obtained, were mainly medium weathered limestone.

### 3 Spectral Analysis and Reconstruction Method of Rock Joint Surface Based on DCT Theory

#### 3.1 Rock Joint Spectral Analysis and Reconstruction Method

The rock joint surface collected in the field is resampled according to the standard raster model in Sect. 2, then, the time domain signal  $[z]$  for DCT transformation can be obtained. In the application of DCT [18–20], the joint surface sample is decomposed into  $N \times N$  cosine surface waves distributed from low frequency to high frequency,

and each surface wave is consistent with the size of the joint surface. The spectrum  $[D]$  is formed by extracting the amplitude of each cosine surface wave and arranging them in a matrix form (Eqs. (1)–(5)).

$$z_0 = \frac{1}{N^2} \sum_{x=0}^{N-1} \sum_{y=0}^{N-1} z[x, y] \tag{1}$$

$$D[0, 0] = \frac{1}{N^2} \sum_{x=0}^{N-1} \sum_{y=0}^{N-1} z[x, y]/z_0 = 1 \tag{2}$$

$$D[0, v] = \frac{2}{N^2} \sum_{x=0}^{N-1} \sum_{y=0}^{N-1} z[x, y] \cos \frac{(2y + 1)v\pi}{2N} /z_0; (v = 1, 2, \dots, N - 1) \tag{3}$$

$$D[u, 0] = \frac{2}{N^2} \sum_{x=0}^{N-1} \sum_{y=0}^{N-1} z[x, y] \cos \frac{(2x + 1)u\pi}{2N} /z_0; (u = 1, 2, \dots, N - 1) \tag{4}$$

$$D[u, v] = \frac{4}{N^2} \sum_{x=0}^{N-1} \sum_{y=0}^{N-1} z[x, y] \cos \frac{(2x + 1)u\pi}{2N} \cos \frac{(2y + 1)v\pi}{2N} /z_0; \tag{5}$$

$$(v = 1, 2, \dots, N - 1; u = 1, 2, \dots, N - 1)$$

where  $z[x, y]$  is the time domain signal and  $D[u, v]$  is the frequency domain signal (the time domain signal has the same size as the frequency domain signal);  $N$  is the signal length in each dimension, which means that the signal must be a square matrix containing a total of  $N \times N$  discrete points;  $z_0$  is the mean value of  $[z]$ ;  $x = 1, 2, \dots, N - 1$  and  $y = 1, 2, \dots, N - 1$ .

In the application of the IDCT, the new signal  $[Z]$  superimposes  $N \times N$  cosine surface waves on the original mean surface  $z = z_0$ , which also forms the reconstructed rock joint surface Eq. (6). The value of the element in the spectrum matrix  $[D]$  multiplied by  $z_0$  corresponds to the amplitude of the cosine surface wave at the same location. Based on a real case of the joint surface spectrum decomposition, the corresponding schematic diagram of Eq. (6) is shown in Fig. 3a.

$$Z[x, y] = z_0 + z_0 \left\{ \sum_{v=1}^{N-1} D[0, v] \cos \frac{(2y + 1)v\pi}{2N} + \sum_{u=1}^{N-1} D[u, 0] \cos \frac{(2x + 1)u\pi}{2N} + \sum_{u=1}^{N-1} \sum_{v=1}^{N-1} D[u, v] \cos \frac{(2x + 1)u\pi}{2N} \cos \frac{(2y + 1)v\pi}{2N} \right\} \tag{6}$$

It can be clearly seen from Fig. 3b, that, the amplitude elements on the main diagonal of the spectrum matrix  $[D]$  shows an exponential change [20, 21], although

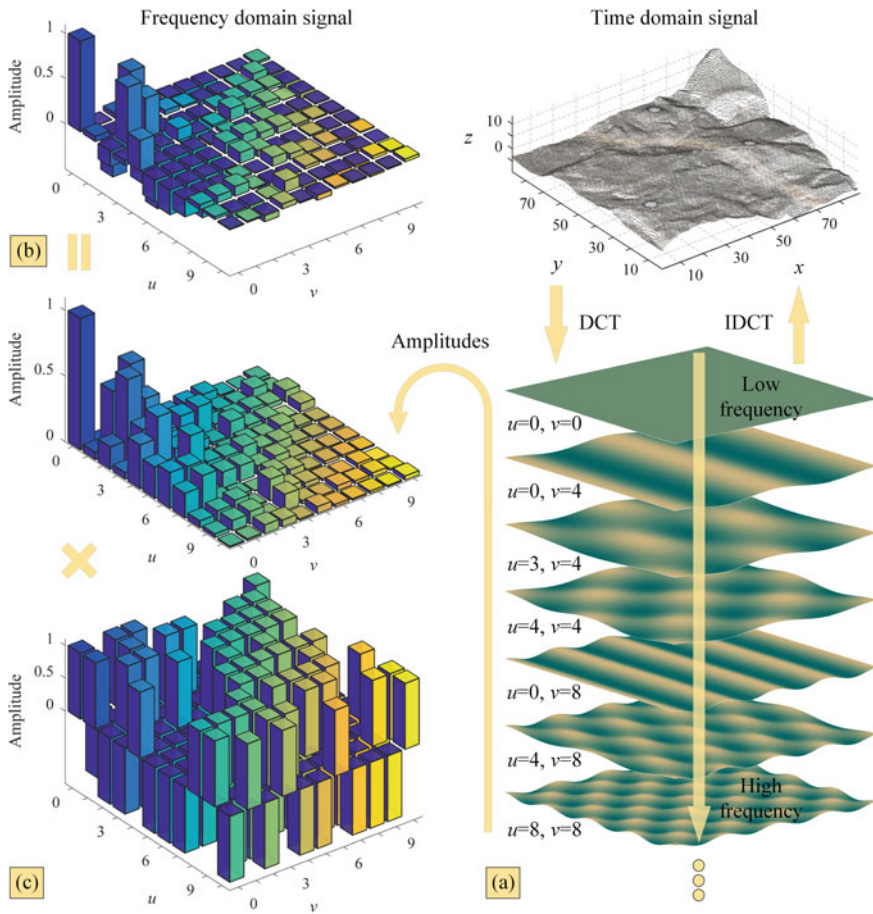


Fig. 3 Schematic diagram of discrete cosine transform

the local values fluctuate. The pattern of variation is more pronounced after removing the negative sign (Eqs. (7) and (8)):

$$D'[u, v] = |D[u, v]|; \varphi'[u, v] = D[u, v]/|D[u, v]|; \quad (7)$$

$$(v = 1, 2, \dots, N - 1; u = 1, 2, \dots, N - 1)$$

$$D[u, v] = D'[u, v] \cdot \varphi'[u, v]; (v = 1, 2, \dots, N - 1; u = 1, 2, \dots, N - 1) \quad (8)$$

where  $[D']$  is a positive matrix named “the modified spectrum” and  $[\varphi']$  is named “the symbol matrix” consisting entirely of  $-1$  and  $1$ . Compared to the matrix  $[D']$ , the symbol matrix  $[\varphi']$  exhibits randomness (Fig. 3c).

The different  $z_0$  values will affect the level of the matrix  $[D]$ , in fact, the morphology of the joint surface has no relationship with the mean value of  $[z]$  ( $z_0$ ).

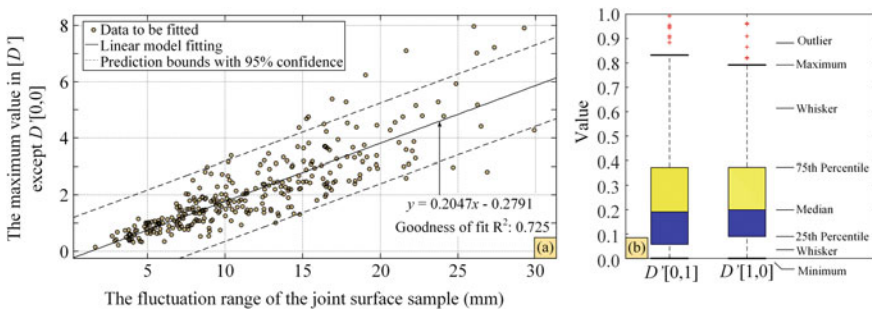
Therefore, to facilitate the calculation and ensure the uniformity of the spectrum during the analysis for different joint surfaces, defining  $z_0 = 1$ . Then,  $z_0 = D [0, 0] = 1$ . Equation (6) is transformed into Eq. (9).

$$Z[x, y] = 1 + \sum_{v=1}^{N-1} D[0, v] \cos \frac{(2y + 1)v\pi}{2N} + \sum_{u=1}^{N-1} D[u, 0] \cos \frac{(2x + 1)u\pi}{2N} + \sum_{u=1}^{N-1} \sum_{v=1}^{N-1} D[u, v] \cos \frac{(2x + 1)u\pi}{2N} \cos \frac{(2y + 1)v\pi}{2N} \tag{9}$$

### 3.2 Empirical Formula for Spectral Reconstruction

The rock joint spectral analysis method was applied to the databases with 205 samples being analyzed. It can be observed that the spectral peaks of all samples are in the low-frequency region (the upper left corner of the spectrum matrix), and its value varies greatly. Therefore, the range of the  $z$ -axis coordinate values were calculated to measure the degree of undulation of each joint surface. Then, a scatter plot was generated with the ranges for all samples on the  $x$ -axis and the spectral peaks on the  $y$ -axis, and the trend line was fitted. It can be seen from Fig. 4a that the range varies linearly with the spectral peak. The goodness of fit  $R^2$  is 0.725, which is highly correlated.

A box plot of  $D' [0, 1]$  and  $D' [1, 0]$  in all sample spectrums (Fig. 4b) is then evaluated, confirming that the values of the two elements are much smaller than those of other low-frequency regions. In fact, the cosine surface waves in this frequency band are only half a cycle length, showing the tilt of the joint surface. The tilt has little relationship with the degree of undulation of the joint surface, so in the analysis process,  $D' [0, 1]$  and  $D' [1, 0]$  can be regarded as 0.



**Fig. 4** Rock joint spectrum statistics: **a** the relationship between the range of the  $z$ -axis coordinate values and the spectral peak. **b** Box plots of  $D' [0, 1]$  and  $D' [1, 0]$

Further, the mean values of all sample spectrums were calculated and presented in scatter form in Fig. 5a, b. It can be seen that after filtering out the local random features of the single sample spectrum, the spectrum shows a more pronounced exponential change. And it can be seen that the values of each row in the spectrum orthogonal to the main diagonal are substantially equal and can be regarded as the same level. Based on this, the fitting model for the discrete cosine transform spectrum is proposed (Eq. 10) with reference to the fitting empirical formula for the discrete Fourier transform spectrum in Mollon [21] and Zhao [20]. The model assumes that elements at the same level in the spectrum have equal values, and define the descriptors  $D_0, D_1, D_2, D_3, \dots, D_8, \dots, D_{N-1}$  (Fig. 5c), arranged from the top left to the bottom right of the spectrum. In the lower right corner of the spectrum matrix, the values are insignificant to affect the morphology of the joint surface and can be ignored in the fitting model.

$$\begin{cases} n = v + u; (v = 0, 1, 2, \dots, N - 1; u = 0, 1, 2, \dots, N - 1) \\ D_0 = 1 \\ D_1 = 0 \\ D_n = 2^{\alpha \cdot \log_2(\frac{n}{3}) + \log_2(D_3)}; 3 < n < 8 \\ D_n = 2^{\beta \cdot \log_2(\frac{n}{8}) + \log_2(D_8)}; 8 < n < N - 1 \end{cases} \quad (10)$$

where  $\alpha, \beta$  are constant parameters and dimensionless coefficients of correction, with  $\alpha \in [-2, 0]$ , and  $\beta \in [-2, 0]$ .

Regard the mean values of the elements at the same level as the raw data for the least squares fitting, forming the spectrum mean surface (the red part in Fig. 5a, b). Then, apply the aforementioned fitting model to fit the spectrum mean surface (the green part in Fig. 5a, b). After fitting,  $D_2 = 1.2575, D_3 = 0.7513, D_8 = 0.1454, \alpha = -1.6524, \beta = -1.7578$ , goodness of fit NRMSE = 0.70383, indicating good fitting effect. From the front view (Fig. 5a) and the side view (Fig. 5b), it can be seen that the fitted surface and the mean surface almost coincide, which is consistent with

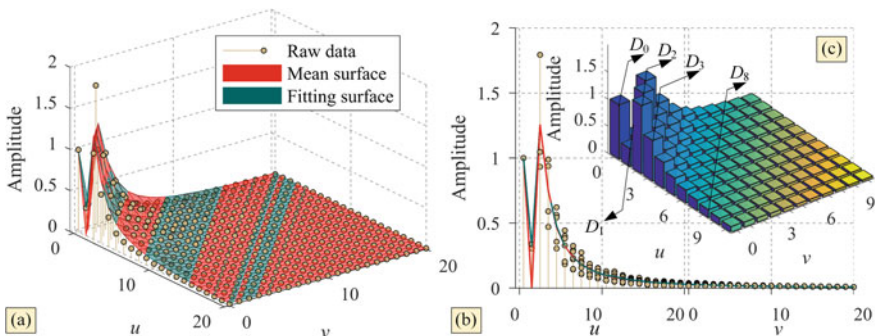


Fig. 5 Fitting of the spectral mean surfaces



the distribution of discrete points in spectrum. For visual effects, only the upper left corner of the spectrum is displayed.

## 4 Relationship Between Spectral Descriptors and Joint Surface Undulation

To study further the influences of spectral descriptors on joint surface undulation, the spectrum fitted in Sect. 3.2 is divided into three parts according to the segmentation characteristics of the fitting function, and the contribution of each part is explored separately (the fixed values  $D_0 = 1$ ,  $D_1 = 0$  are not discussed). The first part is  $D_2$ ; the second part is  $D_3, D_4, \dots, D_7$ , which is dominated by  $D_3$ ; the third part is  $D_8, D_9, \dots, D_{N-1}$ , which is dominated by  $D_8$ . After that, the spectrum fitted in Sect. 3.2 ( $D_2 = 1.2575, D_3 = 0.7513, D_8 = 0.1454, \alpha = -1.6524, \beta = -1.7578$ ) is disassembled into the aforementioned three parts, and the corresponding joint surfaces are reconstructed using the IDCT algorithm. The visualizations of the results correspond to Fig. 6a, b, and c. Figure 6d is a model reconstructed with the three parts of the spectrum superimposed.

It can be seen that the three parts of the spectrum control the undulation of the joint surface independently, from three levels of macroscopic to mesoscopic. By combining the three parts of the spectrum, a rock joint model that is practically close to the practice can be reconstructed. In other words, applying the fitting model in Sect. 3.2, the joint surface with specific undulation can be reconstructed by adjusting the values of  $D_2, D_3$  and  $D_8$  within a certain range. For visual effects, only the upper left corner of the spectrum is displayed. The displayed grids on the joint surfaces are also sparsely processed.

## 5 Discussion

The research is not deep enough and fails to validate the correlation between the proposed method and the shear strength properties of rock. The roughness of rock joint can only be qualitatively evaluated through visual undulation. More in-depth study of a quantifiable parameter needs to be combined with a shear test.

Due to the limited length of this paper, the details of the methodology including both software-hardware components of the image acquisition system are not expanded, which will be further discussed in future works.

The color space of rocks is suitable for describing the weathering degree of joints. Tools such as support vector machines and neural networks can be used to classify rock types and weathering degrees by the feature parameters of color vectors and texture. However, the effect of rock color and mineralogy on the performance of the

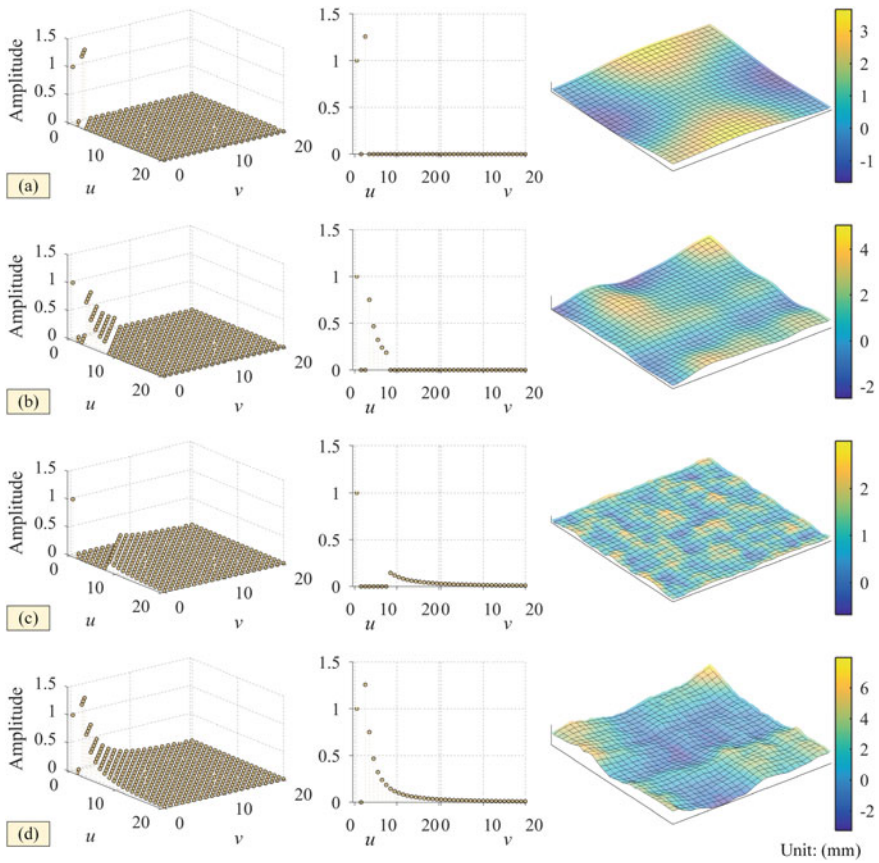


Fig. 6 Illustrative joint surfaces generated using the proposed framework

proposed method is neglected in this paper, which will also be further discussed in future works.

## 6 Conclusions

In this paper, a novel method for spectral analysis and rapid random reconstruction of joint surfaces is proposed, which is beneficial for field identification of discontinuities and providing virtual test samples for numerical modeling. By integrating DCT and IDCT, sample is decomposed into spectrum  $[D]$ . Then, the new joint surface is reconstructed using the modified spectrums. Through analysis, the following conclusion can be drawn.

- (1) The spectrum of joint surface shows a pronounced exponential change, and can be well characterized using an empirical model;
- (2) The joint surface with specific undulation can be reconstructed by adjusting the values of  $D_2$ ,  $D_3$  and  $D_8$  within a certain range.

**Acknowledgements** This study was financially supported by the National Natural Science Foundation of China (Nos. 51208522; 51478477; 51878668; 51978666), the Guizhou Provincial Department of Transportation Foundation (Nos. 2017-123-032; 2017-123-033; 2018-123-040), the Guizhou Provincial Department of Science and Technology - Science and Technology Support Program Key Project (No. [2018]2815), and the Fundamental Research Funds for the Central Universities of Central South University (2020zzts167, 2020zzts154, No. 2019zzts009). All financial supports were greatly appreciated.

**Conflict of Interest** The authors declare that they have no conflict of interest.

## References

1. Barton N (1976) The shear strength of rock and rock joints. *Int J Rock Mech Min Sci Geomech Abstr* 13:255–279
2. Barton N, Choubey V (1977) The shear strength of rock joints in theory and practice. *Rock Mech Felsmechanik M Canique Roches* 10:1–54
3. Tse R, Cruden DM (1979) Estimating joint roughness coefficients. *Int J Rock Mech Min Sci Geomech Abstr* 16:303–307
4. Yang ZY, Lo SC, Di CC (2001) Reassessing the joint roughness coefficient (JRC) estimation using Z 2. *Rock Mech Rock Eng* 34:243–251
5. Yu X, Vayssade B (1991) Joint profiles and their roughness parameters. *Int J Rock Mech Min Sci Geomech Abstr* 28:333–336
6. Song Y, Xia C, Tang Z, Song Y (2013) Numerical simulation and test validation for direct shear properties of rough joints under different contact states. *Chin J Rock Mech Eng* 32:2028–2035
7. Cao R, Cao P, Fan X, Xiong X, Lin H (2016) An experimental and numerical study on mechanical behavior of ubiquitous-Joint Brittle Rock-like specimens under uniaxial compression. *Rock Mech Rock Eng* 49:4319–4338
8. Zhang K et al (2016) Strength, fragmentation and fractal properties of mixed flaws. *Acta Geotech* 11:901–912
9. Zhang K, Cao P, Meng J, Li K, Fan W (2015) Modeling the progressive failure of jointed rock slope using fracture mechanics and the strength reduction method. *Rock Mech Rock Eng* 48:771–785
10. Jiang Q et al (2016) Reverse modelling of natural rock joints using 3D scanning and 3D printing. *Comput Geotech* 73:210–220
11. Jia H (2011) Experimental research on joint surface state and the characteristics of shear failure. Central South University
12. Zhao Y, Wan W, Wang W, Wang M, Peng Q (2013) Shear numerical simulation of random morphology rock joint and nonlinear shear dilatancy model. *Chin J Rock Mech Eng* 32:1666–1676
13. Zhao L et al (2017) Fourier-based reconstruction of rock joint and the statistical analysis of its morphology. *J Railw Sci Eng* 14:1606–1614
14. Zhu Z-H, Fu J-Y, Yang J-S, Zhang X-M (2016) Panoramic image stitching for arbitrarily shaped tunnel lining inspection. *Comput Civ Infrastruct Eng* 31:936–953

15. Zhu Z (2017) Study on the multi-view geometry based method and its application for creating tunnel layout panoramic image. Central South University
16. Paixão A, Resende R, Fortunato E (2018) Photogrammetry for digital reconstruction of railway ballast particles—a cost-efficient method. *Constr Build Mater* 191:963–976
17. Rusu RB, Marton ZC, Blodow N, Dolha M, Beetz M (2008) Towards 3D Point cloud based object maps for household environments. *Rob Auton Syst* 56:927–941
18. Ahmed N, Natarajan T, Rao KR (1974) Discrete Cosine Transform. *IEEE Trans Comput C*–23:90–93
19. Rao KR, Yip P (1990) Discrete cosine transform. In: *Discrete cosine transform: algorithms, advantages, applications*. Academic, pp 1–6. <https://doi.org/10.1016/B978-0-08-092534-9.50007-2>
20. Zhao L, Huang D, Dan H-C, Zhang S, Li D (2017) Reconstruction of granular railway ballast based on inverse discrete Fourier transform method. *Granul Matter* 19:74
21. Mollon G, Zhao J (2014) 3D generation of realistic granular samples based on random fields theory and Fourier shape descriptors. *Comput Methods Appl Mech Eng* 279:46–65

# Numerical Study of the Long-Term Settlement of Screw–Shaft Pile Reinforced Subgrade Under Cyclic Train Load



Fu- Hao Li , Xiao-Lei Zhang, and Shi-Jin Feng

**Abstract** High-speed railways (HSR) set strict limits on subgrade settlement. Excessive settlement, especially the differential settlement at the transition part between viaduct lines and embankment lines, could lead to discomfort on HSR trains and even accidents like derailments. Thus, proper ground treatment measures are inevitably needed. Screw-shaft pile reinforced subgrade was adopted in the transition section of Yancheng–Nantong HSR. However, limited research has been done to investigate the performance of screw-shaft pile reinforced subgrade. In this paper, numerical models were established to analyze the performance, especially the long-term settlement, of the reinforced subgrade. It was found that shaft-screw pile reinforced subgrade could control the long-term settlement better than the traditional shaft pile subgrade. The advantage becomes greater when the train speed increases. Moreover, the application of shaft-screw pile reinforced subgrade could reduce the material usage by about 10%. Briefly, shaft-screw reinforced subgrade could satisfy the settlement control requirements and achieve greater cost efficiency in sandy subgrades.

**Keywords** Shaft-screw pile · Reinforced subgrade · Long-term settlement · Dynamic train load

## 1 Introduction

The increasing operation speed of high-speed railway (HSR) passenger trains poses greater challenges to the settlement control. Chinese authorities require that the post-construction settlement should not exceed 15 mm [1]. However, the settlement caused

---

F.- H. Li (✉) · X.-L. Zhang · S.-J. Feng  
Key Laboratory of Geotechnical and Underground Engineering of Ministry of Education,  
Department of Geotechnical Engineering, Tongji University, Shanghai 200092, China  
e-mail: [1832297@tongji.edu.cn](mailto:1832297@tongji.edu.cn)

X.-L. Zhang  
e-mail: [Xiaolei\\_Zhang@tongji.edu.cn](mailto:Xiaolei_Zhang@tongji.edu.cn)

S.-J. Feng  
e-mail: [fsjgly@tongji.edu.cn](mailto:fsjgly@tongji.edu.cn)

by the train load could exceed the requirements in some cases [2]. Therefore, large-scale ground treatment is always needed, and the cost-efficient ground treatment method is of great importance.

The shaft-screw pile has been widely used as foundations of residential building or wind turbines [3, 4]. It is believed that the shaft-screw pile could enhance the bearing capacity and reduce the material usage at the same time. Sakr et al. [5] proposed two models for analyzing the bearing capacity of a single shaft-screw pile. Chen et al. [6] found that a single shaft-screw pile have 30% higher bearing capacity than the shaft pile featuring the same pile diameter. Sakr, Guo, and Stephen et al. studied the performance of single shaft-screw pile in soil sand, cohesive soil, and glaciolacustrine clay, respectively [5, 7, 8].

Afore-mentioned researches reveal that the single shaft-screw pile has better performance under static load than the traditional shaft pile. However, not much work have been done to determine the performance of shaft-screw subgrade under cyclic train load. Shaft-screw pile reinforced subgrade is applied in Yancheng–Nantong HSR for a balance between cost efficiency and settlement control performance. And this paper aims to investigate the long-term settlement control performance of the shaft-screw pile reinforced subgrade.

## **2 In-Situ Static Load Test and Geometry Simplification for Shaft-Screw Pile**

### ***2.1 In-Situ Static Load Test***

In-situ static load tests were conducted in three sites in Nantong, China, to verify the construction process and evaluate the performance of the shaft-screw pile. The load was applied to the pile at a relatively slow rate. The load for each stage read as 0, 259, 388, 518, 648, 777, 907, 1036, 1166, 1296 kN. The load for each stage in the unloading process read as 1296, 1036, 777, 518, 259, 0 kN. The steady-state settlement of each stage was recorded and depicted in Fig. 1. In all three tests, the settlement in the first loading process is significantly smaller than the later process. Then, the settlement increased almost linearly with the load in Pile 1 and Pile 2. However, the settlement increased dramatically in Pile 3 when the load was increased from 388 to 648 kN. Ultimately, these three piles reached the maximum settlement of 12.49 mm, 11.42 mm, and 11.82 mm, respectively. As for the unloading process, three piles reached the maximum rebound of 2.62 mm, 2.45 mm, and 2.13 mm, respectively. Other results of the in-situ static load test could be found in Table 1.

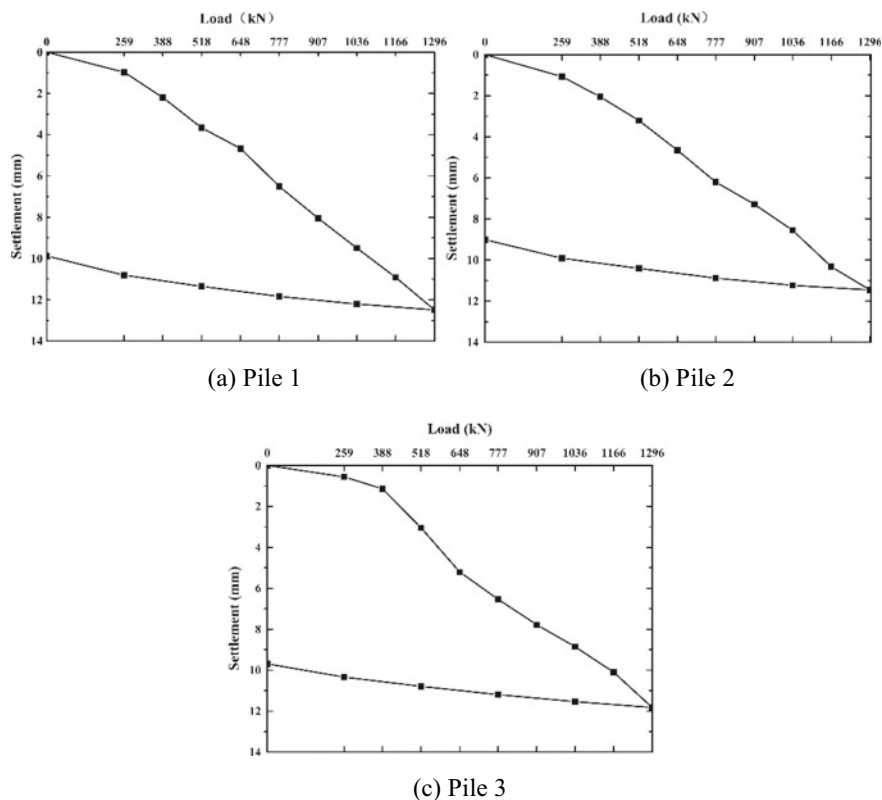


Fig. 1 Load-settlement curves for single shaft-screw piles analyzed

Table 1 In-situ static load test for single piles

No.	Strength designation of concrete	Spacing (m)	Maximum settlement (mm)	Maximum rebound (mm)	Rebound rate (%)
1	C30	2.2	12.49	2.62	21.0
2	C30	2.2	11.42	2.45	21.4
3	C35	2.2	11.82	2.13	18.0

## 2.2 Geometry Simplification for Shaft-Screw Pile

The complexity of the screw-shaft pile geometry demands great computing resources and time for numerical analysis, especially for the dynamic analysis. To keep the balance between the accuracy and the efficiency of the computing, a 2D shaft-screw pile numerical model was developed based on Plaxis 2D. The geometry parameters were set according to cross section of the shaft-screw pile. All parameters related

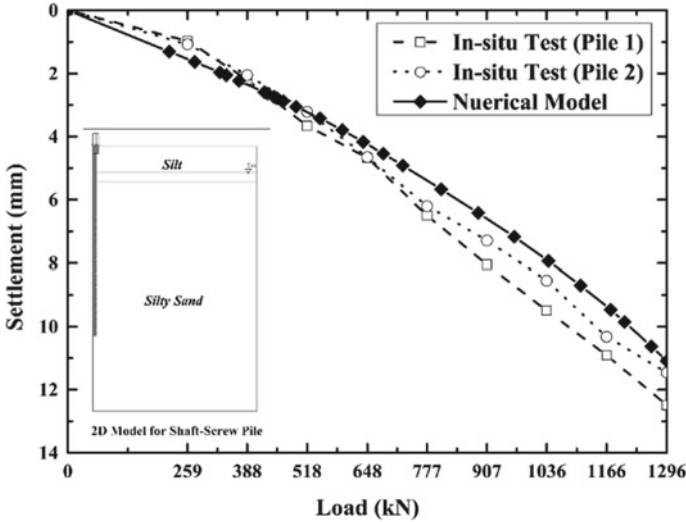


Fig. 2 Model validation

to the numerical model could be found in Sect. 3. The symmetry of the pile-ground system was considered in the numerical model, and uniform load was applied on the top of the pile. Then, the static load test was simulated by the 2D numerical model to verify the validity of the simplification (see in Fig. 2). The settlement of numerical model reached 11.09 mm, which showed great agreement with the in-situ static load (12.49 mm for pile 1 and 11.46 mm for pile 2). The results showed in Fig. 3 indicate that the 2D numerical model is appropriate for the settlement analysis in the engineering practice.

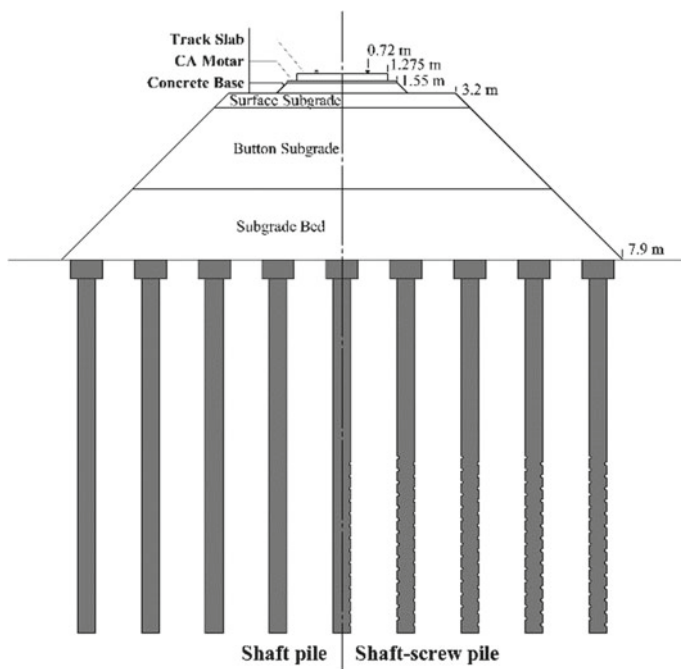
### 3 Parameters for Numerical Models

Numerical models for both the shaft pile and shaft-screw pile reinforced subgrade were developed based on the simplification method proposed in Sect. 2. Some parameters involved and some illustration of the numerical models were included in this section.

#### 3.1 Shaft-Screw Pile Reinforced Subgrade

Two-dimensional numerical models were established for both shaft pile and shaft-screw pile reinforced subgrades (see in Fig. 3) based on Plaxis 2D. Numerical models concern a straight high-speed railway (HSR) of single line and ballast-less





**Fig. 3** Reinforced subgrade

CRTS II slab structure. The slab track is composed of rail (60 kg/m), rail-pad, track slab, concrete asphalt (CA) mortar, and concrete base. The composite embankment consists of surface subgrade, bottom subgrade, subgrade bed, and subgrade foundation. Parameters of the slab track and the embankment are included in Table 2.

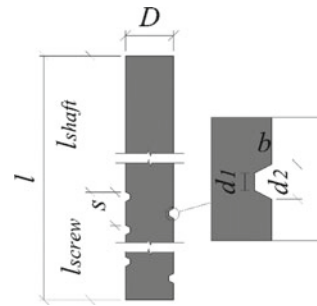
**Table 2** Parameters of the slab track and the embankment

Components	Depth (m)	Density (kg/m <sup>3</sup> )	Elastic modulus (MPa)	Poisson's ratio
Rail	–	7800	$2.10 \times 10^5$	0.30
Rail slab	0.20	2500	$3.50 \times 10^5$	0.22
CA mortar	0.05	2000	$1.00 \times 10^5$	0.30
Concrete base	0.3	2500	$3.00 \times 10^5$	0.20
Embankment (surface subgrade)	0.4	2300	200.0	0.25
Embankment (button subgrade)	2.3	1950	150.0	0.35
Embankment (surface bed)	2.0	2100	110.0	0.30

The geometry of the shaft-screw pile was simplified according to the methods in Sect. 2. Some parameters involved in the numerical model are depicted in Fig. 4 and Table 3. The strength grade of the cap and the pile body are C25 and C30, respectively. The material properties for different kinds of concrete are specifically defined in Chinese criterion (C25:  $\rho = 2.37 \times 10^3 \text{ kg/m}^3$ ,  $E = 2.5 \times 10^7 \text{ MPa}$ ,  $\nu = 0.27$ ; C30:  $\rho = 2.39 \times 10^3 \text{ kg/m}^3$ ,  $E = 3.0 \times 10^7 \text{ MPa}$ ,  $\nu = 0.30$ ).

The soil layer in the numerical model is set according to the site investigation report (see in Table 4). The Mohr–Coulomb strength criteria were adopted in the numerical analysis. As for the boundary, the absorbing boundary condition offered in Plaxis 2D is applied. Horizontal displacement is constrained at all boundaries

**Fig. 4** Geometry of shaft-screw pile



**Table 3** Geometry parameters of the shaft-screw pile

Item	Value
Pile length ( $l$ )	10 m
Length of shaft part ( $l_{\text{shaft}}$ )	5 m
Length of screw part ( $l_{\text{screw}}$ )	5 m
Pile diameter ( $D$ )	500 mm
Screw spacing ( $S$ )	350 mm
Width of screw ( $b$ )	50 mm
Thickness of screw bottom ( $d_1$ )	100 mm
Thickness of screw ( $d_2$ )	50 mm

**Table 4** Soil distribution

	Silt	Silt sand
Depth ( $h$ ) (m)	0–2.8	2.8–21.0
Natural weight ( $\gamma$ ) ( $\text{kN/m}^3$ )	18.740	18.740
Saturate weight ( $\gamma_{\text{sat}}$ ) ( $\text{kN/m}^3$ )	20.600	20.600
Elastic module ( $E$ ) ( $\text{kN/m}^2$ )	7190	8500
Poisson's ratio ( $\nu$ )	0.30	0.30
Cohesion ( $c$ ) ( $\text{kN/m}^2$ )	26.8	6.1
Friction angle ( $\varphi$ )	12.4°	24.9°

while vertical displacement is constrained at boundaries except the symmetry axial of the model.

### 3.2 Train Load

A widely used high-speed train, namely CRH3, which origins from ICE-3, is considered in this part. Each CRH3 train consists of four motor cars and four trailer cars. The CRH3 train is supposed to operate at the speed of up to 350 km/h. The configuration of the CRH3 train is depicted in Fig. 5 [9].

The train load is reduced to a point load applied on the track in numerical models. The axle weight, the spacing of wheel axles, and the train speed, which are believed to be the most important factors [10], are considered when determining the train load. It is assumed that the normal force would sustain between the gap of the passage of two adjacent wheel in a wheel pair [11]. The amplitude of the normal force is calculated as:

$$F = \frac{W \times g}{n} = \frac{4 \times 10^4 \times 9.81}{8} = 49050 \text{ N}$$

where  $W$  represents the mass of the wagon and  $n$  represents the total number of wheels in a wagon. The speed of the train is set as 300 km/h, and the normal force variation of the whole train is shown in Fig. 6a. Then, the Fourier series function is

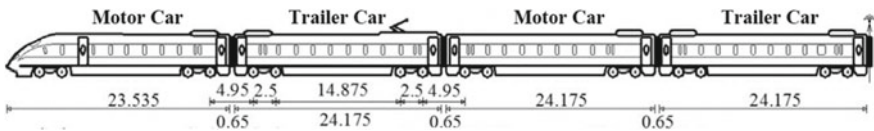
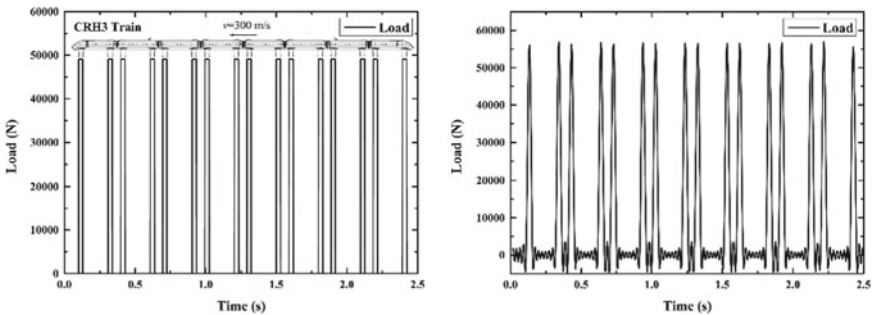


Fig. 5 Configuration of CRH3A train



(a) Normal force due to wagon wheels

(b) Dynamic train load

Fig. 6 Train load simulation

applied to smooth the load–time curve. The Fourier series function read as:

$$f(t) = a_0 + \sum_{n=1}^{\infty} \left[ a_n \cos\left(\frac{2n\pi t}{T}\right) + b_n \sin\left(\frac{2n\pi t}{T}\right) \right]$$

The optimized dynamic train load is shown in Fig. 6b.

### 4 Long-Term Settlement Under Cyclic Train Load

The safety and comfort of high-speed railway set demanding requirements on the settlement control. Monismith et al. [12] proposed an empirical method for cumulative plastic deformation calculation:

$$\varepsilon_p = AN^b$$

where  $\varepsilon_p$  represents the cumulative plastic strain and  $N$  represents the number of load applications. The parameters  $A$  and  $b$  depend on the soil type, soil properties, and the stress state. Further, Li and Selig [13] investigated the influential factors for  $A$  and  $b$ . It is found that the parameter  $A$  depends on the soil type, the soil physical state as well as the deviator stress, while the parameter  $b$  is independent on the physical state and deviator stress. It is recommended that parameter  $A$  could be calculated as:

$$A = a(\sigma_d/\sigma_s)^m$$

where  $\sigma_d$  and  $\sigma_s$  read as dynamic deviator stress and static failure stress, respectively. The parameter  $a$  and  $m$  could be determined by the material. Recommended values for parameter  $a$ ,  $b$ , and  $m$  are given in Table 5.

The dynamic train load is applied on the model for once. The vertical displacement of both shaft-screw pile and shaft pile reinforced subgrade during the first loading process is depicted in Fig. 7. Generally, the deeper the observation point lies, the smaller the displacement is generated, which could be due to the fact that deeper soil would not be disturbed severely by the external train load. The residual settlement of shaft-screw pile reinforced subgrade, mainly varying from 0.14 to 0.18 mm, is

**Table 5** Recommended values for a, b, and m

Soil type	Parameter		
	<i>a</i>	<i>b</i>	<i>m</i>
CH (Clay with high plasticity)	1.2	0.18	2.4
CL (Clay with low plasticity)	1.1	0.16	2
MH (Elastic silt)	0.84	0.13	2
ML (Silt)	0.64	0.1	1.7

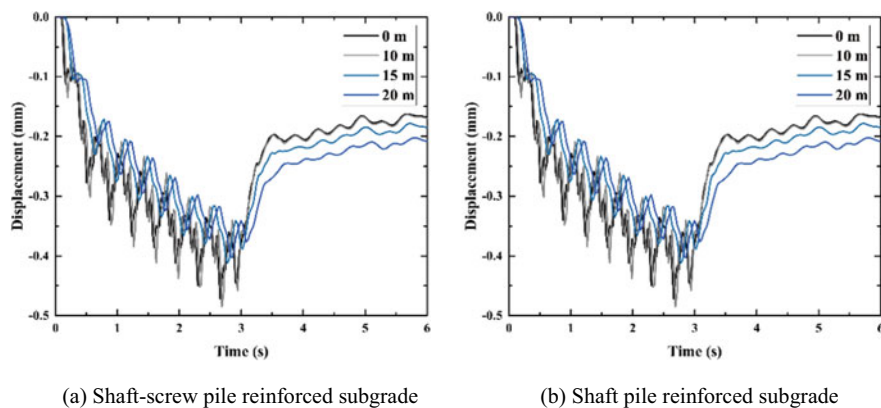


Fig. 7 Time histories of vertical displacement during the first load cycle

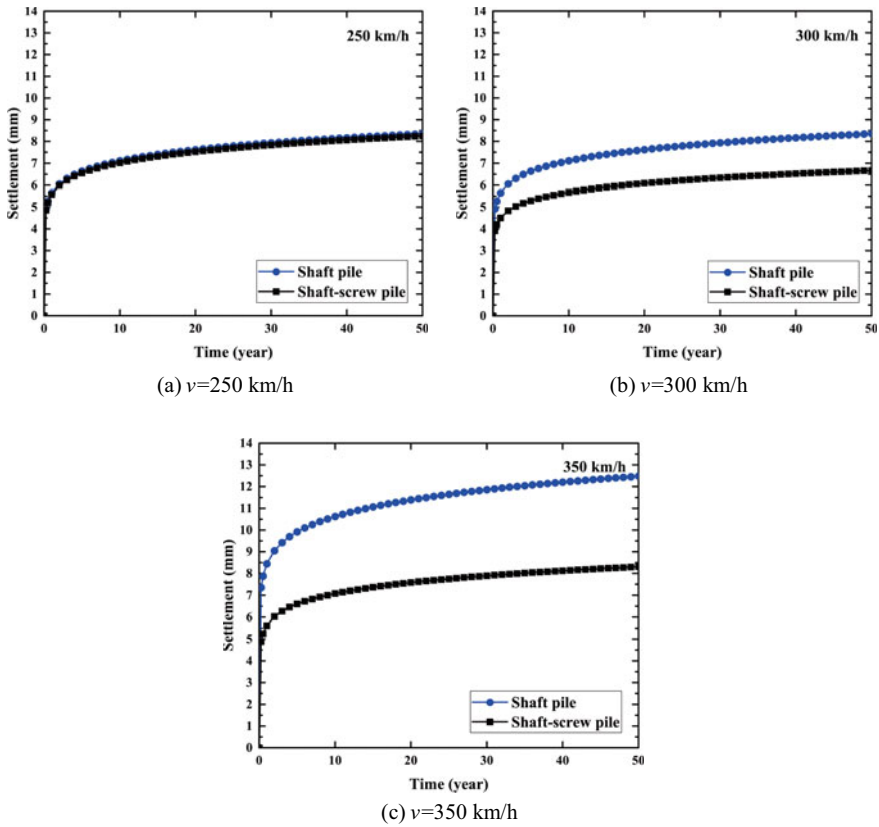
slightly smaller than that of the shaft pile reinforced subgrade, mainly varying from 0.16 to 0.21 mm.

Then, long-term settlement for both subgrades was calculated based on the method proposed by Li and Selig [13]. The parameter  $a$ ,  $b$ , and  $m$  were set as 0.64, 0.1, and 1.7, respectively. Fifty train passages are assumed per day, and the settlement after half year to fifty years' operation was calculated. The results are depicted in Fig. 8. The settlement increases dramatically in the first five years and then develops relatively slowly. Generally, the settlement of shaft-screw pile reinforced subgrade is smaller than that of the shaft pile reinforced subgrade. In the case of 250 km/h, the long-term settlement of shaft-screw pile reinforced subgrade (8.25 mm) is slightly smaller than that in the shaft one (8.35 mm). When the train operate at higher speed, the settlement control effect of shaft-screw pile reinforced subgrade is far better than the shaft pile reinforced subgrade. In the case of 300 km/h, the long-term settlement of shaft-screw pile reinforced subgrade (6.67 mm) is about 20.2% smaller than that in the shaft one (8.36 mm) and in the case of 350 km/h, the long-term settlement of shaft-screw pile reinforced subgrade (8.31 mm) is about 33.4% smaller than that in the shaft one (12.48 mm).

The results here show the superiority of shaft-screw reinforced subgrade's capacity of settlement control. The advantage even enlarges if the train operates at a higher speed.

## 5 Conclusions

The settlement control performance of a new kind of subgrade, shaft-screw pile reinforced subgrade, was investigated by numerical methods. The settlement control performance of shaft-screw pile reinforced subgrade was compared with that of the traditional shaft pile reinforced subgrade. It can be concluded that: (1) The dynamic



**Fig. 8** Comparison of long-term settlement between shaft-screw pile and shaft pile reinforced subgrade

responses of the soil decrease with the depth, and the response of shaft-screw reinforced subgrade is slightly weaker than that of the traditional shaft pile reinforced subgrade. (2) The long-term settlement of the subgrade increases with the operation time, and the shaft-screw pile reinforced subgrade shows better settlement control capacity. (3) Generally, the long-term settlement of the subgrade increases with the operation speed. The settlement control performance of shaft-screw pile reinforced subgrade is far better than shaft pile reinforced subgrade at higher speed.

The shaft-screw reinforced subgrade has great capacity of settlement control. Moreover, the application of the shaft-screw pile could save about 10% of material usage.

## References

1. National Railway Administration of the PRC. Codes for design of High Speed Railway. TB 10621–2014.
2. Chai JC, Miura N (2002) Traffic-load-induced permanent deformation of road on soft subsoil. *J Geotech Geoenviron Eng* 128(11):907–916
3. Sakr M (2009) Performance of helical piles in oil sand. *Can Geotech J* 46:1046–1061. <https://doi.org/10.1139/T09-044>
4. Pack JS Design of helical piles for heavily loaded structures. Pack JS Deep Foundations, pp 353–367
5. Byrne BW, Houlsby GT (2015) Helical piles: an innovative foundation design option for offshore wind turbines. *Philos Trans R Soc A Math Phys Eng Sci* 373
6. Chen Y, Deng A, Wang A, Sun H (2018) Performance of screw–shaft pile in sand: model test and DEM simulation. *Comput Geotech* 104:118–130. <https://doi.org/10.1016/j.compgeo.2018.08.013>
7. Guo Z, Deng L (2017) Field behaviour of screw micropiles subjected to axial loading in cohesive soils. *Can Geotech J* 55:34–44
8. Lanyi-Bennett SA, Deng L (2018) Axial load testing of helical pile groups in glaciolacustrine clay. *Can Geotech J* 56:187–197
9. Feng SJ, Zhang XL, Wang L et al (2017) In situ experimental study on high speed train induced ground vibrations with the ballast-less track. *Soil Dyn Earthq Eng* 102:195–214. <https://doi.org/10.1016/j.soildyn.2017.09.001>
10. Hall L (2003) Simulations and analyses of train-induced ground vibrations in finite element models. *Soil Dyn Earthq Eng* 23:403–413. [https://doi.org/10.1016/S0267-7261\(02\)00209-9](https://doi.org/10.1016/S0267-7261(02)00209-9)
11. Nejati HR, Ahmadi M, Hashemolhosseini H (2012) Numerical analysis of ground surface vibration induced by underground train movement. *Tunn Undergr Space Technol* 29:1–9. <https://doi.org/10.1016/j.tust.2011.12.006>
12. Monismith CL, Ogawa N, Freeme CR (1975) Permanent deformation characteristics of subgrade soils due to repeated loading. In: Transportation research record No 537. Transportation Research Board, Washington DC, pp 1–17
13. Li D, Selig ET (1996) Cumulative plastic deformation for fine-grained subgrade soils. *J Geotech Eng* 122:1006–1013. [https://doi.org/10.1061/\(ASCE\)1090-0241\(1998\)124:11\(1153.x\)](https://doi.org/10.1061/(ASCE)1090-0241(1998)124:11(1153.x))

# Influence of Pile Side Grouting Reinforcement on the Compressive Load Bearing Capacity of Existing Piles



Xinran Li, Quanmei Gong, Yao Shan, and Xiaofan Nie

**Abstract** With the rapid development of road network, it is inevitable that new tunnels will be constructed under existing highway or railway bridges. Open excavation method is a typical way for building a new tunnel under bridge, leading to significant influences of the existing pile friction. Accounting for these issues, pile side grouting reinforcement method has been widely employed to improve the load bearing capacity of existing piles. However, the mechanism of this method is still not clear. In this paper, the compressive load capacity of pile with side grouting reinforcement is investigated. The research results reflect the effect and mechanism of pile side reinforcement on the enhancement of pile friction. For the existing pile in this paper, the reinforcement width has a reasonable range. The compressive load bearing capacity of the pile cannot be improved indefinitely with the increasing of the reinforcement width. Pile with a reinforcement width within 1000 mm shows similar characteristics of enlarged diameter pile. Although ultimate compressive load bearing capacity of these piles is greatly improved, they need a larger displacement to exert load bearing capacity. Shear strength and friction characteristics of the contact surface between the reinforced zone and the pile and supporting capacity of the soil under reinforced zone are the keys to enhance the pile compressive load bearing capacity.

---

X. Li · Q. Gong · Y. Shan (✉) · X. Nie

Shanghai Key Laboratory of Rail Infrastructure Durability and System Safety, Tongji University, Shanghai 201804, China

e-mail: [shanyao@tongji.edu.cn](mailto:shanyao@tongji.edu.cn)

Key Laboratory of Road and Traffic Engineering of the Ministry of Education, Tongji University, Shanghai 201804, China

X. Li

e-mail: [1910121@tongji.edu.cn](mailto:1910121@tongji.edu.cn)

Q. Gong

e-mail: [gongqm@tongji.edu.cn](mailto:gongqm@tongji.edu.cn)

X. Nie

e-mail: [lostoking@outlook.com](mailto:lostoking@outlook.com)



**Keywords** Existing pile · Pile side grouting reinforcement · Bearing capacity · Friction

## 1 Introduction

With the rapid development of road network, new planned tunnels or foundation pits will be constructed beneath existing elevated highways. The stress release of soil around piles decreases the normal stress of pile–soil interfaces during the foundation pit construction, and the existing piles in the foundation pit will be exposed, leading to serious friction loss of existing piles [1]. Especially for friction piles, the friction loss reduces the compressive load bearing capacity of pile and seriously threatens the safety of the foundation pit construction and the bridge.

The soil mechanics parameters have a great influence on the interaction of soil and pile at the bottom of the foundation pit. The increase of the soil friction angle and cohesion significantly improves the pile compressive load bearing capacity [2]. Studies have shown that the use of cement slurry for soil reinforcement can effectively improve the mechanical properties of the soil. Relevant direct shear tests and drained triaxial compression tests proved that the friction angle and cohesion of the reinforced soil increase with the increase of cement content [3, 4].

In order to enhance the existing pile ultimate friction, the method of strengthening the soil around pile with cement slurry is proposed. The research on pile side grouting reinforcement mainly focuses on post-grouting which refers to grouting the pile side through grouting pipes reserved on the steel cage after 7–10 days of bored piles construction. The cement slurry fills the defects of the pile–soil interface and penetrates into the soil under pressure. And the properties of pile–soil interface and the mechanical properties of the soil around the pile can be changed, resulting in improvement of the ultimate friction of pile [5, 6]. The significant effect of post-grouting on the pile load bearing capacity is revealed by several studies with model tests, field tests and numerical simulations [6–11]. Relevant codes also propose some calculation methods of ultimate compressive load bearing capacity of single pile after post-grouting [12, 13].

Since the existing piles are not provided with reserved pipes, it is not possible to adopt the method of post-grouting to improve the compressive load bearing capacity of piles. Therefore, pile side grouting reinforcement of existing piles is often implemented by sleeve valve grouting reinforcement, ordinary high-pressure jet grouting reinforcement and metro jet system (MJS) method. The pile–reinforced zone interface characteristics and the friction improvement mechanism may be different among these methods. Therefore, the research results and calculation methods of post-grouting are not fully applicable, and more detailed researches on pile side grouting reinforcement of existing piles are required.

Based on field test, finite element models are established to study the mechanism of pile side grouting reinforcement on friction improvement and explore the

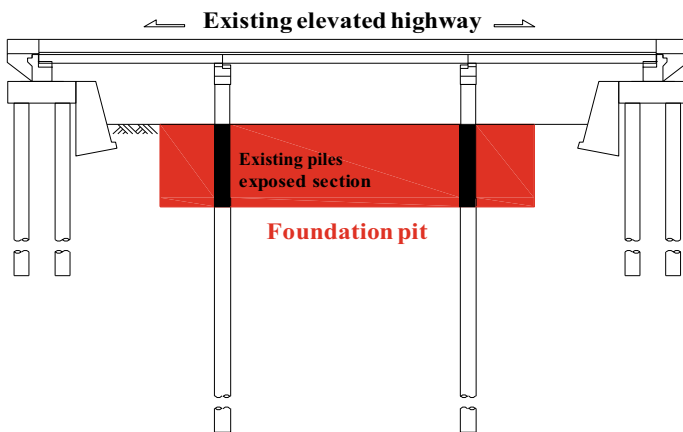
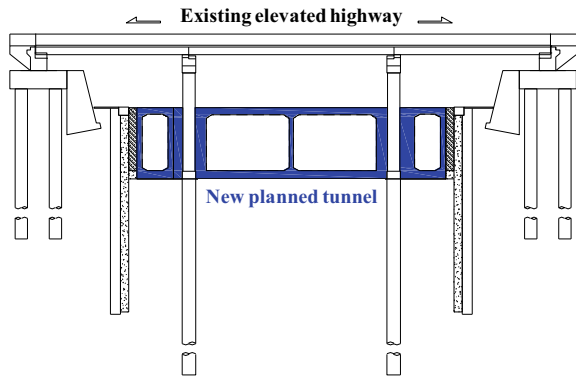
effects of reinforcement width and interface characteristics of pile–reinforced zone on compressive load bearing capacity of piles.

## 2 Field Test

As shown in Fig. 1, construction standard of the new tunnel is urban secondary road, with a designed speed of 40 km/h, and it is planned to traverse under existing elevated highway which is a 3-span simply supported hollow slab bridge with bored pile foundation.

As shown in Fig. 2, the tunnel foundation pit is constructed by open excavation method. The excavation depth is about 6.6–8.2 m, and the excavation width is about 31.5 m. The foundation pit construction exposes part of existing bridge

**Fig. 1** Cross section of new tunnel under existing elevated highway



**Fig. 2** Existing elevated highway and tunnel foundation pit conditions

**Table 1** Typical types and properties of soil in the test site

Soil	$H/(m)$	$\rho/(g/cm^3)$	$c/(kPa)$	$\varphi/(^\circ)$	$E_0/(MPa)$
Fill	0–1.25	1.99	9	15	6
Medium coarse sand	1.25–5	2.00	3	32	23
Coarse sand	5–12	2.01	3	35	30
Gravelly sand	12–20	2.03	2	37	40

Note  $H$ —the depth of soil layer,  $\rho$ —density,  $c$ —cohesion,  $\varphi$ —friction angle and  $E_0$ —deformation modulus

piles. According to the code [13], calculation results indicate that the compressive load bearing capacity of these existing friction piles after excavation cannot meet the original design requirements, so it is necessary to take the measure of pile side grouting reinforcement to improve the compressive load bearing capacity of these piles.

## 2.1 Introduction of the Test Pile

In order to clarify the compressive load bearing capacity of existing friction pile with pile side grouting reinforcement, the MJS method is used to strengthen the soil around the test pile. The test pile's diameter and length are 800 mm and 15 m, respectively. Pile concrete strength grade is C30, and the longitudinal main reinforcement consists of 12  $\Phi$  20 mm HRB400 steel bars. The engineering geological condition of the test site is shown in Table 1.

## 2.2 Pile Side Grouting Reinforcement with MJS Method

The MJS method belongs to special technics of high-pressure jet grouting. This method can monitor earth pressure by adjusting slurry discharge in real time during the grouting process and reduce the impact on environment. This method mixes the slurry and the foundation soil into a cement paste structure, and reinforced zone can wrap the existing pile tightly.

In this paper, the MJS method is used for pile side grouting reinforcement. As shown in Fig. 3, the reinforced zone with a ring width of 2400 mm and a thickness of 3000 mm is all located in the coarse sand stratum. The grouting material is a mixture of water and cement, in which the water-to-cement ratio is 1.0, and the cement content of the reinforced zone reaches 40%.

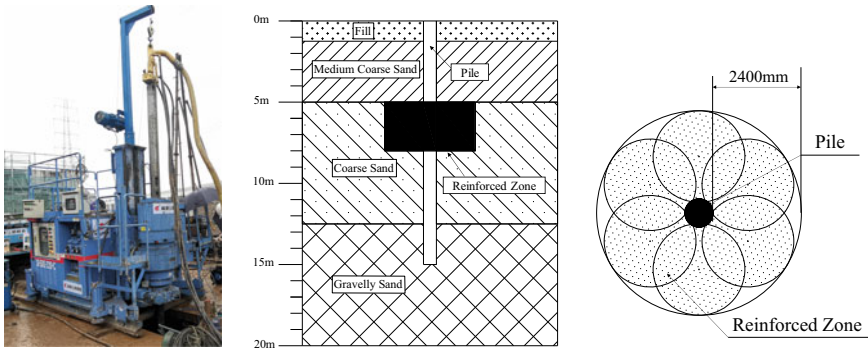


Fig. 3 MJS machinery and scheme of pile side grouting reinforcement

### 2.3 Field Static Load Test

The static load test is carried out based on the code [12]. As shown in Fig. 4, the loading system uses reaction force provided by jack to load and displacement sensor is installed on the pile top. During test, the pile-head load and displacement are measured and recorded by automatic collector. The test uses slow maintenance load method and applies the load step by step until the maximum load. Due to test site restrictions, the maximum load is 5000 kN. The pile-head load and displacement curve and s-lgt curve are shown in Fig. 5.

As shown in Fig. 5, there is neither steep drop in the load–displacement curve nor obvious downward bending in the s-lgt curve. It can be judged that the pile has not reached the compressive load bearing limit value. In order to confirm the ultimate compressive load bearing capacity of this pile, the hyperbolic model proposed by Christon is used to predict it. The comparison between the prediction result and the field test result is shown in Fig. 6. It can be seen that the front curve fits well and the trend is consistent.



Fig. 4 Loading system

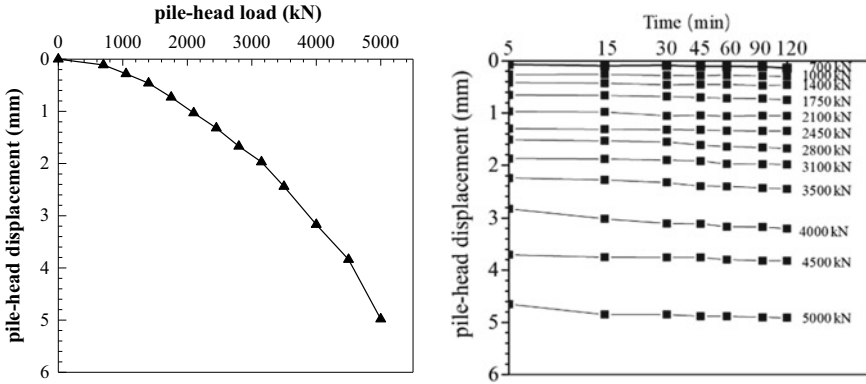


Fig. 5 Results of field test

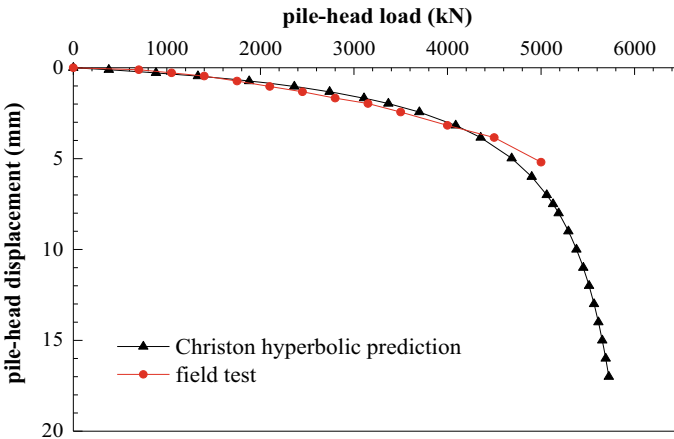


Fig. 6 Comparison between the prediction results and the field test data

### 3 Finite Element Simulation

In order to carry out more detailed research on the compressive load bearing capacity of existing piles after pile side grouting reinforcement, the three-dimensional modeling calculation of the test process is carried out by the ABAQUS finite element software, and the influencing factors of compressive load bearing capacity of piles are analyzed and studied.

### 3.1 Modeling

Since vertical load of pile is an axisymmetric problem, the 1/2 model can be used for simulation and calculation. The size of pile and reinforced zone is the same as those in the field test. As shown in Fig. 7, the length and diameter of the pile and the width and thickness of the reinforced zone are 15 m, 800 mm, 2400 mm and 3000 mm, respectively. The radius of the model is 25 times the diameter of pile, and the length of the model is two times the length of pile.

The pile is defined as linear elastic material, the deformation modulus and Poisson’s ratio of it are 30 GPa and 0.18, respectively. The soil around the pile is defined as Mohr–Coulomb elastoplastic material. The existing engineering shows that the compressive strength of reinforced zone by the MJS method can be up to 8–20 MPa in sand [14]. The reinforced zone is considered to be cement–soil with a cement content of 40% in this paper. The relationship between the deformation modulus and the unconfined compressive strength of cement–soil is presented in the book [5]. In this paper, the Mohr–Coulomb elastoplastic model is used in the reinforced zone. According to reference [3, 15, 16], the parameters are shown in Table 2.

Fig. 7 Sketch of model

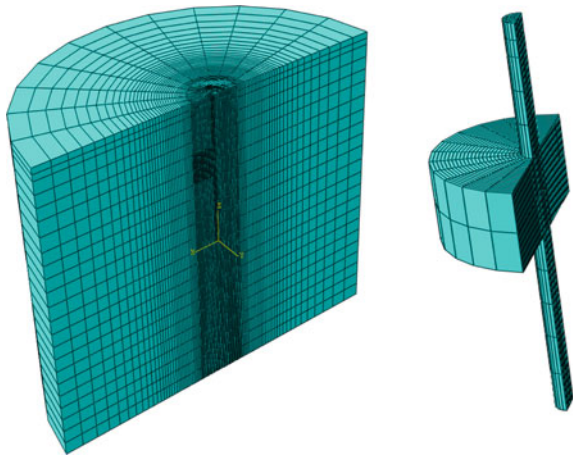


Table 2 Parameters for Mohr–Coulomb elastoplastic model of reinforced zone

Parameter	$E_0$ /(GPa)	$\mu$	$c$ /(kPa)	$\varphi$ /(°)
Value	2	0.2	2500	50

**Table 3** Parameters for contact surface in the finite element model

Contact surface	Pile and fill	Pile and medium coarse sand	Pile and coarse sand	Pile and gravelly sand	Pile and reinforced zone	Reinforced zone and coarse sand
Friction coefficient	0.2	0.6	0.65	0.7	1.2	0.62
Maximum shear stress (kPa)	30	70	80	120	450	80

### 3.2 Contact Surface Setting

Contact surfaces including the pile–soil contact surface, the reinforced zone–soil contact surface and the pile–reinforced zone contact surface are all defined as hard contact in normal direction and penalty stiffness model in tangential contact. Friction coefficient of pile–soil contact surface can refer to the formula that  $\mu = \tan\psi$ , where  $\psi$  is the interface friction angle. The interface friction angle can be taken as  $(0.75\text{--}1.0)\varphi$ , where  $\varphi$  is the soil friction angle [18, 20]. The friction coefficient between concrete pile and sand is 0.5–1.0 [19]. In the same soil layer, the friction coefficient between cement reinforced zone and soil is slightly smaller than that between concrete pile and soil [17]. The parameters of the model are listed in Table 3.

### 3.3 Static Load Test Simulation

Consider the weight of soil and structures and perform initial ground stress balance. This paper uses displacement control method to simulate static load test. The load and corresponding displacement of pile head can be extracted after each step calculation completed. The comparison between the finite element model calculation result and the field test result is shown in Fig. 8.

It could be seen that the pile-head displacement of the finite element model is larger than that measured in the field test, which is caused by two reasons. First, penalty stiffness algorithm used for the tangential behavior of contact surface allows for elastic slip deformation, which meant that relative slip deformation occurs when the surfaces are bonded together. Second, the cement slurry amount of grouting reinforcement in actual engineering might be increased to guarantee the grouting reinforcement quality, and the slurry diffuses into the ground, resulting in the range of reinforced zone is enlarged. From the overall trend, the model calculation result is in good agreement with the field test result, which proves the reliability and applicability of the finite element model.

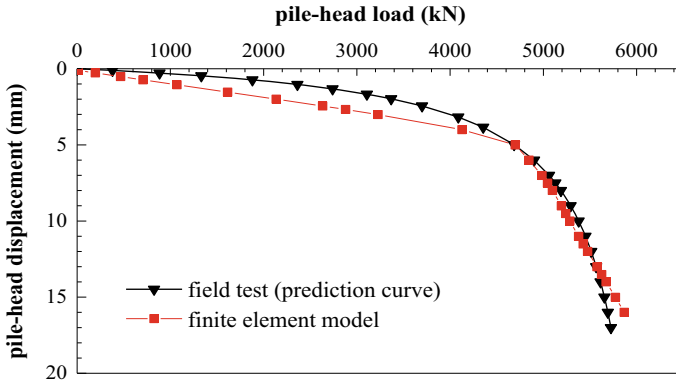


Fig. 8 Comparison between the model calculation result and the field test result

## 4 Factors Influencing Compressive Load Bearing Capacity

### 4.1 Reinforcement Width

Models with different reinforcement widths (1400, 2400, 3400 mm, 4400 m, 5400 mm) are analyzed with depth and thickness of reinforced zone setting as 5 m and 3 m, respectively. The calculation results are shown in Fig. 9a. The compressive load bearing capacity of these reinforced piles is enhanced compared to the unreinforced pile. As the reinforcement width increases from 1400 to 5400 mm, the pile ultimate load bearing capacity decreases. When the reinforcement width is above 4400 mm, the ultimate compressive load bearing capacity of the pile is only about 3800 kN, which is much smaller than that of the pile with a 1400 mm reinforcement width. In order to confirm the optimal width range, models for pile with a reinforcement width within 1400 mm are calculated. The results are shown in Fig. 9b and Table 4. Pile with a 600 mm reinforcement width has the maximum ultimate compressive load bearing capacity of 6332 kN.

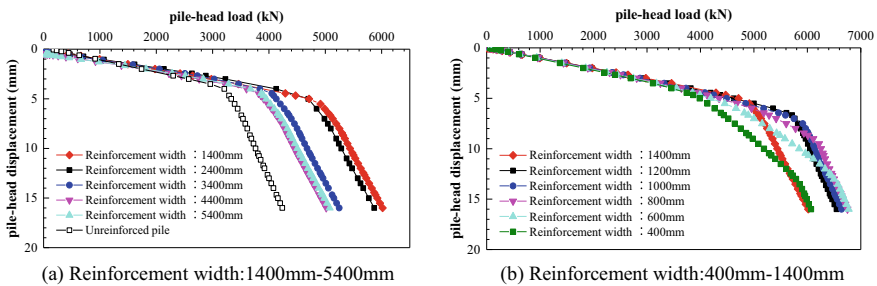


Fig. 9 Comparison among piles with different reinforcement widths and unreinforced pile



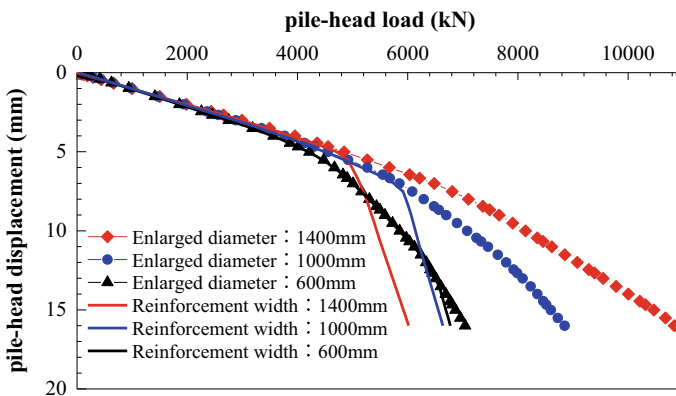
**Table 4** Calculation results of piles with different reinforcement widths

Reinforcement width (mm)	400	600	800	1000	1200	1400
Ultimate compressive load bearing capacity (kN)	5703	6332	6230	6000	5820	4983
Pile-head displacement (mm)	14.2	14	10.5	8	7.6	6.4

As shown in Fig. 9, the pile-head load–displacement curves of the piles with a reinforcement width within 1000 mm have different characteristics compared to the others. These piles need to sacrifice greater displacement to exert bearing capacity, and their curves show slow change characteristics before pile failure, which are similar to expanded diameter pile. The ultimate compressive load bearing capacity of the pile with a 600 mm reinforcement width is larger than that of the 1000 mm one; however, the capacity of the latter can reach 6000 kN as the pile-head displacement is 8 mm, while the former one only exerts 5200 kN under the same displacement.

In order to verify the similarity of load-bearing characteristics between the enlarged diameter pile and the synergy of reinforced zone and the pile, new models are established. The relative displacement and friction between the pile and the reinforced zone are not allowed due to the removal of the pile–reinforced zone contact surface in these new models. The calculation results are shown in Fig. 10. The curves of the new models change slowly, and the load bearing capacity of these piles develops with the increase of the variable section diameter, which reveals the characteristics of enlarged diameter piles. Comparing the calculation results of enlarged diameter piles and side-reinforced pile with the same size of variable section, it can be seen that they have the same bearing performance process before failure. However, the ultimate compressive load bearing capacity of the latter is smaller.

The distribution of the contact pressure on the reinforced zone (enlarged diameter part) and underlying soil interface is shown in Fig. 11. The reinforced zone or enlarged diameter part increases the pile–soil contact area, and the reaction force of



**Fig. 10** Comparison among reinforced piles and enlarged diameter piles

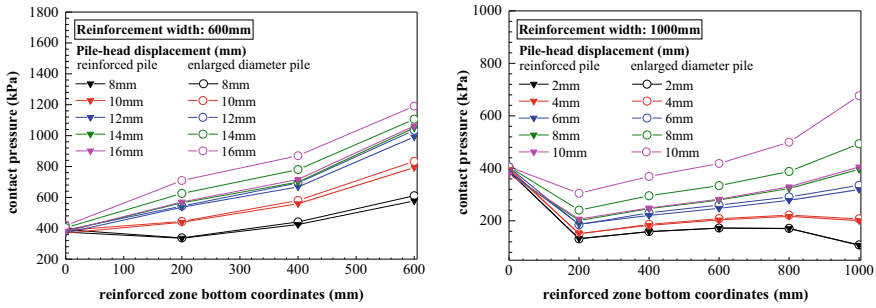


Fig. 11 Contact pressure distribution between reinforced zone and underlying soil

its underlying soil is stimulated with the sinking of the reinforced zone during loading process, assisting pile side friction to share the load transferred from the pile head. After the friction reaches the limit value, the enlarged diameter part can continue to bear larger load, while the contact force of reinforced zone of side-reinforced piles reaches the limit value faster. The contact pressure between reinforced zone and its underlying soil of the pile with a 600 mm (1000 mm) reinforcement width will stop developing when pile-head displacement reaches 14 mm (8 mm), which is also the moment of pile failure.

Analysis of the force state shows that the pile is easy to sink with the reduction of the reinforcement width. The assistance of the reinforced zone to pile stops developing as the total friction between the pile and the reinforced zone is less than the sum of the underlying soil supporting force and the friction between reinforced zone and side soil. Simultaneously, the pile reaches its load bearing capacity limitation. The maximum auxiliary capacity of the reinforced zone is limited by the contact area between reinforced zone and its surrounding soil. Although the reinforced zone with a width less than 600 mm is easier to be pulled down by pile, fully compressing its underlying soil and stimulating soil support force, which works like an enlarged diameter part of the enlarged diameter pile, the pile load bearing capacity improvement is relatively small.

Figure 12 shows the pile side friction before and after the pile reaching ultimate compressive load bearing capacity. The friction of piles with different reinforcement widths has similar development process. The friction of the unreinforced pile section has reached ultimate value, and that of the reinforced pile section distributes unevenly. There are more areas where the friction reaches 400 kPa in the pile–reinforced zone interface of the pile with a 600 mm reinforcement width. Figure 13 shows the development of the total force due to contact pressure between pile and reinforced zone. The contact pressure of the pile with a 600 mm reinforcement width is larger than that of the others, as well as the pile side friction and the ultimate compressive load bearing capacity.

Due to the pile-head load, the pile displacement causes the soil and the reinforced zone to sink. Friction develops at the interfaces, and the soil below the reinforced zone is compressed to limit the displacement of the reinforced zone, resulting in the

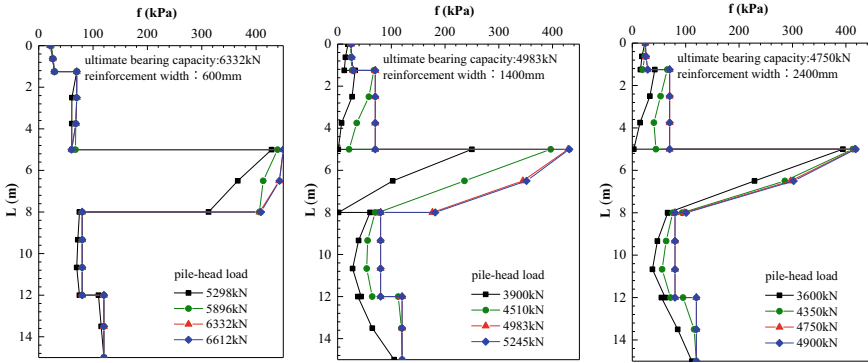


Fig. 12 Friction of piles during loading process

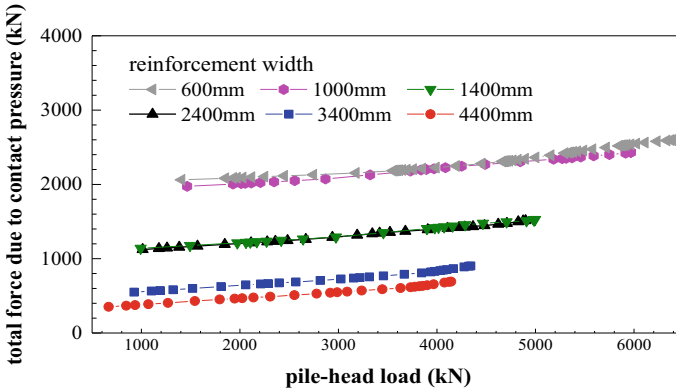


Fig. 13 Total force due to contact pressure

coordinated deformation of the entire pile–soil–reinforced zone system. The pile not only gets extra support by the underlying soil through the reinforced zone, but also be compressed by the deformed reinforced zone. Figure 14 shows the pressure on the reinforced section of the pile with a 2400 mm reinforcement width. The pressure on the upper part is smaller than that of the lower part before loading. The upper part pressure has an additional growth during the loading process, promoting the development of the friction. The piles with an appropriate reinforcement width can stimulate the underlying soil to provide more adequate supporting capacity, which is also beneficial to the development of the friction of the reinforced pile section.

In summary, the reinforced zone improves mechanical properties of the soil around pile and works as a pile enlarged diameter part during loading until pile failure, especially with a small reinforcement width. The pile can get additional support by the underlying soil through reinforced zone and be compressed by the deformation reinforced zone to generate greater friction. In this paper, the pile with a 600 mm

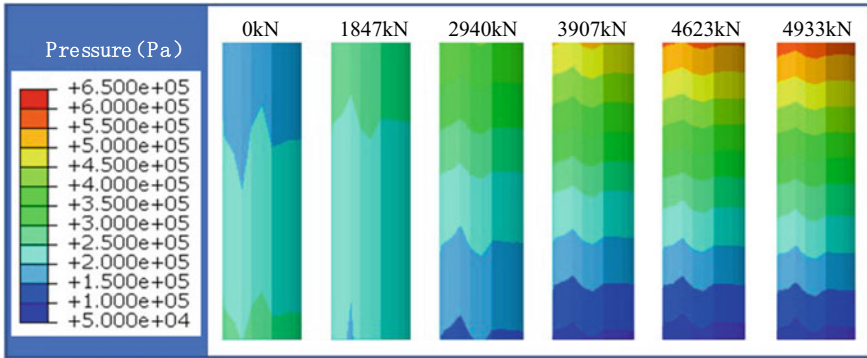


Fig. 14 Pressure on pile of reinforced section

reinforcement width has the maximum ultimate compressive load bearing capacity, but the pile requires a larger displacement to exert its bearing capacity. In actual engineering, the reinforcement width should be designed to meet the requirements of structural deformation limitation and pile load bearing capacity enhancement at the same time. In future research, bearing mechanism is expected to be further explored, and the theoretical calculation method will be given to directly confirm the optimal reinforced zone size.

### 4.2 Characteristics of the Pile–Reinforced Zone Interface

Friction coefficient and maximum shear stress of contact surfaces are key factors affecting pile side friction. Figure 15a shows the result as the friction coefficient of the reinforced zone and pile contact surface is set from 0.8 to 1.6. The compressive load bearing capacity of the pile with a 2400 mm reinforcement width raises when the friction coefficient increases. Figure 15b shows the result of the piles with the

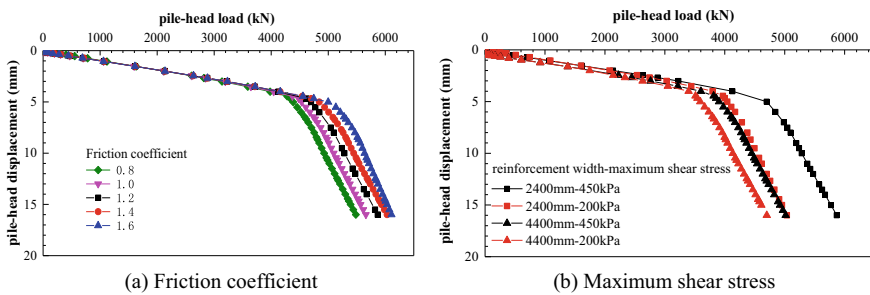


Fig. 15 Comparison among piles with different interface characteristics

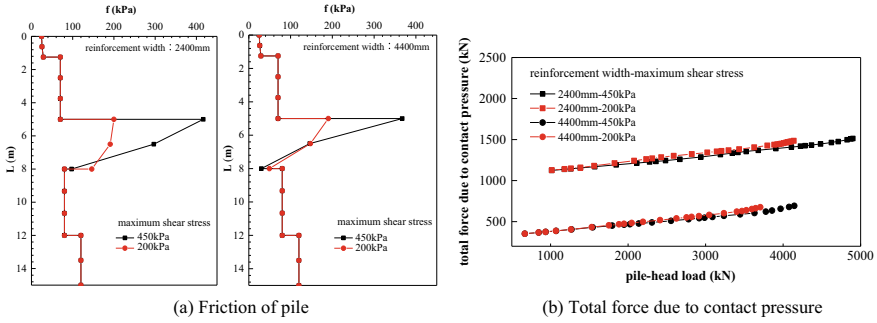


Fig. 16 Comparison among piles with different maximum shear stress

pile–reinforced zone interface maximum shear stress of 200 kPa and 450 kPa. The ultimate compressive load bearing capacity of the pile decreases with the reduction of the maximum shear stress.

Even if the contact pressure of the interfaces is still increasing, due to the interface maximum shear stress, the friction stops developing as the shear stress (friction) reaches the maximum value. Figure 16a shows the pile side friction when the pile reaches ultimate compressive load bearing capacity. The differences in ultimate compressive load bearing capacity among piles are related to the friction of the pile–reinforced zone interface. During loading process, the upper part of the pile reinforced section first reaches the maximum shear stress. Figure 16b shows the total force development due to the pile–reinforced zone interface contact pressure. The force of the piles with the same reinforcement width is consistent; however, the piles have different ultimate compressive load bearing capacity due to the different maximum shear stress limitation.

In actual engineering, the interfaces characteristics are affected by the existing pile itself and the quality of the grouting reinforcement, e.g., the roughness of the pile body and the combination state of pile and reinforced zone. In order to increase the interfaces friction coefficient and shear strength, in addition to ensuring the reinforced zone tightly integrated with pile, it is also possible to improve the mechanical properties of reinforced zone, such as increasing cement content.

### 5 Conclusions

- (1) The numerical model can be used to investigate the compressive load bearing capacity of the existing pile with pile side grouting reinforcement, and the calculation result is consistent with the field test data.
- (2) Pile side grouting reinforcement can effectively improve the compressive load bearing capacity of the existing pile through the increasing of the friction limit value of the pile–reinforced zone interface. Reinforced zone not only improves

- mechanical properties of the soil around pile, but also causes the underlying soil supporting and squeezes the pile after deformation.
- (3) Reinforcement width affects pile load bearing process. Pile with a smaller reinforcement width shows similar characteristic of the enlarged diameter pile. In this paper, the 600 mm reinforcement width can maximize pile bearing capacity, but pile requires a larger displacement to exert its bearing capacity. In actual engineering, the reinforcement width should be designed to meet the requirements of structural deformation limitation and pile bearing capacity enhancement at the same time.
  - (4) The ultimate compressive load bearing capacity of the pile is enhanced with the increase of the interface friction coefficient and shear strength. When the MJS method is used for pile side grouting reinforcement, the construction quality should be strictly controlled to ensure the combination of the reinforced zone and the pile. Increasing the cement content can improve the interface shear strength, allowing the pile to exert greater friction.

**Acknowledgements** This research was supported by National Natural Science Foundation of China (51708424) and the Fundamental Research Funds for the Central Universities, the People's Republic of China.

## References

1. Wenping L (2010) Effect of excavation on pile capacity and engineering application of  $\beta$ -method. *Chin J Geotech Eng* 32(S2):259–262
2. Wei X (2007) Numerical simulation analysis for impact of foundation pit excavation on bottom piles. Shandong University of Science and Technology, Qingdao, Shandong Province, China
3. Maalej Y, Dormieux L, Canou J et al (2007) Strength of a granular medium reinforced by cement grouting. *CR Mec* 335(2):87–92
4. Huaqiang W (2010) Research on reinforcement mechanism of pile shaft grouting and test study. Zhejiang University, Hangzhou, Zhejiang Province, China
5. Zhongmiao Z (2009) Post grouting technology of cast-in-place pile and its engineering application, 1st edn. China Architecture & Building Press, Beijing, China
6. Guoqing Z, Hengchang L, Guangsi Z (2005) Test of grouting surrounding pile for improving bearing capacity. *J China Univ Min Technol* 34(3):265–269
7. Shenggen H, Xiaowei Z, Hui C (2004) Mechanism study on bored cast-in-place piles with post-grouting technology. *Rock Soil Mech* 25(2):251–254
8. Xiangwen L (2010) Study on bearing characteristics of pile foundation with side grouting in deep soft soil. Southwest Jiaotong University, Chengdu, Sichuan Province, China
9. Heming X (2008) FEM analysis for post-grouting to soil around pile sides and post-grouting to soil around pile sides and bottom. Tianjin University, Tianjin, China
10. Thiyyakkandi S, Mcvay M, Bloomquist D et al (2013) Measured and predicted response of a new jetted and grouted precast pile with membranes in cohesionless soils. *J Geotech Geoenviron Eng* 139(8):1334–1345
11. Littlechild BD, Hill SJ, Plumbridge GD et al (2000) Load capacity of foundations on rock. In: *Geo-Denver 2000*, vol 288(100), pp 140–157. Geotechnical Special Publication, Denver, Colorado

12. Ministry of Housing and Urban-Rural Development of the People's Republic of China (2014) Technical code for testing of building foundation piles. China Architecture & Building Press, Beijing, China
13. Ministry of Transport of the People's Republic of China (2007) Code for design of ground base and foundation of highway bridges and culverts. China Communications Press, Beijing, China
14. Zixin Z, Jiayu L (2017) Review and applications of MJS techniques for ground improvement. *J Civ Archit Environ Eng* 39(6):1–11
15. Jiajin Z, Xiaonan G, Kuihua W et al (2015) Numerical simulation of tip bearing capacity of static drill rooted nodular pile. *Rock Soil Mech* 36(1):651–656
16. Jiajin Z, Xiaonan G, Kuihua W et al (2014) Performance of static drill rooted nodular piles under compression. *J Zhejiang Univ (Eng Sci)* 48(5):835–842
17. Mai W (2008) Research on vertically bearing behavior and reliability analysis of concrete-cored DCM pile. Tianjin University, Tianjin, China
18. Kang F, Jianwei Z (2010) Application of ABAQUS in geotechnical engineering. China Water & Power Press, Beijing, China
19. Hongfa X, Huajie W, Shaoping G (2002) Study on the parameters of pile soil contact surface element. *Explor Eng* 5:10–12
20. Randolph MF, Worth CP (1981) Application of the failure state in undrained simple shear to the shaft capacity of driven piles. *Geotechnique* 31(1):143–157

# Influence of Metro Vehicle Operation on Adjacent High-Speed Railway Bridge Pier



Guohui Cheng, Yao Shan, and Xiangliang Zhou

**Abstract** The growing scale of the high-speed railway network and that of the metro leads to an increasing number of intersections between these two traffic modes. To ensure the structural safety during the construction process of metro tunnels constructed beneath existing high-speed elevated lines, rows of isolation piles between these two different kinds of traffic infrastructures have been widely utilized. However, the vibration isolation effect of these piles during the metro vehicle operation process is still not well studied. In this paper, a model that accounts for the interaction between structures (i.e., high-speed bridge, isolation piles and metro tunnels) and soil foundations is established by employing a three-dimensional finite element method to investigate the vibration isolation effect of the isolation piles. The influence of different design parameters of isolation piles on the vibration characteristics of the complete system is investigated. Besides, this paper summarizes the law of wave peaks formation in the vibration magnification area. The results show that: (i) For surface, vibration isolation effect is influenced greatly by the spacing and diameter of isolation piles. The vibration isolation effect of the isolation pile is weakened considerably with increasing pile net spacing and is enhanced with increasing pile diameter. (ii) For high-speed bridge pier top, geometric parameters of isolation piles have little effect on the isolation efficiency. (iii) The increase of pile diameter and spacing makes wave peaks appear easily in the vibration magnifications region.

**Keywords** Vibration isolation · Isolation piles · Finite element

---

G. Cheng · Y. Shan (✉) · X. Zhou

Shanghai Key Laboratory of Rail Infrastructure Durability and System Safety, Tongji University, Shanghai, China

e-mail: [shanyao@tongji.edu.cn](mailto:shanyao@tongji.edu.cn)

Key Laboratory of Road and Traffic Engineering of the Ministry of Education, Tongji University, Shanghai, China

G. Cheng

e-mail: [ghcheng@tongji.edu.cn](mailto:ghcheng@tongji.edu.cn)

X. Zhou

e-mail: [1733262@tongji.edu.cn](mailto:1733262@tongji.edu.cn)



## 1 Introduction

The growing scale of the high-speed railway network and that of the metro network leads to an increasing number of intersections between these two traffic modes. In most of these intersection cases, new constructed metro tunnels beneath existing high-speed railroads are dominant, which brings two issues that need to be taken seriously. First of all, tunnel construction will cause deformation of high-speed railway foundation and endanger traffic safety. Secondly, passenger comfort and structural durability of high-speed railway may be affected by the subway vibration during the operation period. In engineering practice, isolation piles between these two different rail infrastructures have been widely utilized and played an important role in infrastructure deformation controlling in the construction process. As a result, the existing design principle of isolation piles is based on the deformation prediction of infrastructures in constructions, no isolation measure for vibration during operation is considered. Two questions present following this situation: (i) is it possible that the isolation piles would also reduce the influence of metro vehicle operation on adjacent high-speed railway bridge pier? If the answer is yes (ii) how to design the isolation piles to ensure not only the deformation control effect on infrastructures in the construction process, but also the vibration isolation effect between these two rail traffic modes in operation process? To answer these questions, the influence of the isolation piles on dynamic interactions between these two different infrastructures and the environmental dynamic response in the operation stage should be studied.

Isolation piles are generally a row of solid cylindrical piles with the same pile spacing, which is also called row piles. Row pile, trench, and continuous wall are different forms of the vibration isolation barrier. In 1968, Woods [1] designed and carried out a series of in situ experiments to study the effect of a trench on vibration isolation. The amplitude attenuation coefficient was proposed as the evaluation index of the isolation efficiency of the barrier.

$$A_{RC} = \text{Vertical amplitude behind the barrier} / \text{Vertical amplitude without barrier} \quad (1)$$

Although the existence of a trench system can be an effective approach to reduce vibrations, the application of trench was limited by its small depth [2]. Thus, Rechart et al. [3] used low-cost row piles with great applicability as vibration isolation barriers. The follow-up researchers analyzed the influence factors of vibration isolation effect of row piles. The research methods mainly include two categories: (1) analytical method based on wave function expansion method (WFEM), (2) numerical method based on finite element method (FEM), and boundary element method (BEM).

Pao et al. [4] elaborated on the analytical method by a single hole and carried out a lot of numerical analysis that was the beginning of the analytic solution. On this basis, Aviles and Sanchezsesma calculated the vibration isolation of the periodic piles on the two-dimensional (2D) and three-dimensional (3D) level according to

Graf's additive theorem and wave theory [5, 6]. They considered pile spacing affect the efficiency of vibration isolation. After that, scholars analyzed the influence of different sections, materials, and arrangement of piles on the vibration isolation effect [7–12]. Many achievements have been made in the analytical study of isolation pile parameters. However, because of the complexity of wave scattering, the theoretical methods simplified practical engineering. In order to solve the specific engineering problems efficiently and accurately, numerical methods based on FEM and BEM were found. Kattis et al. [13, 14], Kellezi [15], Tsai et al. [16], Xu [17], and Huang et al. [2] analyzed the vibration isolation performance of isolated piles by FEM and BEM method, and the influence of different materials, cross-section forms, and arrangement of the isolated pile on vibration isolation efficiency is studied. For complex engineering, some scholars used the 3D finite element to establish the simulation model. Guo et al. [18] developed a 3D finite element model including isolation piles, soil, and track structure. The vibration isolation efficiency of the isolated pile under the train load is analyzed. In Wang's paper [19], ANSYS software is used to simulate and analyze the periodic layered vibration isolation barrier. Wang investigated the vibration response of the existing building behind the pile row.

In the development of the analytical method, researchers studied the influence of incident waveform, soil parameters, and row pile parameters on the vibration isolation efficiency. The development and application of computer and finite element theory promoted the progress of numerical solutions. Researchers have gradually improved the boundary conditions in the calculation of specific projects, which makes the calculation results more accurate. However, there are still some problems that have not been considered at present: (i) The pile foundation of the bridge has sufficient stiffness and stability. Whether the application of isolation piles can reduce the impact of vibration sources on pile foundation? If so, whether the parameters of isolation piles have the same impact on the effect of vibration isolation as summarized in surface vibration isolation. (ii) What is the formation law of peak value in vibration magnification area and whether it is related to the parameters of the isolation pile?

To answer the above questions, a 3D finite element model including subway tunnels, isolation piles, and pile foundation of the high-speed railway bridge is built in this paper. According to the research results of previous scholars, it can be found that the significant factors affecting the isolation efficiency of single row isolation piles are the net distance between piles and pile diameter, so they are the parameters of isolation piles analyzed in this paper.

Firstly, the influence of isolation pile parameters on the surface isolation efficiency is analyzed through a series of comparative tests. Then, the vibration data in the area behind the isolation pile are extracted to study the relationship between the peak value of the vibration magnification region and pile parameters. Finally, the dynamic response results of the pier top are extracted to analyze vibration isolation efficiency of isolation pile on pile foundation.

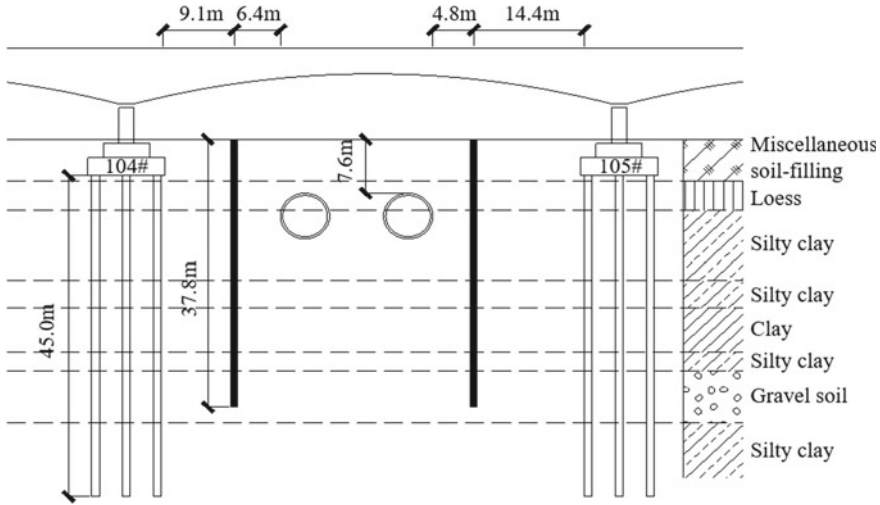


Fig. 1 Cross-sectional sketch of crossing

## 2 Background

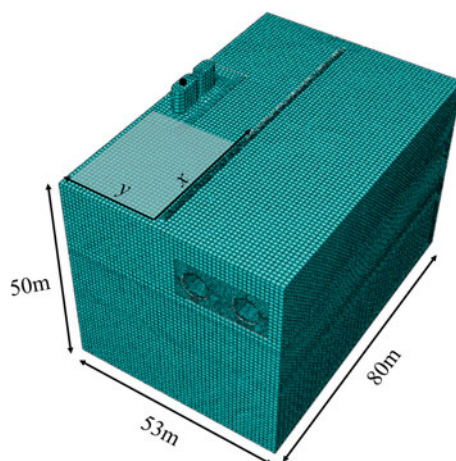
This paper relies on a project in south China, in which two metro tunnels pass under high-speed railway bridge vertically. The cross-sectional and soil layers of the tunnel are shown in Fig. 1. The buried depth of tunnels is 7.6 m, the outer diameter is 6.4 m, and the inner diameter is 5.8 m. The minimum net distance between the tunnel and the pile foundation is 15.5 m. Bored cast-in-place piles with a diameter of 0.8 m are used for isolation piles on both sides of the tunnel, and the length is 37.8 m. The minimum spacing between the isolation pile and the high-speed railway bridge pile is 9.10 m.

This area is a piedmont alluvial plain landform. The strata exposed in the depth of 60 m are mainly loess, silty clay, and gravel soil, with local sandy soil, and the thickness of Quaternary overburden is more than 50 m. The tunnel is mainly located in loess and silty clay.

## 3 Numerical Model

### 3.1 Model Introduction

Limited by the hardware computing capabilities, only a part of the project area can be included in the model. The size of the model should ensure that the calculation results have higher precision while maximizing the calculation efficiency. The calculation results of Lv et al. [20] showed that when the length of the model in the horizontal

**Fig. 2** Finite element model

direction is greater than 8 times the diameter of the tunnel, the calculation results can achieve higher precision. Lei [21] claimed that the range affected by subway vibration was within 60 m from the subway line. To guarantee the calculation accuracy, the length, the width, and the height of the model are chosen as 80 m, 53 m, and 50 m, respectively (refer to Fig. 2).

In ABAQUS, elastic waves will be reflected when propagates to the boundary of the model, which cause a great interference to the calculation of the dynamic response, so that the calculation result cannot reflect the real situation. Therefore, boundary conditions need to be specially treated to reduce or eliminate errors caused by model boundaries. Artificial boundary conditions are used to absorption of elastic waves, thereby simulating an infinite boundary. At present, viscoelastic boundary and infinite element boundary are two widely used artificial boundary methods. The model in this article sets the infinite element boundary.

Discretizing the model region into a finite number of meshes in the finite element model causes a low-pass effect, i.e., waves above a certain frequency are truncated in the model. The magnitude of this cutoff frequency depends on the size of the mesh in the model and the minimum shear wavelength considered. In general, for a finite element model using a lumped mass matrix, a higher calculation accuracy can be obtained when the minimum shear wavelength is longer than 6–8 times the unit lengths [22]. In this paper, under the premise of ensuring accuracy, the model mesh is divided into 0.5–1 m hexahedral elements (finite elements: C3D8R, infinite element: CIN3D8). The overall mesh of the model is shown in Fig. 2.

### 3.2 Material Parameters and Load

In order to improve the calculation efficiency, this paper assumes that the soil is an isotropic homogeneous medium, regardless of the soil microstructure and internal pores, and ignores the initial stress of the soil. Besides, due to the small dynamic strain caused by traffic load, the soil and structure are generally considered to be in the stage of elastic deformation, and the materials in the model are all set to the linear elastic constitutive. According to the on-site geological exploration data, material properties are as follows (The order of soil is the same as Fig. 1) (Table 1).

This paper applies the Rayleigh damping theory to simulate material damping. The theory assumes that the damping matrix of the element is a linear combination of the mass matrix and the stiffness matrix:

$$[C] = \alpha[M] + \beta[K] \tag{2}$$

$\alpha$  and  $\beta$  satisfy the following equation:

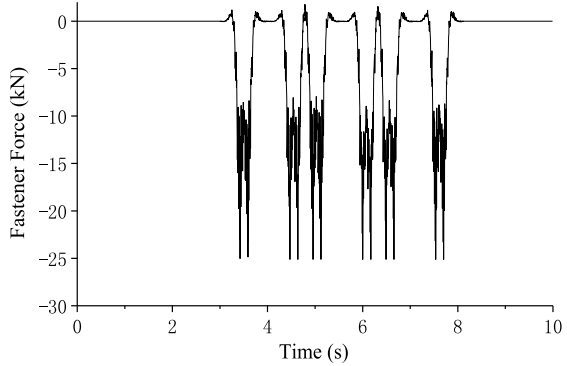
$$\xi_n = \frac{\alpha}{4\pi f_n} + \beta\pi f_n \tag{3}$$

where  $\xi_n$  is the damping ratio at frequency  $f_n$ . The maximum and minimum frequency this paper concern is 50 Hz and 5 Hz, respectively, at which  $\xi_n = 0.05$ . After calculation,  $\alpha = 2.856$ ,  $\beta = 2.894 \times 10^{-4}$ .

**Table 1** Material properties

Material name	Natural density (kg/m <sup>3</sup> )	Dynamic elastic modulus (MPa)	Dynamic Poisson's ratio	Depth
Miscellaneous soil-fill	1900	99	0.432	5.8
Loess	1910	172	0.421	4.2
Silty clay	1940	262	0.411	9.8
Silty clay	1920	606	0.42	3.8
Clay	1940	650	0.39	6.2
Silty clay	1940	1068	0.421	2.7
Gravel soil	2120	1768	0.409	6.3
Silty clay	1940	920	0.41	–
Caps	2500	40,000	0.2	–
High-speed bridge pile	2500	40,000	0.2	–
Shield segment	2500	45,000	0.2	–
Track bed slab	2500	40,000	0.2	–
Isolation pile	2500	40,000	0.2	–

**Fig. 3** Fastener force



The subway load applied in this paper refers to the track fastener force used in the Si’s model [23]. When the subway is running, the fastening force of a fastener on the track is shown in Fig. 3. The phase difference is applied to adjacent fasteners to simulate metro driving.

### 4 Data Analysis

The data of the measuring point (the black point in Fig. 2) is extracted to represent bridge pier top, and the measuring region (the shadow area Fig. 2) represents the surface near the cap. The *x*-direction is parallel to the direction of row piles, and the *y*-direction is perpendicular to it.

For the high-speed bridge pier, the dynamic response evaluation indicator selected is *a<sub>z</sub>*: the maximum vertical acceleration of the pier top. For the surface near the cap, the selection of dynamic response evaluation indicator *a'*(normalized acceleration amplitude) refers to the amplitude attenuation rate proposed by Wood [1], and the calculation is shown in Eq. 4.

$$a' = \frac{a_{\max}}{a_{0-\max}} \tag{4}$$

where *a<sub>max</sub>* is the maximum value of the vertical acceleration at a point in the presence of the piles;*a<sub>0-max</sub>* is the maximum value of the vertical acceleration at the same point in the absence of the piles. The other parameters used in this paper are:

- d*: diameter of isolation pile;
- l*: piles spacing;
- l\**: net spacing of piles (*l\* = l - d*).

The geometrical parameters of piles considered in this work are the diameter *d* and the net spacing *l\**. It is noted that when one parameter is investigated, the other parameters are kept constant. Ding et al. [10] found that: if the spacing of

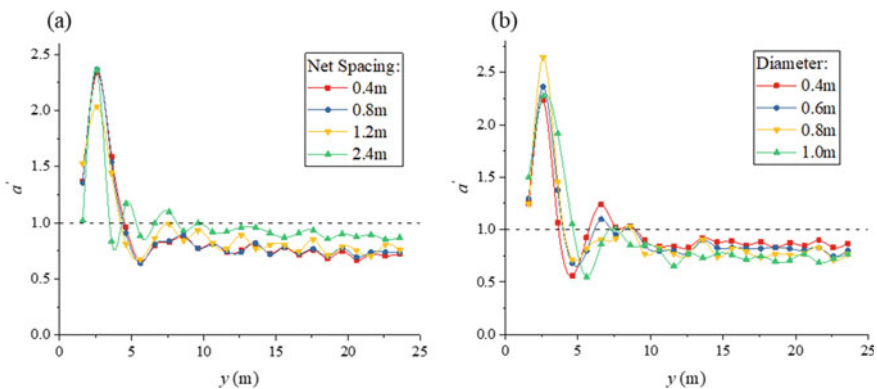
**Table 2** Parameters of isolation piles

Situation	$d$ (m)	$l$ (m)	$l^*$ (m)
Case 1	0.8	1.2	0.4
Case 2	0.8	1.6	0.8
Case 3	0.8	2.4	1.6
Case 4	0.8	3.2	2.4
Case 5	0.4	2.0	1.6
Case 6	0.6	2.2	1.6
Case 7	0.8	2.4	1.6
Case 8	1.0	2.6	1.6

isolation piles is not more than four times the diameter of piles, it could ensure good screening effectiveness. Therefore, considering the construction situation, the different situations are summarized in Table 2. Case 1–4 are used to analyze the influence of net spacing on vibration isolation efficiency, Case 5–8 focus on the diameter.

### 4.1 Vibration Response of Surface

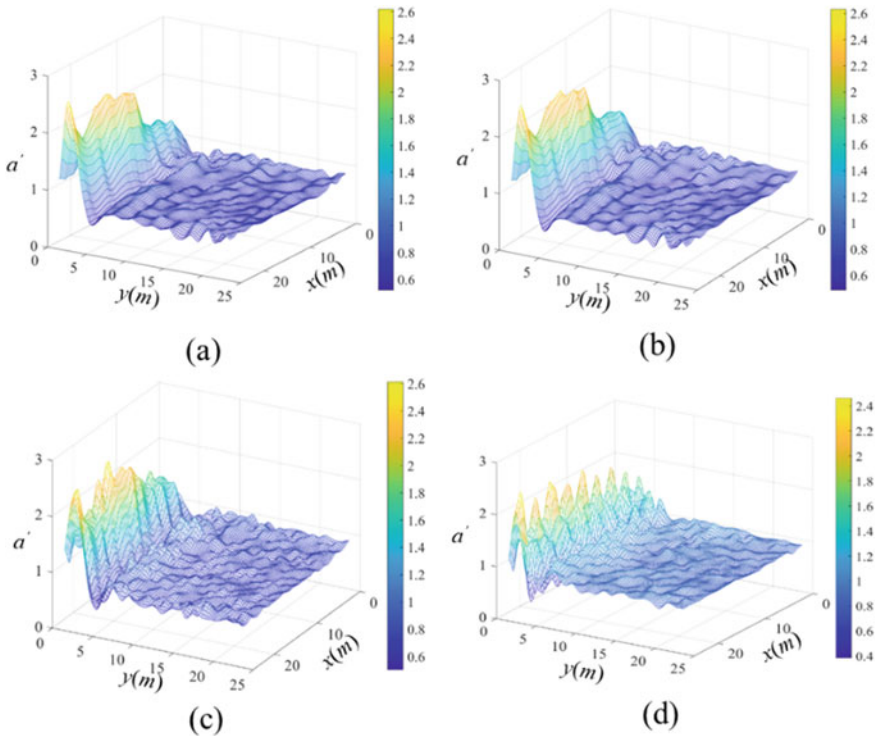
Figure 4 displays the vibration of normalized acceleration amplitude of surface under different net spacing and diameters. It shows that there are vibration magnifications near the isolation pile, which is caused by the scattering of elastic waves between the isolation piles. The wave trough behind the vibration magnification region represents the optimal attenuation region. Figure 4a shows that with the increase of pile spacing, the vibration attenuation decreases. As shown in Fig. 4b, the vibration isolation effect of the isolation pile is enhanced with increasing pile diameter. These laws are in



**Fig. 4** Normalized acceleration amplitude of surface. **a**  $d = 0.8$  m; **b**  $l^* = 1.6$  m

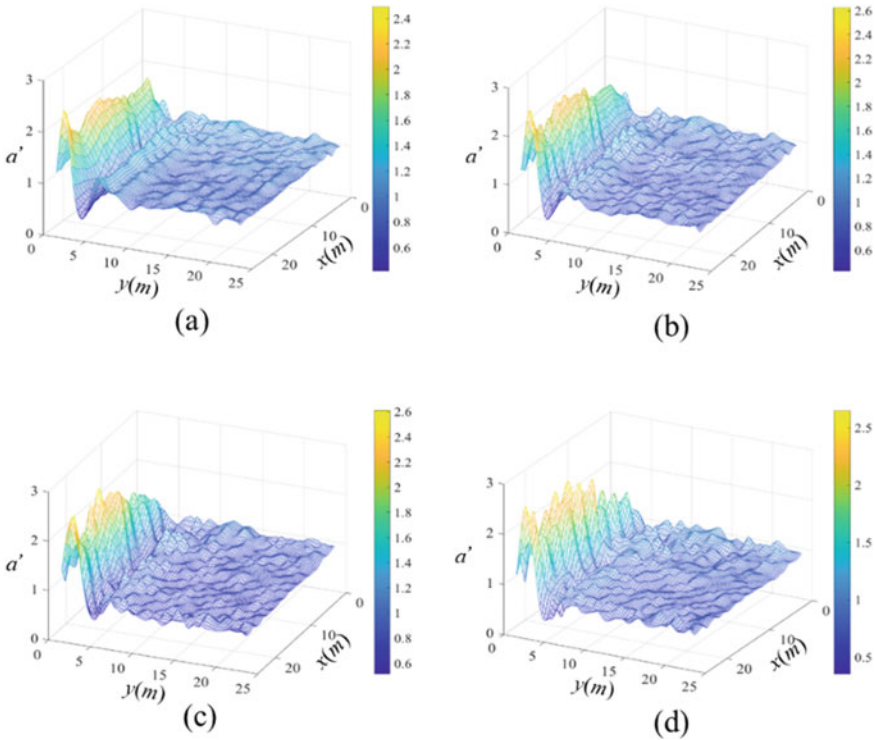
conformity with those of the existing theoretical solutions [6, 7, 10]. It is because that when the spacing of piles is large or the diameter of piles is small, the barrier behaves like a set of independent piles instead of a unit. Besides, according to Fig. 4a, it can be found that the attenuation efficiencies of isolation piles are very close when the pile spacing is 0.8 and 0.4 m, which means that keeping the pile spacing 0.8 m is enough to achieve a high isolation effect.

Figures 5 and 6 are the overall vibration attenuation under different pile spacing and pile diameter. Figure 5 shows that when the net spacing of isolation piles increases from 0.4 m to 2.4 m, more peaks appear in the vibration magnifications region and show strong periodicity in the  $x$ -direction. That is because piles are separated so far enough that they perform like a set of independent obstacles. Figure 6 shows that there is a similar relationship between the wave crest and pile diameter in vibration magnifications region, and the increase of pile diameter leads to the appearance of peaks. This is because the increase of pile diameter increases the distance between adjacent pile-free area, which reduces the interference of incident wave and peaks appear.



**Fig. 5** Three-dimension curved surface of normalized acceleration amplitude under different net spacing. ( $d = 0.8$  m). **a** Case 1; **b** Case 2; **c** Case 3; **d** Case 4





**Fig. 6** Three-dimension curved surface of normalized acceleration amplitude under different pile diameters. ( $l^* = 1.6$  m). **a** Case 5; **b** Case 6; **c** Case 7; **d** Case 8

### 4.2 Vibration Response of Pier

The vibration acceleration data of the feature points mentioned above under different spacing and diameter of piles are extracted; Fig. 7 is drawn according to the maximum vertical acceleration in each case.

Figure 7 shows that the isolation pile can effectively reduce the vibration at the top of the pier. Therefore, the utilization of isolation piles between subway and pile foundation building can play a protective role for the latter.

Figure 7a shows that the vibration attenuation increases slightly with the increase of the net distance between piles. Figure 7b shows that the diameter of the pile has no obvious influence on the isolation effect of the isolation pile. Generally, when isolation piles are used to protect the pile foundation buildings, the geometric parameters have little effect on the isolation efficiency.

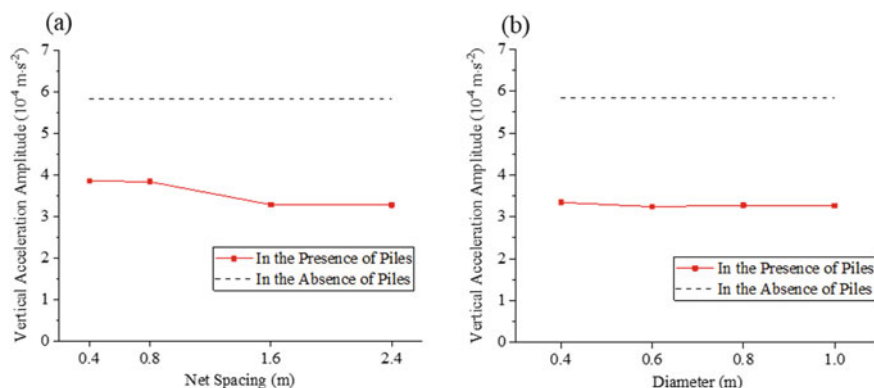


Fig. 7 Vertical vibration amplitude of pier. **a**  $d = 0.8$  m; **b**  $l^* = 1.6$  m

## 5 Conclusions and Future Work

Based on the results of the parametric studies of the passive vibration isolation problem considered, which are depicted in Figs. 4, 5, 6, and 7, one can draw the following conclusions:

1. Isolation plies provide vibration isolations between metro tunnels and high-speed railway bridge in the operation stage.
2. For surface vibration, the vibration isolation effect of the isolation pile is weakened considerably with increasing pile net spacing in the range of 0.4–2.4 m and is enhanced with increasing pile diameter in the range of 0.4–1.0 m.
3. Different from the law of ground vibration isolation, for the vibration of the pier top, geometric parameters have little effect on the isolation efficiency.
4. The increase of pile diameter and spacing makes periodic peaks appear easily in the vibration magnifications region.

Our next step is to apply the high-speed rail load on the top of the pier and study the influence of the isolation piles on dynamic interactions between metro and high-speed rail.

**Acknowledgements** This research was supported by National Natural Science Foundation of China (51708424 and 51761135109) and the Fundamental Research Funds for the Central Universities, the People's Republic of China.

## References

1. Woods R (1968) Screening of surface waves in soils. *Am Soc Civil Eng J Soil Mech* 407–435
2. Huang J, Shi Z (2011) Application of periodic theory to rows of piles for horizontal vibration attenuation. *Int J Geomech* 13(2):132–142

3. Richard F, Woods R, Hall J (1970) *Vibration of soils and foundations*
4. Pao Y, Mow C, Achenbach J (1973) *Diffraction of elastic waves and dynamic stress concentrations*. American Society of Mechanical Engineers Digital Collection
5. Aviles J, Sanchezsesma F (1983) Piles as barriers for elastic waves. *J Geotech Eng* 109(9):1133–1146
6. Aviles J, Sanchezsesma F (1988) Foundation isolation from vibrations using piles as barriers. *J Eng Mech* 114(11):1854–1870
7. Boroomand B, Kaynia A (1991) Vibration isolation by an array of piles. *Soil Dyn Earthq Eng* 11(1):683–691
8. Xia T, Sun M, Chen C et al (2011) Analysis on multiple scattering by an arbitrary configuration of piles as barriers for vibration isolation. *Soil Dyn Earthq Eng* 31(3):535–545
9. Lu J, Nie W (2008) Dynamic response of single pile embedded in half-space saturated soil subjected to Rayleigh waves. *Chin J Geotech Eng* 30(2):225–231
10. Ding G, Cai Y, Xu C (2009) Analysis of vibration isolation of a row of rigid piles to plane SV waves in saturated soil. *Rock Soil Mech* 30(3):849–854
11. Cai Y, Ding G, Xu C (2008) Three-dimensional isolation analysis of a row of pile in saturated soil from incident waves. *J Nat Disasters* 17(2):1–7
12. Xu P (2017) Analysis of isolation effectiveness of shear waves by a row of hollow pipe piles in saturated soils. *Transp Porous Media* 120(1):1–18
13. Sun Y (2003) *Ground vibration caused by railway traffic and vibration isolation of piles*. Tongji University
14. Kattis S, Polyzos D, Beskos D (1999) Vibration isolation by a row of piles using a 3-D frequency domain BEM. *Int J Numer Meth Eng* 46(5):713–728
15. Kattis S, Polyzos D, Beskos D (1999) Modelling of pile wave barriers by effective trenches and their screening effectiveness. *Soil Dyn Earthq Eng* 18(1):1–10
16. Tsai P, Feng Z, Jen T (2008) Three-dimensional analysis of the screening effectiveness of hollow pile barriers for foundation-induced vertical vibration. *Comput Geotech* 35(3):489–499
17. Xu P (2011) Rows of elastic hollow pipe piles as isolation barriers for plane SV waves. *Chin J Geotech Eng* 33(3):392–397
18. Guo B, Sun L, Yan S et al (2014) Numerical analysis of screening efficiency of driven piles in different layouts. *China Earthq Eng J* 36(3):510–515
19. Wang L (2016) *The study on vibration isolation performance of periodic row piles in subway near field buildings*. China Academy of Railway Sciences
20. Lei X (2015) *High speed railway track dynamic: model algorithm and application*. Science Press
21. Lv A, Jiang B, You C (1999) Research on the meshing range of finite element method for back-analysis of displacement. *Chin Civil Eng J* 32(1):26–30
22. Liao Z (2002) *Introduction to wave motion theory in engineering*. Science Press
23. Si J (2018) *The train induced dynamic response of the railway embankment and the underpass metro tunnel system*. Tongji University

# Application Research and Structural Optimization of Vibration Isolation of Row Piles in High-Speed Railway Based on the Concept of Phononic Crystal



Xiaobin Chen and Hao Tang

**Abstract** Phononic crystal is a new type of functional material, which can shield elastic waves at different frequencies by properly setting the parameters and distribution of constituent material. Based on the phononic crystal theory, this paper uses the finite element software COMSOL multi-physics to calculate the band gap characteristics of three-dimensional periodic row piles structure and discusses the influence of soil density, elastic modulus, radius of row piles, configuration mode and section shape. The results show that the radius of row piles and the elastic modulus of soil are the main factors affecting the band gap; the appropriate section shape can be selected according to the frequency range that one needs to shield and the amount of material that is needed to use. Compared with the periodic pile barrier in a square configuration, the pile in a triangle configuration can obtain a higher initial bound frequency, terminal bound frequency and a bigger band gap width. The research results are expected to provide some reference for the vibration isolation design of high-speed railway.

**Keywords** High-speed railway vibration · Phononic crystal · Vibration isolation performance · Numerical simulation · Band gap characteristics

## 1 Introduction

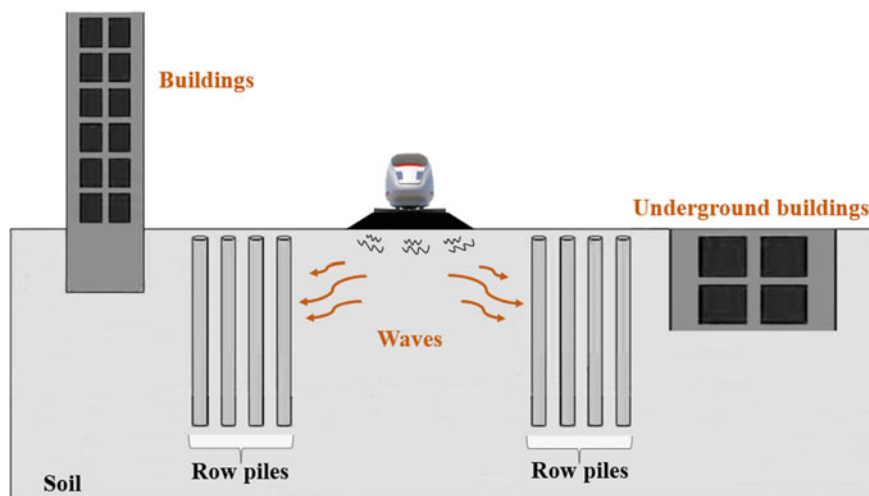
In recent years, with the development of high-speed railway construction and the overall acceleration of existing railway, the impact of ground vibration caused by high-speed train on the surrounding environment has become more and more prominent. Train vibration will have a negative impact on nearby residents, surrounding buildings and the production and use of precision instruments, so it is necessary to study the vibration isolation measures. The high-speed railway is dominated by low-frequency vibration [1]. Yin et al. [2] obtained the conclusion that the environmental vibration frequency of the high-speed railway at 350 and 250 km/h is mainly

---

X. Chen · H. Tang (✉)

School of Civil Engineering, Central South University, Changsha 410075, China

e-mail: [tanghao0908@qq.com](mailto:tanghao0908@qq.com)



**Fig. 1** Vibration reduction diagram of row piles

about 40 and 25 Hz, respectively, through field test. In order to reduce the vibration isolation, the most commonly used method is to set up a barrier on the propagation path of wave. The row pile structure is one of the discontinuous barriers with good effect [3], and its vibration reduction setting is shown in Fig. 1.

Richard et al. [4] first put forward the concept of using single row or multiple rows of cylindrical holes as wave barrier. Aviles and Sanchez-Sesma [5, 6] analyzed the scattering effect of row piles on shear horizontal waves and proposed that rigid piles are more effective than flexible piles, and when the pile diameter and pile length are greater than  $1/4$  and  $1/2$  of the wave length, they will achieve a certain effect of vibration isolation. Gao et al. [7, 8] pointed out that the discontinuous circular section wave barrier can reduce the ground vibration by 60–80%, which proves the good engineering value of the discontinuous vibration isolation barrier. At the same time, he used the elastic dynamic boundary integral equation to study the vibration isolation effect of row piles in three-dimensional layered foundation. The results show that the distribution of soft and hard soil in layered foundation has an influence on the vibration isolation effect of row piles. Qiu [9] made a three-dimensional analysis on the far-field passive vibration isolation of single-row piles and multi-row piles based on the integral equation of Rayleigh wave scattering theory. Li et al. [10] used Rayleigh wave scattering integral equation and found that the main factor affecting the vibration isolation effect of multi-row piles is the number of pile rows, while the influence of section size is relatively small. Wei et al. [11] studied the vibration isolation effect of single-row piles in the railway environment vibration. He established the train, earth and row piles coupling dynamic model by using ANSYS and analyzed the influence of pile depth, pile diameter, section and material on the vibration isolation effect. Meng et al. [12] used COMSOL PDE finite element method to establish a two-dimensional periodic row pile structure and discussed the influence

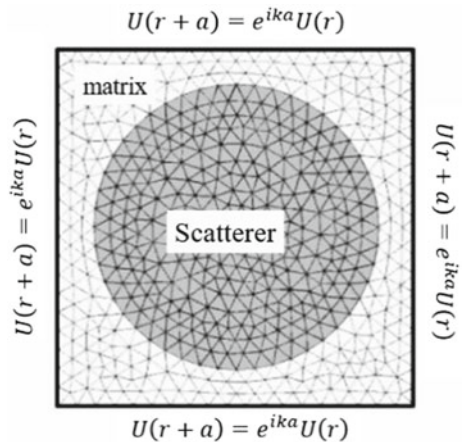
of relevant parameters on its band gap. Liu et al. [13] studied the vibration isolation effect of vibration isolation well and concrete pile through model experiment, and the results show that the vibration isolation effect of concrete pile is better than that of vibration isolation well.

It has long been recognized that the vibration isolation effect of multi-row piles is better than that of single-row piles; however, most of the previous studies on the parameters of row piles are based on the field tests and numerical simulation, and the overall periodicity formed by the regular configuration of row piles is rarely concerned. Based on the band gap characteristics of the phononic crystal, this paper uses the finite element software to establish the three-dimensional periodic structure of row piles. According to the vibration frequency range of the high-speed railway, the vibration isolation effect under different soil density, elastic modulus, row piles radius, configuration mode and section shape is analyzed.

## 2 Calculation Theory of Band Gap Characteristics Based on Finite Element Method

The theoretical study of periodic structure was first carried out in the field of solid-state physics, and continuous achievements have been made. For example, it has been found that elastic waves will transit selectively when propagating in periodic crystals, which is related to the reflection, scattering and diffraction of waves. The phenomenon of selective transmission of waves brings inspiration to the scholars who study vibration isolation. In the study of phononic crystals, the finite element method can be used to calculate the band gap characteristics [14]. When using the finite element software to solve the wave equation, according to Bloch theorem, typical cell can be extracted, as shown in Fig. 2. The cell satisfies the characteristic

**Fig. 2** Typical cell and periodic boundary conditions of periodic row piles



equation, and the boundary displacement matrix  $U(r)$  satisfies the periodic condition:

$$(K - \omega^2 M)U = 0 \tag{1}$$

$$U(r + a) = e^{ika}U(r) \tag{2}$$

where  $\omega$  is the angular frequency,  $K$  is the stiffness matrix,  $M$  is the mass matrix,  $a$  is the global parameter lattice constant vector,  $k$  is the wave vector in the first Brillouin region,  $r$  is the position vector,  $i = -1$ .

The displacement field  $u(r)$  satisfies the following relationship:

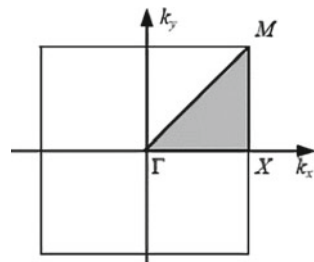
$$u(r) = e^{i(k \cdot r)}u_k(r) \tag{3}$$

where  $u_k(r)$  is a periodic function with the same periodicity as the phononic crystal.

The first Brillouin zone and irreducible Brillouin zone are shown in Fig. 3. It has been proved in solid physics that there will be no new eigenvalues and eigen fields outside the first Brillouin zone. Therefore, when analyzing the propagation characteristics of elastic waves in periodic structures, the calculation can be simplified in the first Brillouin zone. Using the symmetry of the first Brillouin region, the calculation can be further simplified in the irreducible Brillouin region, as shown in the shadow part of the figure. Due to the extreme value of the eigen spectrum can be got at the boundary of the irreducible Brillouin zone, in order to determine the frequency range of band gap, we only need to calculate on the high symmetry boundary ( $M\Gamma\text{-}\Gamma X\text{-}XM$ ).

COMSOL multi-physics is a finite element analysis software with multi-physical field coupling. Compared with other finite element software, its advantage is that it can easily impose periodic boundary conditions. When COMSOL multi-physics is used for the calculation, the band gap of the phononic crystal can be obtained only by using the wave vector  $K$  scan the high symmetry boundary of the irreducible Brillouin zone (IBZ) of the structure and solving formula (1) and formula (2) jointly.

**Fig. 3** First Brillouin zone and irreducible Brillouin zone of periodic piles



### 3 Method Verification

The specific process of calculating the energy band structure of phononic crystals by using COMSOL multi-physics in this paper is as follows: Select the solid mechanics module and select the solution type as the characteristic frequency solution; establish the geometric model of the phononic crystal cell; define the material attribute value of the component; define the global parameter lattice constant  $a$ ; add the Floquet periodic boundary condition, and apply the free boundary at the upper and lower boundaries of the model; last, input the coordinate value of  $M\Gamma-\Gamma X-XM$ , which is the high symmetric boundary of irreducible Brillouin zone, in the parameterized scanning solution setting. After scanning these boundaries for eigenvalues, the energy band structure of the phononic crystal can be obtained by taking the reduced wave vector  $k$  as the abscissa and the eigenvalue as the ordinate.

In order to verify the correctness of COMSOL multi-physics method for calculating the dispersion curve of periodic piles, this paper compares the calculation results with those of Miniaci et al. [15]. The model in the literature is a cross-cavity in the three-dimensional soil, and the calculation results are shown in Fig. 4. The gray area in the figure is the band gap of the model. It can be seen from the figure that the calculation results in this paper are very consistent with those in the literature, which can verify that the calculation method in this paper is correct.

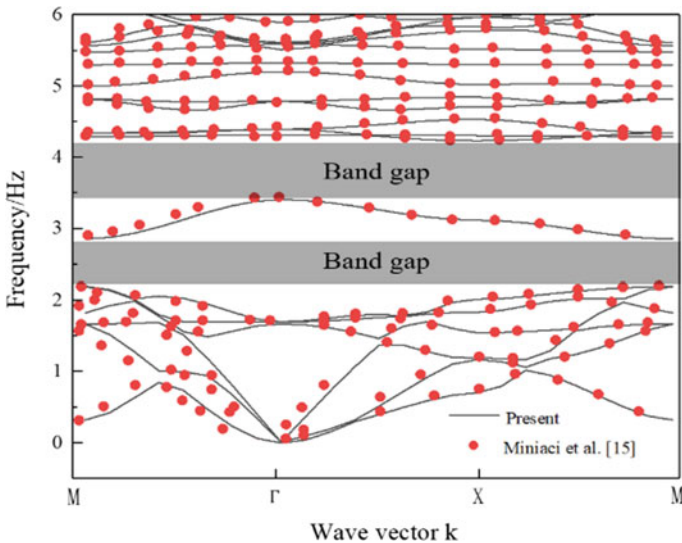


Fig. 4 Dispersion curves of cross-like cavity periodic structure



### 4 Numerical Analysis and Calculation

The dynamic strain of foundation soil caused by railway load excitation is generally less than  $10^{-5}$ , and the soil is completely in the elastic deformation stage. Therefore, in this paper, it is assumed that the pile and soil are isotropic linear elastic materials, the displacement and stress of pile–soil interface are continuous, and the pile of limited length is periodically buried in the soil to form the periodic row piles. This setting can take the influence of pile length into consideration, because the two-dimensional model is equivalent to the infinite length of the pile [16], the three-dimensional model is more suitable for the actual situation.

Material parameters are the main factors that affect the band gap characteristics of periodic row piles [17]. The cell model is established with the soil as the matrix and the pile as the scatterer, as shown in Fig. 5, and the material used for the pile is steel. The material parameters are shown in Table 1. It mainly studies the influence of soil density, elastic modulus, row piles radius, configuration mode and section shape on the band gap. When one material parameter changes, it is assumed that other parameters remain unchanged.

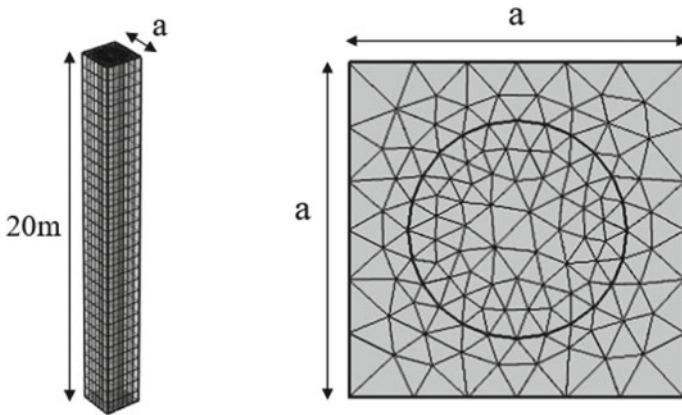


Fig. 5 Cell model in the finite element software

Table 1 Material properties

Material	Elastic modulus (E/Mpa)	Poisson’s ratio ( $\nu$ )	Density ( $\rho/\text{kg/m}^3$ )
Soil	20	0.35	1800
Steel	207,000	0.3	7784

## 5 Analyses of Influencing Factors of Band Gap of Periodic Row Piles

### 5.1 Row Pile Radius

Periodic piles in a square configuration are shown in Fig. 6. The period constant  $a = 2$  m, and the pile length is 20 m. Figure 7 shows the band gap of periodic piles in square configuration versus radius of piles. In the figure, the lower boundary of the gray area represents the initial frequency of band gap (IFBG), the upper boundary represents the terminal frequency of band gap (TFBG), the height of the gray area represents the width of band gap (WBG), and the vibration frequency within the band gap indicates that it cannot pass the row piles barrier. It can be seen from the figure that with the increase of the pile radius, the TFBG and WBG increase

Fig. 6 Periodic piles in a square configuration and IBZ

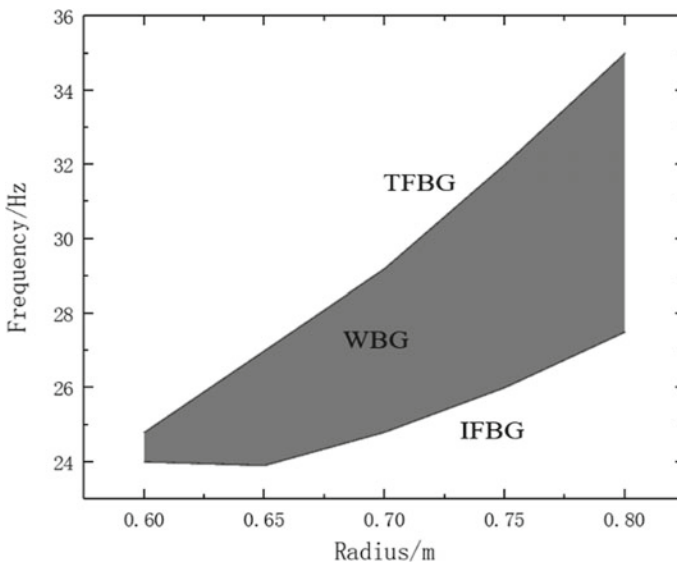
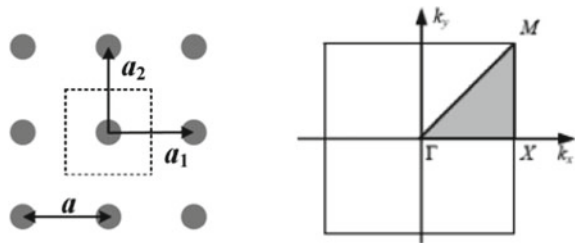
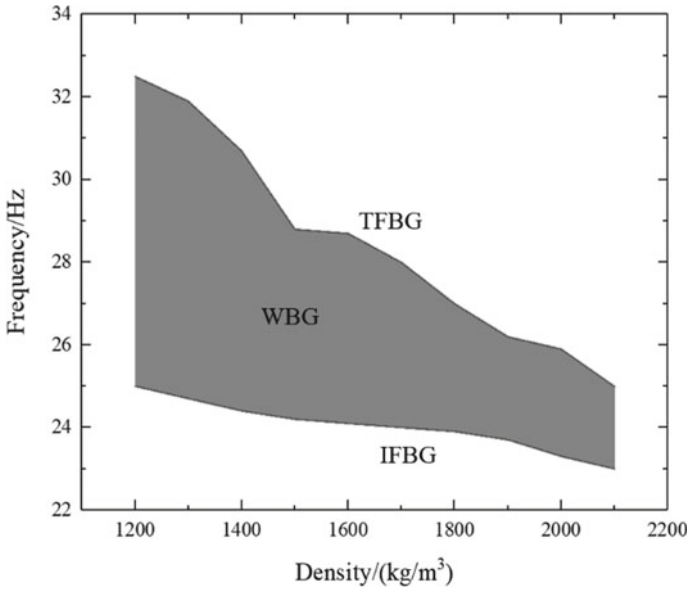


Fig. 7 Band gap of periodic piles in square configuration versus radius of piles



**Fig. 8** Band gap of periodic piles in square configuration versus soil density

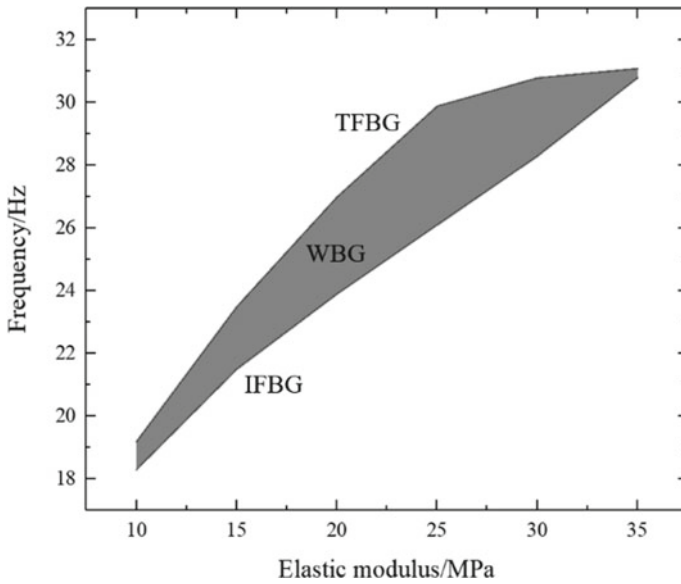
correspondingly, and the IFBG decreases slightly when the radius is 0.65 m, which shows a gradually increasing trend as a whole.

### 5.2 Soil Density and Elastic Modulus

Figures 8 and 9 show the variations of band gap of periodic piles in square configuration with soil density and elastic modulus, respectively. It can be seen that the influence of soil density on the band gap is smaller than that of elastic modulus, and with the increase of soil density, the IFBG and TFBG decrease correspondingly. The WBG slightly increases when the soil density is 2000 kg/m<sup>3</sup>, while the overall trend is gradually decreasing. It can be seen from Fig. 9 that with the increase of the elastic modulus of soil, the IFBG and TFBG increase correspondingly, and the WBG increases first and then decreases, with the maximum value when the soil elastic modulus reaches 25 MPa.

### 5.3 Section Shapes of Piles

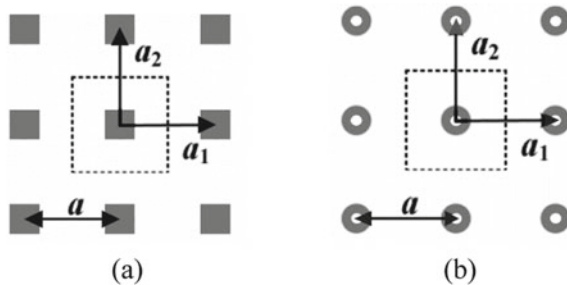
At present, the common section shapes of piles are round pile, square pile and hollow pile. In order to study the influence of different section shapes on the band gap, their



**Fig. 9** Band gap of periodic piles in square configuration versus elastic modulus of soil

period constant is kept at 2 m. At this time, the radius of the circular pile and the side length of the square pile increase with the increase of the filling rate. The outer radius of the hollow pile is kept unchanged at 0.85 m, and the inner radius decreases with the increase of the filling rate. It can be seen from Fig. 11 that when the filling rate is low, the IFBG and TFBG of circular pile and square pile are low. As the filling rate increases, their IFBG, TFBG and WBG increase, and the IFBG, TFBG and WBG of square pile are larger than that of circular pile. When the filling rate is low, the IFBG and TFBG of hollow pile are high. When the filling ratio changes from 0.28 to 0.50, the TFBG basically remains unchanged, while the IFBG gradually increases and the corresponding WBG gradually increases. Therefore, the appropriate section shapes can be selected according to the frequency range that we need to shield and the amount of material that we need to use (Fig. 10).

**Fig. 10** Periodic square piles (a) and hollow piles (b) in a square configuration



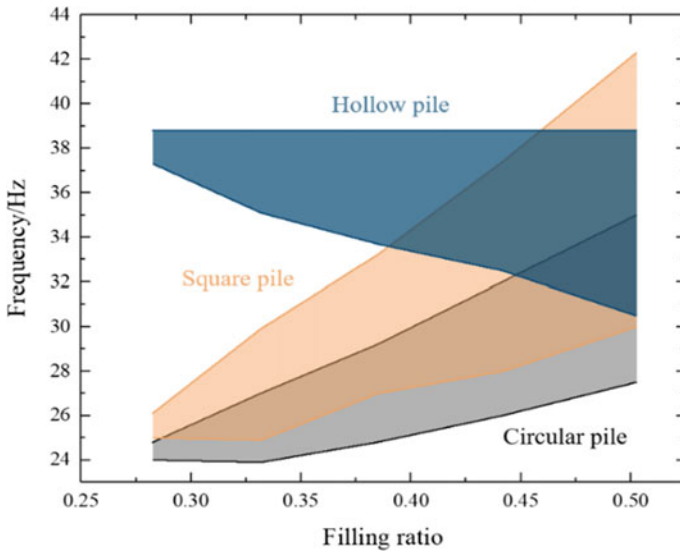
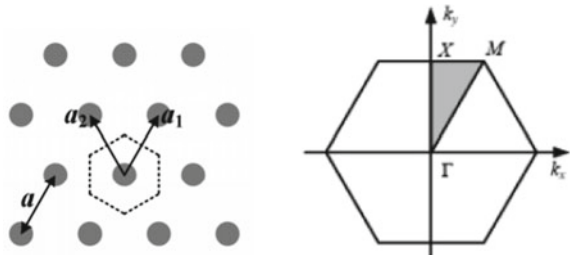


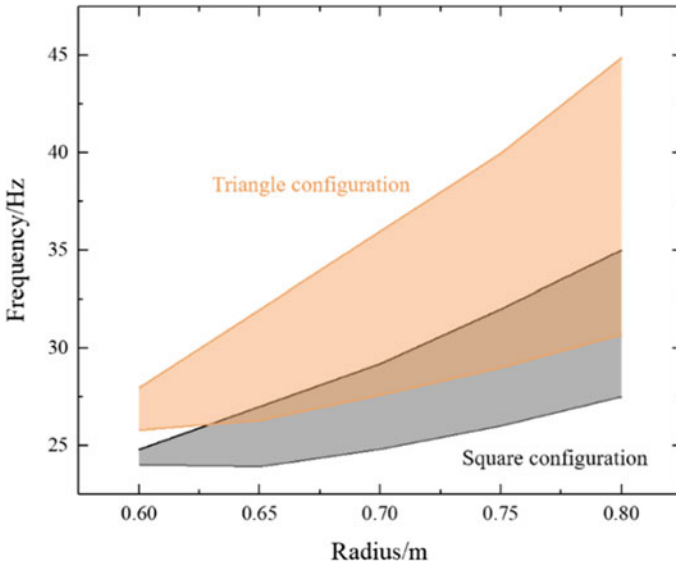
Fig. 11 Band gap of periodic piles in square configuration versus filling ratio

### 5.4 Configuration of Piles

The periodic row piles in triangular configuration are also a common configuration form in engineering, as shown in Fig. 12. Similarly, the period constant  $a = 2$  m. With the increase of filling rate, their IFBG, TFBG and WBG increase. And the IFBG, TFBG and WBG of periodic piles in triangular configuration are larger than those in square configuration. Therefore, when it is necessary to isolate low-frequency vibration, the pile in square configuration can be selected; when it is necessary to isolate higher and wider frequency, the pile in triangular configuration can be selected (Fig. 13).

Fig. 12 Periodic piles in a triangular configuration and IBZ





**Fig. 13** Band gap of periodic piles in square and triangular configuration versus inner radius of piles

## 6 Conclusions

Based on the band gap characteristics of phononic crystals, the three-dimensional periodic piles structure is established by using the finite element software COMSOL multi-physics solid mechanics module, and the band gap characteristics are analyzed. According to the characteristics of high-speed railway vibration frequency, the parameters of different soil density, elastic modulus, pile radius, configuration mode and section shape are discussed.

It can be seen from the analysis results that the radius of row piles and the elastic modulus of soil are the main factors affecting the band gap. With the increase of pile radius, the IFBG, TFBG and WBG increase gradually as a whole. With the increase of soil density, the IFBG, TFBG and WBG decrease gradually. With the increase of the elastic modulus of soil, the IFBG and TFBG increase correspondingly, and the WBG increases first and then decreases; when the filling rate is low, the IFBG and TFBG of circular pile and square pile are low, while those of hollow pile are high. With the increase of the filling rate, the WBG of circular pile, square pile and hollow pile increases gradually. The appropriate section shape can be selected according to the frequency range that needs to be shielded and the material consumption; compared with the periodic piles in square configuration, the piles in triangular configuration can obtain a higher IFBG, TFBG and a larger WBG.

## References

1. Mao KM, Chen GX, Zhang Y, Hong XX, Xiao JH (2012) In-situ testing and analysis of ground vibration caused by CRH trains running on viaduct of Hu-Ning intercity railway. *J Disaster Prev Mitig Eng* 32:267–273. <https://doi.org/10.3969/j.issn.1672-2132.2012.03.002>
2. Yin H, Li YZ, Gu XA, Li YL (2010) Study of the environmental vibration characteristic of high-speed railroad. *Railw Occup Saf Health Environ Prot* 37:32–36. <https://doi.org/10.3969/j.issn.2095-1671.2010.01.009>
3. Gan YY (2018) Vibration reduction analysis of periodic piles with complex damping. Beijing Jiaotong University
4. Richard FE, Hall JR, Woods RD (1970) *Vibrations of soils and foundations*. Prentice-Hall Inc, Upper Saddle River
5. Aviles J, Sanchez-Sesma FJ (1983) Piles as barriers for elastic waves. *J Geotech Eng* 109:1133–1146. [https://doi.org/10.1061/\(ASCE\)0733-9410\(1983\)109:9\(1133\)](https://doi.org/10.1061/(ASCE)0733-9410(1983)109:9(1133))
6. Aviles J, Sanchez-Sesma FJ (1988) Foundation isolation from vibration using piles as barriers. *J Eng Mech* 114:1854–1870. [https://doi.org/10.1061/\(ASCE\)0733-9399\(1988\)114:11\(1854\)](https://doi.org/10.1061/(ASCE)0733-9399(1988)114:11(1854))
7. Gao GY (1998) Theory and application of ground vibration isolation by discontinuous barriers. Zhejiang University
8. Gao GY, Li J, Li N, Song J, Peng ZG (2013) Three-dimensional analysis of far-field passive vibration isolation for row of piles in layered foundation. *Chin J Rock Mech Eng* 2934–2943. <https://doi.org/10.3969/j.issn.1000-6915.2013.z1.046>
9. Qiu C (2003) Three-dimensional analysis of far-field passive vibration isolation for continuous and discontinuous barriers. Tongji University
10. Li ZY (2005) Analysis of multi-row of piles as barriers for isolating vibration in far field. *Chin J Rock Mechan Eng* 24:3990–3995. <https://doi.org/10.3321/j.issn:1000-6915.2005.21.029>
11. Wei HL, Lv SD (2008) Numeric analysis on railway environment vibration isolation by row of piles. *J East China Jiaotong Univ* 25:10–15. <https://doi.org/10.3969/j.issn.1005-0523.2008.02.003>
12. Meng QJ, Shi ZF (2018) Ambient vibration attenuation by periodic pile barriers using periodic theory and COMSOL PDE method. *Rock Soil Mech* 39:4251–4260. <https://doi.org/10.16285/j.rsm.2017.2306>
13. Liu JL, Zhang RH, Zhao XY, Liu H, Zhao Q, Wang AY (2019) The research on the model test on vibration isolation effect of typical. *Earthq Eng Eng Dyn* 39:231–241. <https://doi.org/10.13197/j.eeev.2019.01.233.liujl.027vibrationisolationbarinrailtransit>
14. Liu XN, Hu GK, Sun CT, Huang GL (2011) Wave propagation characterization and design of two-dimensional elastic chiral metamaterial. *J Sound Vib* 330:2536–2553. <https://doi.org/10.1016/j.jsv.2010.12.014>
15. Miniaci M, Krushynska A, Borgia F, Pugno NM (2016) Large scale mechanical metamaterials as seismic shields. *New J Phys* 18:1–14. <https://doi.org/10.1088/1367-2630/18/8/083041>
16. Liu XN, Shi ZF, Mo YL (2015) Comparison of 2D and 3D models for numerical simulation of vibration reduction by periodic pile barriers. *Soil Dyn Earthq Eng* 79:104–107. <https://doi.org/10.1016/j.soildyn.2015.09.009>
17. Zhang B, Liu YQ, Zhang SL, Wang WB (2018) Study on vibration isolation performance of periodic row piles based on bandgap properties. *Railw Eng* 58:148–151. <https://doi.org/10.3969/j.issn.1003-1995.2018.05.35>

# Attenuation Characteristics of Plane Waves by Metabarriers with Negative Parameters



Jiahua Zhou, Xingbo Pu, and Zhifei Shi

**Abstract** Metamaterials have come to the fore in the fields of electromagnetics and acoustics due to their superior performance in targeted frequency ranges. However, the related application such as in vibration mitigation in civil engineering is rare. In this paper, the dispersion relation of a new kind of metabarriers is obtained according to the theory of periodic structure in solid mechanics. The dispersion of the metabarriers is generated by local resonance. A simplified model is established to explain the mechanism of bandgaps. The effective mass density, effective shear modulus and effective bulk modulus of the metabarriers are calculated by finite element method. It is found that the resonance of the oscillator produces a negative effective mass density, which prevents the wave propagating in soil, thus creating bandgaps. At this point, the effective shear modulus and effective bulk modulus of the metabarriers are both positive. The findings of this paper are beneficial for the design of periodic pile barriers to isolate elastic waves propagating in soil.

**Keywords** Metabarriers · Bandgap · Effective parameters · Vibration isolation

## 1 Introduction

Metamaterials are structures or materials made of artificial composites with special properties that natural materials do not have [1]. Through designing the key size of the material, the structure performs extraordinary physical properties. In other words, through artificial design of materials, the obtained composite materials or structures have macroscopic equivalent properties that are not available in nature,

---

J. Zhou · Z. Shi (✉)

School of Civil Engineering, Beijing Jiaotong University, Beijing 100044, PR China

e-mail: [zfshi178@bjtu.edu.cn](mailto:zfshi178@bjtu.edu.cn)

J. Zhou

e-mail: [18115062@bjtu.edu.cn](mailto:18115062@bjtu.edu.cn)

X. Pu

Department of Civil, Chemical, Environment and Materials Engineering DICAM, University of Bologna, 40136 Bologna, Italy



such as arbitrary mass densities and elastic parameters. Metamaterials were originally proposed in electromagnetism. After Smith [2] verified Veselago's negative refraction theory [3] through experiments, materials with abnormal electromagnetic properties such as single negative refractive index materials, near-zero refractive index materials and metamagnetic materials were successively discovered and applied, all of which belong to the category of metamaterials. According to the theory of negative refraction, the metamaterial with small size can control the large wavelength [4–6].

The band gap of phononic crystal can be classified as Bragg scattering [7, 8] and local resonance type [9, 10]. In 2000, Liu first proposed a phononic crystal with local resonance type [9]. They arranged lead sphere coated with soft silicone rubber material in a simple cubic structure made of epoxy matrix to form a three-dimensional, three-component phononic crystal. Through theoretical and experimental studies, it is found that the wavelength corresponding to the band gap of the phononic crystal is larger than the lattice constant, which breaks through the limitation of Bragg scattering mechanism. When the scattering body is not exactly periodic, the band gap also exists in the composite structure. Subsequently, the negative parametric properties of phonon metamaterials and elastic metamaterials were obtained based on different methods [11–19].

By adding multiple oscillators into a unit cell, Lai made it generate resonance under monopolar, dipolar and quadrupolar [20]. Through effective medium theory, band gap was generated because of the existence of negative parameters. Zhou obtained effective parameters by applying local resonance average physical field to the analytical model based on Mie scattering solution [21]. Zhu obtained the effective parameters of anisotropic metamaterial plate by numerical method, which provided a new method for solving the effective parameters [22]. Xu proposed a revised equivalent medium theory to solve the effective parameters of elastic metamaterials along different wave vectors when the wavelength does not meet the condition by means of numerical solution [23].

Piles arranged periodically in soil form periodic barriers, which is a periodic structure with obvious attenuation zone. Jia and Shi proposed the concept called "periodic foundation" to seismic isolation and vibration attenuation in civil engineering [24]. Huang and Shi used the improved plane wave expansion method and finite element method to study the in-plane and out-plane attenuation properties of periodic pile barriers, including solid and hollow piles [25–27]. Meng and Shi studied the attenuation ability of periodic pile barriers in single-phase and saturated soil [28, 29]. It is found that in single-phase soil, the triangular arrangement of piles, soft soil layer and small filling rate can obtain a wide attenuation range. In saturated soil, the frequency of the first attenuation zone will decrease with the increase of the curvature coefficient of soil.

In this paper, the metabarriers formed by piles embedded periodically in soil are studied. The band gaps of the metabarriers are obtained, and their mechanisms are discussed based on local resonance-type unit cell. According to the revised effective medium theory, the effective mass density, effective shear modulus and effective bulk modulus of a unit cell are presented. Meanwhile, metabarriers provide a new idea for the study of the periodic structure band gaps, bring great convenience for the

engineering design of pile rows and provide a new method for the study of effectively reducing the vibration caused by transportation.

## 2 Basic Theory and Model

Without considering damping, the governing equation of elastic waves propagating in continuous and linear isotropic elastic media can be given as follows [30]:

$$\nabla : (\mathbf{C}(\mathbf{r}) : \nabla \mathbf{u}(\mathbf{r})) = \rho(\mathbf{r}) \frac{\partial^2 \mathbf{u}}{\partial t^2} \quad (1)$$

in which  $\nabla = (\frac{\partial}{\partial x}, \frac{\partial}{\partial y}, \frac{\partial}{\partial z})$  is differential operator,  $\mathbf{C}(\mathbf{r})$  is the elastic tensor,  $\rho(\mathbf{r})$  is the material density tensor,  $\mathbf{r} = (x, y, z)$  is the position vector,  $\mathbf{u} = (u_x, u_y, u_z)$  is the displacement vector, and  $t$  is time parameter. According to the Bloch theory [31], the displacement field in the periodic structure can be expressed as follows:

$$\mathbf{u}(\mathbf{r}, t) = \mathbf{u}_{\mathbf{k}} e^{i(\mathbf{k} \cdot \mathbf{r} - \omega t)} \quad (2)$$

where  $\mathbf{k}$  is wave vector, and  $\omega$  is circular frequency. The function  $\mathbf{u}_{\mathbf{k}}$  is a periodic function with periodic constant  $\mathbf{R}$  and can be expressed as follows:

$$\mathbf{u}_{\mathbf{k}}(\mathbf{r}) = \mathbf{u}_{\mathbf{k}}(\mathbf{r} + \mathbf{R}) \quad (3)$$

Substituting Eq. (2) into Eq. (3) results in

$$\mathbf{u}(\mathbf{r} + \mathbf{R}, t) = e^{i\mathbf{k} \cdot \mathbf{R}} \mathbf{u}(\mathbf{r}, t) \quad (4)$$

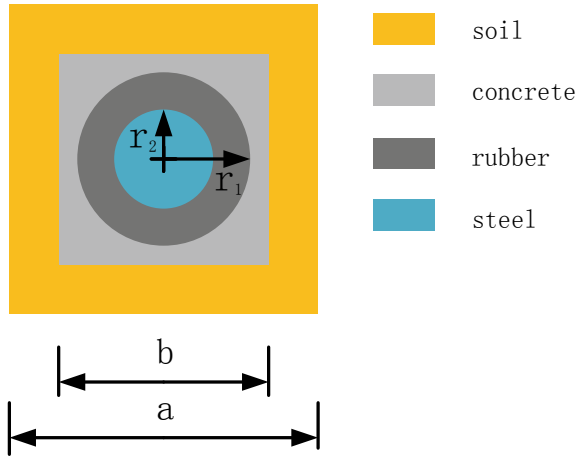
Equation (4) is the periodic boundary condition. Combining Eq. (4) with Eq. (1), the characteristic equation about the wave vector  $\mathbf{k}$  and frequency  $\omega$  can be obtained as follows:

$$(\Omega(\mathbf{k}) - \omega^2 \mathbf{M}) \cdot \mathbf{U} = 0 \quad (5)$$

in which  $\Omega(\mathbf{k})$  is the stiffness matrix and  $\mathbf{M}$  is the matrix of the mass. Stiffness matrix  $\Omega(\mathbf{k})$  is a function of the wave vector  $\mathbf{k}$ . By scanning the first irreducible Brillouin zone of the unit cell, the corresponding frequency can be solved, and then the dispersion relation of the structure can be obtained.

In this paper, the unit cell of metabarriers is shown in Fig. 1. The geometric parameters are taken as  $a = 1$  m,  $b = 0.8$  m,  $r_1 = 0.3$  m,  $r_2 = 0.2$  m. The materials from the inside to the outside are steel, rubber, concrete and soil, respectively. The steel cylinder-coated rubber is a scatter of the unit cell. The material constants of the unit cell are listed in Table 1 [32–34].

**Fig. 1** Bird view of the unit cell



**Table 1** Mass densities and elastic constants of the materials

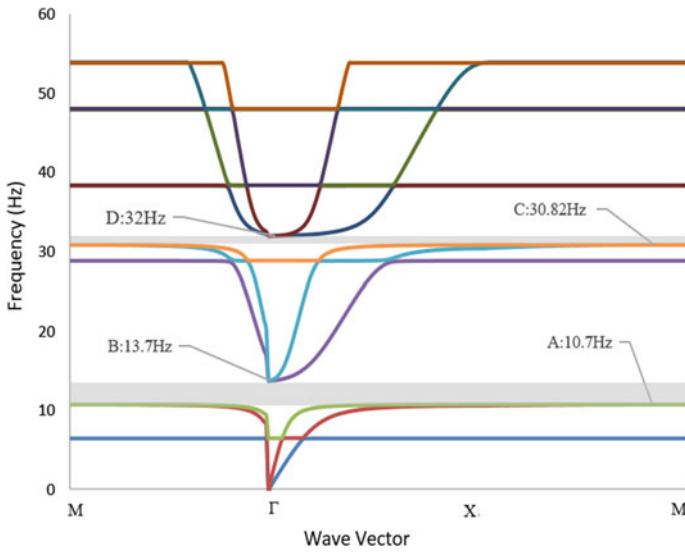
Materials	Mass density $\rho$ (kg/m <sup>3</sup> )	Young's modulus $E$ (Pa)	Poisson's ratio $\nu$
Soil	1800	2e7	0.35
Concrete	2300	25e9	0.2
Rubber	1300	1.175e5	0.47
Steel	7850	2e11	0.3

Referring to the study [35], the unit cell considered in the present paper is simplified as a spring oscillator model, in which the mass of the inner steel column can be regarded as the oscillator, and the rubber coating can be regarded as the spring.

In this paper, a revised medium theory is used to study the dispersion characteristics and vibration absorption mechanism of pile barriers in soil. The band gaps and effective parameters (effective mass density, effective shear modulus and effective bulk modulus) of the unit cell are obtained through the FEM software COMSOL Multiphysics.

### 3 Results and Discussions

The band structure of the unit cell mentioned in Fig. 1 is shown in Fig. 2. There are two band gaps, and the ranges of them are 10.7–13.7 Hz and 30.82–32 Hz. Figure 3 shows the vibration modes at the two band gaps edges. It can be seen from Fig. 3a and b that the resonance modes corresponding to the lower boundary of the first band gap are the translational vibration of the steel column. The rubber coating layer is partly squeezed and partly stretched, while the matrix composed of concrete and soil remains static. The resonance modes in Fig. 3c and d corresponding to the upper



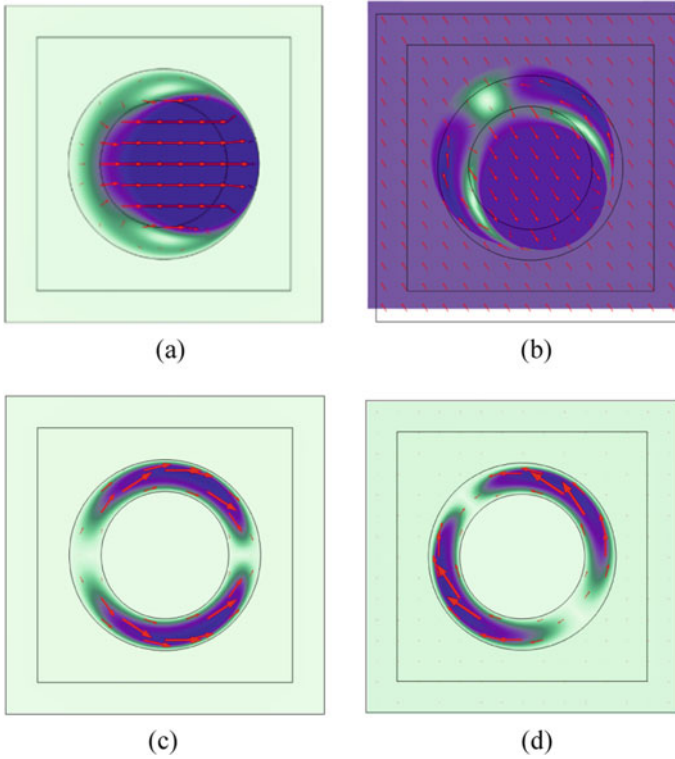
**Fig. 2** Frequency response of unit cell

boundary are the movement of the matrix and the vibrator oppositely, and the rubber is compressed and stretched. Under these two resonance modes, the oscillators in the adjacent unit cells vibrate in opposite phases, and the whole system is in dynamic equilibrium. The modes of the upper and lower boundary of the second band gap are that the rubber coating is stretched or compressed. These band gap resonance patterns generate x- and y-force coupling with plane waves in the matrix, resulting in band gaps generation. For the metabarrier as shown in Fig. 1, the frequencies corresponding to the upper and lower boundary of the first gap can be estimated according to the simplified spring mass model [36]:

$$f_l = \frac{1}{2\pi} \sqrt{\frac{k}{m_1}} \tag{6}$$

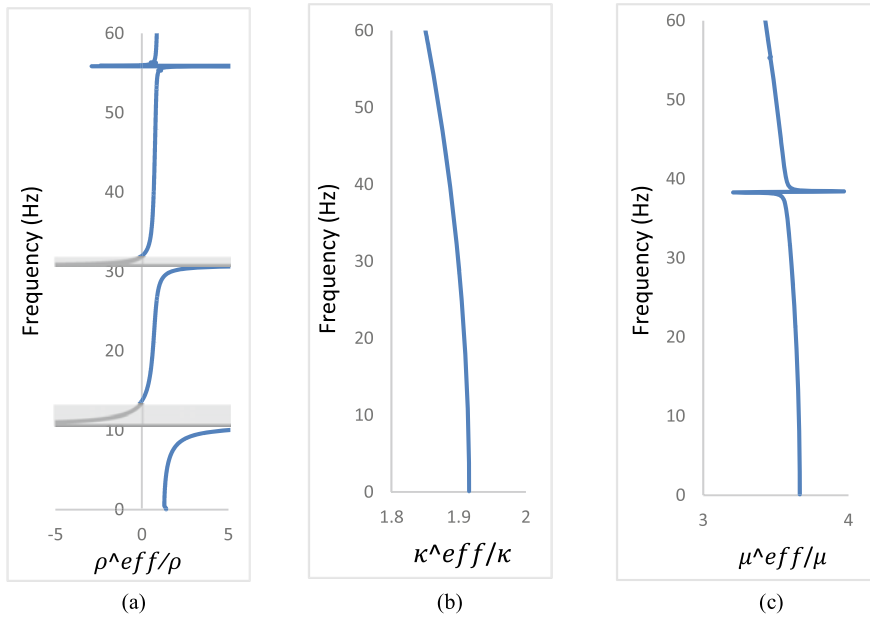
$$f_u = \frac{1}{2\pi} \sqrt{\frac{k(m_1 + m_2)}{m_1 m_2}} \tag{7}$$

in which  $f_l$  is the frequency corresponding to the lower boundary, and  $f_u$  is the frequency corresponding to the upper boundary. The symbol  $k$  is the stiffness of the spring-acting part in the rubber coating obtained by area integral. The symbols  $m_1$  and  $m_2$  are the masses of the core and the substrate corresponding to the spring mass model, respectively. The predicted results by using Eqs. (6) and (7) are 10.61 Hz and 13.68 Hz, respectively, which are basically consistent with the results obtained by FEM.



**Fig. 3** Vibration modes corresponding to the lower and upper boundaries: **a, b** for the first band gap and **c, d** for the second band gap

According to the revised effective medium theory [23], the effective mass density, effective shear modulus and effective bulk modulus of the unit cell are calculated and listed in Fig. 4a, b and c, respectively. It is obvious that both the normalized effective shear modulus  $\mu^{\text{eff}}/\mu$  and the effective bulk modulus  $\kappa^{\text{eff}}/\kappa$  of unit cell are positive within 0–60 Hz. However, for the normalized effective mass density  $\rho^{\text{eff}}/\rho$ , it has negative values in the range of 10.7–13.7 Hz and 30.84–31.96 Hz, which is almost consistent with the range of the two band gaps in the dispersion relation. In addition,  $\rho^{\text{eff}}/\rho$  increases rapidly at the beginning, and the oscillator jumps from positive to negative as it approaches 10.7 Hz. From Fig. 5, it can be observed that when the frequency is below 10.7 Hz (Fig. 5a, b), the oscillator moves in the same direction as the matrix. When the frequency is over 10.7 Hz (Fig. 5c, d), the oscillator jumps and starts to move in the opposite direction to the external matrix, generating negative effective mass density. When the frequency is greater than 13.7 Hz (Fig. 5f), the motion direction of the oscillator changes to be consistent with the direction of the substrate, which is also consistent with the cause of the band gap in the dispersion relation. The same phenomenon also appeared at 30.84 and 31.96 Hz (Fig. 5h, i) as 10.7 Hz and 13.7 Hz, respectively, which will not be repeated. In Fig. 2a, the



**Fig. 4** Dynamic effective parameters of the metabarrier. **a** effective mass density, **b** effective bulk modulus, **c** effective shear modulus

negative effective mass density can also be found between 55.82–55.96 Hz, which is not discussed here because of its extremely narrow band gap.

Theoretically speaking, perfecting filtering properties exist in periodic metabarriers with infinite unit cell. In fact, the distribution of structures is finite in engineering application. In order to validate the effectiveness of metabarriers for reducing ambient vibration, the dynamic responses of a finite 2D metabarriers periodic system are numerically simulated. The schematic diagram of the 2D system is shown in Fig. 6. The geometrical parameters of the numerical model are as follows:  $a = 1$  m,  $L_1 = 2$  m,  $L_2 = 10$  m,  $L_3 = 3$  m,  $L_4 = 5$  m,  $L = 20$  m. A unit displacement is applied at the left end of the model, a continuity period condition is applied to the upper and lower boundaries, and the length of  $L_4$  at the right end of the model is set as the perfect matching layer.

To evaluate the screening effect by metabarriers, the amplitude reduction ratio labeled as  $A_R$  is suggested [37, 38]. The frequency response function (FRF) is introduced,  $FRF = 20 \cdot \log_{10}(\bar{A}/\bar{A}_0)$ , where  $\bar{A}$  is the averaged displacement of reference line 2, and  $\bar{A}_0$  is the averaged displacement of reference line 1. Figure 6b shows the frequency response of Fig. 6a, and the red line and blue line in Fig. 6b represent the frequency response without and with metabarriers, respectively. It can be seen from this figure that when there with metabarriers, the vibration attenuation is obtained in the range of 10.7–13.7 Hz and 30.82–32 Hz (the gray part of the figure), while when there without metabarriers, the vibration attenuation is not obtained. The attenuation

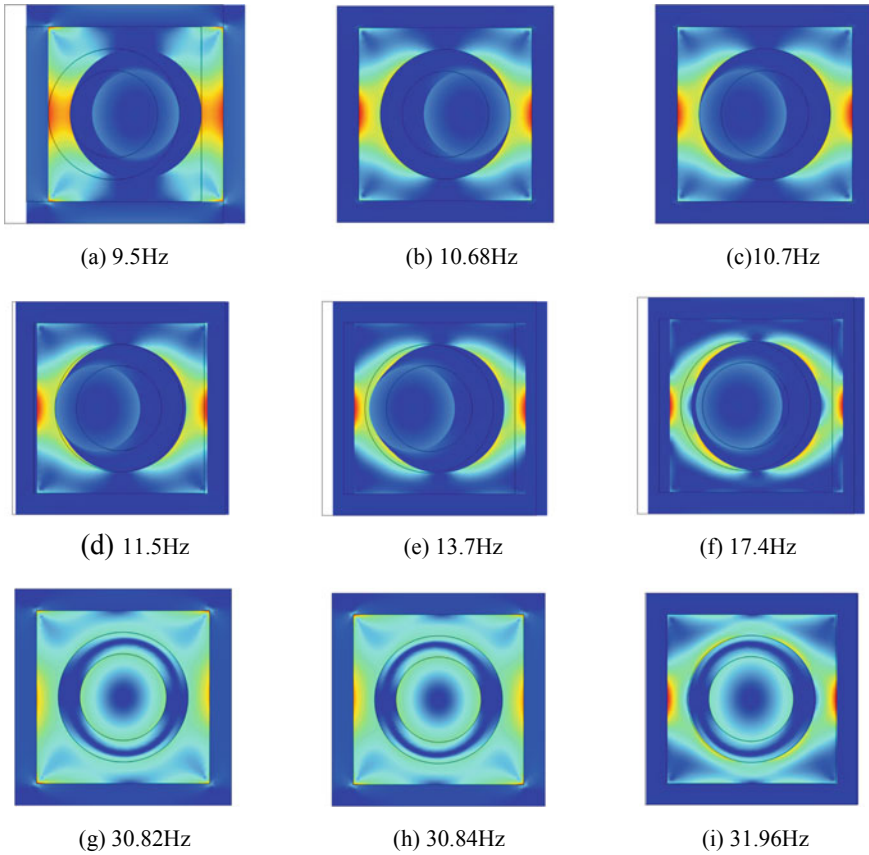
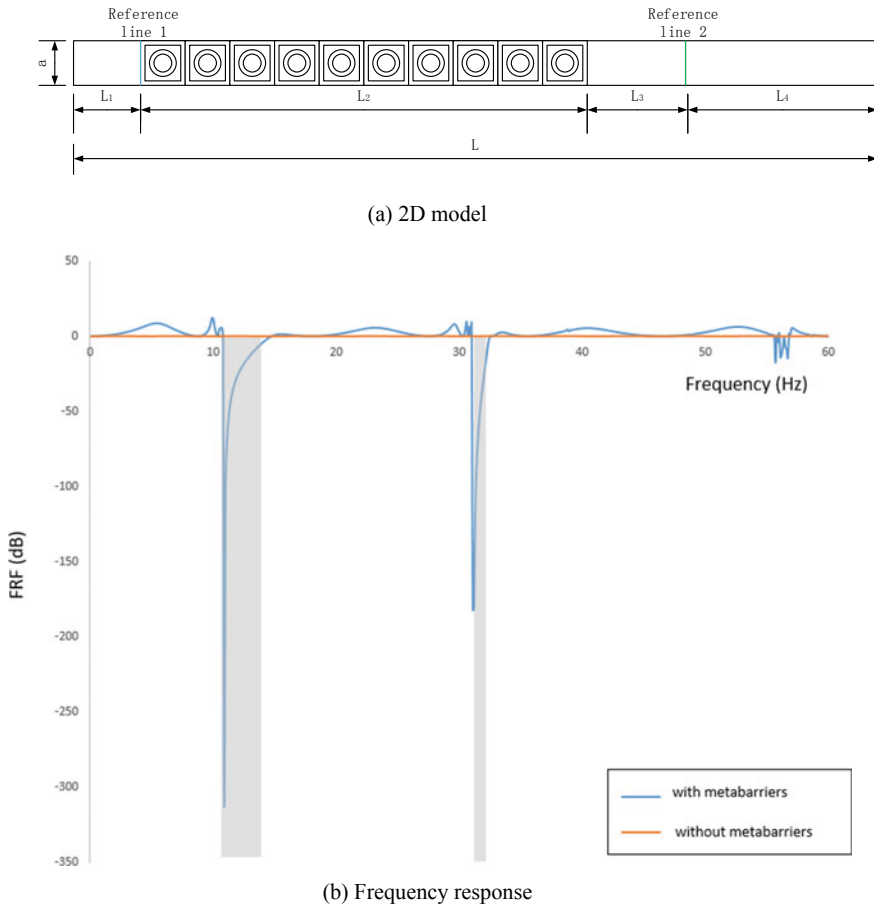


Fig. 5 Strain diagram corresponding to some different frequencies

zone of the metabarriers is in great agreement with the attenuation of the frequency response curve, which further demonstrates the effectiveness of the metabarriers to vibration attenuation.

### 4 Conclusions

In this paper, a new type of metabarriers is proposed for seismic isolation and vibration attenuation in civil engineering. The dispersion relation and modal analysis of the metabarriers indicate that the local resonance of the oscillator causes the band gaps in the range 10.7–13.7 Hz and the region 30.82–32 Hz. According to the revised equivalent medium theory, three effective parameters are obtained. It is found that both the effective shear modulus and the effective bulk modulus are positive in the



**Fig. 6** Schematic diagram of vibration screening problem by periodic metabarriers

range of 0–60 Hz. However, the effective mass density is negative in the region 10.7–13.7 Hz and 30.84–31.96 Hz, which is consistent with the band gaps in the dispersion relation. The results also show that when the effective mass density is negative, the oscillator and matrix move in opposite direction. Otherwise, they move in the same direction. Single negative parameter can make the metabarrier with band gaps.

## References

1. Cui TJ, Smith DR, Liu RP (2010) *Metamaterials: theory, design and application*. Springer, New York
2. Shelby RA, Smith DR, Schultz S (2001) Experimental verification of a negative index of refraction. *Science* 292:77–79



3. Veselago VG (1968) The electrodynamics of substances with simultaneously negative values of permittivity and permeability. *Soviet Phys Uspekhi* 10(4):509
4. Shelby RA, Smith DR, Nemat-Nasser SC et al (2001) Microwave transmission through a two-dimensional, isotropic, left-handed metamaterial. *Appl Phys Lett* 78:489
5. Cummer SA, Christensen J, Alù A (2016) Controlling sound with acoustic metamaterials. *Nat Rev Mater* 1:16001
6. Pendry JB (2000) Negative refraction makes a perfect lens. *Phys Rev Lett* 85:3966
7. Sigalas MM, Economou EN (1992) Elastic and acoustic wave band structure. *J Sound Vib* 158(2):377–382
8. Kushwaha MS, Halevi P (1993) Acoustic band structure of periodic elastic composites. *Phys Rev Lett* 71(13):2022–2025
9. Liu ZY, Zhang X, Mao Y et al (2000) Locally resonant sonic materials. *Science* 289:1734–1736
10. Wang G, Wen JH, Liu YZ (2004) Lumped-mass method for the study of band structure in two dimensional phononic crystal. *Phys Rev B* 69(18):184302
11. Mei J, Liu Z, Wen W et al (2006) Effective mass density of fluid-solid composites. *Phys Rev Lett* 96:024301
12. Ding Y, Liu Z, Qiu C et al (2007) Metamaterial with simultaneously negative bulk modulus and mass density. *Phys Rev Lett* 99:093904
13. Sheng P, Mei J, Liu Z et al (2007) Dynamic mass density and acoustic metamaterials. *Phys B* 394:256–261
14. Lee SH, Park CM, Seo YM et al (2010) Composite acoustic medium with simultaneously negative density and modulus. *Phys Rev Lett* 104:054301
15. Ding C, Hao L, Zhao X (2010) Two-dimensional acoustic metamaterial with negative modulus. *J Appl Phys* 108:074911
16. Liu XN, Hu GK, Huang GL et al (2011) An elastic metamaterial with simultaneously negative mass density and bulk modulus. *Appl Phys Lett* 98:251907
17. Yang M, Ma G, Yang Z et al (2013) Coupled membranes with doubly negative mass density and bulk modulus. *Phys Rev Lett* 110:134301
18. Wang YF, Wang YS, Wang L (2014) Two-dimensional ternary locally resonant phononic crystals with a comblike coating. *J Phys D Appl Phys* 47:015502
19. Wang YF, Wang YS, Zhang C (2016) Two-dimensional locally resonant elastic metamaterials with chiral comb-like interlayers: bandgap and simultaneously double negative properties. *J Acoust Soc Am* 139
20. Lai Y, Wu Y, Sheng P et al (2011) Hybrid elastic solids. *Nat Mater* 10:620–624
21. Zhou X, Hu G (2009) Analytic model of elastic metamaterials with local resonances. *Phys Rev B* 79
22. Zhu R, Liu XN, Huang GL et al (2012) Microstructural design and experimental validation of elastic metamaterial plates with anisotropic mass density. *Phys Rev B* 86
23. Xu YC, Wu JH, Ma FY (2018) Investigation on negative hybrid-resonant bands of elastic metamaterials by revised effective medium theory. *Phys B: Condens Matter* 543:18–26
24. Jia GF, Shi ZF (2010) A new seismic isolation method and its feasibility study. *Earthq Eng Eng Vib* 9(1):75–82
25. Huang JK, Shi ZF (2013) Attenuation zones of periodic pile barriers and its application in vibration reduction for plane waves. *J Sound Vib* 332:4423–4439
26. Huang JK, Shi ZF (2013) Application of periodic theory to rows of piles for horizontal vibration attenuation. *ASCE's Int J Geomech* 13:132–142
27. Huang JK, Shi ZF (2015) Vibration reduction of plane waves using periodic in-filled pile barriers. *ASCE's J Geotech Geoenviron Eng* 141(6):04015018
28. Meng QJ, Shi ZF (2019) Vibration isolation of plane waves by periodic pipe pile barriers in saturated soil. *ASCE's J Aerosp Eng* 32(1):04018114
29. Meng QJ, Shi ZF (2018) Propagation attenuation of plane waves in single-phased soil by periodic pile barriers. *ASCE's Int J Geomech* 18(6):04018035
30. Achenbach JD, Thau SA (1980) Wave propagation in elastic solids. *J Appl Mech* 41(2):544

31. Bloch F (1929) Uber die quantenmechanik der elektronen in kristallgittern. *Z Angew Phys* 52(7–8):555–600
32. Pu X, Shi Z (2017) A novel method for identifying surface waves in periodic structures. *Soil Dyn Earthq Eng* 98:67–71
33. Chen M, Meng D, Jiang H, et al (2018) Investigation on the band gap and negative properties of concentric ring acoustic metamaterial. *Shock Vib (PT.1)*:1–12
34. Muhammad, Lim CW (2019) Elastic waves propagation in thin plate metamaterials and evidence of low frequency pseudo and local resonance bandgaps. *Phys Lett A*
35. Goffaux C, Sánchez-Dehesa J (2003) two dimensional phononic crystals studied using a variational method. *Phys Rev B* 67:144301
36. Wang G, Shao LH, Liu YZ et al (2006) Accurate evaluation of lowest band gaps in ternary locally resonant phononic crystals. *Chin Phys* 15(8):1843–1848
37. Kattis S, Polyzos D, Beskos D (1999) Vibration isolation by a row of piles using a 3-D frequency domain BEM. *Int J Numer Methods Eng* 46:713–728
38. Kattis SE, Polyzos D, Beskos DE (1999) Modelling of pile wave barriers by effective trenches and their screening effectiveness. *Soil Dyn Earthq Eng* 18:1–10

# Shearing Behaviour of Jointed Rocks Under Monotonic and Cyclic Loading with Varying Gouge Materials



Nirali B. Hasilkar, Lalit S. Thakur, and Nikunj Amin

**Abstract** Rock is not homogeneous and isotropic due to the presence of discontinuities and weak planes within its body. This brings in terms of ‘rock material’ and ‘rock mass’ for practical applications. A rock mass is an assemblage of intact rock pieces separated by discontinuities presented in different scales such as microfractures, rock joints, stratification, faults. For design in civil and mining engineering geo-structures, it is often necessary to investigate the behaviour and role of discontinuities on rock mass performance. In many cases, failure is governed by the shear behaviour of discontinuities in excavations. In this context, evaluation of the effects of small repetitive earthquakes on the shear strength parameters of rock joints especially in tunnels and dam foundations is also important. The main scope of work is to study and investigate shearing behaviour of jointed rocks infilled with gouge materials under monotonic and cyclic loading vis-a-vis the theoretical background to shearing behaviour under loading conditions to compare the shear strength values for a variety of jointed rocks. In case of cyclic loading, under the initial loading cycles, the rate of increase of displacement is slow corresponding to the rate of increase of shear stress. In later load cycles, the rate of displacement is rapid with a corresponding increase in shear stress until the peak shear stress value is reached. Under cyclic loading condition, post peak behaviour sometimes exhibits a tendency to drop suddenly and assumes a constant value called residual shear stress.

**Keywords** Shearing behaviour · Jointed rock · Monotonic loading · Cyclic loading · Gouge material

---

N. B. Hasilkar (✉) · L. S. Thakur  
Civil Engineering Department, BITS Edu Campus, Varnama, Vadodara, Gujarat 391240, India  
e-mail: [niralihasilkar.cv@bitseducampus.ac.in](mailto:niralihasilkar.cv@bitseducampus.ac.in)

N. Amin  
Geostruct Engineering and Testing Service, Vadodara, Gujarat 390020, India

## 1 Introduction

Designing a sound and flexible structure over a rock mass needs understanding the failure mechanism and stress–strain behaviour of rocks along discontinuities with their post failure domain. In last few decades, several researchers have evaluated the stress deformational behaviour of rocks by carrying out in situ or laboratory tests. In in situ test being costly, it is desirable that understanding of rock behaviour should be developed to such an extent that the predictions can be based on few carefully selected and less expensive tests in the laboratory.

### 1.1 Rock Material

For construction of slopes, foundations and shallow tunnels, it has been recognized that discontinuities have a major influence on mechanical properties of a rock mass. Calculations for engineering structures in or on a rock mass have to include discontinuity properties, since each has its own variable properties.

For most of the rock engineering problems, engineering properties of a rock mass depend far more on the system of geological separations within rock mass than on the strength of the rock material itself. The strength of a rock mass is in fact its residual strength which, together with its anisotropy, is governed by the interlocking bonds of the unit ‘elements’ forming the rock mass. The deformability of a rock mass and its anisotropy result predominantly from the displacements of the unit elements composing the structure of the rock mass.

With reference to above summary, several theoretical and model studies have been carried out by various researchers which have yielded interesting results. The results of these studies permit one to conclude that the mechanical behaviour of the jointed rock system is dependent on the factors like mechanical behaviour of the individual elements constituting the system, sliding characteristics to joints, configuration of the system and operating stress field.

## 2 Mechanical Behaviour

### 2.1 Mechanical Behaviour of Jointed Rock Under Different Loading

For the field application of the results obtained in laboratory regarding mechanical properties like ultimate strength, elastic limit, etc., of a rock material, it requires an understanding of the effects of many different variables such as form, scale, temperature, service conditions and method of loading. In most of the purposes, the

method of loading is sufficient to distinguish the types of loading as static, cyclic and dynamic.

## ***2.2 Static or Monotonic Loading***

Static or monotonic loading can be applied in two forms depending on the time duration of loading.

### **2.2.1 Short-Term Monotonic Loading**

The short-term monotonic loading is similar to the quick test (referred to with respect to triaxial test of soil). The application of load is very gradually increased either in stress-controlled manner or strain-controlled manner until the structural failure occurs or until the required amount of strain has been applied to the specimen. The stress–strain curve obtained in then is used to determine elastic limit, yield point, yield strength and ultimate strength. Direct or indirect methods can then be employed to calculate the modulus of elasticity of the material from these parameters.

### **2.2.2 Long-Term Monotonic Loading**

The long-term monotonic loading is similar to the consolidated drainage test (referred to in triaxial test) in terms of the rate of loading. The loading rate applied is at such a slow rate that any strain generated, or stress generated due to the loading has time enough to dissipate. This type of loading basically helps in the study of the creep behaviour or flow characteristics of a material necessary for the determination of permanent.

## ***2.3 Cyclic Loading***

Cyclic loading is necessarily the application of repeated positive and negative cycles of load, i.e. compression and tension to cause fluctuating stresses, strains or stress intensities to locations on structural components. The magnitude of these loads shall be as small as 1% of predicted failure loads to as large as 20% of predicted failure loads. The frequency of application of the load or the load cycle frequency is dependent on the purpose of test, type of material and the magnitude of applied loads which is of great considerations when studying fatigue behaviour of materials. Very little attention has been paid to rock fatigue under cyclic or dynamic loads though the phenomenon is of importance in bridge abutments, foundations, dam and road pavements, open cut benches and rock drilling the structures subjected to earthquakes.

Fatigue characteristics are usually presented in the form of S. N. curves (stress level versus the number of cycles required to bring about failure). In which, at high maximum stresses, the number of cycles required to cause failure is small and increases as the maximum stress is lowered. The maximum applied stress level, at which the material can stand an infinite number of cycles, is called fatigue stress.

Tejas Belani (2006) has investigated on Shearing behaviour of jointed rocks using direct shear box. The direct shear tests were conducted on three different types of rocks i.e. limestone, sand stone and marble, having artificial joints prepared to fill the cement- sand gouge within. These tests were conducted to study shearing behaviour of jointed rocks under monotonic loading, effect of gouge to rock shear strength, and influence of various roughness factors with varying asperity amplitudes in different rock specimens.

## ***2.4 Dynamic Loading***

In the first case of loading, the stress effects concerned are virtually static; the inertia forces are treated exactly as though they were ordinary static loads. In impact, the stress conditions are complex and depend upon the properties of the material as well as nature of blow.

It is important to distinguish between impact and very quick static loading. In impact, the loaded member is usually required to absorb a definite amount of energy; in static loading, the member is usually required to resist definite force. Impact loading occurs when a rigid weight is dropped upon a beam during the period of impact, and for some time afterwards, both weight and beam are in a state of vibration, and static equilibrium does not supervene until all the kinetic energy possessed by the weight at the instant of impact has been absorbed by the beam and stored up as strain energy or dissipated as heat.

## **3 Work Outline**

The present study is envisaged to determine the shear strength of three types of rock procured from Gujarat and Rajasthan, i.e. limestone (Rajula), sandstone (Bhuj) and marble (Ambaji).

### ***3.1 Scope of Work***

- The study and investigation on shearing behaviour of cut rocks are filled with gouge materials under monotonic and cyclic loading.
- Examination of shearing behaviour is under theoretical background.

**Table 1** Specific gravity

Material	Average value
Sand (300 $\mu$ passing)	2.56
Limestone	2.62
Sandstone	2.52
Marble	2.71

**Table 2** Compressive strength of rocks and gouge material

Material	Unconfined compressive strength (kg/cm <sup>2</sup> )
Limestone	21.90
Sandstone	41.80
Marble	744.86
Gouge material	264.82

- To compare the shear strength values for variety of jointed rocks.

### 3.2 Scheme of Investigation

**Rocks:** Three types of rocks are used: two belonging to the sedimentary rock group, i.e. limestone and sandstone, and one belonging to the metamorphic rock group, i.e., marble.

**Sand:** Bahadarpur sand is used in preparing the gouge material for filling the rock joints. The sand is sieved through 300 micron I.S. sieve before use.

**Cement:** Ambuja Ordinary Portland Cement of 53 Grade is used for preparing mortar.

**Mortar (Gouge Material):** Mortar is prepared from cement–sand (1:2) having water cement ratio 0.8. It is kept high because it is used as gouge material (grout) for filling the rock joints.

Tables 1 and 2 present specific gravity and strength results, respectively.

## 4 Experimental Work

### 4.1 Sample Preparation

The three types of rocks, viz. limestone, sandstone and marble are procured from different places. Limestone is brought from Rajula quarry, sandstone from Bhuj and marble from Ambaji. The samples of  $10.3 \times 10.3 \times 10.3$  cm are prepared from the chunks by cutting them with the help of large size cutting machine as shown in

Fig. 1. The rock samples, thus, prepared are further sliced into two parts. The artificial asperities with different amplitude of 5, 10 and 15 mm are made in limestone, marble and sandstone samples as shown in Figs. 2 and 3. These samples are then filled with gouge material (cement–sand proportion 1:2) of 2 mm thickness. The samples, thus, prepared are cured for not less than 28 days, and after curing the samples are kept in



Fig. 1 Intact marble specimen

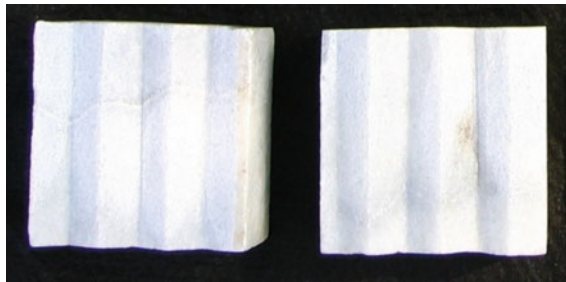


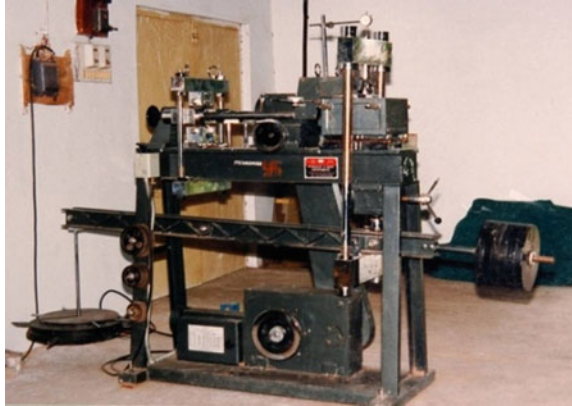
Fig. 2 Cut marble specimen



Fig. 3 Wooden blocks for asperity in cut rock specimens



**Fig. 4** Photograph of direct shear test machine



open air for one day. The samples were then loaded into the large box shear machine as shown in Fig. 4, the gaps between the box and the sample being filled with plaster of pairs.

Large direct shear apparatus was used in this study to determine shear strength of rock samples. The apparatus is designed for a maximum normal load and shear load of 150 kN for large shear box sizes of  $15 \times 15 \times 15$  cm and  $10 \times 10 \times 10$  cm. This instrument is having constant 72 different rates of strain.

## 4.2 Test Procedure

Sample is loaded in the test machine after it is cured for 28 days. It is carefully placed in the shear box with centre of joint exactly aligned to the plane of shear coming in centre of the two halves of the shear boxes. Normal load is applied by putting required number of plates weighing 20 kg. Each test is carried out on three different normal stresses, i.e., 4.5, 9.0 and  $18.0 \text{ kg/cm}^2$ .

### 4.2.1 Monotonic Loading Tests

The test speed of 0.112 mm/min was chosen for this experimental study. The shear load is gradually applied by switching on the forward key of the machine keeping normal load constant. The shear load is measured through proving ring. The measurements of shear displacements and normal displacements are taken with the help of dial gauges having least count 0.001 mm. The shear load measurements are taken at regular intervals. Readings are taken until the proving ring readings become nearly constant. Generally, it is taken for almost 5 mm displacement.

**Table 3** Tests on intact rock specimens

Rock type	Normal stress		
	4.5 kg/cm <sup>2</sup>	9.0 kg/cm <sup>2</sup>	18.0 kg/cm <sup>2</sup>
Sandstone	1	1	1
Marble	1	1	1
Limestone	1	1	1

**Table 4** Distribution of testing samples of sandstone, marble and limestone for varying loading and test conditions

Rock asperity 30 × h (mm)	Monotonic loading at normal stress values (kg/cm <sup>2</sup> )			Cyclic loading at normal stress values (kg/cm <sup>2</sup> )		
	4.5	9	18	4.5	9	18
5	3	3	3	3	3	3
10	3	3	3	3	3	3

### 4.2.2 Cyclic Loading Tests

Strain rate of 0.112 mm/min is being applied during cyclic loading tests. Keeping normal load constant, the shear load is gradually applied by switching on the forward key of the machine and measured as same in monotonic loading tests. The shear load cycle is partitioned as 1/5 value of peak load obtained in monotonic loading tests, so as to create five cycles of loading to reach the peak load. The test is being continued until the proving ring readings become nearly constant.

### 4.3 Experimental Work

See Tables 3 and 4.

### 4.4 Analysis and Discussion

A comparative plot of shear stress versus normal stress for intact sandstone and limestone is shown in Fig. 5, under monotonic loading at shear rate = 0.112 mm/Min. Figure 6 shows a comparative graph of shear stress versus normal stress for jointed sandstone, marble and limestone with rock asperity as 30 × 5 mm. Figure 7 shows a comparative graph of shear stress versus normal stress for jointed sandstone, marble and limestone with rock asperity as 30 × 10 mm under monotonic loading.

The peak shear stress increases with an increase in normal stress. More plastic flow occurs at lower shear rate than higher shear rate as horizontal shear displacement

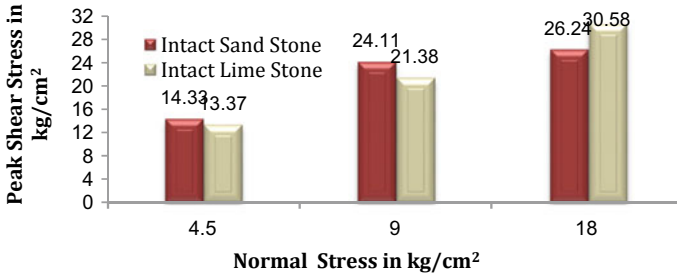


Fig. 5 Peak shear stress versus normal stress of intact sandstone and limestone under monotonic loading

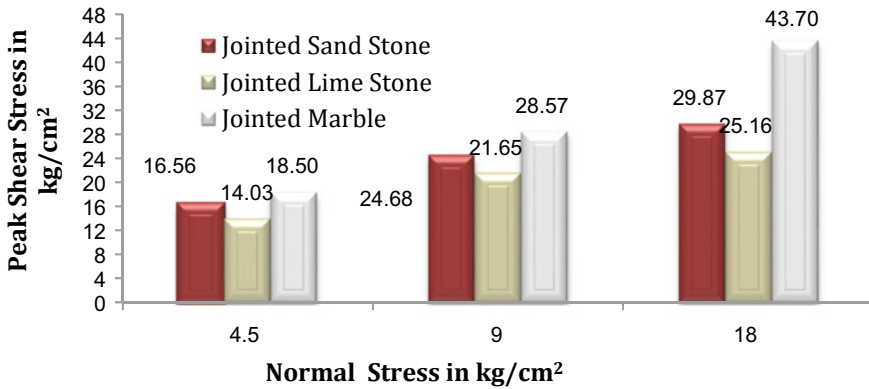


Fig. 6 Peak shear stress versus normal stress of jointed rocks having asperity 30 × 5 mm under monotonic loading

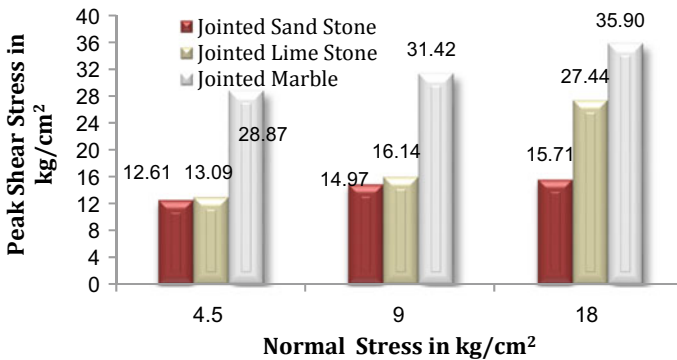


Fig. 7 Peak shear stress versus normal stress of jointed rocks having asperity 30 × 10 mm under monotonic loading

is more at peak shear stress in lower shear rate than higher shear rate. Figures 8, 9, 10, 11, 12 and 13 show comparative graphs of peak shear stress versus normal

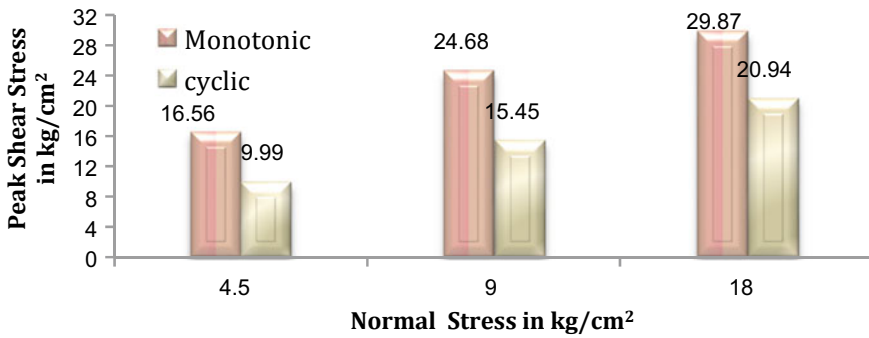


Fig. 8 Peak shear stress versus normal stress of jointed sandstone (30 × 5 mm) under monotonic and cyclic loading

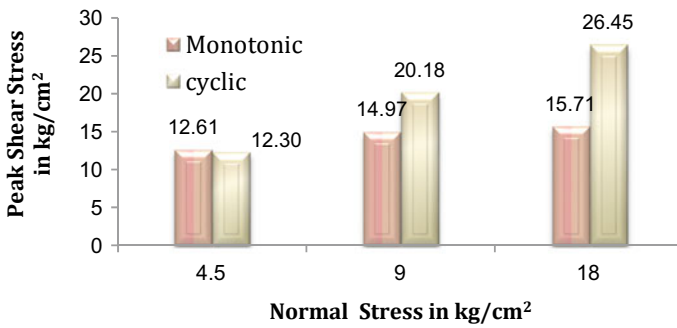


Fig. 9 Peak shear stress versus normal stress of jointed sandstone (30 × 10 mm) under monotonic and cyclic loading

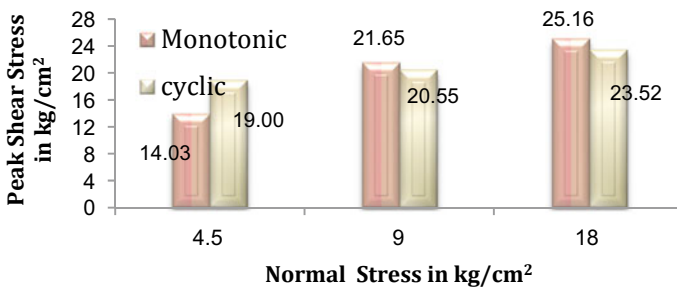
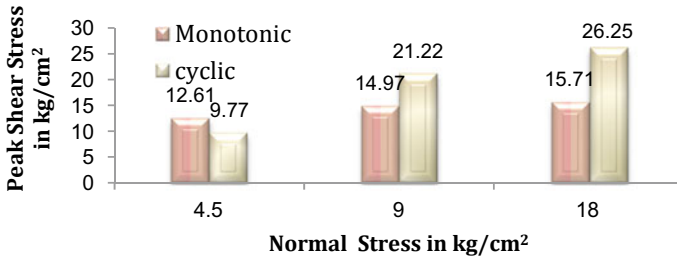
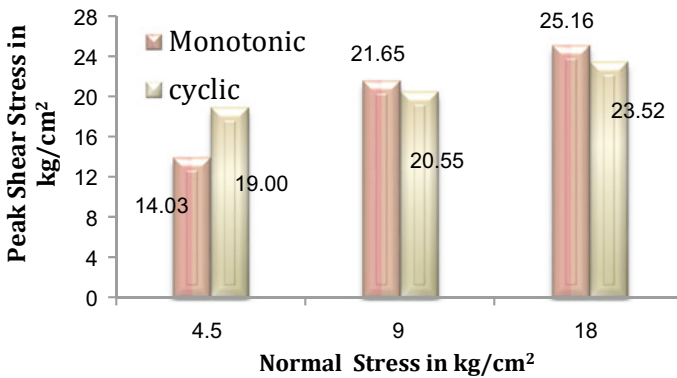


Fig. 10 Peak shear stress versus normal stress of jointed limestone (30 × 5 mm) under monotonic and cyclic loading



**Fig. 11** Peak shear stress versus normal stress of jointed limestone (30 × 10 mm) under monotonic and cyclic loading



**Fig. 12** Peak shear stress versus normal stress of jointed limestone (30 × 5 mm) under monotonic and cyclic loading

stress of jointed sandstone, marble and sandstone with different asperity ratio under monotonic as well as cyclic loading.

It is observed that under the initial cycles of loading the rate of increase of displacement is slow corresponding to the rate of increase of shear stress. While in subsequent load cycles, the rate of displacement is rapid with a corresponding increase in shear stress until the peak shear stress value is reached. Post peak behaviour sometimes exhibits a tendency drop suddenly and assumes a constant value while it becomes decreasing in some few cases. The phenomenon is due to stick and slip process because of slip a drop is observed while graphs show a constant value because of stick phenomenon.

Figures 14, 15, 16 and 17 show the comparisons of experimental and theoretical shear stress of all three types of rocks tested under varying asperity amplitudes, different shear rates and different type of loading. Theoretical shear stress for rock specimens is calculated from Barton’s equation—5. The variation seems within the range of 30–40% with a linear behaviour and is due to the cause that specimens tested we encased in plaster of Paris medium which being soft at the time of testing reduce

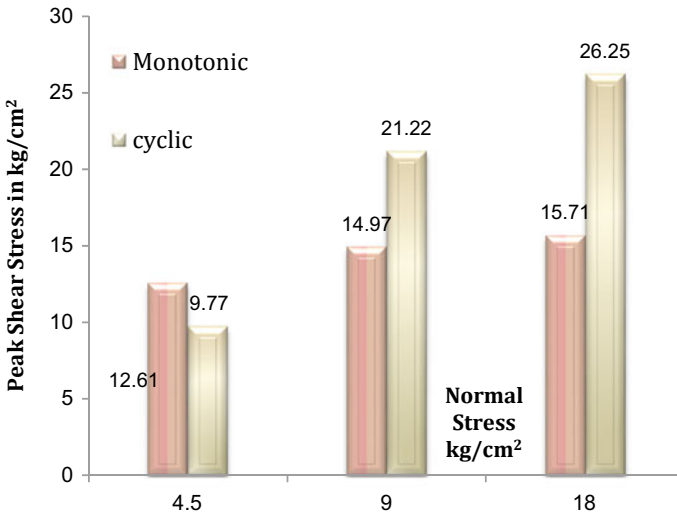


Fig. 13 Peak shear stress versus normal stress of jointed limestone (30 × 10 mm) under monotonic and cyclic loading

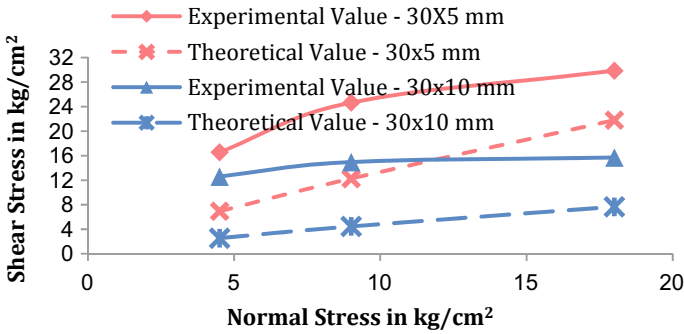


Fig. 14 Experimental and theoretical shear stress of jointed sandstone under monotonic loading

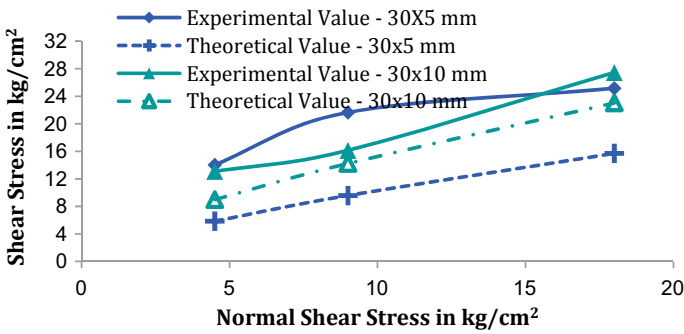


Fig. 15 Experimental and theoretical shear stress of jointed limestone under monotonic loading

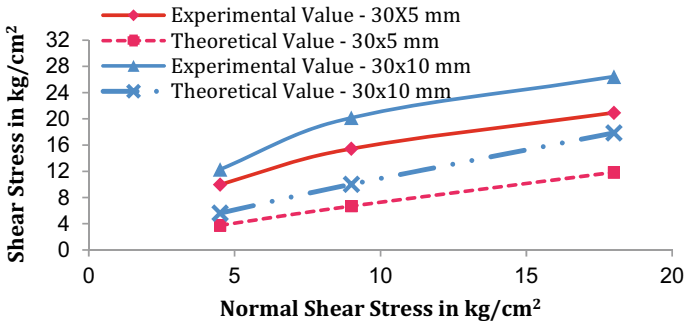


Fig. 16 Experimental and theoretical shear stress of jointed sandstone under cyclic loading

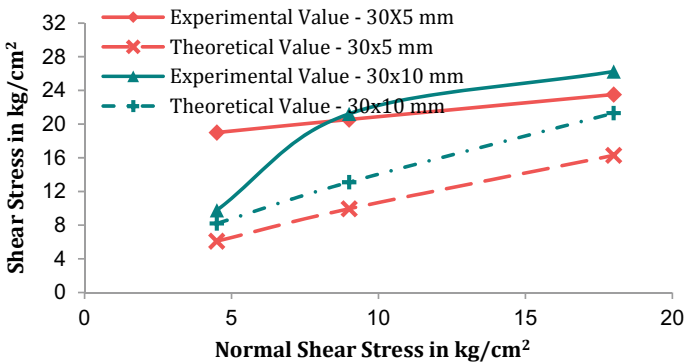


Fig. 17 Experimental and theoretical shear stress of jointed limestone under cyclic loading

the residual strength and also taking a part of the normal stress. The variation may be due to defect in joint thickness, accuracy of cutting the asperities and/or some other manual or mechanical error during experimentation.

## 5 Conclusions

- The shear displacement increases gradually at initial but after the peak shear stress, and the shear displacement increases at faster rate under monotonic loading.
- In case of cyclic loading, under the younger cycles of loading, the rate of increase of displacement is slow corresponding to the rate of increase of shear stress. In older cycles, the rate of displacement is rapid with a corresponding increase in shear stress until the peak shear stress value is reached.
- Under cyclic loading condition, post peak behaviour sometimes exhibits a tendency to drop suddenly and assumes a constant value called residual shear stress.

- Jointed marble specimens show the highest peak shear stress values among all three types of rock for all types of asperities under monotonic loading. While jointed sandstone shows higher peak shear stress value than jointed limestone for  $30 \times 5$  mm asperity and for  $30 \times 10$  mm, limestone and sandstone show nearly same peak shear stress values.
- The jointed rock specimens of all asperities fail at lower shear stress under cyclic loading than monotonic loading. It shows that under cyclic loading.

## References

1. Tejas B (2006) Study of shearing behaviour of jointed rocks using direct shear box, ME Dissertation thesis, M. S. University of Baroda



# Model Research on the Deformation Behavior of Geogrid Supported by Rigid-Flexible Piles Under Cyclic Loading



Kaifu Liu, Yonghao Cai, Yi Hu, Dazhi Wu, and Zhenying Zhang

**Abstract** Geogrid has been widely used in composite foundations or embankments supported by rigid or rigid-flexible piles in the past two decades. However, the research on the deformation behavior of geogrid supported by rigid or rigid-flexible piles under cyclic loading are very limited. Some model tests on the deformation behavior of geogrid supported by rigid-flexible piles were designed and completed under cyclic loading with changing the load amplitude, waveform, and cyclic frequency. The geogrid strain at different locations in the different cyclic process was analyzed based on the model test results. The test results showed that the deformation behavior of geogrid varies with the location. The strain variation trends of geogrid under cyclic loading are consistent with that of applied cyclic load shapes/amplitude. When the waveform of cyclic load is changed singly, the strain of the geogrid will change accordingly. The geogrid strain amplitude at the edge of flexible pile under cyclic load frequency is the largest, and it is also most affected by the cyclic load amplitude.

**Keywords** Model test · Geogrid · Strain · Rigid-flexible pile · Cyclic loading

## 1 Introduction

Soft soil is not suitable for the foundation of large-scale civil engineering structures [1, 2] because of poor shear strength and high compressibility. The geogrid has the characteristics of high strength, small deformation, and good durability. It has been often used in the past two decades in a soft soil embankment with piles to form a reinforced embankment supported by piles to solve the problem of low bearing capacity, overall deformation, and uneven settlement of soft soil embankments [3]. In this composite foundation, piles are used as vertical reinforced material to reduce settlement and improve bearing capacity of soft soil foundation, and geogrids are used as horizontal reinforcement material to reduce differential settlement and lateral

---

K. Liu (✉) · Y. Cai · Y. Hu · D. Wu · Z. Zhang  
School of Civil Engineering and Architecture, Zhejiang Sci-Tech University, Hangzhou, P. R. China  
e-mail: [liukaifu@zstu.edu.cn](mailto:liukaifu@zstu.edu.cn)

displacement of the soils [4]. Many researchers analyzed the mechanism and application of geogrid in the pile-supported composite foundation with geogrid-reinforced cushion. The finite element method was used to analyze the number of layers of geogrids and the influence of the tensile strength of geogrids on settlement [5]. The behavior of geotextile or geogrid in the pile-supported composite foundation with geogrid-reinforced cushion was analyzed by using different numerical methods and software, such as FLAC used by Han et al. [6], Plaxis used by Suleiman et al. [7], and two-dimensional (2D) coupled mechanical and hydraulic numerical implementation method used by Yapage et al. [8]. The effect of geogrid is also studied in the field test by Zheng et al. [9]. Liu et al. [10] explored the deformation behavior of geogrid supported by rigid-flexible piles under static load by the model test. These results are useful for engineering projects.

Geocell could effectively decrease the lateral and axial deformations of the reinforced subballast under cyclic loading [11], and the effect of geogrid stiffness on the reinforced railway under cyclic loading was discussed by using the software Plaxis [12]. The cyclic loading responses of a strip footing supported by a geosynthetic reinforced fill embankment was investigated by several model tests and simulated by the software FLAC [13]. The deformation behavior of geogrid supported by different piles under cyclic loading was studied by Hu [14]. However, the deformation of the geogrid supported by rigid or flexible piles under cyclic loading was rarely studied in the past.

The reinforced concrete piles, steel piles, and deep mixing piles had different rigidity in the composite foundation, so the deformation behavior of the geogrid supported by rigid-flexible piles was different from that supported only by single piles. Considering the effect of pile rigidity and applied load type, some model tests are designed to analyze the deformation behavior of the geogrid supported by rigid-flexible piles under cyclic loading in the present study.

## 2 Materials and Model Tests

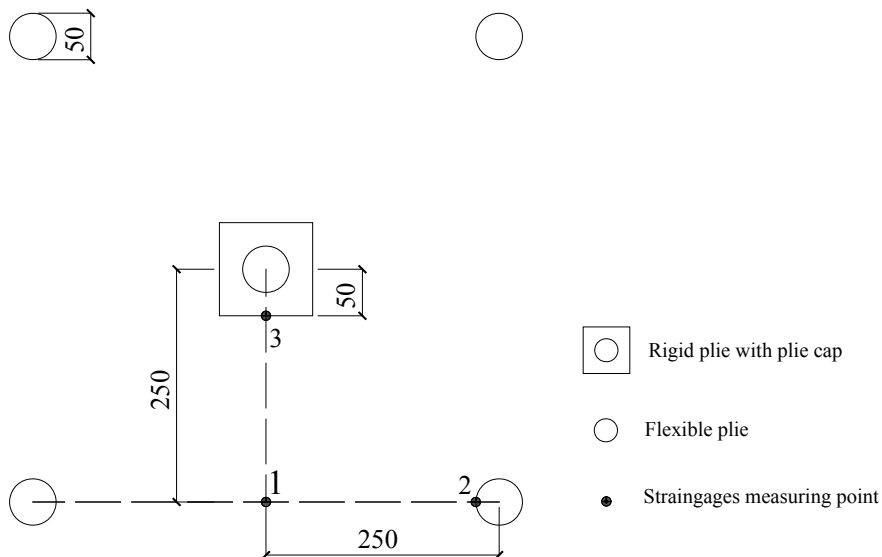
### 2.1 Materials

**Soils.** Soils used in the model tests are as follows: (1) Fine sand, which was used to fill the cushion of composite foundation. (2) Silty clay, which was drying out to facilitate preservations and formulated to the required soil moisture content used in the model test. (3) Mucky clay (saturated), which was formulated to the required soil moisture content of 38.52% (the moisture content of undisturbed soil) when used in the model test (Table 1).

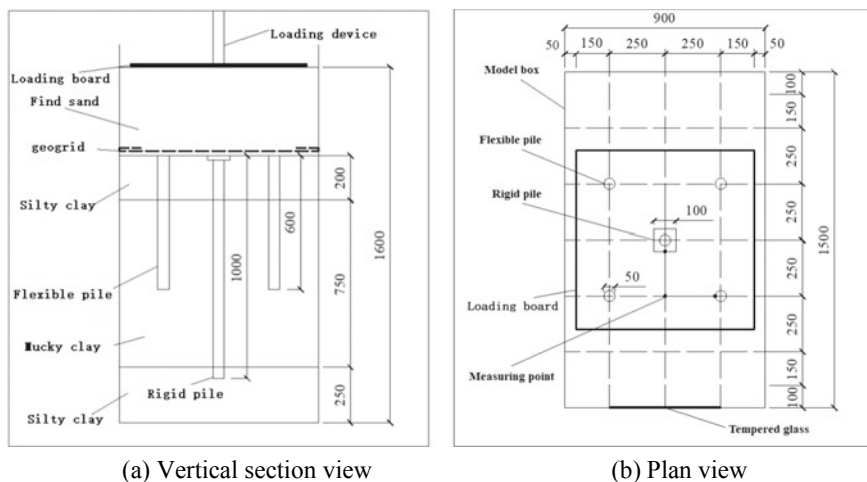
**Model piles.** Four PVC pipes with the length of 600 mm were used to simulate a flexible pile, and a steel pipe with a length of 1000 mm was used to simulate a rigid pile (prestressed concrete pipe pile in the engineering application), both of which were 50 mm in diameter and 2 mm in wall thickness, and shown in Figs. 1 and 2.

**Table 1** Basic physical and mechanical property index of the soils

Soil	Moisture content %	Natural density (g/cm <sup>3</sup> )	Friction angle (°)	Cohesive strength (kPa)
Fine sand	15.35	–	35.00	1.00
Silty clay	27.80	1.783	20.53	10.20
Mucky clay	38.52	1.573	15.00	10.00



**Fig. 1** Layout of strain gauges on the geogrid (Unit: mm)



**Fig. 2** Plan and section vertical view of the test apparatus (Unit: mm)

One steel plate with the square side length of 100 mm and the thickness of 15 mm was put on the steel pipe to simulate the pile cap in the engineering project.

**Geogrid.** The geogrid used in the model tests was produced by Tai'an Luther Engineering Materials Co., Ltd. The type of this biaxial plastic grid was TGSG30-30. The mesh size of the geogrid was  $30 \times 30$  mm, the breaking tensile strength of the geogrid was 30 kN/m, and the elongation at break of the geogrid was 3%.

Some strain gauges were glued on the geogrid to investigate the strain of the geogrid, the location of strain gauges was shown in Fig. 1 (Only one half of the flexible piles and geogrid was shown in Fig. 1).

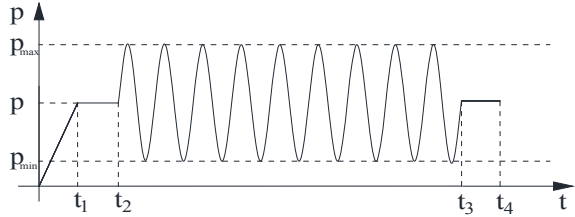
## 2.2 Model Tests

**Test apparatus.** The model test was conducted in a test apparatus which was assembled by steel plates with a thickness of 12 mm in three sides and glass plates with a thickness of 15 mm in another side with dimensions of 1.5 m (length)  $\times$  0.91 m (width)  $\times$  1.7 m (depth). A schematic diagram is shown in Fig. 2. Two rings of channel steel were welded in the height of 0.6 m and 1.2 m to improve the stiffness of steel plate. Place a loading plate at the center of the top surface of the experimental subgrade. The loading actuator directly contacts the loading plate and applies a load. The loading plate size is 800 mm (length)  $\times$  800 mm (width)  $\times$  10 mm (thickness).

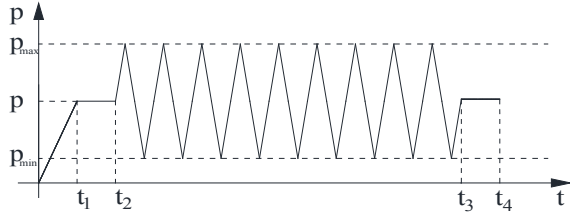
**Foundation of the model test.** The soil layers are from the bottom to the top as the following: (1) Fine sand with a thickness of 400 mm; (2) Silty clay with a thickness of 200 mm (pile cap was in this layer and below the geogrid); (3) Geogrid (the thickness of one geogrid layer cushion was 50 mm) and a mucky clay with a thickness of 750 mm; (4) Silty clay with a thickness of 250 mm. The rigid pile was on the intersection of diagonal lines of the square consisted of the line from the center of four flexible piles.

**Loading equipment and loading process.** The maximum load applied by the equipment was 5 kN. A 20 mm thick square steel plate was used as the loading plate with the side length of 800 mm as shown in Fig. 2b. Cyclic load waveforms of sinusoid and triangular cyclic load (As shown in Fig. 3) were applied in the loading process. Some model tests on the deformation behavior of geogrid supported by rigid-flexible piles were designed under cyclic loading with changing the load amplitude, load waveform, and cyclic load frequency. The loading scheme was given in Table 2. The number of cyclic loading cycles was 100.

**Fig. 3** Cyclic load curves with different waveform



(a) The sinusoid cyclic loading curve



(b) The triangle cyclic loading curve

**Table 2** Loading equipment and loading process

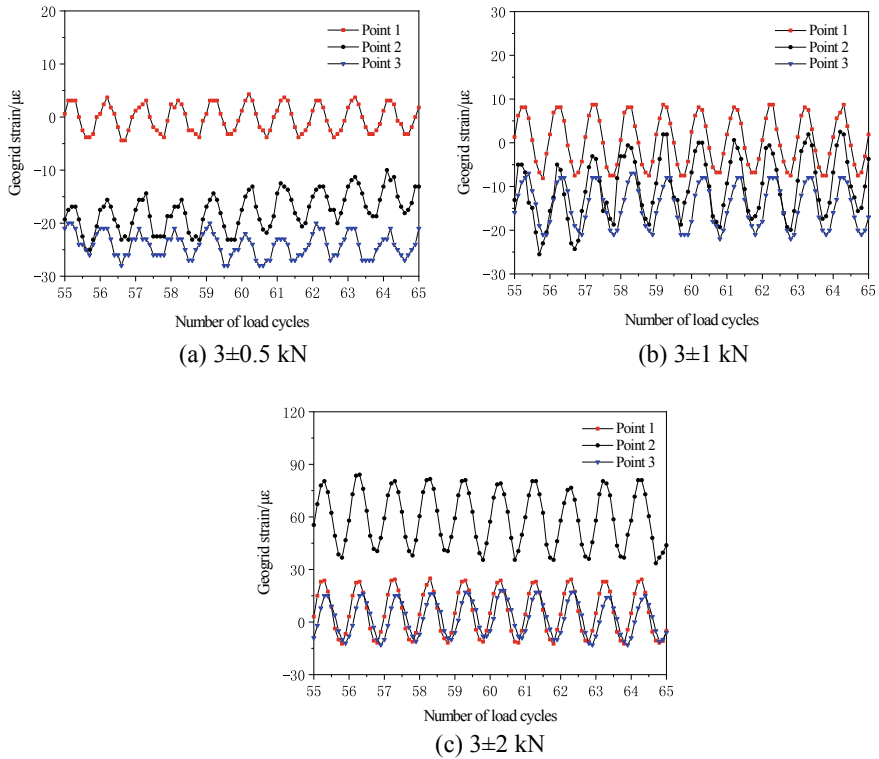
Test number		1	2	3	4	5	6
Load	Pmax/kN	4	4	4	3.5	5	4
	P/kN	3	3	3	3	3	3
	Pmin/kN	2	2	2	2.5	1	2
Load frequency/Hz		0.5	1	2	1	1	1
Number of load cycles		100	100	100	100	100	100
Load waveform		sinusoid	sinusoid	sinusoid	sinusoid	sinusoid	triangle

### 3 Results and Discussion

The geogrid strain changes continuously with the applied load under cyclic loading. Considering that the curve is crowded if strain curves of all load cycles are in the figures, it is impossible to see the strain change of the geogrid. Therefore, only the geogrid strain curves with the number of load cycles from 55 to 65 are selected in this paper.

#### 3.1 Influence of Cyclic Load Amplitude on the Geogrid Strain

Figure 4 shows the geogrid strain-number of load cycles curves at different location under different load amplitude with the cyclic load frequency of 1 Hz. It can be seen from Fig. 4 that the strain value of the geogrid changes with the fluctuation of



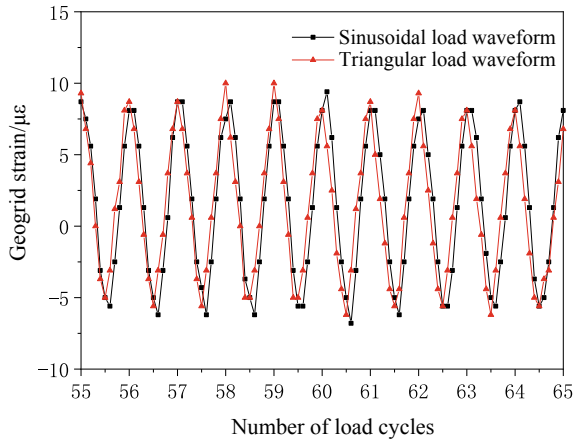
**Fig. 4** Geogrid strain-number of load cycles curves at different location under different load amplitude

applied load of cyclic loading. In other words, the strain variation law of geogrid under cyclic load is consistent with that of applied cyclic load. The geogrid strain at different locations was different under different load amplitude. The value of geogrid strain increased with the increasing of cyclic load amplitude. As shown in Fig. 4c, when the load amplitude was 2 kN, the geogrid strain at the location of point 2 which was near the edge of flexible pile is much larger than those at the location of point 1 and point 3. The geogrid strain was affected by the cyclic load amplitude.

### 3.2 Influence of Cyclic Load Waveform on the Geogrid Strain

Figure 5 shows the geogrid strain-load cycle number curves of point 1 under different load waveform with load frequency of 1 Hz and load amplitude of 1 kN. As shown in Fig. 5, the geogrid strain varied with load waveform. The geogrid strain was similar at different load waveform because there were only ten data points in each load cycle. The geogrid strain changing law was similar to that of load waveform.

**Fig. 5** Geogrid strain-number of load cycles with different load waveform



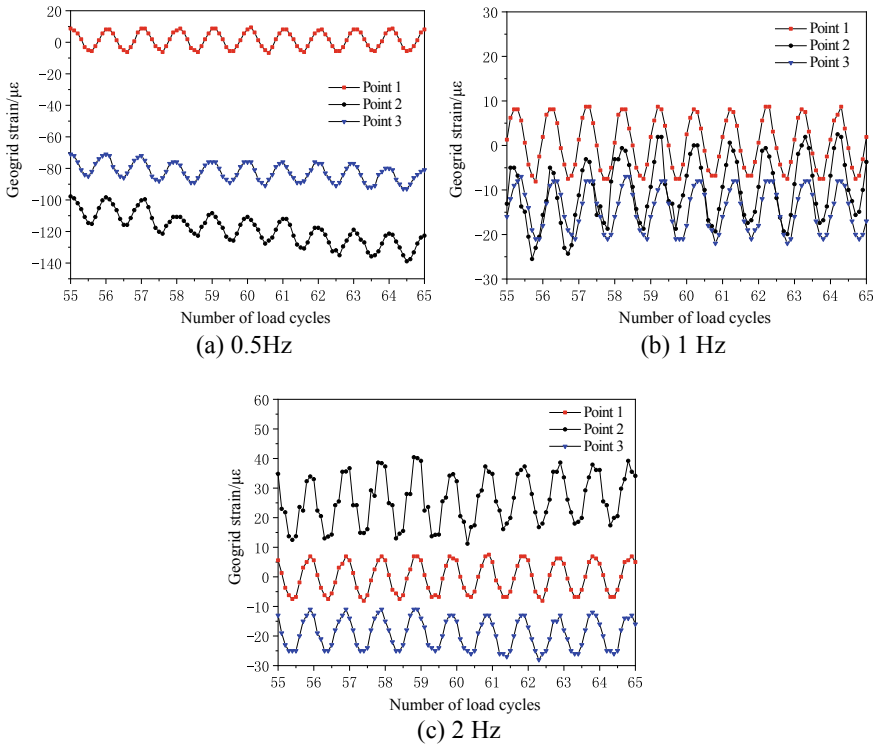
In other words, the geogrid strain would change accordingly when the cyclic load waveform was changed singly.

### 3.3 Influence of Cyclic Load Frequency on the Geogrid Strain

Figure 6 shows geogrid strain-number of load cycles at different locations under different load frequency with the loading amplitude of 1 kN. As shown in Fig. 6, the geogrid strain varied with the geogrid location and cyclic load frequency. The amplitude of geogrid strain variation at the location of point 1 was much smaller than that at the location of point 3 under different load frequency. And the amplitude of geogrid strain variation at the location of point 2 was much larger than that at the location of point 3 under different load frequency. In other words, the geogrid strain amplitude at the location near the edge of flexible pile under cyclic load frequency was the largest and that at the location on the soil was the smallest. Those shows the geogrid near the flexible plies should be carefully considered in the engineering design.

## 4 Conclusions

In this research, we analyzed the deformation behavior of geogrid supported by rigid-flexible piles in composite foundations under cyclic loading by model tests. The deformation behavior of geogrid varied with the position of the geogrid. The strain variation in the geogrid under cyclic load was consistent with that of applied cyclic load characteristics. The geogrid strain would change accordingly when the



**Fig.6** Geogrid strain-number of load cycles at different locations under different load frequency

waveform of cyclic load was changed singly. The geogrid strain amplitude at the edge of flexible pile under different cyclic load frequencies and load amplitudes was the largest, and that on the soil was much smaller. In other words, a geogrid near the flexible plies should be carefully considered in the engineering design.

**Acknowledgements** The authors would like to acknowledge the support provided by the Natural Science Foundation of China (No.51878619) and Natural Science Foundation of Zhejiang Province, China (No. LY13E090010).

**References**

1. Prabakar J, Dendorkar N, Morchhale RK (2004) Influence of fly ash on strength behavior of typical soils. *Constr Build Mater* 18(4):263–267
2. Jia N (2004) Research on settlement shape and treatment of highway widening on soft soil foundation. Zhejiang University, Hangzhou
3. Tang C, Shi B, Gao W et al (2006) Strength and mechanical behavior of short polypropylene fiber reinforced and cement stabilized clayey soil. *Geotext Geomembr* 25(3):194–202



4. Jiao D (2010) Model test research on geogrid-reinforced and pile-supported foundation under cyclic loading. Zhejiang University, Hangzhou
5. Pham HTV, Suleiman MT, White DJ (2004) Numerical analysis of geosynthetic-rammed aggregate pier supported embankments. In: Geotechnical engineering for transportation projects, pp 657–664
6. Han J, Gabr MA (2002) Numerical analysis of geosynthetic-reinforced and pile-supported earth platforms over soft soil. *J Geotech Geoenviron Eng* 128(1):44–53
7. Suleiman MT, Pham H, White DJ (2003) Numerical analyses of geosynthetic-reinforced rammed aggregate pier-supported embankments. Report No. ISU-ERI 3598
8. Yapage NNS, Liyanapathirana DS, Poulos HG (2014) Numerical modeling of geotextile-reinforced embankments over deep cement mixed columns incorporating strain-softening behavior of columns. *Int J Geomech* 15(2):04014047
9. Zheng J, Zhang J, Ma Q et al (2012) Experimental investigation of geogrid-reinforced and pile-supported embankment at bridge approach. *Chin J Geotech Eng* 34(2):355–362
10. Liu K, Cao L, Hu Y et al (2018) Model test on the deformation behavior of geogrid supported by rigid-flexible piles under static load. In: Li L, Cetin B, Yang X (eds) *Proceedings of Geoshanghai 2018 International conference: ground improvement and geosynthetics*. Springer, Singapore, pp 338–346
11. Biabani MM, Indraratna B, Ngo NT (2016) Modelling of geocell-reinforced subballast subjected to cyclic loading. *Geotext Geomembr* 44(4):489–503
12. Nanthakumar S, Muttharam M, Goyal S, Mishra A (2018) Study on the performance of railway ballasted track reinforced with geogrid. *Indian J Sci Technol* 11(23):1–4
13. Alam MJI, Gnanendran CT, Lo SR (2018) Experimental and numerical investigations of the behaviour of footing on geosynthetic reinforced fill slope under cyclic loading. *Geotext Geomembr* 46(8):848–859
14. Hu Yi (2015) Study on bearing behavior of geogrid considering the support of rigid flexible piles. Zhejiang Sci-Tech University, Hangzhou

# Resistance Characteristics of Piles Under Distributed Lateral Loading in the Perpendicular Pile Axis Direction



Atsushi Mohri, Kazuki Sakimoto, Takamune Yamaguchi, Yoshiaki Kikuchi, Shohei Noda, Shinji Taenaka, Shunsuke Moriyasu, and Shin Oikawa

**Abstract** Coastal areas along the Pacific Ocean suffered extensive damage owing to the 2011 tsunami due to the Tohoku earthquake. Hence, reinforcement methods against tsunamis need to be developed for existing caisson type breakwaters. This study proposes installing a row of piles behind the caisson using backfilling, with rubble in the space between, as reinforcement against tsunamis. To determine the cross-section and embedment length of the pile used in this structure, understanding the load condition acting on the pile is necessary. Model experiments were conducted based on bending moment distribution to estimate the external force acting as distributed load on the pile's offshore side. The subgrade reaction acting on the pile from the onshore side was assumed by correcting the coefficient of the subgrade reaction and its depth direction in the Winkler–Spring type subgrade reaction model. There are insufficient points in the external force distribution estimated in this method owing to insufficient evaluation of the subgrade reaction. The impact of the subgrade reaction on a pile's horizontal resistance characteristics depends on its deformation mode. Hence, it is necessary to evaluate the subgrade reaction in the pile deformation mode under distributed load along the perpendicular pile axis direction. This study conducted loading experiments on the piles using different ground conditions and loading methods to examine the difference in horizontal resistance of the piles. The deformation mode of the piles was found to cause changes in the coefficient value of the subgrade reaction and its changing behavior along the depth direction.

**Keywords** Breakwater · Reinforcement · Subgrade reaction

---

A. Mohri (✉) · K. Sakimoto · T. Yamaguchi  
Graduate School of Tokyo University of Science, Yamazaki2641, Noda City, Chiba, Japan  
e-mail: [7619702@ed.tus.ac.jp](mailto:7619702@ed.tus.ac.jp)

Y. Kikuchi · S. Noda  
Tokyo University of Science, Yamazaki2641, Noda City, Chiba, Japan

S. Taenaka · S. Moriyasu · S. Oikawa  
Nippon Steel Corporation, 6-1, Marunouchi 2-chome, Chiyoda-ku, Tokyo, Japan

## 1 Introduction

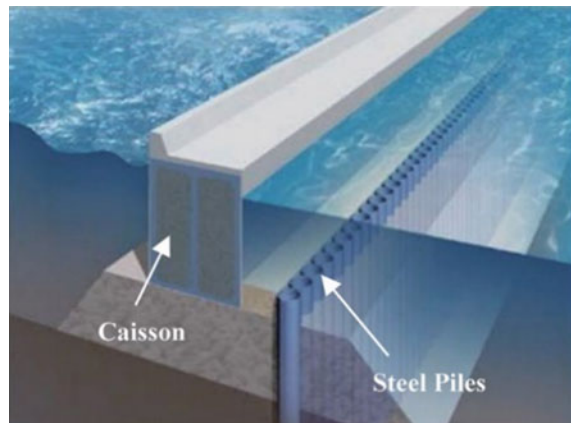
The 2011 tsunami off the Pacific Coast due to the Tohoku earthquake caused extensive damage to the coastal areas of the Pacific Ocean. Several breakwaters that were structurally classified as gravity-type composite breakwaters were destroyed. The main reasons for the gravity-type composite breakwaters to be damaged were the presence of extensive horizontal forces caused by water-level differences between the two sides of the caisson and erosion of the foundation at the rear side of the caisson caused by an overflow of water transported by the tsunami [1]. Therefore, tsunami resistant breakwaters are necessary to reduce the damage caused by large tsunamis.

Moriyasu et al. [2, 3] proposed a method of reinforcing breakwaters by installing steel pipe piles behind a breakwater and filling the space in between with aggregates, as shown in Fig. 1. Passive resistance exerted by the ground can be used to support the steel piles because the horizontal forces acting on the caisson can be effectively transferred to the steel piles through the rubble that fills the space between the piles and the caisson. The fundamental effectiveness of this method of reinforcement was examined by performing static loading experiments [4, 5] and hydraulic flume experiments [3].

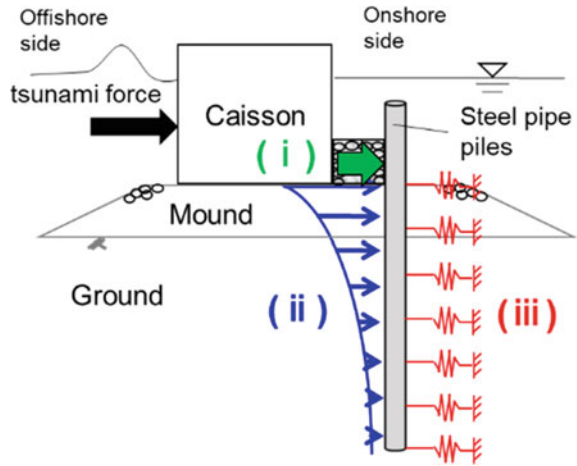
For designing the piles used in this structure, it is important to set the cross-section and embedment length of the steel pipe pile so that the generated stress level of the piles generated by the tsunami force acting on the caisson does not exceed the yield stress level. To determine the cross-section and embedment length of piles, it is necessary to properly grasp the load conditions acting on the piles.

Here, the loads acting on the piles used in this structure are classified into three types as shown in Fig. 2; (i) Earth pressure acting on the protruding part of the piles from the filling with the displacement of the caisson, (ii) Earth pressure acting on rooted part of the piles from the foundation ground due to the slope of the caisson, (iii) Subgrade reaction acting on the piles from the onshore side.

**Fig. 1** Schematic diagram of a reinforced gravity type breakwater [2]



**Fig. 2** Classification of loads acting on piles



Loads (i) and (ii) are external forces acting on the piles as distributed loads. It is important to understand the subgrade reaction that the piles receive from the onshore side against these external forces to predict the maximum bending moment of the pile and the depth of its occurrence.

This study conducted static model experiments to generalize the external force distribution acting on the piles from the offshore side of this structure [6]. In the experiment, the bending strain and bending moment distribution of the pile were calculated. The deflection distribution was obtained by second-order integration of bending moment distribution, and the load distribution acting on the pile was obtained by second-order difference of bending moment distribution. Here, the estimation of the external force distribution was studied by subtracting the assumed subgrade reaction distribution based on the deflection distribution from the load distribution. There were some insufficient points regarding the external force distribution estimated in this method. This is due to a problem in the assumption of subgrade reaction coefficient along the depth direction, which was used to calculate the subgrade reaction distribution.

The impact of the subgrade reaction on the horizontal resistance characteristics of a pile depends on the deformation mode of the pile [7, 8]. In this study, horizontal loading experiments were conducted using different ground conditions and loading methods to examine the difference in the value of subgrade reaction coefficient and its changing behavior along the depth direction.

## 2 Model Loading Test of Reinforced Gravity Type Breakwater

### 2.1 Experimental Outline

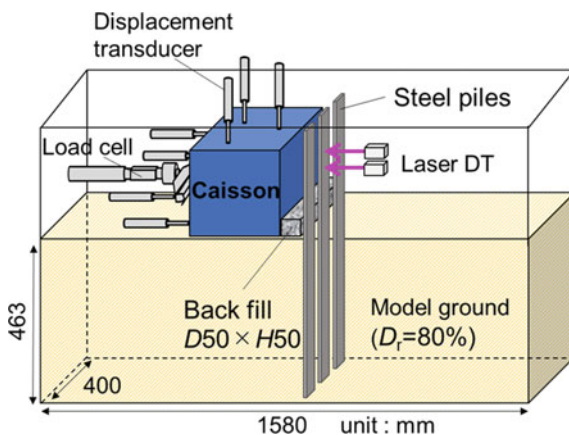
The experiment model was designed at a 1/60 scale. The schematic diagram of the model setup is shown in Fig. 3. A steel sand box that was 1580 mm long, 800 mm high, and 400 mm wide was used to prepare the model ground, as shown in Fig. 3. Dry silica sand #5 ( $\rho_s = 2.647 \text{ g/cm}^3$ ,  $D_{50} = 0.591 \text{ mm}$ ,  $e_{max} = 1.072$ , and  $e_{min} = 0.689$ ) was used to prepare the model ground. The model ground was prepared using a relative density of 80% by the air pluviation method.

The 12 steel piles (800 mm long, 30 mm wide, 2.3 mm thick, and flexural rigidity,  $EI = 6.24 \times 10^3 \text{ kNmm}^2$ ) were set 50 mm behind the caisson (380 mm long, 300 mm high, 300 mm wide,  $\gamma_t = 22 \text{ kN/m}^3$ ). The center to center distance of the piles was 33 mm, and embedment length was 463 mm. A backfill was maintained at a height of 50 mm between the caisson and the steel piles ( $D_{50} \approx 10 \text{ mm}$ ,  $G_s = 2.65$ ,  $\gamma_d = 12.1 \text{ kN/m}^3$ ).

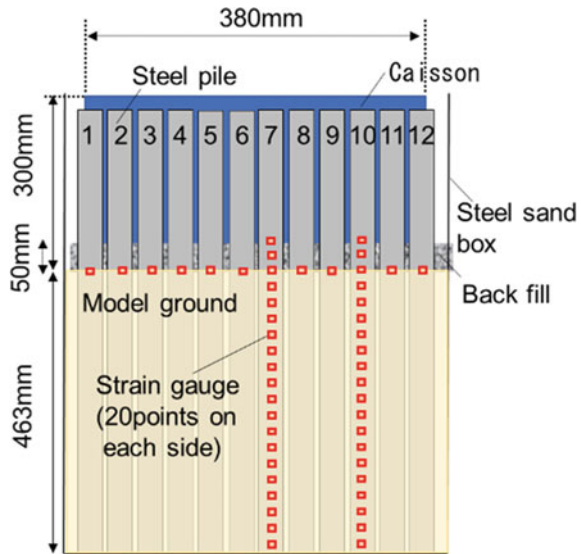
A Teflon sheet was affixed to the loading surface of the caisson model to reduce friction. At the bottom of the caisson, sandpaper #150 was attached. Friction was reduced using a Teflon sheet and a membrane at the contact surface between the ground and the sand box. In the loading experiment, a horizontal load assuming a tsunami force was applied. The horizontal load was applied under displacement control at a height of 150 mm, and the monotonous loading speed was 1 mm/min.

Horizontal displacement of the caisson was measured using LVDTs fixed at 4 points on the load surface and 3 points on the upper surface. 20 strain gauges were attached on both sides along the depth direction of the central pile and a random pile to measure the bending strains, as shown in Fig. 4.

**Fig. 3** Schematic diagram of the experimental model set up



**Fig. 4** Schematic diagram of the experimental model set up (view from the rear side of the caisson)



## 2.2 Experimental Results

Figure 5 shows the bending moment distribution and deflection distribution in the central pile. The figure shows the results when the applied load on the caisson is 700 and 1000 N. In bending moment distribution, the maximum bending moment tends to increase as the applied load on the caisson increases. However, the generation depth  $l_{m, \max}$  does not change significantly. There is no significant change in the first zero-point depth of the bending moment  $l_{m1}$ , which is an important index for determining the embedment length of the pile. Generally, piles receiving horizontal force at the pile head experience an increase in the characteristics of  $l_{m, \max}$  and  $l_{m1}$  with increase in load level. In this experiment, the horizontal force acting on the piles from the offshore side is considered a distributed load, which is different from the general tendency.

Figure 6 shows the load distribution obtained by second-order differentiation of bending moment distribution of the central pile. This load distribution is considered to be the resultant force, which is classified into three categories, as shown in Fig. 2. Therefore, the subgrade reaction model [9] of the PHRI method of type S model, shown in Eq. (1), was applied to the subgrade reaction that was received from onshore side owing to the displacement of the pile.

$$p = k_s x y^{0.5} \quad (1)$$

In the PHRI method of type S model, the subgrade reaction coefficient is considered to be unique to the ground when a horizontal load acts on the pile head. Therefore, a constant coefficient of subgrade reaction can be used without depending on

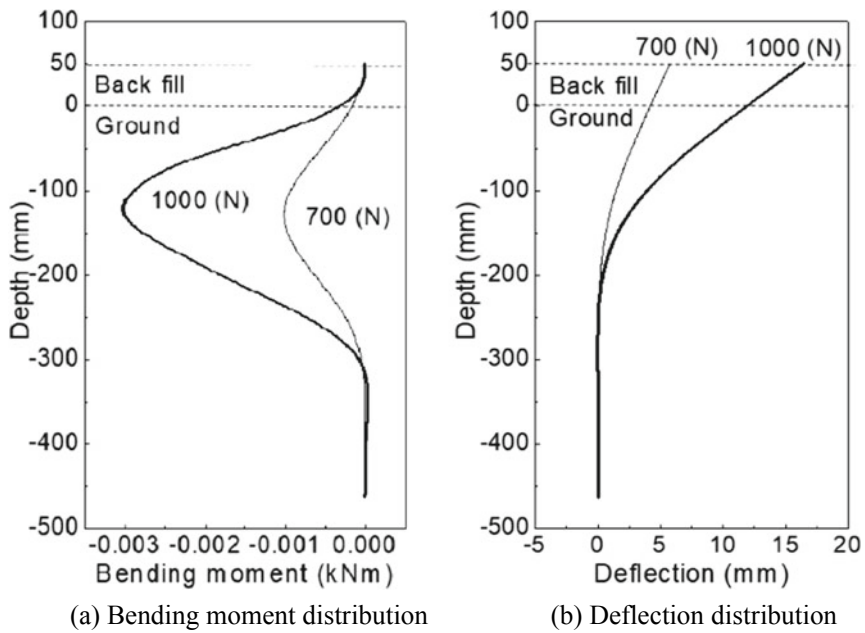
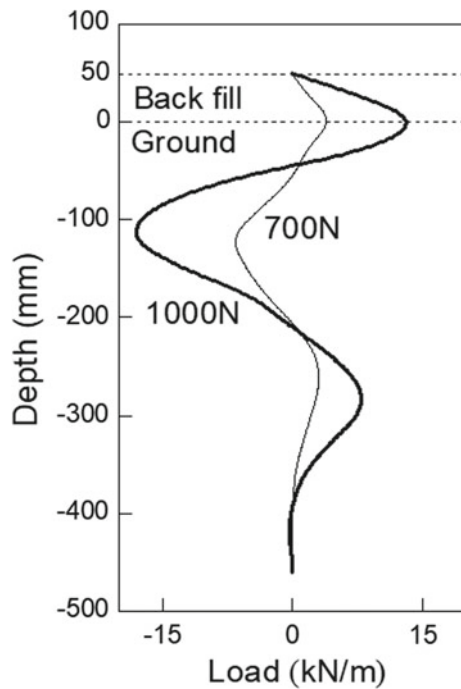


Fig. 5 Bending moment distribution and deflection distribution of the central pile

Fig. 6 Load distribution

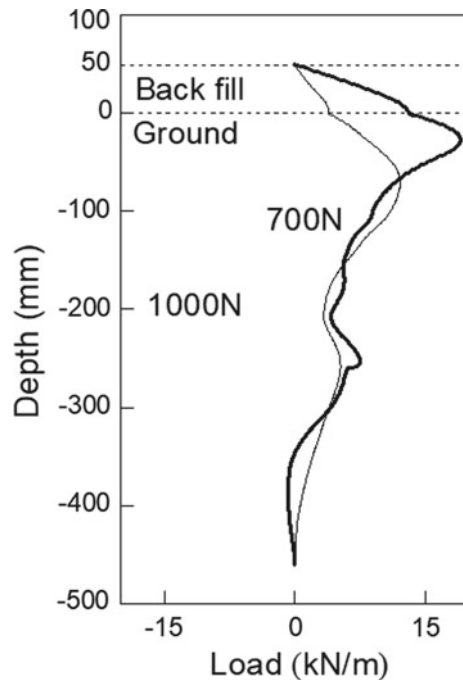


the flexural rigidity,  $EI$ , or displacement of the pile. This model is derived based on the results of horizontal loading tests of piles under various conditions and represents the behavior of the pile by assuming nonlinearity in the  $p$ - $y$  relationship [10].

Generally, the behavior of the subgrade reaction of a pile under a horizontal load depends on the deformation mode of the pile. To consider this phenomenon using the Winkler–Spring type model, it is necessary to change the subgrade reaction coefficient depending on the deformation mode of the pile. The depth distribution of the subgrade reaction coefficient used in the PHRI method of type S model was modified based on the results obtained from the horizontal loading test of the pile. The subgrade reaction distribution was calculated using the deflection distribution shown in Fig. 5b and the corrected coefficient of subgrade reaction.

By subtracting the obtained subgrade reaction distribution based on the assumption from the load distribution, as shown in Fig. 6, the external force distribution acting on the pile from the offshore side was estimated. Figure 7 shows the external force distribution estimated in this experiment. This result shows that the estimated external force acting on the backfill and the shallow section near the ground surface increases as the applied load on the caisson increases. At a depth of approximately –100 mm, the estimated external force tends to decrease as the applied load increases. This can be attributed to the fact that the vertical stress acting on the ground surface directly below the caisson decreased because of the increased frictional force acting upward on the contact surface between the caisson and the backfill, which was owing

**Fig. 7** Estimated external force distribution





to the increase in the applied load. However, there are some problems in the accuracy of the estimated external force distribution because of discontinuous behavior in the estimated external force distribution and the interval of negative values.

The fact that there are insufficient points in the estimated external force distribution is assumed to be caused by a problem with the accuracy of the coefficient distribution of the subgrade reaction that is used in the assumption of the subgrade reaction distribution. As the behavior of the subgrade reaction varies depending on the deformation mode of the pile, it is necessary to assume the coefficient distribution of subgrade reaction corresponding to the deformation mode of the pile. Therefore, loading experiments were conducted using different ground conditions and pile loading conditions to examine the differences in coefficient distribution of the subgrade reaction.

### 3 Horizontal Loading Test on Piles

#### 3.1 Experimental Outline

In the horizontal loading test of piles, the steel sand box shown in Fig. 3 was used.

Figure 8 shows the experimental conditions. In Case 4, horizontal load is applied at two depths (hereinafter referred to as the two-stage loading experiment). The two-stage loading position was depth  $x = 0$  and  $x = -100$  mm with reference to the ground surface on the rear side of the piles. Each horizontal load was applied simultaneously to control the load. Except Case 1, the ground height difference between the front and rear side was 200 or 225 mm. In this loading test, as the pile’s penetration length with respect to the horizontal force is sufficient, the difference in the ground height for each test case is considered to have no effect on the behavior of the pile.

The pile behavior was analyzed based on the bending strain obtained by the strain gauges attached to both sides along the depth direction. As shown in Fig. 9, the model

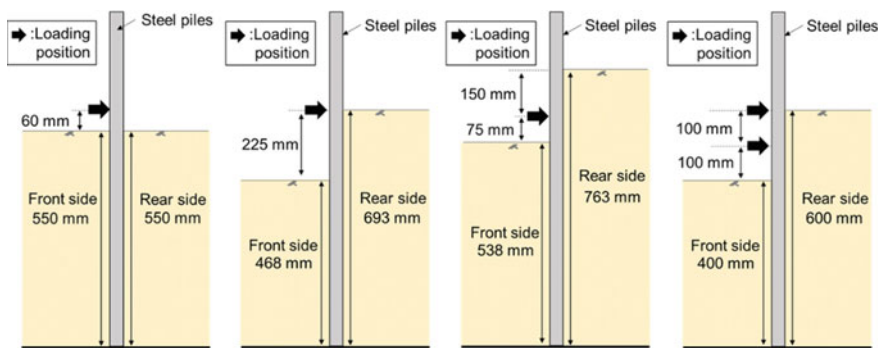
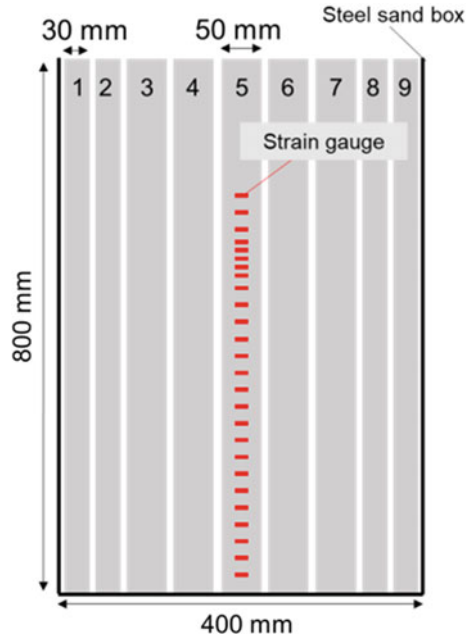


Fig. 8 Details of the experimental cases

**Fig. 9** Schematic diagram of the pile condition

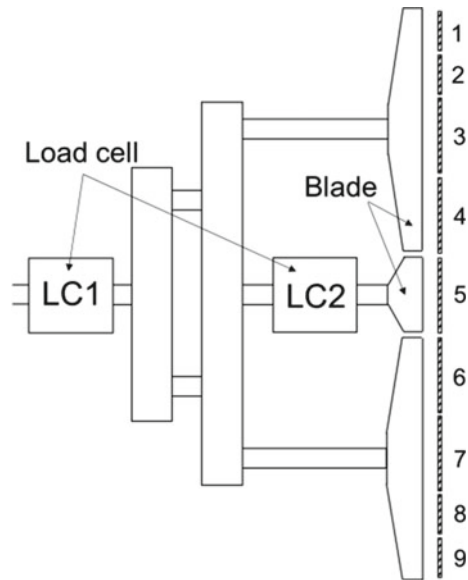


consisted of 50 and 30 mm wide steel plate piles (2.3 mm thick,  $E = 2.05 \times 10^5$  N/mm<sup>2</sup>). For Case 1 to Case 3, strain gauges were attached only to the central pile (pile 5), as shown in Fig. 9. In Case 4, strain gauges were attached to pile 4 and pile 7 in addition to pile 5 to investigate the difference in behavior of each pile.

A horizontal load was applied under the load control. The blade shown in Fig. 10 is attached to the shaft of the Bero-frame cylinder. The blade is divided into three parts at the contact point with the pile. LC1 and LC2 in the figure are load cells. LC1 measures the total load on the piles arranged in a row, and LC2 measures the load acting on one central pile. Additionally, the horizontal displacement of the loading point was measured by a displacement meter fixed to the steel sand box frame.

In this study, two types of sand were used. In Case 1 to Case 3, silica sand #5 ( $G_s = 2.647$  g/cm<sup>3</sup>,  $e_{\max} = 1.072$ ,  $e_{\min} = 0.689$ ) was used at a relative density of 80%, and for Case 4, Tohoku silica sand #5 ( $G_s = 2.651$ ,  $e_{\max} = 0.813$ , and  $e_{\min} = 0.526$ ) was used at a relative density of 90%. Silica sand #5 is the same material used in the model loading experiment in Fig. 3. In Case 4, the weight equivalent to the difference in ground height was applied to the ground surface on the front side of the pile as lead pressure using lead shots.

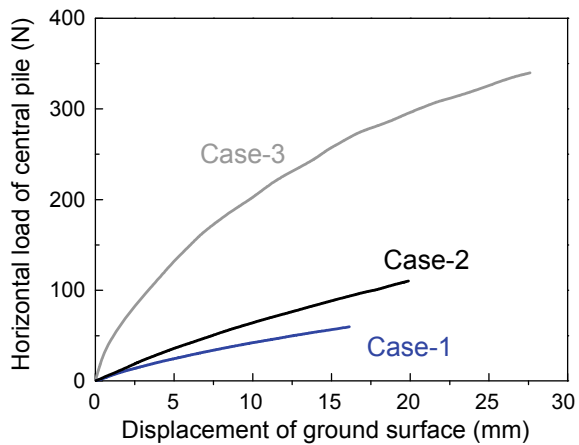
**Fig. 10** Structure of loading blade



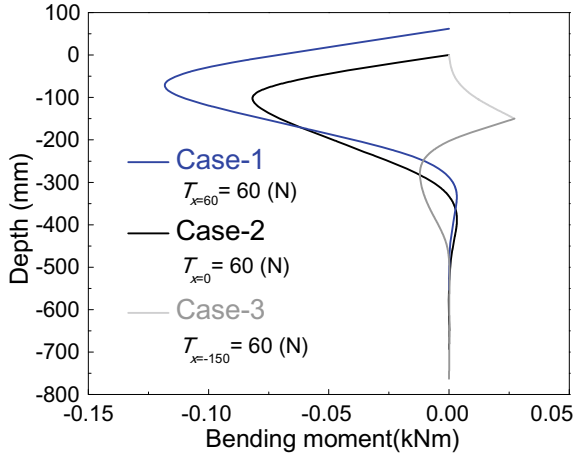
### 3.2 Experimental Results of Horizontal Loading Test

Figure 11 shows the relationship between the horizontal load on the central pile and displacement of the ground surface in Case 1 to Case 3. The horizontal load on the central pile is directly measured by LC2, as shown in Fig. 10. From this result, it can be observed that for different loading positions, the displacement of the ground surface of the pile with the same horizontal load differs greatly. In this case, the horizontal loading test was carried out in a single stage. The displacement of the pile

**Fig. 11** Relationship between horizontal loads on central pile and displacement of ground surface



**Fig. 12** Comparison of bending moment distribution



is considered to decrease with the same load as the position of the external force is deeper in the ground.

Figure 12 shows the bending moment distribution of the central pile when the horizontal load on the central pile measured by the load cell LC2 in Case 1 to Case 3 is 60 N.

From this result, it can be observed that the bending moment distribution varies greatly and the deformation mode of the pile changes even if the loading position is different under the same horizontal load.

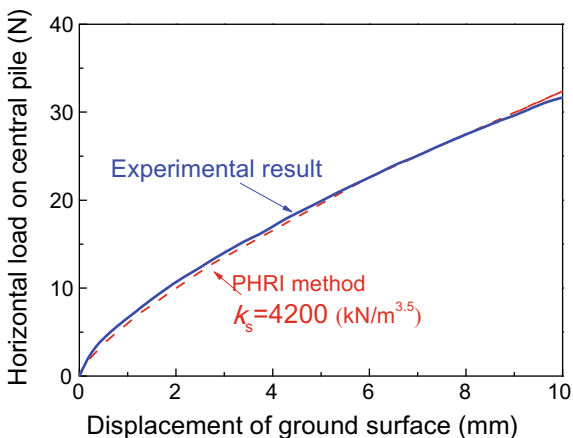
The behavior of the pile was compared with the calculated results based on the beam theory in elastic media, as shown in Eq. (2).

$$\frac{EI}{B} \frac{d^4 y}{dx^4} + p = 0 \tag{2}$$

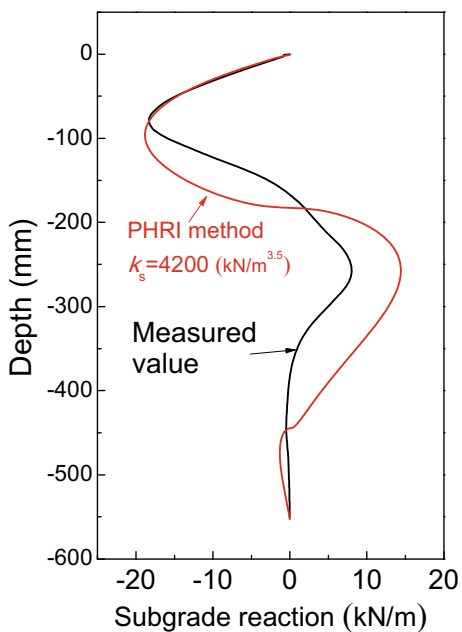
Here, the PHRI method of the type S model was used for modeling the subgrade reaction.

Figure 13 shows the relationship between the displacement of the ground surface and the pile head load of the central pile in Case 1. The figure also shows the relationship obtained by assuming the subgrade reaction coefficient as a constant, regardless of the displacement level, using a model of the PHRI method of the type S model. From this result, it can be seen that the  $k_s$  obtained from the relationship between the pile head load and ground surface displacement is approximately 4200 kN/m<sup>3.5</sup>. Figure 14 shows a comparison of the subgrade reaction distribution obtained by second-order differentiation of bending moment distribution when the pile head load is 32 N in Case 1 and the subgrade reaction distribution based on the PHRI method of the type S model. In the ground reaction force distribution of the PHRI method of type S model,  $k_s = 4200$  kN/m<sup>3.5</sup> is applied along the depth direction. In the experimental results, the maximum bending moment depth ( $l_{m, \max}$ ) with 32 N action was

**Fig. 13** Relationship between horizontal load on central pile and displacement of ground surface



**Fig. 14** Subgrade reaction distribution in Case 1



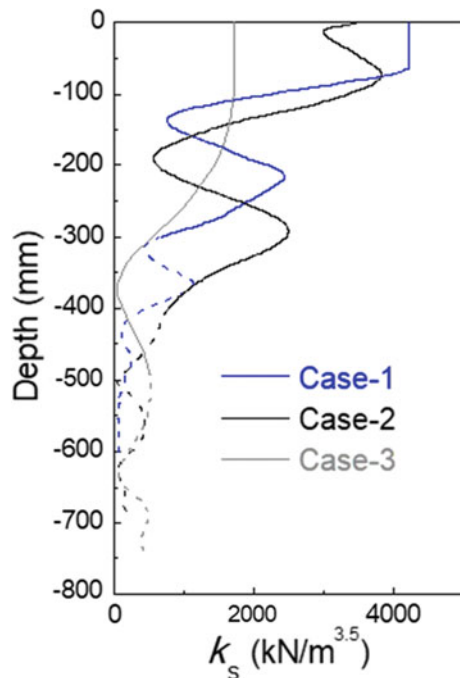
approximately  $-80 \text{ mm}$ . From this result, it can be observed that in the section from the ground surface to about  $l_{m, \max}$ , the subgrade reaction model of the PHRI method can estimate the experimental result accurately, but there is a large divergence that is deeper than  $l_{m, \max}$ . Additionally, based on the subgrade reaction distribution of the experimental results, it can be seen that  $k_s$  has a behavior that decreases when the divergence is deeper than  $l_{m, \max}$ .

The tendency of  $k_s$  to change along the depth direction is considered to indicate the behavior of the subgrade reaction affected by the deformation mode of the pile. Therefore, the depth distribution of  $k_s$  based on the experimental results of Case 1 to Case 3 was calculated and compared.

Figure 15 shows the depth distribution of  $k_s$  based on the bending moment distribution of the central pile in the experimental results for Case 1 to Case 3. Here, the  $k_s$  calculation accuracy is insufficient in the section deeper than the depth of the first zero-point depth of the bending moment ( $l_{m1}$ ), and this section is shown as a dotted line. From this result, it is clear that  $k_s$  does not show a constant value along the depth direction as assumed in the PHRI model. As seen in Fig. 14, for deformation modes like Case 1,  $k_s$  shows a constant value in the section from the ground surface to  $l_{m, \max}$ , but changes in the section deeper than  $l_{m, \max}$ . In Case 1 and Case 2, the change behavior of  $k_s$  along the depth direction tends to be relatively similar. In Case 2,  $k_s$  fluctuates in the interval shallower than  $l_{m, \max}$ , and the value is smaller than  $k_s$  in Case 1. This difference is due to the difference in ground height between the front side and rear side of the piles in Case 2.

Case 2 and Case 3, which differ only in the loading position under the same ground conditions, have different  $k_s$  values in the shallow section, and Case 2 shows a value about twice as large. The difference is much larger than the difference between Case 1 and Case 2. Additionally, the change behavior of  $k_s$  along the depth direction is more gradual than other cases.

**Fig. 15**  $k_s$  distribution in Case 1–Case 3



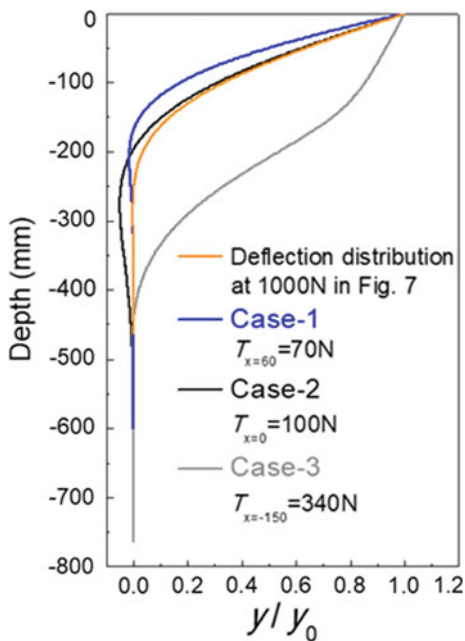
Thus, when the deformation mode of the piles is different, not only the  $k_s$  value in the shallow section of the ground is different, but also the  $k_s$  value for depth distribution is different.

Figures 5, 6, and 7 shows the estimation results of the pile behavior and external force distribution acting from the offshore side in the model experiment. As described above, it is necessary to assume the subgrade reaction distribution while estimating the external force distribution. At this time, horizontal loading tests of the piles were conducted to obtain the coefficient distribution of subgrade reaction.

Figure 16 shows the depth distribution of  $y/y_0$  obtained by normalizing the deflection distribution of the central pile in each case with the ground surface displacement  $y_0$ . Here, as the load level and displacement level of the pile differ depending on the experiment case,  $y/y_0$  divided by the ground surface displacement  $y_0$  is shown. The horizontal load  $T$  on the central pile in each case is shown with a legend in the figure. The figure also shows the result of normalizing the deflection distribution (Fig. 5) with  $y_0$  when the applied load on the caisson is 1000 N. The pile deformation mode and  $k_s$  values obtained in the horizontal loading test of the piles under the pile conditions shown in Fig. 4 were almost consistent with those of Case 1. It can be seen that the deformation mode of the pile when the applied load on the caisson is 1000 N is close to Case 2 and is significantly different from Case 1 and Case 3.

From the above examination, it was found that when the loading position on the pile is different, the deformation mode of the pile is also different, which affects the coefficient value and its distribution. Hence, a two-stage loading experiment was conducted as Case 4.

Fig. 16 Normalized deflection distribution



**Fig. 17** Relationship between the ground surface displacement and horizontal load of the central pile

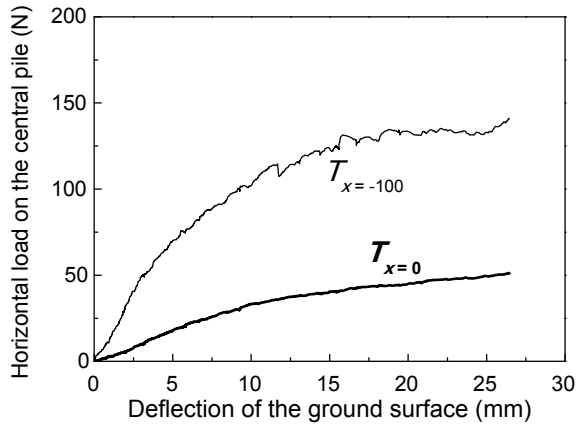
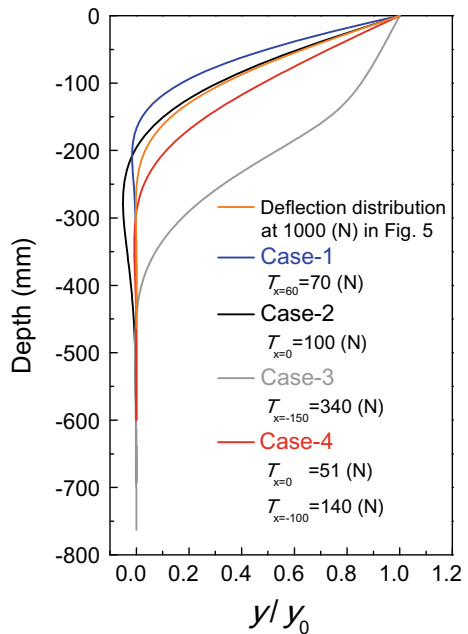


Figure 17 shows the relationship between the ground surface displacement of the central pile and the horizontal load  $T$  of the upper and lower stages measured by LC2 in Case 4.

Figure 18 shows the relationship between the depth distribution of  $y/y_0$  shown in Fig. 16 and the result obtained from the deflection distribution of the central pile in Case 4. The upper and lower horizontal force  $T$  in Case 4 are shown together with the legend in the figure. This result shows that the pile deformation mode in Case 4 is a

**Fig. 18** Normalized deflection distribution

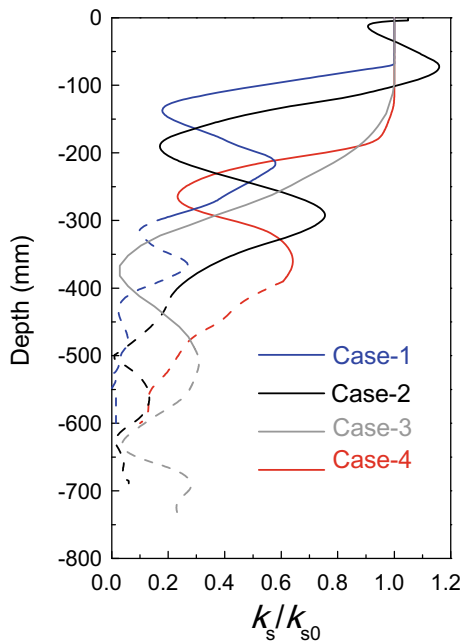




behavior between Case 2 and Case 1. Case 4 also differs from the deformation mode when the applied load on the caisson is 1000 N. To match the pile deformation mode in the model experiment, it is necessary to devise the upper and lower horizontal load levels and loading positions. It is believed that more accurate external force distribution can be estimated by obtaining  $k_s$  and its depth distribution from the result of the loading experiment conducted with such consideration. However, if the ground and pile bending stiffness are different, the deformation mode of the pile may be different. Hence, it is necessary to organize and generalize the coefficient distribution of subgrade reaction in various deformation modes of piles for practical application.

Figure 19 shows the depth distribution of  $k_s$  obtained from the bending moment distribution of the central pile in all cases. The horizontal axis in the figure uses  $k_s/k_{s0}$  normalized with  $k_{s0}$  as the average  $k_s$  at the shallow depth in each case, and the change in behavior along the depth direction is compared. In Case 4, the average  $k_s$  in the shallow section was  $k_s = 3000 \text{ kN/m}^{3.5}$ . Therefore, the  $k_{s0}$  of Case 4 was set to  $k_{s0} = 3000 \text{ kN/m}^{3.5}$ . The  $l_{m, \text{max}}$  in Case 4 was approximately  $-200 \text{ mm}$ . From the results in Fig. 19, it can be observed that  $k_s/k_{s0}$  shows a constant value in the section from the ground surface to about  $l_{m, \text{max}}$ . And the change in behavior in the section deeper than  $l_{m, \text{max}}$  is similar to the tendency of Case 1 and Case 2.

**Fig. 19** Normalized depth distribution of  $k_s$



## 4 Conclusions

In the structure of a breakwater reinforced with steel pipe piles, it is important to design the cross-section and embedment length of the pile. It is important to understand the subgrade reaction that the piles receive from the onshore side against these external forces to predict the maximum bending moment of the pile and the depth of its occurrence. The piles used in this structure received distributed load along the perpendicular pile axis direction from the offshore side. However, insufficient knowledge has been obtained about pile resistance when it receives such a distributed load. The change in reaction force behavior cannot be considered. Therefore, the change in subgrade reaction due to the difference in deformation mode of the pile cannot be considered. In this study, loading experiments were conducted on the piles using different ground conditions and loading methods to examine the difference in the horizontal resistance of the piles.

The displacement of the pile is considered to decrease with the same load as the position of the external force moves deeper in the ground. The bending moment distribution varies greatly and the deformation mode of the pile changes even when the loading position is different under the same horizontal load.

The behavior of the pile from the experimental results was compared with the calculated results based on the PHRI method of a type S model. In the PHRI method of type S model, the subgrade reaction coefficient ( $k_s$ ) is considered to be unique to the ground when the horizontal load acts on the pile head. However, it has been found that owing to the influence of the pile deformation mode, it does not take a certain value in the depth direction. Therefore, the depth distribution of  $k_s$  was calculated based on the bending moment distribution of the pile in the experimental results, and the difference was observed when the loading method was different. As a result, it was found that there was a difference in the value of  $k_s$  when the loading position on the pile was changed. There was a difference in the change behavior of  $k_s$  along the depth direction. These results were believed to be caused by different deformation modes of the pile depending on the loading position on the pile.

When the subgrade reaction is expressed by the Winkler-Spring type PHRI method, it is necessary to assume the value of the coefficient of subgrade reaction and its depth distribution according to the deformation mode of the pile. In future, it will be necessary to study for generalization.

**Acknowledgements** The authors would like to thank Mr. Suganuma and Ms. Sakoda (Tokyo University of Science) for their support in this study. This work was also supported by JSPS KAKENHI, grant number JP1804352.

## References

1. Arikawa T, Sato M, Shimosako K, Tomita T, Tatsumi D, Yeom G, Takahashi T (2012) Investigation of the failure mechanism of Kamaishi breakwaters due to tsunami-initial report focusing

- on hydraulic characteristics. Technical note of Port and Airport Research Institute, No. 1251, p 52
2. Moriyasu S, Oikawa S, Taenaka S, Harata N, Tanaka R, Tsujii M, Kubota K (2016) Development of new type of breakwater reinforced with steel piles against a huge tsunami. Nippon Steel & Sumitomo Metal Technical Report No. 113
  3. Arikawa T, Oikawa S, Moriyasu S, Okada K, Tanaka R, Mizutani T, Kikuchi Y, Yahiro A, Shimosako K (2015) Stability of the breakwater with steel pipe piles under tsunami overflow. Technical note of Port and Airport Research Institute No. 1298, p 44
  4. Kikuchi Y, Kawabe S, Taenaka S, Moriyasu S (2015) Horizontal loading experiments on reinforced gravity type breakwater with steel walls. Japan Geotech Soc Special Publ 2:1267–1272
  5. Suguro M, Kiuchi Y, Kiko M, Nagasawa S, Moriyasu S (2015) Load-displacement properties of gravity type breakwater reinforced by steel pipe piles. Japan Geotech Soc Special Publ 1(6):1–5
  6. Hikichi K, Kikuchi Y, Hyodo T, Mohri A, Akita K, Shoji N, Taenaka S, Moriyasu S, Oikawa S (2018) Estimation of external force acting on steel pile of steel pile reinforced breakwater. In: Proceedings of the 1st international conference on press-in engineering 2018, pp 281–288
  7. Iwata N, Nakai T, Zhang F, Inoue T, Takei H (2007) Influence of 3D effects, wall deflection process and wall deflection mode in retaining wall problems. Soils Found 47(4):685–699
  8. Nakai T (1985) Finite element computations for active and passive earth pressure problems of retaining wall. Soils Found 25(3):98–112
  9. Kubo K (1967) Experimental study on the lateral resistance of piles (Part 2)—effect of soil condition on lateral resistance of piles—. Mon Rep Transp Tech Res Inst 11(12):1–27
  10. Kikuchi Y (2009) Horizontal subgrade reaction model for estimation of lateral resistance of pile. Rep Port Airport Res Inst 48(4):3–22

# Dynamic Behaviors of Piled Embankment Under High-Speed Train Loads



Xiang Duan, Ying Wu, Xuecheng Bian, and Jianqun Jiang

**Abstract** Piled embankments over the soft soil can effectively reduce the post-construction settlement by soil arch effects. To investigate the soil arch effect under train moving loads, the authors established a full three-dimensional finite element model including train set, track structure and piled embankment. Based on the model, dynamic stress under moving train loads is calculated and the influence of soil arch effect is discussed. The numerical analysis reveals that: (1) soil arch effect leads to the redistribution of dynamic stress in piled embankment; (2) geogrids contribute to reducing the dynamic stress on the interpile soils; (3) track structures decide the dynamic stress distribution in the superficial layer in piled embankment, while the dynamic stress distribution at deep layer is mainly related to the pile foundation.

**Keywords** Piled embankment · Soil arch effect · Dynamic stress

## 1 Introduction

Piled embankments are widely adopted in China high-speed railway constructions over soft soil areas [1]. Because of soil arch effect, piles instead of the soft subsoil will bear extra traffic loads and consequently reduce the post-construction settlement effectively. Researches and experiments till now have established several theories and models of soil arches, and most of them are mainly concerned about the soil arches under the static load [2–5]. However, with the increase of train speed, dynamic effect tends to be more critical to the soil arches in piled embankment, which attracts increasing attention to the studies on soil arch effect under dynamic loads [1, 6, 7].

In this paper, a full three-dimensional finite element model (FEM) of train, track and piled embankment is developed to investigate the dynamic behaviors of piled embankment under high speed train loads. Based on the simulation results, the effect of train speed, track structures and the geogrid reinforced are discussed.

---

X. Duan · Y. Wu · X. Bian (✉) · J. Jiang  
Zhejiang University, Yuhangtang Road 388, Hangzhou, China  
e-mail: [Bianxc@zju.edu.cn](mailto:Bianxc@zju.edu.cn)

## 2 Three-Dimensional FEM Model of Train–Track–Embankment.

To simulate the dynamic behaviors of piled embankment under train loads, author has established a three-dimensional FEM model using ABAQUS software. This model consists of the train set, track structure, piled embankment and soft soil foundation. Considering the symmetry of track structure along the train moving direction, a half model is adopted so the calculation time can be greatly saved. Details and the parameters of the ballastless track are shown in Fig. 1 and Table 1.

To consider the moving train loads, the train set model of 8 CRH3 vehicles (as shown in Fig. 1b) is adopted in simulation and the Hertz contact theory is employed to simulate the train–track interaction. For the signal vehicle, it is simplified as multi-rigid body system with 10 degrees of freedom (only the movement at the vertical direction is considered) consisting of vehicles, bogies, wheels and two groups of spring-damping suspension system.

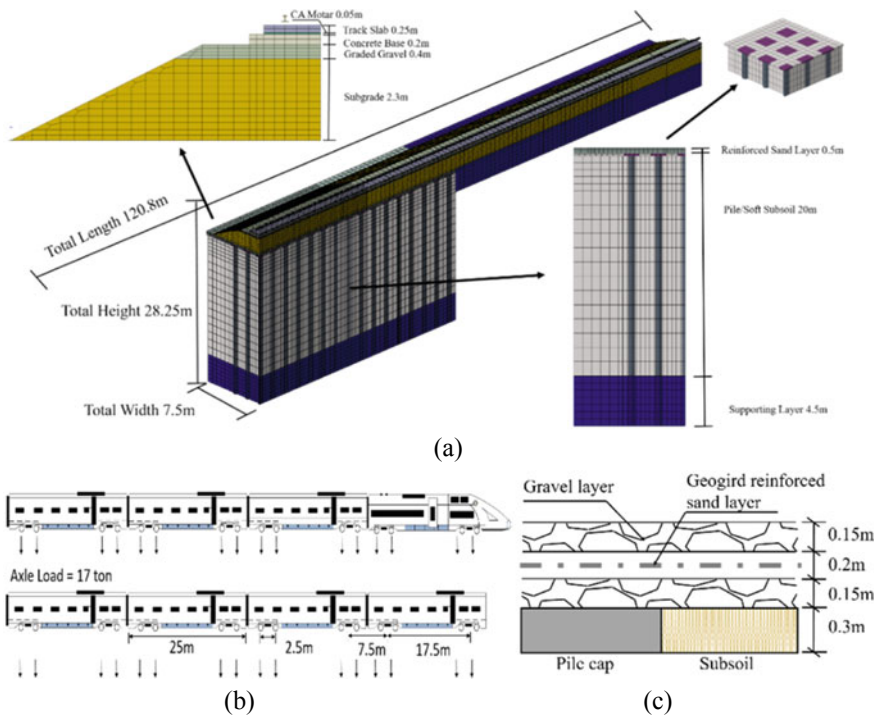


Fig. 1 Details of three-dimensional FEM model: a overall, b train set and c reinforced layer

**Table 1** Parameters of piled embankment model

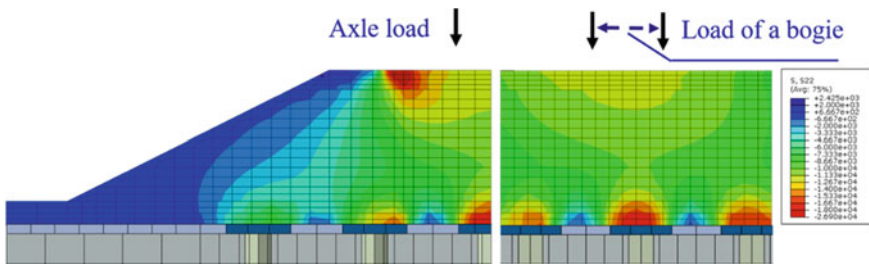
Material	Modulus (MPa)	Density (kg/m <sup>3</sup> )	Poisson's ratio
Track slab	30,000	2700	0.2
CA mortar	315	1800	0.3
Concrete base	25,000	2700	0.2
Graded gravel	300	2000	0.35
Subgrade	200	1920	0.35
Pile cap	38,000	2500	0.2
Pile	30,000	2500	0.2
Subsoil	30	1900	0.3
Supporting layer	20,000,000	1700	0.4

### 3 Dynamic Behavior of Piled Embankment

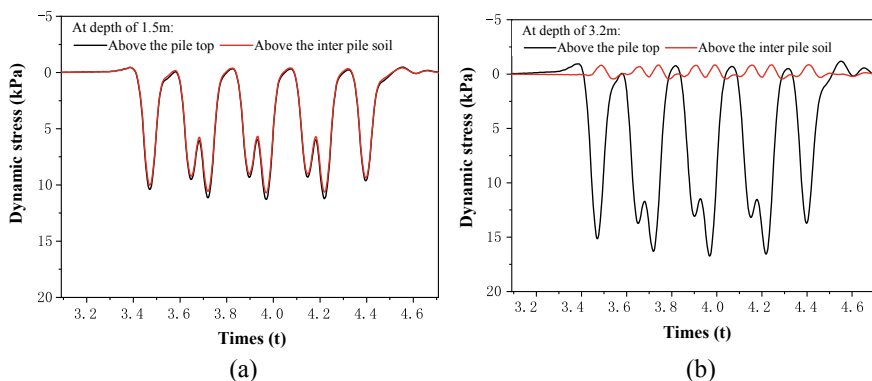
#### 3.1 Dynamic Stress in Piled Embankment

Dynamic stress plays a critical role in accumulative settlement under train loads. Due to soil arch effect, train loads are more likely to transfer to the piles instead of the interpile subsoil and leads to the redistribution of dynamic stress in piled embankment. Figure 2 shows the dynamic stress distribution under train loads. Different from the general rule that the dynamic stress is more uniform as the depth increases, the calculation results illustrate increasingly non-uniform distribution occurs at the positions nearby the piles. It shows that with the position closer to the piles, the more dynamic stress tends to transfer to the subsoil above the pile tops, which indicates that the soil arch still works effectively under train loads.

Figure 3a and b illustrate the dynamic stress histories at depth of 1.5 m (far enough from the piles) and 3.2 m (interface of piles and embankment). At the depth of 1.5 m, dynamic stress above the piles (the black line) and the interpile soils (the red line) meets each other perfectly. However, at the depth of 3.2 m, dynamic stress above



**Fig. 2** Dynamic stress distribution under train loads



**Fig. 3** Dynamic stress histories: **a** above the pile top and **b** above the interpile soil

the pile tops reaches to the peak value of 17.2 kPa while the dynamic stress above the interpile soil fluctuates around 0 kPa. It reveals at the position far away from the piles dynamic stress distributes uniformly, while at the position nearby the piles, soil above the piles undertakes the most traffic loads due to soil arch effect.

### 3.2 The Effect of Soil Arches Under Moving Train Loads

To further investigate the redistribution due to the soil arch effect, a combined Boussinesq solution based on the train load transfer mechanism is proposed as the general distribution in the natural embankment. In previous studies, the train load of one axle is confirmed to be undertaken by 7 or 8 fasteners, while for the two axles in one bogie the loads will be transferred to the neighboring 12 fasteners. Figure 4 shows the load distribution of 12 fasteners under the load of one bogie. Here the black dash lines are the load distribution for each axle, while the pink line refers the combined distribution for the whole bogie. By simplified the bogie load as uniformly distributed stress on the embankment and combining all the bogies of a train set, the combined Boussinesq solution is developed and compared with the calculation results.

Figure 5 illustrates the comparison of the combined Boussinesq solution and the calculated dynamic stress distribution along depths at train speed of 50 m/s (180 km/h) with and without geogrids respectively. In this figure, red lines and black lines are represent of the dynamic stress distribution above the pile tops and interpile soil, while the continuous lines and dash point lines are the dynamic stress in the reinforced and unreinforced cases. As a comparison, the Boussinesq solution proposed above is also illustrated with the blue dash line representing the stress distribution in natural embankment. Generally, it is indicated that distribution of dynamic soil stress along soil depth clearly shows the soil arch effect. At the superficial layer of the embankment, dynamic stress above the interpile soil (beneath the fastener) are 2 kPa

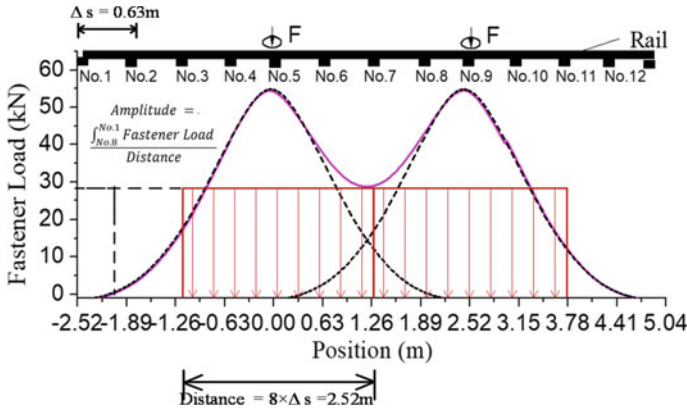


Fig. 4 Simplification of bogie loads

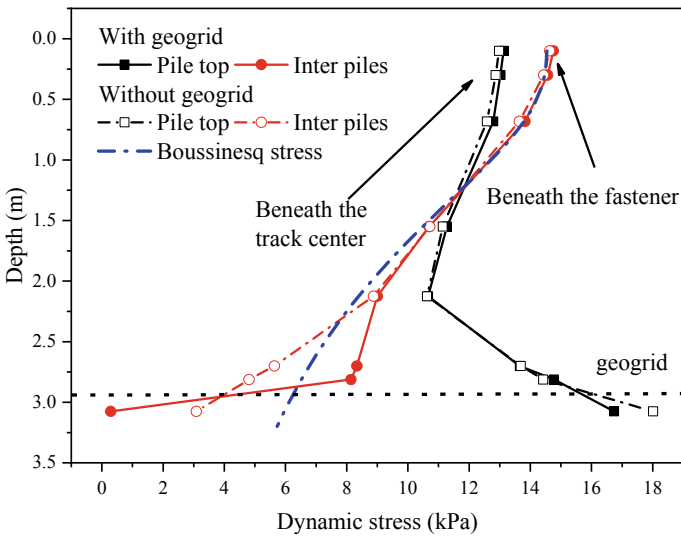


Fig. 5 Redistribution of dynamic stress along with depth

greater than the stress above the piles (beneath the track center). The stress decreases with the depths, and the attenuation tendency meets the proposed Boussinesq solution well, especially the distribution above the interpile soil. However, at the position nearby the pile tops, dynamic stress starts to deviate from the Boussinesq solution. For the distribution above the piles, stress starts to grow increasingly from about 2 m deep and reaches to the maximum stress of 16.8 kPa (18 kPa without geogrid). For the distribution above the interpile soil, stress keeps decreasing and becomes less than the Boussinesq solution at the bottom of the embankment. It reveals that soil arch effect significantly affects the dynamic stress distribution, especially at the positions



near pile tops. The piles will undertake the most traffic loads transferring from the interpile soil so that the subsoil settlement due to the traffic loads can be well limited.

Furthermore, geogrids also show the remarkable influence to the dynamic stress distribution. With the usage of geogrid reinforcement, dynamic stress above the piles is barely changed at the position above the geogrid and then slightly decreases from 17.9 to 16.8 kPa at the position beneath the geogrids. However, dynamic stress above the interpiles is significantly strengthened and even exceeds the proposed Boussinesq solutions at the position above the geogrids, while the stress rapidly decreases from 4 kPa to almost 0 kPa at the position beneath the geogrids. It reveals that the geogrids lead to the dynamic stress further transferring and limit the settlement accumulation under traffic loads.

### 3.3 Influence of Track Structure

The types of track structure, especially the ballasted and ballastless track, are also the key factors for the dynamic behaviors and stress distribution of embankment. To investigate the influence of track structure, a corresponding model with ballasted track is also analyzed and its dynamic stress distribution is compared with the ballastless track at 50 m/s as illustrated in Fig. 6. At the superficial layer of piled embankment, dynamic stress under ballasted track is much greater than the stress under ballastless track, but also attenuates more sharply along with the depth. It is mainly due to the different characters of two track structures. However, at the position nearly the piles, the dynamic stress under the ballasted and ballastless track tends to be similar both

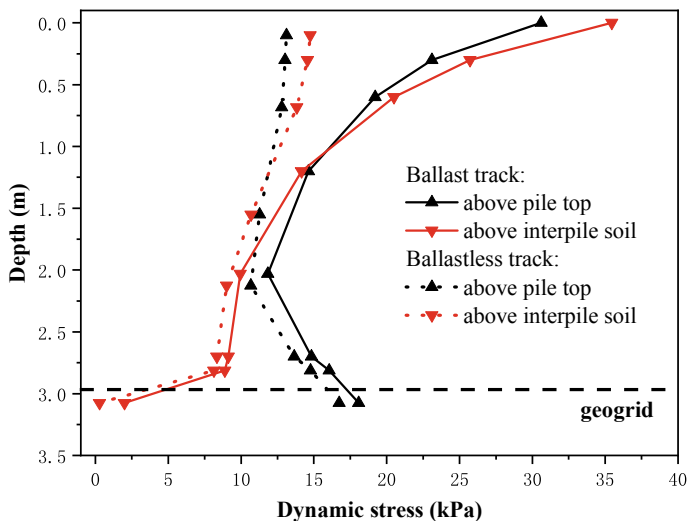


Fig. 6 Dynamic stress distribution under ballasted and ballastless track

in shapes and amplitudes. Dynamic stress under the ballasted track is slightly greater than the stress under the ballastless track mainly due to the dynamic amplification factor is higher in ballasted track. It is indicated that at the position far away from piles, the type of track structures is dominant in the dynamic stress distribution, while at the position nearby the piles the dynamic stress distribution is mainly decided by the pile foundation.

## 4 Conclusion

To investigate the dynamic behaviors of piled embankment under moving train loads, a three-dimensional FEM model is established. The dynamic stress redistribution due to the soil arch effect is then calculated and discussed. The research indicated that:

1. In piled embankment, soil arch effect will also lead to the redistribution of dynamic stress, where the piles undertake extra dynamic load instead of the interpile soils.
2. The Boussinesq solution can describe the soil stress distribution in embankment well at superficial layer of embankment, but with the depth increase the distribution significantly impacted by soil arches and deviates from the Boussinesq solution.
3. The usage of geogrid will further strengthen the redistribution at the position beneath the geogrids.
4. The dynamic stress distribution at the superficial layer of embankment is determined by the type of track structures, while the redistribution at the position nearby the piles is mainly decided by the pile foundation.

## References

1. Chen R, Wang Y, Ye X, Bian X et al (2016) Tensile force of geogrids embedded in pile-supported reinforced embankment: a full-scale experimental study. *Geotext Geomembr* 44(2):157–169
2. Hewlett W, Randolph M (1988) Analysis of piled embankments. *Ground Eng* 21(3):12–18
3. Chen Y, Jia N, Chen R (2004) Soil arch analysis of pile-supported embankments. *China J Highw Transp* 17(4):1–6
4. Giroud J, Bonaparte R, Beech J et al (1990) Design of soil layer-geosynthetic systems overlying voids. *Geotext Geomembr* 9(1):11–50
5. Huang J, Han J (2009) 3D coupled mechanical and hydraulic modeling of a geosynthetic-reinforced deep mixed column-supported embankment. *Geotext Geomembr* 27(4):272–280
6. Zhuang Y, Wang K (2018) Finite element analysis on the dynamic behavior of soil arching effect in piled embankment. *Transp Geotech* 14:8–21
7. Thach P, Liu H, Kong G (2013) Vibration analysis of pile-supported embankments under high-speed train passage. *Soil Dyn Earthq Eng* 55(6):92–99

# Settlement and Capacity of Piles Under Large Number of Cyclic Loads



Renpeng Chen , Chunyin Peng , Jianfu Wang, and Hanlin Wang 

**Abstract** This study reports a group of field tests on cyclically loaded piles installed in soft clay in Huzhou, China. Two 29.5 m long pipe piles were instrumented with transducers to measure the accumulated settlement at the pile-head, the pore water pressure and total pressure at the pile-soil interface, and axial load at the pile end, respectively. The major objective of the field testing is to gain a better understanding of the evolution of the pile-head settlement and the effective stress at the pile-soil interface. The results of cyclic loading tests under different combinations of static load and cyclic load are discussed with reference to changes in the pile capacity, the permanent settlement, and the radial stresses. It is found that the permanent settlement of piles can be characterized as quickly stabilized (QS), progressively developing (PD), and dramatically failed (DF) patterns. Under low-level loading (QS pattern), the pile-shaft earth pressure is nearly undisturbed, final gains in effective stress are observed due to slight dissipation of pore pressure. For intermediate-level loading (PD pattern), significant reductions in pore pressure, earth pressure, and effective stress are observed after cyclic loading. Regarding high-level loading (DF pattern), the quick accumulation of pore water pressure leads to a slight increase in earth pressure, resulting in a continuous decrease in effective stress.

**Keywords** Field testing · Cyclic loading · Long-term behaviors · Soft clay

---

R. Chen (✉) · C. Peng · J. Wang  
Zhejiang University, Hangzhou 310058, China  
e-mail: [chenrp@zju.edu.cn](mailto:chenrp@zju.edu.cn)

C. Peng  
e-mail: [cypeng@zju.edu.cn](mailto:cypeng@zju.edu.cn)

J. Wang  
e-mail: [21712010@zju.edu.cn](mailto:21712010@zju.edu.cn)

R. Chen  
Hunan University, Changsha 410082, China

H. Wang  
The Hong Kong Polytechnic University, Hung Hom, Kowloon, Hong Kong, China  
e-mail: [hanlin.wang@polyu.edu.hk](mailto:hanlin.wang@polyu.edu.hk)

## 1 Introduction

The accumulated settlement of piled-embankment in high-speed railways is required to be rigorously controlled [1], especially in southeastern China where extensive soft clays are often encountered. These piles undertake not only the self-weight of the embankment but also the cyclic load induced by the moving trains. Considering the unfavorable characteristics of soft clay such as high compressibility, low strength, and low permeability, a better understanding of the cyclic behaviors of piles appears important in the design of piled-embankment. The static and cyclic loading levels, the number of cycles, and the soil characteristics affect the pile-head settlement significantly [2].

Plenty of experiments have been performed to explore the cyclic behaviors of piles under cyclic loading. Concerning sand, interesting results are reported by Poulos [2], Al-Douri and Poulos [3], Gavin and O'Kelly [4], Jardine and Standing [5], Blanc and Thorel [6], and Matos et al. [7]. In most of these studies, significant degradation in the shaft capacity was observed when the piles were subjected to limited cycles (hundreds or thousands of cycles) under large cyclic loads (the cyclic amplitude > 50% of the ultimate capacity). Concerning saturated clay, Poulos carried out model tests in reconstituted saturated clay. He found that the significant reduction in shaft friction leads to failure of the model pile (Diameter  $D = 20$  mm). An analysis was proposed to predict the ultimate capacity under cyclic loading [8, 9]. Huang and Liu argue that the pile behavior remains elastic at very low cyclic loading levels, higher cyclic load level leads to more severe degradation in the pile capacity [10]. Muhammed et al. conducted cyclic loading tests on the model pile ( $D = 36$  mm) in saturated clay, the pore water pressure is found to increase initially to its peak then drops gradually with the number of cycles. The shaft friction degrades at the beginning before increasing again until the end of cyclic loading [11, 12].

In general, existing studies mainly focused on model piles driven in sand under short-term loading (for hundreds or thousands of cycles), simulating the effect of waves or winds on offshore structures (the cyclic load amplitude > 50% of the ultimate capacity). However, the piled-embankment in the high-speed railways suffers long-term cyclic loadings (more than  $10^4$  cycles) at small cyclic amplitudes (less than 20% of the ultimate capacity). To date, field study on cyclic behaviors of industrial piles in soft clay to large number of cycles is scarcely reported.

This study reports a program of cyclic loadings on industrial piles installed in soft clay. These piles were instrumented with pore pressure transducers (PPT), earth pressure transducers (EPT), and axial load transducers (ALT). Three loading procedures were performed on the pile in sequence: initial static loading (to obtain the initial capacity), cyclic loadings (to characterize the cyclic behaviors), and final static loading (to determine the changes in pile capacity after cyclic loadings). The soil characteristics are identified before describing the pile-head settlement. Finally, the changes in the pore pressure, the earth pressure, and the effective stress are analyzed.

## 2 Experimental Setup

### 2.1 Field Profiles

The field testing site was a leveled ground along the Hushan Expressway in Huzhou, China. Two prestressed concrete pipe piles (Pile A and Pile B) were installed to a depth of 30 m, with a spacing of 13.2 m. Samples were collected from six drilling boreholes (to a maximum depth of 62 m) to determine basic soil properties. Two cone penetration tests (CPT1 and CPT2) and two vane shear tests (VST1 and VST2) were conducted for site investigations (see soil profile in Fig. 1). The surface layer (CL1, 0–5 m) is grayish-yellow clay of intermediate plasticity. The middle layer (CL2, 5–30 m) is grey clay of high dry strength. The bottom layer (CL3, 30–35 m) is taupe clay of low plasticity with occasional silt partings. Based on the classification standards recommended by ASTM [13], these soils (0–35 m) were identified as Lean Clay (CL). Basic physical and mechanical parameters of each layer are illustrated in Fig. 1. Intact samples from CL2 indicates a cohesion  $c'_{cu}$  of 6.5 kPa and an effective friction angle  $\phi'_{cu}$  of  $25.5^\circ$  in consolidated-undrained triaxial tests.

Two cone penetration tests (CPT) were conducted to a depth of 35 m. CPT1 was carried out at a distance of about 35 m from Pile B while CPT2 was performed about 10 m from the same pile. The CPT results indicate a cone tip resistance  $q_c$  of about 2 MPa and a sleeve friction  $f_s$  of about 20 kPa. Two vane shear tests (VST1 and VST2, with a spacing of 4 m) were conducted to determine the in-situ undrained shear strength  $s_u$ . The ratio of the intact  $s_u$  to the effective overburden stress  $\sigma'_v$  appeared to stabilize with the depth, with ratios of 0.16 and 0.21 for VST1 and VST2, respectively.

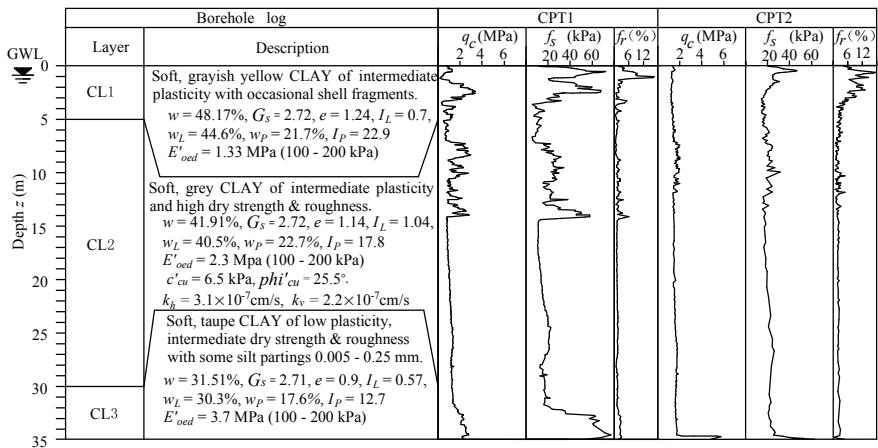
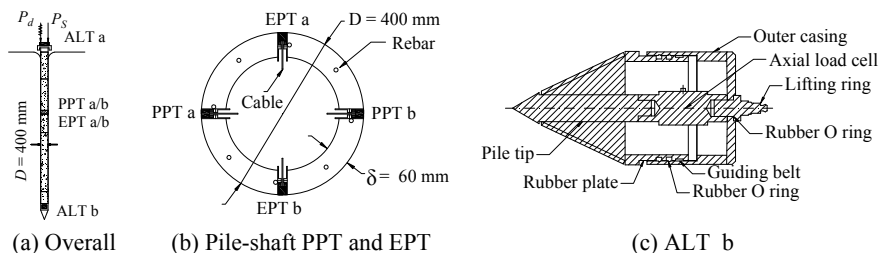


Fig. 1 Soil profile and physical parameters of the testing site



**Fig. 2** The instrumentation details of transducers at the pile-shaft and the pile-end

## 2.2 Testing Preparations

The closed-ended pile had a length of 29.5 m with an outer diameter of 400 mm. Each prestressed concrete pile was instrumented with an axial load transducer (ALT a) at the pile-head to measure the applied load. Pore pressure transducers (PPT) and earth pressure transducers (EPT) were mounted at the same depth (10 m) to obtain the effective stress at the pile-soil interface. Another axial load transducer (ALT b) was designed to measure the pile-tip load. The casing of ALT b is designed to prevent smearing or inclusion of pore water or soil particles (see Fig. 2).

The testing system consisted of a reaction device, a loading device, and a measuring device. The reaction device was made up of a main reaction beam (9000 × 400 × 700 mm) and four secondary reaction beams (supported by two concrete-block cribbings and balanced by a stack of concrete blocks weighing about 1800 kN). In the loading device, the hydraulic actuator (travel: 500 mm; capacity: 1000 kN) was powered by a servo-controlled hydraulic pump. The measuring device included laser displacement transducers (LDT, independent of the loading system), axial load transducers (ALT a, ALT b), pore pressure transducers (PPT a, PPT b), and earth pressure transducers (EPT a, EPT b). All transducers were connected to a dynamic data-acquisition device reading at 100 Hz.

## 2.3 Testing Program

A series of static and cyclic loading tests were conducted on Pile A and Pile B. Three testing procedures were performed on each pile in sequence: initial static loading, cyclic loadings, and final static loading. In the initial static loading (SLA1, SLB1), the undisturbed compressive capacity of the pile was obtained, following the guidelines recommended by ASTM [14]. In the cyclic loadings, the sinusoidal loading waveform was applied as:

$$P(t) = P_s + \frac{P_c}{2}[1 + \sin(\omega t)] \quad (1)$$

**Table 1** Cyclic loading program of the field testing on Pile A and Pile B

Procedure	Pile A		Pile B	
1	SLA1		SLB1	
2	SLR	CLR	SLR	CLR
	0.01	0.17, 0.33, 0.44, 0.65	0.03	0.15, 0.29, 0.46, 0.57
	0.17	0.16, 0.24, 0.33, 0.50	0.16	0.15, 0.24, 0.31, 0.48
	0.33	0.08, 0.17, 0.25, 0.50	0.32	0.08, 0.16, 0.24, 0.32, 0.40, 0.48
	0.50	0.08, 0.17, 0.24, 0.33	0.48	0.08, 0.16, 0.24, 0.33
		0.64	0.08, 0.16	
3	SLA2		SLB2	

where  $P(t)$  was the applied sinusoidal load changing with time  $t$ ;  $P_s$  was static load;  $P_c$  was the peak to trough amplitude of cyclic load;  $\omega$  was circular frequency. Note that the duration and rest periods in a load cycle have rarely been investigated [15]. Qiu reported that the duration of the rest period barely influence the permanent deformation of the soil in highway pavements at low load frequency [16], Liu and Xiao hold the same argument [17]. Therefore, a continuous sinusoidal wave without intervals was applied in this study. The static load ratio ( $SLR = P_s/P_u$ ,  $P_u$  is the ultimate capacity) and the cyclic load ratio ( $CLR = P_c/P_u$ ) were defined to evaluate the loading characteristics. As indicated in Table 1, sixteen cyclic loading combinations were performed on Pile A. The SLR was 0.01, 0.17, 0.33, and 0.50, respectively, with CLR ranging from 0.08 to 0.67. Twenty similar cyclic loadings were conducted on Pile B. Each cyclic combination was terminated either after a maximum number of 50,000 cycles or reaching failure, with loading frequency ranging from 0.3 to 3 Hz depending on the loading system performance. Another static loading test was conducted on the pile (SLA2, SLB2) after cyclic loadings.

### 3 Results and Discussions

#### 3.1 Pile Compressive Capacity

The settlement required for failure is defined as 20 mm (about 5%  $d$ ,  $d$  is the pile diameter). The initial capacities of Pile A and Pile B are 490 kN and 510 kN, respectively. These two piles were subjected to 16 and 20 different cyclic loadings (see Table 1) before conducting final static loadings (SLA2, SLB2). The static compressive capacities for Pile A and Pile B increase by 22% and 24%, respectively. Both the shaft friction and the base resistance are improved.

### 3.2 Pile Head Settlement

The permanent settlement of piles under long-term cyclic loadings can be characterized as three patterns: quickly stabilized (QS), progressively developing (PD), and dramatically failed (DF). Note that the permanent settlement  $s$  is obtained as the mean value of the peak  $s_p$  and the trough  $s_t$  in a settlement waveform.

Figure 3a shows a typical curve of quickly stabilized (QS) settlement against time. The pile-head settlement increased to 3 mm when the pile was loaded to 225 kN from 10 kN. The settlement remained horizontal or even reduced slightly during the cyclic loading period. After the termination of cyclic loading (unloaded back to 10 kN), the pile-head settlement tended to rebound to the previous position. Figure 3b illustrates three typical curves of normalized settlement  $s/d$  of quickly stabilized (QS) pattern. In these three tests, the permanent settlement presented similar stable trends. In terms of quickly stabilized (QS) pattern, only negligible settlements were observed under cyclic loading over a very large number of cycles ( $s < 1\%D$  in  $5 \times 10^4$  cycles). Summarizing the loading conditions of quickly stabilized (QS) pattern, there exists a critical combination below which the pile-head settlement remains nearly undisturbed:  $CLR \leq 0.2$  ( $0 < SLR \leq 0.2$ ) or  $10SLR + 5CLR \leq 6$  ( $0.2 < SLR \leq 0.6$ ).

Figure 4a indicates the typical test result of progressively developing (PD) pattern. An initial settlement of 3 mm was caused when the pile was loaded to 250 kN. As the cyclic loading (ranging from 200 to 300 kN) proceeded, the settlement kept increasing with a final peak settlement of 5 mm. Nevertheless, no failure was observed until the end of the cyclic loading. Figure 4b illustrates three normalized settlement curves of progressively developing (PD) pattern. The permanent displacement accumulated progressively with the number of cycles in the semi-log coordinates. This trend continued developing without reaching failure till the end of cyclic loading ( $0.1\%D \leq s < 5\%D$  in  $5 \times 10^4$  cycles). Concerning progressively developing (PD) pattern,

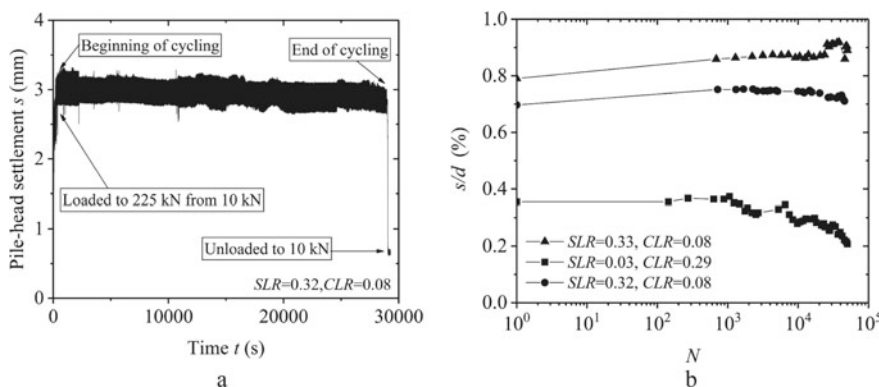
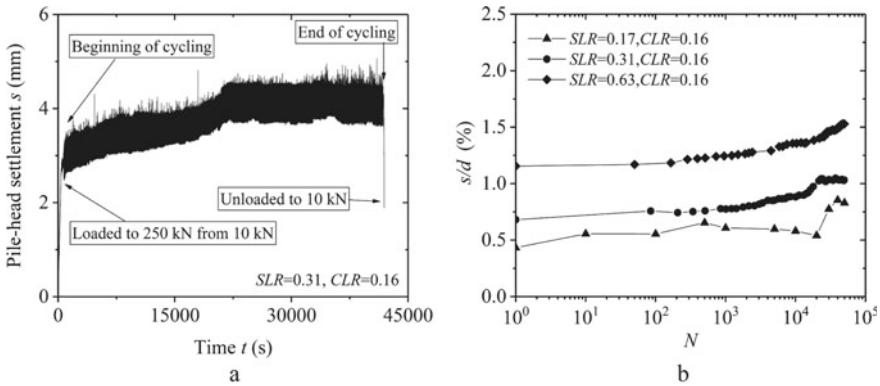


Fig. 3 Typical QS pile-head settlement against: a) time; b) number of cycles

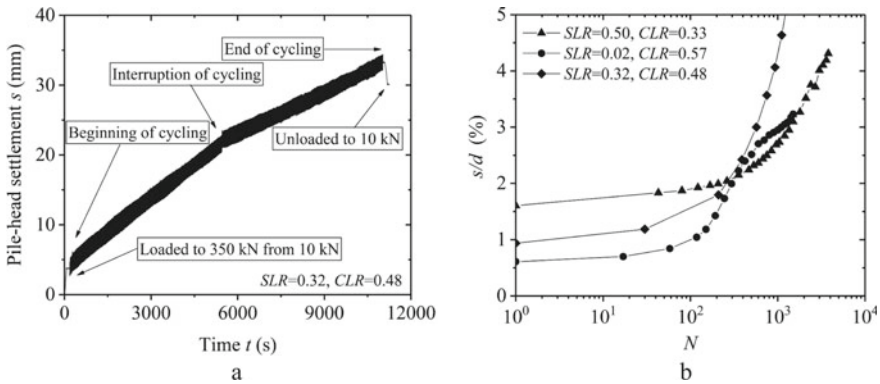




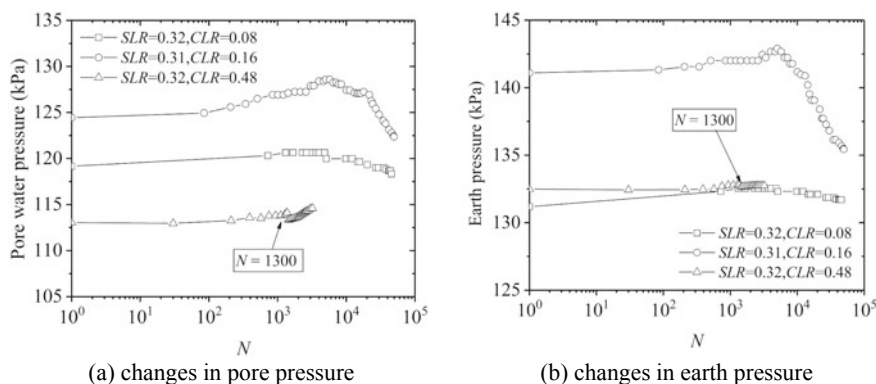
**Fig. 4** Typical PD pile-head settlement against: **a** time; **b** number of cycles

there is an upper limit under which the settlement keeps increasing without failing:  $0.2 < CLR \leq 0.5$  ( $0 \leq SLR \leq 0.2$ ) or  $5SLR + 8CLR \leq 5$  ( $0.2 < SLR \leq 1$ ).

Figure 5a presents the typical displacement behavior of dramatically failed (DF) pattern. Prior to cycling, a downward movement of 4 mm was induced when the pile head was statically loaded to 350 kN. In the cyclic loading period (ranging from 200 to 500 kN), the pile-head settlement increased significantly with the number of cycles. Cyclic failure was triggered after 5000 s (about 1300 cycles) with a settlement of 23 mm. After a pause of 6 h, the pile was cyclically loaded again with the same load combination, the settlement reached 34 mm after 3200 cycles. Figure 5b shows typical normalized settlements of dramatically failed (DF) pattern. The pile-head settlement developed dramatically with the number of cycles in the semi-log coordinates, reaching failure at hundreds or thousands of cycles ( $s > 1\%D$  in  $10^4$  cycles or  $s > 5\%D$  in  $5 \times 10^4$  cycles). Concerning dramatically failed (DF) pattern, there is a lower limit above which the pile-head settlement accumulates significantly,



**Fig. 5** Typical DF pile-head settlement against: **a** time; **b** number of cycles



**Fig. 6** The variations in pile-shaft pore water pressure and earth pressure

plunging failures are observed within limited loading cycles (generally thousands of cycles):  $CLR > 0.5$  ( $0 \leq SLR \leq 0.2$ ) or  $5SLR + 8CLR > 5$  ( $0.2 < SLR \leq 1$ ). Note that the cyclic loading level (CLR) plays a dominant role in determining the settlement patterns of piles under different cyclic loading conditions. In general, if the settlement is required to be rigorously controlled, the total load applied at the pile-head is suggested to be controlled as  $CLR < 0.2$  or  $10SLR + 5CLR \leq 6$ . In order to prevent significant settlement or plunging failure, the total load is suggested to be controlled as  $0.2 < CLR \leq 0.5$  or  $5SLR + 8CLR \leq 5$ .

### 3.3 Pile Shaft Stress

The pore pressure and earth pressure at the pile-soil interface during cyclic loadings were obtained from transducers instrumented along the pile shaft (see Fig. 6). Under low-level cyclic loading (quickly stabilized QS pattern), the pore pressure increases slightly at early stages and then decreases gradually, indicating that the effects of cyclic loading can be neglected. In terms of intermediate-level loading (progressively developing PD pattern), the pore pressure increases significantly at early stages due to partly blocked horizontal drainage channels caused by plastic cyclic shearing on the pile-shaft clay. The pile-soil system is subsequently disturbed by long-term cyclic loading, stronger dissipation through vertical drainage channels results in a significant reduction in pore pressure. For high-level loading (dramatically failed DF pattern), the horizontal drainage channels are quickly blocked by severe shear contraction, prompting a continuous increase in the pore pressure.

As indicated in Fig. 6b, the earth (total) pressure under low-level loading (quickly stabilized QS pattern) is nearly undisturbed by cyclic loadings, since the cyclic loading appears elastic (no significant accumulation of plastic deformation). For intermediate-level loading (progressively developing PD pattern), the earth

pressure increases slightly before reducing significantly below the initial value. Regarding high-level loading (dramatically failed DF pattern), the earth pressure keeps increasing due to the continuous accumulation of pore water pressure.

Figure 7a shows the variations of effective stresses under different cyclic loading. The effective stress under low-level loading (quickly stabilized QS pattern) obtains final gains after cyclic loading, indicating an enhancement in the pile-soil stiffness. For intermediate-level loading (progressively developing PD pattern), the effective stress decreases below the initial value despite some recovery occurs at the end of the cyclic loading, suggesting degradation of the pile-soil stiffness. The pile shaft effective stress decrease continuously under high-level loading (dramatically failed DF pattern), the loss of effective stress keeps developing with the number of cycles. As the pore water pressure accumulates, the pile-shaft effective stress drops accordingly.

Figure 7b illustrates the changes in the base resistance of piles under different cyclic loadings. For piles under low-level loading (quickly stabilized QS pattern), the pile tip resistance tends to decrease with the number of cycles. As the effective stress obtains final gains at the end of cyclic loading (see Fig. 7a), the shaft friction undertakes more axial load. Therefore, the base resistance decreases with the number of cycles. Concerning intermediate-level loading (progressively developing PD pattern), the pile shaft friction reduces slightly due to the decrease in effective stress. The base resistance increases as a result of axial load redistribution. For high-level loading (dramatically failed DF pattern), the pile-soil system is severely damaged by cyclic shearing, the decrease in effective stress leads to degradation in shaft friction. Therefore, the base resistance increases significantly due to axial load redistribution. Piles under higher cyclic loads (CLRs) lead to more obvious improvements in base resistance.

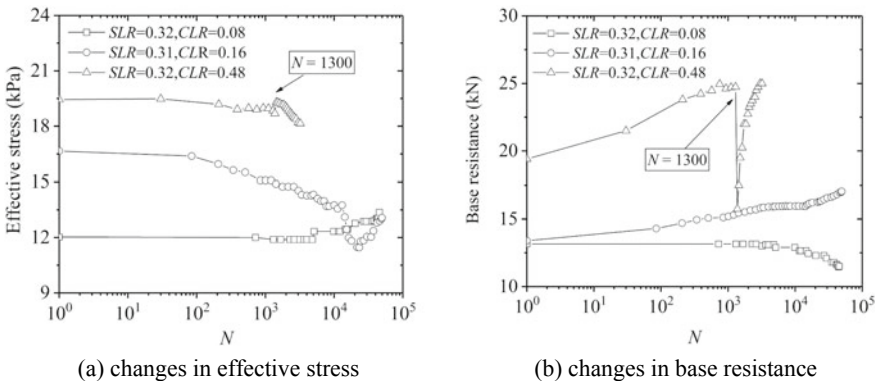


Fig. 7 Variations in effective stresses and base resistance

## 4 Conclusions

This study investigates the long-term behaviors of piles under different combinations of cyclic loading. The piles are instrumented with various transducers, allowing the pile-head settlement, the pore water pressure and the earth pressure at the pile-soil interface, and the pile-end axial load to be measured. Three loading procedures are applied in sequence: initial static loading, cyclic loadings, and final static loading. The variations of effective stress at the pile-soil interface and the base resistance are analyzed.

The permanent settlement of piles under cyclic loading can be characterized as three patterns: quickly stabilized (QS), progressively developing (PD), and dramatically failed (DF). Under low-level loading ( $CLR \leq 0.2$  or  $10SLR + 5CLR \leq 6$ ), the permanent settlement is negligible, the effects of cyclic loading can be neglected. Regarding intermediate-level loading ( $0.2 < CLR \leq 0.5$  or  $5SLR + 8CLR \leq 5$ ), the settlement keeps developing without reaching failure, higher cyclic load leads to larger pile-head settlement. Concerning high-level loading ( $CLR > 0.5$  or  $5SLR + 8CLR > 5$ ), the pile-head settlement develops dramatically, plunging failure occurs.

The stresses at the pile-soil interface present varied responses under different loading conditions. For low-level loading, the earth pressure is nearly undisturbed, the dissipation of pore pressure leads to final gains in effective stress. The base resistance decreases due to enforcement in shaft friction. For intermediate-level loading, the earth pressure and the pore pressure obtain initial growth before decreasing at later stages of the cyclic loading. The pile-soil system is damaged gradually, resulting in a progressive loss in effective stress. The shaft friction degrades with the number of cycles, prompting an increase in the base resistance. In terms of high-level loading, the pronounced damage in drainage channels leads to a quick accumulation of the pore pressure, the decrease in the effective stress leads to a significant degradation in the shaft friction, the base resistance increases with the number of cycles as a result of axial load redistribution.

**Acknowledgements** Support from the Hunan Provincial Science and Technology Department (Grant No. 2019RS1030) is acknowledged. The authors express their appreciation to professorate senior engineer Zhenghui Jiang from Zhejiang Institute of Communications CO., LTD for providing the testing site. The help with the experiments from Mr. Yong Xu and Dr. Wei Cheng from the Geotechnical Institute of Zhejiang University is also acknowledged.

## References

1. Wang HL, Cui YJ, Lamas-Lopez F, Dupla JC, Canou J, Calon N, Saussine G, Aïmedieu P, Chen RP (2018) Permanent deformation of track-bed materials at various inclusion contents under large number of loading cycles. *J Geotech Geoenviron Eng* 144(8):04018044
2. Poulos HG (1989) Cyclic axial loading analysis of piles in sand. *J Geotech Eng* 115(6):836–852
3. Gavin KG, O’Kelly BC (2007) Effect of friction fatigue on pile capacity in dense sand. *J Geotech Geoenviron Eng* 133(1):63–71

4. Al-Douri RH, Poulos HG (1995) Predicted and observed cyclic performance of piles in calcareous sand. *J Geotech Eng* 121(1):1–16
5. Jardine RJ, Standing JR (2012) Field axial cyclic loading experiments on piles driven in sand. *Soils Found* 52(4):723–736
6. Blanc M, Thorel L (2016) Effects of cyclic axial loading sequences on piles in sand. *Geotech Lett* 6(2):163–167
7. Matos R, Pinto P, Rebelo C, Veljkovic M, Simões Da Silva L (2018) Axial monotonic and cyclic testing of micropiles in loose sand. *Geotech Test J* 41(3):526–542
8. Poulos HG (1980) Development of an analysis for cyclic axial loading of piles. *Numer Meth Geomech* 4:1513–1530
9. Poulos HG (1981) Some aspects of skin friction of piles in clay under cyclic loading. *Geotech Eng* 12(1):1–17
10. Huang M, Liu Y (2015) Axial capacity degradation of single piles in soft clay under cyclic loading. *Soils Found* 55(2):315–328
11. Muhammed RD, Canou J, Dupla JC, Tabbagh A (2018) Evaluation of local soil-pile friction in saturated clays under cyclic loading. *Soils Found* 58(6):1299–1312
12. Muhammed RD, Canou J, Dupla JC, Tabbagh A (2019) Evaluation of local friction and pore-water pressure evolution along instrumented probes in saturated clay for large numbers of cycles. *Can Geotech J* 56(12):1953–1967
13. ASTM (2017) Standard practice for classification of soils for engineering purposes (Unified Soil Classification System). American Society for Testing and Materials, West Conshohocken, PA, USA
14. ASTM (2013) Standard test methods for deep foundations under static axial compressive load. American Society for Testing and Materials, West Conshohocken, PA, USA
15. Li D, Selig ET (1994) Resilient modulus for fine-grained subgrade soils. *J Geotech Eng* 120(6):939–957
16. Qiu YJ (1998) Permanent deformation of subgrade soils: laboratory investigation and application in mechanistic-based pavement design. Ph.D. Thesis, University of Arkansas, Ann Arbor
17. Liu J, Xiao J (2010) Experimental study on the stability of railroad silt subgrade with increasing train speed. *J Geotech Geoenviron Eng* 136(6):833–841